

Engineering Materials

Carlton A. Taft  
Sergio R. de Lazaro *Editors*

# Research Topics in Bioactivity, Environment and Energy

Experimental and Theoretical Tools

MOREMEDIA



Springer

# **Engineering Materials**

This series provides topical information on innovative, structural and functional materials and composites with applications in optical, electrical, mechanical, civil, aeronautical, medical, bio- and nano-engineering. The individual volumes are complete, comprehensive monographs covering the structure, properties, manufacturing process and applications of these materials. This multidisciplinary series is devoted to professionals, students and all those interested in the latest developments in the Materials Science field, that look for a carefully selected collection of high quality review articles on their respective field of expertise.

**Indexed at Compendex (2021)**

Carlton A. Taft · Sergio R. de Lazaro  
Editors

# Research Topics in Bioactivity, Environment and Energy

Experimental and Theoretical Tools

 Springer

*Editors*

Carlton A. Taft  
Centro Brasileiro de Pesquisas Físicas  
Rio de Janeiro, Brazil

Sergio R. de Lazaro  
Departamento de Química  
Federal University of São Carlos  
São Carlos, Brazil

ISSN 1612-1317

ISSN 1868-1212 (electronic)

Engineering Materials

ISBN 978-3-031-07621-3

ISBN 978-3-031-07622-0 (eBook)

<https://doi.org/10.1007/978-3-031-07622-0>

© The Editor(s) (if applicable) and The Author(s), under exclusive license to Springer Nature Switzerland AG 2022

This work is subject to copyright. All rights are solely and exclusively licensed by the Publisher, whether the whole or part of the material is concerned, specifically the rights of translation, reprinting, reuse of illustrations, recitation, broadcasting, reproduction on microfilms or in any other physical way, and transmission or information storage and retrieval, electronic adaptation, computer software, or by similar or dissimilar methodology now known or hereafter developed.

The use of general descriptive names, registered names, trademarks, service marks, etc. in this publication does not imply, even in the absence of a specific statement, that such names are exempt from the relevant protective laws and regulations and therefore free for general use.

The publisher, the authors, and the editors are safe to assume that the advice and information in this book are believed to be true and accurate at the date of publication. Neither the publisher nor the authors or the editors give a warranty, expressed or implied, with respect to the material contained herein or for any errors or omissions that may have been made. The publisher remains neutral with regard to jurisdictional claims in published maps and institutional affiliations.

This Springer imprint is published by the registered company Springer Nature Switzerland AG  
The registered company address is: Gewerbestrasse 11, 6330 Cham, Switzerland

# Preface

The chapters of this book address science and technology as potential solutions for some of the world's major challenges, i.e., those related to energy, environment, and bioactivity. The twenty seven chapters (experimental, theoretical, reviews, and research) are written by groups of selected scientists that are teaching/researching on the forefront of their respective fields and thus able to clearly present an accessible introductory phase, basic fundamentals as well as new results, future trends and predictions, making reading/comprehension accessible for both early/non-workers as for advanced research scientists.

The Part I (thirteen chapters) reports research and reviews of applications in 'Energy, Materials and Environment'. The Chapter "[Theory and Computation in Photo-Electro-Chemical Catalysis: Highlights, Challenges, and Prospects](#)" addresses the challenges and prospects (computational modeling) of photo-electro-chemical catalysis, materials, processes, and systems for efficient and cost-effective photo-electro-chemical conversions (PEC) of solar energy to fuels, one of the essential elements of broad strategies towards renewable energy. The Chapter "[Emerging Metal-Halide Perovskite Materials for Enhanced Solar Cells and Light-Emitting Applications](#)" presents the current state of the art of progress in understanding the structure-composition-property relationship of solar cells and light-emitting devices based on emerging metal-halide perovskite materials synthesized by spin-coating techniques. In the Chapter "[SrTi<sub>1-x</sub>Sn<sub>x</sub>O<sub>3</sub> Thin Films as Photocatalysts for Organic Dye Degradation: Influence of the Composition, Deposition Method, and Growth Orientation](#)" the photocatalytic activity of SrTi<sub>1-x</sub>Sn<sub>x</sub>O<sub>3</sub> films for organic dye degradation is investigated. In the Chapter "[SrSnO<sub>3</sub> Applied in the Reduction of NO by CO: Influence of Transition Metal Doping on the Catalytic Activity](#)" doped perovskite SrSnO<sub>3</sub> is investigated for usage in the catalytic reduction of CO and NO. The Chapter "[Advances in the Synthesis and Applications of Self-Activated Fluorescent Nano- and Micro-Hydroxyapatite](#)" addresses hydroxyapatite (HA) with important applications including fluorescence imaging, biosensing, theranostics, nanomedicine, and luminescent materials. The Chapter "[Spintronic Properties in Complex Perovskites: A Concordance Between Experiments and Ab-Initio Calculations](#)" reports theoretical and experimental investigation of complex

perovskite-type systems with a wide range of applications such as anode materials for solid oxide fuel cells, highly active catalysts in electrochemical energy conversion reactions, substrates or high-efficiency solar cells, piezoelectric or dielectric sensors, magnetoelectric/magnetoresistive devices, magnetic and spintronic semiconductors with usage in dynamic random access memories (DRAM) or nonferroelectric random access memories (NVFRAM), hard disk read-write heads for high capacity storage of information in magnetic media, devices for electron current polarization and magnetic sensors among others. The Chapter “[Graphenylene-Like Structures as a New Class of Multifunctional Materials Alternatives to Graphene](#)” reviews an important class of graphene analog, namely, graphenylene, with interesting physicochemical properties such as chemical and structural stability, an intrinsic gap, and the presence of periodic nanoscopic pores making it a promising candidate for various technological applications including gas separation, construction of semiconducting nanodevices, and Li (Na)-ion batteries. Chapter “[Computer Simulations of MOF Systems: Key Applications](#)” deals with Metal-Organic Frameworks (MOF) class of materials with attractive structural characteristics including a wide variety of pore arrangements, types, and volumes with more than 70,000 known crystallographic structures, which makes them very attractive for numerous applications. Chapter “[Advanced DFT Atomistic Approaches for Electronic, Optical, and Structural Properties of Semiconductor Oxides](#)” focuses on DFT simulations for electronic, optical, and structural properties elucidating mechanisms for technological applications. Chapter “[Computational Simulations to Predict the Morphology of Nanostructures and Their Properties](#)” presents studies of property/morphology relationships of materials including molybdates and tungstates from computational simulations of the most exposed surfaces that can be characterized via structural, electronic properties and relative stabilities for applications in photoluminescence, photocatalysis, sensors and storage devices. The Chapter “[Unraveling the Surface Chemistry of the Heterogeneous Catalytic Decomposition of O<sub>3</sub> for Selectivity Concerning O<sub>2</sub> or HO<sup>•</sup> Formation](#)” is of environmental interest since it investigates the O<sub>3</sub> decomposition on heterogenous catalysts which is highly relevant for atmospheric applications and wastewater treatment. Chapter “[NH<sub>3</sub> Synthesis by Electrochemical Process Under Ambient Condition](#)” promotes incentive for researchers to look for new carbon free emission possibilities to maintain the NH<sub>3</sub> production minimizing the environmental and economic impact of the common synthesis route of this important fertilizer. In Chapter “[Overview: Catalysts, Feedstocks in Biodiesel Production](#)” authors make an overview of catalysts, feedstocks in biodiesel production emphasizing the search for alternative energy sources which are renewable, sustainable, and environmental friendly, emphasizing the search for materials with potential for energetic applications such as those discussed in the previous chapters.

The subsequent Chapters are dedicated to ‘Bioactivity’ with emphasis on drug discovery and medicinal applications. Chapter “[In Silico Drug Design and in Vivo Acute Toxicity Assay of Chalcone Analogs with Biological Antiparkinsonian Activity](#)” studies in silico drug design and evaluate the in vivo acute toxicity of molecules with the prediction of monoamine oxidase B (MAO-B) activity for the development of drugs that are candidates for the treatment of parkinson disease.

Chapter “[Electronic and Structural Insights of BCR-ABL Inhibitors Under LMC Treatment Perspective](#)” aims to shed light on the development of new potential drugs (tyrosine kinase inhibitors) against neoplasms related to chronic myeloid leukemia using computational studies of the electronic structure and molecular docking of the drugs to better understand conformations of the protein active site. Chapter “[Pathophysiology, Molecular Interaction Mechanism, Metabolism, Pharmacotherapy and New Perspectives in the Pharmacological Treatment of Chemical Dependence on the Main Illicit Drugs Consumed in the World](#)” reviews chemical dependence focusing on the mechanism of molecular interactions, metabolism, consequent symptomatology during drug withdrawal, current pharmacological treatments and search to increase the pharmacotherapeutic arsenal against this pathology. Chapter “[MAO Inhibitors from Natural Sources for Major Depression Treatment](#)” describes the chemical features of the main active ingredients found in selected medicinal plants with antidepressant properties; comparing with pharmacophoric features of available MAO inhibitors drugs in order to validate promising antidepressants. Chapter “[Lead Optimization in Drug Discovery](#)” reviews the computational techniques used for the lead optimization stage to outline which paths can be followed and used for the rational discovery of new drugs. Chapter “[Pulsed Electric Field and Ultrasound Applied to Proteins, Enzymes and Peptides](#)” addresses protein substrates such as those used in food supplements, flavoring agents, culture media, antioxidants, antihypertensives, anti-inflammatory drugs, and polyphenol oxidase inhibitors. Chapter “[Vaccine History: From Smallpox to Covid-19](#)” makes a timely review of vaccines starting from smallpox to Covid-19. Chapter “[Structural Aspects of Organic Compounds as Proteasome Inhibitors Addressed to Several Diseases](#)” addresses the usage of proteasome inhibitors for treating different diseases, including pathogenesis of cancer cells, inflammatory responses, and some protozoan infections. Chapter “[Phytotechnological and Pharmaceutical Potential of Eugenia Genus](#)” discusses technological products obtained from species of the Eugenia genus emphasizing their biological potential as well as technology used for future development of products with commercial value. Chapter “[How Basic Programming Knowledge can Help the Drug Discovery Process](#)” helps us understand the important support of programming knowledge for the drug discovery process. Chapter “[Ligand-Based Drug Design for Selection of Molecules with Pharmacological Activity in Essential Tremor](#)” presents research involving ligand-based drug design methods for selection of molecules with pharmacological activity in essential tremor. Chapter “[Intramolecular Hydrogen Bonding Patterns and Conformational Preferences of Ouabain—A Molecule with Cardiotonic and Antiviral Activities](#)” investigates conformational preferences and intramolecular hydrogen bonding to better understand the cardiotonic and antiviral properties of ouabain. Chapter “[Molecular Modeling of Acetylcholinesterase Inhibitors for the Treatment of Alzheimer’s Disease](#)” presents research using molecular modeling of acetylcholinesterase inhibitors to obtain drugs for the treatment of alzheimer’s disease.

It is our expectation that this book will be helpful and will stimulate readers with a wide degree of scientific training/interests, offer at least for early/non-workers



an overview of carefully selected fundamental concepts/research areas, and serve as a valuable source of information for scientists working on frontier line projects involving energy, materials, environment, and bioactivity.

The editors would like to thank authors, colleagues, and collaborators for their participation in this Book Project. We look forward for you to obtain a copy of the Book.

Rio de Janeiro, Brazil  
São Carlos, Brazil

Carlton A. Taft  
Sergio R. de Lazaro

# Contents

## Energy, Materials and Environment

<b>Theory and Computation in Photo-Electro-Chemical Catalysis: Highlights, Challenges, and Prospects</b> .....	3
Taifeng Liu and Michel Dupuis	
<b>Emerging Metal-Halide Perovskite Materials for Enhanced Solar Cells and Light-Emitting Applications</b> .....	45
Felipe Moreira Pinto, Mary Carmen Mate Durek de Conti, Swayandipta Dey, Esteban Velilla, Carlton A. Taft, and Felipe de Almeida La Porta	
<b>SrTi<sub>1-x</sub>Sn<sub>x</sub>O<sub>3</sub> Thin Films as Photocatalysts for Organic Dye Degradation: Influence of the Composition, Deposition Method, and Growth Orientation</b> .....	87
A. L. M. de Oliveira, L. Chantelle, J. F. D. Figueiredo, I. A. de Sousa Filho, R. Lebullenger, S. Deputier, I. T. Weber, M. Guilloux-Viry, I. M. G. Santos, and V. Bouquet	
<b>SrSnO<sub>3</sub> Applied in the Reduction of NO by CO: Influence of Transition Metal Doping on the Catalytic Activity</b> .....	111
Guilherme L. Lucena, Danniely M. Ribeiro, João Jarllys N. de Souza, Fagner Ticiano Gomes Vieira, Cristiane A. Pereira, Ernesto A. Urquieta-González, Ary S. Maia, and Ieda Maria Garcia dos Santos	
<b>Advances in the Synthesis and Applications of Self-Activated Fluorescent Nano- and Micro-Hydroxyapatite</b> .....	149
Thales Rafael Machado, Jussara Soares da Silva, Eloisa Cordoncillo, Héctor Beltrán-Mir, Juan Andrés, Valtencir Zucolotto, and Elson Longo	

<b>Spintronic Properties in Complex Perovskites: A Concordance Between Experiments and Ab-Initio Calculations</b> .....	183
J. Roa-Rojas, C. E. Deluque Toro, A. V. Gil Rebaza, X. A. Velásquez Moya, and D. A. Landínez Téllez	
<b>Graphenylene-Like Structures as a New Class of Multifunctional Materials Alternatives to Graphene</b> .....	209
Nicolas F. Martins, Guilherme S. L. Fabris, Anderson R. Albuquerque, Ricardo Paupitz, and Julio R. Sambrano	
<b>Computer Simulations of MOF Systems: Key Applications</b> .....	231
Nailton Martins Rodrigues and João Batista Lopes Martins	
<b>Advanced DFT Atomistic Approaches for Electronic, Optical, and Structural Properties of Semiconductor Oxides</b> .....	255
Sergio R. de Lazaro, Renan A. P. Ribeiro, Marisa C. Oliveira, and Elson Longo	
<b>Computational Simulations to Predict the Morphology of Nanostructures and Their Properties</b> .....	267
José A. S. Laranjeira, Mateus M. Ferrer, Anderson R. Albuquerque, Carlos A. Paskocimas, Julio R. Sambrano, and Guilherme S. L. Fabris	
<b>Unraveling the Surface Chemistry of the Heterogeneous Catalytic Decomposition of O<sub>3</sub> for Selectivity Concerning O<sub>2</sub> or HO<sup>•</sup> Formation</b> .....	289
Raciél Jaimes López, Daniela Palomares Reyna, and Jorge Vazquez-Arenas	
<b>NH<sub>3</sub> Synthesis by Electrochemical Process Under Ambient Condition</b> .....	307
Juliana F. de Brito, Sirlon F. Blaskievicz, Marina Medina, Anelisse Brunca Silva, Marcos Vinícius de L. Tinoco, and Lucia Helena Mascaro	
<b>Overview: Catalysts, Feedstocks in Biodiesel Production</b> .....	337
Carlton A. Taft and Jose Gabriel Solano Canchaya	
<b>Bioactivity</b>	
<b>In Silico Drug Design and in Vivo Acute Toxicity Assay of Chalcone Analogs with Biological Antiparkinsonian Activity</b> .....	361
Bianca L. B. Marino, Jaderson V. Ferreira, L. Brenda Sánchez-Ortiz, José C. T. Carvalho, Irlon M. Ferreira, Suzane Q. Gomes, Carlos Henrique Tomich de Paula da Silva, Carlton A. Taft, and Lorane Izabel da Silva Hage-Melim	

<b>Electronic and Structural Insights of BCR-ABL Inhibitors Under LMC Treatment Perspective</b> .....	389
Érica C. M. Nascimento, Letícia de A. Nascimento, Luiz F. M. A. Benicio, José L. L. Alcântara, Washington A. de Pereira, and João B. L. Martins	
<b>Pathophysiology, Molecular Interaction Mechanism, Metabolism, Pharmacotherapy and New Perspectives in the Pharmacological Treatment of Chemical Dependence on the Main Illicit Drugs Consumed in the World</b> .....	405
Jaderson V. Ferreira, Gisele A. Chaves, Mateus A. Batista, Lenir C. Correia, Lucilene R. Souza, Daniel C. Costa, Mariana P. Barcelos, Carlos Henrique Tomich de Paula da Silva, Carlton A. Taft, and Lorane Izabel da Silva Hage-Melim	
<b>MAO Inhibitors from Natural Sources for Major Depression Treatment</b> .....	451
Luisa Nunes Souza, Jonas Ferro da Silva Neto, Maria Vitória da Silva Paula Cirilo, Gabriel Sousa Albuquerque, Clayson Moura Gomes, Leonardo Luiz Borges, Carlton A. Taft, and Vinicius Barreto da Silva	
<b>Advances in Computational Techniques for Discovery and Development of Drugs Against Leishmaniasis, a Brief Review</b> .....	465
Rai C. Silva, Cleydson B. R. Santos, Carlton A. Taft, Guilherme M. Silva, and Carlos Henrique Tomich de Paula da Silva	
<b>Lead Optimization in Drug Discovery</b> .....	481
Mariana Pegrucci Barcelos, Suzane Quintana Gomes, Leonardo Bruno Federico, Isaque Antonio Galindo Francischini, Lorane Izabel da Silva Hage-Melim, Guilherme Martins Silva, and Carlos Henrique Tomich de Paula da Silva	
<b>Pulsed Electric Field and Ultrasound Applied to Proteins, Enzymes and Peptides</b> .....	501
Igor Carvalho Fontes Sampaio, Isabela Viana Lopes de Moura, Jacson Nunes dos Santos, Josilene Borges Torres Lima Matos, Cleveland Maximino Jones, and Paulo Fernando de Almeida	
<b>Vaccine History: From Smallpox to Covid-19</b> .....	519
Camila Puton, Fernanda Gabriel Aires Saad, Ricelly Pires Vieira, Eduarda de Soares Libânio, Vinicius Barreto da Silva, Wilson de Melo Cruvinel, Leonardo Luiz Borges, Carlton A. Taft, and Clayson Moura Gomes	

<b>Structural Aspects of Organic Compounds as Proteasome Inhibitors Addressed to Several Diseases</b> .....	545
Suzane Quintana Gomes, Guilherme Martins Silva, Mariana Pegrucci Barcelos, Lorane Izabel da Silva Hage-Melim, and Carlos Henrique Tomich de Paula da Silva	
<b>Phytotechnological and Pharmaceutical Potential of <i>Eugenia</i> Genus</b> ....	569
Monatha Nayara Guimarães Teófilo, Elisa Flávia Luiz Cardoso Bailão, José Realino de Paula, Clayson Moura Gomes, Vinicius Barreto da Silva, Carlton A. Taft, Joelma Abadia Marciano de Paula, and Leonardo Luiz Borges	
<b>How Basic Programming Knowledge can Help the Drug Discovery Process</b> .....	583
Leonardo Bruno Federico, Mariana Pegrucci Barcelos, Suzane Quintana Gomes, Isaque Isaque Antonio Galindo Francischini, Anderson Luiz Pena da Costa, Lorane Izabel da Silva Hage-Melim, and Carlos Henrique Tomich de Paula da Silva	
<b>Ligand-Based Drug Design for Selection of Molecules with Pharmacological Activity in Essential Tremor</b> .....	603
Ana C. J. Silva, Suzane Q. Gomes, Mariana P. Barcelos, Carlos Henrique Tomich de Paula da Silva, Carlton A. Taft, and Lorane Izabel da Silva Hage-Melim	
<b>Intramolecular Hydrogen Bonding Patterns and Conformational Preferences of Ouabain—A Molecule with Cardiotonic and Antiviral Activities</b> .....	671
Liliana Mammino	
<b>Molecular Modeling of Acetylcholinesterase Inhibitors for the Treatment of Alzheimer's Disease</b> .....	697
Anderson Mendes Oliveira, Anna Eláyne da Silva Silva, Abraão Alves Pinheiro, Lenir Cabral Correia, Francinaldo Sarges Braga, Laira Rafaelle Pinto Gemaque, Cleydson Breno Rodrigues dos Santos, Carlos Henrique Tomich de Paula da Silva, Carlton A. Taft, and Lorane Izabel da Silva Hage-Melim	

# **Energy, Materials and Environment**

# Theory and Computation in Photo-Electro-Chemical Catalysis: Highlights, Challenges, and Prospects



Taifeng Liu and Michel Dupuis

**Abstract** Computation and simulation is a powerful approach to aid in characterizing, understanding, and ultimately making predictions about materials, processes, and systems for efficient and cost-effective photo-electro-chemical (PEC) conversions of solar energy to fuels, one of the essential elements of broad strategies toward renewable energy. Solar energy-driven water splitting using semi-conductor-based photo-catalysts is perceived as the most desirable opportunity. For robust PEC technologies, viable materials and systems must exhibit good *visible light absorption* and carrier generation, good *carrier transport*, and good carrier *redox reactivity*. Overall conversion efficiencies of systems have improved in recent years. Challenges remain to achieve the needed performance characteristics, including several fundamental science issues toward the discovery and development of semiconductor photo-electrode materials that permit high overall efficiency in devices. Modern first principles-based multi-scale approaches are proving extremely valuable in providing fundamental understanding of many experimental observations in PEC catalysis. Here we highlight illustrative examples of the application of theory and computation to study carrier transport and carrier utilization in semiconducting electrodes. The examples address strategies to enhance charge carrier separation and strategies to mitigate stability and high over-potentials in redox reactivity of carriers. The growing body of computational studies in these areas suggests a bright and impactful future of theory and computation in the field of renewable and sustainable energies.

---

T. Liu

National and Local Joint Engineering Research Center for Applied Technology of Hybrid Nanomaterials, Henan University, Kaifeng 475004, China  
e-mail: [tliu@vip.henu.edu.cn](mailto:tliu@vip.henu.edu.cn)

M. Dupuis (✉)

Department of Chemical and Biological Engineering, University at Buffalo, State University of New York, Buffalo, NY 14260, USA  
e-mail: [mdupuis2@buffalo.edu](mailto:mdupuis2@buffalo.edu)

## 1 Introduction

Computation and modeling is now playing a major role in essentially all areas of chemistry and materials sciences. Efficient and powerful theories have been developed and methods implemented in the past couple of decades that deal with the atomic, mesoscale, and macroscale levels of characterization and understanding of processes and systems. Beyond characterization and understanding, the ultimate objective of computation and modeling is to predict new molecules, new materials, new processes, and new chemistries that go beyond the current state of synthesis, efficiencies, and capabilities. Photo-electro-chemical conversions of solar energy to fuels comprise one of the essential elements of broad strategies toward renewable energy. In fact, solar energy-driven water splitting using semi-conductor-based photo-catalysts is perceived as the most attractive, challenging, and yet highest pay-off opportunity. In this chapter we highlight from a computation and modeling-driven perspective where computation has become a powerful contributor and can emerge as a driver of progress in solar energy conversion technologies. In Sect. 1 of this chapter, we discuss the fundamentals of PEC and give an overview of where computation has a role. In Sect. 2, we highlight our research involvement in this field in collaborations with others. We end the chapter with an outlook, in particular mentioning areas of computational and theoretical limitations and challenges.

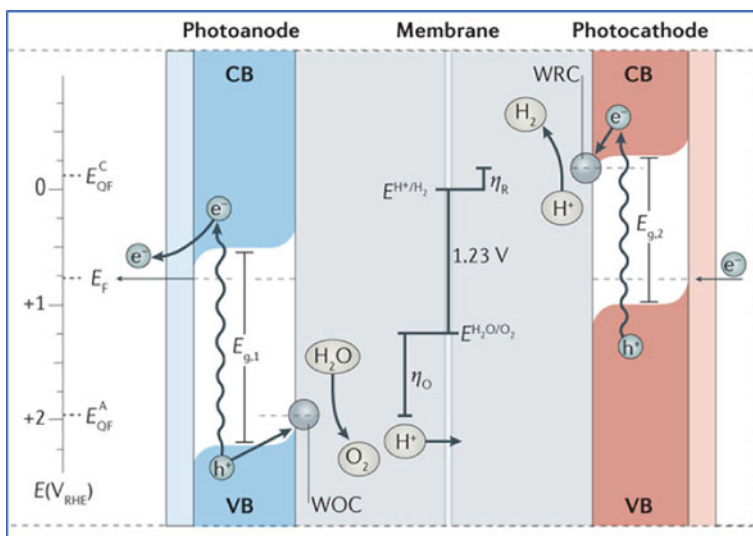
## 2 Photo-Electro-Chemical Catalysis and the Role of Computation

### 2.1 *Fundamental Science Concepts for Photo-Electro-Chemical Conversions*

Efficient and cost-effective conversion of solar energy into electrical and chemical energy is widely accepted as an essential element of a broad strategy toward renewable energy [1–7]. In fact, solar energy-driven water splitting using semi-conductor-based photo-catalysts is perceived as the most desirable opportunity [8–10]. An illustration of the science of photo-electro-chemical conversion, also referred often as photocatalysis, is seen in the schematics of PEC devices in Fig. 1 adapted from Sivula and van de Krol [11], and of the chemical processes taking place in such devices yielding water splitting in Fig. 2, reproduced from Yang et al. [12] Sunlight absorbed by an anode semiconductor material excite the electrons in the material and create electron  $e^-$  and hole  $h^+$  carriers that migrate to the electrode surface to split water through water oxidation at an anode and proton reduction at a cathode. The overall process converts essentially solar energy into chemical fuels.

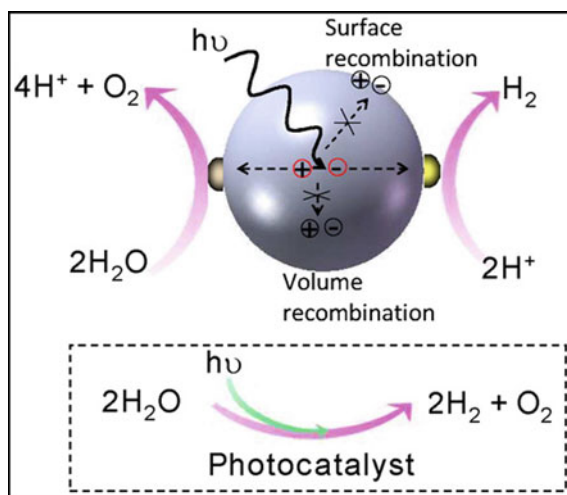
For robust photo-electro-chemical conversion technologies, viable materials and systems must exhibit good *visible light absorption* and carrier generation, good





**Fig. 1** Schematic of a PEC device for water splitting. Under the right circumstances, absorption of sunlight in a semiconductor anode electrode gives rise to catalytically active electrons  $e^-$  and holes  $h^+$ . Holes go on to oxidize water while electrons go on to the cathode where they reduce protons to evolve  $H_2$ . The sunlight is the source of the energy required to split water. Illustration adapted from Sivula and van de Krol [11], with permission

**Fig. 2** Light absorption and charge carrier generation, carrier transport, and carrier redox reactivity are the three critical characteristics for viable photo-catalytic systems. The present proposal addresses issues on charge carrier structure, transport, and reactivity. Illustration from Yang et al. [12], with permission



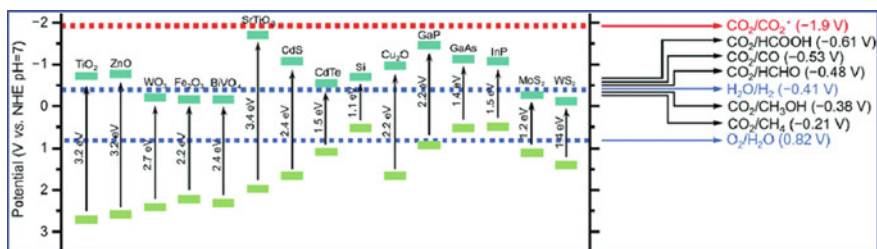


**Fig. 3** Band structure and potentials of selected semiconductors positioned relative to the Normal Hydrogen Electrode (NHE) at  $\text{pH} = 7$ , with standard potentials for selected conversion chemistries also indicated (illustration from Zhang et al. [22], with permission)

*carrier transport*, and good *carrier redox reactivity* [9, 11], as depicted in Fig. 2. Overall conversion efficiencies of PEC systems have improved in recent years [13–17]. Challenges remain to achieve the needed performance characteristics [11, 16–21] including several fundamental science issues. Among those are (a) understanding and predicting material structure and properties, and their relationships to light absorption, carrier generation, transport, and reactivity efficiencies in single, multi-phase, and/or multi-materials systems; (b) tailoring and optimizing the composition, phase, microstructure, and integration of materials to achieve superior light harvesting, charge carrier transport, and overall energy conversion performance. The biggest challenge to enabling practical PEC science and technology is the discovery and development of semiconductor photo-electrode materials that permit high overall efficiency in devices.

The physical chemistry fundamentals and challenges that come into play in PEC's are illustrated in Figs. 3 and 4[22]. Absorption of sunlight by the semiconductor electrode is the first step in the creation of charge carriers that ultimately get involved in the redox chemistries of water splitting at the electrode/electrolyte interface. For water oxidation at an anode electrode, the  $\text{h}^+$  charge carrier states at or near the maximum of the valence band need be below the  $\text{O}_2/\text{H}_2\text{O}$  potential, while, at a cathode, the  $\text{e}^-$  carrier states at or near the conduction band minimum need be higher than the  $\text{H}_2/\text{H}_2\text{O}$  potential. These points make the thermodynamics requirements clearly.

To create charge carriers, sunlight photons need have an energy greater than the band gap of the material. The sun radiation spectrum displayed in Fig. 4 shows that ~42% of the light that reaches the earth is visible. Thus, to make good use of solar light on earth, the challenge is to have materials that absorb strongly in the visible region of light AND that have bands edges (valence and conduction bands) well positioned vs the standard redox potentials of the relevant chemistries.

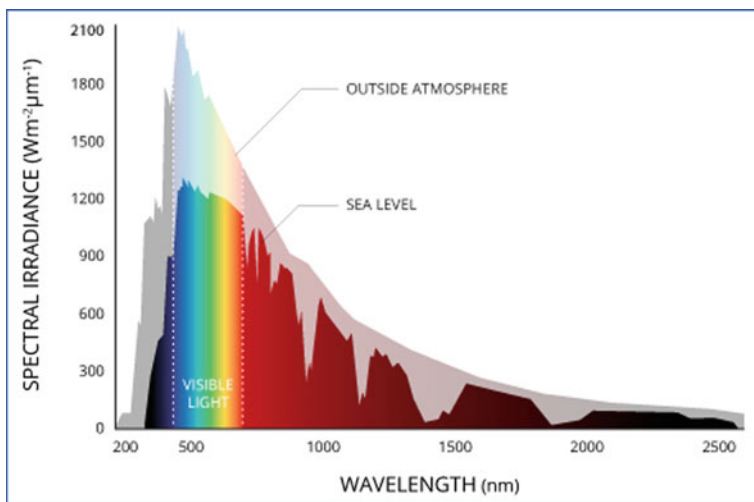


**Fig. 4** Solar irradiance (Figure reproduced from <https://www.fondriest.com>). Visible light radiation makes up  $\sim 42\%$  of light that reaches the earth, indicating that the best PEC's will absorb light in the visible

## 2.2 Fundamental Challenges in Photo-Electro-Chemical Conversions

Based on the fundamentals enunciated above, it is possible to formulate broad strategies to improve PEC efficiency. Those include: a. band structure and band gap engineering of existing materials [15] for improved visible light absorption; b. surface engineering [16] and multi-phase or multi-material junction engineering [16] for improved charge separation; and c. hetero- and homo-junction engineering for improved light absorption, charge separation, and redox band alignment. Beyond engineering existing electrode materials for improved properties, much research is also devoted to the discovery of semiconductor materials with inherently better properties [11, 15] than current materials ( $\text{TiO}_2$ ,  $\text{WO}_3$ ,  $\text{Fe}_2\text{O}_3$ ,  $\text{CuWO}_4$ , and  $\text{BiVO}_4$ —the highest performing oxide to date).

*Light absorption:* Band structure and band gap engineering are widely pursued to extend material absorption into the visible region and enhance carrier generation [23–25]. Band structure engineering includes cation and anion doping and substitution to reduce the band gap, usually through up-shifting of the valence band edge and down-shifting of the conduction band edge. We note that band structure engineering is very conducive to data science-based discovery, and recent such computational investigations have been reported [23–27]. It must be realized that engineering the band gap shifts also the band edges, thus affecting the redox surface chemistry at the solid/electrolyte interfaces [11, 15].

*Charge carrier structure:* The generation and dynamics of charge carriers in early times following light absorption has been studied extensively in recent years

because of the availability of time-resolved techniques. The impetus for this research arose from the thought that detailed knowledge of charge carrier characteristics (exciton generation and lifetime) would lead to the identification of design principles, and to the design and discovery of intrinsically better photocatalytic materials. The experimental techniques to generate this information are many. They include a variety of time-resolved techniques such as transient UV-vis spectroscopies to detect the changes in UV-vis spectra due carriers' thermodynamic and structural features [28–30] and transient microwave conductivity (TRMC) measurements [31, 32]. Other approaches include time-resolved photo-charge (TRPC) measurements for lifetime of charge carriers [33, 34] and for electron-hole separation distance [35]; and time-resolved terahertz THz spectroscopy (TRTS) for ultrafast carrier dynamics and conductivity mechanisms and measurements [36, 37]. Electron paramagnetic resonance (EPR) is also useful to get information about trapping of photogenerated electron [38]. Transient extreme-ultraviolet (XUV) spectroscopy is an emerging powerful capability. A notable point is that it yields descriptions of exciton and polaron structures and dynamics in terms of 'localized' atomistic and chemical concepts as the absorption is interpreted in terms of oxidation states of atoms [39–43]. Theoretical methods have emerged also recently that afford the characterization of exciton structures and lifetimes, based on non-adiabatic molecular dynamics combined with density functional theory and other wavefunction types [44–47], with recent applications in photovoltaics [48–50].

*Carrier transport:* The overarching issue about 'carrier transport' is charge separation. Promoting charge separation means reducing charge recombination and making use of as many  $e^-$  and  $h^+$  carriers as possible that were created by light absorption. This number is one of the quantifiers of conversion efficiency. Physical situations that promote charge separation include single phase facet selective materials [51, 52], multi-phase and/or multi-material junctions [53, 54], single-phase homo-junctions [55–57], and the use of cocatalysts [12, 58, 59]. *Surface engineering* [16] refers to utilization and manipulation of all these situations. *Crystal facet engineering and interface engineering* are emerging as promising approaches to enhance carrier separation and overall water splitting efficiency, both for hydrogen evolution and oxygen evolution [51, 54, 60, 61]. *Facet engineering* deals with the growth of crystal facets that exhibit selectively either reduction or oxidation chemistry. Facet selectivity has been reported for a number of semiconductor materials, including bismuth vanadate  $\text{BiVO}_4$  (BVO) [51], strontium titanate  $\text{SrTiO}_3$ , [62] copper oxide  $\text{Cu}_2\text{O}$  [52, 63, 64], and titania  $\text{TiO}_2$ , [61, 65, 66] for example. Other examples include tungsten oxide  $\text{WO}_3$ , gallium oxide  $\text{Ga}_2\text{O}_3$ , tantalum nitride  $\text{Ta}_3\text{N}_5$ , and several tantalates. *Interface engineering* is the design of mixed-phase interfaces such as in  $\text{TiO}_2$ , [67–69] and gallium oxide  $\text{Ga}_2\text{O}_3$ , [53] or multi-materials interfaces such as  $\text{BiVO}_4/\text{Cu}_2\text{O}$  [63],  $\text{WO}_3/\text{TiO}_2$ , [70]  $\text{WO}_3/\text{BiVO}_4$ , [71] and many other combinations, all interfaces that enhance charge separation.

*Redox chemistry at electrode/electrolyte interface:* There are numerous studies about solar fuels [9, 17] (water splitting,  $\text{CO}_2$  and CO reduction and conversion, along with  $\text{N}_2$  reduction to  $\text{NH}_3$ ) but a relatively small number have focused on understanding the details of the chemical reactions at the surfaces in contrast to the

more global and effective conversion efficiencies. From the perspective of overall solar conversion efficiency, detailed knowledge of surface reaction mechanisms and kinetics is needed, as importantly as details about light absorption, carrier generation, transport and separation [15]. For surface reaction kinetics, transient IR spectroscopy (TRIR) is playing an increasingly important role when attempting to identify and characterize the reactions intermediates [72–74]. It has been used for a number of materials, including  $\text{BiVO}_4$ ,  $\text{TiO}_2$ ,  $\text{SrTiO}_3$ , and others. For water splitting, the emphasis has been on water oxidation as it is the more challenging process compared to proton reduction. [75].

Water oxidation with  $\text{O}_2$  evolution (OER) is most often discussed in terms of a four proton-coupled-electron transfer steps with  $^*\text{OH}$ ,  $^*\text{O}$ , and  $^*\text{OOH}$  intermediate species [76]. The design of better catalysts relies on Sabatier's principle of bonding strength [77]. Still, not all cases fall into this framework. Nucleophilic attack of hole-carrying surface lattice oxygen sites have been proposed as mechanism [73]. Other proposals include O-O coupling in adsorbates (adsorbate evolution mechanism AEM) or direct O-O coupling to a lattice oxygen (lattice oxygen oxidation mechanism LOM) [78]. To date, to the best our understanding, it remains challenging to predict which mechanism applies to which class of materials. Even if volcano plots can be derived from universal scaling of binding energies of intermediates  $^*\text{OH}$  and  $^*\text{O}$ , there are large differences in binding strengths within classes of materials (oxide perovskites are an example) [79]. An increased understanding of the structure-redox activity of materials and of the chemical factors that govern the reaction mechanisms is highly desirable.

## 2.3 *Computation and Simulation for Photo-Electro-Chemical Catalysis*

The field of photo-electro-chemical catalysis is ripe for the application of existing computation and simulation methods, and the development of new methods for the characterization of the fundamental science in the three phases of PEC operations outlined earlier. The scientific challenges that can be addressed by computational means are summarized in Table 1.

### 2.3.1 **Computational Materials Screening and Discovery**

Characterization of processes in the phase of light absorption and carrier generation fall under the umbrella of 'computational materials screening and discovery', some aspects of it were mentioned earlier. The objective is to discover improved or new materials that absorb strongly in and near the visible range of light and generate  $e^-$  and  $h^+$  charge carriers with a high degree of efficiency while exhibiting low recombination rates. Systematic calculations of material structure and stability, of

**Table 1** Opportunities for theory and computation in photo-electro-chemical catalysis. HER = hydrogen evolution Reaction, OER = oxygen evolution reaction, CO<sub>2</sub>RR = CO<sub>2</sub> reduction reaction, CORR = CO reduction reaction, N<sub>2</sub>RR = N<sub>2</sub> reduction reaction

---

<ul style="list-style-type: none"> <li>• <u>Light absorption and carrier generation:</u>  <i>Computational materials screening &amp; discovery</i> <ul style="list-style-type: none"> <li>– structure and stability and phonons</li> <li>– band structure and band gap engineering</li> <li>– doping and defects (vacancies)</li> <li>– work function</li> <li>– d-d transitions</li> </ul> </li> <li>• <u>Carrier transport and separation:</u>  <i>Computational modeling of <math>e^-/h^+</math> carrier dynamics in crystalline single-phase, multi-phase, and multi-materials systems</i> <ul style="list-style-type: none"> <li>– transport</li> <li>– trapping, defect-mediated recombination</li> <li>– enhanced charge separation</li> </ul> </li> </ul>
ofacet selectivity ophase separation—multi-phase oe <sup>-</sup> /h <sup>+</sup> transport layers—multi-material odoping—homojunctions
<ul style="list-style-type: none"> <li>• <u>Redox alignment and reactivity:</u>  <i>Computational modeling of <math>e^-/h^+</math> catalytic utilization</i> <ul style="list-style-type: none"> <li>– HER, OER</li> <li>– CO<sub>2</sub>RR, CORR, N<sub>2</sub>RR</li> </ul> </li> </ul>

---

their phonons, of their band gaps and band structures, of the effects of doping and defects (such as vacancies), and of their work functions, are widely pursued and found in the literature [23–25]. They are aided by modern approaches of machine learning (ML) and artificial intelligence (AI) as extensive databases have become well established and widely used, such as from The Materials Project and from the AFLOW consortium [24–26, 80–83].

A challenge affecting selected transition metals semiconductors deals with *d-d* transitions. Such transitions occur in semiconductors with partially occupied *d* bands, such as hematite Fe<sub>2</sub>O<sub>3</sub>. Hematite absorbs light in the visible range, around ~2 eV, a range that is highly desirable in the quest for materials that are chemically photo-active while absorbing a large fraction of solar radiation. However, excitations of *d* electrons within the *d* band occur in the same range of excitation energies, *they are intra-band excitations and do not lead to  $e^-/h^+$  separation* because of the electronic structure of the resulting excited state, in contrast to valence-to-conduction band excitations that lead to carriers that are mobile within the separated bands. In these situations of *d-d* transitions, the materials are plagued with absorption that is not efficient for photocatalytic  $e^-/h^+$  activity. The characterization, understanding, and control of *d-d* transition remains a challenging problem of computational modeling and design of efficient PEC devices.

### 2.3.2 Computational Modeling of $e^-/h^+$ Carrier Dynamics in Crystalline Single-Phase, Multi-Phase, and Multi-Materials Systems

Upon creation of charge carriers, the dynamics of carriers are the essential elements of the phenomena involved in carrier transport and separation. Their computational modeling falls under the umbrella of ‘computation modeling of  $e^-/h^+$  carrier dynamics in crystalline single-phase, multi-phase, and multi-materials systems.’ Issues are the carrier transport proper, be it by band transport [84] or by polaron hopping with activation barriers [85–90]. Transport in crystalline semiconductors is affected by dopants and defects that may lead to trapping (thus reducing transport efficiency) and defect-mediated recombination (thus eliminating  $e^-$  and  $h^+$  and affecting overall efficiency). Trapping energies can be obtained from first-principles calculations. To the best of our knowledge, computational investigations of recombination are not widely carried out. Both trapping (relatively ‘standard’ calculations) and recombination (challenging theoretical models) can be addressed with solid state quantum chemical calculations.

The overarching objective here toward tailoring efficient PEC materials is to *enhance charge separation* to increase PEC overall efficiency (number of molecules of  $H_2$  and  $O_2$  that evolve per absorbed photon. Several strategies are being pursued, that fall in three main categories: 1. synthesis of electrodes with designed and tailored structures and that exhibit facet selectivity, whereby oxidation and reduction occur at specific facets; 2. phase separation in junctions of materials that exhibit more than one stable phases. Titania and gallium oxide are two examples mentioned above with experimental and computational evidence that  $e^-$  carriers are more thermodynamically stable in one phase and the  $h^+$  carriers in the other phase. Multi-material junctions and co-catalysts are other design features that are particularly conducive to enhanced charge separation, again owing to the different thermodynamic stability of  $e^-$  and  $h^+$  among materials. Obvious examples are those of  $e^-/h^+$  transport layers, with junctions between materials enducing charge separation due to differential thermodynamic stability between electron and hole carriers.

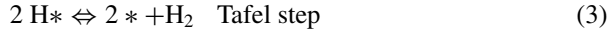
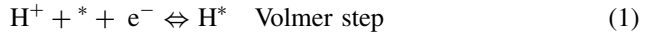
### 2.3.3 Computational Modeling of $e^-/h^+$ Catalytic Utilization

This domain of modeling encompasses all the aspects of chemical reactivity by the charge carriers  $e^-$  and/or  $h^+$  at the semiconductor/electrolyte interfaces. In the context of water splitting, the hydrogen evolution reaction (HER) occurs at a cathode while the water oxidation reaction (oxygen evolution reaction OER) occurs at an anode. (In the chemical equations below, \* represent an empty site for adsorption and  $H^*$ , or  $OH^*$ , or  $X^*$  in general, denotes an H atom adsorbed at that site, or an OH or X group adsorbed at that site).

The multi-step mechanism of HER has been the subject of much research, an informative review of which is given by Lasia [91]. The mechanism is a combination

of the Volmer reaction and the Heyrovsky electrochemical reaction or the chemical hydrogen desorption reaction.

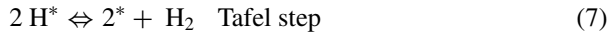
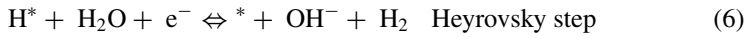
In acidic conditions, the steps have the form:



for an overall reaction:



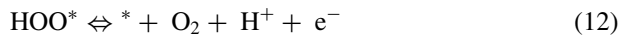
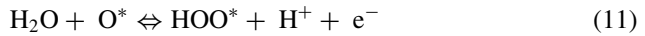
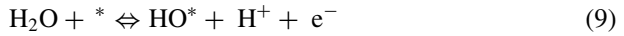
In alkaline conditions, the equivalent steps have the form:



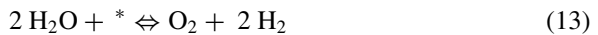
for an overall reaction:



Similarly, the OER mechanism is written as a sequence of four coupled (proton + electron) steps, popularized by the group of Norskov: [76]



for an overall reaction:





The computational modeling of the carrier utilization involves the determination of the reaction energy profiles associated with the formation of the intermediates as listed above. Knowing these profiles gives an indication of the ‘thermodynamic overpotential’, the energy beyond the minimum energy required to dissociate  $\text{H}_2\text{O}$  into  $\text{O}_2$  plus four (proton + electron) pairs (4.92 eV) in water oxidation. Note that, most often computational studies do not focus on determining transition states and activation barriers for the elementary steps, but simply on the thermodynamics stability of the intermediates, keeping in mind that activation energies and thermodynamics stability are connected by the Bell-Evans-Polanyi principle [92, 93].

### 3 Computation and Modeling of Carrier Structure, Dynamics, and Utilization

In recent years our group has pursued a research program focused on the science of PEC from a computational focus strongly integrated with experimental investigations by collaborators. Our emphasis has been on theory and simulation of ‘carrier transport’ in PEC systems. We highlight below some of this work and the key findings. We also point to new subjects of investigation as we view them timely and of fundamental importance considering current happenings in this field of research. However, ahead of this, we think it is important to make two significant observations that bring a stronger light of impact and timeliness to the research ideas. One is about ‘facet selectivity’ and its potentially far-reaching impact beyond water oxidation and PEC’s. The second is about exciton structure and dynamics, and the far-reaching cross-validation between theory and experiment in this field.

The first remark is about intrinsic *facet selectivity*. Many materials (as discussed) exhibit the property whereby, within a single crystal, some crystal facets are active in oxidation, and other facets are active in reduction. The property was discovered about water oxidation on BVO as reported in *Nature Communications* [51]. That report inspired our research. In a very recent paper entitled “Facet-dependent active sites of a single  $\text{Cu}_2\text{O}$  particle photocatalyst for  $\text{CO}_2$  reduction to methanol” in *Nature Energy* [94], Wu et al. showed that facet (110) of a single  $\text{Cu}_2\text{O}$  crystal is active for  $\text{CO}_2$  conversion to methanol as a photocatalyst, while facet (110) is inert. In addition,  $\text{Cu}_2\text{O}$  oxidizes water as it reduces  $\text{CO}_2$ . In other words,  $\text{Cu}_2\text{O}$  performs the two functions, with water oxidation as the source of protons for the reduction of  $\text{CO}_2$ .  $\text{CO}_2$  conversion is arguably the world’s greatest challenge in energy and environment. This report renders the research on facet selectivity in photocatalytic particles even more relevant and potentially impactful.

The second remark is about the ‘chemical’ characterization of exciton structures from XUV spectroscopy [39–41]. In brief, the XUV technique permits the identification of an element’s oxidation state in ultra-fast time-resolution. For hematite  $\text{Fe}_2\text{O}_3$ , [40] a ‘benchmark’ photo-electrode materials that has the merit of very favorable light absorption characteristics and natural abundance, the Baker group describes

how charge localization and small polaron formation occur within  $\sim 660$  fs, and that the electron-hole  $e^-/h^+$  exciton, created within 100 fs, has a radius of a single Fe-O bond length. For  $\text{CuFeO}_2$ , an earth-abundant metal oxide that is attracting much interest as a photocathode [15, 41, 95] for proton reduction by photo-generated electrons, the Baker group reported that O  $2p$  holes thermalize within  $\sim 500$  fs into Cu  $3d$  hybridized 3d holes. Beyond the novel insights that come from the ability to elucidate site-specific charge carrier dynamics in real time, *the ‘localized chemical’ picture of excitons is particularly noteworthy and exciting for electronic structure theorists.* Traditionally, electronic structure in the solid state is discussed in terms of band theory (valence band, conduction band, band gap, gap states, exciton, band bending) most often determined from density functional theory (DFT). The results are not easily translated into ‘localized’ concepts of chemistry. We view the Baker results as a unique opportunity to validate experiment by theory using advanced quantum chemical theories, and, conversely, validate the quantum chemical theories by experiment. We will come back to this point later in Sect. 3 of this chapter on ‘Challenges and outlook’.

### 3.1 Overview of Our Multiscale Modeling Framework

As indicated above, the overall research ideas and directions about PEC’s deal with the timely societal challenges of renewable energy, specifically the efficient and cost-effective conversion of solar energy to electrical and chemical energies. The scope of this use-inspired fundamental research program centers around fundamental characterization of solar energy-to-fuels conversion systems, with theoretical studies in the three stages of photo-electro-chemical PEC conversion, mainly ‘light absorption’, ‘carrier transport’, and ‘carrier reactivity’ as illustrated in Fig. 5. The research aims to advance fundamental knowledge and understanding in PEC to lead ultimately to the design of systems with enhanced overall conversion efficiencies.

Among the three research thrusts elaborated earlier, one focuses on ‘carrier transport’, with the aim to understand, characterize, and generate design principles to control the factors that lead to enhanced separation of photo-generated electron and holes toward higher solar energy-to-fuel conversion efficiency. To this end we view it as a powerful approach to model the space-charge distribution dynamics of charge carriers by combining first-principles atomistic computation and mesoscale kinetics simulation. The research relies on existing software tools DFT-based quantum mechanical (QM) modules as well as our group’s own developed QM tools and a powerful and versatile lattice based kinetic Monte-Carlo (KMC) capability. The early applications of these tools are starting to provide the theoretical foundations for strategies to enhance carrier transport and conversion efficiency. At the most fundamental level, the research addresses how the flow of charge carriers in complex crystalline environments of single phase, multi-phase, and multi-materials semiconductor systems can be tailored to enhance redox reactivity in photo-electro-chemical

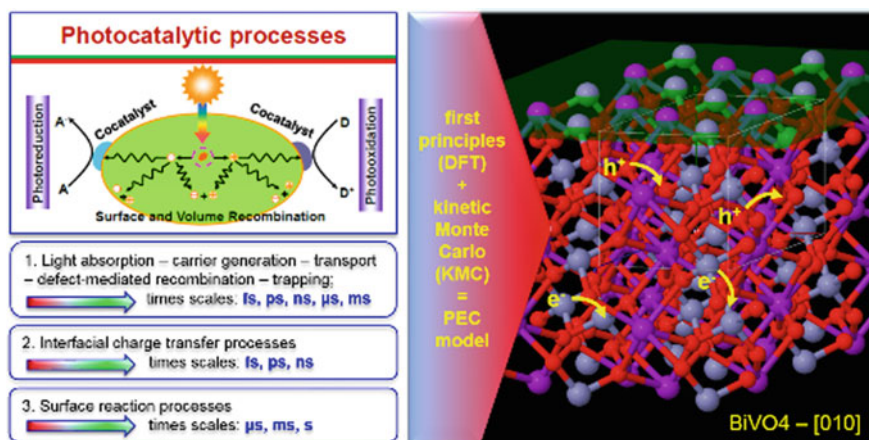


**Fig. 5** Combining first-principles computation and mesoscale kinetics modeling is critical for *qualitative and quantitative* understanding of the science and performance of photo-electro-chemical devices accounting for light absorption and carrier generation, carrier transport, and carrier redox reactivity. Initially the modeling will provide the foundation for crystal facet engineering and interface engineering as they pertain to the rational design of efficient solar energy conversion materials

conversion. This research aligns well with broad themes addressing ‘charge transport and reactivity’ and ‘chemistry at complex interfaces.’

Our general modeling framework is depicted in Fig. 6. It starts with solid state DFT calculations of single polarons in a supercell, with their localized character and the localized lattice distortion associated with polarons. Then, site-to-site hops get identified and the energy profiles associated with the hops are determined via DFT calculations along a pathway whereby the polaron structure at the initial site is

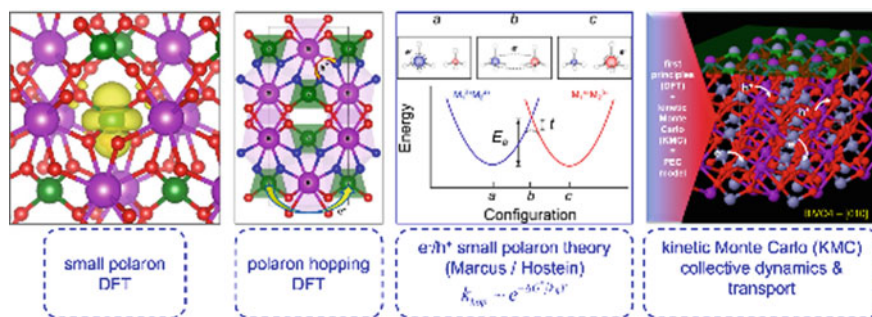


**Fig. 6** General framework of multiscale modeling of carrier transport in semiconductor electrodes of PEC systems: from left to right, DFT calculations of polaron structure and hopping via the Marcus/Holstein theory, to KMC modeling of the collective dynamics of multiple polarons at experimentally relevant concentrations of charge carriers. The diagram of the potential energy profile is reproduced from Rettie et al. [85] with permission

morphed into the polaron structure at the final site. The calculated profile approximates closely the profile displayed in Fig. 6. The hopping rate is determined from Marcus / Holstein theory, based on the rate expression for diabatic hopping or for adiabatic hopping (thermal hopping assisted by phonons). The calculated rates serve as input to the lattice based larger scale model of a solid or particle using the kinetic Monte Carlo methodology to describe the spatial and temporal dynamic distribution of a set of polarons, the number of which can be chosen consistent with experimental concentration of charge carriers. This multiscale methodology has been used and described in many publications by our group and other groups as well [86, 87, 90, 96–104].

*About DFT for polarons:* From a theoretical standpoint, the ability to obtain qualitatively correct descriptions of localized polarons hinges on overcoming the self-interaction error that plagues current functionals of the density that are the foundation of DFT. Many current polaron calculations by us [87, 97, 105, 106] and others [107–112] use the DFT+U methodology to overcome the self-interaction error of DFT. Admittedly, the approach has an ad hoc aspect in the choice of the on-site Hubbard+U parameter, and some prefer the use of hybrid functionals [113–115]. Localization of the unpaired electron or hole is the essence of the Marcus/Holstein small polaron model. Practical experience shows that the activation barrier is not overly sensitive to the choice of +U value. Nonetheless, care must be applied. In the same vein, the amount of exact exchange in hybrid functionals varies from one functional to the other. Care must be applied here too. In any case, we note a broad similarity in results between DFT+U and the popular PBE0 and HSE06 hybrid functionals for a number of oxide perovskites (including strontium, barium, and lead titanates, STO, BTO, and PBO) [112]. Our use of a +U parameter on oxygen to ‘create’ localized holes on O atoms is less pervasive in the literature than +U on metal ions, but it is found [74, 101, 107]. While there are examples in the literature that +U on oxygen does not introduce significant artifacts in the DFT wavefunction [101], even with +U(oxygen) ~8 eV, a value used by us [101] and others [74], we recently demonstrated that, in the case of BVO, the +U vs hybrid is not a resolved issue, and that varying the fraction of exact exchange in hybrid functional leads to substantially different descriptions of  $h^+$  polarons in BVO [102]. This issue is elaborated upon further down in Sect. 3 of this chapter on ‘Challenges’. ‘Tricks of the trade’ to generate polaronic wavefunctions are described in a recent review [86].

*About Lattice based KMC for charge carrier dynamics and transport:* We use the kinetic Monte Carlo KMC methodology embodied in a new Python code to characterize the temporal and spatial carrier dynamics in semiconductor electrodes. A flowchart for the KMC code is shown in Fig. 7, as an object-oriented framework written in Python language that is hosted as a repository on GitHub. The code consists of three essential components, a ‘*Model Engine*’, a ‘*KMC Engine*’, and a ‘*Analysis Engine*’. The ‘*Model Engine*’ includes two object definitions, one called ‘*Material*’ with all physical parameters related to the material of interest, system size, atomic coordinates etc.; the other object is ‘*Neighbors*’ with the lists of hopping neighbors. The second component of the code, the ‘*KMC Engine*’, includes a collection of ‘objects’ driving the execution of the stochastic ‘moves’ corresponding to processes

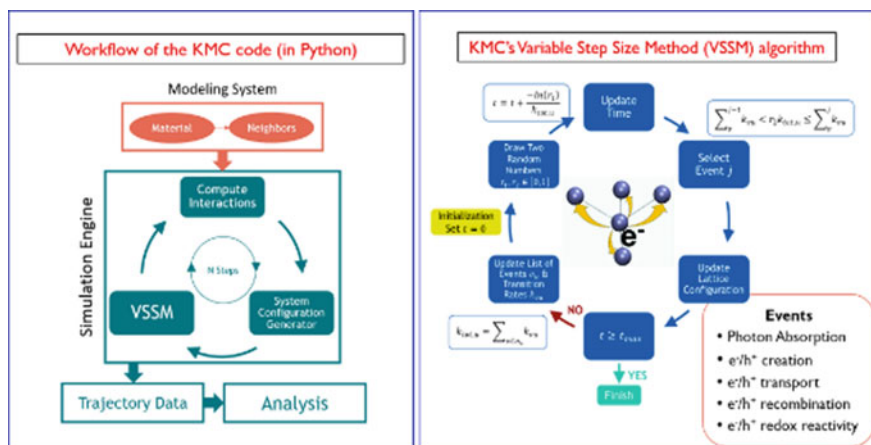


**Fig. 7** Flow chart of PyCT, a Python-based charge transport, cross-platform, object-oriented, lattice based KMC code for carrier transport [89]

for which the rate constants are provided, and therefore treated in the model. The “*Analysis Engine*” includes a collection of objects to analyze the KMC trajectories of the charge carrier distribution.

A simulation starts with a random distribution of excess charges ( $-1$  for electrons,  $+1$  for holes) on lattice sites that are assigned the full oxidation state charges of the constituent ions of the material. The number of excess charges should be consistent with the charge carrier concentration resulting from the absorption of light. The ‘*Model Engine*’ object includes the species locations and their associated hopping neighbors and generates a list of candidate hops and occupation states. The ‘*KMC engine*’ uses the variable step size method (VSSM) implementation [116] of KMC with the elementary rates coming from first-principle calculations (preferably) or from experiments.

The interactions governing the system are electrostatic (long range) in nature and individual rates are affected at any given time ‘ $t$ ’ by the distribution of charges at that time, requiring the evaluation of the *change* in energy upon a ‘move’. An ‘object’ calculates the *change* in energy and the concurrent change in the activation barrier and associated process rate (using the Bell-Evans-Polanyi principle [92, 93]), making use of the Ewald summation approach. For example, an electron involved in a set of possible hops (one of which gets randomly selected) will experience an increased hopping barrier (slower rate) when the hop brings the electron closer to other electrons (increased electrostatic repulsion) or a decreased hopping barrier (faster rate) when the hop takes the electron farther away from other electrons (decreased electrostatic repulsion i.e. electrostatic stabilization). The treatment of long-range electrostatics in these charge models for polaron transport required the use of the Ewald summation [100].

Lattice based KMC simulation is particularly well suited [116–118] to describe the dynamics of space-charge distribution in complex systems such as those considered here. KMC is a stochastic approach to solving coupled kinetics equations for a set of processes with varied rates (see Fig. 5). Processes of interest here include all processes dealing of the fate of charge carriers: photon absorption, exciton creation, dynamics, and recombination, carrier separation, diffusion, and recombination, and carrier reactivity. They span many orders of magnitude in time scales: a. bulk exciton dynamics, charge carrier formation, carrier separation, carrier recombination, carrier trapping, with time scale from femtoseconds up to milliseconds; b. interfacial charge transfer with time scales from femtoseconds to nanoseconds; and c. surface reaction processes in the case of photocatalytic systems, with time scales from microseconds to seconds. A lattice based KMC model allows also to account for local effects (near surface vs. bulk trapping, vacancy and doping defects at relevant concentrations, phase boundaries, interfaces, and homo-junctions) as it provides a spatial and temporal resolution of space-charge distribution. Our recent KMC studies of BVO and W/Mo-doped BVO highlighted below illustrate the unique insights afforded by our (QM+KMC) model. It is worth noting that hopping barriers for the systems of interest here (BVO, STO, W-doped BVO,  $\text{TiO}_2$ , and  $\text{Ga}_2\text{O}_3$ ) are in the range of  $\sim 0.1$  eV up to  $\sim 0.5$  eV, while thermodynamic junction potentials in mixed-phase systems due to band alignment (rutile-anatase mixed-phase  $\text{TiO}_2$ , mixed-phase  $\alpha$ - $\beta$   $\text{Ga}_2\text{O}_3$ ) are in the range of  $\sim 0.2$  to  $0.4$  eV [53, 119–122]. Accordingly, KMC modeling of mixed-phase interfaces makes sense and ought to provide a good description of space-charge separation dynamics induced by interfaces.

The rate constants used in the KMC model may come from experiment or from theory. A complete characterization of transport and PEC conversions efficiency requires that KMC include *all relevant processes*, each described at an appropriate level of accuracy. Thus, comparison with experimental data is important. Through a sensitivity analysis, KMC can also reveal which processes affect the overall efficiency most. With lattice based KMC, we can introduce inhomogeneity in the model, due for example to defects such as doping and vacancies. Defects can be readily introduced at concentrations relevant to experiment, including with a concentration gradient (homo-junction [57]). In these cases, it is necessary to calculate the rates for processes that occur in the vicinity of defects and to include them in the list of possible KMC ‘events’. If needed, defect migration could also be included among the KMC processes. Lattice based KMC model is also well suited to capture the spatial inhomogeneity in light absorption, whereby absorption is depth-dependent and strongest near the crystalline surface.

We note that KMC simulations have been used to investigate thermal catalytic processes on surfaces [116] and also carrier transport in organic photo-voltaic systems [123, 124], both of which are distinctly different from transport in crystalline systems due to the nature of the crystalline network and the underlying interactions. To the best of our knowledge, very few studies have used lattice based KMC to study charge and ion transport in crystalline systems [118, 125]. Our objective has been to go beyond that work and build a set of tools that will allow us to increase understanding of photo-electro-chemical conversion systems in all phases of absorption, transport, and redox

reactivity. Lastly, we aspire to use ab initio data in preference over empirical data as much as possible to, ultimately, have predictive ability and gain new insights that are hard to extract from experiment.

At present, we continue to address facet selectivity in BVO. We are at a stage where we need to include ‘surface reactions’ among the KMC events and  $e^-/h^+$  separation in homo-junctions (W-doped BVO), a task that requires a 2D periodic KMC implementation to model gradient doping. Other systems to investigate could include facet-selective STO, and charge-separating mixed-phase interfaces ( $\text{TiO}_2$  and  $\text{Ga}_2\text{O}_3$ ). In all cases, we will determine the space-charge distribution dynamics of charge carriers in realistic computational models with shapes and sizes relevant to experiment (see Figs. 8 and 9).

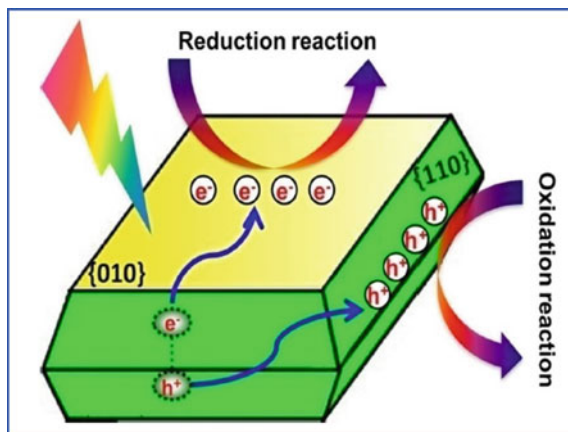


**Fig. 8** Facet selectivity enhances charge separation and reactivity and promotes solar energy conversion efficiency [51, 60]

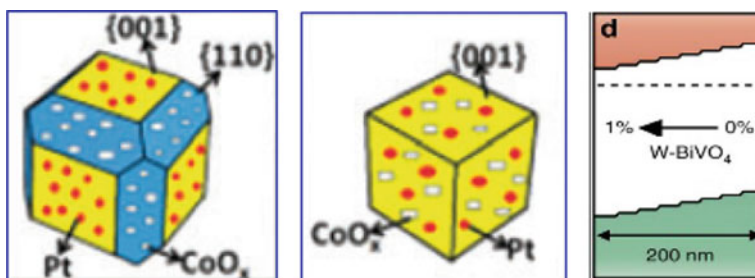


**Fig. 9** Selective spatial charge separation is observed for 18-facet STO (left panel) but not for 6-facet STO (middle panel) [60]. Homo-junction from doping concentration gradient in W-BVO promotes charge separation (right panel) [57]. KMC can provide a fundamental characterization of these systems

Considering the significance of the discovery of facet selectivity in  $\text{Cu}_2\text{O}$  for photocatalytic water oxidation concurrently with  $\text{CO}_2$  reduction, we will want to investigate carrier transport in  $\text{Cu}_2\text{O}$ . A number of DFT studies of  $\text{Cu}_2\text{O}$  have appeared that discuss the nature and origin of carriers, but none have addressed transport [64, 126–129]. Conduction in  $\text{Cu}_2\text{O}$  is known to be polaronic [126]. Clearly, characterizing computationally  $\text{h}^+$  polarons in  $\text{Cu}_2\text{O}$  is challenging in itself due to the electron-rich  $3d$  states of Cu contributing strongly to the top of the valence band. Electron correlated electronic structure calculations beyond DFT are likely to be required as a prerequisite to periodic DFT calculations.

Nanoparticle sizes in experiments are upward of  $\sim 500$  nm in size. Our initial simulations dealt with cell sizes of  $\sim 50$  Å and up to  $50 \text{ e}^-$  or  $\text{h}^+$  carriers. Parallel implementation and execution of the code should allow simulations up to  $\sim 100$  to  $200$  nm in size with  $\sim 100$  electrons. Such sizes and carrier densities are in regimes relevant to experimental situations. Note that  $\text{h}^+$  mobility simulations are significantly more demanding than  $\text{e}^-$  mobility simulations owing to the larger number of anions (oxygens) compared to cations (metals). Two capabilities that ought to be implemented to model finite size particles and facet selectivity include the treatment of free-space boundaries (in KMC configurational energy calculation by Ewald summation) and the inclusion of surface reaction events among the KMC events that carriers can undergo.

Regarding surface reaction events, in our lattice based KMC model, carriers occupy lattice sites at any given time. Their next moves are stochastically determined among the possible events for these sites. To include surface reactions in the model, we need to append a new event, a ‘OER redox reaction event’, to the list of events available to carriers at surface exposed sites. We will need reaction rates for these ‘surface reaction events’, quantities that we can determine from the Marcus-Gerischer model for electron transfer at electrodes [130–133] following the protocol by the Bieberle-Hutter group for water oxidation on hematite  $\text{Fe}_2\text{O}_3$ , based on the four intermediates of the traditional PCET mechanism [134, 135]. Each step has a Gerisher rate determined from the DFT step free energy and the valence band maximum level. The needed data are available for the (010) and (011) facets of BVO [136], and can be easily determined for STO and other semi-conductors. To insure consistency of data from one surface to another, we can use the facet work function or the bismuth Bi or Vanadium V core levels to align the VB and CB energy levels across facets [101]. We should be able to extract a single effective OER rate from the four elementary rates to be used in the KMC model.

An important question to address is accuracy in KMC modeling. By in large, mobility data extracted from KMC simulations are most sensitive to the activation barriers of the processes, owing to the exponential dependence of hopping rates, both in the non-adiabatic and in the adiabatic regimes. It is worth noting that  $k_B T$  at  $300$  °K is  $\sim 0.026$  eV. Accordingly, a change in  $\Delta G^*$  by  $\sim 0.060$  eV brings a factor of  $\sim 10$  change in mobility. Reaching this level of accuracy (nearly chemical accuracy in chemistry) is a tall order but it is not out of reach. DFT calculations mentioned earlier for BVO yielded activation barriers of  $\sim 0.37$  eV for electron polarons (without



the electronic coupling adjustment), compared to  $\sim 0.30$  eV experimentally [100]. Previous calculations on  $\text{Fe}_2\text{O}_3$  and  $\text{TiO}_2$  yielded similar or closer agreement [87, 97, 105]. Nonetheless validation of this type is constantly useful and required.

In a brief conclusion of where we are to date, we note that we are able to model separately  $e^-$  and  $h^+$  polarons and their dynamics in semiconductors like bismuth vanadate  $\text{BiVO}_4$ . [89, 90] The methodology is however general and can be extended to more complex modeling that include other elementary processes, such as polaron generation, polaron recombination, and polaron surface redox reactivity, as long as we have rates. Extending the mesoscale modeling of the PEC systems, through combined QM and lattice based KMC studies has the potential to lead us to solid theoretical foundations of facet selectivity in nanoparticles. This effort will take us closer to a more global simulation model of PEC's from the level of atomic-scale description, all the way to microscale description, for example in nanoparticles of  $\text{BiVO}_4$  and  $\text{SrTiO}_3$  for which experimental data is available. We should remark that there are a great many number of materials that are being evaluated, experimentally mostly, for use as anode and cathode materials [15]. There might be merit in investigating their transport properties systematically by computation and simulation. Nonetheless, resolving our understanding of the phenomenon of facet selectivity is likely to be uniquely impactful with great prospects in technology.

### 3.2 Mesoscale Modeling in Photo-Electro-Catalysis

As indicated earlier, our vision, depicted in Fig. 5 above, is to have the ability to simulate the overall efficiency of solar-to-fuel conversion in photo-electro-chemical devices [137]. The modeling starts from first-principle characterization of all essential elementary processes in light absorption, carrier transport, and redox reactivity (across several orders of magnitude in time scales). The modeling continues with the determination of the complex and collective kinetics of carrier transport and activity in mesoscale models [125, 138]. The ultimate outcome is the conversion efficiency, e.g. the number of product molecules per absorbed photons, a number which depends on the three phases of PEC conversion (absorption, transport, and redox reactivity). For a given system, one or more of these phases could be the limiting factor.

Our initial efforts have been on 'carrier transport' broadly speaking, including the development of necessary tools to model 'transport' qualitatively and quantitatively. We stipulated that both quantum chemical tools and mesoscale kinetic tools would be required and that the ability to combine first-principles characterization with mesoscale kinetics modeling would prove to be critically important for both *qualitative and quantitative* understanding. Our  $\text{BiVO}_4$  studies to date bear this point [90, 100]. The necessity to combine scales is likely to be pervasive due to the complexity of materials and device architectures for PEC conversion.

With regard to 'carrier transport', physical situations that promote charge separation and, as a consequence, conversion efficiency include multi-phase and/or multi-material junctions [53, 54], single-phase homo-junctions [55–57], and the use of

cocatalysts [12, 58, 59]. *Crystal facet engineering and interface engineering* are emerging as highly promising approaches to enhance carrier separation and overall water splitting efficiency, both for hydrogen evolution and oxygen evolution [51, 54, 60, 61]. At the present, synthesis efforts in this field appear Edisonian. We envision that our efforts with multi-scale computation and simulation will be an important contribution toward reaching rational design.

*Facet engineering* (Fig. 8) involves the synthesis of crystals with exquisite control of facet growth, and a concomitant separation of photo-excited electrons and holes [51, 60]. For example, in bismuth vanadate  $\text{BiVO}_4$  (BVO) photo-generated electrons accumulate mainly on (010) facets and holes on (110) facets as inferred from noble metals (Au, Ag, and Pt) depositing selectively on exposed (010) facets (reduction) and metal oxide ( $\text{PbO}_2$  and  $\text{MnO}_x$ ) particles on (110) facets (oxidation) [51]. Similar observations exist for several other semiconductors [61, 139]. Perhaps a most dramatic example is found in the observation of facet selectivity for 18-facet cubic strontium titanate  $\text{SrTiO}_3$  (STO) and the absence of facet selectivity for 6-facet cubic STO [60, 140] as illustrated in Fig. 9.

Several explanations have been put forward to rationalize the observed selective photo-deposition: a. preferred migration of holes and electrons to specific crystal facets under photo-illumination [12]. b. preferred selective sorption of metal and oxides on surface sites [13]. c. different conduction band and valence band levels for different facets. d. different internal electric fields along particular directions [11]. In catalysis, corners, edges, kinks are often thought of as sites with higher activity because of the stronger electrostatic potentials and fields at these sites. While such an argument may apply here as well, it does not explain why deposition/precipitation from oxidation or reduction occurs all over the flat surfaces, including away from corners.

Below, we will highlight progress we have made in addressing facet selectivity in BVO. To date we showed that there is no directional anisotropy in  $e^-$  or  $h^+$  transport (*no kinetic* factor of facet selectivity). We established that  $h^+$  transport is bimodal, with a rattling mode that is not transport-efficient and a slower transport-efficient mode [100]. We showed also that the near-surface thermodynamic stability of  $e^-$  or  $h^+$  is qualitatively similar for different facets (*no thermodynamic* factors of facet selectivity) [101]. These findings point to the need to account for the kinetics of the interfacial redox reactions to ‘see’ facet selectivity in simulation. In addition, we considered sulfur-doped BVO and established that sulfur-to-sulfur hopping transport of  $h^+$  replaces the ineffective bimodal oxygen-to-oxygen transport. These observations are very significant with regards to modeling PEC systems. Indeed, they are a clear demonstration that mesoscale modeling is essential to characterize and understand the attributes of PEC systems. Mesoscale modeling captures the critical connection between elementary hopping rates and crystal structure and topology with regards to transport. Interpretations based on elementary hop characterization, even if at the quantum level of theory, have the potential to be misleading.

*Multi-phase junctions and homo-junctions: multi-phase junctions* have long been thought as promoting redox activity. Indeed mixed-phase titania  $\text{TiO}_2$  is known to be more active than single phase titania [141–143]. It is also well established that the

degree of interconnectivity between crystallites and the structure of grain boundaries affects transport of carriers in materials [144–150]. Characterizing, quantifying, and understanding the fundamental parameters that control the diffusive  $e^-/h^+$  transport across structurally complex interfaces is essential for an overall assessment of transport. *Homo-junctions* are ‘interfaces’ within a material that occur at the boundaries of layers with different levels of doping (more about homo-junctions below). While doping is generally used to increase the concentration of charge carriers and tune band edges, doping with a gradient concentration has been shown to enhance carrier separation by creating homo-junctions, and leading to increased overall catalytic efficiency [55–57]. It is noteworthy that doping levels in homo-junctions are low and yet, they affect carrier transport, separation, and conversion efficiency at the larger scale. *The characterization of these effects requires mesoscale modeling.* Their physics are traditionally described in terms of band bending and carrier depletion regions. In our work, we like to give a chemistry-based, atomistic-derived description and characterization at the mesoscale of carrier transport across multi-phase junctions and homo-junctions with doping levels relevant to experiment.

In summary, both facet engineering and junction engineering share the common trait regarding carrier transport simulation: they require combined atomistic and mesoscale kinetic modeling to provide a fundamental understanding of the factors that create and affect space-charge distributions and their temporal evolutions. *The combined modeling can give important insights on what the bottlenecks for ‘good’ transport are.* The ability to characterize and predict these effects will ultimately enable the control of carrier transport, separation, and redox reactivity.

### 3.3 Highlights

*The overarching theme of our PEC research is to characterize and model the transport of photo-generated electrons and holes in complex crystalline materials to establish the theoretical foundation for facet and interface engineering,* two strategies used to tailor charge separation and to promote redox activity. The enabling elements of these strategies originate in the dynamics of charge carriers at the mesoscale. The leading factors that control charge separation can be several, thermodynamics, dynamics, or surface reactivity. Manipulating carrier separation in facet-selective, mixed-phase, and doped systems offers opportunities to control and enhance solar energy conversion efficiency.

Describing the *mesoscale* behavior of carriers is a challenge that requires modeling beyond traditional ways of single species ( $e^-$  or  $h^+$  polaron) and individual processes (polaron stability, trapping, and hopping), even if done at the quantum chemical (QM) level of theory. Our approach to investigating facet and phase selectivity has been to create *lattice based kinetic Monte Carlo (KMC) models of space-charge distribution dynamics and reactivity* based on individual processes characterized at first principles levels of theory (Fig. 6). Note that it is critically important to *validate* the models using relevant, available, computed and/or experimental data for well-characterized

materials. To accomplish these tasks, we *developed*, as needed, selected original QM and KMC tools and methodologies.

To date, we have made major progress toward this goal, to the point that we are getting closer to being able to use the model to *formulate and predict design* points for absorption, transport, and reactivity for enhanced overall photocatalytic performance. We are at a point where we need to include surface reaction processes in our mesoscale models. This is a major objective at present. In addition, we have identified selected other important fundamental contributions that we can make and that will advance the state-of-the-art in studies of condensed phase and interfacial molecular science in photo-electro-chemical conversions.

### 3.3.1 Carrier Transport: The Case of Bismuth Vanadate BVO

Our goal was to model  $e^-/h^+$  transport in doped and undoped materials such as bismuth vanadate  $\text{BiVO}_4$  (BVO), tantalum nitride  $\text{Ta}_3\text{N}_5$ , and other materials (like strontium titanate  $\text{SrTiO}_3$  (STO)) that exhibit the intriguing phenomenon of *facet selectivity* in oxidation and reduction chemistry (Fig. 8 above). Oxidation occurs on some facets, reduction on other facets. We aimed to establish the theoretical foundation for facet selectivity and other strategies to enhance carrier separation and improve solar energy conversion performance. The combined QM+KMC mesoscale approach that we used has proven essential to understand the nature of intrinsic carrier transport and the role of cation and anion doping in affecting transport. The insights from mesoscale modeling are a step toward *screening of photo-active materials* with superior photocatalytic performance. Structural and chemical descriptors of ‘good’ transport and carrier separation ability are starting to emerge.

- *Mesoscale transport dynamics in  $\text{BiVO}_4$* : We recently completed a study of carrier transport in BVO. DFT calculations indicated that thermodynamic stability is not a factor in facet selectivity. A thorough characterization of  $e^-$  and  $h^+$  hopping pathways in BVO yielded activation energies  $\sim 0.36$  eV for electrons, and as low as  $\sim 0.17$  eV for holes. Mesoscale KMC modeling revealed that hole transport is not nearly as efficient as the low barrier would suggest. Hole transport is *bi-modal*, with very fast but not transport-efficient hops (‘rattling’ motion) and slower but transport-efficient hops [100], as depicted in Fig. 10. It emerged from this work that strategies to eliminate hole ‘rattling’ will improve hole transport efficiency and water oxidation performance.

This work illustrates how mesoscale modeling is critically important to reveal fundamental characteristics of carrier transport. KMC captures the connection between elementary hopping rates and material structure and topology. Interpretations based on elementary hop characterization alone, even if at the quantum level of theory, have the potential to be misleading.

Toward modeling facet selectivity in BVO, we have investigated the thermodynamic stability of  $e^-/h^+$  on ‘bulk’ sites compared to ‘near-surface’ or ‘surface’ sites [101]. A cursory look at the data plotted in Fig. 11 does not appear to reveal striking

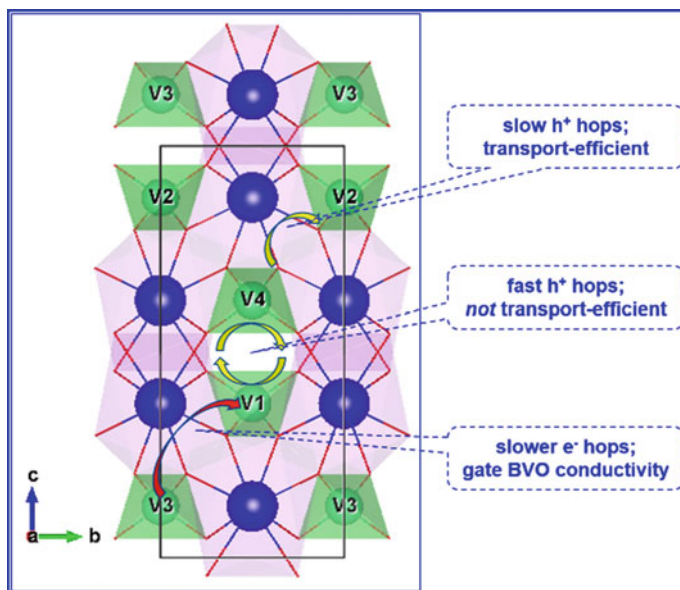


**Fig. 10** Bimodal h<sup>+</sup> transport in BVO. e<sup>-</sup> transport gates BVO conductivity [89]

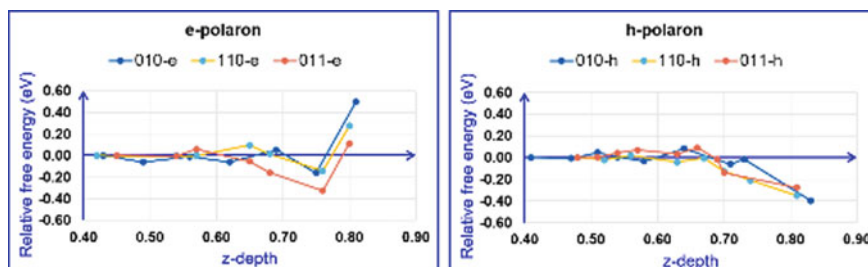


**Fig. 11** Bulk versus surface stability of e<sup>-</sup>/h<sup>+</sup> polaron in BVO [101]

preferences in stability from one facet over the others. e<sup>-</sup> polarons prefer sub-surface sites over exposed surface sites and bulk sites. The stronger stability for the (011) surface may affect the space-charge distribution dynamics and, perhaps, the facet selectivity of e<sup>-</sup> polarons. New KMC simulations are in progress and are expected to reveal such effects. h<sup>+</sup> polarons appear to have a more homogeneous behavior across facets.

*Cation and anion doping in BiVO<sub>4</sub>:* cation doping of BVO with W/Mo has been shown to enhance conversion efficiency in BVO-based devices. We studied how W/Mo doping of BVO affects carrier mobility and electric conductivity [90]. W/Mo doping results in a small decrease in electron mobility. However, the increase in carrier density upon doping overshadows the marginal decrease in electron mobility,

resulting into an increased electronic conductivity. Work in progress deals with modeling homo-junctions, layered systems with a gradient of W-doping concentration and anion-doped BVO with ~25% level of sulfur doping, that have been shown to enhance charge separation. Simulations show that hole ‘rattling’ is eliminated by S-doping, as hole transport is reduced to S-to-S hopping.

### 3.3.2 Carrier Utilization: Solar-To-Fuels Surface Reactions

We pointed out in Sect. 1 that improved detailed knowledge and understanding of the interface reactions is needed to design better performing solar fuels catalysts [9, 15, 17]. Time-resolved IR spectroscopy is useful to characterize the reactions intermediates [72–74] and it has been used for a number of materials, including BiVO<sub>4</sub>, TiO<sub>2</sub>, SrTiO<sub>3</sub>, and others. For water splitting, the emphasis has been more on water oxidation than on proton reduction as it is the bottleneck process in overall water splitting [75, 151–154].

The mechanism prevalently considered for water oxidation is the four proton-coupled-electron transfer (PCET) mechanism with \*OH, \*O, and \*OOH intermediate species [76]. Underlying the design of improved catalysts in general and in particular those based on the thermodynamics of the 4-step PCET model (also called ‘adsorbate evolution mechanism’ with cationic active sites), is the reliance on Sabatier’s principle of bonding strength [77] in conjunction with the Bell-Evans-Polanyi principle that ties kinetic barriers and step energies [92, 93]. Not all cases of water oxidation catalysts fall into the four-step PCET framework and other mechanisms have been proposed [73, 78]. One such mechanism is the ‘lattice oxygen mechanism’ (LOM) whereby lattice oxygens appear to be active specie [155–157]. To the best of our knowledge, *it remains challenging to predict which mechanism applies to which class of materials*. An increased understanding of the structure-redox activity of materials and of the chemical factors that govern the reaction mechanisms is highly desirable. Improved understanding can come from computation of reaction energy profiles and of properties of the intermediates (IR frequencies, charge and spin populations, and other quantities) as described below.

OER takes place on semiconductors that are not defect-free in general, and oxygen vacancies (Ovac’s) are the most common defects [158–162]. The overall effect of Ovac’s is broadly understood as improving carrier concentration and conductivity in the bulk, but it is not fully clear why and how they might improve surface reactivity and PEC conversion efficiency, for a number of materials including BVO [163–165], WO<sub>3</sub>, and hematite Fe<sub>2</sub>O<sub>3</sub> [166] and other materials. *This is an important question as experimentalists are making progress in synthesizing materials with varying levels of vacancy concentrations* [167]. From an experimental point of view, the features associated with excess electron arising from Ovac’s are often described in the solid-state terminology of gap states, deep trap states, and overlap of the gap state densities with the electronic states of the reactive water molecule. There is also some discussion of the degree of ionicity on the metal-oxygen bonds of the

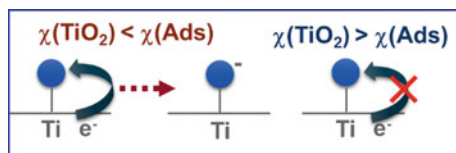


**Fig. 12** Illustration of charge transfer of excess electrons from Ovac from the surface to the adsorbate, depending on the relative electronegativity  $\chi$  of the surface and the adsorbate [167]

semiconductor when attempting to explain the trapping and reacting potentials of the defects [156, 163, 166].

We have been interested, for some time, in the role of excess electrons on the surface chemistry of oxides. As we did for charge carriers, our approach to the question of the effect of Ovac's on reactivity is to provide a chemistry-oriented understanding. It started with a '*universal*' role of excess electrons on the surface chemistry of  $\text{TiO}_2$  that we verbalized [168]. In this work we noted that excess electrons arising from Ovac's or interstitial Ti atoms can participate in charge transfer from the solid to an adsorbate, depicted in Fig. 12. The charge transfer makes the metal-adsorbate bond more ionic, and therefore stronger. The amount of stabilization depends on the electronegativity of the solid surface and of the adsorbate. Accordingly, the stabilization energy is different for  $\text{*OH}$ ,  $\text{*O}$ , and  $\text{*OOH}$  along the OER reaction coordinate. We confirmed this hypothesis in several of our studies: a. OER on oxygen-deficient  $\text{BaTiO}_3$ ; [169] b. OER on  $\text{Ga}_2\text{O}_3$ ; [170] c. comparison of 1e-, 2e-, and 4e- processes on oxygen-deficient rutile, anatase, and brookite [171].

For these systems, we investigated the stability of Ovac's on the surface versus sub-surface, the work function of the oxygen-deficient surfaces, the relative position of the gap states. We analyzed the structural data (bond lengths), the electron atomic populations on the cationic sites and adsorbates, and the spin atomic populations using Bader analysis. These data led us to characterize the amount of charge transfer from the solid to the adsorbate on the pristine surfaces compared to the reduced surfaces. Strong charge transfer correlate with strong free energy stabilization. The OER energy diagrams exhibit variations in step free energies consistent with the amount of charge transfer and charge transfer, as seen in Fig. 16.

The presence of Ovac's may or may not lower the overpotential, depending on how much stabilization is gained in one intermediate over the other ones. Too strong a stabilization in one intermediate is not desirable as it makes a step free energy too large and increases the overpotential (Sabatier principle). Among the intermediates  $\text{*OH}$  has a strong electronegativity. So has  $\text{*O}$  in its dangling structure. In contrast,  $\text{*O}$  as a peroxo species (O atoms inserted in a metal-O-metal motif to give a metal-O-O-metal motif) does not have a strong electronegativity since all of its valencies are full. Lastly,  $\text{*OOH}$  has a weaker electronegativity. These differences lead to strongly changing reaction energy profiles and overpotentials, as depicted in Fig. 13 for rutile. *Thus, knowing and predicting the charge transfer ability of the material is key to manipulating the overpotential.*

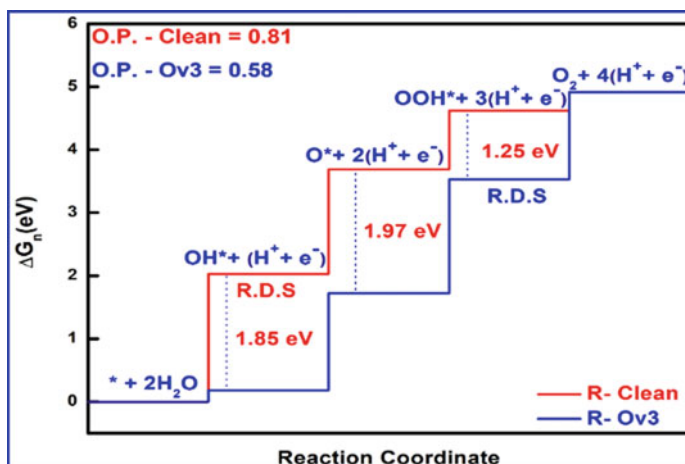


**Fig. 13** OER free energy reaction profile and associated overpotential for pristine and oxygen-deficient rutile. O\* is a peroxo species for the clean surface and a dangling O\* species for the oxygen-deficient surface [171]

We uncovered two types of charge transfer: a. in some cases the pristine surface transfers electron density to the adsorbate, and the excess electrons from Ovac stabilize the electron-deficient solid. b. in other cases the pristine surface transfers no or little charge density to the adsorbate, and the excess Ovac electrons are directly involved in the charge transfer [171]. These studies were carried with the VASP code [172, 173] with charge analyses performed with the Bader theory of atoms in molecules [174].

We plan to carry out similar studies for BVO and  $\text{Fe}_2\text{O}_3$  in the presence of oxygen vacancies. With the recent availability of detailed experimental measurements about the gap states [163], we will be in a position to compare work functions and gap state levels, to correlate these quantities with charge transfer, and to assess theory vs. experiment. The charge transfer analysis will be the connection between data on surfaces and the reaction thermodynamics. Of special interest will be comparisons between the traditional 4 PCET-step mechanism and the lattice oxygen mechanism that has been suggested for  $\text{Fe}_2\text{O}_3$ . We will make use of the extensive study by Hegner et al. of the structure of Ovac's in BVO [165]. These authors have identified two distinctive structural motifs of Ovac's in BVO with comparable formation energies. Our work will characterize these structures from the point of view of their charge transfer ability to the OER intermediates. For the key intermediates on pristine surfaces and on oxygen-deficient surfaces, we will go on to determine their spectroscopic IR signature.



## 4 Challenges in Computation and Modeling in Photo-Electro-Catalysis

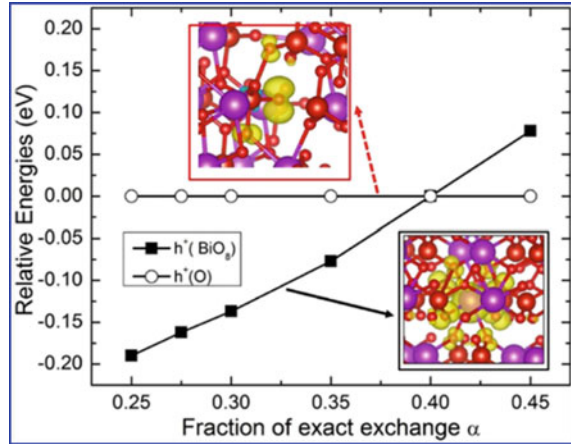
While computation and modelling in photo-electro-catalysis has been broadly successful in providing fundamental characterization and understanding of the physics and chemistry of PEC's, there remain some important challenges about the consistent reliability of predictions. It is well understood and accepted for example that functionals of the density that account for the 'local' density only (LDA), or those of the 'generalized gradient approximation' type (GGA) under-estimate consistently band gaps. A correction to the inherent 'self-interaction' of electrons in DFT is required, and this is commonly achieved by the use of the DFT+U formalism or the use of hybrid functionals. For the description of excitons and polarons the challenge remains. The two approaches yield qualitatively different descriptions of polarons as illustrated below. This observation underscores the need for theorists to develop functionals of density for DFT and/or other advanced theories, perhaps based on wavefunction theories, that provide computational characterizations that are more consistently reliable. Careful cross-validation of theory and experiment is critically important. In what follows we highlight work in our group that points to this type of challenges in functionals of the density, and other that is underway about validation.

### 4.1 Challenge to DFT: Accurate and Reliable Functionals for Polarons and Excitons

As mentioned, when modelling the polaron in materials, corrections to electron self-interaction need be included in the DFT formalism, in the form of DFT+U [175] or hybrid functionals [176] like PBE0 [177] and HSE06 [178]. These approaches have ad hoc parameters that researchers adjust often, mainly by choosing the +U values or the fraction of the exact exchange mixed into the functional.

About polarons in  $\text{BiVO}_4$  (BVO), that  $e^-$  and  $h^+$  polarons exist is confirmed by experiment [179–181]. For  $e^-$  polarons, there is a general concurrence that they are localized on the V sites in BVO, and that they form small polarons. The DFT+U approach [89, 182–184] and the hybrid functional approach [115, 185, 186] yield the same picture of  $e^-$  polarons. For the  $h^+$  polarons in BVO, there are very notable differences between these theories. Using HSE06 functional (with 25% fraction of the HF exchange), Kweon and Hwang [187, 188] reported that the charge of the excess hole spreads over one  $\text{BiO}_8$  dodecahedron or across many Bi and O atoms, depending on the BVO phase. Using PBE0 functional (with 22% fraction of HF exchange) and molecular dynamics (MD) Wiktor [185] et al. found that the hole charge is distributed between one bismuth and eight oxygen atoms, and in about 20% of the MD configurations the hole appears localized on a single oxygen atom. In contrast, using a DFT + U level of theory with  $U_{\text{eff}} = 9$  eV, Pasumarthi [184] et al. and Liu [183] et al. found that an excess hole localizes strongly on a single

**Fig. 14** Relative energies of the two holes polaron structures  $h^+(\text{BiO}_8)$  and  $h^+(\text{O})$  obtained with HSE( $\alpha$ ) for each value of  $\alpha$  when  $\alpha$  varies from 0.25 to 0.40: square symbols are for the hole distributed over one Bi atom and the neighboring oxygen atoms,  $h^+(\text{BiO}_8)$ ; circle symbols are for the hole localized on two or one oxygen atom,  $h^+(\text{O})$  [102]



oxygen atom. The optimized structure exhibits a Bi-O bond lengthening in the range of  $\sim 0.12$  to  $\sim 0.18$  Å. Recently, Liu [189] et al. re-investigated the structure of hole polarons in BVO using hybrid DFT with varying fractions ( $\alpha$ ) of the exact exchange interaction that enters hybrid functionals. For values of  $\alpha$ , from  $\alpha = 0.25$  to  $\alpha = 0.45$ , both the  $h^+(\text{BiO}_8)$  hole structure and the  $h^+(\text{O})$  hole structure were obtained. For the smaller values of  $\alpha$ , the  $h^+(\text{BiO}_8)$  structure was found to be lower in energy, while for the larger values of  $\alpha$ , the  $h^+(\text{O})$  structure was found to be more stable as shown in Fig. 14. For  $\alpha = 0.25$ , the diffusivity of  $h^+(\text{BiO}_8)$  holes determined from the Marcus/Holstein two-state model was determined to be in close agreement with published THz experimental data.

Another example of contrasting findings is about  $e^-$  and  $h^+$  polarons in oxynitrides and nitrides. The charge transport mechanism in these materials proved to be more complex than in metal oxides, as the N 2p state is less strongly localized than the O 2p orbital. Using time resolved microwave conductivity (TRMC) measurements, Respinis [190] et al. observed the carrier mobility increased with the nitrogen content from  $1 \times 10^{-5} \text{ cm}^{-2} \text{ V}^{-1} \text{ s}^{-1}$  in  $\text{Ta}_2\text{O}_5$ , to  $1 \times 10^{-2} \text{ cm}^{-2} \text{ V}^{-1} \text{ s}^{-1}$  in  $\beta\text{-TaON}$ , up to  $1 \times 10^{-1} \text{ cm}^{-2} \text{ V}^{-1} \text{ s}^{-1}$  in  $\text{Ta}_3\text{N}_5$ . Lee [191] et al. predicted the formation of spin-polarized polarons in  $\text{Ta}_2\text{O}_5$  with oxygen vacancies using hybrid functionals. Morbec and Galli [192] reported charge transport properties of the  $\text{Ta}_3\text{N}_5$  from first principles calculations. They found that small  $e^-$  polarons may occur but  $h^+$  polarons are not energetically stable according to the DFT+U approach. The estimated polaronic mobility for electron calculated by DFT+U approach is at least three orders of magnitude smaller than that of the measured value. Accordingly, the authors suggested that the main transport mechanism for both  $e^-$  and  $h^+$  is band-like. Dey [193] et al. studied small polaron formation in  $\beta\text{-TaON}$  using DFT + U approach. They found that an excess electron tends to form a localized small polaron on a Ta site. The calculated diffusion barrier was  $\sim 0.3$  eV, and the calculated mobility  $\sim 9.41 \times 10^{-5} \text{ cm}^2 \text{ V}^{-1} \text{ s}^{-1}$  in pristine TaON, calculated values that are at least two orders of magnitude smaller than the measured values. Liu [194] et al. investigated the charge

transport properties in  $\text{Ta}_2\text{O}_5$ ,  $\text{TaON}$ , and  $\text{Ta}_3\text{N}_5$  by polaron hopping and band-like models. From the polaron binding energies and hybrid functional calculations, they found the charge transport mechanism to be small polaron hopping in  $\text{Ta}_2\text{O}_5$ , whereas in  $\text{TaON}$  and  $\text{Ta}_3\text{N}_5$  hopping may not occur. Furthermore, the calculated mobility from the band-like model was not found consistent with experimental results neither.

These examples underscore the challenges with DFT approaches when investigating polarons in semiconductor. Which method to use (DFT+U or hybrid functional), and what values of +U values or of the fraction of HF exchange, are unsettled questions. There is a clear need for more accurate theoretical treatments, possibly some derived from molecular wavefunction formalisms and extended to the solid state.

## 4.2 *Exciton Structure and Dynamics: Cross-Validation of Theory and Experiment.*

In the same vein of validation of theory and experiment, recent experimental findings and chemical descriptions of excitons and polarons in selected oxides can be viewed as challenges to theory! The theoretical characterization of these ‘species’ with the most advanced tools of electronic structure of molecules and solids should prove a fertile ground for cross-validation of theory and experiment.

*Exciton in  $\text{Fe}_2\text{O}_3$ :* Emerging XUV experimental techniques are providing remarkable descriptions of the electronic structure of excited states (excitons) in short times following the event of light absorption [40]. By following the oxidation states of the elements through XUZ spectroscopy, the Baker group assigned a generation time of less than 100 fs to  $e^-/h^+$  excitons in  $\text{Fe}_2\text{O}_3$ ,  $\text{Co}_3\text{O}_4$ , and  $\text{NiO}$ , and a small polaron relaxation time of  $\sim 660$  fs. Perhaps most striking is the assignment of the exciton radius of a single metal-oxygen bond length, as schematically displayed in Fig. 15. To the best of our knowledge, this is the first atomic scale ‘localized’ description of an exciton (excited state) in a ‘strongly correlated’ extended system. In fact, discussions of excitons are most often in terms of band theory, rarely in terms of ‘localized’ concepts as in the present cases.

Highly accurate excited-state methods have been developed in recent years in chemistry, but, typically, they are not benchmarked against metal oxide data. Time-dependent DFT (TDDFT) is also extensively used in chemistry as it permits to investigate larger systems at reduced computational costs. The availability of the ‘localized’ atomistic pictures for the materials mentioned above offers the opportunity to validate experiment against ‘molecular-based theories of excited states while validating excited states theories applied to strongly correlated systems against experiment. Beyond  $\text{Fe}_2\text{O}_3$ , we could consider similar investigations of  $\text{Co}_3\text{O}_4$ , and  $\text{NiO}$  for which XUV characterization is available. Perhaps most intriguing would be similar exciton studies of BVO, a material in which the configuration of the metal cation is

**Fig. 15** Illustration of exciton in  $\text{Fe}_2\text{O}_3$ , based on XUV characterization of Biswas et al. [39]. The exciton radius is found to be of a single metal oxygen bond length. An electron is excited from an O  $2p$  lone pair state into the  $3d$  state of an Fe atom directly linked to the O atom. High-level excited state calculations will be carried out to validate the experiment-derived description, while the experimental data will help to validate the theories

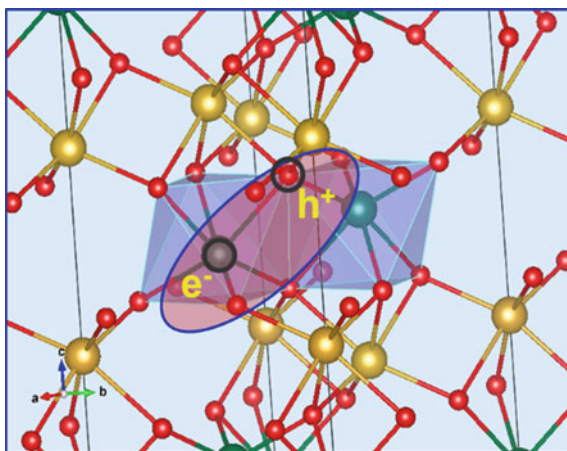
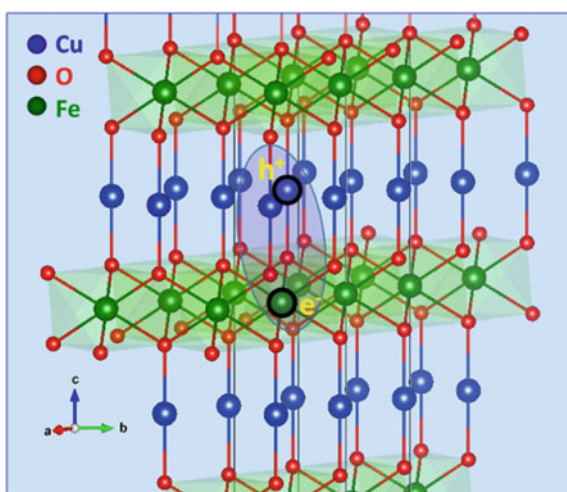


**Fig. 16**  $h^+$  polaron structure in  $\text{CuFeO}_2$  adapted from Ref. [41]. The hole thermalizes into a Cu  $3d$  state, with potential mobility anisotropy in the Cu layer versus across the  $\text{FeO}_2$  layer



formally  $V 3d^0$  and whether the exciton radius might be or not a single metal-oxygen bond length.

The significance of such studies cannot be over-emphasized. They are far-reaching in that address a fundamental issue heretofore not enunciated, mainly the description as ‘localized’ of excitons in oxides such as hematite  $\text{Fe}_2\text{O}_3$ . At the same time, such studies would serve as stringent validation, as they’d provide a critical validation of excited state theories against experiment for strongly correlated systems like metal oxides.

*$h^+$  polaron in  $\text{CuFeO}_2$* : delafossite  $\text{CuFeO}_2$  is another material of interest. It is an earth-abundant metal oxide with good stability in aqueous environments and

favorable light absorption properties. It is attracting very strong attention as a photocathode [15, 41] for proton reduction. Electron-hole separation efficiency (exciton lifetime), carrier mobility, and existence of surface states promoting carrier recombination, are issues that can benefit from theoretical characterization [15, 95]. The XUV spectroscopy-based description by Baker et al. of the ‘localized’, site-specific, structure and dynamics of holes that evolve from O  $2p$  holes into hybridized Cu  $3d$  holes within  $\sim 500$  fs is interesting and challenging [41]. The structure is depicted in Fig. 16. It shows a hole localized in a Cu  $3d$  state rather than an O  $2p$  state. From a fundamental understanding, it is important to know why holes localize on Cu. Few DFT studies of  $\text{CuFeO}_2$  have been reported. The density of states suggests that O  $2p$  states and Cu  $3d$  states contribute to the top of the valence band, indicative of a strong mixing of the atomic states [195]. We note the symmetric environment around Cu sites (Fig. 16), so that the super-exchange interaction of O  $2p$  holes may turn a double-well oxygen hole into a single-well Cu hole [196]. We are in a unique position to be able to validate the XUV picture, as well as to establish the characteristics of  $e^-$  and  $h^+$  transport in  $\text{CuFeO}_2$ . Beyond the electronic structure issue, there is the potential for a strong anisotropy in mobility in the Cu layer vs. across the  $\text{FeO}_6$  layers, clearly seen in Fig. 16.

## 5 Conclusion and Outlook

In this chapter we presented a broad overview of photo-electro-catalysis, a high risk, high-payoff domain of renewable energy. Efficient and cost-effective inter-conversion of electrical and chemical energy is widely accepted as an essential element of a broad strategy toward renewable energy. Current system conversion efficiencies, including for solar water splitting, are however far from the level needed for practical applications. From the standpoint of computation and modeling, there is already a wide body of research that has been instrumental in leading to new understanding and predictions of improved electrode materials for PECs with enhanced conversion efficiencies. The research encompasses computation and modeling for material structure, carrier transport, and redox reactivity. Modern DFT capabilities and multiscale models have already led to the characterization of new materials, of small polaron structures and dynamics [97, 105, 168], and new redox-active semiconductors, all contributions that are impactful in the field [107, 109]. Continuing developments and application, supported by cross-validation of experiment and theory, are expected to significantly advance the field further in years to come.

**Acknowledgements** MD gratefully acknowledges support from the U.S. Department of Energy, Office of Science, Office of Basic Energy Sciences, under Award Number DE-SC0019086. TL acknowledges support from the National Natural Science Foundation of China (grants # 21703054 and #22173026). The authors gratefully acknowledge many stimulating and guiding discussions with Professor Can Li, Director, and many staff members in the Solar Energy Division of the Dalian Laboratory for Clean Energy at the Dalian Institute for Chemical Physics in Dalian, China, where much of the work described in this chapter was initiated.

## References

1. Nocera, D.G.: The artificial leaf. *Acc. Chem. Res.* **45**, 767–776 (2012)
2. USDOE/BES. Basic Research Needs for Catalysis Science (2017). <https://www.science.energy.gov/bes/community-resources/reports/>
3. NSF. Catalytic Chemistry Workshop on Defining Critical Directions for the Future (2011). [http://www.faculty.chemistry.harvard.edu/files/friend-lab/files/nsf\\_catreport\\_final\\_august\\_2011\\_mar2013\\_1.pdf](http://www.faculty.chemistry.harvard.edu/files/friend-lab/files/nsf_catreport_final_august_2011_mar2013_1.pdf)
4. USDOE/BES. Computational Materials Science and Chemistry: Accelerating Discovery and Innovation through Simulation-based Engineering and Science (2010). <https://www.science.energy.gov/bes/community-resources/reports/>
5. USDOE/BES. Science for Energy Technology: Strengthening the Link Between Basic Research and Industry (2010). <https://www.science.energy.gov/bes/community-resources/reports/>
6. USDOE/BES. Basic Research Needs for Solar Energy Utilization (2005). <https://www.science.energy.gov/bes/community-resources/reports/>
7. Cook, T.R., Dogutan, D.K., Reece, S.Y., Surendranath, Y., Teets, T.S., Nocera, D.G.: Solar energy supply and storage for the legacy and non legacy worlds. *Chem. Rev.* **110**, 6474–6502 (2010)
8. Maeda, K., Teramura, K., Lu, D.L., Takata, T., Saito, N., Inoue, Y., Domen, K.: Photocatalyst releasing hydrogen from water—enhancing catalytic performance holds promise for hydrogen production by water splitting in sunlight. *Nature* **440**, 295 (2006)
9. Han, H., Li, C.: Photocatalysis in solar fuel production. *Natl. Sci. Rev.* **2**, 145–147 (2015)
10. Shi, J., Li, C.: Photoelectrochemical approach using photocatalysts. In: Sugiyama, M., Fujii, K., Nakamura, S. (Eds.) *Solar to Chemical Energy Conversion: Theory and Application*. Lecture Notes in Energy, Vol. 32, pp. 319–344 (2016)
11. Sivula, K., van de Krol, R.: Semiconducting materials for photoelectrochemical energy conversion. *Nat. Rev. Mater.* **1** (2016)
12. Yang, J.H., Wang, D.G., Han, H.X., Li, C.: Roles of cocatalysts in photocatalysis and photoelectrocatalysis. *Acc. Chem. Res.* **46**, 1900–1909 (2013)
13. Kudo, A., Miseki, Y.: Heterogeneous photocatalyst materials for water splitting. *Chem. Soc. Rev.* **38**, 253–278 (2009)
14. Osterloh, F.E.: Inorganic materials as catalysts for photochemical splitting of water. *Chem. Mater.* **20**, 35–54 (2008)
15. Abdi, F.F., Berglund, S.P.: Recent developments in complex metal oxide photoelectrodes. *J. Phys. D-Appl. Phys.* **50**, 193002–193024 (2017)
16. Wang, Z., Li, C., Domen, K.: Recent developments in heterogeneous photocatalysts for solar-driven overall water splitting. *Chem. Soc. Rev.* **48**, 2109–2125 (2019)
17. Montoya, J.H., Seitz, L.C., Chakhranont, P., Vojvodic, A., Jaramillo, T.F., Norskov, J.K.: Materials for solar fuels and chemicals. *Nat. Mater.* **16**, 70–81 (2017)
18. Yao, T.T., An, X.R., Han, H.X., Chen, J.Q., Li, C.: Photoelectrocatalytic materials for solar water splitting. *Adv. Energy Mater.* **8** (2018)
19. Chen, S.S., Qi, Y., Li, C., Domen, K., Zhang, F.X.: Surface strategies for particulate photocatalysts toward artificial photosynthesis. *Joule* **2**, 2260–2288 (2018)
20. Sivula, K.: A step toward economically viable solar fuel production. *Chem* **4**, 2490–2492 (2018)
21. Chu, S., Li, W., Yan, Y., Hamaan, T., Shih, I., Wang, D., Mi, Z.: Roadmap on solar water splitting: current status and future prospects. *Nano Fut.* **1**, 2399 (2017)
22. Zhang, N., Long, R., Gao, C., Xiong, Y.J.: Recent progress on advanced design for photoelectrochemical reduction of CO<sub>2</sub> to fuels. *Sci. China Mater.* **61**, 771–805 (2018)
23. Yin, W.J., Wei, S.H., Al-Jassim, M.M., Yan, Y.: Double-hole-mediated coupling of dopants and its impact on band gap engineering in TiO<sub>2</sub>. *Phys. Rev. Lett.* **106**, 066801–066804 (2011)

24. Dey, P., Bible, J., Datta, S., Broderick, S., Jasinski, J., Sunkara, M., Menon, M., Rajan, K.: Informatics-aided bandgap engineering for solar materials. *Comput. Mater. Sci.* **83**, 185–195 (2014)
25. Castelli, I.E., Huser, F., Pandey, M., Li, H., Thygesen, K.S., Seger, B., Jain, A., Persson, K.A., Ceder, G., Jacobsen, K.W.: New light-harvesting materials using accurate and efficient bandgap calculations. *Adv. Energy Mater.* **5**, 1400915–1400921 (2015)
26. Jain, A., Hautier, G., Moore, C.J., Ong, S.P., Fischer, C.C., Mueller, T., Persson, K.A., Ceder, G.: A high-throughput infrastructure for density functional theory calculations. *Comput. Mater. Sci.* **50**, 2295–2310 (2011)
27. Wu, Y., Lazic, P., Hautier, G., Persson, K., Ceder, G.: First principles high throughput screening of oxynitrides for water-splitting photocatalysts. *Energy Environ. Sci.* **6**, 157–168 (2013)
28. Godin, R., Wang, Y., Zwijnenburg, M.A., Tang, J.W., Durrant, J.R.: Time-resolved spectroscopic investigation of charge trapping in carbon nitrides photocatalysts for hydrogen generation. *J. Am. Chem. Soc.* **139**, 5216–5224 (2017)
29. Godin, R., Kafizas, A., Durrant, J.R.: Electron transfer dynamics in fuel producing photosystems. *Curr. Opin. Electrochem.* **2**, 136–143 (2017)
30. Kafizas, A., Godin, R., Durrant, J.R.: Charge carrier dynamics in metal oxide photoelectrodes for water oxidation. In: Mi, Z., Wang, L., Jagadish, C. (Eds.) *Semiconductors for Photocatalysis. Semiconductors and Semimetals*, Vol. 97, pp. 3–46 (2017)
31. Colbeau-Justin, C., Valenzuela, M.A.: Time-resolved microwave conductivity (TRMC) a useful characterization tool for charge carrier transfer in photocatalysis: a short review. *Rev. Mex. Fis.* **59**, 191–200 (2013)
32. Zarifi, M.H., Mohammadpour, A., Farsinezhad, S., Wiltshire, B.D., Nosrati, M., Askar, A.M., Daneshmand, M., Shankar, K.: Time-resolved microwave photoconductivity (TRMC) using planar microwave resonators: application to the study of long-lived charge pairs in photoexcited titania nanotube arrays. *J. Phys. Chem. C* **119**, 14358–14365 (2015)
33. Paulus, C., Wilke, K., Breuer, H.D.: Time resolved photocharge (TRPC) measurements on titanium dioxide: charge carrier dynamics and photocatalytic activity. *J. Inf. Record.* **24**, 299–306 (1998)
34. Wilke, K., Breuer, H.D.: The influence of transition metal doping on the physical and photocatalytic properties of titania. *J. Photochem. Photobiol. Chem.* **121**, 49–53 (1999)
35. Sadeghi, M., Liu, W., Zhang, T.G., Stavropoulos, P., Levy, B.: Role of photoinduced charge carrier separation distance in heterogeneous photocatalysis: oxidative degradation of CH<sub>3</sub>OH vapor in contact with Pt/TiO<sub>2</sub> and cofumed TiO<sub>2</sub>-Fe<sub>2</sub>O<sub>3</sub>. *J. Phys. Chem.* **100**, 19466–19474 (1996)
36. Butler, K.T., Dringoli, B.J., Zhou, L., Rao, P.M., Walsh, A., Titova, L.V.: Ultrafast carrier dynamics in BiVO<sub>4</sub> thin film photoanode material: interplay between free carriers, trapped carriers and low-frequency lattice vibrations. *J. Mater. Chem. A* **4**, 18516–18523 (2016)
37. Dringoli, B.J., Butler, K.T., Zhou, L., Giri, B., Rao, P.M., Walsh, A., Titova, L.V.: Ultrafast carrier dynamics in BiVO<sub>4</sub>: interplay between free carriers, trapped carriers and low-frequency lattice vibrations. In: 2016 41st International Conference on Infrared, Millimeter, and Terahertz Waves; International Conference on Infrared Millimeter and Terahertz Waves (2016)
38. Berger, T., Sterrer, M., Diwald, O., Knozinger, E., Panayotov, D., Thompson, T.L., Yates, J.T.: Light-induced charge separation in anatase TiO<sub>2</sub> particles. *J. Phys. Chem. B* **109**, 6061–6068 (2005)
39. Husek, J., Cirri, A., Biswas, S., Baker, L.R.: Surface electron dynamics in hematite (alpha-Fe<sub>2</sub>O<sub>3</sub>): correlation between ultrafast surface electron trapping and small polaron formation. *Chem. Sci.* **8**, 8170–8178 (2017)
40. Biswas, S., Husek, J., Londo, S., Baker, L.R.: Highly localized charge transfer excitons in metal oxide semiconductors. *Nano Lett.* **18**, 1228–1233 (2018)
41. Husek, J., Cirri, A., Biswas, S., Asthagiri, A., Baker, L.R.: Hole thermalization dynamics facilitate ultrafast spatial charge separation in CuFeO<sub>2</sub> solar photocathodes. *J. Phys. Chem. C* **122**, 11300–11304 (2018)

42. Carneiro, L., Cushing, S., Liu, C., Leone, S.: Evidence for small polaron formation leading to intrinsic photoexcited charge trapping in  $\alpha\text{-Fe}_2\text{O}_3$ . *Abstr. Papers Am. Chem. Soc.* **253** (2017)
43. Carneiro, L.M., Cushing, S.K., Liu, C., Su, Y.D., Yang, P.D., Alivisatos, A.P., Leone, S.R.: Excitation-wavelength-dependent small polaron trapping of photoexcited carriers in  $\alpha\text{-Fe}_2\text{O}_3$ . *Nat. Mater.* **16**, 819+ (2017)
44. Akimov, A.V., Prezhdo, O.V.: The PYXAID program for non-adiabatic molecular dynamics in condensed matter systems. *J. Chem. Theory Comput.* **9**, 4959–4972 (2013)
45. Akimov, A.V., Prezhdo, O.V.: Advanced capabilities of the PYXAID program: integration schemes, decoherence effects, multiexcitonic states, and field-matter interaction. *J. Chem. Theory Comput.* **10**, 789–804 (2014)
46. Akimov, A.V.: Nonadiabatic molecular dynamics with tight-binding fragment molecular orbitals. *J. Chem. Theory Comput.* **12**, 5719–5736 (2016)
47. Akimov, A.V.: Libra: an open-source “methodology discovery” library for quantum and classical dynamics simulations. *J. Comput. Chem.* **37**, 1626–1649 (2016)
48. Long, R., Fang, W., Akimov, A.V.: Nonradiative electron-hole recombination rate is greatly reduced by defects in monolayer black phosphorus: ab initio time domain study. *J. Phys. Chem. Lett.* **7**, 653–659 (2016)
49. Madjet, M.E.-A., Akimov, A.V., El-Mellouhi, F., Berdiyrov, G.R., Ashhab, S., Tabet, N., Kais, S.: Enhancing the carrier thermalization time in organometallic perovskites by halide mixing. *Phys. Chem. Chem. Phys.* **18**, 5219–5231 (2016)
50. Nijamudheen, A., Akimov, A.V.: Criticality of symmetry in rational design of chalcogenide perovskites. *J. Phys. Chem. Lett.* **9**, 248–257 (2018)
51. Li, R., Zhang, F., Wang, D., Yang, J., Li, M., Zhu, J., Zhou, X., Han, H., Li, C.: Spatial separation of photogenerated electrons and holes among 010 and 110 crystal facets of  $\text{BiVO}_4$ . *Nat Commun* **4**, 1432–1438 (2013)
52. Chen, R.T., Zhu, J., An, H.Y., Fan, F.T., Li, C.: Unravelling charge separation via surface built-in electric fields within single particulate photocatalysts. *Faraday Discuss.* **198**, 473–479 (2017)
53. Wang, X., Xu, Q., Li, M., Shen, S., Wang, X., Wang, Y., Feng, Z., Shi, J., Han, H., Li, C.: Photocatalytic overall water splitting promoted by an  $\alpha$ - $\beta$  phase junction on  $\text{Ga}_2\text{O}_3$ . *Angew. Chem. Int. Ed.* **51**, 13089–13092 (2012)
54. Marschall, R.: Semiconductor composites: strategies for enhancing charge carrier separation to improve photocatalytic activity. *Adv. Func. Mater.* **24**, 2421–2440 (2014)
55. Liu, C., Li, X.B., Su, J.Z., Guo, L.J.: Enhanced charge separation in copper incorporated  $\text{BiVO}_4$  with gradient doping concentration profile for photoelectrochemical water splitting. *Int. J. Hydrogen Energy* **41**, 12842–12851 (2016)
56. Han, L.H., Abdi, F.F., van de Krol, R., Liu, R., Huang, Z.Q., Lewerenz, H.J., Dam, B., Zeman, M., Smets, A.H.M.: Efficient water-splitting device based on a bismuth vanadate photoanode and thin-film silicon solar cells. *Chemosuschem* **7**, 2832–2838 (2014)
57. Abdi, F.F., Han, L.H., Smets, A.H.M., Zeman, M., Dam, B., van de Krol, R.: Efficient solar water splitting by enhanced charge separation in a bismuth vanadate-silicon tandem photoelectrode. *Nat. Commun.* **4**, 2195–2201 (2013)
58. Maeda, K., Xiong, A., Yoshinaga, T., Ikeda, T., Sakamoto, N., Hisatomi, T., Takashima, M., Lu, D., Kanehara, M., Setoyama, T., Teranishi, T., Domen, K.: Photocatalytic overall water splitting promoted by two different cocatalysts for hydrogen and oxygen evolution under visible light. *Angewandte Chemie-International Edition* **49**, 4096–4099 (2010)
59. Zong, X., Yan, H., Wu, G., Ma, G., Wen, F., Wang, L., Li, C.: Enhancement of photocatalytic H<sub>2</sub> evolution on CdS by loading  $\text{MOS}_2$  as cocatalyst under visible light irradiation. *J. Am. Chem. Soc.* **130**, 7176–7177 (2008)
60. Mu, L., Yue, Z., Li, A., Wang, S., Wang, Z., Yang, J., Wang, Y., Liu, T., Chen, R., Zhu, J., Fan, F., Li, R., Li, C.: Enhancing charge separation on high symmetry  $\text{SrTiO}_3$  exposed with anisotropic facets for photocatalytic water splitting. *Energy Environ. Sci.* **9**, 2463–2469 (2016)



61. Selcuk, S., Selloni, A.: Facet-dependent trapping and dynamics of excess electrons at anatase TiO<sub>2</sub> surfaces and aqueous interfaces. *Nat. Mater.* **15**, 1107–1113 (2016)
62. Mu, L.C., Zhao, Y., Li, A.L., Wang, S.Y., Wang, Z.L., Yang, J.X., Wang, Y., Liu, T.F., Chen, R.T., Zhu, J., Fan, F.T., Li, R.G., Li, C.: Enhancing charge separation on high symmetry SrTiO<sub>3</sub> exposed with anisotropic facets for photocatalytic water splitting. *Energy Environ. Sci.* **9**, 2463–2469 (2016)
63. Li, R., Tao, X., Chen, R., Fan, F., Li, C.: Synergetic effect of dual co-catalysts on the activity of p-type Cu<sub>2</sub>O crystals with anisotropic facets. *Chem. Eur. J.* **21**, 14337–14341 (2015)
64. Wang, L., Ge, J., Wang, A., Deng, M., Wang, X., Bai, S., Li, R., Jiang, J., Zhang, Q., Luo, Y., Xiong, Y.: Designing p-type semiconductor-metal hybrid structures for improved photocatalysis. *Angew. Chem. Int. Ed. Engl.* **53**, 5107–5111 (2014)
65. Liu, C., Han, X.G., Xie, S.F., Kuang, Q., Wang, X., Jin, M.S., Xie, Z.X., Zheng, L.S.: Enhancing the photocatalytic activity of anatase TiO<sub>2</sub> by improving the specific facet-induced spontaneous separation of photogenerated electrons and holes. *Chem. Asian J.* **8**, 282–289 (2013)
66. Roy, N., Sohn, Y., Pradhan, D.: Synergy of low-energy 101 and high-energy 001 TiO<sub>2</sub> crystal facets for enhanced photocatalysis. *ACS Nano* **7**, 2532–2540 (2013)
67. Gao, Y., Zhu, D., An, H., Yan, P., Huang, B., Chen, R., Fan, F., Li, C.: Directly probing charge separation at interface of TiO<sub>2</sub> phase junction. *J. Phys. Chem. Lett.* **8**, 1419–1423 (2017)
68. Zhang, X.R., Lin, Y.H., He, D.Q., Zhang, J.F., Fan, Z.Y., Xie, T.F.: Interface junction at anatase/rutile in mixed-phase TiO<sub>2</sub>: formation and photo-generated charge carriers properties. *Chem. Phys. Lett.* **504**, 71–75 (2011)
69. Garcia, J.C., Nolan, M., Deskins, N.A.: The nature of interfaces and charge trapping sites in photocatalytic mixed-phase TiO<sub>2</sub> from first principles modeling. *J. Chem. Phys.* **142**, 024708–024717 (2015)
70. Sotelo-Vazquez, C., Quesada-Cabrera, R., Ling, M., Scanlon, D.O., Kafizas, A., Thakur, P.K., Lee, T.L., Taylor, A., Watson, G.W., Palgrave, R.G., Durrant, J.R., Blackman, C.S., Parkin, I.P.: Evidence and effect of photogenerated charge transfer for enhanced photocatalysis in WO<sub>3</sub>/TiO<sub>2</sub> heterojunction films: a computational and experimental study. *Adv. Funct. Mater.* **27** (2017)
71. Selim, S., Francas, L., Garcia-Tecedor, M., Corby, S., Blackman, C., Gimenez, S., Durrant, J.R., Kafizas, A.: WO<sub>3</sub>/BiVO<sub>4</sub>: impact of charge separation at the timescale of water oxidation. *Chem. Sci.* **10**, 2643–2652 (2019)
72. Paz, Y.: Transient IR spectroscopy as a tool for studying photocatalytic materials. *J. Phys. Condens. Matter* **31**, 503004–503025 (2019)
73. Nakamura, R., Nakato, Y.: Primary intermediates of oxygen photoevolution reaction on TiO<sub>2</sub> (rutile) particles, revealed by in situ FTIR absorption and photoluminescence measurements. *J. Am. Chem. Soc.* **126**, 1290–1298 (2004)
74. Herlihy, D.M., Waegle, M.M., Chen, X.H., Pemmaraju, C.D., Prendergast, D., Cuk, T.: Detecting the oxyl radical of photocatalytic water oxidation at an n-SrTiO<sub>3</sub>/aqueous interface through its subsurface vibration. *Nat. Chem.* **8**, 549–555 (2016)
75. Ye, S., Ding, C.M., Liu, M.Y., Wang, A.Q., Huang, Q.G., Li, C.: Water oxidation catalysts for artificial photosynthesis. *Adv. Mater.*
76. Valdes, A., Qu, Z.W., Kroes, G.J., Rossmeisl, J., Norskov, J.K.: Oxidation and photo-oxidation of water on TiO<sub>2</sub> surface. *J. Phys. Chem. C* **112**, 9872–9879 (2008)
77. Medford, A.J., Vojvodic, A., Hummelshoj, J.S., Voss, J., Abild-Pedersen, F., Studt, F., Bligaard, T., Nilsson, A., Norskov, J.K.: From the Sabatier principle to a predictive theory of transition-metal heterogeneous catalysis. *J. Catal.* **328**, 36–42 (2015)
78. Huang, Z.F., Song, J.J., Du, Y.H., Xi, S.B., Dou, S., Nsanzimana, J.M.V., Wang, C., Xu, Z.C.J., Wang, X.: Chemical and structural origin of lattice oxygen oxidation in Co-Zn oxyhydroxide oxygen evolution electrocatalysts. *Nat. Energy* **4**, 329–338 (2019)
79. Man, I.C., Su, H.Y., Calle-Vallejo, F., Hansen, H.A., Martinez, J.I., Inoglu, N.G., Kitchin, J., Jaramillo, T.F., Norskov, J.K., Rossmeisl, J.: Universality in oxygen evolution electrocatalysis on oxide surfaces. *ChemCatChem* **3**, 1159–1165 (2011)

80. Jain, A., Shyue Ping, O., Hautier, G., Chen, W., Richards, W.D., Dacek, S., Cholia, S., Gunter, D., Skinner, D., Ceder, G., Persson, K.A.: Commentary: the materials project: a materials genome approach to accelerating materials innovation. *Appl. Mater.* **1** (2013)
81. Ong, S.P., Cholia, S., Jain, A., Brafman, M., Gunter, D., Ceder, G., Persson, K.A.: The materials application programming interface (API): a simple, flexible and efficient API for materials data based on representational state transfer (REST) principles. *Comput. Mater. Sci.* **97**, 209–215 (2015)
82. Curtarolo, S., Setyawan, W., Hart, G.L.W., Jahnatek, M., Chepulskii, R.V., Taylor, R.H., Wang, S., Xue, J., Yang, K., Levy, O., Mehl, M.J., Stokes, H.T., Demchenko, D.O., Morgan, D.: AFLOW: an automatic framework for high-throughput materials discovery. *Comput. Mater. Sci.* **58**, 218–226 (2012)
83. Curtarolo, S., Setyawan, W., Wang, S., Xue, J., Yang, K., Taylor, R.H., Nelson, L.J., Hart, G.L.W., Sanvito, S., Buongiorno-Nardelli, M., Mingo, N., Levy, O.: AFLOWLIB.ORG: A distributed materials properties repository from high-throughput ab initio calculations. *Comput. Mater. Sci.* **58**, 227–235 (2012)
84. Hautier, G., Miglio, A., Ceder, G., Rignanese, G.M., Gonze, X.: Identification and design principles of low hole effective mass p-type transparent conducting oxides. *Nat. Commun.* **4**, 2292–2298 (2013)
85. Rettie, A.J.E., Chemelewski, W.D., Emin, D., Mullins, C.B.: Unravelling small-polaron transport in metal oxide photoelectrodes. *J. Phys. Chem. Lett.* **7**, 471–479 (2016)
86. Deskins, N.A., Rao, P.M., Dupuis, M.: Charge carrier management in semiconductors: modeling charge transport and recombination. *Springer Handbook of Inorganic Photochemistry* (2022)
87. Rosso, K.M., Smith, D.M.A., Dupuis, M.: An ab initio model of electron transport in hematite ( $\alpha$ -Fe<sub>2</sub>O<sub>3</sub>) basal planes. *J. Chem. Phys.* **118**, 6455–6466 (2003)
88. Rosso, K.M., Dupuis, M.: Reorganization energy associated with small polaron mobility in iron oxide. *J. Chem. Phys.* **120**, 7050–7054 (2004)
89. Liu, T.F., Pasumarthi, V., LaPorte, C., Feng, Z.C., Li, Q.Y., Yang, J.J., Li, C., Dupuis, M.: Bimodal hole transport in bulk BiVO<sub>4</sub> from computation. *J. Mater. Chem. A* **6**, 3714–3723 (2018)
90. Pasumarthi, V., Liu, T., Dupuis, M., Li, C.: Charge carrier transport dynamics in W/Mo-doped BiVO<sub>4</sub>: first principles-based mesoscale characterization. *J. Mater. Chem. A* **7**, 3054–3065 (2019)
91. Lasia, A.: Mechanism and kinetics of the hydrogen evolution reaction. *Int. J. Hydrogen Energy* **44**, 19484–19518 (2019)
92. Evans, M.G., Polanyi, M.: *J. Chem. Soc. Faraday Trans.* **32**, 1340 (1936)
93. Bell, R.P.: The theory of reactions involving proton transfers. *Proc. R. Soc. Lond. Ser. A* **154**, 414 (1936)
94. Wu, Y.A., McNulty, I., Liu, C., Lau, K.C., Liu, Q., Paulikas, A.P., Sun, C.-J., Cai, Z., Guest, J.R., Ren, Y., Stamenkovic, V., Curtiss, L.A., Liu, Y.: Facet-dependent active sites of a single Cu<sub>2</sub>O particle photocatalyst for CO<sub>2</sub> reduction to methanol. *Nat. Energy* **4**, 957–968 (2019)
95. Prevot, M.S., Jeanbourquin, X.A., Bouree, W.S., Abdi, F., Friedrich, D., van de Krol, R., Gijjaro, N., Le Formal, F., Sivula, K.: Evaluating charge carrier transport and surface states in CuFeO<sub>2</sub> photocathodes. *Chem. Mater.* **29**, 4952–4962 (2017)
96. Rosso, K.M., Dupuis, M.: Electron transfer in environmental systems: a frontier for theoretical chemistry. *Theoret. Chem. Acc.* **116**, 124–136 (2006)
97. Deskins, N.A., Dupuis, M.: Electron transport via polaron hopping in bulk TiO<sub>2</sub>: a density functional theory characterization. *Phys. Rev. B* **75**, 195212–195221 (2007)
98. Deskins, N.A., Dupuis, M.: Intrinsic hole migration rates in TiO<sub>2</sub> from density functional theory. *J. Phys. Chem. C* **113**, 346–358 (2009)
99. Liu, T., Dupuis, M., Li, C.: Band structure engineering: insights from defects, band gap, and electron mobility, from study of magnesium tantalate. *J. Phys. Chem. C* **120**, 6930–6937 (2016)

100. Liu, T., Pasumarthi, V., LaPorte, C., Feng, Z., Li, Q., Yang, J., Li, C., Dupuis, M.: Bimodal hole transport in bulk  $\text{BiVO}_4$  from computation. *J. Mater. Chem.* **6**, 3714–3723 (2018)
101. Liu, T.F., Zhao, Q.Y., Li, C., Lyu, Y., Dupuis, M.: Photocatalytic facet selectivity in  $\text{BiVO}_4$  nanoparticles: polaron electronic structure and thermodynamic stability considerations for photocatalysis. *J. Phys. Chem. C* **123**, 20142–20151 (2019)
102. Liu, T.F., Cui, M.S., Dupuis, M.: Hole polaron transport in bismuth vanadate  $\text{BiVO}_4$  from hybrid density functional theory. *J. Phys. Chem. C* **124**, 23038–23044 (2020)
103. Morbec, J.M., Narkeviciute, I., Jaramillo, T.F., Galli, G.: Optoelectronic properties of  $\text{Ta}_3\text{N}_5$ : a joint theoretical and experimental study. *Phys. Rev. B* **90** (2014)
104. Plata, J.J., Marquez, A.M., Sanz, J.F.: Transport properties in the  $\text{CeO}_{2-x}(111)$  surface: from charge distribution to ion-electron collaborative migration. *J. Phys. Chem. C* **117**, 25497–25503 (2013)
105. Iordanova, N., Dupuis, M., Rosso, K.M.: Charge transport in metal oxides: a theoretical study of hematite  $\alpha\text{-Fe}_2\text{O}_3$ . *J. Chem. Phys.* **122**, 144305 (2005)
106. Morbec, J.M., Galli, G.: Charge transport properties of bulk  $\text{Ta}_3\text{N}_5$  from first principles. *Phys. Rev. B* **93**, 035201–035206 (2016)
107. Plata, J.J., Marquez, A.M., Fdez Sanz, J.: Electron mobility via polaron hopping in bulk ceria: a first-principles study. *J. Phys. Chem. C* **117**, 14502–14509 (2013)
108. Shepidchenko, A., Sanyal, B., Klintonberg, M., Mirbt, S.: Small hole polaron in  $\text{CdTe}$ : Cd-vacancy revisited. *Sci. Rep.* **5**, 14509–14514 (2015)
109. Adelstein, N., Neaton, J.B., Asta, M., De Jonghe, L.C.: Density functional theory based calculation of small-polaron mobility in hematite. *Phys. Rev. B* **89**, 245115–245123 (2014)
110. Kanan, D.K., Carter, E.A.: Ab initio study of electron and hole transport in pure and doped  $\text{MnO}$  and  $\text{MnO}:\text{ZnO}$  alloy. *J. Mater. Chem. A* **1**, 9246–9256 (2013)
111. Erhart, P., Klein, A., Åberg, D., Sadigh, B.: Efficacy of the DFT plus U formalism for modeling hole polarons in perovskite oxides. *Phys. Rev. B* **90**, 035204 (2014)
112. Kweon, K.E., Hwang, G.S.: Surface structure and hole localization in bismuth vanadate: a first principles study. *Appl. Phys. Lett.* **103**, 131603–131607 (2013)
113. Kweon, K.E., Hwang, G.S.: Structural phase-dependent hole localization and transport in bismuth vanadate. *Phys. Rev. B* **87**, 205202–205207 (2013)
114. Kweon, K.E., Hwang, G.S., Kim, J., Kim, S., Kim, S.: Electron small polarons and their transport in bismuth vanadate: a first principles study. *Phys. Chem. Chem. Phys.* **17**, 256–260 (2015)
115. Hoffmann, M.J., Matera, S., Reuter, K.: kmos: a lattice kinetic Monte Carlo framework. *Comput. Phys. Commun.* **185**, 2138–2150 (2014)
116. Leetmaa, M., Skorodumova, N.V.: KMCLib: a general framework for lattice kinetic Monte Carlo (KMC) simulations. *Comput. Phys. Commun.* **185**, 2340–2349 (2014)
117. Yu, J., Sushko, M.L., Kerisit, S., Rosso, K.M., Liu, J.: Kinetic Monte Carlo study of ambipolar lithium ion and electron-polaron diffusion into nanostructured  $\text{TiO}_2$ . *J. Phys. Chem. Lett.* **3**, 2076–2081 (2012)
118. Mi, Y., Weng, Y.X.: Band alignment and controllable electron migration between rutile and anatase  $\text{TiO}_2$ . *Sci. Rep.* **5**, 11482–11491 (2015)
119. Wang, X., Kafizas, A., Li, X., Moniz, S.J.A., Reardon, P.J.T., Tang, J., Parkin, I.P., Durrant, J.R.: Transient absorption spectroscopy of anatase and rutile: the impact of morphology and phase on photocatalytic activity. *J. Phys. Chem. C* **119**, 10439–10447 (2015)
120. Li, A., Wang, Z., Yin, H., Wang, S., Yan, P., Huang, B., Wang, X., Li, R., Zong, X., Han, H., Li, C.: Understanding the anatase–rutile phase junction in charge separation and transfer in a  $\text{TiO}_2$  electrode for photoelectrochemical water splitting. *Chem. Sci.* **7**, 6076–6082 (2016)
121. Jin, S.Q., Wang, X., Wang, X.L., Ju, M.G., Shen, S., Liang, W.Z., Zhao, Y., Feng, Z.C., Playford, H.Y., Walton, R.I., Li, C.: Effect of phase junction structure on the photocatalytic performance in overall water splitting:  $\text{Ga}_2\text{O}_3$  photocatalyst as an example. *J. Phys. Chem. C* **119**, 18221–18228 (2015)
122. Oberhofer, H., Reuter, K., Blumberger, J.: Charge transport in molecular materials: an assessment of computational methods. *Chem. Rev.* **117**, 10319–10357 (2017)

123. van der Kaap, N.J., Koster, L.J.A.: Massively parallel kinetic Monte Carlo simulations of charge carrier transport in organic semiconductors. *J. Comput. Phys.* **307**, 321–332 (2016)
124. Kerisit, S., Rosso, K.M.: Kinetic Monte Carlo model of charge transport in hematite ( $\alpha\text{-Fe}_2\text{O}_3$ ). *J. Chem. Phys.* **127**, 124706–124715 (2007)
125. Scanlon, D.O., Morgan, B.J., Watson, G.W.: Modeling the polaronic nature of p-type defects in  $\text{Cu}_2\text{O}$ : The failure of GGA and GGA plus U. *J. Chem. Phys.* **131** (2009)
126. Scanlon, D.O., Morgan, B.J., Watson, G.W., Walsh, A.: Acceptor levels in p-type  $\text{Cu}_2\text{O}$ : rationalizing theory and experiment. *Phys. Rev. Lett.* **103** (2009)
127. Scanlon, D.O., Watson, G.W.: Undoped n-type  $\text{Cu}_2\text{O}$ : fact or fiction? *J. Phys. Chem. Lett.* **1**, 2582–2585 (2010)
128. Yu, X., Zhang, X., Wang, S., Feng, G.: A first principle study on the magnetic properties of  $\text{Cu}_2\text{O}$  surfaces. *Curr. Appl. Phys.* **15**, 1303–1311 (2015)
129. Marcus, R.A.: Electron transfer at electrodes and in solution - comparison of theory and experiment. *Electrochim. Acta* **13**, 995–1000 (1968)
130. Marcus, R.A.: Electron-transfer reactions in chemistry—theory and experiment. *Rev. Mod. Phys.* **65**, 599–610 (1993)
131. Gerischer, H.: Charge transfer processes at semiconductor-electrolyte interfaces in connection with problems of catalysis. *Surf. Sci.* **18**, 97 (1969)
132. Gerischer, H.: On role of electrons and holes in surface reactions on semiconductors. *Surf. Sci.* **13**, 265 (1969)
133. Zhang, X.Q., Bieberle-Hutter, A.: Modeling and simulations in photoelectrochemical water oxidation: from single level to multiscale modeling. *Chemsuschem* **9**, 1223–1242 (2016)
134. George, K., van Berkel, M., Zhang, X.Q., Sinha, R., Bieberle-Huller, A.: Impedance spectra and surface coverages simulated directly from the electrochemical reaction mechanism: a nonlinear state-space approach. *J. Phys. Chem. C* **123**, 9981–9992 (2019)
135. Yang, J., Wang, D., Zhou, X., Li, C.: A theoretical study on the mechanism of photocatalytic oxygen evolution on  $\text{BiVO}_4$  in aqueous solution. *Chemistry* **19**, 1320–1326 (2013)
136. Coridan, R.H., Nielander, A.C., Francis, S.A., McDowell, M.T., Dix, V., Chatman, S.M., Lewis, N.S.: Methods for comparing the performance of energy-conversion systems for use in solar fuels and solar electricity generation. *Energy Environ. Sci.* **8**, 2886–2901 (2015)
137. Liu, D.J., Garcia, A., Wang, J., Ackerman, D.M., Wang, C.J., Evans, J.W.: Kinetic Monte Carlo simulation of statistical mechanical models and coarse-grained mesoscale descriptions of catalytic reaction-diffusion processes: 1D nanoporous and 2D surface systems. *Chem. Rev.* **115**, 5979–6050 (2015)
138. Chen, X., Liu, L., Yu, P.Y., Mao, S.S.: Increasing solar absorption for photocatalysis with black hydrogenated titanium dioxide nanocrystals. *Science* **331**, 746–750 (2011)
139. Li, D., Liu, Y., Shi, W.W., Shao, C.Y., Wang, S.Y., Ding, C.M., Liu, T.F., Fan, F.T., Shi, J.Y., Li, C.: Crystallographic-orientation-dependent charge separation of  $\text{BiVO}_4$  for solar water oxidation. *ACS Energy Lett.* **4**, 825–831 (2019)
140. Ohno, T., Sarukawa, K., Tokieda, K., Matsumura, M.: Morphology of a  $\text{TiO}_2$  photocatalyst (Degussa, P-25) consisting of anatase and rutile crystalline phases. *J. Catal.* **203**, 82–86 (2001)
141. Ohno, T., Tokieda, K., Higashida, S., Matsumura, M.: Synergism between rutile and anatase  $\text{TiO}_2$  particles in photocatalytic oxidation of naphthalene. *Appl. Catal. General* **244**, 383–391 (2003)
142. Wu, C.Y., Yue, Y.H., Deng, X.Y., Hua, W.M., Gao, Z.: Investigation on the synergetic effect between anatase and rutile nanoparticles in gas-phase photocatalytic oxidations. *Catal. Today* **93–5**, 863–869 (2004)
143. Frank, A.J., Kopidakis, N., van de Lagemaat, J.: Electrons in nanostructured  $\text{TiO}_2$  solar cells: transport, recombination and photovoltaic properties. *Coord. Chem. Rev.* **248**, 1165–1179 (2004)
144. Kopidakis, N., Benkstein, K.D., van de Lagemaat, J., Frank, A.J., Yuan, Q., Schiff, E.A.: Temperature dependence of the electron diffusion coefficient in electrolyte-filled  $\text{TiO}_2$  nanoparticle films: evidence against multiple trapping in exponential conduction-band tails. *Phys. Rev. B* **73**, 045326–045332 (2006)

145. Green, A.N.M., Chandler, R.E., Haque, S.A., Nelson, J., Durrant, J.R.: Transient absorption studies and numerical modeling of iodine photoreduction by nanocrystalline TiO<sub>2</sub> films. *J. Phys. Chem. B* **109**, 142–150 (2005)
146. Hendry, E., Wang, F., Shan, J., Heinz, T.F., Bonn, M.: Electron transport in TiO<sub>2</sub> probed by THz time-domain spectroscopy. *Phys. Rev. B* **69**, 081101–081104 (2004)
147. Ulbricht, R., Hendry, E., Shan, J., Heinz, T.F., Bonn, M.: Carrier dynamics in semiconductors studied with time-resolved terahertz spectroscopy. *Rev. Mod. Phys.* **83**, 543–586 (2011)
148. Hurum, D.C., Agrios, A.G., Gray, K.A., Rajh, T., Thurnauer, M.C.: Explaining the enhanced photocatalytic activity of Degussa P25 mixed-phase TiO<sub>2</sub> using EPR. *J. Phys. Chem. B* **107**, 4545–4549 (2003)
149. Kawahara, T., Konishi, Y., Tada, H., Tohge, N., Nishii, J., Ito, S.: A patterned TiO<sub>2</sub>(anatase)/TiO<sub>2</sub>(rutile) bilayer-type photocatalyst: effect of the anatase/rutile junction on the photocatalytic activity. *Angew. Chem. Int. Ed.* **41**, 2811–2813 (2002)
150. Zou, Z.G., Ye, J.H., Sayama, K., Arakawa, H.: Direct splitting of water under visible light irradiation with an oxide semiconductor photocatalyst. *Nature* **414**, 625–627 (2001)
151. Young, K.J., Martini, L.A., Milot, R.L., Snoeberger, R.C., Batista, V.S., Schmuttenmaer, C.A., Crabtree, R.H., Brudvig, G.W.: Light-driven water oxidation for solar fuels. *Coord. Chem. Rev.* **256**, 2503–2520 (2012)
152. Kanan, M.W., Nocera, D.G.: In situ formation of an oxygen-evolving catalyst in neutral water containing phosphate and Co<sup>2+</sup>. *Science* **321**, 1072–1075 (2008)
153. Karkas, M.D., Verho, O., Johnston, E.V., Akermark, B.: Artificial photosynthesis: molecular systems for catalytic water oxidation. *Chem. Rev.* **114**, 11863–12001 (2014)
154. Mueller, D.N., Machala, M.L., Bluhm, H., Chueh, W.C.: Redox activity of surface oxygen anions in oxygen-deficient perovskite oxides during electrochemical reactions. *Nat. Commun.* **6** (2015)
155. Grimaud, A., Hong, W.T., Shao-Horn, Y., Tarascon, J.M.: Anionic redox processes for electrochemical devices. *Nat. Mater.* **15**, 121–126 (2016)
156. Mefford, J.T., Rong, X., Abakumov, A.M., Hardin, W.G., Dai, S., Kolpak, A.M., Johnston, K.P., Stevenson, K.J.: Water electrolysis on La<sub>1-x</sub>Sr<sub>x</sub>CoO<sub>3</sub>-delta perovskite electrocatalysts. *Nat. Commun.* **7** (2016)
157. Di Valentin, C., Pacchioni, G., Selloni, A.: Electronic structure of defect states in hydroxylated and reduced rutile TiO<sub>2</sub>(110) surfaces. *Phys. Rev. Lett.* **97** (2006)
158. Scheiber, P., Fidler, M., Dulub, O., Schmid, M., Diebold, U., Hou, W.Y., Aschauer, U., Selloni, A.: (Sub)Surface mobility of oxygen vacancies at the TiO<sub>2</sub> anatase (101) surface. *Phys. Rev. Lett.* **109** (2012)
159. Brawand, N.P., Goldey, M.B., Voros, M., Galli, G.: Defect states and charge transport in quantum dot solids. *Chem. Mater.* **29**, 1255–1262 (2017)
160. Fu, Q., Wu, T., Fu, G., Gao, T.L., Han, J.C., Yao, T., Zhang, Y.M., Zhong, W.W., Wang, X.J., Song, B.: Skutterudite-type ternary Co<sub>1-x</sub>Ni<sub>x</sub>P<sub>3</sub> nanoneedle array electrocatalysts for enhanced hydrogen and oxygen evolution. *ACS Energy Lett.* **3**, 1744–1752 (2018)
161. Huang, J.Z., Han, J.C., Wang, R., Zhang, Y.Y., Wang, X.J., Zhang, X.H., Zhang, Z.H., Zhang, Y.M., Song, B., Jin, S.: Improving electrocatalysts for oxygen evolution using Ni<sub>x</sub>Fe<sub>3-x</sub>O<sub>4</sub>/Ni hybrid nanostructures formed by solvothermal synthesis. *ACS Energy Lett.* **3**, 1698–1707 (2018)
162. Selim, S., Pastor, E., Garcia-Tecedor, M., Morris, M.R., Francas, L., Sachs, M., Moss, B., Corby, S., Mesa, C.A., Gimenez, S., Kafizas, A., Bakulin, A.A., Durrant, J.R.: Impact of oxygen vacancy occupancy on charge carrier dynamics in BiVO<sub>4</sub> photoanodes. *J. Am. Chem. Soc.* **141**, 18791–18798 (2019)
163. Wu, J.M., Chen, Y., Pan, L., Wang, P.H., Cui, Y., Kong, D.C., Wang, L., Zhang, X.W., Zou, J.J.: Multi-layer monoclinic BiVO<sub>4</sub> with oxygen vacancies and V<sup>4+</sup> species for highly efficient visible-light photoelectrochemical applications. *Appl. Catal. B Environ.* **221**, 187–195 (2018)
164. Hegner, F.S., Forrer, D., Galan-Mascaros, J.R., Lopez, N., Selloni, A.: Versatile nature of oxygen vacancies in bismuth vanadate bulk and (001) surface. *J. Phys. Chem. Lett.* **10**, 6672–6678 (2019)

165. Wang, Z.L., Mao, X., Chen, P., Xiao, M., Monny, S.A., Wang, S.C., Konarova, M., Du, A.J., Wang, L.Z.: Understanding the roles of oxygen vacancies in hematite-based photoelectrochemical processes. *Angew. Chem. Int. Ed.* **58**, 1030–1034 (2019)
166. Chen, C.-F., King, G., Dickerson, R.M., Papin, P.A., Gupta, S., Kellogg, W.R., Wu, G.: Oxygen-deficient  $\text{BaTiO}_{3-x}$  perovskite as an efficient bifunctional oxygen electrocatalyst. *Nano Energy* **13**, 423–432 (2015)
167. Deskins, N.A., Rousseau, R., Dupuis, M.: Defining the role of excess electrons in the surface chemistry of  $\text{TiO}_2$ . *J. Phys. Chem. C* **114**, 5891–5897 (2010)
168. Tyminska, N., Wu, G., Dupuis, M.: Water oxidation on oxygen-deficient barium titanate: a first-principles study. *J. Phys. Chem. C* **121**, 8378–8389 (2017)
169. Liu, T.F., Feng, Z.C., Li, Q.Y., Yang, J.J., Li, C., Dupuis, M.: Role of oxygen vacancies on oxygen evolution reaction activity: beta- $\text{Ga}_2\text{O}_3$  as a case study. *Chem. Mater.* **30**, 7714–7726 (2018)
170. Malik, A.S., Liu, T., Dupuis, M., Li, R., Li, C.: Water oxidation on  $\text{TiO}_2$ : a comparative study of 1e-, 2e-, and 4e- processes on rutile, anatase, and brookite. II the role of oxygen vacancies *ACS Catal.* (2020)
171. Kresse, G., Furthmüller, J.: Efficient iterative schemes for ab initio total-energy calculations using a plane-wave basis set. *Phys. Rev. B* **54**, 11169–11186 (1996)
172. Kresse, G., Furthmüller, J.: Efficiency of ab-initio total energy calculations for metals and semiconductors using a plane-wave basis set. *Comput. Mater. Sci.* **6**, 15–50 (1996)
173. Bader, R.F.W.: *Atoms in Molecules—A Quantum Theory*. Oxford University Press, New York (1990)
174. Dudarev, S.L., Botton, G.A., Savrasov, S.Y., Humphreys, C.J., Sutton, A.P.: Electron-energy-loss spectra and the structural stability of nickel oxide: an LSDA+U study. *Phys. Rev. B* **57**, 1505–1509 (1998)
175. Becke, A.D.: A new mixing of Hartree-Fock and local density-functional theories. *J. Chem. Phys.* **98**, 1372–1377 (1993)
176. Adamo, C., Barone, V.: Toward reliable density functional methods without adjustable parameters: the PBE0 model. *J. Chem. Phys.* **110**, 6158–6170 (1999)
177. Heyd, J., Scuseria, G.E., Ernzerhof, M.: Hybrid functionals based on a screened Coulomb potential. *J. Chem. Phys.* **118**, 8207–8215 (2003)
178. Rettie, A.J., Chemelewski, W.D., Lindemuth, J., McCloy, J.S., Marshall, L.G., Zhou, J., Emin, D., Mullins, C.B.: Anisotropic small-polaron hopping in W:  $\text{BiVO}_4$  single crystals. *Appl. Phys. Lett.* **106**, 022106 (2015)
179. Rettie, A.J., Lee, H.C., Marshall, L.G., Lin, J.-F., Capan, C., Lindemuth, J., McCloy, J.S., Zhou, J., Bard, A.J., Mullins, C.B.: Combined charge carrier transport and photoelectrochemical characterization of  $\text{BiVO}_4$  single crystals: intrinsic behavior of a complex metal oxide. *J. Am. Chem. Soc.* **135**, 11389–11396 (2013)
180. Ziwrtsch, M., Müller, S.n., Hempel, H., Unold, T., Abdi, F.F., van de Krol, R., Friedrich, D., Eichberger, R.: Direct time-resolved observation of carrier trapping and polaron conductivity in  $\text{BiVO}_4$ . *ACS Energy Lett.* **1**, 888–894 (2016)
181. Liu, T., Zhou, X., Dupuis, M., Li, C.: The nature of photogenerated charge separation among different crystal facets of  $\text{BiVO}_4$  studied by density functional theory. *Phys. Chem. Chem. Phys.* **17**, 23503–23510 (2015)
182. Pasumarthi, V., Liu, T., Dupuis, M., Li, C.: Charge carrier transport dynamics in W/Mo-doped  $\text{BiVO}_4$ : first principles-based mesoscale characterization. *J. Mater. Chem. A* **7**, 3054–3065 (2019)
183. Wiktor, J., Ambrosio, F., Pasquarello, A.: Role of polarons in water splitting: the case of  $\text{BiVO}_4$ . *ACS Energy Lett.* **3**, 1693–1697 (2018)
184. Wu, F., Ping, Y.: Combining Landau-Zener theory and kinetic Monte Carlo sampling for small polaron mobility of doped  $\text{BiVO}_4$  from first-principles. *J. Mater. Chem. A* **6**, 20025–20036 (2018)
185. Kweon, K.E., Hwang, G.S.: Surface structure and hole localization in bismuth vanadate: a first principles study. *Appl. Phys. Lett.* **103**, 131603 (2013)

186. Kweon, K.E., Hwang, G.S.: Structural phase-dependent hole localization and transport in bismuth vanadate. *Phys. Rev. B* **87**, 205202 (2013)
187. de Respinis, M., Fravventura, M., Abdi, F.F., Schreuders, H., Savenije, T.J., Smith, W.A., Dam, B., van de Krol, R.: Oxynitrogenography: controlled synthesis of single-phase tantalum oxynitride photoabsorbers. *Chem. Mater.* **27**, 7091–7099 (2015)
188. Lee, J., Lu, W.D., Kioupakis, E.: Electronic and optical properties of oxygen vacancies in amorphous Ta<sub>2</sub>O<sub>5</sub> from first principles. *Nanoscale* **9**, 1120–1127 (2017)
189. Morbec, J.M., Galli, G.: Charge transport properties of bulk Ta<sub>3</sub>N<sub>5</sub> from first principles. *Phys. Rev. B* **93**, 035201 (2016)
190. Dey, M., Singh, A., Singh, A.K.: Formation of a small electron polaron in tantalum oxynitride: origin of low mobility. *J. Phys. Chem. C* **125**, 11548–11554 (2021)
191. Zhao, Q., Cui, M., Liu, T.: Charge carrier transport mechanism in Ta<sub>2</sub>O<sub>5</sub>, TaON, and Ta<sub>3</sub>N<sub>5</sub> studied by applying polaron hopping and bandlike models. *ChemPhysChem* e202100859
192. Shi, L.R., Yan, X.W., Ju, L., Tian, J.L., Xia, Z.C.: The effect of oxygen vacancy on magnetism of geometrically frustrated triangular lattice CuFeO<sub>2</sub>: Ab initio study. *J. Magnet. Magnet. Mater.* **486** (2019)
193. Gajdos, F., Oberhofer, H., Dupuis, M., Blumberger, J.: On the inapplicability of electron-hopping models for the organic semiconductor phenyl-C61-butyrac acid methyl ester (PCBM). *J. Phys. Chem. Lett.* **4**, 1012–1017 (2013)
194. Behara, P.K., Dupuis, M.: Electron transfer in extended systems by density functional theory: calculation of the electronic coupling. *Phys. Chem. Chem. Phys.* **22**, 10609–10623 (2019)
195. Green, M.A., Ho-Baillie, A., Snaith, H.J.: The emergence of perovskite solar cells. *Nat. Photonics* **8**, 506–514 (2014)
196. Park, N.G.: Perovskite solar cells: an emerging photovoltaic technology. *Mater. Today* **18**, 65–72 (2015)

# Emerging Metal-Halide Perovskite Materials for Enhanced Solar Cells and Light-Emitting Applications



Felipe Moreira Pinto, Mary Carmen Mate Durek de Conti,  
Swayandipta Dey, Esteban Velilla, Carlton A. Taft,  
and Felipe de Almeida La Porta

## 1 Introduction

Since the photovoltaic effect was observed for the first time, in particular, many multi-functional materials have widely been developed to facilitate the direct conversion of solar radiation into electricity; thus, enabling the emergence of a promising technology to circumvent the problem of the energy crisis [1–8]. This nearly 70-year-old

---

F. M. Pinto

Engineering Department, Federal University of Lavras, Lavras, Brazil

M. C. M. D. de Conti · F. de Almeida La Porta (✉)

State University of Londrina, Rodovia Celso Garcia Cid, 445, km 380, Londrina, Paraná

86057-970, Brazil

e-mail: [felipelaporta@utfpr.edu.br](mailto:felipelaporta@utfpr.edu.br)

M. C. M. D. de Conti

Federal Technological University of Paraná, Nature Sciences Academic, Avenida Alberto

Carazzai, 1640 CEP, Cornélio Procopio, PR 86300-000, Brazil

S. Dey

Department of Applied Physics, Institute for Complex Molecular Systems (ICMS), Eindhoven

University of Technology, Postbus 513, 5600 MB Eindhoven, The Netherlands

E. Velilla

Centro de Investigación, Innovación y Desarrollo de Materiales—CIDEMAT, Universidad de

Antioquia, Medellín, Colombia

C. A. Taft

Centro Brasileiro de Pesquisas Físicas, CBPF, Rio de Janeiro, Brazil

F. de Almeida La Porta

Laboratory of Nanotechnology and Computational Chemistry, Federal Technological University

of Paraná, Londrina, Brazil

E. Velilla

Grupo en Manejo Eficiente de la Energía – GIMEL, Universidad de Antioquia, Medellín,

Colombia



technology has quickly developed, branching out into different approaches, almost all of which are based on the operating principle of solar cells. In sum, the basic principles related to the working mechanism of solar cells have been a long study and, in turn, are well established in the literature [1]. Wafer-based silicon solar cells have widely been dominant in this field. Yet, it is well-known that such photovoltaic panels, based on single-crystal silicon, are extremely difficult to manufacture and, in addition, have a relatively high cost [2–4]. Also, as we know, the presence of complex defects on silicon-based solar cells significantly reduction in their photovoltaic performance [5, 7–9].

Hence, especially as a result of high energy demand and consumption, it is fundamentally important to develop alternatives for wafer-based single-crystal silicon that can be cheaper and more efficient. In the middle of the challenges for the use of solar energy on a large scale, metal-halide perovskite materials are emerging as promising alternatives to single-crystal silicon [10–15]. Particularly, such emerging materials have a versatile, easily obtainable structure that is, in turn, tolerant to “defects”, but even so, unlike what happens in silicon, electrons manage to permeate these imperfections [16–21]. Consequently, a wide variety of strategies have widely been developed to design single-junction metal-halide perovskite solar cells architectures at a low-cost. Thus, within a decade, the single-junction metal-halide perovskite solar cells had a spectacular increase of their power conversion efficiency (PCE) from 3.8 to 25.7%, that is, making this promising technology to large-scale commercialization [22, 23] as shown in Fig. 1a. Despite this remarkable and impressive progress towards marketing of metal-halide perovskite-based technologies in the future, it should be noted that these PEC results usually are obtained more precisely for the small perovskite-based solar modules (i.e., with area up to 0.1 cm<sup>2</sup>) [23–31]. However, it is essential to highlight that perovskite-based solar module area scaling-up has a significant PEC decrease (see inset in Fig. 1a). Thus, the quality of the metal-halide perovskite layer is widely recognized as the key to obtaining high PEC values. Therefore, from this perspective, it should note that the fabrication of metal-halide perovskite films quality in large-area is still a challenge to future commercializing of this technology [23–31].

In terms of devices, many directions were systematically investigated, and from this perspective, four well-established architectures stand out [32–34] Fig. 1b illustrated the architecture standard planar and mesoporous (n–i–p) devices as well as inverted planar and mesoporous (p–i–n) devices. In addition to these architectures, in particular, there is also the mesoscopic structure that is based on the stacking of a mesoporous TiO<sub>2</sub> layer, ZrO<sub>2</sub> spacer layer, and a carbon electrode and does not require an additional hole transporting layer (HTL) [32, 33, 35, 36]. However, it is important to emphasize that this mesoscopic architecture will not be discussed in this chapter.

Also, it is well-known that the best PEC results related to photovoltaic performance are for perovskite-based solar cells containing lead. In general, there is great concern about the toxicity of compounds based on lead, due to their high levels of bioaccumulation as well as a high reactivity [37–42]. These metal, for example, do not exist naturally in any living organism; do not perform nutritional or biochemical

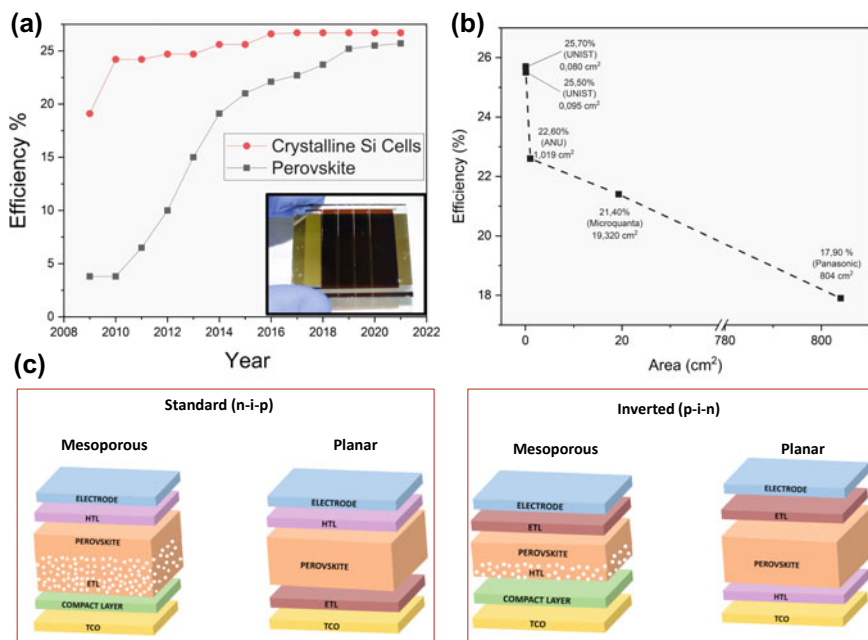


**Fig. 1** **a** Comparative representation of the progress in recent years on the PEC efficiency for silicon- and perovskite-based solar cell technologies (adapted from Refs. [28, 29]). The digital picture inset in **(a)** shows a perovskite-based solar cell device manufactured in our laboratory. **b** Measures compared without distinction between eligible cell areas: total area, opening area and designated lighting area (adapted from Refs. [28, 29]). **c** Schematic representation of the four main types of metal-halide perovskite solar cells architectures (adapted from Ref. [31])

functions, so the presence of these metals is highly harmful in any concentration [43]. Therefore, from this perspective, mainly due to the high toxicity of lead, there are currently several studies aimed at replacing this element with other metallic ions, such as  $\text{Sn}^{2+}$ ,  $\text{Ge}^{2+}$ ,  $\text{Cu}^+$ ,  $\text{Ag}^+$ ,  $\text{Bi}^{3+}$ ,  $\text{Sb}^{3+}$ ,  $\text{In}^{3+}$  and so on [44–50]. Until now, these emerging metal-halide perovskite-based devices are still suffering from film instability, which usually leads to reduced lifetime of these devices. Further, mainly owing to their myriad outstanding properties, it is notable that these emerging metal-halide perovskite materials to be promising candidates for next-generation of light emitters.

Hence, this chapter compiled the current progress in understanding the structure-composition-property relationship of light emitters and solar cells devices based on emerging metal-halide perovskite materials. Here, a particular emphasis has been put on the structure design and advanced characterization of these emerging metal-halide perovskites prepared by spin coating as a strategy.

## 2 Emerging Metal-Halide Perovskite Structures

From a geochemical point of view, it is well known that the name perovskite is due to the mineral  $\text{CaTiO}_3$  (calcium titanate), which was the first example of this family of discovered materials in 1839 by the mineralogist Gustavus Rose [51]. Thus, this fascinating class of perovskite materials (all-inorganic or hybrid) has the general formula  $\text{ABX}_3$ , where A and B are cations and X are anions (most often  $\text{O}^{2-}$  or halide ions  $\text{F}^-$ ,  $\text{Cl}^-$ ,  $\text{Br}^-$  and  $\text{I}^-$ ), although perovskites with nitrides ( $\text{N}^{3-}$ ) and hydrides ( $\text{H}^-$ ) can also be synthesized [51–66].

Among these advanced multi-functional materials, in particular, the inorganic or hybrid metal-halide perovskites, based on the general stoichiometry  $\text{ABX}_3$  (e.g.,  $\text{CsPbX}_3$  with X being Cl, Br, I or a mixture thereof), have myriad properties that are key to use in diverse optoelectronic technologies [22, 42, 67–73]. As is well-known, the charge balance of a perovskite-like structure usually is obtained through the sum of the formal oxidation states of the two metals, which occupy the A and B sites, and of the anion, which must total zero (neutral charge). For instance, in oxide perovskites, it is well-known that the sum of the oxidation states for the two cations must be six, so  $\text{A}^{\text{I}}\text{B}^{\text{V}}\text{O}_3$ ,  $\text{A}^{\text{II}}\text{B}^{\text{IV}}\text{O}_3$  and  $\text{A}^{\text{III}}\text{B}^{\text{III}}\text{O}_3$ . On the other hand, more specifically in the case of the metal-halide perovskites, the sum of the oxidation states for these two cations must be three, so the only possible ternary combination is  $\text{A}^{\text{I}}\text{B}^{\text{II}}\text{X}_3$  [74]. Also, it is well-known that these multi-functional materials can easily be obtained in high complexity structures (such as 3D, 2D, 1D, and 0D) by a wide variety of synthetic strategies [53].

As we know, the ideal metal-halide perovskite has a cubic structure belonging to  $\text{Pm}\bar{3}m$  space group [75, 76]. Until now, most studies have focused on this specific structure; however, it is well-known that depending on the tilting/rotation of the  $[\text{BX}_6]$  polyhedral clusters in the  $\text{ABX}_3$  lattice, particularly this material can also adopt other phases: such as  $\beta$ -tetragonal and two  $\gamma$ - and  $\delta$ -orthorhombic, respectively, in addition to the desired  $\alpha$ -cubic structure [53, 62, 74, 77–85]. Hence, in this perspective, Goldschmidt [86] has introduced an empirical factor, usually known as the Goldschmidt tolerance factor ( $\tau$ ), which is a well-established dimensionless indicator for predicting stability of the cubic perovskite-like structure, which can be defined by the ratios of the ionic radii constituting A, B, and X (Eq. 1). That is:

$$\tau = \frac{R_a + R_x}{\sqrt{2}(R_a + R_b)} \quad (1)$$

Hence, based on this empirical factor the cubic structure is most stable in the range of  $0.8 < \tau < 1.0$  [86]. When the ratio of the ionic radii deviates from the ideal value range, particularly geometric deformations and distortions of the crystal arise, leading to the stabilization of other phases described above [87]. For instance, Li et al. [88] studied 186 complex  $\text{ABX}_3$  systems based on metal-halide perovskites by the Goldschmidt tolerance factor, where they obtained an accuracy of about 96% in predicting the stability of the cubic phase. In the last 95 years, the stability of cubic

metal-halide perovskites has been usually evaluated by using this empirical factor; however, it is well-known that its accuracy is often insufficient [89]. In this regard, several modifications were developed to improve the accuracy of these predictions to accelerate the development process of these materials. Zhang et al. [87] investigated a series of 376  $ABO_3$ -like compounds in order to establish a new criterion to determine the structural stability of perovskite-like compounds. For this, these authors relied on the bond lengths of crystal lattice former (A—O) and crystal lattice modifier (B—O) derived from the bond valence model for the calculations of the tolerance factors, which are found in the range of 0.822–1.139. Therefore, the overall instability for the compounds was identified as being less than 1.2 vu (valence units) as well as increases with decreasing oxidation state of B cations (i.e.,  $A^+B^{5+}O_3$ -type  $>$   $A^{2+}B^{4+}O_3$ -type  $>$   $A^{3+}B^{3+}O_3$ ) [87]. In addition, Bartel et al. [89] have also proposed a new tolerance factor, which is more accurate than the Goldschmidt tolerance factor, defined in the following equation (Eq. 2). That is:

$$\tau = \frac{r_X}{r_B} - n_A \left( n_A - \frac{r_A/r_B}{\ln(r_A/r_B)} \right) \quad (2)$$

where  $n_A$  is the valence of cation A, and  $r_A$  and  $r_B$  are specifically the values of ionic radii of the cations A and B (being  $r_A > r_B$  by definition). According to this new tolerance factor, both oxidic and halide perovskite assume a stable cubic structure when  $\tau < 4.18$  [89]. Also, as mentioned before, mainly due to the high toxicity of lead-based compounds, however, there are currently several studies aimed at replacing this element with other metallic ions, as well as, including the present mixed species in the B site [47–50, 90]. These strategies involving different combinations have been extensively investigated in this field to identify new lead-free halide perovskites (see Fig. 2b) that are potentially promising for applications in solar cells and as light emitters.

In addition to the formal  $ABX_3$  stoichiometry, it is possible to obtain perovskite-like materials ordered by vacancy (e.g.,  $A_2BX_6$  and  $A_3BX_9$ ) where the sites of cations A and B are partially or totally vacant, or replaced by a combination of other cations [91–94]. As we know, double perovskite-like structures, converted into a quaternary formula  $A^I_2B^I B^{III}X_6$  are usually formed by a mixture of monovalent ( $B^I$ ) and trivalent ( $B^{III}$ ) cations coexisting together in the crystal lattice [92–94]. The main strategies used to replace Pb in perovskite-type materials: (i) using homovalent elements (e.g., Sn, Ge, and the other) (ii) based on the use of heterovalent elements (e.g., Bi and Sb) that are usually divided into two subcategories: ion splitting and vacancy-ordered formation [94]. Hence, from this perspective, we believe that a more fundamental understanding of these structural alterations is, of course, the key to the future commercialization of optoelectronic technologies based on inorganic or hybrid halide perovskites.

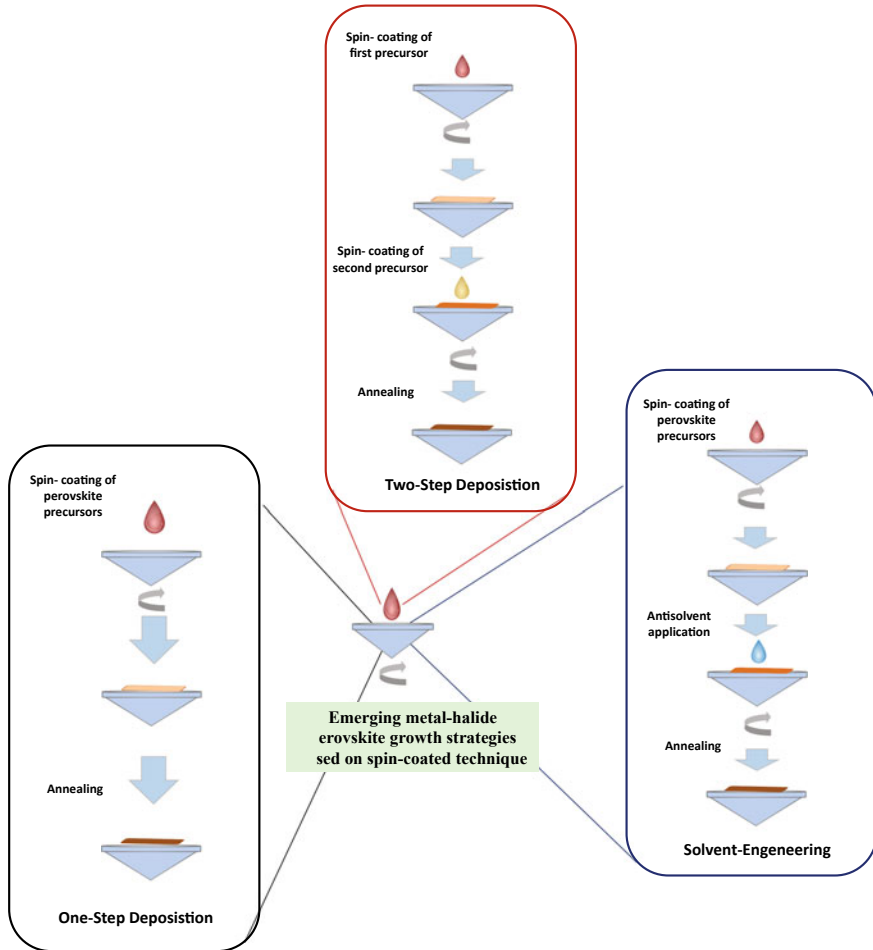


**Fig. 2** Diagram showing the most used techniques for the formation of emerging metal-halide perovskite layers (adapted from Ref. [144])

## 2.1 Homovalent Elements

To replace lead in the all-inorganic and hybrid halide perovskite structure, the easiest is to replace with cations of similarly ionic radii and in the (+2) oxidation state. Thus, in this direction, the most obvious choice would be to replace  $\text{Pb}^{2+}$  with another atom from Group IV in  $\text{AB}(\text{II})\text{X}_3$  lattice. In particular, an interesting alternative is the replacement of this element by tin, since  $\text{Sn}^{2+}$  has a very similar ionic radius to  $\text{Pb}^{2+}$ , 1.35 Å and 1.49 Å, respectively. All-inorganic and hybrid Sn-halide perovskites showed promising optoelectronic properties, as well as, have an attractive bandgap value in the range of 1.2–1.6 eV [95, 96]. In addition, the researchers

have observed for these Sn-based perovskite materials a long diffusion length and electronic mobility than superior to traditional semiconductor materials, such as CdTe and Si, which have been often used in solar panels [44, 72, 97–102]. However, despite the remarkable properties of this  $\text{ASnX}_3$  system, where A can be most often methylammonium (MA), formamidinium (FA), and cesium (Cs), these perovskites are highly sensitive to moisture and the presence of oxygen, which cause a rapid process of oxidation from  $\text{Sn}^{2+}$  to  $\text{Sn}^{4+}$  and, as a result, the perovskite geometry distorts and the optical and electronic properties change significantly during this process [67, 102–104].

Another candidate for replacing Pb in perovskites is germanium itself,  $\text{Ge}^{2+}$ , previously mentioned [105–107]. In the Cs-Ge-X ternary system, there is a bandgap value at room temperature of 1.6 eV for  $\text{CsGeI}_3$ , 2.3 eV for  $\text{CsGeBr}_3$ , and about 3.2 eV for  $\text{CsGeCl}_3$ , respectively. Thus, it is observed that the bandgap increases with the decrease of the ionic radius of the halogens (2.20 Å, 1.96 Å, 1.81 Å) [72]. All-inorganic halide perovskites based on germanium exhibit a crystal structure formed by octahedral clusters of  $[\text{GeX}_6]^{4-}$  similar to that observed in lead halogenate perovskites. Under ambient conditions, in particular, the  $\text{CsGeCl}_3$  phase has a cubic crystal structure, while the bromine ( $\text{CsGeBr}_3$ ) and iodine ( $\text{CsGeI}_3$ ) halides have a distorted rhombohedral structure, which is caused by the second-order Jahn-Teller effect [105]. Sun et al. [106] have investigated the  $\text{MAGeX}_3$  ( $X = \text{Cl}, \text{Br}, \text{I}$ ) properties through theoretical calculations and observed similarity to the  $\text{MAPbI}_3$  compound in terms of the conductivity, stability and optical properties.

Nagane et al. [108] synthesized perovskites varying the composition of Sn-Ge and studied their application in solar cells. For Ge-doping  $\text{MASnI}_3$ , a phase-transition of tetragonal-to-trigonal was observed from the  $\text{CH}_3\text{NH}_3\text{Sn}_{0.25}\text{Ge}_{0.75}\text{I}_3$ , which increases the tolerance factor from 0.84 (pure  $\text{MASnI}_3$ ) to 0.93 ( $\text{MASn}_{0.25}\text{Ge}_{0.75}\text{I}_3$ ), as well as, the stability of such-doped samples [108]. Also, the bandgap of this Sn-Ge based halide perovskites have a bandgap value in the range of 1.3 eV ( $\text{MASnI}_3$ ) to 1.9 eV ( $\text{MASn}_{0.25}\text{Ge}_{0.75}\text{I}_3$ ), respectively. In addition, the  $\text{MASn}_{0.5}\text{Ge}_{0.5}\text{I}_3$  composition showed a bandgap of 1.5 eV with low structural disorder [72]. However, it is known that  $\text{Pb}^{2+}$  has a better applicability due to its superior stability when compared to  $\text{Sn}^{2+}$  and  $\text{Ge}^{2+}$ .

On the other hand, Filip and Giustino have performed a computational screening of all homovalent metal ions (B-site +2 cations) that could replace lead in a perovskite halide configuration [98]. For this computational study, were adopted two criteria that are important for solar cell applications. Firstly, the stability of the cubic perovskite-like structure. Secondly, a direct bandgap value smaller than 2 eV. In this way, a series investigated of perovskite compounds have a reduction from 248 to 25, based on these two criteria, of which 15 have not yet been proposed for used in solar cells. Finally, these authors concluded that the partial replacement of Pb by Mg can help to reduce the toxicity of hybrid halide perovskite, at the same time maintaining its remarkable optoelectronics features [98]. In addition, Korbel et al. [109] performed an extensive study on perovskite-like materials, from over 32,000 possible  $\text{ABX}_3$  combinations, with only 199 hypothetical perovskites being stable (within 25 meV) in nice agreement with study of Filip and Giustino [98].

## 2.2 Heterovalent Elements

### 2.2.1 Ion Splitting Subcategory

Firstly, in this subcategory, we will initially address the mixed anionic compounds, with general formula  $AB(\text{Ch},\text{X})_3$ , where Ch = chalcogen and X = halogen [94, 110, 111]. Such compounds has been recently examined by Sun et al. [112]. These authors found that the  $\text{CsSnS}_2\text{Cl}$  exhibits optical properties most relevant to applications in solar cells than for  $\text{CsSnI}_3$ . In this way, it is well-known that most of the work on  $AB(\text{Ch},\text{X})_3$  is based on the Bi (non-toxic heterovalent elements) replacing the Pb element; causing it to maintain the 3D perovskite structure and charge neutrality, and the anion was replaced by dual (halogen and chalcogen) anions. Among these materials, especially  $\text{MABiSI}_2$  and  $\text{MABiSeI}_2$  being highlighted, due to their optimal bandgap value (1.3–1.4 eV) for applications as solar cells [100]. Also, it is known that the substitution of Pb by Sb or Bi in  $AB(\text{Ch},\text{X})_3$  compounds reduces its dimensionality structural, that is, leading to new and tunable physical properties [113]. As we know, the mixed chalcogenide–halide-based perovskite formation leads to higher stability structural. In turn, it is an exciting feature for lead-free halide perovskites, which still face major stability problems. This fact has been usually assigned to the more covalent bond character found for these compounds [110]. Although none novel absorber materials has been identified from this new class of perovskite-like compounds [97]; however, it is important to emphasize that the research with these chalcogenide-halide-based systems is still in its infancy. Finally, from this perspective, it has been widely recognized that chalcogenide-halide-based systems has latent potential for many optoelectronics applications, and for this reason they promise to shake up this important field of research in the future.

### 2.2.2 Mixed Cationic Compounds

To make up for the problems related to the replacement of Pb by Sb or Bi elements, the strategy of obtaining double halide perovskites,  $A_2B(\text{I})B(\text{III})X_6$  type, with substitution of the B site by mixed cations ( $B = B^+$ ,  $B' = B^{3+}$ ) was explored [114, 115]. Zhao et al. [116] proposed a classification, in terms of electronic structure and chemical stability for the elements that can occupy the BI-site ( $A_2B(\text{I})B(\text{III})X_6$ ). Based on these results, elements of group IA ( $\text{Na}^+$ ,  $\text{K}^+$ , and  $\text{Rb}^+$ ) contribute to the increase BI-s orbital energy, raising the conduction band position. While that elements of group IB ( $\text{Cu}^+$ ,  $\text{Ag}^+$  and  $\text{Au}^+$ ) may provide a significant variation in bandgap value as well as is responsible for changing the valence band of these materials. On the other hand, these authors also identified that use of elements of group IIIA ( $\text{In}^+$  and  $\text{Tl}^+$ ) induces an expansion of the octahedron  $[\text{B}(\text{I})\text{X}(\text{VII})_6]$  clusters as well as contribute to a reduction of the octahedron  $[\text{B}(\text{III})\text{X}(\text{VII})_6]$  clusters. Such structural alterations may contribute to raising the top of valence band in  $A_2B(\text{I})B(\text{III})X_6$  compounds [116]. Also, in such compounds, it has been observed that increasing the ionic radius of

the halogen contributes to a reduction in the bandgap, while the B(III) site change, e.g., from  $\text{Sb}^{3+}$  to  $\text{Bi}^{3+}$ , leads to a significant increase in the bandgap [114]. Finally, the alkali metal cations selected to occupy the B(I)-site not contribute ionicity to the band edges.

$\text{A}_2\text{B(I)B(III)X}_6$  perovskites are also known as “elpasolites”, named after the mineral  $\text{K}_2\text{NaAlF}_6$ . Giustino et al. [39] verified the chemical elements of the periodic table that belong to the elpasolite halides. In their research the authors report 7 elements for the A-site (cations), 8 elements for the B(I)-site (including  $\text{NH}_4^+$  and  $\text{CH}_3\text{NH}_3^+$ ), 34 elements for the B(III)-site (cations) and 5 elements for the X-site (including cyanide  $\text{CN}^-$ ) [39].

Double halide perovskites with alkali metal B(I) cations have 0D dimensionality and have a wide-bandgap feature [94, 117–119]. However, for these complex structures, transition metal cations with multiple oxidation states and/or partially occupied d or f orbitals are not desirable for the B(III)-site [94]. Because they can introduce deep defect states and very low band edges located [94]. Finally, the anions of halides to the X-site, as mentioned before, as the halides change from  $\text{F}^-$ ,  $\text{Cl}^-$ ,  $\text{Br}^-$  to  $\text{I}^-$ , the bandgap generally decreases [116, 120–124].

Furthermore, the vacancy-ordered double perovskite structures, with formula  $\text{A}_3\text{B(III)X}_9$  or  $\text{A}_2\text{B(IV)X}_6$ , has been the focus of several studies and usually are structurally characterized by an antifluorite array of isolated octahedral units linked by A-site cations [125]. These phase transitions in these systems are driven by a mismatch in the ionic radii of the constituent atoms [126].

In the case of the  $\text{A}_3\text{B(III)X}_9$  compounds, the replacing Pb(II) with a group 15 element will result in materials that can assume a 2D or 0D crystal structure [127]. Chang et al. studied the crystal structure of the following synthesized compounds  $\text{Rb}_3\text{Sb}_2\text{Br}_9$ ,  $\text{Rb}_3\text{Sb}_2\text{I}_9$ ,  $\text{Rb}_3\text{Bi}_2\text{Br}_9$ ,  $\text{Rb}_3\text{Bi}_2\text{I}_9$  and  $\text{Tl}_3\text{Bi}_2\text{Br}_9$ . The crystals obtained showed two types of double-layered crystal structures, which are characteristic of the sharing of corners of the  $\text{BX}_6$  octahedron. The differences between the  $\text{A}_3\text{B}_2\text{X}_9$  types can be attributed to specific structural distortions in the close packaging of the underlying  $\text{AX}_3$ . In this way we have two polymorphisms for the compound  $\text{A}_3\text{B}_2\text{X}_9$  [128]. For instance, the  $\text{A}_3\text{Bi}_2\text{X}_9$  vacancy-ordered perovskite-like materials can crystallize most commonly in a trigonal structure (P3m1 space group) of low dimensionality. Likewise, in particular,  $\text{Cs}_3\text{Sb}_2\text{I}_9$  can crystallize into 0D shape (P63/mmc space group) and the 2D  $\langle 111 \rangle$  stacked layer shape (P3m1), respectively [114, 129–131]. Pal et al. [132] suggest that colloidal nanocrystals  $\text{Cs}_3\text{Sb}_2\text{I}_9$  (nanoplatelets and nanorods) and  $\text{Rb}_3\text{Sb}_2\text{I}_9$  have the potential for optoelectronic applications. In addition, Chonamada et al. [133] has been reported the degradation ratio for both polymorphs of  $\text{Cs}_3\text{Sb}_2\text{I}_9$  in form of thin film by the effect of light, water, and heat under an ambient atmosphere. Despite the simplicity of being prepared with controlled particle size and morphology, in general, such materials are highly chemically unstable and this represents a major challenge for their use and commercial exploitation.

For  $\text{A}_2\text{B(IV)X}_6$  vacancy-ordered perovskite-like materials, containing non-toxic transition metals that have a stable +4 oxidation state are promising materials for photovoltaic application [134]. In this sense, Sakai et al. [135] have reported a



series of  $A_2[B(IV)X_6]$  compounds, with  $A = Cs^+$ ,  $B = Pd^{4+}$  and  $X = Br^-$ , with cubic crystal structure (Fm $\bar{3}m$  space group) obtained from direct oxidation of  $Pd^{2+}$  to  $Pd^{4+}$  in solution. Among these systems, the authors identified that  $Cs_2PdBr_6$  has a bandgap of about 1.6 eV and hence is a promising candidate for applications in solar cells and as light emitters [135].

Theoretical and experimental investigations on the  $Cs_2TiI_6$ ,  $Rb_2TiI_6$ ,  $K_2TiI_6$  and  $In_2TiI_6$ , have revealed excellent physical properties for used of such compounds in optoelectronic technologies [136]. The band structures of these  $A_2TiI_6$  vacancy-ordered perovskite-like materials show a very dispersive conduction.

López-Fraguas et al. [137] analyzed the fast structural evolution due to degradation of the  $CsSnI_3$  films leading to the formation of the  $Cs_2SnI_6$ . These authors reported that PLQY for these film decreases significantly. In general, it is well-known that the oxidized  $Sn^{4+}$  ion in perovskite-like structures can act as a p-type dopant, inducing a process of self-doping, that in turn limits its efficiency in energy conversion [72, 138]. To avoid the  $Sn^{2+}$  oxidation process, Lee et al. [107] used the  $SnF_2$  compound as a reducing agent in the formation of  $FASnI_3$ . While that the Umedov et al. [139] have demonstrated the effect of adaptation of the A site (by the addition of Rb and Ag) on the stability of the  $Cs_2SnI_6$  films in ambient air.

### 3 Synthesis Protocol for Emerging Metal-Halide Perovskites

One of the greatest advantages of metal-halide perovskite-based solar cell technology, compared to other technologies, is precisely the manufacturing simplicity with tunable properties [140]. Thus, the long path for the evolution and development of metal-halide perovskite-based devices was marked by a constant improvement of deposition techniques, an evolution achieved from an increase in the understanding of crystallization processes [141]. Particularly, it is well-known that the kinetics of the perovskite formation reaction is relatively fast, and there are several film formation methods that confirm this kinetics. Hence, the quality of the metal-halide perovskite films depends on optimizing parameters related to the concentration of precursors, solvent, temperature, rotation speed, time, and even the post-deposition processes [142–144].

In particular, spin-coating is a solution-based strategy for the simple fabrication of thin films at a low cost, which has received a lot of attention amid the metal-halide perovskite preparation methods [144]. For this reason, in this work we will highlight the recent advances made based on the use of this simple strategy. Figure 2 shows the most used perovskite growth strategies based on spin-coated technique [144]. Of course, spin-coating can produce thin films of high quality with controlled and uniform thickness (i.e., if the viscosity is homogeneous over the entire area of the substrate, regardless of the slip force) [145, 146], even in dry-box conditions and substrate up to 100 cm<sup>2</sup> [147, 148]. During the spin of the substrate, the

centripetal force overcomes the gravitational force and the solute is spread throughout the substrate, forming a film. The substrate in constant speed rotation causes uniform evaporation of the solvent, therefore it is expected that the film thickness will also become uniform [149]. Furthermore, it is well known that the volatility of solvents affects the crystallization process of thin films significantly [150]. Finally, as is well known, the film thickness resulting is, in turn, dependent on the solution concentration of the target material used as well as is usually proportional to the inverse of the spin speed squared (in the case of the same concentration) [145, 146, 150].

### ***3.1 One-Step Deposition***

In this approach, all precursors of the final material are added in a single solution, which is subsequently deposited under the substrate, followed by a heat treatment step. The main aspect of this deposition strategy consists of mixing organic and inorganic precursors in common solvent(s), generally gamma-butyrolactone (GBL), and/or dimethylsulfoxide (DMSO), and/or, dimethylformamide (DMF) as well as the combination of more than one solvent [151–153]. The physical-chemical differences between the organic and inorganic species imply, among other issues, difficulty in obtaining an adequate dissolution of both precursors in a common solvent, resulting, therefore, in films with flaws and moderate coverage rate [151]. Although this approach is extensively used and simple, the precursors used can undergo several chemical reactions in the mixture, influencing both the resulting film and the performance of photovoltaic devices [154].

### ***3.2 Two-Step Deposition***

In this approach, the inorganic and organic compounds are dissolved separately and deposited in sequence (inorganic compound is dissolved in DMSO or DMF and the organic one in Propanol) [143, 155, 156]. The inorganic compound is deposited first, after heat treatment, the organic compound dissolved in propanol is deposited, since inorganic compounds, such as  $\text{PbI}_2$  and others, used do not dissolve in propanol. Additional control over the thin film morphology can then be obtained with this deposition strategy, as it is possible to obtain uniform cuboid perovskite crystals, while the one-step method usually presents an irregular morphology as well as have a high density of pinholes [155]. In addition to the possibility of creating layers of different materials, based on deposition in more than one step makes it possible to create surfaces with different characteristics that can bring greater light absorption and consequently induce higher PCEs values for metal-halide perovskite solar cells [157]. Zheng et al. [158] studied a one-step spin-coating process and compared it with two-step spin-coated, in which the best photovoltaic performances of the perovskite devices with a rough interface of perovskite, which was synthesized with two-step

spin coated as strategy. Despite that, the deposition in two steps or even more steps present an equally challenging and expensive, since there is a production step at each new synthesis step, that is, an additional expense from a commercial point of view. Nevertheless, using this approach, it is possible to obtain perovskite in nanoscale size that can be used as a sensitizer in dye-sensitized solar cells [159, 160] expanding the perovskite applicability to other photovoltaic technologies or light-emitting devices [161–166].

### 3.3 Solvent-Engineering

Among the strategies of film deposition that have brought good results in metal-halide perovskite solar cells is, of course, the solvent engineering protocol [167–170]. Jeon et al. [171] have in addition to using two solvents simultaneously, GBL and DMSO, was the first to report the use of an anti-solvent method, obtaining perovskite films of high crystalline quality, and indeed, high PEC values of about 16.2%. In general, this approach consists of preparing a perovskite solution usually based on a solvent mixture (DMSO/GBL or DMSO/DMF) capable of producing denser layers than the conventional one-step method, taking advantage of the control of the crystallization process [172]. During the last seconds of spin coating rotation, a perovskite non-solvent (e.g., toluene, chlorobenzene, dichlorobenzene or diethyl ether) is placed on the perovskite film, leading to the formation of the  $\text{MA}_2\text{Pb}_3\text{I}_8 \cdot 2\text{DMSO}$  intermediate [168–170]. The DMSO molecules do not allow the direct formation of perovskite to occur, thus forming an intermediate, which with heat treatment loses the DMSO molecules, forming perovskite [167]. This deposition strategy, in particular, have achieved PEC values above 20% [173, 174]. Xiao et al. [175] studied the conventional one-step method followed by a subsequent addition of chlorobenzene (CBZ) leading to an acceleration of the formation of the perovskite layer with greater homogeneity, and consequently higher quality. Jeon et al. [173] observed that with the use of the solvent engineering technique (addition of toluene) there is the formation of a dense film and totally covered in  $\text{TiO}_2$ . In addition to the change for the better in the density and quality of the formed film, there was also an acceleration of the drying process of the perovskite film. Furthermore, it has been observed that solvent engineering strategy lead to a redissolution of the grains and later recrystallization faster, that is, causing the grain size to be close to the film thickness [176]. Although solvent engineering technology is a promising methodology, two important issues remain to be resolved. First, the effect of non-polar solvent on the mechanism of perovskite adduct formation, and second the ratio that leads MAI-PbI<sub>2</sub>-DMSO adduct plays a more important role in the crystallization process than MAI-PbI<sub>2</sub>-dimethylformamide (DMF) is also unclear [172].

## 4 Opportunities in Optoelectronic Technologies

### 4.1 Applications as Light Emitters

With the ever-increasing demand and consumption of various lighting and electronic display devices consuming more than 20% of worldwide electrical energy per year, it is imperative to develop more energy-efficient devices [177–180]. In terms of electroluminescence types, it has been demonstrated that both the narrowband emission derived from free excitons as well as broadband white light emission arising from self-trapped excitons could prove to be quite beneficial in light-emitting applications [179, 181, 182].

As is well-known, the nature of the optoelectronic behavior on semiconducting materials relies on the efficiency of carrier separation between the photogenerated charge carriers and the subsequent carrier recombination for mutual conversion between light and electricity [138, 183–185]. Due to their unique optoelectronic properties such as superior light absorption, excellent carrier transport performance arising from long diffusion lengths, high photoluminescence quantum yields (PLQY), low exciton binding energies, along with their strong defect tolerant behavior make this class of emerging multi-functional materials such potential candidates for developing next generation optoelectronic devices [15, 53, 127, 185–191]. Despite having such fascinating optoelectronic properties, the widescale commercialization process of emerging metal-halide perovskite materials hasn't been kicked off due to intrinsic material toxicity and inferior stability to silicon-based technologies [15, 33, 192]. Therefore, it is imperative to address the existing challenges alongside a continuous search of emerging metal-halide perovskite-based semiconductors, especially lead-free compounds, with improved optoelectronic performance that will hold the key to the future development these field [185, 193–195].

In principle, usually, an excellent light-harvesting material should also be good light-emitting material, but the materials used and the design principles require different approaches whether the materials are applicable in photovoltaic or light-emitting devices [52, 196, 197]. For light-emitting devices, it is well-known that the efficient and fast radiative recombination of excitons is quintessential, whereas, for photovoltaic devices like solar cells, effective charge separation of excitons is critical to extract the charges and convert the charges light to electrical power generation [198–203]. As such, the family of metal-halide perovskites offers a rich variety of convenient frameworks to systematically study the effects of dimensionality, composition, and structural disorder on its electronic configuration and how it affects the optoelectronic properties of the materials [15].

In metal-halide perovskites, within a given dimensionality, the optical response is readily modified through substitution of the halide component leading to alteration in the valence band positions [73, 204, 205]. Generally, in mixed-halide-based perovskites, such as  $\text{CsPb}(\text{Br}_{1-x}\text{Cl}_x)_3$  or  $\text{CsPb}(\text{I}_{1-x}\text{Br}_x)_3$ , it provides emission tunability in the range from 400 to 700 nm with PLQY varying anywhere from 50 to 90%. Whereas, in a mixed cations-based systems, such as  $(\text{FA}_{1-x}\text{Cs}_x)\text{PbI}_3$ , it offers

less optical tunability with bandgaps residing in the range of 1.48–1.73 eV [73, 204, 205]. This bandgap variation in mixed cations-based halide perovskites is primarily due to modified spin-orbit coupling at the edge of the conduction band. Significant changes in the optical properties have been observed upon dimensionality reduction, particularly in the quantum confined two-dimensional layered Ruddlesden-Popper like perovskite analogs (quantum wells). Such complex structures possess enhanced exciton binding energies (reduced PL lifetime) leading to giant oscillator strengths and optical non-linearities [206–210]. Stokes-shifted PL bands also arise from bound exciton states depending on the organic component resulting in modification of dielectric environment [206–208, 211, 212]. Besides being temperature-independent, the strong exciton-phonon coupling has also been reported for some 2D perovskites  $(\text{C}_6\text{H}_5\text{C}_2\text{H}_4\text{NH}_3)_2\text{PbI}_4$ , which directly attributes to polaron formation. On the other hand, self-trapped excitons (and biexcitons) in atomically thin, layered 2D perovskites sheet-like structures display a significant role in the non-linear optical response, mainly due to the enhanced binding energy. Hence, it is well-known that the optical response of 2D perovskite-based LEDs can, in principle, be easily modulated by rational varying the organic cations, organic chain, layer number, and so on. The performed initial reports on physical properties of pure phase 2D perovskite-based LEDs has been realized for  $(\text{CH}_3(\text{CH}_2)_3\text{NH}_3)_2(\text{CH}_3\text{NH}_3)_{n-1}\text{Pb}_n\text{I}_{3n+1}$  Ruddlesden-Popper like systems [206–208]. These vertically oriented films were conducive to efficient charge injection and transport, leading to high electroluminescence efficiency. Due to the phase purity of 2D perovskites, it is expected that LEDs will demonstrate high stability, being operational at low turn-on voltages and could be driven at a high current density of a few  $\text{A}/\text{cm}^2$ . Later in 2017, Chen et al. [213] introduced aromatic alkyl amines into 2D perovskites, which changed the crystal structure from cubic to rod-like and finally a thin film. Interestingly, the electroluminescence of the resultant LEDs was tunable from green to blue just by modifying the structure. Besides modification of materials, altering the device processing and fabrication could also play an important role. For example, in 2018, Yang et al. [214] used a quasi-2D perovskite through composition and phase engineering, thereby obtaining thin films with efficient external PLQY reaching up to 14.36%. In addition, the crystallization process could play a key role affecting the optoelectronic properties of the material. Based on this, Quan et al. [215] explored how different bandgap domains affect the PLQY and LED performance by preparing 2D perovskite-based on  $\text{PEA}_2(\text{MA})_{n-1}\text{Pb}_n\text{Br}_{3n+1}$  and engineered solvent composition during the crystallization process, thereby achieving a EQE of 7.4% with an average brightness of the fabricated LEDs close to  $8400 \text{ cd}/\text{m}^2$ .

Lead-free double perovskite variant based on  $\text{Cs}_2\text{AgInCl}_6$  with low dimensionality has been recently proposed as warm white-light emitters exhibiting a broadband spectrum in the range of 400–800 nm [216, 217]. From stability point of view, all-inorganic perovskite variants exhibit higher stability than organic-inorganic counterparts. In contrast, the 2D or layered organic-inorganic perovskite variants show higher stability against moisture than their 3D all-inorganic counterparts. Some studies also noted that  $\text{A}_3\text{B}(\text{III})_2\text{X}_9$  QDs exhibit wider PL spectra and larger Stokes shift compared to 3D  $\text{MAPbX}_3$  QDs which could be attributed to strong electron-phonon

coupling [218–220]. On the other hand,  $\text{Cs}_3\text{Cu}_2\text{I}_5$  represented an all-inorganic 0D lead-free perovskite variant exhibiting an efficient broadband blue emission with PLQY reaching up to 90% [221].

Ma et al. [222] investigated  $\text{Cs}_3\text{Sb}_2\text{X}_9$  0D particles for application in LED devices, specifically in the 385–640 nm spectral tuning region. Such materials have a high PLQY of about 51.2% and chemical stability. However, it is well-known that the Sb-based halide perovskites are more prone to deep defects when compared to Pb-based halide perovskites. Recently, Hang et al. [223] have reported the relationship between the PLQY and the particle size of  $\text{Cs}_2\text{AgBi}_{1-x}\text{In}_x\text{Cl}_6$  ( $0 < x < 1$ ). Among these materials obtained, the  $\text{Cs}_2\text{AgBi}_{0.125}\text{In}_{0.875}\text{Cl}_6$  stands out because it can break the transition prohibited by parity and retain a direct bandgap, emitting warm white light, with a PLQY of about 70.3%. An interesting feature of these results is the light stability exceeding three months (ca. 2160 h) higher than the study conducted by Luo et al. [217] where the value obtained was 1000 h.

For Sn(II)-based variants, Zhou et al. [224] first reported  $(\text{C}_4\text{N}_2\text{H}_{14}\text{Br})_4\text{SnBr}_6$  with a near unity PLQY, when embedded within an organic matrix in a host-guest fashion, it exhibited a white-light emission with a blue phosphor matrix with a CIE coordinates of (0.35,0.39) and a CCT of 4946 K. Following this work, other two-dimensional Sn-based perovskite variants has been also recently developed with a PLQY of 88% with emission wavelength at 625 nm [225]. Some recent results on the performance of light-emitting devices based on lead-free perovskites are summarized in Table 1. Although these initial few studies are promising, there is still effort required to address a few challenges:

1. The Pb-free perovskite variant LEDs are still far from being commercialized.
2. The PLQY is still a major hindrance as majority of these Pb-free perovskite variants can hardly exceed 80%.
3. The charge generation and recombination, electroluminescence mechanisms are still widely lacking, thus rational design principles (especially with the charge transport layers) has not been well established yet wherein can freely control emission spectra.

**Table 1** Representative results related to electroluminescence peak emission (EL), maximum external quantum efficiency (EQE) and maximum current efficiency ( $\text{CE}_{\text{MAX}}$ ) for lead-free perovskite-based light-emitting devices

Device architecture	EL $\lambda$ (nm)	EQE (%)	$\text{CE}_{\text{max}}$ (cd/A)	References
ITO/PEDOT/CsSnI <sub>3</sub> /PBD/LiF/Al	950	3.8	n/a	[226]
ITO/PEDOT:PSS/MASn(Br <sub>0.2</sub> I <sub>0.8</sub> ) <sub>3</sub> /F8/Ca/Ag	868	0.058	n/a	[227]
ITO/PEDOT:PSS/PEA <sub>2</sub> SnI <sub>4</sub> /TPBi/LiF/Al	633	0.3	n/a	[228]
ITO/PVK/(PEAI) <sub>3,5</sub> (CsI) <sub>5</sub> (SnI <sub>2</sub> ) <sub>4,5</sub> /TmPyPB/LiF/Al	920	3.0	n/a	[229]
ITO/PEDOT:PSS/Poly-TPD/CsCu <sub>2</sub> I <sub>3</sub> /TPBi/LiF/Al	550	0.17	0.46	[230]
ITO/NiO/ Cs <sub>3</sub> Cu <sub>2</sub> I <sub>5</sub> /TPBi/LiF/Al	445	1.12	n/a	[231]
ITO/ZnO:PEI/ Cs <sub>3</sub> Sb <sub>2</sub> Br <sub>9</sub> /TCTA/MoO <sub>3</sub> /Al	408	0.206	n/a	[232]

Research efforts on exploiting the nanocrystalline nature of inorganic and hybrid halide perovskite-based materials for potential light-emitting applications have only been a few years, with lead-free perovskite, even at very early stages. Although there has been a huge boost in the synthesis and solution processing stages utilizing these materials over the last few years, however, must achieve a further understanding of their optical properties by introducing synergistic experimental and theoretical efforts in the development process. These will give more guidance in establishing the structure-property relationships in terms of the material's electronic property and its stability against heat, light, oxygen, humidity, and so on. These joint efforts may open new doors for next-generation advanced lead-free perovskite-based optoelectronics.

## 4.2 Applications as Solar Cells

For perovskite-based solar cells, effective charge separation of excitons is critical to extract the charges and convert the charges light to electrical power generation. Therefore, the efficiency of these devices is conventionally defined as the ratio of the output power to the incident power from the light source, per unit area [1]. This efficiency is traditionally measured at Standard Test Conditions (1 sun of light and device temperature of about 25 °C) and reported by manufacturers in order to compare the performance of one device to another regardless of the solar cells technology [49, 99, 127, 233–258].

In the case of perovskite technology, a broad range of efficiencies have been reported because different elements such as architectures (see Fig. 1c), structures, compositions, and layers to extract the charges have been used to fabricate perovskite solar cells. Therefore, the combination of these elements is reflected not only on the efficiency, but also on the stability of devices, opening a lot of roadmaps to improve, for instance, the efficiency or another parameter according to the application [34, 49, 99, 127, 145, 233–258]. In this regard, it is noted that the protocols to fabricate efficient and reproducible devices display a critical role in the development of this technology [34]. Besides, despite that the precursor-solution chemistry can be considered as the key obtaining high-quality films, the coating procedure and perovskite composition must be optimized simultaneously for achieving higher efficiencies considering the particularities of each architecture (n-i-p, p-i-n or mesoporous) [145]. Figure 3 illustrated the energy-band-alignment diagram of some materials available for fabrication of the single-junction metal-halide perovskite cells. In general, it is well-known that the nuanced structural differences among interfaces of the target perovskite-based devices are critical to its high-performance applications.

On the other hand, it is worth noted that large-scale manufacturing conventionally involved environmental conditions, thus, the protocols and coating procedures to fabricate perovskite devices must be optimized considering the environmental

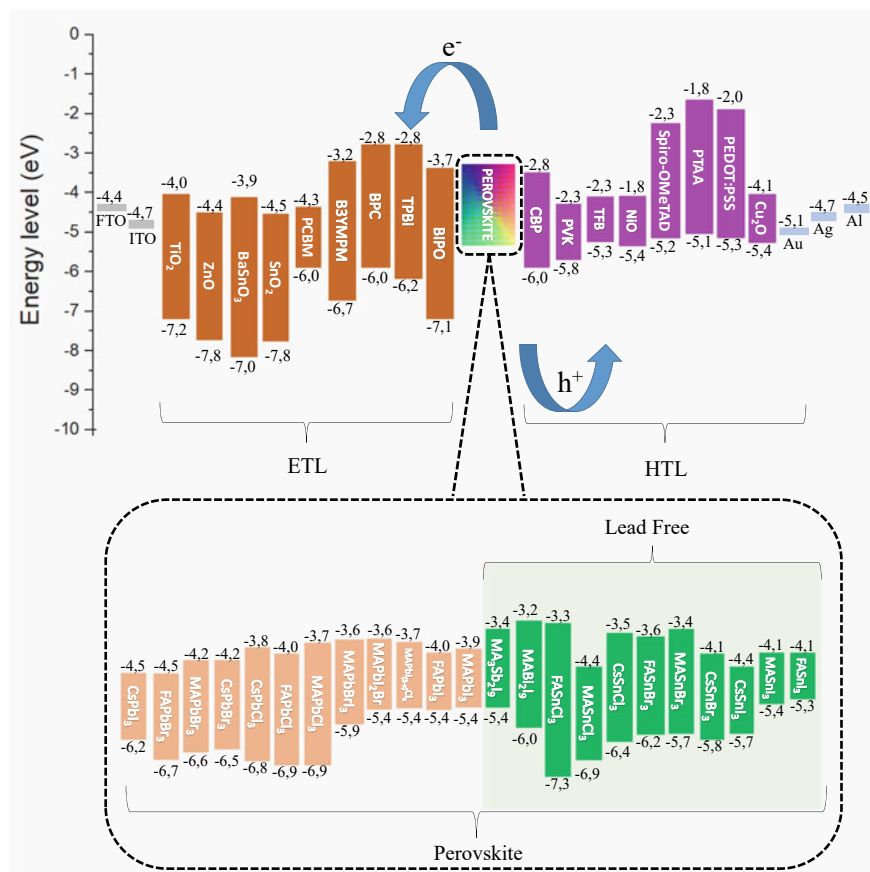


**Fig. 3** Schematic energy-band-alignment diagram of emerging metal-halide perovskite-based solar cells based on different materials usually used as electron-transporting layers (ETL) and as hole-transporting layers (HTL)

factors. Moreover, the environmental impact of perovskite processing is predominantly addressed to use the most environmentally friendly solvent for the fabrication process, and the most environmentally friendly elements to mitigate the main drawback related to the toxicity of conventional perovskites [259–273].

Accordingly, Chen et al. [107] have reported the application of  $\text{Cs}_2\text{SnGeI}_6$ -based solar cells. The performance of these devices showed high stability, with less than 10% deterioration in efficiency after 500 h of continuous operation in  $\text{N}_2$  atmosphere under sunlight. Park et al. [235] manufactured a solar cell with  $\text{Cs}_3\text{Bi}_2\text{I}_9$  perovskite which showed a PEC above 1%. While that the Correa-Baena et al. [260] studied the potential use of  $\text{A}_3\text{Sb}_2\text{I}_9$  ( $\text{A} = \text{Cs}, \text{Rb}$  and  $\text{K}$ ) compounds, as photoabsorbent in solar cell applications.  $\text{Cs}_3\text{Sb}_2\text{I}_9$  has a 0D structure, the highest exciton binding energy ( $175 \pm 9$  meV), an indirect bandgap, and low photocurrent in a solar cell ( $0.13 \text{ mA cm}^{-2}$ ).



Rb<sub>3</sub>Sb<sub>2</sub>I<sub>9</sub> has a 2D structure, a direct bandgap, and among the materials investigated, the lowest exciton binding energy ( $101 \pm 6$  MeV) and the highest photocurrent ( $1.67 \text{ mA cm}^{-2}$ ). K<sub>3</sub>Sb<sub>2</sub>I<sub>9</sub> has a 2D structure, intermediate exciton binding energies ( $129 \pm 9$  MeV) and intermediate photocurrents ( $0.41 \text{ mA cm}^{-2}$ ). Despite remarkably long lifetimes in all compounds (54.9 and 30 ns for Cs, Rb, and K-based materials, respectively), the combination of high exciton binding energy and large effective masses for electrons and holes, results in photocurrents well below  $1 \text{ mA cm}^{-2}$  which limit device performance [260]. Nie et al. [261] have reported MASbSI<sub>2</sub>-based solar cell devices, which showed PEC of about 3.08%, under standard lighting conditions of  $100 \text{ mW/cm}^2$ . Cortecchia et al. [263] have reported 2D MA<sub>2</sub>CuCl<sub>x</sub>Br<sub>4-x</sub> based solar cell devices exhibit a low J<sub>SC</sub> of  $216 \mu\text{A cm}^{-2}$  and V<sub>oc</sub> of 0.256 V, with a PCE of 0.017%. Abulikemu et al. [264] have reported millimeter-scale (CH<sub>3</sub>NH<sub>3</sub>)<sub>3</sub>Bi<sub>2</sub>I<sub>9</sub> based solar cell devices with a PCE of about 0.11%, J<sub>SC</sub> of  $491.89 \mu\text{A cm}^{-2}$  and a V<sub>oc</sub> of 0.7216 V. Ran et al. [256] synthesized a compact thin film of (CH<sub>3</sub>NH<sub>3</sub>)<sub>3</sub>Bi<sub>2</sub>I<sub>9</sub> with a PCE of 0.39% and V<sub>oc</sub> of 0.83 V. These synthesized devices showed low potential loss, but still, a small hysteresis J-V. However, despite these results, the Bi-based perovskite devices have a more stability when compared to Pb-based perovskite devices [256, 264]. Bein et al. [265] manufactured a solar cell with Cs<sub>2</sub>AgBiBr<sub>6</sub> perovskite which showed a PEC of 2.43%, a V<sub>oc</sub> greater than 1 V and good stability at ambient conditions, but with a of relevant hysteresis. In subsequent works, performed by Wu et al. [266] and later Li et al. [267], based on using of solvent engineering strategy, has been reported a relevant decrease in hysteresis of the Cs<sub>2</sub>AgBiBr<sub>6</sub>-based devices. Representative results on lead-free perovskite-based solar cell devices are summarized in Table 2.

Although the growing number of studies related to lead-free perovskite have been published, the most efficient and stable perovskite solar cells are based on lead [268]. These facts highlight that there is still much work to do in this topic to avoid the use of lead on the fabrication of perovskite devices. Moreover, it is worth noted that every innovative technology tries to advance in terms of stability, efficiency, lower costs, stability and sustainability when compared to established/predominant technology [269–273]. Currently, there are some challenges for the economic advancement and use of emerging metal-halide perovskite-based technologies such as the stability (a), toxicity (b), upscaling (c) reproducibility (d).

#### (a) Stability:

In addition to high energy absorption and conversion rates, stability and consequent lifetime are essential factors for a viable commercialization of metal-halide perovskite-based solar cell technologies [271, 272, 274]. Currently, the long-term stability or lifetime ( $T_{80}$ ) of perovskite-based technology on average is only a few months, even for encapsulated devices [275]. This short lifetime is the result of intrinsic and external aspects [276]. Particularly, the intrinsic degradation is mainly related to thermal and light soaking effects. The external degradation is mainly related to moisture ingress into the device. Therefore, various testing protocols have been used to evaluate and report the stability assessment focused mainly on laboratory-scale cells [277–280]. Besides, in

**Table 2.** Summary of lead-free perovskite-based solar cells performance prepared by spin coating

Architecture	V <sub>oc</sub> (V)	J <sub>sc</sub> (mA cm <sup>-2</sup> )	FF (%)	PCE (%)	References
FTO/cp-TiO <sub>2</sub> /mp-TiO <sub>2</sub> /(CH <sub>3</sub> NH <sub>3</sub> ) <sub>3</sub> Bi <sub>2</sub> I <sub>9</sub> /Spiro-OMe TAD/Au	0.88	0.80	49.71	0.34	[233]
FTO/cp-TiO <sub>2</sub> /mp-TiO <sub>2</sub> /MASn(I <sub>0.33</sub> Br <sub>0.67</sub> ) <sub>3</sub> /Spiro-MeOTAD/Au	0.58	11.09	49.50	3.20	[234]
FTO/cp-TiO <sub>2</sub> /mp-TiO <sub>2</sub> /Cs <sub>3</sub> Bi <sub>2</sub> I <sub>9</sub> /HTM/Ag	0.85	2.15	60.00	1.09	[235]
FTO/cp-TiO <sub>2</sub> /mp-TiO <sub>2</sub> /{en} MASnI <sub>3</sub> /PTAA/Au	0.43	24.28	63.72	6.63	[236]
FTO/cp-TiO <sub>2</sub> /mp-TiO <sub>2</sub> /Cs <sub>8</sub> SnBr <sub>3</sub> /Spiro-MeOTAD /Au	0.41	~9.00	58.00	2.10	[237]
FTO/cp-TiO <sub>2</sub> /mp-TiO <sub>2</sub> /CH <sub>3</sub> NH <sub>3</sub> SnI <sub>3</sub> /Spiro-MeOTAD/Au	0.82	12.30	57.00	5.73	[238]
FTO/cp-TiO <sub>2</sub> /mp-TiO <sub>2</sub> /Sb <sub>2</sub> S <sub>3</sub> /PCPDTBT /PEDOT:PSS/Au	0.47	12.00	52.00	2.91	[239]
ITO/cp-TiO <sub>2</sub> /mp-TiO <sub>2</sub> /MA <sub>3</sub> Bi <sub>2</sub> I <sub>9</sub> /Spiro-MeOTAD/MoO <sub>3</sub> /Ag	0.66	0.91	63.63	0.42	[240]
FTO/cp-TiO <sub>2</sub> /mp-TiO <sub>2</sub> /Cs <sub>2</sub> AgBiBr <sub>6</sub> /PTAA/Au	1.02	1.84	67.00	1.26	[241]
FTO/cpt TiO <sub>2</sub> /mp TiO <sub>2</sub> /20% SnF <sub>2</sub> -CsSnI <sub>3</sub> /m-MTDATA/Au	0.24	22.70	37.00	2.02	[242]
ITO/TiO <sub>2</sub> /CsSnI <sub>3</sub> /Spiro-OMeTAD/Au	0.86	23.21	65.00	12.96	[243]
ITO/SnO <sub>2</sub> /Cs <sub>2</sub> AgBiBr <sub>6</sub> /P3HT/Au	1.04	1.78	78.00	1.44	[244]
FTO/TiO <sub>2</sub> /Rb <sub>3</sub> Sb <sub>2</sub> I <sub>9</sub> /Poly-TPD/Au	0.55	2.11	56.97	0.66	[245]
ITO/SnO <sub>2</sub> /C60/ FASnI <sub>3</sub> +SnF <sub>2</sub> +TMAA/Spiro-OMeTAD/Ag	0.31	21.65	64.70	4.34	[246]
ITO/cl-TiO <sub>2</sub> /Cs <sub>2</sub> AgBiBr <sub>6</sub> /Spiro-OMeTAD/Au	1.06	1.55	74.00	1.22	[247]
FTO/b-TiO <sub>2</sub> /n-TiO <sub>2</sub> /CH <sub>3</sub> NH <sub>3</sub> SnCl <sub>3</sub> / PEO:KI/I <sub>2</sub> /Pt	0.60	1.50	59.00	0.55	[248]
ITO/Cu-NiO/Cs <sub>2</sub> AgBiBr <sub>6</sub> /C <sub>60</sub> /BCP/Ag	1.01	3.19	69.2	2.23	[249]
ITO/PEDOT:PSS/MASnBr <sub>7</sub> /PC <sub>61</sub> BM /AI	0.48	17.8	52.00	4.45	[250]
ITO/PEDOT:PSS/FASnI <sub>3</sub> /PC <sub>71</sub> BM/Ag	0.55	22.72	71.2	8.90	[251]
ITO/ PEDOT:PSS/FA <sub>0.8</sub> GA <sub>0.2</sub> SnI <sub>3</sub> (3D/2D)/C60/BCP/Ag anilinium solvent in the second step	0.64	21.10	76.30	10.40	[252]
FTO/PEDOT:PSS/FPSPGI (7.5Ge)/BCP/Ag/Au	0.46	21.92	73.00	7.45	[253]

(continued)

**Table 2** (continued)

Architecture	V <sub>oc</sub> (V)	J <sub>sc</sub> (mA cm <sup>-2</sup> )	FF (%)	PCE (%)	References
ITO/PEDOT:PSS/FA <sub>0.75</sub> MA <sub>0.25</sub> SnI <sub>3</sub> /C <sub>60</sub> /Ag	0.55	19.4	67.00	7.20	[254]
FTO/Cu-NiO <sub>x</sub> /FASnI <sub>3</sub> /PCBM/Ag	0.69	21.15	74.00	10.86	[255]
ITO/PEDOT:PSS/MA <sub>3</sub> Bi <sub>2</sub> I <sub>9</sub> /C <sub>60</sub> /BCP/Ag	0.83	1.39	34.00	0.39	[256]
FTO/PEDOT:PSS/GeI <sub>2</sub> doped (FA <sub>0.9</sub> EA <sub>0.1</sub> ) <sub>0.98</sub> EDA <sub>0.01</sub> SnI <sub>3</sub> /C <sub>60</sub> /BCP/Ag/Au	0.84	20.32	78.00	13.24	[49]
ITO/PEDOT:PSS/MA <sub>0.8</sub> HA <sub>0.2</sub> SnI <sub>3</sub> /PCBM/Al	0.35	11.80	50.00	2.10	[99]
ITO/PEDOT:PSS/MA <sub>3</sub> Sb <sub>2</sub> I <sub>9</sub> +HI/PC <sub>71</sub> BM/C <sub>60</sub> /BCP/Al	0.62	5.41	60.82	2.04	[257]
ITO/PEDOT:PSS/GA <sub>0.2</sub> FA <sub>0.78</sub> SnI <sub>3</sub> -1%EDA <sub>1</sub> /C <sub>60</sub> (20 nm)/BCP/Ag	0.562	20.80	72.60	8.50	[258]

contrast to photovoltaic technologies such as silicon, the performance estimation during the tests could be affected by the performance loss reversibility under day-night cycles [281] and hysteresis effects in the I-V curve [282].

Accordingly, it is possible to find different strategies to improve the lifetime, including alteration of their compositions and dimensionality, interfaces passivation [283], selective charge contacts [284], barrier designs [285], among other strategies. Thus, due that the electrodes and active areas of photovoltaic cells must be protected from ambient exposure conditions, it is mandatory that the strategies used to improve the lifetime are complemented by a proper device encapsulation or external barrier layer to mitigate corrosion processes, increase the electrical insulation, and provide mechanical support [286].

In this regard, it is worth noting that different encapsulating materials and techniques have been used in Perovskite solar devices [287]. For instance, ethylene-vinyl acetate (EVA) as encapsulant was successfully tested following the temperature cycles test suggested by IEC 61,215 [288]. Polyisobutylene (PIB) as a barrier layer shown promising results when the devices were tested in thermal cycles and Damp heat tests [289]. A similar approach using carbon layer as a barrier was probed in solar cells and minimodules, encapsulating the devices with additional glass and epoxy glue, increasing the long stability of devices up to 12,000 h of exposure under continuous illumination of one sun [290]. Besides, several epoxy resins have been tested as encapsulant material to evaluate the outdoor performance of minimodules of perovskite [148, 291].

Although a lot of work has been done on this topic [271, 272, 274], it is important to highlight that there is still a long way to go, particularly regarding incorporation or adaptation of international standards such as IEC 61,215 to evaluate the encapsulation process and improve the lifetime. On the other hand, due that this technology is in its infancy, and there are few statistical data available for large devices operated outdoors [148, 292, 293] it is necessary the outdoor evaluation in order to gain insights related to the stability or degradation processes of this emerging technology [293].

(b) Toxicity

As is well-known, the most perovskite-based devices were developed using a lead-based matrix. However, there is very strict legislation regarding the use of lead, especially due to their high toxicity [53], but these rules make an exception for lead that is used in the solders of conventional photovoltaic modules as well as in other electronic components. This toxicity makes it difficult to accept the technology and may conflict with the ESG (Environmental, Social and Governance) policy that has been sought after worldwide [45]. In this regard, more recently, has been developed lead-free halide perovskites [37, 44, 97, 138]. The most viable substitutes for Pb are Sn and Ge, however, the biggest problem with these metals is that they already have chemical instability in the required oxidation state (2+), resulting in a perovskite with lower stability [166, 269, 294–297]. Sn is the metal that has received the most attention [97, 138, 298] to replace Pb, however, studies [138] have revealed an easy oxidation of

$\text{Sn}^{2+}$ , with an n-type semiconductor behavior, to  $\text{Sn}^{4+}$ , whose behavior becomes that of a p-type semiconductor, which acts as a dopant inside the material, in a process called self-doping. Meanwhile, despite its toxicity, Pb has greater protection against oxidation. The first work using Sn replacing Pb in perovskite was reported by Hao et al. [238], in early 2014. The authors achieved an efficiency of 5.73% with  $\text{MASnI}_3$  perovskite. In the same year, Hao et al. [299], using a methylammonium perovskite with a mixture of lead and tin ( $\text{CH}_3\text{NH}_3\text{Sn}_{(1-x)}\text{Pb}_{(x)}\text{I}_3$ ), and Noel et al. [299], with a study of different solvents in the crystallization of perovskite, they achieved similar efficiencies—5.44 and 6.4%, respectively. Thus, other studies have been carried out in order to improve the stability of perovskite solar cells. However, these are recent studies and not fully understood, requiring intensification of studies for possible practical commercial applications of the devices [300].

(c) Upscaling

There are a number of problems that are caused in perovskite cells with increasing size, since larger areas can bring uniformity and morphology problems [301]. It is necessary to manufacture devices on an industrial scale, making the transition from a laboratory scale to a manufacturing scale [302]. Currently, most studies in the literature are limited to small areas ( $<1 \text{ cm}^2$ ), but devices to photovoltaic commercial sizes ( $>1 \text{ m}^2$ ) must be achieved [154].

Although different techniques have widely been used to fabricate metal-halide perovskite-based devices on larger areas (e.g., such as Doctor blade, Slot-die, Screen printing, and so on) [145], it is to highlight that spin-coting technique has been used successfully in areas up to  $100 \text{ cm}^2$ , obtaining the higher efficiencies [303]. This is an important aspect to remark, because  $100 \text{ cm}^2$  of size is comparable with the size of silicon solar cells used in modules.

Accordingly, in order to improve the performance of perovskite technology beyond cells, the efforts are mainly focus on the cells interconnection passing from cells to, minimodules and modules [292, 304]. In this context, most of the perovskite devices are fabricated using three scribe lines or patterns (P1, P2, and P3) to interconnect the cells in series and mitigate electrical losses [292, 303, 305, 306]. This technique is widely employed in other thin-film photovoltaic technologies as silicon, CIGS, and polymer [307, 308]. In perovskite devices, P1 scribe line is performed on the transparent conductive oxide layer (ITO or FTO) to limit the sub-cells area. P2 scribe line is performed on the charge transport layers (electron and hole layers) and perovskite layer, intended to clear the ITO or FTO layer and allow interconnection between the back electrode and the charge transport layers. Finally, P3 scribe is performed to remove the back-contact layer and separate the cells. Therefore, the active area is limited by P1 and P3 lines. In contrast, the death-area is limited by P3 and P1 lines.

Consequently, the first certificated minimodule of this technology was reported in 2016 by SJTU team, which corresponded to 12.1% of efficiency, 10 serial cells, and an illuminated area of  $36.13 \text{ cm}^2$  [309]. Nowadays, it is possible to find certified PSC module with an efficiency of 17.9% and 55 serial

cells [310]. This considerable progress in the up-scaling shows the effort of the community. Moreover, the multi-junctions with other photovoltaic technologies such as silicon and CIGS, opening new opportunities and challenges to be explored.

(d) Reproducibility

The more robust the synthesis, the more reproducible and less prone to small, subtle changes in the manufacturing process will the perovskite cells be. A robust process is important for reproducibility and scalability for large-scale manufacturing. These small variations in yield and conversion between synthesis batches when they are transferred to larger scales can generate huge losses, creating a certain risk associated with the implementation of large industrial plants. Undoubtedly, the reproducibility and the search for certification of measurements has been and will continue to be one of the biggest challenges for the establishment of perovskite solar cells [311, 312]. Here, it is important to mention that mesoporous structures in both architecture (p-i-n and n-i-p) helps to mitigate pin-holes improving the devices reproducibility. Besides the inverted mesoporous structure (ITO/NiO<sub>x</sub>/Al<sub>2</sub>O<sub>3</sub>/MAPI/PCMB/Rhodamine/Au) has been demonstrated to be feasible for fabricating large-area devices up to 100 cm<sup>2</sup> in dry-box conditions by spin coating, improving the reproducibility and reducing hysteresis [147, 148]. Finally, the standardization of protocols for the fabrication of perovskite devices and ensuring reproducibility is highlighted.

## 5 Conclusions and Outlook

Overall, throughout this chapter, we have highlighted the enormous potential of the emerging metal-halide perovskites for photovoltaic applications. Certainly, the development of this technology will contribute to its popularization and sustainable use in the future. New manufacturing methods, device structure and materials continue to emerge. However, these emerging metal-halide perovskite devices still have several key aspects that need to be improved before their commercial application [313], allowing the introduction of a new and high-tech product on the market [314]. Finally, in this direction, more studies are needed to improve the stability of the devices and other problems still faced, so that it can reach commercialization in the coming years, including the use of new strategies such as Machine Learning [311, 315, 316] for database construction and prediction of the most promising synthesis routes to obtain the highest values of PCEs and ECEs.

**Acknowledgements** The authors gratefully acknowledge the support from the Brazilian agencies CAPES and CNPq.

## References

1. Bisquert, J.: *The Physics of Solar Energy Conversion*, 1st edn. CRC Press (2020)
2. Green, M.A.: The path to 25% silicon solar cell efficiency: history of silicon cell evolution. *Prog. Photovolt. Res. Appl.* **17**(3), 183–189 (2009). <https://doi.org/10.1002/PIP.892>
3. Swanson, R.M.: Approaching the 29% limit efficiency of silicon solar cells. *Conf. Rec. IEEE Photovolt. Spec. Conf.* 889–894 (2005). <https://doi.org/10.1109/PVSC.2005.1488274>
4. Andreani, L.C., Bozzola, A., Kowalczewski, P., Liscidini, M., Redorici, L.: Silicon solar cells: toward the efficiency limits. *Adv. Phys. X* **4**(1), 1548305 (2018). <https://doi.org/10.1080/23746149.2018.1548305>
5. Ohnishi, M., Takeoka, A., Nakano, S., Kuwano, Y.: Advanced photovoltaic technologies and residential applications. *Renew. Energy* **6**(3), 275–282 (1995). [https://doi.org/10.1016/0960-1481\(95\)00019-G](https://doi.org/10.1016/0960-1481(95)00019-G)
6. Raphael, E., Silva, M., Szostak, R., Schiavon, M.A., Nogueira, A.F.: células solares de perovskitas: uma nova tecnologia emergente. *Quim. Nova* (2017). <https://doi.org/10.21577/0100-4042.20170127>
7. Sun, C., et al.: Origins of hydrogen that passivates bulk defects in silicon heterojunction solar cells. *Appl. Phys. Lett.* **115**(25), 252103 (2019). <https://doi.org/10.1063/1.5132368>
8. Quansah, D.A., Adaramola, M.S.: Comparative study of performance degradation in poly- and mono-crystalline-Si solar PV modules deployed in different applications. *Int. J. Hydrogen Energy* **43**(6), 3092–3109 (2018). <https://doi.org/10.1016/j.ijhydene.2017.12.156>
9. Raphael, E., et al.: Células solares de perovskitas: uma nova tecnologia emergente. *Quim.* **41**(1), 61–74 (2018). <https://doi.org/10.21577/0100-4042.20170127>
10. Ling, J.K., et al.: A perspective on the commercial viability of perovskite solar cells. *Sol. RRL* **5**(11), 2100401 (2021). <https://doi.org/10.1002/SOLR.202100401>
11. Tailor, N.K., et al.: Recent progress in morphology optimization in perovskite solar cell. *J. Mater. Chem. A* **8**(41), 21356–21386 (2020). <https://doi.org/10.1039/D0TA00143K>
12. Chang, N.L., Ho-Baillie, A.W.Y., Vak, D., Gao, M., Green, M.A., Egan, R.J.: Manufacturing cost and market potential analysis of demonstrated roll-to-roll perovskite photovoltaic cell processes. *Sol. Energy Mater. Sol. Cells* **174**, 314–324 (2018). <https://doi.org/10.1016/j.solmat.2017.08.038>
13. Moure, C., Peña, O.: Recent advances in perovskites: processing and properties. *Prog. Solid State Chem.* **43**(4), 123–148 (2015). <https://doi.org/10.1016/j.progsolidstchem.2015.09.001>
14. Stranks, S.D., Snaith, H.J.: Metal-halide perovskites for photovoltaic and light-emitting devices. *Nat. Nanotechnol.* **10**(5), 391–402 (2015). <https://doi.org/10.1038/nnano.2015.90>
15. Manser, J.S., Christians, J.A., Kamat, P.V.: Intriguing optoelectronic properties of metal halide perovskites. *Chem. Rev.* **116**(21), 12956–13008 (2016). <https://doi.org/10.1021/ACS.CHEMREV.6B00136>
16. Di Girolamo, D., et al.: Dual effect of humidity on cesium lead bromide: enhancement and degradation of perovskite films. *J. Mater. Chem. A* **7**(19), 12292–12302 (2019). <https://doi.org/10.1039/C9TA00715F>
17. Mattoni, A., Meloni, S.: Defect dynamics in MAPbI<sub>3</sub> polycrystalline films: the trapping effect of grain boundaries. *Helv. Chim. Acta* **103**(9), e2000110 (2020). <https://doi.org/10.1002/HLCA.202000110>
18. Cahen, D., Kronik, L., Hodes, G.: Are defects in lead-halide perovskites healed, tolerated, or both? *ACS Energy Lett.* **6**(11), 4108–4114 (2021). <https://doi.org/10.1021/ACSENERGYLETT.1C02027>
19. Phung, N., et al.: The role of grain boundaries on ionic defect migration in metal halide perovskites. *Adv. Energy Mater.* **10**(20), 1903735 (2020). <https://doi.org/10.1002/AENM.201903735>

20. Pinto, F.M., Suzuki, V.Y., Silva, R.C., La Porta, F.A.: Oxygen defects and surface chemistry of reducible oxides. *Front. Mater.* **6** (2019). <https://doi.org/10.3389/fmats.2019.00260>
21. Zhu, H., et al.: Screening in crystalline liquids protects energetic carriers in hybrid perovskites. *Science (80-)* **353**(6306), 1409–1413 (2016). [https://doi.org/10.1126/SCIENCE.AAF9570/SUPPL\\_FILE/ZHU.SM.PDF](https://doi.org/10.1126/SCIENCE.AAF9570/SUPPL_FILE/ZHU.SM.PDF)
22. Kojima, A., Teshima, K., Shirai, Y., Miyasaka, T.: Organometal halide perovskites as visible-light sensitizers for photovoltaic cells. *J. Am. Chem. Soc.* **131**(17), 6050–6051 (2009). <https://doi.org/10.1021/ja809598r>
23. Green, M., Dunlop, E., Hohl-Ebinger, J., Yoshita, M., Kopidakis, N., Hao, X.: Solar cell efficiency tables (version 57). *Prog. Photovolt. Res. Appl.* **29**(1), 3–15 (2021). <https://doi.org/10.1002/PIP.3371>
24. Rolston, N., et al.: Rapid open-air fabrication of perovskite solar modules. *Joule* **4**(12), 2675–2692 (2020). <https://doi.org/10.1016/J.JOULE.2020.11.001>
25. Tong, G., et al.: Scalable fabrication of >90 cm<sup>2</sup> perovskite solar modules with >1000 h operational stability based on the intermediate phase strategy. *Adv. Energy Mater.* **11**(10), 2003712 (2021). <https://doi.org/10.1002/AENM.202003712>
26. Chen, H., et al.: A solvent- and vacuum-free route to large-area perovskite films for efficient solar modules. *Nature* **550**(7674), 92–95 (2017). <https://doi.org/10.1038/nature23877>
27. Wu, T., et al.: The main progress of perovskite solar cells in 2020–2021. *Nano-Micro Lett.* **13**(1), 1–18 (2021). <https://doi.org/10.1007/S40820-021-00672-W/TABLES/1>
28. Sahoo, S., Manoharan, B., Sivakumar, N.: Introduction. In: *Perovskite Photovoltaics*, pp. 1–24. Elsevier (2018)
29. Best Research-Cell Efficiency Chart (2022). <https://www.nrel.gov/pv/cell-efficiency.htm>
30. Green, M.A., Dunlop, E.D., Hohl-Ebinger, J., Yoshita, M., Kopidakis, N., Hao, X.: Solar cell efficiency tables (version 59). *Prog. Photovolt. Res. Appl.* **30**(1), 3–12 (2022). <https://doi.org/10.1002/pip.3506>
31. Li, D., et al.: A review on scaling up perovskite solar cells. *Adv. Funct. Mater.* **31**(12), 2008621 (2021). <https://doi.org/10.1002/ADFM.202008621>
32. Correa-Baena, J.P., et al.: Promises and challenges of perovskite solar cells. *Science (80-)* **358**(6364), 739–744 (2017). [https://doi.org/10.1126/SCIENCE.AAM6323/SUPPL\\_FILE/AAM6323\\_CORREA-BAENA\\_SM.PDF](https://doi.org/10.1126/SCIENCE.AAM6323/SUPPL_FILE/AAM6323_CORREA-BAENA_SM.PDF)
33. Rong, Y., et al.: Challenges for commercializing perovskite solar cells. *Science (80-)* **361**(6408) (2018). [https://doi.org/10.1126/SCIENCE.AAT8235/ASSET/FA0D3D3C-9EC5-44B8-A024-C9EC9D4B5244/ASSETS/GRAPHIC/361\\_AAT8235\\_FA.JPEG](https://doi.org/10.1126/SCIENCE.AAT8235/ASSET/FA0D3D3C-9EC5-44B8-A024-C9EC9D4B5244/ASSETS/GRAPHIC/361_AAT8235_FA.JPEG)
34. Saliba, M., et al.: How to make over 20% efficient perovskite solar cells in regular (n-i-p) and inverted (p-i-n) architectures. *Chem. Mater.* **30**(13), 4193–4201 (2018). [https://doi.org/10.1021/ACS.CHEMMATER.8B00136/SUPPL\\_FILE/CM8B00136\\_SI\\_004.MPG](https://doi.org/10.1021/ACS.CHEMMATER.8B00136/SUPPL_FILE/CM8B00136_SI_004.MPG)
35. Mei, A., et al.: A hole-conductor-free, fully printable mesoscopic perovskite solar cell with high stability. *Science (80-)* **345**(6194), 295–298 (2014). [https://doi.org/10.1126/SCIENCE.1254763/SUPPL\\_FILE/MEI.SM.PDF](https://doi.org/10.1126/SCIENCE.1254763/SUPPL_FILE/MEI.SM.PDF)
36. Shi, T., et al.: Low-temperature fabrication of carbon-electrode based, hole-conductor-free and mesoscopic perovskite solar cells with power conversion efficiency > 12% and storage-stability > 220 days. *Appl. Phys. Lett.* **117**(16), 163501 (2020). <https://doi.org/10.1063/5.0025442>
37. Wang, R., Wang, J., Tan, S., Duan, Y., Wang, Z.K., Yang, Y.: Opportunities and challenges of lead-free perovskite optoelectronic devices. *Trends Chem.* **1**(4), 368–379 (2019). <https://doi.org/10.1016/J.TRECHM.2019.04.004>
38. Yang, S., Fu, W., Zhang, Z., Chen, H., Li, C.Z.: Recent advances in perovskite solar cells: efficiency, stability and lead-free perovskite. *J. Mater. Chem. A* **5**(23), 11462–11482 (2017). <https://doi.org/10.1039/C7TA00366H>



39. Giustino, F., Snaith, H.J.: Toward lead-free perovskite solar cells. *ACS Energy Lett.* **1**(6), 1233–1240 (2016). <https://doi.org/10.1021/ACSENERGYLETT.6B00499>
40. Shi, Z., et al.: Lead-free organic-inorganic hybrid perovskites for photovoltaic applications: recent advances and perspectives. *Adv. Mater.* **29**(16), 1605005 (2017). <https://doi.org/10.1002/ADMA.201605005>
41. Hailegnaw, B., Kirmayer, S., Edri, E., Hodes, G., Cahen, D.: Rain on methylammonium lead iodide based perovskites: possible environmental effects of perovskite solar cells. *J. Phys. Chem. Lett.* **6**(9), 1543–1547 (2015). [https://doi.org/10.1021/ACS.JPCLETT.5B00504/SUPPL\\_FILE/JZ5B00504\\_SI\\_001.PDF](https://doi.org/10.1021/ACS.JPCLETT.5B00504/SUPPL_FILE/JZ5B00504_SI_001.PDF)
42. Kely, A., Souza, R., Morassuti, C.Y., Batista De Deus, W.: Poluição do ambiente por metais pesados e utilização de vegetais como bioindicadores. *Acta Biomed. Bras.* **9**(3), 95–106 (2018). <https://doi.org/10.18571/ACBM.189>
43. Von Sperling, M.: *Introdução à Qualidade das Águas e ao Tratamento de Esgotos*, 4th edn. Editora UFMG (2014)
44. Wang, Q., Abate, A.: Perovskite solar cells : promises and challenges. In: Kurinec, S.K. (Ed.) *Emerging Photovoltaic Materials: Silicon & Beyond*, 1st edn, pp. 261–356. Scrivener Publishing, Beverly, USA (2019)
45. Li, J., et al.: Biological impact of lead from halide perovskites reveals the risk of introducing a safe threshold. *Nat. Commun.* **11**(310), 1–5 (2020). <https://doi.org/10.1038/s41467-019-13910-y>
46. Joshi, R.L.: Environmental science. *J. Nepal Med. Assoc.* **10**(3), 147–154 (2003). <https://doi.org/10.31729/jnma.1240>
47. Yue, S., et al.: Synthesis, characterization, and stability studies of Ge-based perovskites of controllable mixed cation composition, produced with an ambient surfactant-free approach. *ACS Omega* **4**(19), 18219–18233 (2019). [https://doi.org/10.1021/ACSOMEGA.9B02203/SUPPL\\_FILE/AO9B02203\\_SI\\_001.PDF](https://doi.org/10.1021/ACSOMEGA.9B02203/SUPPL_FILE/AO9B02203_SI_001.PDF)
48. Veronese, A., Patrini, M., Bajoni, D., Ciarrocchi, C., Quadrelli, P., Malavasi, L.: Highly tunable emission by halide engineering in lead-free perovskite-derivative nanocrystals: the Cs<sub>2</sub>SnX<sub>6</sub> (X = Cl, Br, Br/I, I) system. *Front. Chem.* **8**, 35 (2020). <https://doi.org/10.3389/FCHEM.2020.00035/BIBTEX>
49. Nishimura, K., et al.: Lead-free tin-halide perovskite solar cells with 13% efficiency. *Nano Energy* **74**, 104858 (2020). <https://doi.org/10.1016/J.NANOEN.2020.104858>
50. Li, X.L., Li, Z., Zhang, G., Yang, G.J.: Lead-free perovskite [H<sub>3</sub>NC<sub>6</sub>H<sub>4</sub>NH<sub>3</sub>]CuBr<sub>4</sub> with both a bandgap of 1.43 eV and excellent stability. *J. Mater. Chem. A* **8**(11), 5484–5488 (2020). <https://doi.org/10.1039/C9TA12872G>
51. Arul, N.S., Nithya, V.D. (Eds.): *Revolution of Perovskite*. Springer Singapore, Singapore (2020)
52. Huang, Y.T., Kavanagh, S.R., Scanlon, D.O., Walsh, A., Hoye, R.L.Z.: Perovskite-inspired materials for photovoltaics and beyond—from design to devices. *Nanotechnology* **32**(13), 132004 (2021). <https://doi.org/10.1088/1361-6528/ABCF6D>
53. Pinto, F.M., Dey, S., Duarte, T.M., Taft, C.A., La Porta, F.A.: Perovskite-like quantum dots designed for advanced optoelectronic applications. In: de A. Taft, F., La Porta, C.A. (Eds.) *Functional Properties of Advanced Engineering Materials and Biomolecules*, 1st edn, pp. 83–108. Springer, Cham (2021)
54. Hong, X.: Nitride perovskite becomes polar. *Science (80-.)* **374**(6574), 1445–1446 (2021). <https://doi.org/10.1126/science.abm7179>
55. Mazzo, T.M., et al.: Controlling the electronic, structural, and optical properties of novel MgTiO<sub>3</sub>/LaNiO<sub>3</sub> nanostructured films for enhanced optoelectronic devices. *ACS Appl. Nano Mater.* **2**(5), 2612–2620 (2019). <https://doi.org/10.1021/acsnm.8b02110>

56. Sato, T., Noréus, D., Takeshita, H., Häussermann, U.: Hydrides with the perovskite structure: general bonding and stability considerations and the new representative CaNiH<sub>3</sub>. *J. Solid State Chem.* **178**(11), 3381–3388 (2005). <https://doi.org/10.1016/j.jssc.2005.08.026>
57. Surucu, G., Gencer, A., Candan, A., Gullu, H.H., Isik, M.: CaXH<sub>3</sub> (X = Mn, Fe, Co) perovskite-type hydrides for hydrogen storage applications. *Int. J. Energy Res.* **44**(3), 2345–2354 (2020). <https://doi.org/10.1002/er.5062>
58. Flores-Livas, J.A., Sarmiento-Pérez, R., Botti, S., Goedecker, S., Marques, M.A.L.: Rare-earth magnetic nitride perovskites. *J. Phys. Mater.* **2**(2), 025003 (2019). <https://doi.org/10.1088/2515-7639/ab083e>
59. Terranova, U., Viñes, F., de Leeuw, N.H., Illas, F.: Mechanisms of carbon dioxide reduction on strontium titanate perovskites. *J. Mater. Chem. A* **8**(18), 9392–9398 (2020). <https://doi.org/10.1039/D0TA01502D>
60. Assirey, E.A.R.: Perovskite synthesis, properties and their related biochemical and industrial application. *Saudi Pharm. J.* **27**(6), 817–829 (2019). <https://doi.org/10.1016/j.jpsps.2019.05.003>
61. Borowski, M.: Perovskites: Structure. Nova Science Pub Inc., Properties and Uses (2011)
62. Nakata, M.M., Mazzo, T.M., Casali, G.P., La Porta, F.A., Longo, E.: A large red-shift in the photoluminescence emission of Mg<sub>1-x</sub>Sr<sub>x</sub>TiO<sub>3</sub>. *Chem. Phys. Lett.* **622**, 9–14 (2015). <https://doi.org/10.1016/j.cplett.2015.01.011>
63. Fuertes, A.: Nitride tuning of transition metal perovskites. *APL Mater.* **8**(2), 020903 (2020). <https://doi.org/10.1063/1.5140056>
64. Oliveira, L.H., et al.: Optical and gas-sensing properties, and electronic structure of the mixed-phase CaCu<sub>3</sub>Ti<sub>4</sub>O<sub>12</sub>/CaTiO<sub>3</sub> composites. *Mater. Res. Bull.* **93**, 47–55 (2017). <https://doi.org/10.1016/j.materresbull.2017.04.037>
65. Schouwink, P., et al.: Structure and properties of complex hydride perovskite materials. *Nat. Commun.* **5**(1), 5706 (2014). <https://doi.org/10.1038/ncomms6706>
66. Lin, N., Gong, Y., Wang, R., Wang, Y., Zhang, X.: Critical review of perovskite-based materials in advanced oxidation system for wastewater treatment: design, applications and mechanisms. *J. Hazard. Mater.* **424**, 127637 (2022). <https://doi.org/10.1016/j.jhazmat.2021.127637>
67. Chouhan, L., Ghimire, S., Subrahmanyam, C., Miyasaka, T., Biju, V.: Synthesis, optoelectronic properties and applications of halide perovskites. *Chem. Soc. Rev.* **49**(10), 2869–2885 (2020). <https://doi.org/10.1039/C9CS00848A>
68. Ha, S.-T., Su, R., Xing, J., Zhang, Q., Xiong, Q.: Metal halide perovskite nanomaterials: synthesis and applications. *Chem. Sci.* **8**(4), 2522–2536 (2017). <https://doi.org/10.1039/C6SC04474C>
69. Thomas, A., Thankappan, S.: Perovskite Photovoltaics: Basic to Advanced Concepts and Implementation. Academic Press (2018)
70. Xu, W., et al.: Rational molecular passivation for high-performance perovskite light-emitting diodes. *Nat. Photon.* **13**(6), 418–424 (2019). <https://doi.org/10.1038/s41566-019-0390-x>
71. Yakunin, S., et al.: Low-threshold amplified spontaneous emission and lasing from colloidal nanocrystals of caesium lead halide perovskites. *Nat. Commun.* **6**(1), 8056 (2015). <https://doi.org/10.1038/ncomms9056>
72. Jena, A.K., Kulkarni, A., Miyasaka, T.: Halide perovskite photovoltaics: background, status, and future prospects. *Chem. Rev.* **119**(5), 3036–3103 (2019). <https://doi.org/10.1021/acs.chemrev.8b00539>
73. Protesescu, L., et al.: Nanocrystals of cesium lead halide perovskites (CsPbX<sub>3</sub>, X = Cl, Br, and I): novel optoelectronic materials showing bright emission with wide color gamut. *Nano Lett.* **15**(6), 3692–3696 (2015). <https://doi.org/10.1021/nl5048779>
74. Park, N.-G., Grätzel, M., Miyasaka, T. (eds.): Organic-Inorganic Halide Perovskite Photovoltaics. Springer International Publishing, Cham (2016)
75. Quarti, C., Katan, C., Even, J.: Physical properties of bulk, defective, 2D and 0D metal halide perovskite semiconductors from a symmetry perspective. *J. Phys. Mater.* **3**(4), 042001 (2020). <https://doi.org/10.1088/2515-7639/aba6f6>

76. Zhou, Y., Zhao, Y.: Chemical stability and instability of inorganic halide perovskites. *Energy Environ. Sci.* **12**(5), 1495–1511 (2019). <https://doi.org/10.1039/C8EE03559H>
77. Frost, J.M., Walsh, A.: Molecular motion and dynamic crystal structures of hybrid halide perovskites. In: *Organic-Inorganic Halide Perovskite Photovoltaics*. Springer International Publishing, Cham, pp. 1–17 (2016)
78. Glazer, A.M.: The classification of tilted octahedra in perovskites. *Acta Crystallogr. Sect. B Struct. Crystallogr. Cryst. Chem.* **28**(11), 3384–3392 (1972). <https://doi.org/10.1107/S0567740872007976>
79. Halcrow, M.A.: Jahn–Teller distortions in transition metal compounds, and their importance in functional molecular and inorganic materials. *Chem. Soc. Rev.* **42**(4), 1784–1795 (2013). <https://doi.org/10.1039/C2CS35253B>
80. Ullmann, H., Trofimenko, N.: Estimation of effective ionic radii in highly defective perovskite-type oxides from experimental data. *J. Alloys Compd.* **316**(1–2), 153–158 (2001). [https://doi.org/10.1016/S0925-8388\(00\)01448-1](https://doi.org/10.1016/S0925-8388(00)01448-1)
81. Steele, J.A. et al.: Thermal unequilibrium of strained black CsPbI<sub>3</sub> thin films. *Science* (80-) **365**(6454), 679–684 (2019). <https://doi.org/10.1126/science.aax3878>
82. Meggiolaro, D., et al.: Iodine chemistry determines the defect tolerance of lead-halide perovskites. *Energy Environ. Sci.* **11**(3), 702–713 (2018). <https://doi.org/10.1039/C8EE00124C>
83. Shamsi, J., Urban, A.S., Imran, M., De Trizio, L., Manna, L.: Metal halide perovskite nanocrystals: synthesis, post-synthesis modifications, and their optical properties. *Chem. Rev.* **119**(5), 3296–3348 (2019). <https://doi.org/10.1021/acs.chemrev.8b00644>
84. Jing, Q., Xu, Y., Su, Y., Xing, X., Lu, Z.: A systematic study of the synthesis of cesium lead halide nanocrystals: does Cs<sub>4</sub>PbBr<sub>6</sub> or CsPbBr<sub>3</sub> form? *Nanoscale* **11**(4), 1784–1789 (2019). <https://doi.org/10.1039/C8NR08116F>
85. Brivio, F., Walker, A.B., Walsh, A.: Structural and electronic properties of hybrid perovskites for high-efficiency thin-film photovoltaics from first-principles. *APL Mater.* **1**(4), 042111 (2013). <https://doi.org/10.1063/1.4824147>
86. Goldschmidt, V.M.: Die gesetze der krystallochemie. *Naturwissenschaften* **14**(21), 477–485 (1926). <https://doi.org/10.1007/BF01507527>
87. Zhang, H., Li, N., Li, K., Xue, D.: Structural stability and formability of AB<sub>3</sub>O<sub>3</sub>-type perovskite compounds. *Acta Crystallogr. Sect. B Struct. Sci.* **63**(6), 812–818 (2007). <https://doi.org/10.1107/S0108768107046174>
88. Li, C., Lu, X., Ding, W., Feng, L., Gao, Y., Guo, Z.: Formability of ABX<sub>3</sub> (X = F, Cl, Br, I) halide perovskites. *Acta Crystallogr. Sect. B Struct. Sci.* **64**(6), 702–707 (2008). <https://doi.org/10.1107/S0108768108032734>
89. Bartel, C.J., et al.: New tolerance factor to predict the stability of perovskite oxides and halides. *Sci. Adv.* **5**(2) (2019). <https://doi.org/10.1126/sciadv.aav0693>
90. Rao, C.N.R.: Perovskites. In: *Encyclopedia of Physical Science and Technology*, pp. 707–714. Elsevier (2003)
91. Akkerman, Q.A., Manna, L.: What defines a halide perovskite? *ACS Energy Lett.* **5**(2), 604–610 (2020). <https://doi.org/10.1021/acsenergylett.0c00039>
92. Zhou, C., Lin, H., Lee, S., Chaaban, M., Ma, B.: Organic–inorganic metal halide hybrids beyond perovskites. *Mater. Res. Lett.* **6**(10), 552–569 (2018). <https://doi.org/10.1080/21663831.2018.1500951>
93. Adjogri, S.J., Meyer, E.L.: A review on lead-free hybrid halide perovskites as light absorbers for photovoltaic applications based on their structural, optical, and morphological properties. *Molecules* **25**(21), 5039 (2020). <https://doi.org/10.3390/molecules25215039>
94. Xiao, Z., Song, Z., Yan, Y.: From lead halide perovskites to lead-free metal halide perovskites and perovskite derivatives. *Adv. Mater.* **31**(47), 1803792 (2019). <https://doi.org/10.1002/adma.201803792>

95. Gu, S., Lin, R., Han, Q., Gao, Y., Tan, H., Zhu, J.: Tin and mixed lead–tin halide perovskite solar cells: progress and their application in tandem solar cells. *Adv. Mater.* 1907392 (2020). <https://doi.org/10.1002/adma.201907392>
96. Savill, K.J., Ulatowski, A.M., Herz, L.M.: Optoelectronic properties of tin-lead halide perovskites. *ACS Energy Lett.* 6(7), 2413–2426 (2021). <https://doi.org/10.1021/acsenergylett.1c00776>
97. Hoefler, S.F., Trimmel, G., Rath, T.: Progress on lead-free metal halide perovskites for photovoltaic applications: a review. *Monatshefte für Chemie* 148(5), 795–826 (2017). <https://doi.org/10.1007/s00706-017-1933-9>
98. Filip, M.R., Giustino, F.: Computational screening of homovalent lead substitution in organic-inorganic halide perovskites. *J. Phys. Chem. C* 120(1), 166–173 (2016). <https://doi.org/10.1021/acs.jpcc.5b11845>
99. Tsarev, S., et al.: Hydrazinium-assisted stabilisation of methylammonium tin iodide for lead-free perovskite solar cells. *J. Mater. Chem. A* 6(43), 21389–21395 (2018). <https://doi.org/10.1039/C8TA07699E>
100. Shockley, W., Queisser, H.J.: Detailed balance limit of efficiency of p-n junction solar cells. *J. Appl. Phys.* 32(3), 510–519 (1961). <https://doi.org/10.1063/1.1736034>
101. Fan, Q., et al.: Lead-free halide perovskite nanocrystals: crystal structures, synthesis, stabilities, and optical properties. *Angew. Chemie Int. Ed.* 59(3), 1030–1046 (2020). <https://doi.org/10.1002/anie.201904862>
102. Kour, R., et al.: Potential substitutes for replacement of lead in perovskite solar cells: a review. *Glob. Challenges* 3(11), 1900050 (2019). <https://doi.org/10.1002/gch2.201900050>
103. Filip, M.R., Volonakis, G., Giustino, F.: Hybrid halide perovskites: fundamental theory and materials design. In: *Handbook of Materials Modeling*. Springer International Publishing, Cham, pp. 1–30 (2018)
104. Muscarella, L.A., et al.: Air-stable and oriented mixed lead halide perovskite (FA/MA) by the one-step deposition method using zinc iodide and an alkylammonium additive. *ACS Appl. Mater. Interfaces* 11(19), 17555–17562 (2019). <https://doi.org/10.1021/acsmi.9b03810>
105. Men, L., Rosales, B.A., Gentry, N.E., Cady, S.D., Vela, J.: Lead-free semiconductors: soft chemistry, dimensionality control, and manganese-doping of germanium halide perovskites. *ChemNanoMat* 5(3), 334–339 (2019). <https://doi.org/10.1002/cnma.201800497>
106. Sun, P.-P., Li, Q.-S., Yang, L.-N., Li, Z.-S.: Theoretical insights into a potential lead-free hybrid perovskite: substituting Pb 2+ with Ge 2+. *Nanoscale* 8(3), 1503–1512 (2016). <https://doi.org/10.1039/C5NR05337D>
107. Chen, M., et al.: Highly stable and efficient all-inorganic lead-free perovskite solar cells with native-oxide passivation. *Nat. Commun.* 10(1), 16 (2019). <https://doi.org/10.1038/s41467-018-07951-y>
108. Nagane, S., et al.: Lead-free perovskite semiconductors based on germanium-tin solid solutions: structural and optoelectronic properties. *J. Phys. Chem. C* 122(11), 5940–5947 (2018). <https://doi.org/10.1021/acs.jpcc.8b00480>
109. Körbel, S., Marques, M.A.L., Botti, S.: Stability and electronic properties of new inorganic perovskites from high-throughput ab initio calculations. *J. Mater. Chem. C* 4(15), 3157–3167 (2016). <https://doi.org/10.1039/C5TC04172D>
110. Hong, F., Saparov, B., Meng, W., Xiao, Z., Mitzi, D.B., Yan, Y.: Viability of lead-free perovskites with mixed chalcogen and halogen anions for photovoltaic applications. *J. Phys. Chem. C* 120(12), 6435–6441 (2016). <https://doi.org/10.1021/acs.jpcc.6b00920>
111. Li, L., Dong, T.: Photoluminescence tuning in carbon dots: surface passivation or/and functionalization, heteroatom doping. *J. Mater. Chem. C* 6(30), 7944–7970 (2018). <https://doi.org/10.1039/C7TC05878K>
112. Sun, Y.-Y., et al.: Discovering lead-free perovskite solar materials with a split-anion approach. *Nanoscale* 8(12), 6284–6289 (2016). <https://doi.org/10.1039/C5NR04310G>

113. Yang, B., et al.: Lead-free silver-bismuth halide double perovskite nanocrystals. *Angew. Chemie Int. Ed.* **57**(19), 5359–5363 (2018). <https://doi.org/10.1002/anie.201800660>
114. Zhang, Q., Hao, F., Li, J., Zhou, Y., Wei, Y., Lin, H.: Perovskite solar cells: must lead be replaced—and can it be done? *Sci. Technol. Adv. Mater.* **19**(1), 425–442 (2018). <https://doi.org/10.1080/14686996.2018.1460176>
115. Volonakis, G., et al.: Lead-free halide double perovskites via heterovalent substitution of noble metals. *J. Phys. Chem. Lett.* **7**(7), 1254–1259 (2016). <https://doi.org/10.1021/acs.jpcclett.6b00376>
116. Zhao, X.-G., et al.: Design of lead-free inorganic halide perovskites for solar cells via cation-transmutation. *J. Am. Chem. Soc.* **139**(7), 2630–2638 (2017). <https://doi.org/10.1021/jacs.6b09645>
117. Wei, F., et al.: The synthesis, structure and electronic properties of a lead-free hybrid inorganic–organic double perovskite (MA)<sub>2</sub>KBiCl<sub>6</sub> (MA = methylammonium). *Mater. Horizons* **3**(4), 328–332 (2016). <https://doi.org/10.1039/C6MH00053C>
118. Deng, Z., et al.: Synthesis and characterization of the rare-earth hybrid double perovskites: (CH<sub>3</sub>NH<sub>3</sub>)<sub>2</sub>KGdCl<sub>6</sub> and (CH<sub>3</sub>NH<sub>3</sub>)<sub>2</sub>KYCl<sub>6</sub>. *J. Phys. Chem. Lett.* **8**(20), 5015–5020 (2017). <https://doi.org/10.1021/acs.jpcclett.7b02322>
119. Zhao, S., Yamamoto, K., Iikubo, S., Hayase, S., Ma, T.: First-principles study of electronic and optical properties of lead-free double perovskites Cs<sub>2</sub>NaBX<sub>6</sub> (B = Sb, Bi; X = Cl, Br, I). *J. Phys. Chem. Solids* **117**, 117–121 (2018). <https://doi.org/10.1016/j.jpcs.2018.02.032>
120. Meyer, G.: The synthesis and structures of complex rare-earth halides. *Prog. Solid State Chem.* **14**(3), 141–219 (1982). [https://doi.org/10.1016/0079-6786\(82\)90005-X](https://doi.org/10.1016/0079-6786(82)90005-X)
121. Flerov, I.N., Gorev, M.V., Aleksandrov, K.S., Tressaud, A., Granec, J., Couzi, M.: Phase transitions in elpasolites (ordered perovskites). *Mater. Sci. Eng. R Rep.* **24**(3), 81–151 (1998). [https://doi.org/10.1016/S0927-796X\(98\)00015-1](https://doi.org/10.1016/S0927-796X(98)00015-1)
122. Filip, M.R., Liu, X., Miglio, A., Hautier, G., Giustino, F.: Phase diagrams and stability of lead-free halide double perovskites Cs<sub>2</sub>BB'X<sub>6</sub>: B = Sb and Bi, B' = Cu, Ag, and Au, and X = Cl, Br, and I. *J. Phys. Chem. C* **122**(1), 158–170 (2018). <https://doi.org/10.1021/acs.jpcc.7b10370>
123. Xiao, Z., Du, K., Meng, W., Mitzi, D.B., Yan, Y.: Chemical origin of the stability difference between copper(I)- and silver(I)-based halide double perovskites. *Angew. Chemie Int. Ed.* **56**(40), 12107–12111 (2017). <https://doi.org/10.1002/anie.201705113>
124. Zhao, X.-G., Yang, D., Ren, J.-C., Sun, Y., Xiao, Z., Zhang, L.: Rational design of halide double perovskites for optoelectronic applications. *Joule* **2**(9), 1662–1673 (2018). <https://doi.org/10.1016/j.joule.2018.06.017>
125. Maughan, A.E., Ganose, A.M., Scanlon, D.O., Neilson, J.R.: Perspectives and design principles of vacancy-ordered double perovskite halide semiconductors. *Chem. Mater.* **31**(4), 1184–1195 (2019). <https://doi.org/10.1021/acs.chemmater.8b05036>
126. Maughan, A.E., Ganose, A.M., Bordelon, M.M., Miller, E.M., Scanlon, D.O., Neilson, J.R.: Defect tolerance to intolerance in the vacancy-ordered double perovskite semiconductors Cs<sub>2</sub>SnI<sub>6</sub> and Cs<sub>2</sub>TeI<sub>6</sub>. *J. Am. Chem. Soc.* **138**(27), 8453–8464 (2016). <https://doi.org/10.1021/jacs.6b03207>
127. Dey, A., et al.: State of the art and prospects for halide perovskite nanocrystals. *ACS Nano* **15**(7), 10775–10981 (2021). <https://doi.org/10.1021/acsnano.0c08903>
128. Chang, J.-H., Doert, T., Ruck, M.: Structural variety of defect perovskite variants M<sub>3</sub>E<sub>2</sub>X<sub>9</sub> (M = Rb, Tl, E = Bi, Sb, X = Br, I). *Zeitschrift für Anorg. und Allg. Chemie* **642**(13), 736–748 (2016). <https://doi.org/10.1002/zaac.201600179>
129. Shen, Y., et al.: Lead-free, stable, high-efficiency (52%) blue luminescent FA<sub>3</sub>Bi<sub>2</sub>Br<sub>9</sub> perovskite quantum dots. *Nanoscale Horizons* **5**(3), 580–585 (2020). <https://doi.org/10.1039/C9NH00685K>

130. Leng, M., et al.: Surface passivation of bismuth-based perovskite variant quantum dots to achieve efficient blue emission. *Nano Lett.* **18**(9), 6076–6083 (2018). <https://doi.org/10.1021/acs.nanolett.8b03090>
131. Saparov, B., et al.: Thin-film preparation and characterization of Cs<sub>3</sub>Sb<sub>2</sub>I<sub>9</sub>: a lead-free layered perovskite semiconductor. *Chem. Mater.* **27**(16), 5622–5632 (2015). <https://doi.org/10.1021/acs.chemmater.5b01989>
132. Pal, J., Manna, S., Mondal, A., Das, S., Adarsh, K.V., Nag, A.: Colloidal synthesis and photophysics of M<sub>3</sub>Sb<sub>2</sub>I<sub>9</sub> (M=Cs and Rb) nanocrystals: lead-free perovskites. *Angew. Chemie Int. Ed.* **56**(45), 14187–14191 (2017). <https://doi.org/10.1002/anie.201709040>
133. Chonamada, T.D., Dey, A.B., Santra, P.K.: Degradation studies of Cs<sub>3</sub>Sb<sub>2</sub>I<sub>9</sub>: a lead-free perovskite. *ACS Appl. Energy Mater.* **3**(1), 47–55 (2020). <https://doi.org/10.1021/acsaem.9b01899>
134. Lee, B., et al.: Air-stable molecular semiconducting iodosalts for solar cell applications: Cs<sub>2</sub>SnI<sub>6</sub> as a hole conductor. *J. Am. Chem. Soc.* **136**(43), 15379–15385 (2014). <https://doi.org/10.1021/ja508464w>
135. Sakai, N., et al.: Solution-processed cesium hexabromopalladate(IV), Cs<sub>2</sub>PdBr<sub>6</sub>, for optoelectronic applications. *J. Am. Chem. Soc.* **139**(17), 6030–6033 (2017). <https://doi.org/10.1021/jacs.6b13258>
136. Ju, M.-G., et al.: Earth-abundant nontoxic titanium(IV)-based vacancy-ordered double perovskite halides with tunable 1.0 to 1.8 eV bandgaps for photovoltaic applications. *ACS Energy Lett.* **3**(2), 297–304 (2018). <https://doi.org/10.1021/acseenergylett.7b01167>
137. López-Fraguas, E., Masi, S., Mora-Seró, I.: Optical characterization of lead-free Cs<sub>2</sub>SnI<sub>6</sub> double perovskite fabricated from degraded and reconstructed CsSnI<sub>3</sub> films. *ACS Appl. Energy Mater.* **2**(12), 8381–8387 (2019). <https://doi.org/10.1021/acsaem.9b01827>
138. Wang, X., Zhang, T., Lou, Y., Zhao, Y.: All-inorganic lead-free perovskites for optoelectronic applications. *Mater. Chem. Front.* **3**(3), 365–375 (2019). <https://doi.org/10.1039/c8qm00611c>
139. Umedov, S.T., Khadka, D.B., Yanagida, M., Grigorieva, A., Shirai, Y.: A-site tailoring in the vacancy-ordered double perovskite semiconductor Cs<sub>2</sub>SnI<sub>6</sub> for photovoltaic application. *Sol. Energy Mater. Sol. Cells* **230**, 111180 (2021). <https://doi.org/10.1016/j.solmat.2021.111180>
140. Liu, S., et al.: A review on additives for halide perovskite solar cells. *Adv. Energy Mater.* **10**(13), 1–28 (2020). <https://doi.org/10.1002/aenm.201902492>
141. Petrus, M.L., et al.: Capturing the sun: a review of the challenges and perspectives of perovskite solar cells. *Adv. Energy Mater.* **7**(16), 1700264 (2017). <https://doi.org/10.1002/AENM.201700264>
142. Salim, T., Sun, S., Abe, Y., Krishna, A., Grimsdale, A.C., Lam, Y.M.: Perovskite-based solar cells: impact of morphology and device architecture on device performance. *J. Mater. Chem. A* **3**(17), 8943–8969 (2015). <https://doi.org/10.1039/C4TA05226A>
143. Burschka, J., et al.: Sequential deposition as a route to high-performance perovskite-sensitized solar cells. *Nature* **499**(7458), 316–319 (2013). <https://doi.org/10.1038/nature12340>
144. Vaynzof, Y., Vaynzof, Y.: The future of perovskite photovoltaics—thermal evaporation or solution processing? *Adv. Energy Mater.* **10**(48), 2003073 (2020). <https://doi.org/10.1002/AENM.202003073>
145. Park, N.G., Zhu, K.: Scalable fabrication and coating methods for perovskite solar cells and solar modules. *Nat. Rev. Mater.* **5**(5), 333–350 (2020). <https://doi.org/10.1038/s41578-019-0176-2>
146. Chaudhary, K.T.: Thin film deposition: solution based approach. *Thin Film.* (2021). <https://doi.org/10.5772/INTECHOPEN.94455>
147. Ramirez, D., Velilla, E., Montoya, J.F., Jaramillo, F.: Mitigating scalability issues of perovskite photovoltaic technology through a p-i-n meso-superstructured solar cell architecture. *Sol. Energy Mater. Sol. Cells* **195**, 191–197 (2019). <https://doi.org/10.1016/J.SOLMAT.2019.03.014>

148. Velilla, E., Ramirez, D., Uribe, J.I., Montoya, J.F., Jaramillo, F.: Outdoor performance of perovskite solar technology: Silicon comparison and competitive advantages at different irradiances. *Sol. Energy Mater. Sol. Cells* **191**, 15–20 (2019). <https://doi.org/10.1016/J.SOLMAT.2018.10.018>
149. Aguilar, R.G., Ortiz López, J.: Low cost instrumentation for spin-coating deposition of thin films in an undergraduate laboratory. *Am. J. Phys. Educ.* **5**(2), 368 (2011)
150. Hyuck Heo, J., Ho Song, D., Hyuk Im, S., Heo, J.H., Song, D.H., Im, S.H.: Planar CH<sub>3</sub>NH<sub>3</sub>PbBr<sub>3</sub> hybrid solar cells with 10.4% power conversion efficiency, fabricated by controlled crystallization in the spin-coating process. *Adv. Mater.* **26**(48), 8179–8183 (2014). <https://doi.org/10.1002/ADMA.201403140>
151. Eslamian, M.: Inorganic and organic solution-processed thin film devices. *Nano-Micro Lett.* **9**(1), 1–23 (2016). <https://doi.org/10.1007/S40820-016-0106-4>
152. Stranks, S.D., Nayak, P.K., Zhang, W., Stergiopoulos, T., Snaith, H.J.: Formation of thin films of organic-inorganic perovskites for high-efficiency solar cells. *Angew. Chemie Int. Ed.* **54**(11), 3240–3248 (2015). <https://doi.org/10.1002/ANIE.201410214>
153. Huang, P.H., Wang, Y.H., Ke, J.C., Huang, C.J.: The effect of solvents on the performance of CH<sub>3</sub>NH<sub>3</sub>PbI<sub>3</sub> perovskite solar cells. *Energies* **10**(5), 599 (2017). <https://doi.org/10.3390/EN10050599>
154. Howard, I.A., et al.: Coated and printed perovskites for photovoltaic applications. *Adv. Mater.* **31**(26), 1806702 (2019). <https://doi.org/10.1002/ADMA.201806702>
155. Stranks, S.D., Nayak, P.K., Zhang, W., Stergiopoulos, T., Snaith, H.J.: Formation of thin films of organic-inorganic perovskites for high-efficiency solar cells. *Angew. Chemie—Int. Ed.* **54**(11), 3240–3248 (2015). <https://doi.org/10.1002/anie.201410214>
156. El Cohen, B., Gamliel, S., Etgar, L.: Parameters influencing the deposition of methylammonium lead halide iodide in hole conductor free perovskite-based solar cells. *APL Mater.* **2**(8), 081502 (2014). <https://doi.org/10.1063/1.4885548>
157. Burschka, J., et al.: Sequential deposition as a route to high-performance perovskite-sensitized solar cells. *Nature* **499**, 316–319 (2013). <https://doi.org/10.1038/nature12340>
158. Zheng, L., et al.: Improved light absorption and charge transport for perovskite solar cells with rough interfaces by sequential deposition. *Nanoscale* **6**, 8171–8176 (2014). <https://doi.org/10.1039/c4nr01141d>
159. Yoo, S.M., et al.: Preparation of nanoscale inorganic CsPbI<sub>x</sub>Br<sub>3-x</sub> perovskite photosensitizers on the surface of mesoporous TiO<sub>2</sub> film for solid-state sensitized solar cells. *Appl. Surf. Sci.* **551**, 149387 (2021). <https://doi.org/10.1016/J.APSUSC.2021.149387>
160. Yoo, S.M., et al.: Nanoscale perovskite-sensitized solar cell revisited: dye-cell or perovskite-cell? *Chemosuschem* **13**(10), 2571–2576 (2020). <https://doi.org/10.1002/CSSC.202000223>
161. Lee, J.W., Park, N.G.: Two-step deposition method for high-efficiency perovskite solar cells. *MRS Bull.* **40**(8), 654–659 (2015). <https://doi.org/10.1557/MRS.2015.166>
162. Chen, H.: Two-step sequential deposition of organometal halide perovskite for photovoltaic application. *Adv. Funct. Mater.* **27**(8), 1605654 (2017). <https://doi.org/10.1002/ADFM.201605654>
163. Gonzalez-Pedro, V., et al.: General working principles of CH<sub>3</sub>NH<sub>3</sub>PbX<sub>3</sub> perovskite solar cells. *Nano Lett.* **14**(2), 888–893 (2014). [https://doi.org/10.1021/NL404252E/SUPPL\\_FILE/NL404252E\\_SI\\_001.PDF](https://doi.org/10.1021/NL404252E/SUPPL_FILE/NL404252E_SI_001.PDF)
164. Kim, J.S., Cho, H., Wolf, C., Yun, H.J., Heo, J.M., Lee, T.W.: Increased luminescent efficiency of perovskite light emitting diodes based on modified two-step deposition method providing gradient concentration. *APL Mater.* **6**(11), 111101 (2018). <https://doi.org/10.1063/1.5047456>
165. Geon Lee, D., et al.: High efficiency perovskite solar cells exceeding 22% via a photo-assisted two-step sequential deposition. *Adv. Funct. Mater.* **31**(9), 2006718 (2021). <https://doi.org/10.1002/ADFM.202006718>

166. Saki, Z., Byranvand, M.M., Taghavinia, N., Kedia, M., Saliba, M.: Solution-processed perovskite thin-films: the journey from lab: the large-scale solar cells. *Energy Environ. Sci.* **14**(11), 5690–5722 (2021). <https://doi.org/10.1039/d1ee02018h>
167. Ghosh, S., Mishra, S., Singh, T.: Antisolvents in perovskite solar cells: importance, issues, and alternatives. *Adv. Mater. Interfaces* **7**(18), 2000950 (2020). <https://doi.org/10.1002/ADMI.202000950>
168. Guo, Y., et al.: Chemical pathways connecting lead(II) iodide and perovskite via polymeric plumbate(II) fiber. *J. Am. Chem. Soc.* **137**(50), 15907–15914 (2015). [https://doi.org/10.1021/JACS.5B10599/SUPPL\\_FILE/JA5B10599\\_SI\\_006.CIF](https://doi.org/10.1021/JACS.5B10599/SUPPL_FILE/JA5B10599_SI_006.CIF)
169. Xiao, S., et al.: Unveiling a key intermediate in solvent vapor postannealing to enlarge crystalline domains of organometal halide perovskite films. *Adv. Funct. Mater.* **27**(12), 1604944 (2017). <https://doi.org/10.1002/ADFM.201604944>
170. Zhang, K., et al.: A prenucleation strategy for ambient fabrication of perovskite solar cells with high device performance uniformity. *Nat. Commun.* **11**(1), 1–11 (2020). <https://doi.org/10.1038/s41467-020-14715-0>
171. Ahmadian-Yazdi, M.R., Zabihi, F., Habibi, M., Eslamian, M.: Effects of process parameters on the characteristics of mixed-halide perovskite solar cells fabricated by one-step and two-step sequential coating. *Nanoscale Res. Lett.* **11**(1) (2016). <https://doi.org/10.1186/s11671-016-1601-8>
172. Ren, Y., et al.: New insight into solvent engineering technology from evolution of intermediates via one-step spin-coating approach. *Sci. China Mater.* **60**(5), 392–398 (2017). <https://doi.org/10.1007/s40843-017-9027-1>
173. Jeon, N.J., Noh, J.H., Kim, Y.C., Yang, W.S., Ryu, S., Il Seok, S.: Solvent engineering for high-performance inorganic-organic hybrid perovskite solar cells. *Nat. Mater.* **13**(9), 897–903 (2014). <https://doi.org/10.1038/nmat4014>
174. Pascoe, A.R., et al.: Enhancing the Optoelectronic performance of perovskite solar cells via a textured CH<sub>3</sub>NH<sub>3</sub>PbI<sub>3</sub> morphology. *Adv. Funct. Mater.* **26**(8), 1278–1285 (2016). <https://doi.org/10.1002/ADFM.201504190>
175. Xiao, M., et al.: A fast deposition-crystallization procedure for highly efficient lead iodide perovskite thin-film solar cells. *Angew. Chemie Int. Ed.* **53**(37), 9898–9903 (2014). <https://doi.org/10.1002/ANIE.201405334>
176. Xiao, Z., et al.: Solvent annealing of perovskite-induced crystal growth for photovoltaic-device efficiency enhancement. *Adv. Mater.* **26**(37), 6503–6509 (2014). <https://doi.org/10.1002/ADMA.201401685>
177. World Energy Outlook 2019—Analysis—IEA
178. Zissis, G.: Energy consumption and environmental and economic impact of lighting: the current situation. *Handb. Adv. Light. Technol.* 1–13 (2016). [https://doi.org/10.1007/978-3-319-00295-8\\_40-1](https://doi.org/10.1007/978-3-319-00295-8_40-1)
179. Luo, J., Hu, M., Niu, G., Tang, J.: Lead-free halide perovskites and perovskite variants as phosphors toward light-emitting applications. *ACS Appl. Mater. Interfaces* **11**(35), 31575–31584 (2019). <https://doi.org/10.1021/ACSAMI.9B08407>
180. Mandil, C.: Light's labour's lost: policies for energy-efficient lighting. *Energy world* **343**, 14–15 (2006)
181. Jaramillo-Quintero, O.A., Sanchez, R.S., Rincon, M., Mora-Sero, I.: Bright visible-infrared light emitting diodes based on hybrid halide perovskite with spiro-OMeTAD as a hole-injecting layer. *J. Phys. Chem. Lett.* **6**(10), 1883–1890 (2015). [https://doi.org/10.1021/ACS.JPCLETT.5B00732/SUPPL\\_FILE/JZ5B00732\\_SI\\_001.PDF](https://doi.org/10.1021/ACS.JPCLETT.5B00732/SUPPL_FILE/JZ5B00732_SI_001.PDF)
182. Sanchez, R.S., De La Fuente, M.S., Suarez, I., Muñoz-Matutano, G., Martinez-Pastor, J.P., Mora-Sero, I.: Tunable light emission by exciplex state formation between hybrid halide perovskite and core/shell quantum dots: Implications in advanced LEDs and photovoltaics. *Sci. Adv.* **2**(1) (2016). <https://doi.org/10.1126/sciadv.1501104>



183. Yang, B., et al.: Lead-free, air-stable all-inorganic cesium bismuth halide perovskite nanocrystals. *Angew. Chemie—Int. Ed.* **56**(41), 12471–12475 (2017). <https://doi.org/10.1002/anie.201704739>
184. Sun, Q., Wang, J., Yin, W.J., Yan, Y.: Bandgap engineering of stable lead-free oxide double perovskites for photovoltaics. *Adv. Mater.* **30**(15), 1–9 (2018). <https://doi.org/10.1002/adma.201705901>
185. Wang, X., Li, T., Xing, B., Faizan, M., Biswas, K., Zhang, L.: Metal halide semiconductors beyond lead-based perovskites for promising optoelectronic applications. *J. Phys. Chem. Lett.* **12**(43), 10532–10550 (2021). <https://doi.org/10.1021/ACS.JPCLETT.1C02877>
186. Zheng, X., Hou, Y., Sun, H.T., Mohammed, O.F., Sargent, E.H., Bakr, O.M.: Reducing defects in halide perovskite nanocrystals for light-emitting applications. *J. Phys. Chem. Lett.* **10**(10), 2629–2640 (2019). <https://doi.org/10.1021/ACS.JPCLETT.9B00689>
187. Dequillettes, D.W., et al.: Charge-carrier recombination in halide perovskites. *Chem. Rev.* **119**(20), 11007–11019 (2019). [https://doi.org/10.1021/ACS.CHEMREV.9B00169/SUPPL\\_FILE/CR9B00169\\_SI\\_001.PDF](https://doi.org/10.1021/ACS.CHEMREV.9B00169/SUPPL_FILE/CR9B00169_SI_001.PDF)
188. Seth, S., Ahmed, T., De, A., Samanta, A.: Tackling the defects, stability, and photoluminescence of CsPbX<sub>3</sub> perovskite nanocrystals. *ACS Energy Lett.* **4**(7), 1610–1618 (2019). <https://doi.org/10.1021/ACSENERGYLETT.9B00849>
189. Moon, B.J., et al.: Rare-earth-element-ytterbium-substituted lead-free inorganic perovskite nanocrystals for optoelectronic applications. *Adv. Mater.* **31**(33), 1901716 (2019). <https://doi.org/10.1002/ADMA.201901716>
190. Chen, Q., et al.: Under the spotlight: the organic–inorganic hybrid halide perovskite for optoelectronic applications. *Nano Today* **10**(3), 355–396 (2015). <https://doi.org/10.1016/J.NANOTOD.2015.04.009>
191. La Porta, F.A., Masi, S.: Solvent-mediated structural evolution mechanism from Cs<sub>4</sub>PbBr<sub>6</sub> to CsPbBr<sub>3</sub> crystals. *Nanomanufacturing* **1**(2), 67–74 (2021). <https://doi.org/10.3390/nanomanufacturing1020007>
192. Cheng, Y., Ding, L.: Pushing commercialization of perovskite solar cells by improving their intrinsic stability. *Energy Environ. Sci.* **14**(6), 3233–3255 (2021). <https://doi.org/10.1039/D1EE00493J>
193. Bibi, A., et al.: Lead-free halide double perovskites: toward stable and sustainable optoelectronic devices. *Mater. Today* **49**, 123–144 (2021). <https://doi.org/10.1016/J.MATTOD.2020.11.026>
194. Hao, J., Xiao, X.: Recent development of optoelectronic application based on metal halide perovskite nanocrystals. *Front. Chem.* **9**, 1130 (2022). <https://doi.org/10.3389/FCHEM.2021.822106/BIBTEX>
195. Hoeffler, S.F., Trimmel, G., Rath, T.: Progress on lead-free metal halide perovskites for photovoltaic applications: a review. *Monatshefte für Chemie—Chem. Mon.* **148**(5), 795–826 (2017). <https://doi.org/10.1007/s00706-017-1933-9>
196. Sun, J., Yang, J., Lee, J.I., Cho, J.H., Kang, M.S.: Lead-free perovskite nanocrystals for light-emitting devices. *J. Phys. Chem. Lett.* **9**(7), 1573–1583 (2018). <https://doi.org/10.1021/ACS.JPCLETT.8B00301>
197. Manzhos, S., et al.: Materials design and optimization for next-generation solar cell and light-emitting technologies. *J. Phys. Chem. Lett.* **12**(19), 4638–4657 (2021). <https://doi.org/10.1021/ACS.JPCLETT.1C00714>
198. Jeong, S.H., et al.: Characterizing the efficiency of perovskite solar cells and light-emitting diodes. *Joule* **4**(6), 1206–1235 (2020). <https://doi.org/10.1016/J.JOULE.2020.04.007>
199. Wang, F., Liu, X.K., Gao, F.: Fundamentals of solar cells and light-emitting diodes. *Adv. Nanomater. Sol. Cells Light Emit. Diodes* 1–35 (2019). <https://doi.org/10.1016/B978-0-12-813647-8.00001-1>

200. Xu, L., Yuan, S., Zeng, H., Song, J.: A comprehensive review of doping in perovskite nanocrystals/quantum dots: evolution of structure, electronics, optics, and light-emitting diodes. *Mater. Today Nano* **6**, 100036 (2019). <https://doi.org/10.1016/J.MTNANO.2019.100036>
201. Van Le, Q., Won Jang, H., Young Kim, S., V Le, Q., Kim, S.Y., Jang, H.W.: Recent advances toward high-efficiency halide perovskite light-emitting diodes: review and perspective. *Small Meth.* **2**(10), 1700419 (2018). <https://doi.org/10.1002/SMTD.201700419>
202. Guner, T., Demir, M.M.: A review on halide perovskites as color conversion layers in white light emitting diode applications. *Phys. Status Solidi* **215**(13), 1800120 (2018). <https://doi.org/10.1002/PSSA.201800120>
203. Ji, K., et al.: Halide perovskite light-emitting diode technologies. *Adv. Opt. Mater.* **9**(18), 2002128 (2021). <https://doi.org/10.1002/ADOM.202002128>
204. Su, Y., et al.: Highly controllable and efficient synthesis of mixed-halide CsPbX<sub>3</sub> (X = Cl, Br, I) perovskite QDs toward the tunability of entire visible light. *ACS Appl. Mater. Interfaces* **9**(38), 33202–33028 (2017). [https://doi.org/10.1021/ACSAMI.7B10612/SUPPL\\_FILE/AM7B10612\\_SI\\_001.PDF](https://doi.org/10.1021/ACSAMI.7B10612/SUPPL_FILE/AM7B10612_SI_001.PDF)
205. Eperon, G.E., Stranks, S.D., Menelaou, C., Johnston, M.B., Herz, L.M., Snaith, H.J.: Formamidinium lead trihalide: a broadly tunable perovskite for efficient planar heterojunction solar cells. *Energy Environ. Sci.* **7**(3), 982–988 (2014). <https://doi.org/10.1039/C3EE43822H>
206. Ng, Y.F., et al.: Highly efficient Cs-based perovskite light-emitting diodes enabled by energy funneling. *Chem. Commun.* **53**(88), 12004–12007 (2017). <https://doi.org/10.1039/C7CC06615E>
207. Byun, J., et al.: Efficient visible quasi-2D perovskite light-emitting diodes. *Adv. Mater.* **28**(34), 7515–7520 (2016). <https://doi.org/10.1002/ADMA.201601369>
208. Tsai, H., et al.: Stable light-emitting diodes using phase-pure Ruddlesden-popper layered perovskites. *Adv. Mater.* **30**(6), 1704217 (2018). <https://doi.org/10.1002/ADMA.201704217>
209. El-Ballouli, A.O., Bakr, O.M., Mohammed, O.F.: Structurally tunable two-dimensional layered perovskites: from confinement and enhanced charge transport to prolonged hot carrier cooling dynamics. *J. Phys. Chem. Lett.* **11**(14), 5705–5718 (2020). <https://doi.org/10.1021/ACS.JPCLETT.0C00359>
210. Zhang, L., et al.: High-performance quasi-2D perovskite light-emitting diodes: from materials to devices. *Light Sci. Appl.* **10**(1), 1–26 (2021). <https://doi.org/10.1038/s41377-021-00501-0>
211. Yin, J., Li, H., Cortecchia, D., Soci, C., Brédas, J.L.: Excitonic and polaronic properties of 2D hybrid organic-inorganic perovskites. *ACS Energy Lett.* **2**(2), 417–423 (2017). [https://doi.org/10.1021/ACSENERGYLETT.6B00659/SUPPL\\_FILE/NZ6B00659\\_SI\\_001.PDF](https://doi.org/10.1021/ACSENERGYLETT.6B00659/SUPPL_FILE/NZ6B00659_SI_001.PDF)
212. Kahmann, S., Tekelenburg, E.K., Duim, H., Kamminga, M.E., Loi, M.A.: Extrinsic nature of the broad photoluminescence in lead iodide-based Ruddlesden–Popper perovskites. *Nat. Commun.* **11**(1), 1–8 (2020). <https://doi.org/10.1038/s41467-020-15970-x>
213. Chen, Z., et al.: High-performance color-tunable perovskite light emitting devices through structural modulation from bulk to layered film. *Adv. Mater.* **29**(8), 1603157 (2017). <https://doi.org/10.1002/ADMA.201603157>
214. Yang, X., et al.: Efficient green light-emitting diodes based on quasi-two-dimensional composition and phase engineered perovskite with surface passivation. *Nat. Commun.* **9**(1), 1–8 (2018). <https://doi.org/10.1038/s41467-018-02978-7>
215. Quan, L.N., et al.: Tailoring the energy landscape in quasi-2D halide perovskites enables efficient green-light emission. *Nano Lett.* **17**(6), 3701–3709 (2017). [https://doi.org/10.1021/ACS.NANOLETT.7B00976/SUPPL\\_FILE/NL7B00976\\_SI\\_001.PDF](https://doi.org/10.1021/ACS.NANOLETT.7B00976/SUPPL_FILE/NL7B00976_SI_001.PDF)
216. Wei, Q., Ning, Z.: Emerging highly emissive and stable white emitting ‘phosphores’ based on lead-free inorganic halide perovskites. *Sci. China Chem.* **62**(3), 287–288 (2018). <https://doi.org/10.1007/S11426-018-9391-8>

217. Luo, J., et al.: Efficient and stable emission of warm-white light from lead-free halide double perovskites. *Nature* **563**(7732), 541–545 (2018). <https://doi.org/10.1038/s41586-018-0691-0>
218. de Holanda, M.S., Moral, R.F., Marchezi, P.E., Marques, F.C., Nogueira, A.F.: Layered metal halide perovskite solar cells: a review from structure-properties perspective towards maximization of their performance and stability. *EcoMat* **3**(4), e12124 (2021). <https://doi.org/10.1002/EOM2.12124>
219. Pal, J., et al.: Synthesis and optical properties of colloidal M3Bi2I9 (M = Cs, Rb) perovskite nanocrystals. *J. Phys. Chem. C* **122**(19), 10643–10649 (2018). [https://doi.org/10.1021/ACS.JPCC.8B03542/SUPPL\\_FILE/JP8B03542\\_SI\\_001.PDF](https://doi.org/10.1021/ACS.JPCC.8B03542/SUPPL_FILE/JP8B03542_SI_001.PDF)
220. Bass, K.K., et al.: Vibronic structure in room temperature photoluminescence of the halide perovskite Cs3Bi2Br9. *Inorg. Chem.* **56**(1), 42–45 (2017). [https://doi.org/10.1021/ACS.INORGCHEM.6B01571/SUPPL\\_FILE/IC6B01571\\_SI\\_001.PDF](https://doi.org/10.1021/ACS.INORGCHEM.6B01571/SUPPL_FILE/IC6B01571_SI_001.PDF)
221. Jun, T., et al.: Lead-free highly efficient blue-emitting Cs3Cu2I5 with 0D electronic structure. *Adv. Mater.* **30**(43), 1804547 (2018). <https://doi.org/10.1002/ADMA.201804547>
222. Ma, Z., et al.: Electrically-driven violet light-emitting devices based on highly stable lead-free perovskite Cs3Sb2Br9 quantum dots. *ACS Energy Lett.* **5**(2), 385–394 (2020). <https://doi.org/10.1021/acsenerylett.9b02096>
223. Han, P., et al.: Size effect of lead-free halide double perovskite on luminescence property. *Sci. China Chem.* **62**(10), 1405–1413 (2019). <https://doi.org/10.1007/s11426-019-9520-1>
224. Zhou, C., et al.: Luminescent zero-dimensional organic metal halide hybrids with near-unity quantum efficiency. *Chem. Sci.* **9**(3), 586–593 (2018). <https://doi.org/10.1039/C7SC04539E>
225. Zhang, X., et al.: Bright orange electroluminescence from lead-free two-dimensional perovskites. *ACS Energy Lett.* **4**(1), 242–248 (2019). [https://doi.org/10.1021/ACSENERGYLETT.8B02239/SUPPL\\_FILE/NZ8B02239\\_SI\\_001.PDF](https://doi.org/10.1021/ACSENERGYLETT.8B02239/SUPPL_FILE/NZ8B02239_SI_001.PDF)
226. Hong, W.L., et al.: Efficient low-temperature solution-processed lead-free perovskite infrared light-emitting diodes. *Adv. Mater.* **28**(36), 8029–8036 (2016). <https://doi.org/10.1002/adma.201601024>
227. Lai, M.L., et al.: Tunable near-infrared luminescence in tin halide perovskite devices. *J. Phys. Chem. Lett.* **7**(14), 2653–2658 (2016). <https://doi.org/10.1021/acs.jpcllett.6b01047>
228. Liang, H., et al.: High color purity lead-free perovskite light-emitting diodes via Sn stabilization. *Adv. Sci.* **7**(8), 1903213 (2020). <https://doi.org/10.1002/ADVS.201903213>
229. Wang, Y., et al.: Tin-based multiple quantum well perovskites for light-emitting diodes with improved stability. *J. Phys. Chem. Lett.* **10**(3), 453–459 (2019). [https://doi.org/10.1021/ACS.JPCLETT.8B03700/SUPPL\\_FILE/JZ8B03700\\_SI\\_001.PDF](https://doi.org/10.1021/ACS.JPCLETT.8B03700/SUPPL_FILE/JZ8B03700_SI_001.PDF)
230. Ma, Z., et al.: Stable yellow light-emitting devices based on ternary copper halides with broadband emissive self-trapped excitons. *ACS Nano* **14**(4), 4475–4486 (2020). [https://doi.org/10.1021/ACS.NANO.9B10148/SUPPL\\_FILE/NN9B10148\\_SI\\_001.PDF](https://doi.org/10.1021/ACS.NANO.9B10148/SUPPL_FILE/NN9B10148_SI_001.PDF)
231. Wang, L., et al.: Colloidal synthesis of ternary copper halide nanocrystals for high-efficiency deep-blue light-emitting diodes with a half-lifetime above 100 h. *Nano Lett.* **20**(5), 3568–3576 (2020). [https://doi.org/10.1021/ACS.NANO.9B10148/SUPPL\\_FILE/NN9B10148\\_SI\\_001.PDF](https://doi.org/10.1021/ACS.NANO.9B10148/SUPPL_FILE/NN9B10148_SI_001.PDF)
232. Ma, Z., et al.: Electrically-driven violet light-emitting devices based on highly stable lead-free perovskite Cs3Sb2Br9 quantum dots. *ACS Energy Lett.* **5**, 385–394 (2019). <https://doi.org/10.1021/acsenerylett.9b02096>
233. Liu, Z., et al.: Anti-solvent spin-coating for improving morphology of lead-free (CH3NH3)3Bi2I9 perovskite films. *SN Appl. Sci.* **1**(7), 706 (2019). <https://doi.org/10.1007/s42452-019-0727-6>
234. Nguyen, B.P., et al.: Phase formation and local charge transport of lead-free CH3NH3Sn(1-xBrx)3 (0 ≤ x ≤ 1) perovskite solar cells fabricated by solvent optimization. *Sol. Energy* **186**, 136–144 (2019). <https://doi.org/10.1016/j.solener.2019.05.007>

235. Park, B.-W., Philippe, B., Zhang, X., Rensmo, H., Boschloo, G., Johansson, E.M.J.: Bismuth based hybrid perovskites  $A_3Bi_2I_9$  (A: methylammonium or cesium) for solar cell application. *Adv. Mater.* **27**(43), 6806–6813 (2015). <https://doi.org/10.1002/adma.201501978>
236. Ke, W., et al.: Efficient lead-free solar cells based on hollow {en}MASnI<sub>3</sub> perovskites. *J. Am. Chem. Soc.* **139**(41), 14800–14806 (2017). <https://doi.org/10.1021/jacs.7b09018>
237. Gupta, S., Bendikov, T., Hodes, G., Cahen, D.: CsSnBr<sub>3</sub>, a lead-free halide perovskite for long-term solar cell application: insights on SnF<sub>2</sub> addition. *ACS Energy Lett.* **1**(5), 1028–1033 (2016). <https://doi.org/10.1021/acsenerylett.6b00402>
238. Hao, F., Stoumpos, C.C., Cao, D.H., Chang, R.P.H., Kanatzidis, M.G.: Lead-free solid-state organic–inorganic halide perovskite solar cells. *Nat. Photonics* **8**(6), 489–494 (2014). <https://doi.org/10.1038/nphoton.2014.82>
239. Nishikubo, R., et al.: Optoelectronic and energy level exploration of bismuth and antimony-based materials for lead-free solar cells. *Chem. Mater.* **32**(15), 6416–6424 (2020). <https://doi.org/10.1021/acs.chemmater.0c01503>
240. Zhang, X., et al.: Active-layer evolution and efficiency improvement of (CH<sub>3</sub>NH<sub>3</sub>)<sub>3</sub>Bi<sub>2</sub>I<sub>9</sub>-based solar cell on TiO<sub>2</sub>-deposited ITO substrate. *Nano Res.* **9**(10), 2921–2930 (2016). <https://doi.org/10.1007/s12274-016-1177-8>
241. Pantaler, M., et al.: Hysteresis-free lead-free double-perovskite solar cells by interface engineering. *ACS Energy Lett.* **3**(8), 1781–1786 (2018). <https://doi.org/10.1021/acsenerylett.8b00871>
242. Kumar, M.H., et al.: Lead-free halide perovskite solar cells with high photocurrents realized through vacancy modulation. *Adv. Mater.* **26**(41), 7122–7127 (2014). <https://doi.org/10.1002/adma.201401991>
243. Chen, L.-J., Lee, C.-R., Chuang, Y.-J., Wu, Z.-H., Chen, C.: Synthesis and optical properties of lead-free cesium tin halide perovskite quantum rods with high-performance solar cell application. *J. Phys. Chem. Lett.* **7**(24), 5028–5035 (2016). <https://doi.org/10.1021/acs.jpcl.6b02344>
244. Wu, C., et al.: The dawn of lead-free perovskite solar cell: highly stable double perovskite Cs<sub>2</sub>AgBiBr<sub>6</sub> film. *Adv. Sci.* **5**(3), 1700759 (2018). <https://doi.org/10.1002/adv.201700759>
245. Harikesh, P.C., et al.: Rb as an alternative cation for templating inorganic lead-free perovskites for solution processed photovoltaics. *Chem. Mater.* **28**(20), 7496–7504 (2016). <https://doi.org/10.1021/acs.chemmater.6b03310>
246. Zhu, Z., Chueh, C., Li, N., Mao, C., Jen, A.K.-Y.: Realizing efficient lead-free formamidinium tin triiodide perovskite solar cells via a sequential deposition route. *Adv. Mater.* **30**(6), 1703800 (2018). <https://doi.org/10.1002/adma.201703800>
247. Ning, W., et al.: Long electron-hole diffusion length in high-quality lead-free double perovskite films. *Adv. Mater.* **30**(20), 1706246 (2018). <https://doi.org/10.1002/adma.201706246>
248. Rahul, P.K., Singh, R., Singh, V., Singh, B., Bhattacharya, Khan, Z.H.: New class of lead free perovskite material for low-cost solar cell application. *Mater. Res. Bull.* **97**, 572–577 (2018). <https://doi.org/10.1016/j.materresbull.2017.09.054>
249. Gao, W., et al.: High-quality Cs<sub>2</sub>AgBiBr<sub>6</sub> Double perovskite film for lead-free inverted planar heterojunction solar cells with 2.2 % efficiency. *ChemPhysChem* **19**(14), 1696–1700 (2018). <https://doi.org/10.1002/cphc.201800346>
250. Baltakesmez, A., Güzeldir, B., Alkan, Y., Sağlam, M., Biber, M.: Optimizing quality of lead-free perovskite thin film with anti-solvent engineering and co-doping SnBr<sub>2</sub>/SnF<sub>2</sub>; its solar cell performance. *Opt. Mater. (Amst.)* **110**, 110524 (2020). <https://doi.org/10.1016/j.optmat.2020.110524>
251. He, L., et al.: Efficient anti-solvent-free spin-coated and printed Sn-perovskite solar cells with crystal-based precursor solutions. *Matter* **2**(1), 167–180 (2020). <https://doi.org/10.1016/j.matt.2019.10.006>

252. Jokar, E., Cheng, P.-Y., Lin, C.-Y., Narra, S., Shahbazi, S., Wei-Guang Diao, E.: Enhanced performance and stability of 3D/2D tin perovskite solar cells fabricated with a sequential solution deposition. *ACS Energy Lett.* **6**(2), 485–492 (2021). <https://doi.org/10.1021/acseenergylett.0c02305>
253. Ng, C.H., et al.: Reducing trap density and carrier concentration by a Ge additive for an efficient quasi 2D/3D perovskite solar cell. *J. Mater. Chem. A* **8**(6), 2962–2968 (2020). <https://doi.org/10.1039/C9TA11989B>
254. Liu, J., et al.: Lead-free solar cells based on tin halide perovskite films with high coverage and improved aggregation. *Angew. Chemie* **130**(40), 13405–13409 (2018). <https://doi.org/10.1002/ange.201808385>
255. Chen, M., et al.: High-performance lead-free solar cells based on tin-halide perovskite thin films functionalized by a divalent organic cation. *ACS Energy Lett.* **5**(7), 2223–2230 (2020). <https://doi.org/10.1021/acseenergylett.0c00888>
256. Ran, C., et al.: Construction of compact methylammonium bismuth iodide film promoting lead-free inverted planar heterojunction organohalide solar cells with open-circuit voltage over 0.8 V. *J. Phys. Chem. Lett.* **8**(2), 394–400 (2017). <https://doi.org/10.1021/acs.jpcclett.6b02578>
257. Boopathi, K.M., et al.: Solution-processable antimony-based light-absorbing materials beyond lead halide perovskites. *J. Mater. Chem. A* **5**(39), 20843–20850 (2017). <https://doi.org/10.1039/C7TA06679A>
258. Jokar, E., Chien, C.-H., Tsai, C.-M., Fathi, A., Diao, E.W.-G.: Robust tin-based perovskite solar cells with hybrid organic cations to attain efficiency approaching 10%. *Adv. Mater.* **31**(2), 1804835 (2019). <https://doi.org/10.1002/adma.201804835>
259. Vidal, R., et al.: Assessing health and environmental impacts of solvents for producing perovskite solar cells. *Nat. Sustain.* **4**(3), 277–285 (2020). <https://doi.org/10.1038/s41893-020-00645-8>
260. Correa-Baena, J.-P., et al.: A -site cation in inorganic A<sub>3</sub>Sb<sub>2</sub>I<sub>9</sub> perovskite influences structural dimensionality, exciton binding energy, and solar cell performance. *Chem. Mater.* **30**(11), 3734–3742 (2018). <https://doi.org/10.1021/acs.chemmater.8b00676>
261. Nie, R., Mehta, A., Park, B., Kwon, H.-W., Im, J., Il Seok, S.: Mixed sulfur and iodide-based lead-free perovskite solar cells. *J. Am. Chem. Soc.* **140**(3), 872–875 (2018). <https://doi.org/10.1021/jacs.7b11332>
262. Weiss, M., Horn, J., Richter, C., Schlettwein, D.: Preparation and characterization of methylammonium tin iodide layers as photovoltaic absorbers. *Phys. Status Solidi* **213**(4), 975–981 (2016). <https://doi.org/10.1002/PSSA.201532594>
263. Cortecchia, D., et al.: Lead-free MA<sub>2</sub>CuCl<sub>x</sub>Br<sub>4-x</sub> hybrid perovskites. *Inorg. Chem.* **55**(3), 1044–1052 (2016). [https://doi.org/10.1021/ACS.INORGCHEM.5B01896/SUPPL\\_FILE/IC5B01896\\_SI\\_001.PDF](https://doi.org/10.1021/ACS.INORGCHEM.5B01896/SUPPL_FILE/IC5B01896_SI_001.PDF)
264. Abulikemu, M., et al.: Optoelectronic and photovoltaic properties of the air-stable organohalide semiconductor (CH<sub>3</sub>NH<sub>3</sub>)<sub>3</sub>Bi<sub>2</sub>I<sub>9</sub>. *J. Mater. Chem. A* **4**(32), 12504–12515 (2016). <https://doi.org/10.1039/C6TA04657F>
265. Greul, E., Petrus, M.L., Binek, A., Docampo, P., Bein, T.: Highly stable, phase pure Cs<sub>2</sub>AgBiBr<sub>6</sub> double perovskite thin films for optoelectronic applications. *J. Mater. Chem. A* **5**(37), 19972–19981 (2017). <https://doi.org/10.1039/C7TA06816F>
266. Wu, C., et al.: The dawn of lead-free perovskite solar cell: highly stable double perovskite Cs<sub>2</sub>AgBiBr<sub>6</sub> film. *Adv. Sci.* **5**(3), 1700759 (2018). <https://doi.org/10.1002/ADVS.201700759>
267. Li, P., Gao, W., Ran, C., Dong, H., Hou, X., Wu, Z.: Post-treatment engineering of vacuum-deposited Cs<sub>2</sub>NaBiI<sub>6</sub> double perovskite film for enhanced photovoltaic performance. *Phys. Status Solidi* **216**(23), 1900567 (2019). <https://doi.org/10.1002/PSSA.201900567>
268. Ke, W., Kanatzidis, M.G.: Prospects for Low-Toxicity Lead-Free Perovskite Solar Cells, pp. 1–4 (2019)

269. Tiwari, A., Satpute, N.S., Mehare, C.M., Dhoble, S.J.: Challenges, recent advances and improvements for enhancing the efficiencies of ABX<sub>3</sub>-based PeLEDs (perovskites light emitting diodes): A review. *J. Alloys Compd.* **850**, 156827 (2021). <https://doi.org/10.1016/J.JALCOM.2020.156827>
270. Jung, H.S., Park, N.G.: Perovskite solar cells: from materials to devices. *Small* **11**(1), 10–25 (2015). <https://doi.org/10.1002/SMLL.201402767>
271. Salhi, B., Wudil, Y.S., Hossain, M.K., Al-Ahmed, A., Al-Sulaiman, F.A.: Review of recent developments and persistent challenges in stability of perovskite solar cells. *Renew. Sustain. Energy Rev.* **90**, 210–222 (2018). <https://doi.org/10.1016/J.RSER.2018.03.058>
272. Fu, Q., et al.: Recent progress on the long-term stability of perovskite solar cells. *Adv. Sci.* **5**(5), 1700387 (2018). <https://doi.org/10.1002/ADVS.201700387>
273. Wang, Y., Sun, H.: Advances and prospects of lasers developed from colloidal semiconductor nanostructures. *Prog. Quantum Electron.* **60**, 1–29 (2018). <https://doi.org/10.1016/J.PQUANTELEC.2018.05.002>
274. Li, D., et al.: Recent progress on stability issues of organic-inorganic hybrid lead perovskite-based solar cells. *RSC Adv.* **6**, 89356–89366 (2016). <https://doi.org/10.1039/c6ra19801e>
275. He, S., Qiu, L., Ono, L.K., Qi, Y.: How far are we from attaining 10-year lifetime for metal halide perovskite solar cells? *Mater. Sci. Eng. R Rep.* **140**, 100545 (2020). <https://doi.org/10.1016/J.MSER.2020.100545>
276. Boyd, C.C., Cheacharoen, R., Leijtens, T., McGehee, M.D.: Understanding degradation mechanisms and improving stability of perovskite photovoltaics. *Chem. Rev.* **119**(5), 3418–3451 (2018). <https://doi.org/10.1021/ACS.CHEMREV.8B00336>
277. Khenkin, M.V., et al.: Consensus statement for stability assessment and reporting for perovskite photovoltaics based on ISOS procedures. *Nat. Energy* **5**(1), 35–49 (2020). <https://doi.org/10.1038/s41560-019-0529-5>
278. Anoop, K.M., et al.: Bias-dependent stability of perovskite solar cells studied using natural and concentrated sunlight. *Sol. RRL* **4**(2), 1900335 (2020). <https://doi.org/10.1002/SOLR.201900335>
279. Domanski, K., Alharbi, E.A., Hagfeldt, A., Grätzel, M., Tress, W.: Systematic investigation of the impact of operation conditions on the degradation behaviour of perovskite solar cells. *Nat. Energy* **3**(1), 61–67 (2018). <https://doi.org/10.1038/s41560-017-0060-5>
280. Saliba, M., Stollerfoht, M., Wolff, C.M., Neher, D., Abate, A.: Measuring aging stability of perovskite solar cells. *Joule* **2**(6), 1019–1024 (2018). <https://doi.org/10.1016/J.JOULE.2018.05.005>
281. Domanski, K., et al.: Migration of cations induces reversible performance losses over day/night cycling in perovskite solar cells. *Energy Environ. Sci.* **10**(2), 604–613 (2017). <https://doi.org/10.1039/C6EE03352K>
282. Christians, J.A., Manser, J.S., Kamat, P.V.: Best practices in perovskite solar cell efficiency measurements. Avoiding the error of making bad cells look good. *J. Phys. Chem. Lett.* **6**(5), 852–857 (2015). <https://doi.org/10.1021/ACS.JPCLETT.5B00289>
283. Yang, B., et al.: Outstanding passivation effect by a mixed-salt interlayer with internal interactions in perovskite solar cells. *ACS Energy Lett.* **5**(10), 3159–3167 (2020). [https://doi.org/10.1021/ACSENERGYLETT.0C01664/SUPPL\\_FILE/NZOC01664\\_SI\\_001.PDF](https://doi.org/10.1021/ACSENERGYLETT.0C01664/SUPPL_FILE/NZOC01664_SI_001.PDF)
284. Heo, S., et al.: Origins of high performance and degradation in the mixed perovskite solar cells. *Adv. Mater.* **31**(8), 1805438 (2019). <https://doi.org/10.1002/ADMA.201805438>
285. Zhang, S., et al.: Barrier designs in perovskite solar cells for long-term stability. *Adv. Energy Mater.* **10**(35), 2001610 (2020). <https://doi.org/10.1002/AENM.202001610>
286. Hasan, O., Arif, A.F.M.: Performance and life prediction model for photovoltaic modules: effect of encapsulant constitutive behavior. *Sol. Energy Mater. Sol. Cells* **122**, 75–87 (2014). <https://doi.org/10.1016/J.SOLMAT.2013.11.016>
287. Wang, Y., et al.: Encapsulation and stability testing of perovskite solar cells for real life applications. *ACS Mater. Au* (2022). <https://doi.org/10.1021/ACSMATERIALSAU.1C00045>

288. Cheacharoen, R., Rolston, N., Harwood, D., Bush, K.A., Dauskardt, R.H., McGehee, M.D.: Design and understanding of encapsulated perovskite solar cells to withstand temperature cycling. *Energy Environ. Sci.* **11**(1), 144–150 (2018). <https://doi.org/10.1039/C7EE02564E>
289. Shi, L., et al.: Accelerated lifetime testing of organic-inorganic perovskite solar cells encapsulated by polyisobutylene. *ACS Appl. Mater. Interfaces* **9**(30), 25073–25081 (2017). [https://doi.org/10.1021/ACSAMI.7B07625/SUPPL\\_FILE/AM7B07625\\_SI\\_001.PDF](https://doi.org/10.1021/ACSAMI.7B07625/SUPPL_FILE/AM7B07625_SI_001.PDF)
290. Grancini, G., et al.: One-year stable perovskite solar cells by 2D/3D interface engineering. *Nat. Commun.* **8**(1), 1–8 (2017). <https://doi.org/10.1038/ncomms15684>
291. Stoichkov, V., Bristow, N., Troughton, J., De Rossi, F., Watson, T.M., Kettle, J.: Outdoor performance monitoring of perovskite solar cell mini-modules: diurnal performance, observance of reversible degradation and variation with climatic performance. *Sol. Energy* **170**, 549–556 (2018). <https://doi.org/10.1016/J.SOLENER.2018.05.086>
292. Hu, Y., et al.: Standardizing perovskite solar modules beyond cells. *Joule* **3**(9), 2076–2085 (2019). <https://doi.org/10.1016/J.JOULE.2019.08.015>
293. Velilla, E., Jaramillo, F., Mora-Seró, I.: High-throughput analysis of the ideality factor to evaluate the outdoor performance of perovskite solar minimodules. *Nat. Energy* **6**(1), 54–62 (2021). <https://doi.org/10.1038/s41560-020-00747-9>
294. Sharma, P., Kumar, S.: Bioremediation of heavy metals from industrial effluents by endophytes and their metabolic activity: recent advances. *Bioresour. Technol.* 125589 (2021)
295. Wang, J., et al.: Surface structure of mass-selected niobium oxide nanoclusters on Au(111) (2021). <https://doi.org/10.1088/1361-6528/ac1cc0>
296. Canil, L., et al.: Tuning halide perovskite energy levels. *Energy Environ. Sci.* **10**(3), 147–154 (2021). <https://doi.org/10.1039/D0EE02216K>
297. Alderete, B.L., et al.: Evaluation of toxicity and mutagenicity of a synthetic effluent containing azo dye after advanced oxidation process treatment. *Chemosphere* **263**, 128291 (2021)
298. Stroyuk, O.: Lead-free hybrid perovskites for photovoltaics. *Beilstein J. Nanotechnol.* **9**(1), 2209–2235 (2018). <https://doi.org/10.3762/bjnano.9.207>
299. Hao, F., Stoumpos, C.C., Chang, R.P.H., Kanatzidis, M.G.: Anomalous band gap behavior in mixed Sn and Pb perovskites enables broadening of absorption spectrum in solar cells. *J. Am. Chem. Soc.* **136**(22), 8094–8099 (2014). [https://doi.org/10.1021/JA5033259/SUPPL\\_FILE/JA5033259\\_SI\\_001.PDF](https://doi.org/10.1021/JA5033259/SUPPL_FILE/JA5033259_SI_001.PDF)
300. Bin, T., et al.: Perovskite solar cells: film formation and properties. *J. Mater. Chem. A* **3**(17), 9032–9050 (2015). <https://doi.org/10.1039/c4ta05246c>
301. Hwang, K., et al.: Toward large scale roll-to-roll production of fully printed perovskite solar cells. *Adv. Mater.* **27**(7), 1241–1247 (2015). <https://doi.org/10.1002/ADMA.201404598>
302. Galagan, Y.: Perovskite solar cells: toward industrial-scale methods. *J. Phys. Chem. Lett.* **9**(15), 4326–4335 (2018). <https://doi.org/10.1021/ACS.JPCLETT.8B01356>
303. Qiu, L., He, S., Ono, L.K., Liu, S., Qi, Y.: Scalable fabrication of metal halide perovskite solar cells and modules. *ACS Energy Lett.* **4**(9), 2147–2167 (2019). <https://doi.org/10.1021/ACSENERGYLETT.9B01396>
304. Christians, J.A., et al.: Stability at scale: challenges of module interconnects for perovskite photovoltaics. *ACS Energy Lett.* **3**(10), 2502–2503 (2018). [https://doi.org/10.1021/ACSENERGYLETT.8B01498/SUPPL\\_FILE/NZ8B01498\\_SI\\_001.PDF](https://doi.org/10.1021/ACSENERGYLETT.8B01498/SUPPL_FILE/NZ8B01498_SI_001.PDF)
305. Moon, S.J., et al.: Laser-scribing patterning for the production of organometallic halide perovskite solar modules. *IEEE J. Photovoltaics* **5**(4), 1087–1092 (2015). <https://doi.org/10.1109/JPHOTOV.2015.2416913>
306. Velilla Hernández, E.: Computational modeling of the electrical performance and degradation of third-generation photovoltaic modules, under accelerated and real operating conditions. Antioquia University (2021)
307. Booth, H.: Laser processing in industrial solar module manufacturing. *JLMN-J. Laser Micro/Nanoeng.* **5**(3) (2010). <https://doi.org/10.2961/jlmn.2010.03.0001>

308. Burn, A., et al.: All fiber laser scribing of Cu(In,Ga)Se<sub>2</sub> thin-film solar modules. *Phys. Proc. Complete*(41), 713–722 (2013). <https://doi.org/10.1016/J.PHPRO.2013.03.138>
309. Green, M.A., et al.: Solar cell efficiency tables (version 49). *Prog. Photovolt. Res. Appl.* **25**(1), 3–13 (2017). <https://doi.org/10.1002/PIP.2855>
310. Green, M.A., Dunlop, E.D., Hohl-Ebinger, J., Yoshita, M., Kopidakis, N., Hao, X.: Solar cell efficiency tables (Version 58). *Prog. Photovolt. Res. Appl.* **29**(7), 657–667 (2021). <https://doi.org/10.1002/PIP.3444>
311. Odabaşı, Ç., Yıldırım, R.: Assessment of reproducibility, hysteresis, and stability relations in perovskite solar cells using machine learning. *Energy Technol.* **8**(12), 1901449 (2020). <https://doi.org/10.1002/ENTE.201901449>
312. Zhang, Z., et al.: High reproducibility of perovskite solar cells via a complete spin-coating sequential solution deposition process. *Sol. Energy* **122**, 97–103 (2015). <https://doi.org/10.1016/J.SOLENER.2015.08.028>
313. Petrović, M., Chellappan, V., Ramakrishna, S.: Perovskites: Solar cells & engineering applications—materials and device developments. *Sol. Energy* **122**, 678–699 (2015). <https://doi.org/10.1016/J.SOLENER.2015.09.041>
314. Green, M.A., Ho-Baillie, A., Snaith, H.J.: The emergence of perovskite solar cells. *Nat. Photon.* **8**(7), 506–514 (2014). Nature Publishing Group. <https://doi.org/10.1038/nphoton.2014.134>
315. Sun, W., et al.: Machine learning–assisted molecular design and efficiency prediction for high-performance organic photovoltaic materials. *Sci. Adv.* **5**(11) (2019). [https://doi.org/10.1126/SCIADV.AAY4275/SUPPL\\_FILE/AAY4275\\_SM.PDF](https://doi.org/10.1126/SCIADV.AAY4275/SUPPL_FILE/AAY4275_SM.PDF)
316. Li, J., Pradhan, B., Gaur, S., Thomas, J.: Predictions and strategies learned from machine learning to develop high-performing perovskite solar cells. *Adv. Energy Mater.* **9**(46), 1901891 (2019). <https://doi.org/10.1002/AENM.201901891>



# SrTi<sub>1-x</sub>Sn<sub>x</sub>O<sub>3</sub> Thin Films as Photocatalysts for Organic Dye Degradation: Influence of the Composition, Deposition Method, and Growth Orientation



A. L. M. de Oliveira, L. Chantelle, J. F. D. Figueiredo, I. A. de Sousa Filho, R. Lebullenger, S. Deputier, I. T. Weber, M. Guilloux-Viry, I. M. G. Santos, and V. Bouquet

**Abstract** Alkaline earth titanates and stannates with perovskite structure— $A(\text{Ti}/\text{Sn})\text{O}_3$ ,  $A = \text{Ca}, \text{Sr}, \text{Ba}$ —have appeared as emerging materials for photocatalysis applications due to their outstanding physicochemical properties. Particularly,  $\text{SrTiO}_3$  and  $\text{SrSnO}_3$  have been widely applied for hydrogen production and degradation of organic pollutants. Despite this, little is known about photocatalysis using these materials in thin film form. In this chapter, polycrystalline  $\text{SrTi}_{1-x}\text{Sn}_x\text{O}_3$  films were grown on amorphous silica substrate by chemical solution deposition (CSD) and pulsed laser deposition (PLD), and their photocatalytic activity was investigated towards an organic dye degradation. Sn content has a strong influence on the photocatalytic efficiency of the films. The higher photocatalytic photodegradation of the azo dye was achieved for  $\text{SrSnO}_3$  films, whatever the deposition method, with the highest efficiency for the film deposited by CSD with 55 and 90% of degradation and discoloration of the dye, respectively. Oriented and epitaxial  $\text{SrSnO}_3$  thin films were also grown on R-sapphire and (100)  $\text{LaAlO}_3$  single crystal substrates, respectively, and the photocatalytic behaviour was investigated as a function of the growth orientation. In addition, the feasibility to reuse the films in the photocatalytic process was evaluated. Our findings demonstrate the high potential use of  $\text{SrSnO}_3$  thin film materials in photocatalysis.

---

A. L. M. de Oliveira (✉) · J. F. D. Figueiredo · R. Lebullenger · S. Deputier · I. T. Weber · M. Guilloux-Viry · V. Bouquet  
Institut Des Sciences Chimiques de Rennes, UMR 6226, CNRS, Université de Rennes 1, Campus de Beaulieu, 35042 Rennes cedex, France  
e-mail: [andrel\\_tlm@hotmail.com](mailto:andrel_tlm@hotmail.com)

A. L. M. de Oliveira · L. Chantelle · I. M. G. Santos (✉)  
NPE/LACOM, Universidade Federal da Paraíba, João Pessoa, PB, Brazil  
e-mail: [ieda@quimica.ufpb.br](mailto:ieda@quimica.ufpb.br)

J. F. D. Figueiredo  
PGMTR, Universidade Federal de Pernambuco, Recife, PE, Brazil

I. A. de Sousa Filho  
LIMA, Universidade de Brasília, Brasília, DF, Brazil

## 1 Introduction

The use of synthetic dyes has increased considerably in recent years, being extensively used by several countries in industries of paper and textiles [1]. Among the various dyes, the azo dyes, which are characterized by the presence of the  $-N=N-$  groups bonded to aromatic ones, constitute the most important class of dyes used for such purposes. The release of dyes in effluents can lead to serious environmental risks as well as health problems for humans. In this sense, research community as well as public agencies have been very concerned about this problem and the use of new and/or optimized water treatment processes that aim the complete removal and degradation of such substances present in the water is still a need [1, 2]. For instance, heterogeneous photocatalysis is a type of advanced oxidative process considered an emerging technology widely applied in many industrial and scientific processes, especially for hydrogen production and water purification, including dye degradation.

In this context, the search for new materials with desired photocatalytic efficiency continues to be focus of a great variety of studies and perovskite-based compounds have shown favourable catalytic properties for these purposes. Over the last years, thin films have gained a lot of attention due to their flexibility of applications, including photocatalysis [3–7]. Thin films are made up of layers of a material with a thickness less than  $1\ \mu\text{m}$ , supported on a substrate, which can be produced by different methods [8–11] that have a great influence on the quality of the films obtained. The use of films in photocatalysis has some advantage when compared to the use of powders. For instance, preparing a material as a thin film allows to change its structural and microstructural characteristics and properties, besides providing reduction of size by miniaturization [8, 11, 12]. Furthermore, the use of thin films in photocatalytic process is relatively less expensive than the employment of powders, as they can be easily recovered and reused in different batches.

Anatase ( $\text{TiO}_2$ ) thin films had been largely explored for the photocatalytic degradation of textile dyes [4, 13–17]. On the other hand, perovskites, despite the growing interest in the use of these materials as photocatalysts, especially for hydrogen production [18–21], few papers were found reporting its use as thin films for dye degradation. For instance,  $\text{SrTiO}_3$  [22],  $\text{NaNbO}_3$  [23] and  $\text{LaCoO}_3$  [24] films were used in the degradation of methylene blue, and  $\text{La}_{1-x}\text{Sr}_x\text{MnO}_3$ /graphene thin films were applied for acid red 3GN degradation [25].  $\text{SrTiO}_3$  is one of the most studied perovskites for photocatalytic degradation of organic dyes, however most works are conducted in bulk form [26, 27]. Besides being used as photocatalytic material,  $\text{SrTiO}_3$  thin film is also well known for its technological use as oxygen gas sensor [28], dynamic random access memories [29], tunable microwave devices [30], among others. In relation to  $\text{SrSnO}_3$ , this material is attractive for applications in electronic devices [31], as humidity sensors [32], dielectric material used as capacitors [33], as anode material for Li-ion battery [34], among others. In relation to photocatalysis,  $\text{SrSnO}_3$  powders have already been applied for hydrogen production [33–37] and for dye degradation [38–44]. In recent study, our group has reported the application of  $\text{SrSnO}_3$  [45],  $\text{Sr}_{1-x}\text{Ba}_x\text{SnO}_3$  [46],  $\text{SrSnO}_3@\text{ZrO}_2$  [43] and  $\text{SrSnO}_3:\text{Eu}$  [42]

powders towards the remazol yellow gold degradation. Up to our knowledge, nor SrSnO<sub>3</sub> neither SrSnO<sub>3</sub>-SrTiO<sub>3</sub> films have not yet been evaluated for photocatalysis reactions.

In this chapter, we present the preparation of SrTi<sub>1-x</sub>Sn<sub>x</sub>O<sub>3</sub> thin films by chemical solution deposition (CSD) and pulsed laser deposition (PLD) on silica substrate and the investigation about the influence of Sn content on the photocatalytic properties of SrTiO<sub>3</sub>-SrSnO<sub>3</sub> solid solution towards Remazol dye degradation. In addition, SrSnO<sub>3</sub> has been deposited on (012)  $\alpha$ -Al<sub>2</sub>O<sub>3</sub>—R-plane sapphire—and (100) LaAlO<sub>3</sub> single crystals substrates using both methods in order to better understand the influence of nature of growth on the photocatalytic behaviour towards the dye degradation.

## 2 Experimental Details

The synthesis of SrTi<sub>1-x</sub>Sn<sub>x</sub>O<sub>3</sub> ( $x = 0; 0.25; 0.50; 0.75$  and  $1$  coded as STO, STS25, STS50, STS75 and SSO, respectively) thin films was performed by chemical solution deposition (CSD) based on the polymeric precursor method and pulsed laser deposition (PLD). For the deposition, amorphous silica substrate as well as R-sapphire—(012)  $\alpha$ -Al<sub>2</sub>O<sub>3</sub>—and LAO—(100) LaAlO<sub>3</sub>—single crystal substrates were used.

For the preparation of the thin films using CSD, polymeric solutions were prepared according to the methodology described in previous work about SrTi<sub>1-x</sub>Sn<sub>x</sub>O<sub>3</sub> powders [47]. The viscosities of the resulting resins were then adjusted in the range of 25–30 cP controlling the water content using a Brookfield DVII+ Pro viscometer. From these resins, the films were spin coated at 1000 rpm for 3 s and 3000 rpm for 20 s (Spin Coater model KW-4A Chemat Technology) on amorphous silica (10 × 10 mm<sup>2</sup>). Only one layer was deposited for each film. The wet films were heat treated at 400 °C for 4 h to eliminate the organic material, and then crystallized at 650 °C for 2 h in air.

For the PLD deposition, homemade sintered targets were prepared by solid-state reaction using stoichiometric amounts of strontium carbonate (SrCO<sub>3</sub>, Merck), tin oxide (SnO<sub>2</sub>, Aldrich) and titanium oxide (TiO<sub>2</sub>, Alfa Aesar) as starting materials to obtain the desired compositions. Characterizations by X-ray diffraction (XRD) and energy dispersive spectroscopy (EDS) were performed on the different targets to assure that the expected perovskite single-phase structure was obtained. The SrTi<sub>1-x</sub>Sn<sub>x</sub>O<sub>3</sub> (STS) thin films were grown using KrF excimer laser (Tuilaser Excistar,  $\lambda = 248$  nm,  $f = 2$  Hz, 210 mJ/pulse) with a substrate-target distance fixed at 55 mm, at 700 °C for 30 min under an oxygen pressure of 30 Pa. More details about the deposition of SrTi<sub>1-x</sub>Sn<sub>x</sub>O<sub>3</sub> thin films using PLD can also be found in our previous work [8].

The structural characteristics of the films were analysed by X-ray diffraction (XRD). Standard  $\theta$ -2 $\theta$  scans were performed with a two-circle Bruker D8 diffractometer using the monochromatized CuK $\alpha$  radiation. Thin film microstructures were

observed with a field emission scanning electron microscope (FE-SEM, Jeol 6301-F) and the optical properties were evaluated using an UV-vis spectrophotometer (Shimadzu UV-2550, in the range between 190 and 900 nm) in the reflectance mode. Surface roughness was estimated using an Atomic Force Microscope (AFM, Veeco D3100, Nanoscope V) in tapping mode with a silicon Nano World Pointprobe NCH. X-Ray photoelectron spectrometry (XPS) measurements were performed using a PHI 5000 Versa Probe (Physical Electronics Inc., USA) with Al K $\alpha$  X-ray illumination, a pass energy of 29.35 eV and at various photoemission angles using electron neutralization.

The photocatalytic property of the SrTi $_{1-x}$ Sn $_x$ O $_3$  (STS) thin films was investigated for degradation of the Remazol Yellow Gold, RNL (Dystar), in aqueous solution of 10 mg L $^{-1}$  and pH 6. A homemade photoreactor was used with dimension of 10  $\times$  10  $\times$  50 cm $^3$  containing two UV-C Biax<sup>TM</sup> Germicidal lamps (General Electric Lighting, 9 W, with maximum emission wavelength of 254 nm). For the experiment, each film was submerged into the glass vessel containing the dye solution (4 mL) and irradiated during 180 min. The discoloration and degradation of the dye were monitored using a UV-vis spectrophotometer (Perkin Elmer Lambda 1050 UV/VIS/NIR) scanning from 200 to 600 nm. The concentrations of the dye after photocatalysis were estimated by means of an analytical curve obtained from the absorbance bands of the dye at different concentrations. The discoloration was monitored by measuring the absorbance at 415 nm while degradation was monitored by measuring the absorbance band at 240 nm. Percent discoloration and degradation (photocatalytic efficiencies) were calculated considering the initial absorbance of the untreated dye solution and the respective concentrations before ( $C_0$ ) and after photocatalytic ( $C_f$ ) treatment, according to Eq. (1).

$$Efficiency (\%) = \frac{C_0 - C_f}{C_0} \times 100 \quad (1)$$

### 3 Results

#### 3.1 Influence of the Thin Film Composition and Deposition Method on the Photocatalytic Activity

It is known that the crystalline structures of the SrSnO $_3$  (SSO) (ICDD 22-1442) and SrTiO $_3$  (STO) (ICDD 35-0734) are orthorhombic and cubic, respectively. Thus, in order to compare all the compositions in the solid solution, the diffraction peaks were indexed considering a pseudo-cubic unit cell according to the equation of matrix transformation, displayed in Eq. (2) [8].

$$\text{Orthorhombic unit cell : } a_{pc} \approx \frac{a_o}{\sqrt{2}} \approx \frac{b_o}{\sqrt{2}} \approx \frac{c_o}{2} \quad (2)$$

According to the XRD patterns displayed in Fig. 1, all the films deposited on silica are polycrystalline and single-phase with pseudo-cubic perovskite structure. More details about this XRD patterns are presented in our recent book chapter reported in [9], where we reported the preparation of SrTi<sub>1-x</sub>Sn<sub>x</sub>O<sub>3</sub> thin films on silica substrate.

The microstructure of the SrSnO<sub>3</sub> and SrTiO<sub>3</sub> thin films deposited on silica was investigated by field emission scanning electron microscopy (FE-SEM) and the corresponding images can be seen in the inset of Fig. 1 [9]. According to the FE-SEM, the

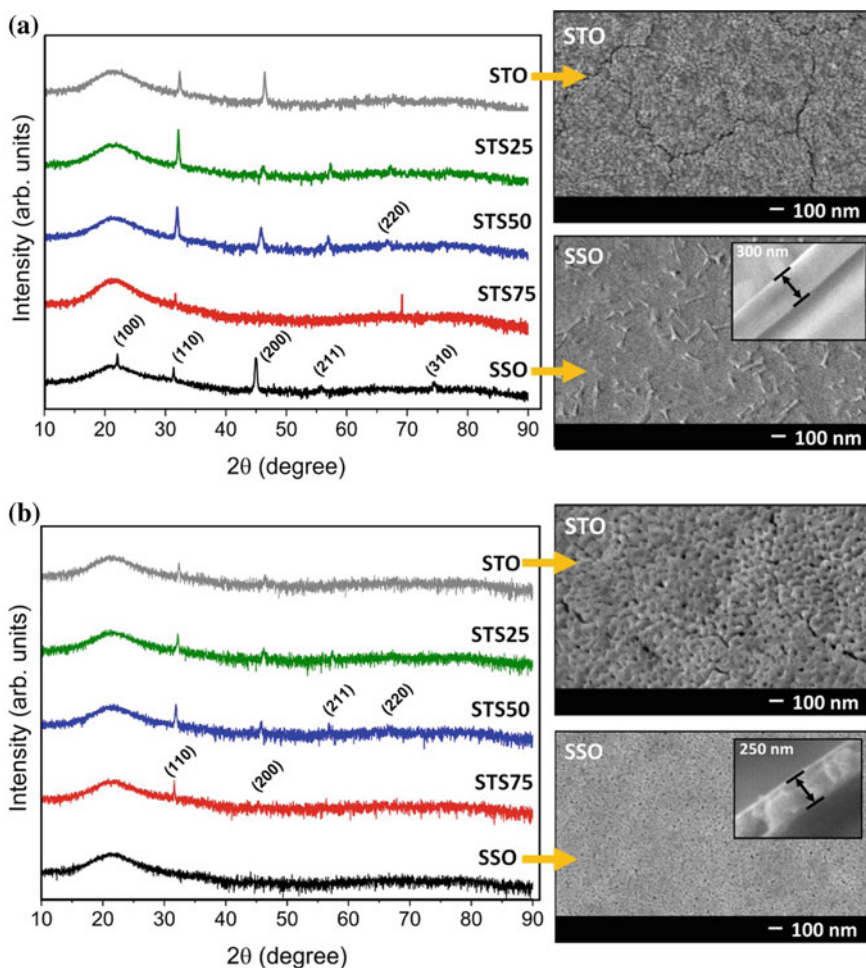


**Fig. 1** XRD patterns of the SrTi<sub>1-x</sub>Sn<sub>x</sub>O<sub>3</sub> thin films deposited on silica substrate by **a** PLD, **b** CSD. Inset: FE-SEM images of the SrTiO<sub>3</sub> and SrSnO<sub>3</sub> thin films deposited on silica substrate by the different methods

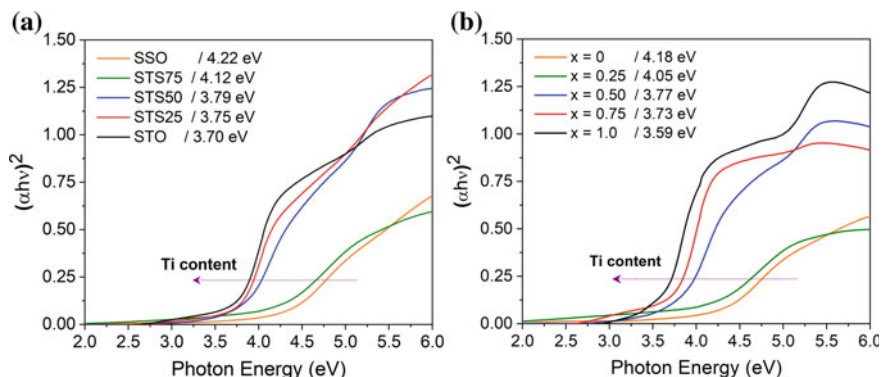


**Fig. 2** UV-vis absorption spectra with the estimated direct  $E_g$  values for  $\text{SrTi}_{1-x}\text{Sn}_x\text{O}_3$  thin films on silica deposited by **a** PLD and **b** CSD

morphology of these films is strongly influenced by the deposition method and the composition of the solid solution. Typically, smaller grains were observed for  $\text{SrSnO}_3$  thin films, in accordance with the observation of Liu et al. [48]. Different deposition method also leads to different microstructures, probably due to different crystallization processes (nucleation and grain growth) [49]. Films deposited by PLD present dense surfaces with the presence of cracks on  $\text{SrTiO}_3$  thin films, usually present when silica is used as substrate. Samples deposited by CSD have a rougher surface, with greater porosity, which can be associated to  $\text{H}_2\text{O}$  and  $\text{CO}_2$  release during decomposition of the polymeric network [49]. Alves et al. [49] have observed this same behaviour for  $\text{SrSnO}_3$  and  $\text{CaSnO}_3$  thin films obtained by the same method. The authors attributed the difference in the microstructures to different crystallization processes (nucleation and grain growth) of the two perovskite materials.

Figure 2a and b show UV-vis spectra for the STS thin films deposited on silica by PLD and CSD, respectively.

The band gaps were calculated using the Tauc method [50]. The results showed an increase of the band gap values according to the amount of  $\text{Sn}^{4+}$  in the solid solution. The band gap of  $\text{SrSnO}_3$  and  $\text{SrTiO}_3$  should be dominated by the orbital splitting of Sn-O and Ti-O octahedra, respectively. In both cases, the top of valence band (VB) is dominated by  $\text{O}_{2p}$  orbitals. It has been reported that the  $\text{Sn}_{5sp}$  orbitals are located at the bottom of the conduction band (CB) of  $\text{SrSnO}_3$ , while  $\text{Ti}_{3d}$  sublevels dominate in  $\text{SrTiO}_3$ . As the  $\text{Ti}_{3d}$  energy levels are lower than  $\text{Sn}_{5sp}$  ones, a band gap decrease is expected when Ti replaces Sn in  $\text{SrSn}_{1-x}\text{Ti}_x\text{O}_3$  lattice and a continuous decrease on the  $E_g$  values from 4.18 to 3.59 eV was observed upon Ti addition along the solid solution. Moreover, due to the lower ionic character for  $\text{Sn}^{4+}\text{-O}^{2-}$  bonds in  $\text{SrSnO}_3$  compared to those  $\text{Ti}^{4+}\text{-O}^{2-}$  in  $\text{SrTiO}_3$ -type structure [2, 51],  $\text{SrSnO}_3$  is expected to have a larger effective crystal field than  $\text{SrTiO}_3$ , resulting in a larger orbital splitting (band gap). Similar behaviour was observed in  $\text{SrSn}_{1-x}\text{Ti}_x\text{O}_3$  thin films on MgO substrates [48] and in  $\text{SrTi}_x\text{Zr}_{1-x}\text{O}_3$  powders [52]. Note that the band gap values obtained in the present work for  $\text{SrTiO}_3$  and  $\text{SrSnO}_3$  agree with the literature data

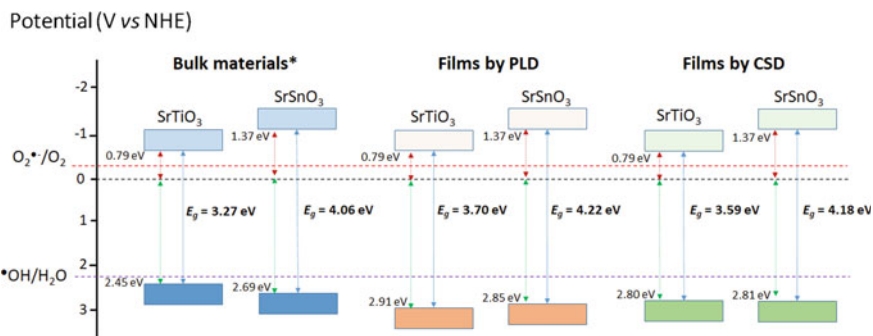
[53, 54], while these values were slightly lower than those previously reported by Liu et al. [48]. This difference might be attributed to the polycrystalline behaviour of our samples as compared to the epitaxial nature of the films prepared by Liu et al. [48].

According to Yuan et al. [55], the increase in the band gap observed for SrSnO<sub>3</sub> is due to the Sn-O-Sn angles deviation from 180°. As the angle deviates from 180° the Sn 5s nonbonding character of the conduction band minimum is lost and antibonding Sn 5s-O 2p contributions become more important. This feature pushes up the energy of the conduction band minimum, resulting in a band gap increase. Other authors report that the lower difference in the covalent character between A-O and B-O bonds can cause changes in the three-dimensional structure of these perovskites, leading to BO<sub>6</sub> octahedra tilts and distortions, thus, affecting the O-B-O bond angles intra-octahedron and B-O-B inter-octahedra. Some other authors associate the decrease in the ionic radius of the cations that occupy the A site in perovskite structure with the band gap values, in ABO<sub>3</sub>-type perovskites such as titanates [2, 56] and stannates [51, 55, 57]. As a result, a variation in band structures may be observed. This phenomenon was demonstrated by Zhang et al. [51] in CaSnO<sub>3</sub>, SrSnO<sub>3</sub> and BaSnO<sub>3</sub> powders and by Borse et al. [21] in Ba(M<sub>0.50</sub>Sn<sub>0.50</sub>)O<sub>3</sub>, (where M=Ti, V, Cr, Zr, Pb and Ce). According to Borse et al. [21], the addition of Ti in the structure of Ba(M<sub>0.50</sub>Sn<sub>0.50</sub>)O<sub>3</sub> led to a decrease in the band gap value, which is due to the main contribution of Ti 3d orbitals to the lower part of the Ba(M<sub>0.50</sub>Sn<sub>0.50</sub>)O<sub>3</sub> conduction band (CB), which shortens the band gap as compared to the experimental value obtained for BaSnO<sub>3</sub> (3.4 eV).

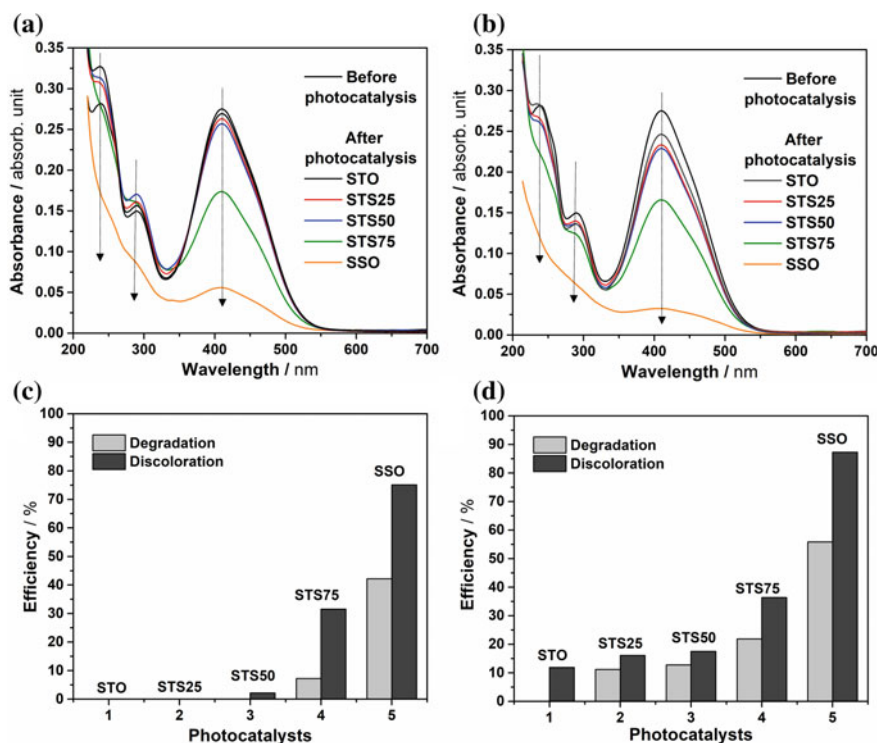
The band gap values calculated in the present work using the Tauc method were used to determine the position of the valence band edge (E<sub>v</sub>), considering the conduction band edge (E<sub>c</sub>) position reported in literature [51, 58]. The band edge positions indicate that all electronic transfers between the film surfaces and the adsorbed molecules are feasible, and all films may present photocatalytic activity.

Figure 4 displays the absorbance spectra of the remazol aqueous solution before and after photocatalysis using STS thin films deposited on silica by PLD and CSD. Comparing the Figs. 4a and b, it is clear that the photocatalytic efficiency is mainly associated to the Sn<sup>4+</sup> content, even considering that the deposition method also has an influence in the photocatalysis due to the microstructure difference. Regardless the deposition method used, SSO films present the highest photoactivity, followed by films with 75% of Sn<sup>4+</sup>. According to Fig. 3, electron transfers between the film surface and the adsorbate are always feasible. On the other hand, a larger energy difference between the E<sub>c</sub> and the •O<sub>2</sub><sup>-</sup>/O<sub>2</sub> level as well as between E<sub>v</sub> and •OH/H<sub>2</sub>O level is observed for SrSnO<sub>3</sub>, which is thermodynamically favourable to the electron transfer.

The literature reported the use of alkaline earth stannates as photocatalysts for organic dye degradation. For instance, Junpoy et al. [59] obtained 85% of discoloration of a solution containing methylene blue after 320 min using rod-like SrSnO<sub>3</sub> as photocatalyst. The authors attributed this efficiency to the formation of •OH radicals and superoxide ions during the photocatalytic process, which could effectively decompose the organic molecules. Wang et al. [57] showed a high photocatalytic activity of CaSnO<sub>3</sub> powders in the degradation of methyl orange, rhodamine B and



**Fig. 3** Comparison between band structure and redox potentials of  $\text{SrTiO}_3$  and  $\text{SrSnO}_3$  materials. \*Data for bulk materials adapted from [51, 58]. The band structure of the films deposited in this work is shown as indicated. For this, the obtained experimental band gap energies of the films and the theoretical VB positions of the bulk materials reported in [51, 58] were considered



**Fig. 4** UV-vis spectra of the remazol aqueous solution before and after photocatalysis and Photocatalytic efficiency of the  $\text{SrTi}_{1-x}\text{Sn}_x\text{O}_3$  thin films deposited on silica by **a, c** PLD and **b, d** CSD



4-hydroxyazobenzene and assigned this efficiency to the tilted SnO<sub>6</sub> octahedra that increase the mobility of the charged carriers, especially the photoinduced electrons, which govern the photocatalytic activity of the materials. In another work Wang et al. [57] have studied the photocatalytic efficiency in the degradation of methyl orange of a series of alkaline earth metal stannates MSnO<sub>3</sub> (M=Ca<sup>2+</sup>, Sr<sup>2+</sup>, Ba<sup>2+</sup>) powders. These authors observed a higher photocatalytic efficiency for CaSnO<sub>3</sub> in comparison with SrSnO<sub>3</sub> and BaSnO<sub>3</sub>. The activities follow the order of CaSnO<sub>3</sub> > SrSnO<sub>3</sub> > BaSnO<sub>3</sub> and the authors attributed the difference of the photocatalytic efficiencies to the slight modification of crystal structure caused by the changing of M<sup>2+</sup> radius.

Some researchers have been trying to associate photocatalysis with distortions in the crystalline lattice [54], as already been demonstrated in alkaline earth stannates [42, 51] and titanates [2] besides alkali metal tantalates and niobates [60]. Such structural distortions can inevitably change the physical, electronic, and photocatalytic properties of these materials. Sato et al. [61] proposed a model considering that charge separation in the initial process of photoexcitation is favoured by dipole moment induced by distorted octahedra. In the present case, we believe that the higher photocatalytic efficiency for the SSO might be attributed to the distorted Sn-O-Sn bond angles (<180°) in the SnO<sub>6</sub> octahedra in comparison to the undistorted Ti-O-Ti (180°) bond angles in the TiO<sub>6</sub> ones of the STO thin film. Such behaviour has been suggested by Arbuñ et al. [2] for Ca, Sr and Ba titanates used for the photodegradation of methylene blue degradation and by Zhang et al. [51, 54] for stannates of these same cations in the photodecomposition of H<sub>2</sub>O and evolution of H<sub>2</sub> and O<sub>2</sub>. Furthermore, Arbuñ et al. [2] studied the photocatalytic efficiency of calcium, strontium and barium titanates and correlated the photocatalytic activity of these materials to their crystalline structures. They reported that the cubic crystalline structure of SrTiO<sub>3</sub> does not favour the mobility of charge carriers and thus has low photocatalytic efficiency. This factor can also be applied to barium and strontium stannates (BaSnO<sub>3</sub> and SrSnO<sub>3</sub>) as demonstrated by Yuan et al. [55]. According to the authors, the increase in the electronegativity of Sr<sup>2+</sup> and the shorter distance of the Sr-O bonds resulted from the octahedral distortion in SrSnO<sub>3</sub> crystal structure in relation to BaSnO<sub>3</sub> can facilitate the transport of charge carriers, especially the photoinduced electrons. These electrons can react with the O<sub>2</sub> adsorbed on the oxide surface, reducing it to a superoxide anionic radical, <sup>•</sup>O<sub>2</sub><sup>-</sup>, or even to other radicals such as HOO<sup>•</sup> or <sup>•</sup>OH, favouring oxidation and subsequent degradation of the dye in water [62].

Silva et al. [26] studied the photocatalytic properties of SrTiO<sub>3</sub> nanoparticles obtained by the microwave assisted hydrothermal method and proposed a mechanism by which the organic dye can be degraded over the prepared samples. According to the authors, two effects are associated with the photocatalytic activity of SrTiO<sub>3</sub>: the first is intrinsic to perovskite-type materials and it is derived from the bulk consisting of asymmetric [TiO<sub>6</sub>] distorted octahedra, which allow the formation of excited octahedral groups [TiO<sub>6</sub>]<sub>d</sub><sup>\*</sup> that favours the creation of intermediate levels within the band gap; the other effect is associated with surface and interface defects of complex clusters [TiO<sub>5</sub>.V<sub>O</sub><sup>z</sup>], which produce extrinsic defects, decrease the band gap and then favour photocatalytic activity. According to the authors, the presence of these

clusters further favours the formation of hydroperoxide ( $\text{HOO}^\bullet$ ) and hydroxide ( $^\bullet\text{OH}$ ) radicals, by capturing electrons/holes and increasing the photocatalytic efficiency of the materials.

In a recent work of our research group involving pure and Eu-doped  $\text{SrSnO}_3$  particles [42], we have observed that charge separation was associated to two different type of distortions in the crystal lattice: i) an intra-octahedral distortion (associated with short-range disorder) that is related to the A-O and B-O interatomic distances as well as to O-Sn-O angles, and ii) an inter-octahedral distortion (associated with medium-range disorder) that is related to the cooperative tilting of the octahedra. The degree of these both type of distortions may introduce intermediate energy levels (associated to deep and shallow defects) that enhanced charge separation upon photoexcitation during photocatalytic process, when they act as electron or hole traps.

The difference of the  $\text{TiO}_6$  and  $\text{SnO}_6$  octahedra environment could lead to different photocatalytic efficiencies of the thin films. The highest efficiency of  $\text{SrSnO}_3$  may be related to these factors, since the network of this perovskite consists of distorted octahedra,  $[\text{SnO}_6]$  when compared to  $\text{SrTiO}_3$ . The formation of complex clusters of the type  $[\text{SnO}_5, \text{V}_\text{O}^z]$  (where  $\text{V}_\text{O}^z = \text{V}_\text{O}^x, \text{V}_\text{O}^\bullet$  ou  $\text{V}_\text{O}^{\bullet\bullet}$ ) is also favoured and together with the formation of electron/hole pairs ( $e^-/h^+$ ) by UV excitation and thus the creation of hydroperoxide and hydroxide radicals, induce photodegradation of the dye. The distorted lattice of  $\text{SrSnO}_3$  can lead to a better charge redistribution compared to  $\text{SrTiO}_3$  which has a very symmetrical lattice.

To better explain the low efficiency observed for Ti-richer films in this work, especially for  $\text{SrTiO}_3$  composition, XPS analyses was performed to evaluate the surface chemical composition and identify the corresponding chemical valence states of Ti cations in  $\text{SrTiO}_3$  thin film deposited on silica by CSD (Fig. 5).

The X-ray photoelectron survey spectra shown in Fig. 5a indicate that the surface composition of the STO thin film contains the expected elements (Sr, Ti and O), while Fig. 5b demonstrates the detailed high-resolution spectrum for Ti 3d. As it can be seen, two peaks corresponding to Ti  $2p_{1/2}$  and  $2p_{3/2}$  were observed at the

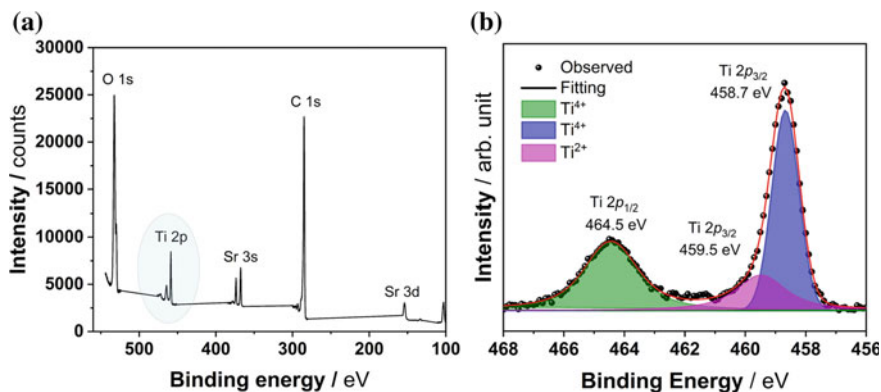


Fig. 5 XPS survey spectrum (a) and high-resolution Ti2p XPS scan (b) of the  $\text{SrTiO}_3$  thin film

binding energies of 464.5 and 458.7, respectively, from which a spin-orbit splitting of 5.8 eV can be calculated. These values are close to those observed by Bukauskas et al. [63] and confirm the existence of Ti<sup>4+</sup> in the sample. No peak assigned to Ti<sup>3+</sup> was observed, whereas a shoulder observed at 459.5 eV might be associated to the presence of Ti<sup>2+</sup> species [63–66]. At the same time, the peak assigned to O 1s was observed at a binding energy of 527.9–530.4 eV, which corresponds to the Ti-O bonds in SrTiO<sub>3</sub> lattice [63–66]. The intensity of O 1s and C 2p peaks and the broadening in C 2p peak may suggest at least a contribution of absorbed H<sub>2</sub>O and CO<sub>2</sub> on the surface of the film. The higher intensity of O 1s and C 2p peaks in comparison to Ti 2p indicate that CO<sub>2</sub> and H<sub>2</sub>O might be adsorbed on the TiO<sub>2</sub>-type layer, especially at Ti<sup>2+</sup> centres on the SrTiO<sub>3</sub> film surface. In addition to that, peaks attributed to Sr 3d from SrTiO<sub>3</sub> film were observed. The comparable and low intensity of both signals might suggest that the SrO framework of the SrTiO<sub>3</sub> lattice might be creating a [Sr-O-Si]-type interface with the SiO<sub>2</sub> substrate. All these results indicate the presence of Ti<sup>2+</sup> on the surface from the exposed TiO terminal, and not from the SrO-end type surface.

Comparing the XPS data with the photocatalytic results, it can be inferred that the presence of cations Ti<sup>4+</sup> and Ti<sup>2+</sup> on the film surface, due to the reduction of Ti<sup>4+</sup> (*d*<sup>0</sup>) to Ti<sup>2+</sup> (*d*<sup>2</sup>) can be responsible for the lower photocatalytic efficiency observed for the Ti-rich samples in this work. The energy levels of Ti<sup>2+</sup> defects are located within the band gap that may not be effective to donate electrons to adsorbed O<sub>2</sub> because it would lead to the formation of Ti<sup>+</sup> or Ti<sup>0</sup> species, which are not usual in these materials and because the energy level of Ti<sup>2+</sup> may be below the \*O<sub>2</sub><sup>-</sup>/O<sub>2</sub> one, preventing electron transfer.

A similar behaviour was observed by Chen et al. [67] in TiO<sub>2</sub> films deposited on alumina. According to Chen et al., these cations can act as defects promoting a higher frequency of significant recombination between the photogenerated electrons/holes (*e*<sup>-</sup>/*h*<sup>+</sup>) pairs, which result in reducing the photocatalytic activity of TiO<sub>2</sub> films.

Another important point is the surface exposed in the film. Fu et al. [68] have shown by theoretical calculations based on DFT that SrTiO<sub>3</sub> contains two types of end surfaces, the SrO and TiO<sub>2</sub> types. The surface composed of SrO is less favourable for the photocatalytic process. In the present work, it seems that Ti<sup>2+</sup> species is related to the exposed TiO terminal. Although a smaller photocatalytic activity was obtained for SrTiO<sub>3</sub> thin films comparing to SrSnO<sub>3</sub> thin films, a discoloration of about 55% was obtained, which can be associated to this more effective surface.

### 3.2 Influence of the Thin Film Growth

To better assess the influence of the thin film growth, SrSnO<sub>3</sub> films were also deposited on two different single crystal substrates by both CSD and PLD methods. The XRD patterns are shown in Fig. 6.

SrSnO<sub>3</sub> films have a high (h00) orientation with a high crystallinity when deposited on LAO single crystal substrate, whatever the deposition method. Phi-scans

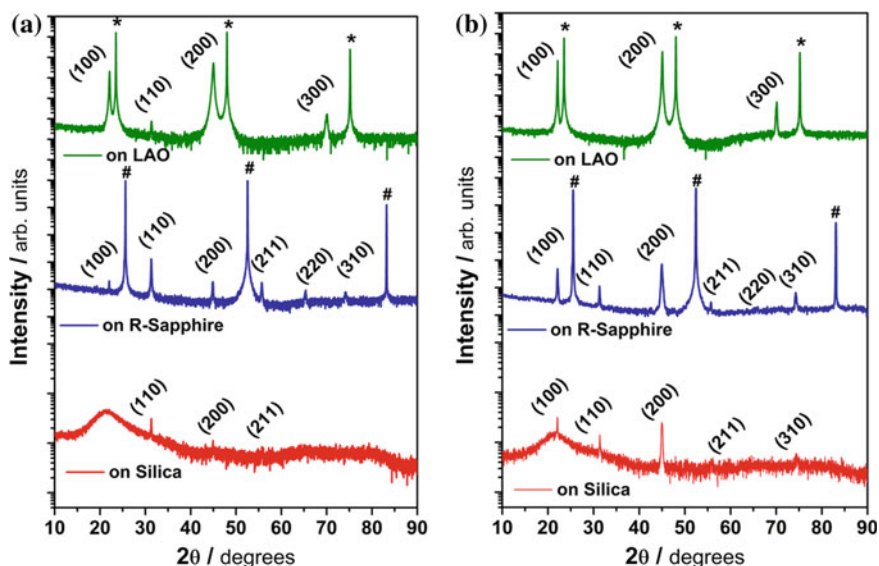


**Fig. 6** XRD patterns of the  $\text{SrSnO}_3$  (SSO) thin films deposited on different substrates by **a** CSD and **b** PLD

(not shown here) revealed an epitaxial growth for these films (in-plane ordering). On R-sapphire, a polycrystalline growth with a preferential (h00) orientation for the film obtained by PLD (textured film) is obtained. The detailed analysis of these films was reported by our research group in a previous work [8]. As already discussed, the films deposited on silica exhibited a polycrystalline characteristic with random orientation. These differences in crystal growth of  $\text{SrSnO}_3$  films are directly related to the substrate nature, which lead also to morphological differences as observed by FE-SEM images in our previous works [8, 9].

The exposed facets on the crystalline surface of the materials are different when they present epitaxial, textured or polycrystalline orientation, with the polycrystalline type showing a greater number of exposed facets on the surface and the epitaxial one with the smallest number (Fig. 6). On the other hand, not all the crystal facets are reactive in the heterogeneous photocatalytic reactions, and this behaviour has been demonstrated for  $\text{TiO}_2$  [63, 65]. Diebold [69] demonstrated that the rutile facets constituted by the plane (110) is the most reactive one. Ohno et al. [70] evaluated the effect of the {110} and {011} facet type in rutile  $\text{TiO}_2$  and {001} and {011} anatase type particles on the photocatalytic activity of these oxides, having demonstrated the higher reactivity of the {110} facet of rutile  $\text{TiO}_2$ . Other studies also support the idea that selective exposure of specific facets to anatase-type  $\text{TiO}_2$  particles can increase their photoactivity [71]. Differently, Silva et al. [17] studied the influence of the exposed facets of  $\text{TiO}_2$  thin films deposited by PLD on various single crystal substrates (C-sapphire, (100)-MgO, -LaAlO<sub>3</sub> and -SrTiO<sub>3</sub>) and on silica in the photodegradation of Remazol dye. The authors demonstrated that the films grown

on C-sapphire presented the highest photocatalytic activity as (001) anatase facet is exposed in larger amount on the film surface. However, the photocatalytic activity of films grown on MgO and silica substrates also presented meaningful activity as compared to the film deposited on C-sapphire. As the films grown on MgO and silica presented high (100) orientation and polycrystalline growth, respectively, it was not possible to derive a simple relationship between film orientation and photocatalytic activity. The authors stated that is not possible to speculate about the nature of exposed facets in (001)-oriented TiO<sub>2</sub> films as they can present either (001) or (101) facets or even a mixture of them, which will depend on the grain morphology.

In relation to perovskites, Zhang et al. [24] deposited LaCoO<sub>3</sub> epitaxial films on (100), (110) and (111) oriented LAO substrates by CSD method. The authors investigated the influence of the film growth on the photocatalytic degradation of methyl orange dye aqueous solution and showed that all films exhibited strong photocatalytic performance. The highest activity was observed for (100) LaCoO<sub>3</sub> thin film with 99.06% of dye degradation after 7 h under UV, followed by the face (111) and (110) LaCoO<sub>3</sub> films with approximately 96% of dye degradation. The authors also evidenced by UV-visible-near infrared spectroscopy that (100) and (111) LCO epitaxial films presented remarkable absorption in the visible range, being much lower for (110) LCO film, which can be an important reason for the different photocatalytic behaviour.

In relation to SrSnO<sub>3</sub> perovskite, Zhang et al. [44] evaluated the dependence of the photocatalytic performance on the exposed facets of the polycrystalline SrSnO<sub>3</sub> particles synthesized by two-step solid state reaction. The authors obtained SrSnO<sub>3</sub> nanocrystals with different morphology (nanorods and self-assembled floral-like structure composed of nanoribbons) and distinct growth direction as a function of the calcination temperature. The photocatalytic activity of the samples was investigated toward methylene blue dye. According to the authors, nanorods grow along the [111] direction, preferentially expose the lower order {001} facets, and present the highest photocatalytic. Curiously, the {001} crystal facets are the most active and stable ones, which was associated to the lower recombination rate of photoinduced charge carriers, the narrower band gap for the photodegradation response and the shorter distance of charge shift by the authors. On the other hand, exposed {111} facets in nanoribbons have a negative effect on the photocatalytic activity.

Based on the known differences among epitaxial, textured, and polycrystalline orientation, SrSnO<sub>3</sub> thin films with these characteristics were evaluated in the photodegradation of Remazol dye. The variation on the absorption spectra of Remazol dye solution after photocatalytic tests clearly indicate a dependence on the deposition method as well as the degree of orientation of the thin films (Fig. 7a and b).

Greater efficiency is achieved with SrSnO<sub>3</sub> films on silica, obtained by the CSD method, with about 55% degradation (Fig. 7c) and 90% discoloration of the RNL solution (Fig. 7d). The lowest efficiency is observed in films deposited on LAO prepared by PLD has about 10% of degradation (Fig. 7c) and 17% of discoloration of the dye solution (Fig. 7d). The results clearly show that as the SrSnO<sub>3</sub> film changes from epitaxial to polycrystalline, the photocatalytic efficiency increases.

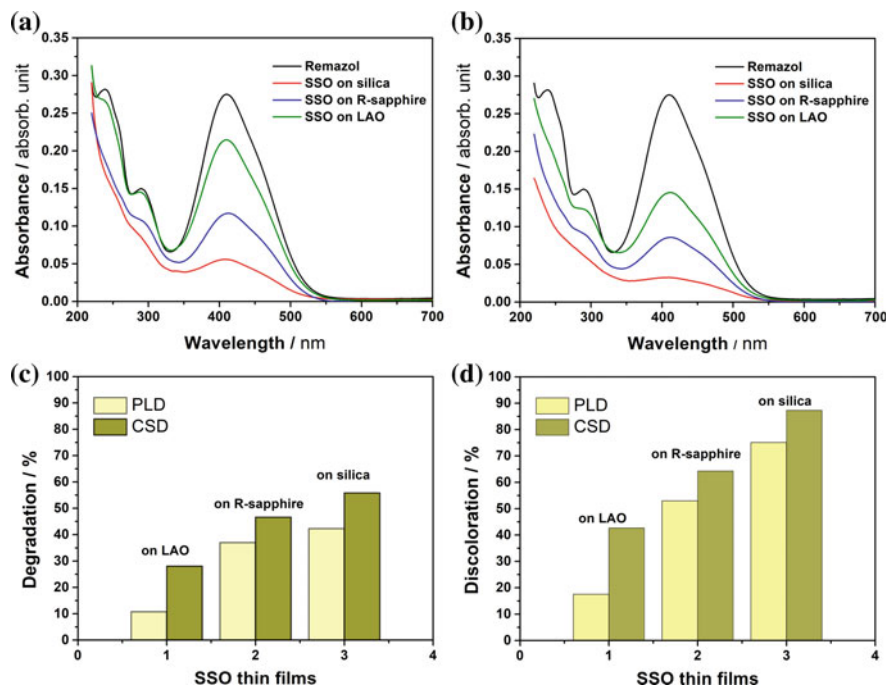


**Fig. 7** UV-vis spectra of the RNL aqueous solution before and after photocatalysis and photocatalytic efficiency of the  $\text{SrSnO}_3$  thin films deposited by **a** PLD and **b** CSD. Degradation and discoloration percentages are displayed in (c) and (d), respectively

As mentioned in the section above, another important factor that may be influencing the properties of  $\text{SrSnO}_3$  films is also the degree of structural order/disorder at short, medium, and long range induced by the nature of the substrate and consequently by the type of film growth. For the epitaxial films grown on LAO, the exposed  $\{h00\}$  facet on the surface seems to have the lowest energy, having the lowest reactivity in the photodegradation reaction of RNL. Moreover, an epitaxial growth induced highly stressed structure leading to a lower photocatalytic activity, as observed by Silva et al. [17]. This is true for both CSD and PLD films. Unlike  $\text{SrSnO}_3$  films deposited on LAO, those ones grown on R-sapphire (which show polycrystalline growth with a preferential  $\{h00\}$  orientation, especially for the film obtained by PLD—textured growth) have a more pronounced photocatalytic efficiency, which may be related to the mix of exposed facets on the film surface, as observed in the XRD patterns. In these films, apart from the larger amount of the exposed  $\{h00\}$  for the film obtained by PLD, other facets can be observed, such as  $\{110\}$  and  $\{310\}$ . The presence of more than one facet on the surface might increase the probability of the existence of more reactive sites that should lead to a higher photocatalytic efficiency. For films deposited on silica, the polycrystalline character without preferential orientation favours photocatalysis even more. In addition to having several exposed facets,

one cannot exclude the fact that polycrystalline films with random orientation growth probably have less defects due to the lower stress present in the film-substrate interface compared to epitaxial or textured films. Although defects usually favour the photocatalysis, the excess of stress might decrease the photocatalytic efficiency in the present case. This fact may be associated to a different type of defects present in the films when compared to those observed in powders, which probably lead to an easier recombination process. As can be seen, the SrSnO<sub>3</sub> films prepared by CSD on silica, but also on the other substrates, have a higher photocatalytic efficiency than the films obtained by PLD, which may be related to the porous microstructure, as displayed in Fig. 1.

Morphological analyses of the surface of SrSnO<sub>3</sub> films deposited on LAO (Fig. 8a), R-sapphire (Fig. 8b) and silica (Fig. 8c) prepared by PLD were performed by FE-SEM before and after photocatalysis.

The morphologies of the films on LAO and sapphire-R did not show significant changes after the photocatalytic tests, unlike the film deposited on silica that showed a higher photocatalytic efficiency for the dye degradation. After photocatalytic test using polycrystalline SrSnO<sub>3</sub> film on silica, a change of surface microstructure was observed, as it seems that a substance stacked on the surface of this film after photocatalysis. During irradiation •OH radicals are formed on the surface of the semiconductor, but these species have a very small lifetime in an aqueous solution and reaction with the dye is favoured if both species are adsorbed on the photocatalyst surface. This may be one of the reasons for the greater efficiency of the SrSnO<sub>3</sub> polycrystalline film on silica observed in this study.

One of the main advantages of heterogeneous photocatalysis is the possibility of catalyst reuse, especially employing thin films as they can be easily removed from the solution, rinsed, and used in subsequent tests. When photocatalyst is used as powders, its recovery becomes quite time-consuming because requires centrifugation, filtration, etc. Moreover, is very likely to lose material during the process. Taking advantage from this facility, consecutive photocatalytic tests were carried out using SrSnO<sub>3</sub> film deposited on silica by PLD. After each cycle, the photocatalytic efficiency of the SrSnO<sub>3</sub> thin film was measured and the percentages of degradation and discoloration of the dye were estimated. After the fourth test, different heat treatments of the film were performed before each new cycle in order to regenerate the photocatalyst. These results are displayed in Fig. 9.

According to the results, the decrease in the photocatalytic efficiency was gradually observed up to the 4th (fourth) cycle. This loss of efficiency has been also observed in other works using TiO<sub>2</sub> [63, 67], and SrTiO<sub>3</sub>/CeO<sub>2</sub> films as photocatalysts [72]. According to Song et al. [72], the observed photocatalytic deactivation of SrTiO<sub>3</sub>/CeO<sub>2</sub> was due, to a certain degree, to the deposition of hydroxides on the photocatalyst surface that block the active sites of the photocatalyst. In the present case, the decrease in the film photocatalytic efficiency observed after each cycle may be due to the inactivation of these active sites on the surface, suggesting that catalyst regeneration could be quite beneficial. The change of the photocatalyst surface was observed right after the 1st photocatalytic test, as shown by the FE-SEM images (Fig. 8b) and confirmed by the AFM images (Figs. 10).

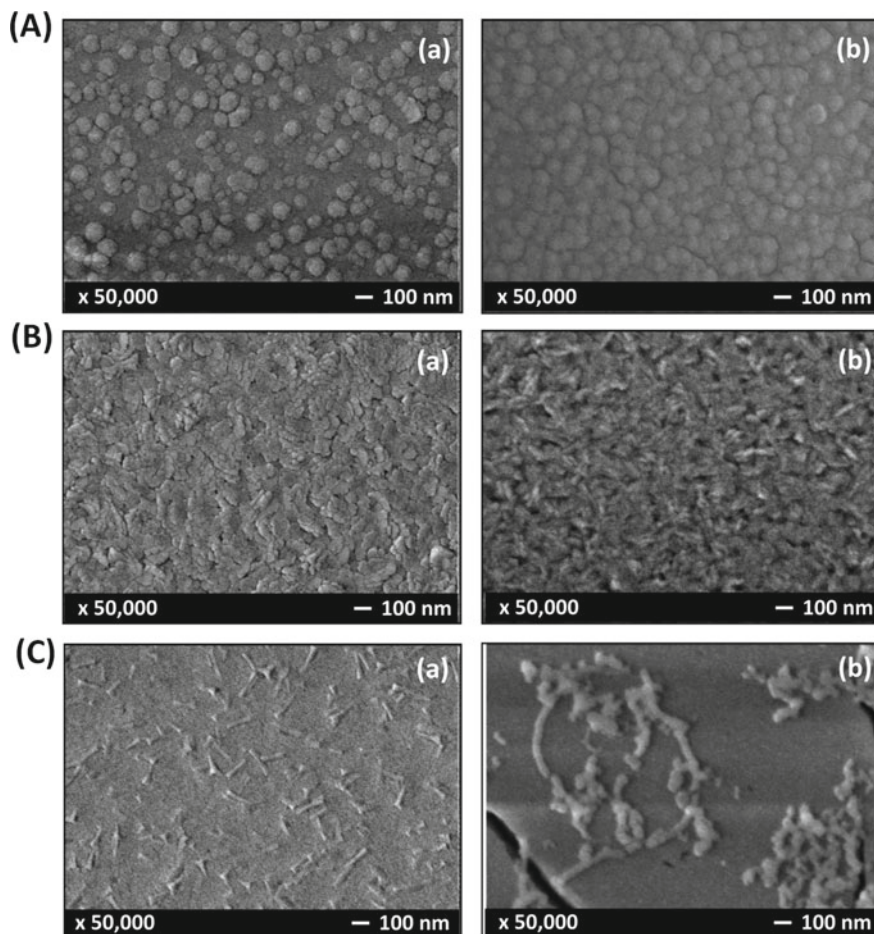


**Fig. 8** FE-SEM images of SrSnO<sub>3</sub> film deposited on LAO (a), R-sapphire (b) and silica (c) by PLD before (a) and after (b) photocatalysis

The film surface before the photocatalytic process has a uniform and homogeneous appearance, with nanostructured granular morphology, in addition to presenting a surface roughness ( $R_{RMS}$ ) of 4 nm. After the 1st photocatalytic cycle of the remazol dye degradation, the thin film surface becomes rougher due to the adsorption of different substances. As a result, the  $R_{RMS}$  roughness of the film surface increases from 4 to 27 nm. This observation suggests that remazol molecules are degraded after photocatalysis and the by-products are adsorbed onto the surface of the SrSnO<sub>3</sub> film, due to the formation of hydroxyl radicals by SrSnO<sub>3</sub>, as reported by [43, 45]. Another possibility is simply the adsorption of dye molecules on the surface of the photocatalyst. This effect leads to a blockage of the film surface that, in further photocatalytic assays, interfere with light penetration and adsorption of more molecules



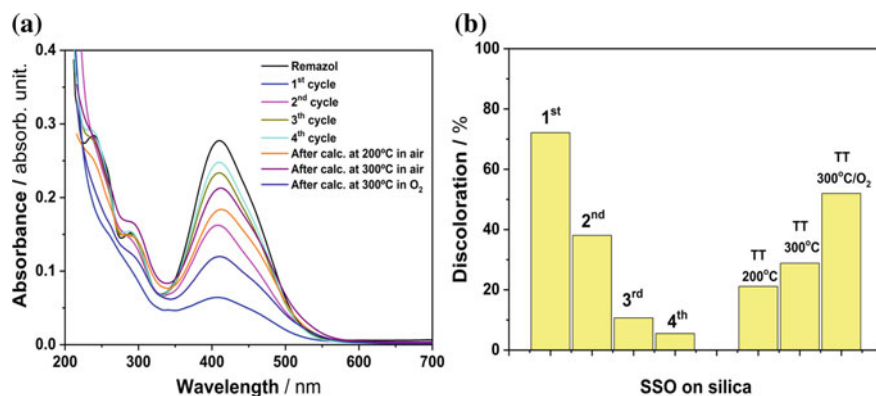


**Fig. 9** UV-vis spectra (a) and discoloration percentage (b) of the RNL aqueous solution before and after successive photocatalytic tests in the presence of SrSnO<sub>3</sub> thin film deposited on silica by PLD

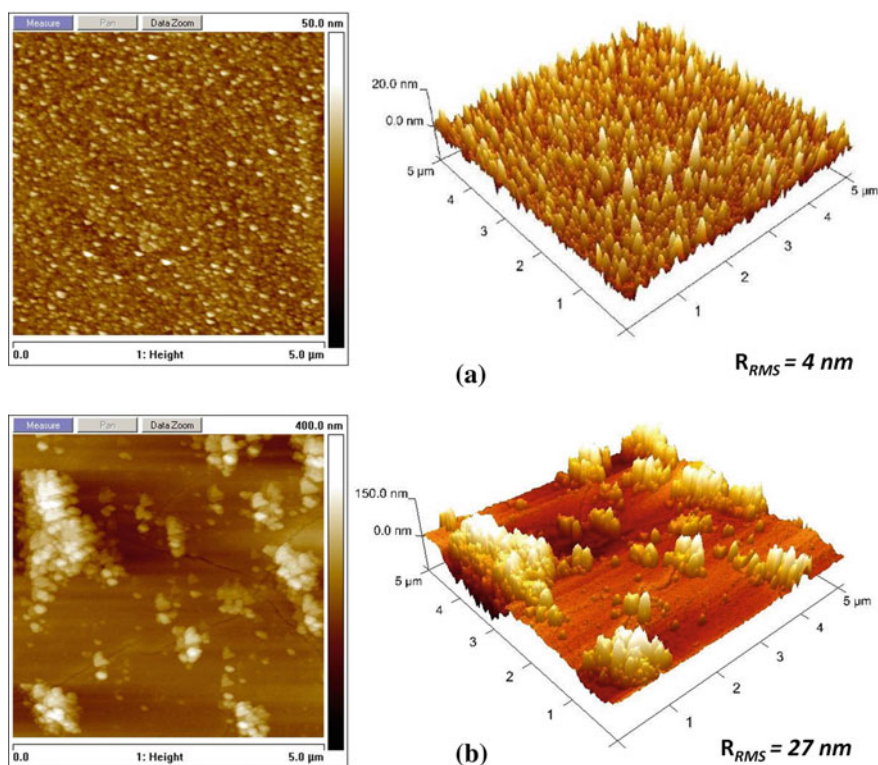


**Fig. 10** AFM images of the SrSnO<sub>3</sub> thin film on silica by PLD before (a) and after (b) the 1<sup>st</sup> photocatalytic test

on the photocatalyst, leading to a loss in efficiency. The change in the morphological aspect of films was also demonstrated through AFM analysis by Chen et al. [67] in  $\text{TiO}_2$ -based thin photocatalyst films after several photocatalytic cycles in the degradation of benzamide.

These results suggest the need of an appropriate treatment for photocatalyst regeneration. To optimize this process, different thermal treatments of the  $\text{SrSnO}_3$  thin film were performed after the fourth successive photocatalytic test and a new test was performed for each procedure. The thermal treatments were chosen based on the melting point and decomposition of the remazol dye [73] and carried out as follows:

1st heat treatment: annealing at 200 °C in air for 2 h (performed before the 5th test).

2nd heat treatment: annealing at 300 °C in air for 2 h (performed before the 6th test).

3rd heat treatment: annealing at 300 °C in  $\text{O}_2$  for 2 h (performed before the 7th test).

After thermal treatment of the  $\text{SrSnO}_3$  film, it is possible to notice a significant improvement in the photocatalytic efficiency, with the best result obtained for a treatment at 300 °C under  $\text{O}_2$  (Fig. 9).

After treatment, the film surface tends to become cleaner (Fig. 11), which favours the penetration of light and activation of the sites on the catalyst surface for further dye degradation tests. These results clearly show the ability of  $\text{SrSnO}_3$  film to be reused in different cyclic tests in remazol photodegradation after adequate thermal treatment for cleaning and reoxidation of the film surface. Therefore, the use of thin films could actually replace, in certain degree, the use of the same catalyst in its powder form.

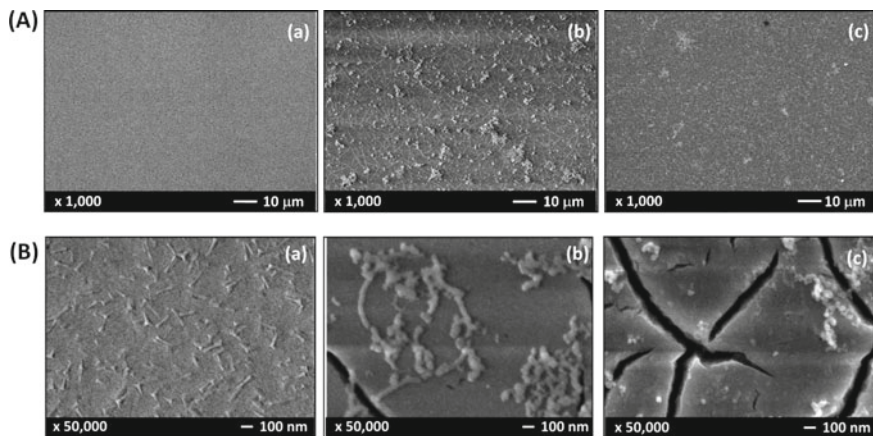


**Fig. 11** FE-SEM images of  $\text{SrSnO}_3$  thin film on silica, showing **a** lower (1000x) and **b** higher (50,000x) magnification of film surface **a** before and **b** after 1st photocatalytic test and **c** after heat treatment at 300 °C in  $\text{O}_2$  for 2 h

## 4 Conclusions

In summary, single phase polycrystalline SrTi<sub>1-x</sub>Sn<sub>x</sub>O<sub>3</sub> ( $x = 0, 0.25, 0.50, 0.75$  and  $1$ ) thin films were successfully prepared by chemical solution deposition (CSD) and pulsed laser deposition (PLD) on amorphous silica substrate. The morphological and optical characteristics were strongly influenced by the composition of the films and deposition method. The composition induced also differences in the photocatalytic efficiency of the thin films, being the Ti<sup>4+</sup>-free sample, i.e., SrSnO<sub>3</sub> (SSO) the most efficient in the degradation of the RNL aqueous solution. XPS analysis revealed mixed valences of Ti (Ti<sup>4+</sup>/Ti<sup>2+</sup>) on the surface of SrTiO<sub>3</sub> and the Ti<sup>2+</sup> centres can act as electron trap favouring the recombination of charge carriers photo-generated in the process. The efficiency of the SSO film prepared by CSD reached 55 and 90% of degradation and discoloration of the dye, respectively, which were higher than the PLD films. The higher photocatalytic efficiency observed for the films prepared by CSD may be attributed to the porous surface, which increase the surface area available for reactions. The results also showed that, besides composition and deposition method, the substrate nature used for depositing thin films have a strong influence on the photocatalytic efficiency. The polycrystalline SrSnO<sub>3</sub> films grown on silica are the most efficient when compared to the oriented ones grown on single crystal substrates. Changes on SSO thin film surface observed by FE-SEM and AFM confirmed the higher efficiency of this photocatalyst, which might be associated to the SnO<sub>6</sub> octahedra tilting that favour the charge separation during photoexcitation. All these results indicated that SrSnO<sub>3</sub> thin film is a promising photocatalyst in the photodegradation of organic dyes and its reuse is possible after heat treatment at 300 °C for 2 h in O<sub>2</sub> atmosphere.

**Acknowledgements** The authors acknowledge the French-Brazilian doctoral college and CAPES-COFECUB (Project 644/09), INCT/CNPq/MCTI and PROINFRA/FINEP/MCTI for financial support and Francis Gouttefangeas for SEM images performed at CMEBA (SCanMat, UMS 2001 CNRS—University of Rennes 1).

## References

1. Singh, K., Arora, S.: Removal of synthetic textile dyes from wastewaters: a critical review on present treatment technologies. *Crit. Rev. Environ. Sci. Technol.* **41**, 807–878 (2011)
2. Arbuji, S.S., Hawaldar, R.R., Varma, S., Waghmode, S.B., Wani, B.N.: Synthesis and characterization of ATiO<sub>3</sub> (A=Ca, Sr and Ba) Perovskites and their photocatalytic activity under solar irradiation. *Sci. Adv. Mater.* **4**, 568–572 (2012)
3. Taheri, M., Abdizadeh, H., Golobostanfard, M.R.: Formation of urchin-like ZnO nanostructures by sol-gel electrophoretic deposition for photocatalytic application. *J. Alloys Comp.* **725**, 291–301 (2017)
4. Alotaibi, A.M., et al.: Zn and N codoped TiO<sub>2</sub> thin films: photocatalytic and bactericidal activity. *ACS Appl. Mater. Interf.* **13**, 10480–10489 (2021)

5. Moulai, F., Fellahi, O., Messaoudi, B., Hadjersi, T., Zerroual, L.: Electrodeposition of nanostructured  $\gamma$ -MnO<sub>2</sub> film for photodegradation of Rhodamine B. *Ionics* **24**, 2099–2109 (2018)
6. Chahkandi, M., Zargazi, M.: New water based EPD thin BiVO<sub>4</sub> film: effective photocatalytic degradation of Amoxicillin antibiotic. *J. Hazard. Mater.* **389**, 121850 (2020)
7. Iborra-Torres, A., Kulak, A.N., Palgrave, R.G., Hyett, G.: Demonstration of visible light-activated photocatalytic self-cleaning by thin films of perovskite tantalum and niobium oxynitrides. *ACS Appl. Mater. Interf.* **12**, 33603–33612 (2020)
8. Oliveira, A.L.M., et al.: Evolution of the structural and microstructural characteristics of SrSn<sub>1-x</sub>Ti<sub>x</sub>O<sub>3</sub> thin films under the influence of the composition, the substrate and the deposition method. *Surf. Coat. Technol.* **313**, 361–373 (2017)
9. Oliveira, A.L.M., et al.: Photoluminescence in alkaline earth stannate thin films grown by physical and chemical methods. In: La Porta, F.A., Taft, C.A. (Eds.), *Functional Properties of Advanced Engineering Materials and Biomolecules*, pp. 155–183. Springer International Publishing, Orgs. Cham (2021)
10. Shwetharani, R., Chandan, H.R., Sakar, M., Balakrishna, G.R., Reddy, K.R., Raghu, A.V.: Photocatalytic semiconductor thin films for hydrogen production and environmental applications. *Int. J. Hydrog. Energy* **45**, 18289–18308 (2020)
11. Pedanekar, R.S., Shaikh, S.K., Rajpure, K.Y.: Thin film photocatalysis for environmental remediation: a status review. *Curr. Appl. Phys.* **20**, 931–952 (2020)
12. Nalajala, N., Patra, K., Bharad, P.A., Gopinath, C.S.: Why the thin film form of a photocatalyst is better than the particulate form for direct solar-to-hydrogen conversion: a poor man's approach. *RSC Adv.* **9**, 6094–6100 (2019)
13. Răileanu, M., et al.: TiO<sub>2</sub>-based nanomaterials with photocatalytic properties for the advanced degradation of xenobiotic compounds from water. A literature survey. *Water, Air, & Soil Pollution* (2013)
14. Han, F., Kambala, V.S.R., Srinivasan, M., Rajarathnam, D., Naidu, R.: Tailored titanium dioxide photocatalysts for the degradation of organic dyes in wastewater treatment: a review. *Appl. Catal. A General* **359**, 25–40 (2009)
15. Rajeshwar, K., et al.: Heterogeneous photocatalytic treatment of organic dyes in air and aqueous media. *J. Photochem. Photobiol. C* **9**, 171–192 (2008)
16. Fujishima, A., Zhang, X., Tryk, D.A.: Heterogeneous photocatalysis: From water photolysis to applications in environmental cleanup. *Int. J. Hydrog. Energy* **32**, 2664–2672 (2007)
17. Silva, V.F., et al.: Influence of the structural characteristics of epitaxial TiO<sub>2</sub> thin films on their photocatalytic properties. *J. Nanosci. Nanotechnol.* **17**, 4326–4334 (2017)
18. Kawasaki, S., et al.: Epitaxial Rh-doped SrTiO<sub>3</sub> thin film photocathode for water splitting under visible light irradiation. *Appl. Phys. Lett.* **101**, 033910 (2012)
19. Huerta-Flores, A.M., Chen, J., Torres-Martínez, J., Ito, A., Moctezuma, E., Goto, T.: Laser assisted chemical vapor deposition of nanostructured NaTaO<sub>3</sub> and SrTiO<sub>3</sub> thin films for efficient photocatalytic hydrogen evolution. *Fuel* **197**, 174–185 (2017)
20. Yilmaz, P., Yeo, D., Chang, H., Loh, L., Dunn, S.: Perovskite BiFeO<sub>3</sub> thin film photocathode performance with visible light activity. *Nanotechnology* **27**, 345402 (2016)
21. Borse, P.H., Lee, J.S., Kim, H.G.: Theoretical band energetics of Ba(M<sub>0.5</sub>Sn<sub>0.5</sub>)O<sub>3</sub> for solar photoactive applications. *J. Appl. Phys.* **100**, 124915 (2006)
22. Katsumata, K.-i., Cordonier, C.E.J., Shichi, T., Fujishima, A.: Photocatalytic activity of NaNbO<sub>3</sub> thin films. *J. Am. Chem. Soc.* **131**, 3856–3857 (2009)
23. Miyauchi, M., Nakajima, A., Fujishima, A., Hashimoto, K., Watanabe, T.: Photoinduced surface reactions on TiO<sub>2</sub> and SrTiO<sub>3</sub> films: photocatalytic oxidation and photoinduced hydrophilicity. *Chem. Mater.* **12**, 3–5 (2000)
24. Zhang, Y.-P., et al.: Orientation-dependent structural and photocatalytic properties of LaCoO<sub>3</sub> epitaxial nano-thin films. *R. Soc. Open Sci.* **5**, 171376 (2018)
25. Hu, J., Ma, J., Wang, L., Huang, H.: Preparation of La<sub>1-x</sub>Sr<sub>x</sub>MnO<sub>3</sub>/graphene thin films and their photocatalytic activity. *Mater. Sci. Eng. B* **180**, 46–53 (2014)

26. Silva, L.F., et al.: Long-range and short-range structures of cube-like shape SrTiO<sub>3</sub> powders: microwave-assisted hydrothermal synthesis and photocatalytic activity. *Phys. Chem. Chem. Phys.* **15**, 12386–12393 (2013)
27. Puangpetch, T., Sreethawong, T., Yoshikawa, S., Chavadej, S.: Synthesis and photocatalytic activity in methyl orange degradation of mesoporous-assembled SrTiO<sub>3</sub> nanocrystals prepared by sol–gel method with the aid of structure-directing surfactant. *J. Mol. Catal. A Chem.* **287**, 70–79 (2008)
28. Hara, T., Ishiguro, T.: Oxygen sensitivity of SrTiO<sub>3</sub> thin film prepared using atomic layer deposition. *Sens. Actuat. B Chem.* **136**, 489–493 (2009)
29. Joshi, P.C., Krupanidhi, S.B.: Structural and electrical characteristics of SrTiO<sub>3</sub> thin films for dynamic random access memory applications. *J. Appl. Phys.* **73**, 7627–7634 (1993)
30. Peng, L.S.J., Heinig, N.F., Moeckly, B.H.: Reactive coevaporation of SrTiO<sub>3</sub> thin films for tunable microwave devices. *MRS Online Proc. Libr.* **688**, 791 (2011)
31. Wakana, H., et al.: Fabrication of high-temperature superconductor single-flux-quantum circuits using a multilayer structure with a smooth surface. *Supercond. Sci. Technol.* **19**, S312–S315 (2006)
32. Shimizu, Y., Shimabukuro, M., Arai, H., Seiyama, T.: Humidity-sensitive characteristics of La<sup>3+</sup>-doped and undoped SrSnO<sub>3</sub>. *J. Electrochem. Soc.* **136**, 1206 (1989)
33. Azad, A.-M., Pang, T.Y., Alim, M.A.: Ultra-low temperature coefficient of capacitance (Tcc) of the SrSnO<sub>3</sub>-based electrical components. *Active Passive Electron. Compon.* **26**, 151–166 (2003)
34. Hu, X., et al.: Rapid synthesis of single-crystalline SrSn(OH)<sub>6</sub> nanowires and the performance of SrSnO<sub>3</sub> nanorods used as anode materials for Li-ion battery. *J. Phys. Chem. C* **114**, 947–952 (2010)
35. Alammar, T., Hamm, I., Grasmik, V., Wark, M., Mudring, A.-V.: Microwave-assisted synthesis of perovskite SrSnO<sub>3</sub> nanocrystals in ionic liquids for photocatalytic applications. *Inorgan. Chem.* **56**, 6920–6932 (2017)
36. Alammar, T., Slowing, I.I., Anderegg, J., Abugoch, J.L.E., Mudring, A.-V.: Ionic-liquid-assisted microwave synthesis of solid solutions of Sr<sub>1-x</sub>Ba<sub>x</sub>SnO<sub>3</sub> perovskite for photocatalytic applications. *ChemSusChem* **10**, 3387–3401 (2017)
37. Chen, D., Ye, J.: SrSnO<sub>3</sub> nanostructures: synthesis, characterization, and photocatalytic properties. *Chem. Mater.* **19**, 4585–4591 (2007)
38. Zhong, F., Zhuang, H., Gu, Q., Long, J.: Structural evolution of alkaline earth metal stannates MSnO<sub>3</sub> (M = Ca, Sr, and Ba) photocatalysts for hydrogen production. *RSC Adv.* **6**, 42474–42481 (2016)
39. Lee, C.W., et al.: Simple synthesis and characterization of SrSnO<sub>3</sub> nanoparticles with enhanced photocatalytic activity. *Int. J. Hydrogen Energy* **37**, 10557–10563 (2012)
40. Sousa Filho, I.A., Arana, L.R., Doungmo, G., Grisolia, C.K., Terrashke, H., Weber, I.T.: SrSnO<sub>3</sub>/g-C<sub>3</sub>N<sub>4</sub> and sunlight: photocatalytic activity and toxicity of degradation byproducts. *J. Environ. Chem. Eng.* **8**, 103633 (2020)
41. Sousa Filho, I.A., Weber, I.T.: SrSnO<sub>3</sub>/g-C<sub>3</sub>N<sub>4</sub> dry phase sunlight photocatalysis. *J. Photochem. Photobiol. A Chem.* **412**, 113255 (2021)
42. Chantelle, L., et al.: Probing the site-selective doping in SrSnO<sub>3</sub>: Eu oxides and its impact on the crystal and electronic structures using synchrotron radiation and DFT simulations. *Inorg. Chem.* **59**, 7666–7680 (2020)
43. Honorio, L.M.C., et al.: Supporting the photocatalysts on ZrO<sub>2</sub>: an effective way to enhance the photocatalytic activity of SrSnO<sub>3</sub>. *Appl. Surf. Sci.* **528**, 146991 (2020)
44. Zhang, X., et al.: Insights into crystal facets of perovskite SrSnO<sub>3</sub> as high-performance photocatalysts toward environmental remediation. *Chem. Eur. J.* **24**, 14111–14118 (2018)
45. Teixeira, A.R.F.A., et al.: SrSnO<sub>3</sub> perovskite obtained by the modified Pechini method—insights about its photocatalytic activity. *J. Photochem. Photobiol. A* **369**, 181–188 (2019)
46. Sales, H.B., et al.: Sr<sub>1-x</sub>Ba<sub>x</sub>SnO<sub>3</sub> system applied in the photocatalytic discoloration of an azo-dye. *Solid State Sci.* **28**, 67–73 (2014)

47. Oliveira, A.L.M., et al.: Effect of the composition on the thermal behaviour of the  $\text{SrSn}_{1-x}\text{Ti}_x\text{O}_3$  precursor prepared by the polymeric precursor method. *J. Therm. Anal. Calorim.* **114**, 565–572 (2013)
48. Liu, Q., et al.: Composition dependence of structural and optical properties in epitaxial  $\text{Sr}(\text{Sn}_{1-x}\text{Ti}_x)\text{O}_3$  films. *Jpn. J. Appl. Phys.* **54**, 031101 (2015)
49. Alves, M.C.F., et al.: Influence of the network modifier on the characteristics of  $\text{MSnO}_3$  (M= Sr and Ca) thin films synthesized by chemical solution deposition. *J. Solid State Chem.* **199**, 34 (2013)
50. Tauc, J.: Optical properties and electronic structure of amorphous Ge and Si. *Mater. Res. Bull.* **3**, 37–46 (1968)
51. Zhang, W., Tang, J., Ye, J.: Structural, photocatalytic, and photophysical properties of perovskite  $\text{MSnO}_3$  (M = Ca, Sr, and Ba) photocatalysts. *J. Mater. Res.* **22**, 1859–1871 (2007)
52. Khunrattanaphon, P., Chavadej, S., Sreethawong, T.: Synthesis and application of novel mesoporous-assembled  $\text{SrTi}_x\text{Zr}_{1-x}\text{O}_3$ -based nanocrystal photocatalysts for azo dye degradation. *Chem. Eng. Jo.* **170**, 292–307 (2011)
53. Piskunov, S., Heifets, E., Eglitis, R.I., Borstel, G.: Bulk properties and electronic structure of  $\text{SrTiO}_3$ ,  $\text{BaTiO}_3$ ,  $\text{PbTiO}_3$  perovskites: an ab initio HF/DFT study. *Comput. Mater. Sci.* **29**, 165–178 (2004)
54. Zhang, W.F., Tang, J., Ye, J.: Photoluminescence and photocatalytic properties of  $\text{SrSnO}_3$  perovskite. *Chem. Phys. Lett.* **418**, 174–178 (2006)
55. Yuan, Y., et al.: Large impact of strontium substitution on photocatalytic water splitting activity of  $\text{BaSnO}_3$ . *Appl. Phys. Lett.* **91**, 094107 (2007)
56. Karakitsou, K.E., Verykios, X.E.: Influence of catalyst parameters and operational variables on the photocatalytic cleavage of water. *J. Catal.* **134**, 629–643 (1992)
57. Wang, W., Bi, J., Wu, L., Li, Z., Fu, X.: Hydrothermal synthesis and catalytic performances of a new photocatalyst  $\text{CaSnO}_3$  with microcube morphology. *Scrip. Mater.* **3**, 186–189 (2009)
58. Wang, C., Qiu, H., Inoue, T., Yao, Q.: Band gap engineering of  $\text{SrTiO}_3$  for water splitting under visible light irradiation. *Int. J. Hydrogen Energy* **39**, 12507–12514 (2014)
59. Junploy, P., Thongtem, S., Thongtem, T.: Photoabsorption and photocatalysis of  $\text{SrSnO}_3$  produced by a cyclic microwave radiation. *Superlatt. Microstruct.* **57**, 1–10 (2013)
60. Kato, H., Kudo, A.: Water splitting into  $\text{H}_2$  and  $\text{O}_2$  on alkali tantalate photocatalysts  $\text{ATaO}_3$  (A = Li, Na, and K). *J. Phys. Chem. B* **105**, 4285–4292 (2001)
61. Sato, J., Kobayashi, H., Inoue, Y.: Photocatalytic activity for water decomposition of indates with octahedrally coordinated  $d^{10}$  configuration. II. Roles of geometric and electronic structures. *J. Phys. Chem. B* **107**, 7970–7975 (2003)
62. Soutsas, K., et al.: Decolorization and degradation of reactive azo dyes via heterogeneous photocatalytic processes. *Desalination* **250**, 345–350 (2010)
63. Bukauskas, V., et al.: Effect of substrate temperature on the arrangement of ultra-thin  $\text{TiO}_2$  films grown by a dc-magnetron sputtering deposition. *Thin Solid Films* **585**, 5–12 (2015)
64. Atuchin, V.V., Kesler, V.G., Pervukhina, N.V., Zhang, Z.: Ti 2p and O 1s core levels and chemical bonding in titanium-bearing oxides. *J. Electron Spectrosc. Related Phenom.* **152**, 18–24 (2006)
65. Xiong, Z., Zhao, X.S.: Nitrogen-doped titanate-anatase core-shell nanobelts with exposed {101} anatase facets and enhanced visible light photocatalytic activity. *J. Am. Chem. Soc.* **134**, 5754–5757 (2012)
66. Tan, H., et al.: A facile and versatile method for preparation of colored  $\text{TiO}_2$  with enhanced solar-driven photocatalytic activity. *Nanoscale* **6**, 10216–10223 (2014)
67. Chen, S.-Z., Zhang, P.-Y., Zhu, W.-P., Chen, L., Xu, S.-M.: Deactivation of  $\text{TiO}_2$  photocatalytic films loaded on aluminium: XPS and AFM analyses. *Appl. Surf. Sci.* **252**, 7532–7538 (2006)
68. Fu, Q., He, T., Li, J.L., Yang, G.W.: Band-engineered  $\text{SrTiO}_3$  nanowires for visible light photocatalysis. *J. Appl. Phys.* **112**, 104322 (2012)
69. Diebold, U.: The surface science of titanium dioxide. *Surf. Sci. Rep.* **48**, 53–229 (2003)
70. Ohno, T., Sarukawa, K., Matsumura, M.: Crystal faces of rutile and anatase  $\text{TiO}_2$  particles and their roles in photocatalytic reactions. *New J. Chem.* **26**, 1167–1170 (2002)

71. Fang, W., Gong, X.-q., Yang, H.: On the unusual properties of anatase TiO<sub>2</sub> exposed by highly reactive facets. *J. Phys. Chem. Lett.* **2**, 725–734 (2011)
72. Song, S., et al.: Photocatalytic degradation of C.I. Direct Red 23 in aqueous solutions under UV irradiation using SrTiO<sub>3</sub>/CeO<sub>2</sub> composite as the catalyst. *J. Hazard. Mater.* **152**, 1301–1308 (2008)
73. Demir, G., Ozcan, K., Tufekci, N., Borat, M.: Decolourization of Remazol yellow PR gran by white rot fungus *phanerochaete chrysosporium*. *J. Environ. Biol.* **28**, 813–7 (2007)
74. Zhu, J., et al.: Nanocrystalline anatase TiO<sub>2</sub> photocatalysts prepared via a facile low temperature nonhydrolytic sol–gel reaction of TiCl<sub>4</sub> and benzyl alcohol. *Appl. Catal. B* **76**, 82–91 (2007)

# SrSnO<sub>3</sub> Applied in the Reduction of NO by CO: Influence of Transition Metal Doping on the Catalytic Activity



Guilherme L. Lucena, Danniely M. Ribeiro, João Jarllys N. de Souza, Fagner Ticiano Gomes Vieira, Cristiane A. Pereira, Ernesto A. Urquieta-González, Ary S. Maia, and Ieda Maria Garcia dos Santos

**Abstract** Strontium stannate (SrSnO<sub>3</sub>) is a perovskite, which has been extensively studied due to its potential technological applications. In this work, SrSnO<sub>3</sub> was doped with transition metals (Cu, Fe, Ni) by the modified Pechini method and evaluated in the catalytic reduction of NO with CO. The perovskite structure was obtained as the major phase for all samples. The catalytic activity of SrSnO<sub>3</sub> was highly improved by all the dopants, as only 10% of conversion was obtained for SrSnO<sub>3</sub>, whereas samples with 5% of Cu presented the highest conversions, reaching 100% of NO into N<sub>2</sub> and 100% of CO into CO<sub>2</sub> at 550 °C. Conversions of 85% of NO into N<sub>2</sub> and 90% of CO into CO<sub>2</sub> were obtained for Ni doped samples at 600 °C, while 62% of conversion was obtained for Fe-doped samples, for both reactions. These results indicate that Cu is the best dopant, which leads to the greatest NO conversion with a smaller amount of dopant.

## 1 Introduction

Atmospheric pollution is related to the increase of concentration of harmful compounds, such as carbon monoxide (CO), nitrogen oxides (NO<sub>x</sub>), sulfur oxides (SO<sub>x</sub>), carbon dioxide (CO<sub>2</sub>), volatile organic compounds (VOC) and halogenated compounds.

---

G. L. Lucena · D. M. Ribeiro · J. J. N. de Souza · F. T. G. Vieira · A. S. Maia · I. M. G. dos Santos (✉)  
NPE-LACOM, Universidade Federal da Paraíba, João Pessoa, PB, Brazil  
e-mail: [ieda@quimica.ufpb.br](mailto:ieda@quimica.ufpb.br)

D. M. Ribeiro  
Instituto Federal da Paraíba, João Pessoa, PB, Brazil

C. A. Pereira · E. A. Urquieta-González  
Research Center on Advanced Materials and Energy, Universidade Federal de São Carlos, São Carlos, SP, Brazil

C. A. Pereira  
Departamento de Engenharia, Universidade Federal de Lavras, Lavras, MG, Brazil



Nitrogen oxides ( $\text{NO}_x$ ) come from natural and human sources, and they are very harmful compounds because they are toxic to human beings, contribute to acid rain, to the destruction of the ozone layer, increase the greenhouse effect and photochemical fog [1–3]. New processes, including new catalysts, have been developed to reduce the emission of pollutants into the atmosphere. Catalysts are used in car exhausts and in industries in order to decrease pollution caused by emission of harmful gases. For instance,  $\text{NO}_x$  elimination does not take place spontaneously, but it can be done using appropriate catalysts. Most of these catalysts are based on noble metals [4], zeolites modified with transition metals [5] and oxide compounds [6].

Perovskite compounds have  $\text{ABO}_3$  stoichiometry and are interesting alternatives to replace the traditional  $\text{NO}_x$  catalysts, due to their greater thermal stability, lower cost, great versatility, and excellent redox property [6]. Most of the perovskites used for NO abatement have lanthanum in the A site and cobalt, nickel, manganese, or iron in the B site [6, 7]. These catalysts have good catalytic activity but not always a good selectivity for  $\text{N}_2$  [8].

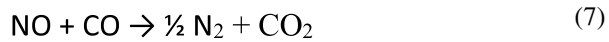
With the aim of developing new catalytic compounds with selectivity for NO abatement, perovskites containing  $\text{Sn}^{4+}$  in the B site and with substitution of lanthanum for alkaline earth metals have been studied by our research group. Among these compounds,  $\text{SrSnO}_3$  was well studied by our research group, after doping with different transition metals, and applied in the NO reduction by CO.

## 1.1 Catalytic Abatement of NO

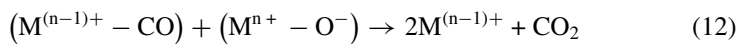
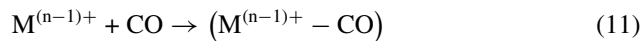
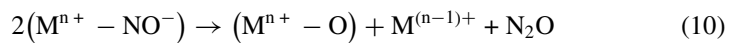
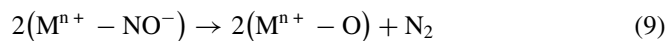
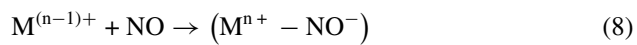
Conversion reaction of NO into  $\text{N}_2$  and  $\text{O}_2$  is extremely slow due to the high dissociation energy of NO molecules, and it hardly occurs at room temperature [9]. The use of catalysts favour the conversion process, but due to the strong adsorption of NO molecules on the catalyst surface, the formation of undesirable intermediates as  $\text{N}_2\text{O}$  and  $\text{NO}_2$  and catalytic deactivation takes place. To avoid these problems, selective catalytic reduction (SCR) is used in the decomposition of NO. In this process, NO conversion is thermodynamically favoured by the presence of reducing agents, as CO,  $\text{NH}_3$ ,  $\text{H}_2$ ,  $\text{CH}_4$ , etc., which decreases the Gibbs free energy ( $\Delta_r G^\circ$ ), compared to the direct decomposition of NO into  $\text{N}_2$  and  $\text{O}_2$  [1, 10, 11].

The use of carbon monoxide (CO) is a promising alternative because it has smaller values of  $\Delta_r G^\circ$  in a broad temperature range and CO is also a pollutant and abatement of both gases is environmentally interesting [12]. The reaction mechanism of NO reduction by CO is very complex. According to literature, in the first step, NO molecules adsorb on the catalyst surface, with dissociation on atomic oxygen and atomic nitrogen, followed by  $\text{N}_2$  formation. In the second step, CO molecules adsorb on the catalyst surface, react with atomic oxygen or lattice oxygen to form  $\text{CO}_2$ . These reactions are presented in Eqs. (1) to (7) [13].





During the catalytic process, the metallic cation is active in the reaction mechanism, being oxidized by NO and reduced by CO, due to the oxygen transfer to this last molecule. Therefore, the behaviour of the metallic catalyst is directly related to the catalyst efficiency [7]. According to Zhang [14], when NO is adsorbed on the perovskite surface, it receives an electron from the metal to form the nitrosyl species ( $\text{NO}^-$ ), which is the first important step of the reduction reaction, Eq. (8). N–O bond in the nitrosyl species is weaker than in NO one favouring the reaction. At low temperatures, adsorbed species on the perovskite surface are dissociated to form  $\text{N}_2$  and  $\text{N}_2\text{O}$ , Eqs. (9) and (10).  $\text{N}_2\text{O}$  is more stable than NO at low temperatures, but it only decomposes above 300 °C, despite the weaker N–O bond. At higher temperatures,  $\text{N}_2\text{O}$  decomposition is easier than NO one and it is favoured when a reducing agent (CO) is added to the reaction, Eqs. (11) and (12). Because of this mechanism,  $\text{N}_2\text{O}$  has been observed as a reaction intermediate by different authors [13–16].



## 1.2 *ASnO<sub>3</sub> Perovskites*

ASnO<sub>3</sub> stannates have interesting physical properties, many of them associated with impurities in the crystalline lattice of structural defects. Alkaline earth stannates have interesting optical, electrical and magnetic properties, with applications as thermally stable capacitors, gas sensors, humidity sensors [17] and as photocatalysts [18]. Despite their technological importance, they are not as studied as the corresponding titanates [19].

The three ASnO<sub>3</sub> compounds have classic perovskite structure (BaSnO<sub>3</sub>, CaSnO<sub>3</sub> and SrSnO<sub>3</sub>). BaSnO<sub>3</sub> has an ideal cubic structure (space group Pm3m), while SrSnO<sub>3</sub> and CaSnO<sub>3</sub> have orthorhombic structure (Pbnm). Despite this, the octahedral site of Sn<sup>4+</sup> is maintained as well as their tridimensional arrangements, while different tiltings among the octahedra lead to meaningful changes in the A site (Ca, Sr and Ba) and in O<sup>2-</sup> site [19, 20]. This distortion is periodically repeated so that a long-range order is observed. Moreover, tilting among the octahedra decreases the conduction band edge with a corresponding increase of the band gap. Therefore, many changes of properties are observed when different modifiers are added to the A site of the stannates with perovskite structure [19, 21].

SrSnO<sub>3</sub> (Fig. 1) is a n-type semiconductor with band gap value above 3.0 eV [19], a valence band (HOMO) corresponding to the non-bridging 2p orbital of O<sup>2-</sup> and a conduction band (LUMO) corresponding to the antibonding orbital resulting from the interaction of the 5 s orbital of Sn<sup>4+</sup> and 2p orbital of O<sup>2-</sup>.

A partial replacement of Sr<sup>2+</sup> and/or Sn<sup>4+</sup> cations leads to structural defects, especially when this replacement is done by a cation with different oxidation state. Therefore, different compounds are formed, but the perovskite structure is maintained. Moreover, cationic vacancies in A and B sites or anionic vacancies are also usual and lead to structural defects and to interesting physical and chemical properties [23, 24]. These structural defects are directly related to the catalytic activity as they act on the reaction mechanisms. For instance, oxygen vacancies are mostly responsible for oxygen mobility inside the crystalline lattice and the more vacancies, the greater the oxygen mobility. Ionic vacancies may favour or not the adsorption of reagents in gaseous phase, but they certainly promote the ion transportation inside the lattice [25].

## 1.3 *Perovskites Applied in the Reduction of NO by CO*

The catalytic properties of perovskites have been studied since the 1950s, for CO oxidation. In 1972, Libby showed its potential application for purification of exhaust gases. Thereafter, perovskite oxides have been recognized as valuable catalysts for NO reduction by CO, due to its high catalytic activity, selectivity, and stability [26, 27].

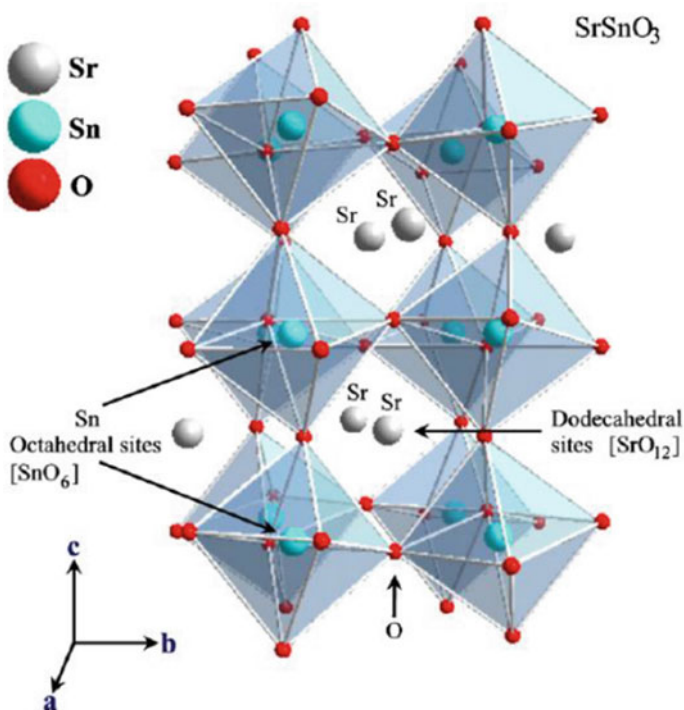


Fig. 1 Orthorhombic structure of SrSnO<sub>3</sub> [22]

Some authors believe that ions in the A site are catalytic inactive and influence the thermal stability of the perovskites, while ions in the B site are catalytic active, with a relatively great distance from one another (0.4 nm), leaving a big space for small molecules to interact selectively in only one active site [28]. For this reason, the choice of the cation in the B site is of great importance for the catalysts as well as for the modification of their catalytic properties, which are determined by the nature of this cation [29].

Most works published concerning perovskites applied in the NO reduction by CO have lanthanum as lattice modifier, associated to transition metals in the B site, as displayed in Table 1.

He et al. [32] studied the influence of the preparation method and of doping on La<sub>0.8</sub>Ce<sub>0.2</sub>B<sub>0.4</sub>Mn<sub>0.6</sub>O<sub>3</sub> (B = Cu or Ag) systems. According to the authors, after adsorption of the NO molecules on the perovskite surface, an electron is transferred from the B site to the NO molecule and the NO<sup>-</sup> molecule is formed simultaneously to the oxidation of the B cation (Cu<sup>+</sup> ↔ Cu<sup>2+</sup> and Mn<sup>3+</sup> ↔ Mn<sup>4+</sup>). The presence of Cu<sup>+</sup> and the redox reaction (Cu<sup>+</sup> ↔ Cu<sup>2+</sup>) may benefit the NO adsorption and its reduction by CO. When the particle size decreases (40–50 nm) and the surface area increases (13.9; 17.9; 5.7 e 14.2 m<sup>2</sup> g<sup>-1</sup>), more defects and larger amounts of Cu<sup>+</sup>

**Table 1** Perovskites applied in the NO reduction by CO

Perovskite	NO conversion (%)	CO conversion (%)	Reference
LaMnO <sub>3</sub>	70 (500 °C)	60 (500 °C)	[11]
La <sub>1-x</sub> Sr <sub>x</sub> MnO <sub>3</sub>	100 (500 °C)	90 (500 °C)	[11]
LaNiO <sub>3</sub>	80 (500 °C)	85 (500°C)	[11]
La <sub>1-x</sub> Sr <sub>x</sub> NiO <sub>3</sub>	100 (500 °C)	90 (500 °C)	[11]
LaFeO <sub>3</sub>	100 (500 °C)	100 (500 °C)	[13]
La <sub>1-x</sub> Sr <sub>x</sub> FeO <sub>3</sub>	100 (550 °C)	100 (550 °C)	[13]
LaCoO <sub>3</sub>	93 (500 °C)	91 (500 °C)	[14]
LaMnO <sub>3</sub>	76 (500 °C)	76 (500 °C)	[14]
LaCo <sub>1-x</sub> Cu <sub>x</sub> O <sub>3</sub>	97 (450 °C)	100 (450 °C)	[14]
LaMn <sub>1-x</sub> Cu <sub>x</sub> O <sub>3</sub>	91 (450 °C)	94 (450 °C)	[15]
La <sub>1-x</sub> Sr <sub>x</sub> AlO <sub>3</sub>	15 (600 °C)	18 (600 °C)	[15]
La <sub>1-x</sub> Sr <sub>x</sub> Al <sub>1-2y</sub> Cu <sub>y</sub> Ru <sub>y</sub> O <sub>3</sub>	100 (400 °C)	100 (400 °C)	[15]
La <sub>1-x</sub> Sr <sub>x</sub> FeO <sub>3</sub>	41 (300 °C)	26 (300 °C)	[30]
LaFeO <sub>3</sub> /CeO <sub>2</sub>	80 (300 °C)	60 (300 °C)	[30]
LaFeO <sub>3</sub>	44 (300°C)	34 (300 °C)	[31]
LaFe <sub>1-x</sub> Cu <sub>x</sub> O <sub>3</sub>	57 (300°C)	42 (300 °C)	[31]
LaFe <sub>1-x</sub> Pd <sub>x</sub> O <sub>3</sub>	96 (300°C)	86 (300 °C)	[31]

ions are formed on the surface and the catalytic activity for NO and CO abatement increases.

Dai et al. [33] evaluated different perovskite type catalysts and correlated the catalytic activity to structural defects (especially oxygen vacancies) and to the redox property (especially of transition metal ions). According to the authors, the oxygen vacancies favor the O<sub>2</sub> and the NO<sub>x</sub> activation and the change of the oxidation state of the B site promotes the redox process of the catalyst. Together, the two effects influence the oxygen mobility in the lattice and improve the catalytic performance for NO reduction by CO. The importance of the oxygen vacancies in the catalytic performance was confirmed by other authors [29, 34], who reported that oxygen vacancies in perovskites have an important role on the catalytic reduction of NO, forming adsorption sites for NO and CO and favoring the dissociation of adsorbed NO species.

In the present work, different transition metals, Fe, Ni and Cu were added into the SrSnO<sub>3</sub> lattice to improve the redox ability of the perovskite and form oxygen vacancies. The pure and doped samples were evaluated in the SCR of NO by CO.

## 2 Materials and Methods

The synthesis of pure and doped (Cu, Fe e Ni) strontium stannate was done by the modified Pechini method, also known as polymeric precursor method. The procedure was carried out in two steps: the synthesis of the tin citrate followed by synthesis of the polymeric resin and calcination. Pure SrSnO<sub>3</sub> and Fe-doped SrSnO<sub>3</sub> was also synthesized using metallic tin, using a route with only one step.

### 2.1 Reagents

The precursors used in the synthesis of pure and doped strontium stannate were: citric acid (99%, Cargill), tin chloride (99.9%, J.T. Baker), tin (99.99%, Vetec), ammonium hydroxide (99.9%, Sigma), copper (II) nitrate (99.0%, Vetec), iron (III) nitrate (99.0%, Vetec), nickel (II) nitrate (99.0%, Vetec), nitric acid (65.0%, Dinamica), ethylene glycol (99.5%, Vetec).

### 2.2 Modified Pechini Method

#### 2.2.1 Two Steps Route

Tin citrate was prepared by dissolution of citric acid in water heated at 70 °C, followed by addition of dihydrated tin chloride, with a stoichiometric ratio of 3 mol of citric acid to 1 mol of tin chloride. The becker was immersed in a container with ice and ammonium hydroxide was slowly added to the solution to induce the precipitation of tin citrate, under a pH value below 3. A molar ratio of 1 mol of tin chloride to 1 mol of ammonium hydroxide was used. The suspension was stored in a refrigerator and supernatant was changed to eliminate the chloride, until a negative result of the chloride test using AgNO<sub>3</sub>. Tin citrated was vacuum filtered, dried in a stove at 60 °C for 24 h, deagglomerated and stored in a refrigerator. Gravimetry was done to determine the amount of tin oxide obtained from the tin citrate.

For the synthesis of the polymeric resin, solutions of the different precursors were prepared. Strontium citrate solution was prepared by dissolution of citric acid and strontium nitrate in a small amount of water. For doped SrSnO<sub>3</sub>, solutions of copper citrate, nickel citrate and iron citrate were also prepared, similarly to the procedure described to strontium citrate. Tin citrate solution was prepared by solubilization of the previously prepared powder in a small amount of nitric acid. Then strontium citrate solution was added into the tin citrate solution under heating at 70 °C and magnetic stirring, followed by addition of the dopant citrate solution (copper citrate or nickel citrate or iron citrate), considering the desired stoichiometry (1, 5, 10 mol %). After homogenization for 15 min, ethylene glycol was added to the solution and

heated up to  $\sim 90$  °C to obtain the polymeric resin. A molar stoichiometric ratio of citric acid:metal of 3:1 was used, besides a mass ratio of citric acid:ethylene glycol of 60:40.

Each polymeric resin was heat treated at 300 °C for 4 h to obtain the polymeric powder precursor, which was deagglomerated and sieved at 100 mesh before milling in an attritor mill for 4 h, in ethanolic medium. After drying, the material was dried, and heat treated with a heating rate of 1 °C min<sup>-1</sup> up to 300 °C for 7 h under oxygen atmosphere. The resulting powder was calcined from 400 to 800 °C, with a heating rate of 5 °C min<sup>-1</sup> for 4 h in a muffle oven.

### 2.2.2 One Step Route

First, tin (Sn) was dissolved in an aqueous solution of nitric acid at 0.1 mol.L<sup>-1</sup> in an ice bath, followed by addition of citric acid. The pH of the solution was adjusted to 3–4 by addition of ammonium hydroxide. The previously prepared strontium citrate solution was added to tin citrate solution under stirring at 60 °C, followed by addition of the iron citrate solution for the doped sample. After 20 min of stirring, ethylene glycol was added, and the solution was heated to 90–100 °C. The same stoichiometric ratios described before were used, as well as the same milling and heat treatment procedure.

## 2.3 Characterization of the Catalysts

The polymeric powder precursors of the pure and doped SrSnO<sub>3</sub> heat treated under oxygen atmosphere were characterized by thermogravimetry (TG) and differential thermal analysis (DTA) using a thermal analyser DTG-60H from Shimadzu. In the analysis, 10 mg of sample were weighed in an alumina crucible, heated with a heating rate of 10 °C min<sup>-1</sup> up to 1200 °C under a synthetic air atmosphere with flow of 50 mL min<sup>-1</sup>.

After calcination from 400 to 800 °C, samples were characterized by X-ray diffraction (XRD), infrared spectroscopy (IR), Raman spectroscopy, UV–visible spectroscopy (UV–vis) and specific surface area.

XRD patterns were obtained in a XRD-6000 diffractometer from Shimadzu operating at 40 kV and 40 mA with CuK $\alpha$  radiation. The  $\theta$ – $2\theta$  XRD patterns were collected in the range of 15–80°, using a step size of 0.02° and step time of 2 s. IR spectra were obtained in an IRPrestige-21 spectrophotometer from Shimadzu, in mid infrared range, from 300 to 2000 cm<sup>-1</sup> using KBr pellets or in the far infrared range, from 240 to 650 cm<sup>-1</sup> using Nujol oil. UV–vis spectra were obtained in a UV-2550 spectrophotometer from Shimadzu, in diffuse reflectance mode, in the range from 190 to 900 nm. The band gap energies were calculated from the absorbance curve according to Wood and Tauc method [35]. Micro-Raman spectra were collected using a Invia micro-Raman from Renishaw operating with an Ar laser (514 nm) and power

of 20 mW. Spectra were obtained in the range from 100 to 1000 cm<sup>-1</sup>, using an objective lens of 50 x. The specific surface area of the catalysts was determined in an ASAP 2420 analyser from Micromeritics, using N<sub>2</sub> adsorption/desorption curves at 77 K. Samples were previously treated at 150 °C for 2 h under ultra-dry N<sub>2</sub> flow.

## 2.4 Catalytic Activity

Materials calcined at 800 °C were evaluated in the catalytic reduction of NO by CO. During the catalytic test, 100 mg of catalyst (previously treated at 500 °C for 1 h under He flow) were diluted in 100 mg of amorphous silica and placed in a fixed bed tubular reactor coupled to a vertical furnace with controlled heating under atmospheric pressure. Reaction was performed between 300 and 700 °C, with space speed of 17,000 h<sup>-1</sup>. The reactor was powered with a continuous gaseous flow (25 mL min<sup>-1</sup>), regulated with the use of mass flow meters, with a mixture of 0.5% of NO and 0.5% of CO under He balance, both as a pattern mixture of 1% mol/mol (gas/He). Reaction products were identified in a GC-17A gas chromatograph from Shimadzu, equipped with a thermal conductivity detector. NO, N<sub>2</sub>, CO and CO<sub>2</sub> were separated at 50 °C, using two packed columns operating in series (Porapack N and Molecular Sieve 13X).

## 3 Results and Discussion

Figure 2 displays the TG and DTA curves of the pristine SrSnO<sub>3</sub> precursor. Four mass loss steps were observed in the TG curve. In the first step, water and adsorbed gases were eliminated from the material surface, corresponding to endothermic transitions in the DTA curve, around 80 °C. The second step was assigned to the combustion reaction of the organic material with elimination of CO<sub>2</sub> and H<sub>2</sub>O, corresponding to an exothermic peak in the DTA curve, between 300 and 600 °C. Mass loss assigned to endothermic peaks above 710 °C (third step) and above 1000 °C were assigned to the carbonate decomposition.

A careful evaluation of the crystallization process of SrSnO<sub>3</sub> was performed after calcination between 400 and 800 °C, and characterization by FTIR and XRD, as displayed in Fig. 3.

According to Nakamoto [36], the hydroxyl group is distinguished from the aqueous group, which displays H–O–H bending modes around 1600 cm<sup>-1</sup>, while the hydroxyl-metal bond, M–OH, displays a vibrational mode between 1000 and 1200 cm<sup>-1</sup>. These two bands were observed in the spectra of Fig. 3a—one band assigned to adsorbed water was observed at 1630 cm<sup>-1</sup>, while one band assigned to M–OH group was observed around 1070 cm<sup>-1</sup>.

Bands assigned to chelated esters were also observed at 1389 and 1547 cm<sup>-1</sup> [36] after calcination at 400 and 500 °C and their intensities decrease after calcination at



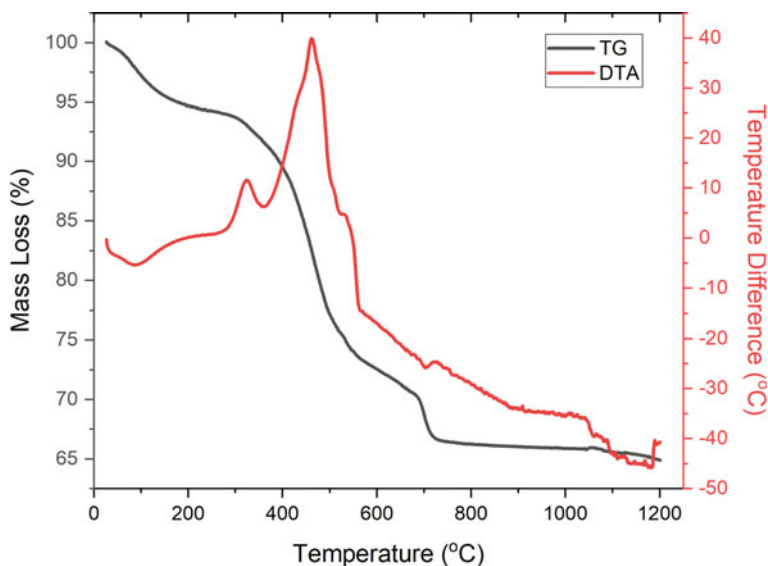


Fig. 2 TG and DTA curves of the  $\text{SrSnO}_3$  precursor

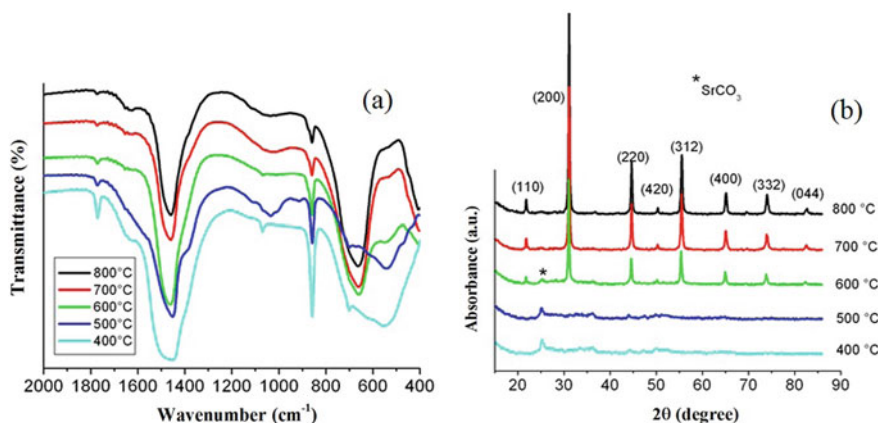


Fig. 3 Infrared spectra (a) and XRD patterns (b) of  $\text{SrSnO}_3$  calcined at different temperatures

and above 600 °C, confirming that the exothermic peak between 300 and 600 °C is related to the combustion of the ester.

According to Nyquist and Kagel [37], absorption bands assigned to carbonates are observed at 1320–1530  $\text{cm}^{-1}$  (strong), at 1040–1100  $\text{cm}^{-1}$  (weak) and at 800–890  $\text{cm}^{-1}$  (medium). In the present work, these bands are observed at 1450, 1080 e 860  $\text{cm}^{-1}$  due to the presence of unidentate carbonate, according to Hodjati et al. [8]. The intensity of these bands decrease after calcination above 700 °C, but they are

not completely eliminated, as the highest calcination temperature was 800 °C and TG/DTA curves indicate the carbonate elimination only above 1200 °C. The high intensity of the band at 1080 cm<sup>-1</sup> is due to the superposition of the hydroxyl band.

The orthorhombic SrSnO<sub>3</sub> perovskite phase has 57 normal modes, with 25 infrared active modes,  $\Gamma_{iv} = 9B_{1u} + 7B_{2u} + 9B_{3u}$  [38]. The perovskite structure has bands assigned to three triply degenerate active modes: the lattice mode  $\nu_1$  (A-BO<sub>3</sub>) between 80 and 140 cm<sup>-1</sup>; the bending mode  $\nu_2$  (O-B-O) between 170 and 280 cm<sup>-1</sup>; and the stretching mode  $\nu_3$  (B-O), between 490 and 680 cm<sup>-1</sup>; while the torsional mode  $F_{2u}$  may become active for perovskites with structure distortion from the ideal cubic symmetry, with the appearance of more bands in the IR spectrum. The  $\nu_3$  mode is observed around 500 cm<sup>-1</sup> for cubic perovskites, and around 660 cm<sup>-1</sup> for orthorhombic ones, due to the octahedral distortion [39]. For instance, Pfaff et al. [40] observed the Sn–O band around 550 cm<sup>-1</sup> for the cubic BaSnO<sub>3</sub> (cúbico), while Last [39] observed this same band around 666 cm<sup>-1</sup>, for the orthorhombic SrSnO<sub>3</sub>. These data agree to Moreira et al. [38], who reported that bands assigned to the stretching of the Sn–O bond are observed around 674 and 530 cm<sup>-1</sup>, while vibrations of the stannate group (SnO<sub>3</sub><sup>2-</sup>) are observed around 300–400 and 600–700 cm<sup>-1</sup>.

In the present work,  $\nu_2$  and  $\nu_3$  modes were observed around 400 and 670 cm<sup>-1</sup>, respectively. The  $\nu_3$  mode was observed around 540 cm<sup>-1</sup>, for samples calcined at 400 and 500 °C. As temperature increases, the intensity of this band decreases, while a high intensity band is observed at 670 cm<sup>-1</sup>. It should be observed that the band previously assigned to the undistorted SnO<sub>6</sub> octahedra of BaSnO<sub>3</sub>, at 540 cm<sup>-1</sup>, was observed at low temperatures, while the band assigned to the distorted SnO<sub>6</sub> octahedra of SrSnO<sub>3</sub>, at 670 cm<sup>-1</sup>, was observed at higher temperatures. This behaviour indicates that the octahedral distortion probably takes place simultaneously to the crystallization process.

This behaviour is in agreement with the XRD patterns of the pure SrSnO<sub>3</sub> (Fig. 3b), which displays an increase of the peaks assigned to the perovskite structure at and above 600 °C, simultaneously to the SnO<sub>6</sub> band at 670 cm<sup>-1</sup>, while no peaks assigned to this phase are observed at 400 and 500 °C. All peaks indicated in Fig. 3b were indexed according to the ICDD index card 77-1798 and confirm that an orthorhombic structure was obtained. Peaks assigned to SrCO<sub>3</sub> were observed after calcination at 400, 500 and 600 °C, in agreement to FTIR spectra.

Azad et al. [41] synthesized SrSnO<sub>3</sub> by solid state reaction (SSR) and self-sustained synthesis (SHS) and observed the formation of the perovskite structure at 1100 °C and 800 °C, respectively. A single-phase material was obtained by the synthesis using the SRS method, while Sr<sub>2</sub>SnO<sub>4</sub> was obtained as a secondary phase when the SHS method was used.

In the present work, the perovskite phase was obtained with good crystallinity at 800 °C. This is an interesting result for catalysis as low calcination temperatures usually lead to materials with greater surface area, which favours the catalytic processes. As all doped SrSnO<sub>3</sub> presented a similar behaviour, the calcination temperature of 800 °C was used for all other samples presented hereafter.

### 3.1 Influence of Doping on the Catalytic Activity of $\text{SrSnO}_3$ : *Me (Me: Fe, Ni, Cu)*

#### 3.1.1 Characterization of the Catalysts

The XRD patterns of doped  $\text{SrSnO}_3$  are presented in Fig. 4. All samples displayed an orthorhombic perovskite structure, according to the ICDD 01-77-1798 index card. For all of the samples, no peaks assigned to the dopants were observed, which indicate that the dopants were incorporated into the perovskite lattice. Moreover, according to the inset in Fig. 4, doping decreases the crystallinity of the perovskite phase, as indicated by the smaller intensities of the (200) peaks. A displacement of these peaks is also observed, which is another indication that dopant got into the perovskite lattice. Similarly to other works published in literature, strontium carbonate ( $\text{SrCO}_3$ ) was observed as a secondary phase for most samples [21].

The lattice parameters were calculated for all samples, as displayed in Table 2. Theoretical data displayed in the ICDD 01-77-1798 index card are displayed for comparison. For  $\text{SrSnO}_3$ , very similar values were obtained compared to the theoretical one. After doping, no meaningful change in the lattice parameters 'a' and 'b' was observed, while an increase in the parameter 'c' was noticed for samples doped with copper and iron, with a small increase of the unit cell volume.

According to literature, the ionic radii of  $\text{Sn}^{4+}$ ,  $\text{Ni}^{2+}$ ,  $\text{Fe}^{3+}$  and  $\text{Cu}^{2+}$  are 69 pm, 69 pm, 65 pm and 73 pm, respectively [42]. The small difference of lattice parameters

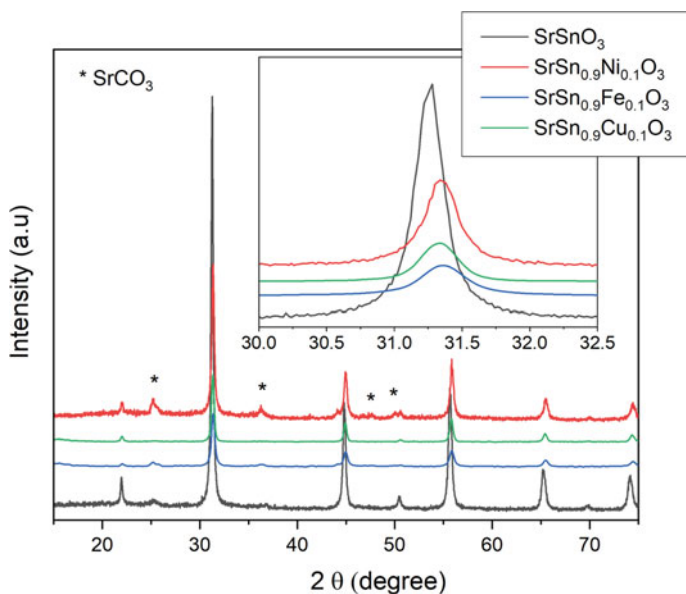


Fig. 4 XRD patterns of the pure and doped  $\text{SrSnO}_3$  calcined at 800 °C

**Table 2** Lattice parameters of the pure and doped SrSnO<sub>3</sub>, calcined at 800 °C for 4 h

Lattice parameter	Theoretical <sup>a</sup>	SrSnO <sub>3</sub>	SrSn <sub>0.9</sub> Fe <sub>0.1</sub> O <sub>3</sub>	SrSn <sub>0.9</sub> Ni <sub>0.1</sub> O <sub>3</sub>	SrSn <sub>0.90</sub> Cu <sub>0.1</sub> O <sub>3</sub>
a (Å)	5.71	5.70	5.70	5.70	5.71
b (Å)	5.71	5.70	5.72	5.70	5.71
c (Å)	8.06	8.06	8.16	8.05	8.10
V(Å <sup>3</sup> )	262.64	262	265	262	264
Crystallite size (nm)	–	34.8	–	23.0	30.3

<sup>a</sup>Obtained from the ICDD 01-77-1798 index card

observed after Ni doping may be assigned to the similar ionic radii of Sn<sup>4+</sup> and Ni<sup>2+</sup>. Curiously, even when Sn<sup>4+</sup> replacement was made with a larger size cation, as Fe<sup>3+</sup>, an increase of the unit cell volume was observed. This behaviour may be due to the lattice distortion related not only to the size difference of the cations, but also due to the formation of oxygen vacancies as Sn<sup>4+</sup> was replaced by cations with smaller oxidation state [43, 44]. This distortion may also be responsible for the smaller crystallite size after doping, as displayed in Table 2, because distortion can make diffusion more difficult.

The infrared spectra of pure and doped SrSnO<sub>3</sub> samples, calcined at 800 °C for 4 h are displayed in Fig. 5. For all samples, the Sn–O stretching band was observed around 670 cm<sup>-1</sup> besides a weak band around 540 cm<sup>-1</sup>, which indicated that different octahedral symmetries are observed in the perovskites. After doping with Ni and Fe, an increase of the intensity of the band assigned to undistorted octahedra at 540 cm<sup>-1</sup> was observed. An absorption band below 400 cm<sup>-1</sup> was assigned to the O–Sn–O bending mode. The presence of carbonate was also observed, as indicated by bands at 860, 1070 and 1470 cm<sup>-1</sup>, as described before.

Raman spectra of the pure and doped SrSnO<sub>3</sub> samples, calcined at 800 °C for 4 h are displayed in Fig. 6. Orthorhombic perovskites display 24 Raman active modes, according to the irreducible representation,  $\Gamma_{\text{Raman}} = 7A_g + 5B_{1g} + 7B_{2g} + 5B_{3g}$ . Not all modes are always observed, as superposition of some modes may occur, as well as a low polarizability of some chemical bonds. Literature data concerning Raman modes for the orthorhombic SrSnO<sub>3</sub> are displayed in Table 3 and the bands observed in the present work are indicated in Fig. 6.

According to [45], bands assigned to strontium carbonate (SrCO<sub>3</sub>) are observed at 148, 180, 214, 236, 244, 258, 511, 690 and 1064 cm<sup>-1</sup>. In the present work, these were observed at 149, 179, 700 and 1070 cm<sup>-1</sup>, while bands at 214, 236, 244 and 258 cm<sup>-1</sup> may be superposed to the bands assigned to SrSnO<sub>3</sub>.

After doping, a symmetry breakage was clearly observed in the Raman spectra. For the sample SrSn<sub>0.9</sub>Ni<sub>0.1</sub>O<sub>3</sub>, no peaks assigned to the perovskite structure were observed, while small intensity bands were observed for SrSn<sub>0.9</sub>Cu<sub>0.1</sub>O<sub>3</sub>. A broad band around 570 cm<sup>-1</sup>, was observed for this sample, which could be related to the formation of oxygen vacancies.

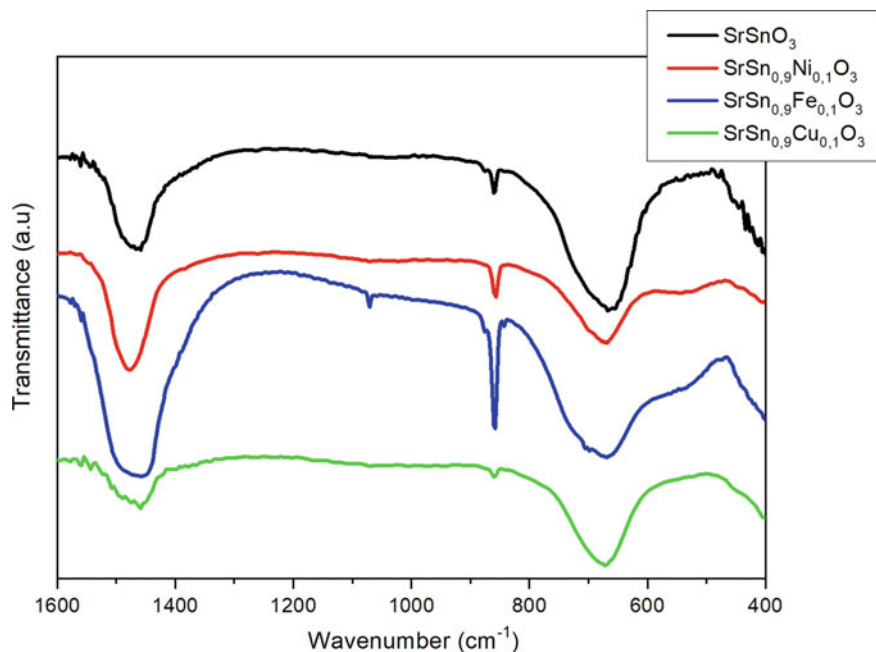


**Fig. 5** Infrared spectra of pure and doped  $\text{SrSnO}_3$  samples, calcined at  $800^\circ\text{C}$  for 4 h

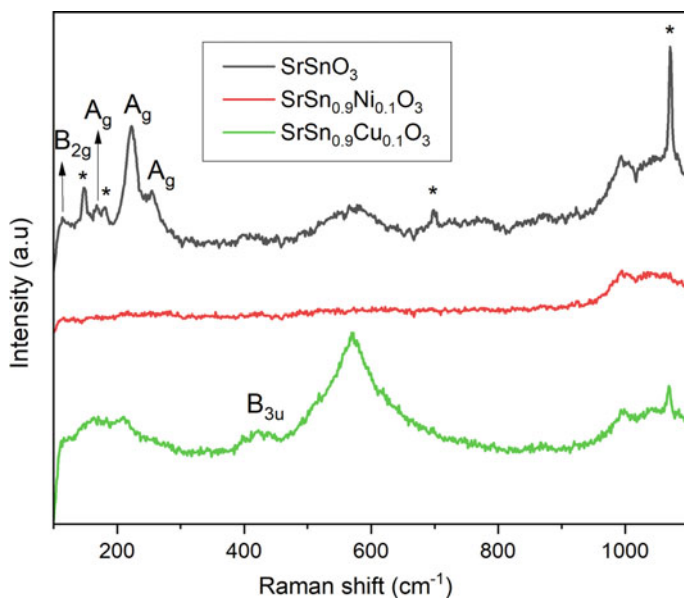


**Fig. 6** Raman spectra of pure and doped  $\text{SrSnO}_3$  samples, calcined at  $800^\circ\text{C}$  for 4 h. Assignments of the peaks was done according to [38, 43]; starred peaks are assigned to  $\text{SrCO}_3$

**Table 3** Raman modes observed for SrSnO<sub>3</sub>, according to literature data [38, 43]

Band (cm <sup>-1</sup> )	Vibrational mode	Assignment
89	A <sub>g</sub>	A-BO <sub>3</sub>
113	B <sub>2g</sub>	Sr-SnO <sub>3</sub>
167	A <sub>g</sub>	Sr-SnO <sub>3</sub>
223	A <sub>g</sub>	Sn-O-Sn
251	A <sub>g</sub>	Sn-O-Sn, O-Sn-O
305	A <sub>u</sub>	SnO <sub>3</sub>
398	–	SnO <sub>3</sub>
410	–	SnO <sub>3</sub>
437	B <sub>3u</sub>	SnO <sub>3</sub>
450	B <sub>3g</sub>	SnO <sub>3</sub>

UV–vis spectra of the pure and doped SrSnO<sub>3</sub> samples, calcined at 800 °C for 4 h are displayed in Fig. 7.

The spectra have similar profiles with a high intensity absorption between 200 and 350 nm, which is assigned to the ligand–metal charge transfer (LMCT), O<sup>2-</sup> → Sn<sup>4+</sup>, as observed by Liu et al. [46] for Sn<sup>4+</sup> in octahedral environment. No other bands were observed for undoped SrSnO<sub>3</sub> above 400 nm, as currently observed for light color materials.

For doped materials, different absorption bands are observed between 300 and 900 nm, depending on the dopant added into the lattice. These bands also depend

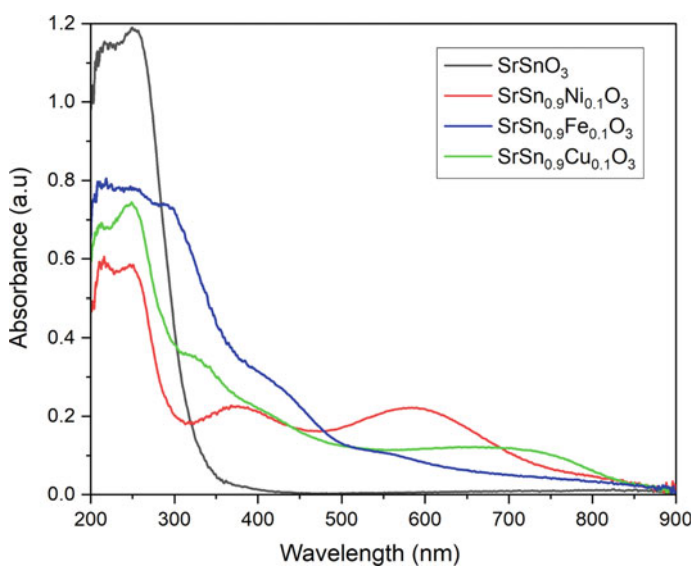


**Fig. 7** UV–vis spectra of the pure and doped SrSnO<sub>3</sub> samples, calcined at 800 °C for 4 h

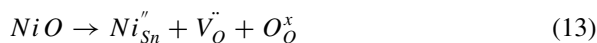
**Table 4** Electronic transitions due to the dopants added into the SrSnO<sub>3</sub> lattice

Material	Band (nm)	Assignment	Range (nm)	Reference
SrSn <sub>0.9</sub> Ni <sub>0.1</sub> O <sub>3</sub>	380	<sup>3</sup> A <sub>2g</sub> ↔ <sup>3</sup> T <sub>1g</sub>	320–450	[48, 49]
	600	<sup>3</sup> A <sub>2g</sub> ↔ <sup>3</sup> T <sub>1g</sub>	490–650	[48, 49]
SrSn <sub>0.9</sub> Fe <sub>0.1</sub> O <sub>3</sub>	315	<sup>6</sup> A <sub>1g</sub> (S) ↔ <sup>4</sup> T <sub>1g</sub> (G), <sup>4</sup> E <sub>g</sub> (G)	303–333	[50, 51]
	430	<sup>6</sup> A <sub>1g</sub> (S) ↔ <sup>4</sup> A <sub>1g</sub> (G), <sup>4</sup> E <sub>g</sub> (G)	416–500	[50, 51]
	560	<sup>6</sup> A <sub>1g</sub> (S) ↔ <sup>4</sup> T <sub>2g</sub> (G)	555–645	[50, 51]
	750	<sup>6</sup> A <sub>1g</sub> (S) ↔ <sup>4</sup> T <sub>1g</sub> (G)	715–800	[50, 51]
SrSn <sub>0.9</sub> Cu <sub>0.1</sub> O <sub>3</sub>	340	Cu <sup>+</sup> : 3d <sup>10</sup> → 3d <sup>9</sup> 4s <sup>1</sup>	320–400	[47]
	440	Cu <sup>+</sup> : 3d <sup>10</sup> → 3d <sup>9</sup> 4s <sup>1</sup>	320–400	[47]
	650, 780	Cu <sup>2+</sup> : <sup>2</sup> B <sub>1g</sub> → <sup>2</sup> E <sub>g</sub> , <sup>2</sup> B <sub>1g</sub> → <sup>2</sup> A <sub>1g</sub> , <sup>2</sup> B <sub>1g</sub> → <sup>2</sup> B <sub>2g</sub>	450–950	[47, 52]

on the oxidation state and coordination of the transition metal and give an indication of redox reactions, during synthesis. Band positions were determined for all of the doped samples and assignments are displayed in Table 4, considering an octahedral environment. For doping with nickel and iron, only bands assigned to Ni<sup>2+</sup> and Fe<sup>3+</sup> were observed, but this result does not exclude the possibility of the presence of other species, since UV–vis spectroscopy does not have high sensitivity. For copper doped SrSnO<sub>3</sub>, Cu<sup>+</sup> and Cu<sup>2+</sup> were observed in a distorted environment, as reported by Rao et al. [47].

SrSnO<sub>3</sub> is a semiconductor with band gap values varying between 3.0 and 4.0 eV [21, 53]. In the present work, a band gap value of 3.7 eV was obtained, similarly to literature data. After doping, a meaningful decrease of this value was observed, as displayed in Table 5, which was assigned to distortions in the perovskite lattice besides the presence of oxygen vacancies and of the dopant itself, which can form intermediate levels inside the band gap.

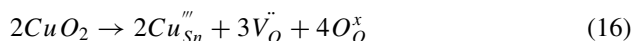
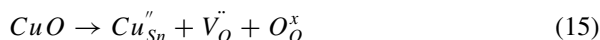
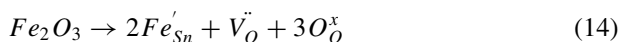
Considering the results obtained, the Kroger Vink notation was used to evaluate the defects formed in the SrSnO<sub>3</sub> lattice due to doping with Ni, Fe or Cu, as displayed in Eqs. (13) to (16). All the charge differences due to doping are probably compensated by the formation of oxygen vacancies, as usually shown in literature.

**Table 5** Band gap energies of the pure and doped SrSnO<sub>3</sub> calcined at 800 °C for 4 h

Sample	Band gap (eV)
SrSnO <sub>3</sub>	3.7
SrSn <sub>0.9</sub> Ni <sub>0.1</sub> O <sub>3</sub>	2.4
SrSn <sub>0.9</sub> Fe <sub>0.1</sub> O <sub>3</sub>	2.4
SrSn <sub>0.90</sub> Cu <sub>0.1</sub> O <sub>3</sub>	1.8

**Table 6** Surface area of the pure and doped SrSnO<sub>3</sub> calcined at 800 °C for 4 h

Sample	Specific surface area (m <sup>2</sup> g <sup>-1</sup> )
SrSnO <sub>3</sub>	18.1
SrSn <sub>0.9</sub> Ni <sub>0.1</sub> O <sub>3</sub>	15.7
SrSn <sub>0.9</sub> Fe <sub>0.1</sub> O <sub>3</sub>	19.3
SrSn <sub>0.90</sub> Cu <sub>0.1</sub> O <sub>3</sub>	21



The specific surface areas of the pure and doped SrSnO<sub>3</sub> calcined at 800 °C for 4 h were determined by the BET equation, as displayed in Table 6. The undoped SrSnO<sub>3</sub> had a slightly larger surface area than the material synthesized by Hodjati et al. [8] by the sol-gel method (16 m<sup>2</sup> g<sup>-1</sup>). After doping, a small decrease of surface area was observed for SrSn<sub>0.9</sub>Ni<sub>0.1</sub>O<sub>3</sub>, while a growing trend was observed for SrSn<sub>0.9</sub>Fe<sub>0.1</sub>O<sub>3</sub> and SrSn<sub>0.90</sub>Cu<sub>0.1</sub>O<sub>3</sub>.

### 3.1.2 Catalytic Tests of NO Reduction by CO

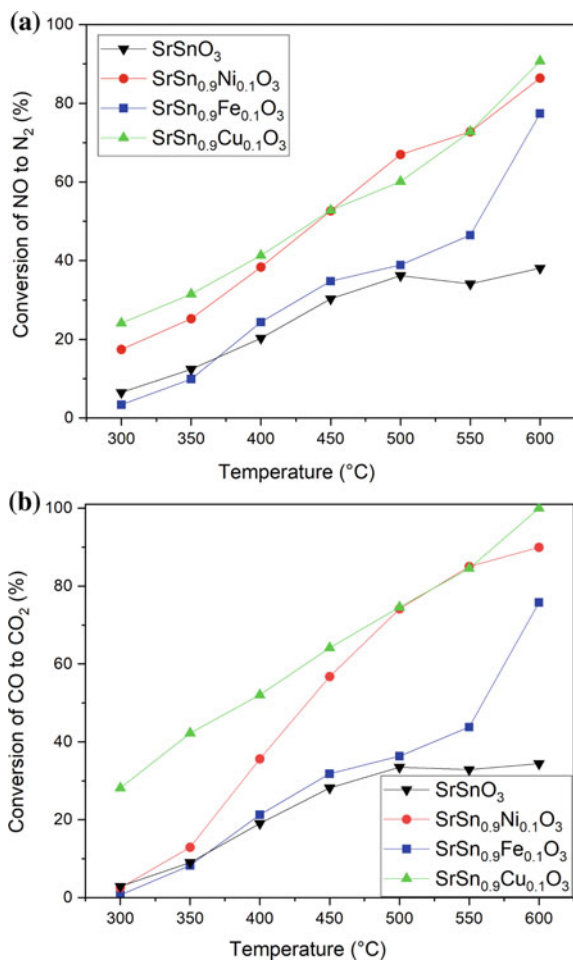
The results of NO conversion into N<sub>2</sub> and CO conversion into CO<sub>2</sub>, using doped and undoped SrSnO<sub>3</sub> as catalysts are displayed in Fig. 8. All samples were catalytic active for the NO reduction and for CO oxidation. The smallest conversion was obtained by the undoped SrSnO<sub>3</sub>, which displayed 34.4% NO conversion into N<sub>2</sub> and 38.1% of conversion of CO into CO<sub>2</sub>, at 600 °C. These values are not much higher than those obtained at 500 °C, with less than 2% of increase. This behavior changed after doping, as a continuous increase of conversion was observed as temperature increased, reaching values above 75% for both reactions at 600 °C, confirming the positive effect of doping on the catalytic activity of SrSnO<sub>3</sub>. This is a very interesting result as Brazil is an important producer of SnO<sub>2</sub> and doped SrSnO<sub>3</sub> can be used as a new catalyst for reaction applications in this temperature range.

Comparing the different dopants, the biggest activity was obtained using SrSn<sub>0.9</sub>Cu<sub>0.1</sub>O<sub>3</sub> as catalyst. For NO reduction, there is no meaningful difference between this catalyst and SrSn<sub>0.9</sub>Ni<sub>0.1</sub>O<sub>3</sub>, as conversions around 90% were obtained with both of them. But for CO oxidation, 100% of CO oxidation was obtained using SrSn<sub>0.9</sub>Cu<sub>0.1</sub>O<sub>3</sub> as catalyst, while 90% of conversion was obtained using SrSn<sub>0.9</sub>Ni<sub>0.1</sub>O<sub>3</sub>.

We believe that the greatest catalytic activity of SrSn<sub>0.9</sub>Cu<sub>0.1</sub>O<sub>3</sub> is related to the redox ability of Cu, making the oxidation and the reduction processes involved in the



**Fig. 8** Conversion of NO to  $N_2$  (a) and CO to  $CO_2$  (b) of the undoped and doped  $SrSnO_3$ , calcined at  $800\text{ }^\circ\text{C}$  for 4 h



catalysis easier. Moreover, Cu-coping leads to the greater amount of oxygen vacancies, as indicated by Eqs. (13) to (16). On the other hand, the sample with smaller amount of oxygen vacancies,  $SrSn_{0.9}Fe_{0.1}O_3$ , had the smallest conversion for all temperatures of the catalytic test. When oxygen vacancies are formed,  $Sn^{4+}$  coordination changes, as fivefold coordinations or even fourfold coordinations may be present in the lattice. Moreover, oxygen vacancies may have three different charges: neutral complexes,  $[SnO_5 \cdot V_O^x]_{complex}$ ; double positive complexes,  $[SnO_5 \cdot V_O^{2+}]_{complex}$ , which capture electrons; and monpositive complexes,  $[SnO_5 \cdot V_O^+]$ , which may capture or donate electrons. The  $[SnO_5 \cdot V_O^{2+}]_{complex}$  or the  $[SnO_5 \cdot V_O^x]_{complex}$  may donate an electron to the adsorbed NO to form  $NO^-$ , which is the active species for NO decomposition [54].

## 3.2 Influence of the Synthesis Procedure on the Catalytic Results of SrSnO<sub>3</sub>: Fe

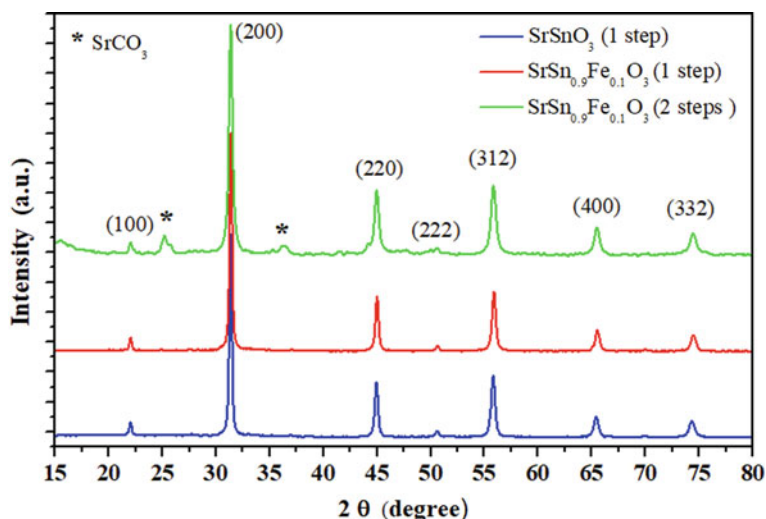
### 3.2.1 Characterization of the Catalysts

Due to the lowest catalytic activity of SrSn<sub>0.9</sub>Fe<sub>0.1</sub>O<sub>3</sub>, this material was chosen to improve the synthesis method in order to evaluate its influence on the catalytic activity. This sample was synthesized using two steps to obtain the polymeric resin, as previously described; and using only one step to obtain the polymeric resin, as described in this section. The XRD patterns of the samples synthesized by the two different routes are presented in Fig. 9.

All samples were identified using the ICDD 01-77-1798 index card, which confirms the formation of the orthorhombic SrSnO<sub>3</sub> with *Pbnm* space group. The samples synthesized using the 1 step route do not have SrCO<sub>3</sub> as secondary phase, probably due to a more homogeneous behaviour of the polymeric resin. The lattice parameters were calculated as displayed in Table 7.

According to the lattice parameters displayed in Table 7, Fe<sup>3+</sup> addition into the SrSnO<sub>3</sub> lattice did not take to meaningful variation of the lattice parameters and very similar unit cell volumes were obtained. Comparing the synthesis route, it was observed that smaller variations were obtained using the 1 step route, probably due to a greater homogeneity of the cations distribution in the polymeric resin, on an atomic scale.

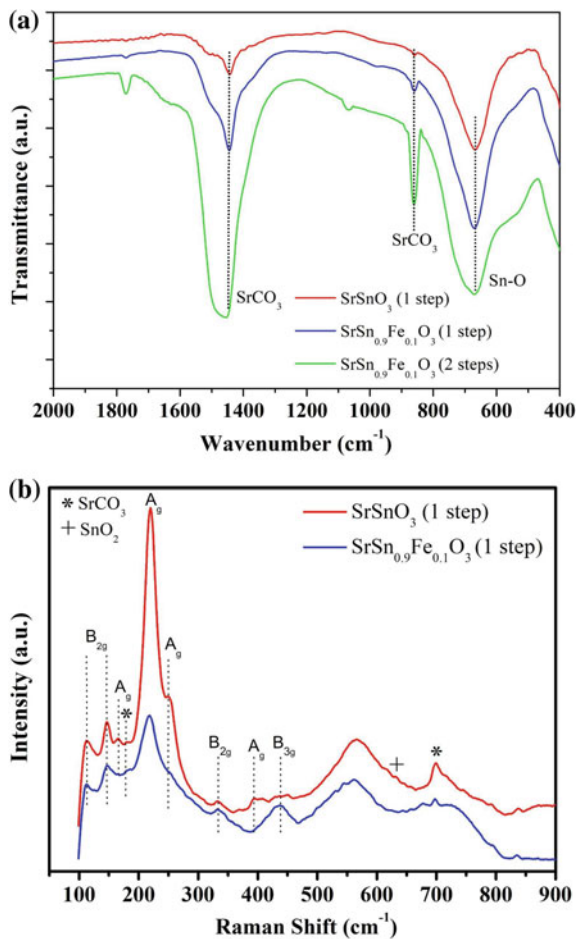
The infrared and Raman spectra of the samples synthesized by the two different routes are displayed in Fig. 10. The infrared spectra were similar to those presented



**Fig. 9** XRD patterns of SrSnO<sub>3</sub> and SrSn<sub>0.9</sub>Fe<sub>0.1</sub>O<sub>3-x</sub>, synthesized by two different routes and calcined at 800 °C

**Table 7** Lattice parameters of  $\text{SrSnO}_3$  and  $\text{SrSn}_{0.9}\text{Fe}_{0.1}\text{O}_{3-x}$ , synthesized by two different routes and calcined at  $800^\circ\text{C}$ 

Synthesis route	Sample	Lattice parameter ( $\text{\AA}$ )			V ( $\text{\AA}^3$ )
		a	b	c	
JCPDS 77-1798	$\text{SrSnO}_3$	5.71	5.71	8.06	263
1 step	$\text{SrSnO}_3$	5.70	5.71	8.02	262
	$\text{SrSn}_{0.9}\text{Fe}_{0.1}\text{O}_3$	5.70	5.69	8.07	261
2 steps	$\text{SrSn}_{0.9}\text{Fe}_{0.1}\text{O}_3$	5.70	5.72	8.16	265

**Fig. 10** Infrared spectra (a) and Raman spectra (b) of  $\text{SrSnO}_3$  and  $\text{SrSn}_{0.9}\text{Fe}_{0.1}\text{O}_{3-x}$ , synthesized by two different routes and calcined at  $800^\circ\text{C}$ 

before and showed the Sn–O stretching band around 670 cm<sup>-1</sup> besides a weak band around 540 cm<sup>-1</sup> and an absorption band below 400 cm<sup>-1</sup>, assigned to the O–Sn–O bending mode. The presence of carbonate was also observed, as indicated by bands at 860, 1070 and 1470 cm<sup>-1</sup>, as described before.

Although similar absorption bands were observed for samples obtained by the two different routes, some meaningful differences may be observed, especially concerning the carbonate bands, which had a higher intensity when the 2 steps route was used during synthesis, in agreement with the XRD patterns. Moreover, the band assigned to undistorted octahedra at 540 cm<sup>-1</sup> had also a higher intensity for the 2 steps route, indicating the change of the Sn<sup>4+</sup> symmetry and confirming the lower homogeneity of the polymeric resin.

The Raman spectra of the samples obtained by the one step route with and without Fe-doping (Fig. 10b) display bands at 113 cm<sup>-1</sup>, 146 cm<sup>-1</sup> and 170 cm<sup>-1</sup> assigned to the Sr–SnO<sub>3</sub> mode; an intense band at 220 cm<sup>-1</sup> (A<sub>g</sub>) assigned to the scissor movement of the Sn–O–Sn group along the *c*-axis; one shoulder at 256 cm<sup>-1</sup> (A<sub>g</sub>) assigned to O–Sn–O and Sn–O–Sn groups along *ab* plane, perpendicular to the *c*-axis [38]. Bands at 332 cm<sup>-1</sup> (B<sub>2g</sub>) and 397 cm<sup>-1</sup> (A<sub>g</sub>) are assigned to Sn–O<sub>3</sub> bonds and to the torsional Sn–O; the symmetric stretching of the Sn–O bond was observed at 565 cm<sup>-1</sup>. Bands assigned to SrCO<sub>3</sub> were observed at 146 cm<sup>-1</sup>, 181 cm<sup>-1</sup> and 700 cm<sup>-1</sup> [55], while one small band assigned to SnO<sub>2</sub> was observed at 646 cm<sup>-1</sup> [21].

Comparing the undoped and doped samples, a small decrease of the intensity of the bands at 113 cm<sup>-1</sup>, 146 cm<sup>-1</sup> and 170 cm<sup>-1</sup> was observed, while the greatest difference was observed in the Sn–O–Sn band at 220 cm<sup>-1</sup>. Besides the decrease of intensity the broadening of this band was also observed as FWHM increased from 15.8 cm<sup>-1</sup> to 23.6 cm<sup>-1</sup>, determined by deconvolution of the peaks. This behavior indicates that the octahedral site was more affected by doping, since Fe<sup>3+</sup> replaces Sn<sup>4+</sup> in the lattice, as expected considering the site preference of Fe<sup>3+</sup>.

The UV–vis spectra of the samples synthesized by the two different routes are displayed in Fig. 11.

For undoped SrSnO<sub>3</sub>, the UV–vis spectrum was very similar to the sample obtained by the 2 steps route, as displayed in Fig. 6, with a high energy absorption between 200 and 350 nm due to the LMCT [46] and almost no absorption above this wavelength. After doping with Fe, absorption bands above 350 nm were observed for both samples, which were deconvolved to identify the electronic transitions.

The Fe<sup>3+</sup> cation has a d<sup>5</sup> electronic configuration in high spin state in octahedral configuration, which means that all electrons are unpaired, as displayed in Fig. 12. Therefore, any electronic transition inside the *d* energy level will only occur if coupled to a spin inversion [51]. Consequently, only spin-forbidden electronic transitions are expected [50]. According to literature [50, 51], these transitions occur from the fundamental state <sup>6</sup>A<sub>1g</sub> (S) to the excited states <sup>4</sup>T<sub>1g</sub> (G), <sup>4</sup>T<sub>2g</sub> (G), <sup>4</sup>A<sub>1g</sub> (G), <sup>4</sup>E<sub>g</sub> (G). All assignments are displayed in Table 8 and confirm that spin-forbidden transitions due to the presence of Fe<sup>3+</sup> are present in the UV–vis spectra.

The band gap values of undoped and Fe-doped SrSnO<sub>3</sub> are displayed in Table 9. The band gap value obtained using the 1-step synthesis route was higher than the

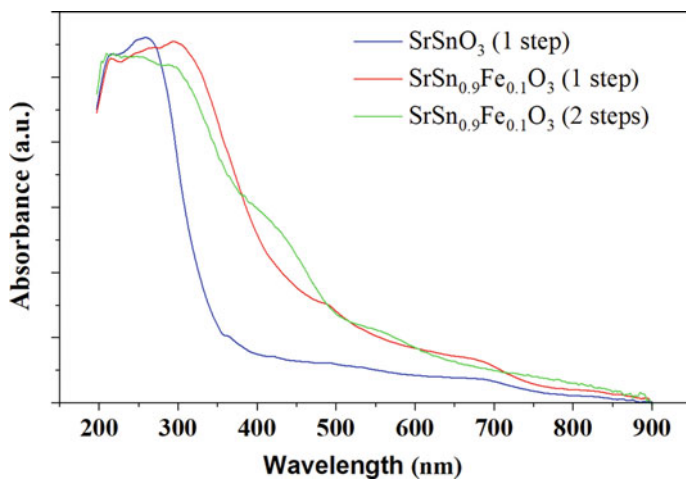


**Fig. 11** UV-vis spectra of  $\text{SrSnO}_3$  and  $\text{SrSn}_{0.9}\text{Fe}_{0.1}\text{O}_{3-x}$ , synthesized by two different routes and calcined at  $800^\circ\text{C}$

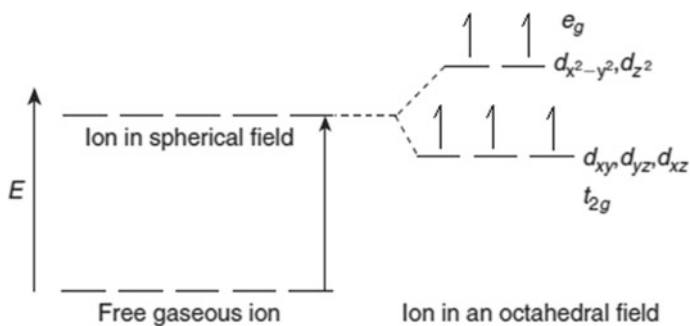


**Fig. 12** Splitting of the octahedral crystal field (high spin) for  $\text{Fe}^{3+}$  [56]

**Table 8** Electronic transitions of  $\text{Fe}^{3+}$  added to the  $\text{SrSnO}_3$  lattice, synthesized by the 1 step and the 2 steps routes

Bands (nm)			Assignment
1 Step	2 Steps	Reference [50, 57, 58]	
318	315	303–333	${}^6\text{A}_{1g}(\text{S}) \leftrightarrow {}^4\text{T}_{1g}(\text{G}), {}^4\text{E}_g(\text{G})$
497	430	416–500	${}^6\text{A}_{1g}(\text{S}) \leftrightarrow {}^4\text{A}_{1g}(\text{G}), {}^4\text{E}_g(\text{G})$
627	560	555–645	${}^6\text{A}_{1g}(\text{S}) \leftrightarrow {}^4\text{T}_{2g}(\text{G})$
–	750	715–800	${}^6\text{A}_{1g}(\text{S}) \leftrightarrow {}^4\text{T}_{1g}(\text{G})$

**Table 9** Band gap values and specific surface area of the undoped and Fe-doped SrSnO<sub>3</sub>, synthesized by the 1 step and the 2 steps routes

	Sample	Band gap energy (eV)	Specific surface area (m <sup>2</sup> g <sup>-1</sup> )
1 step	SrSnO <sub>3</sub>	4.3	11.9
	SrSn <sub>0.9</sub> Fe <sub>0.1</sub> O <sub>3</sub>	2.1	24.4
2 steps	SrSn <sub>0.9</sub> Fe <sub>0.1</sub> O <sub>3</sub>	2.5	19.3

value obtained by the 2-steps route (3.7 eV), displayed in Table 5. This is probably due to a higher short-range order in the final material, due to a more homogeneous polymeric resin, as indicated by the XRD patterns and the IR spectra. After doping, a meaningful decrease of the band gap was observed for both samples, due to the formation of structural defects as displayed in Eq. (14), which form electronic levels inside the band gap. Moreover, d-d electronic transitions assigned to Fe<sup>3+</sup> may also influence the final band gap.

The specific surface area of the undoped and Fe-doped SrSnO<sub>3</sub> are displayed in Table 9. The surface area of the undoped SrSnO<sub>3</sub> obtained by the 1-step route was smaller than the material obtained by the 2-steps route (18.1 m<sup>2</sup> g<sup>-1</sup>), displayed in Table 6, while doping leads to a tendency to increase the surface area, for both routes. The modified Pechini method uses a large amount of organic material, which goes under combustion reaction during heat treatment. As this reaction is highly exothermic, an increase of temperature may occur forming aggregated particles, which decrease the surface area. For this reason, a partial elimination of the organic material is done under oxygen atmosphere, at low temperatures (around 300 °C), but this control is not easy and these surface area variations may occur, with no clear relation to variations of the synthesis routes.

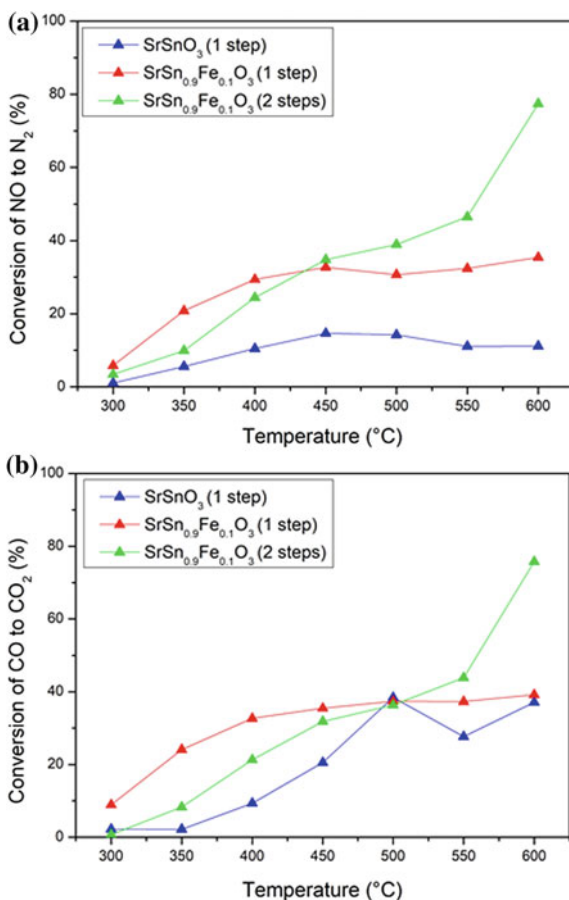
### 3.2.2 Catalytic Tests of NO Reduction by CO

Undoped and Fe-doped SrSnO<sub>3</sub> were applied as catalysts for the NO reduction by CO, as displayed in Fig. 13. Quartz (SiO<sub>2</sub>) was used to dilute the catalyst and its conversion was subtracted from the present results, before plotting.

Conversion of NO to N<sub>2</sub> and CO to CO<sub>2</sub> was favoured by Fe-doping, with a meaningful increase of activity, especially at 600 °C. At this temperature, a 3.2-fold increase was observed for SrSn<sub>0.9</sub>Fe<sub>0.1</sub>O<sub>3</sub> synthesized by the 1-step route, while a 6.9-fold increase was observed for the 2-steps route, for the NO to N<sub>2</sub> conversion. At this same temperature, no meaningful variation was observed comparing SrSnO<sub>3</sub>, SrSn<sub>0.9</sub>Fe<sub>0.1</sub>O<sub>3</sub> synthesized by the 1-step route, while a 1.9-fold increase was observed for SrSn<sub>0.9</sub>Fe<sub>0.1</sub>O<sub>3</sub> synthesized by the 2-step route. This behaviour is due to a higher activity of undoped SrSnO<sub>3</sub> towards CO oxidation.

It is well known that oxygen vacancies are very important for NO reduction due to the formation of active sites, in addition to promoting the dissociation of adsorbed NO species. For instance, Zhang et al. [14] evaluated the catalytic activity of LaCoO<sub>3</sub> in the NO reduction and observed an increase of 20% in the conversion when Co<sup>3+</sup>

**Fig. 13** Conversion of NO to N<sub>2</sub> (a) and CO to CO<sub>2</sub> (b) using the undoped and Fe-doped SrSnO<sub>3</sub>, as catalysts, obtained by two synthesis routes



was partially replaced by Cu<sup>2+</sup>. This improvement was assigned to the formation of oxygen vacancies in the lattice.

A similar behaviour was observed in the present work, when Sn<sup>4+</sup> was replaced by Fe<sup>3+</sup> in the perovskite lattice. Curiously, it seems that the higher short-range disorder induced by the 2-steps synthesis route favoured the catalytic activity. This behaviour may be related to an easier electron transfer of the highly distorted octahedrons favouring the redox reactions involved in the current system.

### 3.3 Influence of the Dopant Amount on the Catalytic Properties of SrSnO<sub>3</sub>: Cu

#### 3.3.1 Characterization of the Catalysts

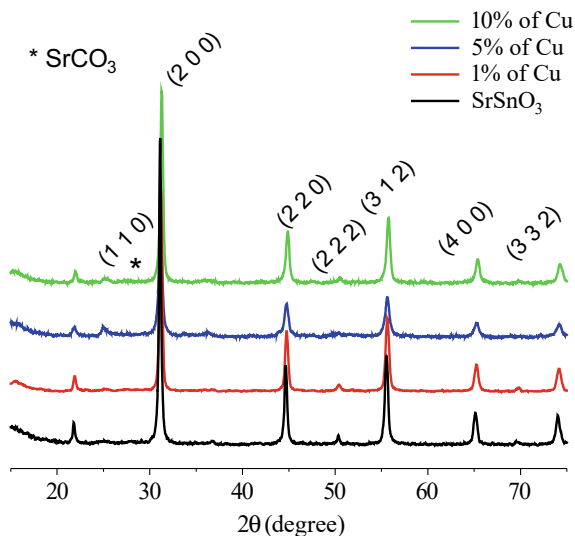
Due to the higher catalytic activity among all dopants, different percentages of Cu were added into the SrSnO<sub>3</sub> lattice, using the 2-steps route, to evaluate its influence in the structural and catalytic properties. The XRD patterns of the Cu-doped materials are displayed in Fig. 14.

Peaks assigned to carbonates were observed at 25.3° and 36.3° with very low intensity except for the sample with 5% of Cu. Peaks assigned to SnO<sub>2</sub> (cassiterite) are usually observed at 26.9°, 33.6°, 51.8° e 64.2°, as reported by Dazhi et al. [59]. Small peaks assigned to SnO<sub>2</sub> were observed for the samples with 5 and 10% of Cu, while peaks assigned to Cu compounds were not identified, which indicated that the dopant was incorporated into the SrSnO<sub>3</sub> lattice.

Pure and Cu-doped SrSnO<sub>3</sub> samples displayed the orthorhombic perovskite with space group *Pbnm* as main phase, according to the ICDD 01-77-1798 index card. Based on this system, lattice parameters of the samples SrSn<sub>1-x</sub>Cu<sub>x</sub>O<sub>3</sub> (*x* = 0, 1, 5 and 10 mol %) were calculated, as displayed in Table 10.

The *a* and *b* lattice parameters were very similar to the theoretical data, calculated from the ICDD 01-77-1798 index card, while *c* parameter was slightly higher and led to a higher unit cell volume. No meaningful change was observed after doping whatever the amount of Cu added into the lattice. Inclination among the octahedra was also calculated and indicated similar absolute values comparing the undoped SrSnO<sub>3</sub>

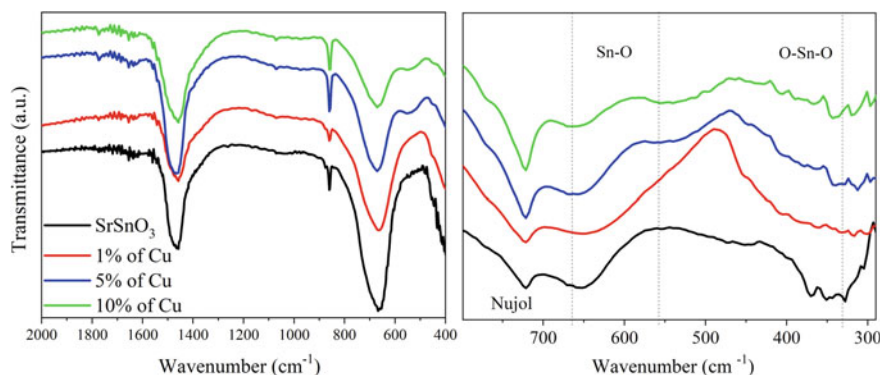
**Fig. 14** XRD patterns of the samples SrSn<sub>1-x</sub>Cu<sub>x</sub>O<sub>3</sub> (*x* = 0, 1, 5 and 10 mol %), calcined at 800 °C for 4 h





**Table 10** Lattice parameters of the samples  $\text{SrSn}_{1-x}\text{Cu}_x\text{O}_3$  ( $x = 0, 1, 5$  and  $10$  mol %), calcined at  $800^\circ\text{C}$  for 4 h

Sample	a (Å)	b (Å)	c (Å)	Volume (Å <sup>3</sup> )	$\Phi$ (°)	$\varphi$ (°)	$\theta$ (°)
Theoretical value	5.71	5.71	8.06	262.64	-3.5	-3.5	0.0
$\text{SrSnO}_3$	5.72	5.72	8.10	265	3.0	3.0	0.0
$\text{SrSn}_{0.99}\text{Cu}_{0.01}\text{O}_3$	5.71	5.71	8.12	265	6.0	2.0	0.0
$\text{SrSn}_{0.95}\text{Cu}_{0.05}\text{O}_3$	5.70	5.71	8.13	265	8.2	5.3	3.4
$\text{SrSn}_{0.9}\text{Cu}_{0.1}\text{O}_3$	5.71	5.71	8.10	264	1.0	4.5	0.0

**Fig. 15** Infrared spectra of the samples  $\text{SrSn}_{1-x}\text{Cu}_x\text{O}_3$  ( $x = 0, 1, 5$  and  $10$  mol %), calcined at  $800^\circ\text{C}$  for 4 h

with the theoretical value, while random variations were observed after doping. The greatest distortion was observed for  $\text{SrSn}_{0.95}\text{Cu}_{0.05}\text{O}_3$ .

Infrared spectra of the samples  $\text{SrSn}_{1-x}\text{Cu}_x\text{O}_3$  ( $x = 0, 1, 5$  and  $10$  mol %), calcined at  $800^\circ\text{C}$  for 4 h are displayed in Fig. 15.

Bands assigned to  $\text{SrCO}_3$  were observed at  $1460\text{ cm}^{-1}$  (strong),  $1070\text{ cm}^{-1}$  (weak) and around  $860\text{ cm}^{-1}$  (medium), confirming the formation of strontium carbonate as secondary phase, in agreement to XRD patterns. According to Mesíková et al. [60], decomposition of  $\text{SrCO}_3$  starts at  $937^\circ\text{C}$  and its total decomposition occurs at  $\sim 1240^\circ\text{C}$ . In the present case, as calcination was done at  $800^\circ\text{C}$ , this phase could not be eliminated. Furthermore, high temperature thermal treatments decrease the specific surface area, which is harmful to catalytic purposes.

All the infrared spectra displayed in Fig. 15 displayed bands at about  $666$  and  $330\text{ cm}^{-1}$ , assigned to the  $\nu_3$  stretching mode (Sn-O) and to the  $\nu_2$  bending mode (O-Sn-O), respectively. The  $\nu_3$  band is characteristic of orthorhombic structures with distortion of the octahedra. These two bands were also present after Cu-doping, with no displacements. On the other hand, a small intensity band was observed at around  $550\text{ cm}^{-1}$ , after doping with 5 and 10 mol% of Cu, which was also assigned to the  $\nu_3$  stretching mode (Sn-O) but currently observed in cubic perovskites, as discussed before. These two bands were observed for measurements in the FAR and

in the MID infrared and indicated that different symmetries of the octahedral sites occur after Cu-doping. These results are in agreement with the XRD tilting angles, which indicated a higher distortion among the octahedra after Cu-doping.

Raman spectra of the samples SrSn<sub>1-x</sub>Cu<sub>x</sub>O<sub>3</sub> ( $x = 0, 1, 5$  and  $10$  mol %), calcined at  $800$  °C for  $4$  h are displayed in Fig. 16.

Bands assigned to SrCO<sub>3</sub> were observed in all of the Raman spectra at  $148, 180$  and  $701$  cm<sup>-1</sup>. The Raman spectrum of the undoped SrSnO<sub>3</sub> displayed 6 active modes assigned to the orthorhombic perovskite, at  $113, 167, 223, 255, 311$  and  $401$  cm<sup>-1</sup> [38]. Bands at  $113$  and  $167$  cm<sup>-1</sup> are assigned to the B<sub>2g</sub> A<sub>g</sub> modes, respectively and correspond to the Sr-SnO<sub>3</sub> lattice mode; the high intensity bands at  $223$  and  $253$  cm<sup>-1</sup> are assigned to the A<sub>g</sub> mode and correspond to the Sn-O-Sn bond; bands at  $311$  and  $401$  cm<sup>-1</sup> are assigned to the B<sub>1g</sub>, A<sub>g</sub> and B<sub>2g</sub> modes, respectively and correspond to the torsional Sn-O<sub>3</sub> mode. A second order broad band was observed around  $570$  cm<sup>-1</sup>, which may be related to the presence of oxygen vacancies.

After Cu-doping, a meaningful decrease in the intensity of the perovskite bands of the Raman spectra was observed, compared to the undoped SrSnO<sub>3</sub>. A broadening of these bands was also observed besides a low definition especially for the sample with  $10\%$  of Cu. On the other hand, the band around  $570$  cm<sup>-1</sup>, assigned to oxygen

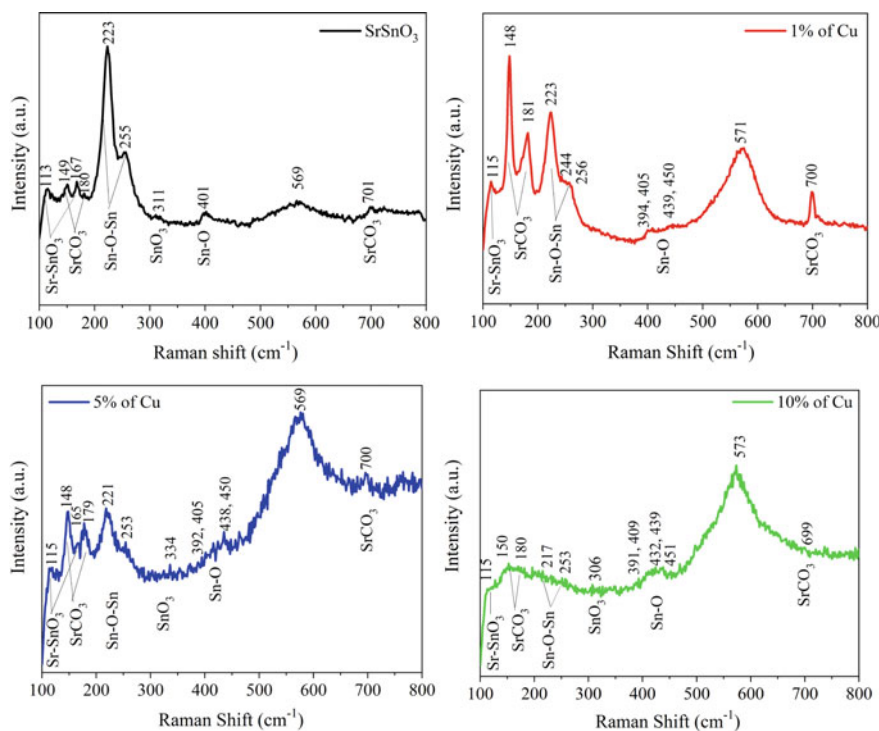
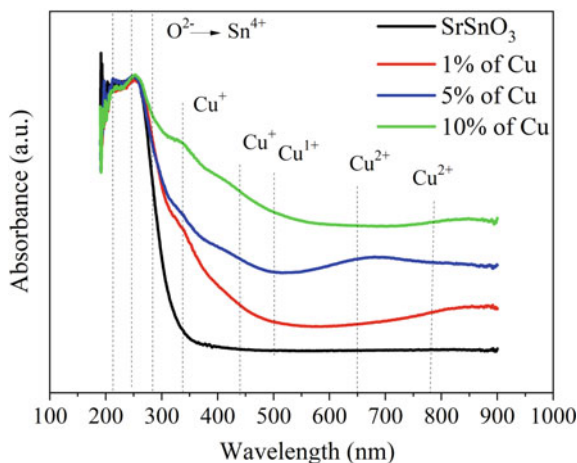


**Fig. 16** Raman spectra of the samples SrSn<sub>1-x</sub>Cu<sub>x</sub>O<sub>3</sub> ( $x = 0, 1, 5$  and  $10$  mol %), calcined at  $800$  °C for  $4$  h

**Fig. 17** UV–vis spectra of the samples  $\text{SrSn}_{1-x}\text{Cu}_x\text{O}_3$  ( $x = 0, 1, 5$  and  $10$  mol %), calcined at  $800^\circ\text{C}$  for  $4$  h



vacancies is clearly observed for all Cu-doped samples. This behavior is a clear indication of the formation of defects after Cu-doping, which leads to a higher short-range disorder, with symmetry loss of the octahedra.

The UV–vis spectra of the samples  $\text{SrSn}_{1-x}\text{Cu}_x\text{O}_3$  ( $x = 0, 1, 5$  and  $10$  mol %), calcined at  $800^\circ\text{C}$  for  $4$  h are displayed in Fig. 17. The electronic transitions were identified considering the deconvolution of the absorption bands.

All of the UV–vis absorption spectra display the same profile, as observed in Fig. 17, with a high intensity absorption band around  $200$  and  $300$  nm due to  $\text{O}^{2-} \rightarrow \text{Sn}^{4+}$  LMCT transitions [46] and low intensity absorption bands between  $300$  and  $900$  nm, assigned to d-d transitions of Cu species. For undoped  $\text{SrSnO}_3$ , absorption is almost zero at this region, as expected.

It is well known that  $\text{Cu}^{2+}$ , with a  $d^9$  electronic configuration, displays a breaking of orbital degeneracy in octahedral crystal-fields, with an  $e_g-t_{2g}$  splitting.  $\text{Cu}^{2+}$  is rarely observed in a regular octahedral symmetry, due to the Jahn Teller effect. When a tetragonal distortion occurs, the  $e_g$  level splits into  ${}^2A_{1g}$  and  ${}^2B_{1g}$  levels, while the  $t_{2g}$  level splits into  ${}^2E_g$  and  ${}^2B_{2g}$  [52, 57]. The  ${}^2B_{1g}$  is the fundamental state and a broad absorption band is observed between  $650$  and  $900$  nm, corresponding to the  ${}^2B_{1g} \rightarrow {}^2B_{2g}$  transition of  $\text{Cu}^{2+}$  ions. This broad band may be assigned to the superposition of the three d-d electronic transitions, corresponding to the  ${}^2B_{1g} \rightarrow {}^2E_g$ ,  ${}^2B_{1g} \rightarrow {}^2A_{1g}$  and  ${}^2B_{1g} \rightarrow {}^2B_{2g}$  transitions [52, 57].

When copper is added into the  $\text{SrSnO}_3$  lattice (Fig. 17), a gradual increase of the absorbance is observed with the formation of absorption bands around  $340$  and  $440$  nm due to the  $3d^{10} \rightarrow 3d^9 4s^1$  electronic transitions of  $\text{Cu}^+$ . As more Cu is added into the lattice, these bands become more intense and one more band is observed around  $500$  nm, also assigned to a forbidden transition of  $\text{Cu}^+$ . Absorption bands were also observed around  $650$  and  $780$  nm, which were assigned to the electronic transitions of  $\text{Cu}^{2+}$  in tetragonally distorted octahedral symmetry.

**Table 11** Band gap values and specific surface area of the samples SrSn<sub>1-x</sub>Cu<sub>x</sub>O<sub>3</sub> (x = 0, 1, 5 and 10 mol %), calcined at 800 °C for 4 h

Sample	Band gap (eV)	Specific surface area (m <sup>2</sup> g <sup>-1</sup> )	D <sub>p</sub> <sup>a</sup> (nm)	D <sub>c</sub> <sup>b</sup> (nm)	D <sub>p</sub> /D <sub>c</sub>
SrSnO <sub>3</sub>	3.8	12	75.2	35.4	2.1
SrSn <sub>0.99</sub> Cu <sub>0.01</sub> O <sub>3</sub>	2.2	16	60.2	30.6	2.0
SrSn <sub>0.95</sub> Cu <sub>0.05</sub> O <sub>3</sub>	2.4	15	60.6	26.6	2.3
SrSn <sub>0.9</sub> Cu <sub>0.1</sub> O <sub>3</sub>	1.8	21	44.6	30.3	1.5

<sup>a</sup>D<sub>p</sub>—particle size<sup>b</sup>D<sub>c</sub>—crystallite size

The band gap energies of SrSn<sub>1-x</sub>Cu<sub>x</sub>O<sub>3</sub> (x = 0, 1, 5 and 10 mol %) are displayed in Table 11. The band gap value of undoped SrSnO<sub>3</sub> was 3.8 eV, in agreement to literature data [20, 61]. After Cu-doping, smaller band gap values were observed, especially when 10 mol% of Cu was added into the SrSnO<sub>3</sub> lattice. This behavior may be related to a greater number of defects with formation of intermediate levels inside the band gap.

The specific surface area of the samples SrSn<sub>1-x</sub>Cu<sub>x</sub>O<sub>3</sub> (x = 0, 1, 5 and 10 mol %) are displayed in Table 11. These data were used to calculate the particle size, while crystallite sizes were calculated from XRD patterns, according to the Scherrer equation. As stated before, the control of the particle size is rather difficult in the modified Pechini method due to the large amount of organic matter, eliminated by an exothermic combustion reaction. This may also influence the crystallite size, which has a random variation.

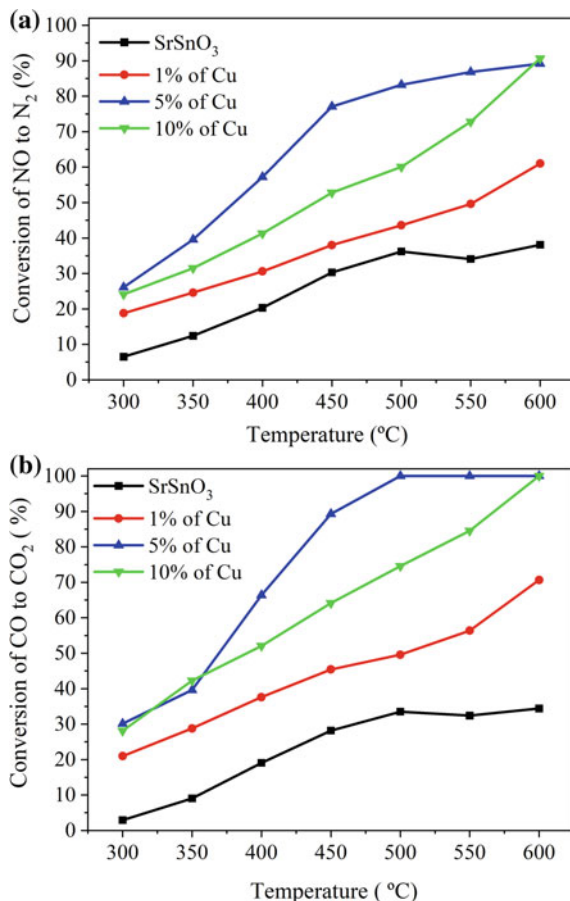
All of the results displayed in this section indicate that copper gets into the SrSnO<sub>3</sub> lattice, with the formation of defects, as oxygen vacancies, which change the symmetry of the octahedra. The formation of the defects is displayed in Eqs. (15) and (16), according to the Kroger Vink notation and considers the presence of reduced Cu<sup>+</sup>, as indicated by the UV–vis spectra. Moreover, the desired perovskite structure was obtained at a relatively low temperature.

### 3.3.2 Catalytic Tests of NO Reduction by CO

Undoped and Cu-doped SrSnO<sub>3</sub> were applied as catalysts for the NO reduction by CO, as displayed in Fig. 18. All samples were active in the NO reduction and in the CO oxidation. For undoped SrSnO<sub>3</sub>, the greatest catalytic conversion of NO into N<sub>2</sub> was 38% and of CO into CO<sub>2</sub> was 34%, both at 600 °C.

Temperature increase had a positive effect in the catalytic activity for all samples, while CO oxidation was slightly greater than NO reduction. In relation to the Cu-doping, its addition into the SrSnO<sub>3</sub> lattice clearly improved the catalytic activity for both reactions, even for the sample with only 1 mol% of Cu. This behaviour may be assigned to the formation of oxygen vacancies as charge compensation species when

**Fig. 18** Conversion of NO to N<sub>2</sub> (a) and CO to CO<sub>2</sub> (b) using SrSn<sub>1-x</sub>Cu<sub>x</sub>O<sub>3</sub> (x = 0, 1, 5 and 10 mol %) as catalysts



Cu replaces Sn<sup>4+</sup> in the perovskite lattice. The formation of Cu<sup>+</sup> species promotes an even greater amount of oxygen vacancies, as displayed in Eqs. (15) and (16).

The highest conversions were obtained when the sample SrSn<sub>0.95</sub>Cu<sub>0.05</sub>O<sub>3</sub> was used as a catalyst, between 350 and 550 °C, while similar conversions were obtained for samples SrSn<sub>0.95</sub>Cu<sub>0.05</sub>O<sub>3</sub> and SrSn<sub>0.9</sub>Cu<sub>0.1</sub>O<sub>3</sub> at low temperatures (300 and 350 °C) and at 600 °C, which was the highest conversion temperature. At this condition, N<sub>2</sub> and CO<sub>2</sub> percentages of conversion were 91% and 100%, respectively. This behaviour may be assigned to a very high deformation of the lattice when 10% of Cu is added to SrSnO<sub>3</sub>, as indicated in the Raman spectra.

According to literature, oxygen vacancies have a very important role in the catalytic activity of perovskites, especially considering the NO reduction. For instance, Zhang et al. [14] also observed an improvement of the catalytic activity after Cu-doping. In their work, the perovskite LaCo<sub>1-x</sub>Cu<sub>x</sub>O<sub>3</sub> was synthesized by solid state reaction and conversion has been improved by 20% after Cu<sup>2+</sup> addition. According to the authors, the high catalytic activity was assigned to the high density

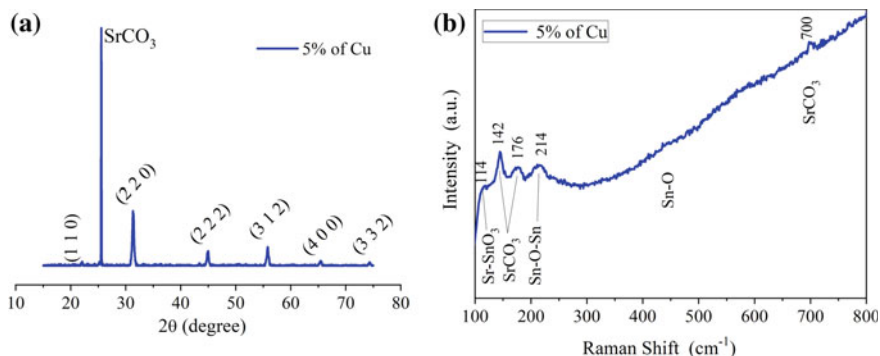


**Fig. 19** XRD pattern (a) and Raman spectrum (b) of the sample SrSn<sub>0.95</sub>Cu<sub>0.05</sub>O<sub>3</sub> after catalytic reaction

of oxygen vacancies, as they form more active site for NO and CO adsorption, as well to the presence of Cu<sup>+</sup> ions and to the Cu<sup>+</sup>/Cu<sup>2+</sup> redox reaction, which favour the NO reduction by CO.

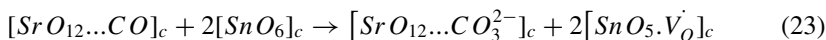
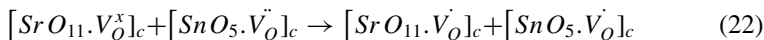
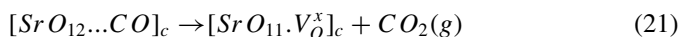
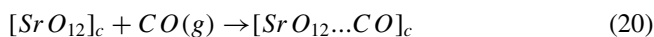
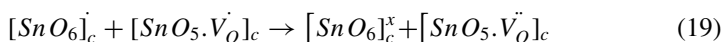
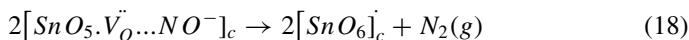
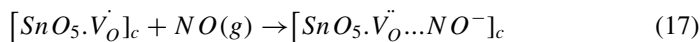
As previously discussed, when NO adsorbs on the perovskite surface, an electron is transferred from the metal (active site), the nitrosyl species (NO<sup>-</sup>) is formed and the bond dissociation is favoured. The oxygen from the NO dissociation is trapped by the oxygen vacancy and the material surface is oxidized. Simultaneously, the metal is reduced by CO, by transfer of the oxygen bonded to the metal to the carbon. As a consequence, the behavior of the catalyst is related to the oxidation state of the metal before reaction (preferably reduced), its affinity with NO molecule and its redox property, which determines the tendency of the metal in the activity site to be oxidized by NO and reduced by CO during the reaction [62].

The SrSn<sub>0.95</sub>Cu<sub>0.05</sub>O<sub>3</sub> sample was characterized by Raman spectroscopy and XRD after the catalytic reaction, as displayed in Fig. 19.

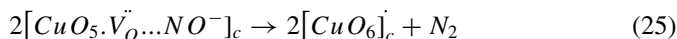
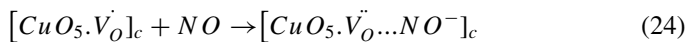
The perovskite structure was maintained after the catalytic reaction, which confirmed the stability of the material. The formation of SrCO<sub>3</sub> was clearly observed in the Raman spectrum and in the XRD pattern and indicated that Sr had an important role in the catalytic mechanism. This element easily forms carbonates, and it may be an important adsorption site for CO. Raman spectrum also suggested an increase of the short-range disorder after the catalytic reaction, as indicated by the smaller intensity and displacement of the Sn-O-Sn peak, from 221 cm<sup>-1</sup> to 214 cm<sup>-1</sup>. The other bands assigned to the perovskite phase were not observed after reaction, and even the high broad band assigned to oxygen vacancies may not be distinguished.

Based on these data, a reaction mechanism was suggested for the NO reduction by CO using Cu-doped SrSnO<sub>3</sub> perovskite as catalyst. In the mechanism, oxygen vacancies cannot be thought as isolated species, as they are associated to the cation in the lattice, changing the symmetry, which is especially important during the catalytic process, as oxygen vacancies may also undergo redox reactions, as discussed before, acting as Lewis acids or bases. During reaction NO probably adsorbs on the

$[SnO_5 \cdot \dot{V}_O]_c$  cluster, which donate an electron to NO, forming the  $NO^-$  species. The N–O bond is weakened, broken and  $N_2$  desorbs from the perovskite surface, while oxygen diffuses to the cluster, where it is trapped, probably by another oxygen vacancy. The CO species adsorbs on the  $[SrO_{11} \cdot \dot{V}_O]_c$  cluster, interacts with the oxygen from the lattice and forms  $CO_2$  or even  $CO_3^{2-}$ , as indicated by the characterization post-catalysis. The symmetry of the octahedra is changed during the reaction, but the overall structure is maintained. Reaction mechanism is displayed in Eqs. (17) to (22).



For Cu-doped samples, a similar mechanism may occur for NO reduction and electron transfers to and from the adsorbed molecules are favoured by the presence of  $Cu^+/Cu^{2+}$  in the perovskite lattice, as displayed in Eqs. (24) and (25).



The reaction mechanism is schematically summarized in Fig. 20, which shows the electron transfer during the catalytic reduction of NO by CO. Cu-doping has a very important role in the process, due to the ability of this cation to easily change its oxidation state, favoring the electron transfer between the surface and the adsorbed species and also inside the perovskite lattice. Oxygen vacancies also have an important role in the process, as they favor the NO adsorption on the perovskite surface. Moreover, they also favor electron transfer, as vacancies may be present as neutral, single positive or double positive species.

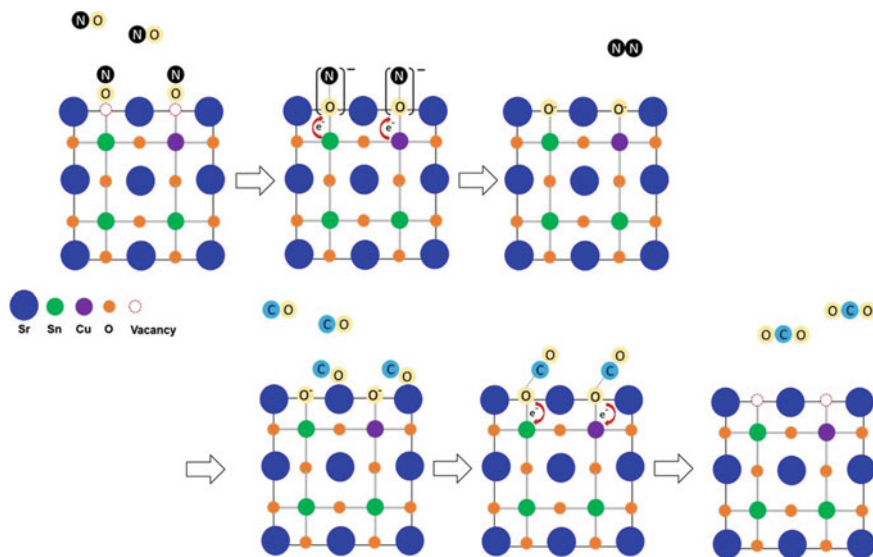


**Fig. 20** Scheme of the reaction mechanism of NO reduction by CO in the presence of Cu-doped SrSnO<sub>3</sub> as catalyst

## 4 Conclusions

SrSnO<sub>3</sub> was synthesized by the modified-Pechini method, without doping and doped with different transition metals (Fe, Ni and Cu), using relatively low temperatures (800 °C), with high crystallinity. Strontium carbonate was observed for almost all synthesis and change in the octahedral symmetry was observed after doping. Specific surface area did not show a meaningful variation, as well as the lattice parameters. The catalytic tests confirmed the importance of doping in the activity of SrSnO<sub>3</sub> towards NO reduction by CO. The highest activity was obtained using 5% of Cu as dopant, which was related to its ability to change its oxidation state, besides the formation of oxygen vacancies due to charge compensation, when it replaces Sn<sup>4+</sup> in the perovskite lattice.

**Acknowledgements** The authors acknowledge Petrobras (Process Number 2014/00327-2), for the financing of this project and CNPq Proc. 151055/2012-2.



## References

1. Song, J., Wang, Z., Cheng, X., Wang, X.: State-of-art review of NO reduction technologies by CO, CH<sub>4</sub> and H<sub>2</sub>. *Process* **9**, 563(1–28) (2021). <https://doi.org/10.3390/pr9030563>
2. Han, L., Cai, S., Gao, M., Hasegawa, J., Wang, P., Zhang, J., Shi, L., Zhang, D.: Selective catalytic reduction of NOx with NH<sub>3</sub> by using novel catalysts: state of the art and future prospects. *Chem. Rev.* **119**(19), 10916–10976 (2019). <https://doi.org/10.1021/acs.chemrev.9b00202>
3. Erickson, L.M., Newark, G., Higgins, M.J., Wang, Z.: Nitrogen oxides and ozone in urban air: a review of 50 plusyears of progress. *Environ. Progr. Sustain. Energy* **39**(e13484), 1–9 (2020). <https://doi.org/10.1002/ep.13484>
4. Lin, Y., Cao, Y., Yao, Q., Chai, O.J.H., Xie, J.: Engineering noble metal nanomaterials for pollutant decomposition. *Ind. Eng. Chem. Res.* **59**, 20561–20581 (2020). <https://doi.org/10.1021/acs.iecr.0c04258>
5. Liu, C., Kubota, H., Amanda, T., Toyao, T., Maeno, Z., Ogura, M., Nakazawa, N., Inagaki, S., Kubota, Y., Shimizu, K.: Selective catalytic reduction of NO over Cu-AFX zeolites: mechanistic insights from in situ/operando spectroscopic and DFT studies. *Catal. Sci. Technol.* **11**, 4459–4470 (2021). <https://doi.org/10.1039/D1CY00282A>
6. Shen, Q., Dong, S., Li, S., Yang, G., Pan, X.: A review on the catalytic decomposition of NO by perovskite-type oxides. *Catalysts* **11**, 622(1–12) (2021). <https://doi.org/10.3390/catal11050622>
7. Zhang, R., Villanueva, A., Alamdari, H., Kaliaguine, S.: Cu and Pd-substituted nanoscale Fe-based perovskites for selective catalytic reduction of NO by propene. *J. Catal.* **237**(2), 368–380 (2006). <https://doi.org/10.1016/j.jcat.2005.11.019>
8. Hodjati, S., Vaezzadeh, K., Petit, C., Pitchon, V., Kiennemann, A.: Absorption/desorption of NOx process on perovskites: performances to remove NOx from a lean exhaust gas. *Appl. Catal. B* **26**(1), 5–16 (2000). [https://doi.org/10.1016/S0926-3373\(99\)00143-5](https://doi.org/10.1016/S0926-3373(99)00143-5)
9. Smith, J.M., Ness, H.C.V., Abbott, M.M.: *Introdução à Termodinâmica da Engenharia Química*. ed. 7, Rio de Janeiro: LTC (2007)
10. Deng, C., Huang, Q., Zhu, X., Hu, Q., Su, W., Qian, J., Dong, L., Li, B., Fan, M., Liang, C.: The influence of Mn-doped CeO<sub>2</sub> on the activity of CuO/CeO<sub>2</sub> in CO oxidation and NO + CO model reaction. *Appl. Surf. Sci.* **389**, 1033–1049 (2016). <https://doi.org/10.1016/j.apsusc.2016.08.035>
11. Tanabe, E.Y., Assaf, E.E.: Óxidos do tipo perovskita para reação de NO com CO. *Quim. Nova* **32**(5), 1129–1133 (2009). <https://doi.org/10.1590/S0100-40422009000500009>
12. Castillo, S., Pineda, M.M., Gómez, R.: Reduction of NO by CO under oxidizing conditions over Pt and Rh supported on Al<sub>2</sub>O<sub>3</sub>-ZrO<sub>2</sub> binary oxides. *Catal. Commun.* **2**(10), 295–300 (2001). [https://doi.org/10.1016/s1566-7367\(01\)00049-8](https://doi.org/10.1016/s1566-7367(01)00049-8)
13. Leontiou, A.A., Ladavos, A.K., Pomonis, P.J.: Catalytic NO reduction with CO on La<sub>1-x</sub>Sr<sub>x</sub>(Fe<sup>3+</sup>/Fe<sup>4+</sup>)O<sub>3±δ</sub> perovskite-type mixed oxides (x = 0.00, 0.15, 0.30, 0.40, 0.60, 0.70, 0.80, and 0.90). *Appl. Catal. A* **241**(1–2), 133–141 (2003). [https://doi.org/10.1016/S0926-860X\(02\)00457-X](https://doi.org/10.1016/S0926-860X(02)00457-X)
14. Zhang, R., Villanueva, A., Alamdari, H., Kaliaguine, S.: Reduction of NO by CO over nanoscale LaCo<sub>1-x</sub>Cu<sub>x</sub>O<sub>3</sub> and LaMn<sub>1-x</sub>Cu<sub>x</sub>O<sub>3</sub> perovskites. *J. Mol. Catal. A: Chem.* **258**(1–2), 22–34 (2006). <https://doi.org/10.1016/j.molcata.2006.05.008>
15. Teraoka, Y., Nii, H., Kagawa, S., Jansson, K., Nygren, M.: Influence of the simultaneous substitution of Cu and Ru in the perovskite-type (La, Sr)M<sub>3</sub>O<sub>3</sub> (M=Al, Mn, Fe, Co) on the catalytic activity for CO oxidation and CO–NO reactions. *Appl. Catal. A* **194–195**, 35–41 (2000). [https://doi.org/10.1016/S0926-860X\(99\)00351-8](https://doi.org/10.1016/S0926-860X(99)00351-8)
16. Hadjarab, B., Bouguelia, A., Trati, M.: Synthesis, physical and photo electrochemical characterization of La-doped SrSnO<sub>3</sub>. *J. Phys. Chem. Solids* **68**(8), 1491–1499 (2007). <https://doi.org/10.1016/j.jpcs.2007.03.013>
17. Azad, A.M., Hon, N.C.: Characterization of BaSnO<sub>3</sub>-based ceramics: Part 1. Synthesis, processing and microstructural development. *J. Alloy. Compd.* **270**(1–2), 95–106 (1998). [https://doi.org/10.1016/S0925-8388\(98\)00370-3](https://doi.org/10.1016/S0925-8388(98)00370-3)

18. Honório, L.M.C., Santos, M.V.B., Filho, E.C.S., Osajima, J.A., Maia, A.S., Santos, I.M.G.: Alkaline earth stannates applied in photocatalysis: prospection and review of literature. *Cerâmica* **64**, 559–569 (2018). <https://doi.org/10.1590/0366-69132018643722480>
19. Zidi, N., Omeiri, S., Hadjarab, B., Bouguelia, A., Akroun, A., Trari, M.: Transport properties and photoelectrochemical characterization of oxygen-deficient ASnO<sub>3</sub> (A= Ca, Sr and Ba). *Physica B* **405**(16), 3355–3359 (2010). <https://doi.org/10.1016/j.physb.2010.05.004>
20. Mizoguchi, H., Eng, H.W., Woodward, P.M.: Probing the electronic structures of ternary perovskite and pyrochlore oxides containing Sn<sup>4++</sup> or Sb<sup>5+</sup>. *Inorg. Chem.* **43**(5), 1667–1680 (2004). <https://doi.org/10.1021/ic034551c>
21. Alves, M.C.F., Souza, S.C., Silva, M.R.S., Paris, E.C., Lima, S.J.G., Gomes, R.M., Longo, E., Souza, A.G., Santos, I.M.G.: Thermal analysis applied in the crystallization study of SrSnO<sub>3</sub>. *J. Therm. Anal. Calorim.* **97**, 179–183 (2009). <https://doi.org/10.1007/s10973-009-0242-x>
22. Bohnemann, J., Libanori, R., Moreira, M.L., Longo, E.: High-efficient microwave synthesis and characterisation of SrSnO<sub>3</sub>. *Chem. Eng. J.* **155**(3), 905–909 (2009). <https://doi.org/10.1016/j.cej.2009.09.004>
23. Peña, M.A., Fierro, J.L.: Chemical structures and performance of perovskite oxides. *Chem. Rev.* **101**(7), 1981–2017 (2001). <https://doi.org/10.1021/cr980129f>
24. Song, S., Xu, L., He, Z., Ying, H., Chen, J., Xiao, X., Yan, B.: Photocatalytic degradation of C.I. Direct Red 23 in aqueous solutions under UV irradiation using SrTiO<sub>3</sub>/CeO<sub>2</sub> composite as the catalyst. *J. Hazard. Mater.* **152**(3), 1301–1308 (2008). <https://doi.org/10.1016/j.jhazmat.2007.08.004>
25. Ferri, D., Forni, L.: Methane combustion on some perovskite-like mixed oxides. *Appl. Catal. B* **16**(2), 119–126 (1998). [https://doi.org/10.1016/S0926-3373\(97\)00065-9](https://doi.org/10.1016/S0926-3373(97)00065-9)
26. Zhu, J., Thomas, A.: Perovskite-type mixed oxides as catalytic material for NO removal. *Appl. Catal. B* **92**(3–4), 225–233 (2009). <https://doi.org/10.1016/j.apcatb.2009.08.008>
27. Chen, L., Si, Z., Wu, X., Weng, D.: DRIFT study of CuO–CeO–TiO<sub>2</sub> mixed oxides for NOx reduction with NH<sub>3</sub> at low temperatures. *ACS Appl. Mater. Interf.* **6**(6), 8134–8145 (2014). <https://doi.org/10.1021/am5004969>
28. Tien-Thao, N., Alamdari, H., Kaliaguine, S.: Characterization and reactivity of nanoscale La(Co, Cu)<sub>0.3</sub> perovskite catalyst precursors for CO hydrogenation. *J. Solid State Chem.* **181**(8), 2006–2019 (2008). <https://doi.org/10.1016/j.jssc.2007.11.016>
29. Zhu, J., Zhao, Z., Xiao, D., Li, J., Yang, X., Wu, Y.: Study of La<sub>2-x</sub>Sr<sub>x</sub>CuO<sub>4</sub> (x = 0.0, 0.5, 1.0) catalysts for NO+CO reaction from the measurements of O<sub>2</sub>-TPD, H<sub>2</sub>-TPR and cyclic voltammetry. *J. Mol. Catal. A: Chem.* **238**(1–2), 35–40 (2005). <https://doi.org/10.1016/j.molcata.2005.03.036>
30. Giannakas, A.E., Leontiou, A.A., Ladavos, A.K., Pomonis, P.J.: Characterization and catalytic investigation of NO + CO reaction on perovskites of the general formula La<sub>x</sub>M<sub>1-x</sub>FeO<sub>3</sub> (M = Sr and/or Ce) prepared via a reverse micelles microemulsion route. *Appl. Catal. A* **309**(2), 254–262 (2006). <https://doi.org/10.1016/j.apcata.2006.05.016>
31. Zhang, R., Alamdari, H., Kaliaguine, S.: Fe-based perovskites substituted by copper and palladium for NO+ CO reaction. *J. Catal.* **242**(2), 241–253 (2006). <https://doi.org/10.1016/j.jcat.2006.05.033>
32. He, H., Liu, M., Dai, H., Qiu, W., Zi, X.: An investigation of NO/CO reaction over perovskite-type oxide La<sub>0.8</sub>Ce<sub>0.2</sub>B<sub>0.4</sub>Mn<sub>0.6</sub>O<sub>3</sub> (B = Cu or Ag) catalysts synthesized by reverse microemulsion. *Catal. Today* **126**(3–4), 290–295 (2007). <https://doi.org/10.1016/j.cattod.2007.06.004>
33. Dai, H., He, H., Li, P., Gao, L., Au, C.H.: The relationship of structural defect–redox property–catalytic performance of perovskites and their related compounds for CO and NO<sub>x</sub> removal. *Catal. Today* **90**(3–4), 231–244 (2004). <https://doi.org/10.1016/j.cattod.2004.04.031>
34. Wu, Y., Li, L., Chu, B., Yi, Y., Qin, Z., Fan, M., Qin, Q., He, H., Zhang, L., Dong, L., Li, B., Dong, L., Li, B., Dong, L.: Catalytic reduction of NO by CO over B-site partially substituted LaM<sub>0.25</sub>Co<sub>0.75</sub>O<sub>3</sub> (M = Cu, Mn, Fe) perovskite oxide catalysts: the correlation between physicochemical properties and catalytic performance. *Appl. Catal. A* **568**, 43–53 (2018). <https://doi.org/10.1016/j.apcata.2018.09.022>

35. Wood, D.L., Tauc, J.: Weak absorption tails in amorphous semiconductors. *Phys. Rev. B* **5**(8), 3144–3151 (1972). <https://doi.org/10.1103/PhysRevB>
36. Nakamoto, K.: *Infrared and Raman Spectra of Inorganic and Coordination Compounds*. John Wiley & Sons, New York, Inc (1986)
37. Nyquist, R.A., Kagel, R.O.: *Infrared Spectra Inorganic Compounds*. Academic Press, New York, Inc (1971)
38. Moreira, E., Henriques, J.M., Azevedo, D.L., Caetano, E.W.S., Freire, V.N., Albuquerque, E.L.: Structural, optoelectronic, infrared and Raman spectra of orthorhombic SrSnO<sub>3</sub> from DFT calculations. *J. Solid State Chem.* **184**(4), 921–928 (2011). <https://doi.org/10.1016/j.jssc.2011.02.009>
39. Last, J.T.: Infrared-absorption studies on barium titanate and related materials. *Phys. Rev.* **105**(6), 1740–1750 (1956). <https://doi.org/10.1103/PhysRev.105.1740>
40. Pfaff, G., Hildenbrand, V.D., Fuess, H.: Spectroscopic study of amorphous precursors for alkaline-earth titanates and stannates. *J. Mater. Sci. Lett.* **17**(23), 1983–1985 (1998). <https://doi.org/10.1023/A:1006652405086>
41. Azad, A.-M., Shyan, L.L.W., Yen, P.T.: Synthesis, processing and microstructural characterization of CaSnO<sub>3</sub> and SrSnO<sub>3</sub> ceramics. *J. Alloy. Compd.* **282**(1–2), 109–124 (1999). [https://doi.org/10.1016/S0925-8388\(98\)00808-1](https://doi.org/10.1016/S0925-8388(98)00808-1)
42. Chiang, Y.M., Bimie III, D.P., Kingery, W.D.: *Physical Ceramics*. John Wiley & Sons, New York (1997)
43. Tarrida, M., Larguem, H., Madon, M.: Structural investigations of (Ca, Sr)ZrO<sub>3</sub> and Ca(Sn, Zr)O<sub>3</sub> perovskite compounds. *Phys. Chem. Miner.* **36**, 403–413 (2009). <https://doi.org/10.1007/s00269-008-0286-7>
44. Doroftei, C., Popa, P.D., Iacomi, F.: Study of the influence of nickel ions substitutes in barium stannates used as humidity resistive sensors. *Sens. Actuators, A* **173**(1), 24–29 (2012). <https://doi.org/10.1016/j.sna.2011.10.007>
45. Kaabar, W., Botta, S., Devonshire, R.: Raman spectroscopic study of mixed carbonate materials. *Spectrochim. Acta Part A Mol. Biomol. Spectrosc.* **78**(1), 136–141 (2011). <https://doi.org/10.1016/j.saa.2010.09.011>
46. Liu, Z.C., Chen, H.R., Huang, W.M., Gu, J.L., Bu, W.B., Hua, Z.L., Shi, J.L.: Synthesis of a new SnO<sub>2</sub>/mesoporous silica composite with room-temperature photoluminescence. *Microporous Mesoporous Mater.* **89**, 270–275 (2006). <https://doi.org/10.1016/j.micromeso.2005.10.037>
47. Rao, L.S., Reddy, M.S., Rao, D.K., Veeraiyah, N.: Influence of redox behavior of copper ions on dielectric and spectroscopic properties of Li<sub>2</sub>O–MoO<sub>3</sub>–B<sub>2</sub>O<sub>3</sub>:CuO glass system. *Solid State Sci.* **11**, 578–587 (2009). <https://doi.org/10.1016/j.solidstatesciences.2008.06.022>
48. Sorlí, S.M.A., Tena, J.A., Badenes, J.C., Calbo, M., Llusar, G.M., Monrós, G.: Structure and color of Ni<sub>x</sub>A<sub>1–3x</sub>B<sub>2x</sub>O<sub>2</sub> (A=Ti, Sn; B=Sb, Nb) solid solutions. *J. Eur. Ceram. Soc.* **24**(8), 2425–2432 (2004). <https://doi.org/10.1016/j.jeurceramsoc.2003.07.012>
49. Dondi, M., Cruciani, G., Guarini, G., Matteucci, F., Raimondo, M.: The role of counterions (Mo, Nb, Sb, W) in Cr-, Mn-, Ni- and V-doped rutile ceramic pigments: Part 2. Colour and technological properties. *Ceram. Int.* **32**(4), 393–405 (2006). <https://doi.org/10.1016/j.ceramint.2005.03.015>
50. Reddy, K.N., Reddy, G.S., Reddy, S.L., Rao, P.S.: Optical absorption and EPR spectral studies of vauquelinite. *Cryst. Res. Technol.* **41**(8), 818–821 (2006). <https://doi.org/10.1080/10420150008211834>
51. Lee, J.D.: *Concise Inorganic Chemistry*, 5th edn. Chapman & Hall, London, Inc (1996)
52. Rajyasree, Ch., Rao, D.K.: Spectroscopic investigations on alkali earth bismuth borate glasses doped with CuO. *J. Non-Cryst. Solids* **357**(3), 836–841 (2011). <https://doi.org/10.1016/j.jnoncrysol.2010.11.008>
53. Liu, Q., Dai, J., Zhang, X., Zhu, G., Liu, Z., Ding, G.: Perovskite-type transparent and conductive oxide films: Sb- and Nd-doped SrSnO<sub>3</sub>. *Thin Solid Films* **519**(18), 6059–6063 (2011). <https://doi.org/10.1016/j.tsf.2011.03.038>
54. Fritz, A., Pitchon, V.: The current state of research on automotive lean NO<sub>x</sub> catalysis. *Appl. Catal. B* **113**(1), 1–5 (1997). [https://doi.org/10.1016/S0926-3373\(96\)00102-6](https://doi.org/10.1016/S0926-3373(96)00102-6)

55. Lin, C.-H., Liu, L.-G.: Post-aragonite phase transitions in strontianite and cerussite—A high-pressure raman spectroscopy study. *J. Phys. Chem. Solids* **58**(6), 977–987 (1997). [https://doi.org/10.1016/S0022-3697\(96\)00201-6](https://doi.org/10.1016/S0022-3697(96)00201-6)
56. House, J.E.: *Inorganic Chemistry*. Academic Press, Canada (2008)
57. Rao, J.L., Murali, A., Rao, E.D.: Electron paramagnetic resonance and optical absorption spectra of Fe(III) ions in alkali zinc boro sulphate glasses. *J. Non-Cryst. Solids* **202**(3), 215–221 (1996). [https://doi.org/10.1016/0022-3093\(96\)00199-8](https://doi.org/10.1016/0022-3093(96)00199-8)
58. Taran, M.N., Langer, K.: Electronic absorption spectra of Fe<sup>3+</sup> in andradite and epidote at different temperatures and pressures. *Eur. J. Miner.* **12**(1), 7–15 (2000). <https://doi.org/10.1127/0935-1221/2000/0012-0007>
59. Dazhi, W., Shulin, W., Jun, C., Suyuan, Z., Fangqing, L.: Microstructure of SnO<sub>2</sub>. *Phys. Rev. B* **49**(20), 14282–14285 (1994). <https://doi.org/10.1103/PhysRevB.49.14282>
60. Mesíková, Z., Sulcová, P., Trojan, M.: Synthesis and description of SrSn<sub>0.6</sub>In<sub>0.4</sub>O<sub>3</sub> perovskite pigments. *J. Therm. Anal. Calorim.* **91**(1), 163–166 (2008). <https://doi.org/10.1007/s10973-007-8312-4>
61. Zidi, N., Omeiri, S., Hadjarab, B., Bouguelia, A., Akroun, A., Trari, M.: Transport properties and photoelectrochemical characterization of oxygen-deficient ASnO<sub>3- $\delta$</sub>  (A= Ca, Sr and Ba). *Physica B* **405**(16), 3355–3359 (2010). <https://doi.org/10.1016/j.physb.2010.05.004>
62. Lima, R.K.C., Batista, M.S., Wallau, M., Sanches, E.A., Mascarenhas, Y.P., Urquieta-González, E.A.: High specific surface area LaFeCo perovskites—Synthesis by nanocasting and catalytic behavior in the reduction of NO with CO. *Appl. Catal. B* **90**(3–4), 441–450 (2009). <https://doi.org/10.1016/j.apcatb.2009.04.004>

# Advances in the Synthesis and Applications of Self-Activated Fluorescent Nano- and Micro-Hydroxyapatite



**Thales Rafael Machado, Jussara Soares da Silva, Eloisa Cordoncillo, Héctor Beltrán-Mir, Juan Andrés, Valtencir Zucolotto, and Elson Longo**

**Abstract** Hydroxyapatite (HA) is the major mineral phase of calcified tissues (i.e., bones and teeth), and the synthetic version of HA has several attractive properties for in vivo applications, ranging from hard tissue repair to drug/gene/protein delivery. In the last decades, HA has been used in combination with lanthanide ions, molecular fluorophores, or inorganic luminescent materials, for the potential use in fluorescence imaging, biosensing and theranostics as well as for the fabrication of optical devices. Recent studies have pointed to the susceptibility of HA to surface and structural defects, which end up impacting its electronic structure and improving its intrinsic fluorescent properties. This chapter highlights the main advances in the synthesis of activator- and dye-free fluorescent nano- and microparticles of HA, in addition to their application in the distinct technological fields and nanomedicine. The available information based on experimental and theoretical approaches about the role of the distinct defects that govern this intrinsic property is also summarized. Lastly, this chapter provides new insights into the design, fabrication and challenges for the further development of HA-based luminescent materials.

---

T. R. Machado (✉) · V. Zucolotto  
GNANO – Nanomedicine and Nanotoxicology Group, Physics Institute of São Carlos, University of São Paulo, São Carlos, SP 89885-000, Brazil  
e-mail: [tmachado.quimica@gmail.com](mailto:tmachado.quimica@gmail.com)

T. R. Machado · J. S. da Silva · E. Longo  
CDMF – Center for the Development of Functional Materials, Federal University of São Carlos, São Carlos, SP 13565-905, Brazil

E. Cordoncillo · H. Beltrán-Mir  
QIO – Inorganic and Organic Chemistry Department, Jaume I University, 12071 Castellón de la Plana, Spain

J. Andrés  
QFA – Physical and Analytical Chemistry Department, Jaume I University, 12071 Castellón de la Plana, Spain

## 1 Introduction and General Concepts

Calcium orthophosphates (CaPs) are a class of materials abundant in nature that can be found both in geological deposits and as the main inorganic constituents of biological hard tissues [1]. The most important and studied CaP is hydroxyapatite (HA,  $\text{Ca}_{10}(\text{PO}_4)_6\text{OH}_2$ ), known as the primary crystalline phase of bones, teeth and tendons, in a non-stoichiometric version containing various foreign ions and ionic vacancies within the crystal lattice often labeled as bioapatite [2–4]. The synthetic version of HA is strongly timely to biomedical applications because of its compositional flexibility, biocompatibility, bioactivity, non-toxicity, and tailorable biodegradability, granting the synthetic HA the superior ability to interact and bond with surrounding tissues [5–7]. Given these advantages, it is often suggested that HA be applied in reconstructive surgery [8] and bone repair [9–12].

HA at nanoscale has been attracting the attention of researchers in the nanomedicine field due to its potential use in intracellular bioimaging [13, 14] and drug/gene delivery systems for various therapeutic applications, including cancer therapy [15–18]. Besides, HA nanoparticles (NPs) can be applied for theranostic purposes since they are capable of performing diagnosis and therapy functions simultaneously [19]. To these ends, HA particles are combined with distinct contrast agents to improve its imaging capability, for example, for fluorescence imaging procedures. In this process, the fluorescence properties of HA is optimized either by doping the particles with lanthanide ions [20–28] or encapsulating organic fluorophores [29–32], or by combining HA with other luminescent materials in the form of composites [33–36]. On the other hand, the induction of self-activated fluorescence in HA is an exciting research area that avoids the necessity to conduct the aforementioned strategies to obtain satisfactory fluorescent properties and that could create a new range of applications for HA in nanomedicine and other technological fields [37].

The origins of self-activated fluorescence properties in materials are based on the formation of localized energy levels within the band gap region induced by defects, including ionic and interstitial vacancies, impurities, length and angle distortions in atomic bonds, dislocations and stresses in the crystalline lattice, boundaries, cracks, pores, and so on [38, 39]. Pure and stoichiometric HA has a band gap energy ( $E_g$ ) greater than 5.3 eV, making photoexcitation of electrons from the valence band (VB) to the conduction band (CB) more difficult, with subsequent radiative recombination of electron–hole pairs ( $e^-h^+$ ) [40]. However, during the synthesis step it is possible to control the nature and the density of defects, resulting in fluorescent HA (f-HA) particles due to the appearance of new energy levels between the VB and the CB [41–43]. Thereby, this chapter brings an overview of the recent investigations on the synthesis and applications of self-activated fluorescent nano- and micro-HA.

## 2 Crystallographic Structure of HA

The stoichiometric HA described under the general formula  $\text{Ca}_{10}(\text{PO}_4)_6(\text{OH})_2$  primarily exhibits monoclinic symmetry with space group  $P2_1/b$ , and after a reversible phase transition from monoclinic to hexagonal polymorph at about 207 °C, it has space group  $P6_3/m$  and lattice constants  $a$  and  $c$  equal to 0.942 and 0.688 nm, respectively [44, 45]. This fact, however, does not imply that natural and biological HA particles, as well as the often-studied synthetic version of HA, adopt a monoclinic pattern. In these cases, the inclusion of foreign ions and the presence of ionic vacancies within the HA crystalline structure typically occur, stabilizing the more disordered and less symmetric hexagonal phase under atmospheric conditions [46].

The crystal structure of hexagonal HA is comprised of a compact assembly of tightly bonded  $[\text{PO}_4]$  tetrahedral clusters with ten Ca species distributed along two nonequivalent crystallographic sites [47]. At the Ca(I) site, nine oxygen atoms belonging to  $[\text{PO}_4]$  are coordinated with the Ca atom, originating  $[\text{CaO}_9]$  clusters. The Ca atoms at this site exhibit a columnar arrangement parallel to the  $c$ -axis. On the other hand, the Ca atoms located at the Ca(II) site are coordinated with six oxygen atoms from  $[\text{PO}_4]$  clusters and one oxygen from the OH group, forming  $[\text{CaO}_7\text{H}]$  clusters (Fig. 1a, b). At the Ca(II) site, the Ca atoms assemble as equilateral triangles lying on opposite sides, where the planes of the triangles are perpendicular to the sixfold screw axis, forming tunnels, i.e., hexagonal channels which are occupied by OH groups along the  $c$ -axis (Fig. 1c,d). The O atoms at the OH site are slightly above or below the Ca(II) triangles. A partial occupancy of 50% at the OH site takes place, and the OH groups are arranged in a disordered fashion, in which the head-to-tail (OH OH OH...) and tail-to-head (HO HO HO...) arrangements alternate along the channel [46].

The peculiar structure of HA supports tremendous lattice distortions, which in turn allow the occurrence of ionic substitutions within several crystallographic sites by species with various sizes and valence states. These substitutions can originate the Ca-deficient ( $\text{Ca/P} < 1.67$ ) or Ca-rich ( $\text{Ca/P} > 1.67$ ) non-stoichiometric versions of HA rather than the stoichiometric ones ( $\text{Ca/P} = 1.67$ ) [50]. The bioapatite present in bone and tooth mineral illustrates this structural flexibility—it is defective and non-stoichiometric due to the high availability of elements in the body that allow the incorporation of various ionic species within the crystalline lattice, including  $\text{F}^-$ ,  $\text{Cl}^-$ ,  $\text{Na}^+$ ,  $\text{K}^+$ ,  $\text{Fe}^{2+}$ ,  $\text{Zn}^{2+}$ ,  $\text{Sr}^{2+}$ ,  $\text{Mg}^{2+}$ ,  $\text{CO}_3^{2-}$ , and citrate ions [51]. Therefore, in order to avoid structure charge imbalance, coupled ionic substitutions and/or vacancy generation (e.g.,  $\text{Ca}^{2+}$  and  $\text{OH}^-$  vacancies) typically occur when ions with different charges from those observed for the groups that comprise the HA structure are incorporated.

One of the most relevant substituting species in HA is  $\text{CO}_3^{2-}$ . The carbonation of HA is energetically favorable, with a formation energy of  $-518.7 \text{ kJ}\cdot\text{mol}^{-1}$ , causing the spontaneous incorporation of  $\text{CO}_3^{2-}$  groups into the HA lattice [52]. In bioapatite, the  $\text{CO}_3^{2-}$  content varies from 2 to 8 wt% depending on the age. In most cases, the synthesis of HA leads to the carbonated version of HA. When  $\text{CO}_3^{2-}$  groups are accommodated at the  $\text{OH}^-$  site (A-type substitution), a  $\text{V}_{\text{OH}}$  vacancy is generated.

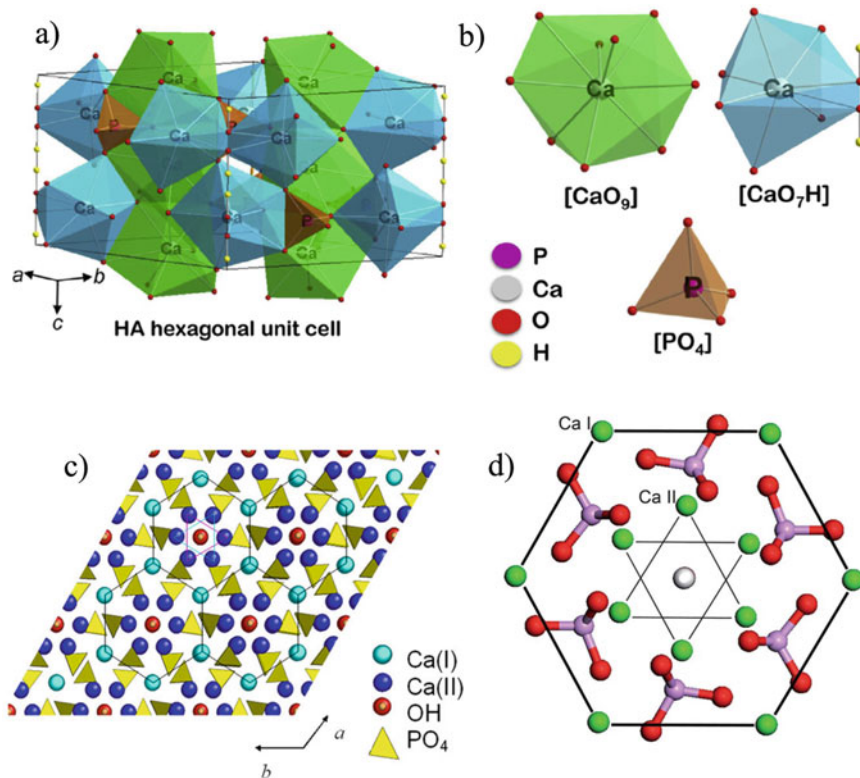


**Fig. 1** Representations of **a** HA hexagonal unit cell, and **b** [PO<sub>4</sub>], [CaO<sub>9</sub>], and [CaO<sub>7</sub>H] polyhedra showing the possible upward and downward orientations for OH<sup>-</sup> groups. Reprinted with permission from Ref. [37]. **c** HA structure along the *c*-axis, where black lines represent the hexagonal networks formed by Ca(I) sites, while cyan and magenta triangles connect staggered Ca(II) sites with different height in relation to the *c*-axis. Reprinted with permission from Ref. [48]. **d** Illustration of one single hexagonal building unit of the HA structure projected in the [001] direction. Reprinted with permission from Ref. [49]

Meanwhile, the substitution of the PO<sub>4</sub><sup>3-</sup> group by CO<sub>3</sub><sup>2-</sup> (B-type substitution) is compensated by the formation of V<sub>Ca</sub> and V<sub>OH</sub> vacancies [53]. A concomitant substitution of the OH<sup>-</sup> and PO<sub>4</sub><sup>3-</sup> groups by CO<sub>3</sub><sup>2-</sup> can also occur (the so-called AB-type substitution). Furthermore, the incorporation of CO<sub>3</sub><sup>2-</sup> into the HA lattice can be charge-compensated by the introduction of foreign ions, such as Na<sup>+</sup>, K<sup>+</sup>, NH<sub>4</sub><sup>+</sup> and H<sub>3</sub>O<sup>+</sup>, depending on the precipitation conditions [54].

Single or multiple substitutions and vacancies, including those associated with CO<sub>3</sub><sup>2-</sup>, significantly affect the lattice parameters, the degree of structural order at long and short ranges, the crystallization mechanisms, and the exposed surfaces, which in turn change, for instance, the biodegradability, bioactivity, biocompatibility and mechanical resistance of the material, allowing researchers to tailor the behavior of HA in biological environments according to the desirable biomedical application



[55]. These structural and compositional changes conducted during the synthesis can also modify the electronic structure and charge distribution of HA nano- and microparticles, leading to self-activated f-HA with improved emission properties.

### 3 Synthesis of Luminescent HA

Wet chemical methods are the most promising approaches for the fabrication of f-HA nano- and microparticles with controlled crystallinity, morphology, and size, as well as for the introduction of several types of defects. The manipulation of the density and chemical nature of the defects is crucial to obtaining f-HA, thus requiring an appropriate choice of the synthesis methodology and experimental parameters. There is a large variety of reported techniques based on chemical precipitation, synthesis from natural bio-resources, hydrothermal-assisted precipitation, and sol-gel method, which will be addressed below.

#### 3.1 Chemical Precipitation

Among the various methods to obtain f-HA, chemical precipitation in aqueous solution is the easiest explored one. This synthesis route is based on the fact that HA is a sparingly soluble salt in neutral and alkaline aqueous solutions and that all intermediates will eventually be converted into HA phase [18]. Calcium hydroxide, calcium nitrate and calcium chloride are generally employed as precursor reagents for  $\text{Ca}^{2+}$ , whereas orthophosphoric acid, diammonium hydrogen phosphate and disodium hydrogen phosphate are commonly used as precursor reagents for  $\text{PO}_4^{3-}$  [56]. Typically, the controlled addition of one reagent to another is made under stirring, and the resulting milky suspension is aged for several hours, or immediately recovered. The aging step is crucial to converting CaP precursor phases into HA, and its duration depends on the other synthesis parameters employed, mainly temperature. At room temperature, HA is obtained only after a few hours, whereas above 90 °C this phase stabilizes almost instantaneously [57]. The aged suspension is then washed, filtered or centrifugated, dried and crushed into a powder.

Shape and size distribution of HA particles as well as their composition and crystallinity are significantly affected by the parameters adopted during the chemical precipitation procedure, including concentration, pH value and rate of addition of precursor solutions, temperature during synthesis, duration of the aging step, and atmosphere [58]. These properties influence not only the osteoconductivity, biocompatibility, bioactivity, and biodegradability of HA [59], but also its intrinsic fluorescence since the density of several types of optically active surface, interface and structural defects is also affected.

Chemical precipitation at room temperature renders poorly crystalline, calcium-deficient AB-type carbonated f-HA particles when  $(\text{NH}_4)_2\text{HPO}_4$  and  $\text{Ca}(\text{OH})_2$  or

CaO are used as  $\text{PO}_4^{3-}$  and  $\text{Ca}^{2+}$  sources, respectively, in air atmosphere and with an aging step of 15 h [60]. In these cases, the f-HA particles have similar rounded shape with average particle size of  $60 \pm 20$  nm. On the other hand, well-crystallized f-HA particles with tunable sizes and shapes, including hexagonal microprisms ( $0.7\text{--}2.5 \mu\text{m} \times 70\text{--}200$  nm), nanorods ( $300\text{--}600$  nm  $\times$   $40\text{--}80$  nm), rice-like NPs ( $50\text{--}60$  nm  $\times$   $12\text{--}25$  nm), microplates and microneedles ( $0.5\text{--}5.5 \mu\text{m} \times 30\text{--}200$  nm) and needle-like NPs ( $200\text{--}700$  nm  $\times$   $20\text{--}50$  nm), are obtained at  $90^\circ\text{C}$  in an aging period of 2 h by varying the rate of addition of  $(\text{NH}_4)_2\text{HPO}_4$  solution to  $\text{Ca}(\text{NO}_3)_2 \cdot 4\text{H}_2\text{O}$  solution (0.15, 7.00 or 600.00 mL/min) as well as the pH value adopted (4.5–5.0 or 9.5–10.0), as summarized in Fig. 2 [39]. The long- and short-range structural order of f-HA particles as well as their compositions vary with these synthesis conditions, ranging from calcium-deficient HA ( $\text{Ca}_{10-x}(\text{HPO}_4)_x(\text{PO}_4)_{6-x}(\text{OH})_{2-x}$  ( $0 < x < 1$ )) in more acidic conditions to compositions closer to those of stoichiometric HA in alkaline conditions.

### 3.1.1 Heat Treatment Steps

The self-activated fluorescence of chemically precipitated HA is significantly affected by posterior heat treatment steps, leading to a large increase of its emission intensity compared to untreated particles. For instance, f-HA nanorods ( $300\text{--}600$  nm  $\times$   $40\text{--}80$  nm) exhibit enhanced fluorescence intensity when obtained via chemical precipitation at  $90^\circ\text{C}$  followed by annealing at  $350$  or  $400^\circ\text{C}$  in air atmosphere [61]. For rounded carbonated calcium-deficient f-HA NPs ( $60 \pm 20$  nm) synthesized at room temperature, the ideal heat treatment setup was found to be between  $400$  and  $450^\circ\text{C}$  [60]. Furthermore, calcium-deficient carbonated f-HA NPs obtained in simulated body fluid (SBF) solution at room temperature can also be made highly fluorescent by annealing at  $400^\circ\text{C}$  [62].

### 3.1.2 Preparation of Doped f-HA

Doping of HA can improve its *in vitro* and *in vivo* behavior, including bioactivity, adsorption of proteins/growth factors, and cell proliferation capability, through the incorporation of several ionic substituents into the HA lattice, as recently reviewed by Tite and colleagues [55]. For instance,  $\text{Mg}^{2+}$ -doped (5 wt.%) f-HA nanorods ( $18\text{--}31$  nm  $\times$   $9\text{--}19$  nm) were obtained by microwave-assisted precipitation at room temperature, leading to a large increase in fluorescence intensity [63]. In another study,  $\text{Sr}^{2+}$ -doped f-HA with enhanced fluorescence properties was prepared by chemical precipitation of HA at  $100^\circ\text{C}$  followed by aging for 24 h at room temperature and a posterior sintering step at  $1000^\circ\text{C}$  for 2 h [64]. Subsequently, an ion exchange process of  $\text{Ca}^{2+}$  by  $\text{Sr}^{2+}$  was carried out by suspending the HA powder in strontium nitrate solution for 5 h. The fluorescence intensity was further improved by soaking the Sr-doped f-HA in SBF up to 32 days due to the incorporation of  $\text{CO}_3^{2-}$  impurity.

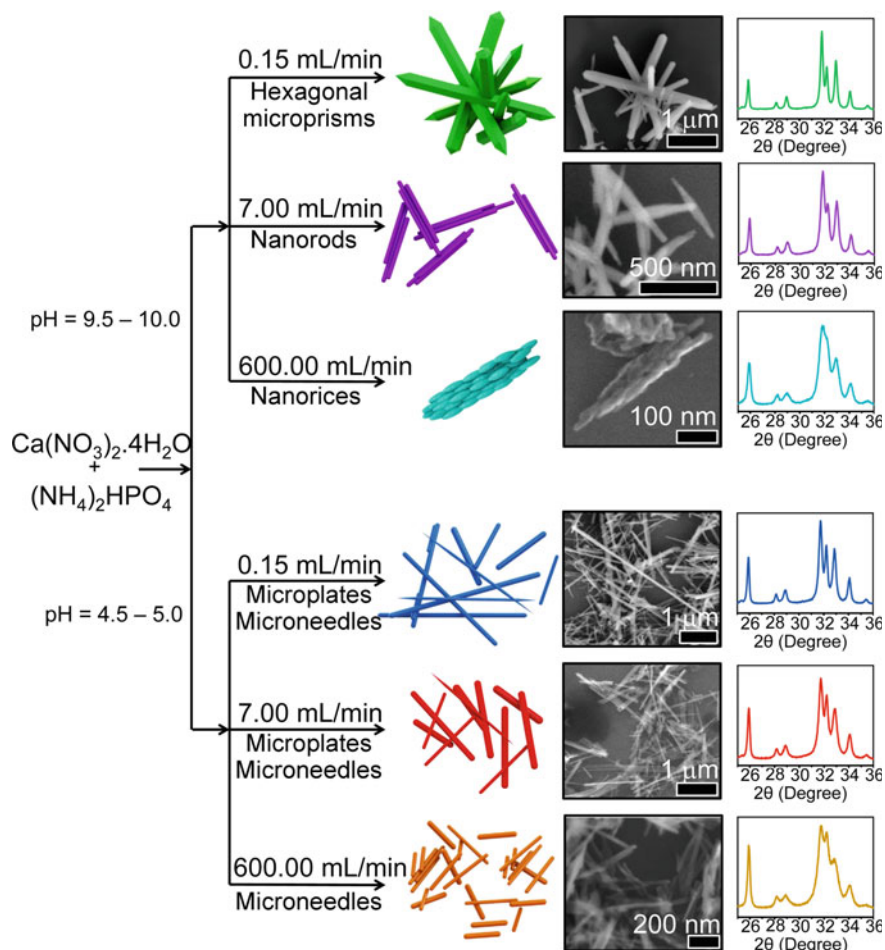


**Fig. 2** Nano- and microparticles of f-HA obtained by chemical precipitation at 90 °C and their corresponding XRD patterns. The particle shape, size, degree of crystallinity and composition can be modified by controlling the pH value adopted and the rate of addition of phosphate solution to calcium solution. Reprinted with permission from Ref. [39]

### 3.1.3 Synthesis of f-HA-Based Composites

The preparation of composite materials containing f-HA nano- and microparticles can be made in order to enhance the intensity of f-HA emission or tune the emission profile of the final composite material. In both cases, charge transfer mechanisms at the interfaces generated between the materials are the main responsible for these behaviors. In this sense, Arul and colleagues [65] prepared polyvinyl alcohol (PVA)/f-HA nanocomposites via microwave-assisted precipitation of f-HA for 30 min at room temperature. The procedure comprised the mixing of 0.5 g of dried powders with

0.0%, 0.5%, 1% and 1.5% of PVA followed by their deposition onto Ti substrate. The authors observed that the intensity of the blue fluorescence of f-HA (centered at 441 nm,  $\lambda_{\text{exc}} = 254$  nm) increased as a function of PVA concentration. In another study, da Silva et al. [66] synthesized a defect-related luminescent composite with tunable emission colors via in situ precipitation of  $\alpha$ -AgVO<sub>3</sub> (AV) in f-HA aqueous suspensions in f-HA/AV molar ratios between 1:1 and 1/32:1. Figueroa-Rosales and colleagues [67] developed f-HA/multi-walled carbon nanotube (MWCNT) composites by chemical precipitation followed by ultrasound bath and microwave radiation. A post-heat treatment step at 250 °C for 6 h was also conducted to improve the fluorescence properties of the final composite materials.

### 3.2 Synthesis from Natural Bio-Resources

The usage of biowastes such as animal bones, fish scale, eggshell and oyster shell among others to prepare HA-based materials is considered a potential waste management strategy to reduce the environmental impact from animal agriculture and food industry [50]. These abundant by-products with no economic value can thereby be converted into value-added products. In addition, HA-based materials obtained from biogenic sources can be well-accepted by living organs due to their physicochemical similarities with bioapatite [56]. In general, HA can be fully extracted from biowaste, acting as the entire source of CaP, or obtained by the reaction of a phosphate precursor with Ca<sup>2+</sup> extracted from a biogenic source.

Kumar and Girija [68] reported the preparation of flower-like f-HA nanostructures from biowaste by the complexation of Ca<sup>2+</sup> from processed and purified eggshell powder (mainly CaCO<sub>3</sub>) with ethylenediamine tetra-acetic acid (EDTA). The Na<sub>2</sub>HPO<sub>4</sub> solution was slowly added to the Ca-EDTA complex, and the resulting solution was then stirred for 30 min, with subsequent pH adjustment to 13. Afterwards, the mixture was irradiated in a microwave oven for 10 min, washed and dried, forming the f-HA precipitate. It was observed that the photoluminescent flower-like NPs were composed of 100–200 nm wide and 0.5–1  $\mu$ m long leaves with Mg<sup>2+</sup> and CO<sub>3</sub><sup>2-</sup> impurities inherited from the eggshells.

In another approach, Goloshchapov and coworkers [69] initially extracted CaO from bird's eggshells through an annealing procedure at 900 °C/2 h, and subsequently mixed the product with distilled water at 100 °C to produce Ca(OH)<sub>2</sub>. Then, a titration was conducted with H<sub>3</sub>PO<sub>4</sub> at room temperature with controlled pH in the 7–9 range (step of 0.5) to obtain distinct levels of CO<sub>3</sub><sup>2-</sup> incorporation. Finally, the precipitate was filtered and dried at 400 °C/1 h to form carbonated f-HA with low crystallinity. Porous rod-like NPs with diameter of ~20 nm and length of ~50 nm were prepared following this methodology, with the best fluorescence intensity being achieved at pH = 8–9 due to the high incorporation of CO<sub>3</sub><sup>2-</sup> impurity into the f-HA lattice in this pH range.

Sinha and coworkers [70] used a simple heat treatment to obtain f-HA from *Labeo Rohita* fish scales acting as a CaP source. After cleaning the scales with boiling water

for 20–25 min followed by 24 h of water immersion at room temperature, the scales were dried, crushed and calcinated at distinct temperatures (from 400 to 1000 °C) for 1 h. The best fluorescence emission intensity was achieved at 800 °C, temperature at which impurities such as collagen and other proteins are more efficiently eliminated without a significant conversion of f-HA into  $\beta$ -TCP phase with poor luminescence.

### 3.3 Hydrothermal-Assisted Precipitation

Zhang and colleagues [71] pioneered the preparation of HA particles with improved fluorescence by using citrate ions ( $\text{Cit}^{3-}$ ) in hydrothermal treatments, being this approach one of the most explored so far. In a typical route, an aqueous solution containing  $\text{Ca}(\text{NO}_3)_2 \cdot 4\text{H}_2\text{O}$  precursor and hexadecyltrimethylammonium bromide (CTAB) surfactant is mixed with another solution containing  $(\text{NH}_4)_2\text{HPO}_4$  precursor and  $\text{Cit}^{3-}$  in a  $\text{Ca}^{2+}:\text{Cit}^{3-}$  ratio of 1:1, which is maintained at 180 °C for 24 h. The f-HA particles with distinct morphologies are obtained depending on the pH adopted for the synthesis (Fig. 3). Short nanorods crystallize in more alkaline environments, with lengths ranging from 50 to 70 nm at pH = 9.0 and 120 nm at pH = 7.0 (Fig. 3a, b). In contrast, in acidic environments more complex structures are formed, including self-assembled bur-like microspheres at pH = 5.0 (Fig. 3c, d) and microflowers at pH = 4.5 (Fig. 3e, f), with diameters of 7–9 and 10 nm, respectively, and microsheets at pH = 4.0, with lengths of 0.7–1 mm (Fig. 3g, h).

It could be noted that the presence of  $\text{Cit}^{3-}$  plays an important role in the final morphology of f-HA due to the formation of the citrate- $\text{Ca}^{2+}$  ion chelating complex, which ends up retarding the preferential growth of HA along the *c*-axis direction. In this specific work, the presence of this complex led to short HA nanorods instead of the nanowires typically observed in hydrothermal synthesis at pH  $\geq 7.0$  without  $\text{Cit}^{3-}$  addition [71, 72]. As also reported by Lin's group [73], the  $\text{Cit}^{3-}$ -based hydrothermal route can also be used to prepare  $\text{Sr}^{2+}$ -substituted f-HA (f-SrHA) microrods and microsheets at shorter reaction times (0.5 and 1 h, respectively) or self-assembled microspheres at larger reaction times (6–48 h) with distinct sizes and crystallinities using  $\text{Sr}(\text{NO}_3)_2$  as  $\text{Sr}^{2+}$  source and at an  $\text{Sr}^{2+}:\text{Cit}^{3-}$  ratio of 1:2.

Further studies have focused on the determination of the ideal precursors to obtain highly fluorescent f-HA particles via  $\text{Cit}^{3-}$ -based synthesis. In this sense, Jiang and colleagues [74] demonstrated that the presence of both  $\text{Cit}^{3-}$  and  $\text{NH}_4^+$  ions in the initial solution originated efficient luminescent centers in f-HA NPs through the combination of  $\text{Na}_3\text{Cit}$  and  $(\text{NH}_4)_2\text{HPO}_4$  or  $(\text{NH}_4)_3\text{Cit}$  and  $\text{Na}_2\text{HPO}_4$  precursors, while no significant radiative emissions were detected when employing  $\text{Na}_3\text{Cit}$  and  $\text{Na}_2\text{HPO}_4$  or only  $(\text{NH}_4)_2\text{HPO}_4$ . Furthermore, Cheng and colleagues [75] observed that by increasing the amount of  $(\text{NH}_4)_3\text{PO}_4 \cdot 3\text{H}_2\text{O}$  in the initial mixture of  $(\text{NH}_4)_3\text{PO}_4 \cdot 3\text{H}_2\text{O}/\text{Na}_3\text{PO}_4 \cdot 12\text{H}_2\text{O}$  precursors it was possible to enhance the fluorescence emission because of the higher concentration of  $\text{NH}_4^+$  ions in the hydrothermal reaction.

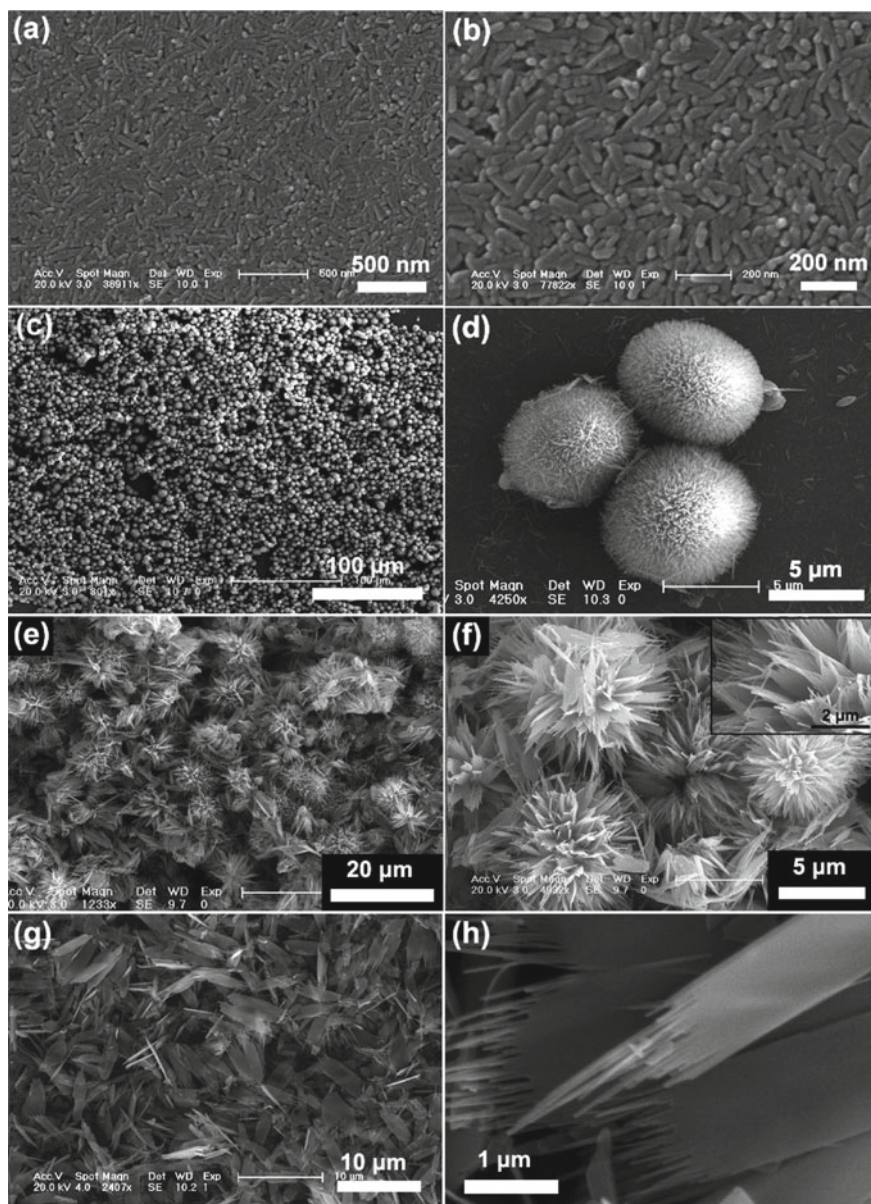


**Fig. 3** Scanning electron microscopy (SEM) images of f-HA particles obtained via hydrothermal treatment in the presence of  $\text{Cit}^{3-}$  showing distinct morphologies resulting from changes in the pH value during the reaction. **a, b** Short nanorods, pH = 7.0; **c, d** bur-like microspheres, pH = 5.0; **e, f** microflowers, pH = 4.5; and **g, h** microsheets, pH = 4.0. Reprinted with permission from Ref. [71]

The usage of distinct precursors during the  $\text{Cit}^{3-}$ -based synthesis of f-HA can also affect the duration of the reaction and bring novel properties to the final material. For instance, shorter reaction times of 3 h at 175 °C and pH = 9 enabled the formation of f-HA nanorods with length of around 100 nm in the presence of polyethylene glycol (PEG) instead of CTAB surfactant, as reported by Yang et al. [76]. On the other hand, Wang and colleagues [77] prepared f-HA nanorods doped with  $\text{Tb}^{3+}$  by the addition of  $\text{Tb}(\text{NO}_3)_3 \cdot 5\text{H}_2\text{O}$  and demonstrated the effect of  $\text{Cit}^{3-}$  and  $\text{Tb}^{3+}$  on the crystal phase, morphology and fluorescent properties of f-HA, evidencing that the radiative emissions can be tuned from blue to green by changing the initial amount of  $\text{Cit}^{3-}$  precursor. Additionally, Li and colleagues [78] synthesized aptamer-capped f-SrHA nanorods doped with  $\text{Gd}^{3+}$  by using  $\text{Gd}(\text{NO}_3)_3 \cdot 6\text{H}_2\text{O}$  precursor and successfully obtained HA NPs with both self-activated fluorescence and paramagnetic properties.

Although it is known that  $\text{Cit}^{3-}$  plays a key role in the improvement of the fluorescent properties of HA, other methodologies based on hydrothermal-assisted precipitation without  $\text{Cit}^{3-}$  precursor also lead to a final material with superior optical properties, as recently demonstrated by Huerta and colleagues [79]. In another work, Park et al. [80] prepared f-SrHA microspheres with Sr/[Ca + Sr] molar ratios of 0, 0.25, 0.50 and 1.00 using poly(aspartic acid) (PASP) as a template. The self-assembled PAPS structure was formed via peptide bonds between  $-\text{COO}^-$  and  $-\text{NH}_3^+$  groups of two different L-aspartic acid (L-Asp) precursor molecules. It was found that another  $-\text{COO}^-$  group of L-Asp monomer interacts with  $\text{Ca}^{2+}$ , forming a chelate. These chelates act as sites for the nucleation and growth of f-SrHA, leading to the occurrence of fluorescent carbon impurity sites. According to the authors, the size, morphology and surface of the particles can be tuned depending on the reaction time and the amount of both L-aspartic acid (L-Asp) and  $\text{Sr}^{2+}$  precursor, which in turn forms weaker chelates with carboxyl groups than  $\text{Ca}^{2+}$  ions.

### 3.4 Sol–Gel Method

Deshmukh and coworkers [81] synthesized self-activated f-HA NPs with a modified sol–gel method using triethylamine (TEA) or acetylacetone (ACA) as stabilizing agents and water or dimethyl sulfoxide (DMSO) as solvents. In this procedure, calcium chloride was first dissolved in DMSO and  $\text{H}_3\text{PO}_4$  was introduced into the former solution by a dropwise addition followed by the influx of TEA or ACA and pH adjustment to 10. The obtained gel was washed, dialyzed, and dried at room temperature. Comparatively, the authors added TEA or ACA stabilizing agent to the  $\text{H}_3\text{PO}_4$  solution, which was in turn added dropwise to the calcium chloride aqueous solution. It was found that the best setup to obtain highly fluorescent HA was with DMSO and ACA. Under these conditions, it was possible to obtain thin rod-like f-HA NPs (62.5 nm in length  $\times$  6.2 nm in diameter) exhibiting a hydrodynamic size of  $57 \pm 10$  nm and a zeta potential of 2.12 mV. When the synthesis was conducted without stabilizing agents, the NPs consisted of rod-like microparticles (1.42  $\mu\text{m}$   $\times$  0.29  $\mu\text{m}$ ).

Although f-HA particles can efficiently load and deliver therapeutic biomolecules (i.e., antibiotics and chemotherapy drugs) in a controllable manner, some researchers have focused on the improvement of their loading capacity by combining them with mesoporous silica (mSi) to fabricate core-shell nanostructures. Yang and coworkers [82] used a modified Pechini sol-gel process to prepare spherical mSi NPs covered by a uniform f-HA layer. Briefly, a water/ethanol mixture, citric acid, CTAB and PEG were added to an acidic solution (pH 2–3) containing both  $\text{Ca}^{2+}$  and  $\text{PO}_4^{3-}$  sources followed by the addition of mSi NPs previously prepared by base catalyzed sol-gel method using a tetraethyl-orthosilicate (TEOS). The diameters of mSi@f-HA NPs were around 200–400 nm, whereas the surface area, average pore diameter and pore volume were  $1348 \text{ m}^2\text{g}^{-1}$ , 2.44 nm and  $0.92 \text{ cm}^3\text{g}^{-1}$ , respectively. These values were several times higher than those typically reported for f-HA (e.g.,  $20\text{--}90 \text{ m}^2\text{g}^{-1}$  of surface area [83, 84]) and had the potential to load superior quantities of biomolecules. Moreover, spherical mSi NPs covered by f-HA nanorods (f-HA@mSi) were also obtained by a similar approach, but using f-HA nanorods previously prepared via  $\text{Cit}^{3-}$ -assisted hydrothermal treatment instead of the soluble salts containing  $\text{Ca}^{2+}$  and  $\text{PO}_4^{3-}$  species [72].

In another study, f-HA nanorods covered by a thin shell of mSi were obtained by base catalyzed sol-gel synthesis of mSi in a dispersion of f-HA nanorods prepared by  $\text{Cit}^{3-}$ -containing hydrothermal treatment [85]. The thickness of the mSi layer of f-HA@mSi nanorods was controlled by the amount of TEOS used (from ~9 nm to ~28 nm), as illustrated in Fig. 4. The final f-HA@mSi NPs were  $68 \times 100$  nm long and  $30 \times 63$  nm wide and exhibited a surface area, an average pore diameter and a pore volume of  $104.6\text{--}223.1 \text{ m}^2\text{g}^{-1}$ ,  $3.649\text{--}3707$  nm and  $0.1664\text{--}0.4763 \text{ cm}^3\text{g}^{-1}$ , respectively—values that varied depending on the thickness of the mSi layer.

## 4 Self-Activated Luminescence

Generally, the self-activated luminescence emission spectrum of f-HA particles obtained by wet methods is composed of a broad band profile centered at 430–530 nm (2.88–2.34 eV) and covering a large part of the UV and visible regions of the electromagnetic spectrum. To achieve such luminescence, f-HA samples are often excited at  $\lambda_{\text{exc}} = 325\text{--}415$  nm (3.81–2.99 eV) in the near-UV region. However, depending on the synthesis and processing approaches, the proposed emission centers responsible for the observed fluorescence are different, and both the emission and the excitation wavelengths can be red-shifted towards less energetic regions by tuning the defects present in the f-HA structure [37].

Considering that neither  $\text{Ca}^{2+}$  nor  $\text{PO}_4^{3-}$  ions emit fluorescence by themselves and that a small amount of energy is often employed to excite f-HA particles in comparison with the calculated values for the optical band gap energy ( $E_g$ ) of pristine HA ( $E_g = 4.60\text{--}5.67$  eV [40, 86, 87]) as well as those experimentally determined (5.41–5.78 eV [61, 88]), the fluorescence in HA has its origin most likely related to the  $e^-$ - $h^+$  pair recombination encompassing localized energy states between the VB and



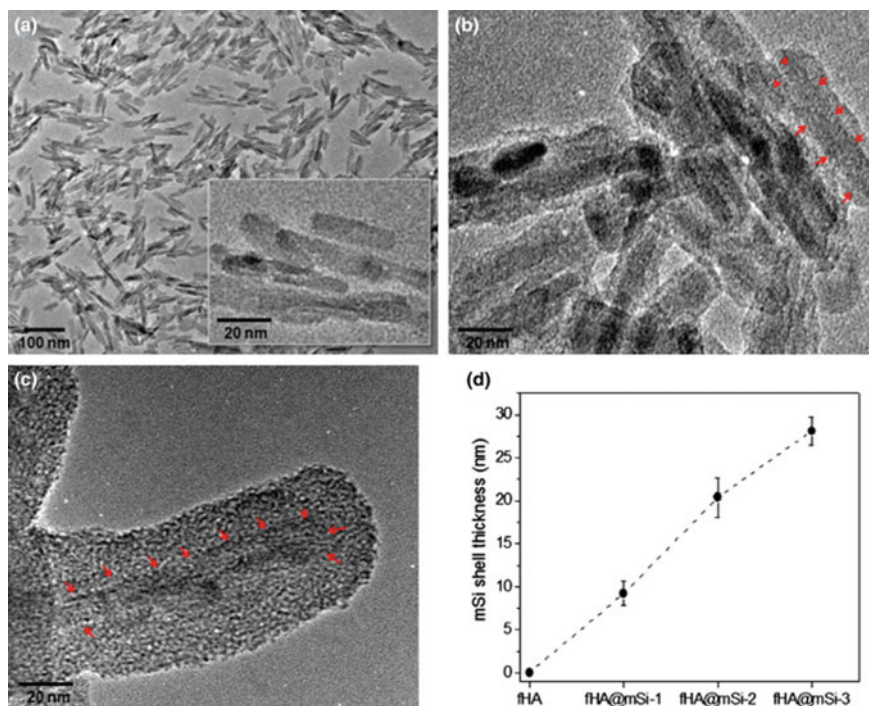


**Fig. 4** Transmission electron microscopy (TEM) images of **a** f-HA nanorods, and **b**, **c** f-HA nanorods covered by a small and a large layer of mSi, respectively. **d** Calculated values of mSi thickness for samples prepared using 50  $\mu\text{L}$  (fHA@mSi-1), 100  $\mu\text{L}$  (fHA@mSi-2), and 150  $\mu\text{L}$  (fHA@mSi-3) of TEOS. Reprinted with permission from Ref. [85]

the CB, i.e., in the forbidden gap of HA. In general, ionic vacancies (e.g.,  $V_{\text{Ca}}$ ,  $V_{\text{OH}}$ , and  $V_{\text{O}}$  vacancies in  $\text{PO}_4^{3-}$ ), ionic substitutions and impurities (e.g.,  $\text{CO}_3^{2-}$ ,  $\text{H}_2\text{O}$  and  $\text{NH}_4^+$ ), and interstitials (e.g.,  $\text{H}_i$ ) in the HA structure induce distortions at both long and short ranges with changes in its lattice parameters, volume, and electronic energy states (an example is shown in Fig. 5a, b), behavior that was evidenced by several theoretical studies based on first-principles calculations [41, 42, 87, 89–93] and experimental approaches [53, 54]. These phenomena have the potential to give rise to several luminescent centers, as a redistribution of electrons takes place between extended and localized electronic levels exhibiting both acceptor- and donor-like characters, consequently leading to self-activated fluorescence in HA in the near-UV and visible regions of the electromagnetic spectrum.

In the case of HA synthesized via wet approaches, the nano- and microparticles are non-stoichiometric and often possess significant density of  $\text{CO}_3^{2-}$  point defects inside the crystalline lattice when obtained in air atmosphere. As previously mentioned, these groups that substitute  $\text{PO}_4^{3-}$  and/or  $\text{OH}^-$  are mainly stabilized by the formation of ionic vacancies ( $V_{\text{Ca}}$  and  $V_{\text{OH}}$ ), the incorporation of  $\text{H}_2\text{O}$  molecules and the occurrence of other ionic substitutions ( $\text{HPO}_4^{2-}$ ,  $\text{Na}^+$ ,

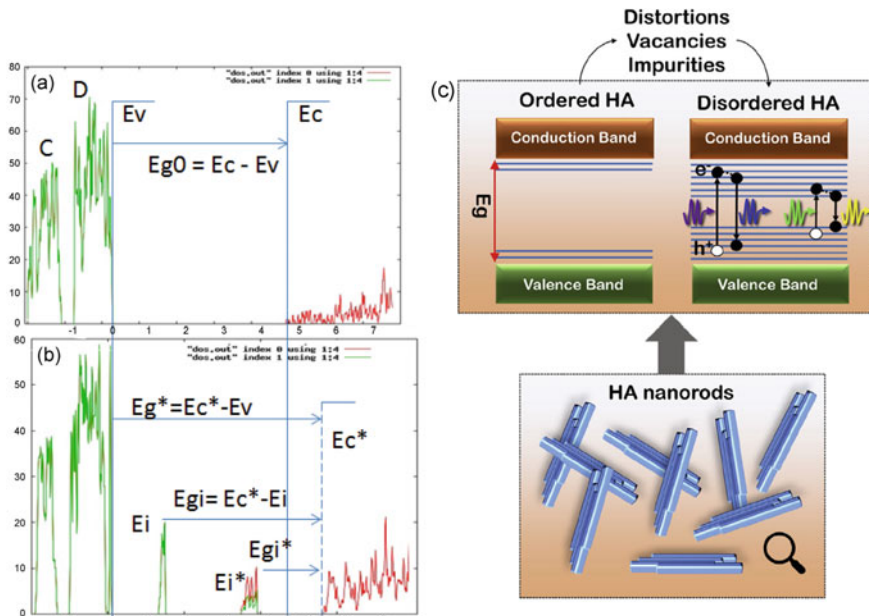


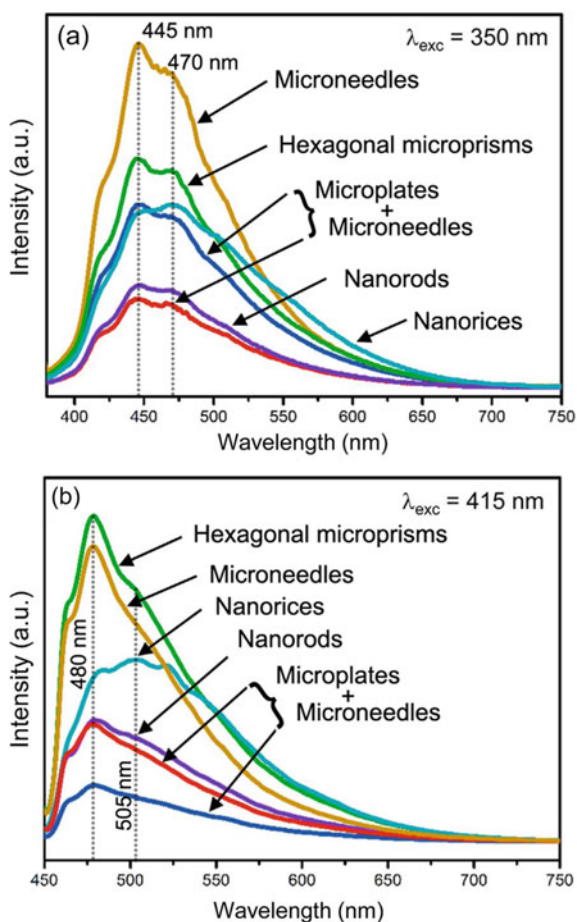
**Fig. 5** Electronic energy levels in the band gap region of HA. **a** Density of states (DOS) image of stoichiometric HA, and **b** DOS image of HA containing point defects that lead to localized states within the forbidden zone with potential for fluorescence emissions in near-UV and visible regions. Legends: energy levels occupied by electrons are represented in green, whereas those represented in red are unoccupied. C and D = upper peaks of the VB; Ev = top of the VB; Ec = bottom of the CB; Ei and Ei\* = fully occupied and half-occupied localized energy states arising from  $V_O$  vacancies in  $PO_4^{3-}$  and  $V_{OH}$  vacancies, respectively. Reprinted with permission from Ref. [41]. **c** General scheme based on the broad band model for the occurrence of self-activated fluorescence in HA nanorods obtained by chemical precipitation. In an ideal ordered HA system, the energy levels in the forbidden zone are minimized. However, the presence of defects causes a higher disorder in the HA system, thus allowing a radiative recombination of  $e^-$ - $h^+$  pairs between the VB and the CB. Reprinted with permission from Ref. [37]

$NH_4^+$ ,  $H_3O^+$ ), depending on the parameters adopted during synthesis [46, 54]. The  $V_{OH}$  vacancies can also occur due to lattice disorder, as proposed by Pasteris and colleagues [94]. Furthermore,  $HPO_4^{2-}$  can incorporate into the HA lattice in more acidic environments, leading to calcium-deficient HA containing both  $V_{Ca}$  and  $V_{OH}$  vacancies [54]. These defects also have profound impact on the atomic arrangement of HA since they promote structural defects as well as distortions in bond lengths and angles in  $[PO_4]$  and Ca coordination clusters. Therefore, the HA structure becomes disordered with a consequent high density of energy levels within the band gap, as demonstrated by the broad band model (Fig. 5c). In this sense, the equilibrium between structural order–disorder effects controls the radiative emissions of f-HA particles.

The understanding of the self-activated fluorescence phenomenon in HA particles and the optimization of the aforementioned defects responsible for the creation

of efficient luminescent centers are an ongoing research area with several studies found in the literature. For instance, in a pioneer experimental study, Aronov and colleagues [95] observed a very wide and continuous fluorescence emission and concluded through electronic trap states spectroscopy that a complex structure of electron/hole bulk and surface localized states are present in f-HA nanoceramics. In a study conducted by our research group [39], it was observed that an asymmetrical broad band emission (Fig. 6) with maxima of intensity centered at 445 and 470 nm ( $\lambda_{\text{exc}} = 350$  nm) or 480 and 505 nm ( $\lambda_{\text{exc}} = 415$  nm) was present in chemically precipitated HA with distinct particle shape, which were composed of five or seven individual emission components, respectively (Fig. S1 and Fig. S2 in Ref. [39]). The main difference between the emission profiles was in their intensities. This behavior was mainly attributed to the different concentrations of  $\text{HPO}_4^{2-}$ ,  $\text{V}_{\text{Ca}}$ ,  $\text{V}_{\text{OH}}$  vacancies, and atomic dislocations from their equilibrium positions, thus leading to distinct densities of localized energy states within the wide band gap of f-HA. Furthermore,

**Fig. 6** Fluorescence emission spectra of f-HA particles with distinct sizes and shapes synthesized via chemical precipitation. **a**  $\lambda_{\text{exc}} = 350$  nm, **b**  $\lambda_{\text{exc}} = 415$  nm. The variations in emission intensity were mainly attributed to distinct densities of point and structural defects that caused changes in energy states within the wide band gap of f-HA. Reprinted with permission from Ref. [39]



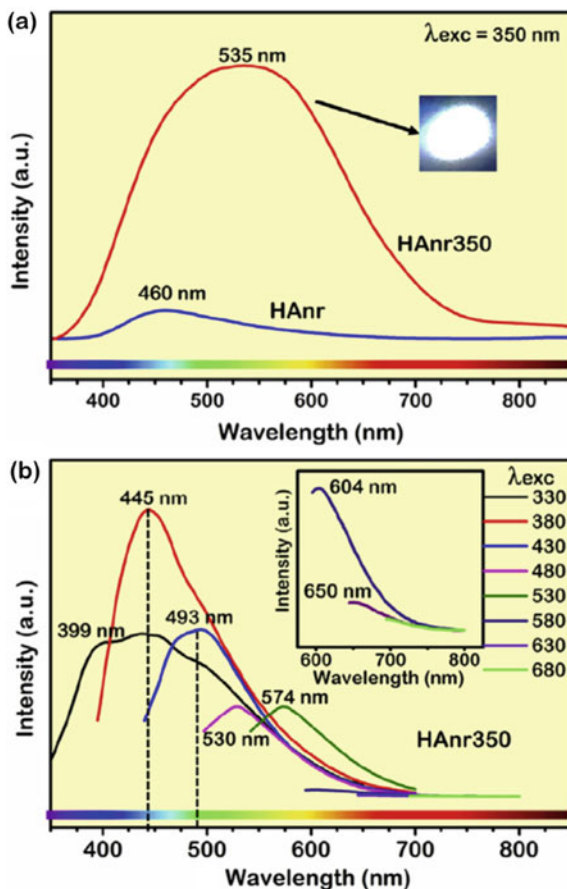
the fluorescence spectra of rice-like f-HA nanoparticles were slightly red-shifted—a behavior that was assigned to the higher density of optically active defects on the surfaces and interfaces of the NPs resulting from their imperfect crystallization and attachment.

In a subsequent study, based on the results obtained by cathodoluminescence, photoluminescence and EPR experiments, Huerta and colleagues [79] suggested that  $V_{Ca}$ ,  $V_{OH}$ , and  $V_O$  vacancies in  $PO_4$  and OH groups, as well as  $V_{OH} + H_i$  complex defect, perturb the electronic structure of f-HA synthesized by hydrothermal-assisted precipitation, being these defects the main responsible for the four individual components observed for the broad band fluorescence emission centered at 517 nm ( $\lambda_{exc} = 325$  nm). Similar emission profiles were obtained in  $Fe^{3+}$ -doped f-HA nanobelts with the general formula  $Ca_{(10-3x)}Fe_{2x}(PO_4)_6(OH)_2$  prepared via an ion exchange procedure posterior to the hydrothermal-assisted precipitation [96]. A general increase in fluorescence intensity was observed in  $Fe^{3+}$  concentrations up to 12.05 at.%, a behavior that was mainly attributed to the formation of extra  $V_{Ca}$  vacancies generated by  $Fe^{3+}$  doping. On the other hand, Kumar and Girija [68] proposed that the emission of f-HA microflowers centered at 430 nm ( $\lambda_{exc} = 344$  nm) may be due to luminescent centers of  $CO_3^{2-}$  and/or defects associated with this substituent.

When posterior thermal treatments are conducted in precipitated f-HA particles, several reactions encompassing the trapped impurities take place, changing the concentration and chemical nature of the point defects and profoundly impacting the structural long- and short-range order of the HA lattice [97]. It was reported that structural  $H_2O$  and  $NH_4^+$  impurities are eliminated at temperatures up to  $\sim 400$  °C, causing a significant decrease in lattice constants  $a$  and  $c$ , whereas  $CO_3^{2-}$  groups are decomposed and/or redistributed via several reactions located in the broad temperature range of 400–1200 °C, leading to distinct steps of increase in lattice parameter  $a$  [98]. At 500 °C, there is a partial filling of hexagonal channels with OH- groups, which is completed at 600–700 °C, suppressing  $V_{OH}$  vacancies.

Together with these temperature-dependent structural and compositional oscillations, the f-HA particles also show dramatic variations in the amplitude, intensity, and center position of their fluorescence emission profile. However, the optimal temperature to achieve the best fluorescence properties was found to be between 350 and 450 °C, which is after the elimination of most part of volatile impurities, with the consequent shrinkage of the crystalline lattice, and when the partial decomposition of  $CO_3^{2-}$  initiates, leading to an improved equilibrium between order–disorder effects and an optimized density of localized energy levels [60, 61]. For example, in this temperature range chemically precipitated f-HA nanorods exhibit very broad emission bands, where the maximum of emission shifts from 460 nm (untreated particles) to 535 nm at 350 °C when excited at  $\lambda_{exc} = 350$  nm, as shown in Fig. 7a; in this case, the fluorescence emission becomes up to 11 times more intense when compared to the raw particles [37]. Additionally, the heat-treated f-HA nanoparticles exhibit multicolor property, causing them to display excitation-dependent emission spectra at  $\lambda_{exc} = 330$ –680 nm due to the thermally-induced high density of defective levels within the band gap region (Fig. 7b). Some studies also pointed out that an important parameter for the fluorescence response of heat-treated f-HA is the initial content

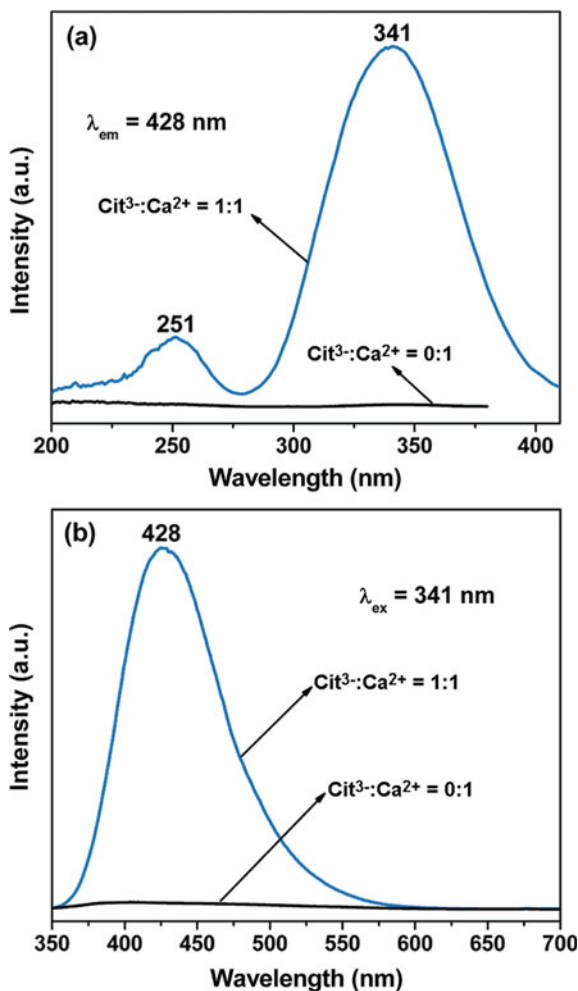
**Fig. 7** **a** Photoluminescence emission spectra ( $\lambda_{\text{exc}} = 350$  nm) of chemically precipitated f-HA nanorods (HAnr) and heat-treated f-HA nanorods at 350 °C/4 h, and **b** excitation-dependent photoluminescence emission spectra of f-HA nanorods heat-treated at 350 °C/4 h. Reprinted with permission from Ref. [37]



of  $\text{CO}_3^{2-}$  and the density of associated defects during the precipitation, leading to significant variations mainly in the intensity of the emission band in the temperature range of 350–450 °C [60, 99].

In the case of f-HA particles obtained by  $\text{Cit}^{3-}$ -based synthesis under hydrothermal conditions, the presence of carbon- and nitrogen-related impurities trapped in the HA lattice seems to play an important role in their fluorescence properties. Zhang and colleagues [71] anticipated that some  $\text{R-C-COO}^-$  units from  $\text{Cit}^{3-}$  suffer a bond cleavage under high pressure and temperature conditions, forming  $\text{R-C}\cdot$  and  $\text{CO}_2^{\cdot-}$  radicals. The latter paramagnetic radical species is then trapped in the HA lattice or interstitial positions, leading to a broad band emission centered at 428 nm ( $\lambda_{\text{exc}} = 341$  nm) not observed in the HA sample obtained without the  $\text{Cit}^{3-}$  precursor, as shown in Fig. 8a,b. It was also indicated that the fluorescence intensity depends on the initial  $\text{Cit}^{3-}:\text{Ca}^{2+}$  molar ratio in f-HA (from 0:1 to 3:1) and the pH value established during synthesis [71, 72]. A similar explanation based on  $\text{CO}_2^{\cdot-}$  radicals for the origin of the emission profile observed in f-SrHA particles

**Fig. 8** **a** Photoluminescence excitation and **b** emission spectra of f-HA NPs obtained by hydrothermal-assisted precipitation in the presence of trisodium citrate precursor (blue line) and without trisodium citrate (black line). Reprinted with permission from Ref. [71]



was reported in Ref. [73]. Further studies demonstrated that the  $\text{Sr}^{2+}:(\text{Ca}^{2+} + \text{Sr}^{2+})$  (from 0 to 1) and  $\text{Cit}^{3-}:\text{Sr}^{2+}$  (from 0:1 to 4:1) molar ratios also affect the fluorescence intensity of f-SrHA particles [83, 100].

However, Jiang and colleagues [74] presented experimental evidence that refuted the presence of  $\text{CO}_2^{\bullet-}$  radicals in f-HA and proposed that the optically active defects are in fact amorphous and nanosized N-rich carbon dots (CDs) trapped in the f-HA lattice or in interstitial positions, thus acting as luminescent centers. As illustrated in Fig. 9, the N-rich CDs are formed under hydrothermal conditions as a product of both  $\text{Cit}^{3-}$  and  $\text{NH}_4^+$  ions, that is, they originate from the precursors containing these ionic species. These findings were further reinforced by a recent study conducted by Cheng and colleagues [75], which used distinct mixtures of  $(\text{NH}_4)_3\text{PO}_4 \cdot 3\text{H}_2\text{O}/\text{Na}_3\text{PO}_4 \cdot 12\text{H}_2\text{O}$  precursors to obtain f-HA NPs via  $\text{Cit}^{3-}$ -based

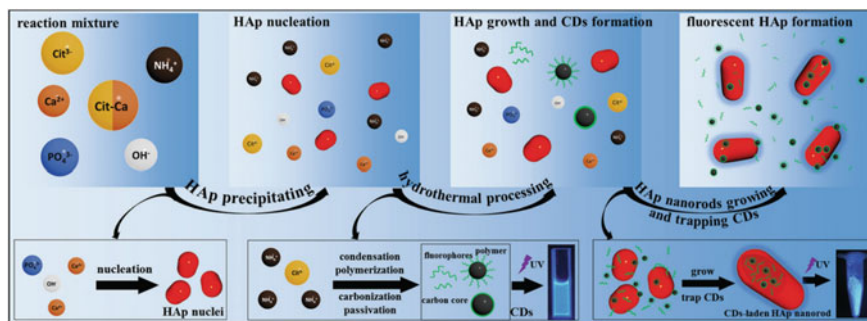


**Fig. 9** Proposed formation mechanism for f-HA via  $\text{Cit}^{3-}$ -assisted hydrothermal treatment. When  $(\text{NH}_4)_2\text{HPO}_4$  precursor solution is added,  $\text{Ca}^{2+}$  ions are released from the chelates formed between  $\text{Ca}^{2+}$  and  $\text{Cit}^{3-}$ , forming the first HA nuclei by the reaction with  $\text{PO}_4^{3-}$  and  $\text{OH}^-$  followed by crystal growth. Then, a reaction encompassing  $\text{Cit}^{3-}$  and  $\text{NH}_4^+$  takes place, forming N-rich CDs containing fluorophore molecules, polymer clusters, and nanosized carbon cores. These cores are gradually trapped in the HA lattice and its interstices, leading to self-activated f-HA. Reprinted with permission from Ref. [74]

hydrothermal treatment. According to the authors, 50/50 or 100/0 mixtures can lead to rod-like NPs with superior colloidal stability and fluorescence emission intensity in comparison with solely  $\text{Na}_3\text{PO}_4 \cdot 12\text{H}_2\text{O}$  precursor. Evidence of CDs as luminescent centers inside f-HA was also demonstrated by Wang and colleagues [77].

Table 1 summarizes the main features and mechanisms in HA particles for the occurrence of self-activated fluorescence according to the synthesis methodology and the experimental setup for the luminescence measurements. Depending on the preparation route and the initial precursors, the proposed defects present in f-HA can significantly change—a fact that guarantees the possible tuning of fluorescence properties in f-HA.

## 5 Applications

Fluorescent HA particles are widely explored for applications ranging from tissue engineering to bioimaging and theragnosis. For these purposes, the luminescent properties of HA-based systems can be tuned by several approaches, such as the encapsulation of organic fluorophores, the doping with luminescent ions, or the combination of HA and other luminescent materials [19]. On the other hand, the self-activated fluorescence has become a great alternative to improve the fluorescence properties of HA particles for various applications, which will be discussed in the next sections.

**Table 1** Main experimental methodologies to obtain fluorescent HA particles

Material	Synthesis approach	Particle morphology	Excitation	Emission	Origins of fluorescence	Ref
f-HA	Chemical precipitation	Nanorods (50–60 nm × 12–25 nm) Nanorods (300–600 nm × 40–80 nm) Microplates and microneedles (0.5–5.5 μm × 0.03–0.2 mm) Prismatic microrods (0.7–2.5 μm × 0.07–0.2 mm)	$\lambda_{exc} = 350$ and 415 nm, krypton ion laser, 7 and 14 mW, respectively	Broad band emission centered between 445–505 nm, depending on the $\lambda_{exc}$ and the particle size and shape	Structural order–disorder. Radiative recombination of $e^-h^+$ pairs in defect-related energy levels within the forbidden zone of HA as an effect of loss of symmetry in [CaO <sub>9</sub> ], [CaO <sub>7</sub> H] and [PO <sub>4</sub> ] clusters in bulk and surface. This effect stems mainly from crystal disorder and V <sub>Ca</sub> and V <sub>OH</sub> vacancies	[39]
f-HA	Chemical precipitation followed by heat treatment steps (200–800 °C)	Nanorods (300–600 nm × 40–80 nm)	$\lambda_{exc} = 350/415$ nm, 300–38 K, krypton ion laser, 7/14/30 mW, $\lambda_{exc} = 330$ –630 nm, Xenon lamp, 450 W	Broad band emission centered between 399–650 nm, depending on the excitation wavelength and source as well as the heat treatment (200–800 °C) and temperature of analysis	Structural order–disorder as in [39]. The thermally-induced elimination or decomposition of trapped impurities (H <sub>2</sub> O, CO <sub>3</sub> <sup>2-</sup> and NH <sub>4</sub> <sup>+</sup> ) from the HA lattice intensifies the radiative recombination of $e^-h^+$ pairs in defect-related energy levels	[37, 61]

(continued)



Table 1 (continued)

Material	Synthesis approach	Particle morphology	Excitation	Emission	Origins of fluorescence	Ref
f-HA	Chemical precipitation using eggshell precursor	Nanorods (~50 nm × 20 nm)	$\lambda_{exc}$ = 405 nm, pump laser	Broad band emission centered at 515 nm. Emission intensity dependent on the heat treatment temperature (400–900 °C) and pH (7–9) during synthesis	CO <sub>3</sub> <sup>2-</sup> luminescent centers substituting PO <sub>4</sub> <sup>3-</sup> groups (B-type) in the HA lattice	[69]
f-HA f-SrHA	Hydrothermal-assisted precipitation	Nanorods 50–70 nm × 25 nm (pH = 9) 120–150 nm × 20 nm (pH = 7) Microspheres 7–9 μm (pH = 5) 10 μm (pH = 4.5)	$\lambda_{exc}$ = 345 nm, Xenon lamp, 150 W	Broad band emission centered at 432 nm. Lifetime = 11.6 ns, quantum yield = 22%. Emission intensity dependent on the Cit <sup>3-</sup> /Sr <sup>2+</sup> molar ratio	CO <sub>2</sub> <sup>*</sup> luminescent centers trapped in the f-HA and f-SrHA lattices and originated from Cit <sup>3-</sup>	[71, 73]
f-HA	Hydrothermal-assisted precipitation	Nanorods (30–200 nm × 20–30 nm)	$\lambda_{exc}$ = 300–370 nm, Xenon lamp, 150 W	Broad band emission centered between 427–442 nm, depending on the $\lambda_{exc}$ . Lifetime = 4.36 ns. Quantum yield = 31.43%	N-rich carbon dot luminescent centers trapped in the HA lattice and originated from Cit <sup>3-</sup> and NH <sub>4</sub> <sup>+</sup> ions	[74]
f-HA	Hydrothermal-assisted precipitation	Nanobelts (0.5–3.0 μm × 10–50 nm)	$\lambda_{exc}$ = 325 nm, He-Cd laser	Broad band emission centered at 517 nm	V <sub>O</sub> vacancy from PO <sub>4</sub> <sup>3-</sup> or OH, V <sub>OH</sub> , V <sub>Ca</sub> , and V <sub>OH</sub> + H <sub>i</sub> vacancies	[79]

(continued)

**Table 1** (continued)

Material	Synthesis approach	Particle morphology	Excitation	Emission	Origins of fluorescence	Ref
f-HA	Sol-gel method	Nanorods (92.8 nm × 23.2 nm) Short nanorods (35 nm × 7 nm) Thin nanorods (62.5 nm × 6.2 nm)	$\lambda_{exc} = 325$ nm, He-Cd laser, 300–15 K;	Broad band emission centered between 502–528 nm, depending on the temperature of analysis. Intensity dependent on the aspect ratio of NPs	Confinement of free electrons in an asymmetric potential created by the elongated shape of NPs with discrete optically active superficial energy levels	[81]

## 5.1 Plain Fluorescence Imaging

Fluorescence imaging is a versatile, non-invasive and low-cost technique with high sensitivity and selectivity that allows the capture of images with high contrast, being potentially used in nanomedicine as a powerful diagnosis tool [101]. Deshmukh and colleagues [81] used f-HA nanorods (62.5 nm × 6.2 nm) obtained by the sol-gel method for in vitro plain fluorescence imaging. The f-HA NPs exhibited a blue fluorescence (maximum at 502 nm,  $\lambda_{\text{exc}} = 325$  nm) stable in phosphate-buffered saline (PBS, pH 7) solution and in Dulbecco's modified Eagle's medium (DMEM). The NPs were well-internalized by both prokaryotic and eukaryotic cells, leading to green and red fluorescence inside the cells, as observed with the aid of an epifluorescence microscope using TRITC and FITC filters (Fig. 10). At dosages up to 1000  $\mu\text{g}\cdot\text{mL}^{-1}$ , the f-HA nanorods displayed a nonhemolytic and low cytotoxic behavior, as determined by MTT and LDH assays, without any significant ROS generation.

Mostly, the application of f-HA NPs is conducted by their excitation in the near-ultraviolet region, which ends up limiting their applicability in deeper tissues due to the high absorption of light by hemoglobin and water. Therefore, it is interesting to use excitation wavelengths closer to the biological window (~650–900 nm), where light has enhanced depth of penetration in tissues [102]. In a recent work, it was demonstrated the multicolor cell imaging capability of f-HA nanorods obtained by chemical precipitation followed by heat treatment at 350 °C/4 h [37]. Using HDFn cells as a model, the internalized f-HA NPs in the cytosol region evidenced the cellular structure by fluorescence emission in confocal microscopy at  $\lambda_{\text{exc}} = 405, 488, 543$  and 594 nm, leading to blue, green, yellow and red colors, respectively. Also, no interference was observed by the co-labeling of cytoskeleton with fluorescein and no evident cytotoxicity was found up to 320  $\mu\text{g}\cdot\text{mL}^{-1}$  of NPs.

The self-activated fluorescence of HA can be also combined with other luminescent species in order to tune its fluorescence emission. Wang and colleagues prepared Tb<sup>3+</sup>-doped f-HA nanorods (51.1 ± 9.7 nm in length) with bright green fluorescence and low cytotoxicity by Cit<sup>3-</sup>-assisted precipitation under hydrothermal treatment [77]. The fluorescence was stable for 72 h in SBF and H<sub>2</sub>O, and a high internalization and labeling capabilities ( $\lambda_{\text{exc}} = 488$  nm) in C6 cell cytoplasm was verified by the conjugation of transferrin receptor on the NPs surfaces.

## 5.2 Fluorescence-Guided Therapy

Since the 1970s, HA has been identified as an efficient system for the transfection of genes applied in the treatment of various pathologies [18]. Currently, CaPs are considered promising pH-responsive nanocarriers for the targeted delivery of distinct bioactive compounds to tumor sites, being widely used in chemotherapy, gene therapy, photodynamic therapy, hyperthermia therapy, and so on [17, 19]. The combination of fluorescent imaging and therapy functions provided by HA represent

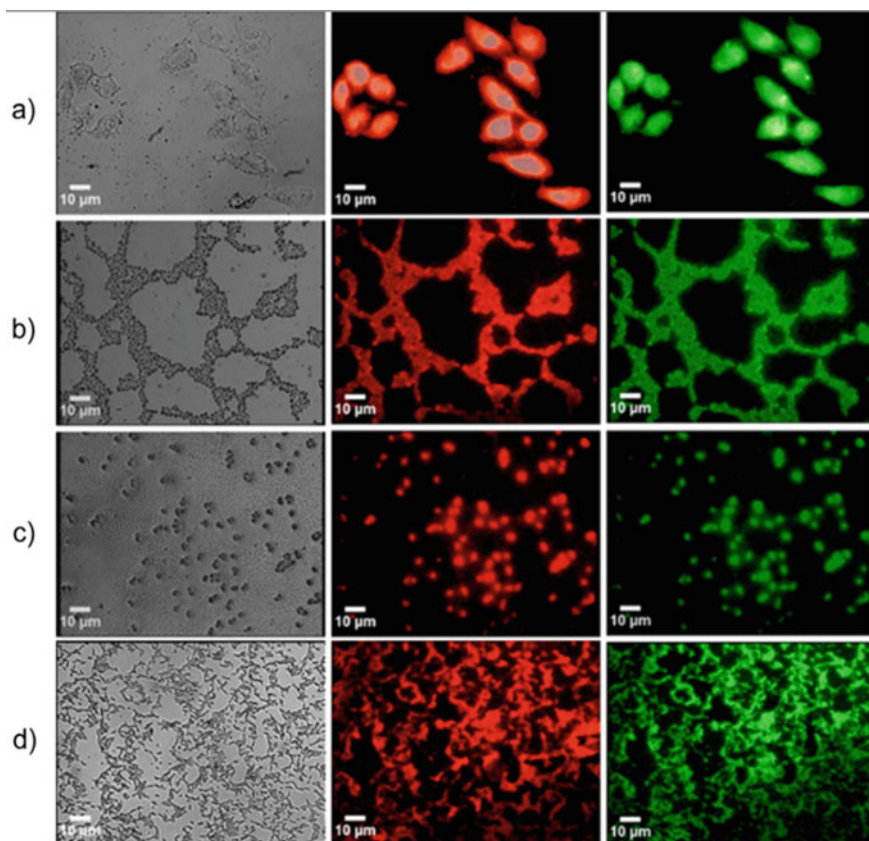


**Fig. 10** Epifluorescence microscopy images of cells containing uptaken f-HA nanorods synthesized via a modified sol–gel procedure using bright field (*left*), FITC filter (*center*) and TRITC filter (*right*), evidencing the bright green and red emissions of f-HA inside the cells. **a** HeLa cells, **b** *Candida albicans*, **c** *Staphylococcus aureus*, **d** *Escherichia coli*. Reprinted with permission from Ref. [81]

the state-of-the-art of nanomedicine and allows the development of efficient therapeutic nanoplateforms with several successfully reported strategies via in vitro and in vivo probes [103].

The f-HA particles can deliver a large variety of bioactive molecules, and the drug loading and release can be monitored by their self-activated fluorescence property. It was shown that the f-HA flower-like nanostructures obtained by eggshell can be loaded with doxycycline hydrochloride (28.3% of loading efficiency), reaching an initial burst release of about 60% for 6 h followed by a slow release of 8% for 54 h, consequently leading to an antibacterial activity against *E. coli* and *B. cereus* [68]. Zhang and colleagues [100] utilized mesoporous f-SrHA nanorods for the delivery of ibuprofen, and demonstrated a loading efficiency of 32.9% and a total drug release of 50.5% after 3 h and 93.9% after 12 h. The ibuprofen-loaded f-SrHA NPs showed

strong blue fluorescence at 432 nm with a continuous increase in emission intensity during drug release, allowing its monitoring. A quenching of luminescent centers by vancomycin loading (efficiency of 16.58%) in mesoporous f-SrHA microflowers was observed by Jiang and colleagues [83], who reported that the cumulative amount of released drug molecules can also be monitored by the emission band centered at 432 nm. In another study, Park and collaborators [80] achieved a higher loading efficiency of 59.1% of vancomycin in f-SrHA microspheres, with a fast release in the first 6 h through the breakage of the hydrogen bonding of vancomycin molecules on the outer surface of the f-SrHAP particle followed by the saturation of drug release after 72 h, as shown in Fig. 11.

To increase the drug loading capability of f-HA particles, they can be combined with mSi. Yang and colleagues [82] used spherical mSi@f-HA NPs (200–400 nm) comprised of a crystalline f-HA layer and an amorphous-mesoporous SiO<sub>2</sub> core to monitor the delivery of captopril. These NPs expressed a loading capability of 33.7%,

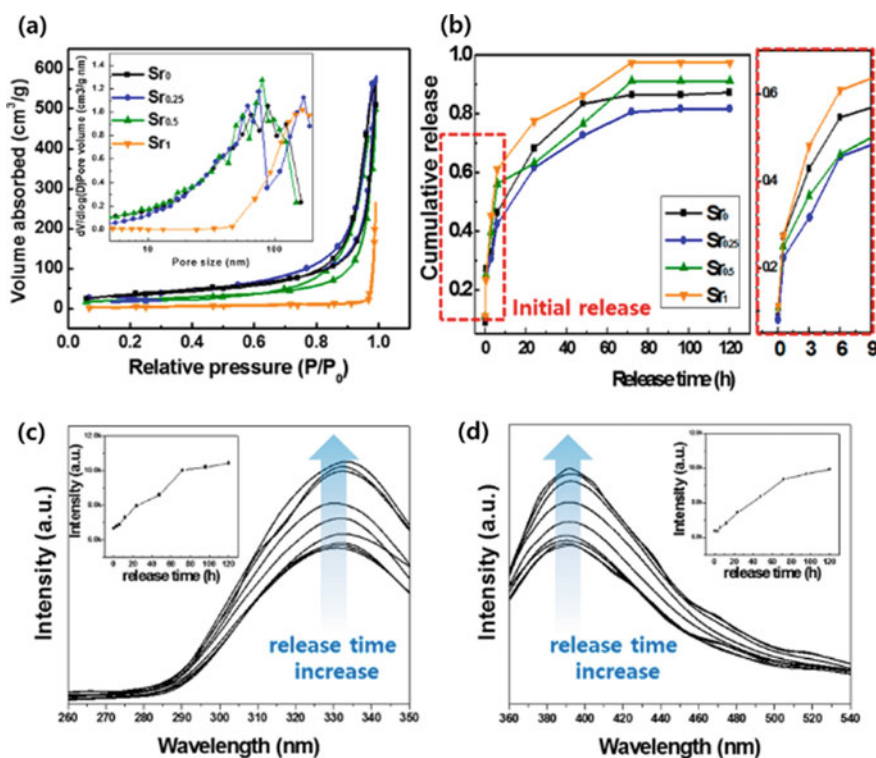


**Fig. 11** **a** N<sub>2</sub> adsorption–desorption isotherm and pore size distributions (inset) of f-SrHA microspheres obtained by hydrothermal treatment, **b** cumulative release of vancomycin from f-SrHA in PBS, and **c, d** Photoluminescence excitation ( $\lambda_{em} = 395$  nm) and emission ( $\lambda_{exc} = 335$  nm) spectra of f-SrHA as a function of vancomycin release time. Reprinted with permission from Ref. [80]

and the captopril release was accompanied by variations in the intensity of blue emission at 410 nm. In another approach, Singh et al. [85] prepared f-HA@mSi nanorods functionalized with amino groups and comprised of a uniform layer of amorphous SiO<sub>2</sub>. The loading capability of fluorescein isothiocyanate (FITC) increased from 1 μg for f-HA nanorods to a maximum of 10 μg for f-HA@mSiO<sub>2</sub> nanorods. The f-HA@mSiO<sub>2</sub> nanorods exhibited self-activated blue fluorescence coexisting with FITC green intracellular signals, demonstrating the in situ imaging ability of the NPs with an uptake efficiency up to 93% in MC3T3-E1 cells. Furthermore, Singh and colleagues [72] covered mSi nanospheres (~200–300 nm) with f-HA nanorods (40 nm × 10 nm) and loaded them with small interfering RNA (siRNA) encoding Plekho-1. The nanocarrier showed a sustainable release over 5 days, an osteoblastic uptake of 96%, and a gene-silencing effect, suppressing Plekho-1 to 18.2%, whereas the self-activated blue fluorescence was used to image the intracellular nanocarrier.

The f-HA particles can also be combined with other contrast agents for multimodal imaging-guided therapy. Li and colleagues [78] prepared Gd<sup>3+</sup>-doped f-SrHA nanorods coated with aptamers, which acted both as capping and targeting agents for the controlled release of doxorubicin (DOX) into breast cancer cells (MCF-7). Since DOX molecules quenched the self-activated blue fluorescence of Gd<sup>3+</sup>-doped f-SrHA nanorods, it was inferred that the increase in emission intensity can be used to monitor the targeted drug release process inside high-level nucleolin expressed MCF-7 cells. In addition, the blue fluorescence and T1-weighted bright contrast from Gd<sup>3+</sup> dopant make these NPs an ideal candidate for both targeted multimodal imaging and therapy.

### 5.3 Biosensing

Fluorescence-based detection is widely applied in biosensing approaches given its high sensitivity, simplicity, and diversity. Moreover, fluorescence sensing based on NPs is an exciting research area with various possibilities of application in biology and medicine due to the superior luminescent properties of the NPs. Specifically, f-HA NPs are biocompatible and can be tailored to have a large surface area in order to immobilize different biomolecules. For instance, a selective in vitro testing of protein kinase A (PKA) activity was conducted by fluorescence using f-HA nanorods, as demonstrated by an assay with HeLa cell lysates [104]. The detection was made by PKA-catalyzed phosphorylation of a peptide substrate, where the resulting phosphopeptides bound to f-HA, quenching its self-activated blue fluorescence. In this specific case, the PKA concentrations in the 1–50 U.L<sup>-1</sup> range were successfully correlated with f-HA fluorescence intensity, and a detection limit of 0.5 U.L<sup>-1</sup> was achieved.

In another approach, a fluorescence assay using f-HA nanorods was developed for the selective detection of alkaline phosphatase (ALP) activity in the human serum [76]. Initially, the fluorescence of f-HA was quenched by the addition of Cu<sup>2+</sup> ions. Then, pyrophosphate ions were introduced to restore the fluorescence intensity of the

NPs due to the formation of a complex between these groups and  $\text{Cu}^{2+}$  ions. When ALP molecules were added to the reaction assay, the hydrolysis of pyrophosphate groups took place, leading to another quenching effect caused by  $\text{Cu}^{2+}$  ions and making ALP detectable in the range of 1–625  $\text{U.L}^{-1}$ .

#### 5.4 Bone Treatment and Regeneration

Self-activated blue luminescence of f-HA nanorods (100 nm) can be utilized as a tool to examine the intracellular molecular mechanism of osteogenesis of bone mesenchymal stem cells (BMSCs) promoted by  $\text{PO}_4^{3-}$  ions, aiming at the development of treatment procedures for bone metabolic diseases [105]. The f-HA NPs can be incorporated into cells via macropinocytosis pathway to the lysosome vesicle that degrades the nanorods due to the acidic pH environment inside the vesicle, thus releasing  $\text{PO}_4^{3-}$  ions (Fig. 12). This latter process is accompanied by the decrease in intensity of HA fluorescence as the particles are dissolved in the 3–48 h interval, as observed by intracellular imaging. Then, the  $\text{PO}_4^{3-}$  ions from f-HA nanorods facilitate the differentiation of BMSCs into osteoblasts by mediating the adenosine-triphosphate (ATP) synthesis in the mitochondria—a process that induces

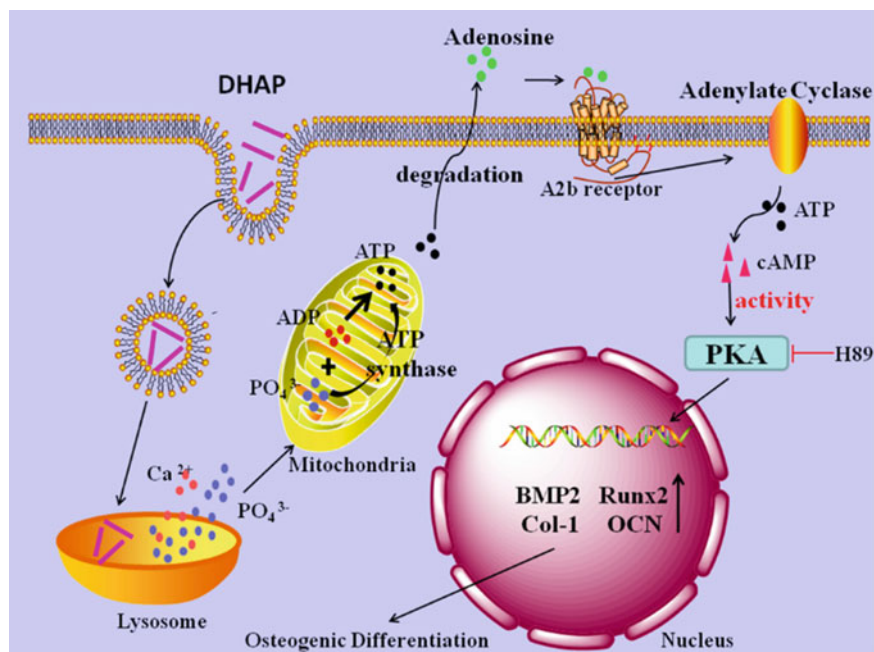


**Fig. 12** Contribution of f-HA nanorods to the osteogenic differentiation of BMSCs. Reprinted with permission from Ref. [105]

the cAMP/PKA pathway—consequently leading to the high mRNA expression of osteogenic differentiation-related genes.

In another study, the self-activated blue luminescence was used to investigate the bone regeneration pathways promoted by f-HA nanorods [106]. It was demonstrated that the NPs can be uptaken by osteoblasts via caveolae-mediated endocytosis and micropinocytosis. Furthermore, these NPs were located in lysosomes, as determined by the intracellular fluorescence signal departing from the NPs. The authors concluded that the f-HA NPs promoted bone regeneration through both intracellular and extracellular pathways. For instance, the intracellular f-HA NPs upregulated the OCN gene expression in the osteoblast cells, the synthesis of collagen and the formation of mineralized nodules, whereas the extracellular f-HA NPs acted as nucleation sites for mineralized nodules, as determined by their blue fluorescence.

Moreover, the preparation of f-HA NPs containing molybdenum oxides ( $\text{MoO}_x$ ) was also reported, exhibiting antibacterial activity for application in bone repair as real-time imaging platforms against bone infection [107].

## 5.5 Other Applications

f-HA nanorods exhibiting strong defect-related blueish- and yellowish-white emission were considered possible candidates for the fabrication of low-cost and non-toxic light-emitting diodes (LEDs) [61]. On the other hand, Cheng and colleagues obtained f-HA nanorods with excellent colloidal stability, and proposed their utilization for long-term storage of confidential information and anti-counterfeit printing [75]. Dispersions of f-HA NPs were used to make inks for infiltration, writing, and printing on commercial paper, showing no background fluorescence. As shown in Fig. 13, the information can be easily observed using a portable UV lamp—but not by the naked eye under natural light. Other applications that take advantage of the fluorescence properties of HA include the characterization of HA-based photocatalysts [41], the structural and compositional changes in bones [108, 109], and early caries detection [69].

## 6 Conclusions and Perspectives

The study of self-activated fluorescence in HA micro- and nanoparticles is an ongoing research topic that has attracted the attention of scientists from various areas with several methodologies available in the current literature. Depending on the synthesis methodology by wet approaches, such as chemical precipitation, hydrothermal-assisted precipitation, synthesis from natural bio-resources and sol-gel method, as well as the correct choice of synthesis parameters and the nature of the precursor compounds, the main features of the fluorescence (i.e., emission color, intensity, and emission band amplitude) can be significantly changed and greatly enhanced. Thus,



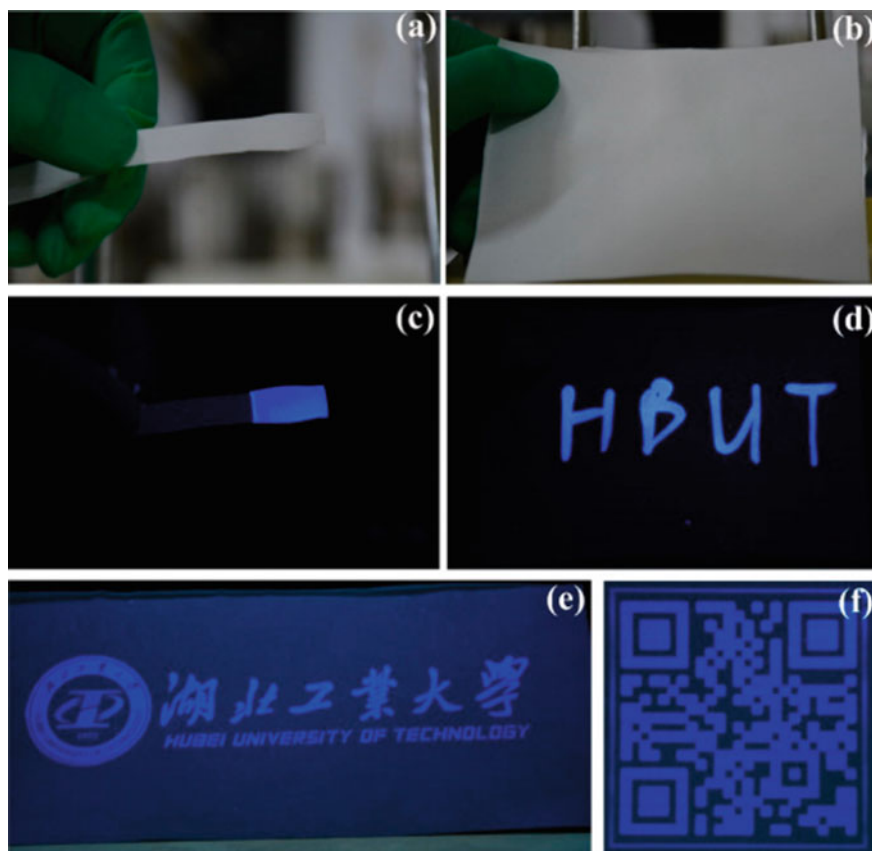


**Fig. 13** Photograph of paper infiltrated with f-HA under **a** natural light, **b**  $\lambda_{\text{exc}} = 365$  nm. Photograph of written paper using f-HA under **c** natural light, **d**  $\lambda_{\text{exc}} = 365$  nm. Photograph of printed paper using f-HA under  $\lambda_{\text{exc}} = 365$  nm evidencing **e** Chinese and English characters, **f** QR code. Reprinted with permission from Ref. [75]

it is essential to have a fine control and optimization of the preparation route in order to obtain improved and reproducible fluorescent properties in f-HA. In this sense, the joint theoretical and experimental approaches can lead to new insights into the main defects that can be manipulated so as to achieve the desirable properties in f-HA.

HA is one of the most interesting materials explored in a vast list of applications, ranging from bone/tooth repair and tissue engineering to bioimaging, biosensing, drug delivery, gene therapy and theranostics. Among the various advantages of HA for these purposes, e.g., biocompatibility, bioactivity, and the capability to load and deliver several biomolecules, its superior structural flexibility is a remarkable feature since the HA crystalline structure accepts distinct foreign substituents, ionic vacancies, interstitials and structural distortions without collapsing. One important effect

of this characteristic is the possibility of stabilizing several defects that act as luminescent centers, leading to self-activated broad band fluorescence in HA particles in the near-UV and visible regions despite the wide optical band gap of HA. The presence of auto-fluorescence properties allows the preparation of f-HA particles by less expensive and complicated approaches while enabling larger possibilities of sophisticated applications in technological and nanomedicine fields. Overall, f-HA particles exhibit good prospects for use in biological applications, being of particular interest. However, considering the wide range of complex compositions, f-HA still needs to be further studied in order to clarify some aspects that are not well-understood and improve its potential for application in large-scale treatments. We strongly believe that this review will be very useful for researchers working in various branches of science and engineering, such as physics, chemistry, materials science, and chemical engineering.

**Acknowledgements** The authors acknowledge the financial support of the following agencies: Conselho Nacional de Desenvolvimento Científico e Tecnológico (CNPq, Grants 164373/2020-9 and 141964/2018-9), and Fundação de Amparo à Pesquisa do Estado de São Paulo (FAPESP, Grant 2013/07296-2). Juan Andres acknowledges Universitat Jaume I for project UJI-B2019-30, and Ministerio de Ciencia, Innovacion y Universidades (Spain) project PGC2018- 094417-B-I00 for supporting this research financially.

## References

1. Dorozhkin, S.V., Epple, M.: *Angew. Chem. Int. Ed.* **41**, 3130 (2002)
2. DileepKumar, V.G., Sridhar, M.S., Aramwit, P., Krut'ko, V.K., Musskaya, O.N., Glazov, I.E., Reddy, N.: *J. Biomater. Sci. Polym. Ed.* **33**, 229 (2022)
3. Chen, I.-H., Lee, T.-M., Huang, C.-L.: *Gels* **7**, 31 (2021)
4. Wang, L., Nancollas, G.H.: *Chem. Rev.* **108**, 4628 (2008)
5. Dessì, M., Alvarez-Perez, M.A., De Santis, R., Ginebra, M.P., Planell, J.A., Ambrosio, L.: *J. Mater. Sci. Mater. Med.* **25**, 283 (2014)
6. Arcos, D., Vallet-Regí, M.: *J. Mater. Chem. B* **8**, 1781 (2020)
7. Shepherd, J.H., Shepherd, D.V., Best, S.M.: 2335 (2012)
8. Lee, D.W., Kim, J.Y., Lew, D.H.: *J. Craniofac. Surg.* **21**, 1084 (2010)
9. Zhou, H., Lee, J.: *Acta Biomater.* **7**, 2769 (2011)
10. Cho, J.-H., Garino, J.P., Choo, S.-K., Han, K.-Y., Kim, J.-H., Oh, H.-K.: *Clin. Orthop. Surg.* **2**, 214 (2010)
11. Choudhury, P., Agrawal, D.C.: *Surf. Coatings Technol.* **206**, 360 (2011)
12. Wang, M.: *Biomaterials* **24**, 2133 (2003)
13. Neacsu, I.A., Stoica, A.E., Vasile, B.S., Andronesu, E.: *Nanomaterials* **9** (2019)
14. Syamchand, S.S., Sony, G.: *Microchim. Acta* **182**, 1567 (2015)
15. Cai, A.Y., Zhu, Y.J., Qi, C.: *Adv. Mater. Interf.* **7**, 1 (2020)
16. Khalifehzadeh, R., Arami, H.: *Adv. Colloid Interf. Sci.* **279**, 102157 (2020)
17. Haider, A., Haider, S., Han, S.S., Kang, I.K.: *RSC Adv.* **7**, 7442 (2017)
18. Uskoković, V., Uskoković, D.P.: *J. Biomed. Mater. Res. - Part B Appl. Biomater.* **96 B** 152 (2011)
19. Qi, C., Lin, J., Fu, L.H., Huang, P.: *Chem. Soc. Rev.* **47**, 357 (2018)
20. Doat, A., Fanjul, M., Pellé, F., Hollande, E., Lebugle, A.: *Biomaterials* **24**, 3365 (2003)

21. Mondéjar, S.P., Kovtun, A., Epple, M.: *J. Mater. Chem.* **17**, 4153 (2007)
22. Li, L., Liu, Y., Tao, J., Zhang, M., Pan, H., Xu, X., Tang, R.: *J. Phys. Chem. C* **112**, 12219 (2008)
23. Yang, P., Quan, Z., Li, C., Kang, X., Lian, H., Lin, J.: *Biomaterials* **29**, 4341 (2008)
24. Chen, F., Huang, P., Zhu, Y.J., Wu, J., Zhang, C.L., Cui, D.X.: *Biomaterials* **32**, 9031 (2011)
25. Hui, J., Zhang, X., Zhang, Z., Wang, S., Tao, L., Wei, Y., Wang, X.: *Nanoscale* **4**, 6967 (2012)
26. Zheng, X., Liu, M., Hui, J., Fan, D., Ma, H., Zhang, X., Wang, Y., Wei, Y.: *Phys. Chem. Chem. Phys.* **17**, 20301 (2015)
27. Xie, Y., He, W., Li, F., Perera, T.S.H., Gan, L., Han, Y., Wang, X., Li, S., Dai, H., *Appl. A.C.S.: Mater. Interf.* **8**, 10212 (2016)
28. Ignjatović, N.L., Mančić, L., Vuković, M., Stojanović, Z., Nikolić, M.G., Škapin, S., Jovanović, S., Veselinović, L., Uskoković, V., Lazić, S., Marković, S., Lazarević, M.M., Uskoković, D.P.: *Sci. Rep.* **9**, 1 (2019)
29. Tabaković, A., Kester, M., Adair, J.H.: *Wiley Interdiscip. Rev. Nanomed. NanoBiotechnol.* **4**, 96 (2012)
30. Liu, H., Chen, F., Xi, P., Chen, B., Huang, L., Cheng, J., Shao, C., Wang, J., Bai, D., Zeng, Z.: *J. Phys. Chem. C* **115**, 18538 (2011)
31. Williams, R.L., Hadley, M.J., Jiang, P.J., Rowson, N.A., Mendes, P.M., Rappoport, J.Z., Grover, L.M.: *J. Mater. Chem. B* **1**, 4370 (2013)
32. Haedicke, K., Kozlova, D., Gräfe, S., Teichgräber, U., Epple, M., Hilger, I.: *Acta Biomater.* **14**, 197 (2015)
33. Guo, Y., Shi, D., Lian, J., Dong, Z., Wang, W., Cho, H., Liu, G., Wang, L., Ewing, R.C.: *Nanotechnology* **19** (2008)
34. Zhao, Y., Shi, L., Fang, J., Feng, X.: *Nanoscale* **7**, 20033 (2015)
35. Liu, M., Liu, H., Sun, S., Li, X., Zhou, Y., Hou, Z., Lin, J.: *Langmuir* **30**, 1176 (2014)
36. Ma, B., Zhang, S., Liu, R., Qiu, J., Zhao, L., Wang, S., Li, J., Sang, Y., Jiang, H., Liu, H.: *Nanoscale* **9**, 2162 (2017)
37. Machado, T.R., Leite, I.S., Inada, N.M., Li, M.S., da Silva, J.S., Andrés, J., Beltrán-Mir, H., Cordoncillo, E., Longo, E.: *Mater. Today Chem.* **14**, 100211 (2019)
38. Lyons, J.L., Janotti, A., Van De Walle, C.G.: *Phys. Rev. Lett.* **108** (2012)
39. Machado, T.R., Sczancoski, J.C., Beltrán-Mir, H., Li, M.S., Andrés, J., Cordoncillo, E., Leite, E., Longo, E.: *Ceram. Int.* **44**, 236 (2018)
40. Slepko, A., Demkov, A.A.: *Phys. Rev. B - Condens. Matter Mater. Phys.* **84**, 1 (2011)
41. Bystrov, V.S., Piccirillo, C., Tobaldi, D.M., Castro, P.M.L., Coutinho, J., Kopyl, S., Pullar, R.C.: *Appl. Catal. B Environ.* **196**, 100 (2016)
42. Matsunaga, K., Kuwabara, A.: *Phys. Rev. B - Condens. Matter Mater. Phys.* **75**, 1 (2007)
43. Anicete-Santos, M., Silva, M.S., Orhan, E., Góes, M.S., Zaghet, M.A., Paiva-Santos, C.O., Pizani, P.S., Cilense, M., Varela, J.A., Longo, E.: *J. Lumin.* **127**, 689 (2007)
44. Ikoma, T., Yamazaki, A., Nakamura, S., Akao, M.: *Netsu Sokutei* **25**, 141 (1998)
45. Narasaraaju, T.S.B., Phebe, D.E.: *J. Mater. Sci.* **31**, 1 (1996)
46. Uskoković, V.: *RSC Adv.* **5**, 36614 (2015)
47. Kay, M.I., Young, R.A., Posner, A.S.: *Nature* **204**, 1050 (1964)
48. Boanini, E., Gazzano, M., Bigi, A.: *Acta Biomater.* **6**, 1882 (2010)
49. Lu, X., Zhang, H., Guo, Y., Wang, Y., Ge, X., Leng, Y., Watari, F.: *Cryst. Eng. Commun.* **13**, 3741 (2011)
50. Bee, S., Hamid, Z.A.A.: *Ceram. Int.* **1** (2020)
51. Wopenka, B., Pasteris, J.D.: *Mater. Sci. Eng. C* **25**, 131 (2005)
52. Peroos, S., Du, Z., De Leeuw, N.H.: *Biomaterials* **27**, 2150 (2006)
53. Fleet, M.: *Carbonated Hydroxyapatite: Materials, Synthesis, and Applications*, 1st edn. Pan Stanford Publishing, New York (2015)
54. Elliot, J.C.: *Structure and Chemistry of the Apatites and Other Calcium Orthophosphates*, 1st edn. Elsevier Publisher, Amsterdam (1994)
55. Tite, T., Popa, A.C., Balescu, L.M., Bogdan, I.M., Pasuk, I., Ferreira, J.M.F., Stan, G.E.: *Materials (Basel)* **11**, 1 (2018)

56. Sadat-Shojai, M., Khorasani, M.T., Dinpanah-Khoshdargi, E., Jamshidi, A.: *Acta Biomater.* **9**, 7591 (2013)
57. Liu, C., Huang, Y., Shen, W., Cui, J.: *Biomaterials* **22**, 301 (2001)
58. Rodríguez-Lorenzo, L.M., Vallet-Regí, M.: *Chem. Mater.* **12**, 2460 (2000)
59. Shavandi, A., Bekhit, A.E.D.A., Sun, Z., Ali, A., *Biomimetics*, J.: *Biomater. Biomed. Eng.* **25**, 98 (2015)
60. Gonzalez, G., Costa-Vera, C., Borrero, L.J., Soto, D., Lozada, L., Chango, J.I., Diaz, J.C., Lascano, L.: *J. Lumin.* **195**, 385 (2018)
61. Machado, T.R., Sczancoski, J.C., Beltrán-Mir, H., Nogueira, I.C., Li, M.S., Andrés, J., Cordoncillo, E., Longo, E.: *J. Solid State Chem.* **249**, 64 (2017)
62. Zollfrank, C., Müller, L., Greil, P., Müller, F.A.: *Acta Biomater.* **1**, 663 (2005)
63. Arul, K.T., Kolanthai, E., Manikandan, E., Bhalerao, G.M., Chandra, V.S., Ramya, J.R., Mudali, U.K., Nair, K.G.M., Kalkura, S.N.: *Mater. Res. Bull.* **67**, 55 (2015)
64. Mahabole, M.P., Bahir, M.M., Kalyankar, N.V., Khairnar, R.S.: *J. Biomed. Sci. Eng.* **05**, 396 (2012)
65. Arul, K.T., Ramya, J.R., Karthikeyan, K.R., Kalkura, S.N.: *Mater. Lett.* **135**, 191 (2014)
66. Soares Da Silva, J., Machado, T.R., Martins, T.A., Assis, M., Foggi, C.C., MacEdo, N.G., Beltrán-Mir, H., Cordoncillo, E., Andrés, J., Longo, E.: *Inorg. Chem.* **58**, 5900 (2019)
67. Figueroa-Rosales, E.X., Martínez-Juárez, J., García-Díaz, E., Hernández-Cruz, D., Sabinas-Hernández, S.A., Robles-Águila, M.J.: *Curr. Comput.-Aided Drug Des.* **11**, 832 (2021)
68. Kumar, G.S., Girija, E.K.: *Ceram. Int.* **39**, 8293 (2013)
69. Goloshchapov, D.L., Minakov, D.A., Domashevskaya, E.P., Seredin, P.V.: *Results Phys.* **7**, 3853 (2017)
70. Sinha, A., Pal, A., Murmu, A.S.S., Amit, U.K.G., Chowdhury, R.: *J. Inst. Eng. Ser. D* (2020)
71. Zhang, C., Yang, J., Quan, Z., Yang, P., Li, C., Hou, Z., Lin, J.: *Cryst. Growth Des.* **9**, 2725 (2009)
72. Singh, R.K., Kim, T.H., Patel, K.D., Kim, J.J., Kim, H.W.: *J. Mater. Chem. B* **2**, 2039 (2014)
73. Zhang, C., Cheng, Z., Yang, P., Xu, Z., Peng, C., Li, G., Lin, J.: *Langmuir* **25**, 13591 (2009)
74. Jiang, D., Zhao, H., Yang, Y., Zhu, Y., Chen, X., Sun, J., Yu, K., Fan, H., Zhang, X.: *J. Mater. Chem. B* **5**, 3749 (2017)
75. Cheng, C., Tong, K., Fang, Y., Wang, J., Liu, Y., Tan, J.: *Coatings* **9**, 1 (2019)
76. Yang, W., Luo, J., Qi, M., Yang, M.: *Anal. Methods* **11**, 2272 (2019)
77. Wang, C., Jeong, K.-J., Kim, J., Kang, S.W., Kang, J., Han, I.H., Lee, I.-W., Oh, S.-J., Lee, J.: *J. Colloid Interf. Sci.* **581**, 21 (2021)
78. Li, Z., Liu, Z., Yin, M., Yang, X., Yuan, Q., Ren, J., Qu, X.: *Biomacromol* **13**, 4257 (2012)
79. Huerta, V.J., Fernández, P., Gómez, V., Graeve, O.A., Herrera, M.: *Appl. Mater. Today* **21**, 100822 (2020)
80. Park, S.Y., Il Kim, K., Park, S.P., Lee, J.H., Jung, H.S.: *Cryst. Growth Des.* **16**, 4318 (2016)
81. Deshmukh, K., Shaik, M.M., Ramanan, S.R., Kowshik, M., *Biomater. A.C.S.: Sci. Eng.* **2**, 1257 (2016)
82. Yang, P., Yang, P., Teng, X., Lin, J., Huang, L.: *J. Mater. Chem.* **21**, 5505 (2011)
83. Jiang, F., Wang, D.P., Ye, S., Zhao, X.: *J. Mater. Sci. Mater. Med.* **25**, 391 (2014)
84. Rodríguez-Ruiz, I., Delgado-López, J.M., Durán-Olivencia, M.A., Iafisco, M., Tampieri, A., Colangelo, D., Prat, M., Gómez-Morales, J.: *Langmuir* **29**, 8213 (2013)
85. Singh, R.K., Kim, T.-H., Patel, K.D., Mahapatra, C., Dashnyam, K., Kang, M.S., Kim, H.-W.: *J. Am. Ceram. Soc.* **97**, 3071 (2014)
86. Rulis, P., Ouyang, L., Ching, W.Y.: *Phys. Rev. B - Condens. Matter Mater. Phys.* **70**, 1 (2004)
87. Bhat, S.S., Waghmare, U.V., Ramamurty, U.: *Cryst. Growth Des.* **14**, 3131 (2014)
88. Jiménez-Flores, Y., Suárez-Quezada, M., Rojas-Trigos, J.B., Lartundo-Rojas, L., Suárez, V., Mantilla, A.: *J. Mater. Sci.* **52**, 9990 (2017)
89. De Leeuw, N.H.: *J. Mater. Chem.* **20**, 5376 (2010)
90. Matsunaga, K.: *Phys. Rev. B - Condens. Matter Mater. Phys.* **77**, 1 (2008)
91. Bystrov, V.S., Coutinho, J., Bystrova, A.V., Dekhtyar, Y.D., Pullar, R.C., Poronin, A., Palcevskis, E., Dindune, A., Alkan, B., Durucan, C., Paramonova, E.V.: *J. Phys. D. Appl. Phys.* **48**, 195302 (2015)

92. Bystrova, A.V., Dekhtyar, Y.D., Popov, A.I., Coutinho, J., Bystrov, V.S.: *Ferroelectrics* **475**, 135 (2015)
93. Bystrov, V.S., Avakyan, L.A., Paramonova, E.V., Coutinho, J.: *J. Phys. Chem. C* **123**, 4856 (2019)
94. Pasteris, J.D., Wopenka, B., Freeman, J.J., Rogers, K., Valsami-Jones, E., Van Der Houwen, J.A.M., Silva, M.J.: *Biomaterials* **25**, 229 (2004)
95. Aronov, D., Chaikina, M., Haddad, J., Karlov, A., Mezinskis, G., Oster, L., Pavlovska, I., Rosenman, G.: *J. Mater. Sci. Mater. Med.* **18**, 865 (2007)
96. Carrera, K., Huerta, V., Orozco, V., Matutes, J., Fernández, P., Graeve, O.A., Herrera, M.: *Mater. Sci. Eng. B Solid-State Mater. Adv. Technol.* **271**, (2021)
97. Tõnsuaadu, K., Gross, K.A., Pluduma, L., Veiderma, M.: *J. Therm. Anal. Calorim.* **110**, 647 (2012)
98. Zyman, Z.Z., Rokhmistrov, D.V., Glushko, V.I., Ivanov, I.G.: *J. Mater. Sci. Mater. Med.* **20**, 1389 (2009)
99. Goloshchapov, D.L., Seredin, P.V., Minakov, D.A., Domashevskaya, E.P.: *Opt. Spectrosc. (English Transl. Opt. i Spektrosk.)* **124**, 187 (2018)
100. Zhang, C., Li, C., Huang, S., Hou, Z., Cheng, Z., Yang, P., Peng, C., Lin, J.: *Biomaterials* **31**, 3374 (2010)
101. Wolfbeis, O.S.: *Chem. Soc. Rev.* **44**, 4743 (2015)
102. Weissleder, R.: *Nat. Biotechnol.* **19**, 316 (2001)
103. Degli Esposti, L., Carella, F., Adamiano, A., Tampieri, A., Iafisco, M.: *Drug Dev. Ind. Pharm.* **44**, 1223 (2018)
104. Zhang, K., Zeng, K., Shen, C., Tian, S., Yang, M.: *Microchim. Acta* **185** (2018)
105. Wang, C., Liu, D., Zhang, C., Sun, J., Feng, W., Liang, X.J., Wang, S., Zhang, J.: *ACS Appl. Mater. Interf.* **8**, 11262 (2016)
106. Dai, C., Zhu, L., Chen, G., Haddleton, D.M.: *RSC Adv.* **9**, 35939 (2019)
107. Placente, D., Ruso, J.M., Baldini, M., Laiuppa, J.A., Sieben, J.M., Santillán, G.E., Messina, P.V.: *Nanoscale* **11**, 17277 (2019)
108. Lambrecht, G., Mallol, C.: *J. Archaeol. Sci. Reports* **31**, 102333 (2020)
109. Sandri, A., Basso, P.R., Corridori, I., Protasoni, M., Segalla, G., Raspanti, M., Spinelli, A.E., Boschi, F.: *J. Biophotonics* **14**, 1 (2021)

# Spintronic Properties in Complex Perovskites: A Concordance Between Experiments and Ab-Initio Calculations



J. Roa-Rojas, C. E. Deluque Toro, A. V. Gil Rebaza, X. A. Velásquez Moya, and D. A. Landínez Téllez

**Abstract** Complex perovskite-type compounds constitute one of the most exciting families of materials due to the wide range of applications such as anode materials for solid oxide fuel cells, highly active catalysts in electrochemical energy conversion reactions, substrates for high-efficiency solar cells, piezoelectric or dielectric sensors, magnetoelectric and magnetoresistive devices, magnetic and spintronic semiconductors with uses in dynamic random access memories (DRAM) or non-ferroelectric random access memories (NVFRAM), hard disk read–write heads for high capacity storage of information in magnetic media and devices for electron current polarization, magnetic sensors, among others. In the present chapter we will focus on the study of the structural, magnetic, ferroelectric, semiconducting and thermophysical properties of complex perovskites with general formula  $A_2BB'O_6$  where A are alkaline earth elements, rare earths or metals of large ionic radius and B and B' are some transition metal elements. For this purpose, we present an exhaustive theoretical–experimental study of these compounds, reporting responses in measurements with different experimental techniques, correlated to ab-initio calculations in the framework of the Density Functional Theory and thermodynamic properties by means of Debye's quasi-harmonic model. The obtained results reveal the applicability of various complex perovskites in the spintronics industry.

---

J. Roa-Rojas · X. A. V. Moya · D. A. L. Téllez

Grupo de Física de Nuevos Materiales, Departamento de Física, Universidad Nacional de Colombia, 111321 Bogotá, D.C, Colombia

C. E. D. Toro

Grupo de Nuevos Materiales, Facultad de Ingeniería, Universidad del Magdalena, Santa Marta, Colombia

A. V. G. Rebaza (✉)

Departamento de Física, Facultad de Ciencias Exactas de la Universidad Nacional de La Plata UNLP, 1900 La Plata, Argentina

e-mail: [arvifis@gmail.com](mailto:arvifis@gmail.com)

Instituto de Física La Plata - IFLP, CCT La Plata CONICET, 1900 La Plata, Argentina

D. A. L. Téllez

Grupo de Estudios de Materiales GEMA, Departamento de Física, Universidad Nacional de Colombia, 111321 Bogotá, D.C, Colombia

## 1 Introduction

The applications of electric charge transport in materials have been known since before the discovery of the electron at the end of the nineteenth century. However, its special applicability in what is known as “electronics” took place in the twentieth century. Electronics, defined as that part of physics that studies the controlled transport of electric charges by means of the laws of electromagnetism, was first associated with vacuum physics, giving rise to electronic devices based on tubes with diode and triode functionality, among others, with which oscillators, amplifiers and modulators were produced.

Around the 1930s, the semiconducting properties of Si and Ge became known, giving rise to p-n junctions and the creation of the first transistor in the 1940s. From that moment on, advances in solid-state physics modified electronics as it was previously known, drastically changing the applications of semiconductor materials, creating new, more efficient and functional devices, and promoting successive miniaturization processes that turned it into microelectronics in the 1950s. Thus, individual components were replaced by the integrated circuit or chip: a Si crystal of small dimensions, containing tiny capacitors, diodes, resistors and transistors appropriately interconnected. These processes were the direct promoters of the transformation between analog and digital processing, with an unusual growth in the 60’s and 70’s that led to the evolution of microprocessors used in personal computers and following the so-called G.E. Moore’s law [1]. At the beginning of this century, the design of processors with nanometer technology (90 nm) gave rise to the so-called nanoelectronics, which gave rise to a race among large companies producing devices for information processing and storage, including USB memories, portable hard disks and innovations in cell phones, among others [2].

Up to this point, the functionalities in electronic devices were obtained by controlling the electron charge transport, aided by semiconductor materials in processing and logic operation [3]. On the other hand, the storage of information, as well as the processes of reading, writing and erasing it, was introduced through the use of magnetic materials [4]. Recently, a new word related to the intrinsic properties of the electron has made the old electronics reach unsuspected levels of applicability and multifunctionality: spintronics. Spin transport electronics (spintronics) is that in which the manipulation of the electron spin and the resulting magnetic moment allows the modification of the functionalities of materials, facilitating the design of more versatile and faster devices than their predecessors and giving rise to a technology in which, in addition to the control of the fundamental charge, the intrinsic spin and the magnetic moment of the electron are controlled [5]. The generation of spin currents can be performed by injection of magnetic spins from a ferromagnetic material, the application of electric and magnetic fields, the introduction of electromagnetic waves, the inclusion of elements that promote Zeeman splitting, the application of thermal gradients and mechanical rotations or geometric modifications [6]. These spin current generation methods applied to the design of spintronic devices are intrinsically related to exotic properties such as giant [7] and colossal

[8] magnetoresistance, half-metallicity [9], exchange-bias [10] multiferroicity [11] and coexistence of ferromagnetism and semiconductivity [12], among others. The design of new magnetic semiconductor materials that allow the control of logic operations as well as the reading and recording of information in a single material could substantially simplify the development of spintronic devices. Efforts to reconcile the two properties, semiconductivity and magnetism, in a single functional material started with the epitaxial growth of tetrahedrally coordinated semiconductor films containing magnetic transition metals [13], up to the so-called dilute magnetic semiconductors, in which spin-dependent magneto-electro-optical properties can be observed [14, 15]. The main obstacle of applicability in spintronic devices at room temperature of the former lies in the difficulty to increase the densities of the included transition metals and hollow carriers [14], while in the latter the major difficulty has to do with the spin-dependent coupling between the semiconductor bands and localized states, which occurs because many of the magnetic particles are not part of the structure of the semiconductor material and remain interstitial or form secondary crystallographic phases [16].

In the present chapter, two ceramic material systems are presented that show semiconducting and ferromagnetic behaviors simultaneously in a single crystalline structure, which may represent an excellent perspective in the generation of new multifunctional materials for applications in spintronic devices. These materials belong to a particular family of oxides known as perovskites [17], which, due to their particular crystallographic characteristics, allow the inclusion of alkaline earth cations, rare earths and transition metals, so that the physical properties can be tuned by modifications in the stoichiometric composition and structural variations of the material [18]. An advantage of perovskites is that their degree of structural complexity depends on the type of substitutions that can be made from their basic formula, which, in turn, allows modifying and even predicting the occurrence of physical properties in new materials [19].

One family of versatile materials that represents a large percentage of the systems currently being investigated in solid physics and chemistry is the so-called perovskites. In general, perovskites are represented by the ideal formula  $ABX_3$ , where A is an alkali earth element, a rare earth, or a metal or semimetal of large ionic radius, B represents a transition metal or lanthanide element, and X, usually, is oxygen or a halogen [20]. Modifications of the atomic radii of A and B introduce structural distortions and new crystalline phases, while inclusions of rare earth elements give the possibility to produce materials with exotic electrical and magnetic properties [21]. Partial substitutions of the A and B cations give rise to complex materials such as double perovskites with generic formula  $A_2BB'O_6$  [22] and even more complex perovskites  $AA'B_2O_6$  [23] and the well-known triple perovskite  $A_2A'B_2B'O_9$  [24]. Their chemical configuration offers multiple possibilities to combine different elements, as well as the possibility to synthesize new materials with a wide variety of physical properties. Depending on the magnetic and electrical characteristics of A, A', B and B' it is relatively easy to create new perovskite systems with promising prospects in the new field of spintronic technology [25]. In the  $A_2BB'O_6$  double perovskites it is possible to obtain materials evidencing



B-B' cation ordering along the crystallographic axes, forming a salt-rock type structure [26], which is not the case for other types of complex perovskite [27]. These structural characteristics limit the crystalline symmetries for the different families of complex perovskites, suggesting the occurrence of structural distortions that also correspond to octahedral inclinations and rotations that influence the physical properties as a result of the intrinsic characteristics of the constituents of the material [28].

Double perovskite-type materials will be presented in this chapter, which are generated from the general formula  $A_2BB'O_6$ . As can be inferred from the title of the chapter, experimental results suggesting macroscopic behaviors applicable in spintronics will be presented. Results of structural properties and electrical, magnetic and optical responses for materials belonging to these families of perovskite-type materials will be duly correlated with predictions from calculation of density of electronic states. These will be performed by means of Density Functional Theory (DFT), which has become a potentially powerful tool for predicting physical properties in perovskite-type materials [29]. Additionally, considering that the macroscopic thermodynamic properties are strongly correlated with the microscopic dynamics of the atoms of the material, and assuming that the collective vibrations of the crystal lattices in these solid materials take place via phonons, it is possible to study the fundamental excitations that are associated with these thermodynamic properties. The most representative function of phonons takes place in insulators and semiconductors, where they make direct contributions to properties such as specific heat and thermal expansion, indicating that they are temperature-dependent properties. In relation to phonons, vibrations in perovskite-type crystals will be considered to have a harmonic character, which will be valid for temperature values below the Debye temperature of the solid. In this way, theoretical methods can constitute a complementary tool for the study of atomic dynamics at relatively high temperatures, through approximations such as the quasi-harmonic Debye model [30]. Thus, the results of the density of electronic states and the behavior of specific heat, Debye temperature, entropy, thermal expansion and the Grüneisen parameter as functions of pressure and temperature will be presented.

The single perovskite-type material  $\text{LaFeO}_3$ , known as lanthanum orthoferrite, has been extensively investigated for more than 60 years because of its G-type antiferromagnetic character [31], as well as for simultaneously exhibiting weak ferromagnetic [32] and ferroelectric [33] responses, so it can be classified as a multiferroic material [34]. Experimentally, the lanthanum orthoferrite  $\text{LaFeO}_3$  adopts an orthorhombic crystal structure, belonging to the space group  $\text{Pnmb}$  (# 62), with tolerance factor  $t = 0.951$  and octahedral distortions given by  $a^+b^-b^-$  [35]. On the other hand, the so-called lanthanum cobaltite  $\text{LaCoO}_3$  has been studied since 1953, showing a total effective magnetic moment greater than the value expected from Hund's rules and  $\text{Co}^{3+}$  electronic spin splittings [36]. Initially, the suggested explanations for this effect were based on contributions due to the appearance of  $\text{Co}^{3+}$  ions in the structure in octahedrally coordinated sites under strong crystal field intensity [37] and spin-orbit type effects, considering a cubic perovskite type structure with trigonal distortions [38]. The exotic electrical and magnetic properties, as well as the different

possible interactions, including the coexistence of low and high spin configurations of the Co cation have been analyzed for many years, including theoretical studies of electronic structure with variations in possible spin configurations and proposals for the occurrence of a transition between a low spin configuration and an intermediate spin state [39]. Despite the apparent similarity in the chemical formula of lanthanide cobaltite and lanthanide orthoferrite,  $\text{LaCoO}_3$  crystallizes in a rhombohedral structure, belonging to space group R-3c (# 167), with a tolerance factor  $t = 1.012$  and out-of-phase distortions on the three octahedral sub-axes according to Glazer's  $a^- a^- a^-$  notation, showing a mostly antiferromagnetic ordering, with incipient ferromagnetic coupling [40] and dielectric response [41]. The interesting properties exhibited by these two materials, as well as their substantial structural differences, in addition to the magnetic nature due to the crystalline field and the types of bonding of the  $\text{Co}^{3+}$  and  $\text{Fe}^{3+}$  cations with oxygen in the  $\text{Co-O}_6$  and  $\text{Fe-O}_6$  octahedra, have direct inference on the exotic physical properties they exhibit. These are the reasons why it is of particular interest to study a complex perovskite-type material from the union of these two simple perovskites to produce the double perovskite  $\text{La}_2\text{CoFeO}_6$  [42]. On the other hand, from the theoretical point of view, the correct determination of the electronic structure of materials containing 3d elements such as Co and Fe in the structure is not easy because of the complex splitting of low spin and high spin electrons due to the crystal field and their interactions with the oxygens in the tetrahedral coordination. Although some calculations have been reported [43], the Hubbard potential applied may not have been exactly the best fit to the experiment, so it is important to revisit the applied concepts, as well as the correction to the exchange potential and correlation considered in the calculations. When La is substituted by rare earths in orthoferrite, its structure remains [44] but its magnetic response depends on the specific cation, showing antiferromagnetism for  $R = \text{Er}$ , Dy [45], ferrimagnetism for  $R = \text{Sm}$  [46] and ferromagnetism for  $R = \text{Tb}$  [47]. On the other hand, the rare earth cobaltite  $\text{RCoO}_3$  crystallizes in an orthorhombic structure (space group Pbnm, #62), evidencing different magnetic responses depending on the cation R [48], with non-collinear antiferromagnetism-type character for  $R = \text{Tb}$  [49]. Due to the ferromagnetic character of the orthoferrite  $\text{TbFeO}_3$  and antiferromagnetic character of the cobaltite  $\text{TbCoO}_3$ , the study of the double perovskite  $\text{Tb}_2\text{FeCoO}_6$  is particularly interesting [50].

Therefore, the investigation of these materials, whose magnetic and electrical transport properties may have interesting implications for the prospects of application in spintronics technology, is of special interest.

## 2 Experimental Techniques

$(\text{La,Tb})_2\text{FeCoO}_6$  samples were produced via the solid reaction method starting from powdered oxides of  $(\text{La,Tb})_2\text{O}_3$ ,  $\text{Fe}_2\text{O}_3$  and  $\text{Co}_2\text{O}_3$  (Sigma-Aldrich, > 99.99% purity). The precursor oxides were dried at a temperature  $T = 120^\circ\text{C}$ , then weighed in stoichiometric proportions, using an analytical balance of 0.1 mg accuracy. The

mixture obtained was crushed in an agate mortar for 3 h. The resulting homogeneous powders were heated at 600 °C for 24 h in a Lindberg-Blue tube furnace, after which it was remixed for 30 min and pressed under the application of 4.5 kN in a 9 mm diameter die to form cylindrical tablet-shaped samples. The samples were then subjected to thermal sintering processes at 800 °C, 1000 °C and 1200 °C for 24 h each to ensure the grain growth process and densification of the samples. The structural analysis of the samples was performed by means of a PANalytical X'pert-Pro X-ray diffractometer ( $\lambda_{\text{CuK}\alpha} = 1.540598 \text{ \AA}$ ), in Bragg–Brentano configuration, with step of  $0.001^\circ$  in  $2\theta$  and time of 10 s. The structural analysis was performed by Rietveld type refinement to determine crystallographic properties of the material. For the surface morphological study, images were taken by scanning electron microscopy (SEM) in a Vega 3 TESCAN equipment. A semi-quantitative electron energy dispersive X-ray energy dispersive spectroscopy (EDS) analysis was performed to determine the composition of the samples. Complex impedance measurement as a function of temperature was carried out using an Agilent-4194A phase gain and impedance analyser, a Janis Research cryogenic system (VPF-475 model) and a Lake Shore 332 temperature controller. These measurements were performed at a temperature variation rate of 1.7 K/min and in a frequency range between 102 and 107 Hz. The I-V curve at room temperature was elaborated from the data measured in a Keithley-6517A DC electrometer and a sample holder with gold-plated silver contacts designed by the authors, which was adapted to the cryogenic system and the temperature controller. The band gap and energy excitation regimes at room temperature were examined by using a VARIAN Cary 5000 UV–Vis–NIR diffuse reflectance spectrophotometer (DRS), which has an integration sphere with a PMT/Pbs detector. The magnetic response was evaluated by means of magnetization measurements as a function of temperature, following the Zero Field Cooling (ZFC) and Field Cooled (FC) procedures under the application of varying magnetic field strengths. Likewise, magnetic hysteresis measurements were performed, varying the applied field intensity in isothermal curves at different temperatures. The equipment used to measure the magnetic response was a VSM-PPMS Quantum Design. Various temperature and applied field regimes were considered for the different measured samples.

### 3 Calculation Methods

As mentioned above, the calculations were performed by means of DFT, since it has been proven that in perovskite-type materials its results agree with those obtained experimentally [51–54]. For the study of the structural, cohesive, electronic and thermodynamic properties of complex perovskites, the VASP code was used, which is based on DFT and the Augmented Wave Projector (PAW) [55–60]. Since the Generalized Gradient Approximation (GGA) does not fully describe the system containing 3d-Fe, 3d-Co and 5d-La orbitals, the exchange and correlation energy was evaluated using the GGA with the inclusion of corrections to the Hubbard U potential (GGA + U) [50–54, 61]. Due to the ferromagnetic characteristic of the material, the value of U

was obtained following the method described for this type of magnetic ordering [62], finding optimal potentials  $U_{\text{Fe}} = 5.3$  eV for Fe and  $U_{\text{Co}} = 3.32$  eV for Co. The ion–electron interactions were described through the PAW [57–59] and all calculations were performed considering spin-polarized configurations. The kinetic energy cutoff for the plane wave expansion of the electronic wave function was 520 eV. Gratings of k-points defined according to the Monkhorst–Pack method [63] were used, where the convergence of the gratings was verified until an energetic accuracy higher than 1 meV/atom was obtained. The Methfessel-Paxton technique [64] with a mixing factor of 0.1 eV was adopted for filling the electronic levels. For these configurations, grids of  $9 \times 9 \times 7$  k-points were considered. These grids represent 284 k-points in the irreducible Brillouin zone. The conjugate gradient method was used to find stable ionic positions, with an energy value of 0.1 meV used as the convergence criterion for the total self-consistent energy calculations. The lattice parameters and internal coordinates of the unit cell were fully optimized by maintaining the spatial symmetry group of the crystal structure, until the forces were less than 30 meV/Å and the energy due to ionic relaxation was less than 1.0 meV/atom. These calculations were performed considering a monoclinic crystalline structure with space group  $P2_1/n$  (#14), in agreement with experimental results for  $(\text{La,Tb})_2\text{FeCoO}_6$  [42, 59]. To determine the Density of States (DOS) parameters, the total energy (E) and external pressure (P) were calculated for different volumes (V) varying around the equilibrium volume ( $V_0$ ) up to  $\pm 5\%$ , allowing relaxation of the internal coordinates. The bulk modulus ( $B_0$ ) and its pressure derivative ( $B'$ ) were obtained by fitting the pressure curves as a function of volume from the Murnaghan equation of state [65].

For the materials for which thermodynamic property calculations were performed, these were carried out following the Debye quasi-harmonic model [66, 67]. In this model, macroscopically measurable thermophysical properties are directly associated with the microscopic dynamics of the atoms within the material when subjected to external changes in pressure and temperature. Considering that the collective vibrations of the crystalline cells of solids occur in the form of phonons, the fundamental excitations associated with these thermodynamic properties can be comfortably calculated. In materials evidencing relatively high electrical resistivities, phonons play a particularly important role, giving relevant contributions to some properties such as specific heat and thermal expansion as a function of temperature. In this way, the crystal lattice vibrations can be expected to exhibit a harmonic character for temperature values below the Debye temperature of the material. In this work, the Debye quasi-harmonic model is applied as part of the study of atomic dynamics in the appropriate temperature regime.

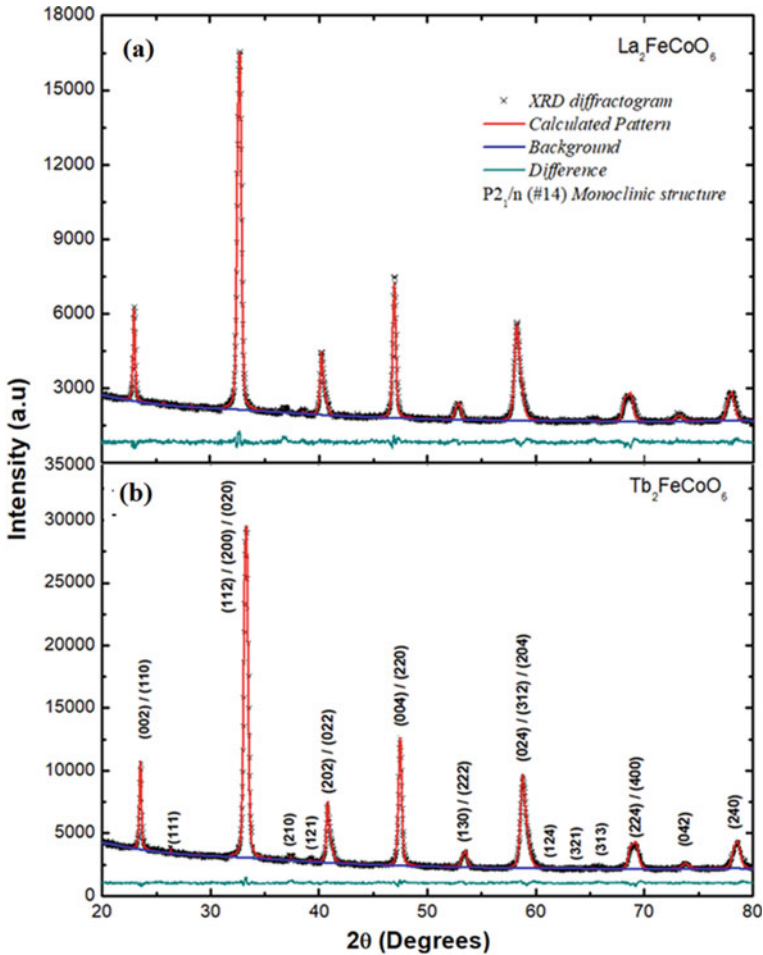


Fig. 1 Diffraction patterns obtained for materials a  $\text{La}_2\text{FeCoO}_6$  and b  $\text{Tb}_2\text{FeCoO}_6$

## 4 Semiconductor Ferromagnetic Features and Thermophysical Properties of Superstructured $(\text{La,Tb})_2\text{CoFeO}_6$ Double Perovskites

### 4.1 Structural Characteristics

The diffraction pattern shown in Fig. 1 was obtained under the same instrumental conditions specified in Sect. 2. Close observation of the diffractograms reveals practically the same reflection peaks for the materials  $\text{La}_2\text{FeCoO}_6$  and  $\text{Tb}_2\text{FeCoO}_6$ , corresponding to perovskite-type monoclinic structure belonging to the  $\text{P2}_1/\text{n}$  (#14) space group.

Although the structure is the same, for  $R = \text{Tb}$  a shift of the diffraction peaks to the right with respect to  $R = \text{La}$  is observed, which is related to the change in lattice parameters, as presented in Table 1 and Fig. 2, where the atomic distribution is exemplified from the results of the Rietveld analysis. This shift is related to a contraction of about 3% in the crystallographic cell of the material for  $R = \text{Tb}$  with respect to  $R = \text{La}$ . The structure depicted in Fig. 2 corresponds to a monoclinic perovskite, belonging to space group  $P2_1/n$ , which characterizes a primitive cell with rotational symmetry of two orders of  $180^\circ$  around a screw-shaped axis, a subsequent translation of half a cell parameter in the  $[010]$  direction and a sliding reflection plane perpendicular to the  $[010]$  direction.

The differences between the ionic radii of the constituent atoms of the material, together with the bond characteristics and electronic correlations, as well as the crystal field effects due to the presence of 3d orbitals in the octahedral coordinations, cause rotations and tilts of the octahedra that influence the magnetic and electric transport responses of the material. In Glazer's notation for octahedral distortions [68], this structure corresponds to the system denoted  $a^-b^+a^-$ , where the superscripts (+) indicate in-phase tilt and (−) out-of-phase tilt. Therefore, in the  $\text{R}_2\text{FeCoO}_6$  material the octahedra rotate out of phase along the  $a$  and  $c$  crystallographic axes, while they rotate in phase along the  $b$  axis. This is corroborated by the appearance of indexed reflections such as (004), (204) and (404) observed in Fig. 1, which are directly related to the in-phase octahedral tilt (*ood*) along the direction of the  $b$  cell parameter.

**Table 1** Lattice parameters, crystal distances and bond angles obtained from the Rietveld refinement

Cation	Anion	Distance (Å)	Bond angles degrees (°)	
La <sub>2</sub> FeCoO <sub>6</sub> crystal parameters; monoclinic angle 90.121(5)°				
Fe	O(1)	2.0250	φ <sub>1</sub>	162.7
Fe	O(2)	2.0187	φ <sub>2</sub>	162.7
Fe	O(3)	2.0107	φ <sub>3</sub>	162.8
Cell parameters (Å)				
Co	O(1)	1.8893	<i>a</i>	5.467(2)
Co	O(2)	1.8963	<i>b</i>	5.505(8)
Co	O(3)	1.9020	<i>c</i>	7.750(3)
Tb <sub>2</sub> FeCoO <sub>6</sub> crystal parameters; monoclinic angle: 89.983(5)°				
Fe	O(1)	2.0159	φ <sub>1</sub>	149.9
Fe	O(2)	2.0151	φ <sub>2</sub>	150.5
Fe	O(3)	2.0157	φ <sub>3</sub>	150.3
Cell parameters (Å)				
Co	O(1)	1.8935	<i>a</i>	5.251(2)
Co	O(2)	1.8931	<i>b</i>	5.437(5)
Co	O(3)	1.8938	<i>c</i>	7.550(3)

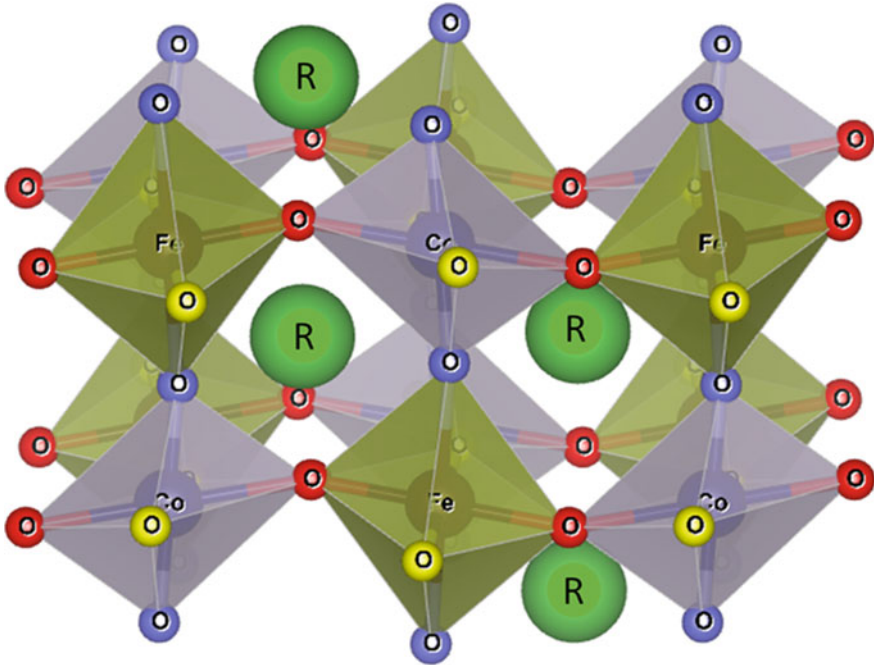


**Fig. 2** Crystallographic structure of  $R_2FeCoO_6$  ( $R = La, Tb$ ) established from Rietveld refinement of XRD experimental data

Table 1 shows evident differences in the Fe-O and Co-O interatomic distances for the three sub-axes, as well as in the  $\varphi_i$  bond angles, both for  $R = La$  and  $R = Tb$ . These differences, which can be clearly seen in Fig. 3, have an impact on the so-called tolerance factor [69, 70]. The obtained values  $\tau_{La} = 0.978$  and  $\tau_{Tb} = 0.921$  are far from the ideal value ( $\tau = 1$ ) corresponding to the cubic perovskite structure, evidencing the degree of structural distortion of the materials analyzed. Meanwhile, the presence of the incipient peaks (111) and (313) in the diffraction pattern suggest reflections due to the occurrence of cation ordering due to the formation of a superstructure with the Fe and Co cations alternating along the crystallographic axes [71, 72].

## 4.2 Ferromagnetic Behavior

A first part in the process of studying the magnetic response is shown in Fig. 4, where graph 4a presents the magnetic susceptibility  $R = La$ , in a temperature range between 50 and 330 K, under the application of magnetic fields of 0.5, 2.0 and 10 kOe, while graph 4b shows the magnetic susceptibility for  $R = Tb$ , in the temperature range  $5 K < H < 340 K$  and in external fields of 2.0, 5.0, 10 and 20 kOe. In both cases

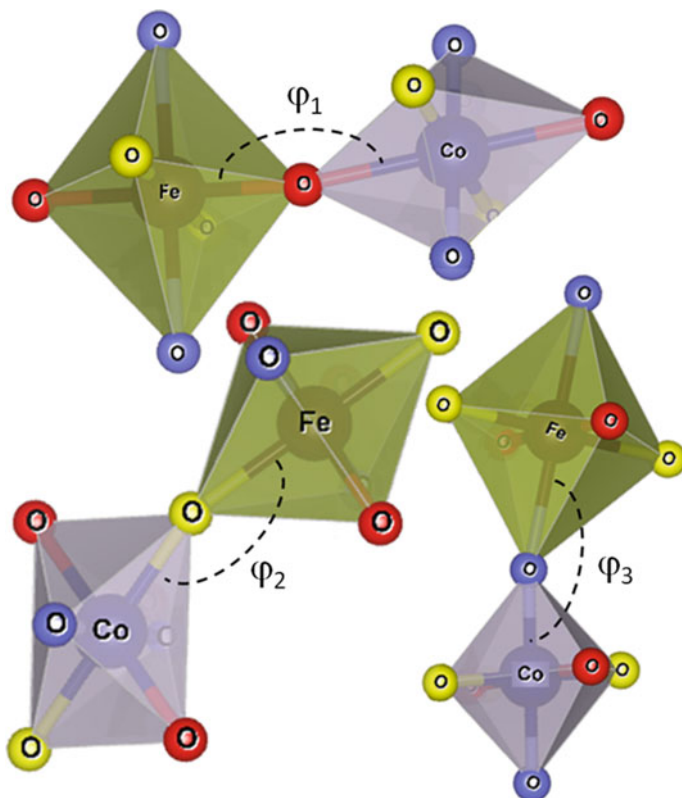
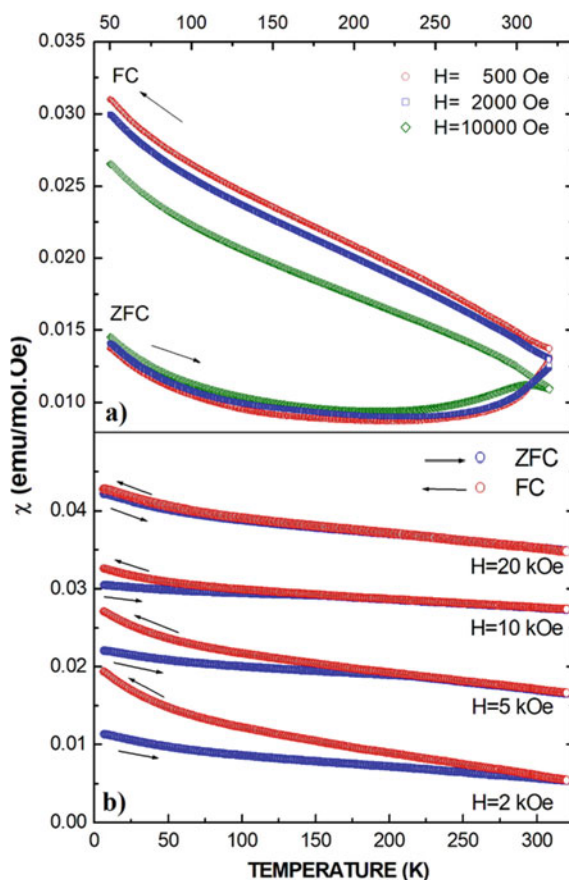


**Fig. 3** Fe-O<sub>1</sub>-Co, Fe-O<sub>2</sub>-Co and Fe-O<sub>3</sub>-Co bond angles between Fe-O<sub>6</sub> and Co-O<sub>6</sub> octahedra in the R<sub>2</sub>FeCoO<sub>6</sub> double perovskites

the thermal procedures applied were the well-known Zero Field Cooling (ZFC) and Field Cooled (FC). For both R = La and R = Tb, the difference in the magnetic field trajectory as a function of temperature between the ZFC and FC recipes suggests the occurrence of some kind of magnetic disorder giving rise to irreversibility effects, with typical features of spin glasses [73]. In double perovskite-type materials, this behavior is attributed to the cationic disorder of the B and B' ions in the A<sub>2</sub>BB'O<sub>6</sub> structure [54]. Meanwhile, for R = La it is not possible to establish the value of the irreversibility temperature, while for R = Tb it can not only be determined but it also evidences a shift towards the lower temperature regime with increasing applied field. This result reveals that the material with R = Tb contains a higher cationic ordering of Fe and Co ions than the compound with R = La. In this ordering, the Fe and Co cations tend to intercalate along the crystallographic axes, ensuring a higher correlation between their magnetic moments in the unit cell and along the whole structure, while the lack of correlation between the magnetic moments in the R = La is due to the low tendency of the crystalline arrangement to form a salt-rock type



**Fig. 4** Magnetic susceptibility measured at low temperatures under the application of various magnetic field intensities for  $\text{La}_2\text{FeCoO}_6$  (a) and  $\text{Tb}_2\text{FeCoO}_6$  (b) double perovskites



superstructure [74]. Due to the non-formation of a superstructure in which the  $\text{FeO}_6$  and  $\text{CoO}_6$  octahedra adopt an alternating distribution along the structure causes the breakdown of the correlation between magnetic domains, which is characteristic of ordered ferromagnetic materials, so that the ferromagnetism remains in the material but the lack of correlation between domains gives rise to the difference between the ZFC and FC responses in magnetic susceptibility. Evidence for this interpretation is in the presence of the peak (111) in the diffractogram corresponding to  $R = \text{Tb}$  in Fig. 1b that is not observed in Fig. 1a for  $R = \text{La}$ , and which is the fingerprint of cation-ordered superstructure formation in double perovskites [75].

The irreversible character could also be associated with effects due to octahedral distortions such as the tilts and rotations of  $\text{FeO}_6$  and  $\text{CoO}_6$ , which take place in phase along the b-direction of the subcell of the octahedrons and out of phase in the a and c directions, introducing blocking of the magnetic domains at low temperatures and making it difficult to align the moments with the applied field during the ZFC procedure. The occurrence of irreversibility only takes place in the ferromagnetic

state, which allows classifying this material and can be corroborated through the finite value of magnetization observed in the susceptibility curves for the two materials under study. This magnetically ordered behavior occurs throughout the temperature region under study. The experimental confirmation of the ferromagnetic response in the two compounds was carried out by measurements of magnetization as a function of the applied magnetic field in isothermal curves at 50, 100, 200 and 300 K for  $R = \text{La}$  (Fig. 5a) and 5, 25, 50, 100, 200 and 300 K for  $R = \text{Tb}$  (Fig. 5b). The applied external field regime was  $-40 \text{ kOe} < H < 40 \text{ kOe}$ .

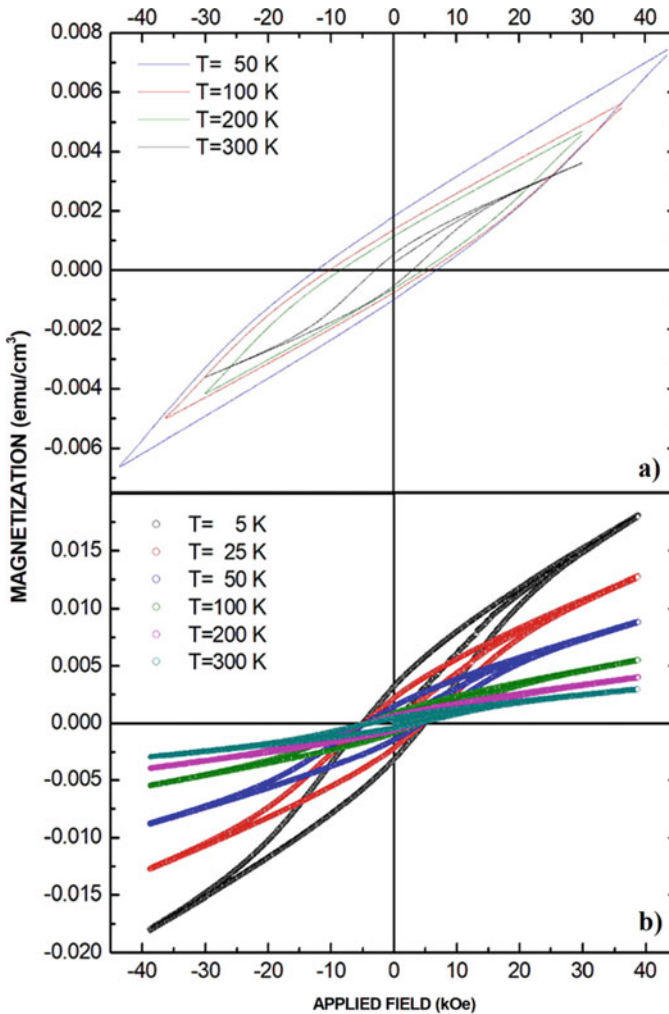
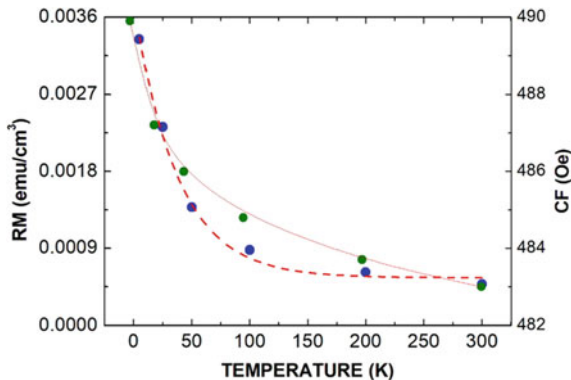


**Fig. 5** Hysteretic magnetization curves as a function of applied magnetic field for rare earth ferrocobaltite with  $R = \text{La}$  (a) and  $R = \text{Tb}$  (b)

**Fig. 6** Decrease in remnant magnetization (left scale) and coercive field (right scale) values with increasing temperature for double perovskite-type lanthanide ferrocobaltites



As predicted from the magnetic susceptibility curves, Fig. 5 evidences a clearly hysteretic behavior characteristic of a ferromagnetic type response for all cases studied at room temperature and below for both R = La (Fig. 5a) and R = Tb (Fig. 5b). Similarly, it is observed that with increasing temperature, there is a decrease in the number of aligned magnetic domains because the increase in entropy decreases the effective exchange energy that characterizes the ferromagnetic feature. For this reason, with increasing temperature, not only the magnetization decreases, as previously observed in the susceptibility curves, but also the magnetic energy of the system decreases as evidenced in the area enclosed by the hysteresis curve. Therefore, the characteristic magnetic parameters are proportionally affected by the change in temperature, observing a systematically decreasing behavior of the coercive field (CF) and remnant magnetization (RM) values. The behavior of the coercive field and remanent magnetization with change in temperature is shown in Fig. 6.

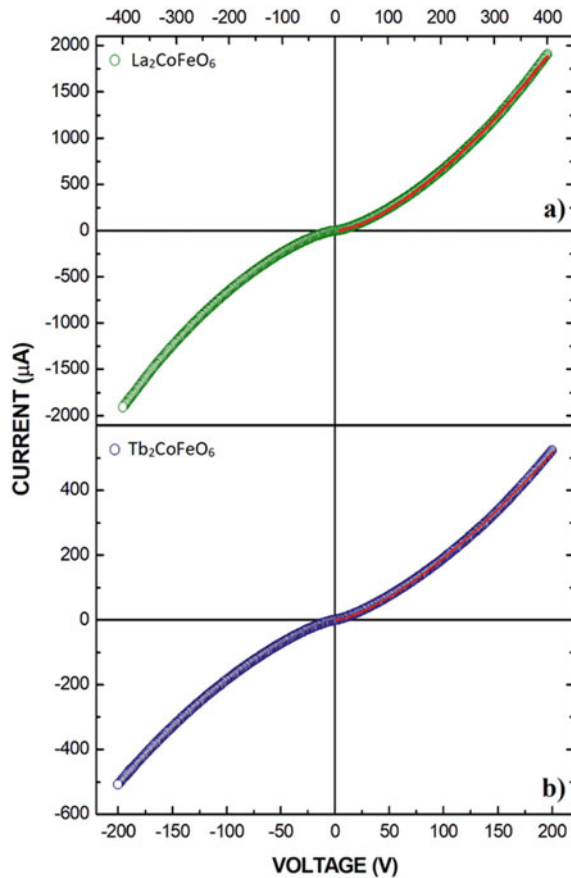
The response obtained for  $R_2\text{FeCoO}_6$  decays exponentially, following an empirical law, where,  $M_o^{La} = 1.12 \text{ emu/g}$  and  $M_o^{Tb} = 2.73 \text{ emu/g}$  represent the spontaneous remanent magnetization for R = La and R = Tb at T = 0 K,  $a_{La} = 2.15 \text{ emu/g}$  and  $a_{Tb} = 15.86 \text{ emu/g}$  are phenomenological constants and  $k_B T_o^{La} = 1.14 \times 10^{-22} \text{ J}$  and  $k_B T_o^{Tb} = 5.52 \times 10^{-22} \text{ J}$  are the magnetic interaction energy corresponding to the exchange potential between the ferromagnetic moments. The obtained value is lower than the energy values calculated for the interaction between ferromagnetic spins in Fe ( $12.1 \times 10^{-22} \text{ J}$ ) and Co ( $51.5 \times 10^{-22} \text{ J}$ ) [76], showing that the ferromagnetic interaction in  $\text{Tb}_2\text{FeCoO}_6$  requires a lower energy cost than in monatomic systems of Fe or Co. Likewise, the coercive fields vary slightly with increasing temperature but decays roughly following Kneller's law [77, 78] given by, where  $H_o^{La} = 108.16 \text{ Oe}$  and  $H_o^{Tb} = 492.64 \text{ Oe}$  represent the coercive fields independent of temperature,  $T_B^{La} = 0.0011 \text{ K}$  and  $T_B^{Tb} = 0.0035 \text{ K}$ , are the blocking temperatures due to the granular feature of the samples, and  $a^{La} \gg 0.35$  and  $a^{Tb} \gg 0.5$  are the Bloch's exponent, which has been observed in ferromagnetic nanoparticles randomly oriented [79], multilayers [80] and bulk spinels [81], suggesting that the variation of the coercive field is sensitive to thermal activation mechanisms, with contributions due to the

occurrence of magnetic multidomain states due to the microstructural anisotropy of crystallites and grains in the material [77].

### 4.3 Electric Response

I-V response measurements were experimentally elaborated with the objective of analyzing the behavior of the electrical response of the materials at room temperature, under application of voltage ranges between  $-400$  V and  $400$  V for  $R = \text{La}$  and between  $-200$  V and  $200$  V for  $R = \text{Tb}$ . The curves obtained are shown in Fig. 7, which clearly shows that the change in applied voltage causes a nonlinear response of the current in the material. The trend followed by the curve has the characteristics observed in varistor type semiconductors [53]. As the voltage increases, the current increases following a power law of the type. Initially, increasing the voltage induces

**Fig. 7** I-V characteristic curves measured on  $\text{La}_2\text{FeCoO}_6$  (a) and  $\text{Tb}_2\text{FeCoO}_6$  (b) samples



small currents due to the occurrence of polarization effects and mixing between dielectric responses and granular boundary relaxation effects. Subsequently, electrons promoted across the gap from the semiconductor valence band conduct, tending to linearize the behavior of the I-V curve for high applied voltages. The fit with the potential spike for the two materials yields the following results:  $I_o^{La} = 0.19 \text{ mA}$ ,  $I_o^{Tb} = 0.27 \text{ mA}$  and  $b \gg 1.53$ ,  $b^{Tb} \gg 1.43$ . This behavior implicitly contains an additional thermal response that contributes to deviating the electrical response from Ohm's law. Thus, the power dissipation is expected to increase rapidly as the applied voltage increases. The dissipation, then, has contributions due to the appearance of Schottky barriers formed by the grain boundaries, which give rise to the nonlinear characteristic of the I-V curve [53]. These barriers are formed by micro-junctions in which a pair of grains can be seen as two consecutive Zener diodes, such that the intergranular boundaries along the material adopt the behavior of resistors that generate currents like those expected in a varistor diode. For high voltage values, the resistance follows the expected ohmic trend, but in this regime the resistivity decreases because the intragranular contributions are more relevant than the intergranular ones. Therefore, the electrical transport due to microstructural defects can be modeled through equivalent electrical circuits that are related to the intra- and intergranular transport currents within the material [82]. According to the model, the I-V figure of merit of the varistor has the form of a power law, as mentioned above, where  $I_o$  is a free constant corresponding to the nonlinear coefficient, whose value close to  $3/2$  is predicted by the quasi-hydrodynamic equations of semiconductors and was attributed to regions of the sample with evanescent carriers [83, 84].

#### 4.4 *Electronic Structures*

It is well known that the macroscopically observable properties of perovskite-type materials can be explained through the study of their electronic behavior [85, 86]. For this reason, the density of electronic states of the compounds  $R_2\text{FeCoO}_6$  following the procedure detailed in Sect. 3. The base magnetic state of the material was considered through ferromagnetic coupling between Fe-O-Fe, Fe-O-Co and Co-O-Co atomic bonds, in addition to possible antiferromagnetic ordering configurations between the aforementioned atoms. In order to explore different configurations of antiparallel spin distribution in the [001], [110] and [111] directions for the antiferromagnetic coupling cases, a  $2 \times 2 \times 2$  supercell of the double perovskite was used. For the ferromagnetic case, all the spins due to the magnetic moments of Fe and Co atoms were considered to be oriented in the direction of application of the external magnetic field. By minimizing the energy for all the mentioned cases, the result reveals that the lowest energy distribution corresponds to a ferromagnetic type of exchange interaction. Since the GGA does not satisfactorily describe the system for the 3d-Fe, 3d-Co, 5d-La and 4f-Tb orbitals, it became necessary to calculate the exchange and correlation energy by means of the generalized gradient approximation including the Hubbard U-correction (GGA + U) [87]. From the ferromagnetic nature of the material, evidenced

both in experimental results and by the energy minimization process, the U correction in the potential was established following the method reported by Liechtenstein et al. [62]. The DOS results as a function of energy are presented in Fig. 8 for (a)  $\text{La}_2\text{FeCoO}_6$  and (b)  $\text{Tb}_2\text{FeCoO}_6$  compounds.

In Fig. 8 the zero-energy value is labeled as Fermi energy  $E_F$ . The correction applied to the exchange potential and correlation was  $U = 5.3$  eV as it was the most in agreement with the experimental results [61]. The first feature observed in Fig. 8 for the total DOS in both materials is the asymmetric character of their electronic states between the up and down spin orientations. For spin up polarization the band gaps clearly correspond to an insulator with values  $E_g^{\text{La}^+} > 3.6$  eV and  $E_g^{\text{Tb}^+} > 3.8$  eV, while for spin down polarization the two materials exhibit semiconducting behavior with  $E_g^{\text{La}^-} = 1.10$  eV and  $E_g^{\text{Tb}^-} = 1.19$  eV. The obtained valence and conduction band configurations for the up and down spin orientations of the compounds with  $R = \text{La}$  and  $R = \text{Tb}$  are summarized in Fig. 9.

The generation of a spin-polarized charge transport channel has been theoretically predicted and experimentally measured in ferromagnetic semiconductors [88, 89]. This type of insulator-semiconductor distribution, which here we will call half-semiconductor in analogy with half-metallic behavior, is unusual in double

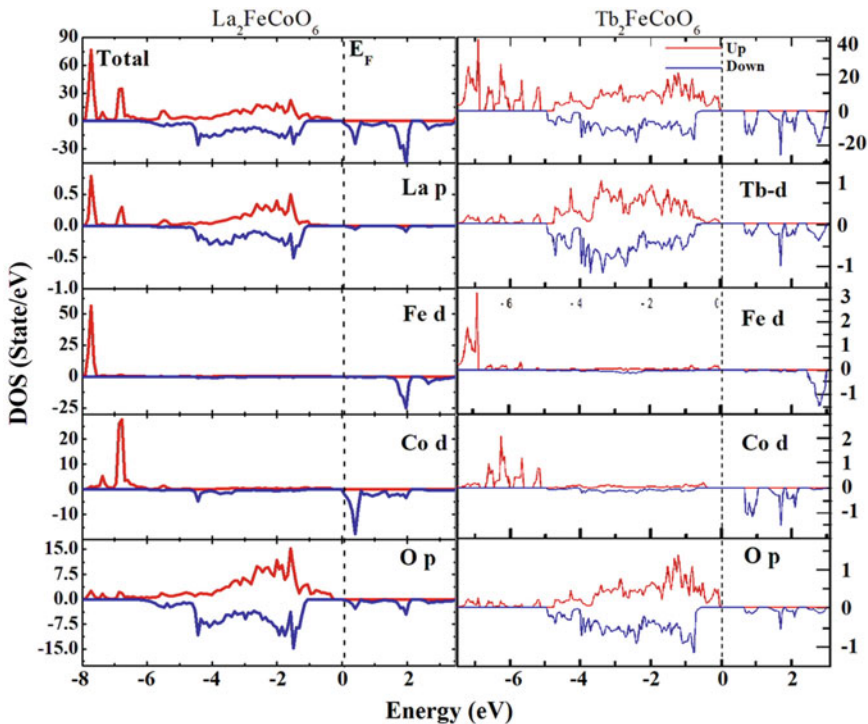


**Fig. 8** Total and partial DOS calculated for **a**  $\text{La}_2\text{FeCoO}_6$  and **b**  $\text{Tb}_2\text{FeCoO}_6$  double perovskites

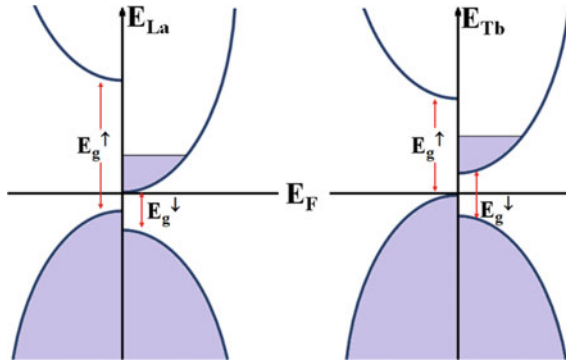


**Fig. 9** Schematics of the valence and conduction bands with spin polarization for  $\text{La}_2\text{FeCoO}_6$  and  $\text{Tb}_2\text{FeCoO}_6$  ferrocobaltites

perovskites based on essentially metallic cations such as Fe and Co. Meanwhile, the occurrence of ferromagnetism and half-semiconductivity in the same crystalline structure is really interesting because it differs substantially from the case of dilute magnetic semiconductors, where there could be no guarantee of control in the positioning of magnetic moments in specific sites of the structural cells of the compound, besides the risk of having interstitial magnetic atoms outside the crystalline cells of the semiconductor material acting as matrix. These results allow inferring possible applications in devices that require magnetic control for the transport of both electric charge and spin moments, what we defined before as spintronics.

Analysis of the hybridizations between the outer electron shells of the atoms in the octahedrally coordinated structural octahedra with the oxygen anions suggest that the microscopic mechanism associated with the ferromagnetic behavior is of the super-exchange type between the high spin electrons of  $\text{Fe}^{2+}_{3d}$  ( $e_g$ ) and the low spin electrons of  $\text{Co}^{4+}_{3d}$  ( $t_{2g}$ ) mediated by the  $\text{O}^{2-}_{2p}$  orbitals, as shown in the diagram in Fig. 10.

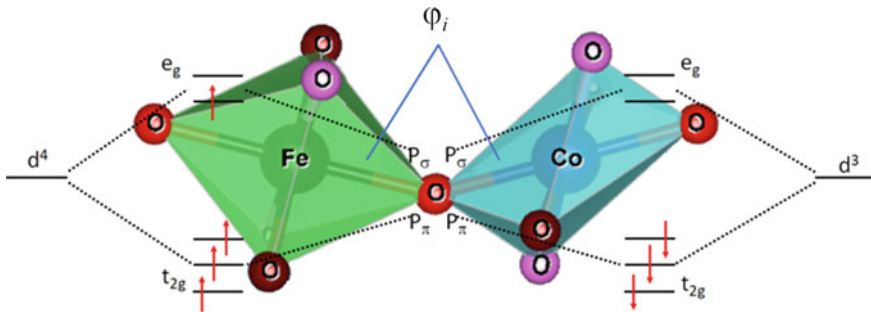


**Fig. 10** Super-exchange interaction between  $e_g$ -moments of Fe and  $t_{2g}$ -moments of Co, giving rise to a weak ferromagnetic response in  $(\text{La},\text{Tb})_2\text{FeCoO}_6$  complex perovskites

In this scenario, the interaction through the pi-bonds Fe-O-Co between the FeO<sub>6</sub> and CoO<sub>6</sub> octahedra, favours a total antiferromagnetic ordering, while through the sigma-bonds it can be observed that the bond angle  $90^\circ < \Phi < 180^\circ$  promotes ferromagnetic dominance through a Goodenough-Kanamori-Anderson type interaction [90].

#### 4.5 Thermophysical Properties

An almost unexplored feature in double perovskite-type materials is the influence of the change in temperature and external pressure on their physical properties. These behaviors could provide relevant information in the study of the macroscopic responses that characterize this family of materials, so their modeling is of particular interest. Considering that during the electronic structure calculation process the equation of state was obtained, it was used in Debye's quasi-harmonic approximation formalism [91], facilitating the calculation of thermophysical properties for (La,Tb)<sub>2</sub>FeCoO<sub>6</sub> materials in the 0 K < T < 900 K temperature regime, obtaining isobaric curves for applied pressures up to 5 GPa. The results of the specific heat at constant volume,  $C_V(T,P)$ , are shown in Fig. 11, where it can be observed that for T > 870 K the Dulong-Petit limit is reached, where the trend of the specific heat becomes independent of the temperature for values  $C_{DP}^{La} = 491$  J/mol.K (Fig. 11a) and  $C_{DP}^{Tb} = 493$  J/mol.K (Fig. 11b). It is evident from the insets of Figs. 11a,b that the specific heat at constant pressure,  $C_P(T,P)$ , has a behavior similar to that of  $C_V(T,P)$  at T < 450 K but does not reach the Dulong-Petit limit in the temperature regime considered in the present work.

A literature search shows that more symmetric perovskite-type cells, such as cubic ones, present low  $C_{DP}$  values, with maximum values of 240 J/mol.K [30], which corresponds to 53% of the value obtained for monoclinic (pseudo-orthorhombic) structures of (La,Tb)<sub>2</sub>FeCoO<sub>6</sub> materials. On the other hand, in perovskites with less

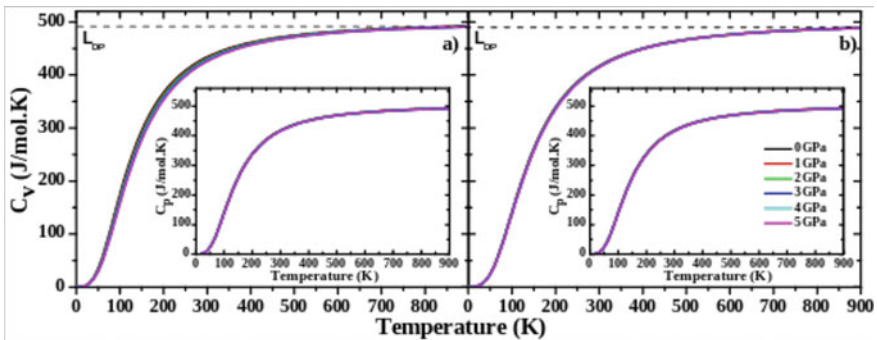


**Fig. 11** Curves of  $C_V(T,P)$  for the La<sub>2</sub>FeCoO<sub>6</sub> (a) and Tb<sub>2</sub>FeCoO<sub>6</sub> (b) double perovskites. The insets represent the respective  $C_P(T,P)$  behaviors



symmetric structures the  $C_{DP}$  value exceeds 475 J/mol.K [53], showing that at low crystalline symmetries effects appear that give rise to nonharmonic contributions to the thermodynamic functions. This anharmonicity seems to increase with structural complexity [92, 93]. The density of states in Fig. 8 shows a very incipient contribution of the La-5p, La-5d and La-6s orbitals to the specific heat, while the majority effect corresponds to the O-2p orbitals. This suggests that at high temperatures the electronic contributions could be superimposed on the phonon contributions produced by the vibrations in the cation-oxygen bonds, as a product of the large absorption of thermal energy, significantly increasing the value of the specific heat.

The dependence of the coefficient of thermal expansion with temperature and pressure calculated for  $(La,Tb)_2FeCoO_6$  materials is shown in Fig. 12. The result shows that for values  $T < 300$  K, the  $\alpha(T,P)$  curves present an abrupt growth with increasing thermal energy, which is expected because, in addition to the strongly anisotropic character originating from the elastic properties of the material, the dramatic octahedral distortions, as well as the elongation of the structural cell along the crystallographic axes, contribute to the appearance of rotations and inclinations of the  $FeO_6$  and  $CoO_6$  octahedra. This behavior occurs because the increase in the thermal energy supplied generates a substantial increase in entropy, randomizing the physical properties and intensifying the phononic effects coming from the vibrations in the intermolecular bonds [67]. At  $T > 300$  K the curve slows down and the change with increasing temperature is less significant because the growth in cell volume tends to stabilize at its maximum value, below which the increase in the coefficient of thermal expansion becomes asymptotic. On the other hand, the effect of the applied pressures partially neutralizes the vibrational activity, so that the increase in the value of the external pressure produces a systematic decrease in entropy which, in turn, shifts the thermal expansion curves towards lower values.

Figure 13 shows the behavior of the Grüneisen parameter  $\gamma(T,P)$ , which grows nonlinearly with increasing thermal energy and decreases with increasing applied pressure. This result takes place due to the variations caused in the vibrational

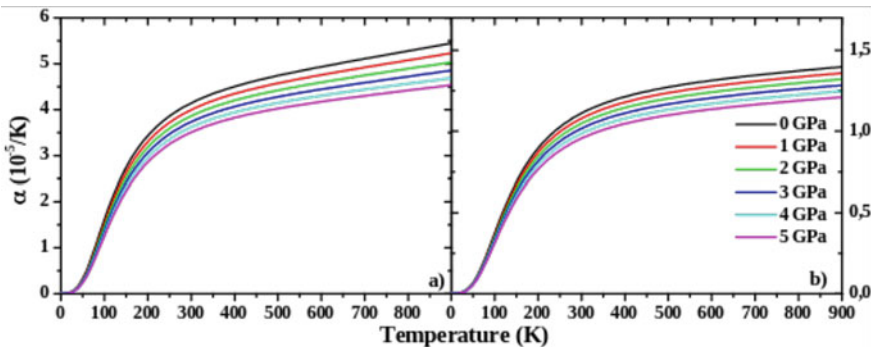


**Fig. 12** Dependence of the coefficient of thermal expansion with temperature and pressure for the  $R_2FeCoO_6$  ferrocobaltites with  $R = La$  (a) and  $R = Tb$  (b)

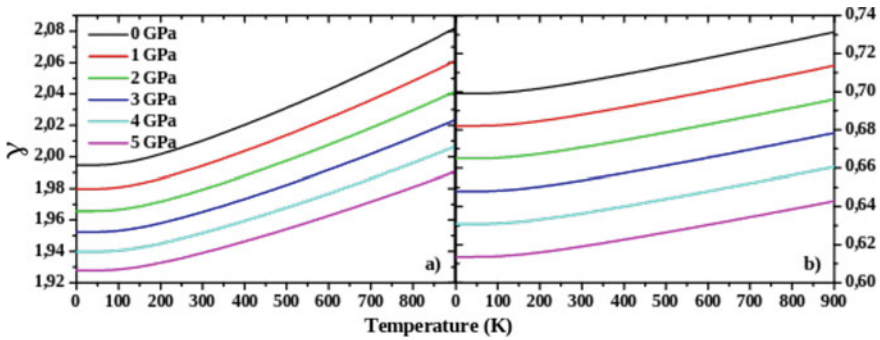


**Fig. 13** Grüneisen parameter  $\gamma(T,P)$  for the  $\text{La}_2\text{FeCoO}_6$  (a) and  $\text{Tb}_2\text{FeCoO}_6$  (b) materials

frequency of the crystal lattice, increasing the elastic waves of the system and increasing the Debye temperature and making the contribution of phonons large due to the low structural symmetry of the system [85]. On the other hand, as the pressure increases, the vibrational frequency of the cation-oxygen bonds throughout the structure also increases, while, simultaneously, the effect of the temperature increase expands the crystalline cells, causing an increase in the wavelength of these vibrations and promoting a decrease in the vibrational frequencies that shifts the Grüneisen parameter curves towards lower values.

## 5 Conclusions

Rietveld analysis of experimental XRD data of the solid-reacted  $(\text{La}, \text{Tb})_2\text{FeCoO}_6$  material reveals its crystallization in a monoclinic superstructure of the double perovskite type belonging to space group  $P2_1/n$  (#14). The unit cell contains distortions due to differences in the sizes and orientation of the  $\text{FeO}_6$  and  $\text{CoO}_6$  octahedra, as well as the angles of the O-Fe-O and O-Co-O bonds along the basal and apical octahedral axes. Magnetic susceptibility reveals magnetic domain disorder effects, which cause ferromagnetic long-range order breaking, leading to irreversibility between curves measured through the ZFC and FC procedures, similar to those characterizing spin glasses. Meanwhile, the magnetization curves exhibit a hysteretic behavior characteristic of weak ferromagnetic materials, which is maintained up to room temperature, with values of the coercive field following Kneller's law in its dependence on temperature. On the other hand, the I-V curves obtained are semiconductor type with strong varistor type tendency, dramatically influenced by the granular nature of the materials.

The results of density of states calculations suggest that the material adopts an antiferromagnetic structure, in which the crystal field effects, and the type of chemical bonding promote a weak ferromagnetic response through a superexchange type mechanism such as that due to a Goodenough-Kanamori-Anderson type interaction.

The energy bands evidence an asymmetry between the spin up and down channels, creating a lower band-gap for one of the spin orientations than for the other, which gives rise to polarized spin currents in the semiconductor ferromagnetic material, suggesting its applicability in spintronic devices such as the so-called spin transistors.

## References

1. Moore, G.E.: Cramming more components onto integrated circuits. *Electronics* **38**(8) April 19 (1965)
2. Kaur, I., Yadav, S., Singh, S., Kumar, V., Arora, S., Bhatnagar, D.: *Solid State Phenom.* **222**, 99 (2015)
3. Rahman, A.: A review on semiconductors including applications and temperature effects in semiconductors. *Am. Sci. Res. J. Eng. Technol. Sci. (ASRJETS)* **7**(1), 50–70 (2014)
4. Comstock, R.L.: Review modern magnetic materials in data storage. *J. Mater. Sci: Mater. Electron.* **13**, 509–523 (2002)
5. Wolf, S.A., Lu, J., Stan, M.R., Chen, E., Tregger, D.M.: The Promise of Nanomagnetism and Spintronics for Future Logic and Universal memory *IEEE* (2010)
6. Hirohata, A., Yamada, K., Nakatani, Y., Prejbeanu, I.-L., Diény, B., Pirro, P., Hillebrands, B.: Review on spintronics: Principles and device applications. *J. Magn. Magn. Mater.* **509**, 166711 (2020)
7. Baibich, M.N., Broto, J.M., Fert, A., Nguyen Van Dau, F., Petroff, F., Etienne, P., Creuzet, G., Friederich, A., Chazelas, J.: *Phys. Rev. Lett.* **61**, 2472 (1988)
8. Jin, S., Tiefel, T.H., McCormack, M., Fastnacht, R.A., Ramesh, R., Chen, L.H.: Thousandfold change in resistivity in magnetoresistive La-Ca-Mn-O films. *Science* **264**, 413–415 (1994)
9. Bonilla, C.M., Landínez Téllez, D.A., Arbey Rodríguez, J., Vera Lopez, E., Roa-Rojas, J.: Half-metallic behavior and electronic structure of Sr<sub>2</sub>CrMoO<sub>6</sub> magnetic system, *Physica B: Condensed Matter* **398** (2), 208–211 (2007)
10. Nogués, J., Schuller, I.K.: Exchange bias. *J. Magn. Magn. Mat.* **192**, 203 (1999)
11. Palkar, V.R., Malik, S.K.: *Solid State Commun.* **134**, 783 (2005)
12. Wolf, S.A., Lu, J., Stan, M.R., Chen, E., Treger, D.M.: *Proc IEEE* **98**, 2155 (2010)
13. Bonanni, A., Dietl, T.: A story of high-temperature ferromagnetism in semiconductors. *Chem. Soc. Rev.* **39**, 528–539 (2010)
14. Chocho, J., Postava, K., Čada, M., Vanwolleghem, M., Halagačka, L., Lampin, J.-F., Pištora, J.: *AIP Adv.* **6**, 155021 (2016)
15. Chen, L., Yan, S., Xu, P.F., Lu, J., Wang, W.Z., Deng, J.J., Qian, X., Ji, Y., Zhao, J.H.: *Appl. Phys. Lett.* **95**, 182505 (2009)
16. Gupta, A., Zhang, R., Kumar, P., Kumar, V., Kumar, A.: *Magnetochemistry* **6**, 15 (2020)
17. Jiang, S., Hu, T., Gild, J., Zhou, N., Nie, J., Qin, M., Harrington, T., Vecchio, K., Luo, J.: *Scr. Mater.* **142**, 116 (2018)
18. Triana, C.A., Landínez Téllez, D.A., Roa-Rojas, J.: *J. Alloys Compd.* **516**, 179 (2012)
19. Cuervo Farfán, J.A., Parra Vargas, C.A., Viana, D.S.F., Milton, F.P., Garcia, D., Landínez Téllez, D.A., Roa-Rojas, J.: *J. Mater. Sci: Mater. Electron.* **29**, 20942 (2018)
20. Hazen, R.M.: Perovskites. *Sci. Am.* **258**, 74–81 (1988)
21. Llamasa, D.P., Landínez-Téllez, D.A., Roa-Rojas, J.: Magnetic and structural behavior of Sr<sub>2</sub>ZrMnO<sub>6</sub> double perovskite. *Phys B.* **404**, 2726–2729 (2009)
22. Moya, X.A.V., Cardona, R., Hernández, J.I.V., Téllez, D.A.L., Roa-Rojas, J.: *J. Electron. Mater.* **47**(7), 3421–3429 (2018)
23. Cuervo Farfán, J.A., Aljure García, D.M., Cardona, R., Arbey Rodríguez, J., Landínez Téllez, D.A., Roa-Rojas, J.: *J. Low Temper. Phys.* **186** (5–6), 295–315 (2017)

24. Cuervo Farfán, J.A., Castellanos Acuña, H.E., Landínez Téllez, D.A., Roa-Rojas, J.: Structural, magnetic, and electrical features of the Nd<sub>2</sub>SrMn<sub>2</sub>TiO<sub>9</sub> perovskite-like compound. *Physica Status Solidi (b)* **253** (6), 1127–1132 (2016)
25. Pilo, J., Miranda, A., Trejo, A., Carvajal, E., Cruz-Irisson, M.: Bidimensional perovskite systems for spintronic applications. *J. Mol. Model.* **23**, 322–325 (2017)
26. Maiti, A., Pal, A.J.: Effect of cation occupancy ordering in double perovskites to overcome hurdles in carrier transport: Cs<sub>2</sub>AgBiBr<sub>6</sub> as a case study. *J. Phys. Chem. C* **125**(29), 16324–16333 (2021)
27. King, G., Woodward, P.M.: *J. Mater. Chem.* **20**, 5785–5796 (2010)
28. Benedek, N.A.: *Inorg. Chem.* **53**, 3769–3777 (2014)
29. Téllez, D.A.L., Buitrago, D.M., Barrera, E.W., Roa-Rojas, J.: Crystalline structure, magnetic response and electronic properties of RE<sub>2</sub>MgTiO<sub>6</sub> (RE = Dy, Gd) double perovskites. *J. Mol. Struct.* **1067**, 205–209 (2014)
30. Deluque Toro, C.E., Mosquera Polo, A.S., Gil Rebaza, A.V., Landínez Téllez, D.A., Roa-Rojas, J.: *J. Low Temp. Phys.* **192**, 265–285 (2018)
31. Koehler, W.C., Wollan, E.O.: Neutron-diffraction study of the magnetic properties of perovskite-like compounds LaBO<sub>3</sub>. *J. Phys. Chem. Solids* **2**, 100 (1957)
32. Phokha, S., Pinitsoontorn, S., Maensiri, S., Rujirawat, S.: Structure, optical and magnetic properties of LaFeO<sub>3</sub> nanoparticles prepared by polymerized complex method. *J. Sol-Gel Sci. Technol.* **71**, 333 (2014)
33. Acharya, S., Mondal, J., Ghosh, S., Roy, S.K., Chakrabarti, P.K.: Multiferroic Behavior of Lanthanum Orthoferrite (LaFeO<sub>3</sub>). *Mater. Lett.* **64**, 415 (2010)
34. Spaldin, N.A.: Multiferroics beyond electric-field control of magnetism. *Proc. R. Soc. A* **476**, 20190542 (2020). <https://doi.org/10.1098/rspa.2019.0542>
35. Dann, S.E., Currie, D.B., Weller, M.T., Thomas, M.F., Al-Rawwas, A.D.: *J. Solid State Chem.* **109**, 134–144 (1994)
36. Jonker, G.H., Van Santen, J.H.: Magnetic compounds with perovskite structure III. ferromagnetic compounds of cobalt. *Physica* **19**, 120 (1953)
37. Goodenough, J.B.: An interpretation of the magnetic properties of the perovskite-type mixed crystals La<sub>1-x</sub>Sr<sub>x</sub>CoO<sub>3-λ</sub>. *J. Chem. Phys. Solids* **6**, 287 (1958)
38. Naiman, C.S., Gilmore, R., DiBartolo, B., Linz, A., Santoro, R.: Lanthanum rhodium and lanthanum cobalt oxides. *J. Appl. Phys.* **36**, 1044 (1965)
39. Korotin, M.A., Ezhov, S.Y., Solovyev, I.V., Anisimov, V.I., Khomskii, D.I., Sawatzky, G.A.: Electronic and spin configurations of Co<sup>3+</sup> and Ni<sup>3+</sup> ions in oxides of K<sub>2</sub>NiF<sub>4</sub> structure: a magnetic susceptibility study, *Phys. Rev. B* **54**, 5309 (1996)
40. Durand, A.M., Belanger, D.P., Booth, C.H., Ye, F., Chi, S., Fernandez-Baca, J.A., Bhat, M.: *J. Phys.: Condens. Matter* **25**, 382203 (2013)
41. Sudheendra, L., Seikh, M.D.M., Raju, A.R., Narayana, C., Rao, C.N.R.: *Ferroelectrics* **306**, 227 (2004)
42. Jaramillo Palacio, J.A., Muñoz Pulido, K.A., Arbey Rodríguez, J., Landínez Téllez, D.A., Roa-Rojas, J.: *J. Adv. Dielectr.* **11**, 2140003 (2021)
43. Fuh, H.-R., Weng, K.-C., Liu, Y.-P., Wang, Y.-K.: *J. Alloys. Compd.* **622**, 657 (2015)
44. Warshi, M.K., Mishra, V., Sagdeo, A., Mishra, V., Kumar, R., Sagdeo, P.R.: Structural, optical and electronic properties of RFeO<sub>3</sub>. *Ceram. Int.* **44**, 8344–8349 (2018)
45. Tang, J., Ke, Y., He, W., Zhang, X., Zhang, W., Li, N., Cheng, Z.: Ultrafast photoinduced multimode antiferromagnetic spin dynamics in exchange-coupled Fe/RFeO<sub>3</sub> (R = Er or Dy) heterostructures. *Adv. Mater.* **30**, 1706439 (2018)
46. Fita, I., Wisniewski, A., Puzniak, R., Zubov, E.E., Markovich, V., Gorodetsky, G.: Common exchange-biased spin switching mechanism in orthoferrites. *Phys. Rev. B* **98**, 094421 (2018)
47. Ke, Y.-J., Zhang, X.-Q., Ma, Y., Cheng, Z.-H.: Anisotropic magnetic entropy change in RFeO<sub>3</sub> single crystals (R = Tb, Tm, or Y). *Sci. Rep.* **6**, 19775 (2016)
48. Panfilov, A.S., Grechnev, G.E., Lyogenkaya, A.A., Pashchenko, V.A., Zhuravleva, I.P., Vasylychko, L.O., Novoselov, D.: Magnetic properties of RCoO<sub>3</sub> cobaltites (R = La, Pr, Nd, Sm, Eu). Effects of hydrostatic and chemical pressure. *Physica B* **553**, 80–87 (2019)

49. Knížek, K., Jiráček, Z., Novák, P., de la Cruz, C.: Non-collinear magnetic structures of TbCoO<sub>3</sub> and DyCoO<sub>3</sub>. *Solid State Sci.* **28**, 26–30 (2014)
50. Estrada Contreras, V.R., Alarcón Suesca, C.E., Deluque Toro, C.E., Landínez Téllez, D.A., Roa-Rojas, J.: Crystalline, ferromagnetic-semiconductor and electronic features of the terbium-based cobalt-ferrite Tb<sub>2</sub>FeCoO<sub>6</sub>. *Ceram. Int.* **47**, 14408–14417 (2021)
51. Cuervo Farfán, J., Arbey Rodríguez, J., Fajardo, F., Vera Lopez, E., Landínez Téllez, D.A., Roa-Rojas, J.: *Physica B: Condensed Matter* **404** (18), 2720–2722 (2009)
52. Gil Rebaza, A.V., Deluque Toro, C.E., Medina Chanduví, H.H., Landínez Téllez, D.A., Roa-Rojas, J.: Thermodynamic evidence of the ferroelectric Berry phase in europium-based ferrobismuthite Eu<sub>2</sub>Bi<sub>2</sub>Fe<sub>4</sub>O<sub>12</sub>. *J. Alloy Compd.* **884**, 161114 (2021)
53. Cuervo Farfán, J.A., Deluque Toro, C.E., Parra Vargas, C.A., Landínez Téllez, D.A., Roa-Rojas, J.: Experimental and theoretical determination of physical properties in the Sm<sub>2</sub>Bi<sub>2</sub>Fe<sub>4</sub>O<sub>12</sub> ferromagnetic semiconductor. *J. Mater. Chem. C* **8**, 14925–14939 (2020)
54. Nieto Camacho, J.A., Cardona Vásquez, J.A., Sarmiento Santos, A., Landínez Téllez, D.A., Roa-Rojas, J.: Study of the microstructure and the optical, electrical, and magnetic feature of the Dy<sub>2</sub>Bi<sub>2</sub>Fe<sub>4</sub>O<sub>12</sub> ferromagnetic semiconductor. *J. Mater. Res. Technol.* **9**, 10686–10697 (2020)
55. Perdew, J.P., Zunger, A.: *Phys. Rev. B* **23**, 5048 (1981)
56. Vladimir, I.: *Strong Coulomb Correlations in Electronic Structure Calculations: beyond the Local Density Approximation*. Gordon and Breach, Amsterdam, The Netherlands (2000)
57. Blöchl, P.E.: *Phys. Rev. B* **50**, 17953 (1994)
58. Kresse, G., Joubert, J.: *Phys. Rev. B* **59**, 1758 (1999)
59. Heyd, J., Scuseria, G.E., Ernzerhof, M.: *J. Chem. Phys.* **118**, 8207 (2003)
60. Kresse, G., Furthmüller, J.: *Comput. Mater. Sci.* **6**, 15 (1996)
61. Deluque Toro, C.E., Muñoz Pulido, K.A., Arbey Rodríguez, J., Landínez Téllez, D.A., Roa-Rojas, J.: *J. Low Temp. Phys.* (2022). <https://doi.org/10.1007/s10909-021-02649-w>
62. Liechtenstein, A.I., Anisimov, V.I., Zaanen, J.: *Phys. Rev. B* **52**, R5467 (1995)
63. Monkhorst, H.J., Pack, J.D.: *Phys. Rev. B* **13**, 5188 (1976)
64. Methfessel, M., Paxton, A.T.: *Phys. Rev. B* **40**, 3616 (1986)
65. Murnaghan, F.D.: *Proc. Natl. Acad. Sci. USA* **30**, 244 (1944)
66. Deluque Toro, C.E., Mosquera Polo, A.S., Gil Rebaza, A.V., Landínez Téllez, D.A., Roa-Rojas, J.: Ab initio study of the electronic structure, elastic properties, magnetic feature and thermodynamic properties of the Ba<sub>2</sub>NiMoO<sub>6</sub> material. *J. Low Temp. Phys.* **192**, 265–285 (2018)
67. Deluque-Toro, C.E., Landínez-Téllez, D.A., Roa-Rojas, J.: Ab-initio analysis of magnetic, structural, electronic and thermodynamic properties of the Ba<sub>2</sub>TiMnO<sub>6</sub> manganite. *DYNA* **85**, 27–36 (2018)
68. Glazer, A.M.: The classification of tilted octahedra in perovskites. *Acta Cryst.* **B28**, 3384 (1972)
69. Goldschmidt, V.M.: Die Gesetze der Krystallochemie. *Naturwissenschaften* **14**, 477 (1926)
70. Cerón, J.A.G., Rodríguez, J.A., Rosales-Rivera, A., Farfán, J.A.C., Vasquez, J.A.C.: *J. Mater. Res. Technol.* **8** (5), 3978–3987 (2019)
71. Landínez Téllez, D.A., Martínez Buitrago, D., Barrera, E.W., Roa-Rojas, J.: *J. Mol. Struct.* **1067**, 205–209 (2014)
72. Woodward, P.M.: Octahedral tilting in perovskites. I. Geometrical considerations, *Acta Cryst. B* **57**, 32–43 (1997)
73. Wang, X.L., James, M., Horvat, J., Dou, S.X.: Spin glass behaviour in ferromagnetic La<sub>2</sub>CoMnO<sub>6</sub> perovskite manganite. *Supercond. Sci. Technol.* **15**, 427–430 (2002)
74. Corredor, L.T., Landínez-Téllez, D.A., Pimentel, J., Jr., Pureur, P., Roa-Rojas, J.: *J. Mod. Phys.* **2**, 154–157 (2011)
75. Ortiz-Díaz, O., Rodríguez Martínez, J.A., Fajardo, F., Landínez Téllez, D.A., Roa-Rojas, J.: *Physica B: Condensed Matter* **398**(2), 248–251 (2007)
76. Snoke, D.W.: *Solid State Physics: Essential Concepts*, Second Edition, pp. 526–597. Cambridge University Press (2020)

77. Bhowmik, R.N., Aneeshkumar, K.S.: Low temperature ferromagnetic properties, magnetic field induced spin order and random spin freezing effect in Ni<sub>1.5</sub>Fe<sub>1.5</sub>O<sub>4</sub> ferrite; prepared at different pH values and annealing temperatures. *J. Magn. Magn. Mater.* **460**, 177–187 (2018)
78. Khan, U., Adeela, N., Javed, K., Riaz, S., Ali, H., Iqbal, M., Han, X.F., Naseem, S.: Influence of cobalt doping on structural and magnetic properties of BiFeO<sub>3</sub> nanoparticles. *J. Nanopart. Res.* **17**, 429 (2015)
79. Nunes, W.C., Folly, W.S.D., Sinnecker, J.P., Novak, M.A.: Temperature dependence of the coercive field in single-domain particle systems. *Phys. Rev. B* **70**, 014419 (2004)
80. Hauschild, J., Fritzsche, H., Bonn, S., Liu, Y.: Determination of the temperature dependence of the coercivity in Fe/Cr (110) multilayers. *Appl. Phys. A* **74**, S1541–S1543 (2002)
81. Felix, J.F., da Silva, E.F. Jr, De Vasconcelos, E.A., de Azevedo, W.M.: Tailoring the electrical properties of ZnO/Polyaniline heterostructures for device applications. *J. Korean Phys. Soc.* **58**, 1256–1260 (2011)
82. Vojta, A., Wen, Q., Clarke, D.R.: Influence of microstructural disorder on the current transport behavior of varistor ceramics. *Comp. Mater. Sci.* **6**, 51 (1996)
83. Pandey, R.K., Stapleton, W.A., Sutanto, I.: The effect of doping with some rare earth oxides on electrical features of ZnO. *IEEE J. Electron Devi. Soc.* **3**, 276–283 (2015)
84. Jünger, A.: *Quasi-hydrodynamic semiconductor equations* (Springer Basel AG) (2001)
85. Alarcón-Suesca, C.E., Deluque Toro, C.E., Gil Rebaza, A.V., Landínez Téllez, D.A., Roa-Rojas, J.: *J. Alloys Comp.* **771**, 1080–1089 (2019)
86. Bonilla, M., Landínez Téllez, D.A., Arbey Rodríguez, J., Albino Aguiar, J., Roa-Rojas, J.: *J. Magn. Magn. Mater.* **320** (14), e397–e399 (2008)
87. Guss, P., Foster, M.E., Wong, B.M., Doty, F.P., Shah, K., Squillante, M.R., Shirwadkar, U., Hawrami, R., Tower, J., Yuan, D.: Results for aliovalent doping of CeBr<sub>3</sub> with Ca<sup>2+</sup>. *J. Appl. Phys.* **115**, 034908 (2014)
88. Bos, J.-W.: *IUCrJ* **4**, 712–713 (2017)
89. Toyosaki, H., Fukumura, T., Yamada, Y., Nakajima, K., Chikyow, T., Hasegawa, T., Koinuma, H., Kawasaki, M.: *Nature Mater.* **3**, 221–224 (2004)
90. Naruse, Y., Takamori, A.: Orbital phase perspective of Goodenough-Kanamori-Anderson Rules (GKA Rules) in superexchange interaction. *ChemRxiv. Cambridge Open Engage, Cambridge* (2020)
91. Deluque Toro, C.E., Landínez Téllez, D.A., Roa-Rojas, J.: *DYNA*, 85, 27 (2018)
92. Andritsos, E.I., Zarkadoula, E., Phillips, A.E., Dove, M.T., Walker, C.J., Brazhkin, V.V., Trachenko, K.: *J. Phys.: Condens. Matter* **25**, 235401 (2013)
93. Bryan, M.S., Pang, J.W.L., Larson, B.C., Chernatynskiy, A., Abernathy, D.L., Gofryk, K., Manley, M.E.: *Phys. Rev. Mater.* **3**, 065405 (2019)

# Graphenylene-Like Structures as a New Class of Multifunctional Materials Alternatives to Graphene



Nicolas F. Martins, Guilherme S. L. Fabris, Anderson R. Albuquerque, Ricardo Paupitz, and Julio R. Sambrano

**Abstract** In the last few decades, the study of materials based on  $sp^2$ -carbon has experienced great development. The advancement of carbon materials science gained great impetus after the discovery of fullerenes and carbon nanotubes, but the experimental finding of graphene caused an unprecedented acceleration in the field. In this context, many other possibilities of carbon allotropes were proposed and synthesized. In this review, we discuss one important class of these graphene analogs, namely the graphenylene. This is a  $sp^2$ -carbon allotrope with quite interesting physicochemical properties, such as chemical and structural stability, an intrinsic gap, and the presence of periodic nanoscopic pores, for instance. All these special properties pose graphenylene as a promising candidate for several technological applications, such as gas separation, construction of semiconducting nanodevices, Li (Na)-ion batteries, and so on. The review focuses on the theoretical determination, based on DFT calculations, of graphenylene's properties and a few other materials structurally related to it. Experimental attempts to obtain its synthesis are also briefly discussed. These materials are discussed in terms of their atomic arrangement, mechanical and electronic characteristics discussing possible technological applications. An additional aspect that is reviewed in the text is the possible existence of inorganic (e.g. boron nitride analog) analogs for this material, which were already discussed in the literature and can bring relevant contributions for technological applications due to their special properties.

---

N. F. Martins · J. R. Sambrano (✉)

Modeling and Molecular Simulation Group, São Paulo State University, Bauru, SP 17033-360, Brazil

e-mail: [jr.sambrano@unesp.br](mailto:jr.sambrano@unesp.br)

G. S. L. Fabris

Department of Materials Engineering, Federal University of Rio Grande Do Norte, Natal 59078-970, Brazil

A. R. Albuquerque

Chemistry Institute, Federal University of Rio Grande Do Norte, Natal 59078-970, Brazil

R. Paupitz

Physics Department, Sao Paulo State University - UNESP, Rio Claro, SP CEP-13506-900, Brazil

## 1 Introduction

Carbon capacity to form  $sp$ ,  $sp^2$ , or  $sp^3$  hybridizations is known as a key characteristic, which leads to the formation of several allotropes, presenting various physical and chemical behaviors very distinct from each other. Around 256 distinct topological types (i.e. different underlying nets) were cataloged from literature in 2006 by Hoffman et al. [1].

The possible existence of several planar materials, formed by structures with high content of  $sp^2$  hybridized carbon atoms, has been investigated for several decades. Starting with a few investigative studies [2–4], nanostructured carbon materials became a subject of interest for the materials science community. The class of molecules made from graphite-like sheets in hollow cage arrangement was theoretically predicted by David E. H. Jones in 1966 [5], being confirmed two decades later. The experimental characterization of the  $C_{60}$  molecule by Kroto et al. (1985) [6], named buckminsterfullerene, sparked interest in new molecular arrangements of carbon allotropes, including non-naturally occurring ones.

The discovery of fullerenes was awarded the Nobel Prize in Chemistry in 1996. Just a few years earlier, Iijima (1991) [7] reported the synthesis of carbon nanotubes using an arc-discharge evaporation method, similar to that used for fullerene synthesis. In 1993, Iijima and Ichihashi [8] controlled the synthesis of single-shell carbon nanotubes, opening the way for new properties to be measured in these materials.

The fact that fullerenes (a 3D molecule; 0D periodicity) and nanotubes (1D) are constructed with  $sp^2$  hybridized carbons and present many remarkable physical and chemical properties, encouraged, even more, the search for carbon allotropes and composed materials that could be useful in technological applications.

A natural question about the possibility of two-dimensional single-layer allotropes of carbon arises from the knowledge of the stacked structure of  $sp^2$  (*-ene* suffix in the nomenclature of  $C = C$  alkenes) sheets in graphite. In this way, graphene-like structures (honeycomb lattice) were known since the 1960s (Boehm et al. [9]) but there were experimental difficulties in isolating single layers to perform electrical measurements, being studied only while supported on metal surfaces. In this century, Novoselov et al. (2004) [10] isolated and investigated new two-dimensional (2D) crystalline materials, rediscovering graphene, with which they performed a series of characterizations that have aroused remarkable scientific and technological interest.

Graphene research has accelerated exponentially in the last decade due to its unique form factor and exceptional physical properties. The global market value of graphene is expected to exceed \$2 billion in this decade. The multitude of special characteristics of the new material and its current (and potential) applications [11–14] motivated many researchers to spend enormous efforts in the proposition and investigation of graphene-like materials. One main goal in this quest was to enable the design of new nanoscopic scaled electronics, possibly based on ion carbon as opposed to the present (microscopic) electronics, which are silicon-based.



However, graphene as a semi-metallic material has a few limitations for its direct use in practical applications [15–18], such as a small ratio between “locked” and “unlocked” currents in electronic devices [19–22]. This difficulty motivated the investigation of a plethora of possible methods to modify, in a controlled way, the band gap energy opening of the material, for instance, chemical modifications such as doping, oxidation, fluorination, or adsorption or even structural modifications by the creation of pores or strain application. Another option being explored is the production of inorganic materials which are structurally related to graphene, such as hexagonal boron nitride (hBN). This research line originated an entirely new family of 2D materials, starting from the hBN cited above, and many other inorganic analogs. Many mono-elemental inorganic graphene analogs were proposed, such as silicene [23], germanene [24], stanene [25], plumbene [26], borophene [27] and phosphorene [28]. In addition to mono-elemental structures, more complex two-dimensional materials were proposed and have been investigated from the theoretical and experimental points of view including the ZnO [29], TiO<sub>2</sub> [30] e AlN [31], GaN [32], GaAs [33], chalcogenides and the Transition-metal dichalcogenides (TMDs) for instance [34].

At this point, it becomes clear that a semiconducting material, possibly also made out of carbon atoms, would be quite convenient for the development of nanoscaled devices useful for electronics. Such material, if also 2-dimensional and chemically stable, could be doped with some electron acceptor (donor) element to obtain n(p)-doped semiconductors which could be used to create n-p junctions and nanometer-scaled electronic devices. Also, such structures could bring new electronic characteristics to be explored technologically. In this context, among many 2-dimensional structures proposed in the last decades, graphenylene rises as an interesting possibility. It was proposed in the 1960s by Balaban et al. [2] and is a sp<sup>2</sup> bonded 2-dimensional carbon allotrope.

After many years of its proposition [35], graphenylene became an object of interest for researchers after a few authors investigated theoretically its physical properties and its possible synthesis routes [36, 37].

A deep bibliographical investigation of the number of papers published over the years 2013 to 2022 in the Web of Science database, shows that the interest in porous materials has increased over the years, as shown in Fig. 1, there is a constant interest in the keyword “biphenylene” and an increase in the use of “graphenylene” term.

The in-depth studies of graphenylene (GP) and graphenylene-like structures are relatively recent. The electronic properties of GP were first investigated in 2012 when Brunetto et al. [35] proposed the material, which was called biphenylene carbon, and calculated its electronic properties. Using the density functional tight-binding approach [38] and a DFT approximation, they showed that the GP band gap were ~0.8 eV, delocalized frontier orbitals, and relatively small effective masses for its charge carriers [39], where this structure can be achieved by the dehydrogenation of a porous graphene nanosheet [40]. Five years later, graphenylene was experimentally obtained [41, 42], through a different path than the proposed by Brunetto and coworkers. Later on, Fabris et al. [43] using the DFTB method alongside an all-electron basis set and B3LYP functional, found that graphenylene has a band gap of 0.83 eV, a similar value to Brunetto’s findings, however with the advantage that

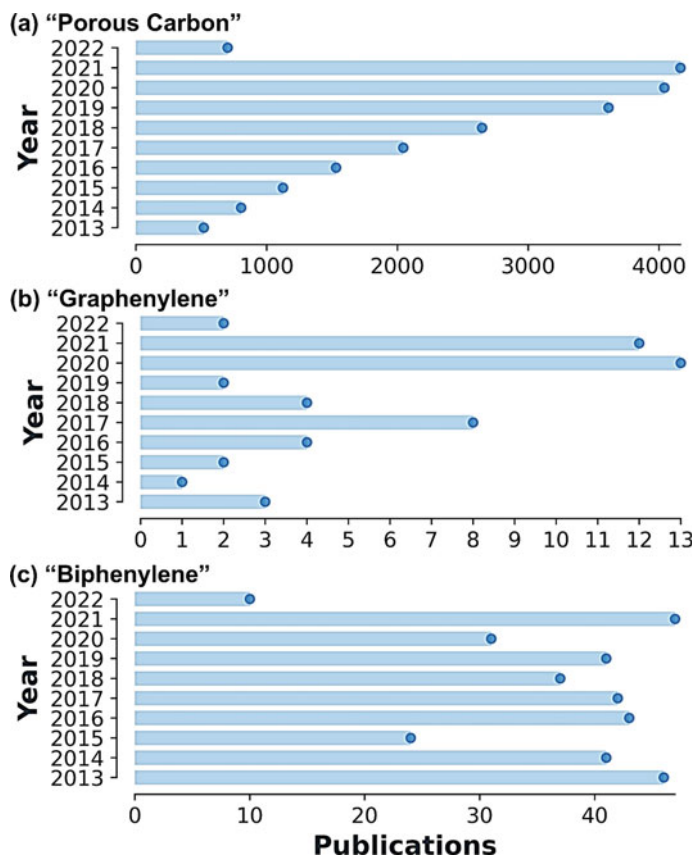


**Fig. 1** Bibliographical research from the year 2013 to 2022 on Web Of Science for the keywords: **a** porous carbon, **b** biphenylene, and **c** graphenylene structures. There is an inconsistency of the official name of graphenylene. The compilation of the results could be affected, although the graphs indicate that there is a constant interest in the keyword “biphenylene” and an increase in the “graphenylene”. This research was done via the “Web of Science” scientific search engine on 02/22/22

the frequencies at  $\Gamma$  point were checked to nonnegative values, demonstrating that the structure is really stable and in a minimum. Recently, the study of graphenylene gained a new impulse after its chemical synthesis and also the synthesis of other similar structures obtained by experimentalists as graphyne [44] and graphdiyne [45].

In the next sections, structural and physical properties as well as possible applications for this intrinsic semiconductor and for a few related materials, including inorganic analogs will be discussed.

## 2 Graphenylene

### 2.1 Structural and Physical Properties

There are three types of rings in graphenylene's structure, indicated in Fig. 2, namely (A) dodecagon ring ( $C_{12}$ ); (B) hexagon ring ( $C_6$ ); and (C) square ring ( $C_4$ ). The GP unit cell belongs to the  $P_6/mmm$  space group with 1 irreducible atom, as illustrated in Fig. 2, with lattice parameters  $a = b = 6.735 \text{ \AA}$ , and C–C bond length of the square ring of  $1.47 \text{ \AA}$ . The hexagon ring has a  $1.35 \text{ \AA}$  and a  $1.47 \text{ \AA}$  bond length, while the central nanopore (dodecagon ring) has a diameter of  $5.47 \text{ \AA}$ , as found by Fabris et al. [43] using density functional theory (DFT) and an all-electron basis set.

The structure of the GP allows indicating 7 points of high symmetry, as marked in Fig. 2, as indicated by Martins et al. [46]. It is really interesting to identify the hollow adsorption sites (A to C) since these locations can be of great importance for a wide range of applications, such as gas separation [37, 47–51], sensors [46, 52], among others [53–60]: (D) the edge of  $C_6$  and  $C_4$  rings; (E) the edge between  $C_{12}$  and  $C_6$  rings; (F) the edge between  $C_{12}$  and  $C_4$  rings; (G) the carbon at the corner of the  $C_4$ ,  $C_6$ , and  $C_{12}$  rings. The rings A, B, and C are especially important to understand the diffusion energy barrier for ions, atoms, and molecules, if they have an appropriate size and their diffusion is allowed, as will be discussed in the next section. Also, the cohesive energy is investigated in this work, where it is found that the GP energy is quite similar to graphene, being slightly less stable, with the h energy of  $-9.7 \text{ eV}$ , higher than the  $-10.4 \text{ eV}$  of graphene [61].

GP has interesting mechanical properties that can be very useful and surpass some existing 2-dimensional materials, combining the versatility of its topology and the graphene similarities. Due to its symmetry, it has only two elastic constants,

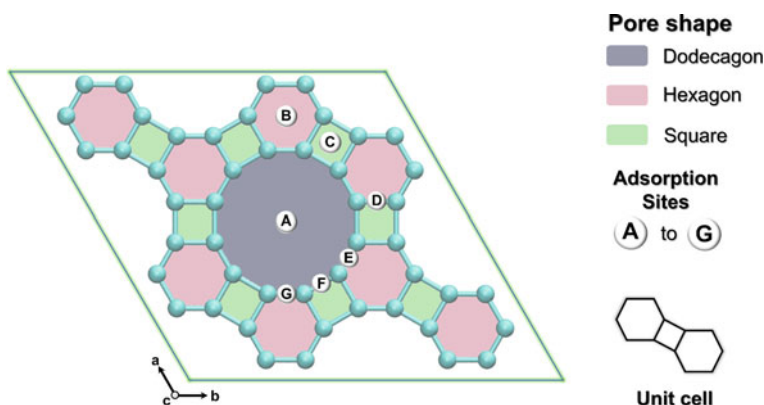


**Fig. 2** Graphenylene structure represented by a cell ( $2 \times 2$ ). The pores are marked in different colors to emphasize their shape and the high symmetry points are labeled from A to G. The inset shows the GP unit cell

labeled  $C_{11}$  and  $C_{12}$ , which represent the longitudinal and transversal expansion or compression, respectively. Through DFT/B3LYP simulations it was observed that  $C_{11} = 695.4$  GPa and  $C_{12} = 180.1$  GPa, which can be used to determine the Young's modulus ( $Y$ ) and the Poisson's ratio ( $\nu$ ) by the following equations:  $Y = (C_{11}^2 - C_{12}^2)/C_{11}$  and  $\nu = C_{12}/C_{11}$ . Meaning that the graphenylene has  $Y = 648.8$  GPa and  $\nu = 0.259$ ; as compared to graphene  $Y_{\text{graphene}} = 1$  TPa and  $\nu_{\text{graphene}} = 0.165$  [43].

Figure 3 it is shown the electronic band structure of graphenylene and compared it with graphene at the same level of theory, namely DFT/B3LYP.

As can be seen in Fig. 3, the band structure of GP has a direct band gap located at the K point with a value of 0.83 eV. The bands of GP are not flat and have some similarities to graphene, mainly composed of  $2p_z$  orbitals, however without the Dirac cone, when taking into consideration the band gap at the K point. It is possible to affirm that the electronic mobility in GP is excellent, as calculated by Brunetto et al. [35], with values of  $m^*/m_e = 0.26$  and  $m^*/m_h = 0.33$ , for the electron and hole effective masses, respectively, being considered an expected value for a good conductor.

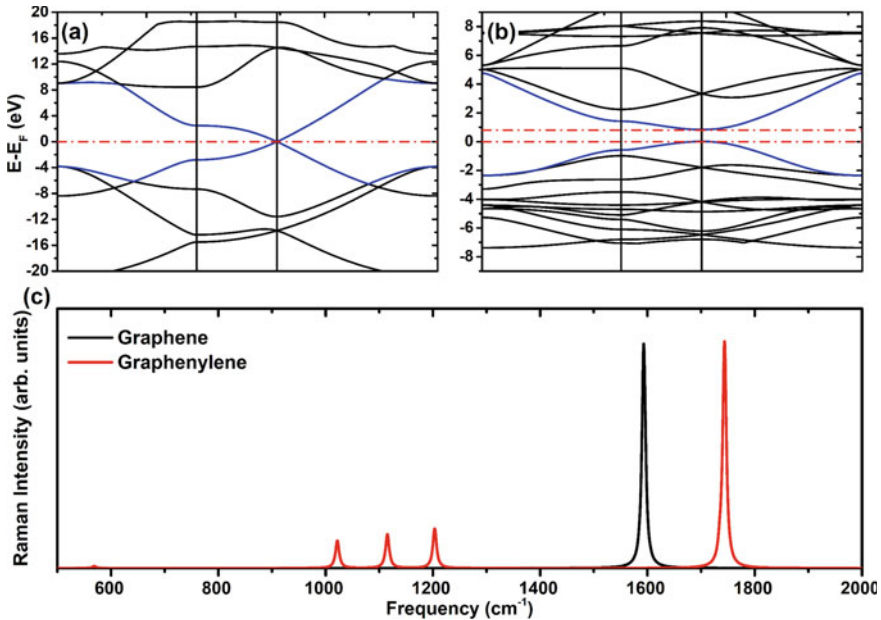


**Fig. 3** Electronic structure of **a** graphene and **b** GP, and the Raman intensities for both structures in **(c)**

## 2.2 Gas Separation

The dodecahedral pore of GP has a radius of 3.20 angstrom. In many cases, the diameter of its central pore is larger than the kinetic diameter of some molecules, facilitating the diffusion of different gases through the material. Song et al. [37] report this via a plane waves DFT study, which shows that the energy barrier of hydrogen gas ( $\text{H}_2$ ) is extremely low (0.20 eV) when compared with other small molecules such as CO (0.99 eV),  $\text{CO}_2$  (1.05 eV) and  $\text{N}_2$  (1.01 eV) whose diffusion could be more difficult.

Membrane-based technology can also serve the cryogenic industry since stable helium isotopes ( $^3\text{He}$  and  $^4\text{He}$ ) can also be separated via GP due to high permeance and great transmission probability from the quantum tunneling of the species [49]. Motallebipour and Karimi-Sabet (2021) [47] also investigate these helium isotopes in the gas phase, attesting that graphenylene has an elevated separation factor and permeance ( $10^{-8} \text{ mol m}^{-2} \text{ s}^{-1} \text{ bar}^{-1}$ ) compared to inorganic graphenylene, resulting in a promising approach to the separation of helium species at high temperatures by the GP membrane. In the same study, IGP is more efficient than GP under steady-state conditions, since it provides acceptable values of separation factor at higher temperatures.

One way to improve the performance of graphenylene is to apply controlled strain on the surface. Zhu et al. [51] show that GP can upgrade the  $\text{H}_2$  permeance by 6 times ( $2.6 \times 10^{-2} \text{ mol s}^{-1} \text{ m}^{-2} \text{ Pa}^{-1}$ ) under a strain of 3.04% compared to the unstrained graphenylene. Depositing a strain between 3.04% and 4.20% the membrane starts to separate  $\text{CO}_2$  and from the range of 5.12–10.78% improves the performance of methane gas ( $\text{CH}_4$ ). These factors indicate that the ability of GP to act as a porous membrane can be tunable after modifications in the structure.

## 2.3 Catalysis and Gas Sensing

Along with the high non-renewable energy consumption, the removal of toxic gases becomes an urgent agenda to minimize harmful effects on the human body. One way to reduce nocive substances from the atmosphere is to use carbon-based catalysts [62], where anchored metals can amplify the catalytic activity of these structures [63]. An example is the first-principles calculations study of Chen et al. [64] that modeled graphenylene as a support for single Ru and Mo atoms and found that the oxidation reactions of CO and NO molecules occur more easily via the Eley–Rideal (ER) mechanism in contrast to the Langmuir–Hinshelwood (LH) model.

Considering the high costs of operation with noble metals, the single-atom catalysts (SACs) on supported monolayer can be an interesting route. Tang et al. [58] considered this alternative with Pt and Pd atoms anchored on GP, denoting that the ER mechanism is energetically more favorable compared to other investigated models since they exhibit a lower energy barrier (<0.35 eV) by the interaction of 2CO and

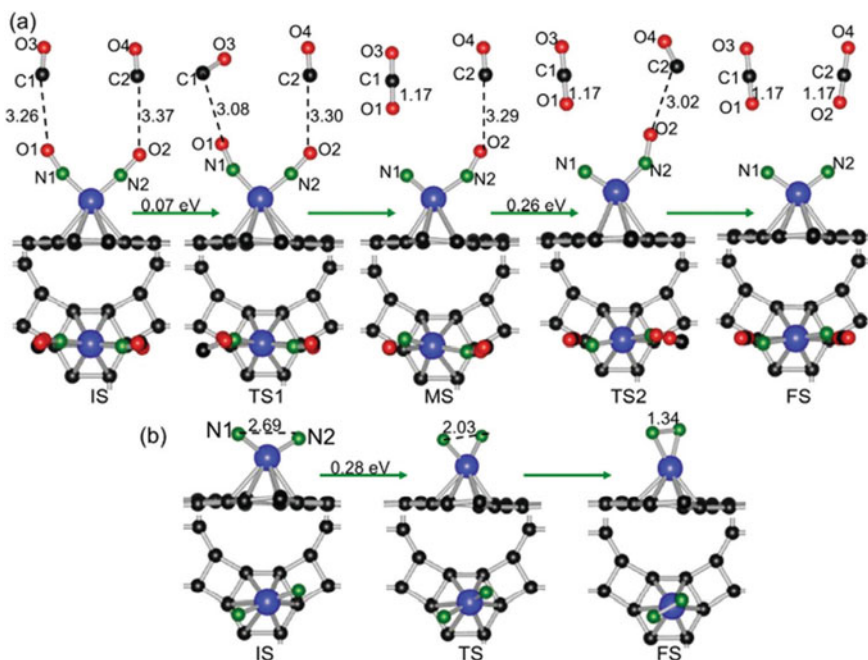


**Fig. 4** Formation processes of the  $N_2$  product on Mn-graphynylene (Reproduced from Ref. [65] with permission from Royal Society of Chemistry)

2NO for the  $2CO_2$  and  $N_2$  products on GP surfaces. Similar results are confirmed once more by Tang et al. (2020), now noting that transition metals (TM) such as Mn, Co, Ni, and Cu can operate as SACs via the ER mechanism in the GP-supported. Figure 4 depicts the reaction states studied by Tang et al. [65].

The Fe atom, another potential TM species in SACs, was also anchored in GP to estimate the behavior of these structures with different molecules (Tang et al., 2020). It is attested that as well to the promising catalytic performance in the oxidation reactions of CO from NO and  $O_2$  molecules, the Fe-GP structure can equally act in CO, NO,  $NO_2$ , and  $O_2$  gas sensing due to the magnetic and electronic properties originated by the Fe atomic orbitals in the adsorbed structure.

## 2.4 Energy Storage and Similar Systems

The progress in research on Li storage in the GP comes from the limitation involving traditional anode materials, such as graphite. Admitting a low cost and excellent chemical stability [66], graphite has a specific capacity limited to  $372 \text{ mAh}\cdot\text{g}^{-1}$  [67], complicating the use of the high energy density of Li in nanoelectronic devices and requiring the development of new anode materials by the industry.

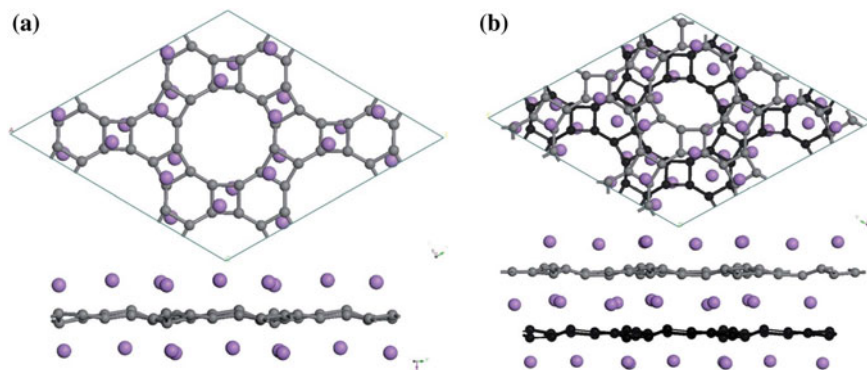


**Fig. 5** **a** Lithium intercalated monolayer graphenylene and **b** lithium-intercalated bilayer graphenylene. The lower and upper layers are represented by dark and gray stick-and-ball styles, respectively. The pink spheres represent lithium atoms (Adapted from Ref. [60] with permission from Royal Society of Chemistry)

Yu [60], via DFT theory, starts the investigation attesting the excellent Li mobility in the intercalations with the monolayer ( $\text{Li}_3\text{C}_6$ ) and bilayer ( $\text{Li}_{2.5}\text{C}_6$ ) of GP, which have specific capabilities of  $1116 \text{ mAh}\cdot\text{g}^{-1}$  and  $930 \text{ mAh}\cdot\text{g}^{-1}$ , respectively, superior values to pristine graphene ( $\text{LiC}_6$ ) with  $740 \text{ mAh}\cdot\text{g}^{-1}$ . Also, adsorption of Li atoms on only one side of the GP, a considerably smaller atomic proportion ( $\text{Li}_{1.5}\text{C}_6$ ) is obtained and, consequently, a smaller specific capacity ( $487 \text{ mAh}\cdot\text{g}^{-1}$ ). The resulting geometries obtained by Yu are shown in Fig. 5.

As an alternative to the usual LIBs, there are the sodium-ion batteries (SIBs), which have been explored in recent years as a natural choice. In this way, Fabris et al. [68] investigate the capability of the GP to also store Na and detects a specific capacity of  $729.89 \text{ mAh}\cdot\text{g}^{-1}$  ( $\text{NaC}_3$ ) with the saturation on both sides of the nanosheet, a very superior value compared to studies of Na in graphite ( $100 \text{ mAh}\cdot\text{g}^{-1}$ ) [69] and doped graphene ( $308 \text{ mAh}\cdot\text{g}^{-1}$ ) [70].

Unique materials like GP may also perform well in clean energy storage, whither the study published by Hussain et al. [54] presents, by theoretical calculations, the potential of graphenylene doped with alkali metals for the retention of  $\text{H}_2$  molecules. In this investigation, it is reported that the GP decorated by 5 atoms of Li, Na, K, and Ca captures 20 hydrogen molecules, where the charge transfer from the alkali metals to the GP polarizes the  $\text{H}_2$  species and stabilizes the adsorption of the molecule in the doped systems, which provides a large energy storage by the decorated graphenylene.

It is also relevant the possibility of use of graphenylene-based membranes applied to water desalination, as discussed by Jahangirzadeh et al. [55]. From the interaction between the functionalized graphenylene in different configurations with familiar salts (sodium and chloride ions), molecular dynamics studies indicate that fluorination in GP pore produces high water permeability ( $11.032 \text{ L}\cdot\text{m}^{-2}\cdot\text{h}^{-1}\cdot\text{bar}^{-1}$ ) and a 99.4% salt rejection, which can be considered a strong evidence that hydrophilic

chemical functions upgrade the capacity of graphenylene to act as a desalination membrane.

## 2.5 Electronic Transport

An interesting characteristic that was recently explored theoretically is the use of graphenylene as a construction element for nanodevices, as shown by Villegas-Lelovsky and Paupitz [59]. In that work, the authors demonstrate that by doping GP, it is possible to tune its electronic transport properties to obtain  $p$ - $n$  junctions, which can be extremely useful for low-dimensional devices. These junctions can be used as part of diodes for instance, with a conducting threshold of  $\sim 1.5$  eV indirect bias and current blocking with opposite bias. The authors also demonstrate that some configurations could result in devices with Zener-like behavior (see Fig. 6).

Furthermore, *ab initio* calculations also show the possibility of establishing diodes based on graphenylene/ $\text{MoX}_2$  van der Waals heterostructures ( $X = \text{S}, \text{Te}$  and  $\text{Se}$ ), that take a high rectification factor ( $10^3$ – $10^4$ ) and optical absorption in the visible spectrum, making these systems promising in photonics and nanoelectronic devices [71].

Using the plane-wave/DFT approach, Liu et al. [56] also analyzes that GP can be functionalized at different concentrations, where hydrogenation and halogenation (F, Cl, Br and I) provide a band gap energy range of 0.075 to 4.98 eV and 0.024 to 4.87 eV, respectively, turning GP a promising material for band gap engineering.

## 3 Experimental Synthesis

In 2009, a new 2D porous structure, with a framework similar to graphene and with a single-atom thickness and nanopores periodically distributed, was fabricated. The hexaiodo-substituted macrocycle cyclohexa-*m*-phenylene (CHP) [40], is shown in Fig. 7b, and the chemical reaction to create this well-designed molecular network is given by the aryl-aryl coupling (see Fig. 7a) which happens on an Ag(111) surface. Figure 7c, d, it is shown the conjugated CHP network and its relationship with graphene.

The surface-assisted coupling reaction started after annealing the substrate for a few minutes in 575 K, as indicated by the STM analysis, and the polymerization reaction initiated above this temperature with a similar time, resulting in the formation of a completely developed polyphenylene network. Figure 8a it is shown an STM image of the polymer network obtained in the deposition on Ag(111) maintained at room temperature and Fig. 8b it is illustrated a high-resolution STM image of the polyphenylene superlattice (with honeycomb pattern) overlaid by the CHP framework to better visualization, and the structural analysis showed that there is a uniform nanopore spacing of 7.4 Å, with a good agreement with the AM1 calculations done



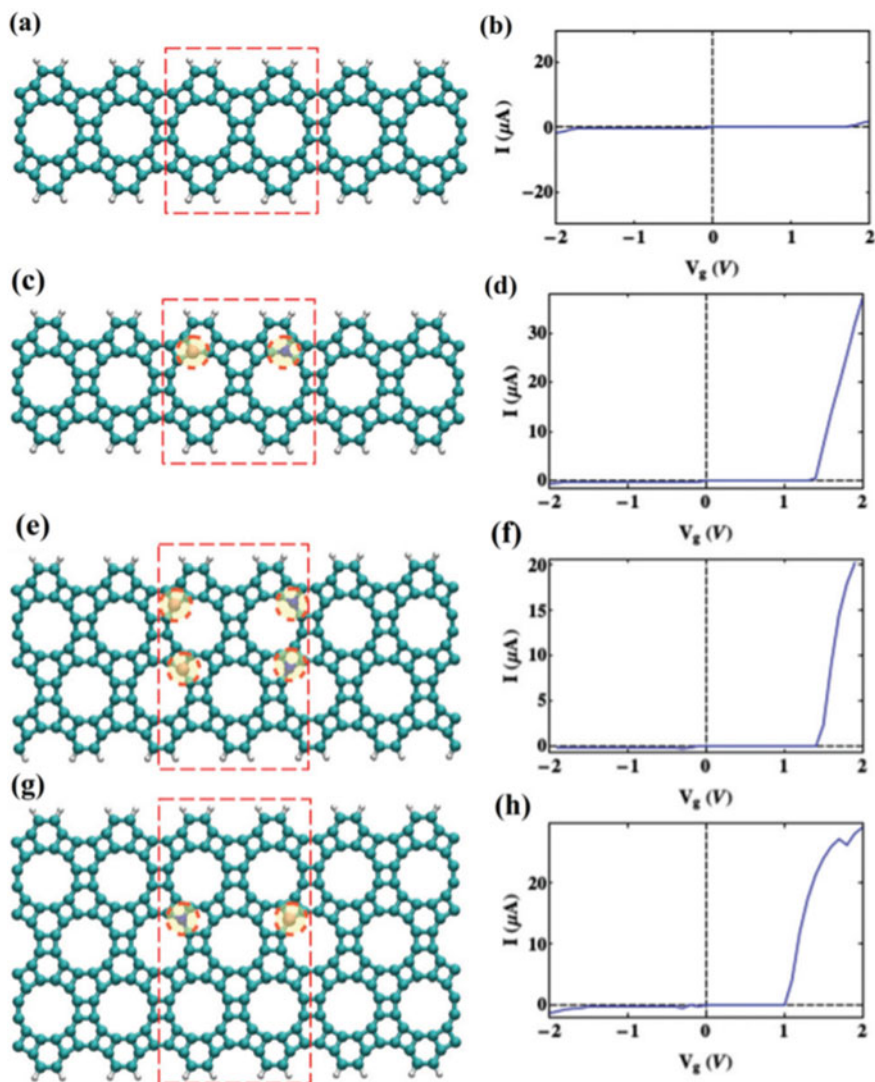


**Fig. 6** Molecular devices composed by p-n junctions from two-unit main layers, one doped with boron and the other with nitrogen: **a** pristine one-row junction and the **b**  $I \times V$  characteristic plot, **c** one-row-pn-junction and the **d**  $I \times V$  characteristic plot, **e** two-rows-pn-junction and the **f**  $I \times V$  characteristic plot, **g** three-row-pn-junction and the **h**  $I \times V$  characteristic plot. Carbon, boron and nitrogen atoms are represented by cyan, pink and blue colors, respectively. The position of the doping atoms, namely boron and nitrogen, is also highlighted with an orange circle delimiting a yellow shaded area to facilitate their localization (Reproduced from Ref. [59] with permission from Royal Society of Chemistry)

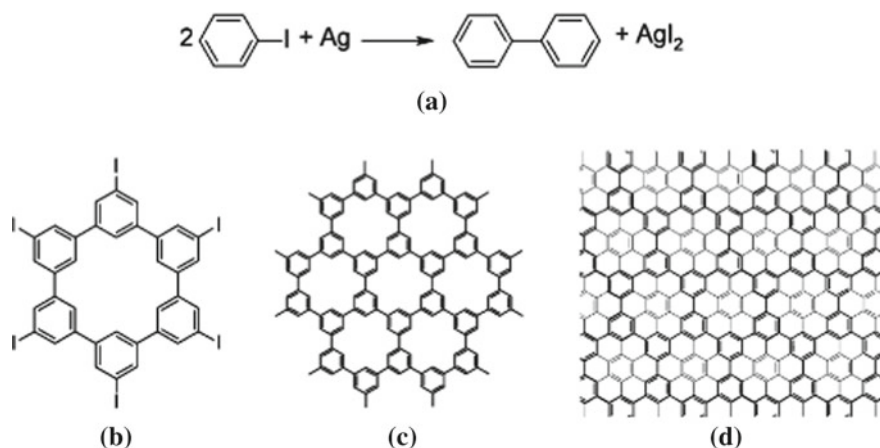


**Fig. 7** a Mechanism of the silver-promoted aryl–aryl coupling of iodobenzene to biphenyl. b Structure of CHP. c Structure of a fraction of the polyphenylene super honeycomb network. d Structural relationship of the polyphenylene super honeycomb network (bold lines) and graphene (thin lines) (Reproduced from Ref. [40] with permission of Royal Society of Chemistry)

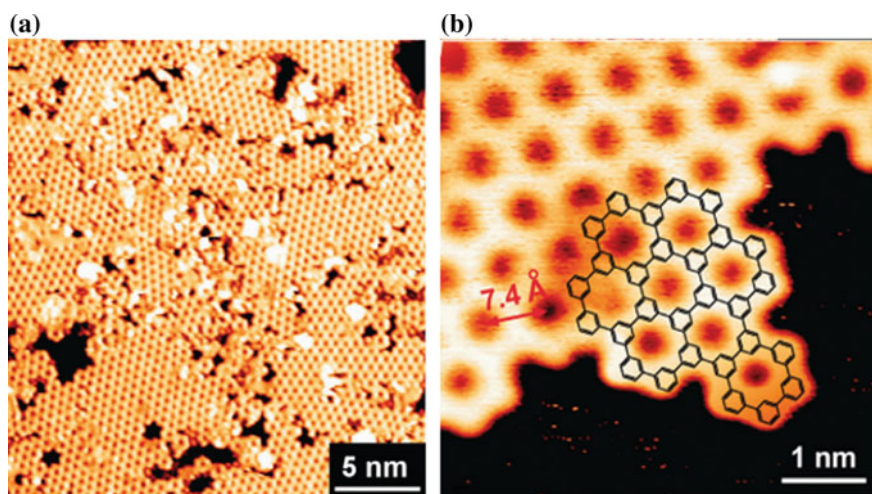


**Fig. 8** a STM image (0.8 V, 50 pA) of the polyphenylene super honeycomb network on Ag(111) formed after polymerization of CHP precursors at 805 K. b STM image (1 V, 50 pA) of an edge of the polymer network, where the structure of the CHP backbone (overlaid chemical structure) can most clearly be recognized (Adapted from Ref. [40] with permission from Royal Society of Chemistry)

by the authors (7.45 Å) and by our previous work (7.5 Å) using the DFT method with an all-electron basis set. These results show that this method constitutes a versatile way to design 2D materials, with the ability to tailor the network and control the pore size and spacing.

Years later, in 2017, Du et al. [41] experimentally discovered a new two-dimensional carbon crystal prepared from the 1,3,5-trihydroxybenzene, different from graphene and similar to the graphenylene, consisting of 4- and 6-carbon atom rings, which was named as 4–6-carbophene.

The chemical reactions to synthesize the graphenylene are described in Fig. 9. The polymerization reaction can happen through intramolecular dehydration of 1,3,5-trihydroxybenzene, as indicated in Fig. 9a, where water molecules are stripped using the aluminum oxide ( $\gamma\text{-Al}_2\text{O}_3$ ), making the benzynes combine with each other, forming small graphenylene fragments. The other possible reaction is from an intermolecular dehydration between 1,3,5-trihydroxybenzene molecules (see Fig. 8b), where those molecules start to join each other and grow quickly (see Fig. 8c). This synthesis was performed in an argon atmosphere at 350–380 °C in a quartz glass tube furnace using  $\gamma\text{-Al}_2\text{O}_3$  as a dehydrant agent.

In Fig. 10 it is shown several moments of the experiment done by Du et al. In Fig. 10a, b can be observed forming graphenylene on a copper foil and in a quartz glass sheet, respectively. The SEM (scanning electron microscopy) of transparent carbon films are shown in Fig. 10c, d. The isolated film is shown in Fig. 10e, f. A more detailed description of the experimental method used and procedures can be found in the original reference.

## 4 Graphenylene-Like (Inorganic Analogs)

### 4.1 Boron Nitride (BN)

A few years ago, Ding et al. [72] proposed an inorganic analog to porous graphene, which we named porous boron nitride (PBN), and investigated its properties using plane-wave DFT, obtaining a band gap of 4.27 eV. Afterward, Perim et al. [73] introduced a graphenylene analog which we named as inorganic graphenylene-like boron nitride (IGP-BN), whereupon using DFT/PBE with localized wave functions they reported a band gap of 4.57 eV and 4.14 eV for PBN and IGP-BN, respectively.

In 2018, this structure was revisited in the paper published by Fabris et al. [43] about graphenylene, where a more detailed study of their structural, electronic, mechanical and vibrational properties was done.

In that study, it was verified that PBN has a direct band gap of 6.45 eV, and IGP-BN has an indirect band gap of 5.52 eV, where a significant displacement of the conduction band towards the valence band was observed for IGP-BN if compared to PBN, and both structures have flat bands, indicating a low electron mobility. For comparison effects, experimentally, the hBN has an indirect band gap of 5.95 eV

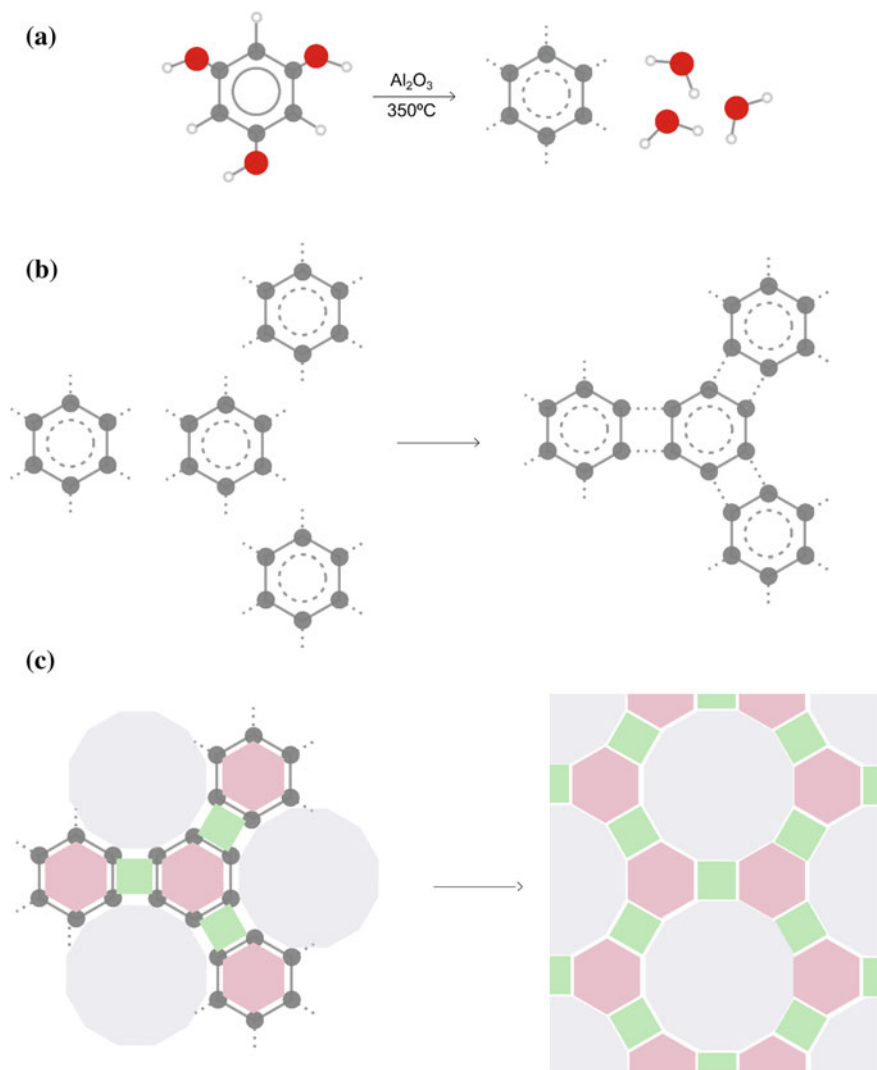


**Fig. 9** Illustration of chemical reaction mechanism from 1,3,5-trihydroxybenzene to 4–6 carbophene 2D crystal. **a** The polymerization reaction via intramolecular dehydration of 1,3,5-trihydroxybenzene. **b** The polymerization reaction via intermolecular dehydration between 1,3,5-trihydroxybenzene molecules. **c** With the joining of more 1,3,5-trihydroxybenzene molecules the fragments of 2D carbon crystal grow up quickly (Adapted from Ref. [41]/Open Access Nature)

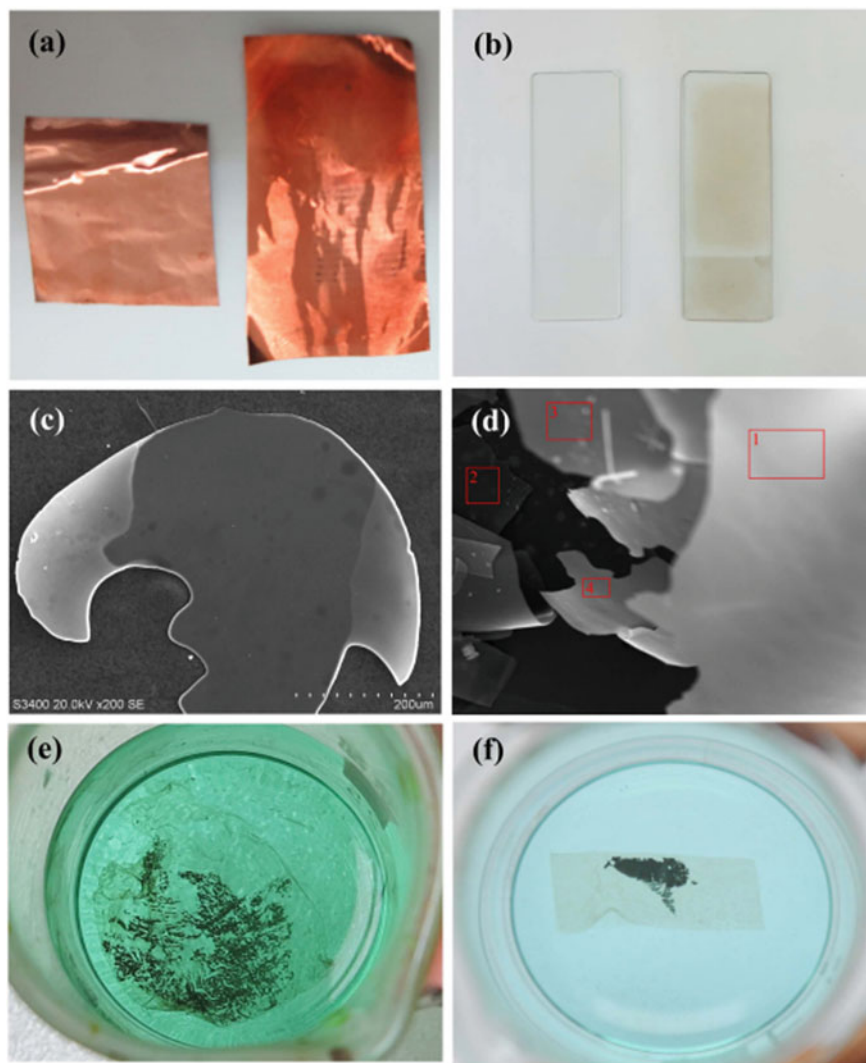


**Fig. 10** The membranes of 2D carbon crystal, coated on the quartz glass sheet and copper foil. **a** Comparison between the copper foil before and after the graphenylene film was coated, from left to right. **b** Comparison between the quartz glass sheet before and after the graphenylene film was coated, from left to right. **c** The SEM image of the graphenylene crystal film separated from the substrate. **d** The SEM image graphenylene crystal film separated from quartz glass sheet. After the carbon films of the 2D crystal are separated from the copper foil and quartz glass sheet, transparent carbon films of graphenylene are obtained. **e, f** The graphenylene films separated from copper foil (Reproduced from Ref. [41]/Open Access Nature)

[74]. For both PBN and IGP-BN, the major contributions in the valence band are given by the  $2p_z$  orbitals of nitrogen atoms and the conduction band is given by  $2p_z$  of boron atoms.

Also, were calculated the elastic constants  $C_{11}$  and  $C_{12}$  of PBN (IGP-BN) which are 379.5 (611.1) GPa and 109.9 (171.8) GPa, respectively, indicating Young's modulus and Poisson's ratio of 347.6 GPa (562.8 GPa) and 0.290 (0.281), respectively. The hBN values for Young's modulus and Poisson's ratio are 858.2 GPa and 0.209, respectively. The IGP-BN seems to be more resistant to deformation in the longitudinal direction than PBN, but with a similar response in the transverse direction, however, both structures have lower values than the pristine hBN.

In another study, Fabris et al. [75] proposed for the first time boron nitride-based porous nanotubes, namely porous boron nitride nanotubes (PBNNTs) and inorganic graphenylene-like boron nitride nanotubes (IGP-BNNTs), and thoroughly investigated the electronic, elastic and piezoelectric properties of the armchair and zigzag conformations of PBNNTs and IGP-BNNTs using DFT/BLYP. This work showed that the porous nanotubes follow a similar trend as observed for single-layers, however an important property rises when the rolling up process occurs, i.e., the construction of PBNNTs nanotubes generates greater piezoelectricity, than those observed in the pristine single-layer. So, the influence of strain on the piezoelectric response was studied, and it was verified that a positive strain in the axis direction reveals a significant increase in the piezoelectricity, which can be modulated up to 20% of strain, obtaining a maximum increase of ~1320%. The mechanical properties analysis showed that the armchair nanotubes have a higher stiffness than the zigzag. From the electronic point of view, band gap energy shows a dependency on the diameter, which for great diameters converge to their respective single-layer values. Moreover, the elastic and piezoelectric properties of these porous nanotubes indicate that they are suitable for potential applications in the reinforcement of fiber composites and movement sensing, due to their piezoelectric response.

The tuning of electronic properties of inorganic graphenylenes has also been verified by Perim et al. [73] which have shown that it is possible to modulate the band gap opening of IGP-BN. Combining DFT calculations and molecular dynamics (DM) simulations, the researchers showed that the selective substitution of BN pairs by carbon atoms can turn the insulating material (4.14 eV) into a semiconductor, with a band gap range of 0.05 to 1.12 eV. Feng and Wang [76] also show that homo-elemental inorganic graphenylene (hIGP-BN) may be anchored by the donor (Tetrathiafulvalene, TTF) and acceptor (Tetracyanoquinodimethane, TCNQ) organic molecules, where the transferred charge from the combined action of TTF and TCNQ modifies the gap from 1.9 eV of hIGP-BN to 0.14 eV, making this graphenylene a tunable material for nanoelectronic devices.

In gas application, the diffusion of  $H_2$  also occurs without very difficulty through IGP-BN, as revealed by Xu et al. [50] where the diameter of 5.35 Å provides a low energy barrier of 0.14 eV and a superior selectivity of the hydrogen molecule compared to other materials such as silicene [77] and graphene [78].

The necessity for new membrane-based technologies also emerges from the problem of separating abundant elements in the atmosphere, such as helium, from

larger and toxic molecules. An alternative for the purification of He in the environment is the use of graphenylene-like structures, as suggested in the study by Wang et al. [49] combining first-principles calculations and molecular dynamics (MD) in the IGP-BN, where it shows a great dependence of the kinetic diameter of the molecule with its surface penetration, a fact corroborated by the almost null diffusion barrier for He (0.06 eV), and selectivities at room temperature (300 K) in the range of  $10^6$ – $10^{31}$  on the gases investigated (Ne, Ar, CO, CO<sub>2</sub>, N<sub>2</sub>, and CH<sub>4</sub>), revealing the excellent separation capacity of the material.

## 4.2 Silicon (Si)

The silicon-based graphenylene, also known as silicenylene (IGP-Si), has been proposed and studied by Fabris et al. [79] in 2017, where using the DFT/B3LYP approach, they showed that the silicenylene is a stable structure and differs than those found for graphenylene, it has a small non-null direct band gap, ~76 meV, at K point with a well-defined, good dispersion and a small enlargement of the Dirac cone, where the 3p<sub>z</sub> orbitals are the major contribution to the band gap region. Also, the structure has a buckling, similar to that found for silicene, and is more susceptible to longitudinal and transversal deformation than silicene, as it has a more distorted network, with a large nanoporous which can be used to new applications, such as gas separation, molecular sieving and energy harvesting.

Silicenylene has calculated elastic constants, C<sub>11</sub> and C<sub>12</sub>, of 110.2 GPa and 39.3 GPa, respectively, resulting in Young's modulus of 96.2 GPa and a Poisson's ratio of 0.36; which compared to silicene, with Young's modulus and Poisson's ratio of 159.57 GPa and 0.283, respectively, indicates that this new structure is significantly less resistant to deformations than their pristine form.

## 4.3 Zinc Oxide (ZnO)

Due to the importance of zinc oxide and its wide range of applications, in 2019, it was proposed a new structure of zinc oxide based on graphenylene architecture, also known as IGP-ZnO, and a porous graphene-based, known as H-gZnO [80].

In this study, both structures were shown to be stable, which was confirmed by non-negative frequencies, and even with its structural modification, the semiconducting properties are maintained. Also, it was theoretically demonstrated that the dehydrogenation of H-gZnO induces a spontaneous interconversion to the IGP-ZnO.

The band structure analysis of the H-gZnO and IGP-ZnO shows that they have a band gap energy of 6.06 eV and 5.42 eV, respectively, which are both higher than graphene-like ZnO (gZnO), 4.55 eV. Furthermore, it was found that around the band gap, the valence band is mainly composed of O 2p<sub>z</sub> orbitals, while the conduction band has a major contribution to the Zn p-orbitals. The analysis of the

mechanical properties showed that the IGP-ZnO has Young's modulus and Poisson's ratio of 177.4 GPa and 0.54, compared to the gZnO, which has 183.2 GPa and 0.65, indicating that, differently from graphenylene and other inorganic analogs, the IGP-ZnO has a very close value of Young's modulus to gZnO, and a lower Poisson's ratio, indicating a better resistance to shear strain.

Therefore, the IGP-ZnO is a stable structure and can be applied in electronic devices that require wide bandgap energy, in addition to acting as a nanofilter for medium/large molecules. In addition, as a great number of porous structures have been proposed for energy harvesting, it is interesting to note that the structural organization of IGP-ZnO and H-gZnO can facilitate redox reactions in these systems.

#### 4.4 Silicon Carbide (SiC)

Proposed in 2021 by Martins et al. [46], inorganic graphenylene-like silicon carbide (IGP-SiC) is a new family member of porous inorganic materials. Using DFT combined with the B1WC hybrid functional, a supercell with 48 atoms (24 of Si and 24 of C) was constructed from the 2H-SiC bulk in the wurtzite phase.

Unlike GP and IGP-BN, which possess 5.47 Å and 5.51 Å diameter [43], respectively, the IGP-SiC has an expansion of the network parameters that provide a central ring with 6.82 Å in diameter. The Si-C bonds of this new structure are narrower compared to GP (22.9%), where the material is more deformable than the organic type, but 3 times more rigid than the Si analog (IGP-Si).

In contrast to graphene-like SiC (g-SiC) which has a direct gap (3.65 eV), IGP-SiC assumes a wide indirect gap (3.22 eV) between the K and M points of the top and bottom of the valence and conduction bands, respectively. The Raman spectra of the IGP-SiC, in comparison to the IGP-Si, also exhibits frequencies closer to those of carbon-based materials (graphene and graphenylene) synthesized, revealing the plausibility of this structure. Molecular Dynamics (MD) simulations report that IGP-SiC has a thermal dynamic stability at approximately 2100 K and, by phonon dispersion calculations, the researchers describe the non-appearance of imaginary frequencies for the material. The summarized data indicate how reasonable the possibility of obtaining the IGP-SiC by experimentalists is.

The investigation of the applicability of inorganic graphenylenes in gas sensing is still incipient, where the study of Martins et al. [46] concerning the IGP-SiC reveals the first potential of these structures. It is reported that the selective doping of 2 Si atoms by 2 Fe atoms in the central ring of the structure provides a considerable increase in the NO gas interaction with the inorganic graphenylene. This doping diminishes the 1.61 eV gap of the Fe-IGP-SiC-NO system to 0.87 eV and results in strong adsorption ( $-58.11$  kcal/mol) of the molecule on the IGP-SiC, producing a candidate material for toxic gas detection.



## 4.5 Gallium Nitride (GaN)

Using the DFT Theory, Fabris et al. [61] present for the first time 1D and 2D porous structures based on gallium nitride (GaN), which are named porous gallium nitride (PGaN), inorganic graphenylene-like gallium nitride (IGP-GaN) and gallium nitride porous nanotubes (PGaNNTs and IGP-GaNNTs). The elastic properties reveal a 146–493 GPa range for Young Modulus, where the 1D structures have stronger bonds that make deformation difficult, in contrast to PGaN and IGP-GaN.

The band structures of 2D porous GaN materials reveal an insulator behavior with an indirect wide gap (4.64–6.0 eV), while the porous GaN nanotubes also assume similar behavior for the armchair (PGaNNTs) (10,10) and IGP-GaNNTs (10,10) and zigzag (PGaNNTs) (10,0) and IGP-GaNNTs (10,0) species. However, with the management of the diameter width of these nanotubes, the band gap decreases at 1 eV compared to PGaN and IGP-GaN, revealing the possibility of electronic modifications of nanotubes by the curvature regulation.

In addition, the researchers evaluate the fingerprint of the porous GaN materials by Raman spectra, where it is explained that high frequencies ( $>1500\text{ cm}^{-1}$ ) occur only for PGaN due to the hydrogen presence, while the IGP-GaN has peaks at low frequencies. Extensive knowledge of Raman spectra for these materials can be of great importance for future experimental studies aiming to obtain their synthesis and explore similar structures.

## 5 Concluding Remarks

In this chapter, we present the graphenylene-like structures as alternatives to graphene in multiple functionalities and gather researchs that demonstrate its potential as an anode in Li (Na) batteries, molecular sieve, sensor and catalyst.

The advance in the predictive power of quantum-computational methods in recent decades has allowed the theoretical prediction of properties of these materials to be very reliable, being able to guide the synthesis of inorganic or hybrid graphenylene analogs for desired applications.

One of the most pronounced properties of monolayer graphenylene is its intrinsic direct band gap, which poses this material as a promising candidate for nanoelectronics applications. Electronic, optical, mechanical, thermal, and chemical properties are easily calculated nowadays, but many interesting applications of graphenylene and graphenylene-like compounds have yet to be demonstrated experimentally.

To date, there have been no practical methods for the large-scale and scalable production of graphenylene (and graphenylene-like) sheets with fine control over the number and the structure of the layers in an unsupported way. Also, to our best knowledge, at this moment there is no other way to synthesize the graphenylene than those presented here.

The subject of monoatomic layers of 2D crystals is now one of the most active fields of research in materials science and condensed matter chemistry/physics under fundamental and practical aspects. Even for structures formed only by  $sp^2$  carbons, not everything resembles graphene. Best of all, many desired properties are superior to graphene and more easily modelable.

There is much to explore from the chemical point of view of modifications of graphenylene as a platform for structures with heteroatoms, dopants, intercalation, formation of nanotubes, in addition to physical modifications, such as deformations and modifications by an electric field. Typical examples of these modifications in graphenylene are the proposition of inorganic systems (e.g. ZnO), and hybrids (e.g. SiC).

There is no doubt about the wide range of possible applications for these materials with extensive surface area and high porosity.

**Acknowledgements** This work was supported by the Brazilian funding agencies FAPESP (2019/08928-9, 2013/07296-2, 2018/03961-5, 2022/00349-2, 2022/03959-6), CAPES - Finance Code 001—(88887.467334/2019-00) and CNPq (420062/2016-5, 312854/2021-8, 2021-3072132021-8). The computational facilities were supported by resources supplied by the Molecular Simulations Laboratory (São Paulo State University, Bauru, Brazil) and High-Performance Computing Center (NPAD) at UFRN.

## References

1. Hoffmann, R., Kabanov, A.A., Golov, A.A., Proserpio, D.M.: *Angew. Chem. Int. Ed.* **55**, 10962 (2016)
2. Balaban, A.T., Harary, F.: *Tetrahedron* **24**, 2505 (1968)
3. Baughman, R.H., Eckhardt, H., Kertesz, M.: *J. Chem. Phys.* **87**, 6687 (1987)
4. Dias, J.R.: *Carbon N. Y.* **22**, 107 (1984)
5. Jones, D.E.H.: *New Sci.* **32**, 245 (1966)
6. Kroto, H.W., Heath, J.R., O'Brien, S.C., Curl, R.F., Smalley, R.E.: *Nature* **318**, 162 (1985)
7. Iijima, S.: *Nature* **354**, 56 (1991)
8. Iijima, S., Ichihashi, T.: *Nature* **363**, 603 (1993)
9. Boehm, H.P., Clauss, A., Fischer, G.O., Hofmann, U.: *Z. Anorg. Allg. Chem.* **316**, 119 (1962)
10. Novoselov, K.S., Geim, A.K., Morozov, S.V., Jiang, D., Zhang, Y., Dubonos, S.V., Grigorieva, I.V., Firsov, A.A.: *Science* **306**, 666 (2004)
11. Bo, Z., Shuai, X., Mao, S., Yang, H., Qian, J., Chen, J., Yan, J., Cen, K.: *Sci. Rep.* **4**, 4684 (2015)
12. Sen Gupta, S., Sreeprasad, T.S., Maliyekkal, S.M., Das, S.K., Pradeep, T.: *ACS Appl. Mater. Interfaces* **4**, 4156 (2012)
13. Shahil, K.M.F., Balandin, A.A.: *Solid State Commun.* **152**, 1331 (2012)
14. Zu, S.-Z., Han, B.-H.: *J. Phys. Chem. C* **113**, 13651 (2009)
15. Fang, Z., Liu, Z., Wang, Y., Ajayan, P.M., Nordlander, P., Halas, N.J.: *Nano Lett.* **12**, 3808 (2012)
16. Goenka, S., Sant, V., Sant, S.: *J. Controlled Release* **173**, 75 (2014)
17. Tang, Z., Wu, H., Cort, J.R., Buchko, G.W., Zhang, Y., Shao, Y., Aksay, I.A., Liu, J., Lin, Y.: *Small* **6**, 1205 (2010)
18. Zeng, M., Liu, Y., Zhao, F., Nie, K., Han, N., Wang, X., Huang, W., Song, X., Zhong, J., Li, Y.: *Adv. Funct. Mater.* **26**, 4397 (2016)

19. Wang, H., Nezhich, D., Kong, J., Palacios, T.: *IEEE Electron Device Lett.* **30**, 547 (2009)
20. Jena, D., Fang, T., Zhang, Q., Xing, H.: *Appl. Phys. Lett.* **93**, 112106 (2008)
21. Liang, G., Neophytou, N., Lundstrom, M.S., Nikonov, D.E.: *J. Appl. Phys.* **102**, 054307 (2007)
22. Teong, H., Lam, K.-T., Bin Khalid, S., Liang, G.: *J. Appl. Phys.* **105**, 084317 (2009)
23. Houssa, M., Dimoulas, A., Molle, A.: *J. Phys. Condens. Matter* **27**, 253002 (2015)
24. Dávila, M.E., Xian, L., Cahangirov, S., Rubio, A., Le Lay, G.: *New J. Phys.* **16**, 095002 (2014)
25. Tang, P., Chen, P., Cao, W., Huang, H., Cahangirov, S., Xian, L., Xu, Y., Zhang, S.-C., Duan, W., Rubio, A.: *Phys. Rev. B* **90**, 121408 (2014)
26. Zhao, H., Zhang, C., Ji, W., Zhang, R., Li, S., Yan, S., Zhang, B., Li, P., Wang, P.: *Sci. Rep.* **6**, 20152 (2016)
27. Piazza, Z.A., Hu, H.-S., Li, W.-L., Zhao, Y.-F., Li, J., Wang, L.-S.: *Nat. Commun.* **5**, 3113 (2014)
28. Xie, Z., Zhang, B., Ge, Y., Zhu, Y., Nie, G., Song, Y., Lim, C.-K., Zhang, H., Prasad, P.N.: *Chem. Rev.* **122**, 1127 (2022)
29. Tusche, C., Meyerheim, H.L., Kirschner, J.: *Phys. Rev. Lett.* **99**, 026102 (2007)
30. Eivari, H.A., Ghasemi, S.A., Tahmasbi, H., Rostami, S., Faraji, S., Rasoulkhani, R., Goedecker, S., Amsler, M.: *Chem. Mater.* **29**, 8594 (2017)
31. de Almeida, E.F., de Brito Mota, F., de Castilho, C.M.C., Kakanakova-Georgieva, A., Gueorguiev, G.K.: *Eur. Phys. J. B* **85**, 48 (2012)
32. Al Balushi, Z.Y., Wang, K., Ghosh, R.K., Vilá, R.A., Eichfeld, S.M., Caldwell, J.D., Qin, X., Lin, Y.-C., DeSario, P.A., Stone, G., Subramanian, S., Paul, D.F., Wallace, R.M., Datta, S., Redwing, J.M., Robinson, J.A.: *Nat. Mater.* **15**, 1166 (2016)
33. Şahin, H., Cahangirov, S., Topsakal, M., Bekaroglu, E., Akturk, E., Senger, R. T., Ciraci, S.: *Phys. Rev. B - Condens. Matter Mater. Phys.* **80**, 1 (2009)
34. Yuan, D., Dou, Y., Wu, Z., Tian, Y., Ye, K.-H., Lin, Z., Dou, S.X., Zhang, S.: *Chem. Rev.* **122**, 957 (2022)
35. Brunetto, G., Autreto, P.A.S., Machado, L.D., Santos, B.I., dos Santos, R.P.B., Galvão, D.S.: *J. Phys. Chem. C* **116**, 12810 (2012)
36. Lu, H., Li, S.-D.: *J. Mater. Chem. C* **1**, 3677 (2013)
37. Song, Q., Wang, B., Deng, K., Feng, X., Wagner, M., Gale, J.D., Müllen, K., Zhi, L.: *J. Mater. Chem. C* **1**, 38 (2013)
38. Elstner, M., Porezag, D., Jungnickel, G., Elsner, J., Haugk, M., Frauenheim, T., Suhai, S., Seifert, G.: *Phys. Rev. B* **58**, 7260 (1998)
39. Haneef, H.F., Zeidell, A.M., Jurchescu, O.D.: *J. Mater. Chem. C* **8**, 759 (2020)
40. Bieri, M., Treier, M., Cai, J., Ait-Mansour, K., Ruffieux, P., Gröning, O., Gröning, P., Kastler, M., Rieger, R., Feng, X., Müllen, K., Fasel, R.: *Chem. Commun.* 6919 (2009)
41. Du, Q.-S., Tang, P.-D., Huang, H.-L., Du, F.-L., Huang, K., Xie, N.-Z., Long, S.-Y., Li, Y.-M., Qiu, J.-S., Huang, R.-B.: *Sci. Rep.* **7**, 40796 (2017)
42. Totani, R., Grazioli, C., Zhang, T., Bidermane, I., Lüder, J., De Simone, M., Coreno, M., Brena, B., Lozzi, L., Puglia, C.: *J. Chem. Phys.* **146** (2017)
43. Fabris, G.S.L., Marana, N.L., Longo, E., Sambrano, J.R.: *J. Solid State Chem.* **258**, 247 (2018)
44. Yang, C., Li, Y., Chen, Y., Li, Q., Wu, L., Cui, X.: *Small* **15**, 1804710 (2019)
45. Zheng, Y., Feng, Q., Tang, N., Du, Y.: *New Carbon Mater.* **33**, 516 (2018)
46. Martins, N.F., Fabris, G.S.L., Albuquerque, A.R., Sambrano, J.R.: *FlatChem* **30**, 100286 (2021)
47. Motallebipour, M.S., Karimi-Sabet, J.: *Phys. Chem. Chem. Phys.* **23**, 14706 (2021)
48. Rezaee, P., Naeij, H.R.: *Carbon N. Y.* **157**, 779 (2020)
49. Wang, L., Li, F., Wang, J., Li, Y., Li, W., Yang, Y., Zhao, M., Qu, Y.: *Phys. Chem. Chem. Phys.* **22**, 9789 (2020)
50. Xu, J., Zhou, S., Sang, P., Li, J., Zhao, L.: *J. Mater. Sci.* **52**, 10285 (2017)
51. Zhu, L., Jin, Y., Xue, Q., Li, X., Zheng, H., Wu, T., Ling, C.: *J. Mater. Chem. A* **4**, 15015 (2016)
52. Tang, Y., Chen, W., Wang, Z., Zhao, G., Cui, Y., Li, Z., Li, Y., Feng, Z., Dai, X.: *Appl. Surf. Sci.* **530** (2020)
53. Hankel, M., Searles, D.J.: *Phys. Chem. Chem. Phys.* **18**, 14205 (2016)
54. Hussain, T., Hankel, M., Searles, D.J.: *J. Phys. Chem. C* **121**, 14393 (2017)

55. Jahangirzadeh, M., Azamat, J., Erfan-Niya, H.: *Comput. Mater. Sci.* **203**, 111126 (2022)
56. Liu, W., Miao, M., Liu, J.: *RSC Adv.* **5**, 70766 (2015)
57. Meftakhutdinov, R.M., Sibatov, R.T., Kochaev, A.I.: *J. Phys. Condens. Matter* **32**, 345301 (2020)
58. Tang, Y., Chen, W., Zhao, G., Teng, D., Cui, Y., Li, Z., Feng, Z., Dai, X.: *ChemPhysChem* **22**, 606 (2021)
59. Villegas-Lelovsky, L., Paupitz, R.: *Phys. Chem. Chem. Phys.* **22**, 28365 (2020)
60. Yu, Y.X.: *J. Mater. Chem. A* **1**, 13559 (2013)
61. Fabris, G.S.L., Paskocimas, C.A., Sambrano, J.R., Paupitz, R.: *J. Solid State Chem.* **303**, 122513 (2021)
62. Liu, X., Dai, L.: *Nat. Rev. Mater.* **1**, 16064 (2016)
63. Pérez-Mayoral, E., Calvino-Casilda, V., Soriano, E.: *Catal. Sci. Technol.* **6**, 1265 (2016)
64. Chen, W., Wang, Z., Cui, Y., Li, Z., Li, Y., Dai, X., Tang, Y.: *New J. Chem.* **44**, 15733 (2020)
65. Tang, Y., Chen, W., Zhang, H., Wang, Z., Teng, D., Cui, Y., Feng, Z., Dai, X.: *Phys. Chem. Chem. Phys.* **22**, 16224 (2020)
66. Asenbauer, J., Eisenmann, T., Kuenzel, M., Kazzazi, A., Chen, Z., Bresser, D.: *Sustain. Energy Fuels* **4**, 5387 (2020)
67. Tarascon, J.-M., Armand, M.: *Nature* **414**, 359 (2001)
68. Fabris, G.S.L., Albuquerque, A.R., Dovesi, R., Sambrano, J.R.: *Mater. Sci. Eng. B: Solid-State Mater. Adv. Technol.* **268**, 115121 (2021)
69. Jache, B., Adelhelm, P.: *Angew. Chem. Int. Ed.* **53**, 10169 (2014)
70. Wasalathilake, K.C., Ayoko, G.A., Yan, C.: *Carbon N. Y.* **140**, 276 (2018)
71. Meftakhutdinov, R.M., Sibatov, R.T., Kochaev, A.I., Evseev, D.A.: *Phys. Chem. Chem. Phys.* **23**, 14315 (2021)
72. Ding, Y., Wang, Y., Shi, S., Tang, W.: *J. Phys. Chem. C* **115**, 5334 (2011)
73. Perim, E., Paupitz, R., Autreto, P.A.S., Galvao, D.S.: *J. Phys. Chem. C* **118**, 23670 (2014)
74. Cassabois, G., Valvin, P., Gil, B.: *Nat. Photonics* **10**, 262 (2016)
75. Fabris, G.S.L., Marana, N.L., Longo, E., Sambrano, J.R.: *ACS Omega* **3**, 13413 (2018)
76. Feng, J.-R., Wang, G.-C.: *Comput. Mater. Sci.* **111**, 366 (2016)
77. Hu, W., Wu, X., Li, Z., Yang, J.: *Phys. Chem. Chem. Phys.* **15**, 5753 (2013)
78. Jiang, D., Cooper, V.R., Dai, S.: *Nano Lett.* **9**, 4019 (2009)
79. Fabris, G.S.L., Marana, N.L., Longo, E., Sambrano, J.R.: *Theor. Chem. Acc.* **137** (2018)
80. Fabris, G.S.L., Marana, N.L., Laranjeira, J.A.S., Longo, E., Sambrano, J.R.: *Mater. Lett.* **275**, 128067 (2020)

# Computer Simulations of MOF Systems: Key Applications



Nailton Martins Rodrigues and João Batista Lopes Martins

**Abstract** Metal–organic frameworks are a class of materials with structural characteristics that make them very attractive for a wide variety of applications, and among these, the wide variety of pore arrangements, types, and volumes stand out. In 2017 it was estimated that more than 70,000 crystallographic structures of MOFs were deposited in the Cambridge Structural Database, and a large number has not been evaluated for its use in some applications. Studies investigating applications of these structures are predominantly carried out using experimental techniques. Although works carried out with computer simulation have shown a significant increase in publications, this area still has a multitude of possible investigations for various structures that can be performed with computer simulation methods, bringing contributions and insights from data with quality and consistent with experimental results.

## 1 Introduction

The class of coordinating polymers known as the Metal–Organic Framework (MOFs) are structures that stand out due to their porosity [1]. They can have two or three dimensions [2], and are formed from the coordination of an organic ligand (usually containing O-, N- and S-donor atoms) to the metal ion [3]. As a result of the reticular synthesis [1, 4], a structure is obtained. This structure contains a part with inorganic characteristics constituted by the metallic ion and the atoms of its coordination polyhedron. The other part contains organic characteristics that basically constitute the ligands used in the synthesis. The organic part is also often called the spacer [5] since the pore volume depends mainly on the size of the ligand used [6].

Other notations for the different parts and clusters of MOFs are also used. The ligand and the metal are often called “linkers”, the coordinating polyhedron of “Primary Building Unit” (PBU), and a finite combination of PBUs can be called Secondary Building Unit (SBU), as described by D’Vries et al. [7] and by Sani

---

N. M. Rodrigues (✉) · J. B. L. Martins  
Instituto de Química, Universidade de Brasília, Brasília, DF 70910-900, Brazil  
e-mail: [nailton.rodrigues@unb.br](mailto:nailton.rodrigues@unb.br)

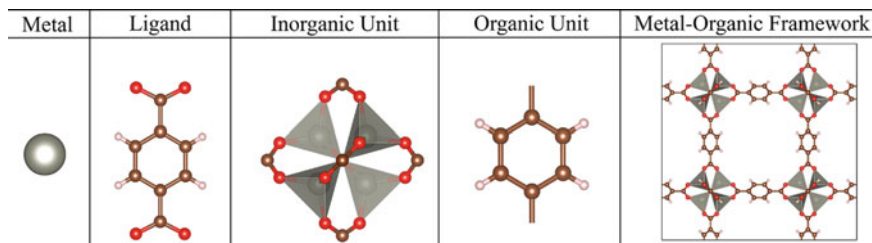


**Fig. 1** Simplified illustration of the parts that make up the MOF-5 (IRMOF-1), that arise by the combination by the zinc metal and the 1,4-benzenedicarboxylate ligand. Atom color label: oxygen: red, carbon: brown, hydrogen: white, zinc: grey

et al. [8]. For Giliopoulos the coordination polyhedron and the  $-\text{CO}_2$  group is called complex/SBU [9]. Yaghi et al. designates the coordinating polyhedron as an “Inorganic Unit”, the ligand of “Organic Unit”, polygons and polyhedra bounded by carboxylate carbons of “Inorganic SBU”, and also the “Organic SBU” as an arrangement formed by the union of ligands [10]. In this context, this review will adopt the designation of the parts that make up these structures only by organic and inorganic units, aiming to facilitate the discussion, as shown in Fig. 1.

In addition to being the spacer responsible for the pore volume, the ligand has a key role in terms of the versatility of this crystalline material. Combining different ligands and metal ions provides thousands of possibilities [11] for the formation of structures with pores from characteristic chemical environments. These structures, combined with its high chemical and thermal stability, and the possibility of obtaining different pore volumes and surface area [12], enable a wide range of applications, ranging from drug delivery [13, 14], markers for the identification of gunshot residues [15], catalysts [16], in gas capture [17], storage [18], and separation [19], pesticide capture [20], removal of radioactive elements [21], among others [22].

Several types of pores are possible in MOFs, which is a big challenge compared to other porous structures [12]. However, the same synthesis process can generate interpenetrated and non-interpenetrated structures with distinct characteristics [23]. The non-interpenetrated structures are the most reported in the literature, and applications such as  $\text{N}_2$  adsorption in the interpenetrated and non-interpenetrated structures show significant differences [24].

For structures that have transition metal, the term MOF is the most commonly used, for those with lanthanides, the term Lanthanide Metal–Organic Frameworks (Ln-MOFs) [25–27] and Lanthanide Organic Frameworks (LOFs) are widely used, and the last term is widely used currently [28–30]. LOFs are widely studied in terms of their luminescent properties [31, 32], but other applications that do not exploit these properties are also reported [33, 34].

In 2017 it was reported that there are approximately 70,000 crystallographic structures of MOF included in the Cambridge Structural Database (CCDC) [35], making the possibility of applications and studies involving such structures enormous. A MOF that has been widely studied, either by experimental or theoretical bias, is the

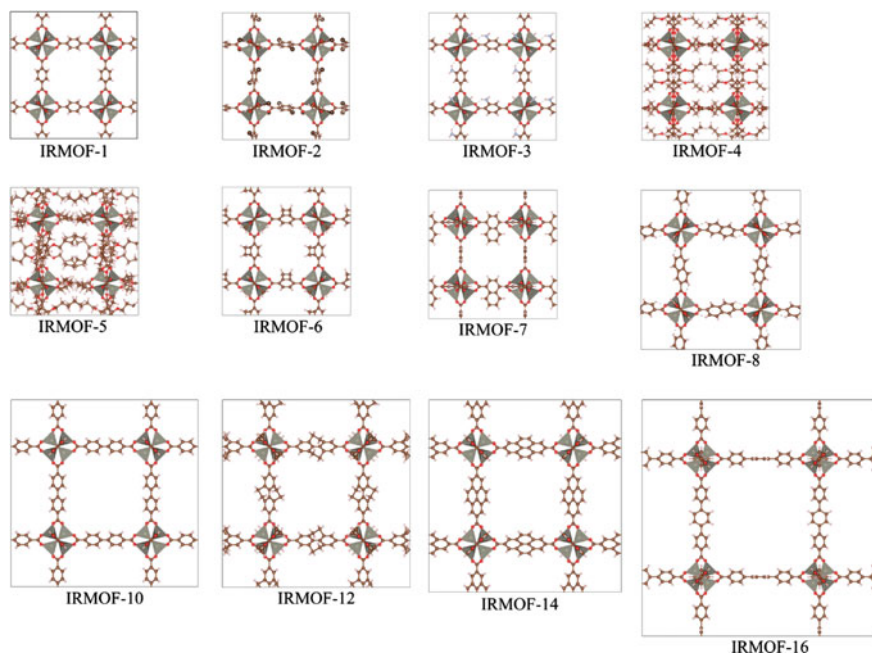


**Fig. 2** Crystallographic unit cells of non-interpenetrated IRMOFs that have cubic cells. Atom color label: oxygen: red, carbon: brown, hydrogen: white, zinc: grey

MOF-5 [36, 37], which is also known as IRMOF-1 since generated a new group of structures that differ from each other only with regard to their organic unit. Therefore, these structures are called iso-reticular MOF (IRMOFs), and were reported in the works published by Yaghi's group [38, 39], and one of its characteristics are the different pore volumes that come from the spacers used (see Fig. 2).

Experimental works involving MOFs are widely found in the literature. Performing a search in ScienceDirect for the pattern “Metal Organic Framework” shows that this field has grown exponentially in the last 20 years, as can be seen in Fig. 3. Regarding the use of computer simulation techniques, it is possible to observe that the term DFT (Density Functional Theory) combined with “Metal–Organic Framework” appears with considerable frequency and constant growth. When “Metal–Organic Framework” is combined with “Molecular Dynamics”, “Semiempirical” or with “Grand Canonical Monte Carlo”, the results are now expressed in smaller figures. Thus, it is possible to verify that DFT is the most used among the theoretical calculation methodologies, associated with experimental data [40, 41] or purely theoretical [42].

The data in Fig. 3 constitute a scenario demonstrating that experimental techniques dominate studies involving the field of MOFs. Therefore, the use of theoretical techniques needs to be improved. In this way, throughout this review, results of works that used theoretical techniques will be addressed, and their contributions and advantages.

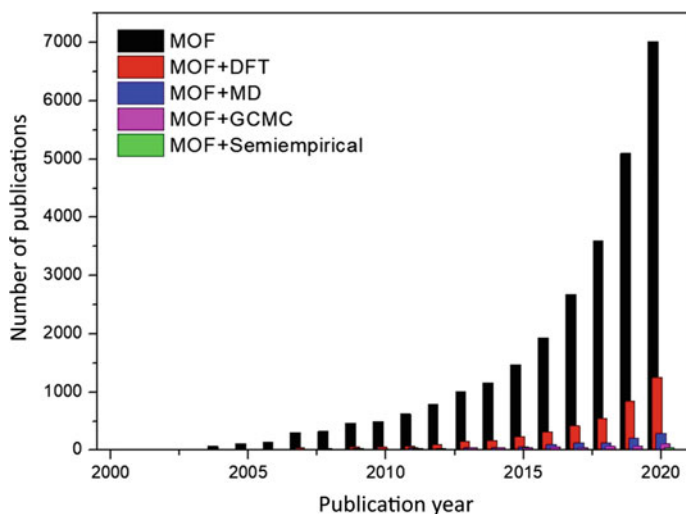


**Fig. 3** Number of scientific publications depending on the year of publication, for articles that contain the terms: “Metal–Organic Framework” (MOF), “Metal–Organic Framework” DFT (MOF + DFT), “Metal–Organic Framework” Semiempirical (MOF + Semiempirical), “Metal–Organic Framework” “Molecular Dynamics” (MOF + MD), “Metal–Organic Framework” “Grand Canonical Monte Carlo” (MOF + GCMC)

## 2 Most Used Theoretical Methods

MOF systems require performing periodic boundary conditions calculations for crystalline materials to obtain properties that depend on a good description of the equilibrium geometry. Among the calculation methods used to investigate these structures, the DFT method are the most used due to the valuable cost–benefit relationship. This is partly due to the good results that it enables, but which can vary substantively depending on the functional and the set of base functions used in the calculation [43].

In the DFT method, the energy of a system is dependent on the electronic density ( $\rho$ ) according to Eq. 1, and its minimum energy value for a system corresponds to the ground state.

$$E = E_v[\rho] \quad (1)$$

In the description of the Hamiltonian for the DFT method, the dependence on the electron density is included, and from the evolution of the mathematical treatment keeping the electronic density as a fundamental quantity, system energy can be written as:

$$E = \langle \Psi | T + V | \Psi \rangle + \int \rho(r)v(r)dr \quad (2)$$



where  $T$  is the kinetic energy,  $V$  is the electron–electron repulsion term and  $v$  is the external potential.

Because electron density does not predict electron spin states, it is necessary to include correlation and exchange functionals. Among these there is a large number of functionals available, being the B3LYP [44] and the PBE [45] two examples of functionals commonly used in studies on the MOF systems [46]. The last one is the most used in solid state calculations, which is the most suitable for treating unit or primitive cells of solid such as MOFs [47].

MOF unit cells can contain a few hundred or even thousands of atoms, making the DFT method less efficient since the computational time required is very large. In this way, semiempirical methods become a good alternative when there is no possibility of generating primitive cells from the unit cell and the system has a high number of atoms (Fig. 4). These methods have become very attractive due to the inclusion of approximations and parametrizations that make these methods faster when compared to the DFT, and due to the possibility of parallelization [48], use of Graphics Processing Unit (GPU) [49, 50] and with the solid-phase calculation methodology [51] included in the MOPAC program [52].

The semiempirical methods were developed based on the Hartree–Fock method [53], which tries to solve the Schrödinger equation with some restrictions and mathematical approximations [24, 54] that are included in the Hamiltonian operator. The semiempirical methods most used today are the AM1 [55], PM3 [56], PM6 [57], PM7 [58] and RM1 [59] semiempirical Hamiltonians, contained in the MOPAC program [52] and are in a constant development [60]. For MOF with Lanthanide atoms in its structure, the calculation can be performed using the RM1 method [61] or from the other methods using the Sparkle model [62], which consists of an approach that treats the lanthanide(III) ion as a  $+3e$  Coulombic charge. This approximation considered that the interaction between the ion and the atoms of the coordination polyhedron has an electrostatic character essentially [63].

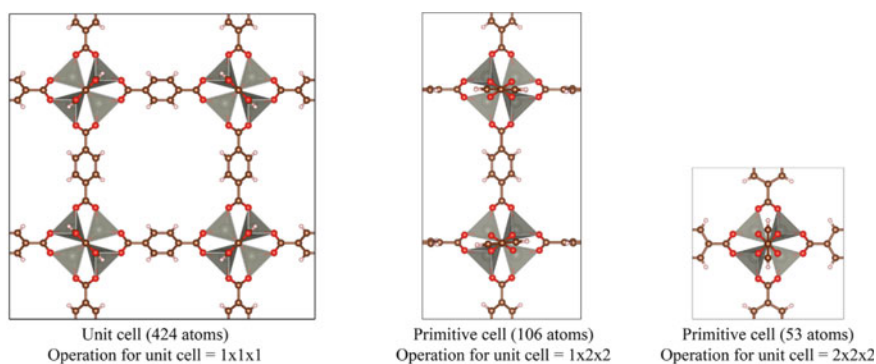


**Fig. 4** IRMOF-1 unit cell and your primitive cell. Primitive cells can be transformed into a unit cell by the operation  $1 \times 2 \times 2$  and  $2 \times 2 \times 2$  in their respective lattice parameters  $a$ ,  $b$ , and  $c$ . Atom color label: oxygen: red, carbon: brown, hydrogen: white, zinc: grey

When a study requires an assessment of the behavior of a system over a period of time, Molecular Dynamics simulation is a method capable of providing such data. In this method, a force field model describes the structure of MOF and the molecules that make up the system. The force field describes bonds, angles, torsions, and the weak and strong interactions that govern the balanced system. The strength of this method is that the system configuration can change its position over time, and this is done by taking into account the movements of molecules in their degrees of freedom.

The movement of molecules is dependent on the interactions that occur in the system, which are described by the potentials. The positions that are generated at a given moment are described using Newton's equations of motion. For the system configuration at a given instant or even from temporal averages for a specific time interval, the macroscopic properties can be obtained using concepts from statistical thermodynamics.

As a method that uses fundamental concepts and approximations to describe the system and its behavior, force field makes possible to treat systems with thousands of atoms, be it gas, liquid, supercritical fluids, among others. It, provides data such as the diffusion of molecules in MOFs [64] and even desalination studies using MOFs [65].

If a study needs to obtain adsorption isotherms for a given gas and quantify the adsorption of any molecule on a given MOF, the Grand Canonical Monte Carlo (GCMC) method can be used for this purpose [66]. GCMC basically applies the Monte Carlo method, which performs random distributions of a given sample to the grand canonical ensemble [67]. The Grand Canonical ensemble deals with a system in contact and equilibrium with a large thermal and particle reservoir [68]. In the simulation, the volume ( $V$ ), temperature ( $T$ ), and chemical potential ( $\mu$ ) are kept fixed. The system is kept in equilibrium, which allows the number of adsorbed molecules to vary, moving from the reservoir to the simulation box throughout the calculation. The simulation box can be the unit cell, a super cell or others model [69].

In GCMC simulation, the interactions between molecules and between molecules and MOF can be described in terms of a force field consisting only of non-binding parameters, with the fixed MOF [70] and only the rotation and translation modes of the free gas or molecule [71], simplifying the process. The potential energy for the interactions can be calculated using the Lennard–Jones equation with the Coulomb potential described in Eq. 3.

$$V_{ij}(r_{ij}) = 4\varepsilon_{ij} \left[ \left( \frac{\sigma_{ij}}{r_{ij}} \right)^{12} - \left( \frac{\sigma_{ij}}{r_{ij}} \right)^6 \right] + \frac{q_i q_j}{4\sigma \varepsilon_0 r_{ij}^2} \quad (3)$$

where  $r_{ij}$  is the distance between atoms  $i$  and  $j$  that have charges  $q_i$  and  $q_j$ , whereas  $\varepsilon$  and  $\sigma$  refer respectively to the minimum potential and the separation (distance) when  $V = 0$ , which are previously adjusted parameters.

Coulomb potential well describes strong interactions and long-distance interactions. The Lennard–Jones potential well describes van der Waals which are weak interactions [72]. From these interactions, it is possible to obtain absolute and excess

adsorption isotherms (reflects experimental data). For the vast majority of MOFs and including IRMOFs, the isotherm profile is type 1 (according to IUPAC) [73], which is since they are microporous materials [74, 75]. Regarding adsorption, it can be physical or governed by weak intermolecular forces such as van der Waals forces, or chemistry, involving stronger interaction forces, with the final result being the formation of an intramolecular chemical bond [76].

The interaction energies (adsorption) for each molecule can be obtained from calculations using DFT [77], semiempirical [78], and other methods [79]. This is an important data and can complement information about which adsorption sites are more or less favorable [80, 81]. Among other information that combined with theoretical data are the adsorption isotherms [82], diffusion dynamics [83], radial distribution [84], nature of the bonds [85], among others [86, 87], which can provide extremely important information for the use of MOFs in various applications [88].

### 3 Fuel Gas Storage

The storage of gases such as hydrogen ( $H_2$ ) and methane ( $CH_4$ ) gas requires the use of high pressures (200–300 bar at room temperature) [89, 90] both for storage and distribution [91]. For safe gas storage, aiming for use in motor vehicles, it is necessary to use highly resistant cylinders capable of withstanding the application of high pressures, making the process very expensive [92]. Applications that need high pressure bring a strong risk of explosion, and in this context, natural gas storage (50 to 98% of methane in volume) [93] can be see cited.  $H_2$  and  $CH_4$  require the application of high pressures to store a considerable amount of these gases. However, gas storage in a cylinder containing a porous material such as activated carbon promotes more excellent gas storage at much lower pressures [94, 95], and this is due to the occurrence of physical adsorption of the gas in the pores and surface of the active carbon, facilitating the gas storage process [96, 97]. Among several porous materials, MOFs have great potential to be used due to their regular porosity, high surface area, chemical stability that maintains the structure constant even after removing adsorbed molecules, among other characteristics already discussed [98].

Methane gas storage capacity in 15 IRMOF new structures was evaluated by Yaghi's group. They demonstrated that IRMOF-6 was the one that demonstrated the highest degree of adsorption and efficiency for the storage of methane, which resulted in a 70% increase in the storage of this gas in a cylinder under a pressure of around 205 atm. This high efficiency was attributed to the large surface area, and this pressure can be used without risk in motor vehicles [39].

Conducting a study of the adsorption of hydrogen molecules on IRMOF-1, IRMOF-6 and IRMOF-20, Fischer et al. [99] obtained adsorption isotherms from GCMC simulations. It was reported that the Lennard–Jones potential is a good alternative for obtaining theoretical adsorption isotherms because this potential describes the Van der Waals interactions very well, and it governs the physical adsorption of hydrogen molecules with MOF sites [100].

Our recent study of methane adsorption isotherm in IRMOF-1 with GCMC, using the Lennard–Jones parameters of the GenericMOF force field (contained in the RASPA program) [101] for the MOF atoms and for the pseudo methane atom (simple sphere model) [102], and the adsorption isotherm was obtained and is present in Fig. 5 (red line). Comparing the theoretical isotherm with the experimental isotherm obtained by Furukawa et al. [34], it is possible to observe an agreement between the isotherms, and that more significant deviations are observed for high pressures. These results support the assertion that the Lennard–Jones potential describes the interactions and, consequently, the adsorption isotherm.

Gases such as hydrogen and methane preferentially adsorb on the inorganic unit [32], and the preferred interaction position is over the oxygens [103], which are coordinated to the metallic centers. The organic unit is configured as a deficient region for adsorption and ways to increase the molecule affinity, such as  $H_2$ , to this unit are investigated. For example, doping with Li, Be, Mg, and Al in the aromatic ring of IRMOF-1 [104]. In this process, the metal interacts with the ring and has a strong ionic character (partially positive charge) obtained from the charge transfer from metal to the aromatic ring. Among the metals mentioned, Li and Al demonstrate a greater affinity with  $H_2$  molecule from interaction energy values calculated with the DFT method. Volkova et al. concluded that for the doping of aromatic rings with Li atoms, in addition to the increase in the interaction energy, the adsorption obtained with GCMC is more than double without Li at 300 K and 100 bar [105]. Doping the aromatic rings of IRMOF-6 with Al in a similar strategy to those mentioned above, increases the interaction energy with the organic unit. However, in relation to the adsorption of  $H_2$  and  $CH_4$  simulated with GCMC a non-significant increase

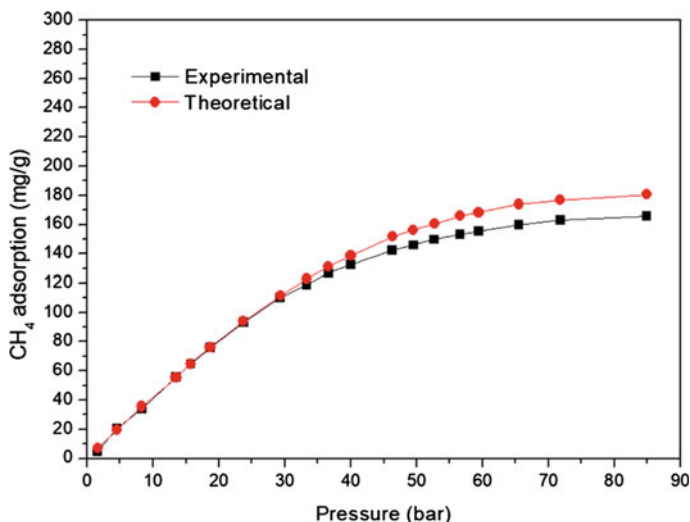


**Fig. 5** Comparison between the  $CH_4$  adsorption isotherms in IRMOF-1 at 298.15 K obtained with GCMC and the experimental data

was seen because the size of the Al atom reduces the pore volume, making it a non-viable alternative [106]. The studies cited used DFT, MP2, semiempirical and GCMC, which are important methods to obtain the properties such as interaction energies and adsorption isotherms.

Replace ring carbon atoms [107] or hydrogen atoms contained in the ring by groups with different properties can increase the adsorption on the organic unit, making the MOF more attractive [108]. After modification, the minimum geometry of these new structures can be calculated using, for example, DFT or semiempirical from calculations with periodic boundary conditions [109], and after this process, they can be used in other investigations [88, 110].

## 4 Polluting Gas Capture

An application that focuses on promoting a reduction in the environmental impacts of contaminating gases already present in the atmosphere concerns the use of MOFs in gas capture as hydrogen sulfide ( $\text{H}_2\text{S}$ ), carbon dioxide ( $\text{CO}_2$ ), sulfur dioxide ( $\text{SO}_2$ ) [111] and nitrogen dioxide ( $\text{NO}_2$ ) [11], which are very harmful toxic molecules that can cause severe environmental damage.

One of the big problems facing our society today is looking for ways, in the short term, to control the emission of polluting gases, and in the long term, to promote the reduction in the concentration of polluting gases in the atmosphere. Investigations on promoting the capture of such gases has already been reported in the literature [61], and its principle consists of capture from adsorption on MOFs for further conversion into less harmful molecules [112]. Insights on how to promote  $\text{H}_2\text{S}$  capture were discussed by Chen et al., which consisted of investigation the interaction of gases (including  $\text{H}_2\text{S}$ ) with different inorganic clusters and subunits. This theoretical work was carried out using DFT calculations. They observed that unsaturated metal centers showed strong interaction with  $\text{H}_2\text{S}$  molecules, and adding amino-group to the organic unit increases polarization and facilitates interaction with  $\text{H}_2\text{S}$  [89].

In general, molecules tend to interact more strongly with metal atoms or with oxygens in the coordination sphere, and the interaction energy has a strong relationship with the metal component of the MOF, so that the value of the interaction energy is a determining factor in the decomposition of adsorbed molecules that can be converted into less harmful molecules through reactions within the pore [113].

From GCMC simulations for the  $\text{H}_2\text{S}$  adsorption on IRMOF-1 at 298 K, it was possible to observe that the  $\text{H}_2\text{S}$  molecules adsorb on the MOF even at low pressures. Our results demonstrate that under ambient conditions (298 K and 1 bar), the molecules preferentially adsorb on the inorganic unit (Fig. 6a). At a pressure of 3 bar (Fig. 6b) it is already possible to observe that the adsorption of molecules on the organic unit already occurs. At 20 bar (Fig. 6c) the molecules occupy all regions of the pore and start to interact with each other more frequently.

The organic unit is a less efficient region in capturing polluting gases, but its importance in the process is remarkable, and once the inorganic unit is saturated,

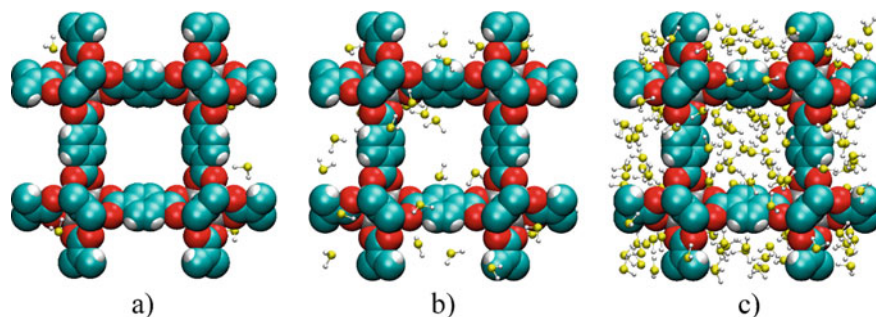


**Fig. 6** Comparison between  $\text{H}_2\text{S}$  adsorption in IRMOF-1 at 298 K and pressure at **a** 1 bar, **b** 3 bar, and **c** 20 bar, obtained with GCMC in RASPA program

it becomes the site to be adsorbed. Its saturation occurs at higher pressures [31], and changes in the organic unit can facilitate adsorption by shifting saturation to increasingly lower pressures [114, 115].

The first reference in the literature on the use of MOFs in  $\text{H}_2\text{S}$  capture was reported by Hamon et al. [116]. In this study, the authors demonstrated the reversibility and recycling capacity of MOFs evaluated through  $\text{CH}_4$  adsorption experiments at room temperature, before and after the  $\text{H}_2\text{S}$  adsorption process, reaching good results for MIL-101(Cr) [116].

Gutiérrez-Sevillano et al. studied the adsorption of  $\text{H}_2\text{S}$  on MOFs Cu-BTC, MIL-47, and IRMOF-1 through GCMC. In addition to developing their own force fields to describe the interactions that occur in these systems, they studied the influence of the number of sites on the adsorption properties of  $\text{H}_2\text{S}$  in the evaluated MOFs [117].

## 5 Gas Separation

Another application that gained prominence, concerns in the gas separation process using MOFs, such as the purification of natural gas and the purification of noble gases [118].

The application of MOFs in natural gas purification is one of the main objectives in removing molecules such as  $\text{H}_2\text{S}$  and  $\text{CO}_2$  usually present in different compositions. The adsorption sites selectivity of MOFs can promote the separation of gases, enhancing the purity of a given gas or set of gases. In 2006, theoretical works evaluating the potential of MOFs in natural gas purification were reported using GCMC to evaluate the separation capacity of MOF CuBTC for a mixture of  $\text{CO}_2$  with  $\text{CH}_4$  and  $\text{C}_2\text{H}_6$ , where selective adsorption of  $\text{CO}_2$  was verified, and the results were in agreement with experimental data [63].

Studies investigating the gas separation processes in MOFs usually use the GCMC method [119]. Yang and Zhong, for example, used GCMC to study the removal of

CO<sub>2</sub> through the use of a set of MOFs for the consequent formation of light alkanes [63] and synthetic gas [120], and this method is already consolidated as an excellent candidate to be used in these studies [106]. However, studies with other methods or a combination of methods are reported [106].

Methane, the main component of natural gas is a strong candidate to replace oil as the primary energy source in the transport sector. This is motivated by the fact that it is a cleaner fuel than gasoline and diesel, with a low production cost [121]. In addition to 95% methane and traces of ethane and propane, natural gas has contaminants such as H<sub>2</sub>S and CO<sub>2</sub> [122]. In addition to being very toxic and corrosive, these contaminants tend to reduce the combustion power of natural gas. Therefore, ways to promote the development of technologies to remove this contaminant are fundamental [123].

In the separation of natural gas, IRMOF-1 and Cu-BTC were constantly cited [124], and its pore volume is highlighted. Compared to other adsorbents like silicate, C168 schwarzite, the IRMOF-1 stood out and showed a greater ability to adsorb pure CO<sub>2</sub> and this gas from a mixture of CO<sub>2</sub> and CH<sub>4</sub>, which the CO<sub>2</sub> is preferentially adsorbed, and this results in selective adsorption promoting the separation of gases [106].

The separation between H<sub>2</sub>S and CH<sub>4</sub>, has a behavior like CO<sub>2</sub> and CH<sub>4</sub>, and the IRMOF-1 has been efficient in this process. H<sub>2</sub>S molecules adsorb preferentially in the inorganic unit of IRMOF-1, and the selectivity increases with the reduction of the temperature, and the interaction with the inorganic unit has an electrostatic character [106]. After suturing the inorganic unit, the H<sub>2</sub>S molecules start to interact with the organic unit and between them.

In gas separation, the use of optimal conditions to maximize the process is an important step. In the separation between CH<sub>4</sub> and H<sub>2</sub>S performed by IRMOF-1, it was noted that for a mixture in the 50:50 ratio, variations in temperature already affect the quality of the separation, and temperature around 323 K unfavorable the methane separation for gas purification. On the other hand, at lower temperatures (273 K) the separation is maximized and at pressures greater than 14 bar the H<sub>2</sub>S approaches 100% of adsorbed molecules, so it is a favorable condition for the purification of CH<sub>4</sub> [125].

A more detailed analysis of the potential for separating CH<sub>4</sub> and H<sub>2</sub>S is done regarding the number of molecules adsorbed per unit cell. Table 1 shows our GCMC results for the number of molecules adsorbed for each gas of a binary mixture of

**Table 1** Number of molecules adsorbed per IRMOF-1 unit cell at different pressures and temperatures, for a mixture of CH<sub>4</sub> and H<sub>2</sub>S in a 50:50 ratio. In parentheses the values in percentage

Temperature	Pressure			
	3 bar		15 bar	
	CH <sub>4</sub>	H <sub>2</sub> S	CH <sub>4</sub>	H <sub>2</sub> S
273 K	4.71 (12.31%)	33.56 (87.69%)	0.35 (0.18%)	195.84 (99.82%)
298 K	2.32 (16.28%)	11.93 (83.72%)	3.62 (2.30%)	153.88 (97.70%)
323 K	1.92 (20.21%)	7.58 (79.79%)	8.86 (10.04%)	79.38 (89.96%)

CH<sub>4</sub> and H<sub>2</sub>S in a 50:50 ratio and inserted in IRMOF-1, at temperatures of 273, 298, and 323 K and pressures of 3 and 15 bar. To better understand how the number of adsorbed molecules varies as a function of temperature, it is necessary to observe the data in Table 1.

From the results in Table 1, it is possible to observe that the increase in temperature reduces the percentage of H<sub>2</sub>S molecules adsorbed on IRMOF-1, and the increase in pressure increases the percentage of adsorbed H<sub>2</sub>S molecules. Thus, it is possible to suggest that a combination of low temperature (273 K) and high pressure (15 bar) can maximize the separation process since under these conditions, 99.82% of the molecules adsorbed on IRMOF-1 were H<sub>2</sub>S molecules.

The separation of noble gases also exploits physical adsorption, which is a key point of this application. The fact that a noble gas interacts with a given MOF more intensely than another promotes a selectivity, and if we think of MOF as a kind of molecular sieve, the gas that interacts with greater intensity must be retained in the MOF structure. The gas that interacts with less intensity or does not interact must be free and purified. Finally, the gas trapped in the MOF can be released by heating the system or converted into less harmful molecules [126].

## 6 Drug Delivery

Some treatments may use drug delivery systems, and research has shown that MOFs can be used in this type of application [127]. In this way, different bio-compatible MOFs have been studied and several combinations between drugs and MOFs have been evaluated for this application. Moreover, Erucar [28] evaluates the storage performance of 24 bio-compatibles MOF for three molecules, such as ibuprofen. Among these 24 structures, the bio-MOF-100 and MOF-74 were highlighted as promising for this application.

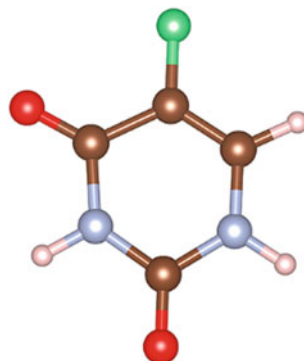
The use of MOFs as drug delivery, due to the drug-MOF system formation (or Drug@MOF) [128] has the possibility of providing a continuous and controlled release of the drug in the plasma [129] that can make some treatments more viable. Conventional dosages tend to result in drug concentrations beyond the therapeutic range, in the toxic range [130], generating side effects that can promote the end of treatment before eradicating the disease. Thus, several drug carriers have been developed [131], and they yield significant contributions to this area [132].

Among the wide variety of existing drugs, it is possible to highlight 5-fluorouracil (Fig. 7), which is one of the drugs used in chemotherapy treatments for tumors such as the esophagus, bladder, ovary, prostate, and breast [133], and the use of MOF as a carrier of this drug has been investigated both experimentally [133] and theoretical [134].

Using experimental combined with computer simulation, Yan et al., in 2019 studied the use of a Zn-MOF ([Zn<sub>3</sub>(OH)<sub>2</sub>(H<sub>2</sub>tccp)<sub>2</sub>(bpy)<sub>2</sub>](H<sub>2</sub>O)<sub>3</sub>(DMF)<sub>3</sub>) as 5-fluorouracil carrier. It was seen that the pore capture capacity of this MOF was 30.7% and that a controlled release in artificial plasma solution was provided. The



**Fig. 7** 5-fluorouracil structure calculated using DFT with B3LYP functional and the 6-311++G\*\* basis set. Atom color label: oxygen: red, carbon: brown, hydrogen: white, nitrogen: blue, fluorine: green



system was chosen as an efficient inhibitor of ovarian cancer cell proliferation from *in vitro* and *in vivo* tests [135].

Investigating 5-fluorouracil and caffeine adsorption on ZIF-8 to quantify the adsorption and evaluate the effect of water and methanol solvents in this process, Proenza and Longo [134] used GCMC and Gibbs-Ensemble Monte Carlo (GEMC). In all simulations, the GenericMOF force field contained in the RASPA program was used [101] to describe MOF, 5-fluorouracil, and caffeine, while for solvent, OPLS/2016 was used [136]. This work demonstrated that only solvent molecules had access to the pore, the others were adsorbed on the surface, so pore size is a relevant factor. A proposed force field for use in MOFs is a significant advance, and its use has generated data consistent with experimental results [137].

5-Fluorouracil molecules interact well with the inorganic unit of MOFs through the electrostatic interaction performed between oxygen atoms of 5-Fluorouracil and metal atoms of the inorganic unit, as well as for hydrogen bonding between hydrogen atoms of the N–H of 5-Fluorouracil and oxygen atoms that constitute the coordinating polyhedron of the inorganic unit. It is also observed that 5-Fluorouracil molecules interact well through hydrogen bonding, which makes the formed system have greater stability [138].

We have recently studied the adsorption of 5-Fluorouracil molecules on IRMOF-1 and IRMOF-10, from distribution density data (Fig. 8) obtained in the RASPA program [138]. It is possible to observe that for IRMOF-1 and molecules of 5-fluorouracil, the most recurrent regions (green regions) are close to the inorganic unit. For the IRMOF-10, which has a greater pore volume, the molecules have a more homogeneous distribution (light green and light blue), evidencing that as the pore of MOF increases, a greater possibility of interaction starts to occur due to the greater volume available, reducing repulsion.

The use of computational tools in research leads to the formation of a Drug@MOF system, that can provide relevant information capable of understanding the factors that make one system better than another. Relevant factors that we can mention in this context are the types and energies of interactions that occur between the drug and MOF and between the drug molecules [138], the quantification of adsorption [139]

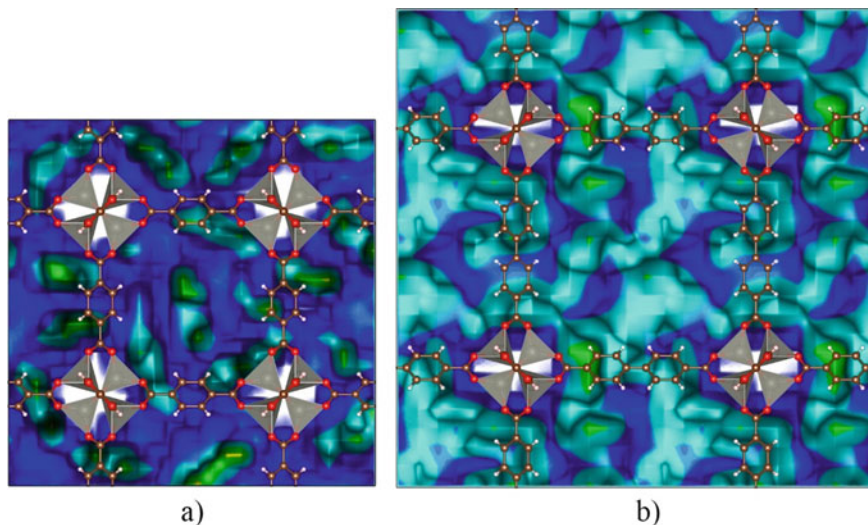


**Fig. 8** Maps of 5-fluorouracil density in **a** IRMOF-1 and **b** IRMOF-10, at 298 K and 1 bar, obtained by the GCMC. The map is color coded from white to green. White indicates zero probability, blue indicates low incidence, and green indicates high probability regions. Atom color label: oxygen: red, carbon: brown, hydrogen: white, zinc: grey

at room temperature and pressures, and finally, the influence of different solvents on the formation of the system [140].

## 7 Final Remarks

Studies involving applications of MOFs are recurrent and growing over the last 20 years. These works pointed out several applications, some of these applications were discussed here as well as new results were presented, always focusing on demonstrating how theoretical strategies and methods can significantly contribute to these studies.

Theoretical works have great potential, due to the possibility of providing data consistent with experimental results or even other data and observations that cannot be obtained by experimental techniques. Obtaining a certain property or behavior of a system requires the use of a specific method. In this process, the size of the studied system can be the limiting factor in the choice of a method.

There is an enormous number of MOFs to be studied and evaluated in various applications, and in this context theoretical methods can provide relevant data for such systems, that can choose an ideal system for a given application.

## References

1. Li, H., Eddaoudi, M., O'Keeffe, M., Yaghi, O.M.: Design and synthesis of an exceptionally stable and highly porous metal-organic framework. *Nature* **402**, 276–279 (1999). <https://doi.org/10.1038/46248>
2. Sillar, K., Hofmann, A., Sauer, J.: Ab initio study of hydrogen adsorption in MOF-5. *J. Am. Chem. Soc.* **131**, 4143–4150 (2009). <https://doi.org/10.1021/ja8099079>
3. Kuppler, R.J., Timmons, D.J., Fang, Q.-R., Li, J.-R., Makal, T.A., Young, M.D., et al.: Potential applications of metal-organic frameworks. *Coord. Chem. Rev.* **253**, 3042–3066 (2009). <https://doi.org/10.1016/j.ccr.2009.05.019>
4. Cao, Y., Zhao, Y., Song, F., Zhong, Q.: Alkali metal cation doping of metal-organic framework for enhancing carbon dioxide adsorption capacity. *J. Energy Chem.* **23**, 468–474 (2014). [https://doi.org/10.1016/s2095-4956\(14\)60173-x](https://doi.org/10.1016/s2095-4956(14)60173-x)
5. Pal, A., Mitra, A., Chand, S., Lin, J.-B., Das, M.C.: Two 2D microporous MOFs based on bent carboxylates and a linear spacer for selective CO<sub>2</sub> adsorption. *CrystEngComm* **21**, 535–543 (2019). <https://doi.org/10.1039/c8ce01925h>
6. Zhang, X., Lin, R.B., Wang, J., Wang, B., Liang, B., Yildirim, T., et al.: Optimization of the pore structures of MOFs for record high hydrogen volumetric working capacity. *Adv. Mater.* **32**, e1907995 (2020). <https://doi.org/10.1002/adma.201907995>
7. D'Vries, R.F., Iglesias, M., Snejko, N., Alvarez-Garcia, S., Gutiérrez-Puebla, E., Monge, M.A.: Mixed lanthanide succinate–sulfate 3D MOFs: catalysts in nitroaromatic reduction reactions and emitting materials. *J. Mater. Chem.* **22**, 1191–1198 (2012). <https://doi.org/10.1039/c1jm14677g>
8. Sani, Y.M., Daud, W.M.A.W., Abdul Aziz, A.R.: Activity of solid acid catalysts for biodiesel production: a critical review. *Appl. Catal. A* **470**, 140–161 (2014). <https://doi.org/10.1016/j.apcata.2013.10.052>
9. Giliopoulos, D., Zamboulis, A., Giannakoudakis, D., Bikiaris, D., Triantafyllidis, K.: Polymer/metal organic framework (MOF) nanocomposites for biomedical applications. *Molecules* **25**, (2020). <http://doi.org/https://doi.org/10.3390/molecules25010185>
10. Yaghi, O.M., O'Keeffe, M., Ockwig, N.W., Chae, H.K., Eddaoudi, M., Kim, J.: Reticular synthesis and the design of new materials. *Nature* **423**, 705–714 (2003). <https://doi.org/10.1038/nature01650>
11. Tan, K., Zuluaga, S., Wang, H., Canepa, P., Soliman, K., Cure, J., et al.: Interaction of acid gases SO<sub>2</sub> and NO<sub>2</sub> with coordinatively unsaturated metal organic frameworks: M-MOF-74 (M = Zn, Mg, Ni, Co). *Chem. Mater.* **29**, 4227–4235 (2017). <https://doi.org/10.1021/acs.chemmater.7b00005>
12. Schnobrich, J.K., Koh, K., Sura, K.N., Matzger, A.J.: A framework for predicting surface areas in microporous coordination polymers. *Langmuir: ACS J. Surf. Colloids* **26**, 5808–5814 (2010). <https://doi.org/10.1021/la9037292>
13. Ma, Z., Moulton, B.: Recent advances of discrete coordination complexes and coordination polymers in drug delivery. *Coord. Chem. Rev.* **255**, 1623–1641 (2011). <https://doi.org/10.1016/j.ccr.2011.01.031>
14. Vasconcelos, I.B., Silva, T.G.d., Militão, G.C.G., Soares, T.A., Rodrigues, N.M., Rodrigues, M.O., et al.: Cytotoxicity and slow release of the anti-cancer drug doxorubicin from ZIF-8. *RSC Adv.* **2**, 9437 (2012). <https://doi.org/10.1039/c2ra21087h>
15. Weber, I.T., de Melo, A.J., Lucena, M.A., Rodrigues, M.O., Alves, S., Jr.: High photoluminescent metal-organic frameworks as optical markers for the identification of gunshot residues. *Anal Chem* **83**, 4720–4723 (2011). <https://doi.org/10.1021/ac200680a>
16. Nguyen, H.T.T., Doan, D.N.A., Truong, T.: Unprecedented salt-promoted direct arylation of acidic sp<sup>2</sup> CH bonds under heterogeneous Ni-MOF-74 catalysis: synthesis of bioactive azole derivatives. *J. Mol. Catal. A: Chem.* **426**, 141–149 (2017). <https://doi.org/10.1016/j.molcata.2016.11.009>

17. Ishak, M.A.I., Jumbri, K., Daud, S., Abdul Rahman, M.B., Abdul Wahab, R., Yamagishi, H., et al.: Molecular simulation on the stability and adsorption properties of choline-based ionic liquids/IRMOF-1 hybrid composite for selective H<sub>2</sub>S/CO<sub>2</sub> capture. *J. Hazard. Mater.* **399**, 123008 (2020). <https://doi.org/10.1016/j.jhazmat.2020.123008>
18. Xia, L., Liu, Q.: Adsorption of H<sub>2</sub> on aluminum-based metal-organic frameworks: a computational study. *Comput. Mater. Sci.* **126**, 176–181 (2017). <https://doi.org/10.1016/j.commat.2016.09.039>
19. Wu, Y., Chen, H., Liu, D., Qian, Y., Xi, H.: Adsorption and separation of ethane/ethylene on ZIFs with various topologies: combining GCMC simulation with the ideal adsorbed solution theory (IAST). *Chem. Eng. Sci.* **124**, 144–153 (2015). <https://doi.org/10.1016/j.ces.2014.07.019>
20. Zhu, X., Li, B., Yang, J., Li, Y., Zhao, W., Shi, J., et al.: Effective adsorption and enhanced removal of organophosphorus pesticides from aqueous solution by Zr-based MOFs of UiO-67. *ACS Appl. Mater. Interfaces* **7**, 223–231 (2015). <https://doi.org/10.1021/am5059074>
21. Yang, W., Pan, Q., Song, S., Zhang, H.: Metal-organic framework-based materials for the recovery of uranium from aqueous solutions. *Inorg. Chem. Front.* **6**, 1924–1937 (2019). <https://doi.org/10.1039/c9qi00386j>
22. Qian, Y., Zhang, F., Pang, H.: A review of MOFs and their composites-based photocatalysts: synthesis and applications. *Adv. Funct. Mater.* **31**, 2104231 (2021). <https://doi.org/10.1002/adfm.202104231>
23. Pan, L., Adams, K.M., Hernandez, H.E., Wang, X., Zheng, C., Hattori, Y., et al.: Porous lanthanide-organic frameworks: synthesis, characterization, and unprecedented gas adsorption properties. *J. Am. Chem. Soc.* **125**, 3062–3067 (2003). <https://doi.org/10.1021/ja028996w>
24. Plakhutin, B.N., Davidson, E.R.: Koopmans' theorem in the restricted open-shell Hartree-Fock method. I. A variational approach. *J. Phys. Chem. A* **113**, 12386–12395 (2009). <https://doi.org/10.1021/jp9002593>
25. Sousa Filho, P., Galaço, A., Serra, O.: Terras Raras: Tabela Periódica, Descobrimiento, Exploração No Brasil E Aplicações. *Quím. Nova* (2019). <http://doi.org/https://doi.org/10.21577/0100-4042.20170438>
26. Rankine, D., Avellaneda, A., Hill, M.R., Doonan, C.J., Sumbly, C.J.: Control of framework interpenetration for in situ modified hydroxyl functionalised IRMOFs. *Chem. Commun.* **48**, 10328–10330 (2012). <https://doi.org/10.1039/c2cc35565e>
27. He, Y., Furukawa, H., Wu, C., O'Keeffe, M., Chen, B.: A mesoporous lanthanide-organic framework constructed from a dendritic hexacarboxylate with cages of 2.4 nm. *CrystEngComm* **15**, 9328 (2013). <http://doi.org/https://doi.org/10.1039/c3ce41062e>
28. Erucar, I., Keskin, S.: Efficient storage of drug and cosmetic molecules in biocompatible metal organic frameworks: a molecular simulation study. *Ind. Eng. Chem. Res.* **55**, 1929–1939 (2016). <https://doi.org/10.1021/acs.iecr.5b04556>
29. Lee, J.S., Vlasisavljevich, B., Britt, D.K., Brown, C.M., Haranczyk, M., Neaton, J.B., et al.: Understanding small-molecule interactions in metal-organic frameworks: coupling experiment with theory. *Adv. Mater.* **27**, 5785–5796 (2015). <https://doi.org/10.1002/adma.201500966>
30. Chaemchuen, S., Kabir, N.A., Zhou, K., Verpoort, F.: Metal-organic frameworks for upgrading biogas via CO<sub>2</sub> adsorption to biogas green energy. *Chem. Soc. Rev.* **42**, 9304–9332 (2013). <https://doi.org/10.1039/c3cs60244c>
31. Sarmiento-Perez, R.A., Rodriguez-Albelo, L.M., Gomez, A., Autie-Perez, M., Lewis, D.W., Ruiz-Salvador, A.R.: Surprising role of the BDC organic ligand in the adsorption of CO<sub>2</sub> by MOF-5. *Microporous Mesoporous Mater.* **163**, 186–191 (2012). <https://doi.org/10.1016/j.micromeso.2012.07.011>
32. Rowsell, J.L., Yaghi, O.M.: Strategies for hydrogen storage in metal-organic frameworks. *Angew. Chem.* **44**, 4670–4679 (2005). <https://doi.org/10.1002/anie.200462786>
33. Zhao, X.-Y., Wang, J., Hao, H.-G., Yang, H., Yang, Q.-S., Zhao, W.-Y.: A water-stable europium-MOF sensor for the selective, sensitive ratiometric fluorescence detection of anthrax biomarker. *Microchem. J.* **166**, 106253 (2021). <https://doi.org/10.1016/j.microc.2021.106253>

34. Furukawa, H., Ko, N., Go, Y.B., Aratani, N., Choi, S.B., Choi, E., et al.: Ultrahigh porosity in metal-organic frameworks. *Science* **329**, 424–428 (2010). <https://doi.org/10.1126/science.1192160>
35. Moghadam, P.Z., Li, A., Wiggin, S.B., Tao, A., Maloney, A.G.P., Wood, P.A., et al.: Development of a Cambridge structural database subset: a collection of metal-organic frameworks for past, present, and future. *Chem. Mater.* **29**, 2618–2625 (2017). <https://doi.org/10.1021/acs.chemmater.7b00441>
36. Ataei, F., Dorrnian, D., Motakef-Kazemi, N.: Synthesis of MOF-5 nanostructures by laser ablation method in liquid and evaluation of its properties. *J. Mater. Sci.: Mater. Electron.* **32**, 3819–3833 (2021). <https://doi.org/10.1007/s10854-020-05126-4>
37. Li, Q., Thonhauser, T.: A theoretical study of the hydrogen-storage potential of (H<sub>2</sub>)<sub>4</sub>CH<sub>4</sub> in metal organic framework materials and carbon nanotubes. *J. Phys. Condens. Matter: Inst. Phys. J.* **24**, 424204 (2012). <https://doi.org/10.1088/0953-8984/24/42/424204>
38. Yaghi, O.M., Li, H., Eddaoudi, M., O’Keeffe, M.: Design and synthesis of an exceptionally stable and highly porous metal-organic framework. *Nature* **402**, 276–279 (1999). <https://doi.org/10.1038/46248>
39. Eddaoudi, M., Kim, J., Rosi, N., Vodak, D., Wachter, J., O’Keeffe, M., et al.: Systematic design of pore size and functionality in isorecticular MOFs and their application in methane storage. *Science* **295**, 469–472 (2002). <https://doi.org/10.1126/science.1067208>
40. Sun, W., Li, H., Li, H., Li, S., Cao, X.: Adsorption mechanisms of ibuprofen and naproxen to UiO-66 and UiO-66-NH<sub>2</sub>: batch experiment and DFT calculation. *Chem. Eng. J.* **360**, 645–653 (2019). <https://doi.org/10.1016/j.cej.2018.12.021>
41. Zhao, J., Wang, C., Wang, S., Zhou, Y.: Experimental and DFT study of selective adsorption mechanisms of Pb(II) by UiO-66-NH<sub>2</sub> modified with 1,8-dihydroxyanthraquinone. *J. Ind. Eng. Chem.* **83**, 111–122 (2020). <https://doi.org/10.1016/j.jiec.2019.11.019>
42. Gao, Y., Zeng, X.C.: Ab initio study of hydrogen adsorption on benzenoid linkers in metal-organic framework materials. *J. Phys.: Condens. Matter* **19**, 386220 (2007). <https://doi.org/10.1088/0953-8984/19/38/386220>
43. Wellendorff, J., Silbaugh, T.L., Garcia-Pintos, D., Nørskov, J.K., Bligaard, T., Studt, F., et al.: A benchmark database for adsorption bond energies to transition metal surfaces and comparison to selected DFT functionals. *Surf. Sci.* **640**, 36–44 (2015). <https://doi.org/10.1016/j.susc.2015.03.023>
44. Becke, A.D.: Density-functional thermochemistry. III. The role of exact exchange. *J. Chem. Phys.* **98**, 5648–5652 (1993). <https://doi.org/10.1063/1.464913>
45. Paier, J., Hirschl, R., Marsman, M., Kresse, G.: The Perdew-Burke-Ernzerhof exchange-correlation functional applied to the G2–1 test set using a plane-wave basis set. *J. Chem. Phys.* **122**, 234102 (2005). <https://doi.org/10.1063/1.1926272>
46. de Oliveira, A., de Lima, G.F., De Abreu, H.A.: Structural and electronic properties of M-MOF-74 (M = Mg, Co or Mn). *Chem. Phys. Lett.* **691**, 283–290 (2018). <https://doi.org/10.1016/j.cplett.2017.11.027>
47. Prasetyo, N., Pambudi, F.I.: Toward hydrogen storage material in fluorinated zirconium metal-organic framework (MOF-801): a periodic density functional theory (DFT) study of fluorination and adsorption. *Int. J. Hydrogen Energy* **46**, 4222–4228 (2021). <https://doi.org/10.1016/j.ijhydene.2020.10.222>
48. Maia, J.D.C., Carvalho, G.A.U., Manguiera, C.P., Santana, S.R., Cabral, L.A.F., Rocha, G.B.: GPU linear algebra libraries and GPGPU programming for accelerating MOPAC semiempirical quantum chemistry calculations. *J. Chem. Theory Comput.* **8**, 3072–3081 (2012). <https://doi.org/10.1021/Ct3004645>
49. Maia, J.D., Urquiza Carvalho, G.A., Manguiera, C.P., Jr., Santana, S.R., Cabral, L.A., Rocha, G.B.: GPU linear algebra libraries and GPGPU programming for accelerating MOPAC semiempirical quantum chemistry calculations. *J. Chem. Theory Comput.* **8**, 3072–3081 (2012). <https://doi.org/10.1021/ct3004645>
50. Maia, J.D.C., Dos Anjos Formiga Cabral, L., Rocha, G.B.: GPU algorithms for density matrix methods on MOPAC: linear scaling electronic structure calculations for large molecular systems. *J. Mol. Model.* **26**, 313 (2020). <https://doi.org/10.1007/s00894-020-04571-6>

51. Stewart, J.J.: Application of the PM6 method to modeling the solid state. *J. Mol. Model.* **14**, 499–535 (2008). <https://doi.org/10.1007/s00894-008-0299-7>
52. Stewart, J.J.P.: MOPAC. <http://openmopac.net/>. Accessed 27 Apr 2021
53. Slater, J.C.: A simplification of the Hartree-Fock method. *Phys. Rev.* **81**, 385–390 (1951). <https://doi.org/10.1103/PhysRev.81.385>
54. Zanghellini, J., Kitzler, M., Brabec, T., Scrinzi, A.: Testing the multi-configuration time-dependent Hartree-Fock method. *J. Phys. B: At. Mol. Opt. Phys.* **37**, 763–773 (2004). <https://doi.org/10.1088/0953-4075/37/4/004>
55. Dewar, M.J.S., Zoebisch, E.G., Healy, E.F., Stewart, J.J.P.: Development and use of quantum mechanical molecular models. 76. AM1: a new general purpose quantum mechanical molecular model. *J. Am. Chem. Soc.* **107**, 3902–3909 (1985). <https://doi.org/10.1021/ja00299a024>
56. Stewart, J.J.P.: Optimization of parameters for semiempirical methods I. *Method. J. Comput. Chem.* **10**, 209–220 (1989). <https://doi.org/10.1002/jcc.540100208>
57. Stewart, J.J.: Optimization of parameters for semiempirical methods V: modification of NDDO approximations and application to 70 elements. *J. Mol. Model.* **13**, 1173–1213 (2007). <https://doi.org/10.1007/s00894-007-0233-4>
58. Stewart, J.J.: Optimization of parameters for semiempirical methods VI: more modifications to the NDDO approximations and re-optimization of parameters. *J. Mol. Model.* **19**, 1–32 (2013). <https://doi.org/10.1007/s00894-012-1667-x>
59. Rocha, G.B., Freire, R.O., Simas, A.M., Stewart, J.J.: RM1: a reparameterization of AM1 for H, C, N, O, P, S, F, Cl, Br, and I. *J. Comput. Chem.* **27**, 1101–1111 (2006). <https://doi.org/10.1002/jcc.20425>
60. Peng, X., Cheng, X., Cao, D.: Computer simulations for the adsorption and separation of CO<sub>2</sub>/CH<sub>4</sub>/H<sub>2</sub>/N<sub>2</sub> gases by UMCM-1 and UMCM-2 metal organic frameworks. *J. Mater. Chem.* **21**, 11259 (2011). <https://doi.org/10.1039/c1jm10264h>
61. Martínez-Ahumada, E., López-Olvera, A., Jancik, V., Sánchez-Bautista, J.E., González-Zamora, E., Martis, V., et al.: MOF materials for the capture of highly toxic H<sub>2</sub>S and SO<sub>2</sub>. *Organometallics* **39**, 883–915 (2020). <https://doi.org/10.1021/acs.organomet.9b00735>
62. de Andrade, A.V.M., da Costa, N.B., Simas, A.M., de Sá, G.F.: Sparkle model for the quantum chemical AM1 calculation of europium complexes. *Chem. Phys. Lett.* **227**, 349–353 (1994). [https://doi.org/10.1016/0009-2614\(94\)00829-9](https://doi.org/10.1016/0009-2614(94)00829-9)
63. Yang, Q., Zhong, C.: Electrostatic-field-induced enhancement of gas mixture separation in metal-organic frameworks: a computational study. *Chemphyschem: Eur. J. Chem. Phys. Phys. Chem.* **7**, 1417–1421 (2006). <https://doi.org/10.1002/cphc.200600191>
64. Amirjalayer, S., Tafipolsky, M., Schmid, R.: Molecular dynamics simulation of benzene diffusion in MOF-5: importance of lattice dynamics. *Angew. Chem.* **46**, 463–466 (2007). <https://doi.org/10.1002/anie.200601746>
65. Mashhadzadeh, A.H., Taghizadeh, A., Taghizadeh, M., Munir, M.T., Habibzadeh, S., Salmankhani, A., et al.: Metal-organic framework (MOF) through the lens of molecular dynamics simulation: current status and future perspective. *J. Compos. Sci.* **4**, 75 (2020). <https://doi.org/10.3390/jcs4020075>
66. Sun, B., Kayal, S., Chakraborty, A.: Study of HKUST (copper benzene-1,3,5-tricarboxylate, Cu-BTC MOF)-1 metal organic frameworks for CH<sub>4</sub> adsorption: an experimental investigation with GCMC (grand canonical Monte-Carlo) simulation. *Energy* **76**, 419–427 (2014). <https://doi.org/10.1016/j.energy.2014.08.033>
67. Moulin, F., Picaud, S., Hoang, P.N., Jedlovsky, P.: Grand canonical Monte Carlo simulation of the adsorption isotherms of water molecules on model soot particles. *J. Chem. Phys.* **127**, 164719 (2007). <https://doi.org/10.1063/1.2799516>
68. Guioth, J., Bertin, E.: Nonequilibrium grand-canonical ensemble built from a physical particle reservoir. *Phys. Rev. E* **103**, 022107 (2021). <https://doi.org/10.1103/PhysRevE.103.022107>
69. Byrne, M.P., O’Gorman, P.A.: Understanding decreases in land relative humidity with global warming: conceptual model and GCM simulations. *J. Clim.* **29**, 9045–9061 (2016). <https://doi.org/10.1175/jcli-d-16-0351.1>

70. Gurdal, Y., Keskin, S.: A new approach for predicting gas separation performances of MOF membranes. *J. Membr. Sci.* **519**, 45–54 (2016). <https://doi.org/10.1016/j.memsci.2016.07.039>
71. Ho, T.A., Wang, Y., Criscenti, L.J.: Chemo-mechanical coupling in kerogen gas adsorption/desorption. *Phys. Chem. Chem. Phys.* **20**, 12390–12395 (2018). <https://doi.org/10.1039/C8CP01068D>
72. Magomedov, M.N.: The calculation of the parameters of the Mie-Lennard-Jones potential. *High Temp.* **44**, 513–529 (2006). <https://doi.org/10.1007/s10740-006-0064-5>
73. Sing, K.S.W.: Reporting physisorption data for gas/solid systems with special reference to the determination of surface area and porosity (Recommendations 1984). *Pure Appl. Chem.* **57**, (1985). <http://doi.org/https://doi.org/10.1351/pac198557040603>
74. Koh, K., Wong-Foy, A.G., Matzger, A.J.: MOF@MOF: microporous core-shell architectures. *Chem. Commun.* 6162–6164 (2009). <http://doi.org/https://doi.org/10.1039/b904526k>
75. Díaz-García, M., Mayoral, Á., Díaz, I., Sánchez-Sánchez, M.: Nanoscaled M-MOF-74 materials prepared at room temperature. *Cryst. Growth Des.* **14**, 2479–2487 (2014). <https://doi.org/10.1021/cg500190h>
76. Yoo, C.J., Lee, L.C., Jones, C.W.: Probing intramolecular versus intermolecular CO<sub>2</sub> adsorption on amine-grafted SBA-15. *Langmuir: ACS J. Surf. Colloids* **31**, 13350–13360 (2015). <https://doi.org/10.1021/acs.langmuir.5b03657>
77. Mueller, T., Ceder, G.: A density functional theory study of hydrogen adsorption in MOF-5. *J. Phys. Chem. B* **109**, 17974–17983 (2005). <https://doi.org/10.1021/jp051202q>
78. Daniel, C.R.A., Rodrigues, N.M., da Costa, N.B., Freire, R.O.: Are quantum chemistry semiempirical methods effective to predict solid state structure and adsorption in metal organic frameworks? *J. Phys. Chem. C* **119**, 23398–23406 (2015). <https://doi.org/10.1021/acs.jpcc.5b05599>
79. Gomez, D.A., Combariza, A.F., Sastre, G.: Quantum-chemistry calculations of hydrogen adsorption in MOF-5. *Phys. Chem. Chem. Phys.* **11**, 9250–9258 (2009). <https://doi.org/10.1039/b909021e>
80. Fischer, M., Gomes, J.R.B., Jorge, M.: Computational approaches to study adsorption in MOFs with unsaturated metal sites. *Mol. Simul.* **40**, 537–556 (2014). <https://doi.org/10.1080/08927022.2013.829228>
81. Campbell, C., Ferreira-Rangel, C.A., Fischer, M., Gomes, J.R.B., Jorge, M.: A transferable model for adsorption in MOFs with unsaturated metal sites. *J. Phys. Chem. C* **121**, 441–458 (2016). <https://doi.org/10.1021/acs.jpcc.6b10751>
82. Liu, J., Culp, J.T., Natesakhawat, S., Bockrath, B.C., Zande, B., Sankar, S.G., et al.: Experimental and theoretical studies of gas adsorption in Cu<sub>3</sub>(BTC)<sub>2</sub>: an effective activation procedure. *J. Phys. Chem. C* **111**, 9305–9313 (2007). <https://doi.org/10.1021/jp071449i>
83. Skoulidas, A.I.: Molecular dynamics simulations of gas diffusion in metal-organic frameworks: argon in CuBTC. *J. Am. Chem. Soc.* **126**, 1356–1357 (2004). <https://doi.org/10.1021/ja039215+>
84. Gaillac, R., Pullumbi, P., Beyer, K.A., Chapman, K.W., Keen, D.A., Bennett, T.D., et al.: Liquid metal-organic frameworks. *Nat. Mater.* **16**, 1149–1154 (2017). <https://doi.org/10.1038/nmat4998>
85. Gupta, M., Chatterjee, N., De, D., Saha, R., Chattaraj, P.K., Oliver, C.L., et al.: Metal-organic frameworks of Cu(II) constructed from functionalized ligands for high capacity H<sub>2</sub> and CO<sub>2</sub> gas adsorption and catalytic studies. *Inorg. Chem.* **59**, 1810–1822 (2020). <https://doi.org/10.1021/acs.inorgchem.9b03012>
86. Titov, K., Zeng, Z., Ryder, M.R., Chaudhari, A.K., Civalleri, B., Kelley, C.S., et al.: Probing dielectric properties of metal-organic frameworks: MIL-53(Al) as a model system for theoretical predictions and experimental measurements via synchrotron far- and mid-infrared spectroscopy. *J. Phys. Chem. Lett.* **8**, 5035–5040 (2017). <https://doi.org/10.1021/acs.jpcclett.7b02003>
87. Kaur, H., Sundriyal, S., Kumar, V., Sharma, A.L., Kim, K.-H., Wang, B., et al.: Theoretical prediction of thermal and electronic properties of metal-organic frameworks. *J. Ind. Eng. Chem.* **80**, 136–151 (2019). <https://doi.org/10.1016/j.jiec.2019.07.041>

88. Li, L., Ma, W., Shen, S., Huang, H., Bai, Y., Liu, H.: A combined experimental and theoretical study on the extraction of uranium by amino-derived metal-organic frameworks through post-synthetic strategy. *ACS Appl. Mater. Interfaces* **8**, 31032–31041 (2016). <https://doi.org/10.1021/acsami.6b11332>
89. Chen, Z., Ling, L., Wang, B., Fan, H., Shangguan, J., Mi, J.: Adsorptive desulfurization with metal-organic frameworks: a density functional theory investigation. *Appl. Surf. Sci.* **387**, 483–490 (2016). <https://doi.org/10.1016/j.apsusc.2016.06.078>
90. Simon, C.M., Kim, J., Gomez-Gualdrón, D.A., Camp, J.S., Chung, Y.G., Martin, R.L., et al.: The materials genome in action: identifying the performance limits for methane storage. *Energy Environ. Sci.* **8**, 1190–1199 (2015). <https://doi.org/10.1039/c4ee03515a>
91. Tranchemontagne, D.J., Park, K.S., Furukawa, H., Eckert, J., Knobler, C.B., Yaghi, O.M.: Hydrogen storage in new metal-organic frameworks. *J. Phys. Chem. C* **116**, 13143–13151 (2012). <https://doi.org/10.1021/jp302356q>
92. Mason, J.A., Veenstra, M., Long, J.R.: Evaluating metal-organic frameworks for natural gas storage. *Chem. Sci.* **5**, 32–51 (2014). <https://doi.org/10.1039/c3sc52633j>
93. Liu, Y., Chen, B., Chen, Y., Zhang, S., Guo, W., Cai, Y., et al.: Methane storage in a hydrated form as promoted by leucines for possible application to natural gas transportation and storage. *Energy Technol.* **3**, 815–819 (2015). <https://doi.org/10.1002/ente.201500048>
94. Neto, H.A.S., Garcia, H.L., Araujo, R.G.O., Garcia, C.A.B.: Adsorção em coluna de leito fixo aplicada para a préconcentração de cádmio em amostras de água. *Sci. Plena* **14**, 1–10 (2018). <http://doi.org/https://doi.org/10.14808/sci.plena.2018.064208>
95. Makal, T.A., Li, J.R., Lu, W., Zhou, H.C.: Methane storage in advanced porous materials. *Chem. Soc. Rev.* **41**, 7761–7779 (2012). <https://doi.org/10.1039/c2cs35251f>
96. Jin, H., Lee, Y.S., Hong, I.: Hydrogen adsorption characteristics of activated carbon. *Catal. Today* **120**, 399–406 (2007). <https://doi.org/10.1016/j.cattod.2006.09.012>
97. Yang, J., Sudik, A., Wolverton, C., Siegel, D.J.: High capacity hydrogen storage materials: attributes for automotive applications and techniques for materials discovery. *Chem. Soc. Rev.* **39**, 656–675 (2010). <https://doi.org/10.1039/b802882f>
98. Baumann, A.E., Burns, D.A., Liu, B., Thoi, V.S.: Metal-organic framework functionalization and design strategies for advanced electrochemical energy storage devices. *Commun. Chem.* **2**, (2019). <http://doi.org/https://doi.org/10.1038/s42004-019-0184-6>
99. Fischer, M., Hoffmann, F., Fröba, M.: Molecular simulation of hydrogen adsorption in metal-organic frameworks. *Colloids Surf., A* **357**, 35–42 (2010). <https://doi.org/10.1016/j.colsurfa.2009.11.025>
100. Chand, S., Pal, A., Saha, R., Das, P., Sahoo, R., Chattaraj, P.K., et al.: Two closely related Zn(II)-MOFs for their large difference in CO<sub>2</sub> uptake capacities and selective CO<sub>2</sub> sorption. *Inorg. Chem.* **59**, 7056–7066 (2020). <https://doi.org/10.1021/acs.inorgchem.0c00551>
101. Dubbeldam, D., Calero, S., Ellis, D.E., Snurr, R.Q.: RASPA: molecular simulation software for adsorption and diffusion in flexible nanoporous materials. *Mol. Simul.* **42**, 81–101 (2015). <https://doi.org/10.1080/08927022.2015.1010082>
102. Borah, B., Zhang, H., Snurr, R.Q.: Diffusion of methane and other alkanes in metal-organic frameworks for natural gas storage. *Chem. Eng. Sci.* **124**, 135–143 (2015). <https://doi.org/10.1016/j.ces.2014.09.031>
103. Rostami, S., Nakhaei Pour, A., Salimi, A., Abolghasempour, A.: Hydrogen adsorption in metal-organic frameworks (MOFs): effects of adsorbent architecture. *Int. J. Hydrogen Energy* (2018). <https://doi.org/10.1016/j.ijhydene.2018.02.160>
104. Dixit, M., Maark, T.A., Pal, S.: Ab initio and periodic DFT investigation of hydrogen storage on light metal-decorated MOF-5. *Int. J. Hydrogen Energy* **36**, 10816–10827 (2011). <https://doi.org/10.1016/j.ijhydene.2011.05.165>
105. Volkova, E.I., Vakhrushev, A.V., Suetin, M.: Improved design of metal-organic frameworks for efficient hydrogen storage at ambient temperature: a multiscale theoretical investigation. *Int. J. Hydrogen Energy* **39**, 8347–8350 (2014). <https://doi.org/10.1016/j.ijhydene.2014.03.167>



106. Yu, S., Jing, G., Li, S., Li, Z., Ju, X.: Tuning the hydrogen storage properties of MOF-650: a combined DFT and GCMC simulations study. *Int. J. Hydrogen Energy* **45**, 6757–6764 (2020). <https://doi.org/10.1016/j.ijhydene.2019.12.114>
107. Lotfi, R., Saboohi, Y.: Effect of metal doping, boron substitution and functional groups on hydrogen adsorption of MOF-5: a DFT-D study. *Comput. Theor. Chem.* **1044**, 36–43 (2014). <https://doi.org/10.1016/j.comptc.2014.05.012>
108. Zhao, D., Timmons, D.J., Yuan, D., Zhou, H.C.: Tuning the topology and functionality of metal-organic frameworks by ligand design. *Acc. Chem. Res.* **44**, 123–133 (2011). <https://doi.org/10.1021/ar100112y>
109. Rodrigues, N.M., Daniel, C.R.A., Rodrigues, Ed.S.M., da Costa, N.B., Gimenez, Id.F., Freire, R.O.: Lanthanide organic frameworks geometry prediction accuracies of quantum chemical calculations. *J. Mol. Struct.* **1184**, 310–315 (2019). <https://doi.org/10.1016/j.molstruc.2019.01.079>
110. Ha, N.T.T., Lefedova, O.V., Ha, N.N.: Theoretical study on the adsorption of carbon dioxide on individual and alkali-metal doped MOF-5s. *Russ. J. Phys. Chem. A* **90**, 220–225 (2015). <https://doi.org/10.1134/s0036024415120201>
111. Li, L., Yang, D., Fisher, T.R., Qiao, Q., Yang, Z., Hu, N., et al.: Molecular dynamics simulations for loading-dependent diffusion of CO<sub>2</sub>, SO<sub>2</sub>, CH<sub>4</sub>, and their binary mixtures in ZIF-10: the role of hydrogen bond. *Langmuir: ACS J. Surf. Colloids* **33**, 11543–11553 (2017). <https://doi.org/10.1021/acs.langmuir.7b01537>
112. Verma, P., Zhang, S., Song, S., Mori, K., Kuwahara, Y., Wen, M., et al.: Recent strategies for enhancing the catalytic activity of CO<sub>2</sub> hydrogenation to formate/formic acid over Pd-based catalyst. *J. CO<sub>2</sub> Util.* **54**, 101765 (2021). <http://doi.org/https://doi.org/10.1016/j.jcou.2021.101765>
113. Gupta, M., De, D., Tomar, K., Bharadwaj, P.K.: From Zn(II)-carboxylate to double-walled Zn(II)-carboxylate phosphate MOF: change in the framework topology, capture and conversion of CO<sub>2</sub>, and catalysis of strecker reaction. *Inorg. Chem.* **56**, 14605–14611 (2017). <https://doi.org/10.1021/acs.inorgchem.7b02443>
114. Alhamami, M., Doan, H., Cheng, C.H.: A review on breathing behaviors of metal-organic-frameworks (MOFs) for gas adsorption. *Materials* **7**, 3198–3250 (2014). <https://doi.org/10.3390/ma7043198>
115. Cessford, N.F., Seaton, N.A., Düren, T.: Evaluation of ideal adsorbed solution theory as a tool for the design of metal-organic framework materials. *Ind. Eng. Chem. Res.* **51**, 4911–4921 (2012). <https://doi.org/10.1021/ie202219w>
116. Hamon, L., Serre, C., Devic, T., Loiseau, T., Millange, F., Ferey, G., et al.: Comparative study of hydrogen sulfide adsorption in the MIL-53(Al, Cr, Fe), MIL-47(V), MIL-100(Cr), and MIL-101(Cr) metal-organic frameworks at room temperature. *J. Am. Chem. Soc.* **131**, 8775–8777 (2009). <https://doi.org/10.1021/ja901587t>
117. Gutiérrez-Sevillano, J.J., Martín-Calvo, A., Dubbeldam, D., Calero, S., Hamad, S.: Adsorption of hydrogen sulphide on metal-organic frameworks. *RSC Adv.* **3**, 14737 (2013). <https://doi.org/10.1039/c3ra41682h>
118. Vazhappilly, T., Ghanty, T.K.: Adsorption control of Xe and Kr in SBMOF-2 metal-organic framework by ligand functionalization and different metal atoms. *Comput. Mater. Sci.* **189**, 110264 (2021). <https://doi.org/10.1016/j.commatsci.2020.110264>
119. Ustinov, E.: Kinetic Monte Carlo approach for molecular modeling of adsorption. *Curr. Opin. Chem. Eng.* **24**, 1–11 (2019). <https://doi.org/10.1016/j.coche.2018.12.004>
120. Yang, Q., Zhong, C.: Molecular simulation of carbon dioxide/methane/hydrogen mixture adsorption in metal-organic frameworks. *J. Phys. Chem. B* **110**, 17776–17783 (2006). <https://doi.org/10.1021/jp062723w>
121. Service, R.F.: Stepping on the gas. *Science* **346**, 538–541 (2014). <https://doi.org/10.1126/science.346.6209.538>

122. Bhatt, P.M., Belmabkhout, Y., Assen, A.H., Weseliński, Ł.J., Jiang, H., Cadiau, A., et al.: Isoreticular rare earth fcu -MOFs for the selective removal of H<sub>2</sub>S from CO<sub>2</sub> containing gases. *Chem. Eng. J.* **324**, 392–396 (2017). <https://doi.org/10.1016/j.cej.2017.05.008>
123. Shah, M.S., Tsapatsis, M., Siepmann, J.L.: Hydrogen sulfide capture: from absorption in polar liquids to oxide, zeolite, and metal-organic framework adsorbents and membranes. *Chem. Rev.* **117**, 9755–9803 (2017). <https://doi.org/10.1021/acs.chemrev.7b00095>
124. Martin-Calvo, A., Garcia-Perez, E., Manuel Castillo, J., Calero, S.: Molecular simulations for adsorption and separation of natural gas in IRMOF-1 and Cu-BTC metal-organic frameworks. *Phys. Chem. Chem. Phys.* **10**, 7085–7091 (2008). <https://doi.org/10.1039/b807470d>
125. Rodrigues, N.M., Dos Santos, L.J., Rodrigues, E.S.M., Martins, J.B.L.: Removal of hydrogen sulfide from a binary mixture with methane gas, using IRMOF-1: a theoretical investigation. *J. Mol. Model.* **27**, 240 (2021). <https://doi.org/10.1007/s00894-021-04863-5>
126. Wang, H.H., Hou, L., Li, Y.Z., Jiang, C.Y., Wang, Y.Y., Zhu, Z.: Porous MOF with highly efficient selectivity and chemical conversion for CO<sub>2</sub>. *ACS Appl. Mater. Interfaces* **9**, 17969–17976 (2017). <https://doi.org/10.1021/acsami.7b03835>
127. Sun, Y., Zheng, L., Yang, Y., Qian, X., Fu, T., Li, X., et al.: Metal-organic framework nanocarriers for drug delivery in biomedical applications. *Nano-micro Lett.* **12**, 103 (2020). <https://doi.org/10.1007/s40820-020-00423-3>
128. Vasconcelos, I.B., Wanderley, K.A., Rodrigues, N.M., da Costa, N.B., Freire, R.O., Junior, S.A.: Host-guest interaction of ZnBDC-MOF + doxorubicin: a theoretical and experimental study. *J. Mol. Struct.* **1131**, 36–42 (2017). <https://doi.org/10.1016/j.molstruc.2016.11.034>
129. He, S., Wu, L., Li, X., Sun, H., Xiong, T., Liu, J., et al.: Metal-organic frameworks for advanced drug delivery. *Acta Pharm. Sin. B* **11**, 2362–2395 (2021). <https://doi.org/10.1016/j.apsb.2021.03.019>
130. Wen, H., Jung, H., Li, X.: Drug delivery approaches in addressing clinical pharmacology-related issues: opportunities and challenges. *AAPS J.* **17**, 1327–1340 (2015). <https://doi.org/10.1208/s12248-015-9814-9>
131. Saeb, M.R., Rabiee, N., Mozafari, M., Mostafavi, E.: Metal-organic frameworks-based nano-materials for drug delivery. *Materials* **14**, (2021). <http://doi.org/https://doi.org/10.3390/ma14133652>
132. Ferey, G., Mellot-Draznieks, C., Serre, C., Millange, F., Dutour, J., Surble, S., et al.: A chromium terephthalate-based solid with unusually large pore volumes and surface area. *Science* **309**, 2040–2042 (2005). <https://doi.org/10.1126/science.1116275>
133. Lucena, F.R., de Araujo, L.C., Rodrigues Mdo, D., da Silva, T.G., Pereira, V.R., Militao, G.C., et al.: Induction of cancer cell death by apoptosis and slow release of 5-fluoracil from metal-organic frameworks Cu-BTC. *Biomed. Pharmacother. = Biomed. Pharmacother.* **67**, 707–713 (2013). <http://doi.org/https://doi.org/10.1016/j.biopha.2013.06.003>
134. Proenza, Y.G., Longo, R.L.: Simulation of the adsorption and release of large drugs by ZIF-8. *J. Chem. Inf. Model.* **60**, 644–652 (2020). <https://doi.org/10.1021/acs.jcim.9b00893>
135. Yan, Z., Li, X., Fan, Q., Bai, H., Wu, S., Zhang, Z.-F., et al.: A water-stable and biofriendly Zn-MOF with pyrazine decorated pores as 5-Fu delivery system to induce human ovarian cancer cells apoptosis and abrogate their growth. *J. Mol. Struct.* **1204**, 127477 (2020). <https://doi.org/10.1016/j.molstruc.2019.127477>
136. Gonzalez-Salgado, D., Vega, C.: A new intermolecular potential for simulations of methanol: the OPLS/2016 model. *J. Chem. Phys.* **145**, 034508 (2016). <https://doi.org/10.1063/1.4958320>
137. Li, L., Duan, Y., Liao, S., Ke, Q., Qiao, Z., Wei, Y.: Adsorption and separation of propane/propylene on various ZIF-8 polymorphs: insights from GCMC simulations and the ideal adsorbed solution theory (IAST). *Chem. Eng. J.* **386**, 123945 (2020). <https://doi.org/10.1016/j.cej.2019.123945>

138. Rodrigues, N.M., Martins, J.B.L.: Theoretical evaluation of the performance of IRMOFs and M-MOF-74 in the formation of 5-fluorouracil@MOF. *RSC Adv.* **11**, 31090–31097 (2021). <https://doi.org/10.1039/d1ra05068k>
139. Kotzabasaki, M., Galdadas, I., Tylianakis, E., Klontzas, E., Cournia, Z., Froudakis, G.E.: Multiscale simulations reveal IRMOF-74-III as a potent drug carrier for gemcitabine delivery. *J. Mater. Chem. B* **5**, 3277–3282 (2017). <https://doi.org/10.1039/c7tb00220c>
140. Sose, A.T., Cornell, H.D., Gibbons, B.J., Burris, A.A., Morris, A.J., Deshmukh, S.A.: Modelling drug adsorption in metal–organic frameworks: the role of solvent. *RSC Adv.* **11**, 17064–17071 (2021). <https://doi.org/10.1039/d1ra01746b>

# Advanced DFT Atomistic Approaches for Electronic, Optical, and Structural Properties of Semiconductor Oxides



Sergio R. de Lazaro, Renan A. P. Ribeiro, Marisa C. Oliveira,  
and Elson Longo

**Abstract** The Density Functional Theory (DFT) has been growing on a large scale since the last few years on Quantum simulations applied to materials, mainly semiconductor oxides. The increase of the DFT approaches overtaken the Hartree–Fock approximation. The main factors were associated with the computational cost and the description of the electronic structure because of the prevision on bandgap using exchange–correlation formalism. Semiconductor oxides have been a lot researched due to technological aims. The high chemical stability, crystalline structures accessible from simple chemical synthesis, connection with Quantum modeling, precise modulation on the bandgap engineering from doping, application on electronic devices employed mainly in the electronic industry are arguments for the high number of articles in such area. The main subject of this chapter is to present a brief collection of molecular descriptions using DFT atomistic simulations for the electronic, optical, and structural properties creating molecular mechanisms for technological applications. More specific, a deep understanding of the molecular structure for materials in crystalline form is a crucial point to develop advanced materials based on semiconductor oxides. Then, an explanation on electronic profiles in bulk and surfaces, excited states, and morphology is our purpose to a new age in the materials chemistry field.

---

S. R. de Lazaro (✉)

State University of Ponta Grossa, Ponta Grossa, Parana, Brazil

e-mail: [srlazaro@uepg.br](mailto:srlazaro@uepg.br)

R. A. P. Ribeiro

State University of Minas Gerais, Divinopolis, Minas Gerais, Brazil

M. C. Oliveira · E. Longo

São Carlos Federal University, São Carlos, São Paulo, Brazil

## 1 Early Overview

Quantum phenomena observed and discussed in the early XX century were the start point for a new era, a new vision on the microscopic properties part of matter causing a revolution in the natural sciences. Consequences from these new experiments were the challenge to elucidate the radiation-matter interaction, an effect so impressive that traditional physics was incapable of solving from the movement laws knowledge until that moment. Something changed on the physical matter simultaneously; it remains the same. Indeed, the study of Planck [1] on the black body radiation was fundamental, the Planck's universal constant ( $h = 6.626 \times 10^{-34} \text{ J}\cdot\text{s}^{-1}$ ) was the primary key to connect the microscopic world to macroscopic dimension introducing an excellent concept about energy packet or quantum, associated to discrete energy levels for electromagnetic waves (light). Other experiments, such as the photoelectric phenomenon [2], the double-slit experiment [3], electron diffraction [4], Compton scattering [5], and Crookes' tube or cathode ray tube [6], are examples of the scientific revolution converging to particle-wave duality proposed by de Broglie [7]. Then, many great scientists focused on how to contribute to these radiation-matter interaction experiments resulting in assiduous scientific discussions. In general, the scientists were building an understanding of the connection between the size or dimension of matter and its properties, showing the need to develop a new mechanics for the radiation-matter effects called Quantum Mechanics. The main point of the quantum idea was the first mathematical model for hydrogen atom developed by Bohr [8] and Schrödinger [9]. Here, we focus on the Schrödinger approach presented as  $H\Psi = E\Psi$ , where  $H$  is the Hamiltonian or the description of the energies involved in the system,  $\Psi$  is the wavefunction with all dynamic information on the system, and  $E$  is the total energy of the system. Such differential equation successfully represented the properties of the hydrogen atom under spherical coordinates, automatically creating the atomic orbitals and discrete energetic levels. This representation is more advanced for the electronic distribution around the hydrogen nucleus denominated as a quantum atomic model. The mathematical formalism for the Schrödinger Equation is knowledge as an equation of eigenfunction and eigenvalues from an operator and a wavefunction; however, the solution of the equation for many-body systems is complex, and the electronic repulsion is a critical factor. Hartree contributed to this big problem by applying numerical calculation on wavefunction, approximating it as a product of single mono-electronic wavefunctions called a self-consistent field (SCF). At the same time, Fock rebuilt the eigenfunction-eigenvalue equation adapting it for the new wavefunction obtained from the SCF procedure. This complex mathematical formalism is knowledge as Hartree-Fock (HF) formalism [10–13]. Posteriorly, Slater inserted into Hartree's wavefunction the spin, generating a spin-orbital wavefunction; therefore, the new wavefunction has four dimensions, three dimensions from spherical and spatial descriptions ( $r, \theta, \phi$  or  $x, y, z$ ) and the spin dimension representing a physical state complete for electrons around the atomic nucleus. Further, Roothaan-Hall described the linear combination of atomic orbitals (LCAO) [14, 15], creating the base to build the first round of the mono-electronic wavefunctions

implemented on the SCF procedure. The Achilles' hell or weak point of the HF formalism is the absence of the correlation term, denying a more formal description of the exchange–correlation interaction among electrons influencing the total energy of the system and molecular orbitals energies.

Hohenberg and Kohn [16] presented two theorems to develop the Density Functional Theory (DFT) in 1960s decade; the first theorem indicated in Eq. (1) defines the electron density ( $n(r)$ ) for a ground state total energy, the total number of electrons ( $N$ ) is distributed in a volume featuring a system. Another point, the  $n(r)$ , is associated with the square of the independent densities ( $\Psi_i(r)$ ), indicating the probability of finding one electron into  $N$  electrons. The second theorem is the formalism to minimize the total energy developing the self-consistency for the first theorem. Posteriorly, Kohn and Sham [17] show a formalism for the total electron density similar to the HF approach, Eq. (2); now, the  $\Psi_i(r)$  are Kohn–Sham orbitals, i. e., one electron wavefunction for independent electrons, e. i. are the eigenvalues connected to  $\Psi_i(r)$  orbitals,  $\hbar = h/2\pi$ ,  $m$  is the electron mass ( $9.10938356 \times 10^{-31}$  kg),  $\nabla^2$  is Laplace operator,  $V(r)$  Coulomb electronic repulsion,  $V_{ext}(r)$  is Coulomb electron-nuclei attractive interactions, and  $V_{xc}(r)$  is the exchange–correlation potential precisely defined from the exchange–correlation energy derivative. The novelties introduced by the DFT were the electronic density  $n(r)$  as a fundamental concept to yield a wavefunction, in opposite to the HF statement, the reduction of the freedom degree for the electrons, once  $n(r)$  is dependent only ( $x,y,z$ ) dimension; and the detailed description of the exchange–correlation term ( $E_{xc}$ ) from a functional for  $V_{xc}(r)$   $\delta(r)$ . The freedom degree for the electrons' report and the exact  $E_{xc}$  term from DFT theorems decrease the computational cost on the impact in the simulation time. Although the DFT formalism has simplified the calculation on many-body problems, the universal functional is unknown, promoting a high diversity of mathematical descriptions for this challenge; furthermore, the DFT was developed on the electronic ground state, the simulation of excited states was adapted from HF formalism.

$$n(r) = \sum_{i=1}^{occ} |\Psi_i(r)|^2 \quad (1)$$

$$\left[ \frac{-\hbar^2}{2m} \nabla^2 + V(r) + V_{ext} + V_{xc}(r) \right] \Psi_i(r) = \varepsilon_i(r) \Psi_i(r) \quad (2)$$

$$V_{xc}(r) = \frac{\delta E_{xc}[n(r)]}{\delta(r)}$$

Hartree–Fock formalism was the first implemented as code in early computers, causing success in science; together with the Hückel [18] and semi-empirical approaches, the simulations of atomic and molecular electronic structures initiated a new era in chemical research offering molecular interpretations from molecular geometry and electronic levels never seen before. The general computation chemistry allowed verifying that HF method simulated in good level ionic compounds as gas as solid phases; the complexity of the covalent bond is weakly described because of the absence of the correlation term. Then, post-HF approaches as perturbation

theory and the complete description for electronic states from configuration interaction (CI) showed the limit of the power computation. The limit of the HF formalism is the huge exponential increase of the interactions among particles in the system. The massive calculations in post-HF reports are a challenge in recent days with high processing and storage capacity in supercomputers.

Covalent-ionic and covalent interactions on molecules and solids reaching good agreements with experimental data showing that the correlation energy included in functional terms is essential to describe the electronic interaction at such a level. From this aspect, the DFT implementation in programs proposed a decrease in computational cost. The reduction in the description of the particles variables and more concise mathematical formalism performed a change from HF to DFT calculations. Initially, the Local-density approximation (LDA) functional demonstrated the challenge of the DFT; posteriorly, the Generalized Gradient Approximation [19] (GGA) raised a functional class denominated as pure functionals describing the exchange and correlation terms independently reaching high applicability for many chemical compounds, for instance, Perdew–Burke–Ernzerhof [20, 21] (PBE), Perdew–Wang [22, 23] (PW91), Becke [24] (B), and Lee–Yang–Parr [25] (LYP) functionals. After, hybrid functionals were more successful in adjusting electronic properties, making the electronic levels in frontier energy levels or valence bands more detailed. Next, examples for PBE (Eq. 3) and B3LYP (Eq. 4) functionals.

$$E_X^{PBE} = 1 + \kappa - \frac{\kappa}{1 + \frac{\mu s^2}{\kappa}}; s = \frac{|\nabla n(r)|}{2(3\pi^2)^{\frac{1}{3}}n(r)^{\frac{4}{3}}} \quad (3)$$

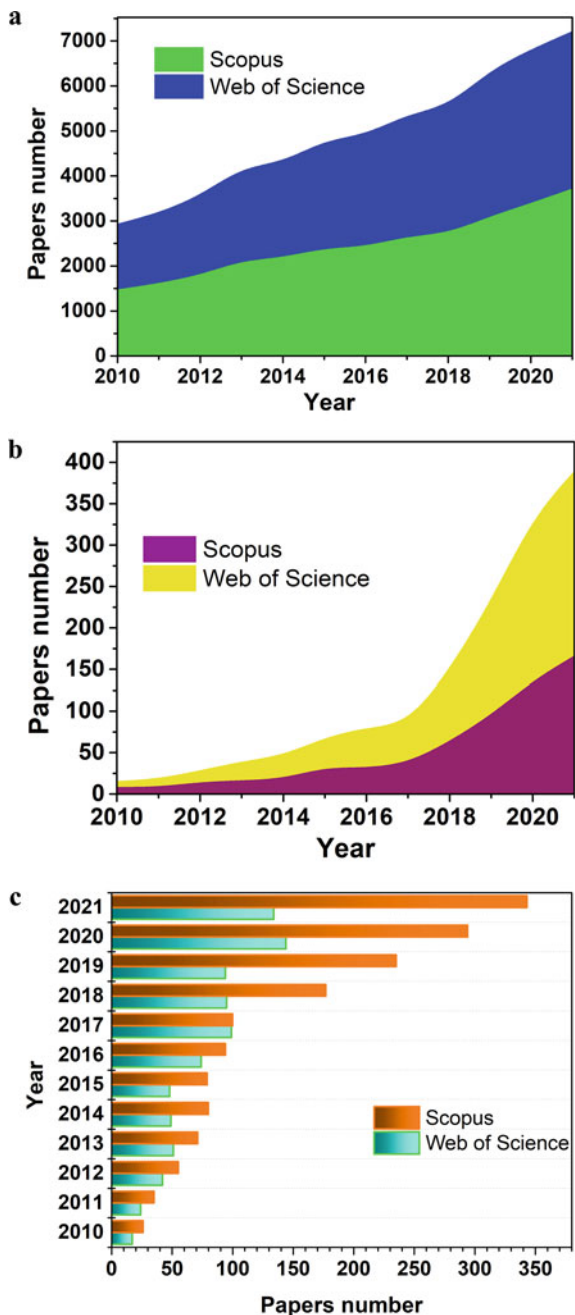
where,  $\kappa$  and  $\mu$  are non-empirical constants, and  $n(r)$  is the electronic density.

$$E_{XC}^{B3LYP} = (1 - a)E_X^{LSDA} + aE_X^{HF} + b\Delta E_X^{B88} + c\Delta E_C^{LYP} + (1 - c)\Delta E_C^{VWN} \quad (4)$$

where a, b, and c represent semi-empirical coefficients calculated from optimized experimental data,  $E_X^{LSDA}$  is the exchange energy for open-shell DFT calculations (for closed-shell calculation the LDA is equivalent to LSDA),  $E_X^{HF}$  is the Hartree–Fock exact exchange energy,  $\Delta E_X^{B88}$  is the gradient correction for exchange Becke energy,  $\Delta E_C^{LYP}$  is the local correlation energy proposed by Lee–Yang–Parr, and  $\Delta E_C^{VWN}$  is the local correlation energy proposed by Vosko et al. [26].

Independently of the room conditions, the HF and DFT quantum calculations in a vacuum and 0 K temperature present an excellent performance to clarify and predict the materials' structural, electronic, and optical properties. Figure 1a shows analysis from Scopus and Web of Science databases applying the “theoretical” and “DFT” search topics between 2010 and 2021 (Fig. 1a). In 2010, were published close to 3000 papers; while in 2021, the number of documents reached 7000, more than double, showing a high widespread on the topics and a linear growing up of published papers number by year as viable quantum simulation contributions. The DFT performance

**Fig. 1 a** Data on “DFT” and “theoretical” keywords analyzed between 2010 and 2021 in the Scopus and Web of Science databases, **b** data on “advanced materials” and “DFT” keywords analyzed between 2010 and 2021 in the Scopus and Web of Science databases, and **c** data on “semiconductor oxides” and “DFT” keywords analyzed between 2010 and 2021 in the Scopus and Web of Science databases





has been motivated in molecular systems with expressive electronic correlation effect, mainly the covalent interaction and magnetic ordering. Then, in Fig. 1b, the analysis is on the “advanced materials” and “DFT” topics search; the “advanced materials” is an expression used for representing a large complex materials group drive to technological and environmental applications because of the bandgap light absorption at ultraviolet range possible from the ionic-covalent chemical bond. An example successful for advanced materials are the semiconductor oxides class (Fig. 1c) formed by transition metals and chalcogenide and halogen anions; the ionic bond is made by high electronegativity difference, while the p and d orbitals overlap to create a covalent bond. The DFT description has reached a high implementation on solid-state chemistry; the goal is to represent an electronic system, so complex was the start of finding more quantum simulations at this level.

## 2 Structural Disorder and Photoluminescence

Structural property is the main point to initiate a quantum simulation. The full relaxed atomic positions in a representative simulation level contribute significantly to the goal of results. In truth, the atomic position creates length chemical bonds, angles, and dihedrals information in a minimum energy point from a minimization complex of the attractive and repulsive interactions represented by Coulomb and exchange–correlation integrals. DFT theoretical results using PBE, PBE0, B3LYP, and HSE06 [27, 28] functionals calculate structural parameters describing in good agreement the short-range distance and arrangement of atoms; the same in pure compositions is essential to represent structural effects as Jahn–Teller [29], cationic or anionic replacements [30, 31], and cationic or anionic vacancies [32]. Previsions on crystalline distortions by DFT calculations are valuable tools for the perturbations caused by these effects [33, 34], indicating that chemical bonds are tensile; consequently, the crystal energy is modified. A relevant discussion based on  $[AO_x]$  and  $[BO_y]$  clusters in the A and B crystalline sites clarifies the crystalline structures reordering from minimizing the atomic interactions [35, 36]. The lattice parameters and internal position on the unit cell are calculated with success presenting good prevision on pure and doping on type-Perovskite semiconductor oxides. This kind of oxide class is widely investigated because of its high versatility for synthesizing and manipulating properties. The features are double cations in the crystalline structure in  $ABO_z$  chemical composition following the Goldsmith rule [37] for ionic radius. In particular, there are A–O ionic bonds and B–O covalent bonds determinants for solid versatility. The experimental results in low annealing temperatures present a high crystalline disorder in a very close amorphous phase for  $SrTiO_3$  and  $SrZrO_3$  materials.

Highly disordered solids were investigated in the 2000s decade [38–41], displaced atomic positions simulated by DFT formalism introduced an approach based on clusters analysis. Semiconductor oxides presented photoluminescence (PL) effect in infrared irradiation analyzed by Raman scattering. The PL intensity depends on the annealing temperature. The initial PL profile is a high and wide signal in

low annealing temperatures, progressing to common and wide signs increasing the annealing temperature. The wide of the signal is connected to charge transfer between cation and oxygen atoms of the crystalline structure. Applying the order–disorder concept on  $[AO_x]$  and  $[BO_y]$  clusters was essential to evaluate this optical property from the crystalline structure. DFT calculations highly displacement around 0.5 Å showed distorted  $[AO_x]$  and  $[BO_y]$  clusters, promoting straining on the chemical bonds causing disorder effects [42, 43]. Such perturbation on the crystalline order creates a high polarization in the  $[AO_x]$  and  $[BO_y]$  clusters detected by Raman spectroscopy. The vibrational modes associated with the structural disorder cause the high and large PL signals. From the increase of the  $[AO_x]$  and  $[BO_y]$  clusters order, the crystalline order decreases the  $[AO_x]$  and  $[BO_y]$  disorder responsible for the dipoles connected to Raman modes; consequently, the PL vanishes. The strain caused on the chemical bonds from  $[AO_x]$  and  $[BO_y]$  clusters is discussed as a Jahn–Teller distortion. The A and B cations are moved from the regular crystalline position indicating a shortening as stretching of the chemical bonds on the  $[AO_x]$  and  $[BO_y]$  clusters. The calculated bandgap for the disordered structures are lower than the bandgap for the ordered structures; it is an essential point, the disorder on  $[AO_x]$  and  $[BO_y]$  clusters inserts energetic intermediary levels decreasing the bandgap and favoring an electronic excitation from incident infrared radiation, the initial charge transfer for the PL phenomenon occurs from 2p orbitals of the oxygen atoms localized on the top of the Valence Band (VB) to the 3d orbitals of the transition metals (B) on the bottom of the Conduction Band (CB).

There are two models in the DFT investigation on the photoluminescence effect in disordered semiconductor oxides. First, a crystalline structure representing the ordered structure and null photoluminescence. At the same time, the other has the B atom displaced, meaning the disordered system and presence of the photoluminescence property. Two manuscripts published in 2008s investigating the  $SrTiO_3$  (ST) in the  $Pm3m$  phase [44], and  $SrZrO_3$  (SZ) in the  $Pbmn$  phase [45] were essential to propose the initial molecular mechanism connecting the energetic intermediary levels. Disorder structural for the PL effect, the correspondence between PL intensity and temperature with decreased bandgap reported by Ultraviolet wavelength analysis for the ST material showing the increase of bandgap regarding temperature, the increase of the crystalline ordering increases the bandgap. Electronic paramagnetic resonance (EPR) spectroscopy applied on ST samples identified electrons unpaired at low annealing temperatures or low crystalline ordering; a low EPR signal persisted to more temperatures indicating a structural disorder in the  $[SrO_{12}]$  and  $[TiO_6]$  clusters. The charge separation associated with the disorder structural created the charge localization analyzed by spin moment in EPR spectroscopy. However, the irradiation source is the Infrared irradiation (IR) detected by Raman scattering showing the charge transfer indicates the electronic model for the PL phenomenon from quantum DFT calculations, the evidence connecting experimental and theoretical results are robust. The model can be introduced in three steps:

- (i) Charge separation before excitation by IR irradiation
- (ii) Electronic promotion from light irradiation creating the excited states

- (iii) Electronic decay emitting photons providing the PL effect detected by Raman scattering.

Another type-Perovskite material as  $\text{CaTiO}_3$  in *Pbmn* orthorhombic phase [46] published in 2009s proposes an analysis of the atomic displacements of 0.5 Å in the z-direction to create oxygen vacancies ( $V_o$ ) disordering of the crystalline structure. Then, the deformation on the ordered  $[\text{TiO}_6]$  and  $[\text{CaO}_{12}]$  clusters were created charge separations showed as  $V_o$  localized between clusters become them  $[\text{TiO}_6]'$  and  $[\text{CaO}_{12}]'$  negative charge points or donors of charge and  $[\text{TiO}_5 \dots V_o]$  and  $[\text{CaO}_{11} \dots V_o]$  positive charge points or receptors of charge. The models simulated in CRYSTAL06 code from DFT approach and B3LYP functional allowed a benchmark on how the disorder in all sites contributes to evidence the photoluminescence inserting energetic intermediary levels into bandgap indicated by a similar tendency among experimental and theoretical bandgaps.

After publications, new works improved the DFT approach, clarifying the PL created by order–disorder in semiconductor oxides. It was verified that the atomic displacement of 0.5 Å was drastic; in truth, an atomic displacement of 0.2 Å [47] and 0.3 Å [48] on the chemical bond in the  $[\text{AO}]$  and  $[\text{BO}]$  clusters is enough to evidence the disorder effect promoting the dipole moment. Open-shell DFT calculation simulated excited electronic state fundamental to advance on PL modeling, now a description more accurate of the electronic excitation as excited singlet or triplet states [35] indicate how the electronic correlation break between the paired electrons on the VB allows for relaxing the atomic positions and for finding the vibrational Raman modes associated to PL. Then, the excited states calculated by open-shell DFT approach situate in more accuracy the energetic intermediary levels suggested in DFT investigations before; the modulation of such levels is essential to build an electronic mechanism to elucidate the complex charge transfer inside of the PL phenomenon reported in disordered semiconductor oxides promoting a start point to other materials.

In solid-state chemistry, the vacancies are charge densities created from atomic replacement, atomic displacement, absence of cation or anion in bulk or surface dimensions. In all possibilities are formed dangling bonds; then, the vacancies and dangling bonds are intrinsically connected. The primary role of vacancies is to modify the electronic density distribution generating an increase of charge (electron carrier) or a decrease of charge (hole carrier) localized on intermediate energetic levels. The Tb-doped  $\text{CaMoO}_4$  material [49] is a semiconductor oxide with optical property promoted from cationic replacement. Two  $\text{Tb}^{3+}$  cations replace two  $\text{Ca}^{2+}$  cations, creating a double negative calcium vacancy ( $V_{\text{Ca}}''$ ). The high defect density causes a high structural disorder among  $[\text{MoO}_4]$ ,  $[\text{CaO}_8]$ , and  $[\text{TbO}_8]$  clusters creating the PL effect. The decrease of the PL intensity from pure  $\text{CaMoO}_4$  and Tb-doped  $\text{CaMoO}_4$  is a consequence of the high defect density.

Then, advanced DFT calculations using open-shell formalism for electron interactions to describe the singlet (s), excited singlet ( $s^*$ ), and triplet ( $t^*$ ) electronic states and atomic displacement of 0.1 Å in z-direction for the  $s^*$  and  $t^*$  excited states presented a robust electronic mechanism to clarify the PL emission in the crystalline

form of the Tb-doped  $\text{CaMoO}_4$  material. In the  $s$  and  $s^*$  electronic states, the DOS analyses indicate the VB is composed by O 2p orbitals; while Mo 4d orbitals and Tb 4f orbitals contribute to the bottom of the CB; the charge transfer profile in the PL phenomenon has origin from O atom to Mo, Tb atoms. Moreover, the  $t^*$  excited state identified the energetic intermediary levels associated with the Tb atoms. The bandgap decreased mainly because of the high structural distortion induced by the  $t^*$  electronic state separating the electronic levels between Mo and Tb atoms.

The  $\text{MgMoO}_4$  material in the wolframite-type  $\beta$  monoclinic phase ( $\beta\text{-MgMoO}_4$ ) [50] has a distorted crystalline structure formed by two  $[\text{MgO}_6]$  octahedral clusters, and two  $[\text{MoO}_4]$  tetrahedral clusters, the interconnection between octahedral and tetrahedral clusters introduces a disorder on the crystalline structure, the slight displacement in the cations regular positions deforms the length and angles bonds detected by Raman scattering creating the PL phenomenon. In  $\beta\text{-MgMoO}_4$ , the PL effect is opposite to other commented materials before. The increase of the heat treatment increases the PL intensity; furthermore, the origin of the PL is the charge transfer between  $[\text{MgO}_6]$  and  $[\text{MoO}_4]$  clusters suggesting that an intrinsic disorder promotes the PL emission. Excited states DFT calculations simulated the singlet ( $s$ ), excited singlet ( $s^*$ ), and triplet ( $t^*$ ) electronic states indicating that the charge transfer is associated directly with the change of the electronic states essential for the PL mechanism. The Mo atoms displaced from the off-centering position promotes an initial charge transfer creating the  $s \rightarrow s^*$  excitation process; the DFT simulation indicates that the charge transfer path occurs between Mo 4d orbitals and O 2p orbitals in the  $[\text{MoO}_4]$  clusters; however, both  $[\text{MgO}_6]$  and  $[\text{MoO}_4]$  clusters are distorted. The charge transfer connected to the following electronic process,  $s^* \rightarrow t^*$ , increases the  $[\text{MoO}_4]$  clusters structural distortion and decreases the deformation on the  $[\text{MgO}_6]$  clusters. Complementary DFT simulations using surface modeling showed  $[\text{MgO}_6]$  clusters on the (100) and (010) low index surfaces distorted by double oxygen vacancies ( $\text{V}_\text{o}^\times$ ), creating the  $[\text{MgO}_4 \cdot 2\text{V}_\text{o}^\times]$  clusters. Then, in the  $\beta\text{-MgMoO}_4$  material, the PL effect is a white-light emission, a prominent colors spectrum, indicating several possibilities for the electronic decay from the energetic intermediary levels because of the structural disorder localized on  $[\text{MgO}_6]$  and  $[\text{MoO}_4]$  bulk clusters and  $[\text{MgO}_4 \cdot 2\text{V}_\text{o}^\times]$  surface clusters.

Elson Longo's researcher always commented that the perfect crystalline ordering as cubic symmetry was boring because the high ordering on molecular clusters did not provide ferroelectric or optical properties. For example,  $\text{SrTiO}_3$  only presents properties when its structure is pseudocubic, that is, with a high density of defects. From the structural disorder, the optical property, PL effect, the application of the material is possible. Therefore, the modeling on the PL phenomenon analyzed by Raman scattering promoted the development of a broad set of tools in the DFT approach in advanced materials, semiconductor oxides. The clarity on a complex effect was possible because of the several concepts in solid-state theory and many-body quantum computational and the knowledge scale initiated on simple quantum models, but with an essential idea, the disorder on molecular clusters of the crystalline structure revolutionized the materials science field. This is the central concept to

evaluate the many correspondences between crystalline structure and properties in advanced materials.

### 3 Conclusions

After 20 years of research history on molecular theory in solid-state chemistry or chemistry of materials has been written on the fascinating photoluminescence emission in disordered materials. Disordered clusters simulations carried out from DFT approaches have shown an impact significant to clarify the molecular effects on semiconductor oxides highly disordered. The atomic displacement creating vacancies, charger transfer, and energetic intermediary levels are essential for connecting the electron–hole pair to electrical and optical properties. The molecular dynamic represented by open-shell DFT calculations in excited states, excited singlet, and triplet allows locating the electrons on the crystalline structure in more agreement. Such stationary simulations indicate a good level of correspondence between theoretical and experimental results, the step by step of molecular mechanism intrinsically associated with the photoluminescence phenomenon in advanced disordered materials.

**Acknowledgements** The authors acknowledge the financial support of CNPq, CAPES, FAPESP, and FAPEMIG. S. R. Lázaro gratefully thanks the financial assistance of CNPq (164266/2020-8). M. C. Oliveira gratefully thanks the financial assistance from FAPESP (project no. 2021/01651-1). E. Longo acknowledges the financial support from FAPESP (project no. 2013/07296-2). R. A. P. Ribeiro is grateful for the financial assistance from FAPEMIG (project no. APQ-00079-21) and UEMG for the Productivity Program.

### References

1. Planck, M.: *Ann. Phys.* **309**, 553 (1901)
2. Einstein, A.: *Ann. Phys.* **322**, 132 (1905)
3. Young, T.: *Philos. Trans. R. Soc. Lond.* **91**, 23 (1801)
4. Davisson, C., Germer, L.H.: *Nature* **119**, 558 (1927)
5. Compton, A.H.: *Phys. Rev.* **21**, 483 (1923)
6. Crookes, W.: *Philos. Trans. R. Soc. Lond.* **170**, 135 (1879)
7. de Broglie, L.: *Ann. Phys.* **10**, 22 (1925)
8. Bohr, N.: *Lond., Edinb., Dublin Philos. Mag. J. Sci.* **26**, 476 (1913)
9. Schrödinger, E.: *Phys. Rev.* **28**, 1049 (1926)
10. Hartree, D.R.: *Math. Proc. Camb. Philos. Soc.* **24**, 111 (1928)
11. Slater, J.C.: *Phys. Rev.* **35**, 210 (1930)
12. Slater, J.C.: *Phys. Rev.* **32**, 339 (1928)
13. Fock, V.: *Z. Phys.* **61**, 126 (1930)
14. Roothaan, C.C.J.: *Rev. Mod. Phys.* **23**, 69 (1951)
15. Hall, G.G.: *Proc. R. Soc. Lond. Ser. A. Math. Phys. Sci.* **205**, 541 (1951)
16. Hohenberg, P., Kohn, W.: *Phys. Rev.* **136**, B864 (1964)

17. Kohn, W., Sham, L.J.: *Phys. Rev.* **140**, A1133 (1965)
18. Hoffmann, R.: *J. Chem. Phys.* **39**, 1397 (1963)
19. Perdew, J.P., Chevary, J.A., Vosko, S.H., Jackson, K.A., Pederson, M.R., Singh, D.J., Fiolhais, C.: *Phys. Rev. B* **46**, 6671 (1992)
20. Perdew, J.P., Burke, K., Ernzerhof, M.: *Phys. Rev. Lett.* **77**, 3865 (1996)
21. Perdew, J.P., Burke, K., Ernzerhof, M.: *Phys. Rev. Lett.* **78**, 1396 (1997)
22. Perdew, J.P., Yue, W.: *Phys. Rev. B* **33**, 8800 (1986)
23. Perdew, J.P., Yue, W.: *Phys. Rev. B* **40**, 3399 (1989)
24. Becke, A.D.: *Phys. Rev. A* **38**, 3098 (1988)
25. Lee, C., Yang, W., Parr, R.G.: *Phys. Rev. B* **37**, 785 (1988)
26. Vosko, S.H., Wilk, L., Nusair, M.: *Can. J. Phys.* **58**, 1200 (1980)
27. Krukau, A.V., Vydrov, O.A., Izmaylov, A.F., Scuseria, G.E.: *J. Chem. Phys.* **125**, 224106 (2006)
28. Zhao, Y., Truhlar, D.G., Zhao, Y., Truhlar, D.G.: *Theor. Chem. Acc.* **120**, 215 (2008)
29. Song, G., Zhang, W.: *Phys. Rev. B* **94**, 064409 (2016)
30. Soares, G.B., Ribeiro, R.A.P., de Lazaro, S.R., Ribeiro, C.: *RSC Adv.* **6**, 89687 (2016)
31. Lacerda, L.H.S., de Lazaro, S.R.: *Solid State Ion.* **297**, 36 (2016)
32. Ribeiro, R.A.P., Longo, E., Andrés, J., de Lazaro, S.R.: *Phys. Chem. Chem. Phys.* **20**, 28382 (2018)
33. Beltrán, A., Gracia, L., Longo, E., Andrés, J.: *J. Phys. Chem. C* **118**, 3724 (2014)
34. Longo, E., Avansi, W., Bettini, J., Andrés, J., Gracia, L.: *Sci. Rep.* **6**, 21498 (2016)
35. Gracia, L., Andrés, J., Longo, V.M., Varela, J.A., Longo, E.: *Chem. Phys. Lett.* **493**, 141 (2010)
36. Ribeiro, R.A.P., Oliveira, M.C., de Sousa, A.G., Bomio, M.R.D., Motta, F.V., Gracia, L., de Lazaro, S.R., Longo, E., Andrés, J.: *J. Appl. Phys.* **126**, (2019)
37. Padgett, J.: *Phonology* **12**, 147 (1995)
38. Pontes, F.M., Pinheiro, C.D., Longo, E., Leite, E.R., de Lazaro, S.R., Magnani, R., Pizani, P.S., Boschi, T.M., Lanciotti, F.: *J. Lumin.* **104**, 175 (2003)
39. Pontes, F.M., Pinheiro, C.D., Longo, E., Leite, E.R., de Lazaro, S.R., Varela, J.A., Pizani, P.S., Boschi, T.M., Lanciotti, F.: *Mater. Chem. Phys.* **78**, 227 (2003)
40. Mara, M.S.C.C., Gurgel, M.F.C., Lazaro, S.R., Boschi, T.M., Pizani, P.S., Leite, E.R., Beltran, A., Longo, E.: *Int. J. Quantum Chem.* **103**, 580 (2005)
41. Choy, S.H., Wang, D.Y., Dai, J.Y., Chan, H.L.W., Choy, C.L.: *Integr. Ferroelectr.* **80**, 107 (2006)
42. de Lazaro, S., Milanez, J., de Figueiredo, A.T., Longo, V.M., Mastelaro, V.R., de Vicente, F.S., Hernandes, A.C., Varela, J.A., Longo, E.: *Appl. Phys. Lett.* **90**, (2007)
43. de Figueiredo, A.T., Longo, V.M., de Lazaro, S., Mastelaro, V.R., de Vicente, F.S., Hernandes, A.C., Siu Li, M., Varela, J.A., Longo, E.: *J. Lumin.* **126**, (2007)
44. Longo, V.M., de Figueiredo, A.T., de Lazaro, S., Gurgel, M.F., Costa, M.G.S., Paiva-Santos, C.O., Varela, J.A., Longo, E., Mastelaro, V.R., de Vicente, F.S., Hernandes, A.C., Franco, R.W.A.: *J. Appl. Phys.* **104**, 023515 (2008)
45. Longo, V.M., Cavalcante, L.S., Erlo, R., Mastelaro, V.R., de Figueiredo, A.T., Sambrano, J.R., de Lazaro, S., Freitas, A.Z., Gomes, L., Vieira, N.D., Varela, J.A., Longo, E.: *Acta Mater.* **56**, 2191 (2008)
46. Milanez, J., de Figueiredo, A.T., de Lazaro, S., Longo, V.M., Erlo, R., Mastelaro, V.R., Franco, R.W.A., Longo, E., Varela, J.A.: *J. Appl. Phys.* **106**, 043526 (2009)
47. Sczancoski, J.C., Cavalcante, L.S., Marana, N.L., da Silva, R.O., Tranquilin, R.L., Joya, M.R., Pizani, P.S., Varela, J.A., Sambrano, J.R., Siu Li, M., Longo, E., Andrés, J.: *Curr. Appl. Phys.* **10**, 614 (2010)
48. Valéria, V., Longo, M., das Graça, M., Sampaio Costa, G., Zirpole, A., Simões, S., Lúcia, I.L., Rosa, V., Oliveira, C., Santos, P., Andrés, J.A., Longo, E., Varela, J.A.J.A.: *Phys. Chem. Chem. Phys.* **12**, 7566 (2010)
49. Tranquilin, R.L., Oliveira, M.C., Santiago, A.A.G., Lovisa, L.X., Ribeiro, R.A.P., Longo, E., de Lazaro, S.R., Almeida, C.R.R., Paskocimas, C.A., Motta, F.V., Bomio, M.R.D.: *ChemPhysChem* (2020)
50. Santiago, A.A.G., Oliveira, M.C., Ribeiro, R.A.P., Tranquilin, R.L., Longo, E., de Lázaro, S.R., Motta, F.V., Bomio, M.R.D.: *Cryst. Growth Des.* **20**, 6592 (2020)

# Computational Simulations to Predict the Morphology of Nanostructures and Their Properties



José A. S. Laranjeira, Mateus M. Ferrer, Anderson R. Albuquerque, Carlos A. Paskocimas, Julio R. Sambrano, and Guilherme S. L. Fabris

**Abstract** The ability to synthesize nano and nanocrystals with well-defined morphologies with good homogeneity is essential for applications that depend on electronic, optical, magnetic, catalytic and/or chemical properties. The morphology determines the types of interfaces generated with the external environment. However, controlling the shape and size of nanocrystals is a complex process not only depending on the chemical formula and structure, but also on external conditions that can be or not controllable. The nanocrystals surfaces have distinct atomic structures and electronic properties and, consequently, these properties can be controlled by modifying their morphology. Within this context, Wulff's construction can be used to estimate the relation of the electronic, structural, and energetic properties with the morphologies. In addition, this method allows the study of growth mechanisms of metals, binary oxides, and complex crystals. This methodology can be applied to an infinity of materials, in special, the molybdates ( $\text{AMoO}_4$ ) and tungstates ( $\text{AWO}_4$ ) family, that urges from the combination of the  $(\text{MoO}_4)^{-2}$  or  $(\text{WO}_4)^{-2}$  ions, respectively, with a bivalent cation ( $\text{A}^{2+}$ ). These materials have attracted great interest because of their applications in photoluminescence, photocatalysis, sensors and loads of storage devices; in addition to having high thermochemical stability and being subject to changes in their optical and dielectric properties from doping with transition metals or rare earths. In this sense, this chapter presents the study of the property/morphology relationship of these materials studied according to computational

---

J. A. S. Laranjeira · J. R. Sambrano

Modeling and Molecular Simulation Group, São Paulo State University, Bauru, SP, Brazil

M. M. Ferrer

Graduate Program in Materials Science and Engineering, Technological Development Center, Federal University of Pelotas, Pelotas, RS 96010-610, Brazil

A. R. Albuquerque

Chemistry Institute, Federal University of Rio Grande Do Norte, Natal, RN 59078-970, Brazil

C. A. Paskocimas · G. S. L. Fabris (✉)

Department of Materials Engineering, Federal University of Rio Grande Do Norte, Natal 59078-970, Brazil

e-mail: [guilherme.fabris@unesp.br](mailto:guilherme.fabris@unesp.br)

simulations of the most exposed surfaces so that each surface can be characterized through its structural and electronic properties, together with the relative stabilities.

## 1 Introduction

Quantum mechanics is the base of modern chemistry, and through this theory we can predict and understand the chemical behavior of the compounds, however as Paul Dirac stated: “The exact application of these laws leads to equations much too complicated to be soluble” [1]. Dirac pointed out that the wave functions of a system described via quantum mechanics grows exponentially with the number of particles present in this system, so that it is not possible to obtain information of complex systems only using analytical methods [2], and to assist and surpass this challenge, a new area has emerged in the last decades and gained great attention, known as computational chemistry.

The Computational Chemistry has been in constant expansion, especially due to the great advances in computational science and its technologies [3]. Among the subareas, the quantum chemistry methods have been frequently used in the chemical industry and in the academy research as a path to generate information at the atomic level, understand the concepts and relate them to fundamental process [4]. The success of such a theory can be concluded from the constant increase of the number of experimental studies associated with quantum chemistry [5]. High-accuracy simulations at the quantum level can help predict and/or design new multifunctional materials. However, to achieve this deep level, the development of hardware to the construction of quantum computers is necessary [6], together with the continuous development of state-of-art computational methods, such as artificial intelligence and machine learning.

Recently there has been remarkable progress in the area of machine learning (ML) with advances in the development of ML algorithms and better hardware features available. Considering certain conditions, such as good training data (set of known inputs and outputs) and the ML algorithm, it is possible to predict properties only determined through quantum chemistry without loss of precision and with computational cost comparable to molecular dynamics calculations [7]. The advantages of having a computational tool remarkably faster than the traditional methods of quantum chemistry can be easily observed, since all studies that require a large number of quantum chemistry calculations benefit in large scale from this tool. There are numerous examples of the use of ML in diverse fields such as molecular dynamics,[8] metadynamics [9, 10], Monte Carlo simulations [10, 11], chemical simulations of real-time virtual reality [12] and the discovery of new drugs at scales previously unthinkable [13].

Unexpected variability in the morphology of nanoparticles can have detrimental effects on their expected behavior and functionalization. This represents a major challenge in the study of morphologies, as the selection of experimentally significant samples is increasingly difficult and requires a priori knowledge of sizes, shapes



and structural complexity for an efficient control of their properties [14]. In this context, the use of ML can be extremely advantageous, enabling early predictions of properties of a material based on its structural characteristics. The structure/properties relationship can be used to inform both real and hypothetical synthesis and processing strategies [15]. However, ML strategies need a large amount of training data, data that can be provided efficiently and with proven accuracy in relation to experimental data by quantum chemistry methods [16].

Even though that quantum computation is evolving at a rapid pace, this technology is not widely available due to its costs and low quantity of quantum algorithms, and as the full complexity can't be achieved, computational chemistry still can't replace the experimental studies, so that the theoreticians and experimentalists can walk together and complement each other. There are many theories and algorithms to study chemical systems, among them one of the most used are the density functional theory (DFT) [17]. This theory has been widely used in the study of systems that have a considerable number of atoms, and usually has a lower computational cost if compared to other quantum methods, such as Hartree-Fock [18], or variational methods [19], for example.

In the 60's, Hohenberg and Kohn [20] proposed that the electronic density could be used as a basic variable and formulate the variational principles to minimize the total energy, following that, Kohn and Sham proposed a self-consistent equation that could be used to describe the electronic behavior of molecular systems [17, 20], and the method arise from the Kohn-Sham equations solving are call DFT. Furthermore, a considerable number of computational packages have been developed to create models exploring the DFT, such as VASP (*Vienna Ab initio Simulation Package*) [21], SIESTA [22], CASTEP [23], QUANTUM ESPRESSO [24], and CRYSTAL [25].

For the structures that we will show in the next section, the simulations were performed using the CRYSTAL17 software, a program developed by the Theoretical and Computational Chemistry research group of University of Turin (UNITO) [26]. The CRYSTAL software allows us to apply HF and DFT methods to periodic systems in 3D (bulk), 2D (surfaces), 1D (nanotubes, nanowires and polymers) and 0D (atoms and molecules), using the linear combination of atomic orbitals (LCAO) method [27].

The ability to obtain or synthesize nano and microstructures with well-defined morphologies with good homogeneity is an essential requirement for applications of materials that play an important role in the electronic, optical, magnetic, catalytic, chemical, as well as other physical properties [28–36]. However, controlling the shape and size of nanocrystals is a complex process and not only depends on the composition and internal structure of the material, but also external growth conditions, such as, synthesis process, temperature, solvent and additives [37]. Furthermore, the control of the relative growth rate of a nanoparticle faces is responsible for the transformations in the morphology, due to the favoring of the growth of certain faces over others. These transformations occurs owing to the geometric restrictions imposed by the crystal structure, and are directly correlated to the surface energy value of each face [38].

Computer simulation using quantum mechanics methods have been used to study the morphological transformations of nanoparticles, and the properties related to their surfaces for a variety of materials. These surfaces can have different geometries and electronic properties, as well as exhibit different physical-chemistry properties that can be controlled by modifying the shape of their particles [39–41].

In 1878, J. W. Gibbs defined the surface energy ( $E_{surf}$ ) of a finite crystal as the difference between the finite crystal energy and the energy of the material of the same configuration of atoms located in a periodic crystal. In 1901, G. Wulff finds a theoretical way to evaluate the energy of the crystal to theoretically build the morphologies of his own experimental works, where the morphologies can be determined by the free energy of various surfaces, minimizing them at a constant volume [42].

Therefore, the Wulff construction, together with the surface models obtained from the DFT calculations, can be used to obtain the electronic, structural and energetic properties that control the morphologies and transformation mechanisms of metals, binary oxides and complex crystals [37].

Among the most studied materials using this approach are the ceramic materials, which can be defined as all inorganic solids with the exception of pure metals, formed by metallic and non-metallic elements with ionic and covalent bonds [43]. In this way, ceramic compounds of perovskite and scheelite structures have been widely studied in recent years, as they are of extreme interest for basic science and because of their potential for technological application [44].

With this in mind, for our study and exploration it was chosen the scheelite family, especially the molybdates and tungstates. The scheelites family have the general form  $ABO_4$  (where, A=Cd, Mn, Ca, Sr, Ba or Pb and B=W or Mo), where the  $A^{2+}$  cation is coordinated to 8 oxygen ions and the  $B^{6+}$  cation is coordinated to 4 oxygen ions, so that the unit cell has two  $ABO_4$  units [45]. Both molybdates and tungstates have inspired great interest due to their applications in photoluminescence [46], photocatalysis [47], sensors [48], and as a means of charge storage [49]; in addition to having high thermochemical stability [50] and being subject to changes in their optical and dielectric properties from doping with transition metals or rare earths [51, 52].

The increase in global demand for energy generates an intense search for sustainable alternative resources and processes [53]. Currently, energy supply relies on fossil fuels as one of the main sources of energy, which are rapidly being depleted. Within this context, the use of solar energy in photocatalytic mechanisms seems to be possible as an efficient solution to solve energy and environment problems [54]. In the last decade, semiconductor photocatalysts with particular morphologies have attracted intense interest in many fields of research [55], including splitting water to produce  $H_2$ , which is an attractive and clean fuel for fuel cells and cell-powered car engines. of fuel and, therefore, its production from water and available sunlight in abundance is a highly advantageous alternative [56]. Compounds that have scheelite structure are interesting candidates for photocatalyst design [57], there are reports in the literature of the functionalization of tungstates and molybdates of this family for use in photolytic water breakdown and  $H_2$  production [58].

Furthermore, due to the reasons mentioned above, by the importance of this material to industry and lack of deep understanding of the surfaces behavior and shapes, in this chapter it is computationally predicted the morphological transformations of the scheelite nanostructures and investigated its intrinsic properties.

## 2 Methodology

### 2.1 Computational Model

To build a computational model using DFT, three elements are needed: a molecular structure, a basis set and a functional. If we change any of these elements, we have a new computational model and the results obtained by the new model will most likely be different from the first one. When a computational model is proposed, its initial structure parameters can be obtained from experimental data, if available. Experimental data constitute the first criterion of a model's ability to reproduce, predict or estimate properties of a given system.

Usually, the first step consists of a testing phase of a series of "pure" and hybrid functionals together with various combinations of basis set available to describe the electronic structure of the elements that constitute the structure in question. The basis sets used in this chapter were obtained from a database on the CRYSTAL program website (<http://www.crystal.unito.it/basis-sets.php>).

After the preliminary choice of the functional and the basis set, as a result of the geometry optimization process of the unit cell (bulk) and the comparison of the data obtained with the experimental results, we have two possible paths to proceed: (I) To conclude that this choice accurately reproduces the electronic and structural properties of the system in question or else; (II) improve our computational model following the steps described by the flowchart in Fig. 1.

1. Choice of functional and basis set;
2. Structure optimization;
3. Comparison of structural and electronic properties with experimental data;
4. If the results are accurate enough, this will be the final model to be used in further studies;
5. Otherwise, the percentage of Hartree-Fock in the exchange functional is modified;
6. If we obtain a model that has the desired accuracy, this will be our final model;
7. Otherwise, an optimization of the coefficients and/or exponents of the set of functions of bases selected in function of the total energy of the system fixed to the experimental parameters is carried out;
8. Structure optimization;
9. This is the final model.

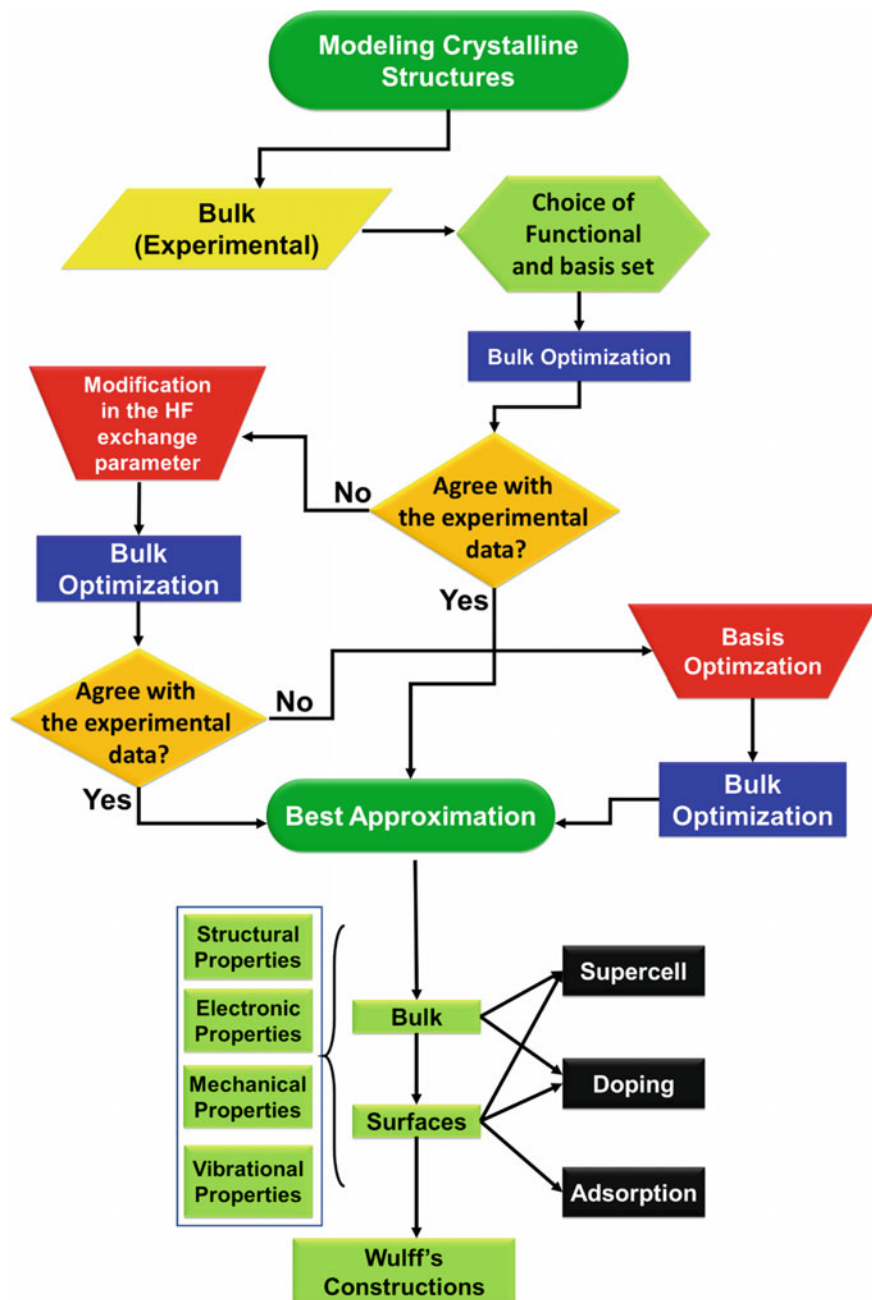


**Fig. 1** Modeling processes of crystalline structures from the construction of the computational model to the Wulff constructions (Adapted from E.O. Gomes et al. [59])

After obtaining the appropriate computational model, which accurately represents the lattice parameters of the unit cell and its internal coordinates, together with the band gap energy, the surfaces (slabs) will be generated in predetermined directions.

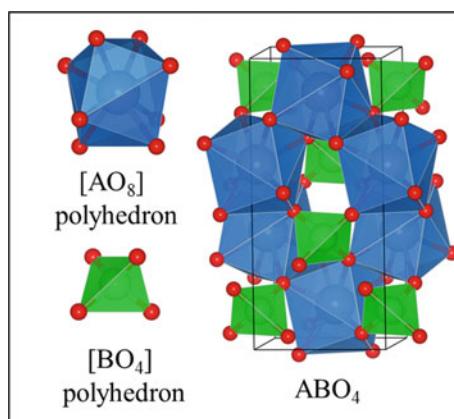
### 2.1.1 Scheelites Compounds $\text{AMoO}_4$ and $\text{AWO}_4$

The compounds of the  $\text{ABO}_4$  ( $\text{A}=\text{Ba}$ ,  $\text{Ca}$ ,  $\text{Cd}$ ,  $\text{Pb}$  or  $\text{Sr}$  e  $\text{B}=\text{Mo}$  or  $\text{W}$ ) type are named Scheelites in honor of the Swedish chemist Carl Wilhelm Scheele [60], who was responsible for the discovery of the chemical elements molybdenum ( $\text{Mo}$ ) and tungsten ( $\text{W}$ ). Thus, the scheelites are characterized by being a family of molybdates and tungstates that have a tetragonal structure, space group  $\text{I4}_{1/a}$  ( $n^\circ$  88) and point group  $\text{C}_{4h}^6$  at NTP [61, 62].

In these structures, the atoms that occupy the A site, called as lattice modifiers, are coordinated by eight oxygen atoms in a dodecahedron configuration, while the atoms present in the B site, the lattice formers, are coordinated to four oxygen atoms, in a tetrahedral structure. These compounds have wide scientific and technological applications, such as: photoluminescence (PL), optical fibers [63], humidity sensors [64, 65], catalysts [66–68], lasers [69, 70], photoluminescent devices [71], among others [72] in addition to exhibiting magnetic [73, 74], catalytic properties [75, 76] and sparkling [77, 78]. Figure 2 is a representation of the structure of the Scheelite structure and its respective coordination polyhedra.

The compounds  $\text{PbMoO}_4$ ,  $\text{PbWO}_4$ ,  $\text{SrMoO}_4$  and  $\text{SrWO}_4$  belong to the scheelite group with two molecular formulas per unit cell. For maximum accuracy between the results obtained by theoretical models via DFT and experimental results, it is necessary to choose an exchange-correlation functional. Although there is a large number of functionals available in the literature, many of them cannot describe the structural and electronic parameters simultaneously with good accuracy of all kinds

**Fig. 2** Unit cell of the scheelite structure



of systems. As an example, it can be mentioned the generalized gradient approximation (GGA) or local density approximation (LDA) functionals, which tend to underestimate the band gap value ( $E_{gap}$ ) of the materials.

There are several studies in the literature that compare the results of several functionals [79–82], showing that a single functional is not capable of providing good results for any material, and for different materials one should seek the functional that best describes its properties, since the choice of the functional in a DFT simulations has a fundamental role.

In the simulations shown here, the choice of functionals used in each structure followed the algorithm demonstrated in Fig. 1. The functionals tried were PBEXC [83], B3LYP [84], BLYP [85], B1WC [86], PBE0 [87], HSE06 [88, 89], PBESOL0 [87] and WC1LYP [80]. Among those functionals, the B3LYP-D3 showed the best results for the PbMoO<sub>4</sub>, WC1LYP for SrMoO<sub>4</sub> and PbWO<sub>4</sub>, while B1WC for SrWO<sub>4</sub>.

The B3LYP-D3 functional, it is the B3LYP functional added to the D3 dispersion correction [90], the B3LYP can be represented through the equation  $E_{xc} = 0.80 * (E_x^{LDA} + B * E_x^{BECKE}) + 0.20 * E_x^{HF} + E_c^{LDA} + 0.81 * (E_c^{GGA} - E_c^{LDA})$ , where  $E_x^{LDA}$  e  $E_c^{LDA}$ , the LDA exchange-correlation functional,  $E_c^{GGA}$  the GGA correlation functional,  $E_x^{HF}$  the HF exchange functional and  $E_x^{BECKE}$  is the Becke exchange functional, and by definition the value of the percentage of the exchange functional by HF is 20% in the B3LYP.

In the case of WC1LYP, this functional can be described through the expression  $E_{xc} = 0.84 * E_x^{WC} + 0.16 * E_x^{HF} + E_c^{LYP}$ , where  $E_x^{WC}$  is the WC exchange functional,  $E_x^{HF}$  the HG exchange functional and  $E_c^{LYP}$  is the LYP correlation functional, in which by definition the default HF percentage for this functional is 16%, since it is the value that multiplies the term of the HF exchange functional [80]. In PbWO<sub>4</sub>, the WC1LYP functional was used as described, in the case of SrMoO<sub>4</sub> we modified this parameter seeking greater accuracy of the results, through systematic variations, a value of 10% was found for the HF exchange functional. The B1WC functional is very similar to WC1LYP, the only difference between them is in the correlation functional, while WC1LYP uses the LYP functional, the B1WC functional uses the PWGGA [86]. the numerical values for the parameters are the same, in SrWO<sub>4</sub> the parameter that multiplies  $E_x^{HF}$  has been changed to 0.10 for better results (Table 1).

**Table 1** Lattice parameters and band gap energy for PbMoO<sub>4</sub> (B3LYP), PbWO<sub>4</sub> (WC1LYP), SrMoO<sub>4</sub> (WC1LYP-H10%) e SrWO<sub>4</sub> (B1WC-H10%)

Material	Functional	a (Å)	c (Å)	$E_{gap}$ (eV)
PbMoO <sub>4</sub>	B3LYP	5.41 (0.4%) [91]	11.83 (2.2%)	3.48 (0.8%) [62]
PbWO <sub>4</sub>	WC1LYP	5.44 (0.1%) [91]	12.03 (0.1%)	3.98 (2.3%) [92]
SrMoO <sub>4</sub>	WC1LYP (10%)	5.48 (1.6%) [93]	12.12 (0.7%)	4.42 (0.5%) [94]
SrWO <sub>4</sub>	B1WC (10%)	5.41 (0.2%) [95]	11.99 (0.2%)	5.01 (1.4%) [96]

\* The values in parentheses indicate the percentage differences from the experimental

## 2.2 Surfaces

The surfaces are constituted by models that indefinitely extend through the xOy plane, and are finite in the z axis, thus constituting a two-dimensional (2D) model, called slabs. In our calculations, for the same plane (*hkl*) several slabs are simulated as a function of the increase in the number of atomic layers to incorporate the bulk characteristics into the 2D model. This increment is done until convergence is obtained in the surface energy ( $E_{surf}$ ) calculation for these slabs, which is described from the expression  $E_{surf} = (E_{slab} - nE_{bulk})/2A$ , where  $E_{slab}$  is the slab total energy,  $E_{bulk}$  is the bulk total energy,  $n$  is the number of molecular units in the bulk present in the slab, and  $A$  is the slab unit cell area.

Structural properties of the outermost layers of the (001), (100), (101), (110), (111) and (112) surfaces, and the band gap energy ( $E_{gap}$ ) calculated for each of the corresponding models are described in Table 2. For all materials, the outermost coordination polyhedra centered on A ( $A = \text{Sr}$  or  $\text{Pb}$ ) exhibited a 6 coordination for the (001) and (112) surfaces and 5 coordination for the (100), (101) and (110) surfaces; the only difference occurred for the plane (111), which for  $\text{PbWO}_4$  and  $\text{SrWO}_4$  presented coordination 4 while in the cases of  $\text{PbMoO}_4$  and  $\text{SrMoO}_4$  it presented coordination 5.

Observing the results shown in Table 2, it is possible to relate the coordination of the outermost polyhedra centered on A, with the stability of each plane. The surfaces (001) and (112) are the most stable for all materials, and are the ones with the greatest coordinations in their outermost polyhedra. For the outermost coordination polyhedra centered on B ( $B = \text{Mo}$  or  $\text{W}$ ), in all models the coordination was kept equal to the *bulk*.

For  $\text{PbMoO}_4$  and  $\text{SrMoO}_4$ , it is observed that the plane that has the highest  $E_{surf}$  is (100), while for  $\text{PbWO}_4$  and  $\text{SrWO}_4$  is the (111), this can be directly related to the lower coordination of the outermost polyhedra centered on A exhibited by these materials. Besides that, it is observed that the surfaces that exhibited the highest and lowest  $E_{gap}$  values were (111) and (001) for  $\text{PbMoO}_4$ , (112) and (111) for  $\text{PbWO}_4$ , (101) and (111)  $\text{SrMoO}_4$ , and (101) and (100) for  $\text{SrWO}_4$ . Further on, as we will see, the knowledge of these values together with the energies of the valence band maximum (VBM) and the conduction band minimum (CBM), is very important for the search for new applications for these materials, mainly in the photocatalysis field.

## 2.3 Electronic and Structural Descriptors

The use of a single value to describe the coordination of an atom in relatively distorted polyhedra can be a difficult task. There are several surfaces in which the polyhedra have the same coordination number ( $cn$ ), but due to the different distortions suffered by the polyhedra in the geometry optimization process, the atoms are not bonded in the same way as for the bulk. It is then necessary to use a parameter that, when

**Table 2** Low Miller Index surfaces ( $hkl$ ) modeled for each of the materials, coordination of the outermost polyhedra centered on A (Pb or Sr) and B (Mo or W), surface energy ( $E_{surf}$ ), band gap energy ( $E_{gap}$ )

PbMoO <sub>4</sub>						
Surface	(001)	(100)	(101)	(110)	(111)	(112)
Pb-centered	[PbO <sub>6</sub> ]	[PbO <sub>5</sub> ]	[PbO <sub>5</sub> ]	[PbO <sub>5</sub> ]	[PbO <sub>5</sub> ]	[PbO <sub>6</sub> ]
Mo-centered	[MoO <sub>4</sub> ]	[MoO <sub>4</sub> ]	[MoO <sub>4</sub> ]	[MoO <sub>4</sub> ]	[MoO <sub>4</sub> ]	[MoO <sub>4</sub> ]
$E_{surf}$	0.66	0.81	0.68	0.81	0.72	0.68
$E_{gap}$	3.47	3.59	3.57	3.54	3.98	3.51
PbWO <sub>4</sub>						
Surface	(001)	(100)	(101)	(110)	(111)	(112)
Pb-centered	[PbO <sub>6</sub> ]	[PbO <sub>5</sub> ]	[PbO <sub>5</sub> ]	[PbO <sub>5</sub> ]	[PbO <sub>4</sub> ]	[PbO <sub>6</sub> ]
W-centered	[MoO <sub>4</sub> ]	[MoO <sub>4</sub> ]	[MoO <sub>4</sub> ]	[MoO <sub>4</sub> ]	[MoO <sub>4</sub> ]	[MoO <sub>4</sub> ]
$E_{surf}$	0.27	0.40	0.29	0.39	0.73	0.28
$E_{gap}$	3.97	4.12	4.04	4.11	3.07	4.14
SrMoO <sub>4</sub>						
Surface	(001)	(100)	(101)	(110)	(111)	(112)
Sr-centered	[SrO <sub>6</sub> ]	[SrO <sub>5</sub> ]	[SrO <sub>5</sub> ]	[SrO <sub>5</sub> ]	[SrO <sub>5</sub> ]	[SrO <sub>6</sub> ]
Mo-centered	[MoO <sub>4</sub> ]	[MoO <sub>4</sub> ]	[MoO <sub>4</sub> ]	[MoO <sub>4</sub> ]	[MoO <sub>4</sub> ]	[MoO <sub>4</sub> ]
$E_{surf}$	0.60	1.16	0.72	0.76	1.00	0.68
$E_{gap}$	4.38	3.25	4.45	4.00	3.15	4.20
SrWO <sub>4</sub>						
Surface	(001)	(100)	(101)	(110)	(111)	(112)
Sr-centered	[SrO <sub>6</sub> ]	[SrO <sub>5</sub> ]	[SrO <sub>5</sub> ]	[SrO <sub>5</sub> ]	[SrO <sub>4</sub> ]	[SrO <sub>6</sub> ]
W-centered	[WO <sub>4</sub> ]	[WO <sub>4</sub> ]	[WO <sub>4</sub> ]	[WO <sub>4</sub> ]	[WO <sub>4</sub> ]	[WO <sub>4</sub> ]
$E_{surf}$	0.57	1.15	0.77	0.81	0.95	0.66
$E_{gap}$	4.95	3.81	5.14	4.78	4.97	4.92

counting the number of coordinated atoms, evaluates the distortions that occur in the polyhedra. For this, it is possible to rely on a model capable of providing an average coordination number ( $ECoN$ ), evaluating all surrounding atoms through a scheme in which they are weighted, no longer being counted as whole atoms, but as fractional atoms with values between 0 and 1, and this number gets closer to zero as the distance between two atoms tends to a very large value.

In this work  $ECoN$  is given by the following equation [97, 98]:

$$ECoN = \sum_i w_i \quad (1)$$

where the quantity called “bond weight” of the  $i$ -th bond is given by:



$$w_i = \exp \left[ 1 - \left( \frac{l_i}{l_{av}} \right)^6 \right] \tag{2}$$

where  $l_i$  is the bond length of the  $i$ -th bond and  $l_{av}$  is a weighted average bond length defined by:

$$l_{av} = \frac{\sum_i l_i \exp \left[ 1 - \left( l_i / l_{min} \right)^6 \right]}{\sum_i \exp \left[ 1 - \left( l_i / l_{min} \right)^6 \right]} \tag{3}$$

To evaluate the effect of the coordination breakdown on the polyhedra coordination in each plane, related to the respective relative stabilities of each surface through the values of  $E_{surf}$ , we will use the sum of each of the effective coordination numbers ( $ECoN$ ) of the outermost clusters centered on A and B (Fig. 3).

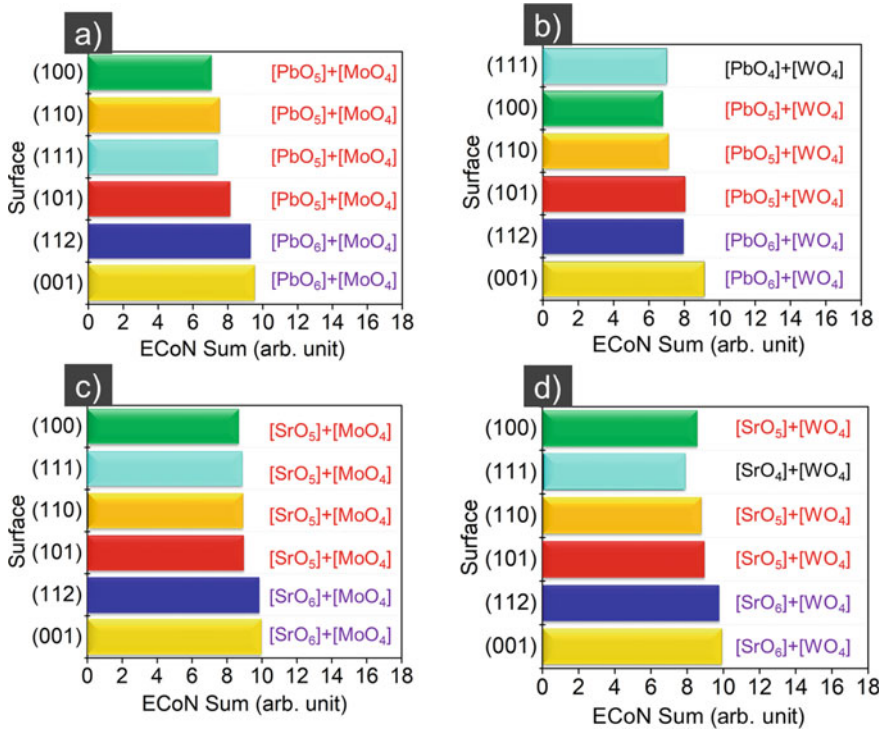


**Fig. 3** Sum of the effective coordination numbers ( $ECoN$ ) of the outermost polyhedra centered on A and B for each one of the surfaces, arranged in the order of stability for **a** PbMoO<sub>4</sub>, **b** PbWO<sub>4</sub>, **c** SrMoO<sub>4</sub> and **d** SrWO<sub>4</sub>

According to Fig. 3, it is possible to see the tendency of an inverse relationship between the greater effective coordination of the outermost polyhedra and the relative stability of the surfaces: as the value of the sum of the  $ECoN$  decreases, the surface energy increases. This relationship is not exact, because here only the most external polyhedra were taken into account. Some models there are more coordination polyhedra in addition to the most external ones in which coordination breaks occur, and these are also decisive for the relative stability of the models.

As a result of the coordination breaks that occur in the  $(hkl)$  surfaces, changes occur in the charge distribution in the outermost regions of each surface, and the terminations are determinant for the type of interaction that each surface can exhibit. Each of the surfaces has the same charge distribution patterns, with a single change occurring in the (111) plane, where the molybdates exhibit a different pattern than the tungstates. This change is associated with the coordination changes observed for these models (Table 2). The (100) plane exhibits a different pattern from that observed for the other surfaces, with regions of positive potential alternating in continuous bands with regions of negative potential (Fig. 4).

The surfaces (101), (110) and (100) are the ones that exhibit regions with highest density of positive charges, in that order, while the (001) plane is the one that exhibits the regions with the highest density of negative charges. It is possible to observe that the exchange of Sr for Pb in the structures generates a greater presence of regions with a density of positive charges, so it can be inferred that for these structures, the presence of Pb makes the systems more accessible to interactions with negatively charged systems. In the case of (111) surface, the exchange of Mo for W generates a slight decrease in the area of the regions with a density of positive charges. For the (111) surface, the exchange of Mo for W generates a slight decrease in the area of the regions with a density of positive charges.

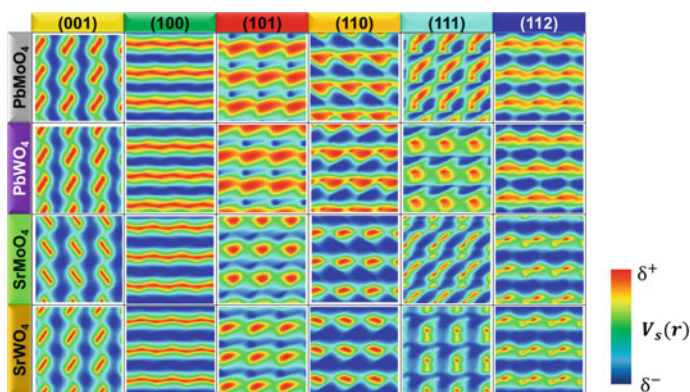


**Fig. 4** Electrostatic potential isosurfaces ( $V_S(r)$ ) for the surfaces (001), (100), (101), (110), (111) and (112) of  $PbMoO_4$ ,  $PbWO_4$ ,  $SrMoO_4$  and  $SrWO_4$

### 2.4 Representation of Morphological Transformations

It is possible to represent the morphological transformations systematically, when instead of using the  $E_{surf}$  values for each surface, using the dimensionless ratio between the  $E_{surf}$  surface energies and the lowest surface energy for the simulated  $E_{surf(hkl)}$  surfaces is used (Eq. 3). Through this type of representation, each possible morphology can be associated with a vector  $\Upsilon^\Gamma (1 \times n)$  ( $n$  is the number of simulated surfaces ( $hkl$ )), where its elements are  $\Gamma_{(hkl)}$ , which are associated with each of the surfaces ( $hkl$ ) can be obtained by the product of the vector associated with a vector  $\Upsilon_{DFT}^\Gamma (1 \times n)$  (Eq. 5) and the modifier diagonal matrix  $\tau (n \times n)$ , according to Eq. (6). The elements of the vector indicated in Eq. (6) are sufficient information to represent any morphology that contains the surfaces ( $hkl$ ) present in the morphological map.

$$\Gamma_{(hkl)} = \frac{E_{surf}}{E_{surf(hkl)}} \tag{4}$$

$$\Upsilon^\Gamma (1 \times n) = \Upsilon_{DFT}^\Gamma \tau = [\Gamma_{(001)} \dots \Gamma_{(hkl)}] = [\tau_{(001)} \dots 0 \dots \dots \dots 0 \dots \tau_{(hkl)}] \tag{5}$$

$$\Upsilon^\Gamma = [\Gamma_{(001)} \dots \Gamma_{(hkl)}] \tag{6}$$

Because the reference crystal ( $v_{n+1}$ ) being the ideal crystal, obtained through geometry optimization, its modification matrix is the identity matrix itself. However, for the other vertices, the modification matrix corresponds to matrices that relate the surface energy variation for one plane at a time, until the value of  $\Gamma_{(hkl)}$  which corresponds to the maximum exposure for each one of the vertices in the graph.

Using the  $E_{surf}$  values determined from the obtained relaxed structures, the thermodynamic crystals for each structure were generated (Fig. 5). All structures have the (001), (101) and (112) surfaces exposed, varying the relative exposure rate. In  $PbMoO_4$  the surface (101) dominates the crystal morphology, followed by (112), (001) and (111); in  $PbWO_4$  the surface (112) dominates the morphology, followed by the surfaces (101) and (001); in  $SrMoO_4$  the same occurs as for  $PbWO_4$  with the difference that the plane (110) is exposed; in  $SrWO_4$  the same occurs as for the decreasing order of relative exposure is the same observed in the last three cases, without the presence of any additional plane besides (001), (101) and (112).

Starting from the dimensionless ratio  $\Gamma_{(hkl)} = E_{surf(hkl)}/E_{surf(001)}$ , a matrix of surface energy ratios for  $PbMoO_4$  was constructed and it is shown in Fig. 6a. The column  $v_7$  corresponds to the reasons  $\Gamma_{(hkl)}$  of the thermodynamic crystal of the  $PbMoO_4$ . The columns  $v_1, v_2, v_3, v_4, v_5$  and  $v_6$ , correspond to the reasons  $\Gamma_{(hkl)}$  so that the plans (001), (100), (101), (110), (111) and (112), have higher relative exposure, respectively. Figure 6b, represents the crystals that can be obtained by modifying the values of  $\Gamma_{(hkl)}$  to one or two surfaces from the thermodynamic crystal. The elements  $e_{1-6}$  represent the crystals shown in Fig. 6a, where the values of  $\Gamma_{(hkl)}$  were modified so that each of the surfaces would have greater relative exposure, the elements  $e_{7-21}$  represent all combinations of changes that occurred in  $\Gamma_{(hkl)}$  in Fig. 6a taken in pairs.

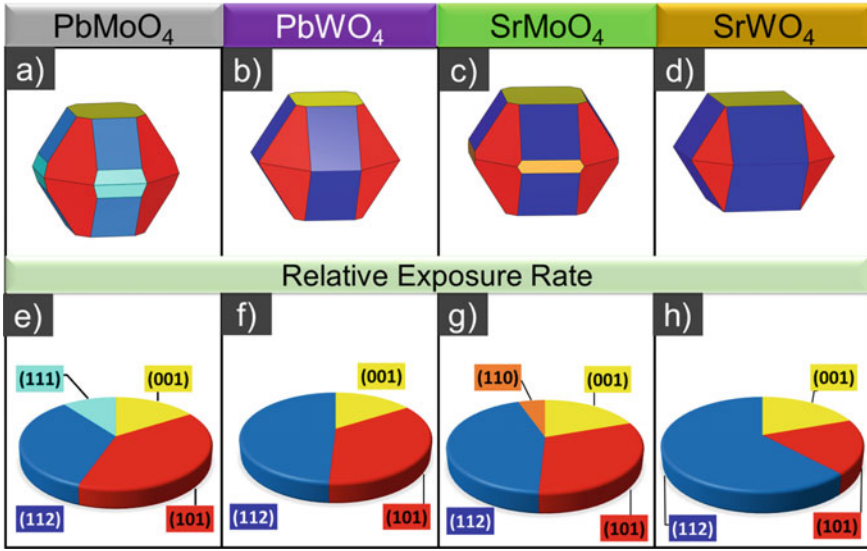


**Fig. 5** Thermodynamic crystals for the **a**  $\text{PbMoO}_4$ , **b**  $\text{PbWO}_4$ , **c**  $\text{SrMoO}_4$  and **d**  $\text{SrWO}_4$ , and exposure relative rates in thermodynamic crystals for each one of the surfaces for the **e**  $\text{PbMoO}_4$ , **f**  $\text{PbWO}_4$ , **g**  $\text{SrMoO}_4$  and **h**  $\text{SrWO}_4$

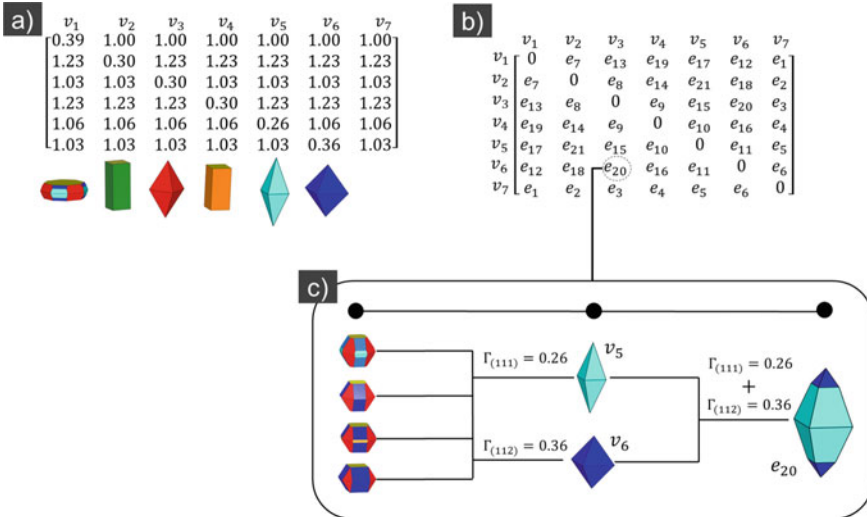


**Fig. 6** **a** Ratios between surface energies, **b** Representative matrix of morphological transformations and **c** shows that through variations in  $\Gamma_{(hkl)}$  it is possible to arrive at any morphology for any of the materials in this work

In Fig. 6c, for example, starting from the thermodynamic crystals for each of the materials, applying the modification in the values of  $\Gamma_{(111)}$  and  $\Gamma_{(112)}$  at the same time, one reaches the crystal  $e_{20}$ . The same reasoning can be applied to obtaining any elements of the modification matrix. The advantage of using the dimensionless ratio  $\Gamma_{(hkl)}$  is that regardless of the system chosen, a change in the value of  $\Gamma_{(hkl)}$  corresponds to the same morphological transformation. The surface energy ratio matrix (Fig. 6a) can be used with the same values for any system present in this work and the same morphologies will be obtained, except (001), where the surfaces present in the ideal crystal even with a lower rate of relative exposure, are found in the morphology of  $v_1$ .

An application arising from the elements of the surface energy matrix and the construction of Wulff crystals is the determination of the density of states (DOS) of crystalline particles,  $\rho_{particle}(\epsilon)$ . As an approximation, assuming an additive linear model that is based on the contribution of each of the exposed surfaces to the electronic structure, it is possible to determine the DOS of any morphology of interest, just by knowing the relative exposure rate of each of the surfaces. In this way, the DOS of a nanoparticle can be given by the equation:

$$\rho_{particula}(\epsilon) = \frac{\sum_{(hkl)} [A_{hkl}]_{particula} \rho_{hkl}(\epsilon)}{\sum_{(hkl)} [A_{hkl}]_{particula}} \quad (7)$$

where,  $A_{hkl}$  is the total surface ( $hkl$ ) area exposed in the particle, and  $\rho_{hkl}$  is the DOS of the respective surface ( $hkl$ ).

Through the model of Eq. (7), the DOS of the thermodynamically stable crystals of each material were estimated (Fig. 7). For the thermodynamically stable crystals of the  $\text{PbMoO}_4$ ,  $\text{PbWO}_4$  and  $\text{SrWO}_4$  the surface (101) was the one with the highest electronic contribution, followed by (111) in the case of  $\text{PbMoO}_4$ , (112) and (001) for the others, only for the  $\text{SrMoO}_4$  the plane (112) was the one with the highest electronic contribution, followed by plans (101), (110) and (001).

For regions close to the valence band maximum (VBM), the (101) plane presented the highest electronic contribution, while the (112) and (001) were surfaces with the highest contribution in the close to conduction band (CB). Although this is a qualitative estimate, we can compare the values of  $E_{gap}$  for each of the particles, the thermodynamic crystal of the  $\text{PbMoO}_4$  was the one that exhibited the lowest value of  $E_{gap}$ , 2.12 eV. The thermodynamic crystals of the  $\text{PbWO}_4$  and  $\text{SrMoO}_4$  have the same values as  $E_{gap}$ , 2.75 eV; while  $\text{SrWO}_4$  was the one that exhibited the highest value of  $E_{gap}$ , 3.43 eV.

The development of this new methodology is important for the analysis and prediction of properties in a rational way, in addition, ways to associate this methodology with other electronic and structural descriptors of our models have been sought. It is worth mentioning that despite the possibility of estimating the DOS of a nanoparticle, it is not safe to say that the band gap of the nanoparticle in question coincides exactly with the band gap observed experimentally for the morphology in question, and these representations have a qualitative character [99].

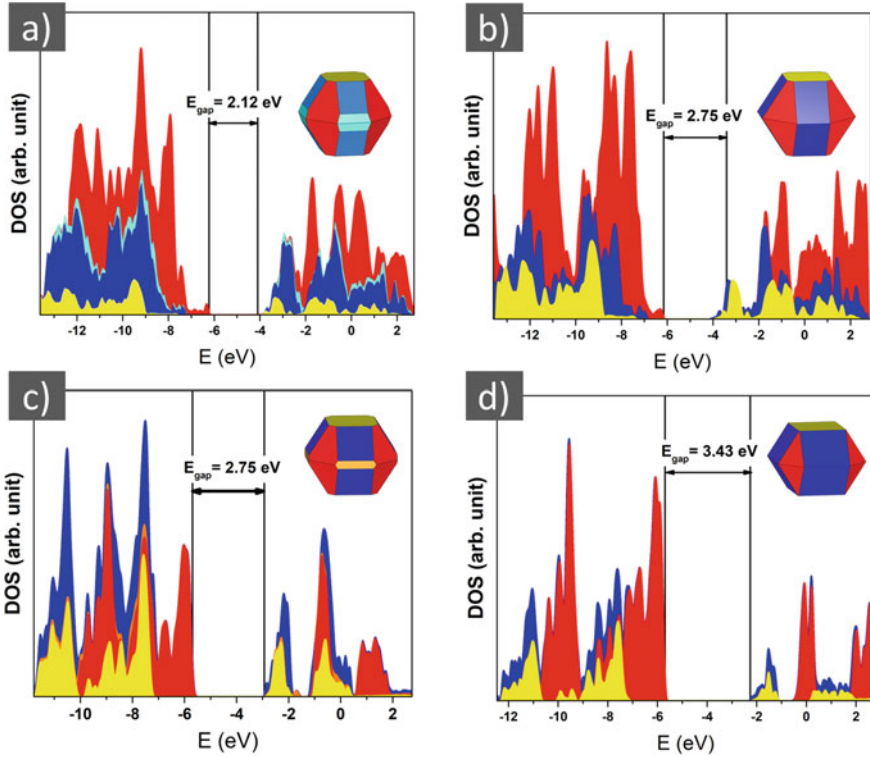


**Fig. 7** Density of states (DOS) for each thermodynamic crystals ( $v_7$ ) built using the Wulff's model for **a**  $\text{PbMoO}_4$ , **b**  $\text{PbWO}_4$ , **c**  $\text{SrMoO}_4$  and **d**  $\text{SrWO}_4$

### 3 $\text{H}_2$ Production by Water-Splitting Using $\text{ABO}_4$ Compounds

Among the renewable energy sources, photocatalytic water separation provides a promising method for the generation of clean, low-cost and environmentally sustainable energy through the production of  $\text{H}_2$  using solar energy. There are several reports in the literature of metal oxides that are usable for the production of  $\text{H}_2$  through water separation [53]. For catalysis to occur on the surface of a semiconductor, it is necessary that a photon of energy equal to or greater than its value of  $E_{\text{gap}}$  reach the surface, so that an electron ( $e^-$ ) is excited by being promoted to the conduction band (CB), leaving a hole ( $h^+$ ) in the valence band (VB). Besides that, the excited electron and the hole can recombine or be trapped in a metastable state, and they can also participate in reactions with electron donors and acceptors adsorbed on the semiconductor surface. Under proper conditions, the excited electron can reduce  $\text{H}^+$  ions producing  $\text{H}_2$  gas and the hole can generate  $\text{O}_2$  [83].

The efficient separation of pairs  $e^- - h^+$  is crucial for catalysis. The choice of a system requires prior knowledge about the levels of the VBM and the CBM in relation to the redox potential of the molecule of  $H_2O$ . When the analysis is done for the vacuum level, the energy of the CBM needs to be lower than the redox potential  $H_2O/O_2$  and the VBM energy be higher than redox potential  $H^+/H_2$ .

To evaluate the applicability of the systems studied for the production of  $H_2$  through the photocatalytic breakdown of the water molecule, two dashed lines representing the  $E^\circ(H^+/H_2)$  and  $E^\circ(O_2/H_2O)$  redox potentials were introduced in Figure 8. The redox potentials were adjusted considering the compensation of the band alignment concerning to the vacuum level for all simulated planes of each material.

Observing the alignment of bands for  $PbMoO_4$  systems in which the (100), (101) and (111) surfaces are exposed, the results shows a favorable condition for the production of  $H_2$  through photocatalytic of the water molecule. The materials  $PbWO_4$ ,  $SrMoO_4$  and  $SrWO_4$  are promising candidates for the production of  $H_2$ , because for all surfaces, VBM is below the redox potential  $H_2O/O_2$  and CBM is above the redox potential  $H^+/H_2$ . Still observing the alignment of bands, it is possible to notice that for all materials, the plane (101) is the one that exhibits the highest value of CBM and VBM. For the  $PbMoO_4$  and  $PbWO_4$  the plane that exhibits lower values of CBM and VBM is the (001). For the  $SrMoO_4$  and  $SrWO_4$ , the plane (100) is the one with the lowest CBM value.

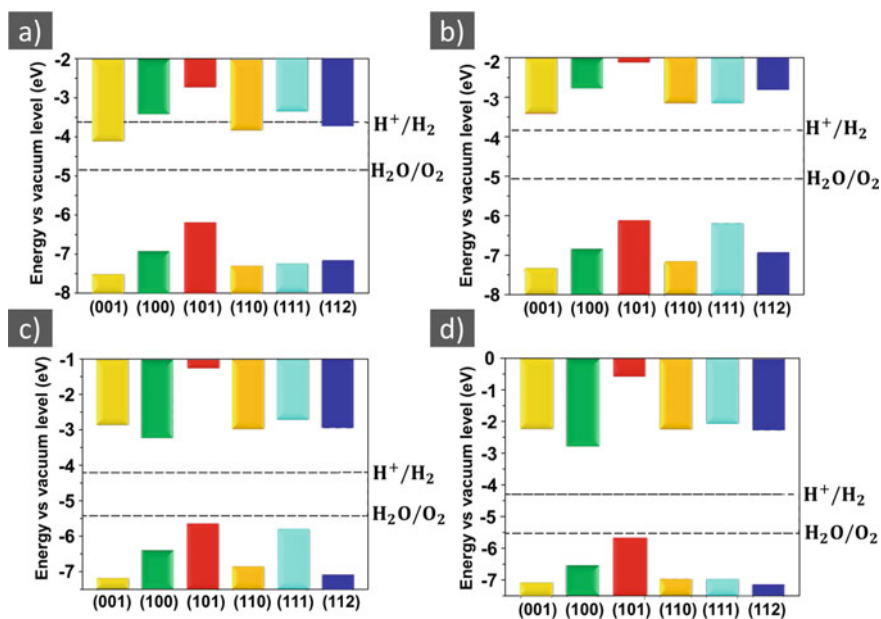


**Fig. 8** Band alignment (valence band and conduction band VS vacuum level) to **a**  $PbMoO_4$ , **b**  $PbWO_4$ , **c**  $SrMoO_4$  and **d**  $SrWO_4$

## 4 Concluding Remarks

In this chapter, we demonstrate that computer modeling of low Miller index (*hkl*) surfaces of scheelite  $ABO_4$  ( $A=\text{Sr}$  or  $\text{Pb}$  e  $B=\text{Mo}$  or  $\text{W}$ ) compounds, in addition to revealing properties not yet studied for these materials, and it can serve to show what are the relationships between atoms A or B that are present in their structures. Also, we saw their potential applications, generating motivation for further studies where a family analysis of compounds of the tungstates and molybdates of the scheelite group would be carried out.

Using the  $E_{surf}$  values and the Wulff's construction, the morphologies of the thermodynamic crystals were estimated for each of the materials, it was shown that considering this crystal as a starting point, it is possible, through the modulation of one or more  $E_{surf}$  values, to propose several stabilization routes for any type of morphology that is within the truncation imposed by the material's spatial group.

The exchange of atoms A or B, and even the formation of heterostructures constituted by these materials in association with the study of their surfaces, can result in new functionalization mechanisms of these materials for several applications. As seen in the present chapter, when the possible production of  $\text{H}_2$  was analyzed through the photolytic breakage of the  $\text{H}_2\text{O}$  molecule, where it was observed that due to the difference in relation to the electronic properties of each of the surfaces, systems with a certain plane (*hkl*) exposed in their nanoparticles may result in potential candidates for this type of application.

We see that the intrinsic atomic properties and the electronic properties of coordination polyhedra that had their coordination broken and that appear in the exposed surfaces of the morphologies are fundamental to explain the mechanisms of semiconductor functionalization in general. The approach used for computational modeling of crystalline solids and their surfaces (*hkl*) can be used for all known structures generating several contributions to materials engineering.

**Acknowledgements** This work was supported by the Brazilian funding agencies FAPESP (2019/08928-9, 2013/07296-2, 2020/01144-0), FAPERGS (21/2551-0000695-1), CAPES—Finance Code 001—(88887.467334/2019-00) and CNPq (grant no. 420062/2016-5, 312854/2021-8, 307213/2021-8 and 432242/2018-0, 482473/2010-0, 446126/2014-4, 308548/2014-0 and 307236/2018-8). The computational facilities were supported by resources supplied by the Molecular Simulations Laboratory (São Paulo State University, Bauru, Brazil) and High-Performance Computing Center (NPAD) at UFRN.

## References

1. Simões, A.: Phys. Perspect. **4**, 253 (2002)
2. Koper, M.T.M.: Mod. Aspect. Electrochem. **36**, 51 (2004)
3. Houk, K.N., Liu, F.: Acc. Chem. Res. **50**, 539 (2017)
4. Bauer, B., Bravyi, S., Motta, M.: Chem. Rev. **120**, 12685 (2020)
5. Vermeire, F.H., Green, W.H.: Chem. Eng. J. **418**, 129307 (2021)



6. Gaita-Ariño, A., Luis, F., Hill, S., Coronado, E.: *Nat. Chem.* **11**, 301 (2019)
7. Dral, P.O.: *J. Phys. Chem. Lett.* **11**, 2336 (2020)
8. Agrawal, P.M., Raff, L.M., Hagan, M.T., Komanduri, R.: *J. Chem. Phys.* **124**, 134306 (2006)
9. Behler, J., Martoňák, R., Donadio, D., Parrinello, M.: *Phys. Status Solidi (b)* **245**, 2618 (2008)
10. Prudente, F.V., Acioli, P.H., Neto, J.J.S.: *J. Chem. Phys.* **109**, 8801 (1998)
11. Brown, D.F.R., Gibbs, M.N., Clary, D.C.: *J. Chem. Phys.* **105**, 7597 (1998)
12. Amabilino, S., Bratholm, L.A., Bennie, S.J., Vaucher, A.C., Reiher, M., Glowacki, D.R.: *J. Phys. Chem. A* **123**, 4486 (2019)
13. Butler, K.T., Davies, D.W., Cartwright, H., Isayev, O., Walsh, A.: *Nature* **559**, 547 (2018)
14. Fernandez, M., Barnard, A.S.: *ACS Nano* **9**, 11980 (2015)
15. Yan, T., Sun, B., Barnard, A.S.: *Nanoscale* **10**, 21818 (2018)
16. Lie, M.H., Arup, U., Grytnes, J.-A., Ohlson, M.: *Biodivers. Conserv.* **18**, 5 (2009)
17. Hohenberg, P., Kohn, W.: *Phys. Rev.* **136**, B864 (1964)
18. Corà, F., Patel, A., Harrison, N.M., Dovesi, R., Callow, C.R.A.: *J. Am. Chem. Soc.* **118**, 12174 (1996)
19. Higgott, O., Wang, D., Brierley, S.: *Quantum* **3**, 156 (2019)
20. Kohn, W., Sham, L.J.: *Phys. Rev.* **140**, A1133 (1965)
21. Hafner, J.: *J. Comput. Chem.* **29**, 2044 (2008)
22. Soler, J.M., Artacho, E., Gale, J.D., García, A., Junquera, J., Ordejón, P., Sánchez-Portal, D.: *J. Phys. Condens. Matter* **14**, 2745 (2002)
23. Clark, S.J., Segall, M.D., Pickard, C.J., Hasnip, P.J., Probert, M.I.J., Refson, K., Payne, M.C.: *Zeitschrift Fur Kristallographie* **220**, 567 (2005)
24. Giannozzi, P., Andreussi, O., Brumme, T., Bunau, O., Buongiorno Nardelli, M., Calandra, M., Car, R., Cavazzoni, C., Ceresoli, D., Cococcioni, M., Colonna, N., Carnimeo, I., Dal Corso, A., de Gironcoli, S., Delugas, P., Distasio, R.A., Ferretti, A., Floris, A., Fratesi, G., Fugallo, G., Gebauer, R., Gerstmann, U., Giustino, F., Gorni, T., Jia, J., Kawamura, M., Ko, H.Y., Kokalj, A., Küçükbenli, E., Lazzeri, M., Marsili, M., Marzari, N., Mauri, F., Nguyen, N.L., Nguyen, H.V., Otero-De-La-Roza, A., Paulatto, L., Poncé, S., Rocca, D., Sabatini, R., Santra, B., Schlipf, M., Seitsonen, A.P., Smogunov, A., Timrov, I., Thonhauser, T., Umari, P., Vast, N., Wu, X., Baroni, S.: *J. Phys. Condens. Matter* **29**, 465901 (2017)
25. Dovesi, R., Orlando, R., Civalieri, B., Roetti, C., Saunders, V.R., Zicovich-Wilson, C.M.: *Zeitschrift Fur Kristallographie* **220**, 571 (2005)
26. Dovesi, R., Saunders, V., Roetti, C., Orlando, R., Zicovich-Wilson, C.M., Pascale, F., Civalieri, B., Doll, K., Harrison, N., Bush, I., Llunel, M., Causà, M., Noël, Y., Maschio, L., Erba, A., Rérat, M., Casassa, S. (2018)
27. Platonenko, A., Popov, A.I.: *Opt. Mater.* **99**, 109529 (2020)
28. Wu, W., Wang, J., Zhang, T., Jiang, S., Ma, X., Zhang, G., Zhang, X., Chen, X., Li, B.: *J. Mater. Chem. xdc* **7**, 5451 (2019)
29. Tsiwah, E.A., Ding, Y., Li, Z., Zhao, Z., Wang, M., Hu, C., Liu, X., Sun, C., Zhao, X., Xie, Y.: *CrystEngComm* **19**, 7041 (2017)
30. Li, M., Yang, Y., Ling, Y., Qiu, W., Wang, F., Liu, T., Song, Y., Liu, X., Fang, P., Tong, Y., Li, Y.: *Nano Lett.* **17**, 2490 (2017)
31. Oliveira, M.C., Gracia, L., Nogueira, I.C., Gurgel, M.F.C., Mercury, J.M.R., Longo, E., Andrés, J.: *Cryst. Res. Technol.* **51**, 634 (2016)
32. Yu, L., Li, D., Yue, M., Yao, J., Lu, S.: *Chem. Phys.* **326**, 478 (2006)
33. Liang, Q., Qiao, F., Cui, X., Hou, X.: *Mater. Sci. Semicond. Process.* **89**, 154 (2019)
34. Lin, X.M., Sorensen, C.M., Klabunde, K.J., Hadjipanayis, G.C.: *Langmuir* **14**, 7140 (1998)
35. Li, M., Zhang, X., Lu, S., Yang, P.: *RSC Adv.* **6**, 103382 (2016)
36. Ren, Y.K., Ding, X.H., Wu, Y.H., Zhu, J., Hayat, T., Alsaedi, A., Xu, Y.F., Li, Z.Q., Yang, S.F., Dai, S.Y.: *J. Mater. Chem. A* **5**, 20327 (2017)
37. Gouveia, A.F., Gracia, L., Longo, E., San-Miguel, M.A., Andrés, J.: *Comput. Mater. Sci.* **188**, 110217 (2021)
38. Harker, D., Donnay, J.: *Am. Miner.* **22**, 446 (1937)

39. Barbosa, M. A., Fabris, G. S. L., Ferrer, M.M., Azevedo, D.H.M., Sambrano, J.R.: *Mater. Res.* **20**, 920 (2017)
40. Ferrer, M.M., Fabris, G.S.L., de Faria, B.V., Martins, J.B.L., Moreira, M.L., Sambrano, J.R.: *Heliyon* **5** (2019)
41. Gouveia, A.F., Ferrer, M.M., Sambrano, J.R., Andrés, J., Longo, E.: *Chem. Phys. Lett.* **660**, 87 (2016)
42. Wulff, G.: *Zeitschrift Für Kristallographie. Crystal. Mater.* **34** (1901)
43. Yu, Y., Shi, T., Ma, Y., Sun, F., Pan, J., Yang, Y.: *Mater. Sci.* **26**, 58 (2020)
44. Assirey, E.A.R.: *Saudi Pharmaceut. J.* **27**, 817 (2019)
45. Kuzmin, A., Purans, J.: *Radiat. Meas.* **33**, 583 (2001)
46. Wang, S., Gao, H., Sun, G., Li, Y., Wang, Y., Liu, H., Chen, C.: *Opt. Mater.* **99**, 109562 (2020)
47. Ray, S.K., Hur, J.: *Ceram. Int.* **46**, 20608 (2020)
48. Ahmed, N., Kraus, H., Kim, H.J., Mokina, V., Tsiumra, V., Wagner, A., Zhydashchuk, Y., Mykhaylyk, V.B.: *Materialia* **4**, 287 (2018)
49. Culver, S.P., Rabuffetti, F.A., Zhou, S., Mecklenburg, M., Song, Y., Melot, B.C., Brutchey, R.L.: *Chem. Mater.* **25**, 4129 (2013)
50. Hsu, L.C.: *Econ. Geol.* **72**, 664 (1977)
51. Karolewicz, M., Fuks, H., Tomaszewicz, E.: *J. Therm. Anal. Calorim.* **138**, 2219 (2019)
52. Huang, Y., Seo, H.J., Feng, Q., Yuan, S.: *Mater. Sci. Eng. B* **121**, 103 (2005)
53. Rajaambal, S., Sivaranjani, K., Gopinath, C.S.: *J. Chem. Sci.* **127**, 33 (2015)
54. Abe, R.: *Chem. Soc. Japan* **84**, 1000 (2011)
55. Gouveia, A.F., Assis, M., Cavalcante, L.S., Longo, E., Andrés, J.: *Front. Res. Today* **1**, 1005 (2018)
56. Peng, Y., Jiang, K., Hill, W., Lu, Z., Yao, H., Wang, H.: *ACS Appl. Mater. Interf.* **11**, 3971 (2019)
57. Rahimi-Nasrabadi, M.: *J. Mater. Sci. Mater. Electron.* **28**, 2200 (2016)
58. Kato, H., Matsudo, N., Kudo, A.: *Chem. Lett.* **33**, 1216 (2004)
59. Gomes, E.O., Fabris, G.S.L., Ferrer, M.M., Motta, F.V., Bomio, M.R.D., Andres, J., Longo, E., Sambrano, J.R.: *Comput. Mater. Sci.* **170**, 109176 (2019)
60. Lennartson, A.: *The Chemical Works of Carl Wilhelm Scheele*. Springer, Cham (2017)
61. Shivakumara, C., Saraf, R., Behera, S., Dhananjaya, N., Nagabhushana, H.: *Mater. Res. Bull.* **61**, 422 (2015)
62. Hazen, R.M., Finger, L.W., Mariathasan, J.W.E.: *J. Phys. Chem. Solids* **46**, 253 (1985)
63. Zhu, F., Xiao, Z., Zhang, F., Yan, L., Huang, A.: *J. Lumin.* **131**, 22 (2011)
64. Blank, T.A., Eksperiandova, L.P., Belikov, K.N.: *Sens. Actuators, B Chem.* **228**, 416 (2016)
65. Arularasu, M.V., Sundaram, R., Magdalane, C.M., Kanimozhi, K., Kasinathan, K., Thema, F.T., Letsholathebe, D., Mola, G.T., Maaza, M.: *J. Nanostruct.* **7**, 47 (2017)
66. Sleight, A.W., Aykan, K., Rogers, D.B.: *J. Solid State Chem.* **13**, 231 (1975)
67. Karthik, R., Kumar, J.V., Chen, S.M., Kokulnathan, T., Yang, H.Y., Muthuraj, V.: *ACS Sustain. Chem. Eng.* **6**, 8615 (2018)
68. Chandrasekaran, S., Arumugam, E., Karuppiiah, C., Karuppaiah, S., Haidyrah, A.S., Chandran, B., Yang, C.C.: *Mater. Lett.* **300**, 130274 (2021)
69. Niu, X., Zhang, P., Hang, Y., Zhu, S., Yang, Q., Yin, H., Li, Z., Chen, Z.: *Infrared Phys. Technol.* **121**, 104010 (2022)
70. Loiko, P., Pavlyuk, A., Slimi, S., Solé, R.M., ben Salem, E., Dunina, E., Kornienko, A., Camy, P., Griebner, U., Petrov, V., Díaz, F., Aguiló, M., Mateos, X.: *J. Luminesc.* **231**, 117793 (2021)
71. Czajka, J., Piskula, Z., Szczeszak, A., Lis, S.: *Opt. Mater.* **84**, 422 (2018)
72. Najafvandezh, N., López-Moreno, S., Errandonea, D., Pavone, P., Draxl, C.: *Mater. Today Commun.* **24**, 101089 (2020)
73. Eerenstein, W., Mathur, N.D., Scott, J.F.: *Nature* **442**, 759 (2006)
74. Wiegmann, H., Ponomarev, B.K., van Tol, J., Jansen, A.G.M., Wyder, P., Red'kin, B.S.: *Ferroelectrics* **183**, 195 (2011)
75. Li, C., Chen, G., Sun, J., Rao, J., Han, Z., Hu, Y., Zhou, Y.: *ACS Appl. Mater. Interf.* **7**, 25716 (2015)

76. Ratova, M., West, G.T., Kelly, P.J.: *Vacuum* **115**, 66 (2015)
77. Kaczmarek, A.M., van Deun, R.: *Chem. Soc. Rev.* **42**, 8835 (2013)
78. Nagornaya, L.L., Danevich, F.A., Dubovik, A.M., Grinyov, B.V., Henry, S., Kapustyanyk, V., Kraus, H., Poda, D.V., Kudovbenko, V.M., Mikhailik, V.B., Panasyuk, M., Polischuk, .G., Rudyk, V., Tsybul'skiy, V., Tupitsyna, I.A., Vostretsov, Y.Y.: *IEEE Trans. Nucl. Sci.* **56**, 2513 (2009)
79. Dahlke, E.E., Olson, R.M., Leverenz, H.R., Truhlar, D.G.: *J. Phys. Chem. A* **112**, 3976 (2008)
80. Demichelis, R., Civalleri, B., Ferrabone, M., Dovesi, R.: *Int. J. Quantum Chem.* **110**, 406 (2010)
81. Zhao, Y., Pu, J., Lynch, B.J., Truhlar, D.G.: *Phys. Chem. Chem. Phys.* **6**, 673 (2004)
82. Jacquemin, D., Femenias, A., Chermette, H., Ciofini, I., Adamo, C., André, J.M., Perpète, E.A.: *J. Phys. Chem. A* **110**, 5952 (2006)
83. Babu, V.J., Vempati, S., Uyar, T., Ramakrishna, S.: *Phys. Chem. Chem. Phys.* **17**, 2960 (2015)
84. Becke, A.D.: *J. Chem. Phys.* **104**, 1040 (1998)
85. Becke, A.D.: *Phys. Rev. A* **38**, 3098 (1988)
86. Bilk, D.I., Orlando, R., Shaltaf, R., Rignanese, G.M., Íñiguez, J., Ghosez, P.: *Phys. Rev. B Condens. Matter Mater. Phys.* **77**, 165107 (2008)
87. Adamo, C., Barone, V.: *J. Chem. Phys.* **110**, 6158 (1999)
88. Krukau, A.V., Vydrov, O.A., Izmaylov, A.F., Scuseria, G.E.: *J. Chem. Phys.* **125**, 224106 (2006)
89. Perdew, J.P., Burke, K., Ernzerhof, M.: *Phys. Rev. Lett.* **77**, 3865 (1996)
90. Grimme, S.: *J. Comput. Chem.* **27**, 1787 (2006)
91. Kaurova, I.A., Kuz'micheva, G.M., Brykovskiy, A.A., Rybakov, V.B., Gorobets, Y.N., Shekhovtsov, A.N., Cousson, A.: *Mater. Des.* **97**, 56 (2016)
92. Saraf, R., Shivakumara, C., Behera, S., Nagabhushana, H., Dhananjaya, N.: *Spectrochim. Acta Part A Mol. Biomol. Spectrosc.* **136**, 348 (2015)
93. Azad, A.K., Eriksson, S.G., Ivanov, S.A., Mathieu, R., Svedlindh, P., Eriksen, J., Rundlöf, H.: *J. Alloy. Compd.* **364**, 77 (2004)
94. Bi, J., Wu, L., Zhang, Y., Li, Z., Li, J., Fu, X.: *Appl. Catal. B* **91**, 135 (2009)
95. Culver, S.P., Greaney, M.J., Tinoco, A., Brutchey, R.L.: *Dalton Trans.* **44**, 15042 (2015)
96. Lacomba-Perales, R., Ruiz-Fuertes, J., Errandonea, D., Martínez-García, D., Segura, A.: *Europhys. Lett.* **83**, 37002 (2008)
97. Hoppe, R.: *Zeitschrift Für Kristallographie. Crystal. Mater.* **150**, 23 (1979)
98. Hoppe, R., Voigt, S., Glaum, H., Kissel, J., Müller, H.P., Bernet, K.: *J. Less Common Metals* **156**, 105 (1989)
99. Laranjeira, J.A.S., Fabris, G.S.L., Ferrer, M.M., Albuquerque, A.R., Sambrano, J.R.: *Cryst. Growth Des.* **20**, 4600 (2020)

# Unraveling the Surface Chemistry of the Heterogeneous Catalytic Decomposition of O<sub>3</sub> for Selectivity Concerning O<sub>2</sub> or HO<sup>•</sup> Formation



Raciel Jaimes López, Daniela Palomares Reyna, and Jorge Vazquez-Arenas

**Abstract** Nowadays, the O<sub>3</sub> decomposition on heterogeneous catalysts is highly relevant for atmospheric applications where oxygen is typically formed, and wastewater treatment where the interest is to form hydroxyl radicals (advanced oxidation processes). Although both reaction mechanisms appear not to share a relationship, the surface chemistry and phenomena arising on the catalysts seem to indicate the opposite. Here, experimental and theoretical studies proposed in the literature are revisited to determine these characteristics influencing the catalytic O<sub>3</sub> decomposition on different materials. It is systematically found that strong Lewis sites via a chemisorption process induces oxygen formation, while physisorption involving weak Lewis sites on surface hydroxyl groups decomposes ozone into hydroxyl radicals. Oxygen vacancies could act as active sites in both cases, and the point-of-zero-charge (PZC) is crucial to preserve surface hydroxyl groups at positive pH values slightly above PZC. The regeneration of active sites depends on the multi-valent oxidation state of the surface metal. Thus, the acid character of the catalyst (Lewis), the adsorption energy of O<sub>3</sub>, HO<sup>•</sup> and other oxygenated surface groups, and the charge transfer rate of the metallic redox atoms on the surface can be regarded as molecular descriptors for the design of novel catalysts for either atmospheric or wastewater treatment applications.

**Keywords** Ozone · Hydroxyl radicals · Oxygen · Advanced oxidation process · Atmospheric · Heterogeneous catalysis · Surface activity

---

R. J. López

Escuela Superior de Ingeniería Química e Industrias Extractivas, Instituto Politécnico Nacional, Av. Luis Enrique Erro s/n, Col. Nueva Industrial Vallejo, Ciudad de México 07738, México

D. P. Reyna · J. Vazquez-Arenas (✉)

Centro Mexicano para la Producción más Limpia, Instituto Politécnico Nacional, Av. Acueducto s/n, Col. La Laguna Ticomán, 07340 Ciudad de México, Mexico

e-mail: [jgvazquez@ipn.mx](mailto:jgvazquez@ipn.mx); [jorge\\_gva@hotmail.com](mailto:jorge_gva@hotmail.com)

## 1 Introduction

The elevated pollution of recalcitrant organic compounds (poor degradation due to stability) including pharmaceutical compounds, pesticides, and dyes in topwater reservoirs and groundwater is a major concern worldwide, due to bioaccumulation resulting in numerous diseases for human beings. To tackle this complex problem, diverse advanced oxidation processes have been envisaged, where ozone ( $O_3$ ) has stood out due to its high oxidation potential (2.08 V vs. SHE), and its ease of implementation at the industrial level. However,  $O_3$  is not able to completely mineralize (i.e. transformation into  $CO_2$  and  $H_2O$ ) the recalcitrant organic compounds in many cases, whence its decomposition into ozone has been envisaged to promote the formation of hydroxyl radicals ( $HO^\bullet$ ) in water, which exhibit considerably higher oxidation potentials. On the other hand, the  $O_3$  catalytic decomposition into  $O_2$  is crucial since this gas is very toxic under atmospheric conditions (e.g. laser printers, office photocopiers, sterilizers, and aircraft cabins). Although ozone is valuable in the upper region of the atmosphere because it absorbs harmful ultraviolet radiation [1], it is quite aggressive on the earth's surface because it can cause respiratory diseases, and accentuate the photochemical smog formed between volatile organic compounds and nitrogen oxides [2, 3]. In the range of 0.1–1 ppm, ozone can cause damage to the mucous membranes, irritability in the throat, and headaches [4]. The regulations regarding the permissible limits for exposure during 8 h is 0.1 ppm. Therefore, the problem of  $O_3$  decomposition using catalysis is of technological interest due to its effects on human health.

Catalytic ozonation is divided into homogeneous catalytic ozonation, where metals in the same phase (e.g. ions) are used to promote the reactions, and heterogeneous where solid catalysts of metals, alloys, carbons, zeolites, and oxides are used to accelerate the  $O_3$  decomposition, regardless of the application. To date, heterogeneous catalysis has been preferred because it generates greater stability during radical or oxygen productions, in addition to the fact that the catalyst can be reused without further treatment. There are not many systematic studies conducted to account for the  $O_3$  decomposition on heterogeneous catalysts, where metal oxides ( $Au_2O$ ,  $Fe_2O_3$ ,  $Ni_2O_3$ ,  $AgO$ ,  $Ag_2O$ ,  $CuO$ ,  $Cu_2O$ ) have been found to be more active than metals, based on equal weights [5]. Comparing each unsupported oxide material using equal volume, but without controlling the surface area ( $0.8\text{--}160\text{ m}^2\text{ g}^{-1}$ ), the following order of activity was proposed [6]:  $Ag_2O > NiO > Fe_2O_3 > Co_3O_4 > CeO_2 > Mn_2O_3 > CuO > Pb_2O_3 > Bi_2O_3 > SnO_2 > MoO_3 > V_2O_5 > SiO_2$ . However, the surface factors and phenomena influencing the  $O_3$  decomposition on heterogeneous catalysts have not been comprehensively discussed, to design novel synthesis methods with controlled surface properties for the enhancement of this mechanism for wastewater and atmospheric applications. Specifically, it has not been possible to conclude which surface properties are overriding to determine whether a catalyst will form  $HO^\bullet$  or  $O_2$ , although this is implicitly within the complex mechanism proposed for the decomposition of this gas, based on the stages of initiation, propagation, and termination [7–10], but relevant underlying chemistry causing this mechanistic difference

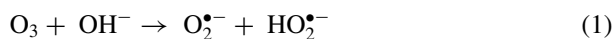
has not been evidenced. Under this idea, the present review critically exposes the experimental and theoretical state of the art of how the surface chemistry and properties of the catalyst affect the divergence of O<sub>3</sub> decomposition into either hydroxyl radicals or oxygen, within the context of the heterogeneous catalytic ozonation. Firstly, the homogeneous reaction mechanism of O<sub>3</sub> decomposition most accepted in the literature is revisited to establish a comparative baseline against reactions arising on heterogeneous catalysts. The surface properties (experiment and theory) promoting the heterogeneous mechanism are then reviewed depending on the catalyst composition, to draw conclusions about the most influential factors affecting this mechanism. It is worthwhile mentioning that textural properties like geometric and surface area, pore size and volume, pore distribution, among others; along with transport phenomena are particularly relevant to enhance O<sub>3</sub> decomposition on heterogeneous catalysts. However, they are herein not regarded since experimental data in the literature is completely varied, and most studies do not report this information.

## 2 Reaction Mechanism of O<sub>3</sub> Decomposition

General, physical and thermodynamic properties of O<sub>3</sub>, as well as its general chemistry, have been formerly discussed [11]. It is known that O<sub>3</sub> can oxidize different chemical species in solution via the direct or indirect homogeneous mechanism. The indirect reactions are of interest since it includes a diversity of interesting species, according to the following stages [7–10]:

### *Initiation step*

Ozone and hydroxide ions react to produce the superoxide anion radical (O<sub>2</sub><sup>•-</sup>) and hydroperoxyl radical (HO<sub>2</sub><sup>•</sup>).

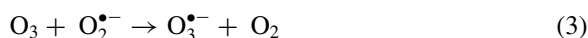


HO<sub>2</sub><sup>•</sup> dissociates to form O<sub>2</sub><sup>•-</sup> and H<sup>+</sup>



### *Radical chain*

O<sub>3</sub> can react with O<sub>2</sub><sup>•-</sup> formed in reactions (1) and (2), to yield ozonide anion radical (O<sub>3</sub><sup>•-</sup>) in one step, followed by the HO<sub>3</sub><sup>•</sup> production which is the predecessor of hydroxyl radicals, as follows:





The end of the reaction produces  $\text{HO}_2^\bullet$  to start again from reaction (1). Chemical species converting  $\text{HO}^\bullet$  into superoxide radicals perform as chain carriers (i.e. promoters). The  $\text{O}_3$  consumption is initiated when the pH is risen in solution resulting in a chain reaction mechanism generating non-selective  $\text{HO}^\bullet$ . Although these radicals are very reactive, since they oxidize the region with the highest electron density of the objective species, they display a very short half-life ( $<10 \mu\text{s}$ ) in concentrations below  $10^{-4} \text{ M}$ .  $\text{O}_2$  is formed on reaction (3) after the formation of some radical intermediate species, before the hydroxyl radical, which could connect these mechanisms to some extent.

#### *Termination*

This stage arises when chemical species react with the hydroxyl radical to yield secondary radicals which do not generate  $\text{HO}_2^\bullet/\text{O}_2^{\bullet-}$ . These scavengers end up in a chain reaction.



Many species can initiate, promote or terminate the chain reaction.

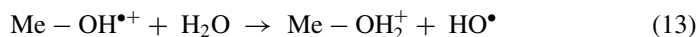
### **3 O<sub>3</sub> Decomposition on Metal Oxides/Hydroxides**

The metal atom of the oxides/hydroxides are assumed as Lewis acidic sites, but when in contact with water molecules of the solvent, they act as Lewis bases, generating surface hydroxyl groups. The predominant charge on the surface hydroxyl groups will depend on the acidity of the interface. Basicity greater than the  $\text{pH}_{\text{PZC}}$  of the oxide will generate an anionic surface charge. In general,  $\text{O}_3$  will react with the surface  $-\text{OH}^-$  to form  $\text{HO}^\bullet$ .

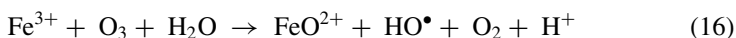
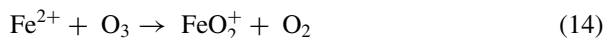
Some catalysts present evidence of their catalytic activity, independent of the presence of  $\text{O}_3$ , as for  $\text{TiO}_2$ .  $\text{TiO}_2$  promotes the decomposition of  $\text{O}_3$  in acidic conditions, while in pH neutral conditions acts as an inhibitor. However, there is evidence

that the effect of the catalyst is due to the direct adsorption of the organic compound on the active sites, and not to the  $O_3$  decomposition [12]. In addition, the surface OH groups are involved in the degradation; which mostly depends on the vacancies arising to a greater extent, in the rutile-type structure.

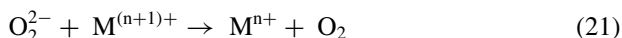
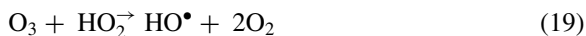
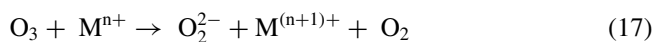
In iron oxide systems, the pH determines the charging properties of the surface hydroxyl species [13].



Therefore, these groups represent the preferred catalytic adsorption sites in FeOOH. In the case of  $Fe_2O_3$ , the oxidation-reduction cycles of the  $Fe^{2+}/Fe^{3+}$  pair are responsible for the generation of  $HO^\bullet$  from  $O_3$  [14].



Liu et al. compared the performance of various types of ferrites. The activity trend found was  $CuFe_2O_4 > NiFe_2O_4 > CoFe_2O_4 > ZnFe_2O_4$  [15]. The proposed mechanism incorporates changes in the oxidation state of the metal site caused by the transfer of electrons to  $O_3$ .



The authors explain the difference in the performance of the oxides based on their mesoporous characteristics, which behave as gels or small granules that are limited



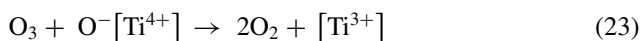
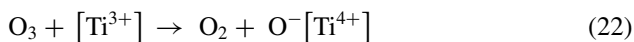
to enter the nanometric pores at high concentrations of organic species, where  $O_3$  reacts with surface hydroxyl groups to generate short-lived  $HO^\bullet$ .

Zhang et al. evaluated the same group of ferrites, where the activity adopted the following order:  $CoFe_2O_4 > NiFe_2O_4 > CuFe_2O_4 > ZnFe_2O_4$  [16]. This behavior was attributed to changes in the oxidation state of the metallic surface as well as the density of surface hydroxyl groups present. Both processes perform at the same time, without being able to deduct the mechanism. The authors proposed the  $HO_3^\bullet$  generation as an intermediate based on the literature, to subsequently generate  $HO^\bullet$ . In this direction, an electron from metal A of  $AFe_2O_3$  can be transferred to  $O_3$  to generate  $O_3^{\bullet-}$  and trivalent A. The  $O_3^{\bullet-}$  reacts with the  $H^+$  to produce  $HO_3^\bullet$  and again  $HO^\bullet$ . The trivalent metal A is reduced by the O of the lattice.

Bulanin and colleagues examined the molecular ozone adsorption on dehydrated oxides using FT-IR spectroscopy at low temperatures (77 K) describing that  $O_3$  retains basic properties [17], generating at least four ways of  $O_3$  adsorption with Lewis acid sites of different strength: physical adsorption; weak hydrogen bonds with surface OH groups; molecular adsorption via coordinative bonding to weak Lewis sites as in  $ZrO_2$ ,  $MgO$  and  $CeO_2$ ; and  $O_3$  dissociation (no molecular adsorption) on strong Lewis sites of  $TiO_2$ ,  $Al_2O_3$  and  $ZnO$  produces a free  $O_2$  molecule and a surface oxygen atom attached to the catalytic surface. These results suggest that depending on the strength of the catalytic surface,  $O_3$  could dissociate rapidly into  $O_2$  as required for atmospheric applications ( $O_3$  chemisorption), or forming  $HO^\bullet$  radicals required for wastewater treatment ( $O_3$  physisorption).

Dhandapani and Oyama reviewed patent literature concerning the composition, preparation, and performance of catalysts promoting  $O_3$  decomposition, suggesting that monoliths can be used to enhance contact between  $O_3$  and catalyst without excessive pressure drop at high flow rates [4]. Conductivity measurements conducted with several metal oxides in the range of  $10^3$ – $10^5 \Omega$  cm resistivity showed the following activity order for the decomposition reaction:  $MnO_2 > Co_3O_4 > NiO > Fe_2O_3 > Ag_2O > Cr_2O_3 > CeO_2 > V_2O_5 > CuO > MoO_3$ , where the first four oxides (along with  $CeO_2$ ) are p-type oxides, while the rest in the last positions of activity towards  $O_3$  decomposition are n-type oxides. These results suggest that p-type semiconductor oxides are required to spur the catalytic decomposition, being consistent with the productions of  $O_2^-$  and  $O_2^{2-}$  species during  $O_3$  decay.

Ding and colleagues revealed that the gaseous  $O_3$  decomposition under high relative humidity without light irradiation was remarkably enhanced from 4.8% on anatase  $TiO_2$  to 100% on aluminum reduced anatase since this last catalyst possesses the most evenly distributed particle size, and mainly largest content of  $Ti^{3+}/Ti^{4+}$  (i.e. several oxidation states) couples and oxygen vacancies ( $V_O$ ), as described in the following mechanism [18]:





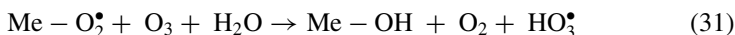
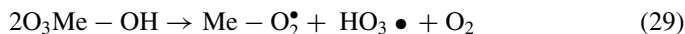
Psaltou et al. examined 18 solid phases categorized in metal oxides/hydroxides, minerals, and carbons to determine the role of Point-of-Zero (PZC) charge and wettability towards the  $\text{O}_3$  decomposition into  $\text{HO}^\bullet$  radicals [19]. They found that neutrally to slight positive hydrophilic surfaces enhance this reaction, although the adsorption capacity is not correlated to the catalytic activity of the materials. Silica alumina, alumina 504, alumina-507,  $\text{SiO}_2$ , Bayoxide, zeolite, calcite, and dolomite presented the best performance to decompose ozone into radicals since these catalysts are neutrally charged with moderate/high wettability around the typical pH value (7) of wastewater treatment plants, thus, no additional pH adjustment is required to increase the oxidation capacity of the  $\text{O}_3$  system.

Ernst et al. evaluated batch experiments on catalytic ozonation in buffered and unbuffered solutions of refractory organic compounds (oxalic, acetic, salicylic, and succinic acids) [20], where the adsorption of the organic model on the catalyst surface is not mandatory for effective oxidation, in fact, this adsorption seems to inhibit the catalytic effect. The reaction mechanism consists of  $\text{O}_3$  adsorption on the catalyst surface, followed by its rapid decomposition due to the presence of hydroxyl surface groups on  $\text{Al}_2\text{O}_3$ , to produce  $\text{O}_2\text{H}$  radicals directly or indirectly.  $\text{O}_2\text{H}$  reacts with another  $\text{O}_3$  molecule to produce  $\text{O}_3^-$  radical, which finally decomposes into  $\text{O}_2$  and  $\text{HO}^\bullet$ . The above mechanism highlights that the oxidation capacity relies on the  $\text{O}_3$  and OH surface groups interaction on the  $\text{Al}_2\text{O}_3$  catalyst.

Other investigations related to aluminum hydroxide/oxide have also attempted to reveal the mechanism of catalytic ozonation for the degradation of taste and odor. Fei et al. revealed that catalytic ozonation in the presence of several aluminum catalysts can substantially promote 2,4,6-trichloroaniline removal compared with the single ozonation [21], according to the following order of activity:  $\gamma\text{-AlOOH} > \gamma\text{-Al}_2\text{O}_3 > \alpha\text{-Al}_2\text{O}_3$ .  $\text{HO}^\bullet$  was found as responsible for the organic elimination, where the charge and density of surface hydroxyl groups influenced the catalytic activity of the materials.

Further experiments were carried out to investigate the relationship between the density of surface hydroxyl groups of aluminum hydroxides/oxides and the concentration of  $\text{HO}^\bullet$  radicals produced from ozone decomposition. Minghao et al. investigated the catalytic activity of  $\text{FeOOH}$  on ozonation of oxalic acid [22], indicating the generation of hydroxyl radicals at acidic and neutral pH conditions, according to the following mechanism:





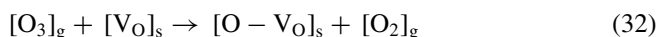
The hydroxyl groups both in a neutral state (Me-OH) and positive charge state (Me-OH<sup>2+</sup>) can perform as the active sites for ozone decomposition into hydroxyl radicals.

The catalytic activity of the metal hydroxides catalyst depends on whether the coexisting Lewis bases are stronger or weaker than ozone, since this oxidizing agent (Lewis base) should be adsorbed and react with the hydroxyl groups on the surface of the catalyst, treated as Bronsted acid.

Lei et al. evaluated that the use of Cu-cordierite in heterogeneous catalytic ozonation considerably promotes the nitrobenzene degradation and mineralization in aqueous solution, compared to sole ozonation [23]. The nitrobenzene adsorption was too small to make a significant contribution to the contaminant elimination during the catalytic ozonation. It was proposed that the catalytic surfaces of metal oxides were covered with hydroxyl groups, due to the chemisorption of dissociative water molecules on the surface ions, when introducing the Cu-cordierite into the aqueous solution. Subsequently, O<sub>3</sub> can react with the surface hydroxyl groups, initiating the HO<sup>•</sup> production on the surface.

The contributions of molecular ozone (39.22%), hydroxyl radicals (45.20%), and surface adsorption (15.57%) were examined during bezafibrate degradation using cobalt-loaded red mud, and tertiary butanol as an organic quencher, confirming the role of this catalyst to form hydroxyl radical reaction [24]. Surface cobalt load developed mesopores, which increased the specific surface area. Co<sub>3</sub>O<sub>4</sub> growing over the mesopore surface contributed to the active functional groups of Co-O-, which was identified as one of the surface catalytic reaction sites.

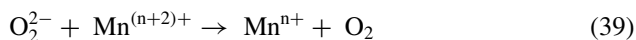
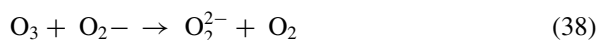
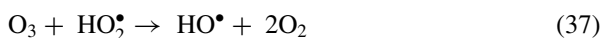
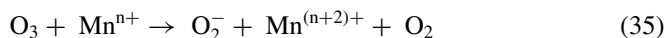
Yang Liu et al. synthesized stable MnO<sub>2</sub> surface for O<sub>3</sub> decomposition under humid conditions [25], disclosing that the combination of a high concentration of active oxygen vacancies and Lewis acid sites generates a weak interaction with water molecules defining the high activity to transform ozone along with the facile recovery of the occupied oxygen vacancies ([V<sub>O</sub>]<sub>s</sub>: active sites for ozone decomposition), according to the following mechanism:



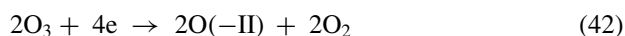
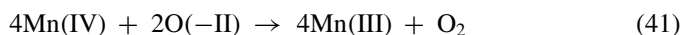
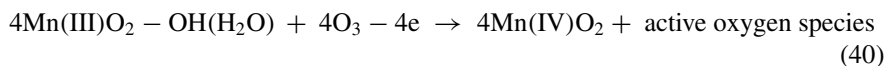


Additionally, these authors connect the weak strength of water adsorption on the catalyst surface (i.e. S-300) with the weakening of the poisoning effect of water during humid decomposition.

The catalytic activity of mesoporous materials on manganese oxide on nitrobenzene ozonation was evaluated by Minghao et al. [26]. The following possible reaction mechanism was proposed ascribing the  $\text{O}_3$  decomposition into  $\text{HO}^\bullet$  to the electron transfer between the catalyst and ozone:



Hui Zhao et al. confirmed by XPS analysis, that the oxidation of Mn(III) to Mn(IV) promotes ozone decomposition, and the oxidation of lattice oxygen reverses the manganese state [27]. An  $\alpha\text{-MnO}_2$  nanotube was used as a catalyst for phenol degradation, identifying the balance of Mn(III)/Mn(IV) vs O(-II)/O(0) as the primary factor influencing the performance.



Lewis acid sites were also confirmed as reaction centers for catalytic ozonation, but the authors were unable to associate the presence of  $\text{HO}^\bullet$  species,  $\text{O}_2^{\bullet-}$ ,  $^\bullet\text{O}_2$ , or  $^\bullet\text{O}$  as responsible for the degradation.

Not only the type of transition metal but also the crystal structure of the oxides influences the catalytic response. To this concern, the type of manganese catalyst ( $\text{MnO}_2$ ,  $\text{Mn}_2\text{O}_3$ , and  $\text{Mn}_3\text{O}_4$ ) presented different catalytic performances in wastewater [28], associated with its higher surface hydroxyl groups, higher electron transfer ability, surface area, or oxygen vacancy.  $\text{MnO}_2$  was found to be more active than others. For phenol, chlorophenol, and cresol eliminations,  $^\bullet\text{O}_2^-$  by a nucleophilic

attack, and  $^1\text{O}_2$  and  $\text{O}_3$  by an electrophilic attack in bulk solution were mainly responsible for the oxidation process. The crystal phase of  $\text{MnO}_2$  was also subjected to analysis by Nawaz et al. [29]. Among phases  $\alpha$ ,  $\beta$ ,  $\delta$ ,  $\gamma$ ,  $\lambda$ , and  $\epsilon$ , phase  $\alpha$  was the most active for the degradation of 4-nitrophenol. It exhibited a lower average oxidation state and stronger oxidation-reduction peaks in voltammetry characterization, which was connected with a higher  $\text{O}_3$  decomposition. The greatest contribution identified for the degradation was in the solvent bulk by  $\text{O}_3$ ,  $\text{O}_2^{\bullet-}$  and  $\text{O}^\bullet$  species.

## 4 $\text{O}_3$ Decomposition on Carbon-Based Materials

Rivera-Utrilla and Sanchez-Polo evaluated the ozonation process using different commercial activated carbons (Ceca AC40, Norit, Merck, Witco, Ceca GAC, Filtrasorb 400, Sorbo) displaying dissimilar physicochemical surface properties [30]. Sorbo, Ceca GAC, and Norit carbons exhibit the greatest  $\text{O}_3$  decomposition due to the largest contents of basal plane electrons and oxygenated surface groups of basic nature (chromene and pyrone). These former basic sites are located at  $\pi$  electron-rich regions within the basal planes of carbon, acting as catalytic centers (Lewis base) to reduce ozone molecules to  $\text{OH}^-$  or  $\text{H}_2\text{O}_2$ , which are precursors of highly oxidative radicals. A large macroporosity in carbon favors the  $\text{O}_3$  entry to the surface active centers, also promoting its decomposition.

Super-fine powdered activated carbon has been proposed and investigated as a novel catalyst for the catalytic ozonation of oxalate by Tianyi et al. [31], revealing that surface reaction was significant occurring according to the Langmuir-Hinshelwood mechanism. The following reactions may describe the pathway of the super-fine powdered activated carbon catalyzed ozonation process:



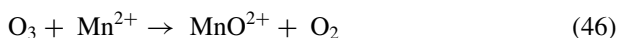
Adsorption of organics (R):



Reaction between adsorbed species:



The surface basicity character along with the type of metallic surface concentration remarkably affects the capacity to transform  $\text{O}_3$  into  $^\bullet\text{OH}$  radicals, since Sanchez-Polo et al. revealed that only metals undergoing  $\text{O}_3$  oxidation are effective [32]. To this concern, surface oxidation of Mn(II)-doped carbon aerogels into Mn(III) and Mn(IV) leads to the following mechanism:



Co(II) and Ti(IV)-doped carbon aerogels displayed no activity whatsoever in this mechanisms. The increase of ozonation cycles promotes the Mn(II) surface oxidation to larger oxidation states, resulting in a catalyst inactivation due to the formation of surface oxygenated species (i.e.  $-\text{C}=\text{O}$ ). In this direction, the  $\text{O}_2$  reduction concentration (rising surface basicity) generates an increase in the surface electronic density, whence the rate of the mechanism is described by reactions (46–48). Thermal activation treatment of aerogels with significant acid surface character ( $\text{pH}_{\text{PZC}} \approx 3\text{--}4$ ) and high surface concentrations ( $\sim 20\%$ ), produces a significant rise in surface basicity because of the removal of surface oxygenated functional groups.

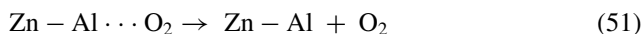
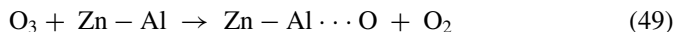
Other strategies such as carbon doping have been studied. Zhiqiang et al. performed a synergetic mechanism of  $\text{HO}^\bullet$  formation and an intra-electron-transfer nonradical reaction in the catalytic ozonation of ketoprofen with the in situ N-doped hollow sphere carbon (NHC) [33]. The high graphitization degree ( $\text{ID}/\text{IG} = 0.78 - 0.88$ ) and low unsaturated oxygen content (0.10–1.38%) of NHC highlighted the dominant role of N-heteroatoms in the  $\text{O}_3/\text{NHC}$  system. The graphitic N forming in the bulk of the graphitic structure served as the “electron-mobility” region to promote ketoprofen degradation with the transfer of electrons from the ketoprofen molecule to  $\text{O}_3$  via a nonradical reaction process. The pyrrolic and pyridinic N located at defects of the graphitic structure acted as the “radical-generation” region to decompose  $\text{O}_3$  into  $^\bullet\text{OH}$  for degrading ketoprofen by a radical oxidation process. This finding provided a brand new insight into engineering N-doped carbonaceous catalysts precisely in the catalytic ozonation process for the efficient treatment of organic-contaminated water.

## 5 $\text{O}_3$ Decomposition on Zeolites

Valdes et al. analyzed the influence of compensating cation content upon the ozone removal using a Chilean natural zeolite (53% clinoptilolite, 40% mordenite, and 7% quartz), concluding that the elimination of zeolite compensating cation content promotes ozone diffusion within the zeolite structure to enhance the  $\text{O}_3$  reduction on its surface active sites [34]. This reaction occurs depending on the adsorption strength on the zeolite surface: ozone adsorption on weak Lewis acid sites or ozone decomposition forming  $\text{O}^\bullet$  and  $\text{O}_2$  on strong Lewis acid sites. The proposal relies on the fact that  $\text{O}_3$  is a Lewis base due to its resonance structure, where one of the oxygen atoms possesses high electron density and consequently affinity to Lewis acid sites on the material.

Ikhlaq et al. analyzed the catalytic ozonation of coumarin on  $\gamma$ -alumina and ZSM-5 zeolites in an aqueous solution to distinguish between radical and non-radical mechanisms [35]. Although both materials eliminated coumarin from the solution, alumina is more active than the zeolite due to the catalytic formation of hydroxyl radicals, displaying the greatest activity around the point of zero charge (pH) where surface hydroxyl species transform  $O_3$  into  $HO^\bullet$  radicals. On the other hand, zeolites generate a direct reaction between adsorbed ozone and adsorbed coumarin (a simple adsorption mechanism), without promoting hydroxyl radical generation.

Brodu et al. examined synthetic ZSM-5 zeolites with different Si/Al<sub>2</sub> ratios and similar specific surface areas and microporous volumes to account for chemical properties defining interactions between these materials and ozone [36]. The total amount of removed  $O_3$  was directly proportional to the total concentration of Lewis acid sites, where two types of Lewis sites were identified:  $O_3$  decay on strong Lewis acid sites and adsorption on mild Lewis acid sites. DRIFT experiments exposed adsorbed peroxide and atomic oxygen species on ZSM-5 zeolites, whereby the ozone interaction with Lewis acid surface sites yields:



## 6 Modelling Studies of $O_3$ Decomposition

Quantum chemistry study methods are ideal to complement the investigation of experimentally proposed mechanisms for surface chemical reactions. Consequently, the literature abounds in density functional theory methods due to their reliability and computational cost, applied both in periodic systems (plane-wave basis-set) and clusters (atomic-center orbitals). In the former, the most popular exchange and correlation functionals are PBE (Perdew–Burke–Ernzerhof) and LDA (Local-density approximations). In cluster modeling, the workhorse continues to be the parameterized B3LYP (Becke, 3-parameter, Lee–Yang–Parr). These simulations are sometimes accompanied by calculations of transition states, reactivity index, and Van der Waals interactions.

Modeling homogeneous catalysis, namely, the reaction of oxygenated species with organic agents is a common practice in the literature. These activities allow obtaining a theoretical foundation of the degradation mechanism of the contaminant as a function of the experimentally observed reaction time. These have made it possible to describe synergistic effects of the chemical environment on the reactivity of  $O_3$  [37], sites of attack by radicals [38], and reaction pathways [39–41]. These

simulations have confirmed the proposed mechanisms based on the chemical intuition of the different oxygenated species, nucleophilic, electrophilic, and radical reactions on specific atoms.

Yu et al. described conclusions drawn from the modeling strategy of these surface reactions via DFT calculations [42]. In their opinion, these studies have not only been able to explain the experimental observations but have also served as a guide to developing new catalysts. In the case of heterogeneous catalysis, they mention: (a) Defects in graphene structures serve as catalytic sites to decompose  $O_3$ . (b) Sites with high valence electron density, or sites with very negative or very positive electrostatic potential lead to redox reactions that are converted into active sites. (c) Mn-doped g-C<sub>3</sub>N<sub>4</sub> has been proposed as a suitable catalyst by DFT methods. (d) The active sites of organic agents in homogeneous phase reactions with the  $O_3$  and  $HO^\bullet$  species have been studied. (e) Consider that DFT is a promising approach, as long as key steps in the  $O_3$  decomposition are undertaken in the future.

Zhang et al. used  $O_3$ - $H_2O_2$  on  $TiO_2$  to remove NO from flue gases [43], where a remarkable increase in the conversion efficiency was achieved by doping with S. Simulations via DFT showed that the presence of S modifies the surface chemical environment, improving the adsorption by hydrogen bonds of -OOH on Ti5c and bridging oxygens. In addition, the Lewis acidity is increased, improving the adsorption of NO and its conversion. The proposed mechanism consists of the adsorption of  $H_2O_2$  on the  $TiO_2$  surface. The formation of Ti-OOH is favored by sulfur doping. This surface termination reacts by transferring electrons to  $O_3$  to form the species  $HO_2^\bullet$  and  $O_3^\bullet$  which in turn, due to the acidic environment, form  $HO^\bullet$  and  $O_2^{\bullet-}$  among other radicals. It should be noted that the authors only modeled by DFT the effects of doping on the adsorption of  $H_2O_2$ , without continuing with the interaction with  $O_3$ .

Using plane-wave DFT calculations, Zhang et al. calculated that the NiO(100) surface is capable of transferring electrons to the  $O_3$  molecule in the adsorption process, because the calculated HOMO on the surface is shifted to very positive energy values [44]. The geometry relaxation produces the decomposition into an  $O_2$  molecule and adsorbed  $O^\bullet$ . Adsorbed  $O^\bullet$  can react with other  $O_3$  to form  $O_2$  and  $O_2^{\bullet-}$  (superoxide radical ion).  $O^\bullet$  can also react with one molecule of  $H_2O$  to form two  $HO^\bullet$ . These processes are described as exothermic or with very low activation energy. In the experimental part of their work, using EPR, they observed the increase in the generation of  $^\bullet OH$  with the introduction of NiO.

### *Carbon materials*

The use of carbon materials lessens some disadvantages of the use of metals, however, their activity for  $O_3$  decomposition is normally lower. The main disadvantage they present is the presence of radical trapping sites, which leads to the decomposition of ozone without the release of  $HO^\bullet$  [45]. The presence of heteroatoms (N, P, F, etc.) in the graphitic structures generate three forms of active sites for ozone: free electrons, free electron pairs, and delocalized electrons.

Structure-reactivity relationships have been a difficult goal but addressed by some authors. Yu et al. studied the mechanism of  $O_3$  decomposition to B-, N-, P-, and



Si-doped graphene [46]. Interestingly, the mechanism they found was the same as Zhang et al. for NiO(100). That is,  $O_3$  decomposes generating  $O_{ads}$  and molecular  $O_2$ . These  $O_{ads}$  represent a crucial active site for the process of generating active oxygen species in the presence of ozone. Two plausible mechanisms for  $O_{ads}$  are the formation of adsorbed  $O_2$  and  $O_2^{*-}$  released from ozone or the formation of two  $\cdot OH$  upon reaction with a molecule of water. The type of species depends on the chemical environment and the authors studied 20 possible descriptors to determine structure-reactivity relationships. One of them, the condensed dual descriptor, showed a large linear correlation with the activation energy of  $O_3$  decomposition.

Using plane-wave DFT methods, Zhang et al. studied the reactivity of different functional groups on graphitic carbon nitrides [47]. Lee et al. obtained a similar result for the physisorption of  $O_3$  in the basal plane of graphene, with an adsorption energy of 0.25 eV [48]. However, they analyzed the dissociative chemisorption of this species, to form an epoxy group in the basal plane, calculating an activation energy of 0.72 eV and an adsorption energy of 0.33. These results imply that the proposed mechanism is also viable on graphene. In addition to graphene, the conclusions can be extrapolated to graphite carbon materials in general. The formation of the epoxide groups was indirectly confirmed experimentally, forming a monolayer of  $Al_2O_3$  with an XPS signal of an epoxy group, on HOPG via atomic layer deposition. This monolayer does not form if HOPG is not initially exposed to  $O_3$ .

Zhang et al. used zero-valent boron to attack two common problems in heterogeneous catalytic ozonation, namely the recovery of active sites, and the scavenging of the  $\cdot OH$  generated [45]. The first is minimized by the spontaneous dissolution of  $B_2O_3$ . The second by the mediated valence circulation of counterions. The free 2p orbital of B can effectively receive the free electron pair of  $O_3$ , generating strong adsorption. This in turn forms  $\cdot OH$  and  $O^*$ .  $O_3$  adsorption promotes internal charge transfer in the ZVB, which enables another B-B bond to continue  $O_3$  decomposition.

The most important steps involve the dissociation of  $O_3$  into O, and migration of O on the surface of the  $B^\circ$  particle. Release of O to generate  $\cdot OH$  from water. The authors propose that in this case, in addition to the known reactivity sites, coordinate binding sites are described, in which the presence of ozone activates the B-B bonds via internal electron transfer. Where this activation to form  $\cdot OH$  overcomes the case of the ending  $-OH^-$ .

## 7 Conclusions

Experimental and theoretical studies proposed in the literature have been revisited with the aim of determining those surface properties and factors strongly influencing the catalytic  $O_3$  decomposition on different materials based on metal hydroxides/oxides, carbon-based materials, and zeolites, among others. Table 1 shows a compendium of surface properties and factors consistently reported, in order to reveal the findings described below. Apparently, each characteristic has a contribution to a certain extent, which could not be weighed, since the reviewed studies do not present

**Table 1** Surface properties and factors reported in the literature accounting for O<sub>3</sub> decomposition on heterogeneous catalysts of wastewater and atmospheric applications

Application	Factors influencing O <sub>3</sub> reduction/removal	References
Gas phase ozone decomposition	p-type semiconductor character required to spur O <sub>3</sub> catalytic decomposition into O <sub>2</sub> <sup>-</sup> and O <sub>2</sub> <sup>2-</sup> intermediates	[4]
Removal of clofibrac acid from aqueous solution	Organic adsorption on catalytic sites more plausible than O <sub>3</sub> decomposition	[12]
Oxalic acid ozonation	Charging properties of the surface hydroxyl species influenced by pH	[13]
Atrazine degradation	Oxidation-reduction cycles of Fe <sup>2+</sup> /Fe <sup>3+</sup> pair	[14]
Degradation of shale gas	Changes in the metal oxidation state when reacting with O <sub>3</sub> promotes the formation of O <sup>2-</sup> and HO <sub>2</sub> <sup>•</sup> species	[15]
Oxalic acid ozonation	Variations in the oxidation state of the metallic surface (Fe <sup>2+</sup> /Fe <sup>3+</sup> ) along with the density of surface hydroxyl groups forming O <sub>3</sub> <sup>•-</sup> and HO <sub>3</sub> <sup>•</sup>	[16]
Ozone adsorption on different oxides	O <sub>3</sub> adsorption relies on strength of Lewis acid sites: physical adsorption; weak hydrogen bonds with surface OH groups; molecular adsorption via coordinative bonding to weak Lewis sites as in ZrO <sub>2</sub> , MgO, and CeO <sub>2</sub> ; and O <sub>3</sub> dissociation (no molecular adsorption) on strong Lewis sites of TiO <sub>2</sub> , Al <sub>2</sub> O <sub>3</sub> and ZnO producing O <sub>2</sub>	[17]
Decomposition of gaseous ozone	Multi-valent oxidation states (Ti <sup>3+</sup> /Ti <sup>4+</sup> ) coupled with oxygen vacancies	[18]
p-chlorobenzoic acid degradation in water	Point-of-Zero charge determines affinity between O <sub>3</sub> and catalyst, where neutral to slight positive surface charge improves •OH production	[19]
Eliminations of oxalic, acetic, salicylic, and succinic acids	Oxidation capacity depends on O <sub>3</sub> and OH surface groups' interaction on Al <sub>2</sub> O <sub>3</sub>	[20]
2, 4, 6-trichloroanisole elimination	Charge and density of surface hydroxyl groups	[21]
Oxalic acid destruction	O <sub>3</sub> (Lewis base) decomposition into HO <sup>•</sup> depends on the strength of hydroxyl groups on the catalyst surface acting as Bronsted acid	[22]
Nitrobenzene degradation	Hydroxyl groups on the catalyst surface	[23]

(continued)

**Table 1** (continued)

Application	Factors influencing O <sub>3</sub> reduction/removal	References
Bezafibrate degradation	Active functional groups of Co–O– performing as surface catalytic sites of HO• production	[24]
O <sub>3</sub> decomposition under humid conditions	The combination of a high concentration of active oxygen vacancies (sites for O <sub>3</sub> decomposition) and Lewis acid sites results in a weak interaction with H <sub>2</sub> O. The weak strength of H <sub>2</sub> O adsorption on the catalyst surface avoids catalyst poisoning	[25]
Nitrobenzene ozonation	Multi-valent oxidation states (Mn <sup>n+</sup> /Mn <sup>(n+2)+</sup> )	[26]
Phenol degradation	Balance of Mn(III) to Mn(IV) oxidation and the oxidation of lattice oxygen O(-II)/O(0) which reverses the Mn state. Lewis acid sites are reaction centers for catalytic ozonation	[27]
Phenol oxidation	Higher electron transfer ability and higher amount of oxygen defects or surface hydroxyl groups	[28]
4-nitrophenol	MnO <sub>2</sub> with a low average oxidation state	[29]
1,3,6-naphthalene-trisulfonic acid degradation	oxygenated surface groups of basic nature (chromene and pyrone) acting as catalytic centers (Lewis base) to reduce O <sub>3</sub>	[30]
Oxalate catalytic ozonation	Surface basicity character due to the removal of surface oxygenated functional groups along with the type of metallic surface concentration undergoing O <sub>3</sub> oxidation	[31]
Efficiency of O <sub>3</sub> transformation into HO•	The capacity of metallic surface oxidation. Surface basicity because of removal of the surface oxygenated functional groups	[32]
Gas O <sub>3</sub> decomposition	Ozone (Lewis base) adsorption on weak Lewis acid sites or ozone decomposition forming O• and O <sub>2</sub> on strong Lewis acid sites	[34]
Catalytic ozonation of coumarin	Surface hydroxyl groups (most reactive at pH close to PZC) transform O <sub>3</sub> into HO•	[35]
Gaseous ozone abatement	O <sub>3</sub> removal was proportional to the total concentration of Lewis acid sites. Two types of Lewis sites were identified: O <sub>3</sub> decay on strong Lewis acid sites and adsorption on mild Lewis acid sites	[36]

an equivalent instrumental analysis, in addition to a similar experimental or theoretical methodology. Accordingly, all the characteristics converging towards a high activity of O<sub>3</sub> decomposition are considered. In particular, this reaction apparently requires surface properties depending on the application (atmospheric or wastewater treatment), on the one hand, the gaseous decay of O<sub>3</sub> (Lewis base) towards O<sub>2</sub> requires strong Lewis sites through a chemisorption process, while the formation of HO• in aqueous solution could arise through physisorption involving weak Lewis sites on the surface -OH groups, as occurs in the ozone homogeneous catalytic decomposition in alkaline media. To this concern, the point-of-zero-charge is critical to maintaining surface hydroxyl groups, which can be achieved at positive pH values slightly above PZC. The oxygen vacancies could perform as active sites of both O<sub>3</sub> reaction processes on the catalyst surfaces. The O<sub>3</sub> decomposition requires a redox process for which the multi-valent oxidation state of the surface metal (e.g. Me<sup>2+</sup>/Me<sup>3+</sup>, M<sup>3+</sup>/Me<sup>4+</sup>) is more a requirement for the regeneration of active sites, rather than a factor stimulating O<sub>3</sub> decay activity. In this way, it can be concluded that the acid character of the catalyst (Lewis), as well as the adsorption energy of O<sub>3</sub>, HO•, and other oxygenated surface species, and the charge transfer rate of the metallic redox atoms on the surface can be considered as molecular descriptors for the design of novel catalysts. Indeed, the magnitude of these properties can tune the kinetics of O<sub>3</sub> decomposition into oxygen or radical species, where manganese oxide phases meet most of the aforementioned factors and surface properties.

**Acknowledgements** The authors thank the support from CONACyT “Ciencia Básica y/o Ciencia de Frontera. Modalidad: Paradigmas y Controversias de la Ciencia 2022” grant no. 320252, Ciencia Básica CONACYT 2018 grant no. A1-S-21608 providing a postdoctoral fellowship for RJL, and SIP-IPN 2194 (modules 20221207 and 20221694).

## References

1. Wang, W., Yung, Y., Lacin, A., Mo, T., Hansen, J.: *Science* **194**, 685 (1976)
2. Thompson, A.M.: *Science* **256**, 1157 (1992)
3. Russell, A., Milford, J., Bergin, M., McBride, S., McNair, L., Yang, Y., Stockwell, W., Croes, B.: *Science* **269**, 491 (1995)
4. Dhandapani, B., Oyama, S.T.: *Appl. Catal. B* **11**, 129 (1997)
5. Schwab, G.-M., Hartmann, G.: *Z. Phys. Chem.* **6**, 56 (1956)
6. Imamura, S., Ikebata, M., Ito, T., Ogita, T.: *Ind. Eng. Chem. Res.* **30**, 217 (1991)
7. Hoigne, J.: *Handbook of Ozone Technology and Applications*, vol. 1 (1982)
8. Tomiyasu, H., Fukutomi, H., Gordon, G.: *Inorg. Chem.* **24**, 2962 (1985)
9. Gottschalk, C., Libra, J.A., Saupé, A.: *Ozonation of Water and Waste Water: A Practical Guide to Understanding Ozone and its Applications*. John Wiley & Sons (2009)
10. Weiss, J.: *Trans. Faraday Soc.* **31**, 668 (1935)
11. Oyama, S.T.: *Catal. Rev.* **42**, 279 (2000)
12. Rosal, R., Gonzalo, M.S., Rodríguez, A., García-Calvo, E.: *J. Hazard. Mater.* **169**, 411 (2009)
13. Sui, M., Sheng, L., Lu, K., Tian, F.: *Appl. Catal. B* **96**, 94 (2010)
14. Zhu, S., Dong, B., Yu, Y., Bu, L., Deng, J., Zhou, S.: *Chem. Eng. J.* **328**, 527 (2017)
15. Liu, P., Ren, Y., Ma, W., Ma, J., Du, Y.: *Chem. Eng. J.* **345**, 98 (2018)

16. Zhang, F., Wei, C., Wu, K., Zhou, H., Hu, Y., Preis, S.: *Appl. Catal. A* **547**, 60 (2017)
17. Bulanin, K., Lavalley, J., Tsyganenko, A.: *Colloids Surf., A* **101**, 153 (1995)
18. Ding, Y., Zhang, X., Chen, L., Wang, X., Zhang, N., Liu, Y., Fang, Y.: *J. Solid State Chem.* **250**, 121 (2017)
19. Psaltou, S., Kaprara, E., Triantafyllidis, K., Mitrakas, M., Zouboulis, A.: *J. Environ. Chem. Eng.* **9**, 106173 (2021)
20. Ernst, M., Lurot, F., Schrotter, J.-C.: Catalytic ozonation of refractory organic model compounds in aqueous solution by aluminum oxide. *Appl. Catal. B* **47**(1), 15–25 (2004)
21. Qi, F., Chen, Z., Xu, B., Shen, J., Ma, J., Joll, C., Heitz, A.: Influence of surface texture and acid–base properties on ozone decomposition catalyzed by aluminum (hydroxyl) oxides. *Appl. Catal. B* **84**(3–4), 684–690 (2008)
22. Sui, M., Sheng, L., Lu, K., Tian, F.: FeOOH catalytic ozonation of oxalic acid and the effect of phosphate binding on its catalytic activity. *Appl. Catal. B* **96**(1–2), 94–100 (2010)
23. Zhao, L., Sun, Z., Ma, J., Liu, H.: Enhancement mechanism of heterogeneous catalytic ozonation by cordierite-supported copper for the degradation of nitrobenzene in aqueous solution. *Environ. Sci. Technol.* **43**(6), 2047–2053 (2009)
24. Xu, B., Qi, F., Zhang, J., Li, H., Sun, D., Robert, D., Chen, Z.: Cobalt modified red mud catalytic ozonation for the degradation of bezafibrate in water: catalyst surface properties characterization and reaction mechanism. *Chem. Eng. J.* **284**, 942–952 (2016)
25. Liu, Y., Zhang, P., Zhan, J., Liu, L.: *Appl. Surf. Sci.* **463**, 374 (2019)
26. Sui, M., Liu, J., Sheng, L.: Mesoporous material supported manganese oxides (MnOx/MCM-41) catalytic ozonation of nitrobenzene in water. *Appl. Catal. B* **106**(1–2), 195–203 (2011)
27. Zhao, H., Dong, Y., Jiang, P., Wang, G., Zhang, J., Li, K., Feng, C.: *New J. Chem.* **38**, 1743 (2014)
28. Nawaz, F., Xie, Y., Xiao, J., Cao, H., Ghazi, Z.A., Guo, Z., Chen, Y.: *Catal. Sci. Technol.* **6**, 7875 (2016)
29. Nawaz, F., Cao, H., Xie, Y., Xiao, J., Chen, Y., Ghazi, Z.A.: *Chemosphere* **168**, 1457 (2017)
30. Rivera-Utrilla, J., Sánchez-Polo, M.: *Appl. Catal. B* **39**, 319 (2002)
31. Chen, T., Gu, W., Li, G., Wang, Q., Liang, P., Zhang, X., Huang, X.: *Front. Environ. Sci. Eng.* **12**, 1 (2018)
32. Sánchez-Polo, M., Rivera-Utrilla, J., Von Gunten, U.: *Water Res.* **40**, 3375 (2006)
33. Sun, Z., Zhao, L., Liu, C., Zhen, Y., Ma, J.: Catalytic ozonation of ketoprofen with in situ N-doped carbon: a novel synergetic mechanism of hydroxyl radical oxidation and an intramolecular electron-transfer nonradical reaction. *Environ. Sci. Technol.* **53**(17), 10342–10351 (2019)
34. Valdés, H., Alejandro, S., Zaror, C.A.: *J. Hazard. Mater.* **227**, 34 (2012)
35. Ikhlaq, A., Brown, D.R., Kasprzyk-Hordern, B.: *Appl. Catal. B* **123**, 94 (2012)
36. Brodu, N., Manero, M.-H., Andriantsiferana, C., Pic, J.-S., Valdés, H.: *Chem. Eng. J.* **231**, 281 (2013)
37. Ren, J., Li, J., Lv, L., Wang, J.: *Environ. Sci. Pollut. Res.* **28**, 12909 (2021)
38. Zhang, Y., Ji, H., Liu, W., Wang, Z., Song, Z., Wang, Y., Liu, C., Xu, B., Qi, F.: *Sci. Total Environ.* **727**, 138696 (2020)
39. Liu, D., Lin, M., Chen, W., Wang, J., Guo, X., Li, X., Li, L.: *Chemosphere* 133544 (2022)
40. Wei, K., Wang, Z., Ouyang, C., Cao, X., Liang, P., Huang, X., Zhang, X.: *Water Res.* **173**, 115536 (2020)
41. He, Y., Wang, L., Chen, Z., Shen, B., Wei, J., Zeng, P., Wen, X.: *Sci. Total Environ.* **785**, 147328 (2021)
42. Yu, G., Wang, Y., Cao, H., Zhao, H., Xie, Y.: *Environ. Sci. Technol.* **54**, 5931 (2020)
43. Zhang, M., Meng, F., Zhang, S., Zeng, Y., Zhong, Q.: *Chem. Eng. J.* **429**, 132475 (2022)
44. Zhang, X., Li, X., Qin, W.: *Chem. Phys. Lett.* **479**, 310 (2009)
45. Zhang, F., Kong, Q., Chen, H., Zhao, X., Yang, B., Preis, S.: *Chem. Eng. J.* 134674 (2022)
46. Yu, G., Xie, Y., Ge, Q., Dai, Q., Xu, J., Cao, H.: *Chem. Eng. J.* **430**, 133114 (2022)
47. Zhang, J., Xin, B., Shan, C., Zhang, W., Dionysiou, D.D., Pan, B.: *Appl. Catal. B* **292**, 120155 (2021)
48. Lee, G., Lee, B., Kim, J., Cho, K.: *J. Phys. Chem. C* **113**, 14225 (2009)

# NH<sub>3</sub> Synthesis by Electrochemical Process Under Ambient Condition



Juliana F. de Brito, Sirlon F. Blaskiewicz, Marina Medina,  
Anelisse Brunca Silva, Marcos Vinícius de L. Tinoco,  
and Lucia Helena Mascaro

**Abstract** The necessity of new methods to substitute the Haber-Bosch process in the synthesis of NH<sub>3</sub> using ambient conditions, generating fewer greenhouse gases, and dispensing less energy, drove the investigation of the electrocatalytic process in the N<sub>2</sub> reduction reaction in the last decade. An impressive number of manuscripts have already been published in this sense, mainly focusing on the reduction of N<sub>2</sub> to NH<sub>3</sub> generation under ambient conditions. The use of diverse catalysts has been investigated targeting an effective reaction for N<sub>2</sub> reduction and NH<sub>3</sub> synthesis under ambient temperature and pressure looking to materials with grate resistance against corrosion, high current density, good stability, and important active sites with preferential adsorption of N<sub>2</sub>. This chapter will present the mechanism and reaction pathway involved in the reduction of N<sub>2</sub> by electrochemical process under ambient conditions and the main catalysts employed for this synthesis. Additionally, it is discussed the implication that the different designed-cells such as single cell, H-cell and MEA can cause in the efficiency of the reduction reaction of N<sub>2</sub>. Finalizing, future perspectives where also pointed in order to, together with what is presented along this revision, promote an incentive for researches to look for new carbon free emissions possibilities to maintain the NH<sub>3</sub> production minimizing the environmental and economic impact of the common synthesis route of this important fertilizer.

## 1 Introduction

The nitrogen cycle performs a crucial role in modern society, however, N-containing natural sources alone, cannot supply human needs, due to its importance in the agriculture and pharmaceutical industry, related to the production of compounds that is the basis of human maintenance [1–3]. The industrial process of ammonia production is still up to date dependent on Haber–Bosch process (HBP) developed

---

J. F. de Brito (✉) · S. F. Blaskiewicz · M. Medina · A. B. Silva · M. V. de L. Tinoco ·  
L. H. Mascaro

Department of Chemistry, Federal University of São Carlos, Rod. Washington Luiz, Km 235, São  
Carlos-SP 13565-905, Brazil  
e-mail: [jfbrito@ymail.com](mailto:jfbrito@ymail.com)

in the early 1920s [3]. The energy consumption of the HBP represents around 3% of all the energy spent on our planet [2, 4–6], in addition to consuming around 5% of all world natural gas production and generating hundreds of millions of tons of CO<sub>2</sub> annually [7, 8]. This scenario motivates intensive studies in different areas such as biocatalysis [9], molecular catalysis [10, 11], and electrocatalysis [12, 13] aiming for high yields and clean routes for ammonia synthesis.

In general, an electrochemical process is related to the charge transport across interfaces between chemical phases [14]. One of the well-known interfaces is found in electrochemical cells, which is defined by two electrodes separated by an electrolyte [14, 15]. The most useful electrochemical system is the cell with three electrodes which is the working and counter electrode, where the half-reactions of reduction and oxidation takes place, and a reference electrode which allows precise monitoring and control of the external potential applied ( $E_{\text{app}}$ ) [14–16]. The use of electric energy from a sustainable source to promote the N<sub>2</sub> reduction reaction (NRR) is one of the most promising routes to produce NH<sub>3</sub> at moderate temperature and atmospheric pressure [3, 17]. A schematic representation of the NRR is presented in Fig. 1 [14, 18].

When an external negative potential is applied at the working electrode, the electrons in the conducting material reach an energy level high enough to be transferred to a vacant orbital of the molecule in the solution, which will define the half-reaction of reduction [14, 16]. At the counter electrode, occurs the half-reaction of oxidation, which depends on the solvent used and the pH of the solution; however, the most common reaction is the water oxidation, represented as Eq. (1) for acidic and Eq. (2) for alkaline environments [14, 15].

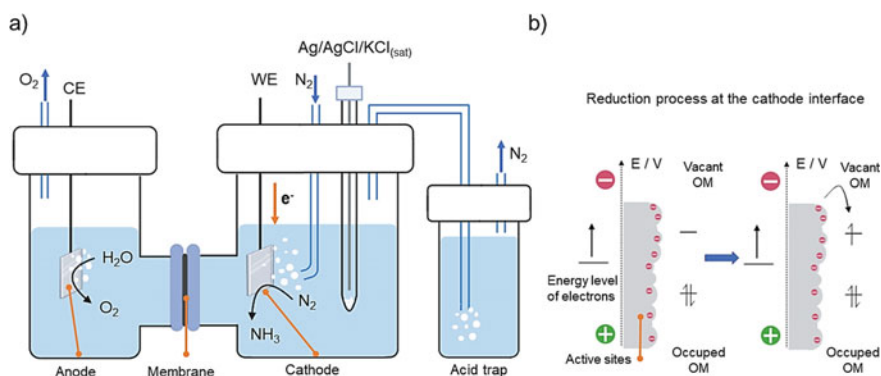
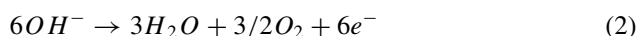
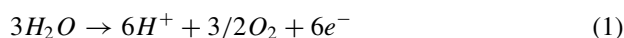
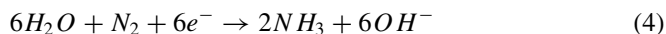
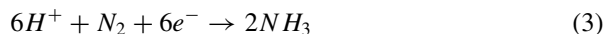
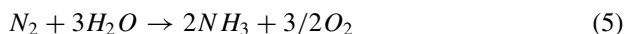


**Fig. 1** a) Scheme of NRR in a H-type cell using silver chlorate as reference electrode and **b** reduction process at the catalyst—electrolyte interface

These equations are important because in NRR the H<sup>+</sup> ions dissociated by water are used to form NH<sub>3</sub> at the cathode, while the water oxidation occurs at the anode [17]. The half-reactions at the cathode of NRR in an acidic condition are shown by the Eq. (3) and an alkaline condition in the Eq. (4).



Coupling the half-reactions in both conditions the overall reaction is the same and is represented by the Eq. (5), as seen, depending on pH different ions need to migrate between the electrodes. In acidic condition the solvated protons are formed at the anode and migrate to cathode, where will form single bonds with nitrogen under electrocatalytic process [16, 17]. By the other side, in alkaline condition, the hydrogen in H<sub>2</sub>O is used to produce NH<sub>3</sub> and OH<sup>-</sup> ions, which need to migrate to the anode to be oxidized to O<sub>2</sub> [17].



The electrochemical NH<sub>3</sub> synthesis from NRR is challenging due to some thermodynamics characteristics of molecular N<sub>2</sub>, such as high thermodynamic dissociation energy (941 kJ mol<sup>-1</sup>), large ionization energy (15.6 eV), and high electron affinity (-1.9 eV), which reduces its reactivity and leads to low process efficiency [19, 20]. Besides that, there are a competition among the NRR and the hydrogen evolution reaction (HER), since these two reactions shows similar thermodynamic potential at room temperature [13]. In this sense, the target of producing ammonia electrochemically with high efficiency is closely aligned to the use of catalysts materials, which were not only highly active for NRR but also chemically stable and made of abundant and nontoxic elements [20].

In the search for materials that act as a catalyst for NH<sub>3</sub> electrosynthesis, the feasibility of N<sub>2</sub> fixation in the catalyst surface is a relevant parameter, since a strong interaction will poison the active site, and the weak one will not allow the N<sub>2</sub> activation, resulting in low faradaic efficiency (FE) and NH<sub>3</sub> yield [21]. The bond strength-catalytic activity analysis is provided by the Sabatier principle and results on the volcano-type relationship of the electrocatalysts materials, which is qualitative guidance for better catalysts choices [22]. Briefly, a great electrocatalyst towards NRR catalysis needs to provide a strong N<sub>2</sub> activation together with intermediate binding for reaction species [19].

In this sense, this chapter will bring a discussion around the electrocatalytic reduction of N<sub>2</sub> for NH<sub>3</sub> synthesis, taking into consideration not only the possible mechanisms pathways but also the theoretically and experimentally most promisor metals, oxides, sulfides and phosphides as catalysts reported in the literature. Figure 2 represents the catalysts that will be addressed in this chapter and the most important factors to build this materials for the electrochemical reduction of N<sub>2</sub>. Additionally, will be



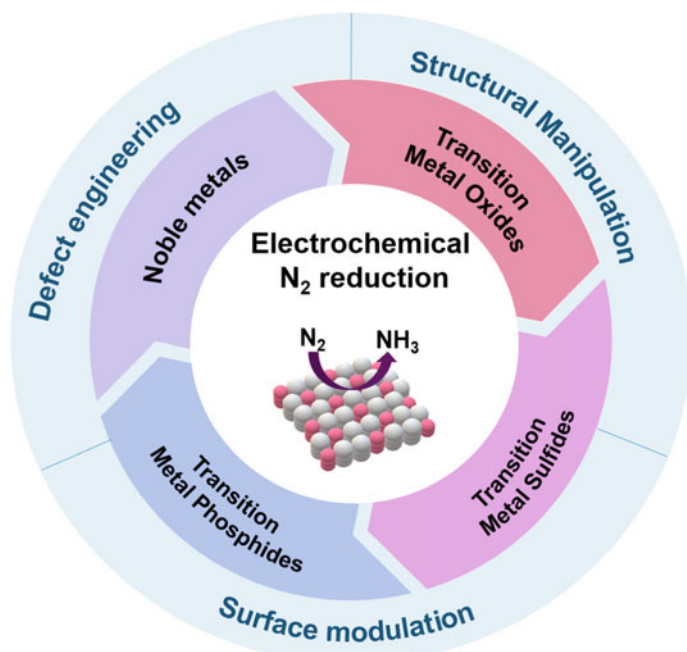
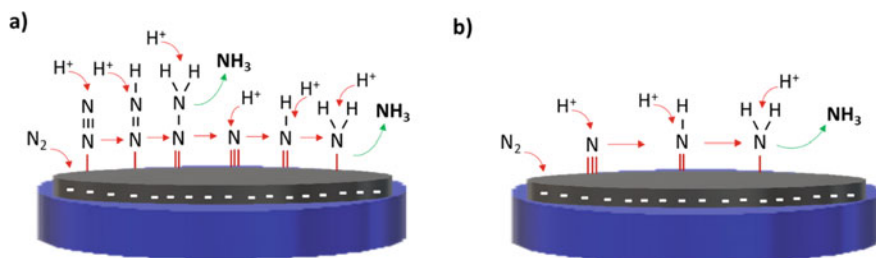


**Fig. 2** Schematic representation of the catalysts and the synthesis factors that will be presented in this chapter

presented the possibilities of reactors for the NRR and the influence of each option in the NH<sub>3</sub> yield, besides the future perspectives to achieve an environmentally friendly option to substitute the HBP.

## 2 N<sub>2</sub> Reduction Mechanism and the Most Favorable Metals and Oxides Electrodes for the Reaction

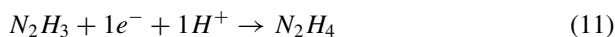
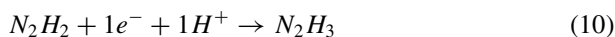
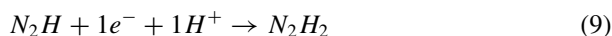
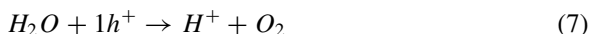
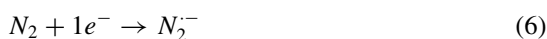
Nitrogen reduction obtained by electrocatalysis technique, mainly under ambient conditions, provides an energy-saving and low-pollution method for the synthetic ammonia industry, benefiting the fertilizer and textile industry [23]. The reaction mechanism for the reduction of N<sub>2</sub> with NH<sub>3</sub> generation using the electrocatalysis technique is based firstly on the generation of the charges in the electrode surface, with the reduction of N<sub>2</sub> in the cathode while the generation of the proton happens in the anode, usually from the water oxidation [23, 24]. There are two different pathways for NH<sub>3</sub> formation, associative (Fig. 3a) and dissociative (Fig. 3b). As can be observed in Fig. 3a, in the associative mechanism both N remain bonded to each other while the hydrogenation occurs until one NH<sub>3</sub> is formed the last N-N bond is broken [25]. It is worth mentioning that the hydrogenation, in this case, can happen

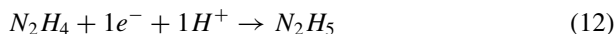


**Fig. 3** Possible reaction mechanisms for the N<sub>2</sub> reduction forming NH<sub>3</sub> by **a** association and **b** dissociation. Adapted from Ref. [26]

preferentially in a distal associative pathway, where the hydrogen is inserted in the outermost N first, as demonstrated in Fig. 3a, or by an associative alternating pathway where the addition of H undergoes alternating each of the two nitrogen centers [26]. On the other hand, the second possible mechanism for the NH<sub>3</sub> synthesis occurs by dissociation of both N species, as can be observed in Fig. 3b. The N≡N bond, in this case, is broken before the beginning of the hydrogenation generating N atoms adsorbed independently in the catalyst surface to the conversion of a single NH<sub>3</sub> molecule [26].

Montoya and co-workers [4] demonstrated that for the associated pathway, the limitation of the N<sub>2</sub> reduction reaction on solid metal surfaces is related to the linear scaling relationship between N<sub>2</sub>H and NH<sub>2</sub> surface sites on transition metals. So, this step should be the target to obtain a good catalyst for the N<sub>2</sub> reduction by electrocatalysis under ambient conditions. To summarize, the reaction pathway for the N<sub>2</sub> reduction reaction with NH<sub>3</sub> formation by an electrochemical process based on DFT calculations reported in the literature [27–29] can be demonstrated by the Eqs. (6)–(13) hereafter.





The most promisor metals to do this conversion of  $N_2$  to  $NH_3$  can be observed in the volcano plot presented by Norskov and coworkers [4], where it is possible to compare the HER and NRR overpotentials as a function of the N surface sites binding-energy ( $N^*$ ), and individual transition metal points for (111) and (211) facets. In both cases, the limiting potentials are less negative for HER than for NRR (at least 0.5 V for Re (111)), suggesting a higher selectivity to HER [4]. For HRR there is a mild difference between the Gibbs free energy and also the limiting potential comparing the metals with (111) and (211) facets. Those differences are more pronounced for the NRR. For (111) facets it is possible to conclude that the lower overpotential on transition metals for  $N_2$  reduction reaction is obtained under Re and Ru catalysts, while for (211) surfaces, the best option could be Ru, Ni, Rh, Ir, and CO.

Figure 4 shows a volcano plot comparing the limiting-potential determining step against the binding energy for  $NH_3$  synthesis by the electrochemical reaction on diverse metal oxides with (110) facets, where the lines were constructed using scaling relations, and take into consideration three of the six electrochemical reaction steps of the  $NH_3$  formation mechanism [30]. The promisor catalysts concerning the oxides explored in this diagram are  $OsO_2$ ,  $ReO_2$  and  $TaO_2$ . However, according to Fig. 4b [30], among than just  $TaO_2$  favors the adsorption of the intermediate NNH over hydrogen adsorption, and thus this surface should be able to reach higher yields of  $NH_3$  formation compared to the other oxides. To be able to suppress the  $H_2$  side-reaction is probably the first biggest challenge around  $N_2$  reduction in the presence of water [26]. As it is known that the design of heterojunctions (or multijunction) catalysts can improve the electrochemical performances of electrodes, those metals

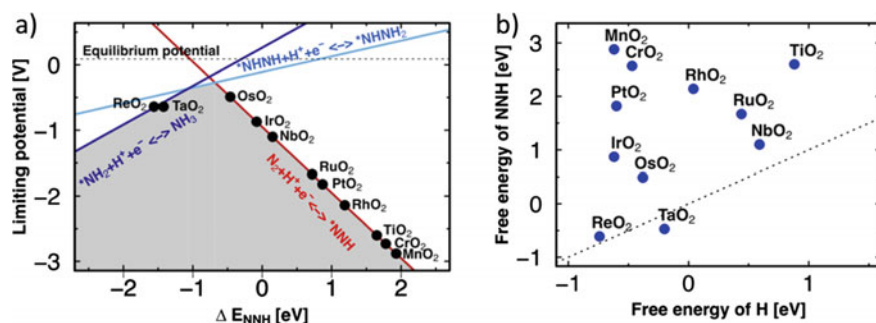


**Fig. 4** a Volcano plot comparing the limiting-potential determining step against the binding energy for  $NH_3$  synthesis by the electrochemical reaction on metal oxides. b Free energy of adsorption of NNH compared to of H on the surface of different metal dioxides. Reproduced with permission from Ref. [30], Copyright 2017 American Chemical Society

and oxides electrodes should be taken into consideration in the build of materials for N<sub>2</sub> reduction reactions.

### 3 Most Relevant Catalysts for the Electrochemical Reduction of N<sub>2</sub>

#### 3.1 Noble Metals

The transition from HBP alternatives through efficient, robust, and stable catalysts remains a huge challenge. Catalysts for the electrochemical ammonia production from dinitrogen reduction, for example, configure a specific research area, due to the potential to compete with the HBP and reduce associated greenhouse gases emissions. The main advantages of working with electrochemical systems are the ease of scaling the system while diminishing dependence on fossil fuels, further leading to a more accessible process.

As mentioned before, the FE achieved for electrochemical NRR are sharply reduced due to the competing HER. There is a wide variety of experimental parameters studied that proved influence directly in the performance, such as the nature of the electrolyte [31–33], however, the primary challenge to make electrocatalytic ammonia synthesis feasible is an electrocatalyst design that suppresses HER while carrying NRR. Though, most electrocatalyst surfaces present a poor specificity towards NRR [34], including hindrances such as multiple electron transfer and high activation energy associated with this reaction. Four main factors can be appointed to be crucial when considering a suitable nitrogen reduction electrocatalyst: size, electronic, coordination, and orientation effects [34].

Amongst the most promising electrocatalysts for ammonia production are the noble metals-based [35, 36], reported in the work of Yanbin and co-workers, where Ag-doped Cu nanosheets achieved an expressive FE of over 20%. The Ag doping induced electron-deficient Cu atoms formation, which enhanced N<sub>2</sub> adsorption, at the same time that suppressed HER [37]. The combination of silver with other materials can be extended for an array with other noble metals, *e. g.* gold [38], leading to an effective ammonia electrocatalyst. A tunable localized surface plasmon resonance (LSPR) can be a primal factor in dinitrogen electrochemical reduction, together with other aspects as the surface area and the Ag/Au ratio in the sample. However, a satisfactory electrocatalyst must show good faradaic efficiency for NRR over HER, in addition to good stability. As demonstrated by El-Sayed and co-workers [35], when silver is converted to silver oxide (Fig. 5a), the faradaic efficiency of an Ag/Au electrocatalyst reduces dramatically (Fig. 5b), from 35.9 to 23.4% for Ag<sub>2</sub>O/Au, it is a substantial decrease of almost 35% of the material activity, which indicates that, according to the catalyst nature, the simple fact of work in an O<sub>2</sub>-free system, considerable influence on the process.

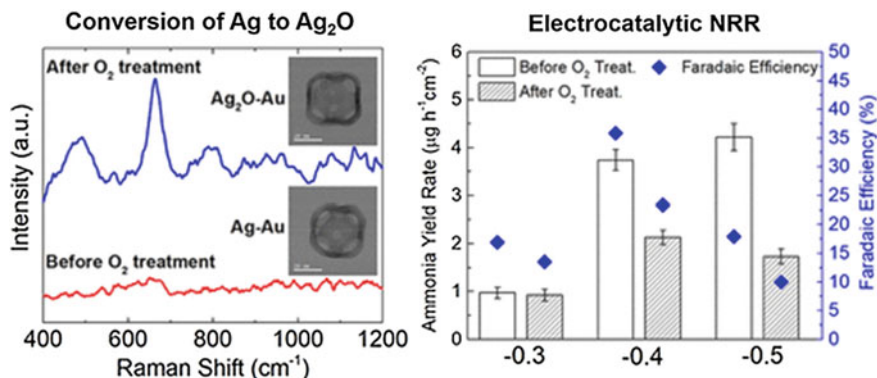


**Fig. 5** **a** Raman spectra of bimetallic Ag/Au-based electrocatalyst before (red line) and after (blue line) O<sub>2</sub> treatment where is possible to observe Ag<sub>2</sub>O-related bands after treatment. **b** Ammonia yield and Faradaic Efficiency at some applied potentials in a 0.5 M LiClO<sub>4</sub> aqueous solution. Reprint with permission from Ref. [35], Copyright© 2019 American Chemical Society

Gold alone is another noble metal with potential for electrochemical nitrogen reduction, with good yields and faradaic efficiency. Although the good responses of gold-based catalysts are being attributed to factors as morphology [39], presence in composites [40], among others, studying how a reaction mechanism occurs is the first step to design architectures that improve this process. Surface-enhanced infrared absorption spectroscopy (SEIRAS) allowed clear some parameters [41]. Throughout the NRR over an Au film, species as the N<sub>2</sub>H<sub>y</sub> species were observed at potentials beneath 0 V *versus* RHE in different wavelengths: 1453 (H-N-H bending), 1298 (H-N-H wagging), and 1109 cm<sup>-1</sup> (N-N stretching). This result indicates that the reduction follows an associative mechanism, with the triple bond in N<sub>2</sub> breaking concerted with the hydrogen insertion. On the other way, the same bands were not observed on a platinum surface under the same conditions, with is consistent with the huge efficiency of Pt for HER, the main competitive reaction found in the electrochemical ammonia synthesis.

### 3.2 Transition Metal Oxides

Transition metal oxides (TMOs) are among the metal-based materials that have been intensively investigated for N<sub>2</sub> electroreduction. In contrast with other transition metal-based materials, TMOs presents facile large-scale preparations and chemical stability. Recently, several TMOs have been reported as NRR catalysts including TiO<sub>2</sub>, Nb<sub>2</sub>O<sub>5</sub>, MnO<sub>2</sub>, VO<sub>x</sub>, CeO<sub>x</sub> and W, Fe, Mo, and Bi oxides [42–44]. Some early theoretical studies [45] have indicated that Ti shows stronger binding with N<sub>2</sub> than with H-atoms which is beneficial for NRR applications. TiO<sub>2</sub>-based materials present excellent chemical stability and strong affinity to N<sub>2</sub> adsorption [30] making them a

potential electrocatalyst for NH<sub>3</sub> synthesis. Yang and co-workers [46] have shown that bulk TiO<sub>2</sub> presents extremely low N<sub>2</sub>-to-NH<sub>3</sub> conversion efficiency (0.95% at –0.15 V *versus* RHE) owing to the high energy barrier for N<sub>2</sub> activation. The authors demonstrated that tailoring the TiO<sub>2</sub> electronic structure by creating oxygen vacancies (OVs) into the TiO<sub>2</sub> surface enhances its NRR catalytic efficiency achieving a higher FE of 9.17%.

Combining oxygen vacancies engineering and morphology control has shown to be even more beneficial for TiO<sub>2</sub> NRR performance. Fang and co-authors [47] showed from DFT studies that introducing oxygen vacancies on 2D-TiO<sub>2</sub> structure lowers the energy barrier for NRR and the RDS for the N<sub>2</sub> reduction on the catalyst surface is 0.25 eV on the OV site while its 2.29 V at defect-free-TiO<sub>2</sub> surface. Moreover, the steps for ammonia formation are thermodynamically more favorable on the OV site leading to higher faradaic efficiency. The effect of Ti<sup>+3</sup> defect sites on TiO<sub>2</sub> in NRR performance was investigated as well. Chen and co-authors [8] demonstrated that Ti<sup>+3</sup> ions are the main catalytic sites in Ti<sub>2</sub>O<sub>3</sub> nanoparticles and significantly lowered the overpotential of the potential-determining step for N<sub>2</sub> conversion. The Ti<sub>2</sub>O<sub>3</sub> electrocatalyst produced an NH<sub>3</sub> yield and FE of 26.01 μg h<sup>-1</sup> mg<sup>-1</sup><sub>cat</sub> and 9.16%, respectively, at –0.25 V *versus* RHE. Even though defect engineering improves TiO<sub>2</sub>-based catalysts performance the faradaic efficiencies remain relatively low. In this sense, other TMOs have been explored for NRR applications.

Nb-based oxides have proved to be active catalysts for N<sub>2</sub> electroreduction [48, 49]. Wang and co-workers [50] reported a Cu-doped niobium oxide anchored on carbon material by solvothermal method coupled with pyrolysis for NRR in acidic and neutral electrolytes. The authors suggest that Cu doping interacts with Nb and induces lattice-disorder formation near the dopant site ensuring more active sites to drive the reaction. Electrochemical tests show that the Cu-Nb<sub>2</sub>O<sub>5</sub>@C electrode exhibits excellent activity and high selectivity N<sub>2</sub> to NH<sub>3</sub> conversion with a yield rate of 28.07 μg h<sup>-1</sup> mg<sup>-1</sup> and a FE of 13.25% at –0.2 V *versus* RHE in acidic electrolyte. Vanadium oxide has also been applied to N<sub>2</sub> electroreduction. Fang and co-workers designed a multivalent vanadium oxide-reduced graphene oxide (mVO<sub>x</sub>-rGO) nanosheets. The hybrid catalyst exhibited a larger NH<sub>3</sub> yield of 18.84 μg h<sup>-1</sup> mg<sup>-1</sup><sub>cat</sub> than V<sub>2</sub>O<sub>5</sub>-rGO with 8.09 μg h<sup>-1</sup> mg<sup>-1</sup><sub>cat</sub>. The authors explained that the high NRR performance occurs not only on phase boundaries but also at the multivalent vanadium oxide surface. In addition, owing to oxygen vacancies mVO<sub>x</sub> adsorb N<sub>2</sub> and water more strongly leading to a better conversion performance [51]. It has already been shown that metal alloying synergy provides an improvement on catalytic efficiency [52]. Furthermore, the natural biological N<sub>2</sub> fixation through the enzymatic pathway involves bimetallic active centers [53]. Recently, many bimetallic oxides have been demonstrated to be good electrocatalysts for NRR (see Table 1).

Chu and co-authors [53] developed FeMoO<sub>4</sub> nanorods for NRR electroreduction. DFT calculations demonstrated that the synergistic effect of Fe and Mo enhances the N<sub>2</sub> adsorption and accelerates charge transfer. In addition, the unsaturated three-fold coordinated Mo acted as the major active site for N<sub>2</sub> activation. Mo-doping strategy also improved NRR electrocatalytic performance of MnO<sub>2</sub> nanoflowers

**Table 1** Summary of reported bimetallic transition metal oxides-based catalysts reported in the literature for NRR under ambient conditions

Catalysts	Experimental conditions	FE (%)	NH <sub>3</sub> yield	References
FeMoO <sub>4</sub>	0.5 mol L <sup>-1</sup> LiClO <sub>4</sub> -0.3 V versus RHE	13.2	45.8 μg h <sup>-1</sup> mg <sup>-1</sup> <sub>cat</sub> (-0.5 V vs. RHE)	[53]
Mo-MnO <sub>2</sub>	0.1 mol L <sup>-1</sup> Na <sub>2</sub> SO <sub>4</sub> -0.4 V versus RHE	12.1	36.6 μg h <sup>-1</sup> mg <sup>-1</sup> <sub>cat</sub> (-0.5 V vs. RHE)	[54]
BiMoO <sub>6</sub>	0.1 mol L <sup>-1</sup> Na <sub>2</sub> SO <sub>4</sub> -0.6 V versus RHE	8.17	20.46 μg h <sup>-1</sup> mg <sup>-1</sup> <sub>cat</sub>	[55]
NiWO <sub>4</sub>	0.1 mol L <sup>-1</sup> HCl -0.3 V versus RHE	19.32	40.05 μg h <sup>-1</sup> mg <sup>-1</sup> <sub>cat</sub>	[56]

[54]. From theoretical studies, the authors revealed that Mo-doping delivered multi-functions for NRR: induced defect level improving MnO<sub>2</sub> conductivity, acted as NRR active site, activated inert Mn sites enhancing the intrinsic NRR activity of the MnO<sub>2</sub>, and suppressed HER. Xing and co-workers [55] reported the development of highly stable Mo-modified bismuth oxide hollow spheres for N<sub>2</sub> electroreduction. The authors explained that the Bi-Mo combination not only enhances NRR catalytic activity but also the stability of Mo-based catalysts. W-based nanomaterials have also been reported as active catalysts for NRR. To overcome the low efficiencies of W-based oxides, Wang and co-authors [56] have developed a porous NiWO<sub>4</sub> catalyst. The obtained catalyst has shown superior catalytic activity and stability NRR performance than the NiO and WO<sub>3</sub> monometallic oxides in a wide pH range. The porous structure provides a better exposition of active sites and facilitate electrolyte transport. These mentioned reports highlight that TMOs are excellent candidates for electrochemical NH<sub>3</sub> synthesis but low efficiencies have been achieved. Thus, to rationally design more efficient catalysts some strategies including surface and defect engineering, heteroatom-doping, and heterostructure construction. must be applied to further improve TMOs catalysts performance for NRR.

### 3.3 Sulfide-Based Catalysts for NRR

The intensive reaction pathways exploration for N<sub>2</sub> fixation on biocatalyst revealed the presence of transition metals (TMs) elements, such as Fe, Co, Mo, Ni, acting in the coenzymes, in which, later studies, pointed out the d orbitals configuration as enhancers of the bonding interaction between the N<sub>2</sub> and the TM catalyst surface [20, 57, 58]. Theoretical investigations based on density functional theory (DFT) calculations about single metal atom catalysts, in the associative mechanism for NH<sub>3</sub> synthesis, reveal the Mo and Fe elements as the most promising candidates [19]. Experimentally, Zhao and co-workers reported that, on the thermodynamic view, the initial hydrogenation step of N<sub>2</sub> occurs spontaneously and preferentially in the

Mo(111) surface; but in the kinetic view, the Fe(110) surface shows better electrocatalytic activity from the potential-dependent rate constant of the rate-determining step [59]. Wang and co-workers prepared a (110)-oriented Mo nanofilm and applied it in the electrochemical reduction of aqueous N<sub>2</sub>, in which a FE of 0.72% was achieved at an overpotential of 0.14 V<sub>RHE</sub> and a NH<sub>3</sub> rate of  $3.08 \times 10^{-11}$  mol s<sup>-1</sup> cm<sup>-2</sup> at -0.49 V *versus* RHE [60].

Although, the TMs can also be in the form of nitrides, carbides, oxides, and sulfides. Taking advantage of enzymatic studies to natural NH<sub>3</sub> synthesis, the TMs sulfides, such as MoS<sub>2</sub> [61], Fe<sub>x</sub>S<sub>y</sub> [62], and Cu<sub>x</sub>S<sub>y</sub> [63], has aroused great attention due to the structural similarity with nitrogenases active site [64]. MoS<sub>2</sub> is a relative nontoxicity and earth-abundant material, which is known as an effective catalyst towards HER, which its layered structure provides not only high surface area but also tunable electronic structure [65]. The presence of Mo and S elements in nitrogenases raise the attention to its catalytic activity towards NRR [20]. Besides that, computational studies appointed the plausibility, in mechanistic terms, of the NH<sub>3</sub> electrosynthesis on the sites where Mo atoms are exposed to the electrolyte [66]. Experimentally, Zhang and co-workers were the first groups that prepared MoS<sub>2</sub> nanosheet hydrothermally on carbon cloth and applied it as a catalyst to NH<sub>3</sub> electrosynthesis under room temperature and atmospheric pressure. The catalyst achieved FE of 1.17% with a NH<sub>3</sub> yield equal to  $8.08 \times 10^{-11}$  mol s<sup>-1</sup> cm<sup>-2</sup> at -0.5 V *versus* RHE in 0.1 M Na<sub>2</sub>SO<sub>4</sub> [67].

Despite the pioneering, greater catalytic efficiency needs to be achieved for large-scale application and various strategies have been adopted to promote the MoS<sub>2</sub> performance for NH<sub>3</sub> electrosynthesis. Xuping Su and co-workers improved the catalyst selectivity towards N<sub>2</sub> reduction by preparing a defect-rich MoS<sub>2</sub> nanoflower, which achieves an FE of 8.34% and a NH<sub>3</sub> yield of 29.28 μg h<sup>-1</sup> mg<sup>-1</sup><sub>cat</sub> at -0.40 V *versus* RHE, against 2.18% and 13.41 μg h<sup>-1</sup> mg<sup>-1</sup><sub>cat</sub> of defect-free counterpart [61]. Matanovic and co-workers with DFT studies also show the improved efficiency by the incorporation of defects and additional elements on MoS<sub>2</sub> nanosheets for improved FE and NH<sub>3</sub> yield [66]. More specifically, sulfur-vacancy (V<sub>S</sub>) defects play a key role in improved MoS<sub>2</sub> nanosheets catalysis towards NRR. Chaoqun and co-workers prepared an optimized V<sub>S</sub>-MoS<sub>2</sub> which achieved a NH<sub>3</sub> average yield rate of  $46.1 \times 10^{-11}$  mol s<sup>-1</sup> cm<sup>-2</sup> at -0.5 V<sub>RHE</sub> with a FE of 4.58% at -0.4 V *versus* RHE. The DFT calculations reveal the improved electrocatalytic efficiency as a consequence of high N<sub>2</sub> selectivity on the catalyst surface [68]. The same sulfur-vacancy effect was observed for amorphous MoS<sub>3</sub>, which achieved a NH<sub>3</sub> yield of 51.7 μg h<sup>-1</sup> mg<sup>-1</sup> and FE of 12.8% at -0.3 V *versus* RHE in 0.5 M LiClO<sub>4</sub> [69]. The poor electrical conductivity is an issue that hinders even the high catalytic efficiency of MoS<sub>2</sub> nanosheets. Based on that, the high surface area and electrical conductance of rGO was used for Xianghong Li and co-workers to prepare a MoS<sub>2</sub> nanosheet-reduced graphene oxide hybrid (MoS<sub>2</sub>-rGO), which achieves FE of 4.58% and a NH<sub>3</sub> yield of 24.82 μg h<sup>-1</sup> mg<sup>-1</sup><sub>cat</sub> at -0.45 V *versus* RHE in 0.1 M LiClO<sub>4</sub> [70].

The interface engineering with the heterostructure design is another strategy to expedite the NRR kinetics and improve the electrocatalytic performance since the strong interfacial interactions of two catalyst materials not only boost the electron



transfer but also optimize the free energies of reaction intermediates [71]. In such an effort, Ke Chu and co-workers prepared a  $\text{MoS}_2/\text{C}_3\text{N}_4$  heterostructure that exhibited a FE of 17.8% and a  $\text{NH}_3$  yield of  $18.5 \mu\text{g h}^{-1} \text{mg}^{-1}_{\text{cat}}$  at  $-0.3 \text{ V}$  versus RHE in  $0.1 \text{ M}$   $\text{LiClO}_4$  solution at ambient conditions. The DFT calculations provide further information that the heterostructure approach provides a decrease in the energy barrier for the stabilization of the intermediate and promotes a more favorable H adsorption on S edge sites of  $\text{MoS}_2$ , leading to high FE [72]. The core/shell heterostructure design is an interesting strategy to balance the selectivity and activity of the electrocatalyst for NRR. Based on that, Jiang and co-workers grow an ultrathin  $\text{MoS}_2$  layer on  $\text{Cu}_{2-x}\text{S}$  quantum dots, which achieves a FE of 6.06% and a  $\text{NH}_3$  yield of  $22.15 \mu\text{g h}^{-1} \text{mg}^{-1}_{\text{cat}}$  at  $-0.5 \text{ V}$  versus RHE. The improved results were attributed to the enhancements of nitrogen adsorption capacity, electrochemical active surface area, and charge transfer rate [73].

The structural differences between the crystalline and amorphous catalyst form are another interesting factor to be analyzed in the catalytic efficiency studies since they afford different elements in contact with the electrolyte that can result in different degrees for  $\text{N}_2$  fixation and consequent  $\text{NH}_3$  synthesis. In such an effort, Patil and co-workers ascribed the presence of more active sites for  $\text{N}_2$  adsorption in the low crystallinity structure of 1 T- $\text{MoS}_2$ , when compared with the corresponding crystalline one. The prepared 1 T- $\text{MoS}_2$  catalyst on Ni foil achieved a FE of 27.66% with a  $\text{NH}_3$  synthesis rate of  $1.05 \mu\text{g min}^{-1} \text{cm}^{-2}$  at  $-0.3 \text{ V}$  versus RHE in  $0.25 \text{ M}$   $\text{LiClO}_4$  electrolyte [74].

The Fe presence on the coenzyme responsible for the natural  $\text{NH}_3$  synthesis increased the efforts for Fe-based catalyst design, and the sulfides have gained interest as a noble-metal-free electrocatalyst [62]. Specifically, the  $\text{Fe}_4\text{S}_4$  clusters play an important role as an electron carrier for the  $\text{N}_2$  fixation on the nitrogenases [75]. Based on that,  $\text{Fe}_3\text{S}_4$  nanosheets were synthesized via hydrothermal route and the obtained catalyst was capable to produce  $\text{NH}_3$  electrochemically at a yield of  $75.4 \mu\text{g h}^{-1} \text{mg}^{-1}_{\text{cat}}$  and a FE of 6.45% at  $-0.4 \text{ V}$  versus RHE [76]. Another strategy to prepare a Fe-based sulfide catalyst was the  $\text{H}_2\text{S}$ -plasma treatment on a Fe foam substrate. The facile and self-supportive strategy provides a catalyst that shows a  $\text{NH}_3$  production rate of  $4.13 \times 10^{-10} \text{ mol s}^{-1} \text{cm}^{-2}$  and a FE of 17.6% at  $-0.30 \text{ V}$  versus RHE in  $0.1 \text{ M}$  KOH. The DFT calculations suggested the well-defined Fe-Fe distance on  $\text{FeS}(011)$  surface as a crucial factor for achieving the catalyst results towards NRR [77].

Intensive efforts have been made to improve the electrochemical conversion of  $\text{N}_2$  to  $\text{NH}_3$ , and they usually are delimited by tempts to mimic the biological mechanism on nitrogenases enzymes. In such an effort, computational analysis has been shown that the increased sulfur sites facilitate the proton transfer to  $\text{N}_2$  fixation [78]. Based on that, Cu-based sulfides catalysts were prepared, taking advantage of the variety  $\text{Cu}_{2-x}\text{S}$  ( $0 \leq x < 1$ ) structures to achieve a higher number of active metal sites. The as-prepared catalyst shows a  $\text{NH}_3$  production rate of  $2.19 \mu\text{mol h}^{-1} \text{cm}^{-2}$  and a FE of 14.1% at  $-0.1 \text{ V}$  versus RHE. The DFT calculations reveal that the catalyst mechanism to NRR mimics the pathway observed in nitrogenases by the hydrogen-bonding interactions on the  $\text{Cu}_{2-x}\text{S}$  surface [79]. However, the stability of the Cu

sulfide-based catalyst acts as a bottleneck to its large-scale application, since the structures usually change to oxides during NRR in a reductively degraded mechanism [80]. Based on that, Kim and co-workers prepared a Cu<sub>9</sub>S<sub>5</sub> catalyst and designed an electrochemical regeneration sulfur method to reconstruct the degraded surface. More interesting, this oxide/sulfur cycle mimics the biocatalyst cycle to N<sub>2</sub> fixation, reconstructing the metal-sulfur bond and restoring the NH<sub>3</sub> electrosynthesis. The Cu<sub>9</sub>S<sub>5</sub> catalyst achieves an efficiency of 10.8 ± 0.4 μg/hcm<sup>2</sup> at -0.5 V versus RHE [63]. Table 2 presents a summary of the NH<sub>3</sub> yield under transition metal sulfides reported in the literature.

**Table 2** Summary of transition metal sulfides-based catalysts reported in the literature for NRR under ambient conditions

Catalyst	Experimental conditions	FE (%)	NH <sub>3</sub> yield	References
Mo(110)	Ultra-pure water -0.49 V versus RHE	0.72	3.09 × 10 <sup>-11</sup> mol s <sup>-1</sup> cm <sup>-2</sup>	[60]
Defect-rich MoS <sub>2</sub>	0.1 mol L <sup>-1</sup> Na <sub>2</sub> SO <sub>4</sub> -0.40 V versus RHE	8.34	29.28 μg h <sup>-1</sup> mg <sup>-1</sup> <sub>cat</sub>	[61]
MoS <sub>2</sub>	0.1 mol L <sup>-1</sup> Na <sub>2</sub> SO <sub>4</sub> -0.50 V versus RHE	1.17	8.08 × 10 <sup>-11</sup> mol s <sup>-1</sup> cm <sup>-2</sup>	[67]
MoS <sub>2</sub> -rGO	0.1 mol L <sup>-1</sup> LiClO <sub>4</sub> -0.45 V versus RHE	4.58	24.82 μg h <sup>-1</sup> mg <sup>-1</sup> <sub>cat</sub>	[70]
MoS <sub>2</sub> /C <sub>3</sub> N <sub>4</sub>	0.1 mol L <sup>-1</sup> LiClO <sub>4</sub> -0.30 V versus RHE	17.8	18.5 μg h <sup>-1</sup> mg <sup>-1</sup> <sub>cat</sub>	[72]
Cu <sub>2-x</sub> S/ MoS <sub>2</sub>	0.1 mol L <sup>-1</sup> Na <sub>2</sub> SO <sub>4</sub> -0.50 V versus RHE	6.06	22.1 μg h <sup>-1</sup> mg <sup>-1</sup> <sub>cat</sub>	[73]
MoS <sub>3</sub>	0.5 mol L <sup>-1</sup> LiClO <sub>4</sub> -0.30 V versus RHE	12.8	51.7 μg h <sup>-1</sup> mg <sup>-1</sup> <sub>cat</sub>	[69]
V <sub>S</sub> -MoS <sub>2</sub>	0.1 mol L <sup>-1</sup> Na <sub>2</sub> SO <sub>4</sub> -0.50 V versus RHE	4.58	46.1 × 10 <sup>-11</sup> mol s <sup>-1</sup> cm <sup>-2</sup>	[68]
1 T-MoS <sub>2</sub>	0.25 mol L <sup>-1</sup> LiClO <sub>4</sub> -0.30 V versus RHE	27.66	1.05 μg min <sup>-1</sup> cm <sup>-2</sup>	[74]
Fe <sub>3</sub> S <sub>4</sub>	0.1 mol L <sup>-1</sup> HCl -0.40 V versus RHE	6.45	75.4 μg h <sup>-1</sup> mg <sup>-1</sup> <sub>cat</sub>	[76]
FeS <sub>x</sub>	0.1 mol L <sup>-1</sup> KOH -0.30 V versus RHE	17.6	4.13 × 10 <sup>-10</sup> mol s <sup>-1</sup> cm <sup>-2</sup>	[77]
Cu <sub>1.81</sub> S	0.1 mol L <sup>-1</sup> KOH -0.10 V versus RHE	14.1	2.19 μmol h <sup>-1</sup> cm <sup>-2</sup>	[79]
Fe-CuS/C	mol L <sup>-1</sup> KOH -0.60 V versus RHE	NI	42 μg h <sup>-1</sup> cm <sup>-2</sup>	[80]
Cu <sub>9</sub> S <sub>5</sub>	0.5 mol L <sup>-1</sup> Na <sub>2</sub> SO <sub>4</sub> -0.50 V versus RHE	NI	10.8 ± 0.4 μg/hcm <sup>2</sup>	[63]

NI: not informed

### 3.4 Transition Metal Phosphide-Based Catalysts

In recent years, transition metal phosphides have presented excellent performances for electroreduction reactions such as HER and CO<sub>2</sub> reduction [81–83] and in the last few years have been gaining attention for electrochemical ammonia synthesis due to their good electrical conductivity and high intrinsic activity. TMPs is a class of compounds in which phosphorous is combined with transition metals. Its distinct electronic structure is derived from the intrinsic charged character of metal (M<sup>δ+</sup>) and phosphorous (P<sup>δ-</sup>) [84, 85] good features for NRR-related intermediates adsorption [86]. Although, TMPs are potential candidates for NRR applications, limited N<sub>2</sub> and preferred H-adsorption severely affect their reaction rate and FE for aqueous NRR [86–88]. Thus, achieving a balance between the HER and NRR is important for obtaining higher faradaic efficiencies for ammonia electrosynthesis [87].

Among the TMPs applied to NRR, Co, Fe, and Mo-based phosphides have been extensively investigated. From a Density Functional Theory Study, Meng and co-workers [89] have shown that CoP is capable of efficiently driving NRR since the N<sub>2</sub> molecules can be strongly adsorbed on the CoP surface and it presents the lowest rate-determining step barrier of 0.724 eV in comparison with reported top-ranking electrocatalysts. The authors also modulated the CoP surface N<sub>2</sub> adsorption capacity by incorporating a hydrophobic layer and confinement of CoP nanoparticles in CNT structure. Moreover, those modifications resulted in an improvement of the Faradaic efficiency from 7.3% for the CoP nanoparticles up to 19.4% for the O-CoP/CNT heterostructure at  $-0.5$  V *versus* RHE.

The electrocatalytic performance of Fe-based phosphides for N<sub>2</sub> electroreduction was investigated by Wu and co-authors [90]. The results have shown that Fe<sub>2</sub>P monolayer presented certain activity towards NRR but required a high onset potential value of 0.48 V to drive the reaction while Fe<sub>3</sub>P monolayer proved to have low activity for the reaction. The authors also verified that the Mo-modified Fe<sub>2</sub>P and Fe<sub>3</sub>P monolayers presented a considerable decrease in the onset potentials to 0.3 and 0.17 V, respectively. Electronic analysis has shown that the heteroatom introduction contributed to N<sub>2</sub> activation by enhancing the degree of matching between the metal atoms and N<sub>2</sub> molecule orbitals. In addition, Luo and co-workers [91] have compared the catalytic activity of bare and Mo-doped FeP nanospheres in acidic electrolytes. Experimental results have shown that Mo-FeP nanospheres presented FE four times higher (7.49%) than the bare iron phosphide electrode. The metal-doping strategy was also used to improve the NRR activity of nickel phosphide nanosheets [92]. The Fe-NiP<sub>2</sub> catalyst presented NH<sub>3</sub> yield 12.2 times higher than pure NiP<sub>2</sub>. From theoretical calculations, it was verified that Fe-introduction lead to optimization of the active center and the electron configuration enhancing NRR efficiency. Another work that explores Fe-based phosphide for NRR was carried by Jiang and co-workers [93]. They reported self-supported Ni-Fe phosphide nanoplates for NRR under ambient conditions. The Ni-Fe-P nanoplates were synthesized by hydrothermal growth of LDHs followed by a low-temperature phosphidation. The catalyst exhibited high faradaic efficiency of 39.9% at  $-0.1$  V versus RHE in 0.1 mol L<sup>-1</sup> Na<sub>2</sub>SO<sub>4</sub> and NH<sub>3</sub>

yield of 16.40  $\mu\text{g h}^{-1} \text{mg}^{-1}_{\text{cat}}$ . The authors attributed the high activity for NRR to the nanostructure and the synergistic effect between Ni and Fe in the active sites.

Many efforts have been made for improving iron phosphide NRR efficiency by inhibiting HER at the catalyst surface. Xu and co-workers [94] built an octadecanethiol (C18) monolayer on Fe<sub>3</sub>P nanoarrays to enhance N<sub>2</sub> interaction and resist proton transfer. The C18@FeP electrocatalyst produced an NH<sub>3</sub> yield of  $1.80 \times 10^{-10} \text{ mol s}^{-1} \text{ cm}^{-2}$  at  $-0.3 \text{ V versus RHE}$  and FE of 11.22%, while the Fe<sub>3</sub>P material presents poor catalytic activity as predicted by Wu et al. [90]. Theoretical calculations suggest that the alkanethiol surface modification leads to in changes ate the reaction mechanism pathway from enzymatic to the consecutive and improved NRR selectivity. The hydrophobic surface coating also enhanced Mo<sub>3</sub>P<sub>4</sub> performance towards N<sub>2</sub> electroreduction. Lin and co-workers [95] have shown that fluorosilane (FAS) coating layer improves NRR efficiency 3.9 times higher in comparison with non-modified Mo<sub>3</sub>P<sub>4</sub> catalyst. The authors explained that FAS-modification weakens H absorption at the catalyst surface and prevents water from closing the electrocatalyst surface.

Investigations demonstrated that other transition metals-based phosphides are potential catalysts for N<sub>2</sub> electroreduction. Drawing on vanadium biological role in nitrogen fixation at nitrogenases [96], V-based catalysts have been explored for NRR [51, 97, 98]. In the work of Wei and co-workers [99], VP nanoparticles were in situ grown on V foil and evaluated as electrocatalysts for NH<sub>3</sub> synthesis. The electrochemical results showed that the VP catalyst produced an NH<sub>3</sub> yield of  $8.35 \times 10^{-11} \text{ mol s}^{-1} \text{ cm}^{-2}$  at  $0 \text{ V versus RHE}$  and FE of 22%. DFT studies demonstrated that the P insertion was beneficial for lowering the N<sub>2</sub> activation energy and accelerating the hydrogenation reaction. Arif and co-workers [100] studied the effect of growing NiFeV-layered double hydroxides (LDH) onto hollow CoVP in NH<sub>3</sub> production efficiency. From experimental tests, the authors observed greater faradaic efficiency (13.8%) for the NiFeV-LDH@CoVP heterostructure in comparison with the bare materials electrodes (CoVP—10.4% and NiFeV-LDH-3.1%). The authors explained that the enhancement at NRR performance can be attributed to some key factors such as the P insertion that weakens the N≡N bond, and to the hollow hierarchical structure that facilitates the access for the surface-active sites for the reactants. Yiran and co-workers [101] predicted by DFT and ab initio molecular dynamics simulation that two-dimensional pentagonal Ti, Zr, and Hf phosphides have improved the adsorption ability of N<sub>2</sub> at their surface. The strong adsorption occurs through the ‘acceptance-donation’ mechanism by the hybridization between transition metal-d and nitrogen- $\pi^*$  orbitals. The authors demonstrated that above the evaluated materials, Penta-TiP follows the distal-pathway mechanism and has the lowest overpotential of 0.56 eV for the RDS. A summary of the NH<sub>3</sub> production using transition metal phosphides and the most relevant experimental conditions reported in the literature is presented in Table 3.

**Table 3** Summary of reported transition metal phosphide-based catalysts reported in the literature for NRR under ambient conditions

Catalysts	Experimental conditions	FE (%)	NH <sub>3</sub> yield	References
O-CoP/CNT	0.1 mol L <sup>-1</sup> Na <sub>2</sub> SO <sub>4</sub> −0.5 V versus RHE	19.4	39.58 μg h <sup>-1</sup> mg <sup>-1</sup> <sub>cat</sub>	[89]
Mo-FeP	0.1 mol L <sup>-1</sup> HCl	7.94 (−0.2 V vs. RHE)	13.1 μg h <sup>-1</sup> mg <sup>-1</sup> <sub>cat</sub> (−0.3 V vs. RHE)	[91]
Fe-Ni <sub>2</sub> P	0.1 mol L <sup>-1</sup> HCl −0.3 V versus RHE	7.92	88.51 μg h <sup>-1</sup> mg <sup>-1</sup> <sub>cat</sub>	[92]
Ni <sub>12</sub> P <sub>5</sub> /FeP <sub>4</sub>	0.1 mol L <sup>-1</sup> Na <sub>2</sub> SO <sub>4</sub> −0.1 V versus RHE	39.9	3.08 × 10 <sup>-10</sup> mol s <sup>-1</sup> cm <sup>2</sup> (16.40 μg h <sup>-1</sup> mg <sup>-1</sup> <sub>cat</sub> )	[93]
C18@Fe <sub>3</sub> P	0.1 mol L <sup>-1</sup> Na <sub>2</sub> SO <sub>4</sub> −0.3 V vs RHE	11.22	8.35 × 10 <sup>-11</sup> mol s <sup>-1</sup> cm <sup>-2</sup>	[94]
Mo <sub>3</sub> P <sub>4</sub>	0.1 mol L <sup>-1</sup> PBS −0.2 V versus RHE	10.1	17.3 μg h <sup>-1</sup> mg <sup>-1</sup> <sub>cat</sub>	[95]
VP	0.1 mol L <sup>-1</sup> HCl 0 V versus RHE	22	8.35 × 10 <sup>-11</sup> mol s <sup>-1</sup> cm <sup>-2</sup>	[99]
NiFeV@CoVP	0.05 mol L <sup>-1</sup> H <sub>2</sub> SO <sub>4</sub> −0.3 V versus RHE	13.8	1.6 × 10 <sup>-6</sup> mol s <sup>-1</sup> cm <sup>-2</sup>	[100]

### 3.5 Rational Catalyst/Support Design

Density functional theory (DFT) calculations are a valuable tool for engineering catalysts that are stable, active and, selective for electrochemical ammonia synthesis, even when considering room temperature and ambient pressure. Skúlason and co-workers [102] studied the thermochemistry of cathodic reaction through DFT calculations to build a free energy profile for a range of transition metal nitrides, then allowing to predict the onset potential for each material for NRR. After considering conditions as catalyst poisoning, structural vacancies, and active crystalline facets, the authors found that the (100) planes of a fcc structure should be the most suitable, with VN, CrN, NbN, and ZrN catalysts being able to generate ammonia at −0.51 V, −0.76 V, −0.65 V and −0.76 V *versus* SHE, respectively. The free energy diagram for the

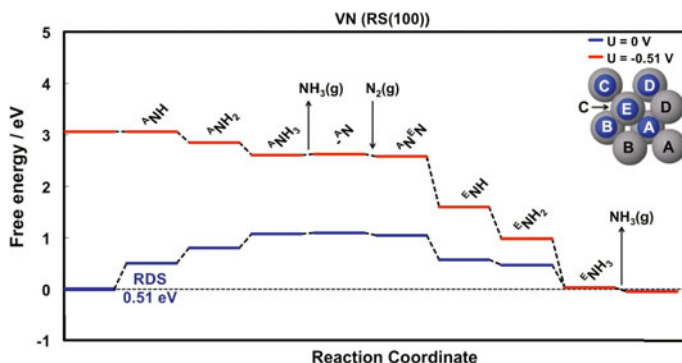


**Fig. 6** Free energy diagram for NH<sub>3</sub> formation via Mars-van Krevelen mechanism on the (100) facet of an fcc structure of VN. The blue line represents the free energy of all the stable intermediates calculated at zero potential while the red line represents the free energy of all the stable intermediates at the onset potential. Reprint with permission from Ref. [102], Copyright© 2015 Elsevier

material that showed the lowest onset potential (VN) is presented in Fig. 6, following the Mars-van Krevelen mechanism [103]. The rate determination step (RDS) for the ammonia electro-synthesis on VN is the first nitrogen atom protonation, with a Gibbs free energy of 0.51 eV. The results also indicate that hydrogen evolution should not compete with NRR, thus leading to a high yield process [104].

Besides vanadium nitride, this metal oxynitride (VON) also presented good activity towards electrochemical NRR [98]. First, computational methods evaluated the nitrogen reduction mechanism in VON considering how to improve activity and selectivity front of hydrogen evolution. One point to mention is the possibility of self-annihilation of the active sites, as the VON structure contains both oxygen and nitrogen anions at the subsurface. Nitrogen vacancies generated in the initial steps of the mechanism, and that directly influence the efficiency of the process can be replaced by the migration of the O or N anions. With a structure containing many oxygen vacancies (oxygen content about 12%), VON achieved a balance amongst the consecutive protonation preference at nitrogen sites over vanadium sites, allowing an onset potential of only 0.4 V *versus* RHE. On the contrary, for a structure with higher oxygen content (about 30%) and more nitrogen vacancies, the required overpotential increased about 0.2 V *versus* RHE in comparison to the previous structure, however presented the lowest energy barrier for N<sub>2</sub> adsorption/dissociation (~0.3 eV), thus leading this catalyst to a higher NH<sub>3</sub> turnover frequency, although with lower stability.

The rational catalyst design for electrochemical NRR is critical and very challenging, mainly due to the need to overcome competition with HER. However, defect engineering has proven to be useful to improve nitrogen adsorption, and, further reduction preferentially to hydrogen. Xiaohui and co-workers [105] presented a plasma-assisted synthesis of different noble metal phosphides (iridium, osmium, rhenium) with abundant surface step atoms. DFT calculations showed that reveal the defects (the low-coordinate step atoms on the edge) can lower the activation

energy for the NRR, achieving  $\text{NH}_3$  yields of  $94 \mu\text{g h}^{-1} \text{mg}^{-1}_{\text{cat}}$  for the iridium-based material. The plasma treatment exposed the  $\text{IrP}_2$  (313) crystal planes instead (111). The (111) index favors only  $\text{H}^+$  adsorption, preferentially leading to hydrogen evolution, otherwise, the (313) plane, in addition to the low coordinated step atoms favors dinitrogen adsorption, resulting in an exceptional catalyst for NRR.

The defect engineering in addition to surface functionalization helps to explain the activity of bidimensional materials as graphene derivatives and MXene-based materials. While MXenes usually exhibit poor catalytic activity towards NRR because their edges typically contain functional groups such as  $\text{OH}^*$  and  $\text{F}^*$  that mitigates the  $\text{N}_2$  adsorption at the active sites, the modification of surface termination of an MXene with an element such as iron, replaces the undesirable terminal groups, as well harshly reduced the surface work function. Lowering the work function increases the density-of-states near the Fermi level, and lowers the energy barrier for effective electron transfer to the absorbed dinitrogen molecule, thus improving the kinetics of the ammonia conversion reaction [106].

The engineering of efficient material architectures based on graphene, in turn, goes through defect engineering and surface functionalization, but also for hybrid materials (composites and heteroatom doping) [107]. N-doping in carbon nanomaterials, for example, may allow the obtention of a metal-free catalyst for NRR, where both pyrrolic and pyridinic sites favor the  $\text{N}_2$  adsorption during the  $\text{NH}_3$  conversion [108]. The graphene defects also can be very suitable for anchor transition metal single-atom and increase catalytic activity by changing the binding energies towards the graphene framework. This is an attractive approach, as long it enables the maximization of elemental utilization efficiency when compared with bulk materials [109, 110]. Different single-atom catalysts (SACs) from transition metal (*e.g.*, Ti) have shown free energy lower than ruthenium for NRR, which can be attributed to back-bonding amongst  $\pi^*$  orbital in  $^*\text{N}_2$  and the d-hybridized Ti orbital [111, 112]. Oschatz and collaborators reported an N-doped carbon nanomaterial containing Au single sites with enhanced performance in nitrogen electroreduction [113]. Even after six cycles of reuse, and at a potential of  $-0.2 \text{ V}$  versus RHE, the faradaic efficiency was about 12%, with an ammonia yield of  $2.32 \mu\text{g h}^{-1} \text{cm}^{-2}$ .

Graphitic carbon nitrides ( $\text{g-C}_3\text{N}_4$ ) configure another type of materials from the “graphene family”, that had been reported as a platform for single-atom stabilization. For nitrogen to ammonia conversion, these materials also had been exploited containing SACs from a range of transition metals [114]. Besides the  $\text{N}_2$  molecule adsorption being a primal factor for the effective ammonia generation, the stabilization of possible reaction intermediates ( $^*\text{NNH}$ ,  $^*\text{NNH}_2$ ,  $^*\text{N}$ ,  $^*\text{NH}$ , and  $^*\text{NH}_2$ ) is also fundamental for the consecutive protonation steps in the mechanism. The pyridinic and pyrrolic nitrogen present on the  $\text{g-C}_3\text{N}_4$  structure facilitate the above-mentioned  $\text{N}_2$  adsorption, while transition metals are suitable for the stabilization of the intermediate. The first protonation step in the NRR is usually the most difficult thermodynamically, with a free energy of about 1 eV for a Ru flat surface for example [45]. This free energy can be reduced to almost half in a  $\text{g-C}_3\text{N}_4$  containing Ru single-atom as demonstrated by Liu and co-workers (Fig. 7) [115]. In their work, the authors screened 20 metals from the 3, 4, and 5d block to explore the effect of the

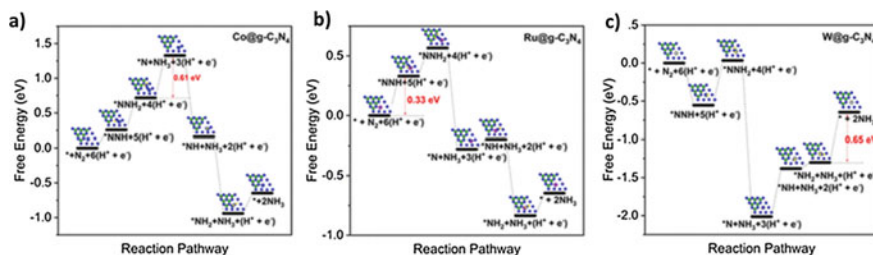


**Fig. 7** Free energy diagram of **a** Co@g-C<sub>3</sub>N<sub>4</sub>, **b** Ru@g-C<sub>3</sub>N<sub>4</sub>, and **c** W@g-C<sub>3</sub>N<sub>4</sub> for NRR through a distal pathway. Reprint with permission from Ref. [115], Copyright© 2019 American Chemical Society

studied metal on NRR, and the most promising were Co, Ru, and W with the lowest free energy for the reaction. The improved activity can be explained in terms of N-atom adsorption energy being changed due to the bonding/antibonding population of the metal center influence. Lastly, the ligand nature could strongly affect the NRR performance, by tuning the adsorption energy of the intermediates, when comparing g-C<sub>3</sub>N<sub>4</sub> with N-doped support.

## 4 Electrochemical Reactors Types for the N<sub>2</sub> Reduction Reaction

The electrochemical production of NH<sub>3</sub> under ambient conditions and heterogeneous catalysts have gained a real interest just in the twenty-first century with the development of different electrocatalytic reactors for liquid and solid electrolytes [22]. The success in the ammonia production laying in the design of a reaction system with an effective catalyst that is not just suitable for N<sub>2</sub> reduction reaction but also is able to minimize the HER [23, 116] and also, in the reactor configuration and its apparatuses, which includes electrolyte, nitrogen flow rate, temperature, etc. [24, 26]. This section will discuss the functionality and the differences among most known reaction systems for the electrocatalytic reduction of N<sub>2</sub>, including single-chamber cell, double-chamber cell, and back-to-back cell (Fig. 8).

The simplest and also first type [117] of reactor to be applied in the reduction of N<sub>2</sub> by electrochemical reaction is the one-compartment cell (or single chamber cell) represented in Fig. 8a. In this type of reactor, the counter and working electrode are in contact with the same electrolyte. The positive points of this configuration are the simplicity and the low cost of this design. There is no need for an exchange membrane or a specific structure of electrode for the reaction. On the other hand, both electrodes in the same compartment lead to a competition between the proton reduction to H<sub>2</sub> formation and the N<sub>2</sub> reduction [116] and, make possible the oxidation of the product NH<sub>3</sub> by the counter electrode [118]. In both cases, resulted in a decrease of



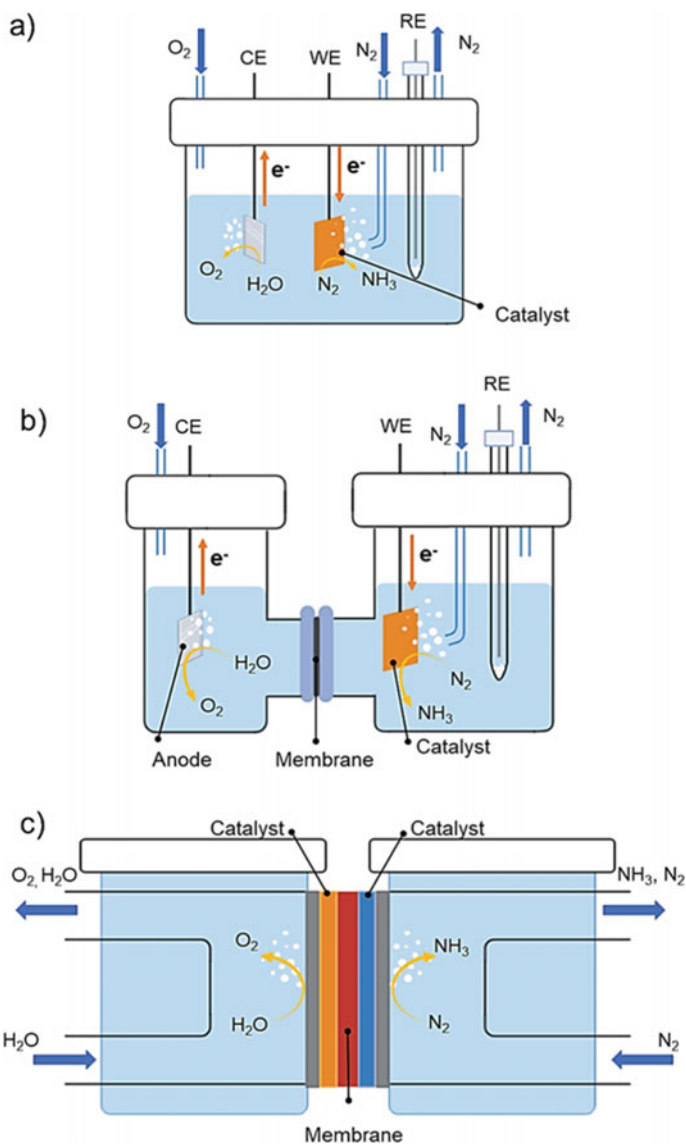


**Fig. 8** Schematic representation of **a** single chamber cell, **b** H-type cell and **c** back-to-back cell for electrochemical N<sub>2</sub> reduction reaction at ambient conditions. Adapted from Ref. [22]

the faradaic efficiency for the N<sub>2</sub> reduction reaction. Additionally, this configuration allows only mono experimental conditions [118].

The most common reactor for the N<sub>2</sub> reduction by electrocatalysis is the so-called two-compartment cell, or double chamber reactor, or H-type cell [2, 3, 27, 119–121] (Fig. 8b). In this configuration, the working and reference electrodes are placed in

one compartment while the counter-electrode is in the other compartment. There is more than 1 advantage of this configuration compared with the single chamber cell. Firstly the fact that two different electrolytes can be applied in the system, being practicable to choose the best electrolyte for both chambers separately [122], and also making possible the use of a gradient in the pH of those compartments, inducing the charge transfer [123]. Secondly, the possibility of the oxidation of the NH<sub>3</sub> formed in the cathodic chamber decreases. However, the migration of NH<sub>3</sub> through the Nafion membrane has been reported in the literature [124], indicating that both compartments should be analyzed.

The last reactor configuration that will be discussed here can be defined as a back-to-back cell, using usually a membrane electrode assembly (MEA) (Fig. 8c). In this type of reactor can be employed liquid electrolyte on both sides [122], liquid on one side and gas phase on the other one[3], or solid-state electrolyte on both sides [24], as it is schematically represented in Fig. 8c. The important point of this configuration is the two porous electrodes (anode and cathode), in general, a gas diffusion electrode (GDE), that are separated by proton (or anion) exchange membrane [22]. This configuration brings the possibility to develop both electrodes, cathode and anode, and that way, to obtain a pair of catalysts more suitable for the interest reaction with the opportunity to develop non-noble metals counter-electrodes. Moreover, the proximity of both electrodes reduces de charge transfer resistance of the electrochemical cell. Additionally, if the cathode has no contact with the liquid electrolyte, there is an inhibition of the H<sub>2</sub> competing reaction [116]. On the other hand, the absence of water can reduce the proton conductivity on the Nafion membrane decreasing the NH<sub>3</sub> production rate [22].

## 5 Conclusions and Future Perspectives

Human maintenance is based on the nitrogen cycle, however, natural N-containing sources alone, cannot supply all the modern human needs, and the industrial Haber-Bosch process of ammonia production, the most important source of nitrogen, presents higher energy consumption and huge production of greenhouse gases. In this sense, there is a race to obtain a clean route for N<sub>2</sub> reduction reaction producing ammonia with high yields. Regarding that, the use of electric energy from a sustainable source to promote the electrochemical NRR is one of the most promising routes to produce NH<sub>3</sub> at moderate temperature and atmospheric pressure, due to the necessity to overcome the large overpotential to activate the extremely stable N<sub>2</sub> molecule.

Undoubtedly the catalyst is the essential piece to obtain an efficient reduction of N<sub>2</sub> with high yields of NH<sub>3</sub>. There are many metals and metal oxides that can be applied with this target, mostly when the combination of them is investigated. It is possible to highlight the use of noble metals, transition metal oxides, phosphide, sulfide, nitrite, and carbon-based catalysts that were reported in the literature delivering motivating results for the synthesis of NH<sub>3</sub> under ambient conditions. However, it is worth paying

attention to the reactor setup that is employed for this reaction. The optimization of the experimental electrochemical parameters and an appropriate design of a reactional cell can improve the process and bring it more close to a large scale. For that, it is important that researchers and engineers join forces to develop the best system possible. It is also important to emphasize that theoretical calculations are helpful tools to predict the interaction of the catalyst with the  $N_2$  and to propose a mechanism for the reduction process.

Finally, from a future perspective, it is possible to predict that there will be a continuous development around the NRR and electrochemical reduction is one of the major candidate processes to replace the HBP. For that will be needed investment in green electrical energy sources, besides the search for a direct reduction of nitrogen from the air, once it is the most predominant element in the atmosphere, and using another proton font than water, which is also extremely necessary for the maintenance of human life. Taking into consideration an environmentally friendly process, the best option for the proton source should be an organic waste that could be oxidized in the anodic compartment if the reaction occurs in an H-type or back-to-back cell. If all those progress were made, the HBP may not be the oldest industrial process running for too long.

## References

1. van de Krol, R., Grätzel, M.: Photoelectrochemical Hydrogen Production. Springer US, Boston, MA (2012). <https://doi.org/10.1007/978-1-4614-1380-6>
2. Li, S.-J., Bao, D., Shi, M.-M., Wulan, B.-R., Yan, J.-M., Jiang, Q.: Amorphizing of Au nanoparticles by CeOx -RGO hybrid support towards highly efficient electrocatalyst for  $N_2$  reduction under ambient conditions. *Adv. Mater.* 1700001 (2017). <https://doi.org/10.1002/adma.201700001>
3. Chen, S., Perathoner, S., Ampelli, C., Mebrahtu, C., Su, D., Centi, G.: Electrocatalytic synthesis of ammonia at room temperature and atmospheric pressure from water and nitrogen on a carbon-nanotube-based electrocatalyst. *Angew. Chemie Int. Ed.* **56**, 2699–2703 (2017). <https://doi.org/10.1002/anie.201609533>
4. Montoya, J.H., Tsai, C., Vojvodic, A., Nørskov, J.K.: The challenge of electrochemical ammonia synthesis: a new perspective on the role of nitrogen scaling relations. *Chemsuschem* **8**, 2180–2186 (2015). <https://doi.org/10.1002/cssc.201500322>
5. Erisman, J.W., Sutton, M.A., Galloway, J., Klimont, Z., Winiwarter, W.: How a century of ammonia synthesis changed the world. *Nat. Geosci.* **1**, 636–639 (2008). <https://doi.org/10.1038/ngeo325>
6. Lindley, B.M., Appel, A.M., Krogh-Jespersen, K., Mayer, J.M., Miller, A.J.M.: Evaluating the thermodynamics of electrocatalytic  $N_2$  reduction in acetonitrile. *ACS Energy Lett.* 698–704 (2016). <https://doi.org/10.1021/acseenergylett.6b00319>
7. Service, R.F.: New recipe produces ammonia from air, water, and sunlight. *Science* (80-.) **345**, 610–610 (2014). <https://doi.org/10.1126/science.345.6197.610>
8. Ali, M., Zhou, F., Chen, K., Kotzur, C., Xiao, C., Bourgeois, L., Zhang, X., MacFarlane, D.R.: Nanostructured photoelectrochemical solar cell for nitrogen reduction using plasmon-enhanced black silicon. *Nat. Commun.* **7**, 11335 (2016). <https://doi.org/10.1038/ncomms11335>
9. Seefeldt, L.C., Hoffman, B.M., Dean, D.R.: *Electron Transf. Nitrogenase Catal.* (2012). <https://doi.org/10.1016/j.cbpa.2012.02.012>

10. Yandulov, D.V., Schrock, R.R.: Catalytic reduction of dinitrogen to ammonia at a single molybdenum center. *76* (2014). <https://doi.org/10.1126/science.1085326>
11. Arashiba, K., Eizawa, A., Tanaka, H., Nakajima, K., Yoshizawa, K., Nishibayashi, Y., Arashiba, K., Eizawa, A., Tanaka, H., Nakajima, K., Yoshizawa, K.: Catalytic nitrogen fixation via direct cleavage of nitrogen—nitrogen triple bond of molecular dinitrogen under ambient reaction conditions catalytic nitrogen fixation via direct cleavage of nitrogen—nitrogen triple bond of molecular dinitrogen under A (2017). <https://doi.org/10.1246/bcsj.20170197>
12. Zhou, F., Azofra, L.M., Ali, M., Kar, M., Simonov, A.N., McDonnell-Worth, C., Sun, C., Zhang, X., MacFarlane, D.R.: Electro-synthesis of ammonia from nitrogen at ambient temperature and pressure in ionic liquids. *Energy Environ. Sci.* **10**, 2516–2520 (2017). <https://doi.org/10.1039/C7EE02716H>
13. Licht, S., Cui, B., Wang, B., Li, F.F., Lau, J., Liu, S. Ammonia synthesis by N<sub>2</sub> and steam electrolysis in molten hydroxide suspensions of nanoscale Fe<sub>2</sub>O<sub>3</sub>. *Science* (80-.), **345** 637–640 (2014). <https://doi.org/10.1126/science.1254234>
14. Bard, A.J., Faulkner, L.R.: *Electrochemical Methods: Fundamentals and Applications*, 2nd edn. John Wiley & Sons, Inc (2004). <https://doi.org/10.1016/j.aca.2010.06.020>
15. Atkins, P.: J, 9th edn. de Paula, *Physical Chemistry* (2010)
16. Castellan, G.W.: *Physical Chemistry*, 3rd edn. (1983)
17. Liu, H., Wei, L., Liu, F., Pei, Z., Shi, J., Wang, Z.J., He, D., Chen, Y.: Homogeneous, heterogeneous, and biological catalysts for electrochemical N<sub>2</sub> reduction toward NH<sub>3</sub> under ambient conditions. *ACS Catal.* 5245–5267 (2019). <https://doi.org/10.1021/acscatal.9b00994>
18. Tang, C., Qiao, S.-Z.: How to explore ambient electrocatalytic nitrogen reduction reliably and insightfully. *Chem. Soc. Rev.* **48**, 3166–3180 (2019). <https://doi.org/10.1039/C9CS00280D>
19. Howalt, J.G., Bligaard, T., Rossmeisl, J., Vegge, T.: DFT based study of transition metal nano-clusters for electrochemical NH<sub>3</sub> production. *Phys. Chem. Chem. Phys.* **15**, 7785–7795 (2013). <https://doi.org/10.1039/c3cp44641g>
20. Pang, Y., Su, C., Jia, G., Xu, L., Shao, Z.: Emerging two-dimensional nanomaterials for electrochemical nitrogen reduction. *Chem. Soc. Rev.* **50**, 12744–12787 (2021). <https://doi.org/10.1039/d1cs00120e>
21. Jia, H.P., Quadrelli, E.A.: Mechanistic aspects of dinitrogen cleavage and hydrogenation to produce ammonia in catalysis and organometallic chemistry: relevance of metal hydride bonds and dihydrogen. *Chem. Soc. Rev.* **43**, 547–564 (2014). <https://doi.org/10.1039/c3cs60206k>
22. Cui, X., Tang, C., Zhang, Q.: A review of electrocatalytic reduction of dinitrogen to ammonia under ambient conditions. *Adv. Energy Mater.* **8**, 1800369 (2018). <https://doi.org/10.1002/aenm.201800369>
23. Li, M., Liu, X., Wang, L., Hou, F., Dou, S.X., Liang, J.: Rational design on photo(electro)catalysts for artificial nitrogen looping. *EcoMat.* **3**, 1–26 (2021). <https://doi.org/10.1002/eom2.12096>
24. Kyriakou, V., Garagounis, I., Vasileiou, E., Vourros, A., Stoukides, M.: Progress in the electrochemical synthesis of ammonia. *Catal. Today.* **286**, 2–13 (2017). <https://doi.org/10.1016/j.cattod.2016.06.014>
25. Guo, C., Ran, J., Vasileff, A., Qiao, S.Z.: Rational design of electrocatalysts and photo(electro)catalysts for nitrogen reduction to ammonia (NH<sub>3</sub>) under ambient conditions. *Energy Environ. Sci.* **11**, 45–56 (2018). <https://doi.org/10.1039/c7ee02220d>
26. Shipman, M.A., Symes, M.D.: Recent progress towards the electrosynthesis of ammonia from sustainable resources. *Catal. Today.* **286**, 57–68 (2017). <https://doi.org/10.1016/j.cattod.2016.05.008>
27. Jin, H., Li, L., Liu, X., Tang, C., Xu, W., Chen, S., Song, L., Zheng, Y., Qiao, S.Z.: Nitrogen vacancies on 2D layered W<sub>2</sub>N<sub>3</sub>: a stable and efficient active site for nitrogen reduction reaction. *Adv. Mater.* **31**, 1–8 (2019). <https://doi.org/10.1002/adma.201902709>
28. Wang, S., Shi, L., Bai, X., Li, Q., Ling, C., Wang, J.: Highly efficient photo-/electrocatalytic reduction of nitrogen into ammonia by dual-metal sites. *ACS Cent. Sci.* **6**, 1762–1771 (2020). <https://doi.org/10.1021/acscentsci.0c00552>

29. Wang, M., Liu, S., Qian, T., Liu, J., Zhou, J., Ji, H., Xiong, J., Zhong, J., Yan, C.: Over 56.55% Faradaic efficiency of ambient ammonia synthesis enabled by positively shifting the reaction potential. *Nat. Commun.* **10**, 1–8 (2019). <https://doi.org/10.1038/s41467-018-08120-x>
30. Höskuldsson, Á.B., Abghoui, Y., Gunnarsdóttir, A.B., Skúlason, E.: Computational screening of rutile oxides for electrochemical ammonia formation. *ACS Sustain. Chem. Eng.* **5**, 10327–10333 (2017). <https://doi.org/10.1021/acssuschemeng.7b02379>
31. Köleli, F., Röpke, D., Aydın, R., Röpke, T.: Investigation of N<sub>2</sub>-fixation on polyaniline electrodes in methanol by electrochemical impedance spectroscopy. *J. Appl. Electrochem.* **41**, 405–413 (2011). <https://doi.org/10.1007/s10800-010-0250-3>
32. Murakami, T., Nishikiori, T., Nohira, T., Ito, Y.: Electrolytic synthesis of ammonia in molten salts under atmospheric pressure. *J. Am. Chem. Soc.* **125**, 334–335 (2003). <https://doi.org/10.1021/ja028891t>
33. Pappenfus, T.M., Lee, K., Thoma, L.M., Dukart, C.R.: Wind to ammonia: electrochemical processes in room temperature ionic liquids. *ECS Trans.* **16**, 89–93 (2019). <https://doi.org/10.1149/1.3159311>
34. Foster, S.L., Bakovic, S.I.P., Duda, R.D., Maheshwari, S., Milton, R.D., Minter, S.D., Janik, M.J., Renner, J.N., Greenlee, L.F.: Catalysts for nitrogen reduction to ammonia. *Nat. Catal.* **1**, 490–500 (2018). <https://doi.org/10.1038/s41929-018-0092-7>
35. Nazemi, M., El-Sayed, M.A.: The role of oxidation of silver in bimetallic gold-silver nanocages on electrocatalytic activity of nitrogen reduction reaction. *J. Phys. Chem. C.* **123**, 11422–11427 (2019). <https://doi.org/10.1021/acs.jpcc.9b01107>
36. Zhang, J., Zhao, B., Liang, W., Zhou, G., Liang, Z., Wang, Y., Qu, J., Sun, Y., Jiang, L.: Three-phase electrolysis by gold nanoparticle on hydrophobic interface for enhanced electrochemical nitrogen reduction reaction. *Adv. Sci.* **7**, 2002630 (2020). <https://doi.org/10.1002/advs.202002630>
37. Y. Qu, T. Dai, Y. Cui, Y. Zhang, Z. Wang, Q. Jiang, Tailoring electronic structure of copper nanosheets by silver doping toward highly efficient electrochemical reduction of nitrogen to ammonia, *Chem. Eng. J.* (2021) 133752. <https://doi.org/10.1016/j.cej.2021.133752>.
38. Nazemi, M., El-Sayed, M.A.: Electrochemical synthesis of ammonia from N<sub>2</sub> and H<sub>2</sub>O under ambient conditions using pore-size-controlled hollow gold nanocatalysts with tunable plasmonic properties. *J. Phys. Chem. Lett.* **9**, 5160–5166 (2018). <https://doi.org/10.1021/acs.jpclett.8b02188>
39. Wang, Z., Li, Y., Yu, H., Xu, Y., Xue, H., Li, X., Wang, H., Wang, L.: Ambient electrochemical synthesis of ammonia from nitrogen and water catalyzed by flower-like gold microstructures. *Chemsuschem* **11**, 3480–3485 (2018). <https://doi.org/10.1002/cssc.201801444>
40. Yang, Y., Wang, S., Wen, H., Ye, T., Chen, J., Li, C., Du, M.: Nanoporous gold embedded ZIF composite for enhanced electrochemical nitrogen fixation. *Angew. Chemie Int. Ed.* **58**, 15362–15366 (2019). <https://doi.org/10.1002/anie.201909770>
41. Yao, Y., Zhu, S., Wang, H., Li, H., Shao, M.: A spectroscopic study on the nitrogen electrochemical reduction reaction on gold and platinum surfaces. *J. Am. Chem. Soc.* **140**, 1496–1501 (2018). <https://doi.org/10.1021/jacs.7b12101>
42. Xu, T., Liang, J., Li, S., Xu, Z., Yue, L., Li, T., Luo, Y., Liu, Q., Shi, X., Asiri, A.M., Yang, C., Sun, X.: Recent advances in nonprecious metal oxide electrocatalysts and photocatalysts for N<sub>2</sub> reduction reaction under ambient condition. *Small Sci.* **1**, 2000069 (2021). <https://doi.org/10.1002/smssc.202000069>
43. Xiao, L., Zhu, S., Liang, Y., Li, Z., Wu, S., Luo, S., Chang, C., Cui, Z.: Nanoporous nickel-molybdenum oxide with an oxygen vacancy for electrocatalytic nitrogen fixation under ambient conditions. *ACS Appl. Mater. Interfaces* **13**, 30722–30730 (2021). <https://doi.org/10.1021/acsmi.1c07613>
44. Wang, Y., Ren, B., Zhen Ou, J., Xu, K., Yang, C., Li, Y., Zhang, H.: Engineering two-dimensional metal oxides and chalcogenides for enhanced electro- and photocatalysis. *Sci. Bull.* **66**, 1228–1252 (2021). <https://doi.org/10.1016/j.scib.2021.02.007>
45. Skúlason, E., Bligaard, T., Gudmundsdóttir, S., Studt, F., Rossmeisl, J., Abild-Pedersen, F., Vegge, T., Jónsson, H., Nørskov, J.K.: A theoretical evaluation of possible transition metal

- electro-catalysts for N<sub>2</sub> reduction. *Phys. Chem. Chem. Phys.* **14**, 1235–1245 (2012). <https://doi.org/10.1039/C1CP22271F>
46. Yang, L., Wu, T., Zhang, R., Zhou, H., Xia, L., Shi, X., Zheng, H., Zhang, Y., Sun, X.: Insights into defective TiO<sub>2</sub> in electrocatalytic N<sub>2</sub> reduction: combining theoretical and experimental studies. *Nanoscale* **11**, 1555–1562 (2019). <https://doi.org/10.1039/c8nr09564g>
  47. Fang, C., Bi, T., Xu, X., Yu, N., Cui, Z., Jiang, R., Geng, B.: Oxygen vacancy-enhanced electrocatalytic performances of TiO<sub>2</sub> nanosheets toward N<sub>2</sub> reduction reaction. *Adv. Mater. Interfaces* **6**, 2–7 (2019). <https://doi.org/10.1002/admi.201901034>
  48. Han, J., Liu, Z., Ma, Y., Cui, G., Xie, F., Wang, F., Wu, Y., Gao, S., Xu, Y., Sun, X.: Ambient N<sub>2</sub> fixation to NH<sub>3</sub> at ambient conditions: Using Nb<sub>2</sub>O<sub>5</sub> nanofiber as a high-performance electrocatalyst. *Nano Energy* **52**, 264–270 (2018). <https://doi.org/10.1016/j.nanoen.2018.07.045>
  49. Kong, W., Liu, Z., Han, J., Xia, L., Wang, Y., Liu, Q., Shi, X., Wu, Y., Xu, Y., Sun, X.: Ambient electrochemical N<sub>2</sub>-to-NH<sub>3</sub> fixation enabled by Nb<sub>2</sub>O<sub>5</sub> nanowire array. *Inorg. Chem. Front.* **6**, 423–427 (2019). <https://doi.org/10.1039/c8qi01049h>
  50. Wang, J., Li, G., Wei, T., Zhou, S., Ji, X., Liu, X.: Dopant-site lattice turbulence of Cu-substituted Nb<sub>2</sub>O<sub>5</sub> for efficient nitrogen electroreduction. *Nanoscale* **13**, 3036–3041 (2021). <https://doi.org/10.1039/d0nr07885a>
  51. Fang, W., Zhao, J., Wu, T., Huang, Y., Yang, L., Liu, C., Zhang, Q., Huang, K., Yan, Q.: Hydrophilic engineering of VOx-based nanosheets for ambient electrochemical ammonia synthesis at neutral pH. *J. Mater. Chem. A* **8**, 5913–5918 (2020). <https://doi.org/10.1039/D0TA00676A>
  52. Santos, H.L.S., Corradini, P.G., Medina, M., Dias, J.A., Mascaro, L.H.: NiMo-NiCu inexpensive composite with high activity for hydrogen evolution reaction (2020). <https://doi.org/10.1021/acscami.0c00262>
  53. Chu, K., Li, Q.Q., Cheng, Y.H., Liu, Y.P.: Efficient electrocatalytic nitrogen fixation on FeMoO<sub>4</sub> nanorods. *ACS Appl. Mater. Interfaces* **12**, 11789–11796 (2020). <https://doi.org/10.1021/acscami.0c00860>
  54. Chu, K., ping Liu, Y., biao Li, Y., li Guo, Y., Tian, Y., Zhang, H.: Multi-functional Mo-doping in MnO<sub>2</sub> nanoflowers toward efficient and robust electrocatalytic nitrogen fixation. *Appl. Catal. B Environ.* **264** (2020). <https://doi.org/10.1016/j.apcatb.2019.118525>
  55. Xing, Z., Kong, W., Wu, T., Xie, H., Wang, T., Luo, Y., Shi, X., Asiri, A.M., Zhang, Y., Sun, X.: Hollow Bi<sub>2</sub>MoO<sub>6</sub> sphere effectively catalyzes the ambient electroreduction of N<sub>2</sub> to NH<sub>3</sub>. *ACS Sustain. Chem. Eng.* **7**, 12692–12696 (2019). <https://doi.org/10.1021/acssuschemeng.9b03141>
  56. Wang, J., Jang, H., Li, G., Kim, M.G., Wu, Z., Liu, X., Cho, J.: Efficient electrocatalytic conversion of N<sub>2</sub> to NH<sub>3</sub> on NiWO<sub>4</sub> under ambient conditions. *Nanoscale* **12**, 1478–1483 (2020). <https://doi.org/10.1039/c9nr08777j>
  57. Dong, W., Chen, X., Peng, J., Liu, W., Jin, X., Ni, G., Liu, Z.: Recent progress on 2D transition metal compounds-based electrocatalysts for efficient nitrogen reduction. *Chem. Res. Chinese Univ.* **36**, 648–661 (2020). <https://doi.org/10.1007/s40242-020-0171-6>
  58. Xue, Z., Zhang, X., Qin, J., Liu, R.: High-throughput identification of high activity and selectivity transition metal single-atom catalysts for nitrogen reduction. *Nano Energy* **80**, 105527 (2021). <https://doi.org/10.1016/j.nanoen.2020.105527>
  59. Shi, J.L., Xiang, S.Q., Zhang, W., Bin Zhao, L.: A thermodynamic and kinetic study of the catalytic performance of Fe, Mo, Rh and Ru for the electrochemical nitrogen reduction reaction. *Phys. Chem. Chem. Phys.* **22**, 25973–25981 (2020). <https://doi.org/10.1039/d0cp05072e>
  60. Yang, D., Chen, T., Wang, Z.: Electrochemical reduction of aqueous nitrogen (N<sub>2</sub>) at a low overpotential on (110)-oriented Mo nanofilm. *J. Mater. Chem. A* **5**, 18967–18971 (2017). <https://doi.org/10.1039/c7ta06139k>
  61. Li, X., Li, T., Ma, Y., Wei, Q., Qiu, W., Guo, H., Shi, X., Zhang, P., Asiri, A.M., Chen, L., Tang, B., Sun, X.: Boosted electrocatalytic N<sub>2</sub> reduction to NH<sub>3</sub> by defect-rich MoS<sub>2</sub> nanoflower 13021 (2018)

62. Ma, B., Zhao, H., Li, T., Liu, Q., Luo, Y., Li, C., Lu, S., Asiri, A.M., Ma, D., Sun, X.: Iron-group electrocatalysts for ambient nitrogen reduction reaction in aqueous media. *Nano Res.* **14**, 555–569 (2021). <https://doi.org/10.1007/s12274-020-3049-5>
63. Kim, H.S., Choi, J., Kong, J., Kim, H., Yoo, S.J., Park, H.S.: Regenerative electrocatalytic redox cycle of copper sulfide for sustainable  $\text{NH}_3$  production under ambient conditions. *ACS Catal.* **11**, 435–445 (2021). <https://doi.org/10.1021/acscatal.0c03985>
64. Abghoui, Y., Sigtryggsson, S.B., Skúlason, E.: Biomimetic nitrogen fixation catalyzed by transition metal sulfide surfaces in an electrolytic cell. *Chemsuschem* **12**, 4265–4273 (2019). <https://doi.org/10.1002/cssc.201901429>
65. Lu, Q., Yu, Y., Ma, Q., Chen, B., Zhang, H.: 2D Transition-metal-dichalcogenide-nanosheet-based composites for photocatalytic and electrocatalytic hydrogen evolution reactions. *Adv. Mater.* **28**, 1917–1933 (2016). <https://doi.org/10.1002/adma.201503270>
66. Matanovic, I., Leung, K., Percival, S.J., Park, J.E., Lu, P., Atanassov, P., Chou, S.S.: Towards defect engineering in hexagonal  $\text{MoS}_2$  nanosheets for tuning hydrogen evolution and nitrogen reduction reactions. *Appl. Mater. Today.* **21**, 100812 (2020). <https://doi.org/10.1016/j.apmt.2020.100812>
67. Zhang, L., Ji, X., Ren, X., Ma, Y., Shi, X., Tian, Z., Asiri, A.M., Chen, L., Tang, B., Sun, X.: Electrochemical ammonia synthesis via nitrogen reduction reaction on a  $\text{MoS}_2$  catalyst: theoretical and experimental studies. *Adv. Mater.* **30**, 2–7 (2018). <https://doi.org/10.1002/adma.201800191>
68. Ma, C., Zhai, N., Liu, B., Yan, S.: Defected  $\text{MoS}_2$ : an efficient electrochemical nitrogen reduction catalyst under mild conditions. *Electrochim. Acta.* **370**, 137695 (2021). <https://doi.org/10.1016/j.electacta.2020.137695>
69. Chu, K., Nan, H., Li, Q., Guo, Y., Tian, Y., Liu, W.: Amorphous  $\text{MoS}_3$  enriched with sulfur vacancies for efficient electrocatalytic nitrogen reduction. *J. Energy Chem.* **53**, 132–138 (2020). <https://doi.org/10.1016/j.jechem.2020.04.074>
70. Li, X., Ren, X., Liu, X., Zhao, J., Sun, X., Zhang, Y., Kuang, X., Yan, T., Wei, Q., Wu, D.: A  $\text{MoS}_2$  nanosheet-reduced graphene oxide hybrid: an efficient electrocatalyst for electrocatalytic  $\text{N}_2$  reduction to  $\text{NH}_3$  under ambient conditions. *J. Mater. Chem. A.* **7**, 2524–2528 (2019). <https://doi.org/10.1039/c8ta10433f>
71. Lv, R., Robinson, J.A., Schaak, R.E., Sun, D., Sun, Y., Mallouk, T.E., Terrones, M.: Transition metal dichalcogenides and beyond: synthesis, properties, and applications of single- and few-layer nanosheets. *Acc. Chem. Res.* **48**, 56–64 (2015). <https://doi.org/10.1021/ar5002846>
72. Chu, K., Liu, Y.P., Li, Y.B., Guo, Y.L., Tian, Y.: Two-dimensional (2D)/2D interface engineering of a  $\text{MoS}_2/\text{C}_3\text{N}_4$  heterostructure for promoted electrocatalytic nitrogen fixation. *ACS Appl. Mater. Interfaces* **12**, 7081–7090 (2020). <https://doi.org/10.1021/acsami.9b18263>
73. Jiang, T., Li, L., Li, L., Liu, Y., Zhang, D., Zhang, D., Li, H., Mao, B., Shi, W.: Ultra-thin shelled  $\text{Cu}_2\text{-xS}/\text{MoS}_2$  quantum dots for enhanced electrocatalytic nitrogen reduction. *Chem. Eng. J.* **426**, 130650 (2021). <https://doi.org/10.1016/j.cej.2021.130650>
74. Patil, S.B., Chou, H.L., Chen, Y.M., Hsieh, S.H., Chen, C.H., Chang, C.C., Li, S.R., Lee, Y.C., Lin, Y.S., Li, H., Chang, Y.J., Lai, Y.H., Wang, D.Y.: Enhanced  $\text{N}_2$  affinity of 1T- $\text{MoS}_2$  with a unique pseudo-six-membered ring consisting of N-Li-S-Mo-S-Mo for high ambient ammonia electrosynthesis performance. *J. Mater. Chem. A.* **9**, 1230–1239 (2021). <https://doi.org/10.1039/d0ta10696h>
75. Buscagan, T.M., Oyala, P.H., Peters, J.C.:  $\text{N}_2$ -to- $\text{NH}_3$  conversion by a triphos-iron catalyst and enhanced turnover under photolysis. *Angew. Chemie - Int. Ed.* **56**, 6921–6926 (2017). <https://doi.org/10.1002/anie.201703244>
76. Zhao, X., Lan, X., Yu, D., Fu, H., Liu, Z., Mu, T.: Deep eutectic-solvothermal synthesis of nanostructured  $\text{Fe}_3\text{S}_4$  for electrochemical  $\text{N}_2$  fixation under ambient conditions. *Chem. Commun.* **54**, 13010–13013 (2018). <https://doi.org/10.1039/c8cc08045c>
77. Xiong, W., Guo, Z., Zhao, S., Wang, Q., Xu, Q., Wang, X.: Facile, cost-effective plasma synthesis of self-supportive  $\text{FeS}$ : X on Fe foam for efficient electrochemical reduction of  $\text{N}_2$  under ambient conditions. *J. Mater. Chem. A.* **7**, 19977–19983 (2019). <https://doi.org/10.1039/c9ta07790a>

78. Raugei, S., Seefeldt, L.C., Hoffman, B.M.: Critical computational analysis illuminates the reductive-elimination mechanism that activates nitrogenase for N<sub>2</sub> reduction. *Proc. Natl. Acad. Sci. U. S. A.* **115**, E10521–E10530 (2018). <https://doi.org/10.1073/pnas.1810211115>
79. Kim, M.C., Nam, H., Choi, J., Kim, H.S., Lee, H.W., Kim, D., Kong, J., Han, S.S., Lee, S.Y., Park, H.S.: Hydrogen bonding-mediated enhancement of bioinspired electrochemical nitrogen reduction on Cu<sub>2</sub>-xS catalysts. *ACS Catal.* **10**, 10577–10584 (2020). <https://doi.org/10.1021/acscatal.0c01730>
80. Kong, J., Kim, M.S., Akbar, R., Park, H.Y., Jang, J.H., Kim, H., Hur, K., Park, H.S.: Electrochemical nitrogen reduction kinetics on a copper sulfide catalyst for NH<sub>3</sub> synthesis at low temperature and atmospheric pressure. *ACS Appl. Mater. Interfaces* (2021). <https://doi.org/10.1021/acsami.1c00850>
81. Theerthagiri, J., Murthy, A.P., Lee, S.J., Karupphasamy, K., Arumugam, S.R., Yu, Y., Hanafiah, M.M., Kim, H.S., Mittal, V., Choi, M.Y.: Recent progress on synthetic strategies and applications of transition metal phosphides in energy storage and conversion. *Ceram. Int.* **47**, 4404–4425 (2021). <https://doi.org/10.1016/j.ceramint.2020.10.098>
82. Pu, Z., Liu, T., Amiin, I.S., Cheng, R., Wang, P., Zhang, C., Ji, P., Hu, W., Liu, J., Mu, S.: Transition-metal phosphides: activity origin, energy-related electrocatalysis applications, and synthetic strategies. *Adv. Funct. Mater.* **30**, 1–23 (2020). <https://doi.org/10.1002/adfm.202004009>
83. Li, Y., Dong, Z., Jiao, L.: Multifunctional transition metal-based phosphides in energy-related electrocatalysis. *Adv. Energy Mater.* **10**, 1–36 (2020). <https://doi.org/10.1002/aenm.201902104>
84. Laursen, A.B., Wexler, R.B., Whitaker, M.J., Izett, E.J., Calvino, K.U.D., Hwang, S., Rucker, R., Wang, H., Li, J., Garfunkel, E., Greenblatt, M., Rappe, A.M., Dismukes, G.C.: Climbing the volcano of electrocatalytic activity while avoiding catalyst corrosion: Ni<sub>3</sub>P, a hydrogen evolution electrocatalyst stable in both acid and alkali. *ACS Catal.* **8**, 4408–4419 (2018). <https://doi.org/10.1021/acscatal.7b04466>
85. Li, Y., Li, R., Wang, D., Xu, H., Meng, F., Dong, D., Jiang, J., Zhang, J., An, M., Yang, P.: A review: target-oriented transition metal phosphide design and synthesis for water splitting. *Int. J. Hydrogen Energy.* **46**, 5131–5149 (2021). <https://doi.org/10.1016/j.ijhydene.2020.11.030>
86. Chanda, D., Xing, R., Xu, T., Liu, Q., Luo, Y., Liu, S., Tufa, R.A., Dolla, T.H., Montini, T., Sun, X.: Electrochemical nitrogen reduction: recent progress and prospects. *Chem. Commun.* **57**, 7335–7349 (2021). <https://doi.org/10.1039/d1cc01451j>
87. Chen, J., Cheng, H., Ding, L.X., Wang, H.: Competing hydrogen evolution reaction: a challenge in electrocatalytic nitrogen fixation. *Mater. Chem. Front.* **5**, 5954–5969 (2021). <https://doi.org/10.1039/d1qm00546d>
88. Li, J., Wei, F., Dong, C., Wang, Z., Xiu, Z., Han, X.: Recent progress of inorganic metal-based catalysts in electrocatalytic synthesis of ammonia. *Mater. Today Energy.* **21** (2021). <https://doi.org/10.1016/j.mtener.2021.100766>
89. Meng, Q., Hou, Y., Yang, F., Cao, C., Zou, Z., Luo, J., Zhou, W., Tong, Z., Chen, S., Zhou, S., Wang, J., Deng, S.: Modulation of surface properties on cobalt phosphide for high-performance ambient ammonia electrosynthesis. *Appl. Catal. B Environ.* **303**, 120874 (2021). <https://doi.org/10.1016/j.apcatb.2021.120874>
90. Wu, J., Li, J., Yu, Y.: Highly stable Mo-doped Fe<sub>2</sub>P and Fe<sub>3</sub>P monolayers as low-onset-potential electrocatalysts for nitrogen fixation†, *Catal. Sci. Technol.* **11**, 1419–1429 (2021). <https://doi.org/10.1039/d0cy02192j>
91. Luo, Y.X., Bin Qiu, W., Liang, R.P., Xia, X.H., Qiu, J.D.: Mo-doped FeP nanospheres for artificial nitrogen fixation. *ACS Appl. Mater. Interfaces* **12**, 17452–17458 (2020). <https://doi.org/10.1021/acsami.0c00011>
92. Guo, C., Liu, X., Gao, L., Kuang, X., Ren, X., Ma, X., Zhao, M., Yang, H., Sun, X., Wei, Q.: Fe-doped Ni<sub>2</sub>P nanosheets with porous structure for electroreduction of nitrogen to ammonia under ambient conditions. *Appl. Catal. B Environ.* **263** (2020). <https://doi.org/10.1016/j.apcatb.2019.118296>



93. Jiang, X., He, M., Tang, M., Zheng, Q., Xu, C., Lin, D.: Nanostructured bimetallic Ni–Fe phosphide nanoplates as an electrocatalyst for efficient N<sub>2</sub> fixation under ambient conditions. *J. Mater. Sci.* **55**, 15252–15262 (2020). <https://doi.org/10.1007/s10853-020-05085-5>
94. Xu, T., Liang, J., Wang, Y., Li, S., Du, Z., Li, T., Liu, Q., Luo, Y., Zhang, F., Shi, X., Tang, B., Kong, Q., Asiri, A.M., Yang, C., Ma, D., Sun, X.: Enhancing electrocatalytic N<sub>2</sub>-to-NH<sub>3</sub> fixation by suppressing hydrogen evolution with alkythiols modified Fe<sub>3</sub>P nanoarrays. *Nano Res.* **12** (2021). <https://doi.org/10.1007/s12274-021-3592-8>
95. Xiao, L., Zhu, S., Liang, Y., Li, Z., Wu, S., Luo, S., Chang, C., Cui, Z.: Effects of hydrophobic layer on selective electrochemical nitrogen fixation of self-supporting nanoporous Mo<sub>4</sub>P<sub>3</sub> catalyst under ambient conditions. *Appl. Catal. B Environ.* **286**, 119895 (2021). <https://doi.org/10.1016/j.apcatb.2021.119895>
96. Tanabe, Y., Nishibayashi, Y.: Recent advances in nitrogen fixation upon vanadium complexes. *Coord. Chem. Rev.* **381**, 135–150 (2019). <https://doi.org/10.1016/j.ccr.2018.11.005>
97. Chang, B., Deng, L., Wang, S., Shi, D., Ai, Z., Jiang, H.: A vanadium–nickel oxynitride layer for enhanced electrocatalytic nitrogen fixation in neutral media 91–96 (2020). <https://doi.org/10.1039/c9ta11378a>
98. Pan, J., Hansen, H.A., Vegge, T.: Vanadium oxynitrides as stable catalysts for electrochemical reduction of nitrogen to ammonia: the role of oxygen. *J. Mater. Chem. A.* **8**, 24098–24107 (2020). <https://doi.org/10.1039/D0TA08313E>
99. Wei, P., Geng, Q., Channa, A.I., Tong, X., Luo, Y., Lu, S., Chen, G., Gao, S., Wang, Z., Sun, X.: Electrocatalytic N<sub>2</sub> reduction to NH<sub>3</sub> with high Faradaic efficiency enabled by vanadium phosphide nanoparticle on V foil. *Nano Res.* **13**, 2967–2972 (2020). <https://doi.org/10.1007/s12274-020-2956-9>
100. Arif, M., Yasin, G., Luo, L., Ye, W., Mushtaq, M.A., Fang, X., Xiang, X., Ji, S., Yan, D.: Hierarchical hollow nanotubes of NiFeV-layered double hydroxides@CoVP heterostructures towards efficient, pH-universal electrocatalytic nitrogen reduction reaction to ammonia. *Appl. Catal. B Environ.* **265**, 118559 (2020). <https://doi.org/10.1016/j.apcatb.2019.118559>
101. Ying, Y., Fan, K., Luo, X., Huang, H.: Predicting two-dimensional pentagonal transition metal monophosphides for efficient electrocatalytic nitrogen reduction †. *J. Mater. Chem. A.* **7**, 11444–11451 (2019). <https://doi.org/10.1039/C8TA11605A>
102. Abghoui, Y., Skúlason, E.: Transition metal nitride catalysts for electrochemical reduction of nitrogen to ammonia at ambient conditions. *Proc. Comput. Sci.* **51**, 1897–1906 (2015). <https://doi.org/10.1016/j.procs.2015.05.433>
103. Vannice, M.A.: An analysis of the Mars–van Krevelen rate expression. *Catal. Today.* **123**, 18–22 (2007). <https://doi.org/10.1016/j.cattod.2007.02.002>
104. Abghoui, Y., Garden, A.L., Hlynsson, V.F., Björgvinsdóttir, S., Ólafsdóttir, H., Skúlason, E.: Enabling electrochemical reduction of nitrogen to ammonia at ambient conditions through rational catalyst design. *Phys. Chem. Chem. Phys.* **17**, 4909–4918 (2015). <https://doi.org/10.1039/C4CP04838E>
105. Yang, X., Ling, F., Zi, X., Wang, Y., Zhang, H., Zhang, H., Zhou, M., Guo, Z., Wang, Y.: Low-coordinate step atoms via plasma-assisted calcinations to enhance electrochemical reduction of nitrogen to ammonia. *Small* **16**, 2000421 (2020). <https://doi.org/10.1002/sml.202000421>

106. Guo, Y., Wang, T., Yang, Q., Li, X., Li, H., Wang, Y., Jiao, T., Huang, Z., Dong, B., Zhang, W., Fan, J., Zhi, C.: Highly efficient electrochemical reduction of nitrogen to ammonia on surface termination modified Ti<sub>3</sub>C<sub>2</sub>T<sub>x</sub> MXene nanosheets. *ACS Nano* **14**, 9089–9097 (2020). <https://doi.org/10.1021/acsnano.0c04284>
107. Majumder, M., Saini, H., Dédék, I., Schneemann, A., Chodankar, N.R., Ramarao, V., Santosh, M.S., Nanjundan, A.K., Kment, Š, Dubal, D., Otyepka, M., Zbořil, R., Jayaramulu, K.: Rational design of graphene derivatives for electrochemical reduction of nitrogen to ammonia. *ACS Nano* **15**, 17275–17298 (2021). <https://doi.org/10.1021/acsnano.1c08455>
108. Liu, Y., Su, Y., Quan, X., Fan, X., Chen, S., Yu, H., Zhao, H., Zhang, Y., Zhao, J.: Facile ammonia synthesis from electrocatalytic N<sub>2</sub> reduction under ambient conditions on n-doped porous carbon. *ACS Catal.* **8**, 1186–1191 (2018). <https://doi.org/10.1021/acscatal.7b02165>
109. Hou, C.-C., Wang, H.-F., Li, C., Xu, Q.: From metal–organic frameworks to single/dual-atom and cluster metal catalysts for energy applications. *Energy Environ. Sci.* **13**, 1658–1693 (2020). <https://doi.org/10.1039/C9EE04040D>
110. Kim, J., Kim, H.-E., Lee, H.: Single-atom catalysts of precious metals for electrochemical reactions. *ChemSuschem* **11**, 104–113 (2018). <https://doi.org/10.1002/cssc.201701306>
111. Choi, C., Back, S., Kim, N.-Y., Lim, J., Kim, Y.-H., Jung, Y.: Suppression of hydrogen evolution reaction in electrochemical N<sub>2</sub> reduction using single-atom catalysts: a computational guideline. *ACS Catal.* **8**, 7517–7525 (2018). <https://doi.org/10.1021/acscatal.8b00905>
112. Guo, X., Huang, S.: Tuning nitrogen reduction reaction activity via controllable Fe magnetic moment: a computational study of single Fe atom supported on defective graphene. *Electrochim. Acta.* **284**, 392–399 (2018). <https://doi.org/10.1016/j.electacta.2018.07.168>
113. Qin, Q., Heil, T., Antonietti, M., Oschatz, M.: Single-site gold catalysts on hierarchical n-doped porous noble carbon for enhanced electrochemical reduction of nitrogen. *Small Meth.* **2**, 1800202 (2018). <https://doi.org/10.1002/smt.201800202>
114. Teixeira, I.F., Barbosa, E.C.M., Tsang, S.C.E., Camargo, P.H.C.: Carbon nitrides and metal nanoparticles: from controlled synthesis to design principles for improved photocatalysis. *Chem. Soc. Rev.* **47**, 7783–7817 (2018). <https://doi.org/10.1039/C8CS00479J>
115. Liu, X., Jiao, Y., Zheng, Y., Jaroniec, M., Qiao, S.-Z.: Building up a picture of the electrocatalytic nitrogen reduction activity of transition metal single-atom catalysts. *J. Am. Chem. Soc.* **141**, 9664–9672 (2019). <https://doi.org/10.1021/jacs.9b03811>
116. Wang, J., Chen, S., Li, Z., Li, G., Liu, X.: Recent advances in electrochemical synthesis of ammonia through nitrogen reduction under ambient conditions. *ChemElectroChem* **7**, 1067–1079 (2020). <https://doi.org/10.1002/celec.201901967>
117. Van Tamelen, E.E., Akermark, B.: Electrolytic reduction of molecular nitrogen. *J. Am. Chem. Soc.* **90**, 4492–4493 (1968). <https://doi.org/10.1021/ja01018a074>
118. Yan, Z., Ji, M., Xia, J., Zhu, H.: Recent advanced materials for electrochemical and photoelectrochemical synthesis of ammonia from dinitrogen: one step closer to a sustainable energy future. *Adv. Energy Mater.* **10**, 1–35 (2020). <https://doi.org/10.1002/aenm.201902020>
119. Ye, W., Arif, M., Fang, X., Mushtaq, M.A., Chen, X., Yan, D.: Efficient photoelectrochemical route for the ambient reduction of N<sub>2</sub> to NH<sub>3</sub> based on nanojunctions assembled from MoS<sub>2</sub> nanosheets and TiO<sub>2</sub>. *ACS Appl. Mater. Interfaces* **11**, 28809–28817 (2019). <https://doi.org/10.1021/acsmi.9b06596>
120. Mushtaq, M.A., Arif, M., Fang, X., Yasin, G., Ye, W., Basharat, M., Zhou, B., Yang, S., Ji, S., Yan, D.: Photoelectrochemical reduction of N<sub>2</sub> to NH<sub>3</sub> under ambient conditions through hierarchical MoSe<sub>2</sub>@g-C<sub>3</sub>N<sub>4</sub> heterojunctions. *J. Mater. Chem. A.* **9**, 2742–2753 (2021). <https://doi.org/10.1039/d0ta10620h>
121. Bai, Y., Lu, J., Bai, H., Fang, Z., Wang, F., Liu, Y., Sun, D., Luo, B., Fan, W., Shi, W.: Understanding the key role of vanadium in p-type BiVO<sub>4</sub> for photoelectrochemical N<sub>2</sub> fixation. *Chem. Eng. J.* **414**, 128773 (2021). <https://doi.org/10.1016/j.cej.2021.128773>

122. de Brito, J.F., Perini, J.A.L., Perathoner, S., Zaroni, M.V.B.: Turning carbon dioxide into fuel concomitantly to the photoanode-driven process of organic pollutant degradation by photoelectrocatalysis. *Electrochim. Acta.* **306**, 277–284 (2019). <https://doi.org/10.1016/j.electacta.2019.03.134>
123. de Brito, J.F., Tavella, F., Genovese, C., Ampelli, C., Zaroni, M.V.B., Centi, G., Perathoner, S.: Role of CuO in the modification of the photocatalytic water splitting behavior of TiO<sub>2</sub> nanotube thin films. *Appl. Catal. B Environ.* **224**, 136–145 (2018). <https://doi.org/10.1016/j.apcatb.2017.09.071>
124. Chen, S., Perathoner, S., Ampelli, C., Mebrahtu, C., Su, D., Centi, G.: Room-temperature electrocatalytic synthesis of NH<sub>3</sub> from H<sub>2</sub>O and N<sub>2</sub> in a gas-liquid-solid three-phase reactor. *ACS Sustain. Chem. Eng.* **5**, 7393–7400 (2017). <https://doi.org/10.1021/acssuschemeng.7b01742>

# Overview: Catalysts, Feedstocks in Biodiesel Production



Carlton A. Taft and Jose Gabriel Solano Canchaya

**Abstract** Considering factors such as cost, and increasing energy demands, the world is searching for alternative energy sources, which are renewable, sustainable and environmental friendly. We mini-review the biodiesel process and as such, we overview FAME production; usage of feedstocks/sources including edible, non-edible, waste, cooking oils, shells, ashes, fats, algal oil; experimental characterization; basic, acid, homogeneous, heterogeneous catalysts and their combinations including (alkaline earth metal oxides, transition metal oxides, zeolites, supported catalysts, hydrocalcite, mixed metal oxides, ion exchange resins, biomass based, sulfated, sulfonated carbon-based, enzyme, bifunctional solid; experimental production with different feedstocks, catalysts and yields; usage of nanomaterials (metal, non-metal oxides, metallic, carbon-based, graphene, MWCNT, core-shell and hybrids); electrocatalytic procedure can be done in absence or presence of catalyst or co-catalyst and does not require elevated temperatures; application of artificial intelligence, machine learning methods. We also overview the production process including comparison of methods, conclusions and outlook. The biodiesel process can benefit from accurate/fast modeling instruments such as materials and biomolecular simulations, including machine learning to better handle, design, optimize, monitor and control the systems. Nano biodiesel catalysts can help with quality, selectivity and secure better yields with existing technologies. We underline a number of early papers published by some of us involving catalysts, feedstock, biodiesel production, with corresponding material simulation as well as alternative energetic routes such as fuel cells. It is of interest to continue accompanying progress in other areas including electric transportation vehicles (responsible for a large part of our energy demands), geothermal, solar, hydro, wind power, fuel cells, materials with potential for energetic technological applications discussed in a number of chapters of this book.

---

C. A. Taft (✉)

Centro Brasileiro de Pesquisas Físicas, Rua Dr. Xavier Sigaud 150, Urca, Rio de Janeiro 22290-180, Brazil  
e-mail: [catff@terra.com.br](mailto:catff@terra.com.br)

J. G. S. Canchaya

Grupo de Métodos Computacionais Aplicados a Nanomateriais-GMCAN, Faculty of Physical Sciences, National University of San Marcos, Avenida Venezuela Cidra 11, Lima, Peru

## 1 Introduction

Due to cost and increasing demands, the world is seeking alternative energy resources which are renewable, environmental-friendly and sustainable. Actually more interest is being paid to heterogeneous catalysis as compared to homogeneous catalysis, in particular regarding the chemical synthesis for biodiesel production, whereas catalysts can be reused/tuned for specific requirements [1–45].

The population of the world has an exponential growth as well as a high standard of living leading to very high increase of total primary energy consumed (TPEC). The transportation of services and goods, is one of the principal contributors to global economy, and is expected to continue to increase yearly. One of the viable, sustainable, cost effective solutions is organic waste matter to produce primary and secondary biofuels.

The biofuels can be categorized as primary biofuels including those produced directly from forests, animal waste, crop residues, plants and secondary biofuels (including those produced from combination of feedstocks, microorganisms, biomass). The secondary generation can be separated into first Generation including those obtained from crops such as sugar cane, corn, barley, soybeans, sunflower oil, etc., via fermentation process. The second generation uses feedstocks which are non-edible (including jathropa, castor oil, wheat straw, grass, waste vegetable oil). The third generation includes microalgas species. The usage of second and third-generation biofuels avoids food security/deforestation/water shortage, requiring, however, solid economics. First generation feedstock yields bioethanol, biodiesel and vegetable oil. Second generation feedstocks yields biodiesel, bioethanol, biomethane, Fischer-Tropsch gasoline, Third generation feedstocks yields biodiesel, butanol, gasoline, methane, ethanol, vegetable oil and jet fuel [1–8].

For all the reasons stated above, the biomass-derived heterogeneous catalysts are now at the fore-front of biodiesel production whereas nano/bifunctional catalysts have become very important due to their high surface area and potential to convert triglycerides/free fatty acids to biodiesel.

Effectively, biofuels, which are good sources of energy and potential fossil fuel substitutes, can be prepared from waste, plants, forestry, agricultural by-products and are gaining great attention due to their sustainable, environmental-friendly nature. Some of the properties are similar to conventional petro-diesel (fossil fuel) whereas other properties are improved, such as better lubrication, high flash point, cetane number, combustion efficiency, lower sulphur content, CO<sub>2</sub> emission and better lubrication.

The lower flash point of petrodiesel (337 K) as compared to biodiesel (423 K) makes the latter non-explosive, non-inflammable, whereas transportation/handling/storage is safe, easy and directly used without additional modifications in engines of automobiles. Considerable investments are being made to make biodiesel more economical and sustainable which is validated by the large number, with exponential increase, of research papers published in this field [1–8].

Fossil fuels will not suddenly stop but there is worldwide effort to attain low carbon footprints whereas biofuels, hydrogen, compressed natural gas, liquefied petroleum gas and alcohol show great potential as alternative energy sources. Biofuels includes bioethanol, biogas and biodiesel, which can be obtained from biomass resources, integrating the challenges of environmental benefits, energy security, renewability, availability and sustainability supporting electricity, transportation fuels, heating and power.

Biodiesel has the advantage of releasing fewer emissions, with more complete combustion because it is highly oxygenated, promoting energy sufficiency, being sulfur-free, with profitable physicochemical properties with the disadvantages, however, of higher maintenance cost, less energy content, high cost of establishment, releasing more nitrogen oxides, separation and purification stage for product and undesirable side reactions. Biodiesel is also an appropriate choice for diesel engines since they indicate 41% less greenhouse emission, no need for significant modifications, physical and chemical advantages. Biodiesel and petrodiesel are miscible in any ratio which has led to usage of their combination in both developed and underdeveloped countries. In this chapter we will focus on biodiesel production including fame production, catalysts, feedstocks, experimental characterization, nanotechnology, material and biomolecular simulations via machine learning applications [1–8].

We overview fame production; edible, non-edible, waste, cooking oils, fats, shells, ashes, algal oil; experimental characterization; basic, acid, homogeneous and heterogeneous catalysts including alkaline earth and transition metal oxides, zeolites, supported catalysts, hydrocalcite, zeolites, mixed metal oxides, biomass based catalysts, ion exchange resins, sulfated and sulfonated carbon-based catalyst, enzyme and bifunctional solid catalysts; nanomaterial stimulants; materials and molecular simulation models such as artificial intelligence and machine learning. We underline some of our previous work in this line of reasearch including biodiesel by hydroesterification of oil from the Microalgae *Scenedesmus dimorphus*; Hydroesterification of *Nannochloropsis Oculata* microalga's biomass to biodiesel using as catalyst pure niobium oxide; niobium oxide supported on alumina and niobium oxide impregnated with phosphoric acid; niobium oxide solid catalyst: esterification of fatty acids, modeling for biodiesel production, production of biodiesel by a two-step niobium oxide catalyzed hydrolysis and esterification [1–4]. We also overview the production process as well as comparison of methods, conclusions and outlook for the future including comments regarding other alternative sources of energy [1–45].

We emphasize the interest to continue accompanying progress in other areas including electric transportation vehicles (responsible for a large part of our energy demands), geothermal, solar, hydro, wind power, fuel/solar cells, materials with potential for energetic technological applications discussed in a number of chapters of this book.

## 2 Fame Production

The process to produce biodiesel is called transesterification/alcoholysis whereas non-edible/edible oils or triglyceride (TG) and alcohol go through a nucleophilic reaction forming byproducts of glycerol and FAME (fatty acid methyl ester). In these reactions an ester is formed at each conversion step whereas three ester molecules are formed during the transesterification process with the conversion of triglyceride to diglyceride, followed by conversion of diglyceride to monoglyceride, and at the end, monoglyceride to glycerol. The reaction of transesterification converts triglyceride of vegetable oil into biodiesel (FAME). Nonetheless, a reaction (esterification) between alcohols and carboxylic acids yielding esters is necessary to convert all vegetable oil free fatty acids (FFA) into biodiesel [1–8].

Often, the high FFA vegetable content is first converted via esterification reaction to FAME using an acid catalyst which is followed by the transesterification reaction using a basic catalyst to convert triglycerides to FAME. The (trans)esterification or simultaneous esterification and transesterification reactions in one-pot can convert both high FFAs of vegetable oils and triglycerides of vegetable oils to FAME reducing time/cost.

Overall, the catalysts can be homogeneous, heterogeneous, bi-functional. The heterogeneous catalyst can also be bi-functional and be a base or an acid. Base includes metal oxides, mixed metal oxides, hydrotalcite, zeolite, bio-mass derived. Acids includes mixed metal oxides, ion exchange resin, sulfated catalyst, sulfonated carbon-based catalysts.

ASTM is the American Society for Testing, which describes biodiesel as a mono-alkyl ester which is produced from animal fats or edible/non-edible oils. Animal fats/vegetable oils comprise mainly triacylglycerol (TAG), an ester of fatty acid and glycerol, whereas the physicochemical properties are strongly influenced by TAG composition which can dictate the biodiesel quality produced. The fatty acids (FA) can be divided into groups with carbon–carbon single bonds and unsaturated FA with at least one carbon–carbon double bond. In vegetable oils the FA mostly found include stearic, linolenic, oleic, linoleic, palmitic, palmitoleic, arachidic, myristic).

The biodiesel production mainly uses non-edible, edible vegetable oils, waste cooking oils and animal fats (yellow grease, tallow, chicken fat, lard) and production by-products of fatty acids of omega-3 originating from fish oil. Algae are also feedstock of promise due to availability in sewage water, shallow ocean water, ponds without dislodging land for food production [1]. Approximately, 27% biodiesel is produced worldwide from soybean oil, whereas 20% from rapeseed and 31% from palm oil. About 75% of biodiesel cost arises from feedstock expenses, making it of interest to consider carefully selection of those expenses whereas each country should use feedstock according to local availability.

India usage for biodiesel production includes soybean, rapeseed, *karanja*, *jatropha*, sunflower; USA usage includes waste oil, soybean, peanuts; Brazil usage includes soybean/palm oil/castor/cotton oil; Canada usage includes animal fat, soybean oil, rapeseed; France usage includes rapeseed, sunflower; UK usage

includes waste cooking oil, rapeseed; Japan usage includes waste cooking oil; China usage includes rapeseed oil, waste cooking oil, Jathropa; Greece usage includes cottonseed; Germany usage includes rapeseed; Norway usage includes animal fats; Spain usage includes linseed oil, sunflower; Italy usage includes rapeseed, sunflower; Mexico usage includes waste oil, animal fat; New Zealand usage includes tallow, waste cooking oil; Ireland usage includes fry ing oil and animal fat, Sweden usage includes cottonseed; Turkey usage includes sunflower/rapeseed; Peru usage includes *jatropha*, palm; Indonesia usage includes jatropha, coconut, palm oil; Malaysia usage includes palm oil; Philippines usage includes *jatropha* oil, coconut; Bangladesh usage includes Pangamia Pinnata oil, rubber seed; Pakistan usage includes *jatropha* oil; Iran usage includes palm, jathropa, algae oil, Thailand usage includes palm, il, jatropha, coconut oil, Iran usage includes *use palm, castor, jathropa*; Singapore and Ghana usage includes palm oil; Zimbabwe usage includes *jatropha* oil, Kenya usage includes castor oil; Mali usage includes jathropa oil; Cuba usage includes neem oil, Jatropha curcas, moringa; Australia usage includes jathropa, waste cooking oil, animal tallow, pangamia and Mali usage includes jathropa oil [1–8].

The selection/usage of first-generation biofuels is important to reduce biodiesel production cost but resulted, however, in the usage of edible oils leading to a food versus oil problem/disturbance of the agricultural farmland allocation. Consequently, in order to mitigate the problems of first-generation biodiesel, non-edible oils were targeted as biodiesel feedstocks. The first generation biofuels also have a larger cost than fossil fuels. In order to mitigate these problems non-edible oils are now targeted as biodiesel feedstock. More than 300 species of non-edible oils are available in South Asia and India (~1 million tons per year of non-edible oils) including *jathropa curcas* oil (JCO) and *pangamia pinata* (*karanja*). The European Union (EU) has reduced the dependency on edible oil and price as well of biodiesel by raising the share of waste cooking oil (second position after rapeseed), recycled vegetable and palm oils. Germany, France, Spain, Netherlands and Poland are the large biodiesel producers in the EU. Non edible crops plantation under proper world-wide administration could strongly reduce our dependence on fossil oils and edible feedstocks [1–8].

### 3 Edible, Non-edible, Waste, Cooking Oils, Waste Fats, Algal Oil

Regarding edible oils, in a number of nations sunflower/rapeseed/palm oil/soybean edible oils have been used as feedstocks for production of biodiesel, i.e., coconut oil (*Cocos nucifera*) from plant coconut; soybean oil (*Cycline max*) from plant soybean; palm oil (*Elaeis guineensis*) from plant Mesocarp of palm oil; sunflower oil (*Helianthus annuus*) obtained from plant sunflower; rapeseed oil (*Brassica napus*) obtained from plant rape [1–8].



Non-edible plant oils, in addition to their evident importance, have low cost and high oil content and do not pose a fuel vs food problem. They can also be grown in areas not suited for agriculture (arid/barren regions) and grow with almost no attention in harsh regions reducing significantly cultivation/biodiesel production costs [1].

Some of the non-edible plant oils used in biodiesel production include *Jatropha curcas* (commercially available), *Madhuca indica* (Mahua)/commercially available), *Moringa oleifera* (moringa seed), *Calophyllum inophyllum*, *Salvadora oleoides* (Pilu), *Nicotiana tabacum* (tobacco), cottonseed oil, apricot seed, rubber seed oil, *Eruca sativa* Gars, terebinth, rubber seed oil, *Pongamia glabra* (Karanja/commercially available), desert date, *Acrocomia aculeata* (macaúba), *Crambe abyssinica* (hochst), *Crotonn megalocarpus*, linseed oil, rubber seed oil, *Sapium sebiferum* (chinese tallow), *Sapindus mukorossi* (soapnut), *Euphorbia tirucalli* (milk bush), *Pistacia chinensis* (bunge seed), *Callophyllum inophyllum*, *Salvadora oleoides* (Pilu), *Nicotiana tabacum* (tobacco), *Eruca sativa* Gars, terebinth, desert date, *Azadirachta indica* (neem)/commercially available), *Acrocomia aculeata* (macauba), *Crambe abyssinica* (hochst), linseed oil, rubber seed oil, *Sapiindus mukorosi* (soapnut), *Sapium sebiferum* (chinese tallow), *Euphorbia tirucalli* (milk bush), *Calophyllum inophyllum* (polanga oil), jojoba, leather pre-fleshings, sal oil [1–8].

Waste cooking oil (WCA) reduces the expense of biodiesel production since it is much cheaper than fresh vegetable oils and, based on their FFA content, can be classified as brown grease for FFA content larger than 15% and yellow grease, otherwise. Billions of tons of WCA are generated annually originating mostly from food processing industries and commercial restaurants whereas the portion not used in biodiesel is likely to be used for production of soap or mostly dumped into rivers contaminating water and contributing to the environmental pollution [1–8].

Animal fats used as feedstocks for biodiesel production includes tallow, chicken fat, lard, with high quantity saturated fatty acids yields, and however, poor cloud/pour points among chemical physical properties, but having high oxidation stability and high cetane number among its chemical physical properties and importantly as well, lower price.

The industrial-scale synthesis of biodiesel production using algal oil [1–8] is considered to be a very promising and highly sustainable as several strains of microalgae can in hours double in size offering the capacity of creating large number of biodiesel litres per hectare each year and the microalgal strains grows in saline water medium, non-arable land and does not compete with production of food. Some of us early reported research on biodiesel by hydroesterification of oil from the Microalgae *Scenedesmus dimorphus* [1].

## 4 Experimental Characterization

We summarize in this section the experimental/analytical techniques used to characterize FAME/catalysts. In order to detect the presence of various functional groups in

the catalyst, Fourier Transform Infrared Spectroscopy (FT-IR) is used. Energy dispersive x-ray spectroscopy (EDX) is used to investigate the chemical composition. To investigate the crystallinity and detection of elements in the catalyst, x-ray diffraction can be used. Scanning Electron Microscopy (SEM) and transmission electron microscopy (TEM) can be used to investigate the surface morphology, structure and particle size. Thermogravimetric analysis (TGA) is used to determine the stability of the catalyst. Quantitative detection of metal oxides are commonly determined by x-ray fluorescence (XRF) and routine determination of the elements as well as chemical state information present in catalyst are done by x-ray photoelectron spectroscopy. Gas chromatography-mass spectroscopy (GC-MS) yields chemical components/percentages of FAME. Brunauer-Emmett-Teller (BET) analysis is used to determine the pore volume/diameter, surface area.  $\text{NH}_2$  and  $\text{CO}_2$  temperature programmed desorption (TPD) analysis is used to study the basicity of the catalyst. NMR can be used to obtain information about degree of carbonization and transformation to FAME. Purity of FAME is obtainable from  $^1\text{H}$  NMR as well as the percentage conversion from vegetable oil [1–8].

## 5 Homogeneous Catalysts

The homogeneous catalysts can be base (KOH, NaOH) as well as acid catalysts (hydrofluoric, sulphuric, hydrochloric, sulphonic). The homogeneous base catalysts  $\text{NaOCH}_3$ , (NaOH, KOH) are easily accessible/cheap and widely investigated in the transesterification process indicating minimum reaction time, ambient temperature and pressure, although in the case of the two latter catalysts, water is formed as byproduct reducing the biodiesel yield. Water is not formed in sodium and potassium methoxide. Alkaline catalysts can be used for transesterification of vegetable oils with low FFA content at least (<2 wt%) [1–8].

The homogeneous base catalyst (KOH) was used under various conditions, with different feedstocks (duck tallow, soybean oil, rapeseed, waste frying oil, palm kernel, *Pongamia pinnata*, frying oil, roselle oil, vegetable oil, crude rubber/palm oil, used olive oil, with different yields (84%, 96%, 95%, 96%, 96%, 92%, 73%, 99%, 87%, 98%, 94%), respectively. The homogeneous base catalyst (NaOH) was used with camola oil, waste cooking oil, cotton seed oil, waste frying oil, sunflower, cotton seed oil, refined palm oil with yields of 98%, 90%, 97%, 97%, 97%, 97%, 95%, respectively.  $\text{NaOCH}_3$  was used as a catalyst for the transesterification of rice bran oil with a 83% biodiesel yield in 60 min [8].

## 6 Acid Catalyst

Due to lower cost and higher reactivity, acid catalysts are not as preferred compared to base catalysts. On one end, the base catalysts have a negative point, i.e. they

can react during transesterification with feedstock FFA yielding saponification consuming/reducing the reactivity of the catalyst. On the other end, acidic catalysts indicate better outcome to transesterification of vegetable oils/fats with more than 2% wt% of FFA. The acid catalysts can be used to bring down the FFA content by prior esterification to a transesterification using base catalyst. However, the usage of acids such HCl, H<sub>3</sub>PO<sub>4</sub>, H<sub>2</sub>SO<sub>4</sub> for direct transesterification indicate major limitations including slow reaction rates, environmental and corrosion related problems. These problems have made acid-catalyzed biodiesel production unpopular. In general, acid catalyzed esterification/transesterification reactions require high temperatures, long reaction times and catalyst loading as compared to base-catalyzed transesterification reactions [1–8].

## 7 Heterogeneous Catalysts

The usage of homogeneous catalysts is uneconomical, labor intensive, with low quality of glycerol produced whereas the catalyst cannot be regenerated. On the other hand, the heterogeneous catalyst can be recovered/reused for catalytic reactions reducing the biodiesel cost. The heterogeneous catalysts, in contrast to the homogeneous catalysts, is recyclable, eco-friendly, reusable, less toxic with reduced energy intake and minimum corrosion providing a route that is more efficient and economical for biodiesel production. The heterogeneous catalysts can be grouped as basic or acidic. Some of these catalysts can promote in one pot both esterification and transesterification reactions simultaneously using high FFA content in vegetable oils/animal fats, without pretreatment.

## 8 Basic Heterogeneous Catalysts

Some of the constraints of basic homogeneous catalysts can be overcome by using basic heterogeneous catalysts which can yield good catalytic production with mild reaction conditions, with the restriction however, of being suited mostly for feedstock with low FFA content in order to avoid saponification reactions and reduction of biodiesel production. As examples, we note that solid base catalysts include alkaline metal oxides, transition metal oxides, hydroxalicates, mixed metal oxides, biomass-based catalysts, zeolites.

## 9 Alkaline Earth Metal Oxides

The alkaline earth metal oxides are insoluble in ethanol and have low toxicities with basicity in the order MgO < CaO < SrO < BaO whereas the first, MgO, is almost

inactive to transesterification. On the other hand CaO is highly insoluble in alcohol, easily available, cheap, non-toxic and although it is widely used in FAME production, it is sensitive to FFA content and loses activity during saponification. Highly active and sensitive to moisture, SrO forms byproducts by reacting with water and CO<sub>2</sub>. Some alkaline earth metal oxide-catalyzed biodiesel production indicated that using CaO with sunflower, soybean and rapeseed oil resulted in yields of 90–95%. BaO with feedstock of palm oil and SrO with soybean oil indicated 95% yield [1–8].

The conventional magnetic stirring process was found to be less efficient than the ultrasonic-assisted biodiesel synthesis (order of four times faster) and in the case of CaO and SrO resulted in biodiesel increase of up to 70% for SrO and CaO underlying the importance of ultrasonication in biodiesel synthesis. Unfortunately, the catalytic reusability test indicated that in the ultrasonic process the catalyst reusability test indicated great decrease of BaO catalytic activity due to leaching.

## 10 Transition Metal Oxides

The transition metal oxides (high reactivity) have high sensitivity towards moisture and low reusability which affects their catalytic efficiency leading to the investigation of other oxides such as metal oxides of Ti, Zn, Zr which show very good catalytic activities, are highly stable and easily available. There have been numerous transition metal oxide-catalyzed biodiesel production yields including Co(n)@chitosan, Cu(n)@chitosan, using soybean oil; SO<sub>4</sub><sup>2-</sup>/ZrO<sub>2</sub>, using crude coconut oil and crude palm kernel oil; (Vanadyl phosphate, Na<sub>2</sub>MnO<sub>4</sub>) using soybean oil; Mn doped ZnO, using Mahua oil [1–8].

Some of us reported production of biodiesel by a two-step niobium oxide catalyzed hydrolysis and esterification [4]. Hydroesterification of *Nannochloropsis Oculata* microalga's biomass to biodiesel using pure niobium oxide, niobium oxide supported on alumina and niobium oxide impregnated with phosphoric acid was early reported by some of us [2]. Our former group also early reported niobium oxide solid catalyst: esterification of fatty acids and modeling for biodiesel production [3].

## 11 Zeolites

The zeolites are essentially aluminosilicates with a microporous crystalline structure depending on synthesis procedures with wide structural modifications yielding excellent acid-base catalysts, whereas catalytic properties can be improved by varying the Si/Al ratio and the pore size and incorporating as well Na<sup>+</sup>, K<sup>+</sup>, Mg<sup>2+</sup> metal ions responsible for the basic nature. Different fame productions were catalyzed by zeolites (La/zeolite beta, KOH@NaX zeolite, La<sub>2</sub>O<sub>3</sub>/NaY zeolite, Sodalite,

CaO@NaY zeolite, KOH/zeolite, Zeolite X, La/zeolite beta, FAK/K-X zeolite, Ba-Zr, Ba-Sr/ZSM-5,  $H_4[W_{12}SiO_4@zeolite H\beta]$  under different conditions with varying reaction conditions (temperature, catalyst loading, reaction time, yields, etc.) [1–8].

## 12 Supported Catalyst

The catalyst support is good for providing high porosity/surface area (where metals are anchored) and reducing mass transfer limitation increasing thus stability/reusability of alkaline earth metal oxides. Silica, alumina,  $ZrO_2$ , ZnO have been proposed for production of FAME [1–8].

Aluminum is well used as support for basic/acidic catalyst in both esterification and transesterification reactions. Aluminum supported biodiesel production catalysts includes CaO@ $Al_2O_3$ , K@KOH@ $Al_2O_3$ , K@ $\gamma-Al_2O_3$ , KI@ $Al_2O_3$ , KOH/La-Ba- $Al_2O_3$  using for feedstock rapeseed oil, microalgae, soybean oil, palm oil, nannochloropsis oculata. In addition to alumina there are other various material catalysts support as well as activated carbon, i.e. KOH/AC, Ag@ZnO,  $K_2SiO_3@AISBA$ , KOH/AC, CaO/ $SiO_2$ , CaO/AC, KF/AC,  $K_2CO_3@KFA$  which have been used with rapeseed oil, microalgae, soybean oil and nannochloropsis oculata [1–8].

## 13 Hydrocalcite

Due to their tunable properties and outstanding performance, hydrocalcites have become important solid catalysts in transesterification. These catalysts belong to the layered double hydroxide (LDH) family with formula  $[Mn^{2+}Mn^{3+}(OH)_{2(n+m)}]^{m+}[A^{x-}]_{m/x} \cdot yH_2O$ , where M is metal and  $A^{x-}$  is an anion with x in the range 0.1–0.5. A number of hydrocalcites (Mg–Al–HT, Mg/Al- $CO_3$ , K/Mg–Al, MgAl- $CO_3$ , K–Mg–Al HT, Zn–Al HT, KF/Ca–Al,  $Zn_5(OH)_8(NO_3)_2 \cdot 2H_2O$ ) using feedstocks soybean oil, sunflower oil, palm oil, poultry fat, microalgae oil, WCO, jathropa oil indicated yields between 75 and 98% [1–8].

## 14 Mixed Metal Oxides

Mixed metal-oxide catalysts are synthesized to increase surface area, stability, basic or acidic strengths in order to prepare stable, reusable, efficient solid catalysts whereas combination of two metal oxides can yield unique properties different from the individual properties. Highly reactive mixed metals for catalysis can be obtained at relatively low temperatures [1–8].

A number of transesterification production of vegetable oils using metal-oxides including (CaO– $CeO_2$ ,  $La_2O_3/ZrO_2$ ,  $TiO_2-MgO$ , SrO/ $SiO_2$ , SrO/CaO,  $TiO_2-ZnO$ ,

ZnO–La<sub>2</sub>O<sub>3</sub>, CaO–ZnO, MgO–ZrO<sub>2</sub>, ZrO<sub>2</sub>@SiO<sub>2</sub>, SiO<sub>2</sub>/ZrO<sub>2</sub> NP, MgO–CaO) and feedstock including (sunflower oil, WCO, olive oil, rapeseed oil, palm oil, soybean oil, palm kernel oil, stearic acid), indicated yields ranging from 49 to 96%.

In particular, solid ZrO<sub>2</sub> base biodiesel catalysts became of considerable interest due to their economic viability and benign environmental nature whereas different types have been developed such as microporous solid base composites. Studies of the physicochemical properties and efficacy/influence of various support materials on biodiesel synthesis indicated higher conversion rates from higher surface areas and higher number of Lewis acid sites. Nanosized mixed metal oxides (SiO<sub>2</sub>/ZrO<sub>2</sub>) prepared via sol-gel strategy indicated 96% biodiesel yield after 3 h reaction time and was reusable for 6 consecutive cycles with small drop in activity.

The mixed metal oxides with high reactivity can be obtained at relatively low temperatures which places them in high demand for catalysis. Various calcium containing mixed metal catalysts for biodiesel production indicated good reactivity using rapeseed oil feedstock whereas CaO–CeO<sub>2</sub> indicated high yield and stability compared to other CaO containing mixed metals and could be reused many times with good yields.

## 15 Biomass Based Catalyst

The bio-waste heterogeneous catalyst for biofuel have gained considerable attention since waste materials have considerable advantages (ecofriendly, non-toxic, economic, cheap, abundant, sustainable, renewable, easily available). Some workers use waste bio-mass as a catalyst for edible low FFA oil as well as edible and non-edible high FFA oil. The biomass catalysts including bones, waste shells, plant ashes, industrial waste making the biodiesel environmental benign and production cost effective [1–8],

A number of solid-base catalysts derived from egg-shells used for FAME production includes chicken eggshell using catalyst (CaO, CaO/W/Mo, CaO/anthill, CaO/Zn, CaO/KF/Fe<sub>3</sub>O<sub>4</sub>, CaO/SiO<sub>2</sub>, CaO/rice husk, CaO/coconut waste, Li/Cao, CaO/Zn, CaO/KF/Fe<sub>3</sub>O<sub>4</sub>, CaO/fly ash, CaO/KF, Na/CaO), using as feedstock (soybean oil, Karanja Oil, WCO, palm oil, rapeseed oil, sunflower oil, JCO, Microalgae *Chlorella vulgaris*, Microalgae/*S. Armatus*, chicken fat, catfish oil, helianthus annuus L oil, cotton oil, *C. sativa* oil, *C. inophyllum* oil, WCPO, Palm oil, Nahor oil, Eucalyptus oil, Neem oil, Soybean oil, *Madhuca indica* oil, SODD, *Jathropa* oil) with yields from 75 to 80%. CaO obtained from chicken eggshell used for biodiesel synthesis after calcination at 1000 C indicated yields over 95% [1–8].

Sea-shell derived and mollusk derived solid catalysts, for biodiesel production, using for catalyst source oyster and pyramidella shell, river snail shell, snail shell, mussel/coacle/scallop shell, mussel shell (*perna varidis*), fresh water mussel shell, mussel/clamp/oyster, angel wing shell, clamshell, short necked clam shell, white

bivalve clamshell, venus clam, abalon shell, T. jourdani shell, A. cristatum shell, cockleshell, obtuse horn shell, biont (turtle) shell, turbonilla striatula shell, chicoreus brunneus shell, Shrimp shell, P. erosa seashell, crab shell), catalyst (CaO, CaO/KI, CaO, KBr/Kaolin, nano-CaO, C/CaO/NaOH, CaO/KOH, CaO-SO<sub>4</sub>, CaO/KF, CaO/Ba, CaO/Na-ZSM-5), and feedstock (soybean oil, jatropha oil, WCO, palm oil, soybean oil, WFO, palm oil, H Wightiana Oil, A. Africana seed oil, castor oil, Chinese tallow oil, karanja oil, Neel oil, Mustard oil, Karanja oil, Neem oil, rapeseed oil) indicated conversion rates from 74 to 99% [1–8].

Waste plant ashes is also serving as heterogeneous catalyst in biodiesel production whereas alkali/alkaline earth elements such as K, Ca, Mg present in the plant biomass ashes can act as highly basic catalysts for biodiesel transesterification using low FFA vegetable oils. The biomass can be washed, dried and burnt, calcinated to produce highly basic ash catalysts. Different plant ash catalyst sources including (oil palm ash, ripe plantain fruit peel, coconut husk, cocoa pod husks, rubber seed shell, wood stem, birch bark, orange peel, cocoa pod husk, walnut shell, sugar beet waste, banana peel, sugar beet waste) and using feedstock such as palm oil, soybean oil, JCO, WCO, sunflower oil, rubber seed oil resulted in high percentage of biodiesel yield under various conditions [1–8].

## 16 Ion Exchange Resin

The ion exchange resin meets many of the requirements for an ideal catalyst since resin is a solid insoluble material able to discharge and retain ions simultaneously and can be broadly categorized into anionic and cationic based on their cross-linkages and functional groups responsible for permutation of ions with properties such as activity at low temperature and easy recovery from liquid mixtures using simple methods. These cationic resins have more active sites, lower residual water production, non-corrosive nature, which are important for FAME reactions/production. They are often used for purification/softening of water at room temperatures. Some ion exchange resins catalysts used in biodiesel production include (D261 anion-exchange resin, Amberlyst A26 OH anion exchange resin, Amberlyst-15, basic anion exchange resin, Amberlyst 15 ion exchange resin, Amberlyst, Basic anion exchange resin, Amberlyst 15 ion exchange resin, Amberlyst, Amberlyst-26, Amberlyst A-26 OH, Amberlite gel resin, Cation-exchange resin, Purolite-PD206), using as feedstocks (soybean oil, acid soybean oil, Hydrolyzed sea ango oil, pongamia oil, *lagenaria vulgaris* seed oil, hydrolyzed sea mango oil, canola oil, tallow fat, WCO, rice bran oil, corn oil) indicated yields from 67 to 95% [1–8].

## 17 Sulfated Catalyst and Sulfonated Carbon-Based Catalyst

Due to their super-acid properties, sulfated catalyst are interesting for transesterification, The sulfated inorganic metal oxides are chemically stable, and have super acidity, redox and acid–base properties for which zirconia is widely studied. A number of sulfated catalysts were indicated to be adequate for biodiesel production. These sulfated catalysts include ( $\text{SO}_4\text{/ZrO}_2$ , ( $\text{SO}_4\text{/SnO}_2\text{-SiO}_2$ ,  $\text{SnSO}_4$ ,  $\text{SO}_4\text{/SnSO}_2\text{/SiO}_2$ ,  $\text{SO}_4\text{/TiO}_2$ ,  $\text{Ti}(\text{SO}_4)\text{O}$ ,  $\text{TiO}_2\text{/PrSO}_3\text{H}$ ) using as feedstocks Neem oil, WCO, Soybean oil, Jatropha oil, Rapeseed oil, WCO) indicated biodiesel production ranging from 51 to 98% under various conditions [1–8].

A number of different sizes, shapes and structure of carbon materials have been developed and used as low-cost catalysts for transesterification. Considered as a new group of the metal-free solid acid catalyst with original carbon structure and Bronstein acidity equivalent to concentrated  $\text{H}_2\text{SO}_4$ ,  $\text{SO}_3\text{H}$ -functionalized acidic carbon materials can be easily prepared by the incomplete carbonization of aromatic compounds in concentrated  $\text{H}_2\text{SO}_4$  or sulfonation of ncompletely carbonized natural organic matter. These materials have lower production costs, high chemical, thermal stability, distinctive surface chemistry and are biogenic-enviroment-friendly.

## 18 Enzyme Catalyst

Enzyme catalysts have been used in recent years to improve the product separation, reaction conditions, ecological benign nature of high-quality biodiesel production on the industrial scale and do not form soap. The enzymes can be immobilized on a matrix on support materials (entrapment, adsorption and covalent bonding). The entrapment method have been used for the large scale production of bacterial/fungal lipases. The immobilized lipase catalyst indicate large tolerance to high thermal stability, pH variation and high substrate selectivity. The lipase catalyst also indicates superior quality, higher yield, freedom from soap formation, lower reaction temperature and ability to work with various feedstocks [1–8].

## 19 Bifunctional Solid Catalyst

Solid acid catalysts, contrary to basic solid catalysts, are insensitive to the FFA content and esterify waste/low cost oils without pretreatment although water formed during the reaction could lead to decomposition of triglycerides to diglycerides resulting in additional catalyst leaching and FFA. It is thus of interest to search for dual type solid catalyst (solid acidic character and solid basic character) to tackle both FFA and easy transesterification of triglycerides to FAME [1–8].



## 20 Nanomaterial Stimulants

It is possible to link efficient biodiesel production with energy optimization and carbon utilization whereas nanomaterials (metallic/metal oxides, non metal oxides, biomolecules, enzymes/biocatalyst and carbon-based) can play important roles in enhancing overall biodiesel production product as well as energy optimization. Biodiesel production is still hampered by numerous hurdles in order to achieve economical viability (cost-intensive pre-treatment steps) and nanotechnology is been used in the pre-treatment step whereas the small size (1–100 nm) brings higher interfacial surface area, high selectivity, porosity, more active sites, high chemical stability/absorption capacity, crystallinity and improved catalytic activities. Nanotechnology deals with syntheses (top-down/physical, bottom-up/chemical methods), characterization, control of size and shape of the nanomaterial [5, 7, 18–30].

Nanomaterials used for biodiesel applications include metal/non-metal oxides ( $\text{TiO}_2$ ,  $\text{Fe}_3\text{O}_4$ ,  $\text{ZnO}$ ,  $\text{CaO}$ ,  $\text{SiO}_2$ ,  $\text{Al}_2\text{O}_3$ ) with higher thermal stability and higher melting points; metallic (Ni, Ag, Au, Rh, Pd, Pt) with higher catalytic activity, moderate temperature, stability; carbon-based (CNT, graphene, MWCNT, fullerenes) with higher stability, inert, higher thermal conductivity, core-shell (Ag/ $\text{SiO}_2$ , Au/ $\text{SiO}_2$ , Ni/ $\text{SiO}_2$ ,  $\text{Fe}_3\text{O}_4$ / $\text{SiO}_2$ , Au/ $\text{TiO}_2$ , Fe/C, FeNi/ $\text{SiO}_2$ , ZnO/ $\text{SiO}_2$ ) with higher stability, improved multifunctional properties and hybrid (FeMo, CuMo) with synergetic catalytic capability.

Nanoferrites are ceramic powders which due to iron oxides in their core component exhibit ferrimagnetic properties. Based on their crystalline structure they are classified as hexagonal ( $\text{MFe}_{12}\text{O}_9$ ), garnet ( $\text{M}_3\text{Fe}_5\text{O}_{12}$ ) and spinel ( $\text{MFe}_2\text{O}_4$ ). Separation and recovery is easily facilitated by using magnetic nanoscale catalyst and applying external magnetic fields [17].

Nanomaterial functions in biofuel production includes for biodiesel (reduces activation energy, improve reaction kinetics, reduces methanol/oil ratio, activate nucleophilic and electrophilic groups by proton transfer); for biogas (ATP-dependent direct uptake of zero-valent iron, electron transfer, and reduction pathways); for biohydrogen (improvement of electron transfer rate, decreases dissolved oxygen (DO) levels in the culture, improve efficacy of the oxygen-sensitive hydrogenase, provide nutrition to microbial growth, accelerate electron transfer between ferredoxin and hydrogenase; acts as an enzyme carrier, enhance the separability of the enzyme during hydrolysis and pretreatment, cofactor for enzymatic activities, aid the structural stability of the enzymes, ability to modulate oxidation-reduction potential); Fischer Tropsch synthesis (improve FTS activity, olefin selectivity, CO conversion rates) [5, 7, 18–30].

Nanomaterials can be used for economic viability/energy optimization whereas low cost biofuel could become a good alternative and tools (mechanical agitation, microwave, microchemical/heat transfer technologies, ultrasonication) could be more widely used. Microchemical technologies could be alternatives for batch reactor systems since microsystems require half the time for maximum extraction

compared to conventional reactors, i.e. batch extraction < microwave-assisted extraction < ultrasonic-assisted extraction < slug-based extraction. Nanofluids are also used in mass/heat transfer operations since they enhance heating/cooling rates whereas it has been observed that heat transfer was regulated by concentration/size/properties of the nanoparticles via transfer coefficients of thermophoresis (movement from temperature gradient), diffusiophoresis (migration of particles to higher concentration), brownian (random fluctuations). Bioethanol, hydrotreated vegetable oils and biodiesel are good choices for the future. In order to increase rates/yields/products strategies like coiled flow interter (CFI) and coiled flow reverser (CFR) have shown to be efficient (changes in centrifugal force/flow direction) compared to batch reactors [5, 7, 18–30].

Mechanical vibration, microcowave, ultrasonication, pulsation have already shown to increase biofuel yields whereas ferrofluids can also move in oscillating magnetic fields for mixing and easily separable. Microchemical technologies such as conduit miniaturization, coiled flow inverters could also be potentially used for biodiesel production, heat transfer fluids and ionic liquids could be used for heating/cooling circuits. Nano-technology based conversion routes can convert waste biomass to biofuels (syngas, biodiesel, HVO) and in combination with microchemical technologies for process intensification could make biofuels more competitive by improving cost-effectiveness whereas the catalytic activity depends on crystallographic arrangement, coordination number and ionization [5, 7, 18–30].

## 21 Electrocatalytic Process for Transesterification

A DC electric field is passed through dissolved ionic substances or molten salts resulting in decomposition in simple substances. Electrocatalytic reactor loaded with mixture of methanol, catalyst, vegetable oil, co-solvent and electrolyte solution. The hydroxyl ions and chlorine reach the anode and oxidized in chlorine and oxygen whereas hydroxyl ions and hydrogen are formed on the cathode. The reaction of methanol with hydroxyl form the methoxide ion strongly nucleophilic and attacks the carbonyl moiety in the glyceride molecule to result in methyl ester and glycerine. The electrocatalytic procedure can be done in absence or presence of catalyst or co-catalyst and does not require elevated temperatures whereas the production by conventional transesterification processes often requires high ambient temperatures and a specialized catalyst. Metals and metal oxides can be used as electrodes. Voltage, electrode type. Stirring rate, co-solvent, electrode type, reaction temperature and duration, concentration of NaCl and oil-to methanol molar ratio can affect the biodiesel yield. The constituent of the cathode plays decisive role and stimulates the search for new materials for making electrodes with high catalytic activity.

## 22 Artificial Intelligence and Machine Learning Methods

Artificial intelligence (AI) is the ability of machines for using computer science techniques like fuzzy logic, machine learning, heuristic algorithms to simulate the human brain activities and can be, among complex tasks, used to make predictions such as biomass/biofuel properties, bioenergy end-use/conversion process performance, supply chain modeling, optimization. The optimization methods include genetic algorithm, response surface methodology and Taguchi method. Artificial Neural Network and Regression and Analytical methods can be used for internal combustion engine research. AI bioenergetic systems applications are still limited although studies indicate great potential for finding solutions for bioenergy development projects [31–45].

Machine learning (ML) methods can be used in industrial processes to monitor, optimize, control systems, diagnose mistakes, forecast maintenance, notify process attacks. Some powerful machine learning algorithms include principal component analysis (PCA), decision trees (DT), linear regression, k-nearest neighbor classifier (KNN), random forests regression (RFR), artificial neural networks (ANN) and support vector machines (SVM) whereas a programmed process uses consecutive iterations based on external variant inputs, gradually updating the problem-solving capability/self-improvement, to solve complicated questions of studies involved. ML technology can be important in processes involved in biodiesel production such as extracting oil, pretreating feedstock, transesterification, reaction, separating products, recovering unreacted alcohol, neutralizing glycerin, washing and purification [31–45].

In the soil phase of biodiesel production, machine learning applications including extreme gradient boosting (GBL, GBD), gene expression programming (GBT), ANN, random forest (RF), supported vector regression (SVR), supported vector machines (SVM), principal component analysis (PCA), partial least square (PLS)) were applied to predict sorghum crop yield, biomass yield in forest, estimate corn production environmental impacts, and land productivity. In the feedstock phase of biodiesel production single and multiple linear regression methods as well as ANN methods were used to predict viscosity, oxidative stability, density, kinematic viscosity and estimate rheological properties [31–45].

Regarding production of biodiesel from renewables, ML can be usefull in all the steps incuding extracting oil, pretreating feedstock, transesterification reaction, separating products, recovering ureacted alcohol including modeling biodiesel-fueled engines and combustion approaches [31–45].

## 23 Comparison of Catalysts in the Production Process

We can compare the catalysts [1–45] used for transesterification/esterification. We start with homogeneous alkali (NaOH, KOH) offering high reactivity, faster reaction

rate, minimum cost, encouraging kinetics, moderate working conditions whereas for high FFA feedstock it is inappropriate; in the presence of FFA and moisture it deactivates, high amount of waste water is required, as a side reaction saponification occurs and is non-recyclable.

Next we have the acid catalysts, HCL, HF, H<sub>2</sub>SO<sub>4</sub>, which are non-reactive to FFA content in oil and moisture, with simultaneous catalyzed esterification/transesterification reactions which, however have slow reaction rates, long reaction times and are corrosive in nature, involving higher reaction temperature/pressure, equipment corrosion, weak catalytic activity, high oil/alcohol requirement and difficulties to recycle.

Heterogeneous alkali catalysts (CaO, SrO, MgO, mixed oxide and hydrotalcite) are non-corrosive, environmentally benign, recyclable, fewer disposal problems, easy separation, higher selectivity and longer catalyst life. They involve slow reaction rates compared to the homogeneous, low FFA requirement in the feedstock (<1 wt%), highly sensitive to water and FFA, saponification as a side reaction, soap formation, high volume of wastewater, leaching of active catalyst sites, diffusion limitations, complex and expensive synthesis route, high cost of catalyst synthesis.

The heterogeneous alkali catalysts include CaO, SrO, MgO, mixed oxide and hydrotalcite, which are non-corrosive, environmentally benign, recyclable, have fewer disposal problems, easy separation, higher selectivity, longer catalyst life, with disadvantages of slow reaction rates compared to homogeneous one, low FFA requirement for feedstock, high sensitivity to water and FFA, saponification as side reaction, soap formation, high volume of wastewater, leaching of catalyst sites, diffusion limitations, complex and expensive synthesis routes.

The acid catalysts include ZrO, TiO, ZnO, ion-exchange resin, sulfonic modified mesostructured silica, which are insensitive to FFA and water content in the oil, catalyze tranesterification and esterification reactions simultaneously, are eco-friendly and recyclable as well as non-corrosive to reactors and their parts but have the disadvantage of moderate reaction rates, long reaction time, higher reaction temperature and pressure, high alcohol/oil requirement, weak catalytic activity, low acidic sites, low micro porosity, leaching of active catalyst sites, diffusion limitations, complex and expensive synthesis routes and high cost of catalyst synthesis.

## 24 Comparison of Industrial Production Methods

Both acid and homogeneous based catalysts have high reactivity compared to heterogeneous catalysts. However, the homogeneous catalysts have low quality glycerol production, inability for catalyst regeneration and lengthy biodiesel production process leading to an uneconomical process with considerable labour and leading to the usage of solid catalysts. Supported solid base catalyst and basic metal oxides indicate excellent activity for biodiesel production with, however, industrial limitations due to their high sensitivity against FFA limits. The acid counterparts also have their limitations as they are not efficient towards the transesterification reactions.

Mixed metal oxides are gaining more attention due to their excellent chemical and thermal stability, high surface area as well as tailored acid-base properties and can be used for (trans)esterification of high FFA content vegetable oils. Enzyme-based catalysts operate at mild reaction conditions, are environmentally benign and display high specificity with however, sensitivity towards poor operational stability, heat, and pH range, limiting industrial applicability. The immobilized lipase has the advantages of high thermal stability, cost-effectiveness and great tolerance to changes of PH, i.e., industrial scale applicability. Bio-waste catalysts are cost-effective, easily available, environmentally benign with industrial scale applicability but are limited by reusability due to leaching of active sites and they also face strong competition for industrial applications with the metal-free carbon based solid acid catalyst (environmental-friendly, biogenic, low production costs, great chemical/thermal stability and surface chemistry). The bifunctional catalysts possess both solid basic character (transesterification to FAME) and solid acidic character (address FFA), are thermostable/insensitive to moisture, very reusable and can be used in industrial scale biodiesel productions.

## 25 Conclusions and Outlook

The industrial globalization/increase in human population and the limited fossil fuel resources sparks the need for alternative/renewable/sustainable fuels such as biodiesel production from methods such as transesterification using homogeneous and heterogeneous catalysts whereas due to limitations of the former and numerous advantages of the latter makes the heterogeneous catalysts the most promising. However, reactivity of solid catalysts are dependent on selection of a number of variable (oil type, temperature, reactor, leaching), leading to nanotechnology as the emerging promising branch of science for biodiesel catalysis including (production of easily recoverable solid-acid or solid-base catalysts, serving as interface between homogeneous and heterogeneous catalysts) whereas magnetic nanoparticle-supported catalyst can be cost effective by possibility of being easily recoverably for the reuse of catalysts. Nanomaterials can be used for economic viability/energy optimization whereas low cost biofuel could become a good alternative. AI can be used to make predictions including biomass/biofuel properties, bioenergy end-use/conversion process performance, supply chain modeling, optimization. ML can be useful in all the steps of biodiesel production from renewables including extracting oil, pretreating feedstock, transesterification reaction, separating products, recovering unreacted alcohol, modeling biodiesel-fueled engines and combustion approaches. Molecular Simulations models of materials and biomolecules can yield a better understanding of the catalytic process involved in biodiesel production.

We must also, however, remain alert for the ongoing progress of new potential, emerging energetic routes including transportation electric vehicles as well as geothermal, solar, hydro, wind power, fuel/solar cells and materials with potential for energetic applications discussed in other chapters of this book.

## References

1. Diaz, G.C., Leite, G.G.T., Cruz, Y.R., Aranda, G.A., Arceo, A.A., Furtado, N.C., Taft, C.A.: Biodiesel by hydroesterification of oil from the microalgae *scenedesmus dimorphus*. *Lett. Org. Chem.* **10**, 263 (2013)
2. Diaz G.C., Cruz Y.R., Leite G.G.T., Aranda, D.A.G., Furtado, N.C., Taft, C.A.: Hydroesterification of nannochloropsis oculata microalga's biomass to biodiesel using as catalyst pure niobium oxide ( $\text{Nb}_2\text{O}_5$ ), niobium oxide supported on alumina ( $\text{Nb}_2\text{O}_5/\text{Al}_2\text{O}_3$ ) and niobium oxide impregnated with phosphoric acid ( $\text{Nb}_2\text{O}_5\text{H}_3\text{PO}_4$ ). *Curr. Org. Chem.* **17**, 1350 (2013)
3. Gonçalves, J.A., Ramos, A.L.D., Rocha, L.L.L., Domingos, A.K., Monteiro, R.S., Peres, J.S., Furtado, N.C., Taft, C.A., Aranda, D.A.G.: Niobium oxide solid catalyst: esterification of fatty acids and modeling for biodiesel production. *J. Phys. Org. Chem.* **24**, 54 (2011)
4. Rocha, L.L.L., Andre Luis Dantas Ramos, A.L.D., Furtado, Nelson C., Taft, C.A., Aranda, D.A.G.: Production of biodiesel by a two-step niobium oxide catalyzed hydrolysis and esterification. *Lett. Org. Chem.* **7**, 571 (2010)
5. La Porta F.A., Taft C.A. (eds.): *Functional Properties of Advanced Engineering Materials and Biomolecules*. Engineering Materials. Springer, Cham (2021). [https://doi.org/10.1007/978-3-030-62226-8\\_2](https://doi.org/10.1007/978-3-030-62226-8_2)
6. Canchaya, J.G.S., Furtado, N.C., Taft, C.A.: An overview of fuel cells and simulation models. *Curr. Phys. Chem.* **5**, 223–252 (2015)
7. La Porta, F.A., Taft, C.A. (eds.): *Emerging Research in Science and Engineering Based on Advanced Experimental and Computational Strategies*. Engineering Materials Springer, Cham (2020). <https://doi.org/10.1007/978-3-030-31403-3>
8. Changmai, B., Vanlaveni, C., Prabhaker, Ingle, A.P., Bhagat, R., Rokhum, S.L.: Widely used catalysts in biodiesel production: a review. *RSC Adv.* **10**, 41625 (2020)
9. Kumar, Y., Yogeshwar, P., Bajpai, S., Jaiswal, P., Yadav, S., Pathak, D.P., Sonker, M., Tiwari, S.K.: Nanomaterials: Stimulants for biofuels and renewables, yield and energy optimization. *Mater. Adv.* **2**, 5318 (2021)
10. Mazaheri, H., Ong, C.H., Amini, Z., Masjuki, H.H., Mofijur, M., Su, C.H., Badruddin, I.A., Khan, T.M.Y.: An overview of biodiesel production via calcium oxide catalysts: current state and perspective. *Energies* **14**, 3950 (2021)
11. Wang, A., Quan, W., Zhang, H., Li, H., Yang, S.: Heterogeneous ZnO-containing catalysts for efficient biodiesel production. *RSC Adv.* **11**, 20465 (2021)
12. Oglio, D.F.D., Garcia, M.A.S., Fiorio, J.L., de Abreu, W.C., Pereira, L.N.S., Braga, A., de Moura, E.M., Guldhe, E., Bus, F., de Moura, C.V.R.: Reusable heterogeneous  $\text{SnO}_2/\text{ZnO}$  catalysts for biodiesel production from acidified/acid oils. *J. Braz. Chem. Soc.* **32**, 182 (2021)
13. Nguyen, H.C., Nguyen, M.L., Su, C.H., Ong, H.C., Juan, H.Y.: Bio-derived catalysts: a current trend of catalysts used in biodiesel production. *Catalysts*, **11**, 812 (2021) <https://doi.org/10.3390/catal11070812>
14. Thangaraj, B., Solomon, P.R.: Clean energy, Biodiesel production by the electrocatalytic process, **19** (2021)
15. Bitire, S. O.: The potential for a sustainable biodiesel production by modified biobased catalyst—A review. *IOP Conf. Ser.: Mater. Sci. Eng.* **1107**, 012206 (2021)
16. Rizwanul Fattah, I.M.R., Ong, H.C., Mahlia, T.M.I., Mofijur, M., Silitonga, A.S., Ashrafur Rahman, S.M.A., Ahmad, A.: State of the art of catalysts for biodiesel production. *Prod. Front. Energy Res.* **8**, 101 (2020). <https://doi.org/10.3389/fenrg.2020.00101>
17. Bharti, M.K., Chalia, S., Thakur, P., Sridhara S.N., Thakur, A., Sharma, P.B.: Nanoferrites heterogeneous catalysts for biodiesel production from soybean and canola oil: a review. *Environ Chem Lett.* <https://doi.org/10.1007/s10311-021-01247-2>
18. Narayan, N., Meiyazhagan, A., Vajtai, R.: Metal nano-particles as green catalysts. *Materials* **12**(21), 3602 (2019)
19. Norizan, M.N., Moklis, M.H., Demon, S.Z.N., Halim, N.A., Samsuri, A., Mohamad, I.S., Knight, V.F., Abdullah, N.: Carbon nanotubes: functionalisation and their application in chemical sensor. *RSC Adv.* **10**(71), 43704 (2020). <https://doi.org/10.1039/d0ra09438b>

20. Chen, H., Zhng, L., Li, M., Xie, G.: Synthesis of core-shell micro/nanoparticles and their tribological application: a review. *Materials*, **13**, 1 (2020). <https://doi.org/10.33390/ma13204590>
21. Nalluri, S.R., Nagarjuna, R., Patra, D., Ganesan, R., Balaji, G.: Large scale solid-state synthesis of catalytically active Fe<sub>3</sub>O<sub>4</sub>@M (M = Au, Ag and Au–Ag Alloy) Core-Shell nanostructures. *Sci. Rep.* **9**(1), 6603 (2019). <https://doi.org/10.1038/s41598-019-43116-7>
22. Ambat, I., Srivastava, V., Haapaniemi, E., Sillanpaa, M.: Nano-magnetic potassium impregnated ceria as catalyst for biodiesel production. *Renew Energy*, **139**, 1428 (2019)
23. Bharti, M.K., Gupta, S., Chalia, S., et al.: Potential of magnetic nano-ferrites in removal of heavy metal from contaminated water: mini review. *J. Supercond. Nov. Magn.* <https://doi.org/10.1007/s10948-020-05657-1>
24. Ghalandari, A., Taghizadeh, M.: Statistical optimization of the biodiesel production process using a magnetic core-mesoporous shell KOH/Fe<sub>3</sub>O<sub>4</sub>@ $\gamma$ -Al<sub>2</sub>O<sub>3</sub> nanocatalyst. *Chem. Eng. Technol.* **42**, 89 (2019)
25. Jeon, Y., Chi, W.S., Hwang, J., et al.: Core-shell nanostructured heteropoly acid-functionalized metal-organic frameworks: bifunctional heterogeneous catalyst for efficient biodiesel production. *Appl. Catal. B Environ.* **242**, 51 (2019)
26. Arya, I., Poona, A., Kumar Dikshit, P.K., Pandit, S., Kumar, J., Singh, H.N., Jha, N.K., Rudayni, H.A., Chaudhary, A.A., Kumar, S.: Current trends and future prospects of nanotechnology in biofuel production. *Catalysts*, **11**, 1308 (2021)
27. Bano, S., Ganie, A.S., Sultana, S., Sabir, S., Khan, M.Z.: Fabrication and optimization of nanocatalyst for biodiesel production: an overview. *Front. Energy Res.* (2020). <https://doi.org/10.3389/fenrg.2020.579014>
28. Bano, S., Adil Shafi Ganie, A.S., Sultana, S., Sabir, S., Zain Khan, M.Z.: Fabrication and optimization of nanocatalyst for biodiesel production: an overview. *Front. Energy Res.* (2020). <https://doi.org/10.3389/fenrg.2020.579014>
29. Mumtaza, M., Baqara, Z., Hussaina, N., Bilal, A.M., Azam, H.M.H., Baqird, Q., Hafiz, M.N., Iqbale, H.M.N.: Application of nanomaterials for enhanced production of biodiesel, biooil, biogas, bioethanol, and biohydrogen via lignocellulosic biomass transformation. *Fuel*, 122840 (2021)
30. Schnedlitz, M., Lasserus, M., Meyer, R., Knez, D., Hofer, F., Ernst, W.E., Hauser, A.W.: Stability of Core-Shell nanoparticle for catalysis at elevated temperatures: structural inversion in the Ni–Au system observed at atomic resolution. *Chem. Mater.* **30**, 1113 (2020). <https://doi.org/10.1021/acs.chemmater.7b05075>
31. Xing, Y., Zheng, Z., Sun, Y., Alikhani, A., Alikhani, M.A.: A review on machine learning applications in biodiesel production studies. *Int. J. Chem. Eng.* (2021), Article ID 2154258. <https://doi.org/10.1155/2021/2154258>
32. Mohd Ali, J., Hussain, M.A., Tade, M.O., Zhang, J.: Artificial Intelligence techniques applied as estimator in chemical process systems-a literature survey. *Expert Syst. Appl.* **42**(14), 5915 (2015)
33. Liao, M., et al.: Applications of artificial intelligence based modeling for bioenergy systems: a review. *GCB Bioenergy*, **13**, 774 (2021)
34. Weichert, D., Link, P., Stoll, A., et al.: A review of machine learning for the optimization of production processes. *Int. J. Adv. Manuf. Technol.* **104**(5), 1889 (2019)
35. Bastos, R.R.C., Da Luz Correa, A.P., Da Luz, P.T.S., Da Rocha Filho, G.N., Zamian, J.R., Da Conceição, L.R.V.: Optimization of biodiesel production using sulfonated carbon-based catalyst from an amazon agro-industrial waste. *Energy Conv Manag* **205**, 112457 (2020)
36. Sandesh, K., Ujwal, P.: Trends and perspectives of liquid biofuel-process and industrial viability. *Energy Conv. Manag.* **10**, 100075 (2021)
37. Bobadilla, M.C., Martinez, R.F., Lorza, L.F., Gomez, S., Gonzalez, E.V.: Optimizing biodiesel production from waste cooking oil using genetic algorithm-based support vector machines. *Energies*, **11**, 2995 (2018)
38. Aghbashlo, M., Peng, W., Tabatabaei, M., et al.: Machine learning technology in biodiesel research: a review. *Prog. Energy Combust. Sci.* **85**, 100904 (2021)

39. Habyarimana, E., Piccard, I., Catellani, M., De Franceschi, P., Dall'Agata, M.: Towards predictive modeling of sorghum biomass yields using fraction of absorbed photosynthetically active radiation derived from sentinel-2 satellite imagery and supervised machine learning techniques. *Agronomy*, **9**, 203 (2019)
40. Yang, P., Zhao, Q., Cai, X.: Machine learning based estimation of land productivity in the contiguous US using biophysical predictors. *Environ. Res. Lett.* **15**(7), 074013 (2020)
41. Mairizal, A.Q., Awad, S., Priadi, C.R., et al.: Experimental study on the effects of feedstock on the properties of biodiesel using multiple linear regressions. *Renew. Energy* **145**, 375 (2020)
42. Tchameni, A.P., Zhao, L., Ribeiro, J.X.F., Li, T.: Predicting the rheological properties of waste vegetable oil biodiesel modified water-based mud using artificial neural network. *Geosyst. Eng.* **22**, 101 (2019)
43. Ahmad, I., Ayub, A., Ibrahim, U., Khattak, M., Kano, M.: Data-based sensing and stochastic analysis of biodiesel production process. *Energies*, **12**, 63 (2019)
44. Kumar, S.: Comparison of linear regression and artificial neural network technique for prediction of a soybean biodiesel yield. *Energy Sour. Part A: Recov. Utiliz. Environ. Effects* **42**, 1425–1435 (2020)
45. Sivamani, S., Selvakumar, S., Rajendran, K., Muthusamy, S.: Artificial neural network-genetic algorithm based Optimization of biodiesel production from *Simarouba glauca*. *Biofuels*, **10**, 393 (2019)



# Bioactivity

# In Silico Drug Design and in Vivo Acute Toxicity Assay of Chalcone Analogs with Biological Antiparkinsonian Activity



**Bianca L. B. Marino, Jaderson V. Ferreira, L. Brenda Sánchez-Ortiz, José C. T. Carvalho, Irlon M. Ferreira, Suzane Q. Gomes, Carlos Henrique Tomich de Paula da Silva, Carlton A. Taft, and Lorane Izabel da Silva Hage-Melim**

**Abstract** Parkinson's disease (PD) is caused by a lack of dopamine, causing an imbalance in the cognitive and motor regions of the brain. Therefore, the search for new inhibitors is important to increase the therapeutic possibilities. Thus, medicinal plants are more studied because they have many substances with varied biological activities. With Medicinal Chemistry, through in silico studies, it is possible to design molecules with defined activity, then confirm this activity in in vitro and in vivo tests. In this study, the animal model used was *Danio rerio* (zebrafish), due to the similarities of its central nervous system with that of humans. Thus, the study aimed to in silico drug design and evaluate the in vivo acute toxicity of molecules with the prediction of MAO-B activity for the development of drugs that are candidates for the treatment of PD. According to the results obtained in silico, it was possible to identify Amburoside A as a promising bioligand from which the analogs PMC1, PMC2, PMC3 were obtained, the last being tested in zebrafish for acute toxicity test with a negative result, indicating that it is a promising molecule to treat Parkinson's disease.

---

**Supplementary Information** The online version contains supplementary material available at [https://doi.org/10.1007/978-3-031-07622-0\\_14](https://doi.org/10.1007/978-3-031-07622-0_14).

---

B. L. B. Marino · J. V. Ferreira · L. I. da S. Hage-Melim (✉)  
Laboratory of Pharmaceutical and Medicinal Chemistry (PharMedChem), Federal University of Amapá, Macapá, Brazil  
e-mail: [loranehage@gmail.com](mailto:loranehage@gmail.com)

L. B. Sánchez-Ortiz · J. C. T. Carvalho  
Laboratory of Research Pharmaceutical, Federal University of Amapá, Macapá, Brazil

I. M. Ferreira  
Laboratory Biocatalysis and Biotransformation in Organic Chemistry, Federal University of Amapá, Macapá, Brazil

S. Q. Gomes · C. H. T. de Paula da Silva  
Computational Laboratory of Pharmaceutical Chemistry, Department of Pharmaceutical Sciences, Faculty of Pharmaceutical Sciences of Ribeirão Preto, University of São Paulo, Ribeirão Preto, São Paulo, Brazil

C. A. Taft  
Centro Brasileiro de Pesquisas Físicas, Rio de Janeiro, Brazil

**Keywords** Parkinson · Medicinal plants · Medicinal chemistry · Zebrafish

## 1 Introduction

The diagnosis of neurodegenerative diseases is gradually increasing in the world population, due to the growing number of people diagnosed. The most diagnosed neurodegenerative disease is Alzheimer's Disease, and the second most common is Parkinson's Disease (PD), which affects people aged 55–60 years [1]. And in Brazil, there was an increase in the frequency of neurodegenerative diseases diagnosed in individuals over the age of 60, including Parkinson's disease. PD is a neurodegenerative disease caused by the death of dopaminergic neurons which are responsible for the synthesis of the neurotransmitter dopamine (AD), affecting the cognitive and motor regions of the brain [2]. The cause of neuron degradation has not yet been discovered, but some hypotheses have emerged to explain the pathophysiology of PD, one of which is the oxidative stress caused by monoamine oxidase B (MAO-B) by degrading dopamine, releasing free radicals, in addition to decreasing the amount of the neurotransmitter in the synaptic cleft [3, 4].

Given the relationship between MAO-B and the pathophysiology of PD, the focus of many studies is on inhibiting this enzyme to decrease its activity and increase AD in the synaptic cleft, in addition to reducing the production of free radicals. However, this class of medication is not widely used in treatment due to its side effects, and this causes patients to fail to adhere to treatment [5, 6]. Thus, there is a growing number of studies with medicinal plants, considering their variety of natural substances, in which they can assist in the development of drugs with better activities, in addition to always seeking to reduce side effects, and there is also greater adherence to the treatment by the Brazilian population when the medication is of natural origin. Among the medicinal plants found in the Brazilian flora, there is *Passiflora incarnata* and *Amburama cearensis* with a potent antioxidant and neuroprotective effect, from which natural substances can be used to plan antiparkinsonian drugs [7, 8].

Since the 18th century, the discovery of new drugs was made at random based on traditional knowledge, empirical practice of using natural products to treat diseases. Although they have not been analyzed correctly, it was possible to identify many molecules with important pharmacological activity. With the advancement of computer technology, there was, consequently, an increase in structural databases making the *in silico* study through molecular modeling, bioinformatics, and artificial intelligence, more accessible and interesting for research, due to its quick access and result with lower cost [9]. A widely used *in silico* approach is the virtual screening process, based on *in vitro* and/or *in vivo* tests, several molecules are subjected to computational tools to simulate various tests, such as pharmacokinetic and toxicological properties, activity prediction and synthetic viability, among others, this approach to drug discovery is called Medicinal Chemistry [10].

The choice of the animal model in the *in vivo* test depends on the objective of the study and the pathology to be studied. In the case of PD, since the 1980s, the

fish *Danio rerio*, popularly known as Zebrafish, started to use, as this fish has many important characteristics for carrying out various studies, such as rapid growth facilitating studies of reproductive toxicity, and lower financial cost for both purchasing and maintaining the environment [11]. In addition, Zebrafish fish have anatomical and functional characteristics similar to those of mammals, such as the brain where dopaminergic neurons, Purkinje cells of the cerebellum and motor neurons are found. Some studies have suggested that the neurotoxin 1-methyl-4-phenyl-1,2,3,6-tetrahydropyridine (MPTP) is metabolized in Zebrafish embryos and larvae by a monoamine oxidase similar to mammalian MAO-B [12].

According to data obtained in the scientific literature, this study aimed to plan MAO-B inhibitor drug candidates from the prototype of natural origin, through Medicinal Chemistry, using in silico planning, synthesis of analogs and evaluation in vivo toxicity.

## 2 Results and Discussion

### 2.1 A Bibliographic Search of Natural Substances

In Fig. 1, the medication, used as a standard, and the natural substances described in the literature and used in this study are observed, respectively: Selegiline (1), Amburoside A (2), Harman (3), Harmaline (4), Harmalol (5), which were designed in the ChemSketch 12.0 software [3, 4, 7, 12–14].

Selegiline was the first MAO-B inhibitor to be discovered. The molecule was synthesized by Zoltán Ecséri at Chinoin Pharmaceuticals (Budapest, Hungary) in 1962, and its selective inhibitory effect of selegiline on one of the MAO isoforms was identified by Knoll and Magyar (1972). Since then, this drug has been used for the treatment of PD, as it is an irreversible inhibitor that in high doses has antidepressant activity, it also has a neuroprotective action against MPTP (1-methyl-4-phenyl-1,2,3,6-tetrahydropyridine) and its sympathomimetic effects are related to methamphetamine metabolites. However, due to its adverse effects such as insomnia, dizziness, headache, bradykinesia, among others, patients abandon treatment [4, 6, 15].

Of the various plants reported in the literature, two plants belonging to the Brazilian flora *Amburana cearensis*, which is native to the Brazilian northeastern region and *Passiflora incarnata* native to the Amazon, were found to enhance the plants of the national flora, in which experimental studies with activity were reported neuroprotective effects in induced PD models [8, 13, 16].

*A. cearensis* (sin. *Torresea cearensis*) is a plant belonging to the Leguminosae family, popularly known by several designations, such as imburana of smell, cherry and coumarou [16]. In a review study of Brazilian plants with inflammatory activity, the natural substances isokaempferide (12.5, 25 and 50 mg/kg) and amburoside A (25 and 50 mg/kg), isolated from the shells of *A. cearensis*, with considerable

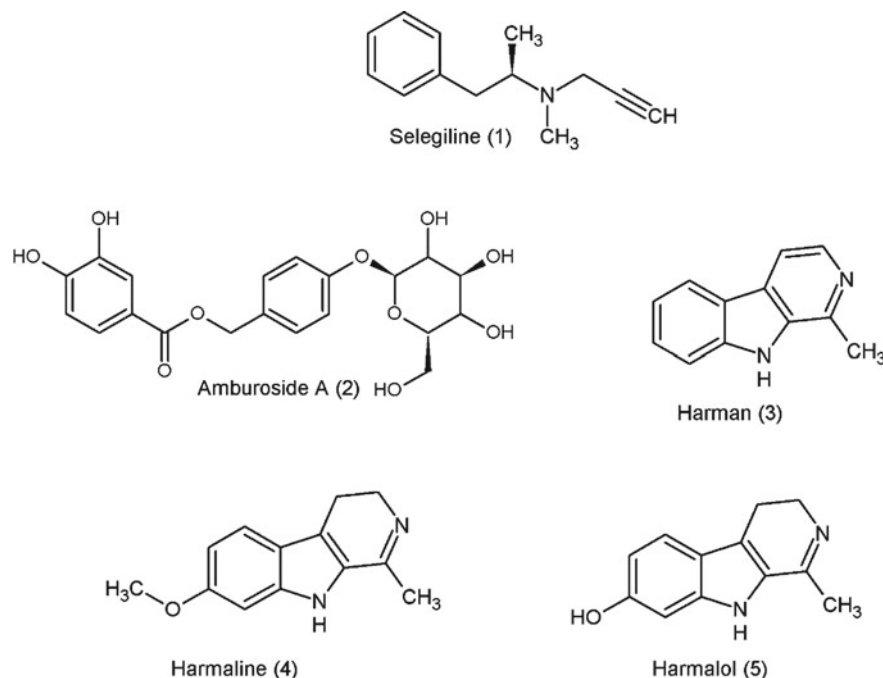


**Fig. 1** Chemical structure of Selegiline (1), and of the natural substances Amburoside A (2), Harman (3), Harmaline (4), Harmalol (5)

anti-inflammatory activity, as they inhibited the migration of neutrophils and leukocytes and the production of TNF- $\alpha$  and prostaglandins E<sub>2</sub> [17]. In another study, the phenolic glycosides found in *A. cearensis*, Amburoside A and B had their biological activity evaluated in cell cultures exposed to the neurotoxin 6-hydroxydopamine (6-OHDA), a hydroxylated derivative of dopamine that is possibly formed endogenously in patients with PD, however, only amburoside A showed neuroprotection [7, 13].

*P. incarnata* popularly known as passion fruit, a word of indigenous origin (tupi), is a herbaceous, climbing plant from northern South America. The main constituents of *P. incarnata* leaves are flavonoids (0.25%), such as vitexin, isovitexin, orientin, isoorientin, apigenin and kampferol. Alkaloids based on the  $\beta$ -carboline ring system, harman, harmalin, harmaline and harmalol are said to be effective anti-Parkinson compounds [15]. Flavonoids with potential antioxidant activity such as antiparkinsonian and for improving memory in the treatment of Alzheimer's disease were also evaluated in which the results showed a significant decrease in free radicals [8]. Other studies with *P. incarnata*, with the aqueous extract of dry leaves, evaluated the effects of the extract in albino mice that were experimentally induced by neuroleptics to develop DP catalepsy, as this is an animal model used to screen for drugs and obtained positive results in terms of activity [18].

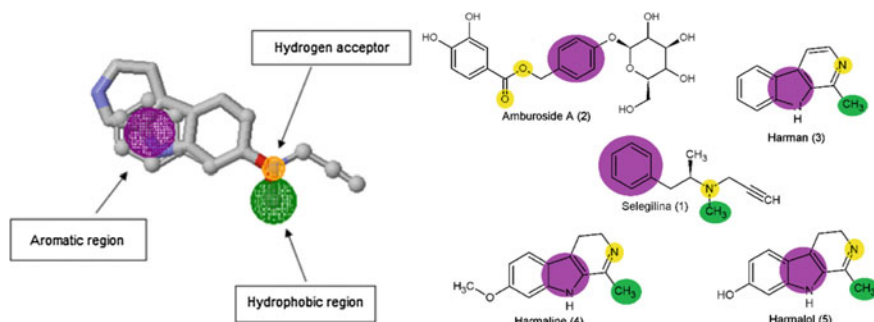


**Fig. 2** Derivation of the pharmacophoric group of Selegiline and the 4 natural substances

## 2.2 Derivation of the Pharmacophoric Pattern

Pharmacophore is the set of electronic and steric characteristics that identifies one or more functional groups or structural subunits, necessary for better molecular recognition by the receptor and, therefore, for the desired pharmacological effect, these are classified by a score [20]. Selegiline and the 4 substances of natural origin were submitted to the webserver PharmaGist obtaining the pharmacophore. Figure 2 shows the result of the pharmacophore with Selegiline as the pivot molecule, however, in the grouping there was only the natural product Harmalina with the score of 4.825 showing the spatial characteristics: a hydrogen bond acceptor group (yellow sphere), a hydrophobic group (sphere green) and an aromatic region (purple sphere). On the basis of these results similar essential regions were identified in the other natural substances.

Hagenow and collaborators [21] identified, for the MAO-B inhibitor, the pharmacophoric pattern with a hydrophobic region, two acceptor regions and an aromatic region. While Mathew et al. [22], find a model with a hydrogen acceptor, a hydrophobic and two aromatic regions. In the present study, the aromatic, hydrogen-accepting and hydrophobic regions were similar to previous studies.

## 2.3 Molecular Docking Study

For the study of docking simulation, the standard drug Selegiline (1) and the natural substances Amburoside A (2), Harman (3), Harmaline (4), Harmalol (5) were considered as a ligand and, as an enzyme, MAO-B. For that, first, the selection was made from the Protein Data Bank (PDB) database of the crystallographic structure of MAO-B deposited in the form of a complex under the code 4A79, with the resolution of 1.89 Å. The software used was GOLD 5.4, which uses the genetic algorithm for the purpose of flexible ligand docking experiments within protein binding sites [23].

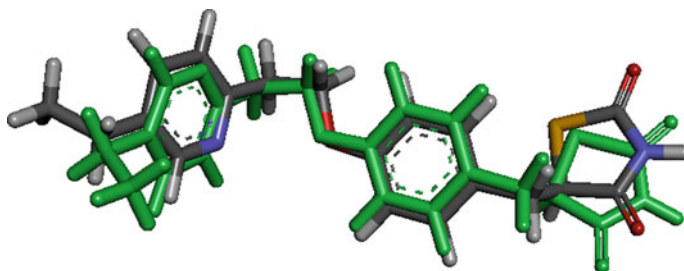


**Fig. 3** Result of the docking simulation with the lowest RMSD for the validation of the 4A79 complex

This was used to identify the MAO-B binding site so that the interaction between the ligands and the enzyme can be simulated.

The validation of the docking simulation software consists of the replication of the experimental result of the positions of the atoms of the ligand in relation to the active site of the enzyme, acquired from the crystallographic complex, and through the GOLD 5.4 software, several coupling tests were performed in an attempt to obtain the same positions of the atoms of the experimental result. The most used method to analyze if the software managed to reproduce the experimental result is the calculation of the Mean Quadratic Deviation (RMSD) in which previous studies showed that results smaller than 2 Å have a high success rate for replicating the experimental result [24]. Through the Discovery Studio Visualizer software [14] it was possible to visualize the RMSD value of 1.381 Å compared to the position of the ligand from the experimental result of the 4A79 complex, shown in Fig. 3.

Hydrophobic interactions occur between nonpolar regions such as aromatic rings and methyls. Conventional hydrogen bonds are characterized when a proton acceptor region interacts with a proton donor region due to the difference in electronegativity. This type of coupling occurs between electronegative atoms such as oxygen and nitrogen [25]. Hydrogen bonds with a distance below or equal to 3 Å are relevant to affirm that there is interaction, while hydrophobic bonds have a distance below or equal to 5 Å so that there is an interaction between amino acids and the natural binding product [26].

Figure 4 shows the possible interactions between the amino acid residues of the active site that were selected as described in the literature: TYR398, TYR435, PHE343, LEU171, TYR326, ILE316, PRO104, PRO104, ILE199, LEU171, CYS172, TRP119 [27] and the standard medicine, Selegiline, along with the studied natural substances. The analysis showed that the possible connections were mostly hydrophobic interactions and had two amino acids in common LEU171 and CYS172, and all the studied molecules had interaction with more than 3 amino acids among the 12 of the active site.

Table 1 shows the results of the docking simulation with the possible interactions for the standard molecule Selegiline (1), and the substances of natural origin Amburoside A (2), Harman (3), Harmaline (4) and Harmalol (5).

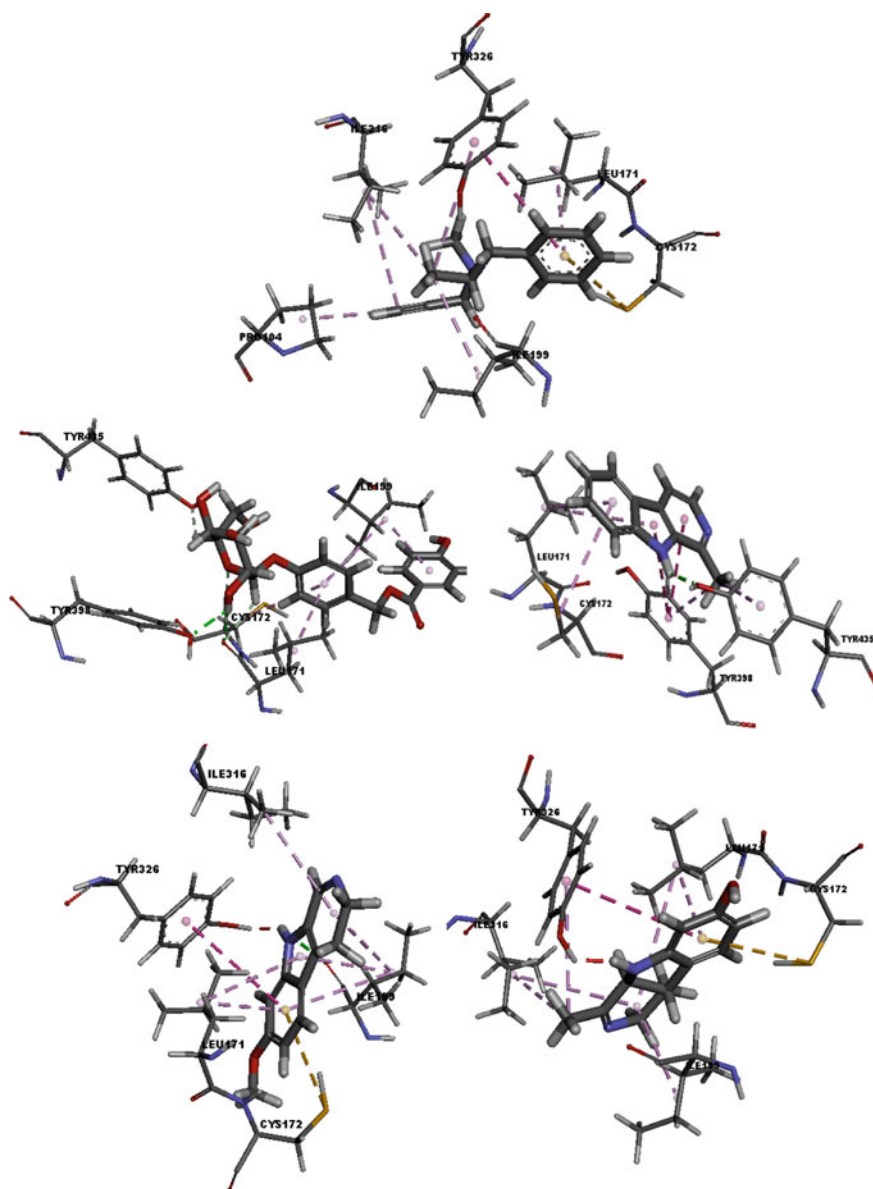


**Fig. 4** Representation of the molecular docking simulation of the amino acid residues of the MAO-B active site and the studied natural substances: Selegiline (1), Amburoside A (2), Harman (3), Harmaline (4) and Harmalol (5)



**Table 1** Docking simulation between the studied molecules and the amino acid residues of the MAO-B enzyme active site

Molecules	Active site amino acids	Atoms involved	Interaction types	Distance (Å)	Score
Selegiline	PRO 104	Alkyl-H	Hydrophobic	3.99	64.54
	LEU171	1343 C-Ph	Hydrophobic	4.24	
	CYS172	S-Ph	Van der Waals	4.73	
	ILE199	Alkyl-C	Hydrophobic	4.22	
	ILE 316	Alkyl-C	Hydrophobic	4.64	
			Hydrophobic	4.84	
	TYR 326	Ph-C	Hydrophobic	5.28	
Hydrophobic			5.46		
Amburoside A	LEU 171	1343 C-Ph	Hydrophobic	3.97	105.20
	CYS 172	H-O	Hydrogen interaction	2.65	
		S-Ph	Hydrophobic	5.06	
	ILE 199	Alkyl-Ph	Hydrophobic	3.83	
			Hydrophobic	4.89	
	TYR 398	O-H	Hydrogen interaction	2.11	
TYR 435	OH-H	Hydrogen interaction	2.51		
Harman	LEU 171	C1343-Ph	Hydrophobic	4.52	64.01
	CYS 172	S-Ph	Hydrophobic	4.83	
	TYR 398	Ph-Ph	Hydrophobic	4.51	
			Hydrophobic	5.36	
			Hydrophobic	4.06	
	TYR 435	Ph-C14	Hydrophobic	3.84	
Hydrogen interaction			2.09		
Harmaline	LEU 171	C1343-Ph	Hydrophobic	4.21	57.32
	CYS 172	S-Ph	Hydrophobic	4.76	
	ILE 199	O-H	Hydrogen interaction	3.08	
			Hydrophobic	4.79	
			Hydrophobic	4.86	
			Hydrophobic	4.22	
	ILE 316	Alkyl-C11	Hydrophobic	4.87	
TYR 326	Ph-Ph	Hydrophobic	3.36		
Harmalol	LEU 171	C1343-Ph	Hydrophobic	4.19	57.50

(continued)

**Table 1** (continued)

Molecules	Active site amino acids	Atoms involved	Interaction types	Distance (Å)	Score
	CYS 172	S-Ph	Hydrophobic	4.88	
	ILE 199	Alkyl-C11	Hydrophobic	4.20	
	ILE 316	Alkyl-C11	Hydrophobic	5.28	
		Alkyl-C15	Hydrophobic	4.72	
	TYR 326	Ph-Ph	Hydrophobic	5.34	
		Ph-C15	Hydrophobic	4.92	

The docking simulation between Selegiline and the MAO-B amino acid residues showed 8 interactions in 6 different amino acid residues from the active site: CYS172, TYR326, PRO104, ILE316, ILE199 and LEU171. All interactions were hydrophobic, with the exception of the interaction with the amino acid residue CYS172 in which a van der Waals interaction was obtained between the sulfur atom of the amino acid CYS172 and the resonance of the aromatic ring of the molecule with a distance of 4.73 Å. With the amino acid residue TYR326, two hydrophobic interactions were observed, one between the resonance of the aromatic ring of the amino acid and the carbon of the methyl radical of the molecule, and the other between the aromatic rings of both the amino acid and the molecule, with distances 5.28 Å and 5.46 Å, respectively. With the amino acid residue PRO104, a hydrophobic interaction was obtained between an alkyl group of the amino acid and the hydrogen atom of the molecule with a distance of 3.99 Å. With the amino acid residue ILE316, two hydrophobic interactions were observed, between an alkyl group of the amino acid and the carbon of the methyl radical, and another interaction between the alkyl group of the amino acid residue and the tertiary carbon of Selegiline, with distances of 4.84 Å and 4.64 Å, respectively. With the amino acid residue ILE199, a hydrophobic interaction was obtained between an alkyl group of the amino acid and the carbon of the methyl radical of the molecule with a distance of 4.22 Å. With the amino acid residue LEU171, a hydrophobic bond was obtained between an alkyl group of the amino acid and the aromatic ring of the molecule with a distance of 4.24 Å, with a score of 64.54.

The simulation between Amburoside A and the MAO-B amino acid residues showed 7 bonds in 5 different amino acids: LEU171, CYS172, TYR398, TYR435 and ILE199. Most of the interactions are of the hydrophobic type (4), and there have also been three interactions of hydrogen between the hydrogen (H) and oxygen (O) atoms. With the amino acid residue LEU171, a hydrophobic interaction was obtained between the alkyl group of the amino acid residue and the aromatic ring of the natural substance with a distance of 3.97 Å. The amino acid residue CYS172 had two interactions, one of the hydrogen interaction type between the H of the amino acid and O of the natural substance with a distance of 2.65 Å, and the other of the hydrophobic type between an alkyl group of the amino acid residue and the ring aromatic of the natural substance, with a distance of 5.06 Å. With the amino acid

residue TYR398, a hydrogen interaction was obtained between the O atoms of the amino acid residue and the H atoms of Amburoside A with a distance of 2.11 Å. The amino acid residue TYR435 showed a hydrogen interaction between the hydroxyl O of the amino acid and the H of Amburoside A with a distance of 2.51 Å. The amino acid residue ILE199 showed two hydrophobic interactions, between alkyl groups of the amino acid residue and the aromatic ring of Amburoside A, with distances of 3.83 and 4.89 Å, with a score of 105.20.

In the simulation between Harman and the MAO-B amino acid residues, 7 interactions were observed in 4 different amino acids: TYR435, TYR398, LEU171 and CYS172. Most interactions are of the hydrophobic type and only one of the hydrogen interaction type. With the amino acid residue TYR435, two interactions were observed, one of the hydrogen interaction type between the O of the amino acid residue and the H of Harman, and another of the hydrophobic type between the aromatic ring of the amino acid residue and the alkyl group, with distances of 2.09 Å and 3.84 Å, respectively. With the amino acid residue TYR398, three hydrophobic interactions were observed, one between the aromatic rings of the amino acid residue and the Harman, another between the aromatic ring of the amino acid residue and the pyrrolidine ring of the Harman, and one between the aromatic ring of the amino acid residue and the alkyl group of the Harman with distances 4.51 Å, 5.36 Å, 4.06 Å, respectively. The amino acid residue LEU171 showed a hydrophobic interaction between the alkyl group of the amino acid residue and the aromatic ring of Harman with a distance of 4.52 Å. The amino acid CYS172 showed a hydrophobic interaction between the alkyl group of the amino acid residue and the aromatic ring of the Harman at a distance of 4.83 Å, with a score of 64.01.

In the simulation between Harmaline and the MAO-B amino acid residues, 8 interactions were observed in 5 different amino acids: ILE199, CYS172, TYR326, ILE316 and LEU171. Most of the bonds were of the hydrophobic type, with only one of the hydrogen interaction type. With the amino acid residue ILE199, a hydrogen interaction was obtained between the O atoms of the amino acid residue and H of Harmaline, and three hydrophobic interactions, one between the alkyl group of the amino acid residue, and the three aromatic rings of the natural product, with distances of 3.08 Å, 4.79 Å, 4.86 Å and 4.22 Å, respectively. With the amino acid residue CYS172, an interaction was obtained between the sulfur atom (S) of the amino acid and the aromatic ring of Harmaline with a distance of 4.76 Å. With the amino acid residue TYR326, a hydrophobic interaction was obtained between the aromatic rings of the amino acid residue and the alkyl group of Harmaline with a distance of 3.36 Å. The amino acid residue ILE316 presented a hydrophobic interaction between alkyl groups of the amino acid residue and the pyridine of Harmaline with a distance of 4.87 Å. The amino acid residue LEU171 presented two hydrophobic interactions, one between the alkyl group of the amino acid and the aromatic ring of Harmaline with a distance of 4.21 Å, with a score of 57.32.

In the simulation between Harmalol and the MAO-B amino acid residues, 7 interactions in 5 different amino acids were observed. All interactions are hydrophobic. With the amino acid CYS172, an interaction was obtained between the sulfur (S) of the amino acid residue and the aromatic ring of Harmalol with a distance of 4.88 Å.

With the amino acid residue TYR326, two interactions were observed, one between the aromatic rings of the amino acid residue, with the alkyl group of Harmalol, with distances of 5.34 Å and 4.92 Å, respectively. With the amino acid residue LEU171, an interaction was obtained between the alkyl group of the amino acid residue and the aromatic ring of Harmalol with a distance of 4.19 Å. The amino acid residue ILE199 showed an interaction between the alkyl groups of the amino acid and the pyridine group of Harmalol with a distance of 4.20 Å. The amino acid residue ILE316 showed two interactions between the alkyl groups of the amino acid residue and the aromatic ring of Harmalol with distances of 5.28 and 4.72 Å, with a score of 57.50.

However, the standard molecule Selegiline an irreversible MAO-B inhibitor drug, this irreversibility characteristic is associated with the adverse effects of the inhibitors due to inactivating, totally or partially, the enzyme for a long period of time, in some cases causing the destruction of some functional groups of the active site, in which it is related to the type of bonds covalent, and in this case, it is assumed that the covalent bond is between the sulfur atom of the CYS172 residue and the molecule, in addition to being the only one that presented weak interaction with the amino acid residue PRO104 but important for conformation and stabilization of the interaction, with it is assumed that these two interactions may be the cause of the side effects of this drug. For the docking results, Selegiline showed 8 interactions in six different amino acids, being CYS172, TYR326, PRO104, ILE316, ILE199, LEU171, and the closest result to the standard molecule was the natural product Harmaline for presenting 8 interactions with the same amino acids the which Selegiline also interacted, with the exception of PRO104. Therefore, it can be deduced that Harmaline is more likely among the four substances of natural origin to present inhibitory activity of the MAO-B enzyme, in the same way as Selegiline, indicating irreversible inhibition. However, the natural substance Amburoside A showed 7 possible interactions in which 3 were with amino acids equal to which Selegiline interacted, and 2 different amino acids belonging to the active site, and its score was higher (105.20) in relation to the other molecules, indicating that probably the inhibitory action of Amburoside A is different from Selegiline and may be reversible, a characteristic that is desired in the planning of drugs with inhibitory action on MAO-B.

The study by Dhiman et al. [28]. presented the docking for the piperine, alkali of *Piper nigrum* in which they demonstrated possible links with TYR326, TYR398, PHE168, TRP119, PHE103, ILE199, CYS172, PHE343 and TYR188. Emphasizing that the natural substances in the present study also showed interactions with these amino acid residues, with Amburoside A being the highlight, out of the five amino acid residues that interacted, three are present in the study by Dhiman et al. [29].

Hagenow and collaborators [21] docked two compounds for MAO-A and MAO-B. With that, it was observed that the compounds had interaction with the amino acid residues LEU164, PHE168, PRO102, GLN206 and CYS172, the latter also interacting with the studied natural products.

## 2.4 Prediction of Pharmacokinetics (ADME) and Toxicological Properties

### 2.4.1 Prediction of Pharmacokinetic Properties

The *in silico* models of ADME properties, in comparison with traditional experimental tests, have greater applicability to meet the huge demand generated in the large-scale screening of new molecules. In addition, *in vitro* and *in vivo* tests have disadvantages that limit their use on a large scale: they are complex and expensive in terms of materials, infrastructure and qualified personal. Therefore, the *in silico* study is used as a complementary tool in research, being more used in the screening stage [29, 30].

For these reasons, there is great interest in the industry in the generation of ADME models *in silico* that can quickly assist in the selection of promising molecules and guide the elimination of compounds with an inappropriate pharmacokinetic profile. On the other hand, the integration of ADME models (*in silico*, *in vitro* and *in vivo*) seems to be an essential path to be followed in all stages of the drug discovery process. For the pharmacokinetic properties, the QikProp program was used, in which it predicts important parameters to be evaluated, mainly, in the absorption and distribution of a certain molecule in comparison with 95% of other molecules already known in the database. In addition, the program performs screening of molecules with the potential to be orally administered drugs through the Lipinski rule [31]. In this study, the parameters included for evaluation were: Human Oral Absorption (HOA), Caco-2 cells, Madin-Darby canine kidney cells (MDCK), blood-brain barrier (BBB), LogP, hydrogen donor, hydrogen acceptor. The results of the ADME prediction of this study are shown in Table 2.

To estimate Human Oral Absorption (HOA), the QikProp software predicts through the number of violations of Lipinski's Rule of Five (RO5) and the percentage of HOA. The analysis of RO5 is made by the number of violations of this rule, being allowed only one violation for the following parameters to be considered a molecule with good bioavailability by oral route: less than 5 hydrogen donors, less than 10

**Table 2** Pharmacokinetic properties of Selegiline (1) and natural substances: amburoside A (2), Harman (3), Harmaline (4) and Harmalol (5)

Molecules	Absorption				Distribution		
	AOH (%)	Donor de H	Acceptor de H	LogP	pCaco-2 (nm/s)	pMDCK (nm/s)	LogBB (C <sub>cerebral</sub> /C <sub>blood</sub> )
1	100	1	1	6.41	909.5	5376.77	0.291
2	28.757	6	10	-2.51	10.649	3.648	-3.76
3	100	1	1	-0.96	4456.5	2487.91	-0.725
4	100	2	1	-2.08	3375.0	1842.24	-3.3
5	78.236	3	1	-0.45	336.8	168.814	-0.051

hydrogen acceptors, molecular weight less than 500 daltons and LogP less than 5 [32]. All the molecules under study, including the pivot, showed zero violations in relation to RO5, with the exception of Amburoside A, which presented only one violation, 6 hydrogen bonding donor groups, however, it continues to have a satisfactory result for oral absorption. While for the percentage result, where >80% high absorption, 25–80% medium and <25% low absorption, natural substances showed between medium and high absorption. Therefore, both Selegiline (standard molecule) and substances of natural origin present satisfactory results of physicochemical properties to be considered good drugs for oral administration.

Caco-2 cells are useful for measuring parameters of cell permeability *in vitro*, an important test to assess the intestinal absorption of drugs. In addition, *in vitro* cell permeability is often also determined with Madin-Darby canine kidney cells (MDCK), which have a shorter growth time than Caco-2 cells. Values above 500 nm/s for both properties are considered ideal. For the permeability parameter in Caco-2 cells, the studied molecules showed results above 500 nm/s, with the exception of Amburoside A and Harmalol that showed values below 500 nm/s, while the molecules that showed results above 500 nm/s were Harman (3) and Harmaline (4), indicating that most will probably be well absorbed in the body. For MDCK cells, most of the studied molecules also showed satisfactory results with greater evidence for Harman (3), Harmaline (4) and Harmalol (5) (Table 2).

The blood–brain barrier (BBB) is a complex structure consisting of cellular elements and an extracellular matrix. It plays a fundamental role in determining the types of molecules that can selectively act in the CNS, therefore, this is one of the most important parameters for this study, considering that the studied molecules and the proposed analogs must have an action in the CNS, that is, present good permeability in the blood–brain barrier. The range indicating the possibility of crossing this barrier is  $-3.0$  and  $1.2$ . And for this parameter, the studied molecules showed good permeability, emphasizing that the natural substances Harman (3) and Harmalol (5) presented better results of LogBB; (Table 2).

Dhiman et al. [28] performed the ADMET in the QiqProp software of compounds derived from the alkaline piperine prediction of natural substances derived from piperine that have potential inhibitory activity for MAO. In this study, natural substances showed between medium and good results for the analyzed parameters, and none showed more than one violation of Lipinski's RO5. Jiang et al. [33] produced a pharmacokinetic study of Harman and Harmaline *in vitro* and *in vivo* using the rat animal model, with intravenous administration, natural substances were detected in the striatum 300 min after administration, indicated that they have good blood–brain barrier permeability, confirming the *in silico* result obtained in the present study.

According to the two studies mentioned above, natural substances with MAO-B inhibitory activity have satisfactory results to be considered good in the absorption and distribution properties, for further research. Although the natural substance Amburoside A has presented results that are not so satisfactory, it can be modified based on the pharmacophore and molecular docking, highlighting the result obtained for this last parameter, to improve its pharmacokinetic characteristics, as

in vitro results were quite satisfactory in the study by Ribeiro et al. [18] and Almeida [7], indicating that it has potential activity.

#### 2.4.2 Prediction of Toxicological Properties

In the planning and development of new drugs, the study of toxicological properties is very important, since the relationship between damage and effectiveness is the factor in choosing a drug for a given treatment [34].

The study of the mutagenic and carcinogenic properties of molecules is carried out in animals to obtain results that they would probably have in humans. However, the cost of researching toxicological properties is quite high when the study involves several molecules, with which new tools and methodologies for the prediction of these properties appear [35].

As an example, the DEREK software, which contains a subset of about 50 rules that describe toxicophoric substructures responsible, for example, for skin sensitization [36] and makes this prediction considering the presence of alkyl halides, aldehydes,  $\alpha$ ,  $\beta$  compounds unsaturated, aromatic amines, phenols, hydroquinones, isothiazolinones, alkyl sulfonates and aromatic nitro groups in the test molecules [37]. Improvements are constantly being made to alerts and predictions are included, such as alerts for 1,2-diketones and isothiazolinones improving the definition of the toxicophoric group [38].

In the prediction of toxicological properties, only Amburoside A (2) presented a toxic action of altering the chromosome responsible for human reasoning, indicating the catechol group as the toxicophoric group, this group did not present interaction in the molecular docking and is also not part of the pharmacophore, therefore, it can be modified to not present more toxicity. And no natural substance showed warnings about Genotoxicity, Mutagenicity and Carcinogenicity, irritation, reproductive effects and neurotoxicity (Table 3).

Mathew et al. [22] carried out in vitro toxicity studies with chalcones that had potential MAO inhibitory activity. The results showed that the majority of chalcones

**Table 3** Toxicological properties of Selegiline (1) and natural substances: amburoside A (2), Harmaline (3), Harman (4), Harmalol (5)

Molecules	Human carcinogenicity	Mutagenicity in bacteria in vitro	In vitro mutagenicity <i>Salmonella typhimurium</i>	Chromosome damages human in vitro
1	Absence of alert	Absence of alert	Absence of alert	Absence of alert
2	Absence of alert	Absence of alert	Absence of alert	Catechol
3	Absence of alert	Absence of alert	Absence of alert	Absence of alert
4	Absence of alert	Absence of alert	Absence of alert	Absence of alert
5	Absence of alert	Absence of alert	Absence of alert	Absence of alert

did not show toxicity to liver cells at 1  $\mu\text{M}$ . Upon increasing the concentration to 5  $\mu\text{M}$ , some compounds exhibited moderate toxicity.

Is et al. [39] presented a study with MAO inhibitors in which the toxicological properties were evaluated in silico, in which the two molecules were subjected to 26 different QSAR models of toxicity, such as mutagenicity, carcinogenicity, cytotoxicity, anemia, genotoxicity, hepatotoxicity, liver necrosis and neurotoxicity, presented low probability and/or negative results for the QSAR models, indicating that they are probably not toxic.

With the results of in silico toxicity of natural substances, it can be deduced that the probability of these substances being toxic is minimal, mainly because they have in silico studies of MAO-B inhibitors in which most of the molecules showed no or moderate toxicity, confirming the study conducted in that research.

## 2.5 Structural Modifications, Activity Prediction and Synthetic Viability

### 2.5.1 Structural Modifications

First, the bioligand Amburoside A was selected because it presented experimental results for in vitro MAO-B inhibitory activity described in the literature and in the present in silico study of molecular docking it presented quantities of interactions similar to Selegiline (standard molecule) in some different amino acids, indicating that it probably has an inhibitory action differently from Selegiline, and may be reversible inhibition since it did not present covalent binding. With that, the modifications had the objective to improve the pharmacokinetic and toxicological properties and to specify the biological activity. In general, based on the probable pharmacophore, glucose was removed and the radicals of the aromatic ring of the catechol group were modified, in which it was identified as a probable toxicological region, the ester group was removed to increase liposolubility to improve the passage in the blood–brain barrier and thus, facilitating the synthetic process (Fig. 5).

The molecules obtained are from the chalcone family, in which they have an open chain containing a phenyl ring attached to the carbonyl group and the other benzene ring linked by a three-carbon enone fragment, that is, they are  $\alpha$ ,  $\beta$ - ketones unsaturated, in which one aromatic ring is directly linked to carbonyl and the other to carbon  $\beta$  of olefinic function, this family is widely used due to its various biological activities such as cancer, inflammation and diabetes, with this, many drugs based on chalcones have been approved for clinical use [40].

In the study by Tran et al. [41], chalcone analogs were synthesized for antibacterial activity of methicillin-resistant *Staphylococcus aureus*. One of these synthesized chalcones has the same structure as PMCI and has low antibacterial activity. Another study carried out with the synthesis of chalcones as potential antidiabetic agents, also used the structure of PMCI, but it did not obtain results for antidiabetic activity [42].



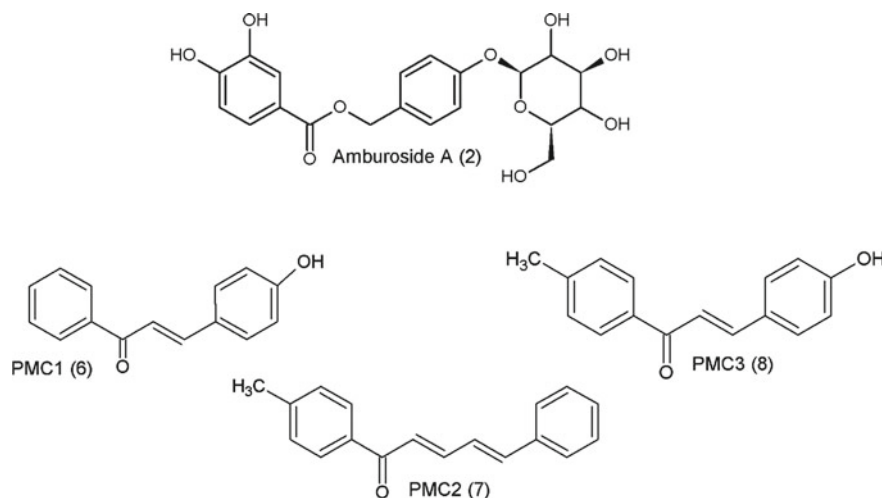


**Fig. 5** Natural substance Amburoside A (2) and the three analogs entitled PMC1 (6), PMC2 (7), PMC (8)

Salama et al. [43] carried out a study on the synthesis of new tetrazole derivatives, in which one of these synthesized molecules has the same structure as PMC2. However, no biological activity tests were performed, the study aimed to show the possibility of synthesizing through the reaction of dienones with the reagent tetrachlorosilane-sodium azide and its structural contribution of NMR.

In the study by Bai et al. [44], molecules were synthesized to assess antitumor activity. Among these molecules, one has a chemical structure similar to PMC3, however, it did not show antitumor activity *in vitro*.

In general, there are few *in vivo* studies of neuroprotective and antioxidant biological activity, mainly in PD, with chalcones. In a study by Chen et al. [45], they obtained a positive result for the cytoprotective activity of a chalcone, in which the cells were subjected to a toxin that decreases the Parkin, Parkin1 and DJ-1 proteins that are associated with PD, and after the treatment with the synthesized chalcone was observed a significant increase of these proteins. Therefore, using the chalcone family to treat neurodegenerative diseases is very promising.

### 2.5.2 Activity Prediction

The activity prediction performed by the PASS web server is based on the structural formula of the substance, with great precision for more than 3500 pharmacotherapeutic effects, being the parameter of the probability of being active ( $P_a$ ) and the probability of being inactive ( $P_i$ ) and it is only considered a molecule probably active when  $P_a > P_i$ . If  $P_a > 0.7$ , the substance is very likely to exhibit activity in the experiments, but the possibility that the substance is the analog of a known pharmaceutical

agent is also high. If  $0.5 < Pa < 0.7$ , the substance is likely to exhibit activity in the experiments, but the probability is less, and it is different from the substance in which the pharmaceutical action is known. If  $Pa < 0.5$ , they are unlikely to exhibit activity in the substance test. However, if the presence of this activity is confirmed in the experiment, the substance may be a new chemical entity [46, 47].

However, for the prediction of MAO-B inhibitory activity, analog 1 (PMC1) presented the value of Pa 0.238, analog 2 (PMC2) presented the value of Pa 0.198 and analog 3 (PMC3) presented the value of Pa 0.282. These results demonstrate great progress for the development of these molecules planned as potential MAO inhibitors, specifically MAO-B, as they were compared with a variety of molecules that already have activity, mostly, proven to inhibit MAO-B, indicating that the planning is following the objective of the study (Table 4).

The SEA web server performs the prediction of biological activity indicating the biological target based on chemical similarity, and can assume that a particular molecule may have an affinity with a certain target. As in the study by McCarroll and collaborators, who used SEA for a virtual screening in order to identify whether some molecules would have action on targets other than the Zebrafish GABA receptor and compare with the in vivo assay [48].

SEA mainly uses two values to perform the activity prediction by chemical similarity. The E-value is the value of the expectation that the similarity is not random between the sets, in which the values closer to zero or less than  $1 \times 10^{-10}$  consider that the activity prediction is not likely to be occurring by chance. While the Tanimoto Coefficient (Tc) is the expected chemical similarity of value 1 [49].

For the PMC1 molecule, DP-related activities were obtained, represented by the values of E-value  $4.426e^{-35}$  and Tc of 0.86 for human enzyme MAO-B, and the values of E-value  $2.509e^{-11}$  and Tc of 0.69 for human MAO-A enzyme, indicating that PMC1 has a greater affinity for the MAO-B enzyme and greater probability of not being a random alignment. For PMC2, results were obtained for E-value  $2.342e^{-24}$  and Tc 0.58 for human MAO-B enzyme, E-value  $9.906e^{-08}$  and Tc 0.29 for MAO-B mouse enzyme, and E-value  $1.408e^{-07}$  and Tc 0.57 for human MAO-A enzyme, indicating that PMC2 has similar characteristics to interact with both the human enzyme MAO-A and MAO-B. For PMC3, E-value  $7.283e^{-14}$  and Tc 1 were obtained for human MAO-A enzyme, E-value  $2.505e^{-28}$  and Tc 0.73 for human MAO-B enzyme, and E-value  $2.683e^{-08}$  and Tc 0.35 for COMT rat enzyme, indicating that PMC3 has a non-significant tendency towards MAO-A instead of

**Table 4** Prediction of biological activity with the PASS webserver for Selegiline and the planned molecules PMC1, PMC2 and PMC3

Molecules	Pa	Pi	Activity
Selegiline	0.366	0.055	Inhibition of monoamine oxidase B
PMC1	0.238	0.005	
PMC2	0.198	0.007	
PMC3	0.282	0.005	

**Table 5** Prediction of biological activity with the SEA webserver for Selegiline and the planned molecules PMC1, PMC2 and PMC3

Molecules	<i>E</i> value	Tanimoto coefficient (Tc)	Activity
Selegiline	4.213e <sup>-38</sup>	1.00	MAO-B rat
	3651e <sup>-35</sup>	1.00	MAO-A rat
	2.909e <sup>-12</sup>	1.00	MAO-B human
	3.929e <sup>-11</sup>	1.00	MAO-B bovine
	2.838e <sup>-12</sup>	0.62	MAO-A human
	5.504e <sup>-07</sup>	0.33	MAO-A bovine
PMC1	4.426e <sup>-35</sup>	0.86	MAO-B human
	2.509e <sup>-11</sup>	0.69	MAO-A human
PMC2	2.342e <sup>-24</sup>	0.58	MAO-B human
	9.906e <sup>-08</sup>	0.29	MAO-B mouse
	1.408e <sup>-07</sup>	0.57	MAO-A human
PMC3	7.283e <sup>-14</sup>	1.00	MAO-A human
	2.505e <sup>-28</sup>	0.73	MAO-B human
	2.683e <sup>-08</sup>	0.35	COMT rat

MAO-B and still has a probable interaction with COMT thus deducing that its action may be multi-target (Table 5).

### 2.5.3 Synthetic Viability

To predict the synthetic viability of the compounds, the SYLVIA software was used, which verifies through calculations the levels of difficulty of synthesis scoring from 1 to 3 for compounds that are easy to synthesize with the background of the image colored green, 3–6 for medium-sized ones with a yellow background and 6–10 for compounds that are very difficult to synthesize with red background [50]. Analog 1 (PMC1) showed a value of 2.52 indicating it is easy to synthesize, analog 2 (PMC2) showed a value of 3.74, that is, medium ease in synthesis, and analog 3 (PMC3) was 2.77, easily synthesized. The proposals are promising because they present biological activity for MAO-B inhibitors and mainly because they are possible to synthesize.

## 2.6 Synthesis of Planned Molecules by Claisen-Schmidt Reaction

The Claisen-Schmidt reaction is a classic reaction (Fig. 6), described by R. L. Claisen and J. G. Schmidt, widely used in the synthesis of chalcones through the aldolic condensation of an acetophenone with an aromatic aldehyde [51]. This reaction can occur in both acidic and basic environments, generating an enol or enolate from

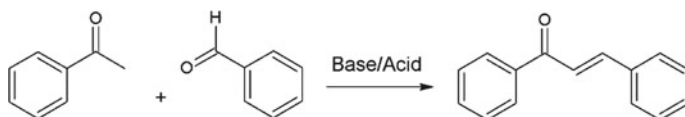


**Fig. 6** Claisen-Schmidt condensation of chalcone

the ketone, respectively, followed by the aldol addition and dehydration, resulting in the aldol adduct. Despite being simple, the Claisen-Schmidt reaction has some disadvantages, such as slow reaction, production of artifacts and most have low yield, ranging from <10% to 100% conversion. To increase the likelihood of better yield, aluminum chloride ( $\text{AlCl}_3$ ) is also used as a Lewis acid for the synthesis of chalcone [40].

Since it is a basic reaction for the synthesis of chalcones, with easily accessible reagents and relatively simple protocol, it was decided to synthesize the analogs proposed in this work to have their toxicities tested in Zebrafish. Molecules 6, 7 and 8, were synthesized with 15%, 46% and 5% yield, respectively. All molecules were synthesized more than once to obtain the minimum amount of 1 g, to be used in the biological experiments.

The structures of the synthesized products were confirmed using the techniques of nuclear magnetic resonance (NMR), infrared spectroscopy (IR), gas chromatography-mass spectrometry (GC-MS) and melting point (m.p.). The  $^1\text{H}$  and  $^{13}\text{C}$  NMR spectra of molecules 6 and 8 showed the characteristic signals expected for these compounds, with emphasis on the  $^1\text{H}$ - $^1\text{H}$  coupling constant of 15,6 Hz, characteristic of double bonds in the trans geometry with values close of to the expected value of 16 Hz. For molecule 7 it was not possible to obtain the coupling constant for double bonds because of the formation of multiplets, but the chemical shifts of  $^1\text{H}$  and  $^{13}\text{C}$  confirmed the structure of the product. The analysis by mass spectrometry showed the m/z for molecules 6, 7 and 8 equals to 224, 248 and 238 Da, consistent with the calculated values for their molecular ions.

## 2.7 Pharmacological Activity in a Zebrafish Model

### 2.7.1 Subjects and Creation Procedure

The animals were kept on the Zebrafish Platform of the Drug Research Laboratory, Biological Sciences and Health Department of the Federal University of Amapá (UNIFAP), Brazil. At a temperature of  $26 \pm 2$  °C with a light cycle of 10 h light/14 h dark. Standardized water (ISSO 1996) was used for the maintenance of adult fish. For the production of standardized water, deionized water was used and the following salts were added:  $\text{CaCl}_2 \times 2\text{H}_2\text{O}$  (117 mg/L),  $\text{MgSO}_4 \times 7\text{H}_2\text{O}$  (49.3 mg/L),  $\text{NaHCO}_3$  (25.9 mg/L) and potassium chloride (2.3 mg/L) (Sigma Aldrich).

The adult fish were fed with commercial feed and *Artemia* saline. These were treated according to the guide for the care and use of experimental animals. The behavior of the fish was assessed by a human observer and filmed, after a week under normal conditions and treatment. This study was submitted and approved by the Committee on Ethics in Animal Use—CEAU of UNIFAP, receiving protocol number 013/2018.

### 2.7.2 Toxicity Test of the Studied Substance

The acute *in vivo* toxicity test in an animal model *Danio rerio*, known as Zebrafish, has a lower cost and time, and can be performed at the beginning of preclinical development, and this justifies the acceptance of this methodology by the drug regulatory bodies [53].

Of the three synthesized molecules, PMC1, PMC2 and PMC3, PMC3 was chosen for the toxicity test because it does not have scientific studies of activity in the central nervous system, and in the prediction test of biological activity *in silico* it showed possible inhibition in two enzymes that are related to the pathophysiology of PD. For acute oral toxicity, the administration of a single dose of PMC3 is considered in this study and observation after 24 h to identify whether there was death in the groups, administering concentrations of 350, 750, 1500 and 2500 mg/kg, according to the recommendations of the OECD protocol 236 [54] after the highest level of the administered dose (2000 mg/kg) it is suggested that there is no mortality in the tested population. Based on this methodology, the acute toxicity test was also performed by the intraperitoneal route, to confirm the possible absence of toxicity of the PMC3 analog by both routes, in which for both routes there was no death or behavior change of the 30 fish tested in total. The results are shown in Table 6.

Due to the chalcones not having good solubility in water, it was necessary to add DMSO and Tween 80 to the distilled water to obtain a mother concentration of 200 mg/mL, so it was possible to dilute according to the bodyweight of each fish. Soon after administration, it was noted that there was an increase in the swimming activity of the fish in both routes, with the same behavior for the control group. The fish were evaluated for 7 days and showed no significant differences in behavior and had a mortality rate of 0%.

**Table 6** Number and percentage of animals killed after treatment with PMC3 orally and intraperitoneally at doses of 350, 750, 1500 and 2500 mg/kg in zebrafish

Dose mg/Kg	Number of dead animals	Percentage %
Control Group	0/3–3	0
350	0/3–3	0
750	0/3–3	0
1500	0/3–3	0
2500	0/3–3	0

N = 3 animals/intraperitoneal route and 3 animals/oral route

### 3 Conclusion

This study was divided into three parts: molecular modeling, synthetic route and acute toxicity in vivo, to obtain a drug candidate with MAO-B inhibitory activity for the treatment of Parkinson's Disease. Thus, the natural substances (Amburoside A, Harman, Harmaline and Harmalol) selected for the in silico study of the pharmacophore, molecular docking, pharmacokinetic and toxicological properties demonstrated satisfactory results indicating a greater probability of good absorption and distribution, in addition to MAO inhibitory activity. –B due to interaction with the active enzyme site provided by docking.

Based on these results, Amburoside A was indicated as a bioligand to propose the modifications, and thus 3 molecules of the chalcone family named PMC1, PMC2 and PMC3 were obtained, although they already exist in the virtual database, these molecules do not have studies for the treatment of disease of the central nervous system, and the majority being for antimicrobial activity in which they did not show good results. Therefore, predictions of activity and synthetic viability were also performed, in which the three molecules showed activity to inhibit MAO. The PMC3 prediction for COMT inhibitory activity is also noteworthy, indicating that this molecule probably has a multi-target action, in addition to presenting easy synthesis. In the synthesis stage, it was possible to synthesize the three molecules with an average yield of 40%, confirming the prediction of synthetic viability. Subsequently, PMC3 was selected to perform the acute toxicity test on Zebrafish, due to its likely multi-target action, and even with the highest dose (2000 mg/kg) administered, the mortality rate in the study population was 0%, indicating the lack of toxicity in this parameter. Thus, this study demonstrates the importance of Molecular Modeling in decreasing the time and cost of research, in addition to proposing three new potential drug candidates for the treatment of Parkinson's Disease.

## 4 Experimental Session

### 4.1 Search for the Structures of Natural Substances

To propose new drug candidates with antiparkinsonian biological activity with the inhibition of the monoamine oxidase B (MAO-B) enzyme for the treatment of PD, first, an online database search was performed with the descriptors “medicinal plants”, “Antiparkinsonian activity” and “natural compounds”, to find natural substances that are described in the literature with antiparkinsonian, antioxidant or neuroprotective activity in vitro or in vivo experiments on animal models with induced PD.

## **4.2 Derivation of the Pharmacophoric Pattern**

The pharmacophore represents the set of functional domains of the studied bioligands through which the possible types of interaction that the ligands in common can make with the receptor site are defined [55]. The pharmacophoric pattern was determined from the online server PharmaGist (<http://bioinfo3d.cs.tau.ac.il/PharmaGist/>) [56] and observed its image on the ZINCPharmer web server (<http://zincpharmer.csb.pitt.edu/pharmer.html>).

## **4.3 Molecular Docking Study**

Molecular docking is a computational method to identify the mode of interaction of ligands at the enzyme or receptor binding site through specific key interactions and to predict the binding affinity between protein-ligand complexes [57]. The GOLD 5.4 software (Genetic Optimization for Ligand Docking) was used to simulate the interaction between the ligands and the MAO-B enzyme through calculations that employs the genetic algorithm for flexible ligand docking experiments within protein binding sites [17].

## **4.4 Prediction of Pharmacokinetics (ADME) and Toxicological Properties**

### **4.4.1 Prediction of Pharmacokinetic Properties (ADME)**

For the pharmacokinetic properties, the parameters of human oral absorption (AOH), cell permeability in Caco-2 and MDCK cells and the penetration of the blood–brain barrier (pBHE) were used, as well as the properties related to the rule of five (logP, molecular mass, hydrogen donors, and hydrogen acceptors) for natural substances, using the QikProp module of the Schrödinger software [58].

### **4.4.2 Prediction of Toxicological Properties**

The natural substance toxicological properties were predicted using the DEREK software (Deductive Estimate of Risk from Existing Knowledge) [34]. DEREK has a system that makes predictions of toxicity, such as mutagenicity, carcinogenicity, skin sensitization, irritation, reproductive effects, neurotoxicity, among others, through the correlation rules implemented in the software [12, 28]

#### **4.5 Structural Modifications, Activity Prediction and Synthetic Viability**

The changes in the structure of the studied molecules were carried out based on the study of docking, on the properties of significant pharmacokinetics and toxicology. In addition, it was also possible to predict the activity of the proposed new compounds using the PASS webserver (<http://www.akosgmbh.de/pass/index.html>), which predicts with high accuracy (70–80%) up to 2000 biological activities for chemical compounds. And SEA (<http://sea.bkslab.org/>) uses the protein-related set of molecules similarity based on the chemical similarity established between its ligands, by searching large compounds databases and creating cross-destination similarity maps.

The prediction of synthetic viability was performed using the SYLVIA software ([http://www.molecular-networks.com/online\\_demos/sylvia/](http://www.molecular-networks.com/online_demos/sylvia/)), in which it indicates whether the molecule has characteristics of easy (green), medium (yellow), or difficult (red) synthesis.

#### **4.6 Synthesis of Planned Molecules by Claisen-Schmidt Reaction**

The search for organic compounds that show activity as MAO-B inhibitors for the treatment of PD was based on chalcone nuclei. The chalcones were synthesized by a Claisen-Schmidt reaction that describes a process in which a benzaldehyde and a methyl ketone are condensed in the presence of catalysts, this reaction is considered one of the most classic reactions in organic chemistry, with the catalysts being strong or acid bases [52].

Typical procedure for PMC1 (6): In a 250 mL flask, 30 mL of ethanol, 4-hydroxybenzaldehyde (5.1 mmol) and acetophenone (5.0 mmol) were stirring for 10 min, then added 6 M NaOH (5 mL) dropwise and remaining in magnetic stirring for 24 h at room temperature. Small pieces of aluminum foil were added to reaction in an attempt to increase the yield. After this period, the mixture was transferred to a Beaker (500 mL) containing approximately 100 g of crushed ice and 10% HCl (15 mL) in manual stirring with a glass stick until the formation of the precipitate. Vacuum filtration was performed to obtain the precipitated solid 6.

Typical procedure for PMC2 (7): In a 250 mL flask, 30 mL of ethanol, cinnamaldehyde (5.1 mmol) and 4-methylacetophenone (5.0 mmol) were stirring for 10 min, then added 6 M NaOH (5 mL) dropwise and remaining in magnetic stirring for 24 h at room temperature. Small pieces of aluminum foil were added to reaction in an attempt to increase the yield. After this period, the mixture was transferred to a Beaker (500 mL) containing approximately 100 g of crushed ice and 10% HCl (15 mL) in manual stirring with a glass stick until the formation of the precipitate. Vacuum filtration was performed to obtain the precipitated solid 7.



Typical procedure for PMC3 (8): In a 250 mL flask, 30 mL of ethanol, 4-hydroxybenzaldehyde (5.1 mmol) and 4-methylacetophenone (5.0 mmol) were stirring for 10 min, then added 6 M NaOH (5 mL) dropwise and remaining in magnetic stirring for 24 h at room temperature. Small pieces of aluminum foil were added to reaction in an attempt to increase the yield. After this period, the mixture was transferred to a Beaker (500 mL) containing approximately 100 g of crushed ice and 10% HCl (15 mL) in manual stirring with a glass stick until the formation of the precipitate. Vacuum filtration was performed to obtain the precipitated solid 8.

All substances were characterized by  $^1\text{H}$  and  $^{13}\text{C}$  NMR, infrared spectroscopy, gas chromatography–mass spectrometry and melting point (supplementary material).

## ***4.7 Acute Toxicity in a Zebrafish Model***

### **4.7.1 Subjects and Creation Procedure**

The adult Zebrafish (approximately 0.3 g in weight) were created on the ZebraFish Platform of the Pharmaceutical Research Laboratory, from the Federal University of Amapá, following standard fish care and maintenance protocols [53]. The environmental variance was maintained, at a minimum, for all behavioral experiments. The adult Zebrafish were kept in deionized water containing 200 mg/L of salt. All animal care procedures were submitted to the Animal Use Ethics Committee of the Federal University of Amapá.

### **4.7.2 Acute Toxicity Test**

This test consists of administering the studied molecule to the fish in a certain dose and, if the fish survives at least 7 days, it indicates a high probability of the substance not being toxic 60. To perform this test, two routes of administration were used, both orally, due to the planned and synthesized substance being indicated as a drug candidate by the oral route, and the intraperitoneal route because it is the route of administration of the neurotoxin used in other studies. For the test, 12 adult fish were used, divided into four groups, containing three fish in each group, and the substance PMC3 fasted once in four different concentrations, 350, 750, 1500 and 2500 mg/kg, with 0.250 g of PMC3 diluted in 900  $\mu\text{g/mL}$  of water, 90  $\mu\text{g/mL}$  of DMSO and 10  $\mu\text{g/mL}$  of Tween 80.

## 5 Ethical considerations

The Ethics Committee on the Use of Animals of the Federal University of Amapá—CEUA-UNIFAP is a deliberative and advisory body of the Higher Administration of the University in normative and consultative matters, in questions about the use of animals for teaching and research. This work was submitted and approved by protocol 013/2018 by this Animal Use Ethics Committee (CEUA).

## References

1. Savica, R., Grossardt, B.R., Rocca, W.A., Bower, J.H.: *Mov Disord.* **33**(4), 537–543 (2018)
2. Wang, D., Hong, R.-Y., Guo, M., Liu, Y., Chen, N., Li, X., Kong D.-X.: *Molecules*, **4003**, 24 (2019)
3. Campos, H.C., Rocha, M.D., Viegas, F.P.D., Nicastro, P.C., Fossaluzza, P.C., Fraga, C.A.M., Barreiro, E.J., Viegas, C., Jr.: *CNS Neurol. Disord. Drug Targets*, **10**(2), 239–250 (2011)
4. Follmer, C., Netto, H.J.C.B.: *Quim. Nova* **36**(2), 306–313 (2013)
5. Finberg, J.P.M., Rabey, J.M.: *Front. Pharmacol.* **340**, 7 (2016)
6. Marino, B.L.B., Souza, L.R., Sousa, K.P.A., Ferreira, J.V., Padilha, E.C., Silva, C.H.T.P., Taft, C.A., Hage-Melim, L.I.S.: *Mini. Rev. Med. Chem.* **20**(9), 754–767 (2020)
7. Almeida, J.R.G.S.: *Sci. Plena*, **6**, 11 (2010)
8. Ingale, S.P., S.B.: *Life*, **36**(4), 200–206 (2017). [https://www.ncbi.nlm.nih.gov/pubmed/?term=Kasture%20SB%5BAuthor%5D&cauthor=true&cauthor\\_uid=29269972](https://www.ncbi.nlm.nih.gov/pubmed/?term=Kasture%20SB%5BAuthor%5D&cauthor=true&cauthor_uid=29269972)"Kasture. <https://www.ncbi.nlm.nih.gov/pmc/articles/PMC5726187/>. [https://www.ncbi.nlm.nih.gov/pmc/articles/PMC5726187/"](https://www.ncbi.nlm.nih.gov/pmc/articles/PMC5726187/)Sci.
9. Pinzi, L., Rastelli, G.: *Int. J. Mol. Sci.* **20**, 4331 (2019)
10. Maia, E.H.B., Assis, L.C., Oliveira, T.A., Silva, A.M., Taranto, A.G.: *Front. Chem.* **343**, 8 (2020)
11. Espino-Saldaña, A.E., Ortiz, R.R., Jaramillo, E.P., Torres, A.M.: *Curr. Neuropharmacol.* **18**, 136–152 (2020)
12. Cariello, N.F., Wilson, J.D., Britt, B.H., Wedd, D.J., Burlinson, B., Gombar, V.: *Mutagenesis* **17**, 321–329 (2002)
13. Leal, L.K., Júnior, H.V.N., Cunha, G.M.A., Moraes, M.O., Pessoa, C., Oliveira, R.A., Silveira, E.R., Canuto, K.M., Viana, G.S.B.: *Neurosci. Lett.* **2**, 86–90 (2005)
14. Accelrys discovery studio. v. 4.0, T.C., San Diego, CA 92121 USA (2007)
15. Ingale, S.P., Sanjay, B.K.: *Orient. Pharm. Exp. Med.* (2014)
16. Canuto, K.M., Silveira, E.R.: *Quim. Nova*, **29**(6), 1241–1243 (2006)
17. Tábi, T., Vécsei, L., Youdim, M.B., Riederer, P., Szökő, É.: *J. Neural Transm.* **127**, 831–842 (2019)
18. Ribeiro, V.P., Arruda, C., El-Salam, M.A., Bastos, J.K.: *Pharm. Biol.* **56**(1), 253–268 (2018)
19. Dhawan, K., Kumar, S.: A, Sharma. *J. Ethnopharmacol.* **78**, 165–170 (2001)
20. Vyas, V., Jain, A., Jain, A., Gupta, A.: Virtual screening: a fast tool for drug design. *Sci. Pharm.* 333–360 (2008)
21. Hagenow, J., Hagenow, S., Grau, K., Khanfar, M., Hefke, L., Proschak, E., Stark, H.: *Drug Des. Dev. Therapy*, **14**, 371–393 (2020)
22. Mathew, B., Adeniyi, A.A., Dev, S., Yurtsever, M., Joy, G., Ucar, G.E., Mathew, Singh-Pillay, A., Soliman, M.E.: *J. Phys. Chem. B.* **121**(6), 1186–1203 (2017). <https://www.ncbi.nlm.nih.gov/pubmed/?term=Matew+2017+pharmacophore+monoamine+oxidase>
23. Verdonk, M.L., Cole, J.C., Hartshom, M.J., Murray, C.W., Taylor, R.D.: *Proteins* **52**(4), 609–623 (2003)

24. Cole, J.C., Murray, C.W., Nissink, J.W.M., Taylor, R.D., Taylor, R.: *Proteins* **60**, 325–332 (2005)
25. Picanço, L.C.S., Castro, L.L., Pinheiro, A.A., Silva, K.R., Souza, L.R., Braga, F.S., Silva, C.H.T.P., Santos, C.B.R., Hage-Melim, L.I.S.: *B. J. Pharm. Res.* **7**, 152–175 (2015)
26. Rodrigues, J.A.R.: *Química Nova*, **6**, 23 (2000)
27. Binda, C., Aldeco, M., Geldenhuys, W.J., Tortorici, M., Mattevi, A., Edmondson, D.E.: *Med. Chem. Lett.* **3**, 39–42 (2012)
28. Dhiman, P., Malik, N., Khatkar, A.: *BMC Chem.* **14**,12 (2020)
29. Yamashita, S., Furubayashi, T., Kataoka, M., Sakane, T., Sezaki, H., Tokuda, H.: *Eur. J. Pharm.* **10**, 195 (2000)
30. Silva, N.S.R., Santos, C.F., Gonçalves, L.K.S., Braga, F.S., Almeida, J.R., Lima, C.S., Brasil, D.S.B., Silva, C.H.T.P., Hage-Melim, L.I.S., Santos, C.B.R.: *B. J. Pharm. Res.* **7**, 247–263 (2015)
31. Fu, C., Shi, H., Chen, H., Zhang, K., Wang, M., Qiu, F.: *ACS Omega* **6**, 889–899 (2021)
32. Lipinski, C.A., Lombardo, F., Dominy, B.W., Feeney, P.J.: *Adv. Drug Deliv. Rev.* **46**(3), 3–26 (2001)
33. Jiang, B., Meng, L., Zou, N., Wang, H., Li, S., Cheng, X., Wang, Z., Chen, W., Wang, C.: *Phytomedicine*, **62**, 152–967 (2019)
34. Ridings, J.E., Barratt, M.D., Gary, R., Earnshaw, C.G., Eggington, C.E., Ellis, M.K., Judson, P.N., Langowski, J.J., Marchant, C.A., Watson, W.P., Yih, T.D.: *Toxicology*, **106**, 267–279 (1996)
35. Muster, W., Breidenbach, A., Fischer, H.: *Drug Discov Today*. **13**, 303–310 (2008)
36. Barratt, M.D., Langowski, J.J.: *J. Chem. Inf. Comput. Sci.* **39**(2), 294–298 (1999)
37. Estrada, E., Patlewicz, G., Gutierrez, Y.: *J. Chem. Inf. Comput. Sci.* **44**(2), 688–698 (2004)
38. Langton, K., Patlewicz, G., Long, A., Marchant, C., Basketter, D.: *Contact Dermatitis* **55**, 342–347 (2006)
39. Is, Y.S., Durdagi, S., Aksoydan, B., Yurtsever, M.: *ACS Chem. Neurosci.* **9**, 1768–1782 (2018)
40. Zhuang, C., Zhang, W., Sheng, C., Zhang, W., Xing, C., Miao, Z.: *Chem. Rev.* **117**(12), 7762–7810 (2017)
41. Tran, T.-D., Do, T.-H., Tran, N.-C., Ngo, T.-D., Huynh, T.-N.-P., Tran, C.-D., Thai, K.-M.: *Bioorg. Med. Chem. Lett.* 4555–4560 (2012)
42. Hsieh, C.-T., Hsieh, T.-J., El-Shazly, M., Chuang, D.-W., Tsai, Y.-H., Yen, C.-T., Wua, S.-F., Wua, Y.-C., Chang, F.-R.: *Bioorg. Med. Chem.* 3912–3915 (2012)
43. Salama, T.A., El-Ahl, A.-A.S., Khalil, A.-G.M., Girges, M.M., Lackner, B., Steindl, C., Elmorsy, S.S.: *Monatshfte fur Chemie*, **134**, 1241–1252 (2003)
44. Bai, X., Shi, W.Q., Chen, H.F., Zhang, P., Li, Y., Yin, S.F.: *Chem. Nat. Compounds*, **48**, 1 (2012)
45. Chen, Y.-F., Wu, S.-N., Gao, J.-M., Liao, Z.-Y., Tseng, Y.-T., Fülöp, F., Chang, F.-R., Lo, Y.-C.: *Molecules*, **25**, 2907 (2020)
46. Filimonov, D., Poroikov, V., Borodina, Y., Glorizova, T.: *J. Chem. Inf. Comput. Sci.* **39**, 666–670 (1999)
47. Ferreira, J.V., Chaves, G.A., Marino, B.L.B., Sousa, K.P.A., Souza, L.R., Brito, M.F.B., Teixeira, H.R.C., Da Silva, C.H.T.P., Santos, C.B., Hage-Melim, L.I.S.: *ChemMedChem* **12**(16), 408–1416 (2017). [https://www.ncbi.nlm.nih.gov/pubmed/?term=Santos%20CBR%5BAuthor%5D&cauthor=true&cauthor\\_uid=28417566](https://www.ncbi.nlm.nih.gov/pubmed/?term=Santos%20CBR%5BAuthor%5D&cauthor=true&cauthor_uid=28417566). [https://www.ncbi.nlm.nih.gov/pubmed/?term=Santos%20CBR%5BAuthor%5D&cauthor=true&cauthor\\_uid=28417566](https://www.ncbi.nlm.nih.gov/pubmed/?term=Santos%20CBR%5BAuthor%5D&cauthor=true&cauthor_uid=28417566)"R
48. McCarroll, M.N., Gendele, L., Kinser, R., Taylor, J., Bruni, G., Myers-Turnbull, D., Helsell, C., Carbajal, A., Rinaldi, C., Kang, H.J., Gong, J.H., Sello, J.K., Tomita, S., Peterson, R.T., Keiser, M.J., Kokel, D.: *Nat. Commun.* **10**, 4078 (2019)
49. Keiser, M.J., Roth, B.L., Armbruster, B.N., Ernsberger, P., Irwin, J.J., Shoichet, B.K.: *Nat Biotech* **25**, 197–206 (2007)
50. Boda, K., Gasteiger, J., Seidel, T.: *J. Comput. Aided Mol. Des.* **21**(6), 311–325 (2007)
51. Rammohan, A., Reddy, J.S., Sravya, G., et al.: Chalcone synthesis, properties and medicinal applications: a review. *Environ. Chem. Lett.* **18**, 433–458 (2020)

52. Se, W.D.: *Bioorg. Med. Chem. Lett.* **15**(24), 5514–5516 (2005)
53. Hyacientha, B.M.S., Picanco, K.R.T., Sanchez-Ortiza, B.L., Silvad, L.B., Pereira, A.C.M., Goes, L.D.M., Borgesa, R.S., Ataide, R.C., Santos, C.B.R., Carvalho, H.O., Anduaga, G.M.G., Navarretec, A., Carvalho, J.C.T.: *Toxicol. Rep.* 217–232 (2020)
54. Organização Para A Cooperação E Desenvolvimento Económico—OECD. Test no. 236: fish embryo acute toxicity test (FET), 22 p. OECD, Paris (2013)
55. Inbar, Y., Schneidman-Duhovny, D., Dror, O., Nussinov, R., Wolfson, H.J.: *Research in Computational Molecular Biology: 11th Annual International Conference, RECOMB, Oakland, CA, USA* (2007)
56. Schneidman-Duhovny, D., Dror, O., Inbar, Y., Nussinov, R., Wolfson, H.J.: *Nucl. Acids. Res.* **36**, W223–W228 (2008)
57. Gupta, S., Mohan, C.G.: *Biomed. Res. Int.* (2014)
58. Schrödinger Release 2018-1: QikProp, Schrödinger, LLC, New York (2018)
59. Bretaud, S., Lee, S., Guo, S.: *Neurotoxicol. Teratol.* **26**, 857–864 (2004)

# Electronic and Structural Insights of BCR-ABL Inhibitors Under LMC Treatment Perspective



Érica C. M. Nascimento, Letícia de A. Nascimento, Luiz F. M. A. Benicio, José L. L. Alcântara, Washington A. de Pereira, and João B. L. Martins

**Abstract** Protein-Tyrosine Kinases (PTK) are responsible for the protein–protein transfer of the phosphate present in ATP molecule. This activity is essential and allowed due to its activation through phosphorylation. However, when an inadequate activation occurs, then triggers neoplasms, such as Chronic Myeloid Leukemia (CML). The treatment of these diseases in their chronic phase occurs through tyrosine kinase inhibitors (TKIs). Examples of TKIs are imatinib, dasatinib, gefitinib, erlotinib, nilotinib, afatinib, sorafenib and ponatinib, which act specifically on the protein target. TKIs are a major scientific development for the treatment of BCR-ABL related cancers. However, the numerous possible mutations of the active site of the protein prevent the action of these inhibitors and consequently induces the spread of the disease. Therefore, the computational study of the electronic structure and the molecular docking of these drugs are essential to understand the conformations of the protein active site. This study also leads to effectively advance in the treatment involving TKIs. For a good direction of these studies, it is necessary to know their electronic properties and the orientation of their respective ligands in the active region of the enzyme. Therefore, this work aims to shed light on the development of new potential drugs centered in protein mutations, against neoplasms related to BCR-ABL.

**Keywords** Tyrosine kinases · Tyrosine kinase inhibitors · Electronic properties · Molecular docking · DFT

---

É. C. M. Nascimento · L. de A. Nascimento · L. F. M. A. Benicio · J. L. L. Alcântara · W. A. de Pereira · J. B. L. Martins (✉)  
Institute of Chemistry, University of Brasília, Brasília, DF, Brazil  
e-mail: [lopes@unb.br](mailto:lopes@unb.br)

L. F. M. A. Benicio  
e-mail: [luiz.moennich@aluno.unb.br](mailto:luiz.moennich@aluno.unb.br)

J. L. L. Alcântara  
e-mail: [jose.lenart@aluno.unb.br](mailto:jose.lenart@aluno.unb.br)

## 1 Introduction

### 1.1 *Chronic Myeloid Leukemia and Tyrosine Kinase Inhibitors*

The class of protein-Tyrosine Kinase (PTK) is responsible for a range of intra- and extracellular processes, such as metabolic regulation, signaling, cell adhesion, cell division and differentiation, as well as apoptosis. PTKs are responsible for transferring the phosphate present in adenosine triphosphate (ATP) [1–3]. This activity is essential and allowed due to its activation through phosphorylation. However an inadequate activation can triggers neoplasms, such as Chronic Myeloid Leukemia (CML) [4–7]. The treatment of these diseases in the chronic phase occurs through tyrosine kinase inhibitors (TKIs), such as imatinib, gefitinib, erlotinib, nilotinib and afatinib, which acts specifically on the protein target. However, the numerous possible mutations of the protein active site prevent the action of these inhibitors, which consequently induces the spread of the disease. Therefore, the computational study of the electronic structure, as well as the study through molecular docking of these drugs plays a key role to understand the conformations of the protein active site and how to effectively advance in the treatment involving TKIs [8].

CML is a clonal chronic myeloproliferative neoplasm, characterized by the reciprocal translocation between chromosomes 9 and 22-t(9;22) (q34;q11), giving rise to the Philadelphia chromosome (Ph). In the Ph chromosome—disease indicator—the gene from the BCR-ABL1 fusion is found, a determinant factor for CML and responsible for the synthesis of the oncoprotein tyrosine kinase BCR-ABL intrinsic to the pathology[6]. In this context, the BCR-ABL protein is present in all patients with CML, and its hyperactivity triggers the release of cell proliferation effectors and apoptosis inhibitors, and its activity is responsible for the initial oncogenesis of CML [9].

Until the advent of imatinib mesylate TKI, in the 2000s, the treatment options that allowed an improvement in the survival rate and quality of life were limited to scarce drugs, such as bisulfan. However, these drugs did not have the desired efficacy and safety for the patient [10, 11]. Thus, the target therapy is through TKIs, which are the first-line for the treatment of cancers related to BCR-ABL and their respective mutations. According to Cortez et al. [12] the biggest challenge for the treatment of CML is primary or acquired drug resistance through tyrosine kinase mutations in the ATP binding region.

In the present study, the inhibitors afatinib, axitinib, dasatinib, gefitinib, erlotinib, imatinib, lapatinib, nilotinib, pazopanib, ponatinib, sorafenib e and tozasertib were analyzed (see Fig. 1). They act competitively with ATP, natural substrate of TK, and binds to the intracellular domain of the TK portion of the EGFR. Then, suppressing its autophosphorylation and consequent cascade signaling of the BCR-ABL signal transduction pathway [13].

Therefore, studies taking into account the wild and mutated forms of the BCR-ABL T315I protein were carried out together with molecular docking studies and

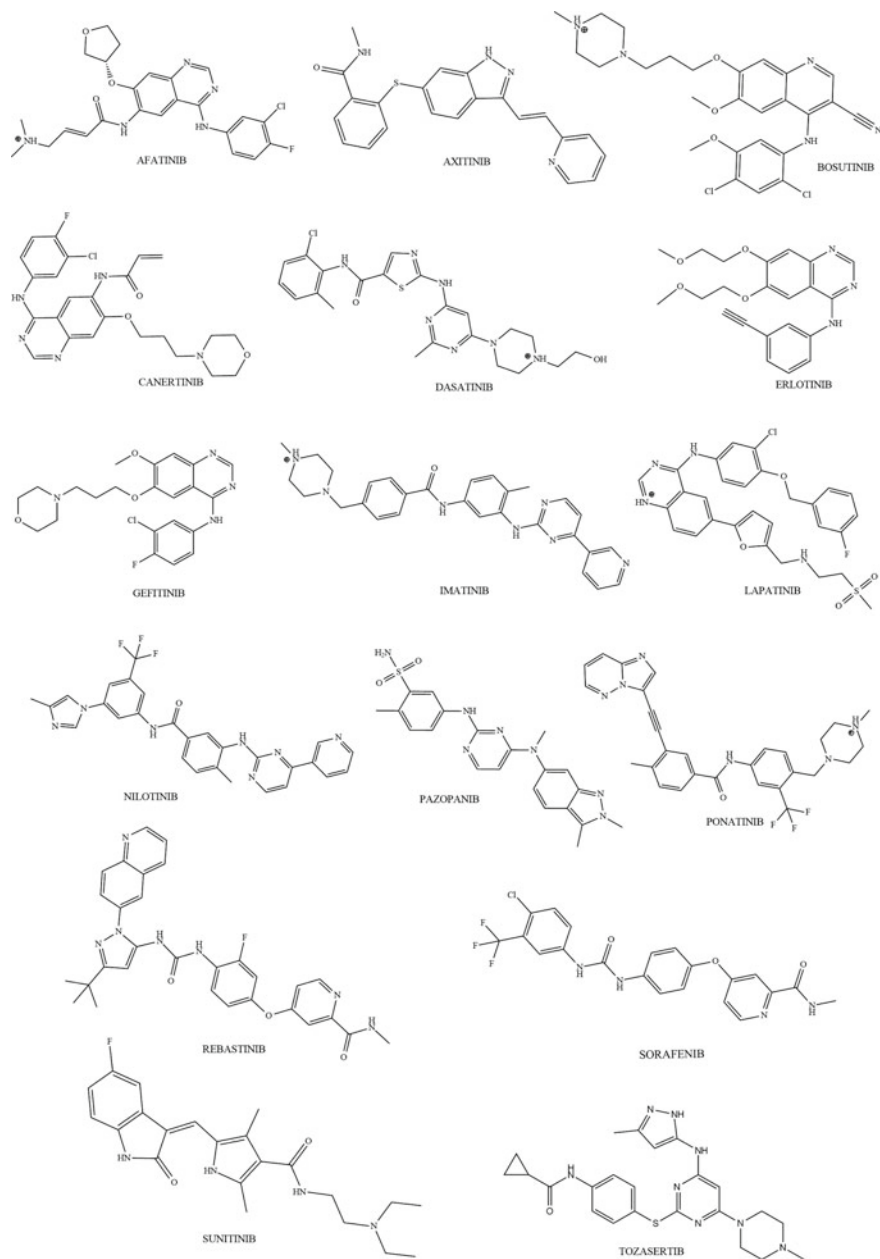


**Fig. 1** 2D molecular structures of studied TKIs

computational calculations, in order to characterize the inhibitor molecular structure. Therefore, to analyze their most primordial residues that present an effective interaction with the inhibitor and the active site of the protein. We have analyzed the positions presented by each of TKIs within the enzyme and the conformation of their orbitals. The aim is to understand the interaction between them, as well as to indicate which inhibitor is more effective in the BCR-ABL inhibition process.

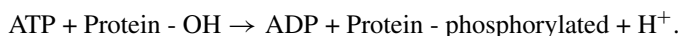
## 1.2 BCR-ABL Protein

The BCR-ABL translocation, known as the Philadelphia Chromosome, results from the fusion of part of the ABL oncogene, located on chromosome 9, with the BCR gene, located on chromosome 22 [14], as well as having a tyrosine kinase activity, thus stimulating cell growth and proliferation [8]. It is activated through signal transduction cascades that start with the addition of a phosphate group coming from ATP (phosphorylation), which binds to the active site of the protein [8].

In this context, the substrate pocket is located in a deep crack where there is located an important residue named “gatekeeper”, that of threonine 315 (Thr315) shown in Fig. 2, which is also involved in binding to ATP, thus being essential to stabilize the active conformation of BCR-ABL [15]. For this reason, the threonine residue is a determinant target for the interaction with the inhibitor. The T315I mutation confers resistance and decreases the molecular interaction to the first and second TKIs generation due to a replacement of the threonine residue by one of isoleucine [15]. Given the extreme importance of the Thr315 residue, in both cases of substrate and inhibitor binding, several studies and research interests were attracted, as it is believed that this region is a great potential pharmaceutical target [15].

Another important region of the protein is the so-called “A-loop” or activation loop (Fig. 3) which plays a central role in the activation of BCR-ABL, and is responsible for indicating the critical role in modulating the kinase activity, as contains a conserved catalytic site, called “DFG-out”, formed by residues Asp381, Phe382, and Gly383 and their respective interactions [15]. In some cases, the “DFG-out” can undergo an inversion in relation to the active conformation of the protein, so this generates a resistance to inhibitors [16].

Protein kinases have been the focus of many targeted treatments. Tyrosine kinases are enzymes responsible for activating many proteins through signal transduction cascades. Proteins are activated by adding a phosphate group to the protein (phosphorylation):



Tyrosine kinase inhibitors can compete with ATP, the phosphorylating entity, the substrate, or both, or they can act allosterically, binding to a site outside the active site, affecting its activity with conformational change. Aiming at the tyrosine kinases that regulate cell growth and proliferation, there are highly effective inhibitors, such



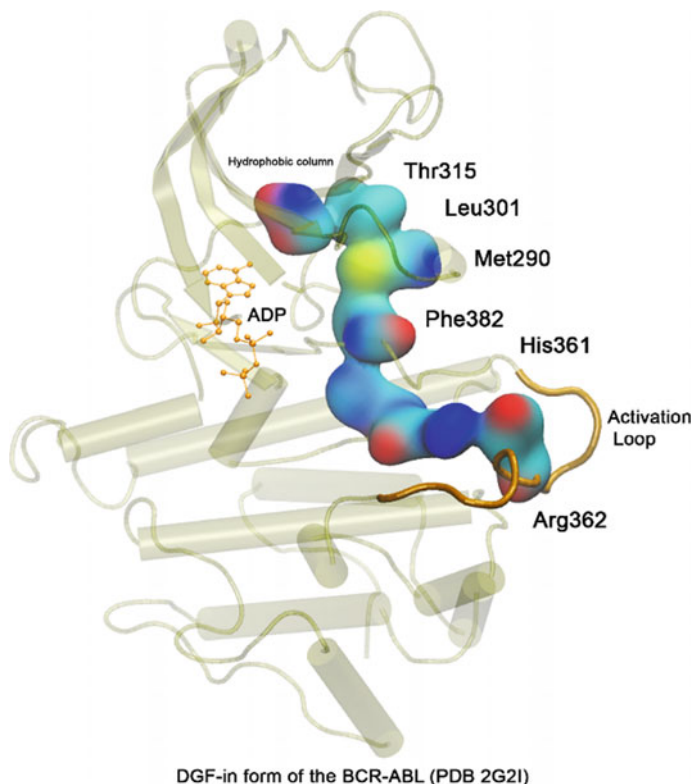


**Fig. 2** Inactive conformation for the ABL domain of PTK, showing the Thr315 gatekeeper residue

as imatinib mesylate, (Gleevec, STI 571), and Nilotinib, (Tasigna, AMN107), for the treatment of CML and gastrointestinal stromal tumors (GIST) [8].

The resistance presented to imatinib inhibitor by some patients leads to the first-generation inhibitors. Subsequent inhibitors nilotinib, bosutinib and dasatinib, are also known as second generation were created and took the lead in inhibiting BCR-ABL as well as other TK mutations such as T315I.

In this sense, the objective of this work is to analyze the characteristics, such as chemical groups, volume and intermolecular forces of the first-generation optimized inhibitors as well as the second-generation ones to compare them with the other inhibitors and ligands presented in this work. Molecular docking methodology was used to qualitatively analyze the interactions between protein-inhibitor of BCR-ABL protein in the wild and mutated state.

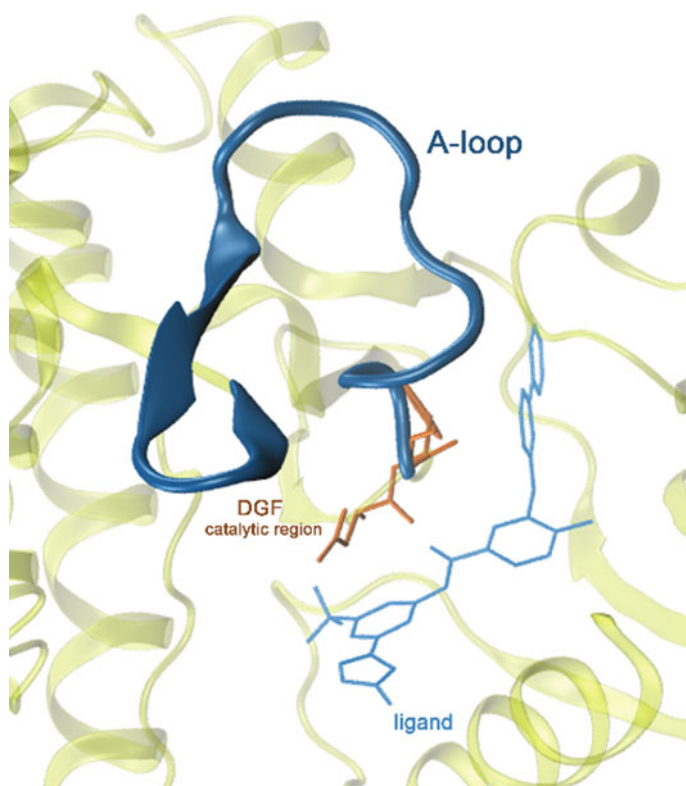


**Fig. 3** BCR-ABL conformation for the A-loop, and the DFG catalytic site with nilotinib molecule complex in light blue

## 2 Methodology

### 2.1 PDB Structures and Molecular Docking

The wild and mutated forms of the BCR-ABL T315I protein were studied together with molecular docking studies and computational calculations. The aim is to investigate the molecular structure of inhibitors and to analyze their most primordial residues that present an effective interaction with the inhibitor and the active site of the protein. We have also analyzed the positions presented by TKIs within the enzyme and the conformation of their orbitals. In such a way, to understand the interaction between them, as well as to indicate descriptors for inhibitor effectiveness.

Although there are several mutations in the ABL-BCR protein, only the T315I mutation was selected due to its characteristic of resistance to imatinib. Ten three-dimensional structures of proteins were taken from the Protein Data Bank (PDB). The two proteins from *Homo sapiens* were selected, being 3QRK (UniProtKB:

P00519) and 3QRJ (UniProtKB: P00519), because they present minor alterations when compared to the literature. The catalytic sites (P1 and S1) of the structures were analyzed, keeping them intact. The ending residues presented in only one of the proteins were removed to obtain better similarity, and the marked difference between the two proteins was only the T315I mutation.

We carried out the study of the interaction of the BCR-ABL protein through docking, in its wild-type oncological conformation, using the structures deposited in the PDB database under the code 3QRK; and its oncological conformation with mutation, under the code 3QRJ(T315I). Two oncological conformations of BCR-ABL T315I were also studied: the wild type 3OXZ and the mutated type 3OY3. We compared the scores obtained, having the maximum DP-987 inhibitor reference, with the IC<sub>50</sub> values, and the most likely conformations with the highest score values obtained. The docking study was carried out with the AutoDock4.2.6 [32] and VMD [33].

Inhibitors used for the treatment of CML, imatinib, ponatinib, nilotinib, bosutinib and dasatinib, were studied; and added inhibitors used in the treatment of other types of cancer: axitinib, erlotinib, gefitinib, lapatinib, pazopanib, sorafenib and tozasertib, to qualitatively and quantitatively assess the interactions of these inhibitors with their therapeutic target. The structures of the inhibitors were taken from DrugBank and PubChem (Table 1). The geometric structures of the ATP molecule (DrugBank ID: DB00171) were also obtained from the DrugBank database and from it the structure of the ADP ligand was generated with the removal of a phosphate group, the two molecules were optimized using the same computational protocol of the other inhibitors.

## 2.2 *Electronic Structure*

The TKI structures were geometry optimized at first using semiempirical PM6 method. Calculations were also performed using density functional theory (DFT) with the functionals B3LYP and  $\omega$ B97XD with the 6-311+G(d,p) basis function using the Gaussian09 computational package [34]. The structural and electronic properties were studied, such as dipole, the SCF orbital energies of frontier orbitals, the highest occupied molecular orbital (HOMO) to the HOMO-4, the lowest unoccupied molecular orbital (LUMO) to LUMO + 4, and the HOMO-LUMO gap. In addition to evaluating the volume and size of the molecules.

**Table 1** Analyzed TKIs

Inhibitor	Target protein	Drugbank ID	References
<i>Afatinib</i>	EGFR	DB08916	Keating [17]
<i>Axitinib</i>	VEGFR	DB06626	Roskoski [18]
<i>Bosutinib</i>	BCR-ABL, Src family	DB06616	Keller-von Amsberg and Schafhausen [19]
<i>Canertinib</i>	pan-erbB	DB05424	Arora and Scholar [20]
<i>Dasatinib</i>	BCR-ABL, Src family, c-KIT, PDGFR, Ephrins	DB01254	Müller et al. [21]
<i>Erlotinib</i>	EGFR	DB00530	Scheffler et al. [22]
<i>Gefitinib</i>	NSCLC	DB00317	Sordella et al. [23]
<i>Imatinib</i>	BCR-ABL, c-KIT, PDGFR	DB00619	Manley et al. [24]
<i>Lapatinib</i>	EGFR	DB01259	Arora and Scholar [20]
<i>Nilotinib</i>	BCR-ABL, c-KIT, PDGFR	DB04868	Fujita et al. [25]
<i>Pazopanib</i>	VEGFR, PDGFR, FGFR	DB06589	Sonpavde et al. [26]
<i>Ponatinib</i>	BCR-ABL, T3151, VEGFR, PDGFR, FGFR, EPH, KIT, RET, Tie-2 e FLT3	DB08901	Zhou et al. [27]
<i>Rebastinib</i>	Tie-2 tyrosine kinase receptor	DB13005	Janku et al. [28]
<i>Sorafenib</i>	RAF kinase, PDGF, VEGF receptor 2 & 3 kinases and c-KIT	DB00398	Keating and Santoro [29]
<i>Sunitinib</i>	RTK, GIST, PDGF-R, VEGFR, RET, CSF-1R, and FLT3	DB01268	Demetri et al. [30]
<i>Tozasertib</i>	BCR-ABL T3151	5494449	Ferreira and Andricopulo [31]

### 3 Results and Discussion

#### 3.1 Frontier Molecular Orbitals

In the present study, the inhibitors afatinib, axitinib, dasatinib, gefitinib, erlotinib, imatinib, lapatinib, nilotinib, pazopanib, ponatinib, sorafenib, and tozasertib were also evaluated (see Fig. 1), which act competitively with ATP, a natural substrate of TK. They also bind to the intracellular domain of the tyrosine portion EGFR kinase, suppressing its autophosphorylation and consequent cascade signaling of the BCR-ABL signal transduction pathway [13].

Figure 4 shows the profile energy of the frontier molecular orbitals (FMO) of the inhibitors obtained with semiempirical PM6 method, and B3LYP and  $\omega$ B97XD functionals. The functionals and semiempirical methods presented almost the same behavior. However, some patterns can be observed. Imatinib, afatinib, dasatinib and ponatinib are in a separate group in both the HOMO – n and the LUMO + n series.

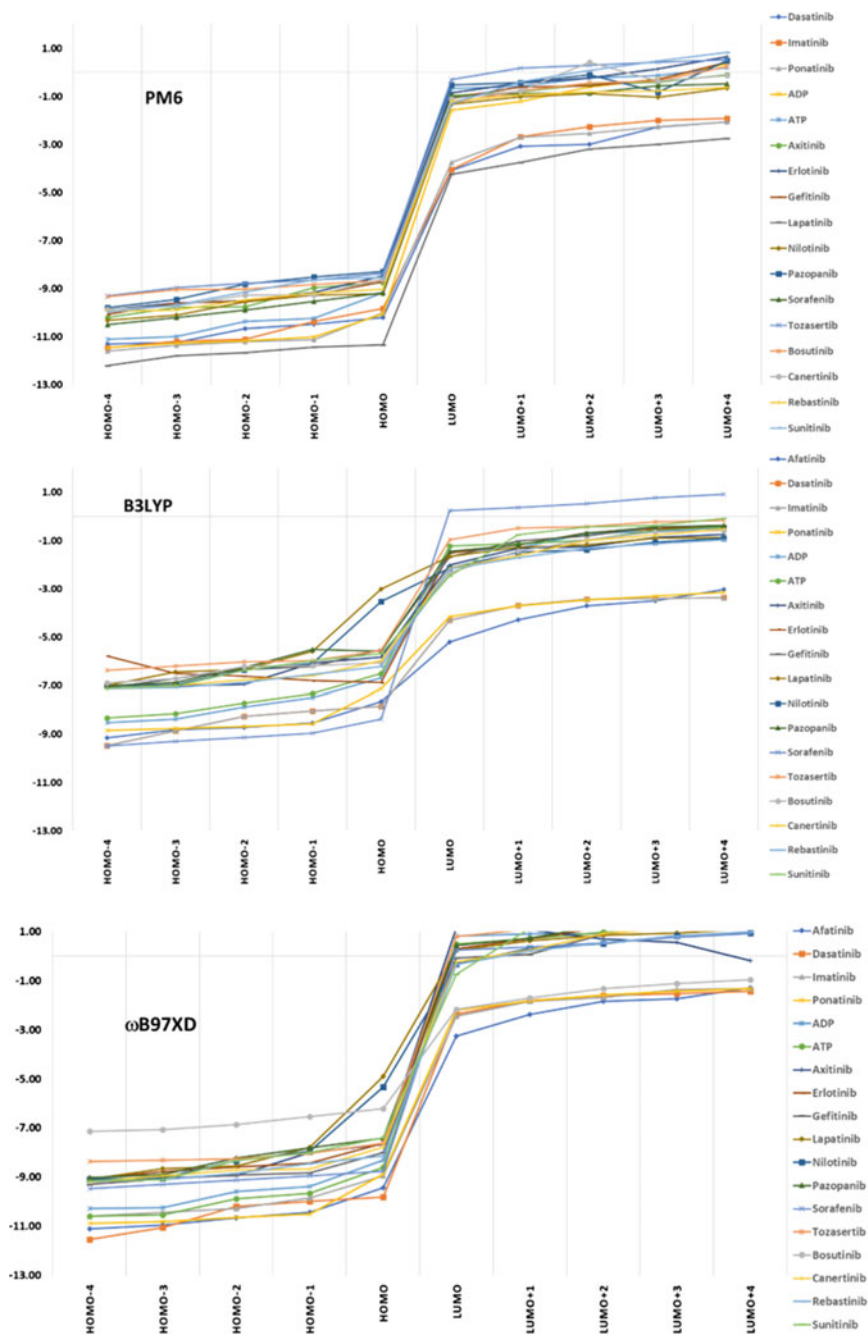


**Fig. 4** Energy profile of the frontier molecular orbitals of TKIs of HOMO to HOMO – 4 and LUMO to LUMO + 4 series. Values are in eV. Calculations were performed with PM6 semiempirical method, and using hybrid functionals B3LYP and  $\omega$ B97XD

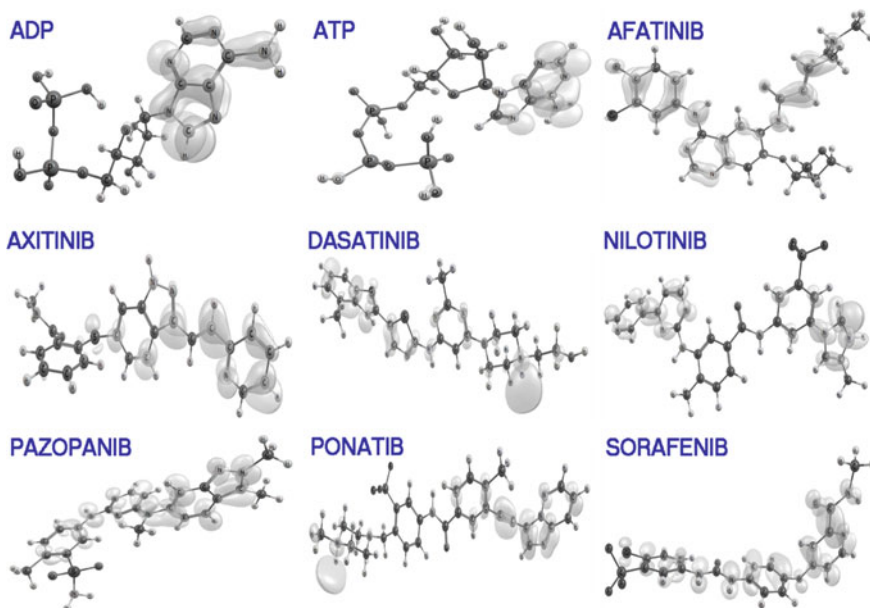


**Fig. 5** The isosurface difference (LUMO-HOMO) distribution and localization for some TKIs studied. Calculations using B3LYP/6-311+G(d,p) level

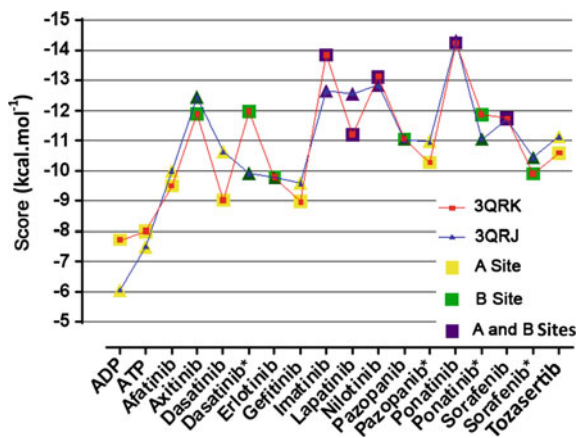
This pattern was observed for all methods, with small variations, always grouping the imatinib, afatinib, dasatinib and ponatinib.

Figure 5 shows the energy difference between the isosurfaces of HOMO and LUMO orbitals. The distribution of the gap of TKIs molecules have different profile, which is the expected behavior in consonance with the kind of kinase protein where it acts more efficiently. The natural substrate ATP, and its product after the phosphorylation of the protein kinase (ADP) have similar distribution and location, in the adenosine group. The VEGFR and PDGFR inhibitors, axitinib, dasatinib, pazopanib, and sorafenib, presents their gap equally distributed throughout the fragments of their molecules. The BCR-ABL type II inhibitors imatinib, nilotinib and ponatinib show similar profile of distribution and location, in the opposite position. The EGFR inhibitor afatinib presented profile similar with ponatinib and sorafenib, both BCR-ABL inhibitors. This can indicate a new use of the afatinib as BCR-ABL inhibitor, or a new molecule derivates of this inhibitor.

### 3.2 Docking and the Electronic Structure Correlation

The protein has two essential sites for inhibition, named P1 site for the interaction site with ATP, and S1 site for the interaction site with protein phosphorylated by the

**Fig. 6** Comparison of docking score values of wild protein 3QRK with mutated protein 3QRJ. Disclaimer for Dasatinib\* referring to Dasatinib at S1 site. Pazopanib\* referring to Pazopanib at P1 site. Ponatinib\* referring to Ponatinib at S1 site, and Sorafenib\* referring to Sorafenib at S1 site



cascade process. Figure 6 illustrates docking score values of wild protein 3QRK and mutated protein 3QRJ. To identify whether the inhibitors were effective, we added the ATP and ADP molecules as a minimum score threshold. Thus, the inhibitors must have inhibition higher than the molecules that would be the natural substrates of the P1 site.

Docking score of inhibitors are suggestive of the binding capacity of inhibitors. The more negative their score, the greater the binding strength of interaction in a set of molecules. We chose substrates as minimum energy thresholds, from which is known that the inhibitor must score more negative than the natural substrate and to become effective for the wild 3QRK and mutant 3QRJ proteins (Table 2).

Mutant protein (3QRJ) has a mutation of the Thr315 residue by an isoleucine, and has a narrower catalytic pocket. Inhibitors showed greater difficulty for inhibition (interaction) of both sites of 3QRJ, especially at the P1 site. This is evidenced by the lower score value of the ATP molecule by the P1 site in the mutated protein than in the wild protein. Figure 7 depicts the correlation of score values with the gap and  $\Delta E$ .

The  $\Delta E$  (HOMO – (HOMO – 1)) shows a range of values between 0.05 and 1.44 eV for all inhibitors, and imatinib, afatinib and ponatinib presents the largest  $\Delta E$  values. This trend is also followed by the gap values for imatinib, afatinib and ponatinib. Ponatinib has the largest score value for both proteins and presents the gap value close to 3.0 eV. Similar conclusions were observed for imatinib, ponatinib and ponatinib derivate molecules in the recent work of Pereira et. al [35]. In order of inhibition of mutated protein: ponatinib ( $-14.25 \text{ kcal mol}^{-1}$ ), nilotinib ( $-12.82 \text{ kcal mol}^{-1}$ ), imatinib ( $-12.65 \text{ kcal mol}^{-1}$ ), lapatinib ( $-12.56 \text{ kcal mol}^{-1}$ ), and axitinib ( $-12.46 \text{ kcal mol}^{-1}$ ).

The docking study demonstrated that for wild-type (3QRK) protein inhibition is favored due to a larger pocket volume [36]. The order of score for the wild protein is ponatinib ( $-14.25 \text{ kcal mol}^{-1}$ ), imatinib ( $-13.84 \text{ kcal mol}^{-1}$ ), nilotinib ( $-13.13 \text{ kcal mol}^{-1}$ ), and axitinib ( $-11.89 \text{ kcal mol}^{-1}$ ). This demonstrates that the

**Table 2** Docking score of inhibitors, for both the wild 3QRK and mutant 3QRJ proteins BCR-ABL. The interaction site (P1 and S1), the gap energy, and the energy difference between HOMO and HOMO-1 using B3LYP/6-311+G(d,p) level

Ligand	3QRK/kcal.mol <sup>-1</sup>	3QRJ/kcal.mol <sup>-1</sup>	Site	Gap/eV	ΔE/eV
ADP	-7.73	-6.07	P1	5.24	0.80
ATP	-8.00	-7.50	P1	5.27	0.88
Afatinib	-9.50	-10.00	P1	2.43	0.82
Axitinib	-11.89	-12.46	S1	3.81	0.24
Dasatinib	-9.03	-10.63	P1	3.54	0.19
Erlotinib	-9.85	-9.79	S1	4.27	0.71
Gefitinib	-8.97	-9.60	P1	3.85	0.70
Imatinib	-13.84	-12.65	P1 and S1	2.70	0.77
Lapatinib	-11.20	-12.56	P1 and S1	3.65	0.29
Nilotinib	-13.13	-12.82	P1 and S1	3.87	0.05
Pazopanib	-11.06	-11.03	S1	4.14	0.32
Ponatinib	-14.25	-14.30	P1 and S1	2.98	1.44
Sorafenib	-11.75	-11.72	P1 and S1	4.80	0.52
Tozasertib	-10.59	-11.14	P1	4.59	0.42

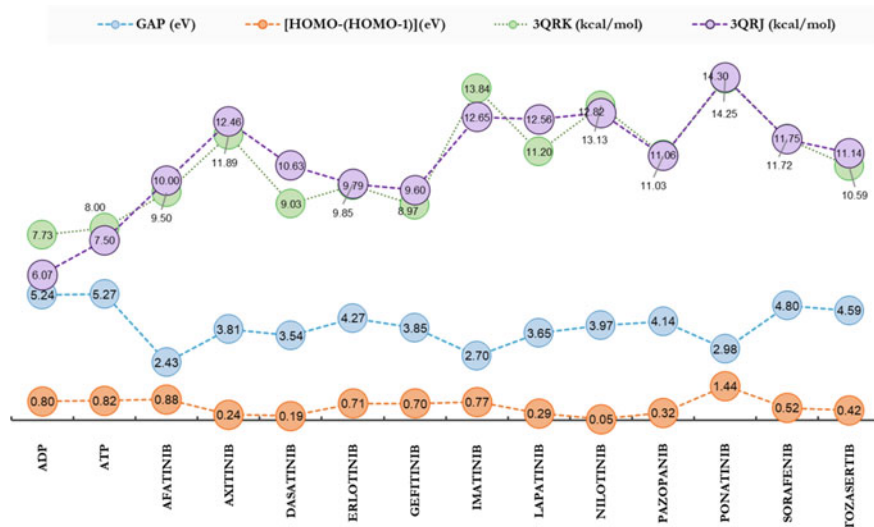


**Fig. 7** Docking score for both the wild 3QRK and mutant 3QRJ proteins BCR-ABL compared to the gap energy, and the energy difference between HOMO and HOMO-1 at B3LYP/6-311+G(d,p) level



inhibitors designed for the disease have high affinity for the protein and consequent inhibition. Otherwise, the inhibitor lapatinib is designed for breast cancer and has high inhibition for the wild protein [37], corroborating the result with the clinical treatment used of imatinib in breast cancer [38].

### 3.3 Comparison of the Docking at P1 and S1 Sites of the Wild and Mutated Proteins

The analysis demonstrates that the inhibitors showed greater inhibition in the wild protein than in the mutant protein, with one exception being ponatinib. On the other hand, ATP has greater interaction with the wild protein than the mutated one, demonstrating that the mutation has its characteristic due to greater interaction with the P1 site. This demonstrates that inhibitors with greater inhibitory activity in the region of the P1 site will present greater inhibition. Ponatinib inhibitor has the highest score value and, its characteristic of inhibiting both sites make it stand out compared to imatinib and nilotinib.

Our results for the wild protein show that classical inhibitors for leukemia have a greater number of interactions with P1 and S1 sites (Fig. 8). Despite not being designed for such protein, these results demonstrate that there is a characteristic correlation of the docking results. For the two proteins, ponatinib stand out with the highest score followed by nilotinib.

The inhibitor tozasertib is an exponent for its strong interaction that occurs with the Glu286 and His361 residues, components of the P1 site in the wild protein. In

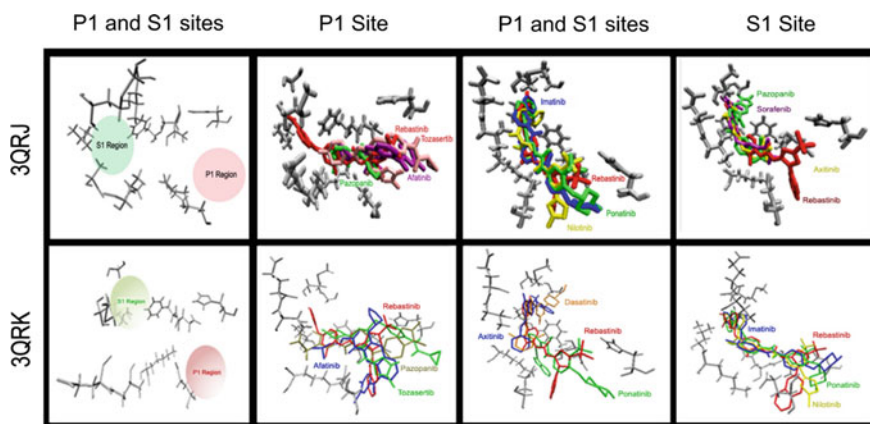


**Fig. 8** Representation of docking from the inhibitor interaction with key amino acids. Column 1: representation of the pocket of P1 and S1 sites; Column 2 represents inhibitors with the highest score at the P1 site; Column 3 represents inhibitors with the highest score at P1 and S1 site; Column 4 represents inhibitors with the highest score at S1 site

the mutated protein, the inclusion of Ile 315 showed no difference for the reported bindings, see Fig. 8.

For S1 site, the best inhibitors are axitinib, dasatinib, ponatinib and pazopanib. The inhibitor axitinib has a high score in both proteins, demonstrating that the site present for protein interaction resulting from the inhibition cascade anchors the inhibitor. Such characteristics indicate a strong candidate as a basis for the design of new hybrid ligand or as a leader molecule in the proposition of new ligands for inhibiting the S1 site. It was observed that inhibitors that contain a sulfur atom in their molecular composition (axitinib, dasatinib, and pazopanib) have a strong interaction with the S1 site.

### Final Remarks

The molecular docking study of a set of tyrosine kinase inhibitors were studied. The molecules include afatinib, axitinib, bosutinib, canertinib, dasatinib, erlotinib, gefitinib, imatinib, lapatinib, nilotinib, pazopanib, ponatinib, rebastinib, sorafenib, sunitinib, tozasertib. They are divided into. The catalytic sites, P1 and S1, of the structures of 3QRK (UniProtKB: P00519) and 3QRJ (UniProtKB: P00519) were analyzed. Quantum chemistry descriptors were used, such as, frontier molecular orbital energies and distribution, and HOMO-LUMO and HOMO-(HOMO-1) energy differences were used to assess the binding affinity of those inhibitors. It is possible to devise some properties that help on the generation of new hybrid ligand with greater inhibition on both sites.

## References

1. Schlessinger, J.: Cell signaling by receptor tyrosine kinases. *Cell* **103**, 211–225 (2000). [https://doi.org/10.1016/s0092-8674\(00\)00114-8](https://doi.org/10.1016/s0092-8674(00)00114-8)
2. Hunter, T., Cooper, J.A.: Protein-tyrosine kinases. *Annu. Rev. Biochem.* **54**, 897–930 (1985). <https://doi.org/10.1146/annurev.bi.54.070185.004341>
3. Cadena, D.L., Gill, G.N.: Receptor tyrosine kinases. *FASEB J* **6**, 2332–2337 (1992). <https://doi.org/10.1096/fasebj.6.6.1312047>
4. Sawyers, C.L.: Chronic Myeloid Leukemia. *N. Engl. J. Med.* **340**, 1330–1340 (1999). <https://doi.org/10.1056/NEJM199904293401706>
5. Faderl, S., Talpaz, M., Estrov, Z., et al.: The biology of chronic Myeloid Leukemia. *N. Engl. J. Med.* **341**, 164–172 (1999). <https://doi.org/10.1056/NEJM199907153410306>
6. Deininger, M.W.N., Goldman, J.M., Melo, J.V.: The molecular biology of chronic myeloid leukemia. *Blood* **96**, 3343–3356 (2000). <https://doi.org/10.1182/blood.V96.10.3343>
7. Maru, Y.: Molecular biology of chronic myeloid leukemia. *Cancer Sci.* **103**, 1601–1610 (2012). <https://doi.org/10.1111/j.1349-7006.2012.02346.x>
8. Fong, C.W.: Binding energies of tyrosine kinase inhibitors: error assessment of computational methods for imatinib and nilotinib binding. *Comput. Biol. Chem.* **28**, 40–54 (2015). <https://doi.org/10.1016/j.compbiolchem.2015.05.002>
9. Bhullar, K.S., Lagarón, N.O., McGowan, E.M., et al.: Kinase-targeted cancer therapies: progress, challenges and future directions. *Mol. Cancer*, **17**, 48 (2018). <https://doi.org/10.1186/s12943-018-0804-2>

10. Jabbour, E.J., Cortes, J.E., Kantarjian, H.M.: Resistance to tyrosine kinase inhibition therapy for chronic myelogenous leukemia: a clinical perspective and emerging treatment options. *Clin. Lymphoma Myeloma Leuk.* **13**, 515–529 (2013). <https://doi.org/10.1016/j.clml.2013.03.018>
11. Jabbour E, Kantarjian H (2018) Chronic myeloid leukemia: 2018 update on diagnosis, therapy and monitoring. *Am J Hematol*, **93**, 442–459. <https://doi.org/10.1002/AJH.25011>
12. Cortes, J.E., Kim, D.-W., le Coutre, P., et al.: A phase 2 trial of ponatinib in Philadelphia chromosome-positive leukemias. *N. Engl. J. Med.* **369**, 1783–1796 (2013). <https://doi.org/10.1056/NEJMoa1306494>
13. Sequist, L.V., Bell, D.W., Lynch, T.J., Haber, D.A.: Molecular predictors of response to epidermal growth factor receptor antagonists in non-small-cell lung cancer. *J. Clin. Oncol.* **25**, 587–595 (2007). <https://doi.org/10.1200/JCO.2006.07.3585>
14. Bentz, M., Cabot, G., Moos, M., et al.: Detection of chimeric BCR-ABL genes on bone marrow samples and blood smears in chronic myeloid and acute lymphoblastic leukemia by in situ hybridization. *Blood* **83**, 1922–1928 (1994)
15. Zhang, H., He, X., Ni, D., et al.: How does the novel T315L mutation of breakpoint cluster region-abelson (BCR-ABL) kinase confer resistance to ponatinib: a comparative molecular dynamics simulation study. *J. Biomol. Struct. Dyn.* **38**, 89–100 (2020). <https://doi.org/10.1080/07391102.2019.1567390>
16. Malkhasian, A.Y.S., Howlin, B.J.: Automated drug design of kinase inhibitors to treat Chronic Myeloid Leukemia. *J. Mol. Graph Model* **91**, 52–60 (2019). <https://doi.org/10.1016/j.jmgm.2019.05.014>
17. Keating, G.M.: Afatinib: a review of its use in the treatment of advanced non-small cell lung cancer. *Drugs* **74**, 207–221 (2014). <https://doi.org/10.1007/s40265-013-0170-8>
18. Roskoski, R., Jr.: Classification of small molecule protein kinase inhibitors based upon the structures of their drug-enzyme complexes. *Pharmacol. Res.* **103**, 26–48 (2016). <https://doi.org/10.1016/j.phrs.2015.10.021>
19. Keller-von Amsberg, G., Schafhausen, P.: Bosutinib in the management of chronic myelogenous leukemia. *Biol. Targets Ther.* **7**, 115–122 (2013)
20. Arora, A., Scholar, E.M.: Role of tyrosine kinase inhibitors in cancer therapy. *J. Pharmacol. Exp. Ther.* **315**, 971–979 (2005). <https://doi.org/10.1124/jpet.105.084145>
21. Müller, M.C., Cortes, J.E., Kim, D.-W., et al.: Dasatinib treatment of chronic-phase chronic myeloid leukemia: analysis of responses according to preexisting BCR-ABL mutations. *Blood* **114**, 4944–4953 (2009). <https://doi.org/10.1182/blood-2009-04-214221>
22. Scheffler, M., Kobe, C., Zander, T., et al.: Monitoring reversible and irreversible EGFR inhibition with erlotinib and afatinib in a patient with EGFR-mutated non-small cell lung cancer (NSCLC) using sequential [18F]fluorothymidine (FLT)-PET. *Lung Cancer* **77**, 617–620 (2012). <https://doi.org/10.1016/j.lungcan.2012.05.110>
23. Sordella, R., Bell, D.W., Haber, D.A., Settleman, J.: Gefitinib-sensitizing EGFR mutations in lung cancer activate anti-apoptotic pathways. *Science* **305**, 1163–1167 (2004). <https://doi.org/10.1126/science.1101637>
24. Manley, P.W., Cowan-Jacob, S.W., Buchdunger, E., et al.: Imatinib: a selective tyrosine kinase inhibitor. *Eur. J. Cancer* **38**, S19–S27 (2002). [https://doi.org/10.1016/S0959-8049\(02\)80599-8](https://doi.org/10.1016/S0959-8049(02)80599-8)
25. Fujita, K.I., Sugiyama, M., Akiyama, Y., et al.: The small-molecule tyrosine kinase inhibitor nilotinib is a potent noncompetitive inhibitor of the SN-38 glucuronidation by human UGT1A1. *Cancer Chemother Pharmacol* **67**, 237–241 (2011). <https://doi.org/10.1007/s00280-010-1445-3>
26. Sonpavde, G., Hutson, T.E., Sternberg, C.N.: Pazopanib, a potent orally administered small-molecule multitargeted tyrosine kinase inhibitor for renal cell carcinoma. *Expert Opin. Investig. Drugs* **17**, 253–261 (2008). <https://doi.org/10.1517/13543784.17.2.253>
27. Zhou, T., Commodore, L., Huang, W.-S., et al.: Structural mechanism of the Pan-BCR-ABL inhibitor ponatinib (AP24534): lessons for overcoming kinase inhibitor resistance. *Chem. Biol. Drug. Des.* **77**, 1–11 (2011). <https://doi.org/10.1111/j.1747-0285.2010.01054.x>
28. Janku, F., Hamilton, E.P., Mathews, C.A., et al.: Open-label, multicenter, phase 1b/2 study of rebastinib in combination with paclitaxel to assess safety and efficacy in patients with advanced

- or metastatic endometrial cancer. *J. Clin. Oncol.* **39**, 5576 (2021). [https://doi.org/10.1200/JCO.2021.39.15\\_suppl.5576](https://doi.org/10.1200/JCO.2021.39.15_suppl.5576)
29. Keating, G.M., Santoro, A.: Sorafenib. *Drugs* **69**, 223–240 (2009). <https://doi.org/10.2165/0003495-200969020-00006>
  30. Demetri, G.D., van Oosterom, A.T., Garrett, C.R., et al.: Efficacy and safety of sunitinib in patients with advanced gastrointestinal stromal tumour after failure of imatinib: a randomised controlled trial. *Lancet (London, England)* **368**, 1329–1338 (2006). [https://doi.org/10.1016/S0140-6736\(06\)69446-4](https://doi.org/10.1016/S0140-6736(06)69446-4)
  31. Ferreira, R.S., Andricopulo, A.D.: Structure-based drug design to overcome drug resistance: challenges and opportunities. *Curr. Pharm. Des.* **20**, 687–693 (2014). <https://doi.org/10.2174/138161282005140214161949>
  32. Morris, G.M., Huey, R., Lindstrom, W., et al.: AutoDock4 and AutoDockTools4: automated docking with selective receptor flexibility. *J. Comput. Chem.* **30**, 2785–2791 (2009). <https://doi.org/10.1002/jcc.21256>
  33. Humphrey, W., Dalke, A., Schulten, K.: VMD: visual molecular dynamics. *J Mol Graph* (1996). [https://doi.org/10.1016/0263-7855\(96\)00018-5](https://doi.org/10.1016/0263-7855(96)00018-5)
  34. Frisch, M.J., Trucks, G.W., Schlegel, H.B., et al.: Gaussian 09, Revision D.01. Gaussian (2009)
  35. Pereira WA, Nascimento ECM, Martins JBL (2021) Electronic and structural study of T315I mutated form in DFG-out conformation of BCR-ABL inhibitors. <https://doi.org/10.11080/0739110220211935320>
  36. Azam, M., Seeliger, M.A., Gray, N.S., et al.: Activation of tyrosine kinases by mutation of the gatekeeper threonine. *Nat. Struct. Mol. Biol.* **15**, 1109–1118 (2008). <https://doi.org/10.1038/nsmb.1486>
  37. Hurvitz, S.A., Shatsky, R., Harbeck, N.: Afatinib in the treatment of breast cancer. *Expert Opin. Investig. Drugs* **23**, 1039–1047 (2014). <https://doi.org/10.1517/13543784.2014.924505>
  38. Breedveld, P., Pluim, D., Cipriani, G., et al.: The effect of Bcrp1 (Abcg2) on the pharmacokinetics and brain penetration of imatinib Mesylate (Gleevec): implications for the use of breast cancer resistance protein and p-glycoprotein inhibitors to enable the brain penetration of imatinib in patients. *Cancer Res.* **65**, 2577–2582 (2005). <https://doi.org/10.1158/0008-5472.CAN-04-2416>
  39. Bernt, K.M., Hunger, S.P.: Current concepts in pediatric Philadelphia chromosome-positive acute lymphoblastic leukemia. *Front. Oncol.* **4** (2014). <https://doi.org/10.3389/fonc.2014.00054>
  40. Morphy, R.: Selectively nonselective kinase inhibition: striking the right balance. *J. Med. Chem.* **53**, 1413–1437 (2010). <https://doi.org/10.1021/jm901132v>
  41. Lu, X., Zhang, Z., Ren, X., et al.: Hybrid pyrimidine alkynyls inhibit the clinically resistance related Bcr-Abl(T315I) mutant. *Bioorg. Med. Chem. Lett.* **25**, 3458–3463 (2015). <https://doi.org/10.1016/j.bmcl.2015.07.006>
  42. Zhou, T., Parillon, L., Li, F., et al.: Crystal structure of the T315I mutant of AbI kinase. *Chem. Biol. Drug Des.* **70**, 171–181 (2007). <https://doi.org/10.1111/j.1747-0285.2007.00556.x>
  43. Pan, X., Wang, F., Zhang, Y., et al.: Design, synthesis and biological activities of Nilotinib derivatives as antitumor agents. *Bioorg. Med. Chem.* **21**, 2527–2534 (2013). <https://doi.org/10.1016/j.bmc.2013.02.036>
  44. Richters, A., Ketzner, J., Getlik, M., et al.: Targeting gain of function and resistance mutations in Abl and KIT by hybrid compound design. *J. Med. Chem.* **56**, 5757–5772 (2013). <https://doi.org/10.1021/jm4004076>

# Pathophysiology, Molecular Interaction Mechanism, Metabolism, Pharmacotherapy and New Perspectives in the Pharmacological Treatment of Chemical Dependence on the Main Illicit Drugs Consumed in the World



Jaderson V. Ferreira, Gisele A. Chaves, Mateus A. Batista, Lenir C. Correia, Lucilene R. Souza, Daniel C. Costa, Mariana P. Barcelos, Carlos Henrique Tomich de Paula da Silva, Carlton A. Taft, and Lorane Izabel da Silva Hage-Melim

**Abstract** Since the early days of mankind, humans have used chemicals from a wide range of origins for psychic changes, whether for religious, occupational or recreational purposes. Among the most widely used illicit substances on the planet, according to the United Nations Office on Drugs and Crime (UNODC), are *Cannabis sativa*, amphetamines, cocaine, opiates, ecstasy and heroin. These are responsible for the dependence of millions of people. Thus, this review is about chemical dependence with a focus on the mechanism of molecular interaction, metabolism and its consequent symptomatology manifested during drug withdrawal, as well as the current pharmacological treatments used during its manifestation and the search to increase pharmacotherapeutic arsenal against this pathology.

**Keywords** Amphetamine · *Cannabis sativa* · Lysergic Acid Diethylamide · Cocaine · Chemical dependency · Withdrawal syndrome

---

J. V. Ferreira · G. A. Chaves · M. A. Batista · L. C. Correia · L. R. Souza · D. C. Costa · L. I. da S. Hage-Melim (✉)

Laboratory of Pharmaceutical and Medicinal Chemistry (PharMedChem), Federal University of Amapá, Macapá, Brazil  
e-mail: [lorane@unifap.br](mailto:lorane@unifap.br)

M. P. Barcelos · C. H. T. de Paula da Silva  
Computational Laboratory of Pharmaceutical Chemistry, Department of Pharmaceutical Sciences, Faculty of Pharmaceutical Sciences of Ribeirão Preto, University of São Paulo, Ribeirão Preto, São Paulo, Brazil

Departamento de Química Faculdade de Filosofia, Ciências e Letras de Ribeirão Preto, Universidade de São Paulo, Ribeirão Preto, São Paulo, Brazil

C. A. Taft  
Centro Brasileiro de Pesquisas Físicas, Rio de Janeiro, Rio de Janeiro, Brazil

## 1 Introduction

Since the dawn of mankind, chemicals that alter behavior and cognition were already employed for the most diverse purposes, from recreational use to religious rituals [1]. Many of these substances today are called ‘drugs of abuse’ which are those that, when used legally or illegally, cause psychological, mental, emotional or social damages [2].

The most commonly used drugs of abuse in the world are cocaine, marijuana, amphetamines, which has its most expressive agent Ecstasy (methylenedioxymethamphetamine) and hallucinogenic substances such as lysergic acid diethylamide (LSD) [3]. Due to the increased use of such substances, in the last 50 years there has been a significant advance in the understanding of the processes by which drug abuse causes dependence, especially with respect to its biomolecular targets [4]. Illicit use of these substances has been increasing in underdeveloped countries, data from the United Nations Office on Drugs and Crime (UNODC) reports large-scale apprehensions of cocaine, *Cannabis sativa*, amphetamines and other proscribed substances worldwide, among which the most commonly found is marijuana. Still according to UNODC data, there are around 200 million users of some drug abuse worldwide [5].

Misuse and consequent chemical dependence are complex disorders regulated by a wide range of biochemical interaction networks and changes in gene expression in the mesolimbic dopaminergic system [6]. Understanding drug-induced changes in molecular and cellular interactions processes help to reveal a better understanding of these specific behavioral changes in chemical dependence [7]. This review introduces the pathophysiology, molecular drug interaction mechanisms and their reference biological targets, the drugs used and the perspectives in the treatments in case of chemical dependence of the main illicit drugs currently used.

## 2 Method

A bibliographical review was carried out in several electronic databases such as PubMed, Scielo, Web of Science, Science Direct and Nature, in order to investigate the publications that refer to the topic of *Cannabis*, LSD, Amphetamines and Cocaine. The descriptors used to capture the relevant articles were: *marijuana*, *cannabis*, Lysergic Acid Diethylamide, cocaine, Physiopathology, symptomatology, chemical dependency, treatment. Among the scientific works used in this research, more than 80% were published in the period from 2013 to 2019.

### 3 *Cannabis sativa*

#### 3.1 *Cannabis*

The *Cannabis sativa* plant, commonly known as marijuana belongs to the Moráceas family, known as “hemp” in India, and grows spontaneously in regions of tropical and temperate climate [8]. The use of Cannabis is predominantly smoked and can also be found in the form of resin in the form of plaques or rods, called hashish. The Leaf can be mixed with crack, or as skunk—a polymorphic form of marijuana [9] that is cultivated in a special way and with psychotropic power 7 to 25 times stronger than common marijuana, with content of the main psychoactive substance,  $\Delta$  [9]-Tetrahydrocannabinol ( $\Delta$  [9]-THC), estimated at 0.2–0.3% of the plant [10]. Figure 1 represents the chemical structure of  $\Delta$  [9]-THC.

##### 3.1.1 Action Mechanism of Cannabis

Two cannabinoid receptor subtypes, CB1 and CB2, have been identified and are responsible for many biochemical and pharmacological effects produced by most cannabinoid compounds [11]. Psychotropic activity is caused by interaction with the  $\Delta$  [9]-THC (Fig. 1) and the cannabinoid receptor CB1 [12], being the activation trigger for this process of conformational changes of this receptor, the interaction of the cannabinoid with the amino acid residue Ser383 and its surroundings (Fig. 2). Despite the differences between cannabinoid receptor CB1 and CB2, most cannabinoid compounds interact similarly in the presence of both receptors [13].

With the conformational change of the cannabinoid receptor CB1 a series of reactions occurs, including inhibition of Adenylate Cyclase, which decreases the production of cAMP (cellular activities depend on the enzyme cyclic adenosine monophosphate—cAMP); opening of the potassium channels ( $K^+$ ), reduction of signal transmission and closure of calcium channels ( $Ca^+$  [2]), leading to a decrease

**Fig. 1** Structural formula of  $\Delta$  [9]-THC

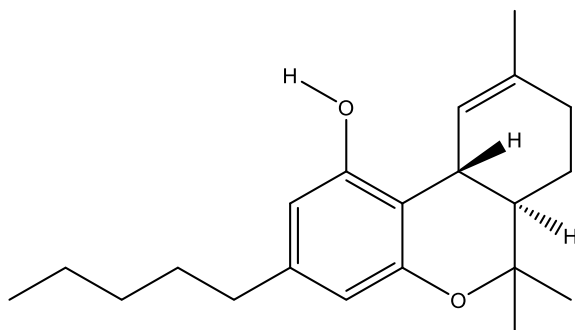
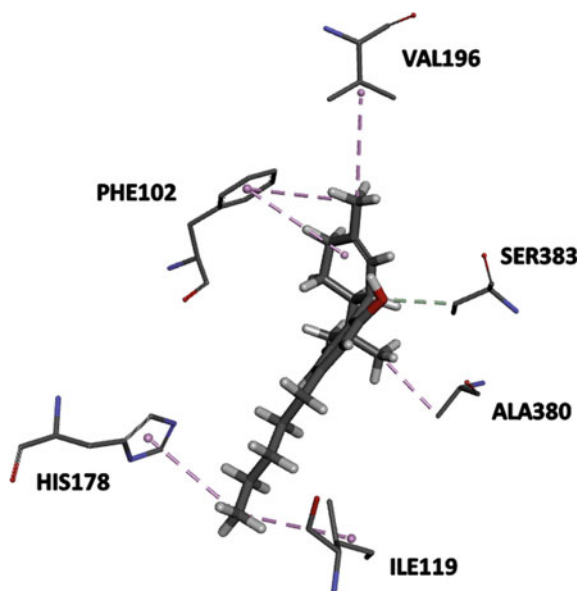


**Fig. 2** Amino acid residues of the cannabinoid receptor CB1 interacting with  $\Delta$  [9]-THC



in the release of neurotransmitters. Whose decreased concentration is related to the psychotropic effects of *C. sativa* [14].

The location of cannabinoid receptor CB1 in the central nervous system (CNS) is directly associated with the behavioral effects produced by cannabinoids. The higher density of these receptors is found in (a) cells of the basal ganglia, involved in the coordination movements of the body [15], (b) in the cerebellum, a region responsible for the coordination of body movements and cognition [16], (c) hippocampus, responsible for learning, memory, fear, and response to stress and (d) cerebral cortex, responsible for cognitive functions [17]. Regions with lower concentrations of cannabinoid receptor CB1 are also involved with reactions derived from the use of *C. sativa*, and these are (a) region of the hypothalamus, related to temperature regulation, hydroelectrolytic balance, and reproductive function, (b) Amygdala responsible for emotional response, (c) column vertebral body responsible for peripheral sensation and (d) brain stem responsible for sleep regulation and motor control [15, 16].

### 3.1.2 Metabolism of *Cannabis Sativa*

$\Delta$  [9]-THC is a very lipophilic molecule and, not by chance, easily crosses the blood–brain barrier (BBB). In addition, it is rapidly distributed to more vascularized organs and tissues, such as the lungs, kidneys, liver, heart salivary glands, pituitary, and thyroid [17]. The decrease in blood pressure of the molecule is mainly due to its first-pass metabolism, although its main metabolite, 11-OH-THC, also has psychoactive power, high liposolubility and acts promptly in the CNS [18].



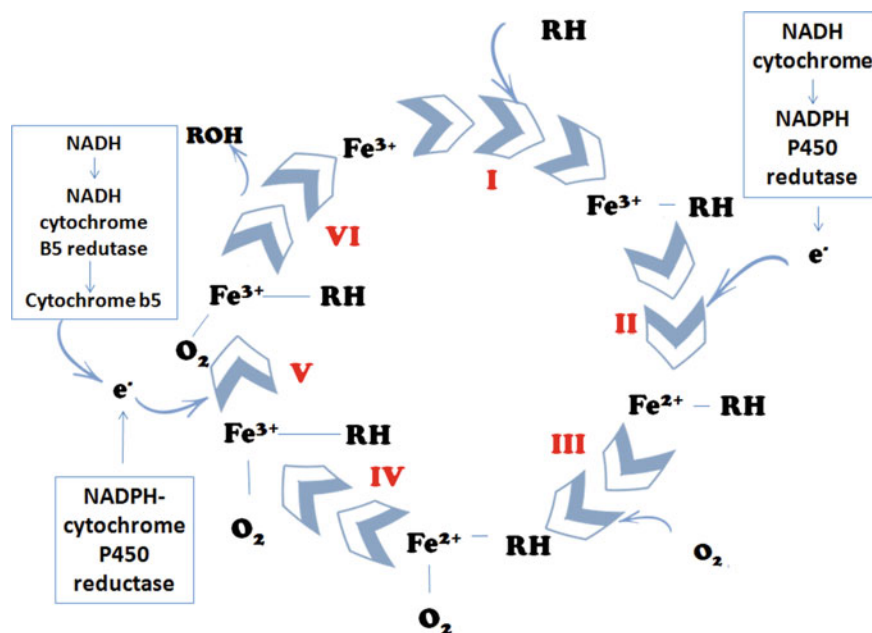


Fig. 3 Catalytic cycle of cytochrome P450. RH represents the substrate of the drug and ROH is the corresponding hydroxylate metabolite [20]

$\Delta$  [9]-THC is rapidly converted to 11-hydroxy-THC (11-OH-THC) in the liver by microsomal hydroxylation, mainly by the isoenzymes CYP2C9, CYP2C19 and CYP2D63 [19]. These enzymes belong to the cytochrome P450 family and are responsible for the aromatic hydroxylation that occurs in the conversion of the compounds mentioned above. This reaction is very common for drugs and xenobiotics that have an aromatic ring, and its mechanism is shown (Fig. 3). Cytochrome has a prosthetic group with iron protoporphyrin (Fig. 4), which is extremely important for the electronic transfer system [20].

The  $\Delta$  [9]-THC substrate is oxidized by the isoenzymes according to the mechanism of action of the cytochrome P450, below is a schematic of the chemical reaction in a simplified way (Fig. 5).

In Fig. 6, the hydroxylation mechanism catalyzed by cytochrome P450 is shown. A radical reaction is observed, and the compound is released after the reaction with water. This step can be repeated, yielding the compound 11-hydroxy-THC (11-OH-THC) [21].

After step 6 present in the catalytic cycle (Fig. 4), the 11-hydroxy-THC (11-OH-THC) can be oxidized again. It would return to the cycle and after all reactions would convert to the 11-N-9-carboxy-9-THC (THC-COOH) (Fig. 7) [23, 24].

Thereafter, cytochrome P450 is involved in oxidation where the inactive metabolite 11-Nor-9-carboxy-9-THC (THC-COOH) is excreted in conjunction with

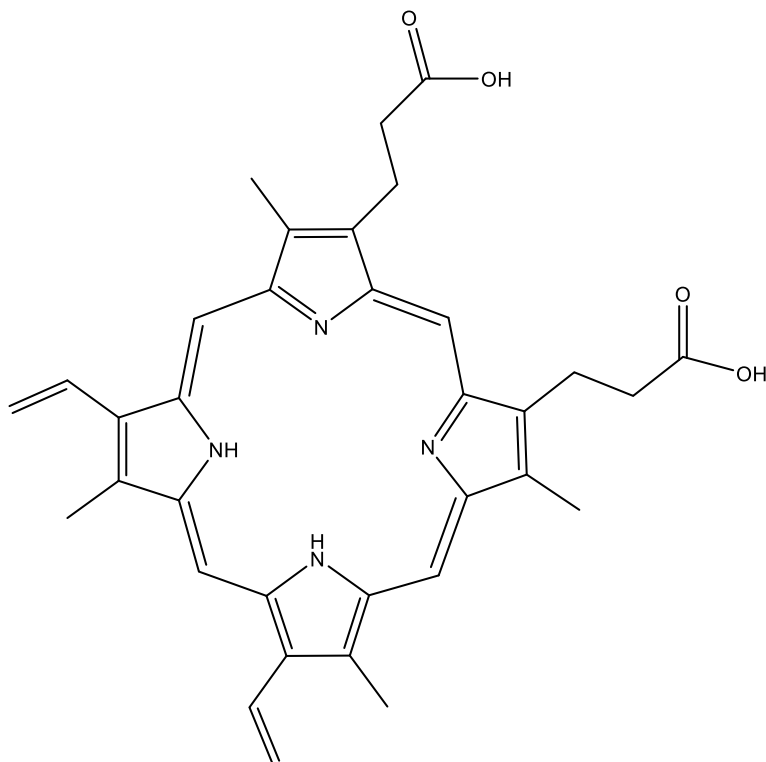


**Fig. 4** Structure of iron protoporphyrin IX, the prosthetic group of cytochrome P450 [20]

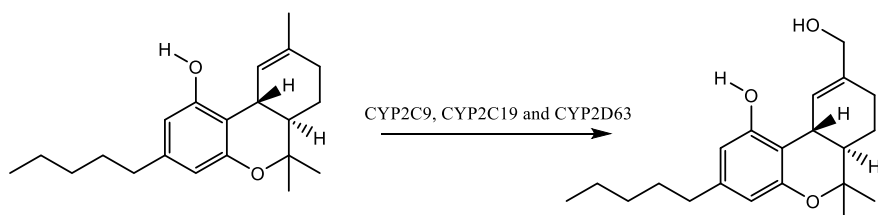


**Fig. 5** Aromatic hydroxylation reaction of  $\Delta^9$ -THC being converted to 11-hydroxy-THC (11-OH-THC) by the isoenzymes CYP2C9, CYP2C19 and CYP2D63

glucuronic acid [25]. The complete reaction of  $\Delta^9$ -THC metabolism is shown below (Fig. 8):

About 100 THC metabolites were identified. In addition to the liver, there are other organs capable of metabolizing cannabinoids, such as the lungs, heart, and intestines, although to a lesser extent (Fig. 9) [26].

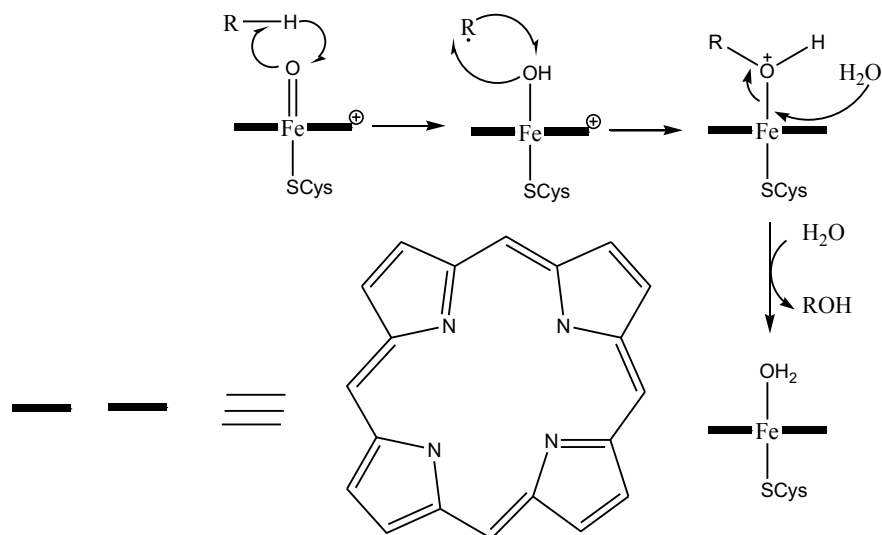


**Fig. 6** Cytochrome P450 catalyzed hydroxylation mechanism [22]

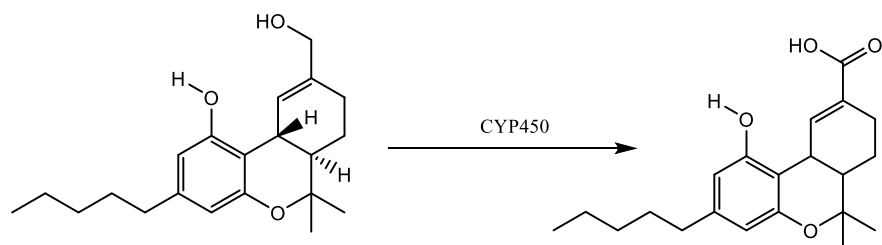


**Fig. 7.** 11-Hydroxy-THC (11-OH-THC) oxidation reaction being converted to 11-Nor-9-carboxy-THC (THC-COOH) by the cytochrome P450

### 3.2 Lysergic Acid Diethylamide (LSD)

Lysergic Acid Diethylamide (LSD) (Fig. 10) was first synthesized from ergot in 1938 and banned by FDA in 1966. At the beginning of their popularization the products contained 0.25 LSD per sugar cube or dose, currently the circulating products contain about 0.4–0.06 mg per dose [27]. Although also found in liquid form (drops), capsules, tablets, gelatin cubes or microdots, is mainly consumed orally in the form of illustrated seals (blotters) [28]. Variations in standard consumption include: swallowed by themselves, wrapped in cigarette paper, mixed with a drink, impregnated with a candy, a biscuit or a drop of sugar. It can also be left on or under the tongue or between the cheek and gum. Other more marginal routes of administration are known: in the smoke, injected or instilled in the eye in liquid form [29].

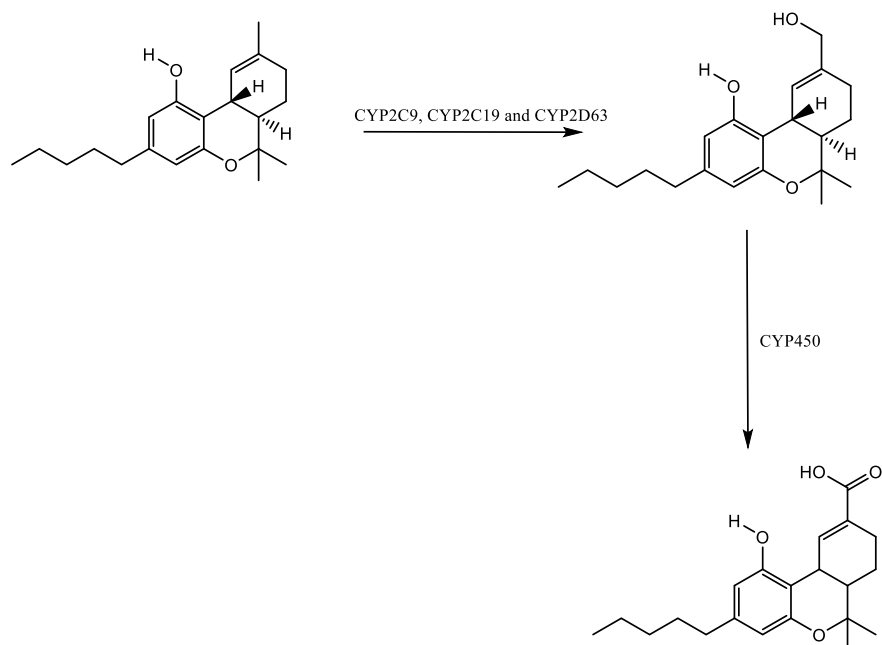


**Fig. 8** Complete reaction of  $\Delta^9$ -THC metabolism and subsequent formations of 11-hydroxy-THC (11-OH-THC) and 11-N-9-carboxy-THC (THC-COOH)

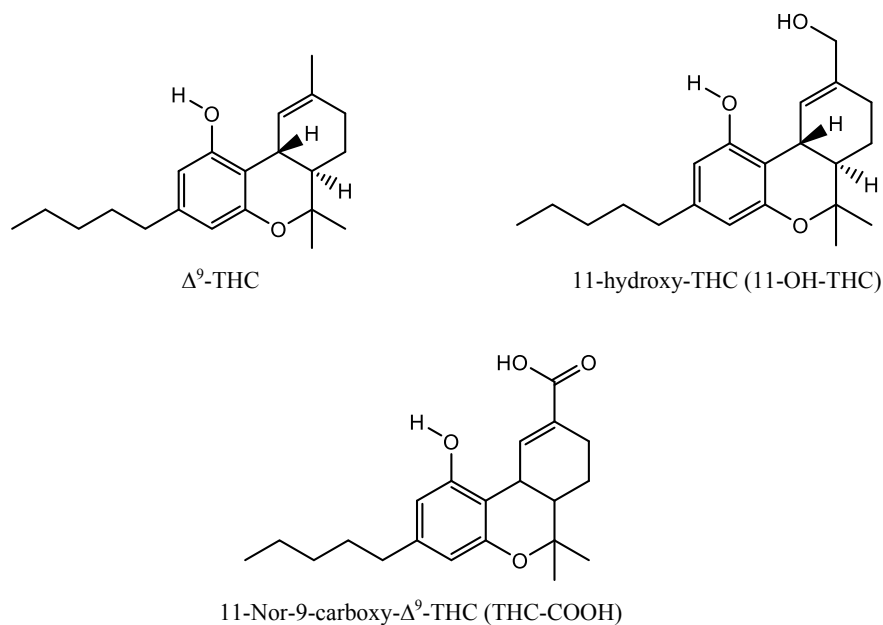
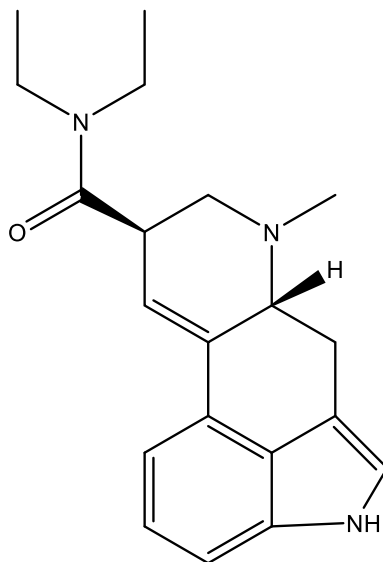


**Fig. 9**  $\Delta^9$ -THC and some of its major metabolites

**Fig. 10** Structural formula of lysergic acid diethylamide



### 3.2.1 Action Mechanism of LSD

The hallucinogenic and psychotic effects of LSD are related to the interaction of this drug in the serotonergic, dopaminergic and adrenergic systems.

#### The Serotonergic System

Serotonin syndrome is characterized by hyperstimulation of postsynaptic serotonergic receptors, presenting symptoms frequently associated with the use of LSD such as tremors, hyperreflexia, muscle spasms, tachycardia, hyperthermia, and delirium [30, 31].

LSD activates different signaling cascades of serotonin (5-HT) receptors, and the interaction with the 5-HT<sub>2A</sub> receptor, coupled to G protein, is the main factor responsible for the hallucinogenic action related to the serotonergic receptor [32]. At this receptor, LSD acts as an agonist increasing the rate in the brain or preventing abstinence from 5-HT. Consequently, when 5-HT binds to 5-HT<sub>2C</sub> receptors, a strong response of inositol triphosphate occurs, a secondary messenger involved in the transduction of the biological signal with or without increased intracellular levels and phosphorylation of calcium [13].

## Dopaminergic System

LSD can directly activate the two major categories of dopaminergic receptor subtypes, D1 and D2 [33]. It is known that the ventral tegmental area receives afferent serotonergic neurons from the raphe nucleus, so that activation of 5-HT<sub>2A</sub> may affect the local dendritic release of dopamine in the mesolimbic and mesocortical pathways [34]. The release of dopamine into the cortical and limbic structures characterizes the first phase (with an estimated duration of 60 min in rats) of the effects of LSD. The second phase (approximately 60–100 min occurs in rats after LSD administration) is mediated by stimulation of D<sub>2</sub> receptors, which is also consistent with the idea that excess dopaminergic activity may be the cause of drug-induced psychosis [35].

## Adrenergic System

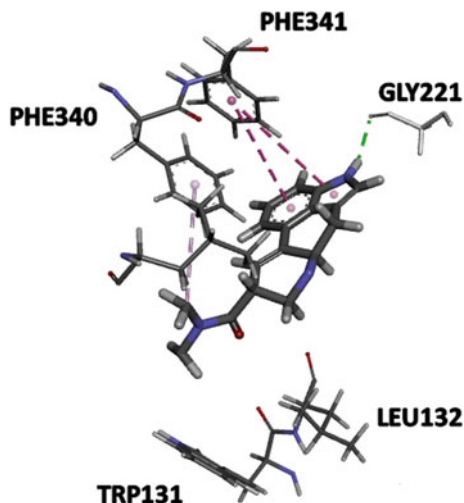
LSD has little affinity for  $\alpha_2$  adrenergic receptors and may also increase glutamatergic transmission in the cortex by the presynaptic activation of the 5-HT<sub>2A</sub> receptor and subsequent activation of  $\alpha$ -amino-3-hydroxy-5-methyl-isoxazole (AMPA) receptors. This fact contributes to the rapid onset of the tolerance effect on the mental responsiveness to the use of LSD in humans (around 4 days) [36].

### 3.2.2 Docking

The simulation of the coupling of the LSD structure bound to one of the molecular targets allowed to clarify the relation of the chemical structure of this drug with its activity, kinetics, and signaling. Although lysergamides are relatively rigid, they are found to have conformational flexibility [37] generating stereochemical differences, mainly related to the amide substitution of these that adopt a restricted conformation in the binding site, a fact that has influence in the hallucinogenic activity, so that these conformations are crucial for the hallucinogenic effects of LSD [38].

The positioning and interactions of diethylamide contribute to the long residence time of LSD in 5-HT<sub>2B</sub> and 5-HT<sub>2A</sub> targets [32]. In the active site of these targets, the ergoline system of LSD forms a narrow slit lined with hydrophobic side chains that comprise aromatic interactions with the phenylalanines of residues Phe340 and Phe341 and bonds of H with residue Gly221. In relation to the diethylamide group of LSD, one ethyl group forms non-polar interactions with residues Leu132 and Trp131, while the other group extends to Leu362 acetate (Fig. 11) [39].

**Fig. 11** Residues of Serotonin Receptor amino acid interacting with lysergic acid diethylamide



### 3.2.3 Metabolism of LSD

At the beginning of this century, studies indicated that LSD metabolism would be converted into phase I biotransformation into hepatic microsomes and human hepatocytes for 2-oxo-3-hydroxysilergic acid diethylamide (OH-LSD) and N-desmethyl—LSD) [40] metabolite present in human urine at concentrations 16–43 times greater than LSD [18].

The LSD is oxidized in OH-LSD by the cytochrome P450 according to the scheme shown in Fig. 12.

Another reaction that occurs also in LSD is dealkylation, which occurs in drugs containing secondary or tertiary amines, an alkoxy or substituted alkyl thiol group. The lost alkyl group becomes its corresponding aldehyde. In the case of dealkylation occurring in LSD for conversion to nor-LSD N-Desmethyl-LSD, the corresponding aldehyde is the methanal [20].

The reaction occurs in two steps, the first being hydroxylation in the methyl group bound to the nitrogen, forming an unstable intermediate. The second step is the decomposition of this intermediate, shown in the figures below:

Due to the extensive metabolism of LSD, research is advancing in the discovery of new metabolites, and the most recent ones conclude that myeloformidases (MPO), abundantly expressed in neutrophils and monocytes and also in neurons and microglia, may also be involved in the metabolism of this substance. This pathway of formation of metabolites would occur concomitantly with the cytochrome P450 system giving rise to another important metabolite, N, N-diethyl-7-formamido-4-methyl-6-oxo-2,3,4,4a,5,6-hexahydrobenzo[f]quinoline-2-carboxamide (FOMBK), which is an open indolic ring compound. Hydrolysis of the FOMBK metabolite leads

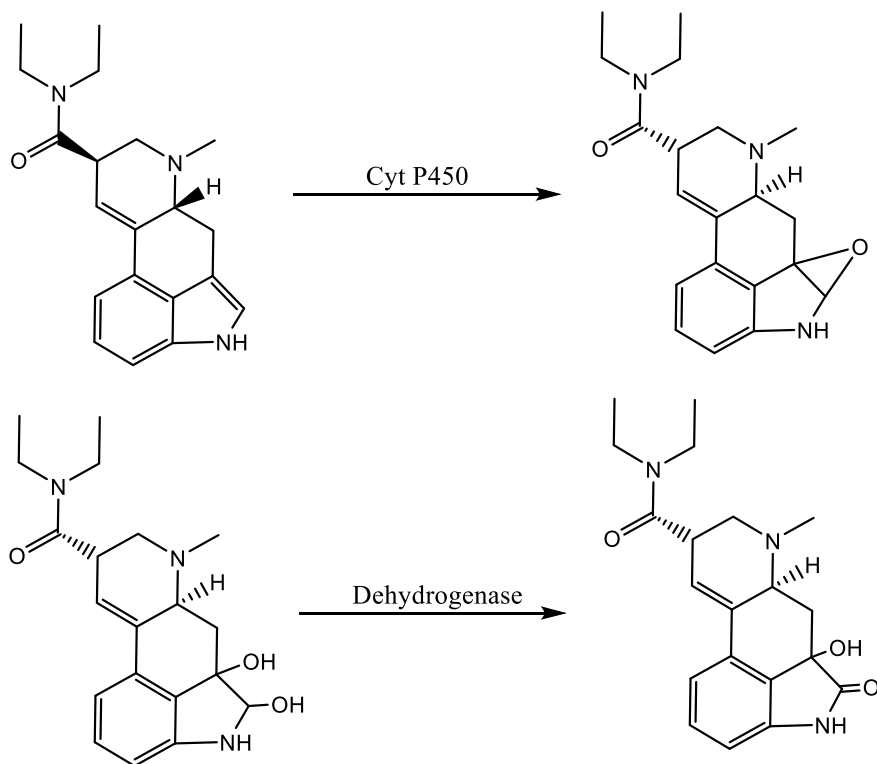


**Fig. 12** LSD metabolic pathway and 2-oxo-3-hydroxy lysergic acid [40]

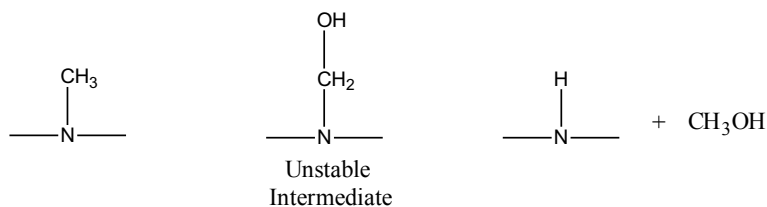


**Fig. 13** Formation of the unstable intermediate in the dealkylation step [20]

to 7-amino-N, N-diethyl-4-methyl-6-oxo-2,3,4,4a, 5,6-hexahydrobenzo [quinoline-2-carboxamide (AOMBK) [41]. The formation of these two products is shown in Fig. 17.

The above scheme first shows the formation of a radical, followed by the reaction with an oxygen molecule. The loss of an oxygen will form the compound O–H-LSD while another alternative would be the formation of an unstable intermediate, which will give rise to OH-LSD and FOMBK. With the exit of a molecule of  $\text{H}_2\text{CO}$ , AOMBK is formed (Fig. 18).



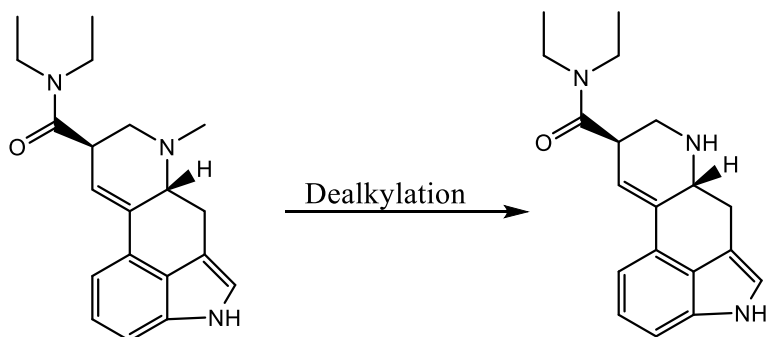


**Fig. 14** LSD dealkylation reaction in nor-LSD N-Desmethyl-LSD

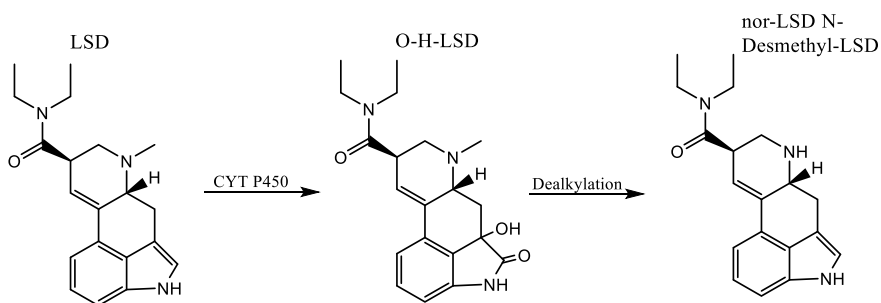


**Fig. 15** Complete reaction of LSD metabolism

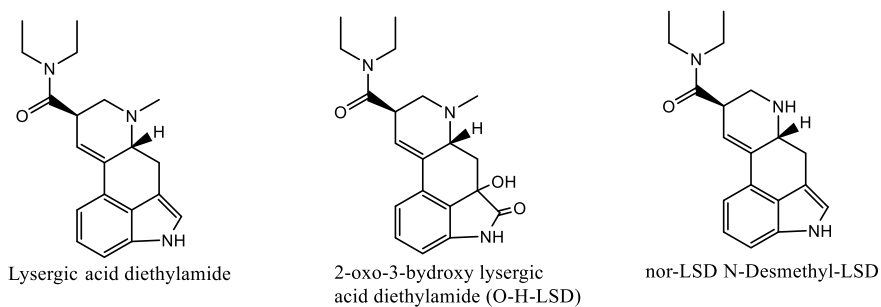


**Fig. 16** LSD and its metabolites

### 3.3 Amphetamine

Amphetamines are substances that have a very complex system that implies several consequences due to inappropriate use. These include a diverse class of synthetic chemicals and naturally occurring alkaloids, e.g. ephedrine and cathinone, which

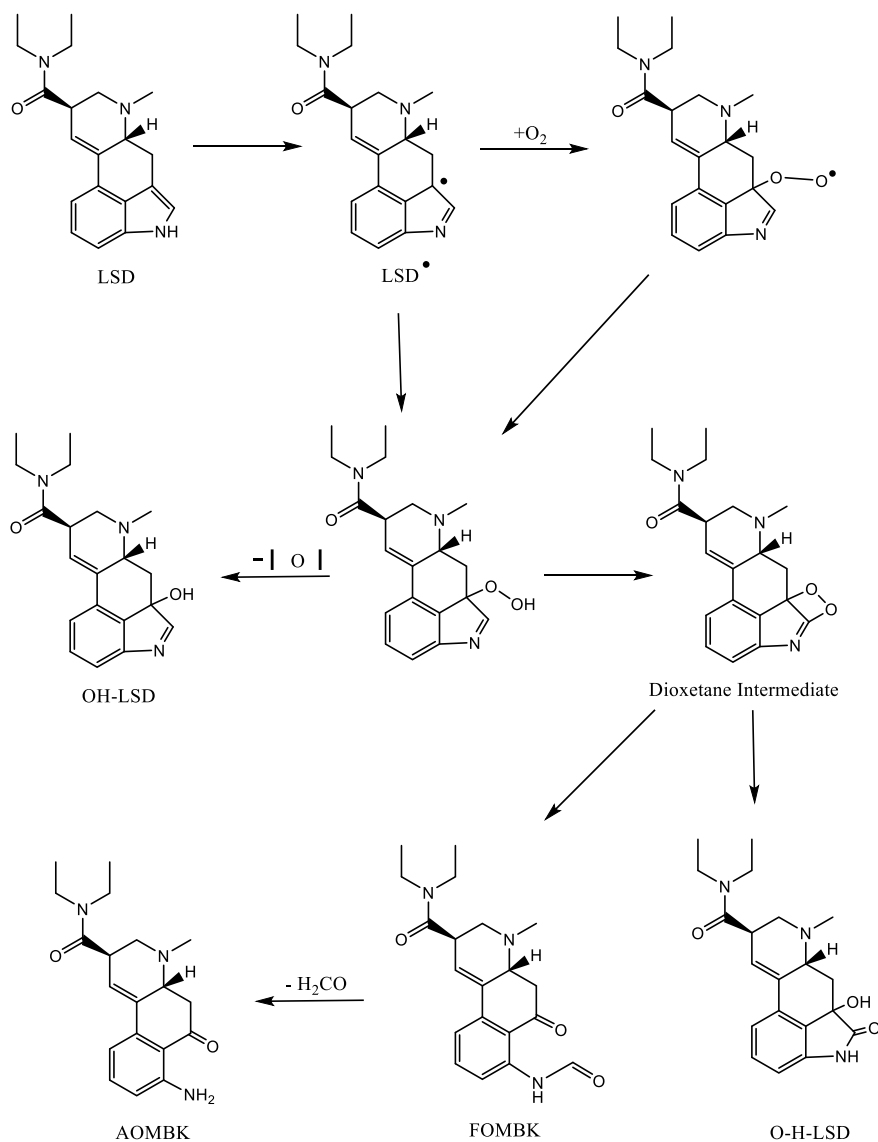


**Fig. 17** Proposed reaction for the formation of AOMBK and FOMBK using MPO [42]

are synthesized in the plant species *Ephedra sinica* and *Catha edulis*, respectively [43, 44].

The complexity to explain the mode of action of these substances is due to the mechanisms of action ranging from the central and peripheral stimulation of the

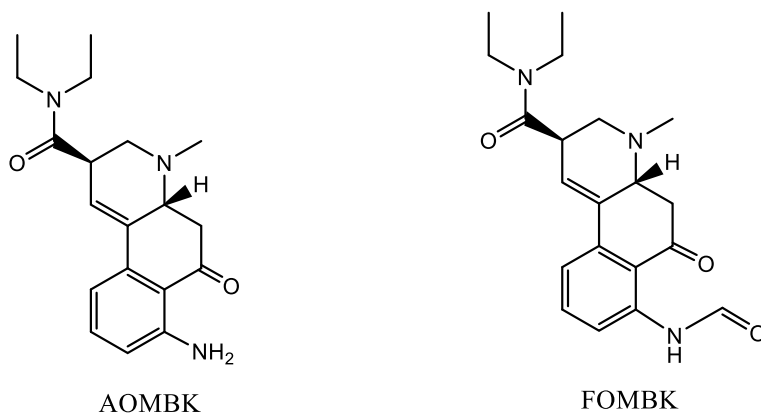


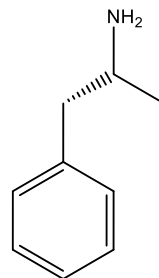
**Fig. 18** LSD and its metabolites

release of endogenous biogenic amines by the binding to the monoamine transporters, which are already difficult to define chemical structures until the blockade of absorption induced by methylphenidate [45].

Amphetamine (Fig. 19) is produced in the laboratory and belongs to the class of phenylethylamines, which are sympathomimetic substances with a predominant action in the CNS, whose induction causes hyperactivity of brain activity. In general, amphetamines and illicit derivatives are used for feelings of euphoria, relaxation, anxiety decline, whose response is dependent on the organism [46]. Due to stimulation of the CNS, the most common users of amphetamines are those whose activities related to this activation, such as the academics that although the intention is the improvement in cognitive performance, present greater difficulties and lower average score in relation to the non-users [47]; the drivers, in relation to the alert state [48]; young people to produce or intensify pleasurable effects or attenuate negative effects; individuals who seek the anorexic effect in search of improvement in self-esteem and the professionals of the arts in search of greater creativity [49].

Methylenedioxyamphetamine commonly called Ecstasy or “Love Pill” and 4-Bromo-2,5-dimethoxy-amphetamine, the “Wind Capsule” [50], are derived from amphetamines and are easily produced illicit drugs in clandestine laboratories and,

**Fig. 19** Structural formula of amphetamine



for this reason, there is a very rapid dispersion of these drugs by society, having influence in the most varied family contexts [51].

### 3.3.1 Action Mechanism of Amphetamine

Amphetamine acts predominantly in the CNS, being an agonist of indirect action of the amines, mainly the dopamine and other neurotransmitters like serotonin and noradrenaline [52]. These competitively inhibit the transport of norepinephrine and dopamine and at high doses also inhibit the reuptake of serotonin [53]; releases dopamine and norepinephrine independent of  $\text{Ca}^{2+}$ , that is, the effect does not depend on the depolarization of the nervous terminal [54]. Similar amphetamine drugs, in addition to acting as agonists in the indirect action of noradrenergic, dopaminergic and serotonergic synapses, also inhibit the enzyme monoamine oxidase (MAO), a flavoenzyme that catalyzes the oxidation of biogenic amines [45].

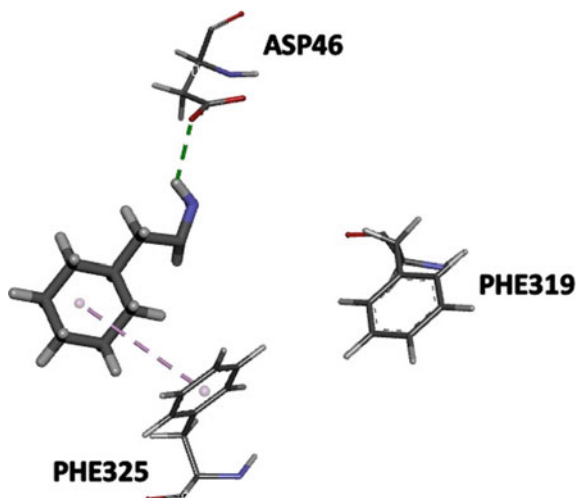
There is a widespread mechanism to explain the action of amphetamines on dopamine levels, which is related to neurotransmitter uptake, a fact that was found due to the administration of dopamine uptake inhibitors to attenuate the effects of amphetamine on the cytoplasmic transporter. This model is known as exchange diffusion, where amphetamine acts directly and/or indirectly on the dopamine transporter. Amphetamine can increase the presence of this transporter on the inside of the cell and this leads to a reverse dopamine transport, decreasing its cytoplasmic concentrations and blocking the reuptake of this neurotransmitter that will be present in the synaptic cleft [55]. This abundant neurotransmitter will interact with various receptors on postsynaptic neurons, specified as type D1-like (D1 and D5) and type D2-like (D2, D3 and D4), these proteins differ in their molecular capacities and pharmacological responses when interconnected with dopamine [56].

The interaction between amphetamine and dopamine occurs through the interaction of the amine group with the carboxylate of Asp46 and is crucial for the hallucinogenic effect, considering that this residue is conserved in neurotransmitters of biogenic amines. In addition to this interaction, the catechol group occupies the cavity in which residues Phe325 and Phe319 [57] (Fig. 20).

### 3.3.2 Metabolism of Amphetamine

In recent years, numerous compounds derived from amphetamines with modified ring systems have reached the market constituting a new class of psychoactive substances (NPS) [58]. Of course, metabolic variation exists in each case, but metabolic O-demethylation is mediated by CYP2D6 (catalyzes the hydroxylation of many amine rings) in man and by CYP2B and CYP2D enzymes in relation to methoxy-amphetamine metabolism in the case of species related to amphetamine. Metabolism continues with the formation of hydroxylated metabolites, p-hydroxyamphetamine (POHA), p-hydroxynorephedrine (POHNOR), and p-hydroxyamphetamine glucuronide (POHAG) [59].

**Fig. 20** Amino acid residues from the dopamine transporter interacting with amphetamine



In the conversion of amphetamine to 4-hydroxyamphetamine, a  $\beta$ -hydroxylation, performed by CYP2D6, occurs. This cytochrome belongs to the P450 family, so it will perform reactions similar to this. To obtain the POHA, the mechanism will be the same as that shown in Fig. 21.

4-hydroxynethedrine is obtained from 4-hydroamfetamine by the action of the enzyme Dopamine- $\beta$ -hydroxylase (DBH), which catalyzes the conversion of dopamine to norepinephrine using ascorbic acid, as can be observed in the following reaction (Fig. 22).

DBH catalyzes the hydroxylation not only of dopamine, but also of other phenylethylamine derivatives, when available (Fig. 23). The minimum requirement appears to be a benzene ring having a two carbon side chain terminating in an amino group [61].

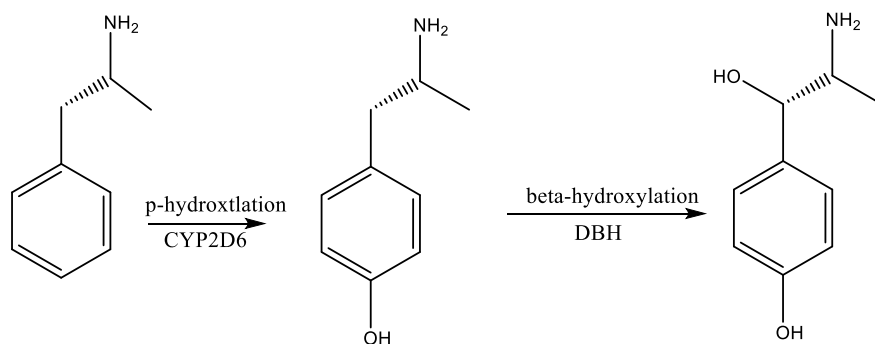


**Fig. 21** Metabolic pathways of amphetamine [60]

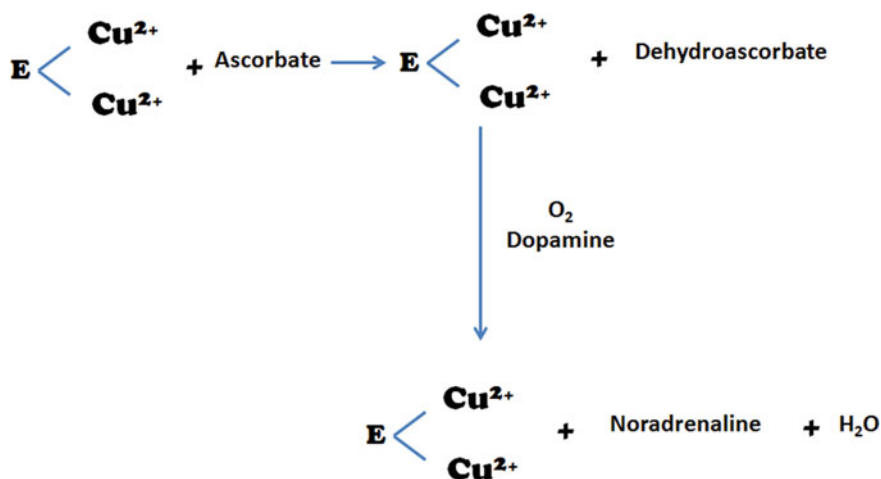


Fig. 22 Mechanism of dopamine  $\beta$ -hydroxylase reaction (DBH) [61]

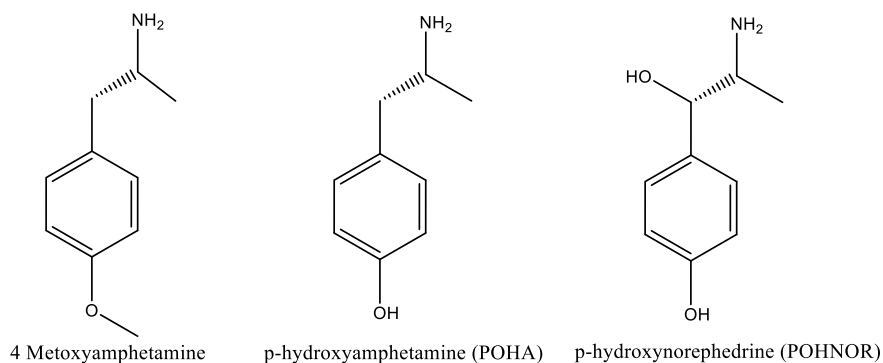
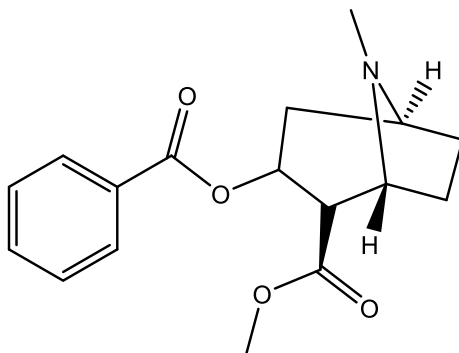


Fig. 23 Amphetamine metabolites

### 3.4 Cocaine

The cocaine alkaloid (COC) (Fig. 24), commonly known as coca, is a drug of abuse that has a relatively short history compared to the *Erythroxylum* plant from which it derives. There are several species of this plant originating in the tropical zone of the South American Andes, of which the most outstanding are *Erythroxylum novogranatense*, *Erythroxylum novogranatense Truxillense* and *Erythroxylum coca* [62], the latter being the most prominent in the illicit use of COC [63].

**Fig. 24** Structural formula of cocaine



### 3.4.1 Action Mechanism of Cocaine

The psychotropic effect of cocaine is caused by stimulation of the CNS due to sodium channel block and neuronal inhibition by catecholamine uptake, changes in synaptic transmissions of noradrenaline, serotonin and dopamine [64], with the last inhibition of neuronal reuptake being the most important involved in the process of dependence [65]. It is important to mention that the amount of norepinephrine and 5-HT in the synaptic cleft is also increased during the cocaine effect, but with less significance [66].

Cocaine has similar actions to catecholamines, not acting directly on adrenergic or dopaminergic receptors, because it is known as an indirectly acting sympathomimetic amine. It can act by blocking the norepinephrine and dopamine reuptake carrier protein in the presynaptic terminal, increasing the levels and effects of these neurotransmitters in the synaptic cleft [67]. The difference between cocaine and amphetamine in relation dopamine reuptake inhibition is related to the inhibition site where these molecules act, while amphetamines occupy the same site as dopamine in the carrier protein, cocaine acts elsewhere, specifically at an allosteric site, causing carrier deformation that prevents interaction with dopamine [68].

Studies on cocaine docking with the neurotransmitter acetylcholine indicate that this interaction occurs mainly by the tryptophan maintained at the center of the active site and, to a lesser extent, by the Tyr195 residue. Thus, this binding occurs competitive and non-competitive, depending on the concentration of the compound [69] (Fig. 25).

### 3.4.2 Metabolism of Cocaine

The first step in the biotransformation of cocaine is catalyzed by CYP3A, where it occurs with oxidative N-demethylation of the substance in its biologically active hepatic metabolite, norcocaine. This conversion occurs by two alternative routes, one involving only the cytochrome P450 and the other requiring the monooxygenase containing the cytochrome P450 and (Flavin Adenine Dinucleotide (FAD)) [70].

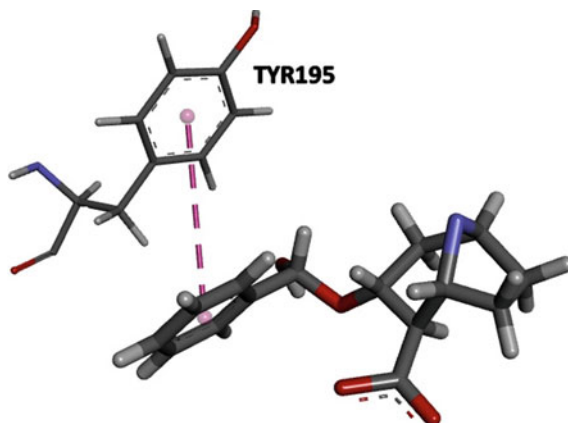


**Fig. 25** Amino acid residues of acetylcholine interacting with cocaine

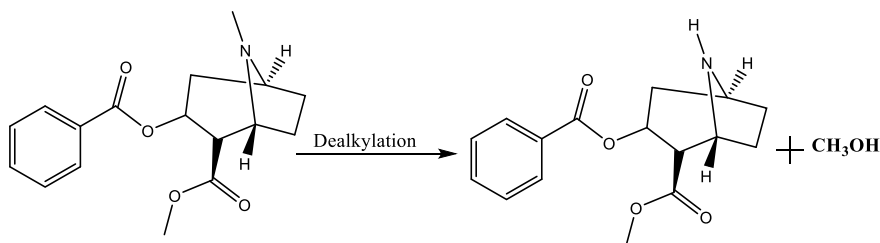
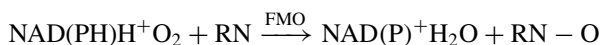


**Fig. 26** Dealkylation reaction of cocaine

In the first route, cocaine is directly N-demethylated in norcocaine by cytochrome P450. In this case the presence of a dealkylation reaction is again present, as can also be seen in LSD (Fig. 26).

The second pathway was found to be a two-step reaction involving cocaine N-oxide as an intermediate, the first step being made by a monooxygenase enzyme containing FAD [20]. The reaction mechanism of this monooxygenase containing FAD is shown in the figure below. This mechanism can be simplified in the following global reaction:



In this route, cocaine is first oxidized to cocaine N-oxide by FMO, followed by N-demethylation catalyzed by cytochrome P450 to norcocaine (Fig. 28).

The major excreted metabolites of cocaine are benzoylecgonine (formed by non-enzymatic hydrolysis), methyl ester of ecgonine (both representing 75–90% of cocaine metabolism) and ecgonine (formed in smaller amounts). Ecgonine



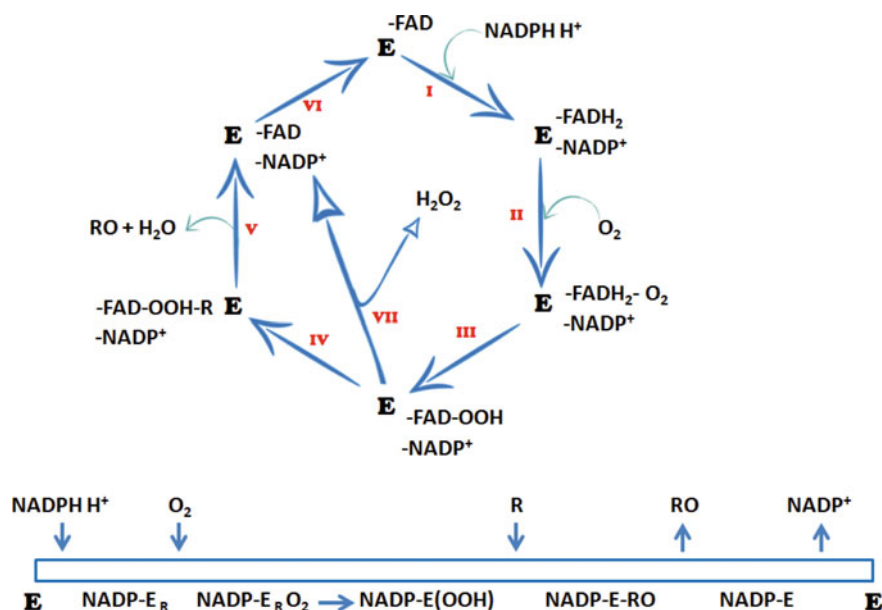
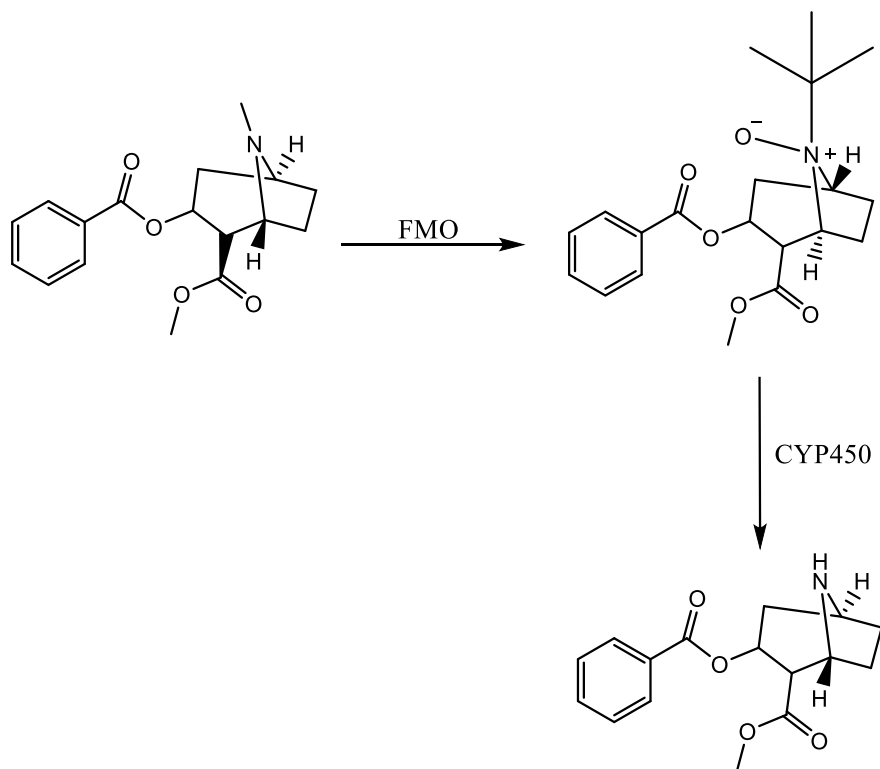


Fig. 27 Oxidation of compounds by microsomal flavin-containing monooxygenase (FMO) [20]

methyl ester undergoes cholinesterase activity (liver and serum enzymes) while benzoylcegonine is formed by non-enzymatic hydrolysis [71, 72].

For the conversion of cocaine to methyl ester of ecgonine, enzymes are used cholinesterase (ChE). In this case, the substrate (cocaine) binds to the amino acid Asn70, and then binds to the active site of choline (cation  $\pi$  site). In the next step, cocaine rotates to the horizontal position for hydrolysis to occur and approaches Ser198 (Fig. 29). After all these steps are completed the final product is obtained, the methyl ester of ecgonine [73] (Fig. 30).

In the case of benzoylcegonine and ecgonine, these compounds are formed by deesterification (hydrolysis) in the liver. In a reaction with water, a bond in the compound is broken, resulting in two compounds. At the same time, a water molecule divides into two, with one hydrogen being transferred to one compound and one hydroxyl to another compound. The hydrogen atom is transferred to the cocaine substrate, giving benzoylcegonine and hydroxyl to the alkyl methyl forming methanol. Methanol, in turn, reacts with cocaine, originating ecgonine methylester and a molecule of water [75] (Figs. 31, 32 and 33).



**Fig. 28** N-oxide cocaine oxidation by FMO, followed by cytochrome P450 catalyzed N-demethylation to form norcocaine

#### 4 Physiopathology of Chemical Dependence

Drug dependence is increasingly recognized as one of the leading causes of death, morbidity, and loss of productivity in developed countries. Due to the urgent clinical and social need to do something about addiction, neuroscience has advanced in the past 50 years favoring extraordinary progress in global efforts to combat addiction [76].

Drug dependence is defined by the 10th Revision of the International Classification of Diseases (ICD-10) with the presence of three or more dependency indicators. These indicators consist of: (a) a strong desire to use the substance, (b) poor use control, (c) withdrawal syndrome by stopping or reducing use, (d) tolerance to the effects of drugs, (e) need for larger doses to achieve the desired psychological effect, (f) a disproportionate amount of time spent by users obtaining, using and recovering from drug use, g) drug persistence, despite problems [77].

To create selective therapies with action on receptors and neurons altered by drugs and thus inhibit drug abuse, it is necessary to understand the neuronal changes

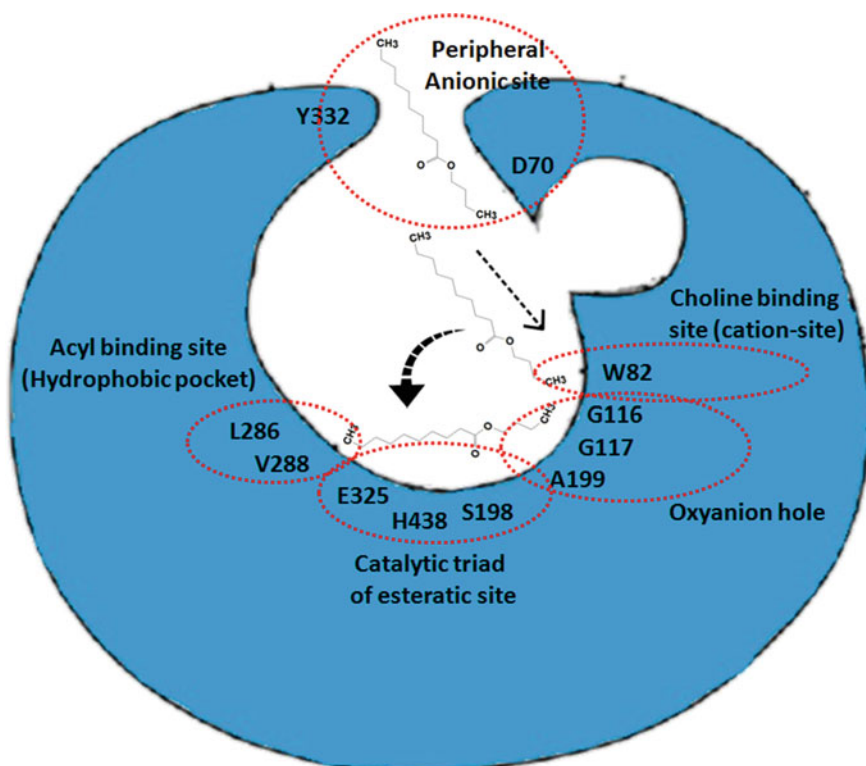


**Fig. 29** Amino acids from cholinesterase involved in the conversion of cocaine into ecgonine [73]

associated with chemical dependence [78]. Since the beginning of research on chemical dependence, the causative behavior of these has been seen as a consequence of alterations in the dopaminergic and GABAergic neurotransmission system, linked to the ability of psychoactive substances to interfere in the release and reuptake of dopamine in the neural circuit complex linked to the reward the brain, specifically the striatum [79]

In this understanding, studies are needed to better understand how each substance causes these dopaminergic changes—which may be implicated in greater direct or indirect release of dopamine, modulation of reuptake into synaptic clefts, availability of receptors, or combination of variables presented at different levels [80].

## 4.1 Cannabis

*Cannabis* consists mainly of three species: *Cannabis sativa*, *Cannabis indica* and *Cannabis ruderalis*. *C. sativa* presents serrated and green leaves, unisex flowers,

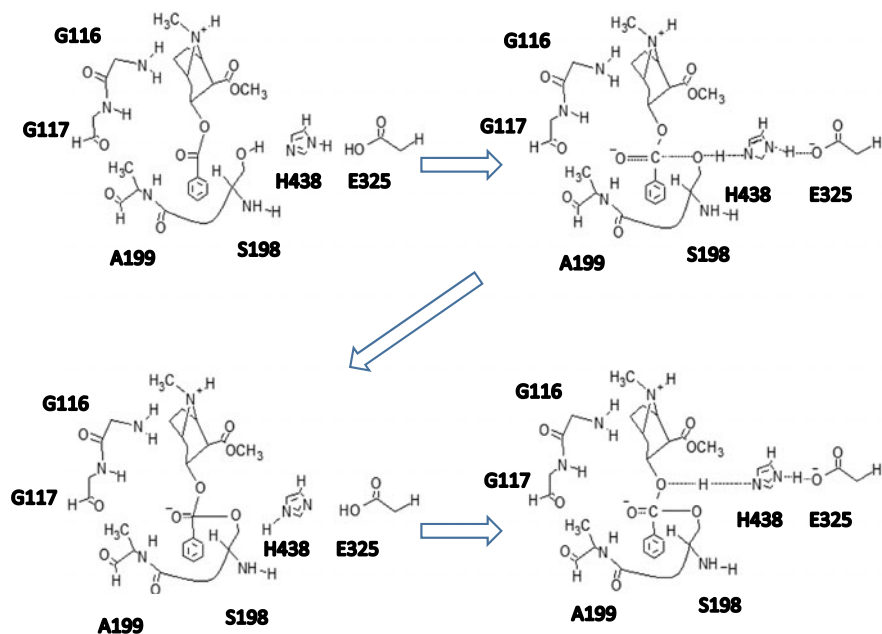


Fig. 30 Schematic representation of the pathway of BChE catalytic hydrolysis with cocaine [74]

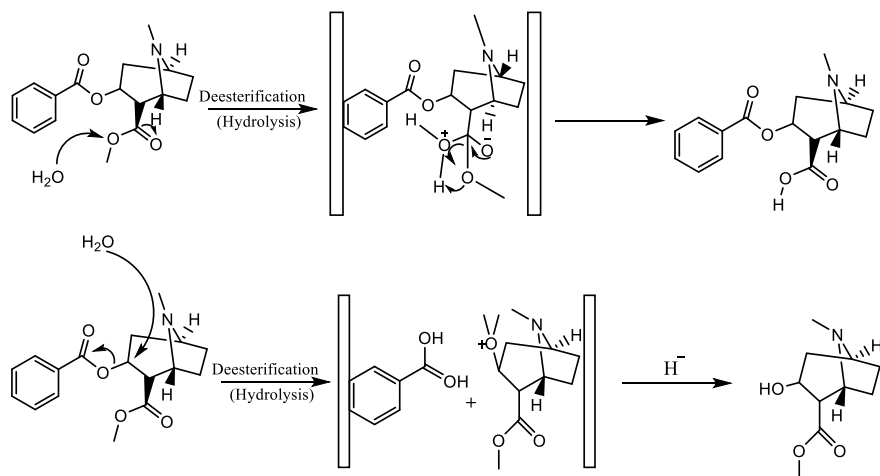
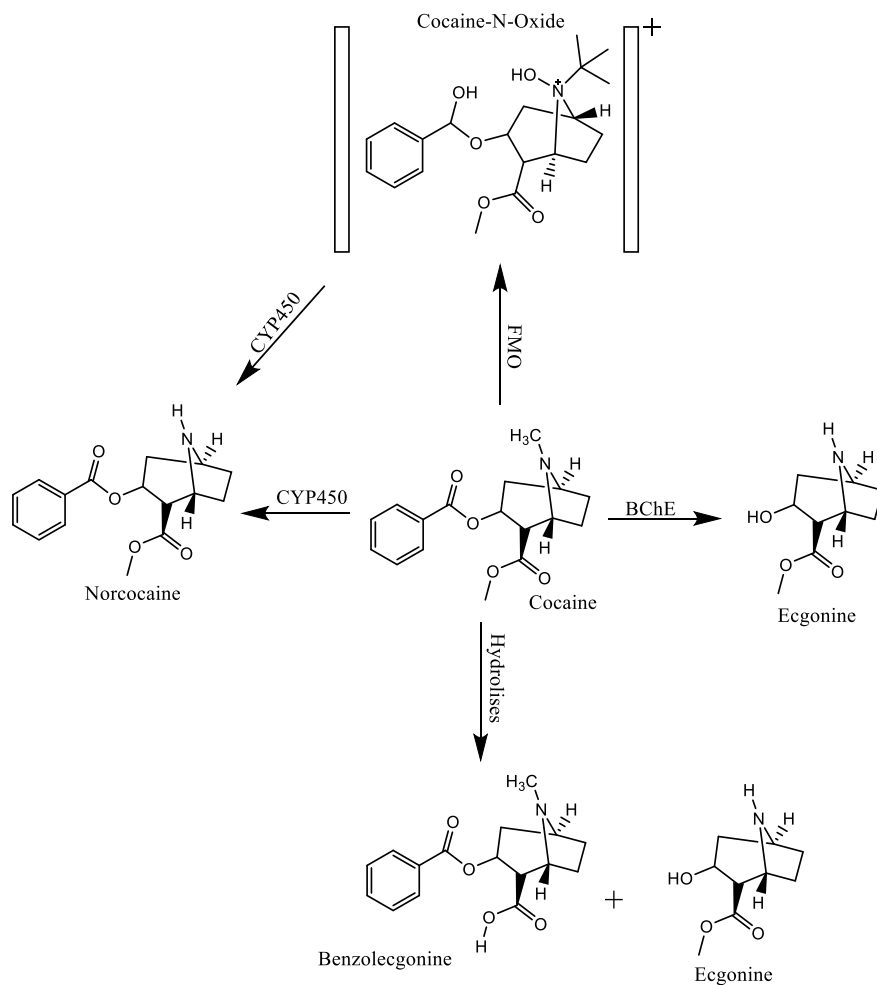


Fig. 31 Formation reaction of benzoylecgonine and ecgonine methylester



**Fig. 32** Pathways to obtaining Cocaine metabolites

granular and composed of fibers arranged on the stem [81]. The biosynthesis of *C. sativa* is concentrating on more than 600 chemical substances, including over 60 different cannabinoids that are recognized for their toxic effects and potential therapeutic [82].

The main component responsible for the psychoactive activity of the plant was identified in the 1960s, known as  $\Delta$  [9]-THC, (Fig. 1). In addition to  $\Delta$  [9]-THC, cannabinol (CBN), carboxylated THC, canabidivarin, Tetrahydrocannabivarin,  $\Delta$  [8]-THC, canabigerol (CBG), cannabichromene (CBC) and Canabidiol (CBD), the latter constituting about 40% of the active substances of the plant [83, 84].

Cannabinoid receptor CB1, identified as molecular targets of exogenous and endogenous cannabinoids, are present in different tissues, such as liver, skeletal

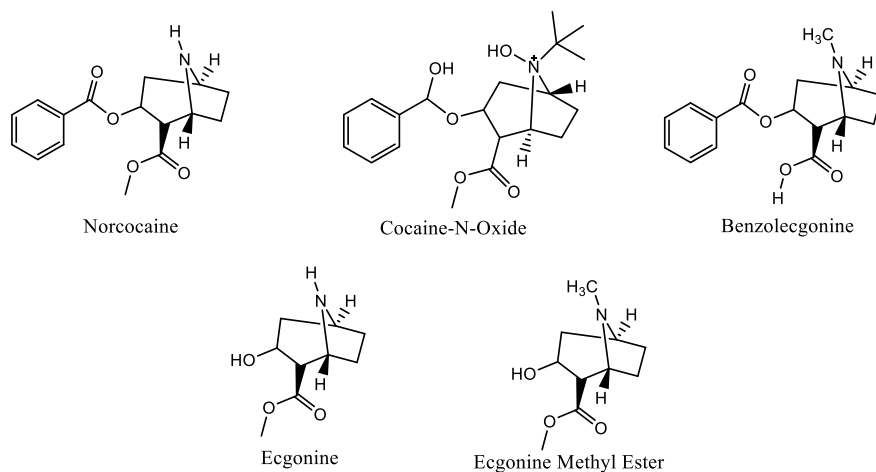


**Fig. 33** Cocaine metabolites

muscle, pancreas and fat [85]. These receptors are found in greater abundance in the ganglia of the base, in the hippocampus and in the cerebellum, mainly in the cerebral mitochondria [86]. CB2 cannabinoid receptors for many decades were thought to be distributed only in peripheral organs related to the immune system, but it is now known that they maintain a wide distribution in the CNS, mainly microglial cells, granular cells of the cerebellum, mast cells and in astrocytes humans [84, 87].

Cannabinoid receptor CB1, responsible for most of the psychotropic effects of cannabinoids, are present in areas associated with motor control, emotional response, learning and memory, targeted behaviors and goals, energy homeostasis and higher cognitive functions [88]. This is a membrane receptor coupled to a G protein that, when activated, inhibits the enzyme Adenylate Cyclase and the activity of the calcium channels, increasing the activity of the potassium channels and modulating the release of other neurotransmitters. In peripheral organs and tissues, cannabinoid receptor CB1 are expressed in lower density [89].

Interactions between  $\Delta$  [9]-THC and cannabinoid receptor CB1 produce acute physical effects such as: dry mouth, dilated conjunctival vessels and accelerated heart rate [90]. This chronic interaction can also cause chronic obstructive pulmonary disease (COPD) and lung cancer, as well as containing levels of benzopyrenes similar to those of tobacco, also reduce the body's immune defenses [91].

## 4.2 LSD

Hallucinogenic drugs are substances capable of inducing perceptual, affective and judgment sensorial changes [92]. There is evidence that the characteristic effects

of LSD and other hallucinogens, for example, psilocybin and mescaline, are mediated by the serotonergic system and the dorsal raphe nucleus acting as agonist or partial agonist connected to 5-HT<sub>2A</sub> receptors. At higher doses, LSD also modulates the ventral tegmentar area by stimulating D<sub>2</sub> dopaminergic receptors, the Trace Amine Associate 1 receptor (TAAR1), and the 5-HT<sub>2A</sub> receptor [35]. The interaction between serotonin-glutamate systems and serotonin-dopamine signaling mediate synaptic activity in specific regions of the brain, such as the frontal cortex, cause hallucinogenic action with distortion of reality and altered senses, perception, cognition, mood, and psychosis [93]. LSD also acts on the locus coeruleus, which receives sensory stimuli from the body and produces sympathomimetic mechanisms [94].

About one hour after ingestion LSD is fully absorbed and reaches a higher plasma concentration in 3 h. Distribution throughout the body easily affects the CNS including being absorbed by the placenta in pregnant women. The effects can last from 6 to 12 h, depending on the dose ingested [95].

Functional magnetic resonance imaging (fMRI) and magnetoencephalography (MEG) research have reported that the use of LSD causes increased blood flow from the visual cortex, increased whole brain functional integration (reduced modulatory organization) and decreased oscillatory power over a wide frequency range [96, 97]. Recent research conducted during rest conditions used complementary neuroimaging techniques that revealed marked changes in brain activity correlated with hallucinogenic effects of LSD such as: (a) increased cerebral blood flow from the visual cortex; (b) the alpha power of the diminished visual cortex; and (c) a functional connectivity profile of the greatly expanded primary visual cortex strongly correlated with visual hallucination classifications, implying that intrinsic brain activity exerts greater influence on visual processing in the brain [98].

### 4.3 Cocaine

The effect of cocaine (Fig. 24) occurs through the competitive inhibition of dopamine transporters, inhibiting the removal of this neurotransmitter from the synaptic and postsynaptic spaces, thus increasing the extracellular concentrations of dopamine [99]. This inhibition prevents the conduction of electrical impulses inside the nerve cells, avoiding the rapid increase of the cellular membrane permeability to the sodium ions during depolarization [100]. Thus, there is an increase in the amount of other neurotransmitters such as norepinephrine, dopamine, serotonin and acetylcholine, involved in motivation, pleasure, cognition, learning, memory, fine motor control and modulation of neuroendocrine signaling [101].

Recent research suggests that cocaine serves as a negative allosteric modulator, altering the function of the dopamine reuptake transporter (DAT), and reversing its transport direction in a co-transport that depends on the burning of dopamine in the synaptic cleft, functioning as an analog of an inverse agonist. Activation of the sympathetic nervous system produces an acute increase in blood pressure, tachycardia, a

predisposition for ventricular arrhythmias and seizures, in addition to mydriasis, hyperglycemia, and hyperthermia [102].

Dopamine is essential as a drug reward mediator [103]. In the short term, cocaine stimulates dopamine neurotransmission by blocking dopamine uptake at D1 and D2 receptors [104], but in the long term the nerve endings mainly in the region of the ventral and dorsal striatum are depleted of this neurotransmitter [105]. This depletion contributes to the dysphoria that develops during cocaine withdrawal and the subsequent desire for more consumption, and this mechanism is responsible for the development of tolerance and dependence patterns [106]. At higher and more regular doses, the involvement of the serotonergic system may occur, directly or indirectly, in mediation of the CNS toxicity [107].

#### 4.4 Amphetamines

Amphetamines (Fig. 19) are a diverse group of compounds that resemble monoamine neurotransmitter transporters. In addition, the structural differences between the various amphetamines highlight the specificity with the carriers [108]. However, amphetamines also bind to targets of non-monoamine transporters such as, for example, adrenergic receptors or traced amine receptors [109, 110].

Human striatum is functionally organized into subdivisions, such as mesolimbic and mesostriated, which have the function of producing pleasure in response to positive events in the individual's life, rewarding the learning process [111].

Amphetamine transporters coupled to the  $\text{Na}^+/\text{Cl}^{-99}$ , channels are responsible for the removal of the synaptic and postsynaptic spaces of dopamine and norepinephrine [112].

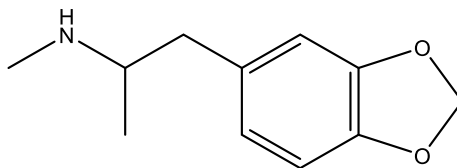
Amphetamine blocks dopamine reabsorption, thereby increasing the concentration of this neurotransmitter at synapses [113]. This fact causes inhibition of appetite [114], euphoria [115], insomnia, accelerated speech, feeling of power [116], irritability [117], impairment of judgment, perspiration, and chills [118]. The resulting mydriasis is harmful and dangerous, especially for drivers because of the increased sensitivity to the presence of car headlamps [48].

The use of amphetamine is also a reason for hypertension and tachycardia that can lead to acute myocardial infarction or cardiac arrhythmias whose concomitance is usually fatal [119]. Vascular and ischemic attacks, which cause decreased attention, concentration and memory problems may occur at the CNS level, in addition to hyperthermia which may lead to seizures [120, 121].

Ecstasy is the common name for MDMA (3,4-methylenedioxyamphetamine) (Fig. 34), a derivative of methamphetamine substituted on the aromatic ring [122]. This is a powerful CNS stimulant, which increases activity in various neurotransmitters and neurohormonal systems. This powerful neurobiological activation can be strongly euphoric, encompassing feelings of intimacy and closeness, and this state of humor is the main motivation of use by recreational users [123] Ecstasy causes dependence, although research suggests that this may be a less potent booster



**Fig. 34** Structural formula of 3,4 methylenedioxymethamphetamine



than other drugs. Although less frequent the phenomenon of tolerance in chronic users may occur [124, 125], being the main withdrawal symptoms such as increased appetite, tiredness and drowsiness, bad mood, paranoia and irritability [126].

## 5 Symptomatology of Withdrawal Syndrome

Abstinence syndrome is the set of signs and symptoms that generate feelings of discomfort and varying degrees of mental and physical suffering [127] that occurs when there is a voluntary or non-voluntary removal of drug use [128]. In general terms, the withdrawal syndrome presents symptoms such as dysphoria, insomnia, anxiety, irritability, nausea, agitation, tachycardia and hypertension. In correct treatment, the initial identification of the type of drug used is important because the complications differ according to the substance [129].

### 5.1 *Cannabis*

The effects of acute *Cannabis* intoxication appear after a few minutes of use with motor and cognitive deficits, such as short-term memory loss, impulsivity, and difficulty remembering events that occurred immediately after use [130]. There are also loss of activities that require coordination and attention, such as driving, as well as reducing the ability to solve problems [131, 132].

In recent years a steady increase in epidemiological studies on the use of *Cannabis* and psychosis (or schizophrenia) has suggested that chronic use of *Cannabis* probably precipitates or worsens schizophrenia in individuals susceptible to this pathology [133], and may trigger anxiety attacks, with panic and depression reactions [134]. Some examples of psychic effects are: depersonalization; altered state of consciousness; lethargy; depression; psychomotor excitation; hallucinations and illusions; panic attacks; somnolence; self-referral and paranoia; anxiety; prejudice of the judgment; irritability and concentration problems [132, 135].

The chronic use of marijuana is capable of causing cognitive impairment in the organization and integration of complex information, so that chronic users have lower verbal memory, reduced processing speed, and executive functioning [136]. Physically, chronic use may cause symptoms of chronic bronchitis induced by respiratory

infections [137] while immunohistopathological and epidemiological evidences suggest the influence of *Cannabis* on the risk of developing lung cancer [91, 138]; reduction in the number of spermatozoa [139], besides influencing the induction of genes linked to the onset of breast cancer [139]. Recent research suggests the influence of *Cannabis* in triggering intracranial arterial stenoses mainly in young users [140].

It is important to mention that the use of *Cannabis* during adolescence can cause lasting effects on brain functions that can compromise the performance of users in adult life in different sectors, whether personal or professional [141].

## 5.2 Cocaine

Cocaine abuse is related to many physical, psychiatric, and social problems [142]. Although some neurological complications may occur in association with cocaine use, there appears to be no consensus among researchers about cognitive deficits arising from drug use [143].

The chronic use of cocaine is related to the vasoactive effects of the substance. There is evidence that abnormalities of cerebral blood flow frequently occur in users even in the absence of evidence of neurological symptoms [144]. Multiple episodes of substance abuse produce a cumulative effect and there is an increased incidence of stroke even in relatively young individuals, so it is suggested that cocaine use should be classified as a risk factor for cardiovascular and cerebrovascular diseases [145].

Among the classic physiological responses to cocaine use are increased blood pressure, heart and respiratory rates, body temperature, pupil dilation, high alertness and increased motor activity [146]. There are numerous and serious cardiovascular consequences for cocaine users with exclusive mechanisms of cardiotoxicity that include sympathomimetic effects, sodium and potassium channel blockade, oxidative stress, mitochondrial damage and consequent rupture of the excitation–contraction coupling [64], in addition to hypertension, tachycardia, seizures and persecutory delirium, characterized by severe cardiopulmonary dysfunction, hyperthermia and acute neurological alterations that frequently lead the user to death [147].

Some cases, probably caused by lack of dopaminergic control, extreme psychomotor agitation, hyperthermia, aggressiveness and hostility, have been described after cocaine use and require intensive care [148].

## 5.3 Amphetamines

Amphetamines activate the reward system of the brain producing highly reinforcing effects, which can lead to abuse and dependence. The recreational use of these lipophilic compounds generates acute and chronic effects through the release of norepinephrine, mainly in the lateral hypothalamic area (LHA) [149], thus activating parts

of the sympathetic nervous system and also decreasing the gastrointestinal activity with the consequent inhibition of appetite [150, 151]. Amphetamines and derivatives also cause chills, a climate of confidence and presumption, mydriasis, xerostomia, wheezing, frantic pulsation, hyperexcitation, feeling of power and euphoria [58, 152]. Consequently the body is agitated with high energy release and increased sexual desire, also occurring the feeling of well-being, joy and reduced fatigue [153].

Some amphetamines are able to act on the serotonergic system, increasing the release of the neurotransmitter at the synapse, responsible for the hallucinogenic effects, so that in removing the drug this system increases anxiety and reduces the ability to cope with stress, a fact that contributes to relapse of use [154].

The psychiatric impairment associated with the use of amphetamines may be cognitive, intellectual or affective [155]. These consequences are correlated with the duration of use as well as the amounts used. Memory, language and attention deficits are also reported among users [156]. Neurological failure may persist for 9 months or more after cessation of amphetamine use, but recovery in attention activity and improvement in cognitive functioning are possible with sustained abstinence [153].

About 40% of chronic users, in addition to developing the phenomenon of tolerance, may develop a toxic reaction, known as “Amphetamine Psychosis” [157] characterized by symptoms such as agitation, irritability, insomnia, hallucinations and delirium. This may require a psychiatric hospitalization because this problem can lead the user to death [158].

Prolonged or intense use of amphetamines may trigger an abstinence syndrome characterized by a sudden change in dysphoric disorder, decreased libido, fatigue, increased appetite, deceleration and sleep disturbances, or accelerated psychomotor activity [159]. The severity of these symptoms is related to the duration and intensity of drug use and symptoms last up to 3 weeks [160, 161].

## 5.4 LSD

The mental changes produced by LSD are variable and abnormal (although the sensory changes resulting from the use are not relevant), however, some consequences are considered terror and panic. At low doses it causes hallucinations, delusions, altered perception of time and space, mental confusion, memory lapses and generalized distortion [162], similar to schizophrenia [163], in addition to undesirable physical effects related to autonomic disorders such as nausea, increased blood pressure and frequency heart failure, body weakness, drowsiness, and increased body temperature [164].

Psychic effects vary depending on the user's emotional state, context, quality and quantity of the product, ranging from extremely pleasant to very unpleasant [165]. Illusions, auditory and visual hallucinations, great sensory sensitivity with the glimpse of brighter colors and perception of imperceptible sounds, synesthesia, mystical experiences, feelings of well-being, ecstatic experiences, and euphoria are

the most common effects [166]. The less common use of intranasal LSD can cause coma, hyperthermia, vomiting, mild gastric bleeding, and respiratory problems [167].

## 6 Pharmacological Treatment for Withdrawal Syndrome

Drug damage can be acute, leading to intoxication or sudden changes called “overdose” and chronic, producing longer lasting changes, such as chemical dependency, and even irreversible changes [168].

One of the first reports on pharmacological treatment for chemical dependence and symptoms related to withdrawal syndrome was carried out by Sigmund Freud in his book *Über Coca*, where he described the use of cocaine to treat psychic disorders and dependence on morphine [169]. In the following months, Freud witnessed the “deep despair” of cocaine-treated patients who had symptoms such as fainting, convulsions, severe insomnia, and unusual patterns of behavior [170]. At that time, delirium tremens were reported—a state of temporary confusion leading to dangerous changes in the regulation of circulation and breathing, leading to the risk of heart attack, stroke or death [171].

The symptoms of cocaine withdrawal are eminently psychic, with depressive and anxious disorders being the most common. They usually appear more intense in the first seven days and appear less intense when the patient is in protected environments [172]. Currently, cocaine users with agitation and withdrawal syndrome can be treated with benzodiazepine [173], GABAergic agonists [174], and antipsychotics or with the combination of drugs [175]. The use of these drugs intramuscular (IM) or intravenous (IV) is recommended if the patient has intense psychomotor agitation and heteroaggressivity and should not accept oral medications [176].

More recently, disulfiram (a substance well known in the treatment of alcohol dependence) [177] and modafinil are used to control withdrawal symptoms in stabilizing clinical and psychiatric conditions resulting from sympathomimetic and neural dysregulation caused by cocaine [178]. Disulfiram, at a dose of 250–500 mg daily, acts in the dopaminergic system, blocking the enzymes D $\beta$ H [179], MAO inhibits the conversion of dopamine to noradrenaline and thus causing a reduction of dopamine in the nucleus accumbens, an integral part of the reward system [180]. Studies with selective D $\beta$ H inhibitors are being conducted for use in minimizing the cardiovascular effects produced by cocaine [181, 182].

Modafinil blocks the reuptake of dopamine and noradrenalin, increasing the concentration in the brain, and increases the activity of the glutamate system, which is generally deficient due to chronic use of cocaine [183]. The dose used is 200 to 400 mg per day, although it does not offer statistically significant benefits, demonstrates the tendency of maintenance in the state of abstinence [184].

Cannabinoids are used as therapeutic agents against nausea and vomiting in terminal patients with cancer and AIDS. *Cannabis* decreases the intensity of spasms and tremors in the case of multiple sclerosis and epilepsy [185]. The main problem

is that chronic use can cause serious side effects on cognitive functions, coordination, learning disabilities and impairment of memory, dependence, and induction of suicide attempts [186].

Research is advancing in the search for pharmacological approaches in *Cannabis* use disorders, obtaining more substantial data on the clinical efficacy of any specific drug to be used in the treatment of chronic users of the plant [187]. Bupropione, a noradrenaline and dopamine reuptake inhibitor, partial serotonin 5HT receptor agonists such as buspirone, are being studied but have reduced effects on *Cannabis* removal [188]. The use of cannabinoid receptor CB1 agonists seems to be the most promising, such as Dronabinol, which is associated with lofexedine,  $\alpha 2$  adrenergic agonist [189]. Naltrexone, an opioid receptor antagonist, may moderate effects and reduce self-administration, whereas cannabinoid receptor CB1 antagonist, such as Rimonabant, has a small reduction in use but causes considerable side effects to psychic changes [190]. In the use of *Cannabis* derivatives, for example, nabiximol showed a reduction in most of the symptoms but was not effective in the long term of abstinence [191].

Initially amphetamines were used for narcolepsy [192] and are currently used for the treatment of Attention Deficit Hyperactivity Disorder (ADHD) in children and restricted obesity [193, 194] with its main mechanism of action being the blockade of neurotransmitter transporters that mediate the reuptake of monoamines potentiating dopaminergic, adrenergic and serotonergic neurotransmission [195]. The first step in treating amphetamine dependence is detoxification that aims to lower blood levels of the drug, but requires prolonged drug treatment. The main symptoms presented at this stage are anxiety and agitation, energy reduction and depressive mood, so in these cases benzodiazepines such as diazepam 5 mg are used orally and neuroleptics such as haloperidol 2 to 5 mg, oral or injectable [196]. It is very important to mention that psychosocial counseling is a factor that should accompany treatment from the beginning of detoxification [197].

LSD has analgesic effects in patients with terminal cancer [198], mainly with improvement of mood and reduction of anxiety [199]. In the mid-last century, LSD-based drugs indicated mental relaxation, anxiety in psychotic nature studies and treatment of alcoholism, with 100 ml ampoules of 100  $\mu$ g, orally or subcutaneously / intravenously. These were allowed and made available for free to psychiatric clinics, however, the abuse of products prompted manufacturers to remove supplies of medicines [150]. LSD acts on several neurotransmitters, but action on serotonin seems to be the most important, due to the clinical presentation of delusions and hallucinations [200]. Benzodiazepine medicinal products such as diazepam 10 mg orally or midazolam 15 mg intramuscularly may be used to control the agitation and symptoms of schizophrenia caused by drug withdrawal [201]. Research advances in the use of isoxazol-9 during the removal of methamphetamine, since this molecule presents preliminary results that contribute directly inhibiting the search behavior of the drug [202].

## 7 Conclusion

This review concludes that drugs, in addition to being included in humanity from the earliest stages, are also present in society, following their own scientific evolution. With the development of new synthetic routes, the appearance of new drugs is not a rare occurrence, which exposes a considerable part of society to chemical dependence. In general, the treatments developed currently have little efficacy and act to combat the symptoms triggered by the withdrawal syndrome in users intensely dependent on *Cannabis*, cocaine, amphetamines, and LSD. Therefore, it is concluded that it is necessary to develop drugs that act selectively on biological targets involved in the process of chemical dependency, as well as those directly involved in the onset of withdrawal symptoms initiated by each drug of abuse.

**Acknowledgements** We acknowledge support from Conselho Nacional de Desenvolvimento Científico e Tecnológico (Brazil) and Coordenação de Aperfeiçoamento de Pessoal de Nível Superior (Capes).

**Conflict of Interest** *The authors declare no conflict of interest.*

## References

1. Ree, E.V.: Drugs, the democratic civilising process and the consumer society. *Int. J. Drug Policy* **13**, 349–353 (2002)
2. Caddy, B.: *Drugs of Abuse*. Science. Pharmaceutical Press, pp. 119–119 (2003). [https://doi.org/10.1016/S1355-0306\(03\)71753-5](https://doi.org/10.1016/S1355-0306(03)71753-5).
3. Degenhardt, L., Hall, W.: Extent of illicit drug use and dependence, and their contribution to the global burden of disease. *Lancet* **379**(9810), 55–70 (2012). [https://doi.org/10.1016/S0140-6736\(11\)61138-0](https://doi.org/10.1016/S0140-6736(11)61138-0)
4. Nutt, D.J., Lingford-Hughes, A., Erritzoe, D., Stokes, P.R.A.: The dopamine theory of addiction: 40 years of highs and lows. *Nat. Rev. Neurosci.* **16**(5), 305–312 (2015). <https://doi.org/10.1038/nrn3939>
5. World Health Organization (WHO): Neurociências: consumo e dependência de substâncias psicoativas RESUMO Organizaçã o Mundial da Saú de Genebra
6. Walker, D.M., Nestler, E.J.: Neuroepigenetics and addiction. In: *Handbook of Clinical Neurology*; Elsevier, vol. 148, pp. 747–765 (2018). <https://doi.org/10.1016/B978-0-444-64076-5.00048-X>
7. Degenhardt, L., Chiu, W.T., Sampson, N., Kessler, R.C., Anthony, J.C., Angermeyer, M., Bruffaerts, R., De Girolamo, G., Gureje, O., Huang, Y., et al.: Toward a global view of alcohol, tobacco, cannabis, and cocaine use: findings from the WHO World Mental Health Surveys. *PLoS Med.* **5**(7), 1053–1067 (2008). <https://doi.org/10.1371/journal.pmed.0050141>
8. Clarke, R.C., Merlin, M.D.: *Cannabis: Evolution and Ethnobotany*, vol. 53 (2013). <https://doi.org/10.1525/j.ctt3fh2f8>
9. Datwyler, S.L., Weiblen, G.D.: Genetic variation in hemp and marijuana (*Cannabis Sativa* L.) according to amplified fragment length polymorphisms. *J. Forensic Sci.* **51**(2), 371–375 (2006). <https://doi.org/10.1111/j.1556-4029.2006.00061.x>
10. Di Forti, M., Murray, R.M.: Cannabis, skunk and spice: the evolving risk of psychosis. *Schizophr. Res.* **153**, S31 (2014). [https://doi.org/10.1016/S0920-9964\(14\)70104-5](https://doi.org/10.1016/S0920-9964(14)70104-5)

11. Mallipedi, S., Janero, D.R., Zvonok, N., Makriyannis, A.: Functional selectivity at G-protein coupled receptors: advancing cannabinoid receptors as drug targets. *Biochem. Pharmacol.*; Elsevier March 15, pp. 1–11 (2017). <https://doi.org/10.1016/j.bcp.2016.11.014>
12. Pertwee, R.G.: Endocannabinoids and their pharmacological actions. In: *Endocannabinoids*; Springer, Cham, pp. 1–37 (2015). [https://doi.org/10.1007/978-3-319-20825-1\\_1](https://doi.org/10.1007/978-3-319-20825-1_1)
13. McCorvy, J.D., Roth, B.L.: Structure and function of serotonin G protein-coupled receptors. *Pharmacol. Ther.* **150**, 129–142 (2015). <https://doi.org/10.1016/j.pharmthera.2015.01.009>
14. Cawston, E.E., Connor, M., Di Marzo, V., Silvestri, R., Glass, M.: Distinct temporal fingerprint for cyclic adenosine monophosphate (cAMP) signaling of indole-2-carboxamides as allosteric modulators of the cannabinoid receptors. *J. Med. Chem.* **58**(15), 5979–5988 (2015). <https://doi.org/10.1021/acs.jmedchem.5b00579>
15. Hu, S.S.J., Mackie, K.: Distribution of the endocannabinoid system in the central nervous system. In: *Endocannabinoids*; Springer, Cham, pp. 59–93 (2015). [https://doi.org/10.1007/978-3-319-20825-1\\_3](https://doi.org/10.1007/978-3-319-20825-1_3)
16. Maccarrone, M., Bab, I., Bfró, T., Cabral, G.A., Dey, S.K., Di Marzo, V., Konje, J.C., Kunos, G., Mechoulam, R., Pacher, P., et al.: Endocannabinoid signaling at the periphery: 50 years after THC. *Trends Pharmacol. Sci.* **36**(5), 277–296 (2015). <https://doi.org/10.1016/j.tips.2015.02.008>
17. Grotenhermen, F.: Clinical pharmacokinetics of cannabinoids. *J. Cannabis Ther.* **3**(1), 3–51 (2003). [https://doi.org/10.1300/J175v03n01\\_02](https://doi.org/10.1300/J175v03n01_02)
18. Angeli, I., Casati, S., Ravelli, A., Minoli, M., Orioli, M.: A novel single-step GC–MS/MS method for cannabinoids and 11-OH-THC metabolite analysis in hair. *J. Pharm. Biomed. Anal.* **155**, 1–6 (2018). <https://doi.org/10.1016/j.jpba.2018.03.031>
19. Matsunaga, T., Iwawaki, Y., Watanabe, K., Yamamoto, I., Kageyama, T., Yoshimura, H.: Metabolism of  $\Delta^9$ -tetrahydrocannabinol by cytochrome P450 isozymes purified from hepatic microsomes of monkeys. *Life Sci.* **56**(23–24), 2089–2095 (1995). [https://doi.org/10.1016/0024-3205\(95\)00193-A](https://doi.org/10.1016/0024-3205(95)00193-A)
20. Kamali, F.: Introduction to drug metabolism (Third Edition). *B. J. Clin. Pharmacol.* **56**(3), 345–345 (2003). <https://doi.org/10.1046/j.1365-2125.2003.01855.x>
21. Elmes, M.W., Kaczocha, M., Berger, W.T., Leung, K.N., Ralph, B.P., Wang, L., Sweeney, J.M., Miyauchi, J.T., Tsirka, S.E., Ojima, I., et al.: Fatty acid-binding proteins (FABPs) are intracellular carriers for  $\Delta^9$ -tetrahydrocannabinol (THC) and cannabidiol (CBD). *J. Biol. Chem.* **290**(14), 8711–8721 (2015). <https://doi.org/10.1074/jbc.M114.618447>
22. Meyer, A.H., Dybala-Defratyka, A., Alaimo, P.J., Geronimo, I., Sanchez, A.D., Cramer, C.J., Elsner, M.: Cytochrome P450-catalyzed dealkylation of atrazine by *Rhodococcus* sp. strain NI86/21 involves hydrogen atom transfer rather than single electron transfer. *Dalton Trans.* **43**(32), 12175–12186 (2014). <https://doi.org/10.1039/c4dt00891j>
23. Coon, M.J.: Enzyme ingenuity in biological oxidations: a trail leading to cytochrome P450. *J. Biol. Chem.* **277**(32), 28351–28363 (2002). <https://doi.org/10.1074/jbc.r200015200>
24. Burstein, S.H.: The cannabinoid acids: nonpsychoactive derivatives with therapeutic potential. *Pharmacol. Ther.* **82**(1), 87–96 (1999). [https://doi.org/10.1016/S0163-7258\(98\)00069-2](https://doi.org/10.1016/S0163-7258(98)00069-2)
25. Akhtar, M.T., Shaari, K., Verpoorte, R.: Biotransformation of tetrahydrocannabinol. *Phytochem. Rev.* **15**(5), 921–934 (2016). <https://doi.org/10.1007/s11101-015-9438-9>
26. Sharma, P., Murthy, P., Bharath, M.M.S.: Chemistry, metabolism, and toxicology of cannabis: clinical implications. *Iran. J. Psychiatr.* **7**(4), 149–156 (2012)
27. Nichols, D.E.: Dark classics in chemical neuroscience: lysergic acid diethylamide (LSD). *ACS Chem. Neurosci.* **9**(10), 2331–2343 (2018). <https://doi.org/10.1021/acchemneuro.8b00043>
28. Gicquel, T., Lepage, S., Morel, I. Histoire Du LSD. De l’ergot de Seigle à l’utilisation Thérapeutique. *La Presse Médicale* **44**(7–8), 832–836 (2015). <https://doi.org/10.1016/j.lpm.2015.04.033>
29. Liester, M.B.: A review of lysergic acid diethylamide (LSD) in the treatment of addictions: historical perspectives and future prospects. *Curr. Drug Abuse Rev.* **7**(3), 146–156 (2014). <https://doi.org/10.2174/1874473708666150107120522>

30. Wang, R.Z., Vashistha, V., Kaur, S., Houchens, N.W.: Serotonin syndrome: preventing, recognizing, and treating it. *Cleveland Clin. J. Med.* **83**(11), 810–817 (2016). <https://doi.org/10.3949/ccjm.83a.15129>
31. Werneke, U., Jamshidi, F., Taylor, D.M., Ott, M.: Conundrums in neurology: diagnosing serotonin syndrome - a meta-analysis of cases. *BMC Neurol.* **16**(1), 97 (2016). <https://doi.org/10.1186/s12883-016-0616-1>
32. López-Giménez, J.F., González-Maeso, J. Hallucinogens and serotonin 5-HT<sub>2A</sub> receptor-mediated signaling pathways. In: *Current Topics in Behavioral Neurosciences*, vol. 36, pp. 45–73. Springer, Berlin, Heidelberg (2018). [https://doi.org/10.1007/7854\\_2017\\_478](https://doi.org/10.1007/7854_2017_478)
33. Halberstadt, A.L. Hallucinogenic drugs: a new study answers old questions about LSD. *Curr. Biol.* Cell Press February 20, R156–R158 (2017). <https://doi.org/10.1016/j.cub.2016.12.058>
34. De Gregorio, D., Posa, L., Ochoa-Sanchez, R., McLaughlin, R., Maione, S., Comai, S., Gobbi, G.: The hallucinogen d-lysergic diethylamide (LSD) decreases dopamine firing activity through 5-HT<sub>1A</sub>, D<sub>2</sub> and TAAR1 receptors. *Pharmacol. Res.* **113**, 81–91 (2016). <https://doi.org/10.1016/j.phrs.2016.08.022>
35. De Gregorio, D., Comai, S., Posa, L., Gobbi, G.: D-lysergic acid diethylamide (LSD) as a model of psychosis: mechanism of action and pharmacology. *Int. J. Mol. Sci. Multidisciplinary Digital Publishing Institute* November 23, 2016, (1953). <https://doi.org/10.3390/ijm17111953>
36. Buchborn, T., Grecksch, G., Dieterich, D.C., Höllt, V.: Tolerance to lysergic acid diethylamide: overview, correlates, and clinical implications. In: *Neuropathology of Drug Addictions and Substance Misuse*, vol. 2, pp. 846–858. Academic Press (2016). <https://doi.org/10.1016/B978-0-12-800212-4.00079-0>
37. Coleman, R.G., Carchia, M., Sterling, T., Irwin, J.J., Shoichet, B.K.: Ligand pose and orientational sampling in molecular docking. *PLoS ONE* **8**(10), e75992 (2013). <https://doi.org/10.1371/journal.pone.0075992>
38. Nichols, D.E. Chemistry and structure–activity relationships of psychedelics. In: *Current Topics in Behavioral Neurosciences*, vol. 36, pp. 1–43. Springer, Berlin, Heidelberg (2018). [https://doi.org/10.1007/7854\\_2017\\_475](https://doi.org/10.1007/7854_2017_475)
39. Wacker, D., Wang, S., McCorvy, J.D., Betz, R.M., Venkatakrishnan, A.J., Levit, A., Lansu, K., Schools, Z.L., Che, T., Nichols, D.E., et al.: Crystal structure of an LSD-bound human serotonin receptor. *Cell* **168**(3), 377–389.e12 (2017). <https://doi.org/10.1016/j.cell.2016.12.033>
40. Klette, K.L., Anderson, C.J., Poch, G.K., Nimrod, A.C., ElSohly, M.A.: Metabolism of lysergic acid diethylamide (LSD) to 2-oxo-3-hydroxy LSD (O-H-LSD) in human liver microsomes and cryopreserved human hepatocytes. *J. Anal. Toxicol.* **24**(7), 550–556 (2000). <https://doi.org/10.1093/jat/24.7.550>
41. Gomes, M.M., Dörr, F.A., Catalani, L.H., Campa, A.: Oxidation of lysergic acid diethylamide (LSD) by peroxidases: a new metabolic pathway. *Forensic Toxicol.* **30**(2), 87–97 (2012). <https://doi.org/10.1007/s11419-011-0131-4>
42. Gomes, M.M., Dörr, F.A., Catalani, L.H., Campa, A.: Oxidation of lysergic acid diethylamide (LSD) by peroxidases: a new metabolic pathway. *Forensic Toxicol.* **30**(2), 87–97 (2012). <https://doi.org/10.1007/s11419-011-0131-4>
43. Strang, J., Babor, T., Caulkins, J., Fischer, B., Foxcroft, D., Humphreys, K.: Drug policy and the public good: evidence for effective interventions. *Lancet* **379**(9810), 71–83 (2012). [https://doi.org/10.1016/S0140-6736\(11\)61674-7](https://doi.org/10.1016/S0140-6736(11)61674-7)
44. Connors, N.J., Hoffman, R.S.: Amphetamines and derivatives. In: *Critical Care Toxicology*, pp. 1–26. Springer International Publishing, Cham (2016). [https://doi.org/10.1007/978-3-319-20790-2\\_4-1](https://doi.org/10.1007/978-3-319-20790-2_4-1)
45. Sitte, H.H., Freissmuth, M.: Amphetamines, new psychoactive drugs and the monoamine transporter cycle. In: *Trends in Pharmacological Sciences*, pp. 41–50. Elsevier Current Trends January 1, 2015 (2015). <https://doi.org/10.1016/j.tips.2014.11.006>
46. Aoun, E.G., Christopher, P.P., Ingraham, J.W.: Emerging drugs of abuse: clinical and legal considerations. *Rhode Island Med. J.* (2013) **97**(6), 41–45 (2014)



47. Geisner, I.M., Huh, D., Crouse, J.M., Lostutter, T.W., Kilmer, J., Larimer, M.E.: Exploring the relationship between stimulant use and gambling in college students. *J. Gambl. Stud.* **32**(3), 1001–1016 (2016). <https://doi.org/10.1007/s10899-015-9586-2>
48. Wille, S.M.R., Richeval, C., Nachon-Phanithavong, M., Gaulier, J.M., Di Fazio, V., Humbert, L., Samyn, N., Allorge, D.: Prevalence of new psychoactive substances and prescription drugs in the Belgian driving under the influence of drugs population. *Drug Test. Anal.* (2017). <https://doi.org/10.1002/dta.2232>
49. Leslie, E.M., Smirnov, A., Cherney, A., Wells, H., Legosz, M., Kemp, R., Najman, J.M.: Simultaneous use of alcohol with methamphetamine but not ecstasy linked with aggression among young adult stimulant users. *Addict. Behav.* **70**, 27–34 (2017). <https://doi.org/10.1016/j.addbeh.2017.01.036>
50. Karinen, R., Høiseth, G.: A literature review of blood concentrations of new psychoactive substances classified as phenethylamines, aminoindanes, arylalkylamines, arylcyclohexylamines, and indolalkylamines. *Forensic Sci. Int.* **276**, 120–125 (2017). <https://doi.org/10.1016/j.forsciint.2017.02.024>
51. Taylor, M.F., Marquis, R., Coall, D., Wilkinson, C.: Substance misuse-related parental child maltreatment: intergenerational implications for grandparents, parents, and grandchildren relationships. *J. Drug Issues* **47**(2), 241–260 (2017). <https://doi.org/10.1177/0022042616683670>
52. Pei, Y., Asif-Malik, A., Canales, J.J.: Trace amines and the trace amine-associated receptor 1: pharmacology, neurochemistry, and clinical implications. *Front. Neurosci.*, *Frontiers April* **5**, 2016 148 (2016). <https://doi.org/10.3389/fnins.2016.00148>
53. Spencer, R.C., Devilbiss, D.M., Berridge, C.W. The cognition-enhancing effects of psychostimulants involve direct action in the prefrontal cortex. *Biol. Psychiatry*. Elsevier June 1, 2015, 940–950 (2015). <https://doi.org/10.1016/j.biopsych.2014.09.013>
54. Cameron, K.N., Solis, E., Ruchala, I., De Felice, L.J., Eltit, J.M.: Amphetamine activates calcium channels through dopamine transporter-mediated depolarization. *Cell Calcium* **58**(5), 457–466 (2015). <https://doi.org/10.1016/j.ceca.2015.06.013>
55. Sulzer, D., Maidment, N.T., Rayport, S.: Amphetamine and other weak bases act to promote reverse transport of dopamine in ventral midbrain neurons. *J. Neurochem.* 527–535 (1993). <https://doi.org/10.1111/j.1471-4159.1993.tb03181.x>
56. Haile, C.N., Kosten, T.R., Kosten, T.A.: Pharmacogenetic treatments for drug addiction: cocaine, amphetamine and methamphetamine. *Am. J. Drug Alcohol Abuse* **35**(3), 161–177 (2009). <https://doi.org/10.1080/00952990902825447>
57. Wang, K.H., Penmatsa, A., Gouaux, E.: Neurotransmitter and psychostimulant recognition by the dopamine transporter. *Nature* **521**(7552), 322–327 (2015). <https://doi.org/10.1038/nature14431>
58. Welter-Luededeke, J., Maurer, H.H.: New psychoactive substances: chemistry, pharmacology, metabolism, and detectability of amphetamine derivatives with modified ring systems. *Ther. Drug Monit.* **38**(1), 4–11 (2015). <https://doi.org/10.1097/FTD.0000000000000240>
59. Feio-Azevedo, R., Costa, V.M., Ferreira, L.P., Branco, P.S., Pereira, F.C., de Lourdes Bastos, M., Carvalho, F., Capela, J.P.: Amphetamine and its metabolite 4-hydroxyamphetamine neurotoxicity in differentiated SH-SY5Y neurons. *Toxicol. Lett.* **229**(229), S241 (2014). <https://doi.org/10.1016/j.toxlet.2014.06.805>
60. Badenhorst, C.P.S., van der Sluis, R., Erasmus, E., van Dijk, A.A.: Glycine conjugation: importance in metabolism, the role of glycine N-acyltransferase, and factors that influence interindividual variation. *Expert Opin. Drug Metab. Toxicol.* **9**(9), 1139–1153 (2013). <https://doi.org/10.1517/17425255.2013.796929>
61. Kaufman, S., Friedman, S.: Dopamine- $\beta$ -hydroxylase. *Pharmacol. Rev.* **17**(2) (1965)
62. Casale, J.F., Mallette, J.R., Jones, L.M.: Chemosystematic identification of fifteen new cocaine-bearing erythroxyllum cultigens grown in Colombia for illicit cocaine production. *Forensic Sci. Int.* **237**, 30–39 (2014). <https://doi.org/10.1016/j.forsciint.2014.01.012>
63. Oliveira, L.F.M.: A Cocaína e Sua Adulteração. *Revista Intertox de Toxicologia, Risco Ambiental e Sociedade* **6**(1), 15–28 (2013)

64. Stankowski, R.V., Kloner, R.A., Rezkalla, S.H.: Cardiovascular consequences of cocaine use. *Trends Cardiovasc. Med.*; Elsevier August 1, 2015; 517–526 (2015). <https://doi.org/10.1016/j.tcm.2014.12.013>
65. Koob, G.F., Volkow, N.D.: Neurobiology of addiction: a neurocircuitry analysis. *Lancet Psychiatry*; Elsevier August 1, 2016; 760–773 (2016). [https://doi.org/10.1016/S2215-0366\(16\)00104-8](https://doi.org/10.1016/S2215-0366(16)00104-8)
66. Simmler, L.D., Anacker, A.M.J., Levin, M.H., Vaswani, N.M., Gresch, P.J., Nackenoff, A.G., Anastasio, N.C., Stutz, S.J., Cunningham, K.A., Wang, J., et al.: Blockade of the 5-HT transporter contributes to the behavioural, neuronal and molecular effects of cocaine. *Br. J. Pharmacol.* **174**(16), 2716–2738 (2017). <https://doi.org/10.1111/bph.13899>
67. Lizasoain, I., Moro, M.A., Lorenzo, P.: Cocaína: aspectos Farmacológicos. *Adicciones* 57–64 (2002). <https://doi.org/10.20882/adicciones.513>
68. Alves, B.E.P.; Carneiro, E.D.O.: *Drogas psicoestimulantes: uma abordagem toxicológica sobre Cocaína e metanfetamina*; Goiás (2013)
69. Hansen, S.B., Taylor, P.: Galanthamine and non-competitive inhibitor binding to ACh-binding protein: evidence for a binding site on non- $\alpha$ -subunit interfaces of heteromeric neuronal nicotinic receptors. *J. Mol. Biol.* **369**(4), 895–901 (2007). <https://doi.org/10.1016/j.jmb.2007.03.067>
70. Gambelungho, C., Rossi, R., Aroni, K., Gili, A., Bacci, M., Pascali, V., Fucci, N.: Norcocaine and cocaethylene distribution patterns in hair samples from light, moderate, and heavy cocaine users. *Drug Test. Anal.* **9**(2), 161–167 (2017). <https://doi.org/10.1002/dta.1903>
71. Ladona, M.G., Gonzalez, M.L., Rane, A., Peter, R.M., de la Torre, R.: Cocaine metabolism in human fetal and adult liver microsomes is related to cytochrome P450 3A expression. *Life Sci.* **68**(4), 431–443 (2000)
72. de Oliveira Silveira, G., Belitsky, Í.T., Loddi, S., Rodrigues de Oliveira, C.D., Zucoloto, A.D., Fruchtingarten, L.V.G., Yonamine, M.: Development of a method for the determination of cocaine, cocaethylene and norcocaine in human breast milk using liquid phase microextraction and gas chromatography-mass spectrometry. *Forensic Sci. Int.* **265**, 22–28 (2016). <https://doi.org/10.1016/j.forsciint.2016.01.007>
73. Ekim, Y.: Butyrylcholinesterase : Structure and Physiological Importance. *Turk. J. Biochem.* **28**(August), 54–61 (2003)
74. Zhan, C.G., Gao, D.: Catalytic mechanism and energy barriers for butyrylcholinesterase-catalyzed hydrolysis of cocaine. *Biophys. J.* **89**(6), 3863–3872 (2005). <https://doi.org/10.1529/biophysj.105.070276>
75. Carvalho, V.M., Da Matta Chasin, A.A., De Carvalho, D.G.: A study on the stability of anhydroecgonine methyl ester (crack biomarker), benzoylecgonine, and cocaine in human urine. *Revista de Psiquiatria Clinica* **35**(1), 17–20 (2008). <https://doi.org/10.1590/S0101-60832008000700005>
76. World Health Organization: Global status report on road safety 2015 (2015)
77. World Health Organization: The ICD-10 classification of mental and behavioural disorders. The ICD-10 classification of mental and behavioural disorders 86–95 (1992)
78. Koob, G.F., Volkow, N.D.: Neurobiology of addiction: a neurocircuitry analysis. *Lancet Psychiatry*; Elsevier August 1, 2016; 760–773 (2016). [https://doi.org/10.1016/S2215-0366\(16\)00104-8](https://doi.org/10.1016/S2215-0366(16)00104-8)
79. Volkow, N.D., Morales, M.: The brain on drugs: from reward to addiction. *Cell* 712–725 (2015). <https://doi.org/10.1016/j.cell.2015.07.046>
80. Miller, J.D., Wilcox, R.E.: Mechanisms of stimulant drug dependence. *J. Addict. Prev.* **5**(1), 1–6 (2017). <https://doi.org/10.13188/2330-2178.1000038>
81. Raman, V., Lata, H., Chandra, S., Khan, I.A., ElSohly, M.A.: Morpho-anatomy of marijuana (*Cannabis Sativa L.*). In: *Cannabis sativa L. - Botany and Biotechnology*, pp. 123–136. Springer International Publishing, Cham (2017). [https://doi.org/10.1007/978-3-319-54564-6\\_5](https://doi.org/10.1007/978-3-319-54564-6_5)
82. Shoeler, T., Bhattacharyya, S.: The effect of cannabis use on memory function: an update. *Subst. Abuse Rehabil.* **4**(January), 11–27 (2013). <https://doi.org/10.2147/SAR.S25869>

83. Gaoni, Y., Mechoulam, R.: Isolation, structure, and partial synthesis of an active constituent of hashish. *J. Am. Chem. Soc.* **86**, 1646–1647 (1964). <https://doi.org/10.1021/ja01062a046>
84. Howlett, A.C., Breivogel, C.S., Childers, S.R., Deadwyler, S.A., Hampson, R.E., Porrino, L.J.: Cannabinoid physiology and pharmacology: 30 years of progress. *Neuropharmacology* **47**, 345–358 (2004). <https://doi.org/10.1016/j.neuropharm.2004.07.030>
85. Hebert-Chatelain, E., Reguero, L., Puente, N., Lutz, B., Chaouloff, F., Rossignol, R., Piazza, P.-V., Benard, G., Grandes, P., Marsicano, G.: Cannabinoid control of brain bioenergetics: exploring the subcellular localization of the CB1 receptor. *Mol. Metab.* **3**(4), 495–504 (2014). <https://doi.org/10.1016/j.molmet.2014.03.007>
86. Zou, S., Kumar, U.: Cannabinoid receptors and the endocannabinoid system: signaling and function in the central nervous system. *Int. J. Mol. Sci.*; Multidisciplinary Digital Publishing Institute March 13, 2018; 833 (2018). <https://doi.org/10.3390/ijms19030833>
87. Onaivi, E.S., Ishiguro, H., Gong, J.-P., Patel, S., Perchuk, A., Meozzi, P.A., Myers, L., Mora, Z., Tagliaferro, P., Gardner, E., et al.: Discovery of the presence and functional expression of cannabinoid CB2 receptors in brain. *Ann. N. Y. Acad. Sci.* **1074**(1), 514–536 (2006). <https://doi.org/10.1196/annals.1369.052>
88. El Khoury, M.-A., Gorgievski, V., Moutsimilli, L., Giros, B., Tzavara, E.T.: Interactions between the cannabinoid and dopaminergic systems: evidence from animal studies. *Prog. Neuropsychopharmacol. Biol. Psychiatry* **38**(1), 36–50 (2012). <https://doi.org/10.1016/j.pnpbp.2011.12.005>
89. Demuth, D.G., Molleman, A.: Cannabinoid signalling. *Life Sci.* **78**(6), 549–563 (2006). <https://doi.org/10.1016/j.lfs.2005.05.055>
90. Marusich, J.A., Craft, R.M., Lefever, T.W., Wiley, J.L.: The impact of gonadal hormones on cannabinoid dependence. *Exp. Clin. Psychopharmacol.* **23**(4), 206–216 (2015). <https://doi.org/10.1037/pha0000027>
91. Tashkin, D.P.: Effects of marijuana smoking on the lung. *Ann. Am. Thorac. Soc.* **10**(3), 239–247 (2013). <https://doi.org/10.1513/AnnalsATS.201212-127FR>
92. Appendino, G., Minassi, A., Tagliatalata-Scafati, O.: Recreational drug discovery: natural products as lead structures for the synthesis of smart drugs. *Nat. Prod. Rep.* **31**(7), 880 (2014). <https://doi.org/10.1039/c4np00010b>
93. de Bartolomeis, A., Buonaguro, E.F., Iasevoli, F.: Serotonin-glutamate and serotonin-dopamine reciprocal interactions as putative molecular targets for novel antipsychotic treatments: from receptor heterodimers to postsynaptic scaffolding and effector proteins. *Psychopharmacology* **225**(1), 1–19 (2013). <https://doi.org/10.1007/s00213-012-2921-8>
94. Fiorella, D., Helsley, S., Lorrain, D.S., Rabin, R.A., Winter, J.C.: The role of the 5-HT<sub>2A</sub> and 5-HT<sub>2C</sub> receptors in the stimulus effects of hallucinogenic drugs III: the mechanistic basis for supersensitivity to the LSD stimulus following serotonin depletion. *Psychopharmacology* **121**(3), 364–372 (1995). <https://doi.org/10.1007/BF02246076>
95. Dolder, P.C., Schmid, Y., Haschke, M., Rentsch, K.M., Liechti, M.E.: Pharmacokinetics and concentration-effect relationship of oral LSD in humans. *Int. J. Neuropsychopharmacol.* **19**(1), pyv072 (2016). <https://doi.org/10.1093/ijnp/pyv072>
96. Tagliazucchi, E., Roseman, L., Kaelen, M., Orban, C., Muthukumaraswamy, S.D., Murphy, K., Laufs, H., Leech, R., McGonigle, J., Crossley, N., et al.: Increased global functional connectivity correlates with LSD-induced ego dissolution. *Curr. Biol.* **26**(8), 1043–1050 (2016). <https://doi.org/10.1016/j.cub.2016.02.010>
97. Carhart-Harris, R.L., Muthukumaraswamy, S., Roseman, L., Kaelen, M., Droog, W., Murphy, K., Tagliazucchi, E., Schenberg, E.E., Nest, T., Orban, C., et al.: Neural correlates of the LSD experience revealed by multimodal neuroimaging. *Proc. Natl. Acad. Sci. U.S.A.* **113**(17), 4853–4858 (2016). <https://doi.org/10.1073/pnas.1518377113>
98. Atasoy, S., Roseman, L., Kaelen, M., Kringelbach, M.L., Deco, G., Carhart-Harris, R.L.: Connectome-harmonic decomposition of human brain activity reveals dynamical repertoire re-organization under LSD. *Sci. Rep.* **7**(1) (2017). <https://doi.org/10.1038/s41598-017-17546-0>

99. Wang, K.H., Penmatsa, A., Gouaux, E.: Neurotransmitter and psychostimulant recognition by the dopamine transporter. *Nature* **521**(7552), 322–327 (2015). <https://doi.org/10.1038/nature14431>
100. Milnes, A., Wilson, S.: Local anesthetics. In: *Oral Sedation for Dental Procedures in Children*, pp. 57–63. Springer, Berlin, Heidelberg (2015). [https://doi.org/10.1007/978-3-662-46626-1\\_5](https://doi.org/10.1007/978-3-662-46626-1_5)
101. De Felice, L.J.: Monoamine transporters as ionotropic receptors. *Trends Neurosci.* **40**(4), 195–196 (2017). <https://doi.org/10.1016/j.tins.2017.02.003>
102. Rubinos, C., Ruland, S.: Neurologic complications in the intensive care unit. *Curr. Neurol. Neurosci. Rep.* (2016). <https://doi.org/10.1007/s11910-016-0651-8>
103. Ikemoto, S., Yang, C., Tan, A.: Basal ganglia circuit loops, dopamine and motivation: a review and enquiry. *Behav. Brain Res.*, September 1, 2015 17–31. <https://doi.org/10.1016/j.bbr.2015.04.018>
104. Xu, H., Das, S., Sturgill, M., Hodgkinson, C., Yuan, Q., Goldman, D., Grasing, K.: Extracellular dopamine, acetylcholine, and activation of dopamine D1 and D2 receptors after selective breeding for cocaine self-administration in rats. *Psychopharmacology* 1–13 (2017). <https://doi.org/10.1007/s00213-017-4640-7>
105. Willuhn, I., Burgeno, L.M., Groblewski, P.A., Phillips, P.E.M.: Excessive cocaine use results from decreased phasic dopamine signaling in the striatum. *Nat. Publ. Group* **17**(5), 704–709 (2014). <https://doi.org/10.1038/nn.3694>
106. Everitt, B.J.: Neural and psychological mechanisms underlying compulsive drug seeking habits and drug memories - indications for novel treatments of addiction. *Eur. J. Neurosci.* **40**(1), 2163–2182 (2014). <https://doi.org/10.1111/ejn.12644>
107. Howell, L.L., Cunningham, K.A.: Serotonin 5-HT<sub>2</sub> receptor interactions with dopamine function: implications for therapeutics in cocaine use disorder. *Pharmacol. Rev.* **67**(1), 176–197 (2015). <https://doi.org/10.1124/pr.114.009514>
108. Sulzer, D.: How addictive drugs disrupt presynaptic dopamine neurotransmission. *Neuron* **69**(4), 628–649 (2011). <https://doi.org/10.1016/j.neuron.2011.02.010>
109. Sulzer, D., Sonders, M.S., Poulsen, N.W., Galli, A.: Mechanisms of neurotransmitter release by amphetamines: a review. *Prog. Neurobiol.* **75**(6), 406–433 (2005). <https://doi.org/10.1016/j.pneurobio.2005.04.003>
110. Bunzow, J.R., Sonders, M.S., Arttamangkul, S., Harrison, L.M., Zhang, G.E., Quigley, D.I., Darland, T., Suchland, K.L., Pasumamula, S., Kennedy, J.L., Olson, S.B., et al.: Amphetamine, 3,4-methylenedioxymethamphetamine, lysergic acid diethylamide, and metabolites of the catecholamine neurotransmitters are agonists of a rat trace amine receptor. *Mol. Pharmacol.* **60**(6), 1181–1188 (2001). <https://doi.org/10.1124/mol.60.6.1181>
111. Feldman Barrett, L., Russel, J.A.: *The Psychological Construction of Emotion* (2014)
112. Vaughan, R.A., Foster, J.D.: Mechanisms of dopamine transporter regulation in normal and disease states. *Trends in Pharmacological Sciences*, pp. 489–496 (2013). <https://doi.org/10.1016/j.tips.2013.07.005>
113. Martinez, D., Slifstein, M., Broft, A., Mawlawi, O., Hwang, D.-R., Huang, Y., Cooper, T., Kegeles, L., Zarahn, E., Abi-Dargham, A., et al.: Imaging human mesolimbic dopamine transmission with positron emission tomography. Part II: amphetamine-induced dopamine release in the functional subdivisions of the striatum. *J. Cereb. Blood Flow Metab.* **23**(3), 285–300 (2003). <https://doi.org/10.1097/01.WCB.0000048520.34839.1A>
114. Chu, S.C., Chen, P.N., Hsieh, Y.S., Yu, C.H., Lin, M.H., Lin, Y.H., Kuo, D.Y.: Involvement of hypothalamic PI3K-STAT3 signalling in regulating appetite suppression mediated by amphetamine. *Br. J. Pharmacol.* **171**(13), 3223–3233 (2014). <https://doi.org/10.1111/bph.12667>
115. Weafer, J., Gorka, S.M., Hedeker, D., Dzemidzic, M., Kareken, D.A., Phan, K.L., de Wit, H.: Associations between behavioral and neural correlates of inhibitory control and amphetamine reward sensitivity. *Neuropsychopharmacology* **42**(9), 1905–1913 (2017). <https://doi.org/10.1038/npp.2017.61>

116. Asaad, G., Brunner: *Mazel clinical psychiatry, co. Hallucinations in clinical psychiatry: a guide for mental health professionals*; Taylor and Francis (1990)
117. Stuckelman, Z.D., Mulqueen, J.M., Ferracioli-Oda, E., Cohen, S.C., Coughlin, C.G., Leckman, J.F., Bloch, M.H.: Risk of irritability with psychostimulant treatment in children With ADHD. *J. Clin. Psychiatry* **78**(06), e648–e655 (2017). <https://doi.org/10.4088/JCP.15r10601>
118. Rasmussen, N.: Amphetamine-type stimulants: the early history of their medical and non-medical uses. *Int. Rev. Neurobiol.* **120**, 9–25 (2015). <https://doi.org/10.1016/bs.irm.2015.02.001>
119. Richards, J.R., Albertson, T.E., Derlet, R.W., Lange, R.A., Olson, K.R., Horowitz, B.Z.: Treatment of toxicity from amphetamines, related derivatives, and analogues: a systematic clinical review. *Drug Alcohol Depend.* 1–13 (2015). <https://doi.org/10.1016/j.drugalcdep.2015.01.040>
120. Pozzi, M., Roccatagliata, D., Sterzi, R.: Drug abuse and intracranial hemorrhage. In: *Neurological Sciences*, vol. 29, pp 269–270. Springer, Milan (2008). <https://doi.org/10.1007/s10072-008-0960-z>
121. Loewenhardt, B., Bernhard, M., Pierskalla, A., Neumann-Haefelin, T., Hofmann, E.: Neurointerventional treatment of amphetamine-induced acute occlusion of the middle cerebral artery by intracranial balloon angioplasty. *Clin. Neuroradiol.* **23**(2), 137–143 (2013). <https://doi.org/10.1007/s00062-011-0122-1>
122. Parrott, A.C.: Is ecstasy MDMA? A review of the proportion of ecstasy tablets containing MDMA, their dosage levels, and the changing perceptions of purity. In: *Psychopharmacology*, pp. 234–241. Springer (2004). <https://doi.org/10.1007/s00213-003-1712-7>
123. Parrott, A.C.: Human psychobiology of MDMA or “Ecstasy”: an overview of 25 years of empirical research. In: *Human Psychopharmacology*, vol. 28, pp. 289–307. Wiley-Blackwell (2013). <https://doi.org/10.1002/hup.2318>
124. Degenhardt, L., Bruno, R., Topp, L.: Is ecstasy a drug of dependence? *Drug Alcohol Depend.* 1–10 (2010). <https://doi.org/10.1016/j.drugalcdep.2009.09.009>
125. Parrott, A.C.: Chronic tolerance to recreational MDMA (3,4-Methylenedioxyamphetamine) or ecstasy. *J. Psychopharmacol.* (Oxford, England) **2005**(19), 71–83 (1994). <https://doi.org/10.1177/0269881105048900>
126. McKetin, R., Copeland, J., Norberg, M.M., Bruno, R., Hides, L., Khawar, L.: The effect of the ecstasy ‘Come-down’ on the diagnosis of ecstasy dependence. *Drug Alcohol Depend.* **139**, 26–32 (2014). <https://doi.org/10.1016/j.drugalcdep.2014.02.697>
127. Nirenberg, M.J.: Dopamine agonist withdrawal syndrome: implications for patient care. *Drugs Aging* **30**(8), 587–592 (2013). <https://doi.org/10.1007/s40266-013-0090-z>
128. Almeida, T., Monteiro, L.: Executive functions and decision making regarding drug addicts in abstinence. *Acta Neuropsychol.* **12**(4), 387–400 (2014). <https://doi.org/10.5604/17307503.1132137>
129. Kubo, C., Kuboki, T. (Eds.): *Psychosomatic medicine* (2006)
130. Day, A.M., Metrik, J., Spillane, N.S., Kahler, C.W.: Working memory and impulsivity predict marijuana-related problems among frequent users. *Drug Alcohol Depend.* **131**(1–3), 171–174 (2013). <https://doi.org/10.1016/j.drugalcdep.2012.12.016>
131. Pan, J.F., Mann, R., Brands, B., Stoduto, G., Wickens, C., Burston, J., Huestis, M.A., Le Foll, B.: Preliminary report on the residual effects of cannabis on young drivers’ performance of driving-related skills. *Drug Alcohol Depend.* **156**, e170–e171 (2015). <https://doi.org/10.1016/j.drugalcdep.2015.07.463>
132. Broyd, S.J., Van Hell, H.H., Beale, C., Yücel, M., Solowij, N.: Acute and chronic effects of cannabinoids on human cognition - a systematic review. *Biol. Psychiatry* 557–567. <https://doi.org/10.1016/j.biopsych.2015.12.002>
133. Nielsen, S.M., Toftdahl, N.G., Nordentoft, M., Hjorth?, C.: Association between alcohol, cannabis, and other illicit substance abuse and risk of developing schizophrenia: a nationwide population based register study. *Psychol. Med.* **47**(09), 1668–1677 (2017). <https://doi.org/10.1017/S0033291717000162>

134. Danielsson, A.-K., Lundin, A., Agardh, E., Allebeck, P., Forsell, Y.: Cannabis use, depression and anxiety: A 3-year prospective population-based study. *J. Affect. Disord.* **193**, 103–108 (2016). <https://doi.org/10.1016/j.jad.2015.12.045>
135. D'Souza, D.C.: Cannabinoids and psychosis. In: *International Review of Neurobiology*, pp. 289–326. Bentham Science Publishers. [https://doi.org/10.1016/S0074-7742\(06\)78010-2](https://doi.org/10.1016/S0074-7742(06)78010-2)
136. Hall, W., Lynskey, M.: Long-term marijuana use and cognitive impairment in middle age. *JAMA Intern. Med.* **6**(3), 2–3 (2016). <https://doi.org/10.1001/jamainternmed.2015.7850>
137. Gates, P., Jaffe, A., Copeland, J.: Cannabis smoking and respiratory health: consideration of the literature. *Respirology* 655–662 (2014). <https://doi.org/10.1111/resp.12298>
138. Joshi, M., Joshi, A., Bartter, T.: Marijuana and lung diseases. *Curr. Opin. Pulm. Med.* **20**(2), 173–179 (2014). <https://doi.org/10.1097/MCP.000000000000026>
139. Gundersen, T.D., Jørgensen, N., Andersson, A.-M., Bang, A.K., Nordkap, L., Skakkebak, N.E., Priskorn, L., Juul, A., Jensen, T.K.: Association between use of marijuana and male reproductive hormones and semen quality: a study among 1,215 healthy young men. *Am. J. Epidemiol.* **182**(6), 473–481 (2015). <https://doi.org/10.1093/aje/kwv135>
140. Wolff, V., Armspach, J.-P., Beaujeux, R., Manisor, M., Rouyer, O., Lauer, V., Meyer, N., Marescaux, C., Geny, B.: High frequency of intracranial arterial stenosis and cannabis use in ischaemic stroke in the young. *Cerebrovascular diseases (Basel, Switzerland)* **37**(6), 438–443 (2014). <https://doi.org/10.1159/000363618>
141. Volkow, N.D., Baler, R.D., Compton, W.M., Weiss, S.R.B.: Adverse health effects of marijuana use. *N. Engl. J. Med.* **370**(23), 2219–2227 (2014). <https://doi.org/10.1056/NEJMra1402309>
142. Verdejo-Garcia, A.: Social cognition in cocaine addiction. *Proc. Natl. Acad. Sci. U.S.A.* **111**(7), 2406–2407 (2014). <https://doi.org/10.1073/pnas.1324287111>
143. Potvin, S., Stavro, K., Rizkallah, É., Pelletier, J.: Cocaine and cognition. *J. Addict. Med.* **8**(5), 368–376 (2014). <https://doi.org/10.1097/ADM.0000000000000066>
144. Chen, W., Liu, P., Volkow, N.D., Pan, Y., Du, C.: Cocaine attenuates blood flow but not neuronal responses to stimulation while preserving neurovascular coupling for resting brain activity. *Mol. Psychiatry* **21**(October), 1–9 (2015). <https://doi.org/10.1038/mp.2015.185>
145. Bachi, K., Mani, V., Jeyachandran, D., Fayad, Z.A., Goldstein, R.Z., Alia-Klein, N.: Vascular disease in cocaine addiction. *Atherosclerosis* 154–162 (2017). <https://doi.org/10.1016/j.atherosclerosis.2017.03.019>
146. Rasimas, J.J., Sinclair, C.M.: Assessment and management of toxidromes in the critical care unit. *Crit. Care Clin.* **33**(3), 521–541 (2017). <https://doi.org/10.1016/j.ccc.2017.03.002>
147. Plush, T., Shakespeare, W., Jacobs, D., Ladi, L., Sethi, S., Gasperino, J.: Cocaine-induced agitated delirium: a case report and review. *J. Intensive Care Med.* **30**(1), 49–57 (2015). <https://doi.org/10.1177/0885066613507420>
148. Greydanus, D.E., Reed, W.J., Hawver, E.K.: Public health aspects of substance use and abuse in adolescence. *Int. Public Health J.* **8**(4), 455–484 (2016)
149. Schmeichel, B.E., Berridge, C.W.: Amphetamine acts within the lateral hypothalamic area to elicit affectively neutral arousal and reinstate drug-seeking. *Int. J. Neuropsychopharmacol./Off. Sci. J. Coll. Int. Neuropsychopharmacol. (CINP)* **17**(1), 63–75 (2014). <https://doi.org/10.1017/S1461145713000734>
150. Dolder, P.C., Schmid, Y., Steuer, A.E., Kraemer, T., Rentsch, K.M., Hammann, F., Liechti, M.E.: Pharmacokinetics and pharmacodynamics of lysergic acid diethylamide in healthy subjects. *Clinical Pharmacokinetics*, pp. 1–12. Springer International Publishing February (2017). <https://doi.org/10.1007/s40262-017-0513-9>
151. Degenhardt, L., Hall, W.: Extent of illicit drug use and dependence, and their contribution to the global burden of disease. *Lancet* **379**(9810), 55–70 (2012). [https://doi.org/10.1016/S0140-6736\(11\)61138-0](https://doi.org/10.1016/S0140-6736(11)61138-0)
152. Vahabzadeh, M., Ghassemi Toussi, A.: Misdiagnosed pruritus; formication due to chronic amphetamine abuse. *Asia Pac. J. Med. Toxicol.* **5**(1), 32–34 (2016). <https://doi.org/10.22038/APJMT.2016.6884>

153. Radfar, S., Rawson, R.: Current research on methamphetamine: epidemiology, medical and psychiatric effects, treatment, and harm reduction efforts. *Addict. Health.* **6**(3–4), 146–154 (2014)
154. Li, H., Scholl, J.L., Tu, W., Hassell, J.E., Watt, M.J., Forster, G.L., Renner, K.J.: Serotonergic responses to stress are enhanced in the central amygdala and inhibited in the ventral hippocampus during amphetamine withdrawal. *Eur. J. Neurosci.* **40**(11), 3684–3692 (2014). <https://doi.org/10.1111/ejn.12735>
155. London, E.D., Kohno, M., Morales, A.M., Ballard, M.E.: Chronic methamphetamine abuse and corticostriatal deficits revealed by neuroimaging. *Brain Res.* **1628**, 174–185 (2015). <https://doi.org/10.1016/j.brainres.2014.10.044>
156. Thanos, P.K., Kim, R., Delis, F., Rocco, M.J., Cho, J., Volkow, N.D.: Effects of chronic methamphetamine on psychomotor and cognitive functions and dopamine signaling in the brain. *Behav. Brain Res.* **320**, 282–290 (2017). <https://doi.org/10.1016/j.bbr.2016.12.010>
157. McKetin, R., Lubman, D.I., Baker, A.L., Dawe, S., Ali, R.L.: Dose-related psychotic symptoms in chronic methamphetamine users: evidence from a prospective longitudinal study. *JAMA Psychiat.* **70**(3), 1–6 (2013). <https://doi.org/10.1001/jamapsychiatry.2013.283>
158. Glasner-Edwards, S., Mooney, L.J.: Methamphetamine psychosis: epidemiology and management. *CNS Drugs* **28**(12), 1115–1126 (2014). <https://doi.org/10.1007/s40263-014-0209-8>
159. Whiteford, H.A., Degenhardt, L., Rehm, J., Baxter, A.J., Ferrari, A.J., Erskine, H.E., Charlson, F.J., Norman, R.E., Flaxman, A.D., Johns, N., et al.: Global burden of disease attributable to mental and substance use disorders: findings from the global burden of disease study 2010. *Lancet* **382**(9904), 1575–1586 (2013). [https://doi.org/10.1016/S0140-6736\(13\)61611-6](https://doi.org/10.1016/S0140-6736(13)61611-6)
160. Bagheri, M., Mokri, A., Khosravi, A., Kabir, K.: Effect of abstinence on depression, anxiety, and quality of life in chronic methamphetamine users in a therapeutic community. *Int. J. High Risk Behav. Addict.* **4**(3), 1–5 (2015). <https://doi.org/10.5812/ijhrba.23903>
161. Wang, G., Shi, J., Chen, N., Xu, L., Li, J., Li, P., Sun, Y., Lu, L.: Effects of length of abstinence on decision-making and craving in methamphetamine abusers. *PLoS ONE* **8**(7), e68791 (2013). <https://doi.org/10.1371/journal.pone.0068791>
162. Baldacchino, A., Arvapalli, V., Oshun, A., Tolomeo, S.: Substance-induced mental disorders. In: *Textbook of Addiction Treatment: International Perspectives*, pp. 1925–1936. Springer Milan, Milano (2015). [https://doi.org/10.1007/978-88-470-5322-9\\_88](https://doi.org/10.1007/978-88-470-5322-9_88)
163. Lev-Ran, S., Feingold, D., Frenkel, A., Lerner, A.G.: Clinical characteristics of individuals with schizophrenia and hallucinogen persisting perception disorder: a preliminary investigation. *J. Dual Diagn.* **10**(2), 79–83 (2014). <https://doi.org/10.1080/15504263.2014.906155>
164. Schmid, Y., Enzler, F., Gasser, P., Grouzmann, E., Preller, K.H., Vollenweider, F.X., Brenneisen, R., Müller, F., Borgwardt, S., Liechti, M.E.: Acute effects of lysergic acid diethylamide in healthy subjects. *Biol. Psychiat.* **78**(8), 544–553 (2015). <https://doi.org/10.1016/j.biopsych.2014.11.015>
165. Liechti, M.E., Dolder, P.C., Schmid, Y.: Alterations of consciousness and mystical-type experiences after acute LSD in humans. *Psychopharmacology* **234**(9–10), 1499–1510 (2017). <https://doi.org/10.1007/s00213-016-4453-0>
166. Grof, S.: *Realms of the Human Unconscious: Observations from Lsd Research*. Souvenir Press (1996)
167. Passie, T., Halpern, J.H., Stichtenoth, D.O., Emrich, H.M., Hintzen, A.: The pharmacology of lysergic acid diethylamide: a review. *CNS Neurosci. Ther.* **14**(4), 295–314 (2008). <https://doi.org/10.1111/j.1755-5949.2008.00059.x>
168. Jones, C.M., Mack, K.A., Paulozzi, L.J., Hsu, J.R., Paulozzi, L., Jones, C., Mack, K., Rudd, R., Jones, C., Mack, K., et al.: Pharmaceutical overdose deaths, United States, 2010. *JAMA* **309**(7), 657 (2013). <https://doi.org/10.1001/jama.2013.272>
169. Bjelić, D.I.: Freud’s cocaine dreams and memories. In: *Intoxication, Modernity, and Colonialism*, pp. 141–187. Palgrave Macmillan US, New York (2016). [https://doi.org/10.1057/978-1-137-58856-2\\_5](https://doi.org/10.1057/978-1-137-58856-2_5)

170. Bramness, J.G.: Prescription drug abuse: risks and prevention. In: *Textbook of Addiction Treatment: International Perspectives*, pp. 637–661. Springer Milan, Milano (2015). [https://doi.org/10.1007/978-88-470-5322-9\\_29](https://doi.org/10.1007/978-88-470-5322-9_29)
171. Bjelić, D.L.: Freud's "Cocaine Episode" on Benjamin's Hashish. In: *Intoxication, Modernity, and Colonialism*, pp. 63–90. Palgrave Macmillan US, New York (2016). [https://doi.org/10.1057/978-1-137-58856-2\\_3](https://doi.org/10.1057/978-1-137-58856-2_3)
172. Alves, C.J., Magalhães, A., Melo, P., de Sousa, L., Tavares, M.A., Monteiro, P.R.R., Summavielle, T.: Long-term effects of chronic cocaine exposure throughout adolescence on anxiety and stress responsiveness in a Wistar rat model. *Neuroscience* **277**, 343–355 (2014). <https://doi.org/10.1016/j.neuroscience.2014.07.008>
173. Richards, J.R., Garber, D., Laurin, E.G., Albertson, T.E., Derlet, R.W., Amsterdam, E.A., Olson, K.R., Ramoska, E.A., Lange, R.A.: Treatment of cocaine cardiovascular toxicity: a systematic review. *Clinical toxicology (Philadelphia, Pa.)* **54**(5), 345–364 (2016). <https://doi.org/10.3109/15563650.2016.1142090>
174. Stephens, D.N., King, S.L., Lambert, J.J., Bellelli, D., Duka, T.: GABAA receptor subtype involvement in addictive behaviour. In: *Genes, Brain and Behavior*, pp. 149–184. Blackwell Publishing Ltd. (2017). <https://doi.org/10.1111/gbb.12321>
175. Kishi, T., Matsuda, Y., Iwata, N., Correll, C.U.: Antipsychotics for cocaine or psychostimulant dependence: systematic review and meta-analysis of randomized placebo-controlled trials. *J. Clin. Psychiatry* **74**(12), e1169–e1180 (2013). <https://doi.org/10.4088/JCP.13r08525>
176. Muzyk, A.J., Leung, J.G., Nelson, S., Embury, E.R., Jones, S.R.: The role of diazepam loading for the treatment of alcohol withdrawal syndrome in hospitalized patients. *Am. J. Addict.* **22**(2), 113–118 (2013). <https://doi.org/10.1111/j.1521-0391.2013.00307.x>
177. Carroll, K.M., Nich, C., Petry, N.M., Eagan, D.A., Shi, J.M., Ball, S.A.: A randomized factorial trial of disulfiram and contingency management to enhance cognitive behavioral therapy for cocaine dependence. *Drug Alcohol Depend.* **160**, 135–142 (2016). <https://doi.org/10.1016/j.drugalcdep.2015.12.036>
178. Haney, M., Rubin, E., Foltin, R.: Modafinil reduces smoked cocaine self-administration in humans: effects vary as a function of cocaine "priming" and cocaine cost. *Neuropsychopharmacology*. S257 (2015). <https://doi.org/10.1016/j.drugalcdep.2016.08.232>
179. Kosten, T.R., Wu, G., Huang, W., Harding, M.J., Hamon, S.C., Lappalainen, J., Nielsen, D.A.: Pharmacogenetic randomized trial for cocaine abuse: disulfiram and dopamine  $\beta$ -hydroxylase. *Biol. Psychiat.* **73**(3), 219–224 (2013). <https://doi.org/10.1016/j.biopsych.2012.07.011>
180. Miller, P.M.: Elsevier Science, *Interventions for Addiction* (2013)
181. Gaval-Cruz, M., Liles, L.C., Iuvone, P.M., Weinschenker, D.: Chronic inhibition of dopamine  $\beta$ -hydroxylase facilitates behavioral responses to cocaine in mice. *PLoS ONE* **7**(11), e50583 (2012). <https://doi.org/10.1371/journal.pone.0050583>
182. De La Garza, R., Bubar, M.J., Carbone, C.L., Moeller, F.G., Newton, T.F., Anastasio, N.C., Harper, T.A., Ware, D.L., Fuller, M.A., Holstein, G.J., et al.: Evaluation of the dopamine  $\beta$ -hydroxylase inhibitor nopicostat in participants who meet criteria for cocaine use disorder. *Prog. Neuropsychopharmacol. Biol. Psychiatry* **59**, 40–48 (2015). <https://doi.org/10.1016/j.pnpbp.2015.01.009>
183. Ellefsen, K.N., Concheiro, M., Pirard, S., Gorelick, D.A., Huestis, M.A.: Pharmacodynamic effects and relationships to plasma and oral fluid pharmacokinetics after intravenous cocaine administration. *Drug Alcohol Depend.* **163**, 116–125 (2016). <https://doi.org/10.1016/j.drugalcdep.2016.04.004>
184. Ballon, J.S., Feifel, D.: A systematic review of modafinil: potential clinical uses and mechanisms of action. *J. Clin. Psychiatry* **67**(4), 554–566 (2006). <https://doi.org/10.4088/JCP.v67n0406>
185. Ryan, J., Sharts-Hopko, N.: The experiences of medical marijuana patients. *J. Neurosci. Nurs.* **49**(3), 185–190 (2017). <https://doi.org/10.1097/JNN.0000000000000283>
186. Salhab, A.: Embattled cannabis: pharmacological, medical, recreational, and adverse effects aspects. *J. Subst. Use* **22**(2), 236–239 (2017). <https://doi.org/10.3109/14659891.2016.1149237>



187. Panlilio, L.V., Justinova, Z., Trigo, J.M., Le Foll, B.: Screening medications for the treatment of cannabis use disorder. *Int. Rev. Neurobiol.* **126**, 87–120 (2016). <https://doi.org/10.1016/bs.irn.2016.02.005>
188. Mason, B.L., Mustafa, A., Filbey, F., Brown, E.S., Mason, B.L.: Novel pharmacotherapeutic interventions for cannabis use disorder. *Curr. Addict. Rep.* **3**(2), 214–220 (2016). <https://doi.org/10.1007/s40429-016-0094-y>
189. Levin, F.R., Mariani, J.J., Pavlicova, M., Brooks, D., Glass, A., Mahony, A., Nunes, E.V., Bisaga, A., Dakwar, E., Carpenter, K.M., et al.: Dronabinol and lofexidine for cannabis use disorder: a randomized, double-blind placebo-controlled trial. *Drug Alcohol Depend.* **159**, 53–60 (2016). <https://doi.org/10.1016/j.drugalcdep.2015.11.025>
190. Onakpoya, I.J., Heneghan, C.J., Aronson, J.K.: Post-marketing withdrawal of anti-obesity medicinal products because of adverse drug reactions: a systematic review. *BMC Med.* **14**(1), 191 (2016). <https://doi.org/10.1186/s12916-016-0735-y>
191. Allsop, D.J., Copeland, J., Lintzeris, N., Dunlop, A.J., Montebello, M., Sadler, C., Rivas, G.R., Holland, R.M., Muhleisen, P., Norberg, M.M., et al.: Nabiximols as an agonist replacement therapy during cannabis withdrawal: a randomized clinical trial. *JAMA Psychiat.* **71**(3), 281–291 (2014). <https://doi.org/10.1001/jamapsychiatry.2013.3947>
192. Gowda, C.R., Lundt, L.P.: Mechanism of action of narcolepsy medications. *CNS spectrums* **19**(1), 25–27, 34 (2014). <https://doi.org/10.1017/S1092852914000583>
193. Punja, S., Shamseer, L., Hartling, L., Urichuk, L., Vandermeer, B., Nikles, J., Vohra, S.: Amphetamines for attention deficit hyperactivity disorder (ADHD) in children and adolescents. In: *Cochrane Database of Systematic Reviews*. Wiley, Chichester, UK (2016). <https://doi.org/10.1002/14651858.CD009996.pub2>
194. Bray, G.A.: Medical treatment of obesity: the past, the present and the future. *Best Pract. Res. Clin. Gastroenterol.* **28**(4), 665–684 (2014). <https://doi.org/10.1016/j.bpg.2014.07.015>
195. Steinkellner, T., Montgomery, T.R., Hofmaier, T., Kudlacek, O., Yang, J.-W., Rickhag, M., Jung, G., Lubec, G., Gether, U., Freissmuth, M., et al.: Amphetamine action at the cocaine- and antidepressant-sensitive serotonin transporter is modulated by alphaCaMKII. *J. Neurosci.* **35**, 11762 (2015). <https://doi.org/10.1523/JNEUROSCI.4034-14.2015>
196. Ling, W., Mooney, L., Haglund, M.: Effects and manifestations of methamphetamine use. *Curr. Psychiatry* **13**(9) (2014)
197. Diaper, A.M., Law, F.D., Melichar, J.K.: Pharmacological strategies for detoxification. *Br. J. Clin. Pharmacol.* **77**(2), 302–314 (2014). <https://doi.org/10.1111/bcp.12245>
198. Geyer, M.A., Richards, W.A., McCann, U., Jesse, R., McKay, C.R., Halberstadt, A.L., Greer, G.R.: Lysergic acid diethylamide and psilocybin revisited. *Biol. Psychiat.* **78**(8), 516–518 (2015). <https://doi.org/10.1016/j.biopsych.2015.08.003>
199. Gasser, P., Holstein, D., Michel, Y., Doblin, R., Yazar-Klosinski, B., Passie, T., Brenneisen, R.: Safety and efficacy of lysergic acid diethylamide-assisted psychotherapy for anxiety associated with life-threatening diseases. *J. Nerv. Ment. Dis.* **202**(7), 513–520 (2014). <https://doi.org/10.1097/NMD.0000000000000113>
200. Komater, M., Vollenweider, F.X.: Serotonergic hallucinogen-induced visual perceptual alterations. *Curr. Top. Behav. Neurosci.* 1–26 (2016). [https://doi.org/10.1007/7854\\_2016\\_461](https://doi.org/10.1007/7854_2016_461)
201. Chaudhry, S.K., Broderick, L., Penzner, J.B., Avery, J.: Benzodiazepine maintenance treatment in schizophrenia. The primary care companion for CNS disorders **17**(6) (2015). <https://doi.org/10.4088/PCC.15101818>
202. Galinato, M.H., Lockner, J.W., Fannon-Pavlich, M.J., Sobieraj, J.C., Staples, M.C., Somkuwar, S.S., Ghofranian, A., Chaing, S., Navarro, A.I., Joea, A., et al.: A synthetic small-molecule isoxazole-9 protects against methamphetamine relapse. *Mol. Psychiatry* (2017). <https://doi.org/10.1038/mp.2017.46>

# MAO Inhibitors from Natural Sources for Major Depression Treatment



Luisa Nunes Souza, Jonas Ferro da Silva Neto,  
Maria Vitória da Silva Paula Cirilo, Gabriel Sousa Albuquerque,  
Clayson Moura Gomes, Leonardo Luiz Borges, Carlton A. Taft,  
and Vinicius Barreto da Silva

**Abstract** Major depressive disorder is a disabling public health concern of high relevance worldwide. Psychotherapy and pharmacotherapy are the main approaches employed to treat patients with depressive symptoms. Antidepressants are drugs able to relieve symptoms of depression that work by affecting neurotransmitters like noradrenaline and serotonin in the brain. Despite antidepressant drugs are one of the most prescribed medicines in medical practice because of their proven clinical benefits, exposure to side effects and lack of efficacy result in outcomes that limit pharmacotherapy performance in some individuals. Thus, the continuous development of therapeutic alternatives is a task of great importance including the design of monoamine oxidase (MAO) inhibitors that work by increasing neurotransmitters in the central nervous system. Medicinal plants have long been an important source of medicines and the results obtained against depression models for some plant species encourage new studies focused on the selection of natural molecules able to act as antidepressant drugs or at least as lead compounds for novel projects. Hence, we describe the chemical features of main active ingredients found in medicinal plants with antidepressant properties, including *Kielmeyera coriacea*, *Rhodiola rosea* and *Banisteriopsis caapi*, also comparing the properties of such natural molecules with pharmacophoric features of available MAO inhibitors drugs in order to validate promising antidepressants.

**Keywords** Antidepressants · Medicinal plants · Drug design · Pharmacophore

---

L. N. Souza · J. F. da Silva Neto · M. V. da Silva Paula Cirilo · G. S. Albuquerque · C. M. Gomes · L. L. Borges · V. B. da Silva (✉)  
Escola de Ciências Médicas e da Vida. Pontifícia Universidade Católica de Goiás, Goiânia, Brazil  
e-mail: [viniciusbarreto.farmacia@gmail.com](mailto:viniciusbarreto.farmacia@gmail.com)

L. L. Borges  
Câmpus Anápolis de Ciências Exatas e Tecnológicas Henrique Santillo, Universidade Estadual de Goiás, Anápolis, Brazil

C. A. Taft  
Centro Brasileiro de Pesquisas Físicas, Rio de Janeiro, Brazil

## 1 Introduction

Major depressive disorder is a disabling public health concern of high relevance worldwide. Depression is also the most common mental disorder, affecting approximately 280 million people worldwide. Around 3.8% of the global population suffer from depression, including 5% among adults and 5.7% among people older than 60 years [1]. The disorder is a disabling and life shortening condition accompanied by functional impairment and marked by typical clinical symptoms, including depressed mood, inability to feel pleasure, feelings of worthlessness and guilt, suicidal ideation and fatigue [2, 3].

The outbreak of severe acute respiratory syndrome caused by SARS-CoV-2 that since 2020 generated COVID-19 pandemic brought about threats not only related to concerns about the physical dimension due to coronavirus virulence but also related to mental status of people due to increased psychological distress associated with social isolation, death of close people, failure of health services and economic recession risks [4–6].

Cognitive therapy and medication are the main approaches used to treat patients with depressive symptoms. Antidepressants are drugs able to relieve symptoms of depression that work by affecting neurotransmitters like noradrenaline and serotonin in the brain. Despite antidepressant drugs are one of the most prescribed medicines in medical practice due to their proven clinical benefits, exposure to side effects and lack of efficacy result in outcomes that limit pharmacotherapy performance in some individuals. Adherence with medication is often poor resulting in more intense symptoms and worse prognosis [7]. Thus, the continuous development of therapeutic alternatives is a task of great importance including the design of molecules that work by affecting neurotransmission in the central nervous system. Medicinal plants have long been an important source of medicines and the results obtained against depression models for some plant species encourage new studies focused on the selection of natural molecules.

## 2 Antidepressant Drugs

Depressed mood is affected by key dysfunctions in brain circuitries mainly supporting emotion regulation and cognitive control [8, 9]. The pathophysiology of depression is not fully understood, and it is not possible to define just one cause. Genetic, biochemical, psychological and social factors must be considered as potential triggers able to induce the depression disorder. Some functional changes observed in neurotransmission characterize the brain of patients with depression. Changes that result in depressed dopaminergic, serotonergic and noradrenergic neurotransmission are well documented when the depressive disorder is considered [10, 11]. Thus, the drugs available to treat depressive disorder are usually designed to enhance neurotransmission.

The pharmacological treatment of depression must be planned taking into account the degree of illness, presence or absence of additional clinical and psychiatric comorbidities, financial cost, tolerability and adverse effects. Pharmacotherapy planning is performed in three stages: (a) acute/initial—aimed at symptomatic resolution; (b) control—aimed at sustaining control of disease symptoms; (c) maintenance—to prevent relapses. Antidepressant drugs are classified according to the chemical structure of drugs or their mechanism of action (Table 1) [12–16].

**Table 1** Pharmacologic class and mechanism of action of antidepressant drugs

Pharmacologic class	Mechanism of action	Examples of drugs
MAO inhibitors	Inhibition of MAO, increasing the concentrations of monoamines neurotransmitters within the central nervous system	Tranylcypromine Moclobemide Selegiline
Tricyclic antidepressants	Inhibition of the reuptake of transmitter amines, increasing their concentrations within the central nervous system	Amitriptyline Imipramine Clomipramine Nortriptyline
Selective serotonin reuptake inhibitors	Inhibition of the presynaptic reuptake of the neurotransmitter serotonin	Fluoxetine Citalopram Escitalopram Fluvoxamine Sertraline Paroxetine
Serotonin and norepinephrine reuptake inhibitors	Reuptake inhibition of both serotonin and norepinephrine, generating potentiation of neurotransmitter activity in the central nervous system	Venlafaxine Desvenlafaxine Duloxetine
Serotonin receptor antagonists and reuptake inhibitors	Inhibition of the reuptake of serotonin, blockade of $\alpha$ -1-adrenergic receptors and antagonism of 5-HT <sub>1a</sub> , 5-HT <sub>1c</sub> and 5-HT <sub>2</sub> receptor subtypes	Trazodone
Norepinephrine reuptake inhibitor	Selective inhibition of noradrenaline reuptake, enhancing noradrenaline activity in the central nervous system	Reboxetine
Norepinephrine and dopamine reuptake inhibitors	Inhibition of the reuptake of the neurotransmitters norepinephrine and dopamine from the synaptic clefts in central nervous system	Bupropion

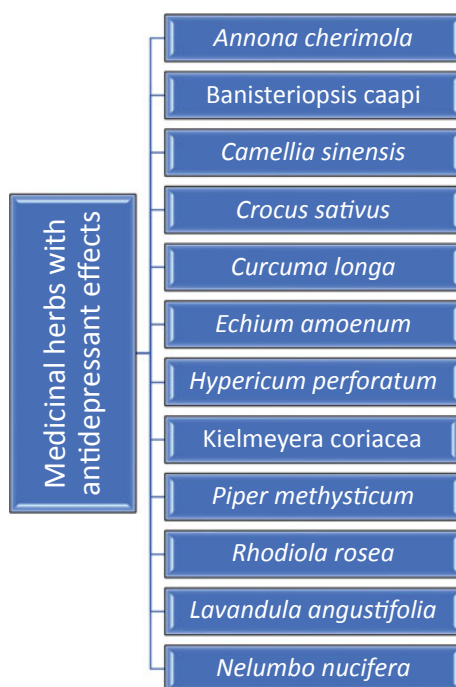
### 3 Medicinal Herbs Against Depression

Medicinal plants are natural sources of chemical compounds able to act with enormous potential in the treatment of various diseases, including disorders that affect the central nervous system, such as depression. Hundreds of plants and their extracts have traditionally been used in folk medicine for generations and some medicinal herbs have been tested as potential antidepressant alternatives (Fig. 1), showing the ability to interfere with neurotransmitters receptors and enzymes related to their metabolism [17–20].

Despite the availability of reports of diverse plants in folk medicine used to treat depression symptoms, their antidepressant activity and the mechanism of action of the phytochemicals active molecules usually are not fully determined. These plant species should be considered as potential sources of natural molecule scaffolds for inspiring the design of improved antidepressant agents [21].

*Rhodiola rosea* L. belong to the genus *Rhodiola* and the family of Crassulaceae. This genus has nearly discrete petals, yellow flowers, stout roots, short root neck, reaches a height of 30–70 cm and has a basal rosette of leaves. *R. rosea* have been used for diverse affections since headache to mental disorders. Antioxidant, anti-cancer, antidiabetic, antistress, antidepressant, neuroprotective, immunomodulatory, anti-inflammatory and analgesic activities have already been described for *R. rosea*. the explanation for such broad bioactivity is probably due to the molecular diversity of

**Fig. 1** Examples of medicinal herbs with antidepressant properties



its phytoconstituents, where rosiridin, an aglycon phytochemical, seems to be one of the most important active ingredients. Other molecules like rhodiolide and salideoside were found to have neurological, cardiological and hepato-protective activity, what is important for preventing/mitigating/reducing stress-induced impairments and disorders related to neuro-endocrine and immune systems [22–23].

*Rhodiola rosea* extracts show the ability to inhibit monoamine oxidase (MAO) in vitro, an enzyme responsible for catalyzing the oxidation of neurotransmitters such as serotonin, dopamine and noradrenaline. Preclinical and clinical studies have shown that the use of *R. rosea* increases the level of serotonin in the central nervous system and the adaptogenic response to stressors. A phase III randomized double-blind placebo-controlled clinical trial using an extract of *R. rosea* L. rhizomes demonstrated an improvement in depression, insomnia, emotional instability, and somatization without important side-effects [24].

Another randomized placebo-controlled trial compared sertraline and the extract of *R. rosea* for treatment of major depressive disorder, showing that the plant was less effective than sertraline, a selective serotonin reuptake inhibitor, but had fewer adverse events and was better tolerated [25]. A third randomized double-blind placebo-controlled clinical trial evaluated the antidepressant effects of a *R. rosea* capsule combined with sertraline. The group which used two capsules of *R. rosea* with one capsule of sertraline had statistically significant reductions in the Hamilton Depression Rating, Beck Depression Inventory and Clinical Impression Change scores than the other groups (sertraline with placebo and sertraline, placebo and one capsule of *R. rosea* groups). Therefore, a preparation of *R. rosea* capsules helped to improve the quality of life and clinical symptoms of depression when combined with sertraline [26].

*Banisteriopsis caapi*, also known as Jabuge, Mariri, Yagé or Caapi, is a native vine from Amazon region. This plant species is often combined with another species, *Psychotria viridis*, also known by locals as “Chacrona”, and generates a sacred indigenous beverage from the northwest Amazon called Ayahuasca, which is a psychoactive plant tea used traditionally by the indigenous of the Upper Amazon and in more recent times by healers and members of religious syncretic groups [27–29].

*B. caapi* is rich in  $\beta$ -carboline or harmala alkaloids, such as harmine, harmaline and tetrahydroharmine (THH) [30–31]. Its unique pharmacology depends on the oral activity of the hallucinogen DMT (*N,N*-dimethyltryptamine), which results from inhibition of MAO enzyme by  $\beta$ -carboline alkaloids. MAO is the enzyme that normally degrades DMT in the liver and gut [32]. Animal studies and clinical research suggests that *B. caapi* preparations show antidepressant activity, a therapeutic effect that has been linked to hippocampal neurogenesis. The three main alkaloids present in *B. caapi*, harmine, harmaline and THH, and the harmine metabolite harmol, also stimulate adult neurogenesis in vitro [33].

The Brazilian cerrado biome is a great source of medicinal plants, with several pharmacologically active species used in folk medicine, contributing to significant knowledge of bioactive compounds. Cerrado is the second main biome in Brazil, located in the middle west region and exhibiting a great diversity of natural plants [34]. The plants of the genus *Kielmeyera* (Clusiaceae) are endemic in South America

and the *Kielmeyera coriacea* species is often documented primarily in savannahs, and it is also known as “pau santo”. This species is rich in xanthenes, substances that have pharmacological properties, such as antitumor, antifungal, antibacterial, and anti-inflammatory activities. Organic extracts from different parts of the plant have been tested against oral microorganisms, and the inner bark extract showed promising results against aerobic and anaerobic oral microorganisms [35]. The hydroethanolic extract of *Kielmeyera coriacea* stems inhibits in a concentration-dependent manner the synaptosomal uptake of serotonin (5-HT), noradrenaline and dopamine [36]. There is a great amount of xanthenes in *K. coriacea* stems and the mainly are 1,3,7-trihydroxy-2-(3-hydroxy-3-methylbutyl)-xanthone, 1,3,7-trihydroxy-2-(3-methyl-but-2-enyl)-xanthone, 2-hydroxy-1-methoxyxanthone, 3-hydroxy-2,4-dimethoxy-xanthone, jacareubin, kielcorin and swertinin. These molecules are the most likely to be related to the antidepressant activity of *K. coriacea* [37].

*R. rosea*, *B. caapi* and *K. coriacea*, as described above, are plant species with phytochemicals with promising antidepressant properties able to inspire the design of optimized drugs. The knowledge of the chemical features of such phytochemicals (Table 2) is a key to develop novel therapeutical agents. Once one of the mechanisms employed by antidepressant drugs is inhibition of MAO, the comparison of

**Table 2** Main phytochemicals found in *R. rosea*, *B. caapi* and *K. coriacea* medicinal plants

Rhodiola rosea	Rosiridin Salidroside Benzyl $\beta$ -D-glucopiranoside Hydroquinone Tyrosol Rosavin Triandrin Epigallocatechin Epigallocatechin 3-gallate
Banisteriopsis caapi	Harmine Tetrahydroharmine Harmaline Harmol Harmine N-oxide Harmic acid methyl ester Harmalinic acid Harmic amide Acetylhornharmine
Kielmeyera coriacea	2-hydroxy-1-methoxyxanthone 3-hydroxy-2,4-dimethoxyxanthone 4-hydroxy-2,3-dimethoxyxanthone 1,3,7-trihydroxy-2-(3-methylbut-2-enyl)-xanthone 1,3,7-trihydroxy-2-(3-hydroxy-3-methylbutyl)-xanthone (Z)-2-ethylhexyl-3-(4-methoxyphenyl)-2-propenoate Swertinin Kielcorin Jacareubin

the chemical features of MAO inhibitor drugs with these plant phytochemicals is a way to verify if MAO inhibition is the main mechanism used by phytoconstituents in order to generate the antidepressant effects observed when the medicinal plants are employed.

## 4 Pharmacophoric Features of MAO Inhibitors and Phytochemicals

A pharmacophore is the ensemble of steric and electronic features necessary to ensure the optimal supramolecular interactions of a bioactive molecule with a specific biological target to generate a therapeutic response [38]. A pharmacophore model built in a ligand-based manner after superimposing a set of active molecules and extracting common chemical features considered essential for their bioactivity is a key drug design strategy for selecting naturally available compounds able to simulate the same features found in the set of active molecules [39, 40].

MAO inhibitors may potentiate the effects of an indirectly-acting sympathomimetic amine called tyramine, leading to their limitation in clinical use due to the risk of inducing hypertensive crisis. Nevertheless, the more recent understanding that the potentiation of tyramine is minimal with MAO-A reversible inhibitors has led to their reintroduction to clinical use for treatment of depression [41]. A group of antidepressant drugs able to inhibit MAO-A selectively and reversibly functions as an appropriate set of active molecules for pharmacophore modeling. Moclobemide, brofaromine, toloxatone, belfloxtone, lazabemide and cimoxatone (Fig. 2) meet such requirements.

On the other hand, plant species with defined medicinal use against depression, including *R. Rosea*, *K. coriacea* and *B. caapi*, are interesting sources of molecular scaffolds in the search for lead compounds against depression. Applying a ligand-based pharmacophore modeling strategy based on superimposition of both set of molecules is a way to enlighten the mechanism of action of these naturally occurring compounds and to answer if MAO-A inhibition is an important approach used by these plants' active ingredients, helping to inspire the design of novel antidepressants in a more diverse chemical space.

The top-ranked pharmacophore models generated with Pharmagist webserver [42] default parameters for MAO-A selective and reversible inhibitors reveal the alignment of one aromatic feature surrounded by hydrogen bond acceptor groups (Fig. 3). The best alignment of hydrogen bond acceptors is achieved when only moclobemide, toloxatone and cimoxatone are considered. In this case, an additional hydrogen bond acceptor feature is added to the model (Fig. 3C).

When *Rhodiola rosea* phytochemicals (Table 2) are aligned with MAO-A selective and reversible inhibitors, the same pattern of an aromatic feature surrounded by hydrogen bond acceptors observed for MAO-A inhibitors is achieved by the top-ranked model generated with Pharmagist webserver default parameters. A number



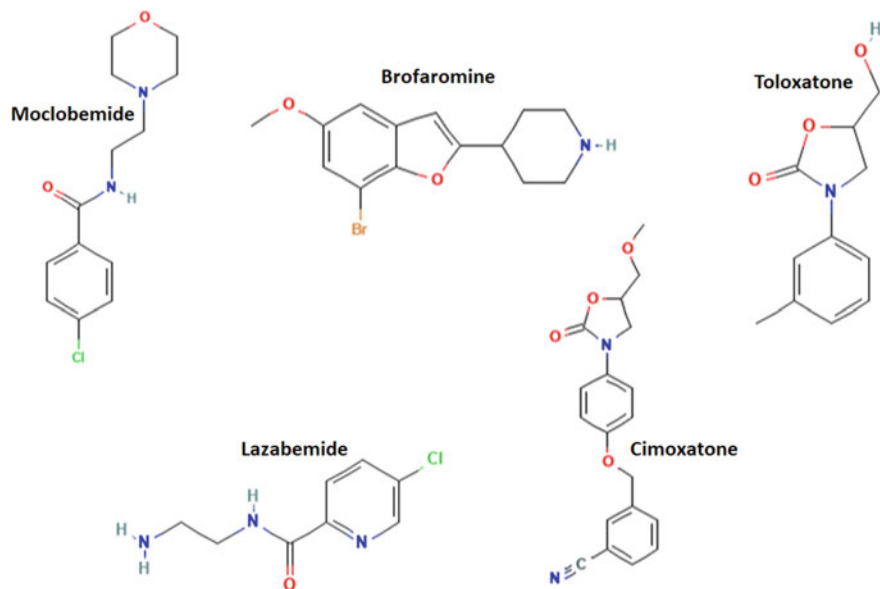


**Fig. 2** Chemical structure depiction of selective and reversible MAO-A inhibitors

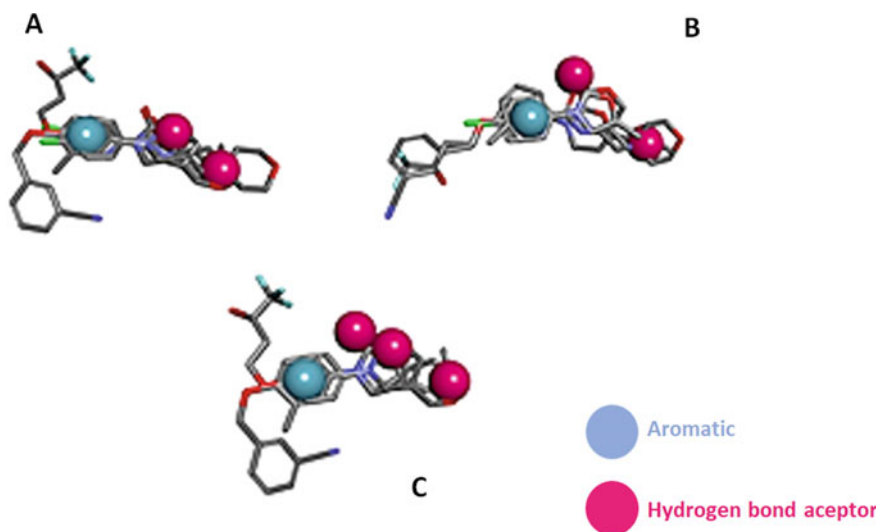


**Fig. 3** Pharmacophoric models generated for MAO-A selective and reversible inhibitors

of eight phytochemicals shared such features with MAO-A inhibitors (Fig. 4), revealing that *Rhodiola rosea* compounds have stereoelctronic features compatible for inhibition of MAO-A.

The model generated for *B. caapi* phytochemicals (Table 2) with MAO-A inhibitors also reveals a similar distribution of features in space, with a number of nine herb molecules aligned. The difference is that the aromatic feature is surrounded by one hydrogen bond acceptor and other hydrogen bond donor feature (Fig. 5). This

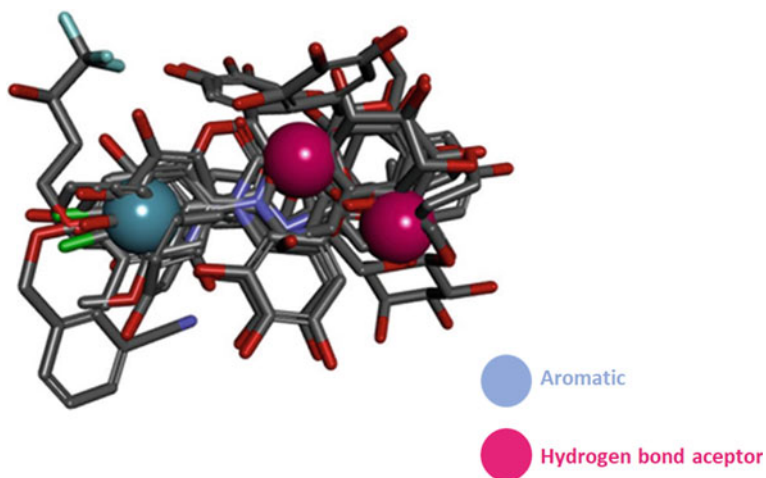


**Fig. 4** Pharmacophoric model generated after combining MAO-A selective and reversible inhibitors and *Rhodiola rosea* phytochemicals

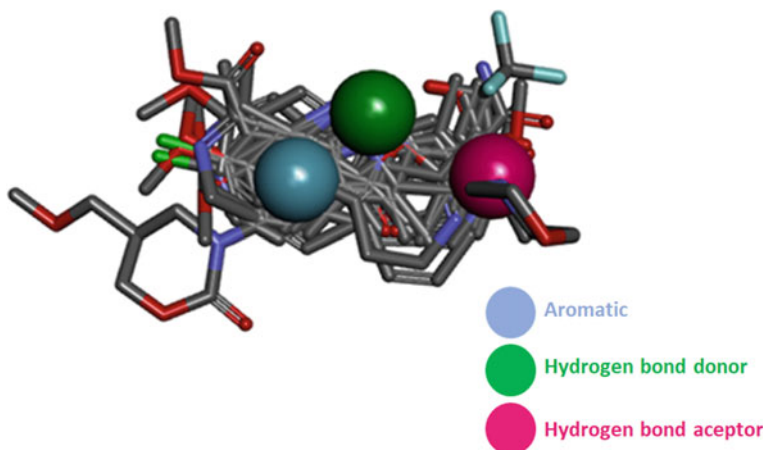


**Fig. 5** Pharmacophoric model generated after combining MAO-A selective and reversible inhibitors and *Banisteriopsis caapi* phytochemicals

occurs because *B. caapi* phytochemicals are indole derivatives with a hydrogen donor function. Thus, basic requirements found in MAO-A inhibitors, including the presence of an aromatic ring and groups with hydrogen bonding capacity are reproduced by *B. caapi* phytochemicals.

Harmine is one of the phytochemicals described for *B. caapi* that had already been identified as a MAO inhibitor with reported crystal structure complexed with MAO-A [43]. Intermolecular interactions observed for harmine with MAO-A active site confirm that aromatic and hydrogen bonding features are crucial for enzyme inhibition (Fig. 6).

At least nine *K. coriacea* phytochemicals (Table 2) also reproduced the basic features found in MAO-A inhibitors. Models combining an aromatic feature with hydrogen bond acceptors were also observed when both sets of molecules are aligned (Fig. 7).

The scaffolds found in *R. rosea*, *B. caapi* and *K. coriacea* molecules were already described as privileged scaffolds for MAO inhibition, including indoles and xanthenes [44], reinforcing that these species provide a rich source of phytochemicals to inspire MAO inhibitors drug design against depression.

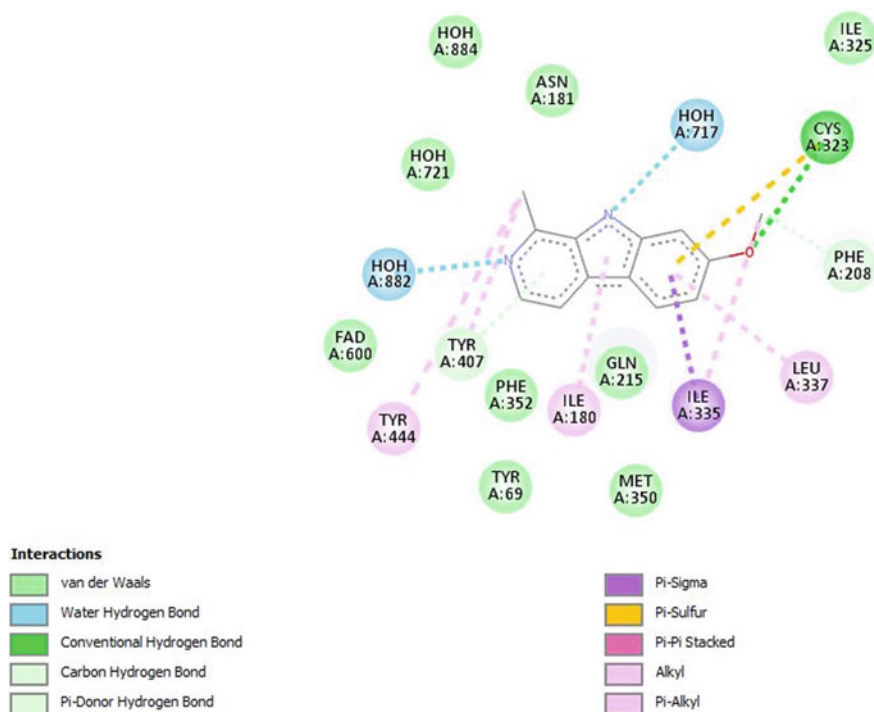


**Fig. 6** Characterization of the intermolecular interactions between MAO-A and harmine crystal structure. Figure generated with Discovery Studio Visualizer v21.1.0.20298

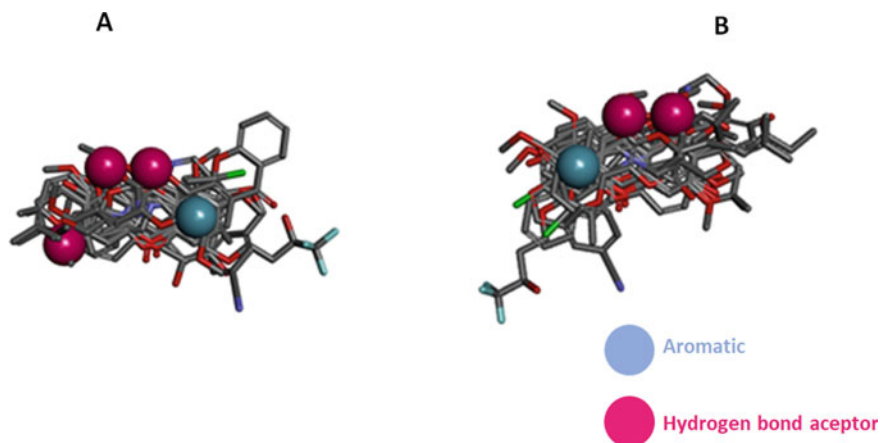


**Fig. 7** Pharmacophoric models generated after combining MAO-A selective and reversible inhibitors and *K. coriacea* phytochemicals

## 5 Conclusion

A variety of phytochemicals from *R. rosea*, *B. caapi* and *K. coriacea* medicinal plants share chemical features considered essential for the antidepressant activity of MAO-A selective and reversible inhibitors. These herb species show promising molecules with therapeutic potential justified by molecular scaffolds that can inspire the design of novel drugs to treat depression.

## References

1. WHO: Depression. [WWW Document] (2020). URL <https://www.who.int/news-room/fact-sheets/detail/depression>. Accessed 1 Jan 2022
2. Meller, F.O., Manosso, L.M., Schäfer, A.A.: The influence of diet quality on depression among adults and elderly: a population-based study. *J. Affect. Disord.* **282**, 1076–1081 (2021)
3. Soares, J.C., Rush, A.J.: Can the digital revolution improve care for mood disorders patients? *J. Affect. Disord.* **282**, 1193–1194 (2021)
4. Wei, N., Huang, B., Lu, S., Hu, J., Zhou, X., Hu, C., Chen, j., Huang, j., Li, S., Wang, Z., Wang, D., Xu, Y., Hu, S.: Efficacy of internet-based integrated intervention on depression and anxiety symptoms in patients with COVID-19. *Randomized Control. Trial* **21**(5), 400–404 (2020)
5. Wathélet, M., Duhem, S., Vaiva, G., Baubet, T., Habran, E., Veerapa, E., Debien, C., Molenda, S., Horn, M., Grandgenèvre, P., Notredame, C., D'Hondt, F.: Factors associated with mental health disorders among university students in France confined during the COVID-19 pandemic. *JAMA Netw. Open* **3**(10), e2025591 (2020)
6. Williams, O.D., Yung, K.C., Grépin, K.A.: The failure of private health services: COVID-19 induced crises in low- and middle-income country (LMIC) health systems. *Glob. Public Health* **16**(8–9), 1320–1333 (2021)

7. Hallgren, M., Kraepelien, M., Öjehagen, A., Lindfors, N., Zeebari, Z., Kaldo, V., Forsell, Y.: Physical exercise and internet-based cognitive-behavioural therapy in the treatment of depression: randomised controlled trial. *Randomized Control.* **207**(3), 227–234 (2015)
8. Wang, Y., Yang, S., Sunc, W., Shia, Y., Duand, H.: Altered functional, interaction hub between affective network and cognitive control network in patients with major depressive disorder. *Behav. Brain Res.* **298**, 301–309 (2016)
9. Brakowski, J., Spinelli, S., Dörig, N., Bosch, O.G., Manoliu, A., Holtforth, M.G., Seifritz, E.: Resting state brain network function in major depression – depression symptomatology, antidepressant treatment effects, future research. *J. Psychiatr. Res.* **92**, 147–159 (2017)
10. Mertens, L.J., Wall, M.B., Roseman, L., Demetriou, L., Nutt, D.J., Carhart-Harris, R.L.: Therapeutic mechanisms of psilocybin: Changes in amygdala and prefrontal functional connectivity during emotional processing after psilocybin for treatment-resistant depression. *J. Psychopharmacol.* **34**(2), 167–180 (2020)
11. Ogawa, S., Tsuchimine, S., Kunugi, H.: Cerebrospinal fluid monoamine metabolite concentrations in depressive disorder: a meta-analysis of historic evidence. *J. Psychiatr. Res.* **105**, 137–146 (2018)
12. Howard, P., Twycross, R., Shuster, J., Mihalyo, M., Wilcock, A.: Antidepressant drugs. *J. Pain Symptom Manag.* **44**(5), 763–783 (2012)
13. Carvalho, L.A.G., de Godoy, J.T., Baldo, A.A., Fortes, B.C.R., Lopes, D.C.S., Noia, D.M., et al.: Tratamento farmacológico da depressão em gestantes: uma revisão da literatura. *Braz. J. Heal Rev.* **3**(4), 10901–10909 (2020)
14. Pereira, M.T.C.G., Souza, F.A.M., Cardoso, F.M.: Tratamento medicamentoso para depressão e prevenção quaternária. *Rev. Bras Med. Família e Comunidade.* **16**(43), 2568 (2021)
15. Woiciekoski, J.V.B., Fronza, D., Lise, A.M.R.: Tratamento farmacológico disponível no Brasil da depressão maior: uma revisão literária. *Revista Thêma et Scientia* **8**(2), 194–224 (2018)
16. Aguiar, C.C., Castro, T.R., Carvalho, A.F., Vale, O.C., Sousa, F.C., Vasconcelos, S.M.: Drogas antidepressivas [Antidepressant drugs]. *Acta Med. Port.* **24**(1), 91–98 (2011)
17. Moragrega, I., Ríos, J.L.: Medicinal plants in the treatment of depression: evidence from preclinical studies. *Plata Med.* **87**(09), 656–685 (2021)
18. Gutiérrez, S.L.G., Chilpa, R.R., Jaime, H.B.: Medicinal Plants for the treatment of “nervios”, anxiety, and depression in Mexican Tradicional Medicine. *Braz. J. Pharmacogn.* **24**, 591–608 (2014)
19. Lee, G., Bae, H.: Therapeutic effects of phytochemicals and medicinal herbs on depression. *Biomed. Res. Int.* **2017**, 6596241 (2017)
20. de Souza, T.J.D., de Faria, P.H.A., Dantas, K.L.S., Pinto, M.N.M., Malerba, G.A., Freitas, M.S., da Silva, S.T., Mayer, P.C.M., Pereira, D.M.S., Figueiredo, C.S.S.S.: Medicinal plants as a therapeutic alternative for major depressive disorder (DMD). *Revista Eletrônica Acervo Saúde* **13**(2), e5646 (2021)
21. Derehi, F.T.G., Ilhan, M., Akkol, E.K.: New drug discovery from medicinal plants and phytoconstituents for depressive disorders. *CNS & Neurol. Disord. Drug Targ.* **18**, 92–102 (2019)
22. Panossian, A., Wikman, G., Sarris, J.: Rosenroot (*Rhodiola rosea*): traditional use, chemical composition, pharmacology and clinical efficacy. *Phytomedicine* **17**(7), 481–493 (2010)
23. Tao, H., Xu, W., Cao, J., Peng, Y., Wang, A., Pei, J., Xiao, J., Wang, S., Wang, Y.: *Rhodiola* species: a comprehensive review of traditional use, phytochemistry, pharmacology, toxicity, and clinical study. *Med. Res. Rev.* **39**(5), 1779–1850 (2019)
24. Darbinyan, V., Aslanyan, G., Amroyan, E., Gabrielyan, E., Malmstrom, C., Panossian, A.: Clinical trial of *Rhodiola rosea* L. extract SHR-5 in the treatment of mild to moderate depression. *Nordic J. Psychiatr.* **61**(5), 343–348 (2007)
25. Mao, J.J., Xie, S.X., Zee, J., Soeller, I., Li, Q.S., Rockwell, K., Amsterdam, J.D.: *Rhodiola rosea* versus sertraline for major depressive disorder: a randomized placebo-controlled trial. *Phytomedicine* **22**(3), 394–399 (2015)
26. Gao, L., Wu, C., Liao, Y., Wang, J.: Antidepressants effects of *Rhodiola* capsule combined with sertraline for major depressive disorder: A randomized double-blind placebo-controlled clinical trial. *J Affect Disord.* **15**, 265–299 (2020)

27. Rodd, R.: Reassessing the Cultural and Psychopharmacological Significance of *Banisteriopsis caapi*: Preparation, Classification and Use Among the Piaroa of Southern Venezuela. *J. Psychoact. Drugs* **40**(3), 301–307 (2008)
28. McKenna, D.J.: The healing vine: ayahuasca as medicine in the 21st century. In: M.J. Winkelman, T.B. Roberts (Eds.), *Psychedelic Medicine: New Evidence for Hallucinogenic Substances as Treatments* (pp. 21–44) (2007)
29. Tupper, K.W.: The globalization of ayahuasca: harm reduction or benefit maximization? *Int. J. Drug Policy* **19**, 297–303 (2008)
30. Riba, J., Valle, M., Urbano, G., Yritia, M., Morte, A., Barbanj, M.J.: Human pharmacology of Ayahuasca: subjective and cardiovascular effects, monoamine metabolite excretion, and pharmacokinetics. *J. Pharmacol. Exp. Ther.* **306**(1), 73–83 (2003)
31. Callaway, J.C., Brito, G.S., Neves, E.S.: Phytochemical analyses of *banisteriopsis caapi* and *psychotria viridis*. *J. Psychoact. Drugs* **37**(2), 145–150 (2005)
32. McKenna, D.J.: Clinical investigations of the therapeutic potential of ayahuasca: rationale and regulatory challenges. *Pharmacol. Ther.* **102**, 111–129 (2004)
33. Morales-García, J.A., Revenga, M.F., Alonso-Gil, S., Rodríguez-Franco, M.I., Feilding, A., Perez-Castillo, A., Riba, J.: The alkaloids of *Banisteriopsis caapi*, the plant source of the Amazonian hallucinogen Ayahuasca, stimulate adult neurogenesis in vitro. *Sci. Rep.* **7**(1), 1–13 (2017)
34. de Carvalho, J.T.G., Baldivia, D.S., Leite, D.F., de Araújo, L.C.A., Espindola, P.P.T., Antunes, K.A., Rocha, P.S., Souza, K.P., dos Santos, E.L.: Medicinal plants from Brazilian cerrado: antioxidant and anticancer potential and protection against chemotherapy toxicity. *Oxid. Med. Cell. Longev.* **2019**, 3685264 (2019)
35. Martins, C.M., do Nascimento, E.A., de Moraes, S.A.L., de Oliveira, A., Chang, R., Cunha, L.C.S., Martins, M.M., Martins, C.H.G., Moraes, T.S., Rodrigues, P.V., da Silva, C.V., de Aquino, F.J.T.: Chemical Constituents and evaluation of antimicrobial and cytotoxic activities of *Kielmeyera coriácea* Mart. & Zucc. essential oils. *Evid.-based Complement. Altern. Med.* **2015**, 842047 (2015)
36. Goulart, Y.C.F., Martins, J.V.C., Santos, A.R., Moreira, L.Y., Calixto, J.B., Cortez, D.A.G., Audi, E.A.: Involvement of serotonin in the antidepressant-like effect of extract from *Kielmeyera coriácea* stems. *Pharm. Biol.* **45**, 169–175 (2007)
37. Sela, V.R., Hattanda, I., Albrecht, C.M., de Almeida, C.B., Obici, S., Cortez, D.A., Audi, E.A.: Effect of xanthone from *Kielmeyera coriácea* stems on serotonergic neurons of the median raphe nucleus. *Phytomedicine* **17**(3–4), 274–278 (2010)
38. Qing, X., Lee, X.Y., Raeymaekers, J.D., Tame, J.R.H., Zhang, K.Y.J., Maeyer, M.D., Voets, A.R.D.: Pharmacophore modeling: advances, limitations, and current utility in drug discovery. *J. Recept. Ligand Channel Res.* **7**, 81–82 (2014)
39. Yang, S.: Pharmacophore modeling and applications in drug discovery: challenges and recent advances. *Drug Discovery Today* **15**, 444–450 (2010)
40. Seidel, T., Wieder, O., Garon, A., Langer, T.: Applications of the pharmacophore concept in natural product inspired drug design. *Mol. Inf.* **39**(11), 2000059 (2020)
41. Finberg, J.P.M.: Update on the pharmacology of selective inhibitors of MAO-A and MAO-B: focus on modulation of CNS monoamine neurotransmitter release. *Pharmacol. Ther.* **143**(2), 133–152 (2014)
42. Schneidman-Duhovny, D., Dror, O., Inbar, Y., Nussinov, R., Wolfson, H.J.: PharmaGist: a webserver for ligand-based pharmacophore detection. *Nucleic Acids Res.* **36**, W223–W228 (2008)
43. Son, S.Y., Ma, J., Kondou, Y., Yoshimura, M., Yamashita, E., Tsukihara, T.: Structure of human monoamine oxidase A at 2.2-Å resolution: the control of opening the entry for substrates/inhibitors. *Proc. Natl. Acad. Sci.* **105**, 5739–5744 (2008)
44. Tripathi, A.C., Upadhyay, S., Paliwal, S., Saraf, S.K.: Privileged scaffolds as MAO inhibitors: retrospect and prospects. *Eur. J. Med. Chem.* **145**, 445–497 (2018)

# Advances in Computational Techniques for Discovery and Development of Drugs Against Leishmaniasis, a Brief Review



Rai C. Silva, Cleydson B. R. Santos, Carlton A. Taft, Guilherme M. Silva, and Carlos Henrique Tomich de Paula da Silva

**Abstract** One-sixth of the world's population, mostly in developing countries, are infected with one or more of the neglected tropical diseases (NTD). Leishmaniasis is a group of manifestations ranging from cutaneous to most severe visceral forms, caused by protozoan parasite *Leishmania* species. It is prevalent in 98 countries and territories, with over 350 million people at risk. In the Americas, cutaneous and mucosal leishmaniasis occurs in 20 countries, being endemic in 18 of them. Depending on the species causing the infection, the disease is characterized by tissue damage such as skin, mucous membranes and internal organs. The search for safer and more effective pharmacological therapies has increased the need to identify new bioactive compounds against these diseases. High-Throughput screening strategies aided by computer programs and large virtual libraries of protein structures and chemical compounds, allow studies for the discovery and drug design of promising compounds, even in the initial stages of drug research, from docking simulations

---

R. C. Silva (✉) · G. M. Silva · C. H. T. de Paula da Silva  
Departamento de Química, Faculdade de Filosofia, Ciências e Letras de Ribeirão Preto,  
Universidade de São Paulo, Av. Prof. Do Café s/n - Monte Alegre, Ribeirão Preto São  
Paulo 14040-903, Brazil  
e-mail: [raics@usp.br](mailto:raics@usp.br)

G. M. Silva  
e-mail: [silvadm@usp.br](mailto:silvadm@usp.br)

C. H. T. de Paula da Silva  
e-mail: [tomich@cfrrp.usp.br](mailto:tomich@cfrrp.usp.br)

C. B. R. Santos  
Laboratory of Modeling and Computational Chemistry, Department of Biological and Health  
Sciences, Federal University of Amapá, Macapá, AP 68902-280, Brazil  
e-mail: [breno@unifap.br](mailto:breno@unifap.br)

C. A. Taft  
Brazilian Center for Physical Research, R. Dr. Xavier Sigaud, 150 - Urca, Rio de  
Janeiro 22290-180, Brazil  
e-mail: [catff@terra.com.br](mailto:catff@terra.com.br)

C. H. T. de Paula da Silva  
Computational Laboratory of Pharmaceutical Chemistry, University of Sao Paulo, Av. Prof. Do  
Café, s/n - Monte Alegre, Ribeirão Preto, São Paulo 14040-903, Brazil

and molecular dynamics, predictions of pharmacokinetic, toxicological profiles, and genomics analysis which allow to optimize the route for the development of new drugs. The purpose of this brief review is to provide information of new approaches to selection of appropriate computational protocol for detecting of new therapeutics for Leishmaniasis treatment.

## 1 Introduction

Leishmaniasis is a group of manifestations ranging from cutaneous to most severe visceral forms, caused by protozoan parasite *Leishmania* species. Visceral form of disease, caused by *Leishmania donovani*, characterised by prolonged fever (>2 weeks), weight loss, anemia, and splenomegaly. It is a disease prevalent in 98 countries and territories, with more than 350 million people at risk. In the Americas, cutaneous and mucosal leishmaniasis occurs in 20 countries, being endemic in 18 of them, however they present different intensities of transmission: low, medium, high, intense and very intense [1].

In the period from 2001 to 2015, 843,931 new cases of cutaneous and mucosal leishmaniasis were reported to the Pan American Health Organization, with an annual average of 56,262 cases, distributed in 17 of the 18 endemic countries [1]. *Leishmania* parasites cycle between two hosts- human and sandfly, in two distinct life stages, as flagellar promastigote or amastigote form [2].

There are no vaccines for human leishmaniasis so far, disease control depends mainly on chemotherapy treatment [3]. However, some vaccines against *L. infantum* in dogs have been reported and marketed. The bioactives of pentavalent antimony [Sb(V)], meglumine antimoniate and sodium stibogluconate—first line of choice in the current treatment of patients with leishmaniasis—, have been used since the 1940s, exhibit high toxicity and strong side effects such as cardiac arrhythmias and kidney damage [4].

Treatment-refractory patients and clinically resistant isolates have been tracked in several locations around the world [5–11]. Other secondary-line drugs such as pentamidine, amphotericin B and miltefosine also exhibit high toxicity, cross-resistance and questionable efficacy, as well as the difficulty of not being economically viable for many countries where the disease reaches severe endemic levels. In fact, there is insufficient information on their efficacy due to the lack of standardization, methodological shortcomings, and substantial differences in the characteristics of studied populations, besides other limitations [12–15].

In other way, there is caution about the environmental risks from the use of insecticides to contain the disease transmission cycles. Canids are inevitably considered to be the main reservoir of *L. infantum* and *L. chagasi* [16], which is suggested to carry the disease in several regions and main compartments. However, the outcome of these areas is questionable, and ethical issues make this alternative impractical in countries, for example, in Western Europe [17–19].



In this study, we started from Google Scholar search therapies for leishmaniasis that yielded 290,156 entries and one of the frequently used academic bibliographic sources, PubMed, recovered over 13,740 published articles (both the basis accessed on 14 January 2022); in several cases, the relationship of advantages to the chemotherapy of the disease is poor, both dog and human leishmaniasis [21, 22]. We visited the literature of findings on some pathogenic protozoa, we addressed aspects in genomics, transcriptomics, proteomics and drug discovery design of ancient and recent Antileishmania bioactives discovered.

### ***1.1 Genomic, Transcriptomic and Proteomic Approaches in Leishmaniasis***

Genomics and proteomics tools have enabled a paradigm shift in drug discovery and development protocol. Bioinformatics plays a key role in exploring genomic, transcriptomic and proteomic information to achieve epiphanies about the molecular mechanisms underlying the disease, and to identify and validate potential drug targets [23].

The technological improvement of tools such as automated DNA sequencing, microarray analysis and protein identification through genomics, transcriptomics and proteomics has produced an expressive amount of information, inducing the application of increasingly complex approaches to the analysis of the data obtained. Such data are freely accessible via the Internet in specialized databases, which are frequently revised and updated according to new experimental findings [24].

During the 1990s, several countries led the integration of international research groups to initiate several projects in search of mapping and sequencing the genomes of a range of parasites. During this period, the sequencing program of three Kinetoplastida species was initiated: *Leishmania major*, *Trypanosoma cruzi* and *Trypanosoma brucei*. From the disclosure of the genomes of those organisms, the project was named Tritryps [25, 26]. The genus *Leishmania* was represented in this initial search for the species *L. major* cepa Friedlin. In the course of further studies, several species of this genus, such as *L. braziliensis*, *L. infantum*, *L. mexicana*, had their genomes unraveled [27].

## **2 Comparative Genomics Between *L. Major*, *L. Infantum* and *L. Braziliensis***

The sequences of the *L. infantum* and *L. braziliensis* genomes were obtained by sequencing using the shotgun approach, with a coverage of five and six times, respectively. A comparative analysis was performed in order to align the sequences of these organisms against the contiguous reference sequences of *L. major* [29].

**Table 1** Comparison of characteristics of Tritryp genomes [28–30]

Parameters	<i>L. infantum</i>	<i>L. major</i>	<i>L. braziliensis</i>
haploid genome (Mpb)	32.1	32.8	32
Chromosomes – by haploid genome	36	36	35
% G + C Content	59.3	59.7	60.4
% Encoding region	44	48	48.5
Genes	8.154	8.298	8.153
Pseudogenes	41	97	161

Although these three species have a similar nucleotide content (about 33 Mb), *L. braziliensis* is genetically more distinct, as had already been observed in the difference in the number of chromosomes, see Table 1. The conservation of synteny, revealed by comparative genomic analyzes between these three species, suggests that the *Leishmania* genome is highly stable and has not undergone major rearrangements during speciation [28, 29].

A comparative analysis between the orthologous genes of the studied species revealed a high level of evolutionary conservation of the species in terms of gene content and order, even with some divergences in the number of copies of specific genes. The most distinct genome in the study (*L. braziliensis*) displays about 47 genes that were not found in the other two species, *L. infantum* has 27 specific genes and *L. major* only 05 [29, 30].

From comparative analyzes between the mentioned genomes, it is verified that the largest number of specific genes for each species studied is found at the ends of the gene groups or in the subtelomeric portions of the chromosomes. The comparison between the three *Leishmania* species showed that the gene variation is well distributed throughout the genome. Insertions, deletions and rearrangements in gene sequences may be responsible for this variation, with emphasis on the loss of function due to gene degeneration, which corresponds to approximately 80% of the total divergences between species [30, 31].

It is worth mentioning that the emergence of new genes can maintain a direct relationship with mechanisms for environmental adaptation and stimulus to the survival of the organism; in the same dynamics there may be the reappearance of some functions in genes of sequences previously identified as pseudogenes. Thus, it is necessary to use complementary methodologies, computational or not, associated with the analysis of genetic, immunological and biochemical aspects to elucidate their biological functions [28, 29].

## 2.1 Transcriptomic

Transcriptomics is a set of analyzes of gene expression - through the qualitative and quantitative study of different RNAs - whether a given organism under a given

condition or in comparison of different situations such as strains resistant or not to a given bioactive compound [30, 32]. The transcriptome and proteome of protozoan parasites, such as *Leishmania* spp., show significant differences between the different stages: amastigotes and promastigotes. These differences are related to the adaptive and survival process of the parasites to the different environments they reach in the hosts. Generally, these adaptations can encompass the expression of proteins that allow bypassing the vertebrate host's immune response or that inhibit the action of the vector's digestive enzymes [32].

After the release of the *L. major* genome, another study allowed the identification of 97.5% of the genes, using a high-density oligonucleotide microarray technique, via photolithography synthesis [32, 33], similar methodology also used to conduct research on *L. donovani* [34], *L. Mexicana* [32].

## 2.2 *Transcriptomics of the Parasite-Vector Interaction*

The interaction between *Leishmania* parasite and vector is determinant for a range of metabolic and biochemical alterations, which trigger substantial changes in the set of proteins of such microorganisms. These adaptations have also been evaluated by semiquantitative PCR, real-time PCR and EST sequencing [35–37].

Another group of collaborators sequenced 2,520 ESTs from *Lu* midgut cDNA libraries. longipalpis, fed in the absence or presence of *L. infantum* [37]. There was a significant increase in the amount of transcripts expressed in the infected vector library. The transcripts with increased expression were correlated with defense/stress/oxidation (7% versus 4% obtained from the uninfected library), ribosomal proteins (16% versus 13%), proteins involved with intracellular mobilization/cytoskeleton/cell adhesion (4% against 1%) and signal transduction (5% against 2%). The findings of these last two studies, which used different analysis techniques, support the importance of more studies focused on the different *Leishmania*-vector systems, for a better understanding of the epidemiological profile of leishmaniasis [37, 38].

## 2.3 *Proteomics*

The global analysis of protein expression in parasites of the genus *Leishmania* has been aimed at identifying and quantifying specific proteins expressed in stages of the biological cycle, proteins enriched from different cellular fractions or organelles and proteins involved in immunostimulation, among others. Such patterns of protein expression have contributed to the functional annotation of proteins and may allow the design of vaccines and the development of new drugs that target specific factors of each life stage [38–44].

The modernization of 2DE (two-dimensional electrophoresis) technology to detect and differentiate antigenic proteins present in cell extracts [45], through their protein expression patterns, different species responsible for American cutaneous leishmaniasis [46] and the development of mass spectrometry (MS) to identify proteins, boosted proteomic studies on these parasites. Thus, proteomic maps have been described for several species of *Leishmania* from the Old and New World [47–50].

The techniques used for the global evaluation of proteins in parasites include the separation by electrophoresis method in one and two dimensions, followed by detection, excision and digestion of bands or protein spots for subsequent identification by combining the peptide mass profile (PMF, Peptide Mass Fingerprinting) or by the masses of the peptide fragments obtained by MS in tandem, using electrospray ionization (ESI) as ionization sources, or even matrix-assisted laser desorption-ionization (MALDI) in combination with several masses, such as Time-Of-Flight (TOF), Quadrupole (Q), Fourier Transform (FT), Orbitrap, or their hybrids [48–51]. Other approaches, also widely used, couple peptide separation by one- or multidimensional liquid chromatography (LC) with mass analysis (LC-MS/MS).

## 2.4 Genetic Target Validation in *Leishmania*

*Leishmania* parasites have specific biological characteristics that make genetic handling difficult; have a strong tendency to aneuploidy, making genetic manipulation of essential genes unstable [52–54]. In most *Leishmania* species, RNA interference does not work, while in species in which RNAi does work, it has not yet been studied to the same extent as *Trypanosoma brucei* organisms, mainly due to the absence of an inducible system for explore the function of essential genes [55].

The promastigote phase of the *Leishmania* parasite can be located in the intestine of the insect vector, however this is not considered the relevant phase for human disease. Therefore, it is widely recommended to confirm the essentiality of a potential biological target using parasites in the amastigote phase of the *Leishmania* life cycle [56]. *Leishmania* possess a very efficient homologous recombination pathway for DNA repair that has been exploited as a basis for generating gene deletions, integrating epitope tags, or expressing transgenes [57–59].

We highlight an interesting set of experimental techniques that can be used for genetic validation in *Leishmania*:

- (I) Gene deletion via homologous substitution, where some drug resistance markers are targeted to the gene of interest by homology flanks through sequential transfections using electroporation. This strategy can be facilitated with CPISPR/Cas9 and short homology flanked cassettes in just one transfection [59–61].
- (II) Facilitated Null Mutant Methodology with Unforced Plasmid Shuffle. An episome that expresses the focus gene is transfected into cell culture or a

- nutritional supplement is administered, favoring its survival to the subsequent deletion of chromosomal alleles of the gene of interest [59–61].
- (III) Plasmid forced mixing. As in II, an episome also expressing the gene of interest is transfected into the parasite to favor the deletion of chromosomal alleles of the gene of interest [59–61].
  - (IV) Another pathway is the DiCre-inducible gene deletion. In this tactic, one allele of the target gene is replaced by a drug-selectable cassette containing a “flow” allele and, in the next step of the transfection stage, the remaining allele is then replaced by another drug resistance marker [59–61].

Drug target validation for antileishmania compounds seeks to acquire the evidence that determines whether a target molecule (protein or enzyme) is selectively inhibited by a bioactive compound resulting in the death of the organism, especially by the relationship of the target structure to a biological process parasite essential. Such evidence that helps to validate target structures may arise from genetic modifications of the pathogen or from inspection of the parasite with specific chemical probes. Well-validated targets will be supported by genetic and chemical evidence, the robustness of the validation will require the amount of evidence obtained [62, 63].

The one example for trypanosomatids being the treatment of human African trypanosomiasis with Eflornithine (difluoromethylornithine, DFMO), a compound that inhibits ornithine decarboxylase [64]. Currently used antileishmanial drugs include pentavalent antimonials, amphotericin B, miltefosine, Meglumine antimoniate, Sodium stibogluconate Paromomycin, pentamidine, see Table 2. There are not target proteins identified, despite extensive research, although amphotericin B is cited to target ergosterol-containing membranes [65, 66].

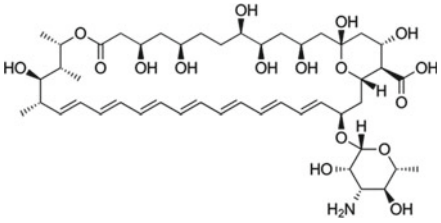
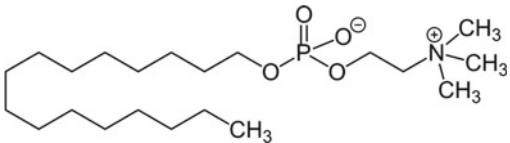
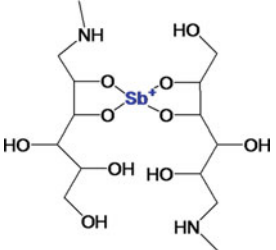
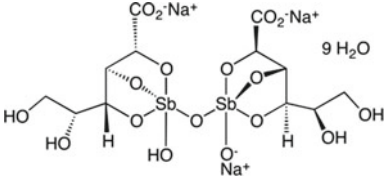
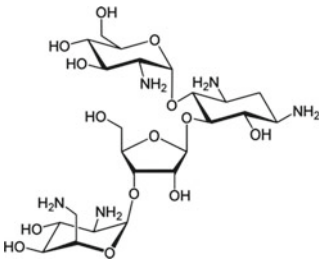
### 3 Aspects of Drug Discovery in Antileishmania Therapy

Drug discovery and development (DDD) of antileishmanial follow the protocol of identification of promising biological target, molecule candidates from natural sources, chemical libraries from pharmaceutical companies or those available for free access, or small chemical collections from university. This selection uses the range of bioactivities such as pharmacokinetic and toxicity tests (ADME/tox), pharmaceutical chemistry and improvement of “druggability” of the macromolecule and biomolecular modification of standard pharmacophoric-based ligand, in addition to improvement of other pharmacokinetic parameters of interest [74, 75].

In another way, by treating “repurposed compounds”—a protocol that can reduce human labor costs and invested resources—the procedure can be significantly reduced, even with all the pre-clinical studies performed, new safety tests and synthetic viability need to be carried out. be carried out seeking to reduce the chances that the selected compound will not fail in the clinical stage [76, 77].

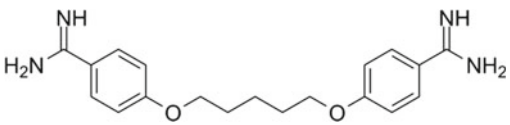
In recent decades, progress has been reasonable and, in most cases, no success is seen beyond academic results. A small number of new chemical entities have

**Table 2** Antileishmanial drugs currently used against cutaneous (C), mucocutaneous (MC) and visceral (V): indication (X) and Literature

Marketed drug	C	MC	V	Literature
			X	[67, 69, 70]
Anfotericin b	X	X	X	[3, 68]
	X	X	X	[68, 70]
Miltefosine	X	X	X	[68, 70]
	X	X	X	[68, 70, 73]
Meglumine antimoniate	X	X	X	[68, 70, 73]
	X		X	[71]
Sodium stibogluconate	X		X	[71]
			X	
Paromomycin			X	

(continued)

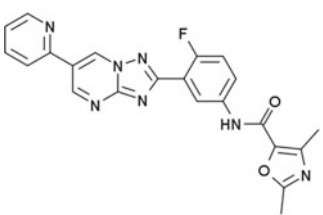
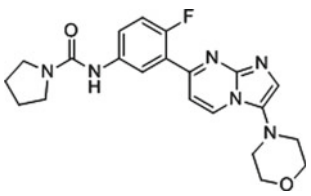
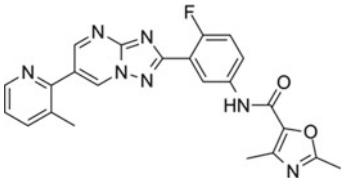
**Table 2** (continued)

Marketed drug	C	MC	V	Literature
 Pentamidine	X	X	X	[68, 72]

been identified for leishmaniasis, and no conclusive evidence has been reached in most cases when tested under real experimental conditions [78]. However, very recently hope has arisen from the discovery of new proteasome inhibitors GNF6702, GSK3494245 and LXE408, with the aid of comparative techniques, displayed in Table 3 [79–81].

Phenotypic screening of three million compounds and hit-to-lead optimization against *Leishmania donovani*, *Trypanosoma cruzi* and *Trypanosoma brucei*

**Table 3** Anti-leishmanials potential that are other clinical studies against cutaneous (C) and visceral (V) leishmaniasis: indication (X) and Year of discovery and bibliography

Hits in silico	L. Visceral	L. Cutaneous	Year and reference
 GNF6702	X	X	(2016) [80]
 GSK3494245	X	X	2019 [81]
 LXE408	X	X	2020 [82]

identified efficacious compound for VL, CL, Chagas disease and trypanosomiasis targeting parasite proteasome [82], led to the identification of a compound termed, GNF6702 with good efficacy for both cultures [82]. The reported compound inhibited the proteasome through a non-competitive mechanism and without inhibiting the mammalian proteasome or cell growth of animals of this class. Inhibitor was in advanced preclinical study and could stand out as a future treatment against leishmanial [79].

Recently, another group of scientists, independent of the previous one, reported studies of target deconvolution and cryoelectron microscopy (cryo-EM) that revealed a small molecule as a potent and selective inhibitor of the chymotrypsin-like activity of the binding of the 20 S proteasome of the parasite *L. tarentolae*, in a region between the  $\beta 4$  and  $\beta 5$  subunits [79]. Both studies present strong clues for understanding the mechanisms of interaction and inhibition of specific catalytic activity for proteasome of *Leishmania* organism.

Was reposted the optimization of GNF6702 that resulted to the selection of the termed LXE408, a molecule with interesting efficacy in murine models of visceral and cutaneous leishmaniasis that is in advanced stage human clinical trials. The same study reported high resolution cryo-MS costructure of LXE408 with *Leishmania tarentolae* proteasome in complexed with the competitive proteasome inhibitor bortezomib, which helps to clarify the non-competitive profile of the proteolytic complex inhibition for this new set of antileishmanial agents [82].

There are also promising compounds of natural origin that show interesting results, antileishmanial activity of strychnobiflavone flavonoid was recently reported against *L. infantum* and *L. amazonensis* amastigotes and promastigotes stages. Biological effect of this compound was verified because of its capacity to interfere in the parasite mitochondrial membrane; however, its mechanism of action has not yet been elucidated [82, 83].

### ***3.1 Insights Based in Bioinformatics Techniques***

In silico and bioinformatics approaches have followed a similar fate, and information on the effect of the next innovation waves (e.g., is not yet abundant enough to envision their possibilities, insofar that we are still waiting for a breakthrough in antiparasitic chemotherapy [16, 84–86].

Most of the papers are focused on a exploration of potential antileishmanial molecules, involving design and synthesis, molecular docking, dynamics simulations, ADME/Tox predictions, artificial intelligence, and automation of drug discovery, antileishmanial activity in vitro and ex vivo (59.49%; doubling the in vivo trials: 25.42%), while we are still waiting for a breakthrough in antiparasitic chemotherapy [87–91].



## 4 Considerations and Perspectives

In this chapter we visit some of the recent knowledge on techniques employed in the search for chemical compounds and structures as potential therapeutic targets. The technical modernization of genomic approaches and systems biology have contributed to the improvement of drug discovery and development platforms, resulting in promising therapies.

Synthetic chemical compounds and Products of natural origin have been demonstrating potent and low-cost alternatives against several types of leishmaniasis, especially *L. infantum* and *L. braziliensis*. Systematic and complementary strategies of genetic manipulation and cell biology, reuse of commercialized drugs, as well as the automation of high-performance screening on compound bases have favored the emergence of new paths for the identification and development of antileishmania drugs. However, instability in the potency of host responses to different pathogens still needs standardization.

## References

1. Pan American Health Organization: Leishmaniasis: Epidemiological Report in the Americas: Washington: Pan American Health Organization (2022). [www.paho.org/leishmaniasis](http://www.paho.org/leishmaniasis)
2. Sundar, S., Singh, B.: Emerging therapeutic targets for treatment of leishmaniasis. *Exp. Opin. Therap. Targ.* **22**, 467–486 (2018)
3. Croft, S.L., Sundar, S., Fairlamb, A.H.: Drug resistance in leishmaniasis. *Clinic. Microb. Rev.* **19**, 111–126 (2006)
4. Faraut-gambarelli, F., Piarroux, R., Deniau, M., Giusiano, B., Marty, P., Michel, G., Faugère, Dumon, H.: In vitro and in vivo resistance of *Leishmania infantum* to meglumine antimoniate: a study of 37 strains collected from patients with visceral leishmaniasis. *Antimic. Agent. Chemoth.* **41**, 827–830 (1997)
5. Lira, R., Sundar, S., Makharia, A., Kenney, R., Gam, A., Saraiva, E., Sacks, D.: Evidence that the high incidence of treatment failures in Indian kalaazar is due to the emergence of antimony-resistant strains of *Leishmania donovani*. *J. Infect. Dis.* **180**, 564–567 (1999)
6. Palacios, R., Osorio, L.E., Grajalew, L.F., Ochoa, M.T.: Treatment failure in children in a randomized clinical trial with 10 and 20 days of meglumine antimonate for cutaneous leishmaniasis due to *Leishmania vianniaspecies*. *Am. J. Trop. Med. Hyg.* **64**, 187–193 (2001)
7. Sundar, S.: Drug resistance in Indian visceral leishmaniasis. *Trop. Med. Inter. Healt.* **6**, 849–854 (2001)
8. Abdo, M.G., El Amin, W.M., Khalil, E.A.G., Mukhtar, M.M.: Antimony-resistant *Leishmania donovani* in eastern Sudan: incidence and in vitro correlation. *East. Mediter. Healt J.* **9**, 837–843 (2003)
9. Das, V.N.R., Ranjan, A., Bimal, S., Siddique, N.A., Pandey, K., Kumar, N.A.W.I.N., Bhat-tacharya, S.K.: Magnitude of unresponsiveness to sodium stibogluconate in the treatment of visceral leishmaniasis in Bihar. *Nat. Med. J. Ind.* **18**, 131–133 (2005)
10. Hadighi, R., Mohebal, M., Boucher, P., Hajjaran, H., Khamesipour, A., Ouellette, M.: Unresponsiveness to Glucantime treatment in Iranian cutaneous leishmaniasis due to drug-resistant *Leishmania tropic* parasites. *PLoS Med.* **3**, e162 (2006)
11. Rojas, R., Valderrama, L., Valderrama, M., Varona, M. X., Ouellette, M., Saravia, N. G.: Resistance to antimony and treatment failure in human *Leishmania* (*Viannia*) infection. *J. Infect. Dis.* **193**, 1.375–1.383 (2006)

12. Vélez, R., Gállego, M.: Commercially approved vaccines for canine leishmaniosis: a review of available data on their safety and efficacy. *Trop. Med. Int. Health.* **25**, 540–557 (2020)
13. Pérez-Victoria, F.J., Sánchez-Cañete, M.P., Seifert, K., Croft, S.L., Sundar, S., Castanys, S., Gamarro, F.: Mechanisms of experimental resistance of *Leishmaniato* miltefosine: implications for clinical use. *Drug Resist. Upd.* **9**, 26–39 (2006)
14. Seifert, K., Pérez-Victoria, F.J., Stettler, M., Sánchez-Cañete, M.P., Castanys, S., Gamarro, F., Croft, S.L.: Inactivation of the miltefosine transporter, LdMT, causes miltefosine resistance that is conferred to the amastigote stage of *Leishmania donovani* and persists in vivo. *Inter. J. Antimic. Agents.* **30**, 229–235 (2007)
15. Kumar, D., Kulshrestha, A., Singh, R., Salotra, P.: In vitro susceptibility of field isolates of *Leishmania donovani* to Miltefosine and amphotericin B: correlation with sodium antimony gluconate susceptibility and implications for treatment in areas of endemicity. *Antimicr. Agents Chemoth.* **53**, 835–838 (2009)
16. Moreno, J., Alvar, J.: Canine leishmaniasis: Epidemiological risk and the experimental model. *Trends Parasitol.* **18**, 399–405 (2002)
17. Costa, C.H.N.: How effective is dog culling in controlling zoonotic visceral leishmaniasis? a critical evaluation of the science, politics and ethics behind this public health policy. *Rev. Soc. Bras. Med. Trop.* **44**, 232–242 (2011)
18. Costa, D.N.C.C., Codeço, C.T., Silva, M.A., Werneck, G.L.: Culling dogs in scenarios of imperfect control: realistic impact on the prevalence of canine visceral leishmaniasis. *PLoS Negl. Trop. Dis.* **7**, e2355 (2013)
19. Sousa-Paula, L.C.D., Silva, L.G.D., Sales, K.G.D.S., Dantas-Torres, F.: Failure of the dog culling strategy in controlling human visceral leishmaniasis in Brazil: a screening coverage issue? *PLoS Negl. Trop. Dis.* **13**, e0007553 (2019)
20. Olías-Molero, A.I., Fontán-Matilla, E., Cuquerella, M., Alunda, J.M.: Scientometric analysis of chemotherapy of canine leishmaniasis (2000–2020). *Parasit. Vectors.* **14**, 36 (2021)
21. Olías-Molero, A.I., de la Fuente, C., Cuquerella, M., Torrado, J.J., Alunda, J.M.: Antileishmanial drug discovery and development: time to reset the model? *Microorganisms* **9**, 2500 (2021)
22. Jiang, Z., Zhou, Y.: Using bioinformatics for drug target identification from the genome. *Am. J. Pharmacogen.* **5**, 387–396 (2005)
23. Hertz-fowler, C., Hall, N.: Parasite genome databases and web-based resources. *Meth. Molec. Bio.* **70**, 45–74 (2004)
24. Degraeve, W.M., Melville, S., Ivens, A., Aslett, M.: Parasite genome initiatives. *Inter. J. Parasit.* **31**, 532–536 (2001)
25. El-Sayed, N.M., Myler, P.J., Blandin, G., Berriman, M., Crabtree, J., Aggarwal, G., Hall, N.: Comparative genomics of trypanosomatid parasitic protozoa. *Science* **309**, 404–409 (2005)
26. Ivens, A.C., Peacock, C.S., Worthey, E.A., Murphy, L., Aggarwal, G., Berriman, M., Myler, P.J.: The genome of the kinetoplast parasite. *Leishmania Major* **309**, 436–442 (2005)
27. Smith, D.F., Peacock, C.S. Cruz, A.K.: Comparative genomics: from genotype to disease phenotype in the leishmaniases. *Inter. J. Parasit.* **37**(1), 173–186 (2007)
28. Myler, P.J.: Searching the Trityp genomes for drug targets. *Drug Targets Kinetoplast. Parasit.* 133–140 (2008)
29. Alves-Ferreira, M., Guimarães, A.C.R., Cuervo, P., de Jesus, J.B.: Abordagens Genômicas, Transcriptômicas e Proteômicas Aplicadas ao Estudo de *Leishmania* spp.
30. Peters, N., Sacks, D.L.: Immune privilege in sites of chronic infection: leishmania and regulatory T-cells. *Immunolog. Rev.* **213**, 159–179 (2006)
31. Cantacessi, C., Dantas-Torres, F., Nolan, M.J., Otranto, D.: The past, present, and future of *Leishmania* genomics and transcriptomics. *Trends Parasit.* **31**, 100–108 (2015)
32. Holzer, T.R., McMaster, W.R., Forney, J.D.: Expression profiling by whole-genome interspecies microarray hybridization reveals differential gene expression in procyclic promastigotes, lesion-derived amastigotes, and axenic amastigotes in *Leishmania mexicana*. *Molec. Biochem. Parasit.* **146**, 198–218 (2006)

33. Leifso, K., Cohen-Freue, G., Dogra, N., Murray, A., McMaster, W.R.: Genomic and proteomic expression analysis of *Leishmaniapromastigote* and *amastigote* life stages: the *Leishmaniagenome* is constitutively expressed. *Molec. Biochem. Parasit.* **152**, 35–46 (2007)
34. Saxena, A., Lahav, T., Holland, N., Aggarwal, G., Anupama, A., Huang, Y., Zilberstein, D.: Analysis of the *Leishmania donovani* transcriptome reveals an ordered progression of transient and permanent changes in gene expression during differentiation. *Molec. Biochem. Parasit.* **152**, 53–65 (2007)
35. Ramalho-Ortigão, M., Jochim, R.C., Anderson, J.M., Lawyer, P.G., Pham, V.M., Kamhawi, S., Valenzuela, J.G.: Exploring the midgut transcriptome of *Phlebotomus papatasi*: comparative analysis of expression profiles of sugar-fed, blood-fed and *Leishmania*-major-infected sandflies. *BMC Genomics* **8**, 300 (2007)
36. Jochim, R.C., Teixeira, C.R., Laughinghouse, A., Mu, J., Oliveira, F., Gomes, R.B., Valenzuela, J.G.: The midgut transcriptome of *Lutzomyia longipalpis*: comparative analysis of cDNA libraries from sugarfed, blood-fed, post-digested and *Leishmania infantum* chagasi-infected sand flies. *BMC Genomics* **9**, 15 (2008)
37. Pitaluga, A.N., Beteille, V., Lobo, A.R., Ortigão-Farias, J.R., Dávila, A.M., Souza, A.A., Traub-Cseko, Y.M.: EST sequencing of blood-fed and *Leishmania*-infected midgut of *Lutzomyia longipalpis*, the principal visceral leishmaniasis vector in the Americas. *Molec. Genetics Genomics.* **282**, 307–317 (2009)
38. Bente, M., Harder, S., Wiesgigl, M., Heukeshoven, J., Gelhaus, C., Krause, E., Bruchhaus, I.: Developmentally induced changes of the proteome in the protozoan parasite *Leishmania donovani*. *Proteomics*, **3**, 1.811–1.829 (2003)
39. Drummel-Smith, J., Brochu, V., Girard, I., Messier, N., Ouellette, M.: Proteome mapping of the protozoan parasite *Leishmania* and application to the study of drug targets and resistance mechanisms. *Molec. Cell. Proteo.* **2**, 146–155 (2003)
40. Nugent, P.G., Karsani, S.A., Wait, R., Tempero, J., Smith, D.F.: Proteomic analysis of *Leishmania mexicana* differentiation. *Molec. Biochem. Parasit.* **136**, 51–62 (2004)
41. Walker, J., Vasquez, J.J., Gomez, M.A., Drummel-Smith, J., Burchmore, R., Girard, I., Ouellette, M.: Identification of developmentally-regulated proteins in *Leishmania panamensis* by proteome profiling of promastigotes and axenic amastigotes. *Molec. Biochem. Parasit.* **147**, 64–73 (2006)
42. Brobey, R.K., Soong, L.: Establishing a liquid-phase IEF in combination with 2-DE for the analysis of *Leishmania* proteins. *Proteomics* **7**, 116–120 (2007)
43. Brobey, R.K., Mei, F.C., Cheng, X., Soong, L.: Comparative two-dimensional gel electrophoresis maps for promastigotes of *Leishmania amazonensis* and *Leishmania major*. *Braz. J. Infec. Disea.* **10**, 1–6 (2006)
44. Cuervo, P., de Jesus, J.B., Junqueira, M., Mendonça-Lima, L., González, L.J., Betancourt, L., Cupolillo, E.: Proteome analysis of *Leishmania (Viannia) braziliensis* by two-dimensional gel electrophoresis and mass spectrometry. *Molec. Biochem. Parasit.* **154**, 6–21 (2007)
45. Handman, E., Mitchell, G.F., Goding, J.W.: Identification and characterization of protein antigens of *Leishmania tropica* isolates. *J. Immunol.* **126**, 508–512 (1981)
46. Saravia, N.G., Gemmell, M.A., Nance, S.L., Anderson, N.L.: Two-dimensional electrophoresis used to differentiate the causal agents of American tegumentary leishmaniasis. *Clin. Chem.* **30**, 2.048–2.052 (1984)
47. Thiel, M., Bruchhaus, I.: Comparative proteome analysis of *Leishmania donovani* at different stages of transformation from promastigotes to amastigotes. *Med. Microb. Immunol.* **190**, 33–36 (2001)
48. Acestor, N., Masina, S., Walker, J., Saravia, N.G., Fasel, N., Quadroni, M.: Establishing two-dimensional gels for the analysis of *Leishmania* proteomes. *Proteomics* **2**, 877–879 (2002)
49. El Fakhry, Y., Ouellette, M., Papadopoulou, B.: A proteomic approach to identify developmentally regulated proteins in *Leishmania infantum*. *Proteomics*, **2**, 1.007–1.017 (2002)
50. Góngora, R., Acestor, N., Quadroni, M., Fasel, N., Saravia, N.G., Walker, J.: Mapping the proteome of *Leishmania Viannia* parasites using two-dimensional polyacrylamide gel electrophoresis and associated technologies. *Biomedica* **23**, 153–160 (2003)

51. Cuervo, P., De Jesus, J.B., Saboia-Vahia, L., Mendonça-Lima, L., Domont, G.B., Cupolillo, E.: Proteomic characterization of the released/secreted proteins of *Leishmania (Viannia) braziliensis* promastigotes. *J. Proteom.* **73**, 79–92 (2009)
52. Sterkers, Y., Lachaud, L., Crobu, L., Bastien, P., Pagès, M.: FISH analysis reveals aneuploidy and continual generation of chromosomal mosaicism in *Leishmania major*. *Cell. Microb.* **13**, 274–283 (2011)
53. Dumetz, F., Imamura, H., Sanders, M., Seblova, V., Myskova, J., Pescher, P., Domagalska, M.A.: Modulation of aneuploidy in *Leishmania donovani* during adaptation to different in vitro and in vivo environments and its impact on gene expression. *MBio* **8**, e00599-e617 (2017)
54. Rogers, M.B., Hilley, J.D., Dickens, N.J., Wilkes, J., Bates, P.A., Depledge, D.P., Mottram, J.C.: Chromosome and gene copy number variation allow major structural change between species and strains of *Leishmania*. *Genome Res.* **21**, 2129–2142 (2011)
55. Lye, L.F., Owens, K., Shi, H., Murta, S.M., Vieira, A.C., Turco, S.J., Beverley, S.M.: Retention and loss of RNA interference pathways in trypanosomatid protozoans. *PLoS Pathog.* **6**, e1001161 (2010)
56. Bates, P.A.: Complete developmental cycle of *Leishmania mexicana* in axenic culture. *Parasitology* **108**, 1–9 (1994)
57. Duncan, S.M., Jones, N.G., Mottram, J.C.: Recent advances in *Leishmania* reverse genetics: manipulating a manipulative parasite. *Molec. Biochem. Parasit.* **216**, 30–38 (2017)
58. Mansoldo, F.R.P., Carta, F., Angeli, A., Cardoso, V.D.S., Supuran, C.T., Vermelho, A.B.: Chagas disease: perspectives on the past and present and challenges in drug discovery. *Molecules* **25**, 5483 (2020)
59. Jones, N.G., Catta-Preta, C.M., Lima, A.P.C., Mottram, J.C.: Genetically validated drug targets in *Leishmania*: current knowledge and future prospects. *ACS Infect. Dis.* **4**, 467–477 (2018)
60. Munjal, A., Khandia, R., Dhama, K., Sachan, S., Karthik, K., Tiwari, R., Joshi, S.K.: Advances in developing therapies to combat Zika virus: current knowledge and future perspectives. *Front. Microb.* **8**, 1469 (2017)
61. Chiurillo, M.A., Lander, N.: The long and winding road of reverse genetics in *Trypanosoma cruzi*. *Microbial Cell.* **8**, 203 (2021)
62. Field, M.C., Horn, D., Fairlamb, A.H., Ferguson, M.A., Gray, D.W., Read, K.D., Gilbert, I.H.: Anti-trypanosomatid drug discovery: an ongoing challenge and a continuing need. *Nat. Rev. Microb.* **15**, 217–231 (2017)
63. Gilbert, I.H.: Drug discovery for neglected diseases: molecular target-based and phenotypic approaches: miniperspectives series on phenotypic screening for anti-infective targets. *J. Med. Chem.* **56**, 7719–7726 (2013)
64. Priotto, G., Pinoges, L., Fursa, I.B., Burke, B., Nicolay, N., Grillet, G., Balasegaram, M.: Safety and effectiveness of first line eflornithine for *Trypanosoma brucei* gambiense sleeping sickness in Sudan: cohort study. *BMJ* **336**, 705–708 (2008)
65. Mbongo, N., Loiseau, P.M., Billion, M.A., Robert-Gero, M.: Mechanism of amphotericin B resistance in *Leishmania donovani* promastigotes. *Antimicrob. Agents Chemoth.* **42**, 352–357 (1998)
66. Saha, A.K., Mukherjee, T., Bhaduri, A.: Mechanism of action of amphotericin B on *Leishmania donovani* promastigotes. *Molec. Biochem. Parasit.* **19**, 195–200 (1986)
67. Sangshetti, J.N., Kalam Khan, F.A., Kulkarni, A.A., Aroteb, R., Patil, R.H.: Antileishmanial drug discovery: Comprehensive review of the last 10 years. *RSC Adv.* **5**, 32376–32415 (2015)
68. Brindha, J., Balamurali, M., Chanda, K.: An overview on the therapeutics of neglected infectious diseases—leishmaniasis and chagas diseases. *Front. Chem.* **9**, 622286 (2021)
69. Hamill, R.J.: Amphotericin B formulations: a comparative review of efficacy and toxicity. *Drugs* **73**, 919–934 (2013)
70. Datta, A., Podder, I., Das, A., Sil, A., Das, N.K.: Therapeutic modalities in post kala-azar dermal leishmaniasis: a systematic review of the effectiveness and safety of the treatment options. *Indian J. Dermatol.* **66**, 34–43 (2021)
71. Sinha, P.K., Jha, T.K., Thakur, C.P., Nath, D., Mukherjee, S., Aditya, A.K., Sundar, S.: Phase 4 pharmacovigilance trial of paromomycin injection for the treatment of visceral leishmaniasis in India. *J. Trop. Med.* 645203 (2011)

72. Lai, A., Fat, E.J., Vrede, M.A., Soetosenojo, R.M., Lai, A., Fat, R.F.: Pentamidine, the drug of choice for the treatment of cutaneous leishmaniasis in Surinam. *Int. J. Dermatol.* **41**, 796–800 (2002)
73. Haldar, A.K., Sen, P., Roy, S.: Use of antimony in the treatment of leishmaniasis: current status and future directions. *Mol. Biol. Int.* **2011**, 571242 (2011)
74. Chávez-Fumagalli, M.A., Schneider, M.S., Lage, D.P., Tavares, G.D.S.V., Mendonça, D.V.C., Santos, T.T.D.O., Coelho, E.A.F.: A computational approach using bioinformatics to screening drug targets for Leishmania infantum species. *Evid.-Based Complement. Altern. Med.* (2018)
75. Silva, R.C., Freitas, H.F., Campos, J.M., Kimani, N.M., Silva, C.H.T.P., Borges, R.S., Pita, S.S.R., Santos, C.B.R.: Natural products-based drug design against SARS-CoV-2 Mpro 3CLpro. *Int. J. Mol. Sci.* **22**, 11739 (2021)
76. Silva, G.M., Borges, R.S., Santos, K.L., Federico, L.B., Francischini, I.A., Gomes, S.Q., Silva, C.H.: Revisiting the proposition of binding pockets and bioactive poses for GSK-3 $\beta$  allosteric modulators addressed to neurodegenerative diseases. *Int. J. Molec. Sci.* **22**, 8252 (2021)
77. Silva, R.C., Poiani, J.G.C., Ramos, R.S., Costa, J.S., Silva, C.H.P., Brasil, D.D.S.B., Santos, C.B.R.: Ligand-and structure-based virtual screening of 16-((diiso-butylamino) methyl)-6 $\alpha$ -hydroxyvouacapane-7 $\beta$ , 17 $\beta$ -lactone, a compound with potential anti-prostate cancer activity. *J. Serb. Chem. Soc.* **84**, 153–174 (2019)
78. Geary, T.G., Woods, D.J., Williams, T., Nwaka, S.: Target identification and mechanism-based screening for anthelmintics: Application of veterinary research programs to search for new antiparasitic drugs for human indications. In: *Antiparasitic and Antibacterial Drug Discovery: From Molecular Targets to Drug Candidates*; Selzer, P.M., Ed.; Wiley-VCH Verlag GmbH & Co.: Weinheim, Germany, 3–15 (2009)
79. Khare, S., Nagle, A.S., Biggart, A., Lai, Y. H., Liang, F., Davis, L.C., Barnes, S.W., Mathison, C.J.N., Barnes, S.W., Mathison, C.J.N.: Proteasome inhibition for treatment of leishmaniasis, chagas disease and sleeping sickness. *Nature* **537**, 229–233 (2016)
80. Wyllie, S., Brand, S., Thomas, M., De Rycker, M., Chung, C.-W., Pena, I., Bingham, R.P., Bueren-Calabuig, J.A., Cantizani, J., Cebrian, D.: Preclinical candidate for the treatment of visceral leishmaniasis that acts through proteasome inhibition. *Proc. Natl. Acad. Sci. USA* **116**, 9318–9323 (2019)
81. Nagle, A., Biggart, A., Be, C., Srinivas, H., Hein, A., Caridha, D., Sciotti, R.J., Pybus, B., Kreishman-Deitrick, M., Bursulaya, B.: Discovery and characterization of clinical candidate LXE408 as a kinetoplastid-selective proteasome Inhibitor for the treatment of leishmaniasis. *J. Med. Chem.* **63**, 10773–10781 (2020)
82. Costa, E.B., Silva, R.C., Espejo-Román, J.M., Neto, M.D.A., Cruz, J.N., Leite, F.H.A., Santos, C.B.R.: Chemometric methods in antimalarial drug design from 1, 2, 4, 5-tetraoxanes analogues. *SAR QSAR Environ. Res.* **31**, 677–695 (2020)
83. Rodrigues, I.A., Mazotto, A.M., Cardoso, V., Alves, R.L., Amaral, A.C.F., Silva, J.R.D.A., Vermelho, A.B.: Natural products: insights into leishmaniasis inflammatory response. *Mediat. Inflamm* (2015)
84. Woods, D.J., Williams, T.M.: The challenges of developing novel antiparasitic drugs. *Invert. Neurosci.* **7**, 245–250 (2007)
85. Schneider, G.: Automating drug discovery. *Nat. Rev. Drug Discov.* **17**, 97–113 (2018)
86. Kaminsky, R.: Where is the breakthrough innovation for parasite control? *Trends Parasitol.* **34**, 99–101 (2018)
87. Nunes, C.M., Pires, M.M., da Silva, K.M., Assis, F.D., Gonçalves Filho, J., Perri, S.H.: Relationship between dog culling and incidence of human visceral leishmaniasis in an endemic area. *Vet. Parasitol.* **170**, 131–133 (2010)
88. Bermudi, P.M.M., Costa, D.N.C.C., Nunes, C.M., Tolezano, J.E., Hiramoto, R.M., Rodas, L.A.C., Cipriano, R.S., Blangiardo, M., Chiaravalloti-Neto, F.: Canine serological survey and dog culling ant its relationship with human visceral leishmaniasis in an endemic urban area. *BMC Infect. Dis.* **20**, 401 (2020)
89. Silva, R.C., Ferreira, I.M., Federico, L.B., Hage-Melim, L.I.D.S., Macêdo, W. J., Porto, A.L., Santos, C.B.R.D.: ADME/Tox Study and Molecular Dynamics Simulations Applied in the

- Design of New Potential GABA-AT Inhibitors. In: La Porta F.A., Taft C.A. (Eds.) *Functional Properties of Advanced Engineering Materials and Biomolecules*. Engineering Materials. Springer, Cham. [https://doi.org/10.1007/978-3-030-62226-8\\_25](https://doi.org/10.1007/978-3-030-62226-8_25)
90. Lobato, C.C., Silva, R.C., Sanches, V.H., dos Santos, K.L., dos Santos, I.V., Carvalho, A.S.D., Santos, C.B.: Application of chemometric techniques for validation of computational methods applied in molecular modeling of 6 $\alpha$ -hidroxycoumarin-7 $\beta$ , 17 $\beta$ -lactone with antiproliferative activity in Leukemia cells. *J. Comput. Theor. Nanosci.* **17**, 4855–4865 (2020)
  91. Pinto, V.D.S., Araújo, J.S., Silva, R.C., Da Costa, G.V., Cruz, J.N., Neto, D.A., Junior, M.: In silico study to identify new antituberculosis molecules from natural sources by hierarchical virtual screening and molecular dynamics simulations. *Pharmaceuticals* **12**, 36 (2019)

# Lead Optimization in Drug Discovery



**Mariana Pegrucci Barcelos, Suzane Quintana Gomes,  
Leonardo Bruno Federico, Isaque Antonio Galindo Francischini,  
Lorane Izabel da Silva Hage-Melim, Guilherme Martins Silva,  
and Carlos Henrique Tomich de Paula da Silva**

**Abstract** The Discovery of a drug with pharmaceutical actions goes through several stages, such as Hit to Lead and Lead Optimization. Hit to Lead comprises the phase in which small molecules are evaluated about their activity and their interaction with the target to generate lead compounds. Data analysis such as potency, selectivity, and other physicochemical properties play an important role in this step, as they form the basis for optimizing the next leads. The final stage of drug discovery is called Lead Optimization, whose function is to maintain or improve the desired properties present in selected compounds and, at the same time, reduce any deficiencies found in their structure. Studies of modifications in compounds for improvement can be carried out in experimental ways such as magnetic resonance and mass spectrometry or also by computational methods. Computational methods used in this phase include pharmacophore studies, molecular docking, molecular dynamics, QSAR, among others. This chapter reports the computational techniques used for the lead optimization stage to present which paths can be followed and used for the rational discovery of new drugs.

---

M. P. Barcelos (✉) · I. A. G. Francischini · C. H. T. de Paula da Silva  
School of Pharmaceutical Sciences of Ribeirão Preto, University of São Paulo, Av. do Café, s/n,  
Ribeirão Preto, São Paulo 14040-903, Brazil  
e-mail: [mpbarcelos@usp.br](mailto:mpbarcelos@usp.br)

S. Q. Gomes · G. M. Silva · C. H. T. de Paula da Silva  
Departamento de Química, Faculdade de Filosofia, Ciências e Letras de Ribeirão Preto (FFCLRP),  
University of São Paulo, Av. Bandeirantes, Ribeirão Preto, São Paulo 3900, 14090-901, Brazil

L. B. Federico  
Computational Laboratory of Pharmaceutical Chemistry, School of Pharmaceutical Sciences of  
Ribeirão Preto, University of São Paulo, Av. do Café, s/n, Ribeirão Preto, São Paulo 14040-903,  
Brazil

L. I. da S. Hage-Melim  
Laboratory of Pharmaceutical and Medicinal Chemistry (PharMedChem), Federal University of  
Amapá, Rodovia Juscelino Kubitschek, km 02, Macapá, Amapá 68903-419, Brazil

## 1 Introduction

Drug Discovery is the multi-step process in which new drug candidates are discovered. One of the steps is the Lead Generation or Hit to lead, that consists of the stage in which small molecules selected after several steps are evaluated and, often optimized, to become lead compounds [1]. Hit molecules are compounds that show the desired activity about other molecules being screened and this activity is confirmed after a test.

The lead generation process begins with the screening stage by High Throughput Screening (HTS) or virtual (VS), in which these hits are selected and evaluated to identify the most promising compounds. Then, these molecules undergo a limited optimization, obtaining compounds with the most adequate pharmacokinetic properties for the research [2]. Through these optimizations, hits are improved about the interaction with the receiving target when compared to the primary hit and this improvement can reach the order of magnitude of nanomolar [1].

After the Hit to Lead step, the compounds go through another step called Lead Optimization [3, 4]. The purpose of this step is to maintain previously acquired favorable pharmacokinetic properties or improve them [2], in addition to making any structural modifications to the Lead compound that aid in the interaction with the target [5].

Several techniques, both experimental and computational, can be used to improve a molecule. Among the most used experimental techniques, we can mention NMR-Based Screening, Mass-Spectrometry-Based Methods, Crystallography-Based Approaches, HST, among others.

Although experimental techniques have been used for a long time in the process of discovering a molecule, computational techniques have been gaining more and more space. The advantages of computational over experimental ones are related to money and time employed, and in the first one, these two factors are smaller [6].

In this chapter, we will focus on the computational methods used for the Lead Optimization step and we will divide them into three large groups: structural studies, conformational studies, and property and activity studies. The first group comprises the pharmacophore, fragmented, and bioisosterism techniques. The second is composed of molecular docking and molecular dynamics. Finally, the last group comprises structure/activity studies (QSAR), Machine Learning/Deep Learning, and ADMETox studies.

## 2 Computational Methods Used in Lead Optimization

Over the past few decades, computational methods have played a large role in drug discovery and development. Its great role is to avoid the high expense with the development part and also to help in getting a compost lead easier. Below we will



list some computational methodologies that can be used in the Lead Optimization step within the Drug Discovery pipeline.

## **2.1 *Fragment-Based, Pharmacophore and Bioisosterism***

### **2.1.1 Fragment-Based**

The use of fragment-based drug discovery (FBDD) started over 20 years ago, being applied in both industry and academia [7]. The advantage of FBDD over HTS (High-Throughput Screening) is the possibility of the use of small libraries with fragments that represents a larger number of drug-like compounds [8]. The principle is based on the fragments that exhibit lower or over potency are further designed to improve the ligand efficiency according to the protein structure to improve the potency to the maximum [9].

To improve the potency of selected fragments, different strategies can be used: growing by design, fragment linking, or merging [7]. After the selection and application of the fragment modification strategy, the evaluation of the groups effect and modifications made to the structures carried out quantitatively, assess whether there was an increase in the affinity between the new compound or if the modifications only led to a non-specific or redundant volume increase. That is, it is verified whether the modifications contributed to the increase in the compound's affinity and, consequently, the fragment's potency, or if the modifications only resulted in a compound with a larger chemical structure without affinity gain about the biological target [10].

In FBDD, the most used strategy is fragment growth, that is, modifications are made to the fragment that increases its size. In this case, information on the structure of the biological target and the binding mode of the fragment to the binding site can be used to direct the synthesis of chemical structures that can interact with this structure.

Fragment linking is based on the process of joining two fragments that link in two different parts of the linking site, through a chemical linker or spacer. In this case, the size and type of spacer will depend not only on the distance between fragments at the site but also on how flexible the linker will be, as it is expected that the spacer implementation will not interfere with the original binding mode of the fragments. Although the addition is a quick way to get new compounds from fragments, often ADMET properties are not considered, resulting in compounds with low permeability due to the high number of rotatable bonds [11, 12].

Fragment merge is a different approach when you have two fragments, but in a situation where they partially occupy the same region of the binding site. In this case, the strategy must be more refined, as it is necessary to understand the parts of the molecules that overlap to create a nucleus that, in addition to fitting into the active site, is also able to improve the ligand's potency when compared to the two fragments initials. Although this type of approach is already established in medicinal chemistry,

it needs high-quality structures to follow in the optimization process, which becomes a disadvantage [7].

The use of *in silico* strategies can also be applied to fragment-to-lead optimization. For example, the use of hot spots at known binding sites can predict which regions of the pocket contribute to the binding structure interaction. Specifically, when you have a hit fragment already known and its binding mode at the binding site, a mapping of the subregions of the binding site around the fragment is performed, using organic probes with different functional groups, shapes, sizes, and polarity, to find regions in this space that can interact favorably with these probes [13]. From the selection of the most favorable probes, the lead compound design process begins, containing the functional groups containing the characteristics indicated by the probes in that region.

The fragment-to-lead process can also be done using SAR and docking techniques. The application of the use of SAR is performed by screening a database of bioactive compounds, commercial or not, applying a screening based on similarity, shape, pharmacophore, or fingerprints to find more complex structures containing the desired hit fragment. This technique can be combined with docking, which allows a more in-depth analysis of the binding pose of the sorted compounds at the binding site, making the selection of more promising compounds containing the desired fragment more efficient. Finally, the molecular docking technique should always be used in combination with other techniques, as in the previous example, as the main function of docking is to predict the position, orientation, and binding scores of molecules at their binding sites [14].

De novo design, specifically de novo design software, is based on knowledge of the fragment binding mode, which is applied in the proposition of new compounds to increase binding affinity. This software applies the same F2L strategies mentioned above. For the most common strategy used in F2L, growing by design, *Autogrow* software uses genetic algorithms to grow the molecule around its fragment, in addition to more modern versions relying on synthetic accessibility and the druggability of the generated molecule analyses [15, 16]. The *GANDI* software uses genetic algorithms to connect different fragments, keeping their predefined poses due to their interactions at the binding site, and inserting fragments of bindings calculated through a scoring function based on a linear combination of force-field binding energy and similarity measures [17]. *BREED* software applies the same principle of fragment merge, that is, it merges different fragments by aligning the 3D coordinates of two fragments and recombining them to generate new molecules. The difference is that the software doesn't just merge the same region partially occupied by the binding site but can recombine the fragments in a strategy called fragment shuffling [18].

### 2.1.2 Pharmacophores

Paul Ehrlich is recognized for coining the concept of pharmacophore: a molecular structure that carries (*phoros*) the essential characteristics responsible for the biological activity of the drug (*pharmacon*), a definition that would be maintained until the

revision of this concept by Peter Günd [19]. According to Peter Günd, a pharmacophore is “a set of structural features in a molecule that is recognized at a receptor site and is responsible for that molecule’s biological activity” [20]. Günd, Wipke, and Langridge were the first to develop software capable of recognizing pharmacophoric patterns in a set of molecules, the *MOLPAT* [21], and in 1989 Güner et al. released the first commercial software with the 3D searching system, *MACCS-3D* [22].

Pharmacophores in the lead optimization process are based on the same principle as the other optimization methods: use the chemical structure of different compounds to optimize the binding affinity and pharmacokinetic properties of the compound. There are two methods of generating pharmacophores: structure-based and ligand-based.

The ligand-based methods in pharmacophore modeling use information (*features*) obtained from a compound or a set of compounds with known activity on a particular biological target to identify the common set of structural features among them. Then, these characteristics are used to identify other similar compounds that are present in the database. Through the ligand-based method, different approaches can be used, such as similarity and substructure search, pharmacophore matching, or 3D shape matching [23]. As pharmacophore models are connected to the structure–activity relationship, complementary analyzes, such as docking, support the analysis and selection of new compounds that interact better with the binding site. There is a vast list of computer programs for modeling pharmacophores [24], being DISCO [25] (Distance Comparisons) and eGASP [26] (Genetic Algorithm Similarity Program) from Tripos, and HipHop [27] from Accelrys, software used in ligand-based approaches. Software developed based on statistical means (3D-QSAR) are CoMFA [28] (Comparative Molecular Field Analysis), Apex-3D [29], and HypoGen [30].

The structure-based method in pharmacophore modeling is based on the complementary analysis of the chemical characteristics of the binding site and their spatial relationships, followed by the creation of a pharmacophore model containing the main selected characteristics. In the use of the structure-based method in pharmacophore modeling, it is important to know a vast number of models can be generated and that not all of them will describe the real characteristics of the binding site, therefore the models must be analyzed with caution. There are two types of methods used in structure-based pharmacophore modeling: based on the macromolecule–ligand or the macromolecule–ligand-based method is used to determine the main sites of interaction between the ligand and the binding site. Examples of software that use this type of approach are *LigandScout* [32], *Pocket v.2* [33], and *GBPM* [34], but for these programs to be used the 3D structure of the structure–ligand complex must be known. If there is no 3D structure of the structure–ligand complex, the macromolecule-based approach is applied. For example, this method can be found in Discovery Studio, which converts the interaction maps into the binding site pharmacophoric characteristics of the catalyst: H-bond acceptor, H-bond donor, and hydrophobic interaction. As this approach can lead to a vast number of pharmacophore models, Barillari et al. proposed the use of hot-spots-guided receptor-based

pharmacophores (HS-Pharm) [35], which is a knowledge-based approach to identify ligand-anchoring atoms in protein cavities. Tintori et al. [36] also developed a computer program capable of generating receptor-based pharmacophoric models. In this case, the *GRID* software calculates the minimum energy pharmacological points for GRID Molecular Interaction Fields (MIFs) at the binding site and converts these points into pharmacophoric features.

Once the pharmacophore model, also called the pharmacophore hypothesis, is obtained, it can be applied in a virtual screening using a database with 3D structures to select potential new ligands with chemical characteristics similar to the model. This technique is called “Pharmacophore-model-based virtual screening”. The disadvantage of using this technique is that if there is any failure during the process of obtaining the pharmacophore hypothesis, the results obtained from the screening will have a higher false-positive rate. Therefore, it is necessary that the pharmacophore model needs to be validated by different methods.

### 2.1.3 Bioisosteres

Bioisosterism is understood as the change of a part of the structure of a bioactive molecule by a substructure that has a similar shape and physicochemical properties. Bioisosterism is applied in the lead generation and optimization phase to improve the pharmacokinetic and pharmacodynamic properties of a compound with known biological activities, in addition to eliminating toxicity effects. Furthermore, bioisosteric substitution can be used in synthetic steps that are difficult to access the desired structure, as well as in the modification of cores that are already protected by patents.

According to Alfred Burger [37], the term bioisosteres refers to compounds or groups that have similar shapes and volumes, a similar distribution of electrons, and similar physicochemical properties. Furthermore, bioisosteres should exhibit similar biochemical behavior and result in similar biological effects. Bioisosteric replacement is based on the selection of bioisosterically suitable groups can be done through the knowledge acquired by the medicinal chemist or using *in silico* tools, so that in both cases it is expected to identify new groups that have a balance not only between shape and size but also in electronic, hydrophobic and hydrogen bonding properties. There is also scaffold hopping, whose objective is to replace the central core of a molecule with a structurally different unit, unlike the bioisosteric replacement that only alters the molecule's functional groups. In other words, scaffold hopping is not used to improve the biological interactions but change the properties of the molecule by modifying the structure of the ligand. Consequently, scaffold hopping is more commonly applied in lead generation steps than in lead optimization steps.

An efficient way to identify bioisosteres based on their properties is to use *in silico* methodologies capable to calculate a variety of descriptors to be used in bioisosteric replacement. A well-known descriptor-based method is called QSAR (Quantitative Structure–Activity Relationship), used to create congeneric series with one position of alteration characterized as relevant in drug design [38]. These descriptors

can also be more detailed and able to quantify the 3D volume overlap and electrostatic distribution of the desired group, acting as complementary descriptors with traditional 2D topological descriptors [39]. A different approach that can be applied in the search for bioisosteres is using a database such as *BIOSTER*, *ChEMBL*, and *SwissBioisostere*. The *BIOSTER* [40] database contains bioisosteric analogs, beyond structurally and biologically related pairs of molecules such as prodrugs, peptide mimetics, and others. *ChEMBL* [41] is an open large-scale bioactivity database, including chemical, bioactivity, and genomic data to be explored by researchers. *SwissBioisostere* [42] provides the molecular substructural replacements and, also, how these replacements are performed from an activity point of view.

As mentioned, the use of bioisosterism in drug discovery can be performed in different ways according to the objectives of the work, but always based on rational approaches. It can be done based on knowledge of medicinal chemists or in silico strategies that involve software, databases, and sets of descriptors. However, if the chosen strategy involves in silico methods, it is important to understand how these programs are validated to ensure that structure–activity relationships are maintained for successful bioisosteres predictions.

## 2.2 Conformational Studies

### 2.2.1 Molecular Docking

Molecular docking is the method used to predict the preferential orientation of a ligand on a receptor, be it a protein or a nucleic acid molecule, in the formation of a stable complex [43]. This orientation can be used to understand the binding affinity between the two molecules, in addition to the formation of their complex, which is useful information for lead optimization, as can be seen in several studies [44] and help in the rational development of medicines, in addition to clarifying biochemical processes [44, 45].

To perform docking simulations, a receiver structure is required. Generally, this structure, when it is a protein, is determined by techniques such as x-ray crystallography, NMR spectroscopy, or cryoelectron microscopy and is available in databases such as Protein Data Bank (PDB) [46] and the Worldwide Protein Data Bank (wwwPDB) [47].

There are other databases with information about link affinities such as PDBIND [48, 49], PDL (27–8), AffinDB (27–9), and BindingDB [50]. Often when it is not possible to obtain the structure by biophysical techniques, one way out is to build a model through homology modeling [51] or threading.

The formation of the complex between the receptor and the ligand provides diverse information at the atomic level about the interaction between molecules, being extremely important for the optimization of compounds [52]. The conformation proposed by docking can be very different from that obtained experimentally,

especially when dealing with a high-flexibility ligand with a small energy barrier between the different conformations [53].

This equality between experimental and *in silico* conformations becomes even more complicated when the binding pocket is composed of amino acids with flexible chains or even the presence of loops in the active site [54].

Protein structure and several ligand banks are the main components of a molecular docking study, but the success of the program to be used depends on the search algorithm and also on the scoring function [55].

The algorithm in docking programs has the function of helping to quickly obtain a new lead compound (when used in virtual screening) or to reproduce the experimental conformation as accurately as possible (when used for validation of experimental data) [56]. There are several search algorithms available such as Incremental Construction [57, 58], Genetic Algorithm [59, 60], Monte Carlo [61], among others; and each has a set of specific search parameters and methods.

Scoring functions are mathematical approximation methods that assess intermolecular binding affinity or binding free energy, to optimize and classify the results to obtain the best guidance after the simulation [62]. There are several scoring functions available [63–66], several of which have been compared and their accuracy tested [67, 68].

A strong relationship between experimental biological activity and predicted binding strength by scoring function was hardly noticed. To overcome this problem, several other approaches have been created [69], but none of them can be applied to molecular docking methodology due to the high demand for computational resources.

The scoring functions are composed of several terms that describe different interactions between the analyzed molecules and their contribution to the overall binding force. However, some terms cannot be accurately predicted and others are still in preliminary studies and are not included in the scoring function [70].

Although it has these disadvantages, molecular docking associated with scoring remains one of the most used tools for obtaining and optimizing hits [71]. There are reports in which docking scores have been successfully used to identify active compounds through virtual screening [72] and filtering out those that did not fit the binding site.

*In silico* optimization of the hit, the compound aims to obtain compounds with improved activities that can be used for final tests. This optimization occurs through the analysis of ligand positions and the interactions performed with the receptor.

Based on other published studies [73, 74], Enyedy and Egan set out to analyze the relationship between molecular docking scores and experimental IC<sub>50</sub> data. They selected three kinases as targets (insertion domain protein receptor kinase—KDR, cyclin-dependent kinase 2—CDK2, and Abelson tyrosine kinase—C-ABL) and over 4300 compounds measured for each kinase [71].

At the end of the study, they concluded that docking scores are useful for optimizing the ligand at the binding site, to reproduce the binding modes observed experimentally. However, these scores were not able to classify the order of compounds and did not always differentiate active from inactive molecules [71].

Thus, although it presents several disadvantages, molecular docking can be used as a methodology to propose optimizations in compounds to obtain the one that will be part of the final tests and, perhaps, gives rise to a new drug.

### 2.2.2 Molecular Dynamics

Several crystallographic studies demonstrate the importance of the flexibility of the molecular target studied and its binding with the ligand, however, this whole process presents a high cost and extensive work. In this way, computational techniques, also called simulations, began to be developed to predict the movements of biomolecules [75], and one of these techniques is molecular dynamics.

Molecular dynamics is a simulation technique developed in the late 1970s [76]. As it is a simulation technique, it aims to obtain information about the behavior of a certain system or process [77]. In this specific case, this technique is used to obtain data related to structural and thermodynamic properties of a biomolecule [78] using simple approximations based on Newtonian physics to simulate atomic movements and reduce computational complexity.

The first step in a molecular dynamics simulation is to obtain the biomolecule. As described above, when the biomolecule to be used is a protein or enzyme, its resolved experimental structure can be obtained from the Protein Data Bank [79] or through techniques such as homology modeling or comparison modeling [80].

In possession of the biomolecule structure, the forces acting on each of the atoms in the system are estimated based on the interactions between bonded and non-bonded atoms [81]. Chemical bonds, atomic angles, and dihedral angles are modeled using simple virtual springs and a sinusoidal function. On the other hand, van der Waals interactions are modeled using the Lennard Jones potential [82] while electrostatic interactions are modeled according to Coulomb's Law [83].

Energy terms are parameterized to fit quantum mechanical calculations and spectroscopic data to reproduce the real behavior of real molecules [81]. Simply put, they identify suitable van der Waals atomic radii, the best partial atomic charges used to calculate electrostatic interaction energies, and so on. These parameters are called the force field [83].

There are several force fields used in molecular dynamics such as AMBER [81, 84], CHARMM [85], and GROMOS [86]. Although they present similar results, the big difference between the aforementioned force fields is related to their parameterization.

After calculating the forces acting on each of the atoms in the system, their positions are moved according to Newton's laws. Simulation time is advanced and the process has been repeated millions of times. Due to the need for several calculations, molecular dynamics simulations are performed on supercomputers or clusters of computers with several processors in parallel [83].

Several studies comparing molecular dynamics simulations with experimental data are being used to validate the technique [87] and many show agreement between

experimental and computational measurements [88–90]. Although there is success in the use of this computational technique, it is still limited by two challenges [91].

The first challenge is the computational cost since simulation routines longer than a microsecond in duration are prohibited and lead, in many cases, to a small sampling of conformational states. The second challenge is that the force fields used require further refinements, as they are poorly suited to systems where quantum effects are important, for example, when transition metals are involved in the bonding [91]. To overcome this last challenge, some researchers have introduced quantum mechanical calculations into classical molecular dynamics force fields [92].

Simulations have played an important role in Drug Design studies as they are excellent tools for identifying sites other than the one already known [93–95]. One of the cases that made use of this technology in drug development based on the integrase of HIV, a biomolecule that was not believed to be a good target [93]. In this case, the simulation showed a possible region for coupling molecules that were not evident in the available crystal structures. Subsequently, through X-ray crystallography, it was shown that the inhibitors bound at this site. This fact led to new experimental studies at Merck and Co [96] and, resulting in the production of a highly effective antiretroviral drug, Raltegravir.

Another important role played by molecular dynamics is the identification of allosteric sites that can be used as sites for the discovery of new drugs. In a study carried out by Ivetac and McCammom [97], simulations were performed on human  $\beta 1$  and  $\beta 2$  adrenergic receptors, and five potential allosteric sites were identified, not evident in any of the existing crystal structures.

Therefore, although it presents some challenges, molecular dynamics simulations are extremely useful to provide information and data where experimental methods cannot. In addition, the advancement of computational power and algorithm design will play a promising role in the design of new drugs.

### ***2.3 Structure–Activity Studies, Machine Learning/Deep Learning, and ADMETox Studies***

One of the most used tools during Drug Discovery processes is the understanding of the structure–activity relationship of a given compound, that is, the study of the effects that this particular ligand analyzed can cause during the interaction with its biological target, and from their understanding rationalize the factors that contribute positively or negatively to this interaction. The interactions of a molecule with its biological target can be hydrophobic, such as Van der Waals, electrostatic, and hydrogen bonding interactions [98].

Thus, for compounds to present therapeutic activity, they must present a certain complementarity to their biological target, where functional groups of the molecule interact with specific residues in the catalytic cavity of the receptor. The greater the



complementarity, the greater the affinity of the molecule structure by the receptor and potentially the greater it's biological activity [98, 99].

To describe the types of interactions between a ligand and its biological receptor, an extensive set of molecular properties can be used since these properties are directly related to the intermolecular forces involved in the ligand-receptor interaction, as well as to the properties of transport and distribution of drugs. Molecular descriptors represent an important tool to predict the properties of substances, classify chemical structures, or look for similarities between them [98–100].

With the advancement of technologies aimed at Drug Discovery, the amount of data generated increased, creating libraries with thousands of structures that could be studied. With that, it was necessary, from chemometrics, the creation of descriptors that allowed computationally the analysis of large amounts of molecules and made it possible to establish a relationship between structure–activity. These descriptors created were: (1) conformational, (2) electronic, (3) information content, (4) quantum mechanics, (5) receptor-related, (6) shape-related, (7) spatial, (8) thermodynamic, and (9) topological, which are currently widely used by computational chemistry in Drug Discovery studies, as a way of understanding the action mechanism of a series of compounds and also as filters for compounds with uninteresting values and properties [99, 101, 102].

There is also a tool to quantify the structure–activity relationship (QSAR), widely used in Drug Discovery processes, which allows quantifying the contribution of each functional group of the molecule to its biological activity, making this correlation through mathematical equations or statistical analysis of data regarding the physicochemical properties of the ligand with its biological activity against the target of interest. All QSAR analyzes are based on the assumption of linear additive contributions of the different structural properties or characteristics of a compound to its biological activity, provided that there are no non-linear transport or binding dependencies on certain physicochemical properties [103, 104].

In this way, QSAR models make it possible to perform, using computational chemistry techniques, the analysis of large sets of molecules from previous experimentally obtained data, becoming a quick and less expensive alternative to performing biological tests in large compound libraries, which requires time, animals and even the synthesis of compounds to be tested [104].

QSAR models can be classified as based on dimensionality from their structural representation or the way each of the descriptor values is derived, represented in Table 1 [104]:

The models can still be classified according to the chemometric method used to quantify the structure–activity relationship, being divided into two categories: Linear Methods, which include linear regression, multiple linear regression, partial least-squares, and main component analysis/regression. The other category is non-linear methods, consisting of artificial neural networks, k-nearest neighbors, and Bayesian neural nets [104, 105].

In this way, with the advancement of technology in the computational and chemoinformatics area, QSAR models have a fundamental role in the search for

**Table 1** Classification of QSAR models based on dimensionality

1D-QSAR correlating activity with global molecular properties like pKa, log P, etc
2D-QSAR correlating activity with structural patterns like connectivity indices, 2D-pharmacophores, etc., without taking into account the 3D representation of these properties
3D-QSAR correlating activity with non-covalent interaction fields surrounding the molecules
4D-QSAR additionally includes an ensemble of ligand configurations in 3D-QSAR
5D-QSAR explicitly represents different induced-fit models in 4D-QSAR
6D-QSAR further incorporating different solvation models in 5D-QSAR

*Source* The authors

new bioactive compounds, being used as filters in virtual screening studies, facilitating the search for compounds with high and low potency toxicity. As no compound needs to be synthesized before computational evaluations by QSAR models, the tool also proves to be important in reducing the work involved in Drug Discovery studies, as well as costs, making it increasingly used [106].

### 2.3.1 Machine Learning/Deep Learning

In recent decades, the advancement of technology in the field of biological, chemical, and computer sciences has generated a huge increase in the amount of data available to be analyzed, which has brought to light a need: the ability to organize and interpret this information with them to generate new outcomes in drug discovery. The creation of GPUs (Graphics Processing Unit) allowed an advance in the area of *Drug Discovery*, with the wide use of Machine Learning techniques [107].

Machine Learning (ML) is one of the branches of Artificial Intelligence (AI) that consists of creating algorithms that can learn from data provided by the programmer to distinguish patterns or sequences when faced with large volumes of information. There are two techniques used in ML: Supervised learning, where training models are developed in which the machine is taught from a given dataset to be able to predict future data values, or continuous variables. In this way, supervised models are effective for classifying data and predicting future values, in addition to allowing the understanding of variables that most influence the processes studied. There is also unsupervised learning, where the machine is used to perform exploratory analyses, being able to put together data sets in a way that makes sense to the user and that the user would not be able to see this pattern. Thus, unsupervised models can identify hidden or intrinsic patterns in large sequences of data, and use them to perform the grouping of information in a way that allows its use [108–110].

In the area of Drug Discovery in the last decade, there has been a significant increase in the use of ML techniques for the discovery of new bioactive molecules, largely due to the amount of information generated and the increase in the chemical and biological space available. The most common way of using ML algorithms is to provide a data series of compounds with biological activity already known to

the machine, as a training set: In this way, the algorithm will be able to identify variables that influence or not the activity biological, and when placed in front of a large database it will be able to distinguish potential active compounds from inactive ones. Many pharmaceutical industries have been adopting the use of ML in their projects to search for new molecules and biological targets, which together with the advancement of technology in the computational area makes the area extremely relevant in the coming years [108, 110–112].

Still, with the advancement of AI techniques, the Deep Learning (DL) approach has also been widely used and is constantly evolving. DL is a technique derived from artificial neural networks and allows the creation of systems and algorithms that can detect patterns from large training data sets labeled or without labels. DL can discover several layers of patterns in datasets that have no organization, making it a tool that acts in a high degree of complexity. The application of DL during the steps of Drug Discovery is vast, including the prediction of bioactivity of compounds, prediction of synthetic pathways, prediction of tertiary structures of proteins in addition to the analysis of biological images [107, 108, 113].

Despite the great advancement of ML and DL techniques in the field of Drug Discovery, there are still some challenges to overcome: There is a great need for experimental data to build predictive models. This need for experimental data also becomes a challenge when it is known that experiments can present inconclusive or inconsistent data, in addition to the cost of performing and repeating experiments. These challenges are likely to be overcome in the coming years, with the engagement of chemists, bioinformatics, and programmers, as well as experimentalists coming together to propose solutions to challenges that are not yet solvable [111, 113, 114].

### 2.3.2 ADMET Studies

Effective drugs with a high level of safety for users come from a combination of excellent pharmacodynamic (PD) and pharmacokinetic (PK) properties, including high affinity and selectivity to the biological target as well as adequate absorption, metabolism, excretion, and low toxicity (ADMET).

In the past, in Drug Development processes, many drugs with potential ended up failing in advanced stages of research, for presenting one or more pharmacokinetic properties below the expected standards, or even for presenting toxicity not predicted during the initial trials. This scenario began to change with the advent of chemoinformatics in the early 1950s and more specifically in the 1990s, where Lipinski et al., provided an enormous contribution to computational models being able to predict pharmacokinetic properties of structures from their properties. physical–chemical [115, 116].

From the 2000s, when we entered the so-called big data era, with the emergence of huge databases that compile thousands of molecules that can be used in Drug Discovery research, there was a need for bioinformatics and data science., the creation of software and algorithms capable of predicting and filtering this massive amount

of structures occurs, providing a basis for the next stages of research and avoiding failures in more advanced stages of the process [115].

Initially, the developed software, such as QikProp, PreADMET, admetSAR, were able to, from the determination of the physicochemical properties of the provided structures, make a correlation with pharmacokinetic parameters, providing estimates of values such as Log P, oral absorption, Log BB, Log D, and Log K, providing a starting point for early discovery or later optimization. Toxicity prediction is also able to be performed using software such as DEREK, METEOR, ADMETlab, etc. The operation of these consists of the use of an approach known as knowledge-based, where data from previously performed experimental tests are fed into the programs, and by correlation, these can predict endpoints such as carcinogenicity, mutagenicity, and teratogenicity [117, 118].

From 2010 onwards, the volume of data generated increased significantly and with the advent of the creation of GPUs (Graphics Processing Unit), it became possible to use Machine Learning (ML) algorithms to study the pharmacokinetics and toxicological effects of a wide range of compounds. ML algorithms are capable of predicting these same properties for a large number of compounds from a given training set, with experimentally determined PK and toxicity properties, in a faster and more efficient way than the software used so far, making with its use increasing exponentially in the processes of Drug Discovery and optimization [115, 117, 119].

In this way, it is possible to conclude that nowadays, it is increasingly necessary to use computational tools for the prediction of pharmacokinetic and toxicological properties, to reduce the discovery time for new drugs and also to prevent drugs with undesirable characteristics advance during the research and fail in final stages that are crucial for their approval, thus preventing the companies and research groups involved in the projects from having losses that make it impossible to continue the search for new molecules [115, 116].

### 3 Conclusion

Drug Discovery is a very vast area, comprising several fields such as medicine, pharmacology, and biotechnology, and it aims to discover new drug candidates. This is an area with several stages, and in this chapter, we focus primarily on the Lead Optimization part.

Several techniques were presented for the improvement of a Lead compound such as pharmacophore, molecular docking, molecular dynamics, ADMETOX studies, machine learning, among others. One technique is not better than the other, as they all have their advantages and disadvantages. Therefore, it is possible to notice that, when used together, they can improve the optimization of a molecule and take this candidate closer and closer to becoming a drug and reaching the people who need it.

## References

1. Deprez-Poulain, R., Deprez, B.: Facts, figures, and trends in lead generation. *Curr. Top. Med. Chem.* **4**(6), 569–580 (2004). <https://doi.org/10.2174/1568026043451168>
2. Hughes, J., Rees, S., Kalindjian, S., Philpott, K.: Principles of early drug discovery. *Br. J. Pharmacol.* **162**(6), 1239–1249 (2011). <https://doi.org/10.1111/j.1476-5381.2010.01127.x>
3. Keserü, G.M., Makara, G.M.: Hit discovery and hit-to-lead approaches. *Drug Discov. Today* **11**(15–16), 741–748 (2006). <https://doi.org/10.1016/j.drudis.2006.06.016>
4. Bleicher, K.H., Böhm, H.-J., Müller, K., Alanine, A.I.: Hit and lead generation: beyond high-throughput screening. *Nat. Rev. Drug. Discov.* **2**(5), 369–378 (2003). <https://doi.org/10.1038/nrd1086>
5. Heifetz, A., James, T., Morao, I., Bodkin, M.J., Biggin, P.C.: Guiding lead optimization with GPCR structure modeling and molecular dynamics. *Curr. Opin. Pharmacol.* **30**, 14–21 (2016). <https://doi.org/10.1016/j.coph.2016.06.004>
6. Leelananda, S.P., Lindert, S.: Computational methods in drug discovery. *Beilstein. J. Org. Chem.* **12**, 2694–2718 (2016). <https://doi.org/10.3762/bjoc.12.267>
7. de Souza Neto, L.R., Moreira-Filho, J.T., Neves, B.J., et al.: In silico strategies to support fragment-to-lead optimization in drug discovery. *Front. Chem.* **8**(February), 1–18 (2020). <https://doi.org/10.3389/fchem.2020.00093>
8. Thomas, S.E., Mendes, V., Kim, S.Y., et al.: Structural biology and the design of new therapeutics: from HIV and cancer to mycobacterial infections: a paper dedicated to John Kendrew. *J. Mol. Biol.* **429**(17), 2677–2693 (2017). <https://doi.org/10.1016/j.jmb.2017.06.014>
9. Patel, D.D., Bauman, J., Arnold, E.: Advantages of crystallographic fragment screening: functional and mechanistic insights from a powerful platform for efficient drug discovery. *Prog. Biophys. Mol. Biol.* **116**, 92–100 (2014)
10. Fischer, M., Hubbard, R.: Fragment-based ligand discovery. *Mol. Interv.* **9**(1), 22–30 (2009)
11. Ichihara, O., Barker, J., Law, R.J., Whittaker, M.: Compound design by fragment-linking. *Mol. Inform.* **30**(4), 298–306 (2011). <https://doi.org/10.1002/minf.201000174>
12. De Fusco, C., Brear, P., Segre, J., et al.: A fragment-based approach leading to the discovery of a novel binding site and the selective CK2 inhibitor CAM4066. *Bioorganic Med. Chem.* **25**(13), 3471–3482 (2017). <https://doi.org/10.1016/j.bmc.2017.04.037>
13. Hall, D.R., Ngan, C.H., Zerbe, B.S., Kozakov, D., Vajda, S.: Hot spot analysis for driving the development of hits into leads in fragment-based drug discovery. *J. Chem. Inf. Model.* **52**(1), 199–209 (2012). <https://doi.org/10.1021/ci200468p>
14. Torres, P.H.M., Sodero, A.C.R., Jofily, P., Silva-Jr, F.P.: Key topics in molecular docking for drug design. *Int. J. Mol. Sci.* **20**(18), 1–29 (2019). <https://doi.org/10.3390/ijms20184574>
15. Durrant, J., Amaro, R.E., McCammon, J.A.: AutoGrow: a novel algorithm for protein inhibitor design. *Chem. Biol. Drug Des.* **73**(2), 168–178 (2009)
16. Durrant, J.D., Lindert, S., McCammon, J.A.: AutoGrow 3.0: an improved algorithm for chemically tractable, semi-automated protein inhibitor design. *J. Mol. Graph Model* **44**, 104–112 (2013). <https://doi.org/10.1016/j.jmgm.2013.05.006>
17. Dey, F., Caffisch, A.: Fragment-based de Novo Ligand design by multiobjective evolutionary optimization. *J. Chem. Inf. Model.* **48**(3), 679–690 (2008). <https://doi.org/10.1021/ci700424b>
18. Pierce, A.C., Rao, G., Bemis, G.W.: BREED: generating novel inhibitors through hybridization of known ligands. application to CDK2, P38, and HIV protease. *J. Med. Chem.* **47**(11), 2768–2775 (2004). <https://doi.org/10.1021/jm030543u>
19. Gund, P.: Evolution of the pharmacophore concept in pharmaceutical research. In: Güner, O.F., (ed.) *Pharmacophore Perception, Development, and Use in Drug Design*. International University Line, La Jolla (2000)
20. Gund, P.: Pharmacophoric pattern searching and receptor mapping. In: Hess H.-J. (ed.) *Annual Reports in Medicinal Chemistry*. Academic, vol. 14 (1979)
21. Gund, P., Wipke, W.T., Langridge, R.: Computer searching of a molecular structure file for pharmacophoric patterns. In: *Proceedings of International Conference on Comp. in Chem. Res. and Edu.* Elsevier (1974)

22. Güner, O.F., Hughes, D.W., Dumont, L.M.: An integrated approach to three-dimensional information management with MACCS-3D. *J. Chem. Inf. Comput. Sci.* **31**(3), 408–414 (1991). <https://doi.org/10.1021/ci00003a007>
23. Khedkar, S.A., Malde, A.K., Coutinho, E.C., Srivastava, S.: Pharmacophore modeling in drug discovery and development: an overview. *Med. Chem. (Los Angeles)*, **3**, 187–197 (2007)
24. Guner, O.: History and evolution of the pharmacophore concept in computer-aided drug design. *Curr. Top. Med. Chem.* **2**(12), 1321–1332 (2005). <https://doi.org/10.2174/1568026023392940>
25. Martin, Y.C.: Distance Comparisons (DISCO): a new strategy for examining 3d structure-activity relationships. In: Hansch, C., Fujita, T., (eds.) *Classical and 3D QSAR in Agrochemistry*. American Chemical Society, Washington D.C. (1995)
26. Jones, G., Willett, P., Glen, R.C.: A genetic algorithm for flexible molecular overlay and pharmacophore elucidation. *J. Comput. Aided Mol. Des.* **9**(6), 532–549 (1995). <https://doi.org/10.1007/BF00124324>
27. Barnum, D., Greene, J., Smellie, A., Sprague, P.: Identification of common functional configurations among molecules. *J. Chem. Inf. Comput. Sci.* **36**(3), 563–571 (1996). <https://doi.org/10.1021/ci950273r>
28. Cramer, R.D., Patterson, D.E., Bunce, J.D.: Comparative molecular field analysis (CoMFA). 1. Effect of shape on binding of steroids to carrier proteins. *J. Am. Chem. Soc.* **110**(18), 5959–5967 (1988)
29. Golender, V.E., Vorpagel, E.R.: Computer-assisted pharmacophore identification. In: Kubinyi, H (ed.) *Drug Design: Theory*. ESCOM, Leiden (1993)
30. Li, H., Sutter, J., Hoffmann, R.: HypoGen: an automated system for generating 3D predictive pharmacophore models. In: Guner, O., (ed.) *Pharmacophore Perception, Development, and Use in Drug Design*. IUL Biotechnology Series, La Jolla (2000)
31. Yang, S.Y.: Pharmacophore modeling and applications in drug discovery: challenges and recent advances. *Drug Discov. Today* **15**(11–12), 444–450 (2010). <https://doi.org/10.1016/j.drudis.2010.03.013>
32. Wolber, G., Langer, T.: LigandScout: 3-D pharmacophores derived from protein-bound ligands and their use as virtual screening filters. *J. Chem. Inf. Model.* **45**(1), 160–169 (2005). <https://doi.org/10.1021/ci049885e>
33. Chen, J., Lai, L.: Pocket vol 2: further developments on receptor-based pharmacophore modeling. *J. Chem. Inf. Model.* **46**(6), 2684–2691 (2006). <https://doi.org/10.1021/ci600246s>
34. Ortuso, F., Langer, T., Alcaro, S.: GBPM: GRID-based pharmacophore model: concept and application studies to protein-protein recognition. *Bioinformatics* **22**(12), 1449–1455 (2006). <https://doi.org/10.1093/bioinformatics/btl115>
35. Barillari, C., Marcou, G., Rognan, D.: Hot-spots-guided receptor-based pharmacophores (HS-pharm): A knowledge-based approach to identify ligand-anchoring atoms in protein cavities and prioritize structure-based pharmacophores. *J. Chem. Inf. Model.* **48**(7), 1396–1410 (2008). <https://doi.org/10.1021/ci800064z>
36. Tintori, C., Corradi, V., Magnani, M., Manetti, F., Botta, M.: Targets looking for drugs: a multistep computational protocol for the development of structure-based pharmacophores and their applications for hit discovery. *J. Chem. Inf. Model.* **48**(11), 2166–2179 (2008). <https://doi.org/10.1021/ci800105p>
37. Burger, A.: *Medicinal Chemistry*, 3d edn. Wiley-Interscience, New York (1970)
38. Todeschini, R., Consonni, V.: *Molecular descriptors for chemoinformatics*. In: *Methods and Principles in Medicinal Chemistry*. Wiley-VCH, Weinheim, Germany (2009)
39. Devereux, M., LA Popelier, P.: In silico techniques for the identification of bioisosteric replacements for drug design. *Curr. Top. Med. Chem.* **10**(6), 657–668 (2010). <https://doi.org/10.2174/156802610791111470>
40. Ujváry, I.: *BIOSTER—A Database of Structurally Analogous Compounds*, vol 46, pp. 92–95 (1995)
41. Gaulton, A., Hersey, A., Nowotka, M.L., et al.: The ChEMBL database in 2017. *Nucleic Acids Res.* **45**(D1), D945–D954 (2017). <https://doi.org/10.1093/nar/gkw1074>

42. Wirth, M., Zoete, V., Michielin, O., Sauer, W.H.B.: SwissBioisostere: a database of molecular replacements for ligand design. *Nucleic Acids Res.* **41**(D1), 1137–1143 (2013). <https://doi.org/10.1093/nar/gks1059>
43. Lengauer, T., Rarey, M.: Computational methods for biomolecular docking. *Curr. Opin. Struct. Biol.* **6**(3), 402–406 (1996). [https://doi.org/10.1016/S0959-440X\(96\)80061-3](https://doi.org/10.1016/S0959-440X(96)80061-3)
44. Kitchen, D.B., Decorez, H., Furr, J.R., Bajorath, J.: Docking and scoring in virtual screening for drug discovery: methods and applications. *Nat. Rev. Drug Discov.* **3**(11), 935–949 (2004). <https://doi.org/10.1038/nrd1549>
45. Mostashari-Rad, T., Arian, R., Sadri, H., et al.: Study of CXCR4 chemokine receptor inhibitors using QSPR and molecular docking methodologies. *J. Theor. Comput. Chem.* **18**(04), 1950018 (2019). <https://doi.org/10.1142/S0219633619500184>
46. Berman, H.M., Battistuz, T., Bhat, T.N., et al.: The protein data bank. *Acta Crystallogr Sect. D Biol. Crystallogr.* **58**(6), 899–907 (2002). <https://doi.org/10.1107/S0907444902003451>
47. Berman, H., Henrick, K., Nakamura, H., Markley, J.L.: The worldwide Protein Data Bank (wwPDB): ensuring a single, uniform archive of PDB data. *Nucleic Acids Res.* **35**(Database), D301–D303 (2007). <https://doi.org/10.1093/nar/gkl1971>
48. Wang, R., Fang, X., Lu, Y., Yang, C.-Y., Wang, S.: The PDBbind database: methodologies and updates. *J. Med. Chem.* **48**(12), 4111–4119 (2005). <https://doi.org/10.1021/jm048957q>
49. Wang, R., Fang, X., Lu, Y., Wang, S.: The PDBbind database: collection of binding affinities for protein–ligand complexes with known three-dimensional structures. *J. Med. Chem.* **47**(12), 2977–2980 (2004). <https://doi.org/10.1021/jm030580l>
50. Liu, T., Lin, Y., Wen, X., Jorissen, R.N., Gilson, M.K.: BindingDB: a web-accessible database of experimentally determined protein–ligand binding affinities. *Nucleic Acids Res.* **35**(suppl 1), D198–D201 (2007). <https://doi.org/10.1093/nar/gkl1999>
51. Chothia, C., Lesk, A.M.: The relation between the divergence of sequence and structure in proteins. *EMBO J.* **5**(4), 823–826 (1986)
52. Wang, G., Zhu, W.: Molecular docking for drug discovery and development: a widely used approach but far from perfect. *Future Med. Chem.* **8**(14) (2016). <https://doi.org/10.4155/fmc-2016-0143>
53. Erickson, J.A., Jalaie, M., Robertson, D.H., Lewis, R.A., Vieth, M.: Lessons in molecular recognition: the effects of ligand and protein flexibility on molecular docking accuracy. *J. Med. Chem.* **47**(1), 45–55 (2004). <https://doi.org/10.1021/jm030209y>
54. Lexa, K.W., Carlson, H.A.: Protein flexibility in docking and surface mapping. *Q. Rev. Biophys.* **45**(3), 301–343 (2012). <https://doi.org/10.1017/S0033583512000066>
55. Meng, X.-Y., Zhang, H.-X., Mezei, M., Cui, M.: Molecular docking: a powerful approach for structure-based drug discovery. *Curr. Comput. Aided-Drug Des.* **7**(2), 146–157 (2011). <https://doi.org/10.2174/157340911795677602>
56. Dias, R., de Azevedo Jr. W.: Molecular docking algorithms. *Curr. Drug Targets.* **9**(12), 1040–1047 (2008). <https://doi.org/10.2174/138945008786949432>
57. Rarey, M., Kramer, B., Lengauer, T., Klebe, G.: A fast flexible docking method using an incremental construction algorithm. *J. Mol. Biol.* **261**(3), 470–489 (1996). <https://doi.org/10.1006/jmbi.1996.0477>
58. Kramer, B., Rarey, M., Lengauer, T.: Evaluation of the FlexX incremental construction algorithm for protein–ligand docking. *Proteins Struct. Funct. Genet.* **37**(2), 228–241 (1999). [https://doi.org/10.1002/\(SICI\)1097-0134\(19991101\)37:2%3c228::AID-PROT8%3e3.0.CO;2-8](https://doi.org/10.1002/(SICI)1097-0134(19991101)37:2%3c228::AID-PROT8%3e3.0.CO;2-8)
59. Morris, G.M., Goodsell, D.S., Halliday, R.S., et al.: Automated docking using a Lamarckian genetic algorithm and an empirical binding free energy function. *J. Comput. Chem.* **19**(14), 1639–1662 (1998). [https://doi.org/10.1002/\(SICI\)1096-987X\(19981115\)19:14%3c1639::AID-JCC10%3e3.0.CO;2-B](https://doi.org/10.1002/(SICI)1096-987X(19981115)19:14%3c1639::AID-JCC10%3e3.0.CO;2-B)
60. Jones, G., Willett, P., Glen, R.C., Leach, A.R., Taylor, R.: Development and validation of a genetic algorithm for flexible docking 1 | Edited by F. E. Cohen. *J. Mol. Biol.* **267**(3), 727–748 (1997). <https://doi.org/10.1006/jmbi.1996.0897>
61. Liu, M., Wang, S.: MCDOCK: a Monte Carlo simulation approach to the molecular docking problem. *J. Comput. Aided Mol. Des.* **13**, 435–451 (1999)

62. Graves, A.P., Brenk, R., Shoichet, B.K.: Decoys for docking. *J. Med. Chem.* **48**(11), 3714–3728 (2005). <https://doi.org/10.1021/jm0491187>
63. Betzi, S., Suhre, K., Chétrit, B., Guerlesquin, F., Morelli, X.: GFScore: a general nonlinear consensus scoring function for high-throughput docking. *J. Chem. Inf. Model* **46**(4), 1704–1712 (2006). <https://doi.org/10.1021/ci0600758>
64. Yang, C.-Y., Wang, R., Wang, S.: M-Score: a knowledge-based potential scoring function accounting for protein atom mobility. *J. Med. Chem.* **49**(20), 5903–5911 (2006). <https://doi.org/10.1021/jm050043w>
65. Krammer, A., Kirchhoff, P.D., Jiang, X., Venkatachalam, C.M., Waldman, M.: LigScore: a novel scoring function for predicting binding affinities. *J. Mol. Graph Model* **23**(5), 395–407 (2005). <https://doi.org/10.1016/j.jmglm.2004.11.007>
66. Velec, H.F.G., Gohlke, H., Klebe, G.: DrugScore CSD knowledge-based scoring function derived from small molecule crystal data with superior recognition rate of near-native ligand poses and better affinity prediction. *J. Med. Chem.* **48**(20), 6296–6303 (2005). <https://doi.org/10.1021/jm050436v>
67. Wang, R., Lu, Y., Fang, X., Wang, S.: An extensive test of 14 scoring functions using the pdbbind refined set of 800 protein–ligand complexes. *J. Chem. Inf. Comput. Sci.* **44**(6), 2114–2125 (2004). <https://doi.org/10.1021/ci049733j>
68. Wang, R., Lu, Y., Wang, S.: Comparative evaluation of 11 scoring functions for molecular docking. *J. Med. Chem.* **46**(12), 2287–2303 (2003). <https://doi.org/10.1021/jm0203783>
69. Reddy, M., Reddy, C., Rathore, R., et al.: Free energy calculations to estimate ligand-binding affinities in structure-based drug design. *Curr. Pharm. Des.* **20**(20), 3323–3337 (2014). <https://doi.org/10.2174/13816128113199990604>
70. Yuriev, E., Agostino, M., Ramsland, P.A.: Challenges and advances in computational docking: 2009 in review. *J. Mol. Recognit.* **24**(2), 149–164 (2011). <https://doi.org/10.1002/jmr.1077>
71. Eynedy, I.J., Egan, W.J.: Can we use docking and scoring for hit-to-lead optimization? *J. Comput. Aided Mol. Des.* **22**(3–4), 161–168 (2008). <https://doi.org/10.1007/s10822-007-9165-4>
72. Vangrevelinghe, E., Zimmermann, K., Schoepfer, J., Portmann, R., Fabbro, D., Furet, P.: Discovery of a potent and selective protein kinase CK2 inhibitor by high-throughput docking. *J. Med. Chem.* **46**(13), 2656–2662 (2003). <https://doi.org/10.1021/jm030827e>
73. Bythway, I., Cochran, S.: Validation of molecular docking calculations involving FGF-1 and FGF-2. *J. Med. Chem.* **47**(7), 1683–1693 (2004). <https://doi.org/10.1021/jm030447t>
74. Friesner, R.A., Murphy, R.B., Repasky, M.P., et al.: Extra precision glide: docking and scoring incorporating a model of hydrophobic enclosure for protein–ligand complexes. *J. Med. Chem.* **49**(21), 6177–6196 (2006). <https://doi.org/10.1021/jm051256o>
75. Durrant, J.D., McCammon, J.A.: Computer-aided drug-discovery techniques that account for receptor flexibility. *Curr. Opin. Pharmacol.* **10**(6), 770–774 (2010). <https://doi.org/10.1016/j.coph.2010.09.001>
76. McCammon, J.A., Gelin, B.R., Karplus, M.: Dynamics of folded proteins. *Nature* **267**(5612), 585–590 (1977). <https://doi.org/10.1038/267585a0>
77. Salo-Ahen, O.M.H., Alanko, I., Bhadane, R., et al.: Molecular dynamics simulations in drug discovery and pharmaceutical development. *Processes*. **9**(1), 71 (2020). <https://doi.org/10.3390/pr9010071>
78. van Gunsteren, W.F., Berendsen, H.J.C.: Computer simulation of molecular dynamics: methodology, applications, and perspectives in chemistry. *Angew. Chemie Int. Ed. English*. **29**(9), 992–1023 (1990). <https://doi.org/10.1002/anie.199009921>
79. Berman, H.M., Westbrook, J., Feng, Z., et al.: The protein data bank. *Nucleic Acids Res.* **28**(1), 235–242 (2000). <https://doi.org/10.1093/nar/28.1.235>
80. Kuhlman, B., Bradley, P.: Advances in protein structure prediction and design. *Nat. Rev. Mol. Cell. Biol.* **20**(11), 681–697 (2019). <https://doi.org/10.1038/s41580-019-0163-x>
81. Cornell, W.D., Cieplak, P., Bayly, C.I., et al.: A second generation force field for the simulation of proteins, nucleic acids, and organic molecules. *J. Am. Chem. Soc.* **117**(19), 5179–5197 (1995). <https://doi.org/10.1021/ja00124a002>



82. Jones, J.E.: On the determination of molecular fields.—II. From the equation of the state of a gas. *Proc. R. Soc. Lond. Ser. A, Contain Pap. Math. Phys. Character.* **106**(738), 463–477 (1924). <https://doi.org/10.1098/rspa.1924.0082>
83. Durrant, J.D., McCammon, J.A.: Molecular dynamics simulations and drug discovery. *BMC Biol.* **9**(1), 71 (2011). <https://doi.org/10.1186/1741-7007-9-71>
84. Wang, J., Wolf, R.M., Caldwell, J.W., Kollman, P.A., Case, D.A.: Development and testing of a general amber force field. *J. Comput. Chem.* **25**(9), 1157–1174 (2004). <https://doi.org/10.1002/jcc.20035>
85. Brooks, B.R., Brucoleri, R.E., Olafson, B.D., States, D.J., Swaminathan, S., Karplus, M.: CHARMM: a program for macromolecular energy, minimization, and dynamics calculations. *J. Comput. Chem.* **4**(2), 187–217 (1983). <https://doi.org/10.1002/jcc.540040211>
86. Christen, M., Hünenberger, P.H., Bakowies, D., et al.: The GROMOS software for biomolecular simulation: GROMOS05. *J. Comput. Chem.* **26**(16), 1719–1751 (2005). <https://doi.org/10.1002/jcc.20303>
87. van Gunsteren, W.F., Dolenc, J., Mark, A.E.: Molecular simulation as an aid to experimentalists. *Curr. Opin. Struct. Biol.* **18**(2), 149–153 (2008). <https://doi.org/10.1016/j.sbi.2007.12.007>
88. LaConte, L.E.W., Voelz, V., Nelson, W., Enz, M., Thomas, D.D.: Molecular dynamics simulation of site-directed spin labeling: experimental validation in muscle fibers. *Biophys. J.* **83**(4), 1854–1866 (2002). [https://doi.org/10.1016/S0006-3495\(02\)73950-7](https://doi.org/10.1016/S0006-3495(02)73950-7)
89. Showalter, S.A., Brüschweiler, R.: Validation of molecular dynamics simulations of biomolecules using NMR spin relaxation as benchmarks: application to the AMBER99SB force field. *J. Chem. Theory Comput.* **3**(3), 961–975 (2007). <https://doi.org/10.1021/ct7000045>
90. Markwick, P.R.L., Cervantes, C.F., Abel, B.L., Komives, E.A., Blackledge, M., McCammon, J.A.: Enhanced conformational space sampling improves the prediction of chemical shifts in proteins. *J. Am. Chem. Soc.* **132**(4), 1220–1221 (2010). <https://doi.org/10.1021/ja9093692>
91. Chodera, J.D., Mobley, D.L., Shirts, M.R., Dixon, R.W., Branson, K., Pande, V.S.: Alchemical free energy methods for drug discovery: progress and challenges. *Curr. Opin. Struct. Biol.* **21**(2), 150–160 (2011). <https://doi.org/10.1016/j.sbi.2011.01.011>
92. Hong, G., Cornish, A.J., Hegg, E.L., Pachter, R.: On understanding proton transfer to the biocatalytic [Fe–Fe]H sub-cluster in [Fe–Fe]H<sub>2</sub>ases: QM/MM MD simulations. *Biochim. Biophys. Acta Bioenerg.* **1807**(5), 510–517 (2011). <https://doi.org/10.1016/j.bbabi.2011.01.011>
93. Schames, J.R., Henschman, R.H., Siegel, J.S., Sotriffer, C.A., Ni, H., McCammon, J.A.: Discovery of a novel binding trench in HIV integrase. *J. Med. Chem.* **47**(8), 1879–1881 (2004). <https://doi.org/10.1021/jm0341913>
94. Durrant, J.D., Keränen, H., Wilson, B.A., McCammon, J.A.: Computational identification of uncharacterized cruzain binding sites. Geary, T.G., (ed.) *PLoS Negl. Trop. Dis.* **4**(5), e676 (2010). <https://doi.org/10.1371/journal.and.0000676>
95. Grant, B.J., Lukman, S., Hocker, H.J., et al.: Novel allosteric sites on ras for lead generation. Srivastava, R.K. (ed.) *PLoS One* **6**(10), e25711 (2011). <https://doi.org/10.1371/journal.pone.0025711>
96. Hazuda, D.J., Anthony, N.J., Gomez, R.P., et al.: A naphthyridine carboxamide provides evidence for discordant resistance between mechanistically identical inhibitors of HIV-1 integrase. *Proc. Natl. Acad. Sci.* **101**(31), 11233–11238 (2004). <https://doi.org/10.1073/pnas.0402357101>
97. Ivetac, A., Andrew, M.J.: Mapping the druggable allosteric space of G-protein coupled receptors: a fragment-based molecular dynamics approach. *Chem. Biol. Drug. Des.* **76**(3), 201–217 (2010). <https://doi.org/10.1111/j.1747-0285.2010.01012.x>
98. Arroio, A., Honório, K.M., da Silva, A.B.F.: Propriedades químico-quânticas empregadas em estudos das relações estrutura-atividade. *Quim. Nova.* **33**(3), 694–699 (2010). <https://doi.org/10.1590/s0100-40422010000300037>

99. Food US.: Annual review structure—activity relationship approaches and applications **22**(8), 1680–1695 (2003)
100. Guha, R.: Chapter 6 On Exploring Structure-Activity Relationships, p. 993 (2013). <https://doi.org/10.1007/978-1-62703-342-8>
101. McKinney, J.D., Richard, A., Waller, C., Newman, M.C., Gerberick, F.: The practice of structure-activity relationships (SAR) in toxicology. *Toxicol. Sci.* **56**(1), 8–17 (2000). <https://doi.org/10.1093/toxsci/56.1.8>
102. Landscapes, A., Cliffs, A.: Structure-Activity Relationship Data Analysis, pp. 507–531 (2010)
103. Kubinyi, H.: QSAR and 3D QSAR in drug design. Part 1: methodology. *Drug Discov. Today* **2**(11), 457–467 (1997). [https://doi.org/10.1016/S1359-6446\(97\)01079-9](https://doi.org/10.1016/S1359-6446(97)01079-9)
104. Verma, J., Khedkar, V., Coutinho, E.: 3D-QSAR in drug design—a review. *Curr. Top. Med. Chem.* **10**(1), 95–115 (2010). <https://doi.org/10.2174/156802610790232260>
105. Gozalbes, R., Doucet, J.P., Derouin, F.: Application of topological descriptions in QSAR and drug design: history and new trends. *Curr. Drug Targets Infect Disord.* **2**(1), 93–102 (2002). <https://doi.org/10.2174/1568005024605909>
106. Neves, B.J., Braga, R.C., Melo-Filho, C.C., Moreira-Filho, J.T., Muratov, E.N., Andrade, C.H.: QSAR-based virtual screening: advances and applications in drug discovery. *Front Pharmacol.* **9**, 1–7 (2018). <https://doi.org/10.3389/fphar.2018.01275>
107. Lipinski, C.F., Maltarollo, V.G., Oliveira, P.R., da Silva, A.B.F., Honorio, K.M.: Advances and perspectives in applying deep learning for drug design and discovery. *Front. Robot. AI* **6**(November), 1–6 (2019). <https://doi.org/10.3389/frobt.2019.00108>
108. Vamathevan, J., Clark, D., Czodrowski, P., et al.: Applications of machine learning in drug discovery and development. *Nat. Rev. Drug Discov.* **18**(6), 463–477 (2019). <https://doi.org/10.1038/s41573-019-0024-5>
109. Lavecchia, A.: Machine-learning approaches in drug discovery: methods and applications. *Drug Discov. Today* **20**(3), 318–331 (2015). <https://doi.org/10.1016/j.drudis.2014.10.012>
110. Stephenson, N., Shane, E., Chase, J., et al.: Survey of machine learning techniques in drug discovery. *Curr. Drug Metab.* **20**(3), 185–193 (2018). <https://doi.org/10.2174/1389200219666180820112457>
111. Hochreiter, S., Klambauer, G., Rarey, M.: Machine learning in drug discovery. *J. Chem. Inf. Model.* **58**(9), 1723–1724 (2018). <https://doi.org/10.1021/acs.jcim.8b00478>
112. Klambauer, G., Hochreiter, S., Rarey, M.: Machine learning in drug discovery. *J. Chem. Inf. Model.* **59**(3), 945–946 (2019). <https://doi.org/10.1021/acs.jcim.9b00136>
113. Gawehn, E., Hiss, J.A., Schneider, G.: Deep learning in drug discovery. *Mol. Inform.* **35**(1), 3–14 (2016). <https://doi.org/10.1002/minf.201501008>
114. Zhang, L., Tan, J., Han, D., Zhu, H.: From machine learning to deep learning: progress in machine intelligence for rational drug discovery. *Drug Discov. Today* **22**(11), 1680–1685 (2017). <https://doi.org/10.1016/j.drudis.2017.08.010>
115. Ferreira, L.L.G., Andricopulo, A.D.: ADMET modeling approaches in drug discovery. *Drug Discov. Today* **24**(5), 1157–1165 (2019). <https://doi.org/10.1016/j.drudis.2019.03.015>
116. Yu, H., Adedoyin, A.: ADME-Tox in drug discovery: integration of experimental and computational technologies. *Drug Discov. Today* **8**(18), 852–861 (2003). [https://doi.org/10.1016/S1359-6446\(03\)02828-9](https://doi.org/10.1016/S1359-6446(03)02828-9)
117. Kar, S., Leszczynski, J.: Open access in silico tools to predict the ADMET profiling of drug candidates. *Expert Opin. Drug Discov.* **15**(12), 1473–1487 (2020). <https://doi.org/10.1080/17460441.2020.1798926>
118. Kazmi, S.R., Jun, R., Yu, M.S., Jung, C., Na, D.: In silico approaches and tools for the prediction of drug metabolism and fate: a review. *Comput. Biol. Med.* **2019**(106), 54–64 (September 2018). <https://doi.org/10.1016/j.combiomed.2019.01.008>
119. Wishart, D.S.: Improving early drug discovery through ADME modelling: an overview. *Drugs R D.* **8**(6), 349–362 (2007). <https://doi.org/10.2165/00126839-200708060-00003>

# Pulsed Electric Field and Ultrasound Applied to Proteins, Enzymes and Peptides



Igor Carvalho Fontes Sampaio , Isabela Viana Lopes de Moura ,  
Jacson Nunes dos Santos , Josilene Borges Torres Lima Matos ,  
Cleveland Maximino Jones , and Paulo Fernando de Almeida 

**Abstract** Currently a multitude of protein substrates are available to obtain value-added peptides on the market, such as those used in food supplements, flavoring agents, culture media, antioxidants, antihypertensives, anti-inflammatory drugs, polyphenol oxidase inhibitors, among others. Enzymatic protein hydrolysis methods have demonstrated advantages due to their substrate specificity, unlikely formation of toxic products and occurrence under mild conditions. The use of isolated or combined proteases with different specificities has been applied in the production of more effective and stable bioactive and shorter reaction times, obtaining different peptide profiles (composition and molecular mass distribution). Several sources of protease extraction have been explored (animal, plant and microbial) in order to make the bioprocess more efficient and economical. Approaches to stimulating enzymatic activity is a field of study with intense activity, bringing it very close to industrial applications and consequent improvement in quality of life. Among these stimulatory technologies, advances have been reported with electrostimulation and ultrasound techniques.

---

I. C. F. Sampaio

Research, Innovation and Development Center, Cariacica, ES 29140-500, Brazil

e-mail: [igorsampaio@outlook.com](mailto:igorsampaio@outlook.com)

I. V. L. de Moura · J. N. dos Santos · J. B. T. L. Matos · P. F. de Almeida (✉)

Laboratory of Biotechnology and Ecology of Microorganisms, Institute of Health Sciences,

Federal University of Bahia, Reitor Miguel Calmon Ave, Salvador, S/N 40110-060, Brazil

e-mail: [pfatk@yahoo.com.br](mailto:pfatk@yahoo.com.br)

I. V. L. de Moura

e-mail: [isabela.lopesm@outlook.com](mailto:isabela.lopesm@outlook.com)

J. N. dos Santos

e-mail: [jacson.jns@gmail.com](mailto:jacson.jns@gmail.com)

J. B. T. L. Matos

e-mail: [josilene.lima@ufba.br](mailto:josilene.lima@ufba.br)

C. M. Jones

Instituto Nacional de Óleo E Gás, State University of Rio de Janeiro, Rio de Janeiro, RJ 20550-013, Brazil

e-mail: [clevelandmjones@gmail.com](mailto:clevelandmjones@gmail.com)

**Keyword** Catalysis · Bioactive peptides · New products · Food · Fine chemistry

## 1 Protein Sources for Obtaining Amino Acids: Current and New Trends

The growing demand for quality proteins for human and animal feed is associated with the need for green or environmentally sustainable methods to obtain these proteins [1, 2]. Thus, there is an intense investigation into the use of new protein sources capable of providing cost-effectiveness and higher biomass conversion rates [3, 4]. The range of protein content of insects is quite broad, with species having between 7 and 91% of their body dry weight [5]. In addition to their high protein content, food-eligible insects have a good amino acid profile, with different insect species exhibiting the presence of essential amino acids [6]. Species like *T. molitor*, *Zophobas morio* and *A. diaperinus* have essential amino acids at levels similar to those found in soy and bovine caseins [7]. Furthermore, it is believed that the systematization of their consumption will allow meeting the protein requirements for human food around the world [8], considering the economic and environmental limitations of animal protein production.

Another alternative form of proteins are those derived from the so-called single cell proteins (SCP) or biomass [9], which can be obtained from different types of microorganisms, such as bacteria, fungi, yeasts and microalgae. One of the advantages of these proteins is their rapid production, considering that most microorganisms have growth rates much higher than those of plants or animals, suggesting a potential alternative for replacing more expensive conventional sources [10].

Despite the fact that microalgae have low cultivation density and slower growth rates than other microorganisms, they are a promising protein source that is not dependent on arable land for production, and can even be grown in non-potable water and without employing organic compounds, unlike other microbes. Another advantage of microalgae is their high concentration of proteins, with several species having protein content reported above 50% (e.g. species of the genus *Chlorella*, *Dunaliella*, *Scenedesmus* and *Spirulina*) [11]. Despite this fact, the bioavailability and protein digestibility of these organisms is reduced due to their complex cellulosic cell wall, and the need to employ cost-effective methods of releasing their contents [12].

In addition to their importance as a protein source, several amino acids or sequences of these have been reported to have bioactive activity, sometimes being referred to as bioactive peptides (BAP): antihypertensives, antioxidants, antidiabetics, immunomodulatory and metal-binding agents [13, 14]. Some potential sources of BAPs are macroalgae [15], vegetables [16], fermented meat products [17] and milk [18]. The consumption and market value of these molecules are expected to increase from US\$40 billion in 2020 to US\$95 billion in 2028, since they can be used to treat a variety of more frequent medical conditions (high blood pressure, cardiovascular disease, diabetes) and also as ingredients of functional foods and

nutraceuticals, employed to improve the health of individuals [19]. Currently, the main way to obtain these molecules is by enzymatic hydrolysis, and there is intense research on optimizing their production and improving their bioactive characteristics. Thus, great technological advances could be achieved with methods that improve the activity of proteolytic enzymes, and favorably modify their products.

## 2 Enzymatic Stimulation

Enzymes are catalyzing macromolecules that accelerate or promote chemical reactions by reducing the activation energy [20]. Although RNAs can also act as catalysts, the present review strictly refers to enzymes made up of amino acids. Currently, a myriad of industrial applications depend directly or indirectly on enzymes, ranging from traditionally well-known areas such as the food industry [21], pharmaceutical [22], wastewater treatment [23], textiles [24], biofuels [25], to others that use them as inputs to provide services, or that even emerged as a result of the development of specific enzymes: immunological and molecular diagnosis [26, 27], special cleaning for biotechnological and fine chemical equipment [28], and bioremediation [29]. This market was valued at US\$8.63 billion in 2019, and is projected to surpass US\$14.0 billion in 2022, given the numerous benefits offered by enzymes, in the most varied industries [30].

Since they confer high efficiency and specificity, the adoption of enzymes has grown exponentially in recent years, replacing, totally or partially, reactions based on acids/bases and high temperatures. Furthermore, these molecules require milder conditions to catalyze the reactions, which, together with the possibility of reuse in several reaction cycles, affords better environmental sustainability to the process [31].

Despite all these advantages, enzymes have optimal activity conditions, losing their stability under extreme conditions of pH and temperature, as well as representing an increase in costs for the industry that adopts them [32]. Thus, to mitigate these limitations and maximize gains, intense research has been directed towards increasing their stability and activity, and obtaining and reusing enzymes [33]. To achieve these goals, some approaches can be employed, such as enzyme modification by physical, chemical or genetic methods [34]; substrate pretreatment; increasing substrate binding of the enzyme; and improving prediction of reactions [35].

Currently, the main hydrolyzing enzymes come from the digestive system of mammals and through microbial pathways. Mammalian enzymes can be used in gastrointestinal digestion assays, in which there is sequential hydrolysis by the enzymes pepsin, trypsin and chymotrypsin [36] in order to obtain peptides from complex protein sources such as meat [37], milk [38] and insects [39].

Many microbial enzymes are available on the market, such as alcalase from *B. licheniformis* (Novozymes), proteinases from *Bacillus sp* (Novozymes), and thermolysins and proteinases from *Aspergillus* (USAI) [40–43]. Notwithstanding the smaller number of plant-derived enzymes for enzymatic hydrolysis, examples of

their use in commercial applications include: papain, bromelain, and ficain, being used in applications such as fermentation, meat softening, milk coagulation, and digestion improvement [39]. In addition, the industry is searching for new protein products. For example, in order to enhance functional properties such as solubility, emulsification, foaming and thermal stability of proteins, the use of different classes of proteases has been investigated [6].

In the field of peptides, several processes can be applied to obtain these molecules, such as the use of enzymatic methods [44], thermal [45], micronization [46] and ultrasound [47]. The literature is clear in indicating that the highest yield of bioactive peptides (BAP) is obtained when using hydrolyzing enzymes [41]. Enzymatic hydrolysis can be performed directly on homogenates of the protein source or on protein isolates. In certain cases, a precedent hydrolysis can be applied to protein denaturation by physical methods [6], such as the use of ultrasound (frequency of 20 kHz, power of 250–600 W) in protein preparations to be lysed with commercial endoproteases from *B. licheniformis* [41].

Thus, intense effort has been directed to the investigation of methods to modify and increase enzymatic activity. Among the physical methods that still need to be better investigated, is the use of ultrasound and pulsed electric fields (electrostimulation).

### 3 Effect of Ultrasound on Enzymes and Peptides

Conceptually, ultrasound is an acoustic mechanical wave with a frequency greater than 18 kHz that needs a medium to propagate [48]. During the propagation of the wave, alternating cycles of compression and rarefaction are produced in the liquid medium, with consequent pressure reduction and formation of microbubbles. This process can lead to a stable cavitation, which leads to a cyclic expansion and compression of these bubbles, generating eddy currents in the liquid medium around bubbles [49]. Furthermore, when in transient cavitation, strong shear waves are generated, causing turbulence, accelerating the mixing of reactants, mass transfer, heat production and even the dissociation of water and dissolved oxygen, to produce free radicals (-OH and -OOH) [50].

Due to its characteristics of high energy efficiency and low investment requirement, ultrasound has been used for several purposes, among which considerable attention has been given to its effect on the activity of enzymes and protein substrates [51, 52]. Its most traditional use has been in enzymatic and microbial inactivation. Despite this ability, new studies have indicated the possibility of its use as an enhancer of enzymatic activity [52–54], which may alter the conformation of enzymes and their functionality and interaction with the substrate, as well as improving the bioactive properties of their peptides. A summary of ultrasound effects is presented in Fig. 1.

The conformational changes in secondary and tertiary structures promoted by ultrasound waves have already been demonstrated [55–57], such as in tyrosinase 6, which had its active site modified, increasing its catalytic activity [58]. Furthermore, it

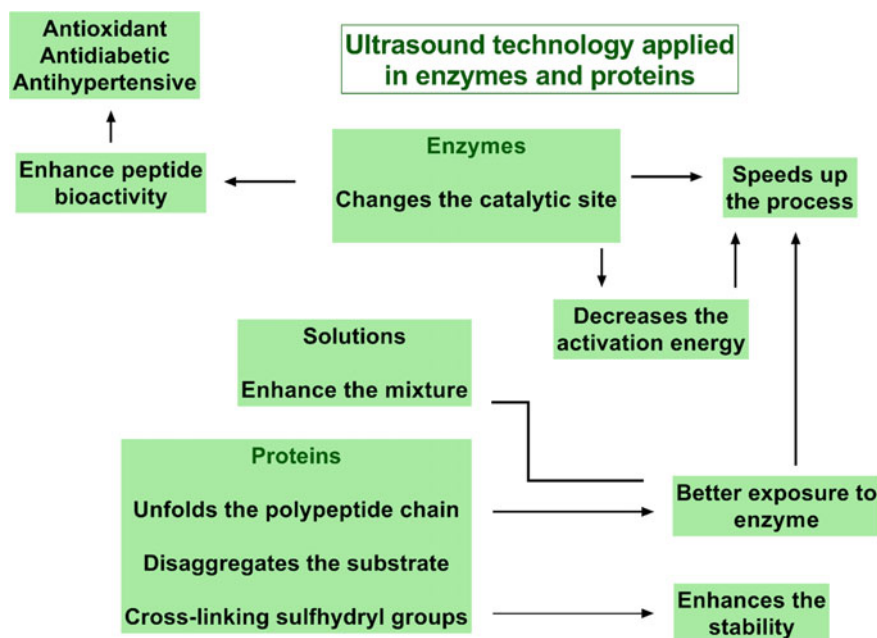


**Fig. 1** Effect of ultrasound on the activity of enzymes and proteins

is believed that these conformational changes promote better exposure of the catalytic site and unfolding of the polypeptide chain, and consequent contact of the enzyme with its substrate [59, 60].

Furthermore, the radicals produced during ultrasonication can promote cross-links in protein molecules, which would alter sulfhydryl groups that modify enzymatic stability [61, 62]. As an example, the enzyme polygalacturonase is more stable when treated with ultrasound. This shows that more investigations need to be carried out with other enzymes, in order to find suitable parameters for the use of ultrasound, to promote enzymatic reactions under optimal conditions and in a more stable way [59]. Another work demonstrated better stability of a sonicated lipase, with evidence that some modifications promoted by ultrasound were irreversible [63, 64].

Furthermore, ultrasonic pretreatment of substrates can destroy aggregations and remove the non-catalyzed cuticle, making the substrate more vulnerable to enzyme attack [65], as well as uncovering regions of the substrate previously inaccessible to enzymes [66], facilitating their combination between enzymes and substrate. Also, ultrasound can directly reduce the degree of polymerization, promoting, in some cases, the homolytic and/or heterolytic cleavage of covalent bonds, the most common method being the breaking of C–C bonds [67], and preferably in the middle of the polymer chains, with consequent reduction their size, an aspect that could increase the speed of the reactions [68].

It is also believed that ultrasound can uncover protein surfaces and create micropores on their surfaces, with a consequent increase in their surface area and improved affinity between enzymes and substrates [69, 70]. It was demonstrated that the ultrasound pretreatment of wheat germ protein increased the hydrophobic amino acid content of the hydrolyzate, evidencing the loosening of the protein structure and better exposure of amino acid residues, and consequent greater vulnerability of proteins to alcalase. Furthermore, the pretreatment of proteins by ultrasound can increase the reaction rate and reduce the activation energy, as well as the gelatin particle size and variation of alpha helix protein structures, making them more susceptible to enzymatic attack [71].

The physical effects of ultrasound (shock waves and microjets) can cause molecules with high energy to collide [72], and protein aggregates can disintegrate under collision, if bound by weak hydrophobic forces, giving ultrasound the ability to homogenize solutions of proteins. Reconstituted whey solutions (5% wv) when sonicated at 20 kHz and 31 W, had their particle size reduced from 200 to 125 nm in a period of 60 min [73]. Similarly, another work reported about 50% reduction in aggregate particle size in whey suspensions with the use of sonication at 20 kHz and 34 W for 2 min [74], and in denatured casein-whey mixtures [75]. Although ultrasound probes are narrower, they have a more intense cavitation region, and result in a more profound effect in whey concentrates [76]. Protein molecules are very susceptible to change when sonicated at higher intensities. Thus, micellar disruption of casein present in reconstituted solutions [77, 78], and better digestibility [78, 79], have been reported. Because of its vast applications, recent studies have reported the use of ultrasound as a way to improve production, extract and functionally modify peptides (Table 1), showing that much remains to be explored in this field.

The application of ultrasound has been demonstrated as a way to reduce the extraction time and increase the yield and antioxidant properties of low molecular weight peptides from bovine bone [80]. This increase in bioactivity was also reported by Rivero-Pino et al. [91] when studying the extraction of BAP from *Tenebrio molitor*, in which peptides that inhibit the enzyme  $\alpha$ -glucosidase had this property improved after using ultrasound for short periods.

Interestingly, this approach was also used to stimulate the fermentation of skimmed milk by *Lactobacillus paracasei* in order to increase the yield of peptides in yogurt, as well as the number of viable cells, while the authors suggest that this effect was due to immediate enzymatic activation after ultrasound application [81]. A similar aspect was also observed when fermenting soybean meal with *Bacillus subtilis* under the effect of ultrasound, with an increase in peptide yield, purity and high ACE-inhibitory antihypertensive activity being reported [92]. Furthermore, an increase in the proteolytic activity of Flavourzyme<sup>®</sup> and Alcalase<sup>®</sup> enzymes was observed after pretreatment of solutions of the nitrogen-fixing plant *Erythrina edulis*, resulting in peptides with better antioxidant and antihypertensive activity. Similar antioxidant activity has also been reported when hydrolyzed chicken feathers were submitted to ultrasound pretreatment [83]. Furthermore, when ultrasound was applied to processed egg protein peptides, an increase was obtained in the contact



**Table 1** Peptides obtained or modified by means of ultrasound

Origin of peptides	Property	Sources
Bovine bone	Antioxidant	[80]
Skimmed milk yogurt ( <i>Lactobacillus paracasei</i> )		[81]
Egg protein		[82]
Chicken feathers		[83]
Whey		[84]
Whey		[85]
Sweet potato		[86]
Nut		[87]
<i>Erythrina edulis</i>	Antihypertensive, Antioxidant	[88]
Fish ( <i>Nemipterus virgatus</i> )	Antioxidant, Anti-inflammatory, Antihypertensive	[89]
Soy Sauce (Moroni Fermentation)	Palatability	[90]
<i>Tenebrio molitor</i>	Antidiabetic	[91]
Whey prebiotic drink		[87]
Soybean meal	Antihypertensive	[92]
Chelated corn with iron		[85]

angle of these peptides, in their antioxidant activity, as well as in the stability of their emulsions [82].

## 4 Electrostimulation on Proteins and Enzymes for the Production of Value-Added Peptides

Another emerging technology for the stimulation of enzymatic activity is the use of pulsed electric fields (PEF). This technique basically consists of submitting samples to high voltage electrical pulses in a very short time (Franco et al. 2020). These pulses are characterized by having an intensity from 0.1 to 80 kV/cm, and the criterion for choosing the voltage varies according to the product and the purpose of this application [93]. It is most commonly used in the food industry, especially in processing, in order to extend the shelf life of the product. Despite traditionally being presented more as a non-thermal method of inactivating microbes [94, 95], more recent applications have been proposed (Fig. 2): increased enzymatic activation [96], microbial control [97], and protein modification [98].

Among the advantages of electrostimulation is the speed of the process, since the application of each cycle lasts for a few micro or milliseconds, in addition to having a low energy expenditure, thus being considered ecofriendly [99–101]. Furthermore, by aligning an electric field along specific orientations of bonds in

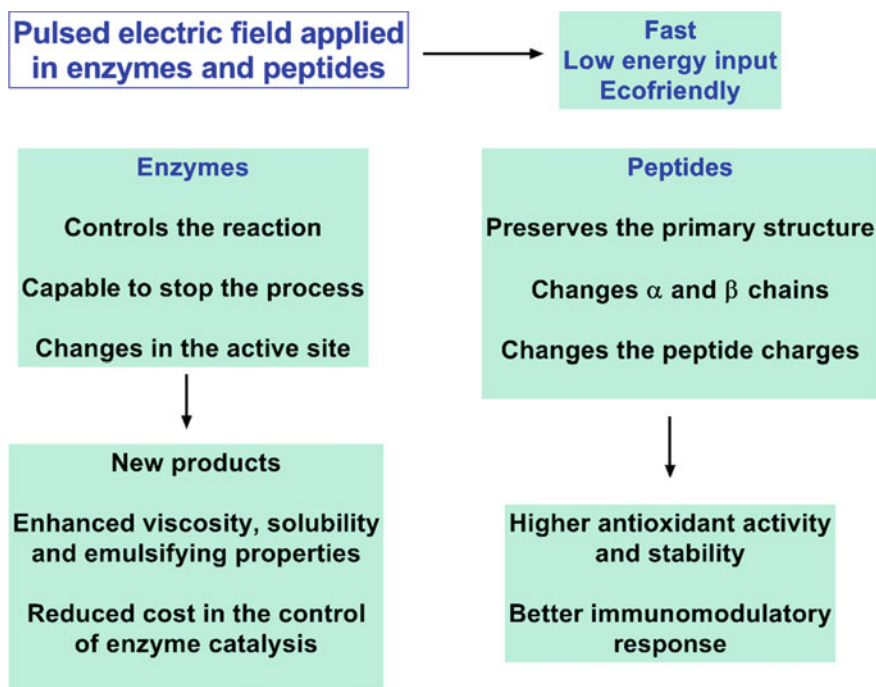


**Fig. 2** Pulsed electric field in enzymes and peptides

a molecule, bonds can be shortened, elongated or broken, making it possible to precisely control chemical reactions, including those catalyzed by enzymes [102].

Studies show that electric field pulses can promote conformation modification and enzymatic activity among different types of enzymes, with examples of activity reduction such as in amylase, glucose oxidase and lipase [103, 104]. On the other hand, increased activity of the anodic region of the laccase enzyme has been reported [105]. Given the relevance and prospects of this topic, researchers performed computational optimization of electric fields to optimize the biocatalytic activity of enzymes [106, 107].

The most accepted theory about the functioning of PEF in biological systems is through electroporation (electro permeabilization). In this way, the application of currents causes a disturbance of the cell membrane, characterized by the formation of both reversible and irreversible pores [93]. The disruption of cell membranes subjected to this process can either make the cell unviable, as is sought by the food industry, as well as favor the extraction of bioactive compounds found inside these cells [108, 109]. Based on this principle, any sample that has a phospholipid membrane can be subjected to PEF, and consequently, the method is applicable to cells regardless of their origin [110]. Thus, it is a versatile alternative to extracting bioactive compounds from different sources, such as animal [111, 112], vegetable [109, 113] and bacteria [114].

Thus, Zhao et al. [115] found an increase in the antioxidant activity of peptides from pineapple, due to a structural change caused by PEF, which the authors attributed to a greater proximity between the alpha chains, but without changes in the order of the amino acids of the peptide. This was especially observed in the treatment with 45 kV/cm. The use of this technology for enzymatic hydrolysis of the biomass of the microalgae *S. almeriensis* has also been reported in the literature, where PEF was related to the acceleration of this process [116], generating the benefit of also allowing the recovery of additional components of the biomass, by allowing the cascade processing of biomass. This proved to be more advantageous than other conventional methods, such as high-pressure homogenization (HPH), used as a comparative study.

Li et al. [117] studied the effects of PEF on alcalase activity at different “voltage lengths”. The greatest increase in catalytic activity was associated with the 10 kV/cm treatment, with an increase of 11.26% compared to the no-PEF treatment. The authors attribute this fact to the changes in secondary and tertiary conformations observed, in addition to changes in the active site also caused by the treatment.

PEF can also be used in the enzymatic hydrolysis of soybean isoflavone glycoside. Lu et al. [101] described changes in secondary and tertiary conformations of the studied compound that were also attributed to PEF treatment. These changes were subsequently identified as responsible for the increase in catalytic activity and acceleration of hydrolysis. When using the electric field pulse, an increase in ovalbumin hydrolysis and digestibility was observed, as well as a reduction in its aggregation, showing a clear application in egg white-based products [118].

An increase in digestibility has also been observed in steaks subjected to PEF [119]. PEF was also reported as a tool for bioprocessing and extraction of functional products from chicken meat residues [120], as well as in modulating protein binding to metals [121], increased yield of enzymes from Jiuzao glutelin extract [122], and improved antioxidant activity of peptides from *Pinus koraiensis* [123] and egg white [124]. Furthermore, stability of the primary structures of peptides submitted to PEF was reported, with alterations in their secondary structure ( $\alpha$ -helix and  $\beta$ -turn), and improvement in antioxidant activity [125].

Interestingly, Zhang et al. [126] submitted peptides from proteins obtained from pine nuts to PEF in order to verify changes in immunomodulatory activity caused by this type of energy. The results showed a higher immunomodulatory response and also the production of nitric oxide, without changes in the primary structure of the BAP. Furthermore, this author also corroborated the stability of the primary structure of the peptides, and the change in their secondary structure [126].

The use of PEF can alter the secondary, tertiary and even quaternary structures of proteins and enzymes, modifying their solubility, viscosity, emulsifying and gelling capacity [127]. The change in the secondary and tertiary structures of proteins can occur through two main pathways: direct stretching, and unfolding by tension forces caused by electric fields [128]. These modifications suggest the prospect of industrial applications, which are the likely reason for the increase in the number of publications and patent filings in this area.

Therefore, there is a confluence of the use of ultrasound and electric field pulse technologies to improve and control the activity of proteolytic enzymes, as well as

to obtain, process and modify peptides, especially in the food and pharmaceutical fields. Given the growing number of publications in these two fields, it is projected that many new products based on modified peptides will emerge, and that there will ensue a reduction in the costs of obtaining this class of molecules.

## References

1. Aiking, H., Boer J.: Protein and sustainability – the potential of insects. *J. Insects Food Feed* **5**, 3–7 (2019). <https://doi.org/10.3920/JIFF2018.0011>
2. Ismail, B.P., Senaratne-Lenagala, L., Stube, A., Brackenridge, A.: Protein demand: review of plant and animal proteins used in alternative protein product development and production. *Anim. Front* **10**, 53–63 (2020). <https://doi.org/10.1093/af/vfaa040>
3. Feng, Y., Chen, X.M., Zhao, M., et al.: Edible insects in China: utilization and prospects. *Insect Sci.* **25**, 184–198 (2018). <https://doi.org/10.1111/1744-7917.12449>
4. Sánchez-Muros, M.J., Barroso, F.G., Manzano-Agugliaro, F.: Insect meal as renewable sources of food for animal feeding: a review. *J. Clean. Prod.* **65**, 16–27 (2014). <https://doi.org/10.1016/j.jclepro.2013.11.068>
5. van Huis, A.: Edible insects are the future? *Proc. Nutr. Soc.* **75**, 294–305 (2016). <https://doi.org/10.1017/S0029665116000069>
6. Nongonierma, A.B., FitzGerald, R.J.: Unlocking the biological potential of proteins from edible insects through enzymatic hydrolysis: a review. *Innov. Food Sci. Emerg. Technol.* **43**, 239–252 (2017). <https://doi.org/10.1016/j.ifset.2017.08.014>
7. Yi, L., Lakemond, C.M.M., Sagis, L.M.C., et al.: Extraction and characterization of protein fractions from five insect species. *Food Chem.* **141**, 3341–3348 (2013). <https://doi.org/10.1016/j.foodchem.2013.05.115>
8. Berggren, Å., Jansson, A., Low, M.: Approaching ecological sustainability in the emerging insects-as-food industry. *Trends Ecol. Evol.* **34**, 132–138 (2019). <https://doi.org/10.1016/j.tree.2018.11.005>
9. Spalvins, K., Zihare, L., Blumberg, D.: Single cell protein production from waste biomass: comparison of various industrial by-products. *Energy Proc.* **147**, 409–418 (2018). <https://doi.org/10.1016/j.egypro.2018.07.111>
10. Sharif, M., Zafar, M.H., Aqib, A.I., et al.: Single cell protein: sources, mechanism of production, nutritional value and its uses in aquaculture nutrition. *Aquaculture* **531**, 735885 (2021). <https://doi.org/10.1016/j.aquaculture.2020.735885>
11. Becker, E.W.: Micro-algae as a source of protein. *Biotechnol. Adv.* **25**, 207–210 (2007). <https://doi.org/10.1016/j.biotechadv.2006.11.002>
12. Bharte, S., Desai, K.: Techniques for harvesting, cell disruption and lipid extraction of microalgae for biofuel production. *Biofuels* **12**, 285–305 (2021). <https://doi.org/10.1080/17597269.2018.1472977>
13. Karami, Z., Akbari-Adergani, B.: Bioactive food derived peptides: a review on correlation between structure of bioactive peptides and their functional properties. *J. Food Sci. Technol.* **56**, 535–547 (2019). <https://doi.org/10.1007/s13197-018-3549-4>
14. Cicero, A.F.G., Fogacci, F., Colletti, A.: Potential role of bioactive peptides in prevention and treatment of chronic diseases: a narrative review. *Br. J. Pharmacol.* **174**, 1378–1394 (2017). <https://doi.org/10.1111/bph.13608>
15. Hamedy, P.A., FitzGerald, R.J.: Bioactive proteins, peptides, and amino acids from macroalgae. *J. Phycol.* **47**, 218–232 (2011). <https://doi.org/10.1111/j.1529-8817.2011.00969.x>
16. Grancieri, M., Martino, H.S.D., Gonzalez de Mejia, E.: Chia seed (*Salvia hispanica* L.) as a source of proteins and bioactive peptides with health benefits: a review. *Comput. Rev. Food Sci. Food Saf.* **18**, 480–499 (2019). <https://doi.org/10.1111/1541-4337.12423>

17. Gallego, M., Mora, L., Escudero, E., Toldrá, F.: Bioactive peptides and free amino acids profiles in different types of European dry-fermented sausages. *Int. J. Food Microbiol.* **276**, 71–78 (2018). <https://doi.org/10.1016/j.ijfoodmicro.2018.04.009>
18. Amorim, F.G., Coitinho, L.B., Dias, A.T., et al.: Identification of new bioactive peptides from Kefir milk through proteopeptidomics: bioprospection of antihypertensive molecules. *Food Chem.* **282**, 109–119 (2019). <https://doi.org/10.1016/j.foodchem.2019.01.010>
19. Verified Market Research: Bioactive Peptides Market size was valued at USD 48.62 Billion in 2020 and is projected to reach USD 95.71 Billion by 2028, growing at a CAGR of 8.86% from 2021 to 2028 (2021)
20. Yang, J., Wei, J., Luo, F., et al.: Enzyme Responsive Peptide-Based AIE Bioprobes, pp. 335–359 (2022)
21. Sindhu, R., Shiburaj, S., Sabu, A., et al.: Enzyme technology in food processing: recent developments and future prospects. In: *Innovative Food Processing Technologies*. Elsevier, pp. 191–215 (2021)
22. Parvizpour, S., Hussin, N., Shamsir, M.S., Razmara, J.: Psychrophilic enzymes: structural adaptation, pharmaceutical and industrial applications. *Appl. Microbiol. Biotechnol.* **105**, 899–907 (2021). <https://doi.org/10.1007/s00253-020-11074-0>
23. Feng, S., Hao Ngo, H., Guo, W., et al.: Roles and applications of enzymes for resistant pollutants removal in wastewater treatment. *Bioresource Technol.* **335**, 125278 (2021). <https://doi.org/10.1016/j.biortech.2021.125278>
24. Zhang, Y., Liu, H., Tang, K., et al.: Effect of different ions in assisting protease to open the collagen fiber bundles in leather making. *J. Clean. Prod.* **293**, 126017 (2021). <https://doi.org/10.1016/j.jclepro.2021.126017>
25. Binod, P., Gnansounou, E., Sindhu, R., Pandey, A.: Enzymes for second generation biofuels: recent developments and future perspectives. *Bioresource Technol. Rep.* **5**, 317–325 (2019). <https://doi.org/10.1016/j.biteb.2018.06.005>
26. Wu, Z., Lu, J., Fu, Q., et al.: A smartphone-based enzyme-linked immunochromatographic sensor for rapid quantitative detection of carcinoembryonic antigen. *Sens. Actuators B Chem.* **329**, 129163 (2021). <https://doi.org/10.1016/j.snb.2020.129163>
27. Dronina, J., Bubniene, U.S., Ramanavicius, A.: The application of DNA polymerases and Cas9 as representative of DNA-modifying enzymes group in DNA sensor design (review). *Biosens. Bioelectron.* **175**, 112867 (2021). <https://doi.org/10.1016/j.bios.2020.112867>
28. Borzouee, F., Varshosaz, J., Cohan, R.A., et al.: A comparative analysis of different enzyme immobilization nanomaterials: progress, constraints and recent trends. *Curr. Med. Chem.* **28**, 3980–4003 (2021). <https://doi.org/10.2174/0929867328999201214225249>
29. Singh, A.K., Bilal, M., Iqbal, H.M.N., et al.: Bioremediation of lignin derivatives and phenolics in wastewater with lignin modifying enzymes: Status, opportunities and challenges. *Sci. Total Environ.* **777**, 145988 (2021). <https://doi.org/10.1016/j.scitotenv.2021.145988>
30. Allied Market Research (2021) Enzymes Market Type (Protease, Carbohydrase, Lipase, Polymerase and Nuclease, and Other Types), Source (Microorganisms, Plants, and Animals), Reaction Type (Hydrolase, Oxidoreductase, Transferase, Lyase, and Other Reaction Types), and Application (Food and
31. Intasian, P., Prakinee, K., Phintha, A., et al.: Enzymes, in vivo biocatalysis, and metabolic engineering for enabling a circular economy and sustainability. *Chem. Rev.* **121**, 10367–10451 (2021). <https://doi.org/10.1021/acs.chemrev.1c00121>
32. Andrade, T.A., Martín, M., Errico, M., Christensen, K.V.: Biodiesel production catalyzed by liquid and immobilized enzymes: optimization and economic analysis. *Chem. Eng. Res. Des.* **141**, 1–14 (2019). <https://doi.org/10.1016/j.cherd.2018.10.026>
33. Ferreira, R., da, G., Azzoni, A.R., Freitas, S.: Techno-economic analysis of the industrial production of a low-cost enzyme using *E. coli*: the case of recombinant  $\beta$ -glucosidase. *Biotechnol. Biofuels* **11**, 81 (2018). <https://doi.org/10.1186/s13068-018-1077-0>
34. Tamura, T., Hamachi, I.: Chemistry for covalent modification of endogenous/native proteins: from test tubes to complex biological systems. *J. Am. Chem. Soc.* **141**, 2782–2799 (2019). <https://doi.org/10.1021/jacs.8b11747>

35. Song, J., Li, F., Leier, A., et al.: PROSPERous: high-throughput prediction of substrate cleavage sites for 90 proteases with improved accuracy. *Bioinformatics* **34**, 684–687 (2018). <https://doi.org/10.1093/bioinformatics/btx670>
36. Rodríguez, M., García Fillería, S.F., Tironi, V.A.: Simulated gastrointestinal digestion of amaranth flour and protein isolate: Comparison of methodologies and release of antioxidant peptides. *Food Res. Int.* **138**, 109735 (2020). <https://doi.org/10.1016/j.foodres.2020.109735>
37. Martini, S., Conte, A., Tagliazucchi, D.: Comparative peptidomic profile and bioactivities of cooked beef, pork, chicken and turkey meat after in vitro gastro-intestinal digestion. *J. Proteomics* **208**, 103500 (2019). <https://doi.org/10.1016/j.jprot.2019.103500>
38. Basilicata, M., Pepe, G., Adesso, S., et al.: Antioxidant properties of buffalo-milk dairy products: a  $\beta$ -Lg peptide released after gastrointestinal digestion of buffalo ricotta cheese reduces oxidative stress in intestinal epithelial cells. *Int. J. Mol. Sci.* **19**, 1955 (2018). <https://doi.org/10.3390/ijms19071955>
39. Zielińska, E., Baraniak, B., Karaś, M.: Identification of antioxidant and anti-inflammatory peptides obtained by simulated gastrointestinal digestion of three edible insect species (*Grylodes sigillatus*, *Tenebrio molitor*, *Schistocerca gregaria*). *Int. J. Food Sci. Technol.* **53**, 2542–2551 (2018). <https://doi.org/10.1111/ijfs.13848>
40. Hall, F.G., Jones, O.G., O’Haire, M.E., Liceaga, A.M.: Functional properties of tropical banded cricket (*Grylodes sigillatus*) protein hydrolysates. *Food Chem.* **224**, 414–422 (2017). <https://doi.org/10.1016/j.foodchem.2016.11.138>
41. Zhou, Z.F., Ren, Z.X., Yu, H.Y., et al.: Effects of different modification techniques on molecular structure and bioactivity of *Bombyx mori* pupa protein. *J. Asia Pac. Entomol.* **20**, 35–41 (2017). <https://doi.org/10.1016/j.aspen.2016.11.008>
42. Vercruyse, L., Smaghe, G., Beckers, T., Van, C.J.: Antioxidative and ACE inhibitory activities in enzymatic hydrolysates of the cotton leafworm, *Spodoptera littoralis*. *Food Chem.* **114**, 38–43 (2009). <https://doi.org/10.1016/j.foodchem.2008.09.011>
43. Vercruyse, L., Smaghe, G., Herregods, G., Van Camp, J.: ACE inhibitory activity in enzymatic hydrolysates of insect protein. *J. Agri. Food Chem.* **53**, 5207–5211 (2005). <https://doi.org/10.1021/jf050337q>
44. Najafian, L., Babji, A.S.: Production of bioactive peptides using enzymatic hydrolysis and identification of antioxidative peptides from patin (*Pangasiusutchi*) sarcoplasmic protein hydrolysate. *J. Funct. Foods* **9**, 280–289 (2014). <https://doi.org/10.1016/j.jff.2014.05.003>
45. Zhang, M., Huang, T., Mu, T.: Improvement of thermal, microwave and ultrasonication pretreatment on the production of antioxidant peptides from sweet potato protein via in vitro gastrointestinal digestion. *Int. J. Food Sci. Technol.* **54**, 2338–2345 (2019). <https://doi.org/10.1111/ijfs.14095>
46. Dhiman, A., Prabhakar, P.K.: Micronization in food processing: A comprehensive review of mechanistic approach, physicochemical, functional properties and self-stability of micronized food materials. *J. Food Eng.* **292**, 110248 (2021). <https://doi.org/10.1016/j.jfoodeng.2020.110248>
47. Habinshuti, I., Mu, T.H., Zhang, M.: Ultrasound microwave-assisted enzymatic production and characterization of antioxidant peptides from sweet potato protein. *Ultrason Sonochem.* **69**, 105262 (2020). <https://doi.org/10.1016/j.ultsonch.2020.105262>
48. Vanga, S.K., Wang, J., Jayaram, S., Raghavan, V.: Effects of pulsed electric fields and ultrasound processing on proteins and enzymes: a review. *Processes* **9**, 722 (2021). <https://doi.org/10.3390/pr9040722>
49. Wang, J., Wang, J., Kranthi Vanga, S., Raghavan, V.: Influence of high-intensity ultrasound on the IgE binding capacity of Act d 2 allergen, secondary structure, and In-vitro digestibility of kiwifruit proteins. *Ultrason Sonochem.* **71**, 105409 (2021). <https://doi.org/10.1016/j.ultsonch.2020.105409>
50. Bhangu, S.K., Ashokkumar, M., Cavalieri, F.: Synthesis of bio-functional nanoparticles from sono-responsive amino acids using high frequency ultrasound. *Ultrason Sonochem.* **63**, 104967 (2020). <https://doi.org/10.1016/j.ultsonch.2020.104967>

51. Rios-Romero, E.A., Ochoa-Martínez, L.A., Morales-Castro, J., et al.: Ultrasound in orange sweet potato juice: bioactive compounds, antioxidant activity, and enzymatic inactivation. *J. Food Process Preserv.* **42**, e13633 (2018). <https://doi.org/10.1111/jfpp.13633>
52. Cao, X., Cai, C., Wang, Y., Zheng, X.: The inactivation kinetics of polyphenol oxidase and peroxidase in bayberry juice during thermal and ultrasound treatments. *Innov. Food Sci. Emerg. Technol.* **45**, 169–178 (2018). <https://doi.org/10.1016/j.ifset.2017.09.018>
53. Gao, X., Feng, T., Liu, E., et al.: Ougan juice debittering using ultrasound-aided enzymatic hydrolysis: Impacts on aroma and taste. *Food Chem.* **345**, 128767 (2021). <https://doi.org/10.1016/j.foodchem.2020.128767>
54. Utekar, P.G., Kininge, M.M., Gogate, P.R.: Intensification of delignification and enzymatic hydrolysis of orange peel waste using ultrasound for enhanced fermentable sugar production. *Chem. Eng. Process Process Intensif.* **168**, 108556 (2021). <https://doi.org/10.1016/j.cep.2021.108556>
55. Chandrapala, J., Zisu, B., Palmer, M., et al.: Effects of ultrasound on the thermal and structural characteristics of proteins in reconstituted whey protein concentrate. *Ultrason Sonochem.* **18**, 951–957 (2011). <https://doi.org/10.1016/j.ultsonch.2010.12.016>
56. Li, H., Hu, Y., Zhao, X., et al.: Effects of different ultrasound powers on the structure and stability of protein from sea cucumber gonad. *LWT* **137**, 110403 (2021). <https://doi.org/10.1016/j.lwt.2020.110403>
57. Zhao, Y., Wen, C., Feng, Y., et al.: Effects of ultrasound-assisted extraction on the structural, functional and antioxidant properties of *Dolichos lablab* L. Protein. *Process Biochem.* **101**, 274–284 (2021). <https://doi.org/10.1016/j.procbio.2020.11.027>
58. Decker, H., Schweikardt, T., Nillius, D., et al.: Similar enzyme activation and catalysis in hemocyanins and tyrosinases. *Gene* **398**, 183–191 (2007). <https://doi.org/10.1016/j.gene.2007.02.051>
59. Wang, D., Yan, L., Ma, X., et al.: Ultrasound promotes enzymatic reactions by acting on different targets: enzymes, substrates and enzymatic reaction systems. *Int. J. Biol. Macromol.* **119**, 453–461 (2018). <https://doi.org/10.1016/j.ijbiomac.2018.07.133>
60. Nadar, S.S., Rathod, V.K.: Ultrasound assisted intensification of enzyme activity and its properties: a mini-review. *World J. Microbiol. Biotechnol.* **33**, 170 (2017). <https://doi.org/10.1007/s11274-017-2322-6>
61. Mirmoghadaie, L., Shojaee Aliabadi, S., Hosseini, S.M.: Recent approaches in physical modification of protein functionality. *Food Chem.* **199**, 619–627 (2016). <https://doi.org/10.1016/j.foodchem.2015.12.067>
62. Soria, A.C., Villamiel, M.: Effect of ultrasound on the technological properties and bioactivity of food: a review. *Trends Food Sci. Technol.* **21**, 323–331 (2010). <https://doi.org/10.1016/j.tifs.2010.04.003>
63. Ma, X., Wang, W., Zou, M., et al.: Properties and structures of commercial polygalacturonase with ultrasound treatment: role of ultrasound in enzyme activation. *RSC Adv.* **5**, 107591–107600 (2015). <https://doi.org/10.1039/C5RA19425C>
64. Osa, R., Zhou, C., Xu, B., et al.: Effects of ultrasound, osmotic dehydration, and osmosonication pretreatments on bioactive compounds, chemical characterization, enzyme inactivation, color, and antioxidant activity of dried ginger slices. *J. Food Biochem.* **43**, e12832 (2019). <https://doi.org/10.1111/jfbc.12832>
65. Yang, C.Y., Fang, T.J.: Kinetics for enzymatic hydrolysis of rice hulls by the ultrasonic pretreatment with a bio-based basic ionic liquid. *Biochem. Eng. J.* **100**, 23–29 (2015). <https://doi.org/10.1016/j.bej.2015.04.012>
66. Pu, Y., Zou, Q., Hou, D., et al.: Molecular weight kinetics and chain scission models for dextran polymers during ultrasonic degradation. *Carbohydr. Polym.* **156**, 71–76 (2017). <https://doi.org/10.1016/j.carbpol.2016.09.017>
67. Gogate, P.R., Prajapat, A.L.: Depolymerization using sonochemical reactors: a critical review. *Ultrason Sonochem.* **27**, 480–494 (2015). <https://doi.org/10.1016/j.ultsonch.2015.06.019>
68. Luo, J., Fang, Z., Smith, R.L.: Ultrasound-enhanced conversion of biomass to biofuels. *Prog. Energy Combust. Sci.* **41**, 56–93 (2014). <https://doi.org/10.1016/j.peccs.2013.11.001>

69. Jin, J., Ma, H., Wang, W., et al.: Effects and mechanism of ultrasound pretreatment on rapeseed protein enzymolysis. *J. Sci. Food Agri.* **96**, 1159–1166 (2016). <https://doi.org/10.1002/jsfa.7198>
70. Quilles Junior, J.C., Ferrarezi, A.L., Borges, J.P., et al.: Ultrasound affects the selectivity and activity of immobilized lipases applied to fatty acid ethyl ester synthesis. *Acta Sci. Technol.* **42**, e46582 (2019). <https://doi.org/10.4025/actascitechnol.v42i1.46582>
71. Priya, G.P.R.: Ultrasound-assisted intensification of activity of free and immobilized enzymes: a review. *Ind. Eng. Chem. Res.* **60**, 9650–9668 (2021). <https://doi.org/10.1021/acs.iecr.1c01217>
72. Li, H., Cabañas-Gac, F., Hadidi, L., et al.: Ultrasound assisted wet media milling synthesis of nanofiber-cage LiFePO<sub>4</sub>/C. *Ultrason Sonochem.* **68**, 105177 (2020). <https://doi.org/10.1016/j.ultrasonch.2020.105177>
73. Zisu, B., Lee, J., Chandrapala, J., et al.: Effect of ultrasound on the physical and functional properties of reconstituted whey protein powders. *J. Dairy Res.* **78**, 226–232 (2011). <https://doi.org/10.1017/S0022029911000070>
74. O’Sullivan, J., Arellano, M., Pichot, R., Norton, I.: The effect of ultrasound treatment on the structural, physical and emulsifying properties of dairy proteins. *Food Hydrocoll.* **42**, 386–396 (2014). <https://doi.org/10.1016/j.foodhyd.2014.05.011>
75. Leon, A.M., Medina, W.T., Park, D.J., Aguilera, J.M.: Properties of microparticles from a whey protein isolate/alginate emulsion gel. *Food Sci. Technol. Int.* **24**, 414–423 (2018). <https://doi.org/10.1177/1082013218762210>
76. Jambtrak, A.R., Mason, T.J., Lelas, V., et al.: Effect of ultrasound treatment on particle size and molecular weight of whey proteins. *J. Food Eng.* **121**, 15–23 (2014). <https://doi.org/10.1016/j.jfoodeng.2013.08.012>
77. Madadlou, A., Mousavi, M.E., Emam-Djomeh, Z., et al.: Comparison of pH-dependent sonodisruption of re-assembled casein micelles by 35 and 130kHz ultrasounds. *J. Food Eng.* **95**, 505–509 (2009). <https://doi.org/10.1016/j.jfoodeng.2009.06.008>
78. Wu, S., Li, G., Xue, Y., et al.: Solubilization of micellar casein powders by high-power ultrasound. *Ultrason Sonochem.* **67**, 105131 (2020). <https://doi.org/10.1016/j.ultrasonch.2020.105131>
79. Yang, M., Zeng, Q., Wang, Y., et al.: Effect of ultrasound pretreatment on the physicochemical properties and simulated gastrointestinal digestibility of micellar casein concentrates. *LWT* **136**, 110319 (2021). <https://doi.org/10.1016/j.lwt.2020.110319>
80. Yang, L., Guo, Z., Wei, J., et al.: Extraction of low molecular weight peptides from bovine bone using ultrasound-assisted double enzyme hydrolysis: impact on the antioxidant activities of the extracted peptides. *LWT* **146**, 111470 (2021). <https://doi.org/10.1016/j.lwt.2021.111470>
81. Huang, G., Chen, S., Tang, Y., et al.: Stimulation of low intensity ultrasound on fermentation of skim milk medium for yield of yoghurt peptides by *Lactobacillus paracasei*. *Ultrason Sonochem.* **51**, 315–324 (2019). <https://doi.org/10.1016/j.ultrasonch.2018.09.033>
82. Ai, M., Zhang, Z., Fan, H., et al.: High-intensity ultrasound together with heat treatment improves the oil-in-water emulsion stability of egg white protein peptides. *Food Hydrocoll.* **111**, 106256 (2021). <https://doi.org/10.1016/j.foodhyd.2020.106256>
83. Alahyaribeik, S., Ullah, A.: Effects of ultrasound-assisted alkaline extraction on antioxidant activity and functional characteristics of chicken feather keratin peptides. *Chem. Select* **5**, 13788–13794 (2020). <https://doi.org/10.1002/slct.202002887>
84. Liu, L., Li, X., Du, L., et al.: Effect of ultrasound assisted heating on structure and antioxidant activity of whey protein peptide grafted with galactose. *LWT* **109**, 130–136 (2019). <https://doi.org/10.1016/j.lwt.2019.04.015>
85. Alizadeh, O., Aliakbarlu, J.: Effects of ultrasound and ohmic heating pretreatments on hydrolysis, antioxidant and antibacterial activities of whey protein concentrate and its fractions. *LWT* **131**, 109913 (2020). <https://doi.org/10.1016/j.lwt.2020.109913>
86. Falade, E.O., Mu, T.H., Zhang, M.: Improvement of microwave-assisted ultrasound enzymatic production and high hydrostatic pressure on emulsifying, rheological and interfacial characteristics of sweet potato protein hydrolysates. *Food Hydrocoll.* **117**, 106684 (2021). <https://doi.org/10.1016/j.foodhyd.2021.106684>



87. Zhao, F., Zhai, X., Liu, X., et al.: Effects of high-intensity ultrasound pretreatment on structure, properties, and enzymolysis of walnut protein isolate. *Molecules* **27**, 208 (2021). <https://doi.org/10.3390/molecules27010208>
88. Guerra-Almonacid, C.M., Torruco-Uco, J.G., Jonh Jairo Méndez-Arteaga, W.M.-A., Rodríguez-Miranda, J.: Effect of ultrasound pretreatment on the antioxidant capacity and anti-hypertensive activity of bioactive peptides obtained from the protein hydrolysates of *Erythrina edulis*. *Emirates J. Food Agric.* **288** (2019). <https://doi.org/10.9755/ejfa.2019.v31.i4.1938>
89. Li, Z., Wang, J., Zheng, B., Guo, Z.: Impact of combined ultrasound-microwave treatment on structural and functional properties of golden threadfin bream (*Nemipterus virgatus*) myofibrillar proteins and hydrolysates. *Ultrason Sonochem.* **65**, 105063 (2020). <https://doi.org/10.1016/j.ultsonch.2020.105063>
90. Gao, X., Zhang, J., Liu, E., et al.: Enhancing the taste of raw soy sauce using low intensity ultrasound treatment during moromi fermentation. *Food Chem.* **298**, 124928 (2019). <https://doi.org/10.1016/j.foodchem.2019.05.202>
91. Rivero-Pino, F., Espejo-Carpio, F.J., Pérez-Gálvez, R., et al.: Effect of ultrasound pretreatment and sequential hydrolysis on the production of *Tenebrio molitor* antidiabetic peptides. *Food Bioprod. Process* **123**, 217–224 (2020). <https://doi.org/10.1016/j.fbp.2020.07.003>
92. Ruan, S., Luo, J., Li, Y., et al.: Ultrasound-assisted liquid-state fermentation of soybean meal with *Bacillus subtilis*: effects on peptides content, ACE inhibitory activity and biomass. *Process Biochem.* **91**, 73–82 (2020). <https://doi.org/10.1016/j.procbio.2019.11.035>
93. López-Gámez, G., Elez-Martínez, P., Martín-Belloso, O., Soliva-Fortuny, R.: Enhancing carotenoid and phenolic contents in plant food matrices by applying non-thermal technologies: bioproduction versus improved extractability. *Trends Food Sci. Technol.* **112**, 622–630 (2021). <https://doi.org/10.1016/j.tifs.2021.04.022>
94. Zhang, S., Sun, L., Ju, H., et al.: Research advances and application of pulsed electric field on proteins and peptides in food. *Food Res. Int.* **139**, 109914 (2021). <https://doi.org/10.1016/j.foodres.2020.109914>
95. Zhu, Z., Wang, F., Xia, Q., et al.: Health promoting benefits of PEF: bioprotective capacity against the oxidative stress and its impact on nutrient and bioactive compound bioaccessibility. In: *Pulsed Electric Fields to Obtain Healthier and Sustainable Food for Tomorrow*. Elsevier, pp. 51–64 (2020)
96. Ohshima, T., Tamura, T., Sato, M.: Influence of pulsed electric field on various enzyme activities. *J. Electrostat.* **65**, 156–161 (2007). <https://doi.org/10.1016/j.elstat.2006.07.005>
97. Buckow, R., Ng, S., Toepfl, S.: Pulsed electric field processing of orange juice: a review on microbial, enzymatic, nutritional, and sensory quality and stability. *Comput. Rev. Food Sci. Food Saf.* **12**, 455–467 (2013). <https://doi.org/10.1111/1541-4337.12026>
98. Xiang, B.Y., Ngadi, M.O., Ochoa-Martínez, L.A., Simpson, M.V.: Pulsed electric field-induced structural modification of whey protein isolate. *Food Bioprocess Technol.* **4**, 1341–1348 (2011). <https://doi.org/10.1007/s11947-009-0266-z>
99. Qian, J.Y., Gu, Y.P., Jiang, W., Chen, W.: Inactivating effect of pulsed electric field on lipase in brown rice. *Innov. Food Sci. Emerg. Technol.* **22**, 89–94 (2014). <https://doi.org/10.1016/j.ifset.2014.01.010>
100. Zhao, W., Yang, R., Zhang, H.Q.: Recent advances in the action of pulsed electric fields on enzymes and food component proteins. *Trends Food Sci. Technol.* **27**, 83–96 (2012). <https://doi.org/10.1016/j.tifs.2012.05.007>
101. Lu, C., Li, F., Yan, X., et al.: Effect of pulsed electric field on soybean isoflavone glycosides hydrolysis by  $\beta$ -glucosidase: Investigation on enzyme characteristics and assisted reaction. *Food Chem.* **378**, 132032 (2022). <https://doi.org/10.1016/j.foodchem.2021.132032>
102. Stuyver, T., Danovich, D., Joy, J., Shaik, S.: External electric field effects on chemical structure and reactivity. *WIREs Comput. Mol. Sci.* **10** (2020). <https://doi.org/10.1002/wcms.1438>
103. Ho, S.Y., Mittal, G.S., Cross, J.D.: Effects of high field electric pulses on the activity of selected enzymes. *J. Food Eng.* **31**, 69–84 (1997). [https://doi.org/10.1016/S0260-8774\(96\)00052-0](https://doi.org/10.1016/S0260-8774(96)00052-0)
104. Zhong, K., Hu, X., Zhao, G., et al.: Inactivation and conformational change of horseradish peroxidase induced by pulsed electric field. *Food Chem.* **92**, 473–479 (2005). <https://doi.org/10.1016/j.foodchem.2004.08.010>

105. Miklavcic, D.: Handbook of Electroporation. Springer International Publishing, Cham (2016)
106. Welborn, V.V., Ruiz Pestana, L., Head-Gordon, T.: Computational optimization of electric fields for better catalysis design. *Nat. Catal.* **1**, 649–655 (2018). <https://doi.org/10.1038/s41929-018-0109-2>
107. Stuyver, T., Huang, J., Mallick, D., et al.: TITAN: a code for modeling and generating electric fields—features and applications to enzymatic reactivity. *J. Comput. Chem.* **41**, 74–82 (2020). <https://doi.org/10.1002/jcc.26072>
108. Franco, D., Munekata, P.E.S., Agregán, R., et al.: Application of pulsed electric fields for obtaining antioxidant extracts from fish residues. *Antioxidants* **9**, 90 (2020). <https://doi.org/10.3390/antiox9020090>
109. López-Gámez, G., Elez-Martínez, P., Martín-Belloso, O., Soliva-Fortuny, R.: Pulsed electric fields affect endogenous enzyme activities, respiration and biosynthesis of phenolic compounds in carrots. *Postharvest Biol. Technol.* **168**, 111284 (2020). <https://doi.org/10.1016/j.postharvbio.2020.111284>
110. Toepfl, S., Kinsella, J., Parniakov, O.: Industrial scale equipment, patents, and commercial applications. In: *Pulsed Electric Fields to Obtain Healthier and Sustainable Food for Tomorrow*. Elsevier, pp. 269–281 (2020)
111. He, Y., Pan, X., Chi, C.F., et al.: Ten new pentapeptides from protein hydrolysate of miuiy croaker (*Miichthys miuiy*) muscle: Preparation, identification, and antioxidant activity evaluation. *LWT* **105**, 1–8 (2019). <https://doi.org/10.1016/j.lwt.2019.01.054>
112. Arihara, K., Yokoyama, I., Ohata, M.: Generation of bioactivities from proteins of animal sources by enzymatic hydrolysis and the Maillard reaction. In: *Biologically Active Peptides*. Elsevier, pp. 403–425 (2021)
113. Talla, G., Gangopadhyay, S., Biswas, C.: Effect of impregnated powder materials on surface integrity aspects of Inconel 625 during electrical discharge machining. *Proc. Inst. Mech. Eng. Part BJ Eng. Manuf.* **232**, 1259–1272 (2018). <https://doi.org/10.1177/0954405416666904>
114. Vaessen, E.M.J., den Besten, H.M.W., Patra, T., et al.: Pulsed electric field for increasing intracellular trehalose content in *Lactobacillus plantarum* WCFS1. *Innov. Food Sci. Emerg. Technol.* **47**, 256–261 (2018). <https://doi.org/10.1016/j.ifset.2018.03.007>
115. Zhao, Y., Liang, R., Yang, Y., Lin, S.: The mechanism of pulsed electric field (PEF) targeting location on the spatial conformation of pine nut peptide. *J. Theor. Biol.* **492**, 110195 (2020). <https://doi.org/10.1016/j.jtbi.2020.110195>
116. Akaberi, S., Gusbeth, C., Silve, A., et al.: Effect of pulsed electric field treatment on enzymatic hydrolysis of proteins of *Scenedesmus almeriensis*. *Algal. Res.* **43**, 101656 (2019). <https://doi.org/10.1016/j.algal.2019.101656>
117. Li, Y., Zhang, S., Bao, Z., et al.: Exploring the activation mechanism of alcalase activity with pulsed electric field treatment: effects on enzyme activity, spatial conformation, molecular dynamics simulation and molecular docking parameters. *Innov. Food Sci. Emerg. Technol.* **76**, 102918 (2022). <https://doi.org/10.1016/j.ifset.2022.102918>
118. Liu, Y.F., Oey, I., Bremer, P., et al.: Proteolytic pattern, protein breakdown and peptide production of ovomucin-depleted egg white processed with heat or pulsed electric fields at different pH. *Food Res. Int.* **108**, 465–474 (2018). <https://doi.org/10.1016/j.foodres.2018.03.075>
119. Bhat, Z.F., Morton, J.D., Mason, S.L., et al.: Pulsed electric field: A new way to improve digestibility of cooked beef. *Meat Sci.* **155**, 79–84 (2019). <https://doi.org/10.1016/j.meatsci.2019.05.005>
120. Ghosh, S., Gillis, A., Sheviriyov, J., et al.: Towards waste meat biorefinery: Extraction of proteins from waste chicken meat with non-thermal pulsed electric fields and mechanical pressing. *J. Clean. Prod.* **208**, 220–231 (2019). <https://doi.org/10.1016/j.jclepro.2018.10.037>
121. Dudev, T., Ilieva, S., Doudeva, L.: How an electric field can modulate the metal ion selectivity of protein binding sites: insights from DFT/PCM calculations. *Phys. Chem. Chem. Phys.* **20**, 24633–24640 (2018). <https://doi.org/10.1039/C8CP04050H>
122. Jiang, Y., Xing, M., Kang, Q., et al.: Pulse electric field assisted process for extraction of Jiuzao glutelin extract and its physicochemical properties and biological activities investigation. *Food Chem.* 132304 (2022). <https://doi.org/10.1016/j.foodchem.2022.132304>

123. Zhang, S., Zhang, M., Xing, J., Lin, S.: A possible mechanism for enhancing the antioxidant activity by pulsed electric field on pine nut peptide Glutamine-Tryptophan-Phenylalanine-Histidine. *J. Food Biochem.* e12714 (2018). <https://doi.org/10.1111/jfbc.12714>
124. Lin, S., Jin, Y., Liu, M., et al.: Research on the preparation of antioxidant peptides derived from egg white with assisting of high-intensity pulsed electric field. *Food Chem.* **139**, 300–306 (2013). <https://doi.org/10.1016/j.foodchem.2013.01.048>
125. Lin, S., Liang, R., Li, X., et al.: Effect of pulsed electric field (PEF) on structures and antioxidant activity of soybean source peptides-SHCMN. *Food Chem.* **213**, 588–594 (2016). <https://doi.org/10.1016/j.foodchem.2016.07.017>
126. Zhang, S., Liang, R., Zhao, Y., et al.: Immunomodulatory activity improvement of pine nut peptides by a pulsed electric field and their structure-activity relationships. *J. Agric. Food Chem.* **67**, 3796–3810 (2019). <https://doi.org/10.1021/acs.jafc.9b00760>
127. Han, Z., Cai, M., Cheng, J.H., Sun, D.W.: Effects of electric fields and electromagnetic wave on food protein structure and functionality: a review. *Trends Food Sci. Technol.* **75**, 1–9 (2018). <https://doi.org/10.1016/j.tifs.2018.02.017>
128. Ohshima, T., Tanino, T., Guionet, A., et al.: Mechanism of pulsed electric field enzyme activity change and pulsed discharge permeabilization of agricultural products. *Jpn. J. Appl. Phys.* **60**, 060501 (2021). <https://doi.org/10.35848/1347-4065/abf479>

# Vaccine History: From Smallpox to Covid-19



**Camila Puton, Fernanda Gabriel Aires Saad, Ricelly Pires Vieira, Eduarda de Soares Libânio, Vinicius Barreto da Silva, Wilson de Melo Cruvinel, Leonardo Luiz Borges, Carlton A. Taft, and Clayson Moura Gomes**

**Abstract** In the early seventeenth century, smallpox was one of the most fearsome communicable diseases in the world. Lady Mary Montagu noted that the disease could be prevented by introducing liquid extracted from smallpox scabs from an infected patient into the skin of healthy individuals. This process, known as “variolation” was used in England and in USA until the first investigations by the English physician Edward Jenner appeared. Jenner created the vaccine for an animal poxvirus from the pustule formed by the vaccinia virus in the teats of cows, where the technique was essentially based on the idea that a virulent agent for animals could be attenuated in humans. In 1885, Louis Pasteur, through a fixed virus which was obtained by successive passages in the nervous tissue of rabbits with the dissecting action of potassium hydroxide, developed the vaccine against rabies, in which similar procedures were adopted in the development of several vaccines of live attenuated viruses. Already in the 1940s, a revolution occurred with the discovery that cells could be cultured in vitro and used as substrates for viral growth. Oral polio vaccine and vaccines against measles, rubella, mumps and chickenpox were made possible by selecting clones by passage in in vitro cell culture. Some RNA virus have segmented genomes that can be manipulated. Co-cultivation of two virus in cell culture with clone selection by plaque formation allows the isolation of virus with segments from both. This regrouping planned to create three main vaccines: live and inactivated influenza as well as one of two rotavirus vaccines. Another discovery in the late nineteenth century was that immunogenicity could be maintained as the substance contained in those killed by heat or chemical treatment. This type of inactivation was first applied to pathogens of typhoid fever, plague and cholera bacilli. In the twentieth century, chemical inactivation was also applied to a virus. The influenza vaccine was

---

C. Puton · F. G. Aires Saad · R. P. Vieira · E. de Soares Libânio · V. B. da Silva · W. de Melo Cruvinel · L. L. Borges · C. M. Gomes (✉)

Escola de Ciências Médicas E da Vida, Pontifícia Universidade Católica de Goiás, Goiânia, GO, Brazil

e-mail: [claysonmoura10@gmail.com](mailto:claysonmoura10@gmail.com)

L. L. Borges

Universidade Estadual de Goiás, Campus Central, Anápolis, GO, Brazil

C. A. Taft

Centro Brasileiro de Pesquisas Físicas, Rio de Janeiro, RJ, Brazil

the first successful inactivated virus vaccine, developed against Polio and Hepatitis A. Besides, several vaccines consist of partially or fully purified proteins. Most of the inactivated flu vaccines used are created by growing the virus in embryonated eggs and then breaking down the entire virus with detergents. The viral hemagglutinin protein is purified to serve as the vaccine antigen, although other influenza virus components may be part of the final product. Early in the history of bacteriology, morphological studies and chemical analyzes showed that many pathogens were surrounded by a polysaccharide capsule and that antibodies against the capsule could promote phagocytosis. The first use of this information to create a vaccine was the development of the meningococcal polysaccharide vaccine. After years of study and development in bacteriology, the scientific community faced the Covid-19 pandemic in 2020, marked by the race against time in the invention of effective vaccines against the SARS-CoV-2 virus. After all, most of vaccines take more than a decade to be formulated and, in the case of the vaccine against the new coronavirus, in less than a year, at least 34 candidate vaccines appeared in clinical analysis. New vaccine production techniques using DNA and RNA recombination techniques are being implemented in this race. In Brazil, the most widely distributed vaccines approved by Anvisa are AstraZeneca, CoronaVac and Pfizer-BioNTech. The AstraZeneca/Oxford vaccine is composed of a non-replicating viral vector, which consists of a defective chimpanzee virus (adenovirus), with a segment of the SARS-CoV-2 genome, responsible for producing the structure present on the viral surface (protein S), being recognized by human cells, triggering an immune response against Coronavirus. The CoronaVac vaccine is composed by the inactivated SARS-CoV-2 virus, along with its complete structure. It is unable to multiply, although it can stimulate the response to produce antibodies. The Pfizer-BioNTech vaccine, on the other hand, consists of a formulated lipid nanoparticle of nucleoside-modified mRNA that encodes the pre-fusion peak glycoprotein of SARS-CoV-2. Despite the small amount of dose applications in Brazil, the Janssen vaccine has recently started its distribution in the country. This is the only vaccine, so far, with a single dose application. It is an adenovirus 26 (Ad26) vector vaccine that contains in its interior genetic material of the S protein contained in the surface spikes of SARS-CoV-2, and that stimulates, after application, the cellular responses of T CD4 + and T CD8 + antibodies. Here, we propose a detailed review of the entire history of vaccination, from Smallpox to Covid-19.

**Keywords** Vaccination · Immunization · Antigen · Pandemics · Coronavirus

## 1 Introduction

In the early seventeenth century, smallpox was one of the most terrible diseases in the world. Lady Mary Montagu observed that the disease could be prevented by introducing fluid extracted from smallpox scabs from an infected patient into the skin of healthy individuals. This process, known as “variolation” was used in England

and in the USA until the first investigations by the English physician Edward Jenner emerged. Jenner created the vaccine using an animal poxvirus from the pustule formed by the vaccinia virus on the teats of cows, the technique was essentially based on the idea that a virulent agent for animals could be attenuated in humans.

In 1885, Louis Pasteur, using a fixed virus which was obtained by successive passages in the nervous tissue of rabbits with the dissecting action of potassium hydroxide, developed the vaccine against rabies, in which similar procedures were adopted in the development of several live attenuated viruses vaccines. Some years after, in the 1940s, a revolution took place with the discovery that cells could be grown *in vitro* and used as substrates for viral growth. The oral polio vaccine and the measles, rubella, mumps, and chickenpox vaccines were made possible through selection of clones by passage in *in vitro* cell culture.

Furthermore, certain RNA viruses have segmented genomes that can be manipulated. Co-cultivation of two viruses in cell culture with selection of clones by plaque formation allows the isolation of viruses with RNA segments from both viruses. This regrouping allowed the creation of three main vaccines: live and inactivated influenza as well as one of two rotavirus vaccines.

Another discovery in the late nineteenth century was that immunogenicity could be maintained if bacteria were carefully killed by heat or chemical treatment. This type of inactivation was first applied to pathogens such as typhoid, plague, and cholera bacilli. In the twentieth century, chemical inactivation was also applied to viruses. The influenza vaccine was the first successfully inactivated virus vaccine, later developed against Polio and Hepatitis A.

In addition, several vaccines consist of partially or fully purified proteins. Most inactivated flu vaccines used today are created by growing the viruses in embryonated eggs and then breaking down the entire virus with detergents. The viral hemagglutinin (HA) protein is purified to serve as the vaccine antigen, although other components of the influenza virus may be present in the final product.

In the beginning of the history of bacteriology, morphological studies and chemical analyzes showed that many pathogens were surrounded by a polysaccharide capsule and that antibodies against the capsule could promote phagocytosis. The first use of this information to make a vaccine was in the development of the meningococcal polysaccharide vaccine.

After years of study and development in bacteriology, the scientific community faced the Covid-19 pandemic in 2019, marked by a race against time in the invention of an effective vaccine against the SARS-CoV2 virus. After all, the vast majority of vaccines take more than a decade to formulate and, in the case of the vaccine against the new coronavirus, in less than a year at least 34 candidate vaccines have emerged in clinical analysis. New vaccine production techniques using DNA and RNA recombination techniques are being implemented in this race.

In Brazil, the most widely distributed vaccines approved by Anvisa are AstraZeneca, CoronaVac and Pfizer-BioNTech. The AstraZeneca/Oxford vaccine is composed of a non-replicating viral vector, which consists of a defective chimpanzee virus (adenovirus) with a segment of the SARS-CoV-2 genome, responsible for the production of the structure present on the viral surface (protein S), being

recognized by human cells, triggering an immune response against the Coronavirus. The CoronaVac vaccine is composed of the inactivated (killed) SARS-CoV-2 virus, with its complete structure. It is unable to multiply, but stimulates the response to produce antibodies. The Pfizer-BioNTech vaccine consists of a formulated lipid nanoparticle of nucleoside-modified mRNA encoding the SARS-CoV-2 pre-fusion spike glycoprotein. Although in smaller distribution in Brazil, the Janssen vaccine had its application recently started. This is the only vaccine, so far, with application in a single dose. It is a vaccine of the adenovirus 26 (Ad26) vector that contains inside the genetic material of the S protein contained in the surface spikes of SARS-CoV-2, and that stimulates, after its application, the cellular responses of T CD4 + and T CD8 + antibodies.

## 2 Vaccination History

Since the beginning of human life there are pathogens that try to enter human bodies in order to reproduce and promote the evolution of their species. In order to survive, humans created a series of natural and adaptive immunological mechanisms against these microorganisms aiming at protection and homeostasis. However, just as humans evolved, microorganisms also managed to find ways to enter the human body by evading the immune system, which was the key of generating life-threatening diseases [1].

In this context, the vaccine emerges as a great partner in the fight for life due to its easy and speed in stimulating the effectiveness of the immune response from the original history of each infection, which can act by originating an immune mechanism that will prevent infection before the pathogen enters the cell or that will provide the necessary repair after cellular infection. Depending on each disease, the vaccine action mechanism differs in terms of its specific target. In 2018, more than 70 vaccines were available for more than 30 different microorganisms [1, 2].

Recalling the historical context, in the early seventeenth century, smallpox was one of the most terrible diseases in the world. Lady Mary Montagu observed that the disease could be prevented by introducing fluid extracted from smallpox scabs from an infected patient into the skin of healthy individuals. This process, known as “variolation” was used in England and the USA until the first investigations by the English physician Edward Jenner emerged [3]. Jenner created the vaccine for an animal poxvirus from the pustule formed by the vaccinia virus on the teats of cows. The technique was essentially based on the idea that a virulent agent for animals could be attenuated in humans [4]. Before vaccination, the risk of contracting the disease was about 30% and those who managed to survive acquired serious sequels. The last known case of smallpox was reported in Somalia in 1977. In 1980, the World Health Organization (WHO) declared eradication of the disease after the implementation of the vaccine as a preventive measure [1].

In 1885, Louis Pasteur, using a fixed virus in which it was obtained by successive passages in the nervous tissue of rabbits with the dissecting action of potassium

hydroxide, developed the vaccine against rabies, in which similar procedures were adopted in the development of several live attenuated virus vaccines [5]. The vaccine mechanism consists of a neutralization directed by viral antibodies that will enter the blood–brain barrier [1]. In the 1940s, a revolution took place with the discovery that cells could grow *in vitro* and could also be used as substrates for viral growth [6].

Oral polio vaccine and measles, rubella, mumps, and chickenpox vaccines were made possible through selection of clones by passage in *in vitro* cell culture [3, 7–10]. The polio vaccine, both in its inactive form (salk) and in its attenuated form (sabin) has unquestionable efficacy. According to WHO, in 2018, 33 cases were identified worldwide. The measles, rubella, mumps and chickenpox vaccine, generally applied in the quadrivalent form, in addition to being effective and universally applicable, can lead to the eradication of these exanthematous diseases with mass vaccination. According to WHO, the United Nations Fund (UNICEF) and the World Bank, between 2000 and 2007 there was a 74% drop in measles deaths due to implemented vaccination campaigns [1, 11].

Furthermore, certain RNA virus have segmented genomes that can be manipulated. Co-cultivation of two viruses in cell culture with selection of clones by plaque formation allows the isolation of viruses with RNA segments from both viruses. This regrouping allowed for the creation of three main vaccines: live and inactivated influenza [10, 12] as well as one of two rotavirus vaccines [13], this being the first to be part of the National Immunization Plan (PNI) in 2007 [11].

Another discovery in the late nineteenth century was that immunogenicity could be maintained if bacteria were carefully killed by heat or chemical treatment. This type of inactivation was first applied to pathogens such as typhoid, plague, and cholera bacilli [14, 15]. According to WHO, these vaccines provide about 85% of protection for 6 months and 50–60% protection in the first year [1].

In the twentieth century, chemical inactivation was also applied to virus. The influenza vaccine was the first successful inactivated virus vaccine, later developed against Polio and Hepatitis A [16–18]. The Hepatitis A vaccine is also presented in the attenuated form [2].

In addition, several vaccines consist of partially or fully purified proteins. Most inactivated flu vaccines used today are generated by growing the virus in embryonated eggs and then breaking down the entire virus with detergents. The viral hemagglutinin (HA) protein is purified to serve as the vaccine antigen, although other components of the influenza virus may be present in the final product [19].

In the beginning of the history of bacteriology, morphological studies and chemical analyzes showed that many pathogens were surrounded by a polysaccharide capsule and that antibodies against the capsule could promote phagocytosis. The first use of this information to make a vaccine was in the development of the meningococcal polysaccharide vaccine [20].

In this scenario, the National Immunization Program (PNI) was implemented in Brazil in 1973 by Oswaldo Cruz, which is considered a worldwide reference, in order to guarantee vaccination coverage to the target population and prevent the emergence of epidemiological outbreaks in the country. Currently, the vaccines contemplated in the PNI 2022 include all previously presented vaccines with the addition of the



vaccine against SARS-CoV2 in the determined age groups [21]. There are several technological groups involved in the process of implementation development and improvements in vaccine production [11].

2022 marks the 49th anniversary of the creation of the PNI, which has already been responsible for helping to create immunization programs in the Gaza Strip, Palestine and the West Bank, in addition to cooperating with the programs of several other conglomerates such as Argentina, the United States, Israel and Philippines. One of the biggest events held by the PNI was the eradication of smallpox, which was certified by the WHO commission and became part of the Brazilian legacy of improvements in public health. In addition to the eradications of previously epidemic diseases on a large scale, the PNI was also responsible for the creation of the Reference Center for Immunobiologicals (CRIES) that participate in the vaccination of immunodeficient individuals and in prophylaxis [22–25].

### 3 Vaccines Immunology

Vaccines against infectious diseases serve as a prophylactic exposure, inducing a controlled immune response to a given infectious agent. Our immune system is divided into innate and adaptive, with the activation of the innate immune system preceding the generation of adaptive immunity. The innate immune system is made up of several types of cells, such as neutrophils, dendritic cells, and macrophages, that function to interact with foreign molecules in a non-specific way. These cells phagocytize infectious agents, produce inflammatory cytokines and activate other immune cells through the secretion of chemokines [26].

The adaptive immune system, divided into humoral and cellular, responds to specific regions of the given infectious agent, called epitopes that compose the antigen. The humoral response depends on the activity of antibodies secreted by B cells, which bind to epitopes and generate the secretion of specific antibodies against the recognized antigen, thus leading to protection against infection [27]. Cellular responses are based on the action of T cells. All nucleated cells have molecules of the Major Histocompatibility Complex Class I (MHC-I) on their surface. When infected with an intracellular infectious agent, cells are able to present linear epitopes of these infectious agents complexed with MHC-I on their surface to alert the immune system of the infection. Cytotoxic T cells (CT) that contain the corresponding T cell receptor are able to bind to MHC-I presenting specific epitopes leading to the death of the infected cell [26].

Helper T cells (TH) are one of the most important in vaccine development. Antigen Presenting Cells (APCs) such as dendritic cells, macrophages and B cells are able to phagocytize, process and present CD4 + epitopes in complex with MHC-II on their surface. These epitopes stimulate CD4 + T cells leading to their maturation into TH cells, which are able to stimulate cells of the innate and adaptive immune system through the secretion of cytokines that are capable of making the immune response stronger and more effective. Depending on the secreted cytokine responses, they are

classified as T helper 1 (TH1) response or T helper 2 (TH2) response. TH2 responses favor the development of a humoral immune response, which has traditionally been the basis for vaccine development. Upon activation, B, TH, and TC cells proliferate to effectively deal with the infection AND some may persist after clearance, resulting in immune memory [27].

Another important concept is herd immunity, knowing that vaccines not only work at the organism level, but also at the population level. If a certain fraction (ranging from 60 to 90%) of the population is immune to an infectious agent, the disease has a very low probability of finding another naive host and spread around. This is important because it is not the entire population that can be vaccinated, there are some contraindications depending on the vaccine, such as disease stage and age Based on the history of the vaccine and the study of the immunological mechanisms involved, several vaccines have emerged such as BCG, Influenza, rubella, yellow fever, among others [28] (Fig. 1).

## 4 Current Vaccines

### 4.1 BCG

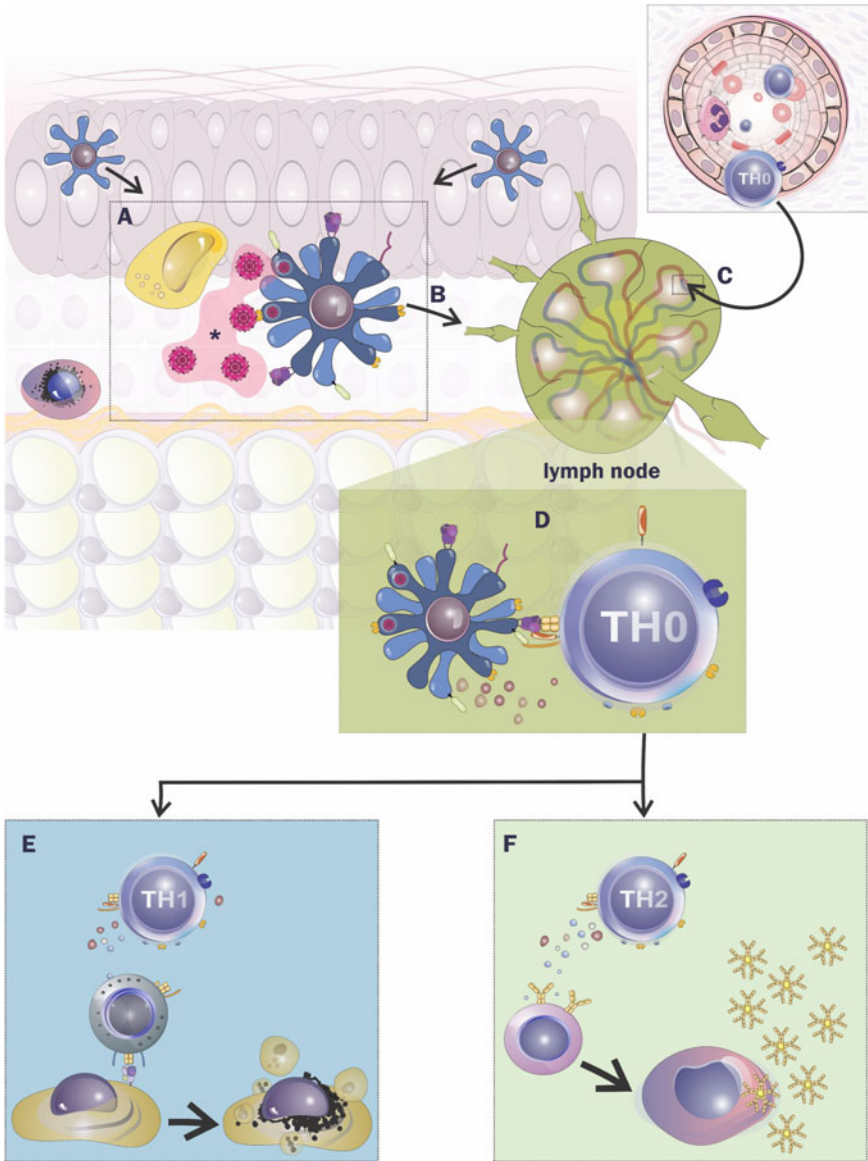
Tuberculosis (TB) is the leading cause of death from an infectious bacterial disease worldwide. The only licensed vaccine for tuberculosis prevention is *Mycobacterium bovis* bacille Calmette-Guérin (BCG), which protects people exposed to *Mycobacterium tuberculosis*. This vaccine was based on the attenuation of the bacteria that naturally cause tuberculosis in cattle and, occasionally, in humans [29].

The creation of this vaccine was analogous to the development of the smallpox vaccine, it was developed between 1906 and 1919 by Camille Calmett and Albert Guerin at the Pasteur Institute (Paris). The researchers obtained an attenuated strain of the original *Mycobacterium bovis* after 13 years of successive passages in culture medium. In 1921, BCG was first administered to a neonate in Paris [30, 31].

Despite the identical name, the BCG vaccines used worldwide correspond to other strains cultivated over the years in different laboratories around the world. Although genotypically similar to *M. bovis*, they differ from each other by genotypic and phenotypic characteristics, with different expressions regarding viability, immunogenicity, reactogenicity and residual virulence [32, 33], with the BCG Moreau-Rio de Janeiro strain being the Brazilian vaccine strain [34].

The BCG vaccine offers more than 70% protection against disseminated TB and tuberculous meningitis in newborns and school-age children. Despite its ability to protect against disease progression and disseminated forms of TB, the effectiveness of BCG against pulmonary TB in adult populations ranges from 0 to 80% [35, 36].

In addition to preventing and reducing morbidity and mortality from tuberculosis, epidemiological studies have shown non-specific benefits of the childhood BCG



vaccine for the prevention of other communicable and non-communicable diseases [37–39].

◀**Fig. 1** A-Innate immunity cells (Dendritic cells and macrophages) recognizing antigens administered in the vaccine (\*). Migration of dendritic cells to recognize antigens from the vaccine. B-Dendritic cells process vaccine antigens and migrate to secondary lymphoid organs (lymph nodes). C-The virgin lymphocytes potentially specific to the antigen are in the process of recirculation and, by stimulating innate immunity, enter the lymph node through the high endothelial venules in search of antigenic peptides for which they are specific. D-Activation of the virgin lymphocyte by the antigen-presenting cell with subsequent differentiation of lymphocytes in specific subpopulations of auxiliary T cells, in this representation, TH1 and TH2 subpopulations. E-Example of TH1 response where the cytokines produced favor the development of a cellular response, in this example, with activation of cytolytic T lymphocytes that eliminate a cell infected by an intracellular pathogen. F-Example of TH2 response where the cytokines produced favor the development of a humoral immune response that results in the activation of B lymphocytes, differentiation of this in plasmotocio and finally production of immunoglobulins specific to the vaccine antigen

A case-control study based in young children in Guinea-Bissau investigated the impact of BCG on the incidence of specific respiratory syncytial virus (RSV) infection, and the results suggested that BCG vaccination can reduce the incidence of acute respiratory tract infections caused by the same [40].

In addition to providing prophylactic protection against infections, BCG has also been shown to be effective as a non-specific immunotherapy in clinical conditions mediated by virus, such as the positive effect of BCG against skin and genital warts caused by the human papillomavirus (HPV) [41].

A randomized controlled trial in 40 healthy human volunteers demonstrated that BCG vaccination, prior to influenza vaccination, increased antibody titer against the 2009 influenza A(H1N1) vaccine strain [42].

In addition, another aspect is the protective effect against cancer in adult life, in which it acts by increasing the development of the immune system and there are several experimental studies in animals that show the inhibitory effect of BCG on tumor growth [43, 44]. As shown in the meta-analysis which suggests that early BCG vaccination may be associated with a reduced risk of leucemia [35]. Furthermore, a retrospective review showed that childhood BCG vaccination was associated with a lower risk of developing lung cancer [46].

## 4.2 Influenza

Seasonal influenza is an acute respiratory infection caused by three types of virus, A, B and C. Influenza virus type A and B have a greater clinical significance, while influenza virus type C is much less frequent and usually causes mild infections, presenting less significant implications for public health. For this reason, influenza vaccines are produced using relevant strains of influenza A and B viroses [47].

Inactivated influenza vaccines were first developed in the late 1930s from virus grown in mouse lungs or chick embryos [48]. The effectiveness of these seasonal vaccines was guaranteed by the correspondence between the circulating strain and

the strain contained in the vaccine and by the dose of cultured virus. There are three types of influenza vaccines, the “inactivated” vaccines, the “live attenuated” cold adapted and the “recombinant HA” vaccines, these are licensed for human use in different countries [49].

These vaccines are generally available as trivalent or quadrivalent formations, containing recent strains of influenza A virus of the H1N1 and H3N2 subtypes in combination with one or two strains of influenza B virus of the Yamagata and/or Victoria strains [50].

The effectiveness of the flu vaccine varies with age, health status and season. Vaccination reduces the risk of influenza disease by about 40% to 60% when circulating virus are well compatible with the vaccine. In addition to preventing influenza infections, vaccines also reduce intensive care admissions and the length of hospital stays [51].

### 4.3 *Rubella*

Rubella is a common childhood disease caused by a virus, the Rubella virus, with worldwide distribution and usually with minimal systemic symptoms [52]. Although it is a disease associated with childhood, between 6 and 25% of women of reproductive age are seronegative for rubella and may develop the disease if exposed [53, 54].

If the mother is infected in the first 20 weeks of pregnancy, the most important complication is the risk of the child being born with Congenital Rubella Syndrome (CRS). CRS often leads to fetal death or serious birth defects, including blindness, deafness, cardiovascular anomalies, and mental retardation [52, 55].

Live attenuated rubella vaccines were discovered by microbiologist Maurice Hilleman, introduced in 1969 and have been widely used since. Seroconversion to the vaccine is 95% in infants older than 11 months and antibodies last for more than 21 years [52].

As vaccines contain live attenuated rubella virus, there was initial concern that vaccinating women who were later found to be pregnant could result in fetal infection and deformity, but a large study showed that there was no association of birth defects in women who received the vaccine dose 3 months before or after conception [56].

### 4.4 *Dengue*

Dengue, a disease caused by the virus belonging to the Flaviviridae family, has 4 serotypes (DENV-1, DENV-2, DENV-3 and DENV-4), transmitted by the mosquito vector *Aedes Aegypti* and has expanded geographically in recent years, reaching a global pandemic. Almost half of the world's population lives in dengue-endemic areas in more than 100 countries, with estimated 390 million cases per year. Dengue

varies from asymptomatic to severe disease, with a mortality rate of approximately 20% if left untreated. In the face of this mass contamination, efforts have been made to develop a vaccine against dengue [57, 58].

Dengvaxia, Sanofi Pasteur's attenuated tetravalent chimeric dengue vaccine, is based on a yellow fever "backbone" (CYD-TDV), with 56 to 61% efficacy against dengue among children in Asia and Latin America. CYD-TDV is associated with an increased risk of severe dengue and hospitalization in seronegatives, so it should only be applied to individuals with evidence of previous infection. It was applied massively in the Philippines in 2016, being incorporated into the school immunization program that began in 2013, with the application of measles, rubella, tetanus and diphtheria vaccines. In 2017, approximately two years after the start of the dengue vaccination program, with approximately 800,000 Filipino children vaccinated with at least 1 dose, it was announced by Sanofi Vaccines that Dengvaxia could be unsafe for some populations. The vaccine should only be applied when serology for dengue is positive, in which cases it would be more likely to reduce serious events [57–59].

The lack of confidence resulting from this event had an impact on vaccination against other viral diseases, causing 500 measles deaths in the following year. In a survey carried out in March 2021, around 60% of Filipinos were unwilling to be vaccinated against viral diseases, that percentage reduced to 33% in May of the same year. Filipinos analyzed in the study did not trust vaccines due to community experiences or information gained through social media or television, even if these were not scientifically proven. In addition, the lack of reliable information that should have been provided, such as that the vaccinated should be seronegative, has become another key point for vaccine mistrust, promoting the growth of conspiracy theories. A new trust was implemented when Filipinos faced the measles outbreak and the resulting deaths, becoming a forced trust, out of fear [59].

A new tetravalent dengue vaccine candidate is TAK-003 (Takeda), based on a live DENV-2 virus, which provides a genetic backbone for all four vaccine virus. The DENV-2 strain is based on an attenuated virus from the laboratory. The two doses of TAK-003 are being evaluated in a phase 3 clinical trial in Latin America and Asia, in the age group between 4 and 16 years [57].

The efficacy of two-dose TAK-003 for the prevention of virologically confirmed dengue induced by any dengue virus serotype starting 30 days after the second injection was 80.2% in the study population. Furthermore, it was effective in preventing dengue leading to hospitalization and in preventing severe dengue. The vaccine was 97.7% effective against DENV-2, 73.7% effective against DENV-1, and 62.6% effective against DENV-3. However, efficacy results against DENV-4 were inconclusive. Efficacy was similar across age groups and between seropositive and seronegative individuals at baseline. Vaccine efficacy was 95.4% against dengue leading to hospitalization. The identified cases provided estimates of vaccine efficacy against three of the serotypes, but not against DENV-4. Vaccine efficacy was highest against DENV-2 (97.7%), the genetic backbone of TAK-003, however, efficacy was modest (62.6–73.7%) against the other three serotypes, chimeric strains in TAK-003 [57].

Adverse events had similar percentages between the vaccine and placebo groups, namely: angioedema, asphyxia, autoimmune hepatitis, disseminated tuberculosis,

drug abuse, hypersensitivity, hyperthyroidism, flu, malaise, aseptic meningitis, patent ductus arteriosus, seizure, septic shock and urticaria. TAK-003 was effective against virologically confirmed dengue regardless of previous exposure to dengue [57].

## 4.5 HIV

Antiretroviral therapy (ART) is an effective measure in preventing clinical progression and death associated with HIV. Although it is an extremely important preventive measure, it has limitations. About 80% of Europeans and North Americans know they are infected with HIV and yet only 30–50% have viral suppression (low probability of sexual transmission). In addition, ART is unable to cure or eradicate HIV infection and due to poor adherence to treatment, viral resistance may occur [60].

Faced with these limiting factors of ART, the vaccine has become an option in trying to solve the failures of this therapy. Among the vaccines under study, there is the HIV mRNA vaccine (iHIVARNA) that targets dendritic cells. Between 2015 and 2016, in Barcelona, the first phase I dose-escalation clinical trial was performed in 21 human patients with naked mRNA containing dendritic cell activation signals (TriMix) and encoding a novel HIV immunogen sequence (HTI) to redirect T-cell immunity in HIV-infected individuals to the most vulnerable viral targets. All 21 patients received either the three doses of TriMix or the different doses of iHIVARNA (HTI with TriMix) administered intranodal inguinally [60].

The vaccine, in general, was safe and well tolerated, with no serious adverse events, deaths or changes in gene expression. Compared to plasmid DNA and viral vectors, mRNA has a better safety profile. mRNA-mediated gene transfer occurs in non-dividing cells and is not restricted to an individual-specific human leukocyte antigen (HLA) allele. As no serious adverse events were observed even with the administration of the highest dose of vaccine (1200 mg mRNA—900 mg HTI mRNA and 300 mg TriMix mRNA), this dose was chosen to proceed with the phase II clinical trial [60].

iHIVARNA, at the highest dose, was able to induce moderate HIV-specific immune responses and moderate increase in T cell responses spanning the HTI sequence during week 8 of administration. The increase in the frequency of specific HIV-1 T cells after vaccination was 80%, compared to 31% at week zero [60]. In addition to the iHIVARNA vaccine, there are other clinical studies underway, as there is still no highly effective preventive vaccine against HIV, among them the study carried out in Baltimore that analyzes the IHV01 vaccine [61].

IHV01 is the FLSC vaccine (subunit encoded by a synthetic gene that expresses a human codon-optimized full-length HIV gp120 sequence joined at its C-terminus to the N-terminus of domains 1 and 2 of human CD4) formulated in phosphate adjuvant aluminum (Alum, AlPO<sub>4</sub>), developed to exploit the potential vulnerabilities of transition state/CD4i envelope structures. Currently studied in a phase Ia clinical trial, with an increase in dose, in Baltimore, United States, its safety, tolerability and

immunogenicity were evaluated. The study was conducted between 2015 and 2017 and 65 participants were included [61].

There was no significant difference in the incidence of adverse events (AE) between the placebo and control groups. In the control group, 81% of vaccinations with IHV01 did not produce localized or systemic reactions, while the incidence was 80% for the placebo group. 98% of AEs were mild or moderate, the most frequent being: pain at the injection site, itching and headache; there were no serious vaccine-related AEs and no intercurrent HIV infections, all participants tested negative for HIV at the end of the study [61].

Responses to the FLSC components of IHV01 increased in all vaccination groups, with the 100% FLSC vaccine response milestone being in all vaccine dose groups (75, 150, and 300 mg) after the fourth dose. (twenty-sixth week). However, the 150 mg dose group reached this milestone after the second vaccination. No significant effects of the vaccine on CD4 counts were found. There was a decrease in MFI binding titers (measurement of antibody titers by median fluorescence intensity) in all three vaccine groups 24 weeks after the final vaccination, although response rates remained above 90% [61].

The IHV01 vaccine was immunogenic, raising antibodies against FLSC and highly conserved CD4i epitopes. The induced antibodies were largely cross-reactive with the gp120, gp140 and V1V2 domains representing various clades of HIV-1. Given these observations, this vaccine can be considered a possible future strategy against HIV [61].

## 4.6 HPV

Human papillomavirus (HPV) infection can cause precancerous (precancerous) and cancerous (malignant) diseases. Lesions resulting from the infection are usually located on the cervix, vagina, vulva, anus, penis, tonsils and base of the tongue. Annually, about 570,000 new cases of cervical cancer occurs in the world, being 70% of the time attributed to HPV types 16 and 18. In view of the various conditions caused by HPV, safe and effective vaccines have been developed to combat prenatal outcomes. There are three vaccines available and prequalified by the World Health Organization (WHO): bivalent, quadrivalent and nine-valent [62, 63].

The bivalent vaccine prevents infections related to HPV types 16 and 18. These two types are the most oncogenic, related to about 70% of cervical cancer cases worldwide [62]. Between 2004 and 2005, in Costa Rica, a clinical study was carried out to evaluate the effectiveness of the bivalent vaccine with adjuvant HPV-16/18 AS04, Cervarix®, GlaxoSmithKline Biologicals, in the prevention of cervical infections by HPV 16/18 and of related illnesses and injuries. The women who participated in the study were followed for 11.1 years. After that time, the efficacy against cervical intraepithelial neoplasia grade 2 and 3 (CIN2 + /CIN3 + ), precancerous lesions, was 100%. The bivalent vaccine demonstrated protection against CIN3 + , an immediate precursor of invasive cervical cancer, even after a decade of vaccination [63].



The quadrivalent vaccine prevents infections related to HPV types 6, 11, 16 and 18. In a study of Chinese women evaluating the quadrivalent vaccine for 78 months, the effectiveness of this vaccine was demonstrated. Efficacy against types 16 and 18 related to NIC1 was 100%, as well as against types 6, 11, 16 and 18 related to NIC1 and NIC2 [64].

The nine-valent vaccine, on the other hand, prevents infections related to HPV types 6, 11, 16, 18, 31, 33, 45, 52 and 58; it is the most extensive of the three vaccines, covering the types present in the quadrivalent vaccine and adding the other five HPV types commonly associated with cervical infections (Huh et al. 2017). In a multicenter clinical trial comparing the quadrivalent and nine-valent vaccines, the greater efficacy of the nine-valent vaccine was demonstrated. Cervical disease of any grade was reduced by 98.4% when related to the nine-valent vaccine. In addition, large reductions in disease related to each individual HPV type covered by it were observed. High efficacy was observed against vulvar and vaginal condylomas, reduction in the number of definitive cervical therapy procedures, cervical biopsy, and 100% reduction in high-grade vulvar and vaginal disease [65].

In another study conducted in 105 study centers located in 18 countries, the nine-valent and quadrivalent vaccines were also compared with the control group (unvaccinated individuals). In this study, the efficacy of the nine-valent vaccine compared to the control for primary outcome of high-grade cervical, vulvar and vaginal disease was 97.4%; for grade three CIN, adenocarcinoma in situ or cervical cancer related to the vaccine types, the efficacy was 100%. In addition, there was a reduction in cervical cytological abnormalities and clinical procedures related to HPV types 31, 33, 45, 52, and 58, as well as a greater reduction in persistent infection related to HPV 16. Finally, a similar safety profile to the quadrivalent vaccine was observed in this vaccine, except for injection site reactions [62].

## 5 Messenger RNA Vaccines and COVID-19

This entire process of study and evolution was challenged by COVID-19 pandemics, the traditionally time-consuming vaccine development process required unprecedented acceleration. mRNA vaccines gained prominence as the first vaccines to be approved for prophylactic treatment and its technology was used by many companies [66, 67]. In March 2020, BioNTech and Pfizer agreed to develop an mRNA-based vaccine for the prevention of COVID-19 [68].

Gene-based vaccines, such as mRNA and DNA vaccines, work by carrying genetic instructions for the production of an antigen by the cells of the vaccine recipient [69]. This potential vaccine has been studied since 1990, when a protein was obtained after injection of the encoding mRNA into the skeletal muscle of a mouse the *in vivo* expression [70]. During the following 10 years, several studies demonstrated that the mRNA could induce an immune response to the protein expressed in many cell types [71, 72].

MRNA technology has several advantages that make it an attractive alternative to traditional vaccines or even DNA vaccines. This type of vaccine has generated primary interest due to its degree of safety. Unlike live attenuated and inactivated vaccines, mRNA vaccines have no association with endotoxin and infection [73].

Another important point of the mRNA vaccine is its efficacy. The mRNA is precise, will express a specific antigen and induce a targeted immune response, promoting a humoral and cellular immune response and induces the innate immune system [74], thereby they minimize adverse effects compared to whole cell vaccines [75].

Furthermore, a third important point of mRNA vaccines is in their production. The process is based on standardized in vitro transcription, making it a robust and scalable manufacture. Also, because it requires less optimization to synthesize new antigen sequences of similar size, it creates a flexibility in manufacturing important for infectious agents that spread rapidly [76, 77].

## 6 COVID-19 Vaccines

Until this date, the National Health Surveillance Agency (ANVISA) has approved four vaccines for COVID-19 in adults, these being: Coronavac/Sinovac, Pfizer/BioNTech, Janssen and AstraZeneca/Oxford [78].

### 6.1 *Pfizer/BioNTech*

In December 2020, the first two vaccines approved for emergency use in the United States are messenger RNA based (mRNA) platforms and were developed by Pfizer/BioNTech and Moderna. Published safety and efficacy trials have reported high efficacy rates of 94–95% after two interval doses, combined with limited side effects and a low rate of adverse reactions [79].

The Pfizer/BioNTech vaccine trial (BNT162b2) reported that the vaccine was 95% effective. The study recruited a total of 43,548 adult volunteers, with half of the participants receiving a placebo injection and the other half receiving the actual vaccine. One hundred and seventy people contracted COVID-19 in both groups: 8 of these participants were in the vaccine group and the other 162 were in the placebo group. Ten of the 170 cases were classified as severe, and 9 of the 10 severe cases were among the participants in the placebo group [80].

### 6.2 *Oxford/AstraZeneca*

The University of Oxford in partnership with British pharmaceutical company AstraZeneca has developed a non-replicating chimpanzee viral vector vaccine. A

completed and published phase 1/2 randomized, blinded study in the *Lancet* journal, had 1,077 healthy participants, aged 18–55 years and recruited from the UK. These participants received the vaccine at a dose of  $5 \times 10^{10}$  vaccine particles ( $n = 543$ ) or a licensed meningococcal vaccine as a placebo ( $n = 534$ ). A group of 10 participants in the group that received the actual vaccine also received a second booster dose of the vaccine 28 days after the first dose. On day 28, specific antibodies peaked in the COVID-19 vaccine group and these levels remained elevated until day 56. In addition, on day 56, a much higher specific antibody response was observed for the 10 participants who received a booster injection. The T-cell response, observed in all participants, peaked on day 14 and remained elevated until day 56. However, an increase in T-cell response after the second dose was not observed in participants in the booster group [81].

The published efficacy, until this date, of this vaccine is 70% in adults under 55 years of age and prevents 100% of hospitalizations and severe forms of the disease [82].

### 6.3 *Coronavac*

Sinovac has developed an inactivated + aluminum adjuvanted vaccine, called CoronaVac. Published data from preclinical trials in mouse and monkey models showed sufficient specific IgG responses and neutralizing antibody titer levels. Mice were injected with doses of 1.5 or 3 or 6  $\mu\text{g}$  of the vaccine along with an aluminum adjuvant or a saline placebo. In addition, vaccinated monkeys were exposed to SARS-CoV-2 and were observed to be protected from the virus with decreased viral loads, unlike the control group [83]. A press release from their Phase 1 study mentioned that they recruited 143 healthy participants aged 18–59 for a randomized, double-blind study, but no results regarding the Phase 1 study have been made available [84]. The Phase 2 randomized, double-blind studies involved 600 participants between the ages of 18 and 59. Participants were divided into two double-dose programs—the 0 and 14-day or the 0 and 28-day regimen. Within each scheme, 120 participants received the 3  $\mu\text{g}$  dose, 120 participants received the 6  $\mu\text{g}$  dose, and 60 participants received a placebo. Local adverse events, such as pain and swelling, were mild to moderate, along with pain, the most common reported event in both regimens and resolved within 3 days. No serious Grade 3 adverse events were reported. Neutralizing antibody (NAb) responses showed high quantifications for doses of 3 and 6  $\mu\text{g}$  in both regimens. 28 days after the second dose, those in the 0- and 14-day regimen had stable NAb levels, but for the 0- and 28-day regimen, NAb levels increased considerably. A similar pattern was also observed for specific antibodies. It was also observed that NAb levels decreased with increasing age, thus suggesting a higher dosing requirement for the elderly. T-cell immunity was not analyzed in this report [85].

The CoronaVac vaccine, composed of inactivated SARS-CoV-2 virus (killed) with its complete structure, with the sum of two doses, prevents 100% of severe and moderate cases, 78% of mild cases and 50.38% of very mild cases [86, 87].

## 6.4 Janssen

The Janssen COVID-19 (Ad26.COVS.S) vaccine, the third vaccine authorized for use in the United States, uses a replication-incompetent human type 26 adenoviral vector platform and is administered as a single intramuscular dose [88].

Twenty-five participants were randomized (median age, 42; range, 22–52; 52% female, 44% male, 4% undifferentiated) and all completed the study by the provisional end point on day 71. Binding and neutralizing antibodies appeared rapidly on day 8 after initial immunization in 90% and 25% of vaccine recipients, respectively. On day 57, binding and neutralizing antibodies were detected in 100% of vaccine recipients after a single immunization. On day 71, the geometric mean titers of peak specific binding antibodies were 2432 to 5729 and the geometric mean titers of neutralizing antibodies were 242 to 449 in the vaccinated groups. A variety of antibody subclasses, Fc receptor binding properties and antiviral functions were induced. CD4 + and CD8 + T cell responses were induced. In this phase 1 study, a single immunization with Ad26.COVS.S induced rapid binding and neutralizing antibody responses as well as cellular immune responses. Two phase 3 clinical trials are underway to determine the efficacy of the Ad26.COVS.S vaccine [89].

One study included 19,630 SARS-CoV-2 negative participants who received Ad26.COVS.S and 19,691 who received placebo. Ad26.COVS.S protected against moderate to severe critical Covid-19 with onset at least 14 days after administration (116 cases in the vaccine group versus 348 in the placebo group; efficacy, 66.9%); and at least 28 days after administration (66 versus 193 cases; efficacy, 66.1%);. Vaccine efficacy was highest against severe-critical Covid-19 (76.7% for onset  $\geq$  14 days and 85.4% for onset  $\geq$  28 days). The incidence of serious adverse events was balanced between the two groups. Three deaths occurred in the vaccine group (none were related to Covid-19) and 16 in the placebo group (5 were related to Covid-19). Therefore, a single dose of Ad26.COVS.S protected against symptomatic Covid-19 and asymptomatic SARS-CoV-2 infection and was effective against severe-critical illness, including hospitalization and death. Safety appeared to be similar to that of other phase 3 trials of Covid-19 vaccines [88].

In February 2021, the Advisory Committee on Immunization Practices (ACIP) issued interim recommendations for the use of the Janssen COVID-19 vaccine among people aged  $\geq$  18 years and in April, the CDC and FDA recommended a pause in Janssen vaccine use following reports of six cases of cerebral venous sinus thrombosis (CVT) with thrombocytopenia (platelet count  $<$  150,000/ $\mu$ L of blood) among Janssen vaccine recipients [90]. Similar thrombotic events, especially among women under 60 years of age, have been described in Europe after receipt of the AstraZeneca

COVID-19 vaccine, which uses an incompetent chimpanzee adenoviral vector for replication [91–93].

## 7 COVID-19 Childhood Vaccines

The results of vaccine studies for COVID-19 in adolescents have several implications. Vaccination confers the direct benefit of disease prevention plus indirect benefits, including community protection. Although children generally have a lower frequency of symptomatic COVID-19 than adults, school activities, youth sports, and other community gatherings may represent important sources of outbreaks and transmission, even among vaccinated adults [94].

Anvisa approved in late 2021 the BNT162b2 vaccine (Pfizer/BioNTech) for immunization against Covid-19 in children from 5 to 11 years old as a safe and effective for this age group. One article aimed to determine the efficacy, immunogenicity and safety of the BNT162b2 vaccine, given 21 days apart in children aged 5–11 years old, providing data/results from two studies: (i) a phase 1 study to determine dosage (selected at a dose of 10  $\mu$ g) and (ii) a phase 2–3 clinical trial, in which participants were randomized in a 2:1 ratio (vaccine at the dosage determined in study 1 vs. placebo). The immune response of the 5–11 years old group was compared to 16–25 years old vaccinated with the same vaccine. Vaccine efficacy was assessed 7 days after the 2nd dose. In the phase 2–3 study, 2,268 children were included—of whom 1,517 received the vaccine (experimental group—EG) and 751 the placebo (control group—CG)—with a mean follow-up of 2.3 months. Regarding vaccine safety, the results showed that in the 5–11 age group the safety profile was quite good, with adverse effects at the inoculation site in 71% to 74% of cases, with fatigue and headache being the most frequent—ranging from 0.1% to 0.9%. Fever was manifested in 8.3% of vaccinees, most frequently after the 2nd vaccine dose. Lymphadenopathies appeared in 0.9% of vaccinees. No cardiovascular (myocarditis or pericarditis) or allergic (hypersensitivity or anaphylaxis) syndromes were detected. About the efficacy, thirty days after the 2nd dose, when compared to the 16–25 year old group, the levels of neutralizing SARS-CoV-2 antibodies in the 5–11 year old group was 1.04 (95% CI 0.93 to 1.18). This level was considered an immunological success previously defined as  $> 0.67$  of the lower limit of the 95% CI. Seven days or more after inoculation with BNT162b2 there were 3 cases of SARS-CoV-2 infection in the vaccinated group and 16 in the placebo group, demonstrating a vaccine efficacy of 90.7% (95% CI 67.7% to 98.3%). No serious post-vaccine cases were detected in either group. Therefore, in children between 5 and 11 years old, two inoculations with 10  $\mu$ g of the BNT162b2 vaccine, given 21 days apart, are safe and effective [95].

The release of Pfizer-BioNTech's vaccine use in adolescents aged 12–17 years was supported by a randomized, placebo-controlled, phase 3 clinical trial that evaluated the safety, immunogenicity, and efficacy of this vaccine. Its comparator was a cohort at the age of 16–25 years old. A total of 2,260 adolescents were included: 1,131

received the vaccine and 1,129 the placebo. The BNT162b2 vaccine had a favorable safety and adverse event profile, with mild to moderate transient reactogenicity: 79–86% injection site pain, 60–66% fatigue, and 55–65% headache; no vaccine-related serious adverse events were observed. The mean neutralizing antibody titers after the second dose met the non-inferiority criterion and indicated an even greater response in the 12–15 year old cohort. The same US research also found eight cases of COVID-19, all in the placebo group [94].

Anvisa has approved the emergency use of CoronaVac in children aged 6 to 17 years old in early 2022 based on phase 1 and 2 clinical trials conducted in China with children and adolescents aged 3 to 17 years old, who received two doses 28 days apart, and proved that the vaccine is safe and effective. In phase 1, 71 young people participated; 28 days after vaccination, 100% of them showed antibodies. In phase 2, 479 children and adolescents participated; in the group receiving 1.5 µg dosage, 96% of the participants showed antibodies; in the group receiving 3 µg, this number was 100%. The adverse reactions were mild to moderate, as pain at the application site and fever being the most common, with symptoms disappearing within 48 h. The results were published in June in the scientific journal *The Lancet Infectious Diseases*. Phase 3 clinical trials are underway with more than 4,000 children and adolescents aged 3–17 years old to investigate the immunogenicity, safety and efficacy of CoronaVac. In Chile, the clinical trials with children have yielded better results than those with adults: not only did they experience fewer adverse effects, but they also showed higher antibody production. In addition, in real-world vaccination, which has been going on for months in China, CoronaVac in children shows the same safety and efficacy as other age groups, and no cases of myocarditis, pericarditis or thrombosis have been identified, as already reported for other vaccines. In the Asian country, more than 211 million doses of CoronaVac have been administered to children [96] (Table 1).

**Table 1** Vaccines, breakthrough year, antigen and efficacy

Vaccine	Breakthrough year	Antigen	Efficacy	References
Smallpox	1796	Orthopoxvirus variolae	90%	[97]
Rabies	1885	Lyssavirus Genus	100%	[98]
Tuberculosis-BCG	1921	Mycobacterium Tuberculosis	78%	[35]
Tetanus	1920	Clostridium tetani	100%	[99]
Diphtheria	1923	Corynebacterium diphtheriae	80–90%	[100]

(continued)

**Table 1** (continued)

Vaccine	Breakthrough year	Antigen	Efficacy	References
Yellow Fever	1930	Arbovirus from Flaviridae family	98–99%	[101]
Influenza	1940	Type A and B virus	40–60%	[49]
Rubella	1969	Rubella virus	95%	[52]
Dengvaxia (Dengue)	2015	CYD-TDV	56–61%	[58]
TAK-003 (Dengue)	2019	DENV-2 virus	97,7% (DENV-2); 73,7% (DENV-1); 62,6% (DENV-3)	[57]
iHIVARNA (HIV)	2017	HIV (dendritic cells)	Ongoing studies	[60]
HPV bivalent	2007	HPV 16 and 18	100%	[62]
HPV quadrivalent	2006	HPV 6,11,16 and 18	100%	[64]
HPV nine-valent	2014	HPV 6, 11, 16, 18, 31, 33, 45, 52 and 58	97,4–100%	[62]
Coronavac/Sinovac	2020	SARS-Cov-2	Prevents 100% of severe and moderate cases, 78% of mild cases and 50.38% of very mild cases	[87]
Pfizer/BioNTech	2020	SARS-Cov-2	95%	[80]
Janssen	2020	SARS-Cov-2	66.9%: moderate-to-severe critical Covid-19 14 days after administration; 66.1%: at least 28 days after administration; Vaccine efficacy was highest against severe-critical Covid-19 76.7% for onset $\geq$ 14 days and 85.4% for onset $\geq$ 28 days	[88]
AstraZeneca/Oxford	2020	SARS-Cov-2	70% in adults under 55 and prevents 100% of hospitalizations and severe forms of the disease	[82]

## References

1. Sell, S.: How vaccines work: immune effector mechanisms and designer vaccines. *Expert Rev. Vaccines* **18**(10), 993–1015 (2019)
2. Shukla, V.V., Shah, R.C.: Vaccinations in primary care. *Indian J. Pediatrics* **85**(12), 1118–1127 (2018)
3. Plotkin, S.: History of vaccination. *Proc. Natl. Acad. Sci.* **111**(34), 12283–12287 (2014)
4. Baxby, D.: Edward Jenner's Inquiry after 200 years. *BMJ* **318**(7180), 390–390 (1999)
5. Pasteur, L.: Méthode pour prévenir la rage après morsure (1885)
6. Enders, J.F., Weller, T.H., Robbins, F.C.: Cultivation of the Lansing strain of poliomyelitis virus in cultures of various human embryonic tissues. *Science* **109**(2822), 85–87 (1949)
7. Sabin, A.B., Hennessen, W.A., Winsser, J.: Studies on variants of poliomyelitis virus. *J. Exp. Med.* **99**(6), 551–576 (1954)
8. Katz, S.L.: Studies on an attenuated measles-virus vaccine. *Am. J. Dis. Child.* **100**(6), 942 (1960)
9. Hilleman, M.R., Buynak, E.B., Weibel, R.E., Stokes, J.: Live, attenuated mumps-virus vaccine. *N. Engl. J. Med.* **278**(5), 227–232 (1968)
10. Takahashi, M., Okuno, Y., Otsuka, T., Osame, J., Takamizawa, A.: Development of a live attenuated varicella vaccine. *Biken J.* **18**(1), 25–33 (1975)
11. Homma, A., Martins, R. de, M., Leal, M. da, L.F., Freire, M., da, S., Couto, A.R.: Atualização em vacinas, imunizações e inovação tecnológica. *Ciência Saúde Coletiva* **16**(2), 445–458 (2011)
12. Francis, T.: The protective effect of vaccination against epidemic influenza B. *J. Am. Med. Assoc.* **131**(4), 275 (1946)
13. Clark, H.F., Offit, P.A., Plotkin, S.A., Heaton, P.M.: The new pentavalent rotavirus vaccine composed of bovine (Strain WC3) -human rotavirus reassortants. *Pediatr. Infect. Dis. J.* **25**(7), 577–583 (2006)
14. Salmon, D., Smith, T.: On a new method of producing immunity from contagious diseases. *Am. Vet. Rev.* **10**, 63–69 (1886)
15. Roux, E., Chamberland, C.: Immunité contre la septicémie conférée par des substances solubles. *Ann. Inst. Pasteur. (Paris)* **1**, 561–572 (1887)
16. Francis, T., Magill, T.P.: The antibody response of human subjects vaccinated with the virus of human influenza. *J. Exp. Med.* **65**(2), 251–259 (1937)
17. Salk, J.E., Krech, U., Youngner, J.S., Bennett, B.L., Lewis, L.J., Bazeley, P.L.: Formaldehyde treatment and safety testing of experimental poliomyelitis vaccines. *Am. J. Public Health Nat. Health* **44**(5), 563–570 (1954)
18. Provost, P.J., Hughes, J.V., Miller, W.J., Giesa, P.A., Banker, F.S., Emini, E.A.: An inactivated hepatitis a viral vaccine of cell culture origin. *J. Med. Virol.* **19**(1), 23–31 (1986)
19. Cate, T.R., Couch, R.B., Kasel, J.A., Six, H.R.: Clinical trials of monovalent influenza A/New Jersey/76 virus vaccines in adults: reactogenicity, antibody response, and antibody persistence. *J. Infect. Dis.* **136**(Supplement 3), S450–S455 (1977)
20. Gotschlich, E.C., Liu, T.Y., Artenstein, M.S.: Human immunity to the meningococcus. *J. Exp. Med.* **129**(6), 1349–1365 (1969)
21. Sociedade Brasileira de Imunizações. Calendário de imunizações 2021–2022 (2021). <https://sbim.org.br/images/calendarios/calend-pg-adulto-20-ou-mais.pdf>
22. Programa Nacional de Imunizações. Ministério da Saúde (2003)
23. Health Information for International Travel. Site CDC (2003)
24. 2º Informe Técnico sobre a Vacinação/Revacinação BCG (1994)
25. World Health Organization. The History of Vaccination
26. Moser, M., Leo, O.: Key concepts in immunology. *Vaccine*. **28**, C2-13 (2010)
27. Siegrist, C.-A.: Mechanisms underlying adverse reactions to vaccines. *J. Comput. Pathol.* **137**, S46-50 (2007)
28. Rashid, H., Khandaker, G., Booy, R.: Vaccination and herd immunity. *Curr. Opin. Infect. Dis.* **25**(3), 243–249 (2012)



29. World Health Organization. Global tuberculosis report (2020)
30. Calmette, A., Guérin, C., Boquet, A., Nègre, L.: La vaccination préventive contre la tuberculose par le "BCG." (1927)
31. Grange, J.M., Gibson, J., Osborn, T.W., Collins, C.H., Yates, M.D.: What is BCG? *Tubercle* **64**(2), 129–139 (1983)
32. Collins, D.M., de Lisle, G.W.: BCG identification by DNA restriction fragment patterns. *Microbiology* **133**(6), 1431–1434 (1987)
33. Milstien, J.B., Gibson, J.J.: Quality control of BCG vaccine by WHO: a review of factors that may influence vaccine effectiveness and safety. *Bull. World Health Organ.* **68**(1), 93–108 (1990)
34. Benévolo-de-Andrade, T.C., Monteiro-Maia, R., Cosgrove, C., Castello-Branco, L.R.R.: BCG Moreau Rio de Janeiro: an oral vaccine against tuberculosis—review. *Mem. Inst. Oswaldo Cruz* **100**(5), 459–465 (2005)
35. Mangtani, P., Abubakar, I., Ariti, C., Beynon, R., Pimpin, L., Fine, P.E.M., et al.: Protection by BCG vaccine against tuberculosis: a systematic review of randomized controlled trials. *Clin. Infect. Dis.* **58**(4), 470–480 (2014)
36. Roy, A., Eisenhut, M., Harris, R.J., Rodrigues, L.C., Sridhar, S., Habermann, S., et al.: Effect of BCG vaccination against *Mycobacterium tuberculosis* infection in children: systematic review and meta-analysis. *BMJ* **5**;349, g4643–g4643 (2014)
37. Benn, C.S., Roth, A., Garly, M.-L., Fisker, A.B., Schaltz-Buchholzer, F., Timmermann, A., et al.: BCG scarring and improved child survival: a combined analysis of studies of BCG scarring. *J. Int. Med.* **288**(6), 614–624 (2020)
38. Garly, M.-L., Martins, C.L., Balé, C., Baldé, M.A., Hedegaard, K.L., Gustafson, P., et al.: BCG scar and positive tuberculin reaction associated with reduced child mortality in West Africa. *Vaccine* **21**(21–22), 2782–2790 (2003)
39. Ahmed, A., Rakshit, S., Adiga, V., Dias, M., Dwarkanath, P., D'Souza, G., et al.: A century of BCG: Impact on tuberculosis control and beyond. *Immunol. Rev.* **301**(1), 98–121 (2021)
40. Stensballe, L.G., Nante, E., Jensen, I.P., Kofoed, P.-E., Poulsen, A., Jensen, H., et al.: Acute lower respiratory tract infections and respiratory syncytial virus in infants in Guinea-Bissau: a beneficial effect of BCG vaccination for girls. *Vaccine* **23**(10), 1251–1257 (2005)
41. Salem, A., Nofal, A., Hosny, D.: Treatment of common and plane warts in children with topical viable bacillus calmette-guerin. *Pediatr. Dermatol.* **30**(1), 60–63 (2013)
42. Leentjens, J., Kox, M., Stokman, R., Gerretsen, J., Diavatopoulos, D.A., van Crevel, R., et al.: BCG vaccination enhances the immunogenicity of subsequent influenza vaccination in healthy volunteers: a randomized, placebo-controlled pilot study. *J. Infect. Dis.* **212**(12), 1930–1938 (2015)
43. Kumral, A., İşcan, B., Tuzun, F., Cilaker Micili, S., Arslan, M.K., Tugyan, K., et al.: Bacillus Calmette-Guérin vaccination: a novel therapeutic approach to preventing hyperoxic lung injury. *J. Matern. Fetal Neonatal Med.* **28**(16), 1950–1956 (2015)
44. Weiss, D.W., Bonhag, R.S., Deome, K.B.: Protective activity of fractions of tubercle bacilli against isologous tumours in mice. *Nature* **190**(4779), 889–891 (1961)
45. Morra, M.E., Kien, N.D., Elmaraezy, A., Abdelaziz, O.A.M., Elsayed, A.L., Halhouli, O., et al.: Early vaccination protects against childhood leukemia: a systematic review and meta-analysis. *Sci. Rep.* **7**(1), 15986 (2017)
46. Usher, N.T., Chang, S., Howard, R.S., Martinez, A., Harrison, L.H., Santosham, M., et al.: Association of BCG vaccination in childhood with subsequent cancer diagnoses. *JAMA Netw. Open* **2**(9), e1912014 (2019)
47. Gattás, V.L., Braga, P.E., Koike, M.E., Lucchesi, M.B.B., Oliveira, M.M.M., de Piorelli, R. de O, et al.: Safety assessment of seasonal trivalent influenza vaccine produced by Instituto Butantan from 2013 to 2017. *Revista do Instituto de Medicina Tropical de São Paulo* **20**;61 (2018)
48. Hirst, G.K., Rickard, E.R., Whitman, L., Horsfall, F.L.: Antibody response of human beings following vaccination with influenza viruses. *J. Exp. Med.* **75**(5), 495–511 (1942)

49. Grohskopf, L.A., Alyanak, E., Broder, K.R., Blanton, L.H., Fry, A.M., Jernigan, D.B., et al.: Prevention and control of seasonal influenza with vaccines: recommendations of the advisory committee on immunization practices—United States, 2020–2021 influenza season. *MMWR Recomm. Rep.* **69**(8), 1–24 (2020)
50. Sekiya, T., Ohno, M., Nomura, N., Handabile, C., Shingai, M., Jackson, D.C., et al.: Selecting and using the appropriate influenza vaccine for each individual. *Viruses* **13**(6), 971 (2021)
51. Eficácia da vacina: quão bem as vacinas contra a gripe funcionam (2020). <https://www.cdc.gov/flu/vaccines-work/vaccineeffect.htm>
52. Banatvala, J., Brown, D.: Rubella. *Lancet* **363**(9415), 1127–1137 (2004)
53. Cutts, F.T., Robertson, S.E., Diaz-Ortega, J.L., Samuel, R.: Control of rubella and congenital rubella syndrome (CRS) in developing countries, Part 1: Burden of disease from CRS. *Bull. World Health Organ.* **75**(1), 55–68 (1997)
54. Mendis, L.: Susceptibility to rubella virus among Sri Lankan women. *Ceylon Med. J.* **34**(2), 73–75 (1989)
55. Lee, J.-Y., Bowden, D.S.: Rubella virus replication and links to teratogenicity. *Clin. Microbiol. Rev.* **13**(4), 571–587 (2000)
56. Rubella prevention. Recommendations of the Immunization Practices Advisory Committee (ACIP). *MMWR Recommendations and reports : morbidity and mortality weekly report Recommendations and reports.* **23;39**(RR-15), 1–18 (1990)
57. Biswal, S., Reynales, H., Saez-Llorens, X., Lopez, P., Borja-Tabora, C., Kosalaraksa, P., et al.: Efficacy of a tetravalent dengue vaccine in healthy children and adolescents. *N. Engl. J. Med.* **381**(21), 2009–2019 (2019)
58. Halstead, S.B., Katzelnick, L.C., Russell, P.K., Markoff, L., Aguiar, M., Dans, L.R., et al.: Ethics of a partially effective dengue vaccine: lessons from the Philippines. *Vaccine* **38**(35), 5572–5576 (2020)
59. Yu, V.G., Lasco, G., David, C.C.: Fear, mistrust, and vaccine hesitancy: narratives of the dengue vaccine controversy in the Philippines. *Vaccine* **39**(35), 4964–4972 (2021)
60. Leal, L., Guardo, A.C., Morón-López, S., Salgado, M., Mothe, B., Heirman, C., et al.: Phase I clinical trial of an intranodally administered mRNA-based therapeutic vaccine against HIV-1 infection. *AIDS* **32**(17), 2533–2545 (2018)
61. Chua, J.V., Davis, C., Husson, J.S., Nelson, A., Prado, I., Flinko, R. et al.: Safety and immunogenicity of an HIV-1 gp120-CD4 chimeric subunit vaccine in a phase 1a randomized controlled trial. *Vaccine* **39**(29), 3879–3891 (2021)
62. Huh, W.K., Joura, E.A., Giuliano, A.R., Iversen, O.-E., de Andrade, R.P., Ault, K.A., et al.: Final efficacy, immunogenicity, and safety analyses of a nine-valent human papillomavirus vaccine in women aged 16–26 years: a randomised, double-blind trial. *Lancet* **390**(10108), 2143–2159 (2017)
63. Porras, C., Tsang, S.H., Herrero, R., Guillén, D., Darragh, T.M., Stoler, M.H., et al.: Efficacy of the bivalent HPV vaccine against HPV 16/18-associated precancer: long-term follow-up results from the costa Rica vaccine trial. *Lancet Oncol.* **21**(12), 1643–1652 (2020)
64. Wei, L., Xie, X., Liu, J., Zhao, Y., Chen, W., Zhao, C., et al.: Efficacy of quadrivalent human papillomavirus vaccine against persistent infection and genital disease in Chinese women: a randomized, placebo-controlled trial with 78-month follow-up. *Vaccine* **37**(27), 3617–3624 (2019)
65. Giuliano, A.R., Joura, E.A., Garland, S.M., Huh, W.K., Iversen, O.-E., Kjaer, S.K., et al.: Nine-valent HPV vaccine efficacy against related diseases and definitive therapy: comparison with historic placebo population. *Gynecol. Oncol.* **154**(1), 110–117 (2019)
66. Krammer, F.: SARS-CoV-2 vaccines in development. *Nature* **586**(7830), 516–527 (2020)
67. Rego, G.N.A., Nucci, M.P., Alves, A.H., Oliveira, F.A., Marti, L.C., Nucci, L.P., et al.: Current clinical trials protocols and the global effort for immunization against SARS-CoV-2. *Vaccines.* **8**(3), 474 (2020)
68. Pfizer and BioNTech to co-develop potential COVID-19 vaccine (2020). <http://www.pfizer.com>

69. Abbasi, J.: COVID-19 and mRNA vaccines—first large test for a new approach. *JAMA* **324**(12), 1125 (2020)
70. Wolff, J.A., Malone, R.W., Williams, P., Chong, W., Acsadi, G., Jani, A., et al.: Direct gene transfer into mouse muscle in vivo. *Science* **247**(4949), 1465–1468 (1990)
71. Conry, R.M., LoBuglio, A.F., Wright, M., Sumerel, L., Pike, M.J., Johannings, F., et al.: Characterization of a messenger RNA polynucleotide vaccine vector. *Can. Res.* **55**(7), 1397–1400 (1995)
72. Qiu, P., Ziegelhoffer, P., Sun, J., Yang, N.S.: Gene gun delivery of mRNA in situ results in efficient transgene expression and genetic immunization. *Gene Ther.* **3**(3), 262–268 (1996)
73. Sahin, U., Karikó, K., Türeci, Ö.: mRNA-based therapeutics—developing a new class of drugs. *Nat. Rev. Drug Discov.* **13**(10), 759–780 (2014)
74. Pollard, C., de Koker, S., Saelens, X., Vanham, G., Grooten, J.: Challenges and advances towards the rational design of mRNA vaccines. *Trends Mol. Med.* **19**(12), 705–713 (2013)
75. Kim, J., Eygeris, Y., Gupta, M., Sahay, G.: Self-assembled mRNA vaccines. *Adv. Drug Deliv. Rev.* **170**, 83–112 (2021)
76. Corbett, K.S., Edwards, D.K., Leist, S.R., Abiona, O.M., Boyoglu-Barnum, S., Gillespie, R.A., et al.: SARS-CoV-2 mRNA vaccine design enabled by prototype pathogen preparedness. *Nature* **586**(7830), 567–571 (2020)
77. Jackson, L.A., Anderson, E.J., Roupheal, N.G., Roberts, P.C., Makhene, M., Coler, R.N., et al.: An mRNA vaccine against SARS-CoV-2—preliminary report. *N. Engl. J. Med.* **383**(20), 1920–1931 (2020)
78. Vacinas - Covid-19 (2022). <https://www.gov.br/anvisa/pt-br/assuntos/paf/coronavirus/vacinas>
79. Anand, P., Stahel, V.P.: The safety of Covid-19 mRNA vaccines: a review. *Patient Saf. Surg.* **15**(1), 20 (2021)
80. Polack, F.P., Thomas, S.J., Kitchin, N., Absalon, J., Gurtman, A., Lockhart, S., et al.: Safety and efficacy of the BNT162b2 mRNA Covid-19 vaccine. *N. Engl. J. Med.* **383**(27), 2603–2615 (2020)
81. Folegatti, P.M., Ewer, K.J., Aley, P.K., Angus, B., Becker, S., Belij-Rammerstorfer, S., et al.: Safety and immunogenicity of the ChAdOx1 nCoV-19 vaccine against SARS-CoV-2: a preliminary report of a phase 1/2, single-blind, randomised controlled trial. *Lancet* **396**(10249), 467–478 (2020)
82. Voysey, M., Clemens, S.A.C., Madhi, S.A., Weckx, L.Y., Folegatti, P.M., Aley, P.K., et al.: Safety and efficacy of the ChAdOx1 nCoV-19 vaccine (AZD1222) against SARS-CoV-2: an interim analysis of four randomised controlled trials in Brazil, South Africa, and the UK. *Lancet* **397**(10269), 99–111 (2021)
83. Gao, Q., Bao, L., Mao, H., Wang, L., Xu, K., Yang, M., et al.: Development of an inactivated vaccine candidate for SARS-CoV-2. *Science* **369**(6499), 77–81 (2020)
84. Sinovac says early data show its Covid-19 vaccine generated immune responses (2020). <https://www.statnews.com/2020/06/14/sinovac-early-data-covid19-vaccine-generated-immune-responses/>
85. Zhang, Y., Zeng, G., Pan, H., Li, C.: Immunogenicity and safety of a SARS-CoV-2 inactivated vaccine in healthy adults aged 18–59 years: report of the randomized, double-blind, and placebo-controlled phase 2 clinical trial. *Medrxiv* (2020)
86. Governo do Estado do Ceará. Quais os mecanismos de ação das vacinas disponíveis? (2021). <https://coronavirus.ceara.gov.br/quais-os-mecanismos-de-acao-das-vacinas-disponiveis/#:~:text=A%20vacina%20CoronaVac%20%C3%A9%20composta,anticorpos>
87. Butantan: Butantan apresenta a eficácia global da vacina Coronavac (2021). <https://pebmed.com.br/butantan-apresenta-a-eficacia-global-da-vacina-coronavac/>
88. Sadoff, J., Gray, G., Vandebosch, A., Cárdenas, V., Shukarev, G., Grinsztejn, B., et al.: Safety and efficacy of single-dose Ad26.COV2.S vaccine against Covid-19. *New Engl. J. Med.* **10;384**(23), 2187–201 (2021)
89. Stephenson, K.E., Le Gars, M., Sadoff, J., de Groot, A.M., Heerwegh, D., Truyers, C., et al.: Immunogenicity of the Ad26.COV2.S Vaccine for COVID-19. *JAMA* **20;325**(15), 1535 (2021)

90. Joint CDC and FDA Statement on Johnson & Johnson COVID-19 Vaccine (2021). <https://www.cdc.gov/media/releases/2021/s0413-JJ-vaccine.html>
91. Greinacher, A., Thiele, T., Warkentin, T.E., Weisser, K., Kyrle, P.A., Eichinger, S.: Thrombotic thrombocytopenia after ChAdOx1 nCov-19 vaccination. *N. Engl. J. Med.* **384**(22), 2092–2101 (2021)
92. Schultz, N.H., Sørvoll, I.H., Michelsen, A.E., Munthe, L.A., Lund-Johansen, F., Ahlen, M.T., et al.: Thrombosis and thrombocytopenia after ChAdOx1 nCoV-19 vaccination. *N. Engl. J. Med.* **384**(22), 2124–2130 (2021)
93. Scully, M., Singh, D., Lown, R., Poles, A., Solomon, T., Levi, M., et al.: Pathologic antibodies to platelet factor 4 after ChAdOx1 nCoV-19 vaccination. *N. Engl. J. Med.* **384**(23), 2202–2211 (2021)
94. Frenck, R.W., Klein, N.P., Kitchin, N., Gurtman, A., Absalon, J., Lockhart, S., et al.: Safety, Immunogenicity, and efficacy of the BNT162b2 Covid-19 vaccine in adolescents. *N. Engl. J. Med.* **385**(3), 239–250 (2021)
95. Walter, E.B., Talaat, K.R., Sabharwal, C., Gurtman, A., Lockhart, S., Paulsen, G.C., et al.: Evaluation of the BNT162b2 Covid-19 vaccine in children 5 to 11 years of age. *N. Engl. J. Med.* **386**(1), 35–46 (2022)
96. Instituto Butantan. Por unanimidade, CoronaVac é aprovada pela Anvisa para uso emergencial em crianças de seis a 17 anos (2022). <https://butantan.gov.br/noticias/por-unanimidade-corona-vac-e-aprovada-pela-anvisa-para-uso-emergencial-em-criancas-de-seis-a-17-anos>
97. Levi, G.C.: Kallás EG Varíola, sua prevenção vacinal e ameaça como agente de bioterrorismo. *Rev. Assoc. Med. Bras.* **48**(4), 357–362 (2002)
98. Erbolato, E.B., da Silva, E.V., Miguel, O., Sureau, P., Germano, P.M.L.: Eficácia da vacina anti-rábica ERA em camundongos, frente a quatro diferentes variantes antigênicas do vírus da raiva. *Rev. Saude Publica* **23**(6), 447–454 (1989)
99. Afshar, M., Raju, M., Ansell, D., Bleck, T.P.: Narrative review: Tetanus-A health threat after natural disasters in developing countries. *Ann. Intern. Med.* **154**, 329–335 (2011)
100. Ministério da Saúde. Vacina Adsorvida Difteria, Tétano e Pertusiis (Acelular)–dTpa-para vacinação de gestantes. <http://conitec.gov.br/images/Incorporados/VacinadTPa-Gestantes-final.pdf>
101. Monath, T.P.: Yellow fever: an update **1**(1), 11–20 (2001)

# Structural Aspects of Organic Compounds as Proteasome Inhibitors Addressed to Several Diseases



Suzane Quintana Gomes, Guilherme Martins Silva,  
Mariana Pegrucci Barcelos, Lorane Izabel da Silva Hage-Melim,  
and Carlos Henrique Tomich de Paula da Silva

**Abstract** The proteasome is a multi-subunit proteolytic complex structure that plays an important role in the cell cycle and has emerged as a key target related to myeloma, mantle cell lymphoma and other cancer types. Furthermore, studies have shown that the use of proteasome inhibitors might also be promising for treating other different diseases. Pathogenesis of cancer cells, inflammatory responses and, recently, some protozoan infections, are significant examples where the proteasome has been explored as a mean of therapeutic intervention. This book chapter provides an overview of relevant structural aspects of organic compounds, aiming to simplify the recognition of common structural features, and also to facilitate the rational discovery of novel proteasome inhibitors with interest in several diseases.

**Keywords** Proteasome inhibitors · Rheumatoid arthritis · Asthma · Multiple sclerosis · Psoriasis · Malaria · Trypanosomiasis · Cancer

---

S. Q. Gomes (✉) · G. M. Silva · C. H. T. de Paula da Silva  
Departamento de Química, Faculdade de Filosofia, Ciências e Letras de Ribeirão Preto,  
Universidade de São Paulo, Av. Bandeirantes, 3900, Ribeirão Preto, São Paulo 14090-901, Brazil  
e-mail: [suzane.quintana@usp.br](mailto:suzane.quintana@usp.br)

C. H. T. de Paula da Silva  
e-mail: [tomich@fcrp.usp.br](mailto:tomich@fcrp.usp.br)

M. P. Barcelos · C. H. T. de Paula da Silva  
School of Pharmaceutical Sciences of Ribeirão Preto, University of São Paulo, Av. do Café, s/n,  
Ribeirão Preto, São Paulo 14040-903, Brazil

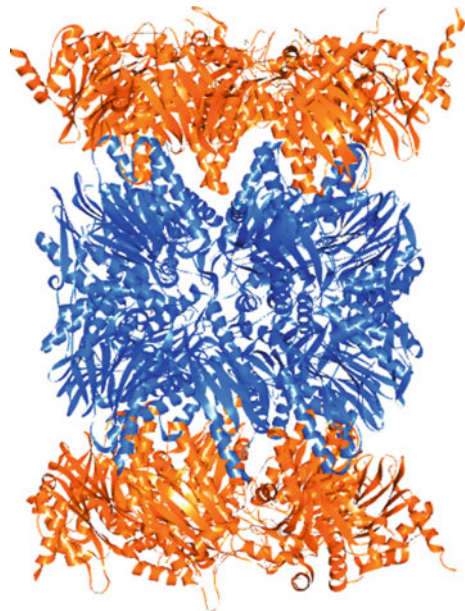
L. I. da S. Hage-Melim  
Laboratório de Química Farmacêutica e Medicinal (PharMedChem), Departamento de Ciências  
Biológicas e da Saúde, Curso de Farmácia, Universidade Federal Do Amapá, Rod. Juscelino  
Kubitschek, KM-02, Macapá 68903-419, Brazil

## 1 General Aspects About Proteasome: Structure and Function

The proteasome is a multi-subunit complex (26S) composed by one catalytic center (sCP or 20S) associated with one or two regulatory particles (RP or 19S) [1]. The catalytic center has a cylindrical shape with a hollow formed by an outer ring containing seven homologues  $\alpha$  subunits, and an inner ring with seven homologues  $\beta$  subunits (Fig. 1) [1]. The regulatory particle is composed by approximately 20 subunits, with divergent functions and structures from the catalytic center [2].

Ubiquitin proteasome-system (UPS) is responsible for initial clearance regulation of misfolded and unnecessary proteins in cells [3]. The clearance process starts with ubiquitin's addition into the proteins that will be degraded, resulting in a poly ubiquitinated protein [4]. Then, the proteolytic complex proteasome 26S recognize this protein and starts its degradation into small peptides varying from 2 to 24 residues in length. Recognition of poly ubiquitinated protein occurs in the regulatory particle (RP or 19S), which is also responsible for the denaturation and transference of tagged protein into the catalytic center of the particle (CP or 20S) [1, 2]. Consequently, the protein is degraded in the catalytic site 20S, which is constituted by a cylindrical central particle with a hollow formed by an outer ring containing seven homologues  $\alpha$  subunits, and an inner ring with seven homologues  $\beta$  subunits. The  $\beta_1$ ,  $\beta_2$  and  $\beta_5$  subunits that composes the inner ring as well as the catalytic site are responsible for caspase-like, trypsin-like and chymotrypsin-like proteolytic activities, respectively, acting in a synergistic way to degrade acid, basic and hydrophobic residues. The

**Fig. 1** Representation of proteasome catalytic center (20S) and its subunits



outer ring constitutes a well-packaged protective barrier for the catalytic site of the proteasome, responsible for preventing any protein present in the biological environment from entering in the active site [5].

The sCP can exist in various isoforms, being one of them expressed in the immune cell as immunoproteasome (iCP). iCP is expressed when cells receive an inflammatory signal or when they are stressed; its main function is to perform the hydrolysis of proteins into peptides, compatible with loading in the class I major histocompatibility complex (MHC-I) [6]. The isoform 20S proteasome, first described in the 1990's, receives this name due to the fact that its subunits are positively controlled by cytones and also because its genes encoding two subunits are within the coding region of the complete class II major histocompatibility complex (MHC-II) [7].

The iCP has three subunits,  $\beta 1i$ ,  $\beta 2i$  and  $\beta 5i$  incorporate in the proteasome during its assembly, which replaces the constitutive counterparts,  $\beta 1$ ,  $\beta 2$  and  $\beta 5$  of sCP [8]. While the substituted subunits  $\beta 2i$  and  $\beta 5i$  maintain their trypsin- and chymotrypsin-like functions,  $\beta 1i$  has chymotrypsin-like activity and not capsase [9]. Its assembly is four times faster when compared to the standard proteasome, but its half-life is shorter due to related immune responses [10]. Some authors suggest that the objective of the immunoproteasome is to degrade defective ribosomal products [11, 12], resulting from cellular stress or an infection, since in these cases there is a greater probability of cells suffering oxidative damage. However, there are conflicting reports stating that it preferentially degrades ubiquitinated proteins [13, 14] or badly folded/oxidized proteins. The iCP is more efficient to degrading proteins into antigenic peptides than sCP, and this is due to modifications in cleave preferences of active subunits of iCP, which consequently leads to iCP producing peptides with more hydrophobic character that can be loaded into major histocompatibility complexes type I (MHC-I) [15].

The potential of proteasome as a target come from its role in the cell cycle. Studies has shown that proteasome is involved in some cell-cycle progression as in cyclins regulation, protein p53, caspases, BCL2 activity and nuclear factor of  $\kappa B$  (NF- $\kappa B$ ) [16]. Cyclin-dependent kinase (CDK) complexes and CDC25 phosphatase family are closely connected in a mechanism present in different phases of the cell growth [17]. In order for the growth process to occur normally, the cyclins are rapidly degraded by the proteasome after their activation in the cell cycle, as well as the CDKs inhibitors [18, 19]. For this reason, when the proteasome is inhibited, a failure occurs in the mechanism of regulation of cyclins and CDKs, leading to a delay or cell cycle arrested.

The short-lived protein p53 can be accumulated in eukaryotic cells when it is under stress conditions, leading to a p53 produced in excess in the organism and inducing cell responses as cell-cycle arrest, DNA repair and apoptosis [20]. To regulate the p53 excess in the organism the own protein expresses an ubiquitin ligase E3 call MDM2, signaling the p53 to be degraded by proteasome in order to return to normal cell concentrations [21, 22]. It is noteworthy that some cancer cells overexpress MDM2, avoiding the accumulation of p53 and, hence, suppressing the cell responses [23]. In this case, proteasome inhibition treatment allows the accumulation of p53, which provides a cellular condition capable to induce apoptosis in these tumors cells.

The nuclear factor of  $\kappa$ B (NF- $\kappa$ B), unlike protein p53, when free in cytoplasm, is capable to activate the factors IAP and BCL2, avoiding the apoptotic process in cell. To regulate NF- $\kappa$ B, the protein I $\kappa$ B binds to the nuclear factor inactivating it [24]. Interestingly, when a cell is stimulated by chemotherapy, I $\kappa$ B is phosphorylated and ubiquitinated followed by proteasome degradation [25]. In a tumor cell is not desirable to find the NF- $\kappa$ B due this ability to activated anti-apoptotic factors and, thus, inhibition of proteasome is one way to keep I $\kappa$ B in cytoplasm to regulate the nuclear factor. Furthermore, free NF- $\kappa$ B are capable to inactivate caspase-8 essential to apoptosis cascade [16]. Hence, inhibiting proteasome also affects positively the caspase activity.

Since proteasome was discovered, it has been used as a key therapeutic target, especially regarding cancer treatment. Nevertheless, due to the proteasome role in cells, it also shows to be a promising target for other different disorders and diseases. In this review, we covered proteasome inhibitors compounds with potential treatment of rheumatoid arthritis, asthma, multiple sclerosis, psoriasis, malaria, trypanosomiasis, and also cancer cells. We report a selection of promising organic molecules to simplify the recognition of core structural similarities, which may be used as a rational guide or route for further modifications on discovery and development of new proteasome inhibitors.

## 2 Proteasome Inhibitors in Inflammatory Diseases

Inflammatory diseases include several conditions that are characterized by inflammation. Some examples of inflammatory diseases for which we will give special emphasis in this review include rheumatoid arthritis, asthma, multiple sclerosis, and psoriasis [26].

An inflammation process may be described as a protective response to homeostatic dysregulation and a diversity of noxious stimuli, such as infection and injury [27]. Such events cascade leads to alteration on regular activities and function of tissues and/or organs, for example, the synthesis and secretion by hepatocytes of acute phase proteins (APPs) in response to Interleukin 6 (IL-6), in order to promote host defense from infection [28]. In fact, this mentioned example of inflammation is related to rheumatoid arthritis. This disease is classified as systemic inflammation, which causes joint damage, disability, decreased quality of life, cardiovascular diseases, and other comorbidities [29]. Some extracellular stimuli are capable to induce inflammatory response, where NF- $\kappa$ B has a well-recognized role in the inflammatory process, being found activated in human synovial tissue on the early as well as the late stage of rheumatoid arthritis [30].

Multiple sclerosis is a chronic inflammatory disease that acts on the central nervous system (CNS), leading to demyelination and neurodegeneration. It is characterized by the onset of recurring clinical symptoms followed by total or partial recovery, namely, the classic relapsing–remitting form of multiple sclerosis. An important role in the inflammatory process involves the NF- $\kappa$ B, as a similar way



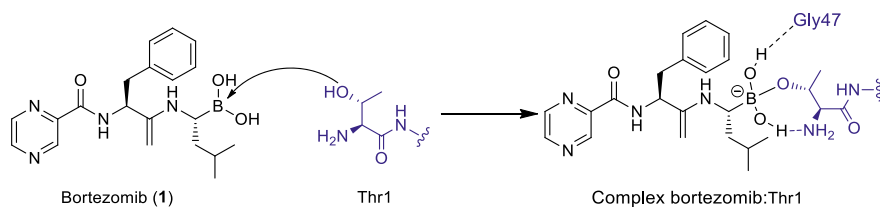
of rheumatoid arthritis [31]. Asthma is also a chronic inflammatory disease that provokes the airflow obstruction in the lung in a reversible model. The nuclear factor NF- $\kappa$ B contributes for the rising of eosinophils and infiltrating cells in the lung's airflow, playing an important role in inflammation [32]. NF- $\kappa$ B is also responsible for the inflammatory process of psoriasis, an autoimmune disease, which skin cells grow up at an abnormally fast rate resulting in skin's inflammation with scales [33].

These pathologies exhibit, in their respective inflammatory processes, a condition in which important proteins may be activated irregularly by the action of other cellular signaling pathways. One example is ubiquitin–proteasome pathway that plays a key role in the selective degradation of proteins that participate in the control of inflammatory processes, as degradation of I $\kappa$ B responsible for inactivating nuclear factor NF- $\kappa$ B. Thus, studies aiming at inhibition of the proteasome has become a potential alternative for the treatment of inflammatory diseases [34, 35].

Most proteasome inhibitors have anti-inflammatory and antiproliferative effects, so that several pathologies and conditions characterized by these processes simultaneously represent attractive options for their development and progress as drugs [35]. Worth mentioning that there are several reviews in the literature describing potential proteasome inhibitors with a diverse therapeutic interest. Thus, here we seek to gather the most relevant information regarding eight major synthetic and natural proteasome inhibitors, in which it is, in fact, demonstrated by means of experimental tests their corresponding anti-inflammatory properties on inflammation process.

Bortezomib (**1**, Fig. 3) belongs to the class of synthetic boronate compounds and it is structurally analogue to the corresponding antecessor, a peptide aldehyde [36]. Its chemical structure is composed by a peptide boronate containing a pyrazinoic acid bound to phenylalanine, and a leucine bound to boronic acid. Bortezomib is a reversible inhibitor, whose mechanism of inhibition starts from a covalent bond between boronic acid and threonine (Thr1), while nitrogen of both Gly47 and Thr1 stabilizes the acidic boronate hydroxyl by a hydrogen bond (Scheme 1) [37], resulting in proteasome complex with Bortezomib represented by PDB ID 5LF3 (Fig. 2). The boronic acid also confers to Bortezomib a slow dissociation and high proteasome specificity.

Bortezomib was initially named PS-341 and it is today marketed as Velcade™ (by Takeda Oncology). Actually, bortezomib represents a proteasome inhibitor that, in principle, has been investigated in the direction of anti-inflammatory diseases, although there are currently many studies concerning its anti-cancer activity [5]. Its



**Scheme 1.** Mechanism of reaction between bortezomib and Thr1 proteasome

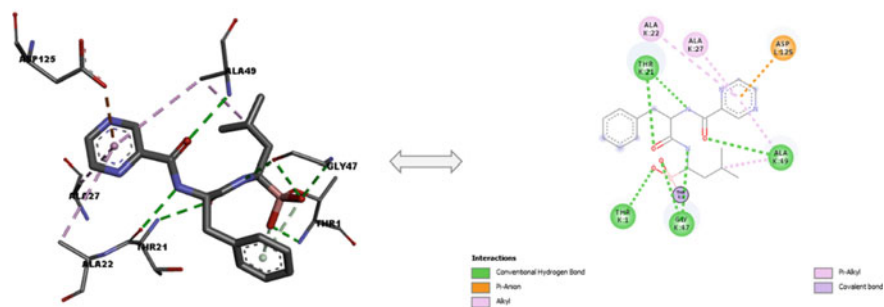


**Fig. 2** Human 20S proteasome complex with Bortezomib (PDB ID: 5LF3, resolution: 2.1 Å)

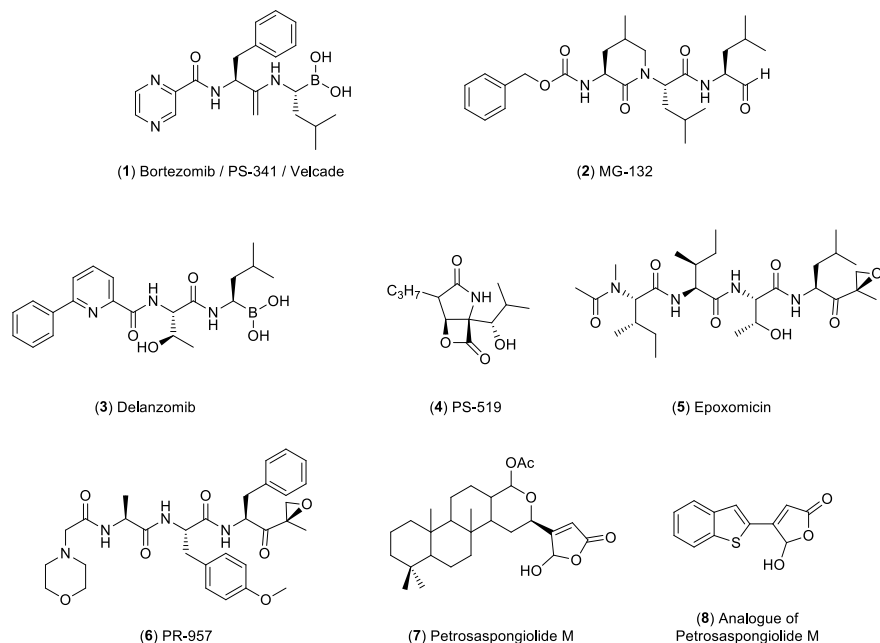
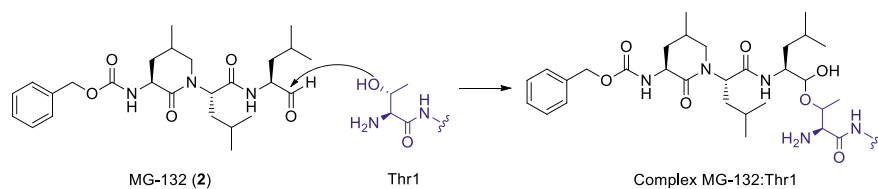


**Fig. 3** Chemical structures of proteasome inhibitors used as anti-inflammatory agents

attenuation on streptococcal cell-wall, as well as on clinical progress of the T cell dependent chronic phase of rheumatoid arthritis was one of the first observations done for this compound as an anti-inflammatory agent [38]. Later, the proteasome inhibitor bortezomib has also shown activity on models related to diseases including lupus nephritis [39], multiple sclerosis [40], colitis [41] and myasthenia gravis [42]. Nevertheless, it is important to straight out that not all effects of this molecule on respective disease models correspond to inhibition of NF- $\kappa$ B activation [43].

MG-132 (**2**, Fig. 3) is one of the first ever synthesized peptide aldehyde. It represents, nowadays, one of the most used proteasome inhibitors in studies of cell biology

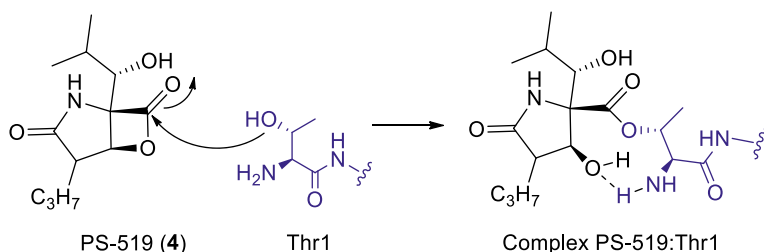


**Scheme 2.** Mechanism of reaction between MG-132 and Thr1 human proteasome

due to its reversible mechanism of action and fast dissociation when compared with boronic acids [5]. Scheme 2 shows the mechanism of reaction between the peptide aldehyde MG-132 and Thr1 and, differently of bortezomib, there is no chemical interactions between the ligand **2** and Thr1 beyond the covalent bond to stabilize the complex. MG-132 has been used in posterior structure–activity relationship projects resulting in many other compounds mentioned here in this review [25].

Potential treatment for rheumatoid arthritis has been verified by Migita et al. [44] when using the proteasome inhibitor MG-132 on *in vitro* experiments, i.e., they observed that accumulation of endogenous substance p53 entails the avoidance of rheumatoid synovial cells to progress into S-phase. Likewise, it has been proposed that NF- $\kappa$ B activation should lead to a decrease in the production of protective proteins against the cytotoxicity of TNF- $\alpha$ , so that use of MG-132 to control NF- $\kappa$ B activity appears as an interesting alternative for the treatment of diseases related to the levels of these protective proteins, such as asthma [45]. More recent studies also show that use of MG-132 temporarily alleviates atopic dermatitis on mice models [46] and that a combined use of MG-132 with rapamycin (an inducer of autophagy) restrains the expression of inflammatory cytokines and the formation of macrophage foam cells as well. This suggests that such combination of compounds may be useful on treating anti-inflammatory process like atherosclerosis [47]. The proteasome inhibitor Delanzomib (**3**, Fig. 3) is known for reducing NF- $\kappa$ B pathway activity and it has been tested to treat fatal lupus nephritis in mice. Results pointed out to improved stabilization of disease, more specifically in reduction in pro-inflammatory cytokines [48, 49].

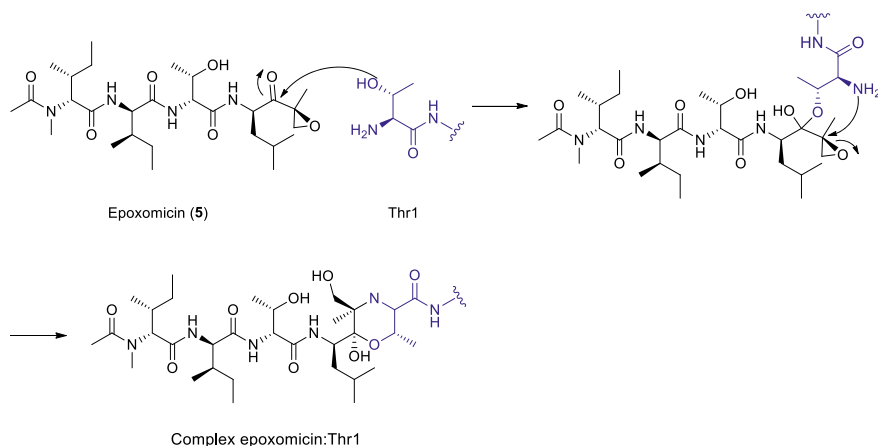
Compound PS-519 (**4**, Fig. 3) is a significant proteasome inhibitor, which acts on inflammatory events associated with ischemia and reperfusion injury [50, 51]. It belongs to the lactacystin class of natural compounds and was synthetically optimized afterwards as a more potent inhibitor of the NF- $\kappa$ B (I $\kappa$ B)  $\alpha$  stabilization, presenting an IC<sub>50</sub> of 1–5  $\mu$ M. Scheme 3 shows that the hydroxyl oxygen forms a covalent bond with the carbonyl after opening the lactone ring, leaving a free hydroxyl capable of making a stabilizing hydrogen bond with the nitrogen of Thr1. PS-519 development is under clinical trials related to several inflammatory diseases as we point out next. The evaluation of proteasome inhibition in rodent models of cerebral ischemia has been carried out and results demonstrated that PS-519 diminishes the expression of cell adhesion proteins, limiting brain tissue damage [52]. Anti-inflammatory effects were also observed on a study concerning asthma, in which an animal model characterized by pulmonary eosinophilia was developed and subsequently tested with low doses of the compound PS-519 [32]. Zollner et al. performed an experiment where



**Scheme 3.** Mechanism of reaction between PS-519 and Thr1 human proteasome

lesioned skin from patients with plaque-stage psoriasis was grafted onto mice lacking functional B- and T-cells [33]. Use of PS-519 to treat these prepared mice led to considerable reduction on inflammatory infiltrate related to psoriasis. Reduction in inflammation and demyelination related to multiple sclerosis models were also observed in treatments with compound PS-519 [53].

Epoxomicin (**5**, Fig. 3) is a natural product that belongs to the family of epoxyketones, which represents an important and potent class of proteasome inhibitors. Scheme 4 shows the reaction mechanism between epoxomicin and Thr1 in two main steps: first the hydroxyl oxygen forms a covalent bond with the epoxomicin carbonyl followed by the nitrogen attack to the epoxy group, resulting in its opening and generation of the piperazine ring (morpholine). This compound well succeeded in tests with disease models such as irritant sensitivity, showing *in vivo* anti-inflammatory activity [54]. In addition, it has been shown that epoxomicin inhibits the 20S proteasome proteolytic activity by binding irreversibly and thus covalently modifying the catalytic proteasome  $\beta$  subunits [55]. The binding mode is assigned by activation of epoxyketone inside the proteasome. It is inferred that epoxide acts as “suicide



**Scheme 4.** Mechanism of reaction between epoxomicin and Thr1 human proteasome

substrate”, which binds in covalent mode with amino acids residues in the active site [54]. Compound PR-957 (**6**, Fig. 3) is also considered a selective proteasome inhibitor due to its ability to control the progression of murine experimental models of diseases such as rheumatoid arthritis, colitis and lupus has been verified [56]. It decreases the production of antibodies as well as reduces the levels of various pro-inflammatory cytokines [43].

There is an interesting article reporting the use of natural extract of *Cymbopogon citratus* as an anti-inflammatory agent. In particular, chlorogenic acid was mentioned as most representative bioactive compound present in the extract, responsible for proteasome inhibition and consequent expression of NF- $\kappa$ B pathway [57]. Petrosaspongiolide M (**7**, Fig. 3) is a marine natural product that has been revealed as a proteasome inhibitor with interesting anti-inflammatory effects. Its initial inhibition studies were described in works of Margarucci et al., in which it presented IC<sub>50</sub> values of 0.64 and 0.15  $\mu$ M, in 20S proteasome activity assay for chymotrypsin-like (CT-L) and caspase-like (Casp-L) activity, respectively [58]. Such compound gave origin to various synthetic analogues such as analogue of Petrosaspongiolide M (**8**, Fig. 3) with IC<sub>50</sub> values of 0.07  $\mu$ M in both same assays mentioned above [59]. Later, it has been shown that **7** interacts with proteasome either by binding the active site in the inner core of its structure or by forming a covalent bond with a lysine residue at the 11S activator particle interface of this protein [60].

### 3 Proteasome Inhibitors in Protozoal Diseases

Malaria and trypanosomiasis are infectious disease caused by pathogenic microorganisms [61]. In this topic, some proteasome inhibitors will be discussed as new and promising alternatives for malaria as well as trypanosomiasis treatments.

Malaria is a parasitic disease capable to lead to death of the host, if not treated. Among protozoan species, four infects humans are known: *Plasmodium vivax*, *Plasmodium malariae*, *Plasmodium ovale*, and *Plasmodium falciparum*—where the last one is responsible for the most serious form of the disease. Malaria is transmitted by female Anopheles mosquito bite injecting sporozoites parasite form into the blood stream. These parasites are lodged in the liver and after one or two weeks, they start a new cycle in the red blood cells, stage responsible for disease symptoms [62].

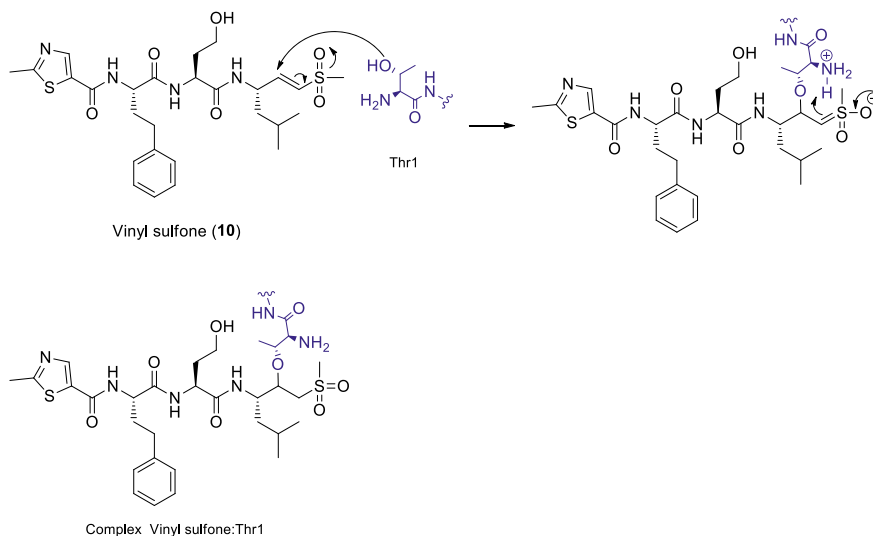
Antimalaria agents like Chloroquine phosphate, Quinine sulfate, Primaquine phosphate, Mefloquine, Halofantrine, Amodiaquine, and Atovaquone act in sexual and asexual protozoan life cycle. They are commonly used in treatment of uncomplicated malaria, but almost all these medicines are ineffective against resistant strains of *Plasmodium* species [63]. For treatment of resistant strains of *P. falciparum*, the current drugs used as first-line therapy are Artemisinin (ART) and Artemisinin Combination Therapies (ACT), Artemisinin (**9**, Fig. 7), isolated from a Chinese plant, and its semi-synthetics derivatives are capable to reduce the protozoan burden rapidly [63, 64]. Despite of the mechanism of action of artemisinin is not completely understood, studies have shown that when proteasome is inhibited, the protozoan exhibit

toxicity in all stages of parasite life cycle [65, 66]. The major challenge of using proteasome as a target is to find a selective drug for *Plasmodium* proteasome over the human counterpart [67].

In some regions of Asia, the growth of the Artemisinin resistance is worrisome because there is no drug that could replace them for the treatment of malaria [68]. Fortunately, others proteasome inhibitors have shown activities against *Plasmodium falciparum*. Studies with epoxomicin (**5**) have shown activities against sexual and asexual protozoan stages, with selectivity regarding human cells lines [69]. Recently, a new *P. falciparum* inhibitor exhibited potent activity and selectivity over human proteasome. This new compound is a non-natural peptide with a vinyl sulfone group (**10**, Fig. 7), which binds to the protozoan proteasome covalently (Scheme 5) and irreversibly, with a large therapeutic window. Furthermore, this new inhibitor has shown a strong synergism with ART (**9**), which could be used in a combined therapy against resistant *P. falciparum* [70].

Trypanosomiasis is a group of parasitic diseases caused by the Kinetoplastide family protozoa. *Trypanosoma brucei* spp., *Trypanosoma cruzi* and *Leishmania* spp. belongs to this family and are responsible to cause sleeping sickness, Chagas disease and leishmaniasis, respectively [71].

In the case of sleeping sickness, the protozoan validated target is ornithine decarboxylase, besides the promising targets which are currently under study such as RNA-editing ligase 1 (REL1), N-myristoyltransferase (NMT), Trypanothione Reductase (TR), Pteridine Reductase-1 (PTR1), among others [72]. Studies with *Trypanosoma brucei* have shown that its proteasome can also be used as target, mostly for trypsin-like activity inhibition, although synthesized compounds have not shown selectivity of protozoan proteasome over human proteasome [73].



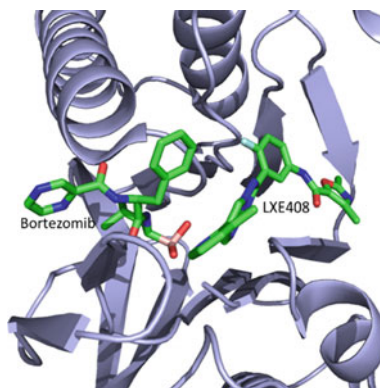
**Scheme 5.** Mechanism of reaction between vinyl sulfone (**10**) and Thr1 human proteasome

Regarding Chagas disease, the main targets are protozoan enzymes and proteases [74]. In 2016, a new study with trypanosomatids has shown important results with proteasome inhibitors to aim a new scaffold capable of inhibiting different trypanosomatids and resistant strains. Based on a High-throughput screening (HTS) study and subsequent structural synthetic modifications, the compound named GNF6702 (**11**, Fig. 7) presented the highest potency of inhibition of the protozoan chymotrypsin-like activity, without affecting the activity of the human proteasome. Without the crystallographic structure of proteasome complexed with the compound GNF6702 but based on its inhibition results, the authors have proposed that **11** acted as a noncompetitive proteasome inhibitor, binding at the interface between  $\beta 4$  and  $\beta 5$  subunits of the protozoan proteasome. GNF6702 presented  $EC_{50}$  of 18 nM, 70 nM and 120 nM for the amastigote forms of *Leishmania donovani*, *Trypanosoma brucei* and *Trypanosoma cruzi*, respectively [74]. In 2020, Nagle et al. published the compound LXE408 (**12**, Fig. 7), an optimized version of GNF6702 with remarkable efficacy in murine models of visceral and cutaneous leishmaniasis, which is currently in Phase I human clinical trials [75]. Also, the authors published the crystallographic structure of the *Leishmania tarentolae* proteasome complexed to LXE408 (PDB ID: 6TCZ, resolution: 3.4 Å) and the crystallographic structure of the *Leishmania tarentolae* proteasome complexed to the compound LXE408 and bortezomib (PDB ID: 6TD5, resolution: 3.2 Å, Fig. 4).

Comparison of these two crystallographic structures indicated that when bortezomib (**1**) is complexed with the compound LXE408 (**12**), bortezomib undergoes conformational changes in its phenyl group—when compared to its crystallographic pose in the binary complex between the compound and the proteasome—while the binding mode of LXE408 remained unchanged (Fig. 4). This result introduces a new understanding of the behavior of these inhibitors in the noncompetitive specific  $\beta 5$  proteasome inhibition binding mode [75].

Unlike compounds used in the treatment of inflammatory diseases that form covalent bonds with the Thr1 residue of the proteasome, protozoan proteasome inhibitors

**Fig. 4** Crystallographic complex of compound LXE408 (**12**) and bortezomib (**1**) in the ligand site of proteasome 20 subunit of *Leishmania tarentolae*



interact with the target by means of intermolecular interactions, mainly hydrophobic and hydrogen bonds, as shown in Fig. 5.

In 2019, Wyllie et al. were the first group to publish the crystallographic structure of trypanosomatids 20S proteasome, specifically *Leishmania tarentolae* complex with compound GSK3494245 (Fig. 6), confirming that this kind of inhibitor binds between the  $\beta 4$  and  $\beta 5$  proteasome subunits in a noncovalent mode. The proteasome inhibitor GSK3494245 (13, Fig. 7) is in Phase I study for the treatment of visceral leishmaniasis, inhibiting the chymotrypsin-like activity with  $IC_{50} = 0.16 \mu\text{M}$ . The oral dose efficacy of 25 mg/kg is similar to the oral dose of miltefosine. Furthermore, GSK3494245 has shown favorable pharmacokinetics and physicochemical properties [76]. Interestingly, in 2021, Thomas et al. [77] reported the original scaffold phenotypic used in the lead-optimization, scaffold-hopping, in silico profiling, and subsequent synthesis utilized to achieve the candidate GSK3494245.

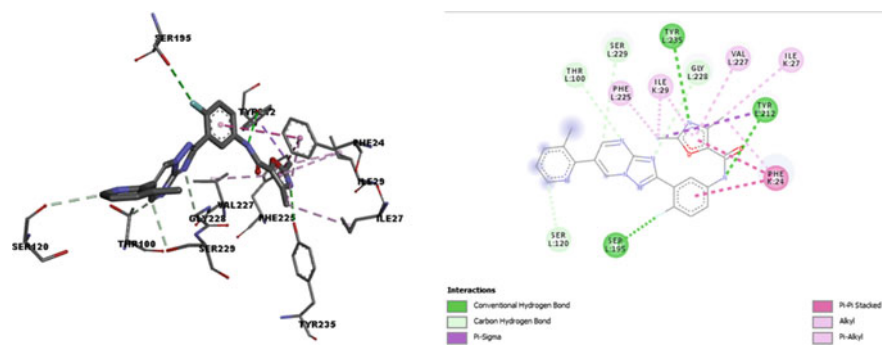


**Fig. 5** *Leishmania tarentolae* 20S proteasome complex with LXE408 (PDB ID: 6TCZ, resolution: 3.4 Å)

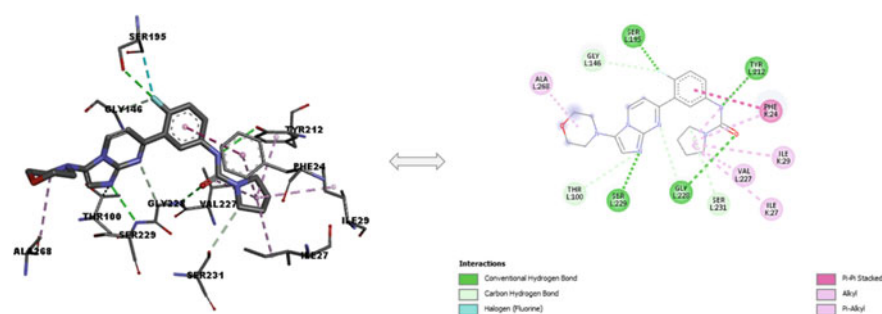


**Fig. 6** *Leishmania tarentolae* 20S proteasome complex with GSK3494245 (PDB ID: 6QM7, resolution of 2.80 Å)



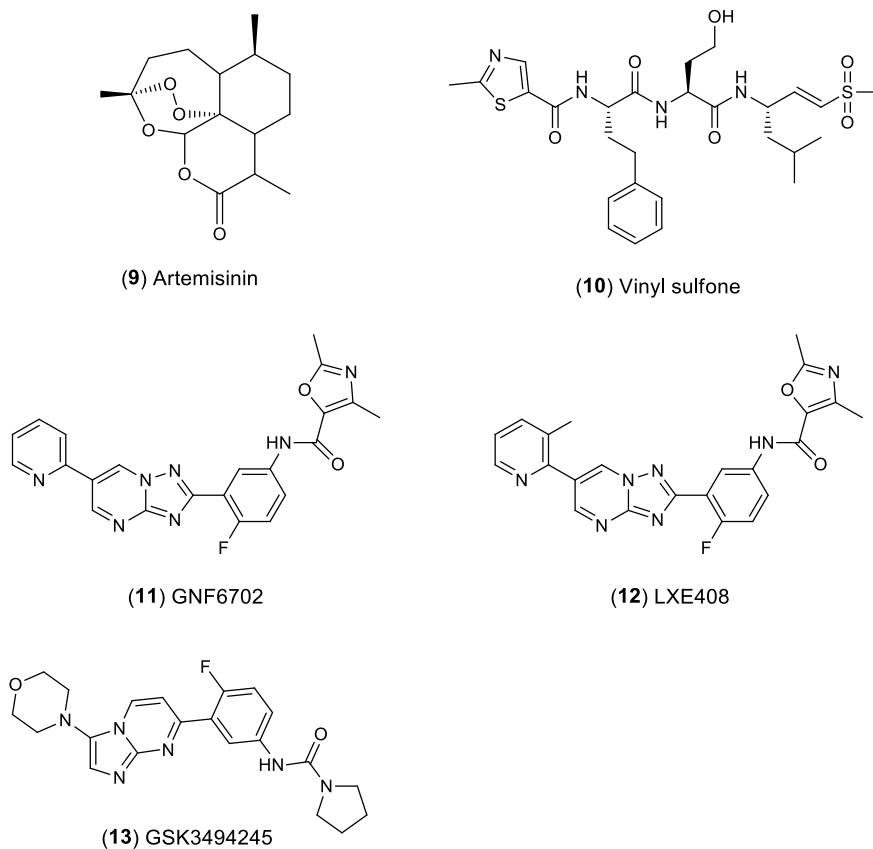


**Fig. 7** Structures of the proteasome inhibitors Artemisinin (9), Vinyl sulfone (10), GNF6702 (11), LXE408 (12), and GSK3494245 (13)

## 4 Proteasome Inhibitors in Cancer Treatment

As discussed earlier, proteasome inhibition can lead to tumor cell apoptosis, enabling the study of new anticancer agents. An important example includes the hematological malignancies, also called blood cancer, which are a neoplastic disease that affect the production of blood cells and, consequently, their functions. Leukemia, lymphoma and myeloma are the three most known types of hematological malignancies [78].

Leukemia is the name given to cancer that affects leukocytes. The person diagnosed with leukemia has an abnormal production of leukocytes, also called white blood cells, which are the blood cells responsible for helping to fight infections. Lymphoma is a cancer of a part of the immune system called the lymph system and usually is triggered when a T or B cell (specific types of white blood cells) becomes abnormal and the production of subsequent abnormal cells is increased. Myeloma is defined in a similar manner as above-mentioned types of hematological malignancies;

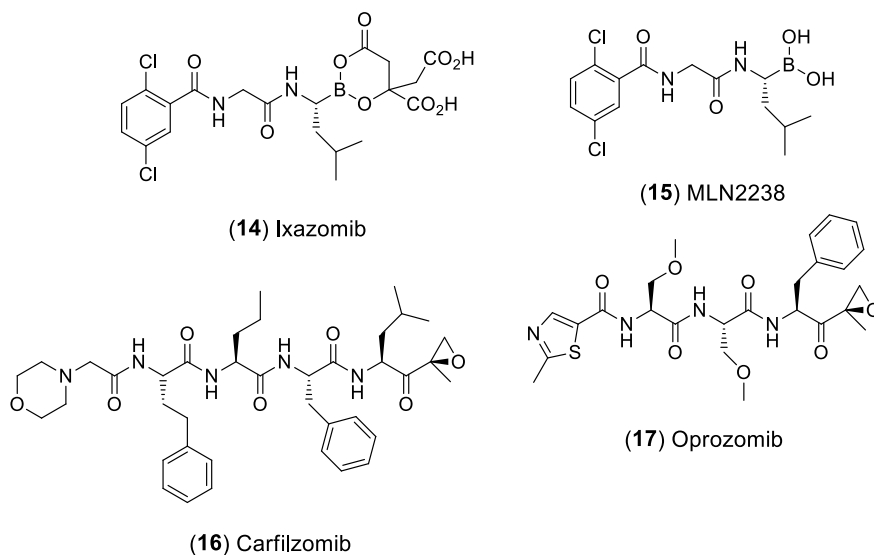


**Fig. 8** Structures of the synthetic proteasome inhibitors Ixazomib (**14**), MLN2238 (**15**), Carfilzomib (**16**) and Oprozomib (**17**)

however, its beginning occurs in plasma cells—another specific type of white blood cell formed in bone marrow [79, 80].

The first proteasome inhibitor (PI) approved by FDA for the treatment of myeloma and mantle cell lymphoma was Bortezomib (**1**, Fig. 3). This inhibitor induces apoptosis of tumor cells and interferes in different paths of tumor progression and, recently, “second generation” PIs have been introduced into the clinical [81–84]. Since then, FDA approved two more proteasome inhibitors: Ixazomib (**14**, Fig. 8) and Carfilzomib (**16**, Fig. 8).

Ixazomib (**14**) is a second-generation boronate discovered by a small-molecule screening [85, 86]. During pre-clinical studies it was found that the structure of **12** was not the active form, but the hydrolyzed structure MLN2238 (**15**, Fig. 8). This new structure was considered the responsible for inhibition of the chymotrypsin-like proteolytic site ( $\beta 5$ ) with an  $IC_{50}$  of 3.4 nmol/L ( $K_i$  of 0.93 nmol/L). In addition, kinetics studies showed that MLN2238 presents a proteasome dissociation six-fold faster when compared to Bortezomib. In 2017, many countries have approved the use of Ixazomib in combination with lenalidomide and dexamethasone for treating multiple myeloma in patients who have received at least one prior therapy [85, 86].

Carfilzomib (**16**, Fig. 8) is a tetrapeptide epoxyketone approved to multiple myeloma. Compared to Bortezomib, Carfilzomib belongs to a different inhibitor's class, consequently exhibiting a distinct mechanism of action i.e. by irreversible inhibition [87]. As described for epoxomicin, the epoxyketone must be activated inside the proteasome. Carfilzomib inhibits a selective chymotrypsin-like activity in both the constitutive and immune proteasome with activity of 3–5 mg/kg [84]. Despite

Carfilzomib activity seems to be lower than the observed for Bortezomib (1 mg/kg), its chymotrypsin-like selectivity has shown to be greater [87].

In an attempt to achieve proteasome inhibitors with good oral bioavailability and also selectivity similar to Carfilzomib, Zhou et al. found a tripeptide epoxyketone as a selective inhibitor of chymotrypsin-like activity in cell-free systems: Oprozomib (**17**, Fig. 8) [52]. A comparative analysis between Carfilzomib and Oprozomib presented an equipotent antitumor activity in xenograft mouse model. Further studies revealed that Oprozomib was capable to increase MM cell apoptosis and decrease angiogenesis with IC<sub>50</sub> of 36 nM for the chymotrypsin-like activity [54].

The proteasome inhibitor Delanzomib (**3**) also belongs to the boronate class of compounds. It is a reversible inhibitor with potency comparable to Bortezomib [88] that shows chymotrypsin-like activity and promotes apoptosis in human multiple myeloma cell lines. Delanzomib is on Phase I/II study for relapsed/refractory myeloma treatment with maximum tolerated dose (MTD), 2.1 mg/m<sup>2</sup> [89]. Investigations also revealed that when Delanzomib is used in combination with dexamethasone and/or lenalidomide, it produces a delay in tumor growth and tumor reduction of multiple myeloma [51, 90].

Natural products also represent a relevant source of proteasome inhibitors. Omuralid (**18**, Fig. 9) represents the structurally related class of  $\beta$ -lactones and numerous of them have been discovered so far. A representative proteasome inhibitor is Salinosporamide A (**19**, Fig. 9), isolated from the *Salinispora tropica*, an obligate marine actinomycete bacteria [91]. Since previous studies, the extract of *Salinispora* A has shown high cytotoxicity against HCT-116 human colon carcinoma and several cancer cells lines. Furthermore it was found that it is able to inhibit chymotrypsin-like catalytic sites of 20S proteasome with a IC<sub>50</sub> of 1.3 nM [92]. Its structure allows the formation of strong interactions with the active site, due to the formation of a tetrahydrofuran ring after the opening of the  $\beta$ -lactone ring [43] capable of stabilizing the adduct and prolonging its inhibition.

Some proteasome inhibitors do not act in a specific target but are capable to induce apoptosis in tumor cells in general. The mechanism of inhibition for nonspecific inhibitors is not well defined and they might probably act on innumerous cellular target [93]. A major example of these type of inhibitors includes the polyphenols found in tea plants. Studies have shown that polyphenols, which contain an ester bond, are able to induce tumor growth arrest or even cell death through inhibition of proteasomal chymotrypsin-like activity [94]. Four ester-bonding polyphenols epigallocatechin-3-gallate EGCG, epigallocatechin EGC, epicatechin-3-gallate ECG, epicatechin CG, were tested on inhibition assays of purified 20S proteasome, from which EGCG (**20**, Fig. 9) presented the lowest IC<sub>50</sub> (86 nM) of the series, while the positive control ( $\beta$ -lactone) presented IC<sub>50</sub> of 600 nM [95]. A mechanism of inhibition has been proposed based on the electrophilic ester carbon susceptible to nucleophilic attack, which is able to form an adduct with the target as  $\beta$ -lactones. Moreover, this hypothesis was supported by non-ester bond-containing polyphenols which are not capable to inhibit the proteasomal chymotrypsin-like activity, probably due its low susceptibility to a nucleophilic attack [94, 95].

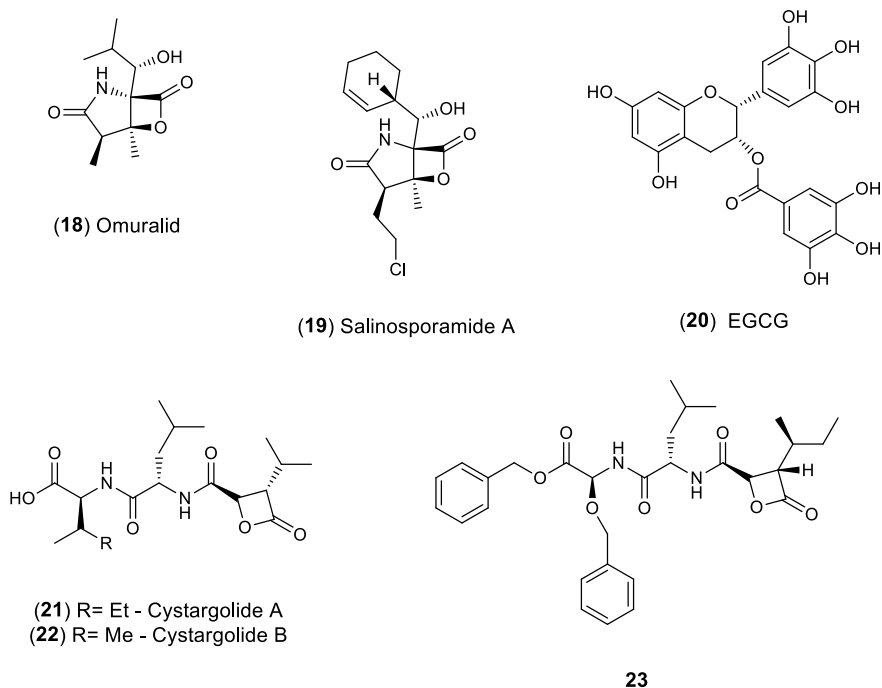


**Fig. 9** Structures of the natural proteasome inhibitors Omuralid (18), Salinosporamid A (19), EGCG (20), Cystargolid A (21) and B (22) and benzyl-O-benzyl-N-(((2R,3S)-3-((S)-sec-butyl)-4-oxooxetane-2-carbonyl)-l-allyl)-l-serinate (23)

Cystargolides A (21, Fig. 9) and B (22, Fig. 9) are also natural products isolated from actinomycete *Kitasatospora cystarginea* with proteasome activity in the micromolar inhibition rate. Based on cystargolide scaffold, Tello-Aburto et al. proposed punctual structure modifications at the  $\beta$ -lactone side chain, the internal dipeptides and the acid derivative, so that 24 new compounds were obtained [96]. Among these compounds, 23 (Fig. 9) exhibited the best results against tumor lines and h $\beta$ 5 combined, with an expressive  $IC_{50}$  of 0.041  $\mu$ M for the multiple myeloma—when compared to Carfilzomib ( $IC_{50} = 0.0067 \mu$ M) [96]. Besides positive results of proteasome inhibition and drug-likeness properties, problems with cellular infiltration must be carefully reviewed detailed to continue this study.

Oxathiazolones HT1171 (24, Fig. 10) and HT2004 (25, Fig. 10) has shown activity towards the human immunoproteasome. Authors have proposed that the hydroxyl group from the threonine present in the active site attacks the functional group oxathiazolone in compounds 24 and 25, generating an intermediate followed by cyclization. As a result, the binding mode of compounds are covalent and irreversible [97].

Ettari et al. have reported new series proteasome inhibitors with potential treatment of hematological malignancies, based on oxathiazolones [98, 99]. These compounds binds in the active site in an irreversible mode by forming a noncovalent bond. From

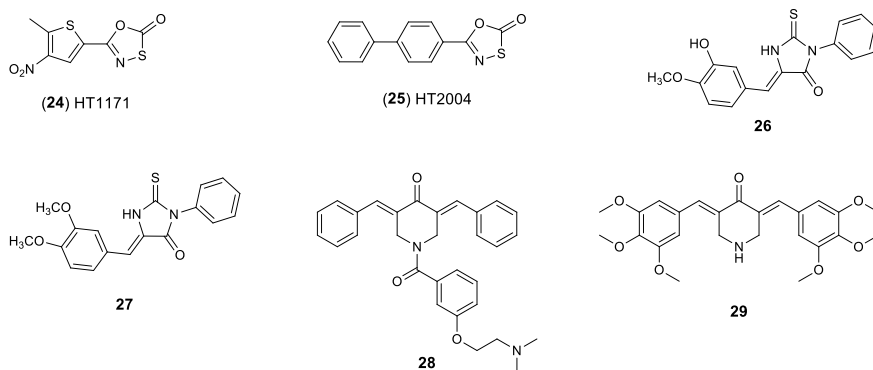


**Fig. 10** Structures of new proteasome inhibitors HT1171 (**24**), HT2004 (**25**), **26**, **27**, **28**, and **29**

these series, two new compounds showed the most expressive activity ( $K_i$ ):  $\beta 5i = 2.35 \mu\text{M}$  and  $\beta 1i = 6.53 \mu\text{M}$  to **26**, (Fig. 10), and  $\beta 5i = 2.01 \mu\text{M}$  and  $\beta 1i = 2.64 \mu\text{M}$  to **27** (Fig. 10), respectively. In addition, these two compounds were tested for growth inhibitory activity against dexamethasone-resistant multiple myeloma cells—using MG-132 as a positive control ( $\text{IC}_{50} = 14.4 \mu\text{M}$ )—, and the result was  $\text{IC}_{50} = 40.7 \mu\text{M}$  for **26** and  $\text{IC}_{50} = 36.7 \mu\text{M}$  for **27** [100].

Piperidones were discovered to be active against cancer cell in a screening of a cytotoxic pharmacophore study [101, 102]. The most promising compound is **28** (Fig. 10), which showed potent activity against breast cancer leading to the design of a series of analogues with increased potency [103]. Among the new molecules, **29** (Fig. 10) has shown a proteasome inhibition of leukemia/lymphoma cells. Compounds **28** and **29** were tested against six leukemia/lymphoma derived cells resulting in respective values of  $\text{IC}_{50}$  ranging from 0.67 to  $3.41 \mu\text{M}$  (**28**), and  $\text{IC}_{50}$  ranging from 0.23 to  $0.52 \mu\text{M}$  (**29**), in which the best results were obtained against Ramos cell line [102, 103]. The inhibition mechanism has not been completely elucidated yet, but these results are interesting to further studies.

## 5 Conclusions

There is a range of diseases and disorders that may be associated with the proteasome as a promising target. For inflammatory diseases, both Bortezomib (**1**) and MG-132 (**2**) presents activity against rheumatoid arthritis, while both Bortezomib and PR-957 (**6**) presents activity against rheumatoid arthritis and lupus. They share structural similarities based on peptides, providing similar activities against inflammatory diseases. Furthermore, they are able to bind covalently with different groups from the  $\beta 5$  Thr1 subunit, providing an extra stabilization and thus representing reversible or irreversible inhibitors. Non-peptide inhibitors like PS-519 (**6**), has shown promising results as proteasome inhibitor against asthma, plaque-stage psoriasis, and multiple

sclerosis. On the other hand, proteasome inhibitor related to malaria and trypanosomiasis do not share a common structure. For malaria, the proteasome inhibitor is a non-natural peptide with a vinyl sulfone group (**10**) which binds covalently to the target, while, for trypanosomiasis, GNF6702 (**11**), LXE408 (**12**), and GSK3494245 (**13**) binds in a noncovalent mode. The most expressive studies concerning proteasome inhibitors involve the treatment of cancer, and the core of these inhibitors are based on synthetic peptides. Bortezomib (**1**), Ixazomib (**14**), in combinatory therapy), Carfilzomib (**16**) and Delazomib (**3**, in combinatory therapy) may be employed to multiple myeloma treatment. There are also interesting examples of natural proteasome inhibitors, such as: Salinosporamide A (**19**), which is cytotoxic against several cancer cells lines; HT1171 (**24**) and HT2004 (**25**), with potential treatment of hematological malignancies; and piperidones scaffold, with potent activity against breast cancer and leukemia/lymphoma. Worth noting that they do not share structural similarities, indicating that these inhibitors structures have much to be explored. Fundamentally, all selected organic molecules presented in this chapter are potential proteasome inhibitors, which can be used in structural modifications studies. This could be conducted by envisioning improvement of potency and target specificity of these inhibitors and thus assisting the rational discovery of novel bioactive agents within this context.

**Conflict of Interest** The authors declare no conflict of interest.

## References

1. Adams, J.: The proteasome: structure, function, and role in the cell. *Cancer Treat. Rev.* **29**, 3–9 (2003)
2. Tanaka, K.: The proteasome: overview of structure and functions. *Proc. Japan Acad. Ser. B Phys. Biol. Sci.* **85**(1), 12–36 (2009)
3. Wong, E., Cuervo, A.M.: Integration of clearance mechanisms: the proteasome and autophagy. *Cold Spring Harb. Perspect. Biol.* **2**(12), a006734 (2010)
4. Pevzner, Y., Metcalf, R., Kantor, M., Sagaro, D., Daniel, K.: Recent advances in proteasome inhibitor discovery. *Expert Opin. Drug Discov.* **8**, 537–568 (2013)
5. Goldberg, A.L.: *Bortezomib in the Treatment of Multiple Myeloma*. Springer Basel, Basel (2011)
6. Zerfas, B.L., Maresh, M.E., Trader, D.J.: The immunoproteasome: an emerging target in cancer and autoimmune and neurological disorders. *J. Med. Chem.* **63**(5), 1841–1858 (2020)
7. Ferrington, D.A., Gregerson, D.S.: Immunoproteasomes: structure, function, and antigen presentation. *Prog. Mol. Biol. Transl. Sci.* **109**, 75–112 (2012)
8. Griffin, T.A., Nandi, D., Cruz, M., Fehling, H.J., Kaer, L.V., Monaco, J.J., Colbert, R.A.: Immunoproteasome assembly: cooperative incorporation of interferon gamma (IFN- $\gamma$ )-inducible subunits. *J. Exp. Med.* **187**(1), 97–104 (1998)
9. Loidl, G., Groll, M., Musiol, H.-J., Ditzel, L., Huber, R., Moroder, L.: Bifunctional inhibitors of the trypsin-like activity of eukaryotic proteasomes. *Chem. Biol.* **6**(4), 197–204 (1999)
10. Heink, S., Ludwig, D., Kloetzel, P.-M., Krüger, E.: IFN- $\gamma$ -induced immune adaptation of the proteasome system is an accelerated and transient response. *Proc. Natl. Acad. Sci. USA* **102**, 9241–9246 (2005)

11. Ferrington, D.A., Husom, A.D., Thompson, L.V.: Altered proteasome structure, function, and oxidation in aged muscle. *FASEB J* **19**(6), 644–646 (2005)
12. McCarthy, M.K., Weinberg, J.B.: The immunoproteasome and viral infection: a complex regulator of inflammation. *Front. Microbiol.* **6**, 21 (2015)
13. Nathan, J.A., Spinnenhirn, V., Schmidtke, G., Basler, M., Groettrup, M., Goldberg, A.L.: Immuno- and constitutive proteasomes do not differ in their abilities to degrade ubiquitinated proteins. *Cell* **152**(5), 1184–1194 (2013)
14. Seifert, U., Bialy, L.P., Ebstein, F., Bech-Otschir, D., Voigt, A., Schröter, F., Prozorovski, T., Lange, N., Steffen, J., Rieger, M., Kuckelkorn, U., Aktas, O., Kloetzel, P.-M., Krüger, E.: Immunoproteasomes preserve protein homeostasis upon Interferon-Induced oxidative stress. *Cell* **142**(4), 613–624 (2010)
15. Zerfas, B.L., Maresh, M.E., Trader, D.J.: The Immunoproteasome: an emerging target in cancer and autoimmune and neurological disorders. *J. Med. Chem.* **63**(5), 1841–1858 (2020)
16. Adams, J.: The proteasome: a suitable antineoplastic target. *Nat. Rev. Cancer* **4**, 349–360 (2004)
17. Murray, A.W.: Recycling the cell cycle: cyclins revisited. *Cell* **116**, 221–234 (2004)
18. Glotzer, M., Murray, A.W., Kirschner, M.W.: Cyclin is degraded by the ubiquitin pathway. *Nature* **349**, 132–138 (1991)
19. Clurman, B.E., Sheaff, R.J., Thress, K., Groudine, M., Roberts, J.M.: Turnover of cyclin E by the ubiquitin-proteasome pathway is regulated by cdk2 binding and cyclin phosphorylation. *Genes Dev.* **10**(16), 1979–1990 (1996)
20. Chène, P.: Inhibiting the p53-MDM2 interaction: an important target for cancer therapy. *Nat. Rev. Cancer* **3**, 102–109 (2003)
21. Honda, R., Tanaka, H., Yasuda, H.: Oncoprotein MDM2 is a ubiquitin ligase E3 for tumor suppressor p53. *FEBS Lett.* **420**, 25–27 (1997)
22. Fang, S., Jensen, J.P.R., Ludwig, L., Vousden, K.H., Weissman, A.M.: Mdm2 is a ring finger-dependent ubiquitin protein ligase for itself and p53. *J. Biol. Chem.* **275**, 8945–8951 (2000)
23. Momand, J., Wu, H.-H., Dasgupta, G.: MDM2—master regulator of the p53 tumor suppressor protein. *Gene* **242**, 15–29 (2000)
24. Karin, M., Cao, Y., Greten, F.R., Li, Z.-W.: NF-kappaB in cancer: from innocent bystander to major culprit. *Nat. Rev. Cancer* **2**, 301–310 (2002)
25. Li, C.C.H., Dai, R.M., Longo, D.L.: Inactivation of NF-κB inhibitor IκBα: ubiquitin-dependent proteolysis and its degradation product. *Biochem. Biophys. Res. Commun.* **215**(1), 292–301 (1995)
26. Tropsha, A.: Best practices for QSAR model development, validation, and exploitation. *Mol. Inform.* **29**, 476–488 (2010)
27. Okin, D., Medzhitov, R.: Evolution of inflammatory diseases. *Curr. Biol.* **22**, R733–R740 (2012)
28. Gabay, C., Kushner, I.: Acute-phase proteins and other systemic responses to inflammation. *N. Engl. J. Med.* **340**, 448–454 (1999)
29. Scott, D.L., Wolfe, F., Huizinga, T.W.: Rheumatoid arthritis. *Lancet* **376**, 1094–1108 (2010)
30. Makarov, S.S.: NF-κB in rheumatoid arthritis: a pivotal regulator of inflammation, hyperplasia, and tissue destruction. *Arthritis. Res. Ther.* **3**, 200 (2001)
31. Correale, J., Gaitán, M.I., Ysraelit, M.C., Fiol, M.P.: Progressive multiple sclerosis: from pathogenic mechanisms to treatment. *Brain* **140**(3), 527–546 (2017)
32. Elliott, P.J., Pien, C.S., McCormack, T.A., Chapman, I.D., Adams, J.: Proteasome inhibition: a novel mechanism to combat asthma. *J. Allergy Clin. Immunol.* **104**(2), 294–300 (1999)
33. Zollner, T.M., Podda, M., Pien, C., Elliott, P.J., Kaufmann, R., Boehncke, W.-H.: Proteasome inhibition reduces superantigen-mediated T cell activation and the severity of psoriasis in a SCID-hu model. *J. Clin. Invest.* **109**, 671–679 (2002)
34. Adams, J., Stein, R.: *Annu. Rep. Med. Chem.* 279–288 (1996)
35. Elliott, P.J., Zollner, T.M., Boehncke, W.-H.: Proteasome inhibition: a new anti-inflammatory strategy. *J. Mol. Med.* **81**, 235–245 (2003)

36. Lee, D.H., Goldberg, A.L.: Proteasome inhibitors: valuable new tools for cell biologists. *Trends Cell Biol.* **8**(10), 397–403 (1998)
37. Groll, M., Berkers, C.R., Ploegh, H.L., Ovaia, H.: Crystal structure of the boronic acid-based proteasome inhibitor bortezomib in complex with the yeast 20S proteasome. *Structure* **14**(3), 451–456 (2006)
38. Palombella, V.J., Conner, E.M., Fuseler, J.W., Destree, A., Davis, J.M., Laroux, F.S., Wolf, R.E., Huang, J., Brand, S., Elliott, P.J., Lazarus, D., McCormack, T., Parent, L., Stein, R., Adams, J., Grisham, M.B.: Role of the proteasome and NF- $\kappa$ B in streptococcal cell wall-induced polyarthritis. *Proc. Natl. Acad. Sci.* **95**, 15671–15676 (1998)
39. Neubert, K., Meister, S., Moser, K., Weisel, F., Maseda, D., Amann, K., Wiethe, C., Winkler, T.H., Kalden, J.R., Manz, R.A., Voll, R.E.: The proteasome inhibitor bortezomib depletes plasma cells and protects mice with lupus-like disease from nephritis. *Nat. Med.* **14**, 748–755 (2008)
40. Fissolo, N., Kraus, M., Reich, M., Ayturan, M., Overkleeft, H., Driessen, C., Weissert, R.: Dual inhibition of proteasomal and lysosomal proteolysis ameliorates autoimmune central nervous system inflammation. *Eur. J. Immunol.* **38**, 2401–2411 (2008)
41. Schmidt, N., Gonzalez, E., Visekruna, A., Kuhl, A.A., Loddenkemper, C., Mollenkopf, H., Kaufmann, S.H.E., Steinhoff, U., Joeris, T.: Targeting the proteasome: partial inhibition of the proteasome by bortezomib or deletion of the immunosubunit LMP7 attenuates experimental colitis. *Gut* **59**, 896–906 (2010)
42. Gomez, A.M., Vrolix, K., Martínez-Martínez, P., Molenaar, P.C., Phernambucq, M., van der Esch, E., Duimel, H., Verheyen, F., Voll, R.E., Manz, R.A., De Baets, M.H., Losenet, M.: Proteasome inhibition with bortezomib depletes plasma cells and autoantibodies in experimental autoimmune myasthenia gravis. *J. Immunol.* **186**, 2503–2513 (2011)
43. Kisselev, A.F., Van Der Linden, W.A., Overkleeft, H.S.: Proteasome inhibitors: an expanding army attacking a unique target. *Chem. Biol.* **19**, 99–115 (2012)
44. Migita, K., Tanaka, F., Yamasaki, S., Shibatomi, K., Ida, H., Kawakami, A., Aoyagi, T., Kawabe, Y., Eguchi, K.: Regulation of rheumatoid synoviocyte proliferation by endogenous p53 induction. *Clin. Exp. Immunol.* **126**, 334–338 (2001)
45. Fujihara, S., Ward, C., Dransfield, I., Hay, R.T., Uings, I.J., Hayes, B., Farrow, S.N., Haslett, C., Rossi, A.G.: Inhibition of nuclear factor- $\kappa$ B activation un-masks the ability of TNF- $\alpha$  to induce human eosinophil apoptosis. *Eur. J. Immunol.* **32**, 457–466 (2002)
46. Ohkusu-Tsukada, K., Ito, D., Takahashi, K.: The Role of Proteasome Inhibitor MG132 in 2,4-Dinitrofluorobenzene-Induced Atopic Dermatitis in NC/Nga Mice. *Int. Arch. Allergy Immunol.* **176**(2), 91–100 (2018)
47. Zhang, W., Xu, W., Chen, W., Zhou, Q.: Interplay of autophagy inducer rapamycin and proteasome inhibitor MG132 in reduction of foam cell formation and inflammatory cytokine expression. *Cell Transplant.* **27**(8), 1235–1248 (2018)
48. Seavey, M.M., Lu, L.D., Stump, K.L., Wallace, N.H., Ruggeri, B.A.: Novel, orally active, proteasome inhibitor, delanzomib (CEP-18770), ameliorates disease symptoms and glomerulonephritis in two preclinical mouse models of SLE. *Int. Immunopharmacol.* **12**, 257–270 (2012)
49. Teicher, B.A., Tomaszewski, J.E.: Proteasome inhibitors. *Biochem. Pharmacol.* **96**, 1–9 (2015)
50. Soucy, F., Grenier, L., Behnke, M.L., Destree, A.T., McCormack, T.A., Adams, J., Plamondon, L.: A novel and efficient synthesis of a highly active analogue of *clasto*-LACTACYSTIN  $\beta$ -Lactone. *J. Am. Chem. Soc.* **121**(43), 9967–9976 (1999)
51. Williams, A.J., Dave, J.R., Tortella, F.C.: Neuroprotection with the proteasome inhibitor MLN519 in focal ischemic brain injury: relation to nuclear factor kappaB (NF-kappaB), inflammatory gene expression, and leukocyte infiltration. *Neurochem. Int.* **49**(2), 106–112 (2006)
52. Berti, R., Williams, A.J., Moffett, J.R., Hale, S.L., Velarde, L.C., Elliott, P.J., Yao, C., Dave, J.R., Tortella, F.C.: Quantitative real-time RT-PCR analysis of inflammatory gene expression associated with ischemia-reperfusion brain injury. *J. Cereb. Blood. Flow. Metab.* **22**(9), 1068–1079 (2002)



53. Vanderlugt, C.L., Rahbe, S.M., Elliott, P.J., Dal Canto, M.C., Miller, S.D.: *J. Autoimmun.* **14**, 205–2011 (2000)
54. Meng, L., Mohan, R., Kwok, B.H.B., Elofsson, M., Sin, N., Crews, C.M.: Epoxomicin, a potent and selective proteasome inhibitor, exhibits in vivo antiinflammatory activity. *Proc. Natl. Acad. Sci. USA* **96**, 10403–10408 (1999)
55. Ramachandran, K.V., Margolis, S.S.: A mammalian nervous-system-specific plasma membrane proteasome complex that modulates neuronal function. *Nat. Struct. Mol. Biol.* **24**(4), 419–430 (2017)
56. Zhou, H.-J., Aujay, M.A., Bennett, M.K., Dajee, M., Demo, S.D., Fang, Y., Ho, M.N., Jiang, J., Kirk, C.J., Laidig, G.J., Lewis, E.R., Lu, Y., Muchamuel, T., Parlati, F., Ring, E., Shenk, K.D., Shields, J., Shwonek, P.J., Stanton, T., Sun, C.M., Sylvain, C., Woo, T.M., Yang, J.: Design and synthesis of an orally bioavailable and selective peptide epoxyketone proteasome inhibitor (PR-047). *J. Med. Chem.* **52**, 3028–3038 (2009)
57. Francisco, V., Costa, G., Figueirinha, A., Marques, C., Pereira, P., Neves, B.M., Lopes, M.C., García-Rodríguez, C., Cruz, M.T., Batista, M.T.: Anti-inflammatory activity of *Cymbopogon citratus* leaves infusion via proteasome and nuclear factor- $\kappa$ B pathway inhibition: contribution of chlorogenic acid. *J. Ethnopharmacol.* **148**, 126–134 (2013)
58. Margarucci, L., Monti, M.C., Tosco, A., Riccio, R., Casapullo, A.: Chemical proteomics discloses petrosaspongiolide M, an antiinflammatory marine sesterterpene, as a proteasome inhibitor. *Angew. Chem. Int. Ed.* **49**, 3960–3963 (2010)
59. Margarucci, L., Tosco, A., De Simone, R., Riccio, R., Monti, M.C., Casapullo, A.: Modulation of proteasome machinery by natural and synthetic analogues of the marine bioactive compound petrosaspongiolide M. *ChemBioChem* **13**, 982–986 (2012)
60. Monti, M.C., Margarucci, L., Riccio, R., Bonfili, L., Mozzicafreddo, M., Eleuteri, A.M., Casapullo, A.: Mechanistic insights on petrosaspongiolide M inhibitory effects on immunoproteasome and autophagy. *Biochim. Biophys. Acta (BBA)—Proteins Proteomics* **1844**(4), 713–721 (2014)
61. World Health Organization. Healthy topics: infectious diseases. [https://www.who.int/topics/infectious\\_diseases/en/](https://www.who.int/topics/infectious_diseases/en/) (2019)
62. Schlitzer, M.: Malaria chemotherapeutics Part I: history of antimalarial drug development, currently used therapeutics, and drugs in clinical development. *ChemMedChem* **2**, 944–986 (2007)
63. Baruah, U.K., Gowthamarajan, K., Vanka, R., Karri, V.V.S.R., Selvaraj, K., Jojo, G.M.: Malaria treatment using novel nano-based drug delivery systems. *J. Drug Target.* **25**, 567–581 (2017)
64. Bridgford, J.L., Xie, S.C., Cobbold, S.A., Pasaje, C.F.A., Herrmann, S., Yang, T., Gillett, D.L., Dick, L.R., Ralph, S.A., Dogovski, C., Spillman, N.J., Tilley, L. Artemisinin kills malaria parasites by damaging proteins and inhibiting the proteasome. *Nat. Commun.* **18**(9(1)) 3801 (2018)
65. Gantt, S.M., Myung, J.M., Briones, M.R.S., Li, W.D., Corey, E.J., Omura, S., Nussenzweig, V., Sinnis, P.: Proteasome inhibitors block development of *Plasmodium* spp. *Antimicrob. Agents Chemother.* **42**(10), 2731–2738 (1998)
66. Prudhomme, J., McDaniel, E., Pons, N., Bertani, S., Fenical, W., Jensen, P., Le Roch, K.: Marine actinomycetes: a new source of compounds against the human malaria parasite. *PLoS ONE* **3**, e2335 (2008)
67. Li, H., O'Donoghue, A.J., van der Linden, W.A., Xie, S.C., Yoo, E., Foe, I.T., Tilley, L., Craik, C.S., da Fonseca, P.C.A., Bogyo, M.: Structure- and function-based design of *Plasmodium*-selective proteasome inhibitors. *Nature* **530**, 233–236 (2016)
68. Dondorp, A.M., Yeung, S., White, L., Nguon, C., Day, N.P.J., Socheat, D., Von Seidlein, L.: Artemisinin resistance: current status and scenarios for containment. *Nat. Rev. Microbiol.* **8**, 272–280 (2010)
69. Czesny, B., Goshu, S., Cook, J.L., Williamson, K.C.: The proteasome inhibitor epoxomicin has potent *Plasmodium falciparum* gametocytocidal activity. *Antimicrob. Agents Chemother.* **53**, 4080–4085 (2009)

70. Yoo, E., Stokes, B.H., de Jong, H., Vanaerschot, M., Kumar, T., Lawrence, N., Njoroge, M., Garcia, A., Van der Westhuyzen, R., Momper, J.D., Ng, C.L., Fidock, D.A., Bogyo, M.: Defining the determinants of specificity of plasmodium proteasome inhibitors. *J. Am. Chem. Soc.* **140**, 11424–11437 (2018)
71. El-Sayed, N.M., Myler, P.J., Blandin, G., Berriman, M., Crabtree, J., Aggarwal, G., Caler, E., Renauld, H., Worthey, E.A., Hertz-Fowler, C., et al.: Comparative genomics of Trypanosomatid Parasitic Protozoa. *Science* **309**(5733), 404–409 (2005)
72. (a) Gilbert, I.H.: Target-based drug discovery for human African trypanosomiasis: selection of molecular target and chemical matter. *Parasitology* **141**, 28–36 (2014). (b) Kourbeli, V., Chontzopoulou, E., Moschovou, K., Pavlos, D., Mavromoustakos, T., Papanastasiou, I.P.: An overview on target-based drug design against Kinetoplastid protozoan infections: human African trypanosomiasis, chagas disease and leishmaniasis. *Molecules* **26**, 4629 (2021)
73. Steverding, D., Spackman, R.W., Royle, H.J., Glenn, R.J.: Trypanocidal activities of trileucine methyl vinyl sulfone proteasome inhibitors. *Parasitol. Res.* **95**, 73–76 (2005)
74. Khare, S., Nagle, A.S., Biggart, A., Lai, Y.H., Liang, F., Davis, L.C., Barnes, S.W., Mathison, C.J.N., Myburgh, E., Gao, M.-Y., et al.: Proteasome inhibition for treatment of leishmaniasis Chagas disease and sleeping sickness. *Nature* **537**, 229–233 (2016)
75. Nagle, A., et al.: Discovery and characterization of clinical candidate LXE408 as a kinetoplastid-selective proteasome inhibitor for the treatment of leishmaniasis. *J. Med. Chem.* **63**, 10773–10781 (2020)
76. Wyllie, S., Brand, S., Thomas, M., De Rycker, M., Chung, C.W., Pena, I., Bingham, R.P., Bueren-Calabuig, J.A., Cantizani, J., Cebrian, D., et al.: Preclinical candidate for the treatment of visceral leishmaniasis that acts through proteasome inhibition. *Proc. Natl. Acad. Sci. USA* **116**(19), 9318–9323 (2019)
77. Thomas, M., Brand, S., De Rycker, M., Zuccotto, F., Lukac, I., Dodd, P.G., Ko, E.J., Manthri, S., McGonagle, K., Osuna-Cabello, M., Riley, J., Pont, C., Simeons, F., Stojanovski, L., Thomas, J., Thompson, S., Viayna, E., Fiandor, J.M., Martin, J., Wyatt, P.G., Miles, T.J., Read, K.D., Marco, M., Gilbert, I.H.: Scaffold-hopping strategy on a series of proteasome inhibitors led to a preclinical candidate for the treatment of visceral leishmaniasis. *J. Med. Chem.* **64**(9), 5905–5930 (2021)
78. American Society of Hematology. For Patients: Blood Cancers. <http://www.hematology.org/Patients/Cancers/> (2019)
79. Abramson, H.N.: The multiple myeloma drug pipeline–2018: a review of small molecules and their therapeutic targets. *Clin. Lymphoma Myeloma Leuk.* **18**, 611–627 (2018)
80. NIH National Cancer Institute. Cancer Types: Lymphoma. <https://www.cancer.gov/types/lymphoma/patient/adult-nhl-treatment-pdq> (2021)
81. Boccadoro, M., Morgan, G., Cavenagh, J.: Preclinical evaluation of the proteasome inhibitor bortezomib in cancer therapy. *Cancer Cell Int.* **5**, 18 (2005)
82. Reddy, N., Czuczman, M.S.: Enhancing activity and overcoming chemoresistance in hematologic malignancies with bortezomib: preclinical mechanistic studies. *Ann. Oncol.* **21**, 1756–1764 (2010)
83. Moreau, P., Richardson, P.G., Cavo, M., Orłowski, R.Z., San Miguel, J.F., Palumbo, A., Harousseau, J.L.: Proteasome inhibitors in multiple myeloma: 10 years later. *Blood* **120**(5), 947–959 (2012)
84. Kupperman, E., Lee, E.C., Cao, Y., Bannerman, B., Fitzgerald, M., Berger, A., Yu, J., Yang, Y., Hales, P., Bruzzese, F., et al.: *Cancer Res.* **70**, 1970–1980 (2010)
85. Hanley, M.J., Gupta, N., Venkatakrisnan, K., Bessudo, A., Sharma, S., O’Neil, B.H., Wang, B., van de Velde, H., Nemunaitis, J.: A phase 1 study to assess the relative bioavailability of two capsule formulations of ixazomib, an oral proteasome inhibitor, in patients with advanced solid tumors or lymphoma. *J. Clin. Pharmacol.* **58**, 114–121 (2018)
86. Demo, S.D., Kirk, C.J., Aujay, M.A., Buchholz, T.J., Dajee, M., Ho, M.N., Jiang, J., Laidig, G.J., Lewis, E.R., Parlati, F., et al.: Antitumor activity of PR-171, a novel irreversible inhibitor of the proteasome. *Cancer Res.* **67**, 6383–6391 (2007)

87. Piva, R., Ruggeri, B., Williams, M., Costa, G., Tamagno, I., Ferrero, D., Giai, V., Coscia, M., Peola, S., Massaia, M., et al.: CEP-18770: a novel, orally active proteasome inhibitor with a tumor-selective pharmacologic profile competitive with bortezomib. *Blood* **111**(5), 2765–2775 (2008)
88. Vogl, D.T., Martin, T.G., Vij, R., Hari, P., Mikhael, J.R., Siegel, D., Wu, K.L., Delforge, M., Gasparetto, C.: Phase I/II study of the novel proteasome inhibitor delanzomib (CEP-18770) for relapsed and refractory multiple myeloma. *Leuk. Lymphoma* **58**, 1872–1879 (2017)
89. Sanchez, E., Li, M., Li, J., Wang, C., Chen, H., Jones-Bolin, S., et al.: CEP-18770 (delanzomib) in combination with dexamethasone and lenalidomide inhibits the growth of multiple myeloma. *Leuk. Res.* **36**, 1422–1427 (2012)
90. Chauhan, D., Catley, L., Li, G., Podar, K., Hideshima, T., Velankar, M., Mitsiades, C., Mitsiades, N., Yasui, H., Letai, A., et al.: A novel orally active proteasome inhibitor induces apoptosis in multiple myeloma cells with mechanisms distinct from Bortezomib. *Cancer Cell* **8**, 407–419 (2005)
91. Feling, R.H., Buchanan, G.O., Mincer, T.J., Kauffman, C.A., Jensen, P.R., Fenical, W.: Salinosporamide A: a highly cytotoxic proteasome inhibitor from a novel microbial source, a marine bacterium of the new genus salinospora. *Angew. Chem. Int. Ed. Engl.* **42**(3), 355–357 (2003)
92. Groll, M., Huber, R., Potts, B.C.: Crystal structures of salinosporamide A (npi-0052) and b (npi-0047) in complex with the 20S proteasome reveal important consequences of beta-lactone ring opening and a mechanism for irreversible binding. *J. Am. Chem. Soc.* **128**, 5136–5141 (2006)
93. da Silva, D.C., Andrade, P.B., Ribeiro, V., Valentao, P., Pereira, D.M.: Recent patents on proteasome inhibitors of natural origin. *Recent Pat. Anticancer. Drug Discov.* **12**, 4–15 (2017)
94. Nam, S., Smith, D.M., Dou, Q.P.: Ester bond-containing tea polyphenols potentially inhibit proteasome activity in vitro and in vivo. *J. Biol. Chem.* **276**(16), 13322–13330 (2001)
95. Groll, M., Ditzel, L., Löwe, J., Stock, D., Bochtler, M., Bartunik, H.D., Huber, R.: Structure of 20S proteasome from yeast at 2.4 Å resolution. *Nature* **386**, 463–471 (1997)
96. Niroula, D., Hallada, L.P., Le Chapelain, C., Ganegamage, S.K., Dotson, D., Rogelj, S., Groll, M., Tello-Aburto, R.: Design, synthesis, and evaluation of cystargolide-based  $\beta$ -lactones as potent proteasome inhibitors. *Eur. J. Med. Chem.* **157**, 962–977 (2018)
97. Fan, H., Angelo, N.G., Warren, J.D., Nathan, C.F., Lin, G.: Oxathiazolones selectively inhibit the human immunoproteasome over the constitutive proteasome. *ACS Med. Chem. Lett.* **5**, 405–410 (2014)
98. Lin, G., Li, D., de Carvalho, L., et al.: Inhibitors selective for mycobacterial versus human proteasomes. *Nature* **461**, 621–626 (2009)
99. Maccari, R., Ettari, R., Adornato, I., Naß, A., Wolber, G., Bitto, A., Mannino, F., Aliquò, F., Bruno, G., Nicolò, F., Previti, S., Grasso, S., Zappalà, M., Ottanà, R.: Identification of 2-thioxoimidazolidin-4-one derivatives as novel noncovalent proteasome and immunoproteasome inhibitors. *Bioorg. Med. Chem. Lett.* **28**(3), 278–283 (2018)
100. Robles-Escajeda, E., Das, U., Ortega, N.M., et al.: A novel curcumin-like dienone induces apoptosis in triple-negative breast cancer cells. *Cell Oncol.* **39**, 265–277 (2016)
101. Nunes, L.M., Hossain, M., Varela-Ramirez, A., Das, U., Ayala-Marin, Y.M., Dimmock, J.R., Aguilera, R.J.: A novel class of piperidones exhibit potent, selective and pro-apoptotic anti-leukemia properties. *Oncol. Lett.* **11**, 3842–3848 (2016)
102. Contreras, L., Calderon, R.I., Varela-Ramirez, A., Zhang, H.Y., Quan, Y., Das, U., Dimmock, J.R., Skouta, R., Aguilera, R.J.: Induction of apoptosis via proteasome inhibition in leukemia/lymphoma cells by two potent piperidones. *Cell. Oncol.* **41**, 623–636 (2018)

# Phytotechnological and Pharmaceutical Potential of *Eugenia* Genus



**Monatha Nayara Guimarães Teófilo, Elisa Flávia Luiz Cardoso Bailão, José Realino de Paula, Clayson Moura Gomes, Vinicius Barreto da Silva, Carlton A. Taft, Joelma Abadia Marciano de Paula, and Leonardo Luiz Borges**

**Abstract** *Eugenia* is the largest Neotropical genus belonging to the Myrtaceae family, comprising more than 1000 species spread across the Antilles, Southeast Asia, Pacific Islands, Argentina, southern Mexico, Cuba, Uruguay, Africa, and Brazil. *Eugenia* genus comprises species employed in folk medicine due to their antioxidant compounds, such as polyphenols, tannins, and flavonoids. Traditionally, plants are widely used to treat inflammatory diseases and metabolic disorders. Various species from this genus possess technological potential as well. The biological properties associated with the phytochemistry profile raise a significant number of potential intermediate and final products. Thus, we approach the technological products obtained from species of the *Eugenia* genus, their biological potential and the main techniques employed in the future development of products with commercial value.

**Keywords** Myrtaceae · Medicinal plants · Cerrado · Intermediate products

## 1 Introduction

Historical records from traditional Chinese, Ayurvedic and Amerindian medicine show that the widespread use of plants for medicinal and nutritional purposes comes from the beginning of humanity [1]. Thus, over the years, the use of natural products has become an alternative practice in conventional medicine around the world; the World Health Organization and government agencies have highlighted the need for

---

M. N. G. Teófilo · E. F. L. C. Bailão · J. A. M. de Paula · L. L. Borges (✉)  
Campus Central, Universidade Estadual de Goiás, Anápolis, GO, Brazil  
e-mail: [leonardo.borges@ueg.br](mailto:leonardo.borges@ueg.br)

J. R. de Paula  
Faculdade de Farmácia, Universidade Federal de Goiás, Goiânia, GO, Brazil

C. M. Gomes · V. B. da Silva · L. L. Borges  
Escola de Ciências Médicas E da Vida, Pontifícia Universidade Católica, de Goiás, Goiânia, GO, Brazil

C. A. Taft  
Centro Brasileiro de Pesquisas Físicas, Rio de Janeiro, RJ, Brazil

studies that establish criteria for safety, efficacy, and quality, valuing the use of medicinal plants in the therapeutic scope [2, 3].

In this context, scientific research aims to prove its use in folk medicine, based on empirical knowledge, classifying and identifying its biochemical composition, and establishing its real benefits of use and better pharmacological properties [1]. Furthermore, the structural diversity of special metabolites present in plants represents a prosperous source of bioactive compounds [3]. Thus, the search for these substances becomes essential due to the ability to treat different pathophysiological conditions and contribute to the conservation and recognition of the biodiversity of Biomes and promoting the sustainability and development of natural resources.

*Eugenia* is the largest Neotropical genus belonging to the Myrtaceae family, comprising more than 1000 species spread across the Antilles, Southeast Asia, Pacific Islands, Argentina, Southern Mexico, Cuba, Uruguay, Africa, and Brazil [4, 5]. In Brazil, the genus has a wide geographic distribution, mainly in the Amazon, Atlantic Forest, and Cerrado [6, 7]. According to the current molecular classification, *Eugenia* belongs to the subtribe Eugeniinae of the tribe Myrteae, subfamily Myrtoideae [8–10].

The species' way of life consists of fruit trees, shrubs, or sub-shrubs, occupying the position of the second most diverse tree genus in species on the planet [9, 11, 12]. The flowers are axillary, branched, tiny, and fragrant with white or possibly pink petals [12]. The fruits are small, less than 10 cm in diameter, globose, pulpy, consisting of few seeds, usually 1–2 [9, 12], and consumed *in natura*; they are rich in minerals, vitamins, and phenolic compounds. Due to their characteristics, many plants are used in landscaping, domestic planting, reforestation, and urban afforestation. Other species, such as *Eugenia dysenterica* (Mart.) DC, are still used in folk medicine as laxatives, anti-inflammatory, and anti-rheumatic agents [13–16].

In addition, the species are rich in essential oils, extracts are also made from them (ethanolic, hydroalcoholic, acetone), and chemical compounds are isolated [17, 18], several nutrients and bioactive substances have been described supporting popular uses [13, 14]. Thus, *Eugenia* genus has aroused much commercial interest due to its edible fruits, ornamental characteristics, essential oils, and therapeutic potential.

## 2 The Pharmaceutical Potential of the *Eugenia* Genus

Species of the *Eugenia* genus have several biological properties, such as gastroprotective [19], antidiabetic [20], antioxidant [21], anticancer [22], anti-inflammatory [23], antimicrobial [17], antipyretic [24], among others [13]. These activities are related to the presence of special metabolites, such as phenolic compounds, mainly flavonoids (myricitrin, quercetin), terpenoids (monoterpenes, triterpenes, sesquiterpenes), and tannins [13, 15]. Traditionally, plants are widely used to treat inflammatory diseases and metabolic disorders [17].

The pharmaceutical potential has been described in several plants, including fruits, seeds, and leaves [13]. For example, extracts from *Eugenia selloi* (O.

Berg) B.D. Jacks.(fruit), *Eugenia kleinii* D. Legrand.(seeds), and *Eugenia brasiliensis* Lam.(pulp) showed anti-inflammatory and antioxidant activity due to the ability to modulate neutrophil migration. Two similar compounds across species that may enhance the observed potential were ellagic acid and quercetin [25–27]. Likewise, the presence of ellagic acid and other  $\alpha$ - and  $\beta$ -amyrin pentacyclic triterpenoid constituents in *Eugenia umbeliflora* O. Berg leaves was reported, showing important anti-inflammatory effects on the extract the behavior of neutrophils and on the decrease of IL- $\beta$  levels [28].

Antiparasitic activities have also been reported; studies with essential oil from the leaves of *Eugenia uniflora* L. and hydroalcoholic extract of *Eugenia pruniflora* Cambess, showed anti-leishmania (*Leishmania amazonensis*) potential against promastigote and amastigote forms using in vivo and in vitro experiments. Biological activity is probably associated with sesquiterpenes and terpenoid fractions [29, 30]. These results are promising and may help in the future in the treatment of leishmaniasis—an infectious, neglected tropical disease of great epidemiological importance [31].

Extracts from the leaves of *Eugenia puniceifolia* (Kunth) DC. (“cerejeira do cerrado”), *E. dysenterica*, *E. umbeliflora*, and the fruit of *Eugenia mattosii* D. Legrand (“cerejeira anã”) showed gastroprotective and antinociceptive effects in vivo, such as increased production of gastric mucus, blockage of production of hydrochloric acid, reduction of more than 60% of ulcerated areas, similar to that compared with cimetidine and omeprazole (medicines used in the treatment of gastritis). These studies indicated the presence of condensed tannins and proanthocyanidins as responsible for the observed biological effects [19, 32–34].

Despite antimicrobial properties, crude extracts from seeds (*E. Kleinii*, *E. brasiliensis*) and leaves (*E. brasiliensis*), obtained greater antifungal potential in *Candida albicans* biofilm than with nystatin (standard) in the phytochemistry of the extract. The majority presence of gallic acid and epicatechin was observed [14]. Likewise, antibiofilm activity was observed in *Lactobacillus acidophilus* from the extract of *E. brasiliensis* (pulp), in addition to catechin, flavonols, anthocyanins, and ellagitannins were found [27]. Essential oils of *E. umbeliflora*, *E. brasiliensis*, and *Eugenia beaurepairiana* (Kiaersk) D. Legrand (“ingábaú”) showed antibacterial properties against *Staphylococcus aureus*, *Escherichia coli*, and *Pseudomonas aeruginosa*, and extract/fractions of *E. mattosii* still show antimycoplasmic activity (*Mycoplasma pneumoniae* and *Mycoplasma genitalium*) [35, 36]. Furthermore, the essential oil of *Eugenia calycina* Cambess (“pitanga vermelha do cerrado”) and its fractions showed selective activity against oral gram-negative bacteria (*Porphyromonas gingivalis*, *Prevotella nigrescens*, among others). These biological properties have been associated with the presence of oxygenated and non-oxygenated sesquiterpenes, thus making it a good measure in treating oral bacterial infections [37].

Ethanol extract from fruits and seeds of *Eugenia involucrata* DC. showed an antitumor effect on PANC-1 (pancreatic adenocarcinoma) cells, involving complex mechanistic pathways, such as oxidative stress and cell proliferation. The primary responsibility for the biological activity of the extract was epicatechin, catechin, and ellagic acid alone or in combination with other chemical constituents present

[22]. On the other hand, the study by Vitek et al. 2016, with an isolated compound (quercetin-3-O-(6''-O-galloil)- $\beta$ -d-glucopyranoside) from the extract of *E. dysenterica* leaves, alone was shown to induce cytotoxicity in cells of the CCRF-CEM lineage (Lymphoblastic Leukemia of T cells) and antiproliferative and cell differentiation effects in a Kasumi-1 lineage (acute myeloid leukemia) [38].

Other reported activities of *Eugenia* spp. consists of antidepressant activity influenced by substances such as  $\alpha$ -amyrin and  $\beta$ -amyrin, betulin, 29-hydroxy-oleanolic acid, and flavonoids [39], potential to inhibit acetylcholinesterase (AChE) activity, correlated with known compounds such as quercetin, catechin, epicatechin, procatechuic acid, and myricitrin [40]. Ability to interact with nicotinic cholinergic receptors [41], and finally, the species show low or no toxicity using in vivo and in vitro studies [25, 27, 42, 43]. Therefore, the phytochemical characteristics of the genus are a promising source in the discovery of bioactive compounds and the development of drugs, proving the great pharmaceutical potential of the species.

### 3 Phytotechnological Potential of the *Eugenia* Genus

Due to the growing recognition of the nutritional and therapeutic benefits of species of the *Eugenia* genus, many of the fruits are being consumed in an industrial version of ice cream/popsicles, juices, jams, sweets, and jellies, such as the “pitanga” of the *E. uniflora* species, the “cereja do rio grande” from *E. involucrata* and the “cagaita” belonging to *E. dysenterica* [44, 45].

In this context, residues from *Eugenia* spp. has been well investigated; Silva et al. [46], observed that the by-product of pitanga fruits (*E. uniflora*) had higher polyphenol content (total anthocyanins, yellow flavonoids,  $\beta$ -carotene, lycopene, resveratrol and coumarins) than their respective pulp, demonstrating that after processing the residues have prospects of use, such as nutraceutical supplements and food inputs [46]. The extract of *E. uniflora* leaves is a healthy alternative for replacing synthetic antioxidants, such as butylated hydroxytoluene (BHT), in goat and pork hamburgers [47, 48]. Due to its antioxidant potential, preserving the quality of the meat without adverse effects on its physical–chemical and sensory properties, and increasing the shelf life to storage time.

Bioactive peptides derived from plants have attracted significant interest from researchers and the pharmaceutical industry. They are chains of amino acids joined by covalent bonds with different biological functions [49]. For example, Lima et al. 2010, showed that a peptide isolated from the fruit of *E. dysenterica* promoted a laxative effect in rats due to the increase in intestinal peristalsis without causing diarrhea and toxic effects. The peptide was identified using modern and practical analysis methods such as high-performance liquid chromatography (HPLC). The molecular mass and degree of purity were determined using Tris/Tricine polyacrylamide gel electrophoresis matrix-assisted laser desorption/ionization-time of flight

mass spectrometry (MALDI-ToF) [50]. Thus promoting perspectives in the technological development of natural pharmaceutical peptides in treating irritable bowel syndrome and chronic constipation.

One application of renewable characteristics that has been studied is the use of the extract of the leaves of *E. dysenterica* as an additive in biofuel. Rial et al. [51], demonstrated the ability of the crude extract to reduce the oxidation of soy biodiesel after 120 days of storage much more effectively than quercetin (standard). This result was associated with flavonoids, tannins, steroids, and triterpenoids, promoting stability and better quality of biodiesel [51].

The spray drying technique also proves to be a promising strategy in developing bioactive intermediate products from *Eugenia* spp. [52]. The study by Iturri et al. [53], was shown to be a good technique in the preservation of phenolic compounds and in obtaining microparticles from the pulp extract of *Eugenia stipitata* McVaugh. In addition, innovatively, Differential Scanning Calorimetry (DSC) was used with the spray dryer to define the drying temperatures and the proportion of the wall material. Therefore, the microparticles with the best conservation of polyphenols and the best antioxidant potential were with maltodextrin (1:9) at 100 °C. Hence, the association between these two techniques results in a quality product, with high concentrations of compounds being economically viable in industrial production [53].

Nanoemulsions have alternative products in the application. Nanoemulsions from the essential oil of *Eugenia brejoensis* Mazine leaves potential antibacterial foods, against *Pseudomonas fluorescens* bacteria found in food. No essential oil compounds were identified as sesquiterpenic hydrocarbons,  $\beta$ -(E)-Caryophyllene,  $\delta$ -cadinene, and bicyclogermacrene [54]. From the extracts, emulsions are also made, as the catechin-rich *E. dysenterica* extract has shown in in vitro experiments, antimicrobial properties against *S. aureus* strains, and angiogenic activity [43]. Demonstrating the possibility of developing dermatological treatment from plant products, with a perspective on the cosmetics industry.

Other technological potentials of species of the *Eugenia* genus include serving as an additive in producing films (food and degradable biofilms) of active nanocomposites and in the coating of minimally processed foods due to antioxidant and antimicrobial activity [55, 56]. Furthermore, protect different organisms (*E. coli*, seeds, and *Drosophila melanogaster*) against toxicity caused by mercuric chloride residues through antioxidant mechanisms or chelation [57], promoting interesting perspectives in environmental conservation. Also, *Eugenia* spp. has shown good yield and extraction results by the supercritical fluid technique, indicating the use of green technologies as alternative and economic conditions in extractive processes [58–60].

Some species still show a predisposition in the development of quality insecticides, with low toxicity and sustainable footprint; an example is a study by Silva et al. [61], in which the essential oil of *E. calycina* showed larvicidal activity against *Aedes aegypti* mosquito, due to the synergistic effect of oxygenated sesquiterpene compounds (spathulenol, aromadendrane-4 $\beta$ ,10 $\alpha$ -diol and 1 $\beta$ -11-dihydroxy-5-eudesmene), with low toxicity in HeLa (human epithelial cell) and Vero (African monkey renal cell) cell lines [61]. Therefore, in addition to the biological properties



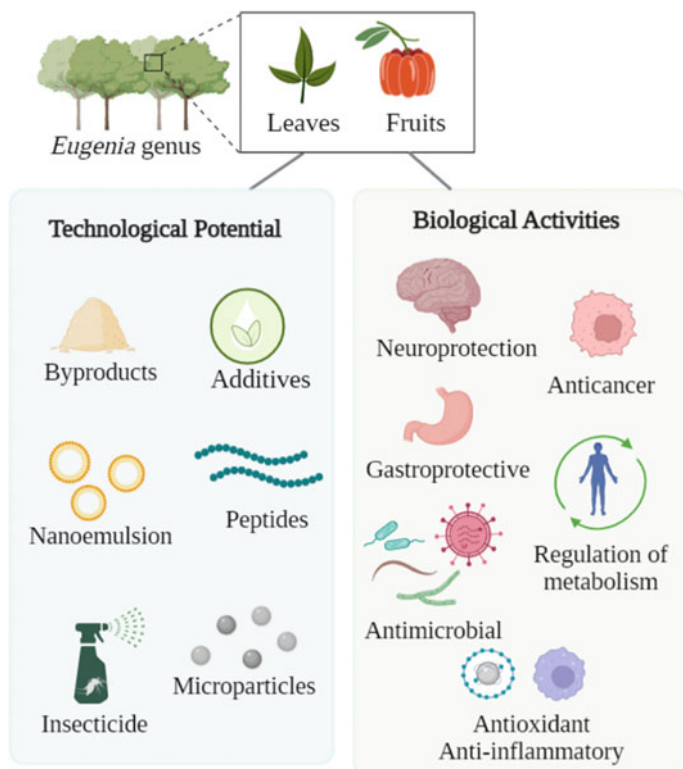


**Fig. 1** Illustration of the biological and technological potential of the *Eugenia* genus

*Eugenia* spp. also demonstrates great technological potential in the development of products with commercial value (Fig. 1).

#### 4 Food Application of *Eugenia* spp.

In recent decades, the food industry and the consumer market have been increasingly interested in phenolic-rich edible fruits as they slow down the rancidity process, improve the quality and the nutritional value of foods, and promote well-being and health [62]. *Eugenia* spp. is an innovation hotspot for food purposes, because of the presence of (i) favorable sensory characteristics and (ii) bioactive phytochemicals with biological activity stronger than that observed in fruits traditionally consumed by the urban population, so being considered superfruits, which encourages its use as nutraceuticals [13, 15, 63, 64]. Nutraceuticals are substances that, other than nutrition, are also used as medicine. A nutraceutical presents physiological benefits or protects chronic body processes, such as aging and chronic diseases. In other terms,

nutraceuticals may be used to improve health, increasing life expectancy [65]. Thus, *Eugenia* spp. has great economic potential since the regular intake of its superfruits should be beneficial for human health [13, 64].

Two *Eugenia* species stand out for food applications: *E. uniflora* and *E. dysenterica*. These species are traditionally consumed in Brazil in natura or prepare several culinary recipes, such as ice creams, jams, jellies, and beverages. Recently, *E. uniflora* was added to traditional kombucha, which contributed to diversifying and improving this beverage's chemical and bioactive characteristics, revealing a sweeter kombucha, with floral and fruity aromas and with a greater antioxidant activity [66]. Since the antioxidant compounds are highly unstable molecules, microencapsulation of *E. uniflora* juice by spray drying demonstrated to be a suitable alternative for the encapsulation and protection of antioxidants for the food industry [67].

*E. uniflora* extracts could also be used in the food industry as natural aroma enrichment of processed foods, in food packaging, or as food preservatives. The characteristic flavor of *E. uniflora* fruits is attributed to the presence of sesquiterpenes and ketones [68]. The flavor intensity of these fruits obtained by supercritical carbon dioxide extraction is correlated to the temperature increase (>50 °C) [69]. The antioxidant molecules in *E. uniflora* could be essential to protect *in natura* or processed food. Biopolymer films loaded with nanocellulose from soybean straw and activated with *E. uniflora* leaf extract displayed a greater resistance and stiffness, higher barrier properties to UV/Vis light, and higher antioxidant activity than those without the extract [55]. *E. uniflora* leaf extract was effective against color deterioration and lipid and protein oxidation, without impairing the sensorial characteristics, on lamb burgers with fat replacement by chia oil emulsion, representing a promising alternative to replace synthetic antioxidants by natural products in lamb burgers [47].

Although its laxative capacity [50], *E. dysenterica* can be used in the food industry [63]. Wines, juices, jellies, and raisins with high antioxidant properties and good consumer acceptance were elaborated using *E. dysenterica* pulp [70–73]. Moreover, *E. dysenterica* fruit extract has the potential to be used as an ingredient of diabetic and obese food formulations since it can inhibit  $\alpha$ -amylase and  $\alpha$ -glucosidase, key enzymes in carbohydrate metabolism, slowing postprandial hyperglycemia [74], and it presents functional properties to both prevent and treat obesity and associated diseases [75, 76]. Recently, *E. dysenterica* juice also demonstrated a postprandial glucose-lowering effect [77]. To prevent deterioration of the bioactive compounds in *E. dysenterica*, spray drying methodology was shown to be a suitable alternative during dehydration of the leaves and fruit [52, 78].

Other *Eugenia* species, considered unexplored Brazilian fruits, has the potential to be applied in the food industry. *E. calycina* presents three times more ellagic acid than blackberry and black raspberry, the main richest classical foods in ellagic acid [62]. Using a thermal ultrasound approach, phenolic compounds extraction from *E. calycina* was more efficient [79]. Fresh and spray dried *Eugenia jambolana* Lam (“jambolan”) has already been used to prepare caprine frozen yogurt containing the probiotic strain *Bifidobacterium animalis* subsp. *lactis* B1-07. The preparation presented a good consumer acceptance and maintained high probiotic survival

rates along with 90-day frozen storage, proving to be a high-quality dairy product for the crescent, healthy-oriented market [80]. The stability of anthocyanins- and anthocyanidins-enriched extracts and formulations of fruit pulp of *E. jambolana* was investigated. The anthocyanins-enriched Sephadex extract presented good stability (36% content reduction) after 1 year at 5 °C [81].

*Eugenia pyriformis* Cambess (“uvaia”) can be considered an energetic matrix containing fructose, sucrose, glucose, and maltotetraose. This fruit presents high levels of macronutrients (ash, lipids, proteins, fibers) and minerals. It contributes to the dietary reference intake regarding dietary fibers and micronutrients, such as Fe, Cu, K, Mg, and Mn. Moreover, *E. pyriformis* presented high levels of total flavonoids, phenolic compounds, and antioxidant activity, terpenes the majority (46.75%) of identified volatile compounds [82, 83]. The influence of in vitro gastrointestinal digestion on the bioaccessibility and bioactivity of phenolic compounds was investigated for *E. pyriformis* fruits. Flavonoids increased their relative intensity, while phenolic acids reduced their power, suggesting that such compounds are more susceptible to being degraded during the digestive process, presumably due to less chemical complexity than flavonoids, which were found mainly in glycosylated form [84].

*E. stipitata* (“arazá”) is being considered a superfruit because of the high content of minerals such as K, Ca, and Mg, sucrose, fructose, maltotetraose, phenolic compounds, and flavonoids, with a good antioxidant capacity, revealing a relevant potential to be used as a functional food [64, 85]. Storage stability tests of freeze-dried *E. stipitata* powders revealed that shelf-lives, calculated considering 90% properties retention as the acceptability limit, were 34 and 50 days to an arazá/maltodextrin mixture and an arazá/Arabic-gum mixture, respectively [86]. Microparticles of maltodextrin and *E. stipitata* pulp (1:9, 100 °C) obtained by spray-drying guided by differential scanning calorimetry (DSC) had good bioactivity conservation after in vitro gastrointestinal digestion, conserving 61% of total polyphenols, and 101%, 85% and 31% of antioxidant capacity. These microparticles had a spherical morphology, presented good thermal stability, and can be stored at a temperature range from 20 to 40 °C without becoming sticky [53].

*E. brasiliensis* (“grumixama”) is also considered a good source of bioactive compounds, such as anthocyanins, flavonols, and ellagitannins [87]. Human urine and plasma after ingestion of polyphenol-rich juice of purple *E. brasiliensis* revealed that a single dose of grumixama juice increased the plasma antioxidant capacity and 114 metabolites were assessed in urine, including 17 amino acids, 47 organic acids, and several other metabolites involved mainly with amino acid metabolism and mitochondrial metabolism [88]. Altogether, these data indicate that *Eugenia* spp. may serve as a raw material for the food industry.

## 5 Conclusion

Species of the *Eugenia* genus are a promising source of bioactive and biotechnological compounds. Essential oils and plant extracts contain special metabolites such

as flavonoids, terpenoids, and tannins, responsible for triggering various biological activities (regulation of metabolism, neuroprotection, gastroprotection, etc.), thus making it an alternative measure as a therapeutic complement and treatment of diseases. In addition, the species show perspective in the industry with the development of technological products playing the role of drugs, environmental remediators, food inputs, additives, insecticides, among others.

## References

1. Hao, D., Xiao, P.: Pharmaceutical resource discovery from traditional medicinal plants: Pharmacophylogeny and pharmacophylogenomics. *Chin. Herb. Med.* (Elsevier BV) **12**, 104–117 (2020)
2. World Health Organization. WHO Traditional Medicine Strategy (2014–2023)
3. Moreira, D. de L., Teixeira, S.S., Monteiro, M.H.D., De-Oliveira, A.C.A.X., Paumgarten, F.J.R.: Traditional use and safety of herbal medicines. *Revista Brasileira de Farmacognosia. Sociedade Brasileira de Farmacognosia* **24**, 248–257 (2014)
4. WCSP. World Checklist of Selected Plant Families. Facilitated by the Royal Botanic Gardens, Kew (2022). <http://wcsp.science.kew.org/>. Cited 21 Jan 2022
5. Mazine, F.F., Faria, J.E.Q., Giaretta, A., Vasconcelos, T., Forest, F., Lucas, E.: Phylogeny and biogeography of the hyper-diverse genus *Eugenia* (Myrtaceae: Myrteae), with emphasis on *E. sect. umbellatae*, the most unmanageable clade. *Taxon. Int. Assoc. Plant Taxon.* **67**, 752–69 (2018)
6. Mazine, F.F., Bünger, M.O., de Faria, J.E.Q., Lucas, E., Souza, V.C.: Sections in *Eugenia* (Myrteae, Myrtaceae): nomenclatural notes and a key. *Phytotaxa* **289**, 225–236 (2016)
7. Mazine, F.F., Bünger, M., Faria, J.E.Q., Fernandes, T., Giaretta, A., Valdemarin, K.S. et al.: *Eugenia* in Flora do Brasil 2020 [Internet]. Jardim Botânico do Rio de Janeiro. <http://reflora.jbrj.gov.br/reflora/floradobrasil/FB10338> (2020). Cited 6 Feb 2022
8. Wilson, P.G., O'Brien, M.M., Heslewood, M.M., Quinn, C.J.: Relationships within Myrtaceae sensu lato based on a matK phylogeny. *Plant Syst. Evol.* **251**, 3–19 (2005)
9. Lucas, E.J., Holst, B., Sobral, M., Mazine, F.F., Nic Lughadha, E.M., Barnes Proença, C.E. et al.: A new subtribal classification of tribe Myrteae (Myrtaceae). *Syst. Botany. Am. Soc. Plant Taxon.* **44**, 560–569 (2019)
10. Berg, O.: *Revisio Myrtacearum Americae*. *Linnaea* **27**, 1–472 (1856)
11. Beech, E., Rivers, M., Oldfield, S., Smith, P.P. GlobalTreeSearch: the first complete global database of tree species and country distributions. *J. Sustain. For.* (Taylor and Francis Inc.) **36**, 454–89 (2017)
12. Landrum, L.R., Kawasaki, M.L.: The genera of Myrtaceae in Brazil: an illustrated synoptic treatment and identification keys. *Brittonia. São Paulo* **49**, 508–536 (1997)
13. de Araújo, F.F., Neri-Numa, I.A., de Paulo Farias, D., da Cunha, G.R.M.C., Pastore, G.M.: Wild Brazilian species of *Eugenia* genera (Myrtaceae) as an innovation hotspot for food and pharmacological purposes. *Food Res. Int.* (Elsevier Ltd.) **57–72** (2019)
14. Sardi, J. de C.O., Freires, I.A., Lazarini, J.G., Infante, J., de Alencar, S.M., Rosalen, P.L.: Unexplored endemic fruit species from Brazil: antibiofilm properties, insights into mode of action, and systemic toxicity of four *Eugenia* spp. *Microb. Pathogen.* (Academic Press) **105**, 280–287 (2017)
15. Bailão, E.F.L.C., Devilla, I.A., Conceição, E.C. da, Borges, L.L. Bioactive compounds found in Brazilian Cerrado fruits. *Int. J. Mol. Sci.* **23760–23783** (2015)
16. Tainá Macedo Garcia Cardoso, Ellen Santos Calmon de Oliveira, Jorge P.P. Carauta, Marcelo da Costa Souza, Débora Medeiros, Luiz José Soares Pinto, et al. *Árvores e Arbustos. Horto Botânico* (2022). <https://museunacional.ufrj.br/hortobotanico/arvoresearbustos.html>. Cited 13 Feb 2022

17. de Souza, A.M., de Oliveira, C.F., de Oliveira, V.B., Betim, F.C.M., Miguel, O.G., Miguel, M.D.: Traditional uses, phytochemistry, and antimicrobial activities of *Eugenia* species—A review. *Planta Med.* **84**, 1232–1248 (2018)
18. da Costa, J.S., da Cruz, E. de N.S., Setzer, W.N., da Silva, J.K.D.R., Maia, J.G.S., Figueiredo, P.L.B.: Essentials oils from Brazilian *Eugenia* and syzygium species and their biological activities. *Biomolecules* (MDPI AG) 1–36 (2020)
19. dos Santos, L., Campos, A., Cechinel Filho, V., Nesello, L.A.N.: Phytochemical profile and gastroprotective activity of *Eugenia mattosii* fruits. *Arquivos de Gastroenterologia. IBEPEGE—Inst. Bras. Estudos Pesquisas Gastroent.* **55**, 138–141 (2018)
20. Bastos, R.G., Salles, B.C.C., Bini, I.F., Castaldini, L.P., Silva, L.C.D., Vilela, A.A. et al.: Phytochemical composition, antioxidant and in vivo antidiabetic activities of the hydroethanolic extract of *Eugenia florida* DC. (Myrtaceae) leaves. *S. Afr. J. Botany* (Elsevier B.V.) **123**, 317–332 (2019)
21. Nicácio, A.E., Rotta, E.M., Boeing, J.S., Barizão, É.O., Kimura, E., Visentainer, J.V. et al.: Antioxidant activity and determination of phenolic compounds from *Eugenia involucrata* DC. Fruits by UHPLC-MS/MS. *Food Anal. Methods.* (Springer New York LLC) **10**, 2718–2728 (2017)
22. Girardelo, J.R., Munari, E.L., Dallorsoleta, J.C.S., Cechinel, G., Goetten, A.L.F., Sales, L.R. et al.: Bioactive compounds, antioxidant capacity and antitumoral activity of ethanolic extracts from fruits and seeds of *Eugenia involucrata* DC. *Food Res. Int.* (Elsevier Ltd.) **137** (2020)
23. Pietrovski, E.F., Magina, M.D.A., Gomig, F., Pietrovski, C.F., Micke, G.A., Barcellos, M., et al.: Topical anti-inflammatory activity of *Eugenia brasiliensis* Lam. (Myrtaceae) leaves. *J. Pharm. Pharmacol.* (Oxford University Press (OUP)) **60**, 479–487 (2010)
24. Amorim, A.C.L., Lima, C.K.F., Hovell, A.M.C., Miranda, A.L.P., Rezende, C.M.: Antinociceptive and hypothermic evaluation of the leaf essential oil and isolated terpenoids from *Eugenia uniflora* L. (Brazilian Pitanga). *Phytomedicine* (Urban und Fischer Verlag Jena) **16**, 923–928 (2009)
25. Lazarini, J.G., Franchin, M., Soares, J.C., Nani, B.D., Massarioli, A.P., de Alencar, S.M. et al.: Anti-inflammatory and antioxidant potential, in vivo toxicity, and polyphenolic composition of *Eugenia selloi* B.D.Jacks. (pitangatuba), a Brazilian native fruit. *PLoS ONE* (Public Library of Science) **15** (2020)
26. Infante, J., Rosalen, P.L., Lazarini, J.G., Franchin, M., de Alencar, S.M.: Antioxidant and anti-inflammatory activities of unexplored Brazilian native fruits. *PLoS ONE* (Public Library of Science) **11** (2016)
27. Lazarini, J.G., Sardi, J. de C.O., Franchin, M., Nani, B.D., Freires, I.A., Infante, J. et al.: Bioprospection of *Eugenia brasiliensis*, a Brazilian native fruit, as a source of anti-inflammatory and antibiofilm compounds. *Biomed. Pharmacother.* (Elsevier Masson SAS) **102**, 132–139 (2018)
28. Goldoni, F.C., Barretta, C., Nunes, R., Broering, M.F., de Faveri, R., Moller, H.T. et al.: Effects of *Eugenia umbelliflora* O. Berg (Myrtaceae)-leaf extract on inflammation and hypersensitivity. *J. Ethnopharmacol.* (Elsevier Ireland Ltd) **244** (2019)
29. Albuquerque, R.D.D.G., Oliveira, A.P., Ferreira, C., Passos, C.L.A., Fialho, E., Soares, D.C. et al.: Anti-leishmania amazonensis activity of the terpenoid fraction from *Eugenia pruniformis* leaves. *Anais da Academia Brasileira de Ciências* (Academia Brasileira de Ciências) **92**, 1–14 (2020)
30. Rodrigues, K.A.D.F., Amorim, L.V., Oliveira, J.M.G. de, Dias, C.N., Moraes, D.F.C., Andrade, E.H.D.A. et al.: *Eugenia uniflora* L. essential oil as a potential anti-leishmania agent: Effects on leishmania amazonensis and possible mechanisms of action. *Evid.-Based Complement. Altern. Med.* **2013** (2013)
31. Organização Pan-Americana da Saúde. Informe epidemiológico das Américas. Washington, D.C. (2020)
32. Basting, R.T., Nishijima, C.M., Lopes, J.A., Santos, R.C., Lucena Périco, L., Laufer, S. et al. Antinociceptive, anti-inflammatory and gastroprotective effects of a hydroalcoholic extract from the leaves of *Eugenia punicifolia* (Kunth) DC. in rodents. *J. Ethnopharmacol.* (Elsevier Ireland Ltd) **157**, 257–267 (2014)

33. Carolina, L., Prado, S., Silva, D.B., Lopes De Oliveira-Silva, G., Renata, K., Hiraki, N. et al.: The gastroprotective effects of *Eugenia dysenterica* (Myrtaceae) Leaf Extract: The Possible Role of Condensed Tannins [Internet]. Biol. Pharm. Bull. (2014). <http://rsb.info.nih.gov/>
34. Meyre-Silva, C., Petry, C.M., Berté, T.E., Becker, R.G., Zanatta, F., Delle-Monache, F. et al.: Phytochemical analyses and gastroprotective effects of *Eugenia umbelliflora* (Myrtaceae) on experimental gastric ulcers. Nat. Prod. Commun. (Natural Product Incorporation) 4, 911–916
35. Magina, M.D.A., Dalmarco, E.M., Wisniewski, A., Simionatto, E.L., Dalmarco, J.B., Pizzolatti, M.G., et al.: Chemical composition and antibacterial activity of essential oils of *Eugenia* species. J. Nat. Med. **63**, 345–350 (2009)
36. Vechi, G., Tenfen, A., Maína Boeder, A., Hernandez-Gómez, L., Maurício Mendes de Córdova, C., Delle Monache, F. et al.: Chemical composition and antimycoplasmic activity of *Eugenia mattosii* leaves, stems and isolated compounds.
37. Sousa, R.M.F., de Moraes, S.A.L., Vieira, R.B.K., Napolitano, D.R., Guzman, V.B., Moraes, T.S. et al.: Chemical composition, cytotoxic, and antibacterial activity of the essential oil from *Eugenia calycina* Cambess. leaves against oral bacteria. Ind. Crop. Prod. (Elsevier B.V.) **65**, 71–78 (2015)
38. Vitek, R., de Novais, L.M.R., Torquato, H.F.V., Paredes-Gamero, E.J., de Carvalho, M.G., de Sousa P.T. et al. Chemical constituents and antileukemic activity of *Eugenia dysenterica*. Nat. Prod. Res. (Taylor and Francis Ltd.) **31**, 1930–1934 (2017)
39. Colla, A.R.S., MacHado, D.G., Bettio, L.E.B., Colla, G., Magina, M.D.A., Brighente, I.M.C. et al.: Involvement of monoaminergic systems in the antidepressant-like effect of *Eugenia brasiliensis* Lam. (Myrtaceae) in the tail suspension test in mice. J. Ethnopharmacol. **143**, 720–31 (2012)
40. Tenfen, A., Vechi, G., Cechinel-Zanchett, C.C., Lorenzetti, T.S., Reginato-Couto, C.E., Siebert, D.A. et al.: Phenolic profile by HPLC-ESI-MS/MS of six Brazilian *Eugenia* species and their potential as cholinesterase inhibitors. Nat. Prod. Res. (Taylor and Francis Ltd.) **35**, 2608–2611 (2021)
41. Grangeiro, M.S., Calheiros-Lima, A.P., Martins, M.F., Arruda, L.F., Garcez-do-Carmo, L., Santos, W.C.: Pharmacological effects of *Eugenia puniceifolia* (Myrtaceae) in cholinergic nicotinic neurotransmission. J. Ethnopharmacol. **108**, 26–30 (2006)
42. da Cunha, F.A.B., Waczuk, E.P., Duarte, A.E., Barros, L.M., Elekofehinti, O.O., Matias, E.F.F. et al.: Cytotoxic and antioxidative potentials of ethanolic extract of *Eugenia uniflora* L. (Myrtaceae) leaves on human blood cells. Biomed. Pharmacother. (Elsevier Masson SAS) **84**, 614–621 (2016)
43. Mazutti da Silva, S.M., Ferreira-Nunes, R., Amore, C.R., Martins, D.H.N., Pic-Taylor, A., Fonseca-Bazzo, Y.M. et al.: Emulsion incorporating *Eugenia dysenterica* aqueous extract entrapped in chitosan microparticles as a novel topical treatment of cutaneous infections. J. Drug Delivery Sci. Technol. (Editions de Sante) **55** (2020)
44. Chang, S.K., Alasalvar, C., Shahidi, F.: Superfruits: Phytochemicals, antioxidant efficacies, and health effects—A comprehensive review. Crit. Al Rev. Food Sci. Nutr. (Taylor and Francis Inc.) 1580–1604 (2019)
45. de Sousa, E.R.B., Camilo, Y.M.V., Vera, R.: Cagaita—*Eugenia dysenterica*. Exotic Fruits (Elsevier) 77–83 (2018)
46. da Silva, L.M.R., de Figueiredo, E.A.T., Ricardo, N.M.P.S., Vieira, I.G.P., de Figueiredo, R.W., Brasil, I.M., et al.: Quantification of bioactive compounds in pulps and by-products of tropical fruits from Brazil. Food Chemistry (Elsevier Ltd) **143**, 398–404 (2014)
47. de Carvalho, F.A.L., Lorenzo, J.M., Pateiro, M., Bermúdez, R., Purriños, L., Trindade, M.A.: Effect of guarana (Paullinia cupana) seed and pitanga (*Eugenia uniflora* L.) leaf extracts on lamb burgers with fat replacement by chia oil emulsion during shelf life storage at 2 °C. Food Res. Int. (Elsevier Ltd) **125** (2019)
48. Lorenzo, J.M., Vargas, F.C., Strozzi, I., Pateiro, M., Furtado, M.M., Sant’Ana, A.S. et al.: Influence of pitanga leaf extracts on lipid and protein oxidation of pork burger during shelf-life. Food Res. Int. (Elsevier Ltd) **114**, 47–54 (2018)

49. Meena, S., Kanthaliya, B., Joshi, A., Khan, F., Arora, J.: Biologia futura: medicinal plants-derived bioactive peptides in functional perspective—a review. *Biologia Futura*. (Akademai Kiado Rt.) 195–208 (2020)
50. Lima, T.B., Silva, O.N., Oliveira, J.T.A., Vasconcelos, I.M., Scalabrin, F.B., Rocha, T.L. et al.: Identification of *E. dysenterica* laxative peptide: A novel strategy in the treatment of chronic constipation and irritable bowel syndrome. *Peptides* **31**, 1426–1433 (2010)
51. Rial, R.C., Merlo, T.C., Michalski Santos, P.H., Dias Melo, L.F., Barbosa, R.A., de Freitas, O.N. et al.: Evaluation of oxidative stability of soybean methyl biodiesel using extract of cagaite leaves (*Eugenia dysenterica* DC.) as additive. *Renew. Energy* (Elsevier Ltd) **152**, 1079–1085 (2020)
52. Daza, L.D., Fujita, A., Fávoro-Trindade, C.S., Rodrigues-Ract, J.N., Granato, D., Genovese, M.I.: Effect of spray drying conditions on the physical properties of Cagaite (*Eugenia dysenterica* DC.) fruit extracts. *Food Bioprod. Process.* (Institution of Chemical Engineers) **97**, 20–29 (2016)
53. Iturri, M.S., Calado, C.M.B., Prentice, C.: Microparticles of *Eugenia stipitata* pulp obtained by spray-drying guided by DSC: an analysis of bioactivity and in vitro gastrointestinal digestion. *Food Chem.* (Elsevier Ltd) **334** (2021)
54. Mendes, J.F., Martins, H.H.A., Otoni, C.G., Santana, N.A., Silva, R.C.S., da Silva, A.G. et al.: Chemical composition and antibacterial activity of *Eugenia brejoensis* essential oil nanoemulsions against *Pseudomonas fluorescens*. *LWT* (Academic Press) **93**, 659–664 (2018)
55. Tessaro, L., Lourenço, R.V., Martelli-Tosi, M., do Amaral Sobral, P.J. Gelatin/chitosan based films loaded with nanocellulose from soybean straw and activated with “Pitanga” (*Eugenia uniflora* L.) leaf hydroethanolic extract in W/O/W emulsion. *Int. J. Biol. Macromol.* (Elsevier B.V.) **186**, 328–340 (2021)
56. Wang, W., Zhang, Y., Yang, Z., He, Q. Effects of incorporation with clove (*Eugenia caryophyllata*) essential oil (CEO) on overall performance of chitosan as active coating. *Int. J. Biol. Macromol.* (Elsevier B.V.) **166**, 578–586 (2021)
57. Cunha, F.A.B., Pinho, A.I., Santos, J.F.S., Sobral-Souza, C.E., Albuquerque, R.S., Matias, E.F.F. et al.: Cytoprotective effect of *Eugenia uniflora* L. against the waste contaminant mercury chloride. *Arab. J. Chem.* (Elsevier B.V.) **12**, 4197–4203 (2019)
58. Klein, E.J., Carvalho, P.I.N., Náthia-Neves, G., Vardanega, R., Meireles, M.A.A., da Silva, E.A. et al.: Techno-economic optimization of uvaia (*Eugenia pyriformis*) extraction using supercritical fluid technology. *J. Supercrit. Fluids* (Elsevier B.V.) **174**
59. Canabarro, N.I., Veggi, P.C., Vardanega, R., Mazutti, M.A., Ferreira, M. do C.: Techno-economic evaluation and mathematical modeling of supercritical CO<sub>2</sub> extraction from *Eugenia uniflora* L. leaves. *J. Appl. Res. Med. Aromatic Plants* (Elsevier GmbH) **18** (2020)
60. Barzotto, I.L.M., Santos, K.A., da Silva, E.A., Sene, A.C., da Silva, N.S., Vieira, L.: Supercritical extraction of *Eugenia involucrata* leaves: Influence of operating conditions on yield and A-tocopherol content. *J. Supercrit. Fluids* (Elsevier B.V.) **143**, 55–63 (2019)
61. Silva, M.V.S.G., Silva, S.A., Teixeira, T.L., de Oliveira, A., Morais, S.A.L., da Silva, C.V. et al.: Essential oil from leaves of *Eugenia calycina* Cambes: natural larvicidal against *Aedes aegypti*. *J. Sci. Food Agric* (John Wiley and Sons Ltd) **101**, 1202–1208 (2021)
62. Peixoto Araujo, N.M., Arruda, H.S., dos Santos, F.N., de Morais, D.R., Pereira, G.A., Pastore, G.M.: LC-MS/MS screening and identification of bioactive compounds in leaves, pulp and seed from *Eugenia calycina* Cambess. *Food Res. Int.* (Elsevier) **137**, 109556 (2020)
63. Bailão, E.F.L.C., de Oliveira, M.G., de Almeida, L.M., Amaral, V.C.S., Chen, L.C., Caramori, S.S. et al.: Food Composition Data: Edible Plants in Cerrado, pp. 179–224 (2021)
64. Soares, J.C., Rosalen, P.L., Lazarini, J.G., Massarioli, A.P., da Silva, C.F., Nani, B.D., et al.: Comprehensive characterization of bioactive phenols from new Brazilian superfruits by LC-ESI-QTOF-MS, and their ROS and RNS scavenging effects and anti-inflammatory activity. *Food Chem.* **281**, 178–188 (2019)
65. Nasri, H., Baradaran, A., Shirzad, H., Rafeian-Kopaei, M.: New concepts in nutraceuticals as alternative for pharmaceuticals [Internet]. *Int. J. Prevent. Med.* (2014). [www.ijpm.ir](http://www.ijpm.ir)

66. Silva Júnior, J.C. da, Magnani, M., Almeida da Costa, W.K., Madruga, M.S., Souza Olegário, L., da Silva Campelo Borges, G. et al. Traditional and flavored kombuchas with pitanga and umbu-cajá pulps: Chemical properties, antioxidants, and bioactive compounds. *Food Biosci.* **44**, 101380 (2021)
67. Ortiz-Basurto, R.I., Rubio-Ibarra, M.E., Ragazzo-Sanchez, J.A., Beristain, C.I., Jiménez-Fernández, M.: Microencapsulation of *Eugenia uniflora* L. juice by spray drying using fructans with different degrees of polymerisation. *Carbohydr. Polymers.* **175**, 603–609 (2017)
68. Malaman, F.S., Moraes, L.A.B., West, C., Ferreira, N.J., Oliveira, A.L.: Supercritical fluid extracts from the Brazilian cherry (*Eugenia uniflora* L.): Relationship between the extracted compounds and the characteristic flavour intensity of the fruit. *Food Chem.* **124**, 85–92 (2011)
69. Oliveira, A.L., Kamimura, E.S., Rabi, J.A.: Response surface analysis of extract yield and flavour intensity of Brazilian cherry (*Eugenia uniflora* L.) obtained by supercritical carbon dioxide extraction. *Innov. Food Sci. & Emerg. Technol.* **10**, 189–94 (2009)
70. Oliveira, M.E.S., Pantoja, L., Duarte, W.F., Collela, C.F., Valarelli, L.T., Schwan, R.F., et al.: Fruit wine produced from cagaita (*Eugenia dysenterica* DC) by both free and immobilised yeast cell fermentation. *Food Res. Int.* **44**, 2391–2400 (2011)
71. Rossini Gomes Santos, P., de Moraes Cardoso, L., de Freitas Bedetti, S., Rossi Hamacek, F., Vlândia Bandeira Moreira, A., Stampini Duarte Martino, H. et al.: Geleia de cagaita (*Eugenia dysenterica* DC.): desenvolvimento, caracterização microbiológica, sensorial, química e estudo da estabilidade.
72. Schiassi, M.C.E.V., de Souza, V.R., Lago, A.M.T., Campos, L.G., Queiroz, F.: Fruits from the Brazilian Cerrado region: Physico-chemical characterization, bioactive compounds, antioxidant activities, and sensory evaluation. *Food Chem.* **245**, 305–311 (2018)
73. Silva, C.D.M. da, Pires, C.R.F., Lima, J.P., Pereira, A.S., Silva, C.A.: Desidratação osmótica para obtenção de cagaita passa. *J. Bioenergy Food Sci.* [Internet] **2**, 226–233 (2015). <http://periodicos.ifap.edu.br/index.php/JBFS/article/view/82>
74. Daniel Daza, L., Fujita, A., Granato, D., Silvia Fávora-Trindade, C., Inés Genovese, M.: Functional properties of encapsulated Cagaita (*Eugenia dysenterica* DC.) fruit extract. *Food Biosci.* **18**, 15–21 (2017)
75. Donado-Pestana, C.M., Belchior, T., Genovese, M.I. Phenolic compounds from cagaita (*Eugenia dysenterica* DC.) fruit prevent body weight and fat mass gain induced by a high-fat, high-sucrose diet. *Food Res. Int.* **77**, 177–185. 2015
76. Donado-Pestana, C.M., dos Santos-Donado, P.R., Daza, L.D., Belchior, T., Festuccia, W.T., Genovese, M.I.: Cagaita fruit (*Eugenia dysenterica* DC.) and obesity: role of polyphenols on already established obesity. *Food Res. Int.* **103**, 40–47 (2018)
77. Araujo, R.L. de, Tomás-Barberán, F.A., Santos, R.F. dos, Martinez-Blazquez, J.A., Genovese, M.I.: Postprandial glucose-lowering effect of cagaita (*Eugenia dysenterica* DC) fruit juice in dysglycemic subjects with metabolic syndrome: An exploratory study. *Food Res. Int. Elsevier Ltd* **142** (2021)
78. Couto, R.O., Martins, F.S., Chaul, L.T., Conceição, E.C., Freitas, L.A.P., Bara, M.T.F., et al.: Spray drying of *Eugenia dysenterica* extract: effects of in-process parameters on product quality. *Rev. Bras* **23**, 115–123 (2013)
79. Peixoto Araujo, N.M., Silva, E.K., Arruda, H.S., Rodrigues de Moraes, D., Angela, A., Meireles, M., Pereira, G.A. et al.: Recovering phenolic compounds from *Eugenia calycina* Cambess employing high-intensity ultrasound treatments: A comparison among its leaves, fruit pulp, and seed as promising sources of bioactive compounds. *Sep. Purif. Technol.* **272**, 118920 (2021)
80. Bezerra, M., Araujo, A., Santos, K., Correia, R.: Caprine frozen yoghurt produced with fresh and spray dried jambolan fruit pulp (*Eugenia jambolana* Lam) and *Bifidobacterium animalis* subsp. *Lactis* BI-07. *LWT—Food Sci. Technol.* **62**, 1099–104
81. Sharma, R.J., Gupta, R.C., Singh, S., Bansal, A.K., Singh, I.P.: Stability of anthocyanins- and anthocyanidins-enriched extracts, and formulations of fruit pulp of *Eugenia jambolana* ('jamun'). *Food Chem.* **190**, 808–817 (2016)



82. Farias, D. de P., de Araújo, F.F., Neri-Numa, I.A., Dias-Audibert, F.L., Delafiori, J., Catharino, R.R. et al.: Distribution of nutrients and functional potential in fractions of *Eugenia pyriformis*: An underutilized native Brazilian fruit. *Food Res. Int.* **137**, 109522 (2020)
83. da Silva, A.P.G., Spricigo, P.C., Purgatto, E., de Alencar, S.M., Sartori, S.F., Jacomino, A.P.: Chemical composition, nutritional value and bioactive compounds in six uvaia accessions. *Food Chem.* **294**, 547–556 (2019)
84. de Paulo, F.D., de Araújo, F.F., Neri-Numa, I.A., Dias-Audibert, F.L., Delafiori, J., Catharino, R.R., et al.: Effect of in vitro digestion on the bioaccessibility and bioactivity of phenolic compounds in fractions of *Eugenia pyriformis* fruit. *Food Res. Int.* **150**, 110767 (2021)
85. de Araújo, F.F., de Paulo Farias, D., Neri-Numa, I.A., Dias-Audibert, F.L., Delafiori, J. de Souza F.G. (et al.). Chemical characterization of *Eugenia stipitata*: A native fruit from the Amazon rich in nutrients and source of bioactive compounds. *Food Res. Int.* (Elsevier Ltd) **139** (2021)
86. Reyes-Álvarez, C.A., Lanari, M.C. Storage stability of freeze-dried arazá (*Eugenia stipitata* Mc Vaugh) powders. Implications of carrier type and glass transition. *LWT* **118**, 108842 (2020)
87. Teixeira, L. de L., Bertoldi, F.C., Lajolo, F.M., Hassimotto, N.M.: Identification of Ellagitannins and Flavonoids from *Eugenia brasiliensis* Lam. (Grumixama) by HPLC-ESI-MS/MS. *J. Agric. Food Chem* **63**, 5417–5427 (2015)
88. Teixeira L. de L., Dörr, F., Dias, C.T.S., Pinto, E., Lajolo, F.M., Villas-Bôas, S.G. et al.: Human urine metabolomic signature after ingestion of polyphenol-rich juice of purple grumixama (*Eugenia brasiliensis* Lam.). *Food Res. Int.* **120**, 544–552 (2019)

# How Basic Programming Knowledge can Help the Drug Discovery Process



**Leonardo Bruno Federico, Mariana Pegrucci Barcelos, Suzane Quintana Gomes, Isaque Isaque Antonio Galindo Francischini, Anderson Luiz Pena da Costa, Lorane Izabel da Silva Hage-Melim, and Carlos Henrique Tomich de Paula da Silva**

**Abstract** In-silico drug design is a well-established and structured process, with several methodologies and software available to researchers in this field. However, depending on the study and the work dynamics of the research group, there may be demands that require more than one software. These may come from different companies, not designed to work together. Still, there may be the need to use such software different from the one planned, for example, using software developed for studies with few molecules in research with extensive databases. In these cases, adapting to these dynamics may cause excess work or excessive consumption of time. An efficient way to deal with these obstacles, which take up unnecessary time in research, can be solved by creating computational scripts. At first sight, the development of skills in programming languages may discourage the drug discovery researcher. On the other hand, basic knowledge of these skills can greatly value computational drug discovery groups. Therefore, this chapter is intended to encourage researchers in this field to develop skills in programming languages. We will also show practical examples of how the basics can help and reduce the time spent on repetitive tasks using Python, recognized as a simple and easy-to-learn language.

---

L. B. Federico (✉)

Computational Laboratory of Pharmaceutical Chemistry, School of Pharmaceutical Sciences of Ribeirão Preto, University of São Paulo, Av. do Café, s/n, Ribeirão Preto, São Paulo 14040-903, Brazil

e-mail: [lbfederico@usp.br](mailto:lbfederico@usp.br)

M. P. Barcelos · I. I. A. G. Francischini · C. H. T. de Paula da Silva

School of Pharmaceutical Sciences of Ribeirão Preto, University of São Paulo, Av. do Café, s/n, Ribeirão Preto, São Paulo 14040-903, Brazil

S. Q. Gomes · C. H. T. de Paula da Silva

Departamento de Química, Faculdade de Filosofia, Ciências e Letras de Ribeirão Preto (FFCLRP), University of São Paulo, Av. Bandeirantes, 3900, Ribeirão Preto, São Paulo 14040-903, Brazil

A. L. P. da Costa · L. I. da S. Hage-Melim

Laboratory of Pharmaceutical and Medicinal Chemistry (PharMedChem), Federal University of Amapá, Rodovia Juscelino Kubitschek, km 02, Macapá, Amapá 68903-419, Brazil

## 1 Introduction

The search for new drug candidates with satisfactory pharmacokinetic and pharmacodynamic profiles, biological activity, low side effects, and high market value has been mobilizing the drug Discovery area over the last three decades [1–3]. The advancement of computer science and the development of more powerful machines has allowed the creation of less costly and faster approaches in the process of discovering new drugs, such as virtual screenings, which start from databases with a high number of compounds in which filters are applied to obtain potential hits at the end of the process [4–6].

Initially, along with the technological advancements in the areas that support computational chemistry, there was also a great increase in the size of the databases of compounds to be treated in the projects for the development of new bioactive molecules [7]. On the other hand, with the growing number of databases containing millions of compounds, there was the need to develop new computational approaches that allowed filtering as many compounds as possible, to select only really promising molecules in *in silico* environments [8, 9]. Since then, different methodologies were created, for example, the use of pharmacokinetic and toxicity prediction software, which at the time were able to successfully filter larger databases [10, 11].

However, with the exponential increase in the size of the databases of chemical compounds used in virtual screenings, the use of non-automated software has become unfeasible, since the time required becomes huge, which makes several projects impracticable [12, 13]. When it was realized that automating a series of tasks would reduce the time spent on projects and increase their viability, the inclusion of programming languages in drug discovery projects began. As a result, programming languages such as Python became extremely used and widespread in research projects for new hits [14, 15].

Terms such as programming language, Python, R, among others, can scare experienced researchers and even dispel researchers who are joining Drug Discovery projects *in silico*, as they carry a stigma of very high complexity [16, 17]. However, these languages are extremely useful in the development of Drug Discovery projects, not limiting their use only to the area of medicinal chemistry, but being able to be applied in several areas such as molecular biology, genetics, pharmacology, among others [18, 19].

The continuous powerful machines development also contributed to the application of advanced techniques that use programming languages in Drug Discovery projects to make them more automated, such as the use of Machine Learning (ML) to automate the treatment of large databases compound data from a small set of molecules with known activity [20, 21].

It is also important to mention that the basic knowledge in the programming language can help the researcher to automate several repetitive tasks from the development of low complexity scripts that allow the reduction of the time spent in routine tasks, such as the analysis of predicted pharmacokinetic and toxicological data for a given database [22, 23].

Since the Python language is considered an easy-to-learn language, with its main characteristic to be multiparadigm, it allows the development of projects in which structured, object-oriented and imperative programming can be used. Thus, this use together helps the simplest solutions among the programming paradigms for different problems, in addition to having a dynamic typing, which allows checking the validity of functions, expressions, variables, or modules present in the programming [24, 25].

The Python programming language was developed by Guido van Russom at Centrum Wiskunde & Informatica in the 1980s and was released to the public in 1991, whose website (<https://www.python.org/>) hosts information about the characteristics of Python language applied to programming and its integration with different systems [26]. The programming software that is available for all current operating systems, as well as other platforms, provides manuals for different levels of knowledge and performance, from beginners to advanced. It is still possible to find on the website a contact channel with the world community that uses this programming language, reports on events related to Python, and a link to several successful projects in different areas [27].

Currently, Python is one of the main programming languages used due to its great versatility. Users have many possibilities of application, such as the development of websites for the web, elaboration of scripts (repetitive tasks performed daily) that can be automated, optimizing routine activities, including remotely; development of computer programs, intelligence technologies for solving specific problems based on the improvement of algorithms (ML), game development, data science, and big data, among others [28–30].

It is worth noting that Python is a programming language widely used by many professionals, with numerous forums and function libraries that are useful for improving existing programs, as well as making it possible to create programs for the most diverse purposes, having as limits only user creativity [31].

Thus, given the versatility that the Python programming language has in several areas, including pharmaceutical research, in this chapter the general aspects of the Python programming language and its application in automation processes will be contextualized, followed by some examples of how Python can be applied to make several steps of the research and discovery of new drugs more agile and faster.

For researchers who are interested in learning and using programming in their projects, even at a basic level, Al Sweigart's book "Automate the Boring Stuff with Python" shows, in a didactic and intuitive way, how to use the advent of the Python language to solve small tasks of lesser complexity and that take a considerable part of the time in Drug Discovery projects from the automation of these processes, thus helping to increase the speed of execution of the projects [32].

Amid the advancement of the use of programming in several areas of research, and along with the massive increase of users of several programming languages around the world, the GitHub platform appears. This platform is a source code and file hosting repository with version control using Git [33]. In this way, users and software developer around the world can contribute to private and open source projects, which allows a greater ability to solve complex codes and also contributes

to the advancement of the use of programming in the area of discovery of new drugs [34].

Finally, this chapter is dedicated to encouraging and demonstrating how having basic knowledge of any programming language can be of great value in Drug Discovery laboratories. The Python language was used as an example due to its versatility and ease of learning, but the great topic discussed here can be extrapolated to any language.

## 2 Hosting Scripts and Software

There are many tools available within the computational world that can be used in the discovery of *in silico* drugs, and the use of some computational skills can make easy the life of a researcher in this area. In this part, we will discuss some tools and computer languages that are intended to help in the discovery of new drugs.

Between the 1980s and 1990s, a revolution in software development began: the open-source software movement [35]. Open-Source Software (OSS) is computer software that has an open-source license allowing the person who acquires it to study, modify, and distribute the software without gain and for any purpose [36].

OSS communities are referred to as meritocracies, since “code is the king” and any decision is based solely on technical merit [37], however, previous studies suggest that there is a complex social structure in open-source contribution [38, 39]. This movement would generate an impact on the computing world, leading to the eventual creation of GitHub in 2008.

GitHub is a collaborative code hosting platform built on top of the version control system, Git. A version system is a system that records changes made to files over time [40]. This site is a social network for code developers as it allows interaction between its users so that they contribute to each other’s projects and also users have profiles that can be filled with identifying information in addition to containing their most recent activities [41].

In recent years, GitHub has become the world’s largest code host [42]. As many of the projects hosted on the site are public, anyone can view the activities carried out in these projects [41]. Studies involving GitHub to date focus on source code language construction [40], effects of branch and pull-based software development [43], associations between crowdsourcing knowledge and development [40], among others. Even today, GitHub’s wealth of data remains underexplored in terms of scholarly publications [42].

As stated earlier, GitHub has several codes on its website and each code is in a programming language chosen by the developer. A programming language is a method of implementing source code that can be turned into a computer software or will provide instructions for processing a computer [44, 45]. For this code to be written there are a series of syntactic and semantic rules.

The main objective for using a programming language is for developers to obtain greater productivity, be able to more easily express their intentions, and allow them

to write more organized and faster software [46]. Another interesting factor is the independence that languages allow about computers since the software is written in a programming language is translated into the computer's machine code instead of being executed directly. This independence was one of the goals in one of the first programming languages created, Fortran [47].

Several programming languages are used in the Drug Discovery area, such as C/C++ for quantum mechanics calculations [48], Fortran 90 or Fortran 77 in some old software packages [49], R language for statistical calculations, and Python that is gaining space due to its ease [50]. Python is a programming language created in 1991 and classified as a high-level language, that is, a programming language with a high level of abstraction, farther from machine code and closer to human language. The great advantage in languages classified in this way is that it is not necessary to know the characteristics of the processor on which it will act, and they are not directly related to the computer's architecture [51].

In addition to being a high-level language, Python is scripted and multi-paradigm, object-oriented, structured, and imperative. Its typing is dynamic, allowing easy code reading and requiring few lines when compared to other programming languages [30]. When Python was designed, the inventor intended his language to address the importance of the programmer. Its design was based on the ABC language, having C-derived syntax, list comprehension, anonymous functions and Haskell anonymous functions [51].

Due to all these characteristics, this programming language is widely used in creating Common Gateway Interface (CGI) in web pages, word processing, and also scientific data. A community formed by scientists, engineers, and researchers who use and promote Python as a language to be used in scientific research [30]. Within the Drug Discovery area, it is possible to find Python working in the creation of some software and packages such as ChemoPy [50], MUBD-DecoyMaker 2.0 [52], PyDPI [53], and TeachOpenCAAD [54].

The freely available open-source ChemoPy package was developed to calculate the most commonly used structural and physicochemical characteristics within drug discovery processes [55]. It allows the user an easy and transparent computation aimed at a comprehensive implementation of these descriptors in a unified way [50]. Another package that follows the same route of calculating structural and physicochemical descriptors is PyDPI, with the difference that it also calculates the interactions between the molecule and the studied target [53].

Due to the large amount of data generated that needs to be analyzed during virtual screening (VS) studies, a small-scale SV based on a benchmarking set [56] has been used. The benchmarking set is a dataset of active and inactive compounds against a specific target and its quality is crucial for making a decision. MUBD-DecoyMaker is an algorithm created to generate unbiased benchmarking datasets for virtual drug screening [52].

Finally, there is also available a Teaching Platform for computer-aided drug design called TeachOpenCADD. This platform is publicly available on GitHub and was developed using Python packages and open-source data [54]. One of the central themes addressed within this platform is Jupyter notebooks.

Jupyter notebooks are open-source browser-based tools that function as virtual notebooks, allowing a workflow with data and visualizations by the operator [56]. They were created to facilitate the documentation, sharing, and reproduction of data analyses. The system originated with the Python language [57] and today supports other languages such as R, C, and Javascript [58]. Due to this capability, they are tools widely used for literate interactive programming [59], one of the available strategies for problems that present a large amount of scientific data [60]. In Drug Discovery, Jupyter Notebooks can assist in the analysis of large sets of molecular structures and molecular dynamics simulations as they integrate interactive calculations and visualizations allowing exploratory analysis of molecular data [60].

A final tool that can be used in silico studies is KNIME (Konstanz Information Miner), a free modular and open-source platform that allows the visual creation of pipelines with the selective execution of analysis steps and data inspection through selective views [61]. This environment condenses active bioinformatics and cheminformatics community [62] and has been used since 2006 in pharmaceutical research [63].

The main objective for which KNIME was created was to perform modular, scalable, and open data processing, in addition to allowing easy integration with different modules. The intention was for it to be a platform for research, collaboration, and integration between various data analysis projects [64]. Therefore, it is possible to notice that several computer programming tools can be used in the area of drug development and that knowledge about basic programming can help throughout this trajectory.

### **3 Process Automation in the Discovery and Planning of New Drugs Through Python Programming Language**

The Python programming language was developed by Guido van Rossum 30 years ago, whose philosophy is a design that can be developed with readable codes, and that allows the language to build programs with an object-oriented approach in a logical and clear, with satisfactory employability for conducting small or large-scale projects [26].

It is also considered a highly versatile language because it can be used in different operating systems and has a large number of users, which favors the exchange of experiences and problem solving through forums or function libraries that have codes ready to be modified as required. The needs of the project meet the needs of numerous segments, including pharmaceutical research, as will be explained later [31].

Therefore, for programs to be developed in Python, as well as other programming languages, some requirements are necessary, such as cognitive abilities related to logic and operability in programming, contemplating (1) the organization of ideas for the orderly elaboration of tasks, followed by (2) the development of algorithms, which are actions that are initiated and executed under conditional conditions defined

by the programmer until the desired result is reached (3) the ability to data abstraction, that is, hide the complexity of the codes from the user interface and of working algorithms to simplify the use, (4) knowledge about the data structures, and (5) the terms that designate such structures, as well as syntax and cohesion of the language in the development of programs [65].

In this context, the Python language has a considerable range of syntactic structures, libraries of functions in an interactive programming environment, in which the scripts that will be executed by the programs are written in lines called REPL (Read–Evaluate–Print Loop), which allow the programmer to write their code and immediately evaluate their results. Every program is made up of basic elements such as expressions, with their appropriate variables, operators, call elements, functions, and organization structures [66].

Expressions are commands written in code, which analyzes and determine decision making based on conditionals defined by the programmer, in which the information (*values*) to be analyzed and processed by the program will be organized into functions, which are tools that receive *inputs*, that is, *values* that can be manipulated to generate *outputs* as set by expressions [66].

These *values* of the program can be of type *integer* or *float*, which, respectively, designate the representation of integer values and decimal values, which are stored in variables that allow the location of the specific information contained in each *value* through symbolic association by names that can be evoked by programmers or users [66].

Therefore, considering that the entire program needs to resort to several *values* so that the expressions operate based on conditionals defined by the program, data organization structures are necessary, both for the manipulation of static data, which do not change, as well as dynamic data, which change over time, such as *lists*, which are structures that store multiple variables that can be modified as defined by the user, and *tuples*, which are structures where the set of *values* contained in a given *tuple* cannot be changed [66].

In this sense, other forms of data structuring are *strings*, which organize *values* sequentially, and *dictionaries*, which can store *integer* or *floating values* in isolation, or even store larger structures such as lists, *strings*, or *tuples* [66].

In summary, once the expressions and their conditionals are defined to be analyzed by functions according to the *values* existing in the program code, it becomes operational to perform real tasks. The sophistication of the program is evaluated by its simplicity concerning the organization of *values* in *lists*, *strings*, *tuples*, or *dictionaries*, which help in the manipulation and processing of the large number of information of a numerical or textual nature, which can be used in different areas, such as, in the automation of tasks, in which the user determines in the program what, when and how the computer should perform tasks such as extracting information present in texts inserted in the program, downloading material of interest to the user directly from the internet, organizing files, filling out spreadsheets, creating and reading of texts in files of different formats, editing images, scheduling tasks, sending emails, SMS messages, among other tasks [66].



About abstraction in the programming process, pattern matching with regular expressions represents a method that allows access to a specific *string*, or several, employing regular expressions that favor textual processing to carry out string operations search or replacement. In these operations, the elements can be restricted, as in the case of access control by passwords, where *input* validation is of vital importance since the *values* entered by the user cannot be different from those existing in the program codes; whereas in other situations, such as searches, the program will need to be robust enough to differentiate an *input* that does not necessarily have to match the program's *value* [66].

The *input* validation is important in the development of programs of the most variable natures to avoid *bugs* and security flaws that can make the program vulnerable. Therefore, the programmer must know the data structures, as well as the terms that designate them more so that he is successful in the elaboration of a program capable of carrying out the tasks that are requested of them with precision and promptly [66].

It is worth noting that in the process of developing a program it is common to found errors related to validation of *inputs*, as well as syntax errors in the codes, and since the Python language presents its codes arranged in lines with REPL, the detection of *bugs* can be done more accurately. However, in certain cases, fixing and removing *bugs* can be a challenging task that requires tools that optimize these tasks, such as *assertions*, which are predicate points in programs that always evaluate the veracity of assumptions at certain points of code execution; *exceptions*, which are entries considered wrong that prevent the progression of program execution; *logging*, which is a tool that has the purpose of keeping a record of all data inputs, processes, data outputs, as well as the final results of the program; and *debuggers*, which are programs used to find inconsistencies in programming code [66].

Consequently, due to the characteristics, the Python programming language and its interactive environment make its use practical and intuitive, which can be applied to the development of programs of different complexities, with easy application structures and support for fault identification and its subsequent removal of program codes [66].

## 4 Python Language Application in Automation Processes

The production of files in programs requires organization in directories that allow the program to locate them and keep any changes implemented in them saved, making such files available on the computer both for reading and editing. Although it is considered a simple process, when the user needs to deal with a large amount of information, process automation represents a means by which repetitive tasks can be performed accurately and quickly if specific programs are created [66].

In this context, task automation requires, in addition to a considerable basic knowledge of the programming language, the additional use of modules that allow the translation and obtainment of *values* in files of different formats such as Microsoft® Excel documents, Microsoft® Word documents, Google Sheets, pdf, which can

respectively be automated to perform many repetitive tasks that consume considerable time and become error-prone when a large number of data or files have to be manipulated [66].

Among the tasks performed in software that can be automated, we can mention: the creation and editing of text files or spreadsheets, copying and pasting from one file to another, organization of files in directories, searches, and online tasks (such as filling and sending forms and reports on a periodic or scheduled basis), manipulating images, sending text messages and emails for various purposes. Emphasizing that each module has its advantages and limitations in the process of implementing software information in programming codes [66].

For example, Microsoft® Excel [67] is a software used to manage spreadsheets, which can be automated with the *openpyxl* (<https://openpyxl.readthedocs.io/en/stable/>) module of Python. However, in addition to excel, different alternatives for creating and editing spreadsheets such as LibreOffice Cal [68] and OpenOffice Calc [69] may be preferred by certain users since they are free. This fact can represent a challenge for automation in Python language in conjunction with the *openpyxl* module in obtaining data in the correct format when sharing or processing the same set of data in different software. It is worth noting that in this task, loading spreadsheets directly into Python enables the interconversion and processing of data from different software automatically, demonstrating the versatility of the Python programming language against different operating systems and programming languages [66].

Google Sheets (<https://workspace.google.com/intl/pt-BR/products/sheets/>) represents a strong competitor as to the Excel program and other spreadsheet editor programs, mainly because it is a free web application, available to any user with a Google or Gmail account, which has its own API (Application Programming Interface) and allows the creation of spreadsheets with online editing, making it possible to access such spreadsheets on any computer connected to the internet. The automation of tasks in Google Sheets can be performed using the Python programming language in association with the *EZSheets* (<https://pypi.org/project/EZSheets/>) module, making it possible to create, read, download, and change spreadsheets automatically. However, there are some limitations regarding Google Sheets processing time, such as its application that requires a web request to execute commands on the data, in addition to having a limited frequency of modifications that can be applied by the programmer or user [66].

About text files in pdf and word format, they present greater complexities regarding color, size, and font style, in addition to layout organization, which make it difficult to use the *Python-doc-x* package (<https://python-docx.readthedocs.io/en/latest/>) and *pyPDF2* (<https://pypi.org/project/PyPDF2/>) modules (respectively used in Microsoft® Word and Adobe pdf), which can generate files that are difficult to read [66].

Regarding task automation in web browsers, many features like a *web browser* in Python, the *request* (<https://docs.python-requests.org/en/latest/>) element, and *beautifulsoup4* (BS4) (<https://www.crummy.com/software/BeautifulSoup/bs4/doc/>) which supports scraping information from web pages can help to automate specific tasks. However, complete automation of web-based tasks can be accomplished with the

*selenium* module, which requires considerable skills to be used in programming [66].

Thus, it is important to point out that the complexity of programming codes for the automation of many of the tasks described so far can be a challenge for the programmer. However, this challenge can be overcome by organizing the codes in a text-readable format that makes viewing and analyzing the codes easier in text editors such as Mu (<https://codewith.mu/>), or in CSV (<https://docs.python.org/3/library/csv.html>) or JSON modules (<https://docs.python.org/3/library/json.html>), which are specific to processing files CSV (Comma-Separated Values), which allow saving and retrieving versions of the same source code that can be edited and further improved by the programmer; and JSON (JavaScript Object Notation), which are files that make codes interconvertible between a version that is easier for humans to understand and another that is easier for computers to understand. Emphasizing that such features do not reduce code complexity but make it more favorable to its analysis and error detection, which can be removed more easily, without the need to redo a code from scratch [66].

When the programmer knows how to write code with data organization structures, its own syntax and knows how to use different modules and *debugging* resources for code implementation, the breadth of tasks that become capable of being automated also expands [66].

Communication by text messages via e-mail can also be automated through programs capable of processing SMTP (Simple Mail Transfer Protocol) and/or IMAP (Internet Message Access Protocol), which together with tools such as the *pyzmail* (<https://pypi.org/project/pyzmail/>) module can be used to automate sending and retrieving emails respectively; and communication by SMS messages can also be automated by Python using services such as *Twilio* (<https://www.twilio.com/pt-br/docs>) that offer modules that allow sending SMS text messages via the internet [66].

In addition to automation processes involving specific modules to edit spreadsheets or download files, the initiation of a program or application is also possible in Python language, allowing the programmer to develop programs that perform different tasks involving autonomous control of the keyboard and mouse of the computer through a technique called GUI (Graphical User Interface Automation). This technique allows tasks involving numerous mouse clicks and keyboard typing to be performed without user monitoring, giving him time to work on other tasks that require human analysis [66].

Among the modules available for developing GUI automation is *pyautogui* (<https://pyautogui.readthedocs.io/en/latest/>), which allows the computer to interact with installed applications through mouse and keyboard control. However, as all other modules presented, *pyautogui* also has its limitations, such as, for example, if the program is not instructed where to click precisely due to lack of instructions, the program will not be able to execute its scripts, therefore, the user must ensure that the location of what must be clicked or typed is correctly informed to the program. In this sense, one of the ways to avoid this type of problem is by determining the

coordinates on the screen through the analysis of a screenshot, which will precisely direct where the program should click [66].

In this way, the image manipulation process can also be automated by the Python language when the programmer is aware of the intrinsic aspects of the language, has skills in using Python. *Pillow* module (<https://pillow.readthedocs.io/en/stable/index.html>) and is proficient in the cartesian location of *pixels* in images, making it possible to edit image contents, resizing, cutting, rotating, copying and pasting, transposing image elements, as well as saving them using programs that automate software such as PowerPoint, Microsoft paint, paintbrush, or adobe photoshop [66].

## 5 The Python Programming Language Applied to Drug Research and Drug Discovery

At this point, after presenting the basic aspects of the Python programming language, some works will be exposed to demonstrate the applicability of Python in the research and development process of new drugs, mainly *in silico* methods, which are constituted by a large variety of computer-simulated tests aimed at predicting the pharmacological properties of molecules with the potential to become new therapeutic agents [70, 71].

For the computational methods in the research of new drugs to be reliable, it is important to structure a workflow with consistent methodologies, which preferably are validated by the execution and interpretation of the results by different researchers to ensure the reproducibility of the experiments *in silico*. Results can also be validated through the same experiments being performed in more than one program with their results being compared or validated directly in *in vitro* or *in vivo* studies [72].

Thus, due to the large number of biochemical, physical–chemical, and quantum data that must be analyzed in the process of screening molecules for later validation at more complex levels of biological organization (cell/tissue/organism), the Python programming language becomes a tool of great value for organizing data and programming algorithms that facilitate the decision-making process, either through machine learning or through the automation of tasks that consume considerable time in their execution, allowing researchers to focus on other stages of the research process, while programs run autonomously what can be automated [72].

The use of the Python programming language can be exemplified in the virtual library ChEMBL (<https://www.ebi.ac.uk/chembl/>), in which structural data and the structure–activity relationship data of numerous molecules are stored and shared among researchers around the world, Python is used to (1) enable the distribution of incompatible data from different databases, which are translated and made compatible through Python; (2) performing virtual operations necessary for structure–activity predictions without the need to download and install large software and/or high financial cost; (3) conducting complex analyzes for the selection of

prototypes or conducting advanced applications, (4) enabling the selection of molecular targets, whose structures have been elucidated, and (5) performing analysis of data from different sources (including the literature, allowing the user to obtaining images in different formats (SDF, SMILES, InChIs) as well as experimental results that provide greater details for the methodological planning of computational studies in drug research and drug development [73].

Python is an open-access programming language that has a large number of programming packages that can be modified and used to produce new tools useful in drug planning and development. For example, *ChemoPy* (<https://github.com/ifyounge/Chemopy>) is a package developed in Python, which allows analysis of 19 QSAR/SAR descriptors, in addition to having 7 molecular fingerprint systems, which can be used to analyze molecular structure files available in four databases, the KEGG (<https://www.genome.jp/kegg/pathway.html>), PubChem (<https://pubmed.ncbi.nlm.nih.gov/>), DrugBank (<https://go.drugbank.com/>), and CAS (<https://www.cas.org/support/documentation/cas-databases>) through ID codes; and the developers point to the possibility of implementing improvements in the program's algorithms [50].

In this context, studies have shown that the use of the Python programming language in the automation applied to the research of new drugs can speed up the process of selection and in silico testing, making it faster and with fewer errors.

The use of the Python language in the Linux environment together with packages such as *panda* and others, helped the researchers to obtain 30 molecules (among billions existing in the PubChem database) that showed satisfactory results in the inhibition of the methyltransferase enzyme of the flaviviruses of Dengue and West Nile in QSAR and molecular docking predictive tests [74].

In another research work, they obtained 1355 compounds in an automated way from the PubChem database, comparing them structurally with other 111 compounds with inhibitory activity on the SARS-CoV-2 protease, reaching a selection of 50 compounds with good performance in in silico tests. Subsequently, the 3 compounds that presented the best results were analyzed employing a molecular dynamics assay, emphasizing that all stages of the research (except the molecular dynamics assay) were conducted in an automated way through algorithms developed to make decisions based on QSAR parameters, Lipinski's rules [75], and thermodynamic parameters in ligand anchoring assays [76].

The Python programming language is not a new resource, but it is very versatile and adaptable to different projects, whose functionality depends on the programmer's creativity in analyzing processes and systematizing solutions to be executed by algorithms defined by their technical competence in the syntax and structuring of the elements of the programming language. Based on this, this chapter introduced the reader to generalities about the main features of Python, its data structures, and programming capabilities for the execution of repetitive tasks that can be automated in association with specific modules that allow the computer to understand and execute appropriate scripts for carrying out specific tasks [77].

In addition, examples of how Python can be used in the discovery of new drugs, and how repetitive steps such as searching and extracting online data, organizing

data in spreadsheets, and making decisions based on algorithms, can be automated and streamlined the drug selection process was presented. Demonstrating that programming in Python is a tool of great potential in pharmaceutical research [66].

In the following sections, examples of programs developed by the authors will be presented in an instructive way for the development of codes and the use of modules used in the automation of tasks performed in pharmaceutical research.

## 6 The Use of Basic Concepts in Python for the Development of Scripts in Drug Discovery: A Practical Approach

Currently, there is a growing interest, from the pharmaceutical industry and research groups that work with drug development, for researchers who, in addition to mastering Structure and Ligand-Based Drug Discovery techniques, know some programming language. The language required is usually Python, but not exclusively. At first glance, this demand may seem wrong since much of the work routine of these professionals is applied in commercial software, however, knowledge in some programming languages can bring benefits to this work routine.

Although most Drug Discovery software is developed aiming to use large amounts of data, with most having a graphical interface, this amount of information can slow down the work and require high-performance computers. The use of these software by command lines in the terminals of the operating system can improve this performance, but sometimes, depending on the study, due to the number of ligands, databases, proteins, among others to be used, this task will continue to demand much time with repetitive tasks. Even so, some software, such as Gromacs [78], designed for molecular dynamics (MD) studies, have several steps to be performed manually, editing text files, or even integrating software from the same or different companies.

Repetitive tasks commonly performed in computer drug development laboratories can be automated using some basic and simple Python concepts. By obtaining knowledge of variables, lists, tuples and dictionaries, logical operators, loops of repetition, conditions, functions, and manipulation of text files, it is now possible to develop scripts for the automation of some tasks.

There are packages for Python aimed at computational Drug Discovery studies, such as Scikit-learn (<https://scikit-learn.org/stable/>) widely used in Machine Learning studies and the RDKit Open-Source Cheminformatics Software (<https://www.rdkit.org/>), an open-source tool with links to Python, which has several functionalities aimed at manipulating chemical structures.

In addition to the packages available for the manipulation of data useful to the drug development process, several companies make available with their licenses an application programming interface (API) with which it is possible to use the features of this software directly in an algorithm developed in Python. With the APIs, it is

possible to use specific functionalities present in the software, and thus, integrate actions from more than one software.

## 6.1 Practical Examples

For a better understanding of how basic concepts in Python can help the drug development process, we will present some Scripts developed to automate and reduce the time spent on simple functions. The scripts were written in Python and are available at [www.github.com/lbfederico](http://www.github.com/lbfederico).

Several users used to the ease and convenience of graphical interfaces in Drug Discovery software report difficulties in starting studies with software that do not offer this option and still require the manipulation of text files, such as Gromacs, one of the most renowned for molecular dynamics studies.

## 6.2 Automating Some Tasks of Gromacs

Gromacs does not have a graphical interface, and some of the steps for developing the software are carried out manually. Generally, MD software, when used for the simulation of ligand-receptor complexes, is carried out in a few complexes, due to the high computational demand required, but, depending on the study, it may be necessary to carry out the same in dozens of complexes. In this last case, the need for a simple file manipulation can further slowdown the study.

Thinking about making this data manipulation easier, we developed 3 simple scripts which automate the initial steps necessary to use Gromacs for MD studies in complexes.

The first script developed (**LigPrep.py**) aims to automate the stages of preparation of the ligands. **LigPrep.py** identifies the files present in the execution directory with the extension *.mol2*, corrects the bond orders (by executing the *sort\_mol2\_bonds.pl* script), sends the corrected ligand to the CGenFF server, which returns the *.srt* topology file. The *.srt* topology file is converted (by running the *cgenff\_charmm2gmx.py* script) to *.pdb*, which is used by *gmx editconf* to generate the *.gro* file for the ligands. Finally, all results are organized in specific directories for each ligand.

The second script was developed to automate the preparation of ligand-receptor complexes. In each directory containing the ligand and receptor topology (*.gro*) files and the system topology file (*topol.top*), the **complex\_topol.py** script merges the protein and ligand topology files into a new file named *complex.gro*, keeping the receiver file vector box and correcting the number of atoms in the file. The **complex\_topol.py** also accesses the *topol.top* file to include the ligand parameters (*.itp* and *.prm*) and adjust the total number of molecules in [molecules].

To prepare the ligand and receptor files to be used for gas phase (vacuum) calculations, the simple **remove\_SOL.py** script was created. This script accesses the

*complex.gro* file and remove all solvent molecules creating the *prot\_ions.gro* file, a file containing only information on the topology of the receptor, ligand, and ions.

We also created the **topol\_POSRES.py** script, which includes the information of the ligands restrictions in the system topology (*.top*) file and the **Analytix\_GMX.py** script, which enters the directories above where it is allocated and executes the commands to trajectory adjustment, rotational and translational adjustment of the trajectory, and graphics generation of RMSD (complex and ligand), RMSF, SASA and Radius of Gyrate. The same script can be used for the gas phase complexes just for trajectory correction, and rotational and translational adjustment.

### 6.3 Automation and Integration of OpenEye Company Software

One of the main steps of virtual screening is aimed at preparing the databases used in these studies [9]. Virtual screening studies generally use varied bases, aiming to diversify the number of compounds present in them. Therefore, it may be that for a given study new bases must be prepared. This process can be performed in a simple way using one to three software from the company OpenEye, Filter, Flipper, and Omega [79].

Such software is simply executed via command lines. The Flipper software is integrated with Omega, but for the preparation of, for example, ten databases, 20 command lines must be written, and it will still be necessary to be attentive to the end of a database so that the next one can be launched. Due to this fact, we developed a simple script that lists all the databases contained in a specific directory and sequentially executes Filter, Flipper, and Omega for each database.

With the same intention described for the preparation of the bases, we also developed a script that automates and integrates the software ROCS and EON [80, 81]. Such pipeline was developed to integrate these two softwares and use them in multiple databases, without the need to write several command lines, nor the need to wait for a calculation to finish before starting the next one.

### 6.4 ROC/AUC Validations for ROCS and GOLD Software

Validation studies in virtual screening campaigns are fundamental steps to ensure the quality of the screenings to be carried out. We developed a script capable of optimizing the steps that determine the quality of the virtual screening studies performed by the ROCS and GOLD software [82]. In the future we will expand the same study to other different software.

The algorithm developed for the validation process using the ROC/AUC curve starts by converting the input molecules into *.smi*, a format required by the DUD-E



website [83] for the generation of decoys, using the oBabel software [84]. After converting the molecules, the user sent them to the DUD-E server, which returns the generated decoys via e-mail. The script accesses the email, gets the file sent in *tar.gz*, unzips it, and converts the decoys to *.mol2* by oBabel.

Aiming at a correct conversion from 2 to 3D format, we used the Omega software to generate only one conformer. After the preparation of the active ligands and decoys, they are sent to the ROCS and GOLD software. In possession of the results, they are manipulated using the Pandas (<https://pandas.pydata.org/>) and NumPy (<https://numpy.org/>) packages and prepared for the correct use of the tools of the SciKit-Learning package (<https://scikit-learn.org/stable/>) and data generation that will be plotted by the Matplotlib package (<https://matplotlib.org/>).

## 7 Conclusion

The process of drug development through computational tools is a process that generally demands time and is also peculiar to each research group, which is dependent on the needs and skills of researchers. Some of these processes may include more than one computer software and often from different companies. As much as this software is developed aiming and allowing this integration, the manipulation of a large amount of data can make this process slow.

Some simple and basic skills in programming can help to automate repetitive tasks, and thus, optimize the time spent on exhausting tasks usually performed in computational laboratories for drug development. Therefore, the basic knowledge of the Python programming language becomes a great help to researchers in the area. This language, developed to be simple writing and learning language, has become very popular, being widely used by drug developers according to a large number of applications available in the GitHub repository.

We hope that with our case reports, the readers of this chapter will feel encouraged to look for our GitHub page, visualize and use our applications, as well as start studying Python.

## References

1. Atanasov, A.G. et al.: Natural products in drug discovery: advances and opportunities. *Nat. Rev. Drug Discov.* **2014** (2021)
2. Koshland, D.E.: Application of a theory of enzyme specificity to protein synthesis. *Proc. Natl. Acad. Sci.* **44**, 98–104 (1958)
3. Holenz, J., Stoy, P.: Advances in lead generation. *Bioorg. Med. Chem. Lett.* (2019). <https://doi.org/10.1016/j.bmcl.2018.12.001>
4. Surabhi, S., Singh, B.: COMPUTER aided drug design: an overview. *J. Drug Deliv. Ther.* (2018). <https://doi.org/10.22270/jddt.v8i5.1894>

5. Baig, M.H., Ahmad, K., Rabbani, G., Danishuddin, M., Choi, I.: Computer aided drug design and its application to the development of potential drugs for neurodegenerative disorders. *Curr. Neuropharmacol.* **16**, 740–748 (2017)
6. Prieto-Martínez, F.D., López-López, E., Eurídice Juárez-Mercado, K., Medina-Franco, J.L.: Computational drug design methods—current and future perspectives. In: *In Silico Drug Design* (2019). <https://doi.org/10.1016/b978-0-12-816125-8.00002-x>
7. Banegas-Luna, A.J., Cerón-Carrasco, J.P., Pérez-Sánchez, H.: A review of ligand-based virtual screening web tools and screening algorithms in large molecular databases in the age of big data. *Future Med. Chem.* (2018). <https://doi.org/10.4155/fmc-2018-0076>
8. Gorgulla, C., et al.: An open-source drug discovery platform enables ultra-large virtual screens. *Nature* (2020). <https://doi.org/10.1038/s41586-020-2117-z>
9. Federico, L.B., Silva, G.M., Barcelos, Mariana Pegrucci Francischini, I.A.G., Taft, C.A., Silva, C.H.T.P.: Key aspects for achieving hits by virtual screening studies. In: La Porta, F.A., Taft, C.A. (eds.) *Functional Properties of Advanced Engineering Materials and Biomolecules*, vol. 780. Springer International Publishing (2021)
10. De Araújo Matos, I., Da Costa Júnior, N.B., Meotti, F.C.: Integration of an Inhibitor-like Rule and Structure-based Virtual Screening for the Discovery of Novel Myeloperoxidase Inhibitors. *J. Chem. Inf. Model.* (2020). <https://doi.org/10.1021/acs.jcim.0c00813>
11. Hage-Melim, L.I. da S. et al.: Virtual screening, ADME/Tox predictions and the drug repurposing concept for future use of old drugs against the COVID-19. *Life Sci.* **256**, 117963 (2020)
12. Fischer, A., Sellner, M., Neranjan, S., Smieško, M., Lill, M.A.: Potential inhibitors for novel coronavirus protease identified by virtual screening of 606 million compounds. *Int. J. Mol. Sci.* (2020). <https://doi.org/10.3390/ijms21103626>
13. Walters, W.P.: Virtual chemical libraries: miniperspective. *J. Med. Chem.* (2018)
14. Rifaioğlu, A.S., et al.: Recent applications of deep learning and machine intelligence on in silico drug discovery: methods, tools and databases. *Brief. Bioinform.* (2019). <https://doi.org/10.1093/bib/bby061>
15. Yang, Z.Y., Yang, Z.J., Lu, A.P., Hou, T.J., Cao, D.S.: Scopy: An integrated negative design python library for desirable HTS/VS database design. *Brief. Bioinform.* (2021). <https://doi.org/10.1093/bib/bbaa194>
16. Pontes, T.B., Miranda, G.L., Celani, G.C.: Algorithm-aided design with python: analysis of technological competence of subjects. *Educ. Sci.* (2018). <https://doi.org/10.3390/educsci8040200>
17. da Silva, H.A., Moura, A.S.: Teaching introductory statistical classes in medical schools using RStudio and R statistical language: evaluating technology acceptance and change in attitude toward statistics. *J. Stat. Educ.* (2020). <https://doi.org/10.1080/10691898.2020.1773354>
18. Jia, L., et al.: Development of interactive biological web applications with R/Shiny. *Brief. Bioinform.* (2022). <https://doi.org/10.1093/bib/bbab415>
19. Zhou, W., Li, X., Han, L., Fan, S.: Application of network pharmacology based on artificial intelligence algorithms in drug development. *Netw. Pharmacol.* (2021). [https://doi.org/10.1007/978-981-16-0753-0\\_2](https://doi.org/10.1007/978-981-16-0753-0_2)
20. Gawehn, E., Hiss, J.A., Brown, J.B., Schneider, G.: Advancing drug discovery via GPU-based deep learning. *Expert Opin. Drug Discov.* (2018). <https://doi.org/10.1080/17460441.2018.1465407>
21. Gawehn, E., Hiss, J.A., Schneider, G.: Deep learning in drug discovery. *Mol. Inform.* **35**, 3–14 (2016)
22. Hessler, G., Baringhaus, K.H.: Artificial intelligence in drug design. *Molecules* (2018). <https://doi.org/10.3390/molecules23102520>
23. Jordan, A.M.: Artificial intelligence in drug design—the storm before the calm? *ACS Med. Chem. Lett.* (2018). <https://doi.org/10.1021/acsmchemlett.8b00500>
24. Kelly, S.: What is Python? Python, PyGame Raspberry Pi Game Dev. 3–5 (2016). <https://doi.org/10.1007/978-1-4842-2517-2>
25. Cunningham, H.C.: *Multiparadigm Programming with Python 3* Ch. pp. 1–26 (2018)

26. Severance, C. Guido van Rossum: The early years of python. *Computer* (Long. Beach. Calif) **48**, 7–9 (2015)
27. Rashed, M.G., Ahsan, R.: Python in computational science: applications and possibilities. *Int. J. Comput. Appl.* **46**, 26–30 (2018)
28. Miller, C., Hersberger, C., Jones, M.: Automation Of Common Building Energy Simulation Workflows Using Python Architecture & Sustainable Building Technologies (SuAT), Institute of Technology in Architecture (ITA), ETH Zurich EXERGY Studios s.r.o., Vienna University of Technology,. In: *Proceedings of BS2013*, pp. 210–217 (2012)
29. Manaswi, N.K.: *Deep Learning with Applications Using Python*. *Deep Learning with Applications Using Python* (2018). <https://doi.org/10.1007/978-1-4842-3516-4>
30. Millman, K.J., Aivazis, M.: Python for scientists and engineers. *Comput. Sci. Eng.* **13**, 9–12 (2011)
31. Nagpal, A., Gabrani, G.: Python for data analytics, scientific and technical applications. In: *Proc.—2019 Amity Int. Conf. Artif. Intell. AICAI 2019*, 140–145 (2019). <https://doi.org/10.1109/AICAI.2019.8701341>
32. AISweigart. *Python编程快速上手*. 人民邮电出版社 (2016)
33. Bouquin, D.R.: GitHub. *J. Med. Libr. Assoc.* (2015). <https://doi.org/10.3163/1536-5050.103.3.019>
34. Sydow, D., et al.: TeachOpenCADD-KNIME: a teaching platform for computer-aided drug design using KNIME workflows. *J. Chem. Inf. Model.* (2019). <https://doi.org/10.1021/acs.jcim.9b00662>
35. Brethauer, D.: Open source software: a history. *Publ. Work.* **7**, 1–20 (2001)
36. Fuggetta, A.: Open source software—an evaluation. *J. Syst. Softw.* **66**, 77–90 (2003)
37. Scacchi, W.: Free/open source software development : recent research results and emerging opportunities. *Manag. Sci.* **52**, 1000–1014 (2007)
38. von Krogh, G., Spaeth, S., Lakhani, K.R.: Community, joining, and specialization in open source software innovation: a case study. *Res. Policy* **32**, 1217–1241 (2003)
39. Ducheneaut, N.: Socialization in an open source software community: a socio-technical analysis. *Comput. Support. Coop. Work* **14**, 323–368 (2005).
40. Thung, F., Bissyandé, T.F., Lo, D., Jiang, L.: Network structure of social coding in GitHub. In: *Proc. Eur. Conf. Softw. Maint. Reengineering, CSMR*, pp. 323–326 (2013). <https://doi.org/10.1109/CSMR.2013.41>
41. Kalliamvakou, E. et al.: The promises and perils of mining GitHub. In: *11th Work. Conf. Min. Softw. Repos. MSR 2014—Proc.*, pp. 92–101 (2014). <https://doi.org/10.1145/2597073.2597074>
42. Gousios, G., Vasilescu, B., Serebrenik, A. & Zaidman, A. Lean ghtorrent: GitHub data on demand. In: *11th Work. Conf. Min. Softw. Repos. MSR 2014—Proc.*, pp. 384–387 (2014). <https://doi.org/10.1145/2597073.2597126>
43. Iriberry, A., Leroy, G.: A life-cycle perspective on online community success. *ACM Comput. Surv.* **41**, 1–29 (2009)
44. Fischer, A.E., Grodzinsky, F.: *The Anatomy of Programming Languages*. Prentice Hall (193AD)
45. Dershem, H.L., Jipping, M.J.: *Programming Languages: Structures and Models*. PWS Publishing Company (1995)
46. Melo, A.C.V. de, Silva, F.S.C. da.: *Princípios de Linguagens de Programação*. Edgard Blücher Ltda (2003)
47. Sammet, J.E.: *Programming Languages: History and Fundamentals*. Prentice Hall (1969)
48. Geldenhuys, W.J., Gaasch, K.E., Mark Watson, D.D.A., C.J.V. der S.: Optimizing the use of open-source software applications in drug discovery. *DTT* **11**, 127–132 (2006)
49. Vriend, G.: WHAT IF: a molecular modeling and drug design program. *Molecules* **8**, 52–56 (1990)
50. Cao, D.S., Xu, Q.S., Hu, Q.N., Liang, Y.Z.: ChemoPy: freely available python package for computational biology and chemoinformatics. *Bioinformatics* **29**, 1092–1094 (2013)

51. Donat, W.: *Introducing Python*. In: *Learn Raspberry Pi Programming with Python*, pp. 55–89. Apress (2018). [https://doi.org/10.1007/978-1-4842-3769-4\\_3](https://doi.org/10.1007/978-1-4842-3769-4_3)
52. Xia, J., Li, S., Ding, Y., Wu, S., Wang, X.S.: MUBD-DecoyMaker 2.0: a python GUI application to generate maximal unbiased benchmarking data sets for virtual drug screening. *Mol. Inform.* **39**, 2–5 (2020)
53. Cao, D.S., et al.: PyDPI: freely available python package for chemoinformatics, bioinformatics, and chemogenomics studies. *J. Chem. Inf. Model.* **53**, 3086–3096 (2013)
54. Sydow, D., Morger, A., Driller, M., Volkamer, A.: TeachopenCadd: a teaching platform for computer-aided drug design using open source packages and data. *J. Cheminform.* **11**, 1–7 (2019)
55. Cao, D.-S., Xu, Q.-S., Liang, Y.-Z., Chen, X., Li, H.-D.: Prediction of aqueous solubility of druglike organic compounds using partial least squares, back-propagation network and support vector machine. *J. Chemom.* (2010). <https://doi.org/10.1002/cem.1321>
56. Irwin, J.J.: Community benchmarks for virtual screening. *J. Comput. Aided. Mol. Des.* **22**, 193–199 (2008)
57. Perez, F., Granger, B.E.: IPython: a system for interactive scientific computing. *Comput. Sci. Eng.* **9**, 21–29 (2007)
58. Pimentel, J.F., Murta, L., Braganholo, V., Freire, J.: A large-scale study about quality and reproducibility of jupyter notebooks. *IEEE Int. Work. Conf. Min. Softw. Repos.* **2019**, 507–517 (2019)
59. Knuth, D.E.: Literate programming. *Comput. J.* **27**, 97–111 (1984)
60. Nguyen, H., Case, D.A., Rose, A.S.: NGLview-interactive molecular graphics for Jupyter notebooks. *Bioinformatics* **34**, 1241–1242 (2018)
61. Warr, W.A.: Scientific workflow systems: Pipeline Pilot and KNIME. *J. Comput. Aided. Mol. Des.* **26**, 801–804 (2012)
62. Beisken, S., Meinel, T., Wiswedel, B., Figueiredo, L.F. De, Berthold, M.: KNIME-CDK : workflow-driven cheminformatics. 2–5 (2013)
63. Berthold, M.R. et al.: KNIME: the konstanz information miner. 4th Int. Ind. Simul. Conf. 2006, ISC 2006 **11**, 58–61 (2006)
64. Fillbrunn, A., et al.: KNIME for reproducible cross-domain analysis of life science data. *J. Biotechnol.* **261**, 149–156 (2017)
65. Ekmekci, B., McAnany, C.E., Mura, C.: An introduction to programming for bioscientists: a python-based primer. *PLoS Comput. Biol.* **12**, 1–43 (2016)
66. Sweigert, A.: *Automate the Boring Stuff with python*. Coding. William Pollock (2020)
67. Corporation, M. Microsoft Corporation. Microsoft Excel (2018). <https://office.microsoft.com/excel>
68. Foundation TD: LibreOffice Calc (2020). <https://www.libreoffice.org/discover/calc/>
69. Foundation TD: OpenOffice Calc (2020). <https://www.openoffice.org/discover/calc/>
70. Lin, X., Li, X., Lin, X.: A review on applications of computational methods in drug screening and design. *Molecules* **25**, 1–17 (2020)
71. Salman, M.M., et al.: Advances in applying computer-aided drug design for neurodegenerative diseases. *Int. J. Mol. Sci.* **22**, 4688 (2021)
72. Temml, V., Kutil, Z.: Structure-based molecular modeling in SAR analysis and lead optimization. *Comput. Struct. Biotechnol. J.* **19**, 1431–1444 (2021)
73. Nowotka, M., Papadatos, G., Davies, M., Dedman, N., Hersey, A.: Want drugs? Use python. *Euroscipy* 25–30 (2015)
74. Geoffrey, B. et al.: A program to automate the discovery of drugs for West Nile and Dengue virus—programmatically screening of over a billion compounds on PubChem, generation of drug leads and automated in silico modelling. *J. Biomol. Struct. Dyn.* **0**, 1–9 (2020)
75. de Brito, M.A.: Pharmacokinetic study with computational tools in the medicinal chemistry course. *Brazilian J. Pharm. Sci.* **47**, 797–805 (2011)
76. Geoffrey, B.A.S., et al.: Automated in Silico identification of drug candidates for coronavirus through a novel programmatic tool and extensive computational (MD, DFT) studies of select drug candidates. *ChemRxiv* (2020). <https://doi.org/10.26434/chemrxiv.12423638>

77. Kumar, K. Why python rocks for research....??? Int. J. Eng. Technol. **6**, 408–410 (2019)
78. Van Der Spoel, D., et al.: GROMACS: fast, flexible, and free. J. Comput. Chem. (2005). <https://doi.org/10.1002/jcc.20291>
79. Hawkins, P.C.D., Nicholls, A.: Conformer generation with OMEGA: learning from the data set and the analysis of failures. J. Chem. Inf. Model. **52**, 2919–2936 (2012)
80. OpenEye Scientific Software. ROCS 3.3.1.2. (2018)
81. OpenEye Scientific Software. EON 2.3.1.2. (2018)
82. Verdonk, M.L., Cole, J.C., Hartshorn, M.J., Murray, C.W., Taylor, R.D.: Improved protein-ligand docking using GOLD marcel. Proteins **52**, 609–623 (2003)
83. Mysinger, M.M., Carchia, M., Irwin, J.J., Shoichet, B.K.: Directory of useful decoys, enhanced (DUD-E): better ligands and decoys for better benchmarking. J. Med. Chem. **55**, 6582–6594 (2012)
84. O’Boyle, N.M., et al.: Open Babel. J. Cheminform. **3**, 1–14 (2011)

# Ligand-Based Drug Design for Selection of Molecules with Pharmacological Activity in Essential Tremor



Ana C. J. Silva, Suzane Q. Gomes, Mariana P. Barcelos,  
Carlos Henrique Tomich de Paula da Silva, Carlton A. Taft,  
and Lorane Izabel da Silva Hage-Melim

**Abstract** Essential tremor (ET) is the most common movement disorder, characterized by producing involuntary oscillatory and rhythmic movements when some specific action is performed. The main pharmacotherapy used to treat the disease is through the use of propranolol, which is a non-selective  $\beta$ -adrenergic receptor antagonist. Some adverse effects are related to the use of this drug, many of which act on the Central Nervous System (CNS), such as fatigue, which can even reach depression. Pharmaceutical chemistry is a science that helps, through different methodologies, the drug design for the treatment of different pathologies. Therefore, it needs other areas of science to contribute to the studies developed. Initially, to design a new drug, it is necessary to choose the therapeutic target, as well as the aspects related to the pathology. In the case of the research in question, the main objective is the drug design that has an activity for essential tremor. Thus, the first stage of the research consisted of selecting molecules contained in the BindingDB database to be screened using the pharmacophore, obtained in the ZincPharmer software. After screening, tests were applied to predict the pharmacokinetic properties using the Qikprop software, toxicological using the DEREK software, analysis of the activity potential and possible target, using the PASS and SEA webservers, respectively. After the analysis of each parameter, the best proposals were chosen, with a total of twelve molecules, to be carried out in the molecular docking study, using the GOLD software, as a way to estimate the activity of the molecules analyzed in these receptors. From a general

---

A. C. J. Silva · L. I. da S. Hage-Melim (✉)

Laboratory of Pharmaceutical and Medicinal Chemistry (PharMedChem), Federal University of Amapá, Macapá, Brazil  
e-mail: [loranehage@gmail.com](mailto:loranehage@gmail.com)

S. Q. Gomes

Departamento de Química, Faculdade de Filosofia, Ciências e Letras de Ribeirão Preto, Universidade de São Paulo, Av. Bandeirantes, 3900, Ribeirão Preto, São Paulo 14090-901, Brazil

M. P. Barcelos · C. H. T. de Paula da Silva

Computational Laboratory of Pharmaceutical Chemistry, Department of Pharmaceutical Sciences, Faculty of Pharmaceutical Sciences of Ribeirão Preto, University of São Paulo, Ribeirão Preto, São Paulo, Brazil

C. A. Taft

Centro Brasileiro de Pesquisas Físicas, Rio de Janeiro, Brazil

perspective, most of the results were favorable, since in different analyses, many of the modifications showed superior results than propranolol in at least one of the criteria. Therefore, the continuation of studies against the proposals is an attractive option, as they can provide favorable results for the development of a drug with better properties for the treatment of essential tremor.

**Keywords** Therapeutic target · Molecular docking · Pharmacotherapy · Pharmaceutical chemistry

## 1 Introduction

For the definition and characterization of essential tremor (ET), it is important to understand the concept of tremor and its different types. Thus, in definition, tremor is characterized as an oscillatory and rhythmic movement of antagonist muscles [1]. By determining the frequency of tremors, it is possible to establish which category the tremor falls into. A physiological tremor occurs at a frequency of 8–13 Hz, which can be exacerbated, with stimulation of the sympathetic nervous system, in situations of stress, physical exercise, withdrawal of alcohol and some drugs, in addition to metabolic disorders, such as hyperthyroidism and hypoglycaemia [2]. The frequency of pathological tremor, on the other hand, is generally slower, occurring in the range of 4–8 Hz and is perceived more in distal parts of the limbs [3].

Also, in relation to pathological tremor, other classifications are established, such as in relation to its phenomenology, location, etiology and frequency, the latter being already addressed [2]. As for phenomenology, tremors are divided into action tremor and rest tremor [4]. Resting tremor is what occurs when the body is relaxed and even so the oscillatory and rhythmic movements are present, being quite characterized by Parkinson's Disease, in addition to other types of tremors such as rubral, delayed tremor, myorhythmia and severe essential tremor [3, 4].

Action tremor, on the other hand, is signaled when there is a contraction of the muscles involved, that is, when a specific movement is performed. This type of tremor can be subdivided into postural, kinetic, intentional, task-specific tremor, and isometric tremor. Postural refers to holding a position against gravity. Kinetics occur during the execution of a certain type of movement of an extremity. When a movement is performed that intends to hit a target, it is called an intentional tremor. On the other hand, task-specific tremor manifests itself almost exclusively during a specific motor act, for example, during the action of writing or handling a musical instrument. Finally, isometric tremor appears when an affected segment is contracted without its displacement [3, 5, 6].

Essential tremor is the most common type of movement disorder, being classified as a type of action tremor, being typical of a kinetic tremor accompanied by a postural tremor that affects mainly the upper limbs [7]. Worldwide, the occurrence of the disease is estimated at 0.5–1% in adults, reaching 5% in people over 65 years of age [8, 9]. However, even if the values indicate a higher incidence at older ages, groups

of younger individuals can be affected by the disease, especially those with family members with a history [10].

Its etiology and pathophysiology are not well known and, therefore, several studies are being carried out to establish whether this type of tremor is a degenerative disease or not. Even with so many controversies, several lines of research indicate that the origin of the disease is due to some cerebellar dysfunction [7].

The ET is found at the frequency of 4–12 Hz (medium frequency), where symptoms are more noticeable in the upper and lower extremities in the initial stage, and in the head and voice when the condition is more evolved [11]. This disorder can intensify with the exposure to external stressful agents and with advancing age. For this reason, ET can be confused with Parkinson's Disease, being a factor that hinders the diagnosis of the disease [12].

The disease is chronic, with progression of symptoms and no cure. For this reason, in early stages, its diagnosis is difficult, in which the tremors may appear unilaterally or asymmetrically, which is different from one of the diagnostic criteria for the disease, as the existence of bilateral and symmetrical tremor in the ET is considered [13].

Although it is not a degenerative disease and is considered benign, ET interferes with the quality of life of patients, in which, in many situations, due to symptoms, they cannot perform some activities, significantly affecting their personal life [14]. As it is a chronic disease, over time, the tremors become more intense, making it difficult to perform motor actions.

This, in turn, can lead to the appearance of psychological disorders, where, due to the inability to perform some so-called "easy" actions, the individual's psychological condition may be affected, and this may develop an anxiety, depression or personality characteristics, and thus, contribute even more to the intensification of symptoms, since the tremors arising from emotional disorders are also triggered [15].

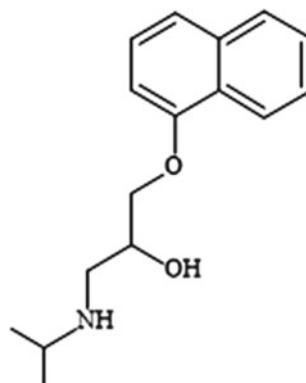
The  $\beta$ -adrenergic receptors are located in different cells of the body, in which when activated, they produce several functions in the body, such as the regulation of the cardiovascular system, the production and release of hormones, in addition to the control of metabolism [16]. The most common receptors found in the cardiovascular system are the  $\beta$ 1 adrenergic receptors, which when activated by catecholamines (adrenaline and noradrenaline) produce a positive chronotropic and ionotropic effect. The  $\beta$ 2 adrenergic receptors are responsible for smooth muscle relaxation in different organs [17].

These receptors are associated with the Gs protein, which has seven transmembrane domains, presenting an N-terminal portion that is exposed to the extracellular environment, where specific substances interact with this region and produce a response chain through intracellular mechanisms, the latter being initiated by the activation of the C-terminal portion, which is in the inner area of the membrane. Activation stimulates the adenylyl cyclase enzyme, which will result in the production of cAMP, causing different types of cellular responses, depending on the location of the receptor [17, 18].

Due to this response produced by the activation of  $\beta$ -adrenergic receptors, several drugs were developed and synthesized in order to inhibit or stimulate the targets



**Fig. 1** Chemical structure of propranolol



addressed in question for the production of a desired therapeutic effect for a certain type of pathology [19].

The usual drug treatment for essential tremor is based on the administration, mainly of beta-blockers, being the main representatives of the class, propranolol and primidone, being the first considered as a reference drug for the treatment of this disorder. Propranolol (Fig. 1) is a non-selective  $\beta$ -adrenergic receptor antagonist, and its action on ET possibly occurs through blocking peripheral  $\beta_2$  adrenoceptors [20]. Its use causes an improvement of 50 to 70% in patients, with the greatest effect on ET that manifests itself in the hands, when compared to other types of action tremor, such as in the head and voice [21].

As already described, the pharmacological mechanism of propranolol is not known for sure, since the drug has peripheral or central action. However, some studies report a possible relationship of propranolol being a membrane stabilizer, which attributes therapeutic activity to ET [22].

There are several contraindications for the use of this drug, such as individuals who have asthma, severe congestive heart failure, diabetes mellitus, peripheral arterial disease and grade atrioventricular blocks [23].

However, even if the initial response to the drug is favorable, during the course of treatment, the dose can be increased in order to maintain the same efficacy when taken at the beginning of the treatment. In addition, some side effects at high doses may appear, such as gastrointestinal disturbances, erectile dysfunction, fatigue, muscle weakness, nausea, weight gain and even depression [20]. Another important aspect related to dose increase is that older individuals are more likely not to tolerate these progressively higher doses. As the most frequently available presentation of propranolol is 40 mg tablets, in certain types of treatment it is necessary to administer up to 8 tablets a day, which is very inconvenient for the patient who is receiving the treatment [24].

The research and development of new drugs is a time-consuming and costly process. Therefore, as a way to reduce possible costs and allow promising results, some tools are employed, such as the use of computational chemistry. This area allows a prior assessment of the possible interaction between molecule and target,

as a way to identify failure in the response of this interaction through computer simulations [25]. In this way, computational chemistry establishes the aspects related to the molecule-receptor complex, with the purpose of verifying as much as possible all the biological processes that may occur.

In this sense, *in silico* studies, which provide computer programs and databases in networks to establish possible chemical relationships of the active molecule with a specific target, mainly help in the selection of molecules with potential therapeutic activity [26]. Among the advantages related to this type of study is the possibility of a prior evaluation, based on the structure, of the pharmacokinetic parameters of the molecules, preventing the synthesis of compounds with inadequate ADME properties, with high expenditure of resources and in a longer period [27]. Thus, the application of *in silico* models before other types of tests, *in vivo* and *in vitro*, is a way to prevent cost and time losses, with a greater probability of obtaining drug candidates [28].

As an initial step for planning a drug, the therapeutic target must be established, as well as aspects related to the pathophysiology in which you want to study. Through different methodologies that are applied, it is possible to obtain new agents with biological activity for the treatment of certain pathology.

## 2 Material and Methods

### 2.1 Molecules Selection

The BindingDB online database (<https://www.bindingdb.org/bind/index.jsp>), allows the identification of different compounds based on their interaction with specific targets, according to the chemical characteristics of the molecule and its ability to binding with a receptor [29]. The webserver has several applications that include, analysis of ligands for a specific target, checking the degree of affinity, according to the structure–activity relationship; identification of a possible candidate as a target, according to the ligands [30].

For this research, the descriptor “Beta adrenergic antagonist” was used on the BindingDB webserver, in order to find possible ligands for beta-adrenergic receptors with antagonist action. Altogether, the first 30 ligands were selected, according to the IC<sub>50</sub> value (Mean Inhibitory Concentration), which indicates the average concentration necessary for a compound to be able to inhibit a target. This criterion is based on the idea that substances with a high IC<sub>50</sub> are less potent than those with a low IC<sub>50</sub>, as they need a higher concentration to reach the same level of inhibition [31].

Each molecule was downloaded in SDF format, with a 2D structure, on the PubChem platform (<https://pubchem.ncbi.nlm.nih.gov>), which is one of the largest databases available, with access public, where it contains information about chemical substances and their respective biological properties [32].

The molecules, after being saved, were analyzed and their partial charges calculated using the “Discovery Studio Visualizer” program. The partial charge is indicated by the average of the partial charge of each atom of the molecule subtracted by the number of protons present [31]. The correction of this allows the optimization in the geometry and energy of the molecules, contributing to the prediction calculations not to have possible errors.

## ***2.2 Identification of Pharmacophore Groups***

This step consisted of identifying the regions of the molecules responsible for attributing biological activity. The molecules, after optimized in Discovery Studio Visualizer and saved in “mol2” format, were compressed into a folder and added to the online platform PharmaGist (<https://bioinfo3d.cs.tau.ac.il/PharmaGist/>), which it is a server that has tools capable of identifying the regions that are common between different molecules, in addition to providing data related to the alignment of the set of molecules, establishing, by quantitative values, the best results [33].

## ***2.3 Pharmacophore-Based Virtual Screening***

The visualization and description of the pharmacophoric groups can be done on the online platform ZINCPharmer (<http://zincpharmer.csb.pitt.edu/>) which allows the 3D alignment of molecules, with the indication of possible regions that confer activity. This program also allows the search for similar molecules based on the pharmacophore. The program generates thousands of conformational isomers of compounds in less than 1 min. The results can be visualized instantly or even the molecules generated in other programs can be downloaded [34].

As a facilitating tool, the program also allows filtering the results, according to the user's specifications, such as the limit number of orientations for each conformation (‘Max Hits per Conf’), the number of orientations of conformations for each molecule (‘Max Hits per Mol’) and/or the total number of targets (‘Max Total Hits’). Another filter used is the Average Square Root Deviation (‘RMSD’), which calculates the orientation of hits, then restricts the hits to those with better geometry for selection [34]. In the research, the value of 1 was used as a minimum parameter for “Max Hits per Conf” and “Max Hits per Mol” and for RMSD, 1.5 and molecular weight less than 500 g/mol. This screening enabled the search for molecules with different conformations, being non-isomers, based on the pharmacophore.

## ***2.4 Determination of Physical and Chemical Properties***

In this step, the physicochemical properties of each resulting molecule in ZINCPharmer were determined, after screening done in the program and of propranolol, in order to compare the values. The physicochemical parameters were evaluated according to the Rule of Five (RO5), developed by Christopher A. Lipinski and collaborators in 1997, which establishes the physicochemical properties as one of the factors that influence the bioavailability of a drug [35]. Therefore, in this study, molecules that did not fit more than two RO5 parameters were disregarded and considered unsuitable to be used as a prototype.

## ***2.5 Prediction of Pharmacokinetic Properties***

For the development of a drug, the understanding of how and when it will reach its place of action becomes necessary, since one wants to understand and control its therapeutic action, configuring its pharmacokinetics. How the drug will be absorbed, its form of distribution, its biotransformation and how it will be excreted by the body are key to the effectiveness of a drug. Thus, according to the physicochemical properties of the molecules, the pharmacokinetics will be different, with greater therapeutic response and less occurrence of adverse effects [36].

Thus, in the present study, the pharmacokinetic properties of the molecules screened by ZINCPharmer were determined, with the aid of the Qikprop software, which offers data related to ADME (absorption, distribution, metabolism and excretion) [37]. The parameters evaluated in the program were: qualitative prediction of human oral absorption (AOH); prediction of the percentage of human oral absorption (%AOH); cell permeability in Caco-2 (pCaco-2) and MDCK (pMDCK) cells; penetration into the blood–brain barrier (logBB); prediction of activity in the Central Nervous System (CNS); prediction of blocking activity in HERG channels (logHERG).

## ***2.6 Prediction of Toxicological Properties***

As for the potential carcinogenicity and mutagenicity of the molecules, predictions of the toxicological properties were made with the aid of the DEREK program (Deductive Estimate of Risk from Existing Knowledge), which allows relating the molecular structure with toxicity, through a series of information contained in the program's database [38].

## 2.7 Activity Prediction: SEA and PASS

For this step, two resources available in the network were used, one being used to determine the potential for activity and inhibition of the proposals and the other to determine whether the modified molecules can interact with the target of the disease to be treated. The 'PASS prediction' program can provide data regarding the biological activity of molecules and is accessed at <<http://www.akosgmbh.de/pass>>. As a way to determine the potential of molecule-receptor binding, the Similarity Ensemble Approach (SEA) server was accessed through the link <<http://sea.bkslab.org/>>, to predict potential targets of the created proposals.

## 2.8 Modifications of the Selected Prototype

After analyzing the data obtained from the in silico predictions, the molecule that best fit the values was selected as the prototype. From this, successive modifications, made in the ChemSketch program, were carried out in order to evaluate, in addition to ADME/Tox predictions, others such as activity, PASS prediction and SEA prediction. In all, 30 (thirty) modifications were made from the selected prototype to obtain a better proposal than the chosen drug.

## 2.9 Molecular Docking Using the Gold Software

Molecular docking programs assess, through a cyclic process, the conformation of the ligand by specific scoring functions, where the conversion of an interaction with a minimum energy occurs [39]. Generally speaking, this type of virtual screening is carried out in three steps. In the first, the docking program predicts the possibility of complexation of different structures with a specific target protein. The second step is to classify this complexation according to energy forces. Finally, they provide the fitting scores, classifying them according to the best results [40].

One of the programs used is GOLD (Genetic Optimisation for Ligand Docking), which uses the genetic algorithm (GA) to optimize docking times and increase the probability of finding the best fit [41].

The search for protein structures was performed on the PDB (Data Bank Proteins) site, which works as a file bank of crystallographic structures [42]. For the research, two targets were selected ( $\beta$ 1 adrenergic—PDB ID: 7VBQ, Resolution: 3.18 Å and  $\beta$ 2 adrenergic—PDB ID: 3NYA, Resolution: 2.50 Å) complexed with carazolol and alprenolol, respectively [43, 44].

To assess the predictive capacity of the in-silico model, the validation method (redocking) was used. As the crystallographic structures are complexed to other molecules, the validation is used precisely to establish whether the program is able

to determine the spatial orientation of the ligand, presenting the origin coordinates, the RMSD (Root Mean Square Deviation), validation radius, in addition to predicting a possible interaction with some amino acid residue of interest [45].

After validation of the selected targets in the PDB, molecular docking was performed with the reference molecule (propranolol), with the prototype and the modifications that showed better results in the pharmacokinetic, toxicological and activity prediction analysis.

## 3 Results and Discussion

### 3.1 Molecules Selection

The planning of a new drug that presents better therapeutic activity for the treatment of ET proved to be important, in which all steps from the selection of molecules to the optimization of prototypes were followed according to the precepts established by medicinal chemistry. Through several studies found in the literature, the use of propranolol has become an effective therapy for the first-line treatment of essential tremor. Based on these studies, it was found that its action target is  $\beta$ -adrenergic receptors, with an antagonist effect [46].

To begin with, we searched the BindingDB online server for molecules that have activity and that can bind to  $\beta$ -adrenergic receptors. The selection criterion was based on the receptor activity and the mean inhibitory concentration values (IC<sub>50</sub>), in order to allow molecules with greater activity against these receptors to be selected in that database. In all, thirty molecules were selected according to the IC<sub>50</sub> (Fig. 2).

After being selected, the partial charges of each molecule were calculated and corrected, since each atom has a partial charge, positive or negative, which is determined according to the chemical nature of each one [31]. An electronic “cloud” is created around the molecule and this influences the potential for intermolecular bonding, since, depending on the partial charges of the atoms, bonding can be carried out with greater or lesser ease. As the electronic cloud is not only in a specific atom but travels around the molecule, electrons tend to approach electronegative atoms and more distant from the electropositive ones, which causes the poor distribution of charge in the molecule, hence the need to correct them [31].

### 3.2 Pharmacophoric Model

According to the IUPAC, a pharmacophoric model is a set of characteristics of steric and electronic resources capable of guaranteeing an interaction with a specific target to trigger or block a biological response [47]. Thus, according to the three-dimensional spatial arrangement, a molecule will have greater binding affinity with a

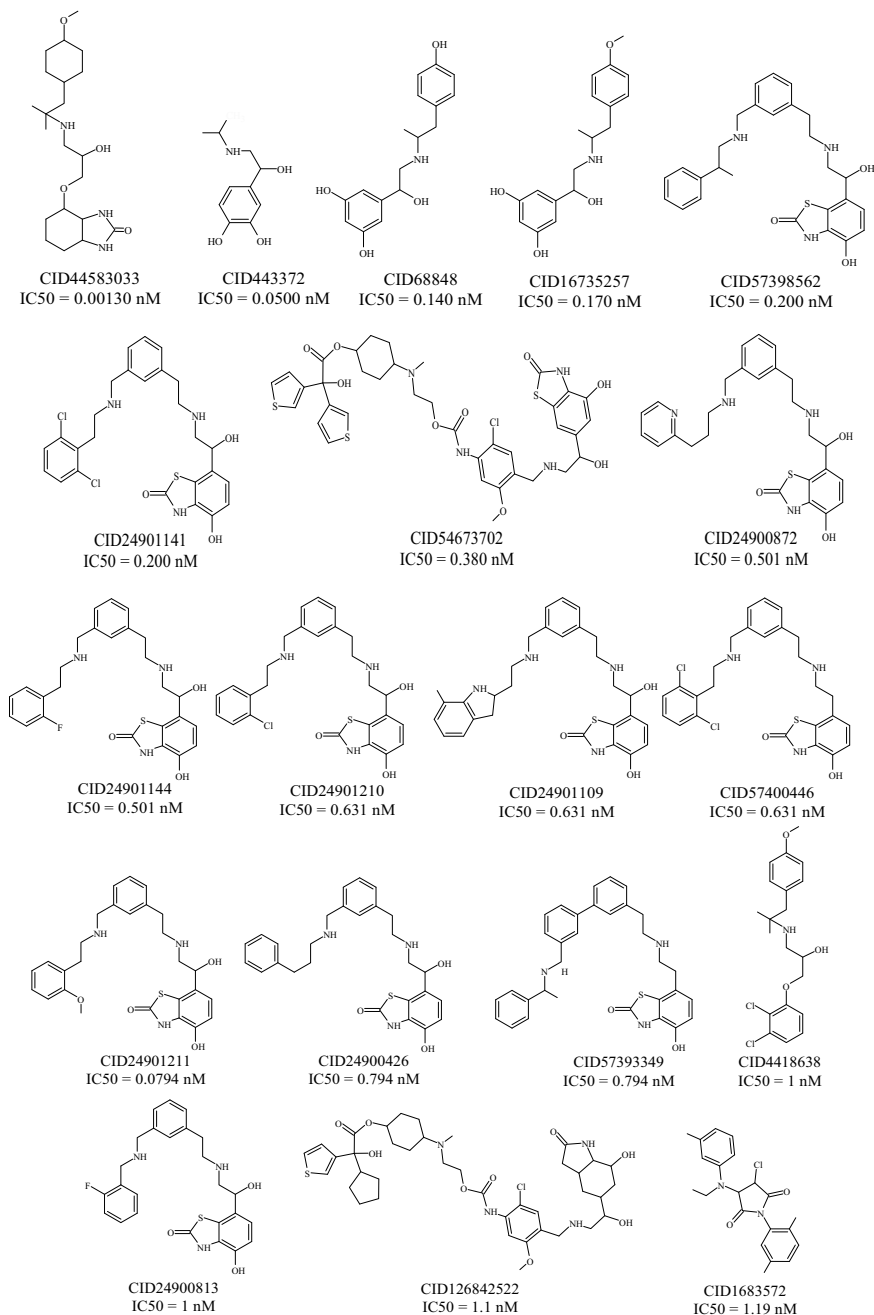


**Fig. 2** Representation of the chemical structures of  $\beta$ -adrenergic receptor antagonists with respective IC<sub>50</sub> values (ascending order) selected from the Binding DB database

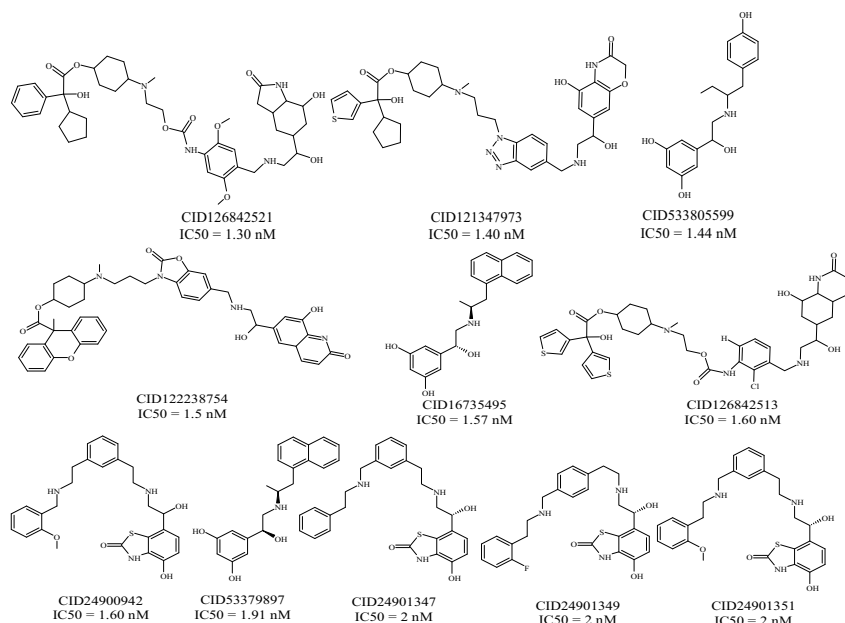


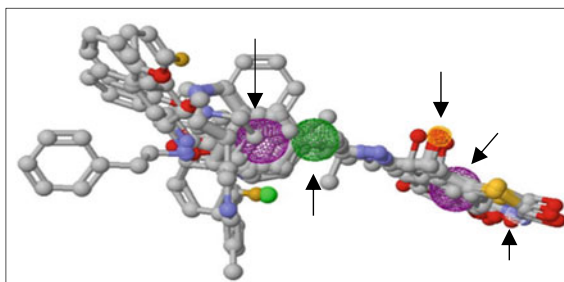
**Fig. 2** (continued)

certain type of receptor and, once verified, the pharmacophore can serve as a powerful model for application in the development of new drugs [33]. In all, twenty-four molecules were aligned, the alignment score being 40,252.

As seen in Fig. 3, the regions that confer activity are highlighted through the representation of colors, in which, purple represents the aromatic regions (2), green indicates hydrophobic region (1), white indicates hydrogen donors (1) and the orange hydrogen acceptor region (1).

Given the regions that present the activity potential of the molecule, when carrying out the modifications, these groups cannot be changed, as the pharmacological action potential can drastically reduce [33].

**Fig. 3** Pharmacophoric groups of aligned molecules.  
 Source PharmaGist





### 3.3 *Pharmacophore-Based Virtual Screening*

Several tools are made available, through computational chemistry, which allow greater ease in the process of discovering new drugs in a favorable time. In this sense, different means of approaches for the selection of molecules that present positive interactions with targets are found in the literature. These types of approaches are called virtual screenings and are classified into two types: ligand structure-based screening and receptor structure-based screening. The first refers to the use of ligands with structures already known and described to serve as a reference for the characterization of new compounds that may present favorable interactions with the target receptor. The second, as the name indicates, considers the structure of the therapeutic target in question, in order to discover new molecules with activity for this type of receptor [48].

In general, in a situation where there are thousands of compounds available for study, virtual screening facilitates the process of identifying compounds that are more likely to be active [31]. One of the search alternatives would be through the pharmacophoric model, where it is possible to perform a screening through the information on the structure of the ligands and thus select molecules, available in databases, that have chemical characteristics similar to those of the ligands [48].

In the related study, the screening was performed on the ZINCPharmer webserver, through the derivation of the pharmacophore. For the refinement, the parameters described in the material and methods section were used. The output file had a quantity of 46 hits, that is, 46 molecules that present regions similar to the pharmacophore. However, after applying the descriptors in order to refine the screening, the number of hits was reduced to 17 molecules (Fig. 4).

### 3.4 *Determination of Physical and Chemical Properties*

Once the pharmacophoric regions have been established, another analysis to be made for planning a drug is in relation to its physicochemical properties, which is necessary to determine the good availability of a substance in the body. To this end, they are evaluated according to the parameters established by Lipinski et al., through the rule of five. You may wonder why this name is given, but this is due to the fact that the established values are all multiples of five. This rule states that for a molecule to be better absorbed, its molecular mass (MM) must be  $\leq 500$ ,  $\log P \leq 5$ , number of hydrogen donors (HDB)  $\leq 5$  and hydrogen acceptors (HAB)  $\leq 10$ . If a molecule does not meet at least three requirements, it will not be considered with satisfactory bioavailability [35]. The results of this analysis of the screened molecules, as well as the reference molecule (Propranolol), are shown in Table 1.

According to the table, it can be seen that none of the molecules presented more than one nonconformity in the parameters established by Lipinski's R05, thus indicating a good bioavailability if administered orally.

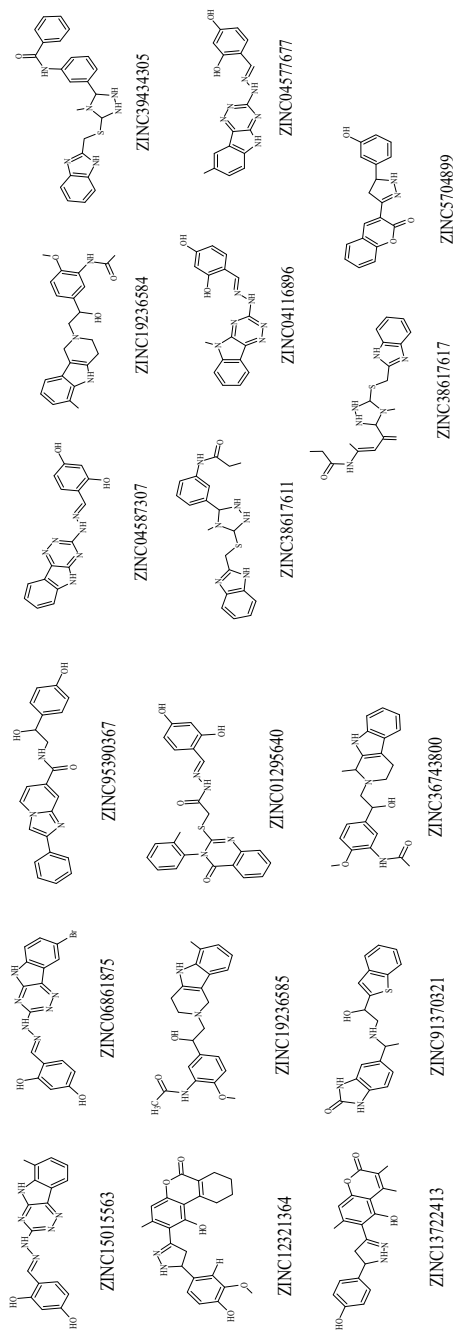


**Fig. 4** Representation of chemical structures sorted from the pharmacophore on the ZINCPharmer webserver

**Table 1** Evaluation of physicochemical properties using Lipinski's rule of five of molecules screened in ZINCPharmer and propranolol

Molecules	LogP	MM	HDB	HAB
PROPRANOLOL	3.0	259.34	2	3
ZINC15015563	2.7	334.3	4	7
ZINC06861875	3.0	399.2	4	7
ZINC95390367	3.2	373.4	3	4
ZINC12321364	3.9	420.5	3	7
ZINC19236585	2.3	393.5	3	4
ZINC01295640	3.7	460.5	3	7
ZINC13722413	3.3	364.4	3	6
ZINC91370321	3.1	353.4	4	5
ZINC36743800	2.3	393.5	3	4
ZINC04587307	2.3	320.3	4	7
ZINC19236584	2.3	393.5	4	5
ZINC39434305	3.8	444.5	4	7
ZINC38617611	3.9	397.5	4	7
ZINC04116896	2.3	334.3	3	7
ZINC45677677	2.7	334.3	4	7
ZINC38617617	3.0	396.5	4	7
ZINC05704899	3.2	306.3	2	5

### 3.5 Prediction of Pharmacokinetic Properties

An essential step for the *in silico* study is the realization of the pharmacokinetic prediction, as it allows to simulate the way a molecule acts in the body, from its absorption to its excretion [36]. Thus, this type of procedure facilitates obtaining pharmacokinetic information from drug candidates before carrying out the pre-clinical and clinical phases, thus optimizing resources and, consequently, results [49]. Prediction of pharmacokinetic properties—ADME (absorption, distribution, metabolism and excretion) were performed using the Qikprop software. The reference values, according to each analyzed parameter (AOH, %AOH, pCaco-2, pMDCK, logBB, SNC, HERG), are listed in Table 2.

Regarding absorption in the gastrointestinal tract, its determination is important to predict the bioavailability of the drug in the body [50]. After its administration, the drug being ingested, depending on its pharmacokinetic properties, can then be better or worse absorbed, thus reaching the therapeutic target for the production of the biological effect [27]. Thus, one of the parameters evaluated is the human oral absorption and its percentage of absorption. Of the screened molecules, only molecules ZINC15015563, ZINC06861875, ZINC91370321, ZINC04587307, ZINC39434305, ZINC38617611, ZINC04577677 and ZINC38617617 obtained

**Table 2** Descriptors and their reference values according to the Qikprop program

Descriptor	Reference value
Human oral absorption	1 low 2 medium 3 high
% Human oral absorption	<25 low >80 high
Permeability in Caco-2 cells Permeability in MDCK cells	<25 low >500 high <25 low >500 high
logBB	-3 a 1.2
SNC	-2 a +2
logHERG	<-5

Source Qikprop 4.4 Manual

average AOH results, while the rest had high values. In relation to %AOH, all molecules presented high values (Table 3).

With the application of new methodologies, some models for in vitro tests were developed to predict drug absorption. Among these tests, to predict permeability across cell membranes, are those performed on Caco-2 cells. These cells are widely used in studies to assess the intestinal absorption of a drug, as their lineage is derived from human colon adenocarcinoma and, therefore, their structural and functional characteristics (in vitro) are very similar to those of the human epithelium [51]. Another type of model used is the Maden Darby Canine Kidney (MDCK) cells, in which, when cultivated in semi-permeable membranes, they differentiate into columnar epithelial cells, with junctions similar to Caco-2 cells. This model is used to assess the in vitro permeability of new compounds. These cells are widely used to understand the renal distal tubular physiology, including the transport of ions, being one of the few models to express adequate amounts of co-transporters [52]. Of all molecules, only three (ZINC39434305, ZINC38617611 and ZINC38617617) showed low permeability in Caco-2 cells. The other molecules were in the range between high and medium permeability. Regarding MDCK cells, three molecules (ZINC39434305, ZINC38617611 and ZINC38617617) presented negative results, while the rest had intermediate values (Table 3).

The blood–brain barrier (BBB) is made up of several components in which it forms a communication network that interconnects the Central Nervous System (CNS) with peripheral tissues, where it regulates the exchange of substances between the blood and this system. Depending on the chemical characteristic of the molecule, it can pass the barrier more easily or not, in which molecules with lipophilic characteristics can penetrate more than the hydrophilic ones. With this, some substances exert greater activity in the CNS and depending on the pathology that wants to be treated, it is more favorable for the drug to be able to pass through the barrier. However, substances that

**Table 3** Pharmacokinetic properties, obtained in Qikprop software, of molecules screened in ZINCPharmer

Molecules	AOH	%AOH	pCaco-2	pMDCK	SNC	logBB	logHERG
PROPRANOLOL	3	100.000	802.562	431.502	1	0.034	-6.433
ZINC15015563	3	74.670	155.093	65.990	-2	-1.717	-6.043
ZINC06861875	3	74.484	129.054	142.997	-2	-1.622	-6.062
<b>ZINC95390367</b>	<b>3</b>	<b>90.224</b>	<b>296.209</b>	<b>132.804</b>	<b>-2</b>	<b>-1.557</b>	<b>-7.439</b>
ZINC12321364	3	85.412	209.368	91.272	-2	-1.403	-5.279
ZINC19236585	3	87.073	221.408	107.266	0	-0.595	-6.748
ZINC01295640	3	87.978	176.947	87.240	-2	-1.973	-7.528
ZINC13722413	2	84.257	245.605	108.460	-2	-1.182	-5.206
ZINC91370321	3	72.088	57.938	39.683	-2	-1.122	-7.120
ZINC36743800	3	87.669	244.429	119.370	0	-0.521	-6.819
ZINC04587307	3	71.421	128.527	53.862	-2	-1.770	-6.164
ZINC19236584	3	88.186	265.537	130.550	0	-0.487	-6.638
ZINC39434305	2	56.205	8.045	5.629	0	-0.388	-9.888
ZINC38617611	2	50.467	7.721	5.387	0	-0.361	-8.761
ZINC04116896	3	81.878	280.994	125.446	-2	-1.447	-6.228
ZINC04577677	3	72.966	128.527	53.862	-2	-1.826	-6.079
ZINC38617617	2	51.223	8.602	6.040	0	-0.290	-8.625
ZINC05704899	3	86.404	373.646	170.699	-1	-0.907	-5.773

manage to overcome the barrier are the most likely to cause more serious adverse effects [53].

For this reason, in this study, for drug planning in the treatment of ET, low penetration into the blood–brain barrier will be considered as a positive result, since it is intended to assess whether, even with less action at the CNS level, the molecules present better responses when compared to propranolol for the treatment of the pathology addressed. Thus, the screened molecules ZINC15015563, ZINC06861875, ZINC95390367, ZINC12321364, ZINC01295640, ZINC13722413, ZINC91370321, ZINC04587307, ZINC04116896, ZINC04577677 and ZINC05704899 showed inactivity in the reference values (in the reference values 2). Regarding the brain/blood partition ( $\log_{BB}$ ), all values are in line with the reference, that is, an unfavorable result for this study, as it indicates a possible penetration of the blood–brain barrier, which may act centrally.

One of the tests to find out if drug candidates may present possible toxicity is through the verification of inhibition in HERG/K + ion channels. This inhibition can cause disturbances in the normal rhythm of the heart, which can cause heart failure and even lead to death [31]. Thus, studies on the mechanisms regarding the inhibition of HERG channels provide significant information regarding the molecular factors, contributing to the *in silico* modeling [54]. According to the reference values of the Qikprop program, worrisome results are those with values lower than -5. In other words, according to the table, all screened molecules presented values for inhibition of HERG/K + channels, thus indicating potential toxicity (Table 3).

Assessing the ADME predictions of the screened molecules, it can be seen that only some criteria fit the values. In this sense, it is important to make changes in its structure in order to obtain more satisfactory results, especially related to the inhibition of HERG channels.

### ***3.6 Prediction of Toxicological Properties***

One of the challenges found for the development of new drugs is the evaluation of their toxicity in humans. In an attempt to reduce the time and expense of materials during this assessment, in addition to the risk associated with the use of these drugs under test, computational toxicology allows the application of computational and mathematical models to predict the possible toxic activity of a molecule from a set of information contained in databases [55].

The DEREK program is able to perceive chemical substructures within molecules and relate them to probable types of toxicity [56]. In the program, the toxicological prediction of the 17 molecules and also of propranolol was carried out, in order to compare the results and highlight which molecule obtained the best response, as described in Table 4. For better understanding, the program provides information regarding the number of alerts, describing the chemical structure that gives it such signaling, in addition to predicting what type of complications in a living organism it may cause.

**Table 4** Prediction of toxicological properties, in the DEREK program, of molecules screened in ZINCPharmer

Description	Total alerts	Condition	Alert
PROPRANOLOL	5	Bladder disorder (equivocal)	Bisoprolol
		Bradycardia (equivocal)	Esmolol
		Carcinogenicity (equivocal)	Ethanolamine or aminoethanethiol
		HERG channel inhibition (plausible)	HERG I Pharmacophore
		Urolithiasis (equivocal)	Bisoprolol
ZINC19236584	2	Hepatotoxicidade (equivocal)	Aminopherol derivative
ZINC36743800		Inibição canal HERG (plausível)	HERG I Pharmacophore
ZINC15015563	2	Skin sensitization (Plausible)	Resorcinol or precursor
ZINC01295640			Hydrazine
ZINC04587307			
ZINC04116896			
ZINC04577677			
ZINC38617611 ZINC38617617	7	HERG channel inhibition (plausible)	HERG I Pharmacophore HERG II Pharmacophore
		Skin sensitization (equivocal)	Hydrazine or precursor
		Hepatotoxicity (plausible)	Hydrazine Benzimidazole or precursor
		Mitochondrial dysfunction (equivocal)	Hydrazine
		Nephrotoxicity (equivocal)	Hydrazine
ZINC06861875	4	Carcinogenicity (plausible)	Resorcinol or 3-aminophenol
		Skin Sensitization (Plausible)	Resorcinol or precursor
			Hydrazine or precursor
	Photoallergenicity (plausible)	Halogenated aromatic compound	
ZINC95390367	2	Bradycardia (equivocal)	Phenylephrine
		Skin sensitization (equivocal)	Phenol replacement or precursor
ZINC12321364	4	Skin sensitization (Plausible)	Catechol or precursor
			Resorcinol or precursor

(continued)

**Table 4** (continued)

Description	Total alerts	Condition	Alert
			Hydrazine or precursor
		Photoallergenicity (plausible)	Coumarin
ZINC12722413	4	Skin sensitization (Plausible)	Phenol replacement or precursor
			Resorcinol or precursor
			Hydrazine or precursor
		Photoallergenicity (plausible)	Coumarin
ZINC91370321	4	Carcinogenicity (equivocal)	Ethanolamine or aminoethiol
		HERG channel inhibition (plausible)	HERG I Pharmacophore
		Hepatotoxicity (plausible)	Thiophene
		Glucocorticoid receptor agonism (plausible)	N-phenethylbenzamide or derivative
ZINC39434305	9	HERG channel inhibition (plausible)	HERG I Pharmacophore
			HERG II Pharmacophore
			HERG III Pharmacophore
		Skin sensitization (equivocal)	Hydrazine or precursor
		Hepatotoxicity (plausible)	Hydrazine
			Benzoamidazole or derivative
		Mitochondrial dysfunction (equivocal)	Hydrazine
		Nephrotoxicity (equivocal)	Hydrazine
		Thyroid toxicity (equivocal)	Benzamide
ZINC5704899	3	Skin sensitization (Plausible)	Phenol replacement or precursor
			Hydrazine or precursor
		Photoallergenicity	Coumarin

It is important to highlight that even if the drug is for oral administration, warnings indicating skin sensitization and photoallergenicity were considered, which are of greater relevance for topical drugs, due to the risks they can bring during the synthesis process.

As observed in the table, it can be inferred that 14 molecules signaled a total of alerts less than or equal to 5 (ZINC19236584, ZINC36743800, ZINC15015563,



ZINC01295640, ZINC04587307, ZINC04116896, ZINC04577677, ZINC06861875, ZINC123740, ZINC12391 two had 7 alerts (ZINC38617611, ZINC38617617) and one with 9 alerts (ZINC39434305). Thus, when compared to the propranolol molecule, in which 5 alerts were signaled, most of the results were favorable for the toxicological analysis.

### 3.7 Activity Prediction: SEA and PASS

Through the “PASS prediction” server, it was possible to determine the activities that the screened molecules present in relation to the symptoms of ET, in order to develop a drug that has a therapeutic activity superior to propranolol.

At the expense of the activity and mechanism of action of the drug propranolol, the variables analyzed in the PASS web server to determine the activity potential were: antiadrenergic activity,  $\beta$ -adrenergic receptor antagonist,  $\beta_1$ -adrenergic receptor antagonist,  $\beta_2$ -receptor antagonist adrenergic and antiparkinsonian/tremor relief (Table 5).

As seen in Table 5, of the 17 molecules analyzed, only 5 presented results in relation to the activity potential for at least one of the variables, it is important to highlight that none of the molecules evaluated presented activity for the relief of tremor. The molecules ZINC95390367 and ZINC91370321 were the ones that

**Table 5** Results of prediction of activity potential and inhibition of molecules screened in ZINCPharmer that presented values in any of the evaluated criteria

Molecules	Pa	Pi	Description
PROPRANOLOL	0.746	0.004	Antiadrenergic
	0.390	0.003	$\beta$ -adrenergic receptor antagonist
	0.282	0.003	$\beta_1$ -adrenergic receptor antagonist
	0.170	0.005	$\beta_2$ -adrenergic receptor antagonist
	0.434	0.008	Antiparkinsonian, tremor relief
ZINC95390367	0.102	0.062	Antiadrenergic
	0.109	0.012	$\beta$ -adrenergic receptor antagonist
	0.098	0.009	$\beta_1$ -adrenergic receptor antagonist
	0.074	0.012	$\beta_2$ -adrenergic receptor antagonist
ZINC19236585	0.092	0.069	Antiadrenergic
	0.067	0.033	$\beta$ -adrenergic receptor antagonist
ZINC91370321	0.197	0.032	Antiadrenergic
ZINC36743800	0.055	0.054	$\beta$ -adrenergic receptor antagonist
ZINC19236584	0.092	0.069	Antiadrenergic
	0.067	0.033	$\beta$ -adrenergic receptor antagonist

**Table 6** Prediction of activity of the molecules sorted in ZINCPharmer on SEA server

Molecules	Description	MAX TC
PROPRANOLOL	Beta-1 adrenergic receptor (B0FL73 CAVPO)	0.46
	Beta-1 adrenergic receptor (B0FL73 CAVPO)	0.47
	Beta-1 adrenergic receptor (ADRB1 RAT)	0.42
	Beta-2 adrenergic receptor (ADRB2 CANLF)	0.42
	Beta-1 adrenergic receptor (ADRB1 HUMAN)	0.42
	Beta-2 adrenergic receptor (ADRB2 HUMAN)	0.42
ZINC95390367	Beta-2 adrenergic receptor (ADRB2 HUMAN)	0.36
	Beta-1 adrenergic receptor (ADRB1 HUMAN)	0.36
<b>ZINC91370321</b>	Beta-2 adrenergic receptor (ADRB2 RAT)	0.30
	Beta-2 adrenergic receptor (ADRB2 HUMAN)	0.48
	Beta-2 adrenergic receptor (ADRB2 BOVIN)	0.37
	Beta-1 adrenergic receptor (ADRB1 MOUSE)	0.29
	Beta-2 adrenergic receptor (ADRB2 MESAU)	0.29

presented the best results among those that were screened, however, they had a lower performance when compared to the propranolol molecule.

As with the other assessments, the prediction in SEA was made in relation to the values given by the drug and prototype. In this server, the potential that molecules have when interacting with the therapeutic target related to the disease to be treated, which in the case in question, essential tremor, was analyzed. Table 6 shows the molecules that showed binding results with  $\beta$ -adrenergic receptors in different types of organisms.

In this server, the criterion that indicates strong binding potential is the “MAX TC” value, in which the closer to 1, the greater the tendency of the molecule to bind to the target/receptor.

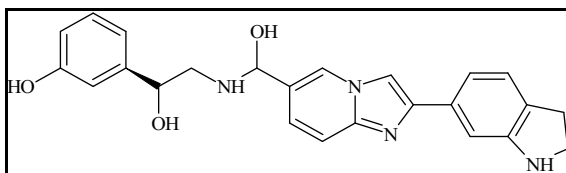
As observed in the table, only two molecules were found to have activity potential in  $\beta$ -adrenergic receptors, the molecule ZINC95390367 being the one that obtained the best results. However, as with PASS, the propranolol molecule had a superior result in this parameter.

### 3.8 Selection and Modification of the Prototype

Evaluating all criteria in each tested segment, it was observed that the molecule that obtained the best results was the description ‘ZINC95390367’ (Fig. 5), in which, despite its performance not being superior to propranolol, when compared to the other molecules tested, presented, in most of the predictions made, superior results.

After selection, the modifications (Fig. 6) were performed according to the pharmacophoric regions, in order to prevent the biological activity potential from not

**Fig. 5** Chemical structure of the molecule selected as a prototype: ZINC95390367



reducing to very low levels [33]. Not only the pharmacophoric model, care was also taken to maintain or improve the pharmacokinetic properties. Therefore, the aromatic regions, the presence of hydrogen donors and acceptors and the hydrophobic regions were maintained, according to the results of the pharmacophoric model, as a way to prevent the reduction of its activity. With this, in order to create other possible structures, some methyls, cyclic groups, electronegative atoms, such as oxygen and nitrogen, were added, in addition to changing the position of some atoms. Not only were they added, but some groups and regions were also removed in order to assess whether they could obtain better results.

Thus, in order to verify whether the modifications had favorable responses when compared to the prototype and to propranolol itself, the pharmacokinetic properties of each modification were analyzed using the Qikprop software (Table 7).

As seen in Table 7, the responses related to human oral absorption and absorption in Caco-2 and MDCK cells, the modified molecules showed results superior to the prototype.

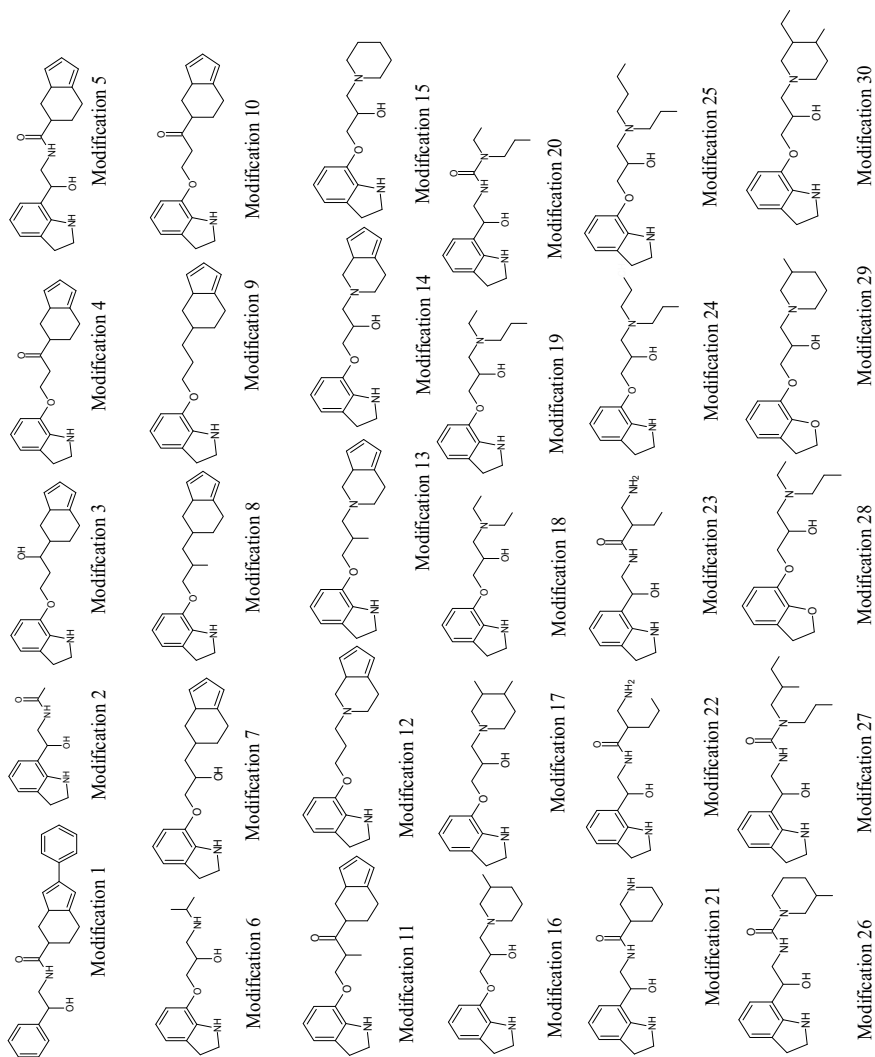
Regarding the action on the CNS, considering a negative response to the high capacity of action at the central level of the molecules, only nine (1, 2, 5, 20, 21, 22, 23, 26 and 27) of the thirty molecules had such a average response, while the rest demonstrated high capacity to exert action in this system. Regarding the brain/blood partition ( $\log_{BB}$ ), all molecules showed negative responses to this study, as they indicate reference values for penetration into the blood–brain barrier.

Of all the molecules analyzed, only eight (2, 3, 5, 20, 21, 23, 26, and 27) showed favorable responses to  $\log_{HERG}$ , that is, they do not present toxicity potential.

To predict the toxicological properties of the modified molecules (Table 8), using the DEREK program, the total number of alerts and which regions responsible for these alerts capable of conferring toxicity on the molecules were evaluated.

As seen in Table 8, it is possible to establish that the toxicological results of the modifications against propranolol were favorable. It is important to point out that only modification 6 showed a response (total alerts) similar to the prototype. But with regard to the rest, no modification had a worse response than those presented by propranolol and prototype.

From the results presented in Table 9, it can be inferred that the responses to the modifications were superior to those of the molecules screened in ZincPharmer, given that the maximum warning that a molecule (modification 6) presented was two: bradycardia and carcinogenicity. Modifications 12, 13, 14, 15, 16, 17, 25, 29 and 30 signaled an alert for HERG channel inhibition. With regard to carcinogenicity, the

**Fig. 6** Chemical structures of modifications made from prototype

**Table 7** Pharmacokinetic properties, obtained in the Qikprop software, of the molecules modified from the prototype

Molecules	AOH	%AOH	pCaco-2	pMDCK	SNC	logBB	logHERG
PROPRANOLOL	3	100.000	802.562	431.502	1	0.034	-6.433
Prototype	3	90.224	296.209	132.804	-2	-1.557	-7.439
1	3	100.000	1.542.867	1.176.738	0	-0.448	-5.453
2	2	63.977	114.047	105.474	0	-0.293	-3.796
3	3	100.000	852.408	460.541	1	0.155	-5.782
4	3	100.000	839.540	453.030	1	0.188	-6.113
5	3	76.519	135.996	130.379	0	-0.317	-4.697
6	2	74.660	165.994	86.920	1	0.373	-6.155
7	3	100.000	810.548	436.144	1	0.133	-5.799
8	3	100.000	1.639.329	933.809	2	0.484	-5.977
9	3	100.000	1.665.677	950.043	2	0.482	-6.385
10	3	100.000	800.107	430.075	1	0.170	-6.097
11	3	100.000	1.005.033	550.283	1	0.271	-6.013
12	3	92.538	378.191	211.673	2	0.841	-7.018
13	3	95.179	433.486	245.314	2	0.911	-6.517
14	3	80.280	177.174	93.265	2	0.481	-6.384
15	2	74.810	142.225	73.549	1	0.372	-6.055
16	3	77.216	158.498	82.685	1	0.430	-5.859
17	3	81.618	208.554	111.241	2	0.533	-6.103
18	3	81.733	299.034	164.220	2	0.575	-5.934
19	3	80.342	195.089	103.499	1	0.304	-6.381
20	3	82.986	312.726	241.437	0	-0.199	-4.215
21	2	49.932	15.233	13.431	0	-0.255	-4.744
22	2	53.842	20.429	14.667	0	-0.522	-5.069
23	2	55.681	32.371	22.476	0	-0.221	-4.702
24	3	83.552	236.534	127.456	1	0.320	-6.512
25	3	86.070	246.704	133.390	1	0.268	-6.664
26	3	76.101	150.318	129.350	0	-0.267	-4.160
27	3	89.402	356.346	265.919	0	-0.301	-4.420
28	3	100.000	1.573.679	893.455	1	0.221	-5.582
29	3	100.000	1.172.081	649.778	1	0.269	-5.708
30	3	80.482	167.949	88.028	1	0.410	-5.628

**Table 8** Prediction of toxicological properties, in the DEREK program, of modified molecules

Molecules	Total alerts	Condition	Alert
Propranolol	5	Bladder Disorder (equivocal)	Bisoprolol
		Bradycardia (equivocal)	Esmolol
		Carcinogenicity (equivocal)	Ethanolamine or aminoethanethiol
		HERG channel inhibition (plausible)	HERG I Pharmacophore
Prototype	2	Bradycardia (equivocal)	Phenylephrine
		Skin sensitization (equivocal)	Phenol replacement or precursor
Modification 1	0	–	–
Modification 2	0	–	–
Modification 3	0	–	–
Modification 4	0	–	–
Modification 5	0	–	–
Modification 6	2	Bradycardia (equivocal)	Esmolol
		Carcinogenicity (equivocal)	Ethanolamine or aminoethanethiol
Modification 7	0	–	–
Modification 8	0	–	–
Modification 9	0	–	–
Modification 10	0	–	–
Modification 11	0	–	–
Modification 12	1	HERG channel inhibition (plausible)	HERG I Pharmacophore
Modification 13	1	HERG channel inhibition (plausible)	HERG I Pharmacophore
Modification 14	1	HERG channel inhibition (plausible)	HERG I Pharmacophore
Modification 15	1	HERG channel inhibition (plausible)	HERG I Pharmacophore
Modification 16	1	HERG channel inhibition (plausible)	HERG I Pharmacophore
Modification 17	1	HERG channel inhibition (plausible)	HERG I Pharmacophore
Modification 18	1	Carcinogenicity (equivocal)	Ethanolamine or aminoethanethiol
Modification 19	1	Carcinogenicity (equivocal)	Ethanolamine or aminoethanethiol
Modification 20	0	–	–

(continued)

**Table 8** (continued)

Molecules	Total alerts	Condiction	Alert
Modification 21	0	–	–
Modification 22	0	–	–
Modification 23	0	–	–
Modification 24	1	Carcinogenicity (equivocal)	Ethanolamine or aminoethanethiol
Modification 25	2	Carcinogenicity (equivocal) HERG channel inhibition	Ethanolamine or aminoethanethiol HERG I Pharmacophore
Modification 26	0	–	–
Modification 27	0	–	–
Modification 28	1	Carcinogenicity (equivocal)	Ethanolamine or aminoethanethiol
Modification 29	1	HERG channel inhibition (plausible)	HERG I Pharmacophore
Modification 30	1	HERG channel inhibition (plausible)	HERG I Pharmacophore

Source Own authorhip

**Table 9** Results of the prediction of the activity potential or inhibition of molecules by the 'PASS Prediction' program of the modified molecules

Molecules	Pa	Pi	Description
Propranolol	0.746	0.004	Antiadrenergic
	0.390	0.003	$\beta$ -adrenergic receptor antagonist
	0.282	0.003	$\beta_1$ -adrenergic receptor antagonist
	0.170	0.005	$\beta_2$ -adrenergic receptor antagonist
	0.434	0.008	Antiparkinsonian, tremor relief
Prototype	0.102	0.062	Antiadrenergic
	0.109	0.012	$\beta$ -adrenergic receptor antagonist
	0.098	0.009	$\beta_1$ -adrenergic receptor antagonist
	0.074	0.012	$\beta_2$ -adrenergic receptor antagonista
Modification 1	0.224	0.027	Antiadrenergic
	0.098	0.015	$\beta$ -adrenergic receptor antagonist
	0.114	0.025	$\beta_1$ -adrenergic receptor antagonist

(continued)

**Table 9** (continued)

Molecules	Pa	Pi	Description
	–	–	$\beta_2$ -adrenergic receptor antagonist
	0.226	0.061	Antiparkinsonian, tremor relief
Modification 2	0.160	0.040	Antiadrenergic
	0.162	0.007	$\beta$ -adrenergic receptor antagonist
	0.127	0.007	$\beta_1$ -adrenergic receptor antagonist
	0.126	0.006	$\beta_2$ -adrenergic receptor antagonist
	0.189	0.079	Antiparkinsonian, tremor relief
Modification 3	0.173	0.037	Antiadrenergic
	0.094	0.016	$\beta$ -adrenergic receptor antagonist
	0.050	0.028	$\beta_1$ -adrenergic receptor antagonist
	0.061	0.017	$\beta_2$ -adrenergic receptor antagonist
	0.190	0.079	Antiparkinsonian, tremor relief
Modification 4	0.097	0.065	Antiadrenergic
	–	–	$\beta$ -adrenergic receptor antagonist
	–	–	$\beta_1$ -adrenergic receptor antagonist
	–	–	$\beta_2$ -adrenergic receptor antagonist
	0.149	0.107	Antiparkinsonian, tremor relief
Modification 5	0.218	0.028	Antiadrenergic
	0.096	0.015	$\beta$ -adrenergic receptor antagonist
	0.087	0.011	$\beta_1$ -adrenergic receptor antagonist
	0.078	0.050	$\beta_2$ -adrenergic receptor antagonist
	0.195	0.076	Antiparkinsonian, tremor relief
Modification 6	0.866	0.004	Antiadrenergic
	0.548	0.002	$\beta$ -adrenergic receptor antagonist
	0.341	0.003	$\beta_1$ -adrenergic receptor antagonist
	0.404	0.002	$\beta_2$ -adrenergic receptor antagonist
	0.414	0.010	Antiparkinsonian, tremor relief
Modification 7	0.267	0.020	Antiadrenergic
	0.084	0.020	$\beta$ -adrenergic receptor antagonist
	0.049	0.029	$\beta_1$ -adrenergic receptor antagonist
	0.059	0.018	$\beta_2$ -adrenergic receptor antagonist
	0.182	0.083	Antiparkinsonian, tremor relief
Modification 8	–	–	Antiadrenergic
	–	–	$\beta$ -adrenergic receptor antagonist

(continued)



**Table 9** (continued)

Molecules	Pa	Pi	Description
	–	–	$\beta_1$ -adrenergic receptor antagonist
	–	–	$\beta_2$ -adrenergic receptor antagonist
	0.205	0.071	Antiparkinsonian, tremor relief
Modification 9	0.172	0.037	Antiadrenergic
	0.060	0.045	$\beta$ -adrenergic receptor antagonist
	–	–	$\beta_1$ -adrenergic receptor antagonist
	–	–	$\beta_2$ -adrenergic receptor antagonist
	0.211	0.068	Antiparkinsonian, tremor relief
Modification 10	0.097	0.065	Antiadrenergic
	–	–	$\beta$ -adrenergic receptor antagonist
	–	–	$\beta_1$ -adrenergic receptor antagonist
	–	–	$\beta_2$ -adrenergic receptor antagonist
	0.149	0.107	Antiparkinsonian, tremor relief
Modification 11	–	–	Antiadrenergic
	–	–	$\beta$ -adrenergic receptor antagonist
	–	–	$\beta_1$ -adrenergic receptor antagonist
	–	–	$\beta_2$ -adrenergic receptor antagonist
	0.157	0.100	Antiparkinsonian, tremor relief
Modification 12	0.376	0.011	Antiadrenergic
	–	–	$\beta$ -adrenergic receptor antagonist
	–	–	$\beta_1$ -adrenergic receptor antagonist
	–	–	$\beta_2$ -adrenergic receptor antagonist
	0.229	0.060	Antiparkinsonian, tremor relief
Modification 13	0.199	0.031	Antiadrenergic
	–	–	$\beta$ -adrenergic receptor antagonist
	–	–	$\beta_1$ -adrenergic receptor antagonist
	–	–	$\beta_2$ -adrenergic receptor antagonist
	0.153	0.104	Antiparkinsonian, tremor relief
Modification 14	0.578	0.005	Antiadrenergic
	–	–	$\beta$ -adrenergic receptor antagonist
	0.060	0.021	$\beta_1$ -adrenergic receptor antagonist
	0.065	0.015	$\beta_2$ -adrenergic receptor antagonist

(continued)

**Table 9** (continued)

Molecules	Pa	Pi	Description
	0.256	0.049	Antiparkinsonian, tremor relief
Modification 15	0.599	0.005	Antiadrenergic
	0.178	0.005	$\beta$ -adrenergic receptor antagonist
	0.104	0.008	$\beta_1$ -adrenergic receptor antagonist
	0.113	0.007	$\beta_2$ -adrenergic receptor antagonist
	0.358	0.019	Antiparkinsonian, tremor relief
Modification 16	0.448	0.008	Antiadrenergic
	0.131	0.009	$\beta$ -adrenergic receptor antagonist
	0.066	0.017	$\beta_1$ -adrenergic receptor antagonist
	0.068	0.014	$\beta_2$ -adrenergic receptor antagonist
	0.346	0.022	Antiparkinsonian, tremor relief
Modification 17	0.399	0.010	Antiadrenergic
	0.134	0.009	$\beta$ -adrenergic receptor antagonist
	0.055	0.024	$\beta_1$ -adrenergic receptor antagonist
	0.058	0.019	$\beta_2$ -adrenergic receptor antagonist
	0.288	0.038	Antiparkinsonian, tremor relief
Modification 18	0.603	0.005	Antiadrenergic
	0.260	0.004	$\beta$ -adrenergic receptor antagonist
	0.151	0.005	$\beta_1$ -adrenergic receptor antagonist
	0.137	0.006	$\beta_2$ -adrenergic receptor antagonist
	0.474	0.005	Antiparkinsonian, tremor relief
Modification 19	0.555	0.005	Antiadrenergic
	0.299	0.003	$\beta$ -adrenergic receptor antagonist
	0.191	0.004	$\beta_1$ -adrenergic receptor antagonist
	0.179	0.005	$\beta_2$ -adrenergic receptor antagonist
	0.524	0.004	Antiparkinsonian, tremor relief
Modification 20	0.211	0.029	Antiadrenergic
	0.167	0.006	$\beta$ -adrenergic receptor antagonist
	0.179	0.004	$\beta_1$ -adrenergic receptor antagonist
	0.193	0.004	$\beta_2$ -adrenergic receptor antagonist
	0.302	0.033	Antiparkinsonian, tremor relief
Modification 21	0.212	0.029	Antiadrenergic
	0.115	0.011	$\beta$ -adrenergic receptor antagonist
	0.114	0.008	$\beta_1$ -adrenergic receptor antagonist

(continued)

**Table 9** (continued)

Molecules	Pa	Pi	Description
	0.071	0.013	$\beta_2$ -adrenergic receptor antagonist
	0.186	0.081	Antiparkinsonian, tremor relief
Modification 22	–	–	Antiadrenergic
	0.084	0.020	$\beta$ -adrenergic receptor antagonist
	0.055	0.024	$\beta_1$ -adrenergic receptor antagonist
	0.058	0.019	$\beta_2$ -adrenergic receptor antagonist
	0.188	0.080	Antiparkinsonian, tremor relief
Modification 23	–	–	Antiadrenergic
	0.078	0.024	$\beta$ -adrenergic receptor antagonist
	0.053	0.026	$\beta_1$ -adrenergic receptor antagonist
	0.052	0.022	$\beta_2$ -adrenergic receptor antagonist
	0.133	0.123	Antiparkinsonian, tremor relief
Modification 24	0.609	0.005	Antiadrenergic
	0.340	0.003	$\beta$ -adrenergic receptor antagonist
	0.237	0.004	$\beta_1$ -adrenergic receptor antagonist
	0.214	0.004	$\beta_2$ -adrenergic receptor antagonist
	0.456	0.006	Antiparkinsonian, tremor relief
Modification 25	0.566	0.005	Antiadrenergic
	0.351	0.003	$\beta$ -adrenergic receptor antagonist
	0.267	0.005	$\beta_1$ -adrenergic receptor antagonist
	0.231	0.004	$\beta_2$ -adrenergic receptor antagonist
	0.446	0.007	Antiparkinsonian, tremor relief
Modification 26	0.323	0.014	Antiadrenergic
	0.121	0.010	$\beta$ -adrenergic receptor antagonist
	0.104	0.009	$\beta_1$ -adrenergic receptor antagonist
	0.062	0.017	$\beta_2$ -adrenergic receptor antagonist
	0.202	0.072	Antiparkinsonian, tremor relief
Modification 27	0.133	0.048	Antiadrenergic
	0.098	0.015	$\beta$ -adrenergic receptor antagonist
	0.094	0.048	$\beta_1$ -adrenergic receptor antagonist
	0.095	0.008	$\beta_2$ -adrenergic receptor antagonist
	0.192	0.078	Antiparkinsonian, tremor relief
Modification 28	0.595	0.005	Antiadrenergic
	0.264	0.004	$\beta$ -adrenergic receptor antagonist

(continued)

**Table 9** (continued)

Molecules	Pa	Pi	Description
	0.192	0.004	$\beta_1$ -adrenergic receptor antagonist
	0.064	0.016	$\beta_2$ -adrenergic receptor antagonist
	0.457	0.006	Antiparkinsonian, tremor relief
Modification 29	0.487	0.007	Antiadrenergic
	0.111	0.012	$\beta$ -adrenergic receptor antagonist
	0.064	0.018	$\beta_1$ -adrenergic receptor antagonist
	–	–	$\beta_2$ -adrenergic receptor antagonist
	0.292	0.036	Antiparkinsonian, tremor relief
Modification 30	0.394	0.014	Antiadrenergic
	0.115	0.011	$\beta$ -adrenergic receptor antagonist
	0.044	0.034	$\beta_1$ -adrenergic receptor antagonist
	0.047	0.025	$\beta_2$ -adrenergic receptor antagonist
	0.257	0.057	Antiparkinsonian, tremor relief

signaled molecules were numbers 18, 19, 24, 25 and 28. The remainder, comprising a total of 17 molecules, did not show any type of signaling with regard to toxicity.

Regarding the activity prediction (Table 9), performed in the “PASS prediction” program, all 30 modifications presented superior results to the prototype, being important to show that some of them (6, 18, 19, 24, 25 and 28) are stood out for having values, in most descriptors, equal to or higher than the prototype and the propranolol molecule itself.

Compared to the first analysis, the prediction results in the SEA web server (Table 10) were higher than the values presented by the prototype. However, when compared

**Table 10** Results of activity predictions by the ‘SEA Prediction’ online server of the modified molecules

Molecules	Description	MAX TC
Propranolol	Beta-1 adrenergic receptor (B0FL73 CAVPO)	0.46
	Beta-2 adrenergic receptor (B0FL73 CAVPO)	0.47
	Beta-1 adrenergic receptor (ADRB1 RAT)	0.42
	Beta-2 adrenergic receptor (ADRB2 CANLF)	0.42
	Beta-1 adrenergic receptor (ADRB1 HUMAN)	0.42
	Beta-2 adrenergic receptor (ADRB2 HUMAN)	0.42
Prototype	Beta-2 adrenergic receptor (ADRB2 HUMAN)	0.36
	Beta-1 adrenergic receptor (ADRB1 HUMAN)	0.36
Modification 1	Beta-1 adrenergic receptor (B0FL73 CAVPO)	0.56
	Beta-2 adrenergic receptor (ADRB2_CAVPO)	0.60

(continued)

**Table 10** (continued)

Molecules	Description	MAX TC
	Beta-1 adrenergic receptor (ADRB1 RAT)	0.56
	Beta-2 adrenergic receptor (ADRB2_BOVIN)	0.56
	Beta-2 adrenergic receptor (ADRB2_CANLF)	0.56
	Beta-2 adrenergic receptor (ADRB2_MOUSE)	0.36
	Beta-1 adrenergic receptor (ADRB1_HUMAN)	0.56
	Beta-2 adrenergic receptor (ADRB2_HUMAN)	0.56
Modification 14	Beta-1 adrenergic receptor (ADRB1 RAT)	0.36
	Beta-2 adrenergic receptor (ADRB2_CANLF)	0.35
	Beta-1 adrenergic receptor (ADRB1_HUMAN)	0.34
	Beta-2 adrenergic receptor (ADRB2_HUMAN)	0.34
Modification 15	Beta-1 adrenergic receptor (B0FL73_CAVPO)	0.31
	Beta-2 adrenergic receptor (ADRB2_CAVPO)	0.32
	Beta-1 adrenergic receptor (ADRB1 RAT)	0.42
	Beta-2 adrenergic receptor (ADRB2_BOVIN)	0.32
	Beta-2 adrenergic receptor (ADRB2_CANLF)	0.43
	Beta-1 adrenergic receptor (ADRB1_HUMAN)	0.42
	Beta-2 adrenergic receptor (ADRB2_HUMAN)	0.46
	Beta-2 adrenergic receptor (ADRB2_HUMAN)	0.46
Modification 16	Beta-1 adrenergic receptor (B0FL73_CAVPO)	0.33
	Beta-2 adrenergic receptor (ADRB2_CAVPO)	0.32
	Beta-1 adrenergic receptor (ADRB1 RAT)	0.38
	Beta-2 adrenergic receptor (ADRB2_BOVIN)	0.34
	Beta-2 adrenergic receptor (ADRB2_CANLF)	0.38
	Beta-1 adrenergic receptor (ADRB1_HUMAN)	0.39
	Beta-2 adrenergic receptor (ADRB2_HUMAN)	0.39
	Beta-2 adrenergic receptor (ADRB2_HUMAN)	0.39
Modification 17	Beta-1 adrenergic receptor (ADRB1 RAT)	0.36
	Beta-2 adrenergic receptor (ADRB2_CANLF)	0.39
	Beta-1 adrenergic receptor (ADRB1_HUMAN)	0.40
	Beta-2 adrenergic receptor (ADRB2_HUMAN)	0.40
Modification 18	Beta-1 adrenergic receptor (B0FL73_CAVPO)	0.30
	Beta-2 adrenergic receptor (ADRB2_CAVPO)	0.33
	Beta-1 adrenergic receptor (ADRB1 RAT)	0.32
	Beta-2 adrenergic receptor (ADRB2_BOVIN)	0.33
	Beta-2 adrenergic receptor (ADRB2_CANLF)	0.32

(continued)

**Table 10** (continued)

Molecules	Description	MAX TC
Modification 19	Beta-1 adrenergic receptor (B0FL73 CAVPO)	0.30
	Beta-2 adrenergic receptor (ADRB2_CAVPO)	0.32
	Beta-1 adrenergic receptor (ADRB1 RAT)	0.31
	Beta-2 adrenergic receptor (ADRB2_BOVIN)	0.31
	Beta-2 adrenergic receptor (ADRB2_CANLF)	0.30
Modification 24	Beta-1 adrenergic receptor (B0FL73 CAVPO)	0.31
	Beta-2 adrenergic receptor (ADRB2_CAVPO)	0.33
	Beta-1 adrenergic receptor (ADRB1 RAT)	0.31
	Beta-2 adrenergic receptor (ADRB2_BOVIN)	0.32
	Beta-2 adrenergic receptor (ADRB2_CANLF)	0.31
Modification 25	Beta-2 adrenergic receptor (ADRB2_CAVPO)	0.31
	Beta-1 adrenergic receptor (ADRB1 RAT)	0.30
	Beta-2 adrenergic receptor (ADRB2_BOVIN)	0.30
	Beta-2 adrenergic receptor (ADRB2_CANLF)	0.29
Modification 28	Beta-1 adrenergic receptor (B0FL73 CAVPO)	0.30
	Beta-2 adrenergic receptor (ADRB2_CAVPO)	0.32
	Beta-2 adrenergic receptor (ADRB2_BOVIN)	0.31
	Beta-2 adrenergic receptor (ADRB2_CANLF)	0.30
Modification 29	Beta-2 adrenergic receptor (ADRB2_CAVPO)	0.30
	Beta-1 adrenergic receptor (ADRB1 RAT)	0.36
	Beta-2 adrenergic receptor (ADRB2_BOVIN)	0.32
	Beta-2 adrenergic receptor (ADRB2_CANLF)	0.36
	Beta-1 adrenergic receptor (ADRB1 HUMAN)	0.41
	Beta-2 adrenergic receptor (ADRB2 HUMAN)	0.41
Modification 30	Beta-1 adrenergic receptor (ADRB1 RAT)	0.35
	Beta-2 adrenergic receptor (ADRB2_BOVIN)	0.32
	Beta-2 adrenergic receptor (ADRB2_CANLF)	0.37
	Beta-1 adrenergic receptor (ADRB1 HUMAN)	0.37
	Beta-2 adrenergic receptor (ADRB2 HUMAN)	0.37

to the propranolol molecule, only one modification (1) showed higher values for all types of targets evaluated in the program.

According to the predictions, it was observed that some modifications (1, 2, 5, 20, 26 and 27) had a better performance in the pharmacokinetic parameters (QikProp), especially when taking into account the low probability of penetration into the CNS, others had better results in activity prediction (6, 18, 19, 24, 25 and 28) in 'Pass prediction', when compared to the results of propranolol and prototype. Regarding SEA, only molecule 1 showed superior results to propranolol and prototype. In the

toxicological parameter, all had a favorable result. Thus, for this research, to perform molecular docking, the following modifications were selected: 1, 2, 5, 6, 18, 19, 20, 25, 26, 27 and 28.

### 3.9 Molecular Docking of Modifications

#### 3.9.1 $\beta$ 1-Adrenergic Receptor

In the validation of the crystallographic structure of the target protein (PDB ID: 7BVQ) with the ligand (carazolol), the value of 0.600 Å was obtained as a result of the RMSD calculation. It is considered as indicative of a good result when the RMSD is less than 2 Å, since it assumes that a correct fit of the ligand occurred in an adequate spatial orientation in the target [45]. The validation radius was 9.345 and the coordinates of origin:  $x = 21.59$ ;  $y = -21.88$ ;  $z = 2.89$ .

The resulting Score given was 86.46, which is nothing more than a value provided by the program itself, which allows establishing the best conformation of the ligand in the active site, that is, the program modulates which are the best ways of fitting that the molecule can do it, providing quantitative data.

According to the origin coordinates obtained in the validation, the binding site was defined for the start of docking. As seen in Fig. 7, all linkers are located in the same region, with many interacting with the same amino acid residues.

It is important to highlight that the analysis was performed based on a comparison with the docking of the propranolol molecule itself (Table 11). In other words, to establish whether the prototype and the modifications had greater interactions with the target than propranolol, the amounts and types of interactions that occurred between ligand and receptor were then analyzed, in order to establish the best ligand-receptor fit. receiver.

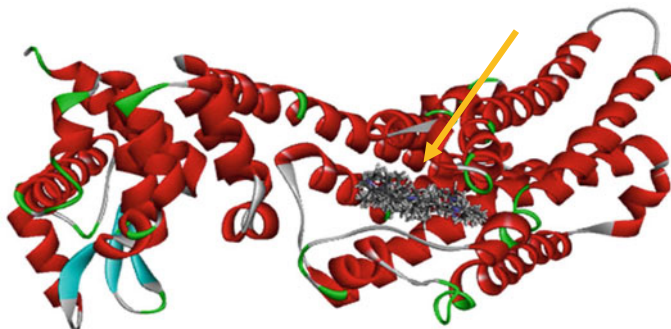


Fig. 7 Overlap of propranolol molecules, prototype and  $\beta$ 1 adrenergic receptor modifications

**Table 11** Propranolol docking, prototype and selected modifications in  $\beta 1$  adrenergic receptor

Molecule	Amino acid	Ligand atoms	Category	Type	Distance
Propranolol	ASN426	H32	Hydrogen bond	Conventional hydrogen bond	2.06
	ASN426	H33	Hydrogen bond	Conventional hydrogen bond	2.09
	PHE404	Ligand	Hydrophobic	Pi-Pi T-shaped	5.01
	PHE404	Ligand	Hydrophobic	Pi-Pi T-shaped	4.72
	PHE335	C18	Hydrophobic	Pi-Alkyl	5.10
	PHE403	C18	Hydrophobic	Pi-Alkyl	5.01
	PHE403	C19	Hydrophobic	Pi-Alkyl	5.47
	PHE422	C18	Hydrophobic	Pi-Alkyl	4.82
	PHE422	C19	Hydrophobic	Pi-Alkyl	4.57
	VAL256	Ligand	Hydrophobic	Pi-Alkyl	4.98
	VAL256	Ligand	Hydrophobic	Pi-Alkyl	4.15
	VAL259	Ligand	Hydrophobic	Pi-Alkyl	4.91
Prototype	SER345	H37	Hydrogen bond	Conventional hydrogen bond	2.67
	ASP255	H43	Hydrogen bond	Conventional hydrogen bond	2.03
	ASP255	H39	Hydrogen bond	Carbon hydrogen bond	2.44
	ASP255	H42	Hydrogen bond	Carbon hydrogen bond	3.03
	ASN426	H46	Hydrogen bond	Carbon hydrogen bond	3.09
	ASP334	H52	Hydrogen bond	Carbon hydrogen bond	2.88
	PHE335	Ligand	Hydrophobic	Pi-Sigma	2.51
	PHE335	Ligand	Hydrophobic	Pi-Pi T-shaped	4.93
	PHE403	Ligand	Hydrophobic	Pi-Pi T-shaped	4.93
	PHE404	Ligand	Hydrophobic	Pi-Pi T-shaped	4.76
	VAL256	Ligand	Hydrophobic	Pi-Alkyl	4.12
	VAL259	Ligand	Hydrophobic	Pi-Alkyl	5.04
	Mod. 1	ASP255	H36	Hydrogen bond	Carbon hydrogen bond
PHE404		Ligand	Hydrophobic	Pi-Pi T-shaped	4.73
PHE422		Ligand	Hydrophobic	Pi-Pi T-shaped	5.20
PHE335		Ligand	Hydrophobic	Pi-Alkyl	5.43
VAL256		Ligand	Hydrophobic	Pi-Alkyl	4.11

(continued)



**Table 11** (continued)

Molecule	Amino acid	Ligand atoms	Category	Type	Distance
Mod. 2	VAL259	Ligand	Hydrophobic	Pi-Alkyl	4.58
	ASN407	O16	Hydrogen bond	Conventional hydrogen bond	2.02
	ALA342	O16	Hydrogen bond	Carbon hydrogen bond	2.79
	VAL256	Ligand	Hydrophobic	Pi-Sigma	2.79
	PHE404	Ligand	Hydrophobic	Pi-Pi T-shaped	5.15
	PHE403	Ligand	Hydrophobic	Pi-Alkyl	4.55
Mod. 5	VAL259	Ligand	Hydrophobic	Pi-Alkyl	4.62
	ASN426	H43	Hydrogen bond	Conventional hydrogen bond	2.07
	ASP255	H48	Hydrogen bond	Conventional hydrogen bond	1.93
	ASN426	H30	Hydrogen bond	Carbon hydrogen bond	2.84
	TRP251	ligand	Hydrophobic	Pi-Pi T-shaped	5.03
	VAL256	Ligand	Hydrophobic	Alkyl	4.57
	VAL259	Ligand	Hydrophobic	Alkyl	4.96
	PHE403	Ligand	Hydrophobic	Pi-Alkyl	5.19
	PHE404	Ligand	Hydrophobic	Pi-Alkyl	5.35
	TRP427	Ligand	Hydrophobic	Pi-Alkyl	4.72
Mod. 6	ASN426	H27	Hydrogen bond	Conventional hydrogen bond	1.74
	ASN426	H37	Hydrogen bond	Conventional hydrogen bond	1.98
	ASN426	H24	Hydrogen bond	Carbon hydrogen bond	2.90
	SER345	H33	Hydrogen bond	Carbon hydrogen bond	2.54
	VAL256	Ligand	Hydrophobic	Pi-Sigma	2.85
	PHE403	Ligand	Hydrophobic	Pi-Pi T-shaped	5.44
	VAL256	Ligand	Hydrophobic	Alkyl	4.51
	VAL423	C18	Hydrophobic	Alkyl	4.45
	PHE404	Ligand	Hydrophobic	Pi-Alkyl	4.95
	PHE422	C13	Hydrophobic	Pi-Alkyl	4.76
	PHE422	C18	Hydrophobic	Pi-Alkyl	4.49
	VAL259	Ligand	Hydrophobic	Pi-Alkyl	4.71
Mod.18	ASN426	O19	Hydrogen bond	Conventional hydrogen bond	2.53

(continued)

**Table 11** (continued)

Molecule	Amino acid	Ligand atoms	Category	Type	Distance
	ASP255	H43	Hydrogen bond	Conventional hydrogen bond	1.84
	ASN426	H25	Hydrogen bond	Carbon hydrogen bond	2.81
	ASN426	H26	Hydrogen bond	Carbon hydrogen bond	3.07
	ASN426	H29	Hydrogen bond	Carbon hydrogen bond	2.35
	PHE404	Ligand	Hydrophobic	Pi-Pi T-shaped	4.82
	TRP251	C12	Hydrophobic	Pi-Alkyl	5.05
	PHE335	C13	Hydrophobic	Pi-Alkyl	4.34
	PHE404	Ligand	Hydrophobic	Pi-Alkyl	4.85
	VAL256	Ligand	Hydrophobic	Pi-Alkyl	4.08
	VAL259	Ligand	Hydrophobic	Pi-Alkyl	4.52
	Mod. 19	TYR430	O19	Hydrogen bond	Conventional hydrogen bond
ASN426		H43	Hydrogen bond	Conventional hydrogen bond	1.66
ASN426		H25	Hydrogen bond	Carbon hydrogen bond	2.96
ASP255		H26	Hydrogen bond	Carbon hydrogen bond	2.53
ASN426		H30	Hydrogen bond	Carbon hydrogen bond	3.0
VAL256		Ligand	Hydrophobic	Pi-Sigma	2.68
PHE403		C12	Hydrophobic	Pi-Alkyl	4.64
PHE404		Ligand	Hydrophobic	Pi-Alkyl	5.16
PHE422		C12	Hydrophobic	Pi-Alkyl	4.77
VAL259		Ligand	Hydrophobic	Pi-Alkyl	4.69
Mod. 20	PHE335	O21	Hydrogen bond	Conventional hydrogen bond	2.16
	ASN426	H28	Hydrogen bond	Conventional hydrogen bond	2.04
	ASP255	H46	Hydrogen bond	Conventional hydrogen bond	2.20
	ASN426	H25	Hydrogen bond	Carbon hydrogen bond	2.36
	ASN426	H31	Hydrogen bond	Carbon hydrogen bond	2.29

(continued)

**Table 11** (continued)

Molecule	Amino acid	Ligand atoms	Category	Type	Distance
	ASP455	H40	Hydrogen bond	Carbon hydrogen bond	2.99
	PHE403	Ligand	Hydrophobic	Pi-Pi T-shaped	4.61
	VAL423	C15	Hydrophobic	Alkyl	3.82
	VAL256	Ligand	Hydrophobic	Alkyl	4.38
	VAL259	Ligand	Hydrophobic	Alkyl	3.99
	TRP427	C15	Hydrophobic	Pi-Alkyl	4.99
Mod. 24	ASN426	H43	Hydrogen bond	Conventional hydrogen bond	1.89
	SER345	H39	Hydrogen Bond	Carbon hydrogen bond	2.57
	VAL256	Ligand	Hydrophobic	Pi-Sigma	2.76
	PHE403	Ligand	Hydrophobic	Pi-Pi T-shaped	5.56
	VAL256	Ligand	Hydrophobic	Alkyl	4.50
	TRP251	C15	Hydrophobic	Pi-Alkyl	5.20
	PHE404	Ligand	Hydrophobic	Pi-Alkyl	4.94
	PHE422	C14	Hydrophobic	Pi-Alkyl	5.22
	VAL259	Ligand	Hydrophobic	Pi-Alkyl	4.66
Mod. 25	ASP255	H44	Hydrogen bond	Conventional hydrogen bond	2.11
	TRP251	Ligand	Hydrophobic	Pi-Pi T-shaped	4.99
	VAL259	C15	Hydrophobic	Alkyl	4.55
	ILE235	Ligand	Hydrophobic	Alkyl	5.02
	TRP400	C15	Hydrophobic	Pi-Alkyl	4.93
	PHE403	C15	Hydrophobic	Pi-Alkyl	4.40
	PHE404	C21	Hydrophobic	Pi-Alkyl	5.20
	TRP427	Ligand	Hydrophobic	Pi-Alkyl	4.59
	TRP427	Ligand	Hydrophobic	Pi-Alkyl	5.27
	ILE235	Ligand	Hydrophobic	Pi-Alkyl	5.36
Mod. 26	ASP255	H45	Hydrogen bond	Conventional hydrogen bond	2.03
	PHE335	Ligand	Hydrophobic	Pi-Pi T-shaped	5.22
	VAL256	Ligand	Hydrophobic	Alkyl	4.31
	VAL259	Ligand	Hydrophobic	Alkyl	4.87
	PHE404	Ligand	Hydrophobic	Pi-Alkyl	4.59
	PHE404	C19	Hydrophobic	Pi-Alkyl	5.40
Mod. 27	ASN426	H31	Hydrogen bond	Conventional hydrogen bond	2.83

(continued)

**Table 11** (continued)

Molecule	Amino acid	Ligand atoms	Category	Type	Distance
	ASP255	H29	Hydrogen bond	Carbon hydrogen bond	2.87
	ASN426	H30	Hydrogen bond	Carbon hydrogen bond	2.94
	CYS333	H33	Hydrogen bond	Carbon hydrogen bond	3.04
	PHE403	Ligand	Hydrophobic	Pi-Pi T-shaped	5.17
	VAL256	Ligand	Hydrophobic	Alkyl	4.48
	ILE235	C22	Hydrophobic	Alkyl	4.03
	TRP251	C23	Hydrophobic	Pi-Alkyl	5.12
	PHE404	Ligand	Hydrophobic	Pi-Alkyl	5.13
	PHE422	C15	Hydrophobic	Pi-Alkyl	5.36
	VAL256	Ligand	Hydrophobic	Pi-Alkyl	4.62
	VAL259	Ligand	Hydrophobic	Pi-Alkyl	4.82
	Mod. 28	ASN426	H42	Hydrogen bond	Conventional hydrogen bond
ASN426		H25	Hydrogen bond	Carbon hydrogen bond	2.44
VAL256		Ligand	Hydrophobic	Alkyl	4.05
TRP251		C15	Hydrophobic	Pi-Alkyl	5.38
PHE404		Ligand	Hydrophobic	Pi-Alkyl	5.08
PHE422		C12	Hydrophobic	Pi-Alkyl	5.22
VAL256		Ligand	Hydrophobic	Pi-Alkyl	5.44
VAL259		Ligand	Hydrophobic	Pi-Alkyl	5.07

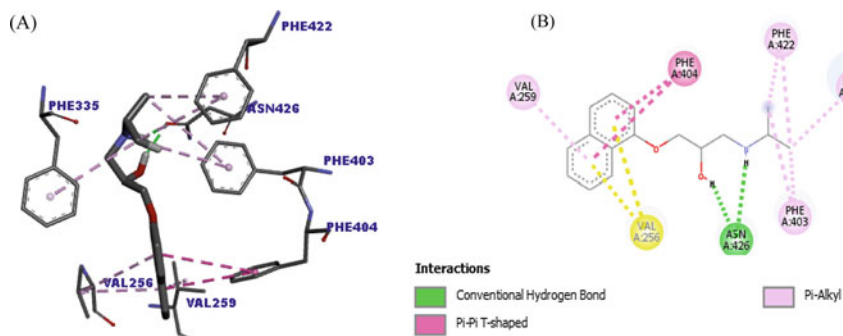


**Fig. 8** Result of the molecular docking of propranolol. **A** 3D model; **B** 2D model. Intermolecular interactions are represented by the colors: hydrogen bonds (green color), pi-pi T-shaped (darker pink color), pi-alkyl (light pink and yellow color for VAL256)

In the propranolol docking (Fig. 8), it was possible to observe two hydrogen bonds, of the conventional type between the atoms H32 and H33 and the O atom of the residue of the amino acid ASN426, at a distance of 2.06 and 2.99 Å, respectively. Hydrogen bonds are considered as one of the strongest intermolecular interactions, due to the high polarity involved in the bond (by the donor hydrogen with an electronegative atom) and the need for closer approximation between the molecules, due to the size of the hydrogen atom [31, 57].

Hydrophobic interactions also occurred, in which two were of the pi-pi T-shaped type. This type of interaction happens in cyclic systems, composed of hybrid atoms ( $sp^2$ ), that is, they establish a double bond between carbons, such as aromatic rings, in which it forms a specific angle of the centroid of each ring (T shape), hence the name “T-shaped” [31, 57]. In the case of the docking in question, there were two interactions between the aromatic portion of PHE404 with the naphthalene ring of propranolol (two benzene rings), with distances of 5.01 and 4.72 Å. The other type of hydrophobic interaction that occurred was the pi-alkyl type, in which it is configured by the link between the alkyl portion with a cyclic ring composed of  $sp^2$  hybrid atoms and, in total, six interactions of this type were found, with amino acids PHE403, PHE402, VAL256 and VAL259.

Thus, the propranolol molecule made a total of twelve interactions with different amino acids present in the active site. This configures, for the present study, that molecules with amounts of interactions equal to or greater than those of propranolol will be considered more, as this may be an indication of a higher action activity. Not only will the quantity be evaluated, but also which types of interactions occur, since there are stronger intermolecular bonds than others, which also influence the analysis.

The prototype (Fig. 9) presented six hydrogen bond-type interactions, two of which were conventional, with the interaction between the atoms of the ligand H37 and H43 with carboline groups from the amino acid residues SER345 and ASP255, in that order. The distance between SER345 and binder H37 was 2.67 Å and between

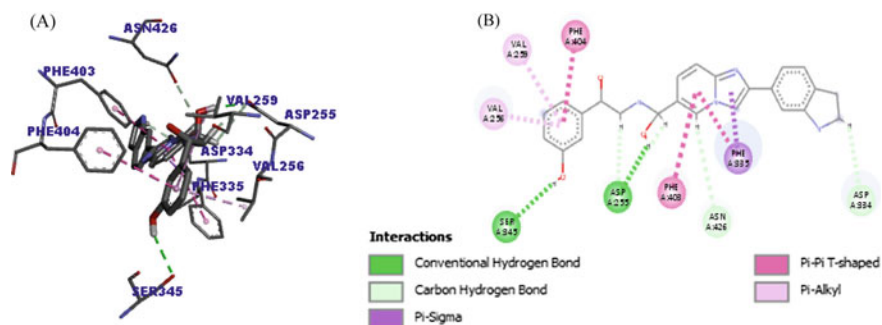


**Fig. 9** Result of the prototype molecular docking in  $\beta_1$ -adrenergic receptor. **A** 3D model; **B** 2D model. Intermolecular interactions are represented by the colors: conventional hydrogen bonds (green color), Carbon-hydrogen bonds (light blue color), pi-sigma (purple color), pi-pi T-shaped (darker pink color), pi-alkyl (light pink color)

ASP255 and binder H43 2.03 Å. The other four hydrogen bonds were of the Carbon-Hydrogen type, which is characterized by having carbon as a hydrogen donor or acceptor, as it has greater electronegativity than hydrogen. This type of interaction occurred between the atoms of the residues of ASP255 with H39 and H42 (with a distance of 2.44 and 3.03 Å, respectively), of ASN426 with H46 (with a distance of 3.09 Å) and ASP334 with the H52 (with a distance of 2.88 Å).

In addition to hydrogen bonds, it was also possible to observe hydrophobic interactions such as pi-pi T-shaped, pi-alkyl and pi-sigma. The latter occurs between single-chain and double-bonded systems, that is, between  $sp^2$  and  $sp^3$  hybrid atoms. The pi-sigma interaction occurred between a hydrogen from PHE335 with the unsaturated cyclopentane of the prototype molecule, and the bonding distance was 2.51 Å. As for the rest of the hydrophobic interactions, three were of the pi-pi T-shaped type, involving amino acids PHE335, PHE403, PHE404 and two of the pi-alkyl type, with the interaction of amino acids VAL1139 and VAL1142.

Regarding the modifications, the first molecule (Fig. 10) showed few interactions when compared to propranolol and the prototype, having a total amount of six. Among these, only one was a carbon-hydrogen hydrogen bond that occurred between the ASP255 and the H36 of the molecule, with a distance of 2.48 Å. The rest of the interactions were of the hydrophobic type, being two pi-pi T-shaped in which residues PHE404 and PHE422 interacted with ligands of the molecule. The other three were of the pi-alkyl type, with the interaction between amino acids PHE335, VAL256 and VAL259.

As in the docking shown in the previous molecule, modification 2 (Fig. 11) also presented six interactions, in which two were hydrogen bonding, one of the conventional type and the other of the carbon-hydrogen type, occurring, in that order, the interaction of amino acids ASN407 and ALA342 with the same atom (O16) as the linker. The distance between interactions was 2.02 and 2.70 Å, respectively. The remaining interactions were hydrophobic, one pi-sigma, one pi-pi T-shaped and two pi-alkyl. The amino acid residues that made the interaction were, namely: VAL256 (pi-sigma), PHE404 (pi-pi T-shaped), PHE403 and VAL259 (pi-alkyl).

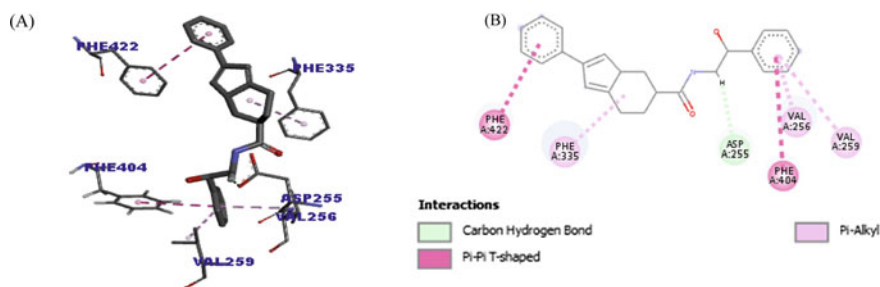


**Fig. 10** Result of molecular docking of modification 1 in  $\beta_1$ -adrenergic receptor. **A** 3D model; **B** 2D model. Intermolecular interactions are represented by the colors: carbon-hydrogen bonds (light blue color), pi-pi T-shaped (darker pink color), pi-alkyl (light pink color)

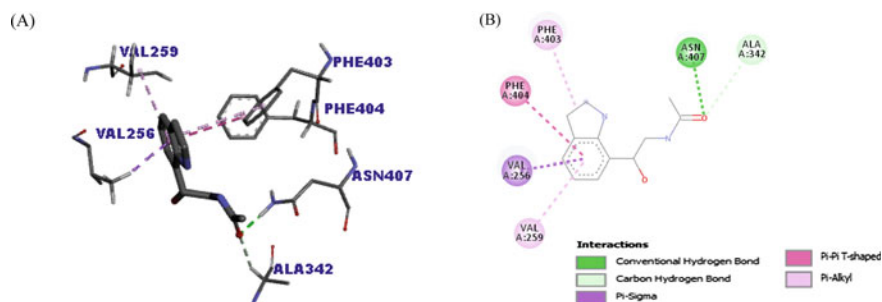


**Fig. 11** Result of molecular docking of modification 2 in  $\beta$ 1-adrenergic receptor. **A** 3D model; **B** 2D model. Intermolecular interactions are represented by the colors: hydrogen bonds (green color), Carbon-hydrogen bonds (light blue color), pi-pi T-shaped (light pink color), pi-sigma (purple color), pi-alkyl (light pink color)

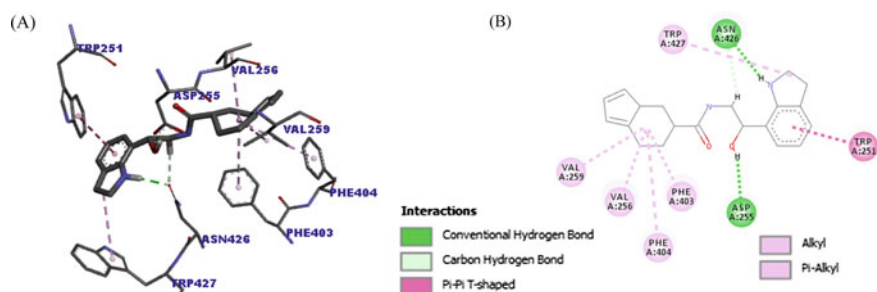


**Fig. 12** Result of molecular docking of modification 5 in  $\beta$ 1-adrenergic receptor. **A** 3D model; **B** 2D model. Intermolecular interactions are represented by the colors: hydrogen bonds (green color), Carbon-hydrogen bonds (light blue color), pi-pi T-shaped (light pink color), pi-alkyl (light pink color)

Regarding the docking of modification 5 (Fig. 12), it was possible to observe nine interactions. Of these, three are hydrogen bonds, two of which are of the conventional type, with the interaction between the residue ASN426 with the H43 of the ligand (distance of 1 Å) and ASP255 with the H48 (distance of 1.93 Å). The other was the carbon-hydrogen type, with interaction between ASN426 and H30, with a distance of 2.4 Å.

The other interactions that appeared were hydrophobic, being: one pi-pi T-shaped, two alkyl and one pi-alkyl. The amino acid residues involved were, in order, TRP251, VAL256, VAL259, PHE403, PHE404 and TRP427.

Modification 6 docking (Fig. 13) has already presented more favorable results when compared to propranolol, as it presented the same amount of interactions, with a total of twelve and with higher intermolecular forces, as it presented four hydrogen bonds. Of these four, two are of the conventional type, in which the ASN426 interacted with the ligand's H27 at a distance of 1.74 Å and ASN425 with the H37 at a distance of 1.98 Å. The other two were of the carbon-hydrogen type in which the

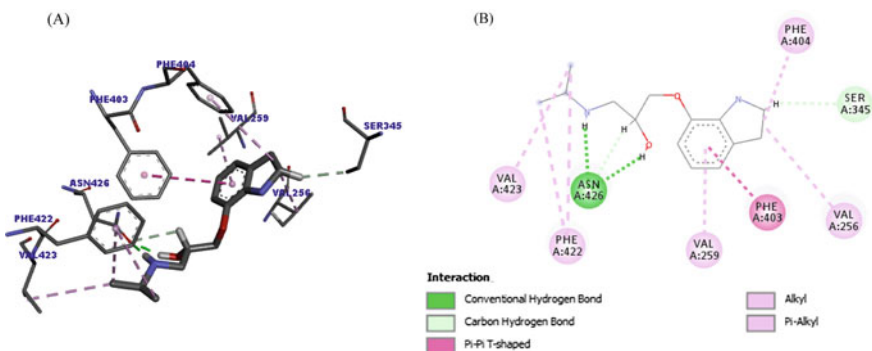


**Fig. 13** Result of molecular docking of modification 6 in  $\beta 1$ -adrenergic receptor. **A** 3D model; **B** 2D model. Intermolecular interactions are represented by the colors: conventional hydrogen bonds (green color), Carbon-hydrogen bonds (light blue color), pi-pi T-shaped (dark pink color), pi-alkyl and alkyl (light pink color)

residue ASN426 interacted with H24, with a distance between molecules of 2.90 Å and SER345 interacted with H33 at a distance of 2.54 Å.

The other eight interactions were hydrophobic, one being pi-sigma, with interaction between VAL256 and an atom of the modified molecule. The other was a pi-pi T-shaped type with PHE403 and the binder. Two were of the alkyl type, with VAL256 interacting with a ligand and VAL423 with C18. Finally, the last four were of the pi-alkyl type, in which PHE422 interacted with two atoms: C13 and C18; and VAL259 and PHE422 with two other ligands on the molecule.

Unlike the previous one, modification 18 (Fig. 14) exhibited one less interaction, that is, a total of eleven, five of which were hydrogen bonds. Two of these bonds were of the conventional type, with the interaction between ASN426 and O19 of the ligand, with a distance of 2.53 Å, and between ASP255 and H43 at a distance

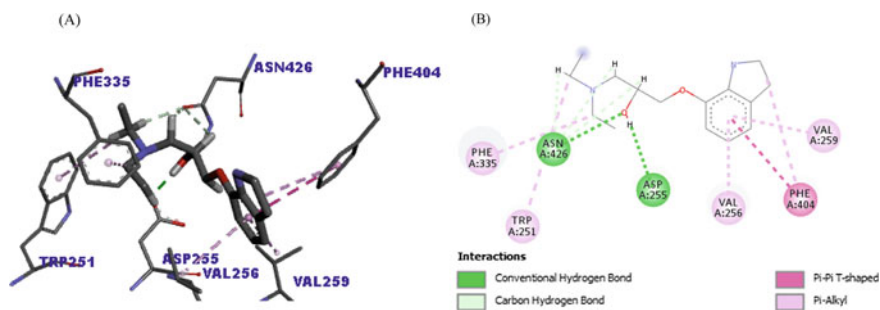


**Fig. 14** Result of molecular docking of modification 18 in  $\beta 1$ -adrenergic receptor. **A** 3D model; **B** 2D model. Intermolecular interactions are represented by the colors: conventional hydrogen bonds (green color), Carbon-hydrogen bonds (light blue color), pi-pi T-shaped (dark pink color), pi-alkyl (light pink color)



between molecules of 1.84 Å. The other three hydrogen bonds were carbon-hydrogen bonds, with a single amino acid interacting with three ligands H25, H26 and H29, with distances of 2.81, 3.07 and 2.35 Å, respectively. It is important to emphasize that, even with a smaller number of interactions than propranolol docking, this modification will be taken into account for the study, since it presented a greater amount of strong intermolecular interactions.

The other interactions visualized were the hydrophobic type, being a pi-pi T-shaped in which PHE404 interacted with a binding atom. The remainder was pi-alkyl, in which TRP251 interacted with C12, PHE 335 with C13 and PHE404, VAL256, VAL259 with other ligands of the molecule.

With regard to modification 19 (Fig. 15), a total of ten interactions can be observed, being divided between five hydrogen bonds and five hydrophobic interactions. As in modification 18, two of these bonds are of the conventional type, in which an interaction between the TYR430 with the O19 of the ligand was verified, at a distance of 2.77 Å and an interaction between the ASN426 with the H43, at a distance of 1.66 Å. The other three bonds, of the carbon-hydrogen type, occurred with the residue of ASP426 and two more ligands, the H25 and H30, having a distance between the molecules of 2.96 and 3 Å, respectively. While the last hydrogen-carbon bond occurred between ASP255 and H26 of the modified molecule. The distance of this last interaction was 2.53 Å.

In sequence, five hydrophobic interactions were observed, being a pi-sigma characterized by the interaction between VAL256 with a benzene ring of the ligand. The other four interactions were pi-alkyl, with the interaction of PHE403 and PHE422, both with C12. An interaction with PHE404 with a ligand and finally VAL259 with another ligand of the molecule.

With respect to modification 20 (Fig. 16), one can observe eleven interactions, six of which are hydrogen bonds. Thus, it is possible to establish a possible higher activity of this modification against this receptor when compared to other molecules already

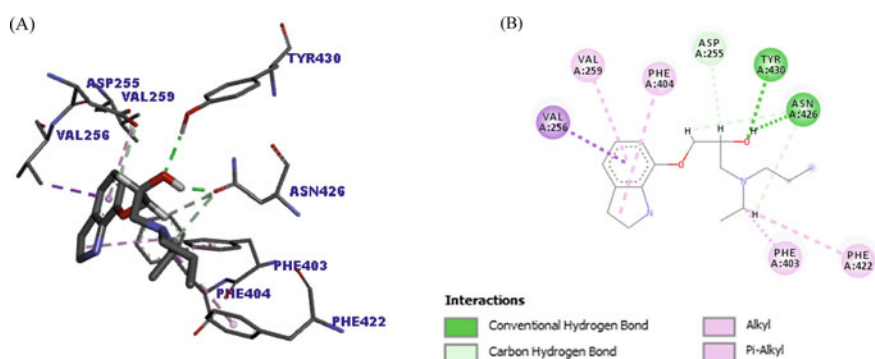


**Fig. 15** Result of molecular docking of modification 19 in  $\beta$ 1-adrenergic receptor. **A** 3D model; **B** 2D model. Intermolecular interactions are represented by the colors: conventional hydrogen bonds (green color), Carbon-hydrogen bonds (light blue color), pi-sigma (purple color), pi-alkyl (light pink color)

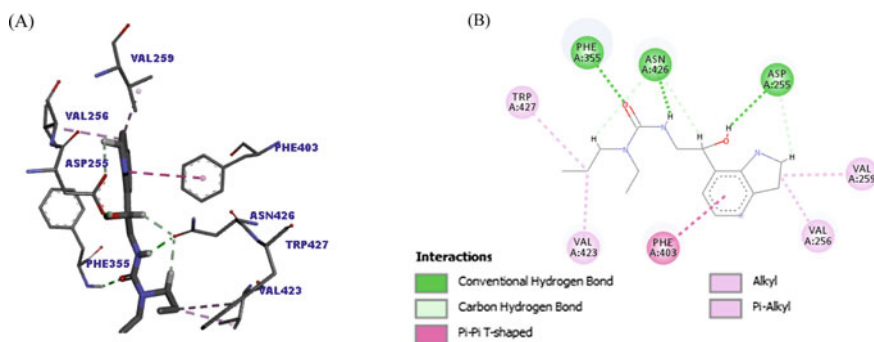


**Fig. 16** Result of molecular docking of modification 20 in  $\beta$ 1-adrenergic receptor. **A** 3D model; **B** 2D model. Intermolecular interactions are represented by the colors: conventional hydrogen bonds (green color), Carbon-hydrogen bonds (light blue color), pi-pi T-shaped (dark pink color), pi-alkyl and alkyl (light pink color)

shown. Of these six connections, three are of the conventional type, in which the PHE335 interacted with the O21, with a distance of 2.16 Å. The ASN426 interacted conventionally with the H28, at 2.94 Å of distance. The ASP255 interacted with the ligand's H46, having a distance between the two of 2.20 Å.

The other three hydrogen bonds are of the carbon-hydrogen type, in which the ASN426 interacted with two more ligands, the H25 and H31, distancing each other, 2.36 and 2.29 Å, respectively. Finally, the ASP455 had such an interaction with the molecule's H40 at a distance of 2.99 Å. The five remaining interactions were hydrophobic, pi-pi T-shaped, alkyl and pi-alkyl. The pi-pi T-shaped interaction happened between PHE403 and a binding atom. The alkyl interactions occurred between VAL423 with C15 and VAL256 and VAL259 with two other ligands. Pi-alkyl occurred between TRP427 and a linker atom of the modified molecule.

The docking of modification 9 (Fig. 17) showed nine interactions, two hydrogen

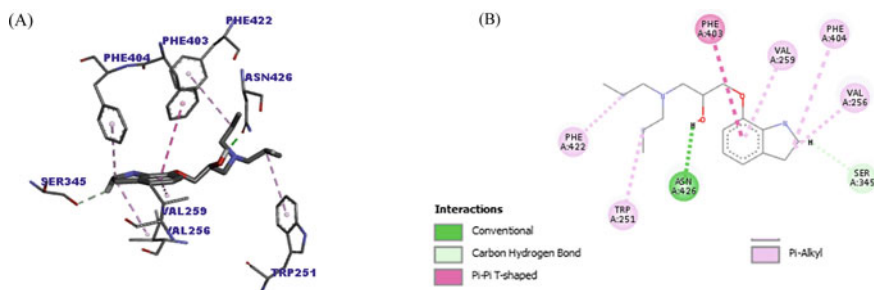


**Fig. 17** Result of molecular docking of modification 24 in  $\beta$ 1-adrenergic receptor. **A** 3D model; **B** 2D model. Intermolecular interactions are represented by the colors: conventional hydrogen bonds (green color), Carbon-hydrogen bonds (light blue color), pi-pi T-shaped (dark pink color), pi-alkyl and alkyl (light pink color)

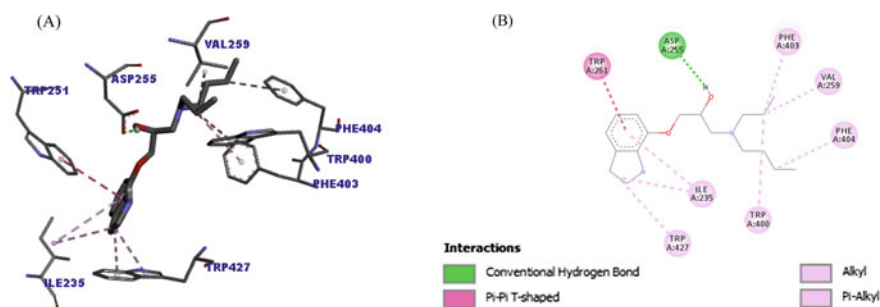


**Fig. 18** Result of molecular docking of modification 25 in  $\beta$ 1-adrenergic receptor. **A** 3D model; **B** 2D model. Intermolecular interactions are represented by the colors: conventional hydrogen bonds (green color), pi-pi T-shaped (light pink color), pi-alkyl and alkyl (light pink color)

bonds, one of the conventional type and the other carbon-hydrogen. The first one was given through the interaction between the residue ASN426 with the H43 of the ligand at a distance of 1.89 Å. The second occurred due to the interaction between SER345 with the H39 of the ligand, with a distance of 2.57 Å.

The others were hydrophobic interactions, being: one pi-sigma, one pi-pi T-shaped, one alkyl and four pi-alkyl. In pi-sigma, the amino acid VAL256 interacted with a linker atom. The interaction pi-pi T-shaped and alkyl, the amino acids involved were PHE403 and VAL256 that were interacting with different ligands. Finally, the pi-alkyl interactions occurred between TRP251 with C15, PHE422 with C14, PHE404 and VAL259 interacting with two other ligands.

About modification 25 (Fig. 18), it is possible to see a total of ten interactions, in which only one is a hydrogen bond and the rest are hydrophobic interactions. Hydrogen bonding, of the conventional type, occurred between ASP255 and H44, with a distance of 2.11 Å.

Of the nine hydrophobic interactions, one is pi-pi T-shaped, two are alkyl, and six are pi-alkyl. In the pi-pi T-shaped interaction, PHE335 interacted with a bonding atom. As for the alkyl type, VAL259 interacted with C15 and ILE235 with linking atom. They also interacted with C15, but in the form of pi-alkyl, the amino acid residues TRP400 and PHE403. PHE404 interacted with C12 and TRP427 bound two other bonding atoms, while ILE235 also made another interaction with another ligand, of the pi-alkyl type.

Modification 26 (Fig. 19) showed a conventional hydrogen bond with the ASP255 and the H45 atom, with a distance between molecules of 2.03 Å. The rest of the interactions were hydrophobic, with a T-shaped pi-pi being performed between the PHE335 with a bonding atom, another two of the alkyl type with VAL256 and VAL259 bonded to different atoms of the molecule. PHE404 performed a pi-alkyl interaction with two atoms, one C19 and the other with a different bonding atom. Thus, it is possible to infer that this modification had a total of six interactions, far below those of references and other molecules already listed above.

As in modification 6, the interactions were similar with modification 27 (Fig. 20)

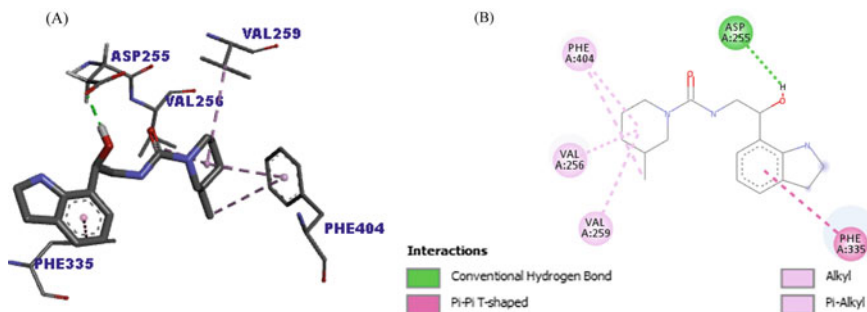


**Fig. 19** Result of molecular docking of modification 26 in  $\beta$ 1-adrenergic receptor. **A** 3D model; **B** 2D model. Intermolecular interactions are represented by the colors: conventional hydrogen bonds (green color), pi-pi T-shaped (light pink color), pi-alkyl and alkyl (light pink color)

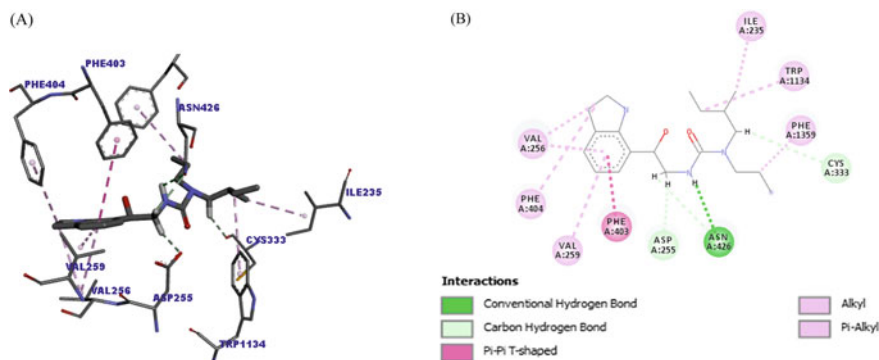


**Fig. 20** Result of molecular docking of modification 27 in  $\beta$ 1-adrenergic receptor. **A** 3D model; **B** 2D model. Intermolecular interactions are represented by the colors: conventional hydrogen bonds (green color), Carbon-hydrogen bonds (light blue color), pi-pi T-shaped (light pink color), pi-alkyl and alkyl (light pink color)

as it had a total of twelve interactions, with types of intermolecular forces greater than that of propranolol, since it also presented four hydrogen bonds, which are higher forces. Of these four, one is of the conventional type, characterized by the interaction between ASN426 interacted with the ligand H31 at a distance of 2.83 Å. The other three hydrogen bonds were of the carbon-hydrogen type in which the ASP255 residue interacted with H29, presenting a distance between molecules of 2.87 Å, ASN426 also interacted with H30 at a distance of 2.94 Å, on the other hand, CYS333 had an interaction of hydrogen with the H33 atom, with a distance of 3.04 Å.

The other eight (8) interactions were hydrophobic, one pi-pi T-shaped, with interaction between PHE403 and a binding atom of the modified molecule. Two were of the alkyl type, with VAL256 interacting with a ligand and ILE235 with C22. Finally, the last five (4) were of the pi-alkyl type, in which TRP251 interacted with C23 and

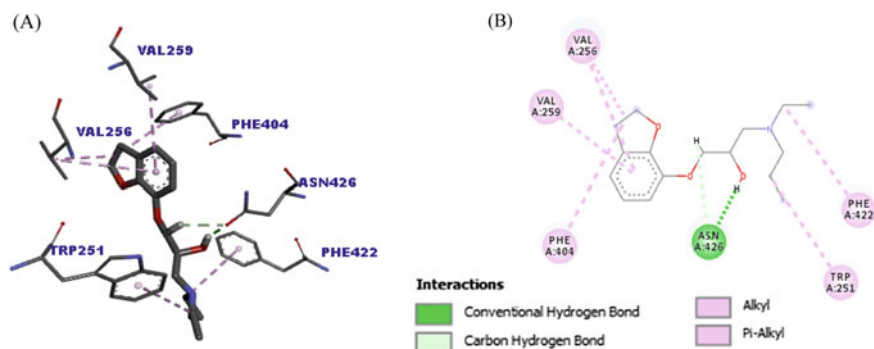


**Fig. 21** Result of molecular docking of modification 28 in  $\beta_1$ -adrenergic receptor. **A** 3D model; **B** 2D model. Intermolecular interactions are represented by the colors: conventional hydrogen bonds (green color), Carbon-hydrogen bonds (light blue color), pi-alkyl and alkyl (light pink color)

PHE422 with C15. Amino acid residues PHE404, VAL256, VAL259 interacted with different atoms of the linker molecule.

The docking of modification 28 (Fig. 21) showed a total of eight interactions, two hydrogen bonds, one of which is of the conventional type expressed by the interaction between ASN426 and H42, with a distance of 1.79 Å, and the other of the carbon-hydrogen type, visualized through the interaction between the ASN426 and with the H25 atom, at a distance of 2.44 Å between the molecules.

The rest of the interactions, with a total of six, were all hydrophobic interactions, being an alkyl interaction, with VAL256 interacting with a binding atom. The remaining five were all pi-alkyl, in which the TRP251 interacted with the C15 and the PHE422 with the C12. Amino acid residues PHE404, VAL256, VAL259 interacted with different atoms of the linker molecule.

Assessing the performance of the molecules, it is possible to infer that the ones that showed the best results for docking were the prototype and modifications 6 and 27, as they showed amounts of interactions equal to those of propranolol and with greater intermolecular forces, thus indicating a possible greater activity on the target.

### 3.9.2 $\beta_2$ -Adrenergic Receptor

In the validation of the crystallographic structure of the target protein (PDB ID: 3NYA) with the ligand (alprenolol), the value of 0.79 Å was obtained as a result of the RMSD calculation. According to this value, it was considered a good result, as the RMSD value was less than 2 Å, thus assuming that the ligand correctly fitted in an appropriate spatial orientation on the target [45, 58]. The validation radius was 9.364 and the origin coordinates:  $x = -2.28$ ;  $y = 4.23$ ;  $z = -51.19$ . The score of this redoing was 68.76.

In view of these values, target validation was accepted and the protein extracted from the PDB database was used to proceed with the docking.

In a study by Wacker et al. [43], as a way to compare the degree of conformation of different substances in  $\beta$ 2-adrenergic receptors, the authors determined the X-ray of the crystal structure of these targets complexed to different substances. And among these, the non-selective  $\beta$ -adrenergic receptor antagonist, alprenolol [59]. Thus, through the study, it was possible to identify the amino acid residues located in the active site, namely: ASN312, TRP109, TR316, ASP113, TRP286, PHE193, PHE289, TR308, ASN293, PHE290, TYR199, SER203, VAL114, THR118, VAL117 and TRP286.

Thus, for the analysis of this docking, the interactions with these specific amino acids were taken into account. According to the origin coordinates obtained in the validation, the binding site was defined for the start of docking. As seen in Fig. 22, all of the linkers lie in the same region, many of which are interacting with the same amino acid residues.

Thus, to establish whether the prototype and the modifications had greater interactions with the target when compared to propranolol in  $\beta$ 2 adrenergic receptor, it was also analyzed the amounts and types of interactions that occurred between ligand and receptor, mainly checking which residues were as a way to compare with the study by Wacker et al. [43] (Table 12).

In the result of the propranolol docking (Fig. 23), one can observe thirteen interactions, four hydrogen bonds and seven hydrophobic. Of the four hydrogen bonds, only one is of the carbon-hydrogen type, in which ASN312 interacts with the H31 of the ligand, at a distance of 2.82 Å. The rest is of the conventional type, with ASN312 interacting with ligands, O15 and H33 at a distance of 2.08 and 2.11 Å, respectively, and ASP113 interacting with H32, at a distance of 2.05 Å.

As for the hydrophobic interactions, two are of the pi-pi T-shaped type, both are interactions with the same amino acid, in this case it is PHE290 interacting with different bonding atoms. Only one is of the alkyl type, in which VAL114 interacts with the C19 of the ligand. Still in relation to this last amino acid (VAL114), it is also possible to notice that it makes another interaction, but of the pi-alkyl type, with



Fig. 22 Overlap of propranolol molecules, prototype and  $\beta$ 2 adrenergic receptor modifications

**Table 12** Propranolol docking, prototype and selected  $\beta_2$  adrenergic receptor modifications

Molecule	Amino acid	Ligand atoms	Category	Type	Distance
Propranolol	ASN312	O15	Hydrogen bond	Conventional hydrogen bond	2.08
	ASP113	H32	Hydrogen bond	Conventional hydrogen bond	2.05
	ASN312	H33	Hydrogen bond	Conventional hydrogen bond	2.11
	ASN312	H31	Hydrogen bond	Carbon hydrogen bond	2.82
	PHE290	Ligand	Hydrophobic	Pi-Pi T-shaped	4.82
	PHE290	Ligand	Hydrophobic	Pi-Pi T-shaped	4.94
	VAL114	C19	Hydrophobic	Alkyl	5.10
	TRP109	C18	Hydrophobic	Pi-Alkyl	4.25
	PHE193	C19	Hydrophobic	Pi-Alkyl	4.15
	VAL114	Ligand	Hydrophobic	Pi-Alkyl	4.32
	VAL117	Ligand	Hydrophobic	Pi-Alkyl	4.76
Prototype	SER204	O10	Hydrogen bond	Conventional hydrogen bond	2.25
	SER203	H40	Hydrogen bond	Conventional hydrogen bond	2.06
	THR195	H43	Hydrogen bond	Conventional hydrogen bond	1.77
	PHE193	H47	Hydrogen bond	Carbon hydrogen bond	2.36
	ASP192	H53	Hydrogen bond	Carbon hydrogen bond	2.89
	PHE194	Ligand	Hydrophobic	Pi-Pi Stacked	4.87
	TYR308	Ligand	Hydrophobic	Pi-Pi Stacked	5.48
	TYR308	Ligand	Hydrophobic	Pi-Pi Stacked	4.43
	PHE290	Ligand	Hydrophobic	Pi-Pi T-shaped	4.81
	LYS305	Ligand	Hydrophobic	Alkyl	3.78
	PHE194	Ligand	Hydrophobic	Pi-Alkyl	4.90
	VAL114	Ligand	Hydrophobic	Pi-Alkyl	4.43
	VAL117	Ligand	Hydrophobic	Pi-Alkyl	5.13
ALA200	Ligand	Hydrophobic	Pi-Alkyl	4.55	
Mod.1	ALA200	O27	Hydrogen Bond	Carbon hydrogen bond	2.43
	SER203	H33	Hydrogen Bond	Carbon hydrogen bond	2.42
	TYR308	Ligand	Hydrophobic	Pi-Pi Stacked	4.14

(continued)

**Table 12** (continued)

Molecule	Amino acid	Ligand atoms	Category	Type	Distance
	PHE290	Ligand	Hydrophobic	Pi-Pi T-shaped	4.83
	ALA200	Ligand	Hydrophobic	Alkyl	4.99
	HIS296	Ligand	Hydrophobic	Pi-Alkyl	5.49
	TYR308	Ligand	Hydrophobic	Pi-Alkyl	5.24
	VAL114	Ligand	Hydrophobic	Pi-Alkyl	4.66
	VAL117	Ligand	Hydrophobic	Pi-Alkyl	5.47
	LYS305	Ligand	Hydrophobic	Pi-Alkyl	5.29
Mod.2	PHE193	O16	Hydrogen Bond	Conventional hydrogen bond	1.68
	ASN312	H24	Hydrogen Bond	Conventional hydrogen bond	1.99
	ASN312	H29	Hydrogen Bond	Conventional hydrogen bond	1.82
	ASP192	O16	Hydrogen Bond	Carbon hydrogen bond	2.79
	PHE193	Ligand	Hydrophobic	Pi-Pi Stacked	4.11
	PHE193	Ligand	Hydrophobic	Pi-Alkyl	4.92
Mod.5	ASP113	H31	Hydrogen bond	Conventional hydrogen bond	2.82
	ASN312	H43	Hydrogen bond	Conventional hydrogen bond	2.06
	ASP113	H48	Hydrogen bond	Conventional hydrogen bond	1.59
	TYR308	H30	Hydrogen bond	Carbon hydrogen bond	2.97
	ASN312	H30	Hydrogen bond	Carbon hydrogen bond	2.84
	TRP109	Ligand	Hydrophobic	Pi-Pi T-shaped	4.86
	VAL114	Ligand	Hydrophobic	Alkyl	4.53
	VAL117	Ligand	Hydrophobic	Alkyl	4.39
	ILE309	Ligand	Hydrophobic	Alkyl	4.10
	PHE290	Ligand	Hydrophobic	Pi-Alkyl	5.15
	TRP313	Ligand	Hydrophobic	Pi-Alkyl	4.85
	Mod.6	ASP113	H37	Hydrogen bond	Conventional hydrogen bond
TRP109		Ligand	Hydrophobic	Pi-Pi T-shaped	4.86
VAL114		C13	Hydrophobic	Alkyl	4.23
VAL117		C13	Hydrophobic	Alkyl	3.67
ILE309		Ligand	Hydrophobic	Alkyl	4.39

(continued)



**Table 12** (continued)

Molecule	Amino acid	Ligand atoms	Category	Type	Distance
	VAL117	C18	Hydrophobic	Alkyl	4.27
	TRP286	C18	Hydrophobic	Pi-Alkyl	4.55
	PHE289	C18	Hydrophobic	Pi-Alkyl	5.11
	TRP313	Ligand	Hydrophobic	Pi-Alkyl	4.67
	TYR316	Ligand	Hydrophobic	Pi-Alkyl	5.46
Mod.18	ASN312	H38	Hydrogen bond	Conventional hydrogen bond	2.05
	ASN312	H43	Hydrogen bond	Conventional hydrogen bond	1.95
	TRP109	Ligand	Hydrophobic	Pi-Pi T-shaped	4.61
	VAL114	C12	Hydrophobic	Alkyl	4.94
	VAL117	C12	Hydrophobic	Alkyl	4.75
	VAL114	C13	Hydrophobic	Alkyl	4.51
	ILE309	Ligand	Hydrophobic	Alkyl	4.09
	PHE289	C12	Hydrophobic	Pi-Alkyl	5.39
	TRP313	Ligand	Hydrophobic	Pi-Alkyl	5.02
Mod.19	TYR308	H43	Hydrogen bond	Conventional hydrogen bond	1.84
	ASP113	H27	Hydrogen bond	Carbon hydrogen bond	2.54
	TRP109	Ligand	Hydrophobic	Pi-Pi T-shaped	4.87
	VAL117	C12	Hydrophobic	Alkyl	4.55
	ILE309	Ligand	Hydrophobic	Alkyl	4.36
	TRP286	C12	Hydrophobic	Pi-Alkyl	5.38
	PHE289	C12	Hydrophobic	Pi-Alkyl	4.99
	PHE289	C15	Hydrophobic	Pi-Alkyl	4.6
	PHE290	C15	Hydrophobic	Pi-Alkyl	5.08
TRP313	Ligand	Hydrophobic	Pi-Alkyl	4.73	
Mod.20	ASN312	H28	Hydrogen bond	Conventional hydrogen bond	2.04
	ASN312	H46	Hydrogen bond	Conventional hydrogen bond	1.97
	ASP113	H27	Hydrogen bond	Carbon hydrogen bond	2.15
	ASN312	H31	Hydrogen bond	Carbon hydrogen bond	2.85
	PHE289	Ligand	Hydrophobic	Pi-Pi T-shaped	5.13
	ILE309	C15	Hydrophobic	Alkyl	3.82

(continued)

**Table 12** (continued)

Molecule	Amino acid	Ligand atoms	Category	Type	Distance
	HIS93	C12	Hydrophobic	Pi-Alkyl	4.72
	TRP109	C12	Hydrophobic	Pi-Alkyl	4.99
	PHE289	Ligand	Hydrophobic	Pi-Alkyl	5.07
	PHE290	Ligand	Hydrophobic	Pi-Alkyl	5.05
	TRP313	C15	Hydrophobic	Pi-Alkyl	5.16
	VAL114	Ligand	Hydrophobic	Pi-Alkyl	5.10
	VAL117	Ligand	Hydrophobic	Pi-Alkyl	5.29
Mod.24	ASN312	H43	Hydrogen Bond	Conventional hydrogen bond	1.75
	TYR308	H29	Hydrogen Bond	Carbon hydrogen bond	2.76
	TRP109	Ligand	Hydrophobic	Pi-Pi T-shaped	4.94
	VAL114	C14	Hydrophobic	Alkyl	4.35
	VAL117	C14	Hydrophobic	Alkyl	3.73
	ILE309	Ligand	Hydrophobic	Alkyl	4.19
	PHE193	C15	Hydrophobic	Pi-Alkyl	4.94
TRP313	Ligand	Hydrophobic	Pi-Alkyl	4.78	
Mod. 25	ASN312	H44	Hydrogen bond	Conventional hydrogen bond	2.04
	ASP113	H27	Hydrogen bond	Carbon hydrogen bond	2.77
	ASP113	H30	Hydrogen bond	Carbon hydrogen bond	2.88
	ASN312	H30	Hydrogen bond	Carbon hydrogen bond	2.79
	SER203	H41	Hydrogen bond	Carbon hydrogen bond	2.99
	ILE309	C15	Hydrophobic	Alkyl	4.28
	VAL114	Ligand	Hydrophobic	Alkyl	4.11
	PHE290	Ligand	Hydrophobic	Pi-Alkyl	5.21
	TYR308	C21	Hydrophobic	Pi-Alkyl	4.83
	VAL114	Ligand	Hydrophobic	Pi-Alkyl	4.86
	VAL117	Ligand	Hydrophobic	Pi-Alkyl	4.67
Mod. 26	ASN312	O20	Hydrogen bond	Conventional hydrogen bond	2.44
	ASN312	H29	Hydrogen bond	Conventional hydrogen bond	2.09
	TYR308	H37	Hydrogen bond	Conventional hydrogen bond	2.12

(continued)

**Table 12** (continued)

Molecule	Amino acid	Ligand atoms	Category	Type	Distance
	ASP113	H45	Hydrogen bond	Conventional hydrogen bond	1.95
	ASN312	H26	Hydrogen bond	Carbon hydrogen bond	2.56
	ASP113	H28	Hydrogen bond	Carbon hydrogen bond	2.88
	ASN312	H32	Hydrogen bond	Carbon hydrogen bond	2.30
	PHE290	Ligand	Hydrophobic	Pi-Pi T-shaped	5.69
	ILE309	Ligand	Hydrophobic	Alkyl	5.34
	ILE309	C19	Hydrophobic	Alkyl	4.31
	HIS93	Ligand	Hydrophobic	Pi-Alkyl	5.45
	TRP109	Ligand	Hydrophobic	Pi-Alkyl	5.06
	PHE193	Ligand	Hydrophobic	Pi-Alkyl	5.10
	TRP313	C19	Hydrophobic	Pi-Alkyl	4.82
	VAL114	Ligand	Hydrophobic	Pi-Alkyl	4.57
	VAL117	Ligand	Hydrophobic	Pi-Alkyl	4.97
Mod. 27	TYR316	O21	Hydrogen bond	Conventional hydrogen bond	2.91
	TYR308	H31	Hydrogen bond	Conventional hydrogen bond	2.58
	TYR308	H39	Hydrogen bond	Conventional hydrogen bond	2.09
	ASN312	H47	Hydrogen bond	Conventional hydrogen bond	1.81
	ASN312	H28	Hydrogen bond	Carbon hydrogen bond	2.65
	PHE289	Ligand	Hydrophobic	Pi-Pi T-shaped	5.43
	ILE309	C22	Hydrophobic	Alkyl	3.72
	TRP109	C23	Hydrophobic	Pi-Alkyl	4.88
	PHE193	Ligand	Hydrophobic	Pi-Alkyl	5.46
	TRP313	C22	Hydrophobic	Pi-Alkyl	4.84
	TRP313	C23	Hydrophobic	Pi-Alkyl	4.69
	TYR316	C23	Hydrophobic	Pi-Alkyl	5.17
	VAL114	Ligand	Hydrophobic	Pi-Alkyl	4.62
	VAL117	Ligand	Hydrophobic	Pi-Alkyl	5.05
	ASN312	H42	Hydrogen Bond	Conventional hydrogen bond	1.76

(continued)

**Table 12** (continued)

Molecule	Amino acid	Ligand atoms	Category	Type	Distance
Mod.28	ASP113	H26	Hydrogen Bond	Carbon hydrogen bond	2.69
	TYR308	Ligand	Hydrophobic	Pi-Pi T-shaped	5.53
	VAL114	C12	Hydrophobic	Alkyl	5.06
	ILE309	Ligand	Hydrophobic	Alkyl	4.26
	PHE193	C15	Hydrophobic	Pi-Alkyl	4.83
	PHE289	C12	Hydrophobic	Pi-Alkyl	5.46
	TRP313	Ligand	Hydrophobic	Pi-Alkyl	4.60
	TYR316	Ligand	Hydrophobic	Pi-Alkyl	5.42
	ILE309	Ligand	Hydrophobic	Pi-Alkyl	5.39

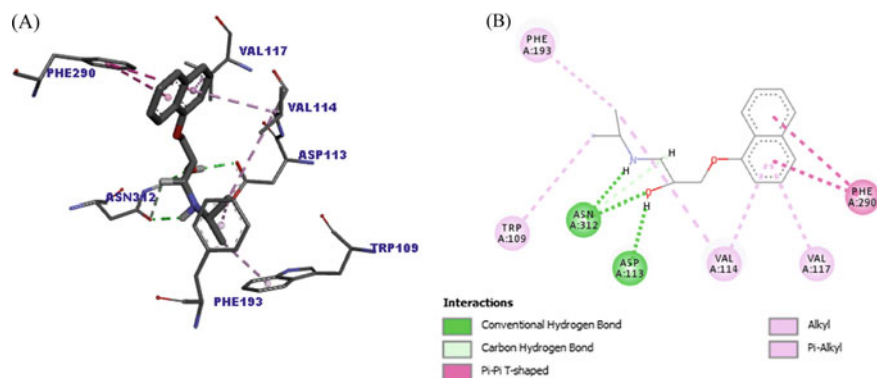


**Fig. 23** Result of the molecular docking of propranolol on the  $\beta_2$ -adrenergic receptor. **A** 3D model; **B** 2D model. Intermolecular interactions are represented by the colors: conventional hydrogen bonds (green color), Carbon-hydrogen bonds (light blue color), pi-pi T-shaped (dark pink), pi-alkyl and alkyl (light pink color)

another atom of the binding molecule. All the rest of the interactions were pi-alkyl, in which TRP109 interacted with C18, PHE193 with C19 and VAL117 with a bonding atom.

The prototype anchorage (Fig. 24), when compared to propranolol, presented better results, since it had three more interactions and with greater forces, as it had greater hydrogen interactions. In all, there were five hydrogen bonds, three of the conventional type and two of the carbon-hydrogen type. The SER204 made a conventional connection with the O10, with a distance of 2.25 Å. SER403 and THR195, also with conventional hydrogen bonding, interacted with H40 and H43, with distances of 2.06 and 1.77 Å, respectively. On the other hand, PHE193 had a carbon-hydrogen interaction with H47, distancing itself from each other by 2.36 Å.

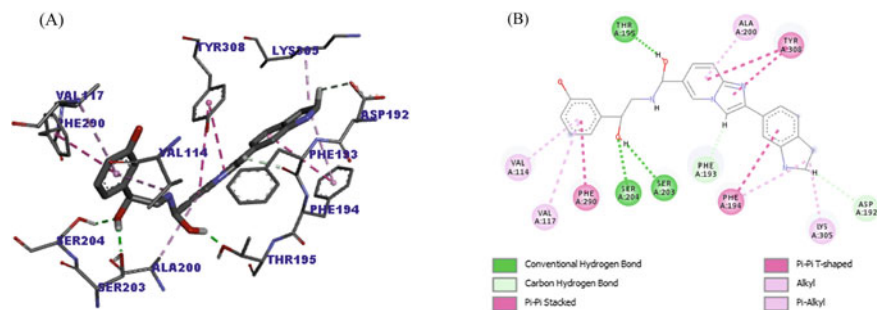


**Fig. 24** Result of the prototype molecular docking in  $\beta$ 2-adrenergic receptor. **A** 3D model; **B** 2D model. Intermolecular interactions are represented by the colors: conventional hydrogen bonds (green color), Carbon-hydrogen bonds (light blue color), pi-pi T-shaped and pi-pi Stacked (dark pink) pi-alkyl and alkyl (color light pink)

Finally, the last carbon-hydrogen interaction detected was with amino acid ASP192 with H53, at a distance of 2.9 Å.

The rest of the interactions were all hydrophobic, with PHE194, TR308, TR308 making pi-pi stacked interactions with different atoms of the ligand. The PHE193 made a connection, also of the pi-pi type, although in another configuration, which is the T-shaped. While the alkyl type appeared only once, through the bond between LYS305 and an atom of the prototype. The pi-alkyl type totaled four interactions between the ligand atoms and the residues of PHE194, VAL114, VAL117 and ALA200.

Modification 1 (Fig. 25) showed a total of ten interactions, two of which were carbon-hydrogen, between ALA200 and O27 and SER20 and the H33 atom at a distance between the molecules of 2.43 and 2.42 Å, respectively.

The other interactions were hydrophobic, being two of the pi-pi type, involving the amino acids TYR308 and PHE290. Only one was of the alkyl type with ALA200, interacting with an atom of the ligand. PHE404 performed a pi-alkyl interaction with two atoms, one C19 and the other with a different bonding atom. The other six bonds

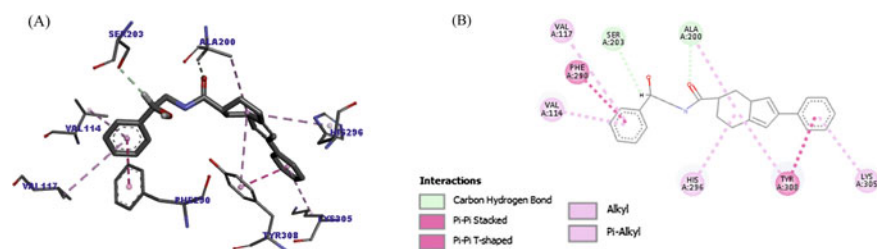


**Fig. 25** Result of molecular docking of modification 1 in  $\beta$ 2-adrenergic receptor. **A** 3D model; **B** 2D model. Intermolecular interactions are represented by the colors: Carbon-hydrogen bonds (light blue color), pi-pi T-shaped and pi-pi Stacked (dark pink), pi-alkyl and alkyl (light pink color)

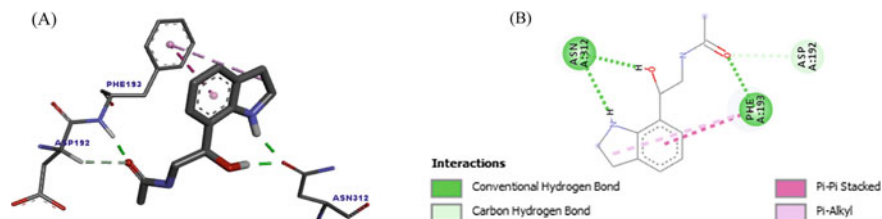


**Fig. 26** Molecular docking result of modification 2 in  $\beta$ 2-adrenergic receptor. **A** 3D model; **B** 2D model. Intermolecular interactions are represented by the colors: conventional hydrogen bonds (green color), Carbon-hydrogen bonds (light blue color), pi-pi Stacked (dark pink) and pi-alkyl (light pink color)

were all pi-alkyl, with the participation of amino acids, namely: HIS296, TYR308, VAL114, VAL117 and LYS305.

Modification 2 docking (Fig. 26) showed only six interactions, in which the vast majority was hydrogen bonding, with a total of four interactions. Three of these interactions was the conventional type, in which PHE193 interacted with O16 (distance 1.68 Å) and ASN312 interacted with two bonding atoms, H24 and H29, with a distance of 1.99 and 1.82 Å, in that order. The other hydrogen bond was a carbon-hydrogen interaction with ASP192 interacting with O16 at a distance of 2.79 Å. Regarding the rest of the interactions, all were hydrophobic, involving the same amino acid residue, which was PHE193, which made a pi-pi Stacked and a pi-alkyl interaction with different atoms of the ligand molecule.

Modification 5 (Fig. 27) showed a total of eleven bonds, equivalent to that of propranolol, differing only in the types of interactions performed. In total, there were five hydrogen bonds, three of the conventional type and two of the carbon-hydrogen type. The ASP113 made two conventional type connections with the H31 and H48, with a distance of 2.82 and 1.59 Å, respectively. TYR308 had interaction

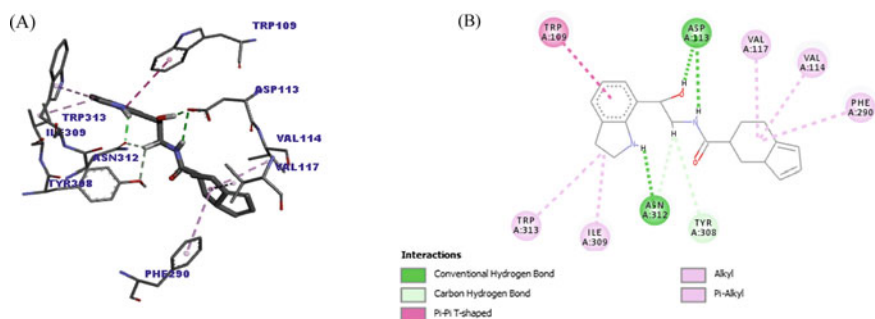


**Fig. 27** Result of molecular docking of modification 5 in  $\beta$ 2-adrenergic receptor. **A** 3D model; **B** 2D model. Intermolecular interactions are represented by the colors: conventional hydrogen bonds (green color), Carbon-hydrogen bonds (light blue color), pi-pi T-shaped (dark pink) and alkyl and pi-alkyl (light pink color)

with carbon-hydrogen type H30 (distance of 2.97 Å). ASN312, on the other hand, made two interactions, one of the conventional type and the other carbon-hydrogen, with H43 and H30, at a distance of 2.06 and 2.84 Å, in that order.

As for the rest of the interactions, all were hydrophobic, in which TRP109 made a pi-pi T-shaped interaction. VAL114, VAL117 and ILE309 performed alkyl type interactions, with different atoms of the ligand. Finally, PHE209 and TRP313 made pi-alkyl type interactions.

Altogether, modification 6 (Fig. 28) showed ten interactions, however, only one with a greater strength, which occurred between ASP113 and H37 that interacted with a conventional hydrogen bond, at a distance of 2.02 Å.

All the rest of the interactions were of the hydrophobic type, being a pi-pi T-shaped, with TRP109 and a binding atom. Four were of the alky type, in which VAL114 interacted with C13, VAL117 also with C13 plus C18 and ILE309 with another atom of the ligand. The other four were pi-alkyl hydrophobic interactions, in which TRP286 and PHE289 interacted with the same atom, C18. Finally, TRP313 and TR316 interacted with other binding atoms of the modified molecule.

Modification 18 (Fig. 29) showed a total of nine interactions, with only two hydrogen bonds, involving only one amino acid, ASN312, which performed conventional hydrogen interactions, with H38 and H48, to one distance between molecules of 2.05 and 1.95 Å, respectively.

As for hydrophobic interactions, only one is pi-pi T-shaped through the binding of TRP109 with an atom of the ligand. The docking still had four alkyl bonds, with VAL114 and VAL117 interacting with the same atom, C12. Also, in relation to VAL114, this amino acid still bound to C13. Finally, the last apparent alkyl bond was that of ILE309 with a linking atom. All the remaining interactions, with a total of two, were of the pi-alkyl type, in which PHE289 interacted with C12 and TRP313 with another binding atom.

The docking of modification 19 (Fig. 30) showed, in total, ten interactions, being a conventional hydrogen interaction with TYR308 and H43 (distance of 1.84 Å) and

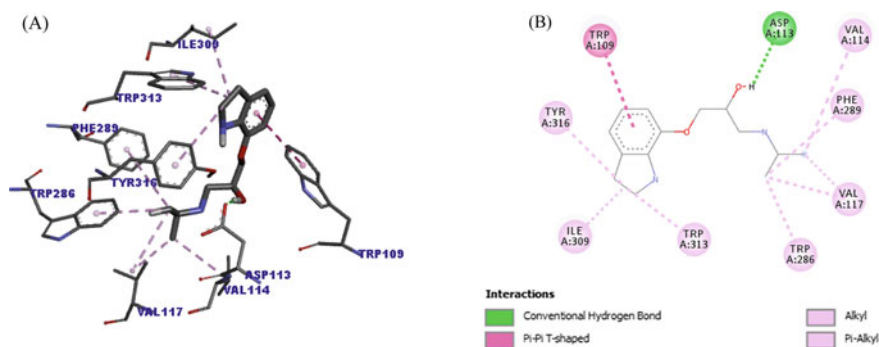


**Fig. 28** Result of molecular docking of modification 6 in  $\beta_2$ -adrenergic receptor. **A** 3D model; **B** 2D model. Intermolecular interactions are represented by the colors: conventional hydrogen bonds (green color), pi-pi T-shaped (dark pink) and alkyl and pi-alkyl (light pink color)

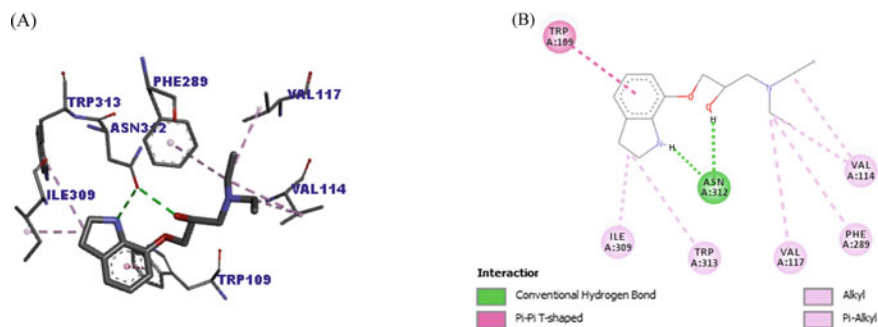


**Fig. 29** Result of molecular docking of modification 18 in  $\beta_2$ -adrenergic receptor. **A** 3D model; **B** 2D model. Intermolecular interactions are represented by the colors: conventional hydrogen bonds (green color), pi-pi T-shaped (dark pink) and alkyl and pi-alkyl (light pink color)

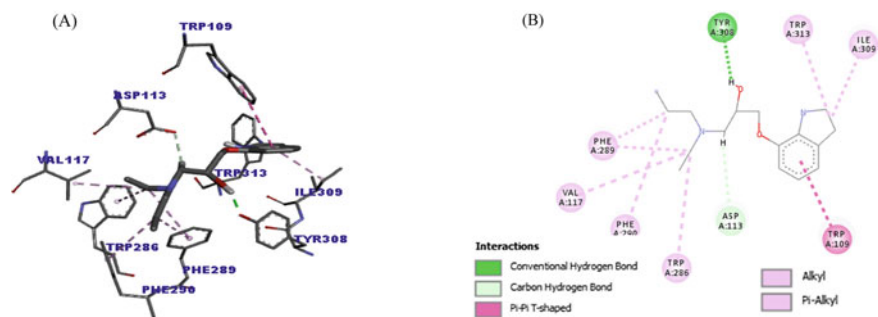


**Fig. 30** Result of molecular docking of modification 19 in  $\beta_2$ -adrenergic receptor. **A** 3D model; **B** 2D model. Intermolecular interactions are represented by the colors: conventional hydrogen bonds (green color), Carbon-hydrogen bonds (light blue color), pi-pi T-shaped (dark pink) and alkyl and pi-alkyl (light pink color)

another of the carbon-hydrogen type, between ASP113 and the H27, at a distance of 2.54 Å.

All other interactions were hydrophobic, only one of which was pi-pi T-shaped, characterized by the interaction between the amino acid TRP109 and the ligand atom. Two were of the alkyl type with VAL117 interacting with C12 and ILE309 with another atom. The rest of the interactions were all pi-alkyl, TRP286 and PHE289 interacted with C12, PHE289 and PHE290 interacted with C15 and TRP313 with some atom of the ligand.

In the result of modification 20 (Fig. 31), one can observe thirteen interactions, having two more interactions than the propranolol molecule, presenting four hydrogen bonds and nine hydrophobic bonds. Of the four hydrogen bonds, two are conventional hydrogen bonds, with the interaction of a single amino acid, ASN312, and two different ligands, H28 and H462, with a distance in Å of 2.04 and 1.97,



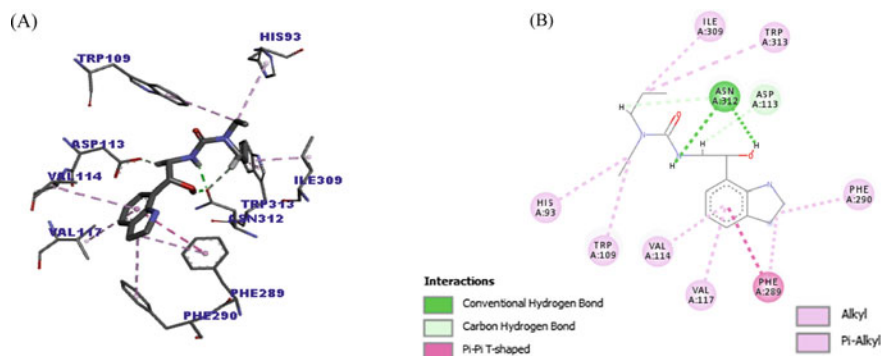


**Fig. 31** Result of molecular docking of modification 20 in  $\beta_2$ -adrenergic receptor. **A** 3D model; **B** 2D model. Intermolecular interactions are represented by the colors: conventional hydrogen bonds (green color), Carbon-hydrogen bonds (light blue color), pi-pi T-shaped (dark pink) and alkyl and pi-alkyl (light pink color)

respectively. The others are carbon-hydrogen bonds, with interaction of ASN312 and H31 (distance of 2.15 Å) and of ASP113 with H27, with a distance of 2.85 Å.

Regarding hydrophobic interactions, one is of the pi-pi T-shaped type, characterized by the bond between PHE289 and a ligand atom. Only one is of the alkyl type, where ILE309 interacts with C15. All the remaining bonds, with a total of seven interactions, were pi-alkyl, in which HIS93 and TRP109 interacted with C12, TRP313 with C15 and PHE289, PHE290, VAL114, VAL117 bonded to other atoms present in the molecule.

The docking of modification 24 (Fig. 32) presented a total of eight interactions, being two hydrogen bonds, being conventionally configured by the interaction

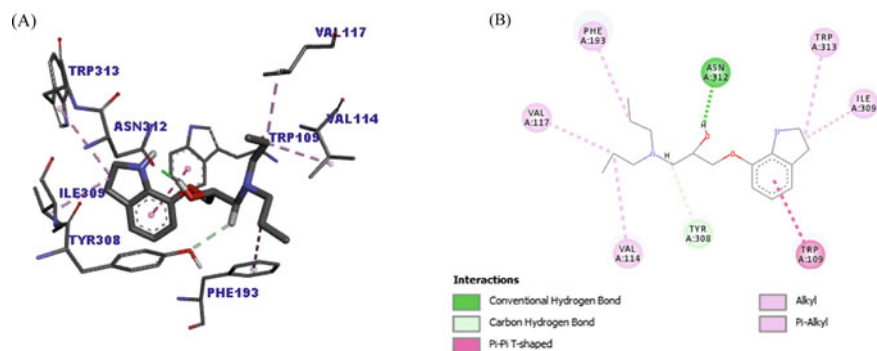


**Fig. 32** Molecular docking result of modification 24 in  $\beta_2$ -adrenergic receptor. **A** 3D model; **B** 2D model. Intermolecular interactions are represented by the colors: conventional hydrogen bonds (green color), Carbon-hydrogen bonds (light blue color), pi-pi T-shaped (dark pink) and alkyl and pi-alkyl (light pink color)

between ASN312 and H43, with a distance of 1.75 Å and the other of the carbon-hydrogen type, visualized through the interaction between the TR308 and with the H29 atom, at a distance of 2.76 Å between the molecules.

The rest of the interactions, with a total of six (6), were hydrophobic interactions, which had a T-shaped pi-pi, with TRP109 interacting with a binding atom. Three bonds, of the alkyl type, occurred with VAL114 and VAL117 interacting with C14 and ILE309 with a linking atom. The last two interactions were of the pi-alkyl type, visualized by PHE193 interacting with C15 and by TRP313 interacting with another ligand.

The remaining five were all pi-alkyl, in which the TRP251 interacted with the C15 and the PHE422 with the C12. Amino acid residues PHE404, VAL256, VAL259 interacted with different atoms of the linker molecule.

Modification 25 (Fig. 33) also presented a total of eleven bonds, equivalent to that of propranolol, differing in terms of the types of interactions. In total, there were six hydrogen bonds, three of the conventional type and three of the carbon-hydrogen type. Those of the conventional type were shown by the interactions between ASN312 and H29 (2.09 Å distance), TYR308 with H37 (2.12 Å distance) and ASP 112 with H45 (1.95 Å distance). While the carbon-hydrogen type, it was characterized by the interaction between ASN312 and the atoms of H26 and H32, with a distance of 2.56 and 2.30 Å, respectively, and by the interaction between the ASP113 with the H28 atom (distance of 2.88 Å).

As for the rest of the interactions, all were hydrophobic interactions, and PHE290 made one of the pi-pi T-shaped type. ILE309, on the other hand, performed two alkyl-type interactions, one with C19 and the other with an atom of the ligand. Finally, the HIS93, TRP109, PHE193, VAL117, VAL117 and TRP313 pi-alkyl type interactions.

The largest number of interactions visualized was that of modification 26 (Fig. 34), in which a total of sixteen connections was made. Of these, seven were hydrogen bonds, being divided into four of the conventional type and three carbon-hydrogen bonds. Regarding conventional connections, ASN312 interacted with O20 and H29, with a distance of 2.44 Å and 2.09 Å, in that order. The others were characterized by

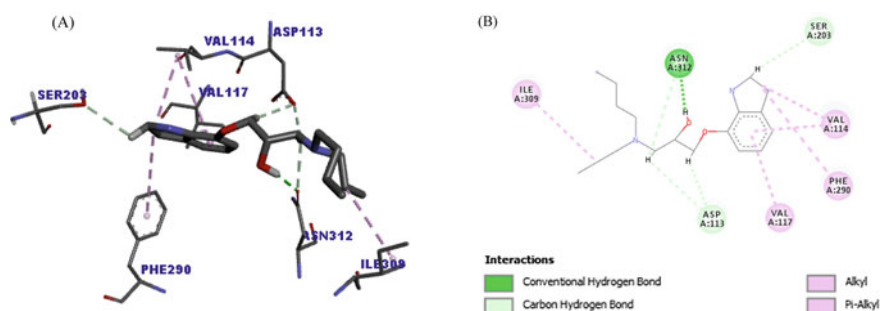


**Fig. 33** Result of molecular docking of modification 25 in  $\beta_2$ -adrenergic receptor. **A** 3D model; **B** 2D model. Intermolecular interactions are represented by the colors: conventional hydrogen bonds (green color), Carbon-hydrogen bonds (light blue color) and alkyl and pi-alkyl (light pink color)

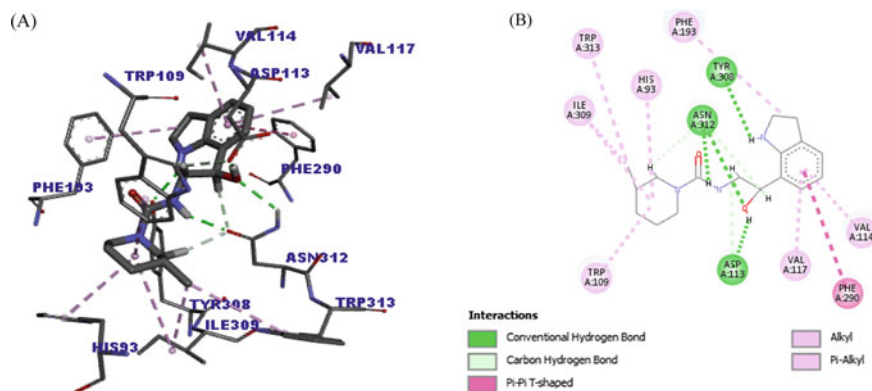


**Fig. 34** Molecular docking result of modification 26 in  $\beta$ 2-adrenergic receptor. **A** 3D model; **B** 2D model. Intermolecular interactions are represented by the colors: conventional hydrogen bonds (green color), Carbon-hydrogen bonds (light blue color), pi-pi T-shaped (dark pink) and alkyl and pi-alkyl (light pink color)

the interaction between TYR208 and H37 (distance of 2.12 Å) and between ASP113 and H45 (distance of 1.95 Å). Regarding carbon-hydrogen, ASP312 has already made two interactions, one with H26 and another with H32, at a distance, respectively, of 2.56 and 2.30 Å and ASP113 made an interaction, also with H32, moving away from the 2.88 Å ligand.

The other interactions, all hydrophobic, showed a pi-pi T-shaped bond, characterized by the interaction between the PHE290 amino acid and the ligand atom. Two were of the alkyl type with ILE309 interacting with C19 and another atom of the ligand. The rest of the interactions, totaling six, were of the pi-alkyl type, with HIS93, TRP109, PHE193, VAL114, VAL117 interacting with different atoms of the ligand and TRP313 with C19.

Regarding the modification 27 docking (Fig. 35), as well as the prototype, when compared to the propranolol it presented better results, since it had three more interactions and with greater forces. In all, there were five hydrogen bonds, four of the conventional type and only one of the carbon-hydrogen type. The TYR316 made conventional connection with the O21 (distance of 2.91 Å). The TYR308 interacted with the H31 and H39, with distances of 2.06 and 1.77 Å, respectively. ASN312, on the other hand, made a conventional bond with H47 and a carbon-hydrogen bond with H28, distancing itself from the ligand 1.81 and 2.65 Å, respectively.

As for the hydrophobic interactions, one was pi-pi T-shaped with PHE289 interacting with a binding atom. Another was an alkyl bond, performed through the interaction between ILE309 and C22. The remainder of the interactions, with a total of seven bonds, were of the pi-alkyl type, with TRP109, TRP313, TYR313 interacting with C23, with ILE309 and TRP313 with C22 and finally, PHE193, VAL114 and VAL117 with different ligands on the molecule.

Finally, the last modification analyzed was number 28 (Fig. 36) and presented a total of ten interactions. It was possible to observe only two hydrogen bonds,

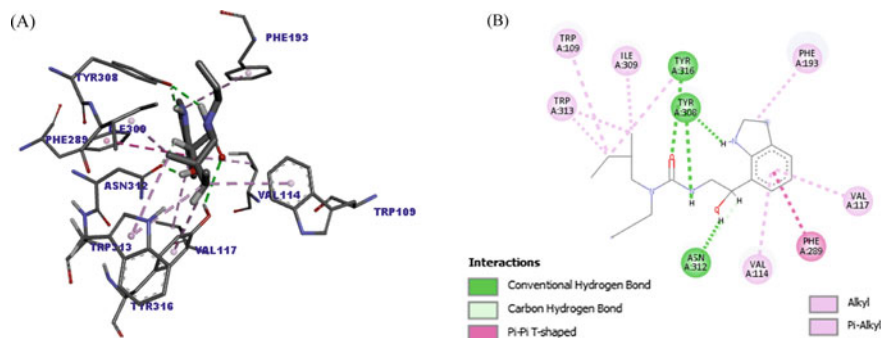


**Fig. 35** Molecular docking result of modification 27 in  $\beta_2$ -adrenergic receptor. **A** 3D model; **B** 2D model. Intermolecular interactions are represented by the colors: conventional hydrogen bonds (green color), Carbon-hydrogen bonds (light blue color), pi-pi T-shaped (dark pink) and alkyl and pi-alkyl (light pink color)

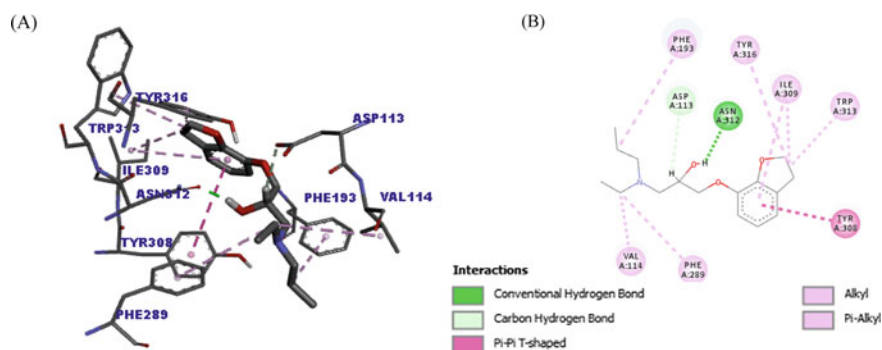


**Fig. 36** Result of molecular docking of modification 28 in  $\beta_2$ -adrenergic receptor. **A** 3D model; **B** 2D model. Intermolecular interactions are represented by the colors: conventional hydrogen bonds (green color), Carbon-hydrogen bonds (light blue color), pi-pi T-shaped (dark pink) and alkyl and pi-alkyl (light pink color)

one conventional, with ASN31 and H42 (distance of 1.76 Å) and another carbon-hydrogen, between ASP113 and H26, at a distance of 2.69 Å.

The rest of the interactions were of the hydrophobic type, in which only one pi-pi T-shaped, characterized by the interaction between the amino acid TYR308 with an atom of the ligand. Two were of the alkyl type with VAL117 interacting with C12 and ILE309 with another atom. The rest of the interactions were all pi-alkyl, PHE193 and PHE289 interacted with C15 and C12, respectively. TRP313, TYR316 and ILE309 made interactions with different atoms.

Unlike the analysis of molecules in  $\beta_1$ -adrenergic receptors, molecular docking in  $\beta_2$ -adrenergic receptors had better results, since a greater number of molecules can be observed (prototype, molecule 5, 20, 25, 26 and 27) with results of interactions equivalent or even greater than that of propranolol. It is important to highlight the result of

molecule 26, which had five more interactions than the drug already commercially distributed, in addition to having interactions with higher binding strengths.

### 3.9.3 Molecule Selectivity

As previously described, the score value is given by the docking program and, in a simplified way, is nothing more than a parameter that allows establishing the best conformation that a ligand can have in the target's active site [58]. With this, it is possible to predict, through the score, if one molecule is more selective than another. In other words, the higher the score, the higher the indicator that a molecule is selective for a specific target, since the molecule had a better fit. Therefore, this stage of the study aimed to compare the scores obtained in each docking of the molecules in the different receptors in order to establish the selectivity of each one in the target proteins (Table 13).

As described in the literature, propranolol is a non-selective  $\beta$ -adrenergic receptor antagonist, which in other words means that it has an effect on both receptors. And it is possible to visualize through the table, where the values of the scores are very close to each other.

In the case of the prototype, it can be seen that the scores for both receptors were quite high, meaning that the molecule had a better fitting performance than propranolol and even to modifications. However, by approximating the values, it indicates a non-selectivity for adrenergic receptors.

From a general perspective, the molecules showed a better fit at  $\beta_2$ -adrenergic receptors, but not with a significant difference to assert selectivity. However, some

**Table 13** Score of molecules analyzed in docking at  $\beta_1$  and  $\beta_2$  adrenergic receptors

Molecule	$\beta_1$ -adrenergic	$\beta_2$ -adrenergic
Propranolol	63.83	65.45
Prototype	90.88	86.29
Modification 1	80.44	82.88
Modification 2	52.75	60.54
Modification 5	81.55	84.34
Modification 6	62.22	64.34
Modification 18	60.74	65.36
Modification 19	61.43	65.47
Modification 20	63.60	68.24
Modification 24	65.17	73.54
Modification 25	69.79	75.48
Modification 26	64.77	70.99
Modification 27	68.61	79.34
Modification 28	61.50	68.51

caveats are necessary, as in the case of modifications 2, 24 and especially modification 27, they presented a slight selectivity for  $\beta$ 2-adrenergic receptors.

## 4 Conclusion

Propranolol is the most commonly used drug for the treatment of ET and its prolonged use produces changes in the users' quality of life. Therefore, the development of a new drug with better properties is a therapeutic option that can provide patients with this disorder with fewer problems related to the use of drugs to treat ET.

After determining the prototype, using computational tools, different modifications were carried out in order to obtain a more promising molecule than the original. From a general perspective, the results were favorable, since in different analyses, many of the modifications presented superior results than those of propranolol. Regarding the pharmacokinetic evaluation, according to the research criteria, including the prototype, seven molecules (1, 2, 5, 20, 26 and 27) obtained favorable responses. Regarding the toxicological evaluation, all modifications had superior results, representing a significant improvement in this regard.

Regarding the activity prediction analysis, in all, six modifications (6, 18, 19, 24, 25 and 28) had positive results, mainly in relation to tremor relief, which is one of the main focuses of the research. As for the analysis in SEA, only one molecule had a favorable performance, being number 1. However, in molecular docking, the results were suggestive that many molecules have the capacity for a better interaction with the targets. In  $\beta$ 1-adrenergic receptor docking, the prototype and modifications number 6 and 27 showed a better fit, signaling quantities of interactions with greater intermolecular forces. Regarding the  $\beta$ 2-adrenergic, the prototype and five other modifications (5, 20, 25, 26 and 27) had a better performance against the docking of the propranolol molecule.

Therefore, it would be of interest to continue with the in-silico studies of these proposals as a way to further improve their properties, in order to enable a drug with better performance for the treatment of Essential Tremor.

## References

1. Ferreira, J.J., et al.: MDS evidence-based review of treatments for essential tremor. *Mov. Disord.* **34**(7), 950–958 (2019). <https://doi.org/10.1002/mds.27700>
2. Carvalho, V., Massano, J.: Tremor: a clinical guide for the non-neurologist. *Acta Med. Port.* **32**(2), 149–157 (2019). <https://doi.org/10.20344/amp.11352>
3. Elble, R.J.: Tremor. USA (2017)
4. Louis, E.D.: Tremor. *Contin. Lifelong Learn. Neurol.* 959–975 (2019)
5. Mansur, P.H.G., et al.: A review on techniques for tremor recording and quantification. *Crit. Rev. Biomed. Eng.* **35**(5), 343–362 (2007). <https://doi.org/10.1615/CritRevBiomedEng.v35.i5.10>

6. Hess, C.W., Pullman, S.L.: Tremor: clinical phenomenology and assessment techniques. *Tremor Other Hyperkinet. Mov.* **2**, 1–15 (2012). <https://doi.org/10.5334/TOHM.115>
7. Haubenberger, D., Hallett, M.: Essential tremor. *N. Engl. J. Med.* **378**(19), 1802–1810 (2018). <https://doi.org/10.1056/NEJMcp1707928>
8. Hopfner, F., Deuschl, G.: Is Essential tremor a single entity? *Eur. J. Neurol.* **25**(1), 71–82 (2018). <https://doi.org/10.1111/ijlh.12426>
9. Shanker, V.: Essential tremor: diagnosis and management. *BMJ* **366** (2019). <https://doi.org/10.1136/bmj.l4485>
10. Louis, E.D.: The roles of age and aging in essential tremor: an epidemiological perspective. *Neuroepidemiology* **52**(1–2), 111–118 (2019). <https://doi.org/10.1159/000492831>
11. Odgerel, Z., et al.: Whole genome sequencing and rare variant analysis in essential tremor families. *PLoS ONE* **14**(8), 1–28 (2019). <https://doi.org/10.1371/journal.pone.0220512>
12. Tarakad, A., Jankovic, J., Clinch, M.D.: Reviews essential tremor and Parkinson's disease : exploring the relationship, 1–10 (2018). <https://doi.org/10.7916/D8MD0GVR>
13. Zesiewicz, T.A., Chari, A., Jahan, I., Miller, A.M., Sullivan, K.L.: Overview of essential tremor. *Neuropsychiatr. Dis. Treat.* **6**(1), 401–408 (2010)
14. Puschmann, A., Wszolek, Z.K.: Diagnosis and treatment of common forms of tremor. *Semin. Neurol.* **31**(1), 65–77 (2011)
15. Louis, E.D.: Non-motor symptoms in essential tremor: a review of the current data and state of the field. *Park. Relat. Disord.* **22**, S115–S118 (2016). <https://doi.org/10.1016/j.parkreldis.2015.08.034>
16. Ippolito, M., Benovic, J.L.: Biased agonism at  $\beta$ -adrenergic receptors. *Cell. Signal.* **80**(November 2020), 109905 (2021). <https://doi.org/10.1016/j.cellsig.2020.109905>
17. Fumagalli, C., Maurizi, N., Marchionni, N., Fornasari, D.:  $\beta$ -blockers: their new life from hypertension to cancer and migraine. *Pharmacol. Res.* **151**(December 2019), 104587 (2020). <https://doi.org/10.1016/j.phrs.2019.104587>
18. Pfeleger, J., Gresham, K., Koch, W.J.: G protein-coupled receptor kinases as therapeutic targets in the heart. *Nat. Rev. Cardiol.* **16**(10), 612–622 (2019). <https://doi.org/10.1038/s41569-019-0220-3>
19. Oliver, E., Mayor Jr, F., D'Ocon, P.: Beta-blockers: historical perspective and mechanisms of action. *Rev. Española Cardiol. (English Ed.)* **72**(10), 853–862 (2019). <https://doi.org/10.1016/j.rec.2019.04.006>
20. Kalam, M.N., Rasool, M.F., Rehman, A.U., Ahmed, N.: Clinical pharmacokinetics of propranolol hydrochloride: a review. *Curr. Drug Metab.* **21**(2), 89–105 (2020)
21. Bhidayasiri, R.: Differential diagnosis of common tremor syndromes. *Postgrad. Med. J.* **81**(962), 756–762 (2005). <https://doi.org/10.1136/pgmj.2005.032979>
22. Jefferson, D., Jenner, P., Marsden, C.D.:  $\beta$ - Adrenoreceptor antagonists in essential tremor. *J. Neurol. Neurosurg. Psychiatry* **42**(10), 904–909 (1979). <https://doi.org/10.1136/jnnp.42.10.904>
23. Hedera, P., Cibulčík, F., Davis, T.L.: Pharmacotherapy of essential tremor. *J. Cent. Nerv. Syst. Dis.* **5**, JCNSD.S6561 (2013). <https://doi.org/10.4137/jcnsd.s6561>
24. Reich, S.G.: Treatment of essential tremor: medical therapy. *Curr. Clin. Neurol.* 165–168 (2019). [https://doi.org/10.1007/978-3-319-97897-0\\_37](https://doi.org/10.1007/978-3-319-97897-0_37)
25. Wang, Y., et al.: In silico ADME/T modelling for rational drug design. *Q. Rev. Biophys.* **48**(4), 488–515 (2015). <https://doi.org/10.1017/S0033583515000190>
26. Winiwarter, S., et al.: In silico ADME in drug design—Enhancing the impact. *ADMET DMPK* **6**(1), 15–33 (2018). <https://doi.org/10.5599/admet.6.1.470>
27. Paul Gleeson, M., Hersey, A., Hannongbua, S.: In-Silico ADME models: a general assessment of their utility in drug discovery applications. *Curr. Top. Med. Chem.* **11**(4), 358–381 (2011). <https://doi.org/10.2174/156802611794480927>
28. Clark, D.E., Grootenhuis, P.D.J.: Predicting Passive Transport, pp. 1193–1203 (2003)
29. Gilson, M.K., Liu, T., Baitaluk, M., Nicola, G., Hwang, L., Chong, J.: BindingDB in 2015: a public database for medicinal chemistry, computational chemistry and systems pharmacology. *Nucleic Acids Res.* **44**(D1), D1045–D1053 (2016). <https://doi.org/10.1093/nar/gkv1072>

30. Liu, T., Lin, Y., Wen, X., Jorissen, R.N., Gilson, M.K.: BindingDB: a web-accessible database of experimentally determined protein-ligand binding affinities. *Nucleic Acids Res.* **35**(SUPPL. 1), 198–201 (2007). <https://doi.org/10.1093/nar/gk1999>
31. Patrick, G.L.: An Introduction to medicinal chemistry (2013)
32. Kim, S., et al.: PubChem substance and compound databases. *Nucleic Acids Res.* **44**(D1), D1202–D1213 (2016). <https://doi.org/10.1093/nar/gkv951>
33. Schneidman-Duhovny, D., Dror, O., Inbar, Y., Nussinov, R., Wolfson, H.J.: PharmaGist: a webserver for ligand-based pharmacophore detection. *Nucleic Acids Res.* **36**(Web Server issue), 223–228 (2008). <https://doi.org/10.1093/nar/gkn187>
34. Koes, D.R., Camacho, C.J.: ZINCPharmer: pharmacophore search of the ZINC database. *Nucleic Acids Res.* **40**(W1), 409–414 (2012). <https://doi.org/10.1093/nar/gks378>
35. Lipinski, C.A.: Lead- and drug-like compounds: the rule-of-five revolution. *Drug Discov. Today Technol.* **1**(4), 337–341 (2004). <https://doi.org/10.1016/j.ddtec.2004.11.007>
36. Chandrasekaran, B., Abed, S.N., Al-Attraqchi, O., Kuche, K., Tekade, R.K.: Computer-Aided Prediction of Pharmacokinetic (ADMET) Properties, vol. 2. Elsevier Inc. (2018)
37. Ntie-Kang, F.: An in silico evaluation of the ADMET profile of the StreptomeDB database. *Springerplus* **2**(1), 1–11 (2013). <https://doi.org/10.1186/2193-1801-2-353>
38. Marchant, C.A.: Prediction of rodent carcinogenicity using the DEREK system for 30 chemicals currently being tested by the National Toxicology Program. *Environ. Health Perspect.* **104**(SUPPL. 5), 1065–1073 (1996). <https://doi.org/10.1289/ehp.96104s51065>
39. Ferreira, L.G., Dos Santos, R.N., Oliva, G., Andricopulo, A.D.: Molecular docking and structure-based drug design strategies **20**(7) (2015)
40. Onodera, K., Satou, K., Hirota, H.: Evaluations of molecular docking programs for virtual screening. *J. Chem. Inf. Model.* **47**(4), 1609–1618 (2007). <https://doi.org/10.1021/ci7000378>
41. Verdonk, M.L., Cole, J.C., Hartshorn, M.J., Murray, C.W., Taylor, R.D.: Improved protein-ligand docking using GOLD. *Proteins Struct. Funct. Genet.* **52**(January), 609–623 (2003)
42. Berman, H.M., et al.: The protein data bank. *Acta Crystallogr. Sect. D Biol. Crystallogr.* **58**(6) I, 899–907 (2002). <https://doi.org/10.1107/S0907444902003451>
43. Wacker, D., et al.: Conserved binding mode of human  $\beta_2$  adrenergic receptor inverse agonists and antagonist revealed by X-ray crystallography. *J. Am. Chem. Soc.* **132**(33), 11443–11445 (2010). <https://doi.org/10.1021/ja105108q>
44. Xu, X. et al.: Binding pathway determines norepinephrine selectivity for the human  $\beta_1$ AR over  $\beta_2$ AR. *Cell Res.* September, 1–11 (2020). <https://doi.org/10.1038/s41422-020-00424-2>
45. López-Camacho, E., García-Godoy, M.J., García-Nieto, J., Nebro, A.J., Aldana-Montes, J.F.: A new multi-objective approach for molecular docking based on rmsd and binding energy. *Lect. Notes Comput. Sci. (including Subser. Lect. Notes Artif. Intell. Lect. Notes Bioinformatics)* **9702**, 65–77 (2016). [https://doi.org/10.1007/978-3-319-38827-4\\_6](https://doi.org/10.1007/978-3-319-38827-4_6)
46. Louis, E.D.: Clinical practice: Essential tremor. *N. Engl. J. Med.* **345**(12), 887–891 (2001). [http://www.ncbi.nlm.nih.gov/entrez/query.fcgi?db=pubmed&cmd=Retrieve&dopt=AbstractPlus&list\\_uids=11565522](http://www.ncbi.nlm.nih.gov/entrez/query.fcgi?db=pubmed&cmd=Retrieve&dopt=AbstractPlus&list_uids=11565522)
47. Yang, S.Y.: Pharmacophore modeling and applications in drug discovery: challenges and recent advances. *Drug Discov. Today* **15**(11–12), 444–450 (2010). <https://doi.org/10.1016/j.drudis.2010.03.013>
48. Drwal, M.N., Griffith, R.: Combination of ligand- and structure-based methods in virtual screening. *Drug Discov. Today Technol.* **10**(3), e395–e401 (2013). <https://doi.org/10.1016/j.ddtec.2013.02.002>
49. Balbach, S., Korn, C.: Pharmaceutical evaluation of early development candidates ‘the 100 mg-approach.’ *Int. J. Pharm.* **275**(1–2), 1–12 (2004). <https://doi.org/10.1016/j.ijpharm.2004.01.034>
50. Pelkonen, O., Boobis, A.R., Gundert-Remy, U.: In vitro prediction of gastrointestinal absorption and bioavailability: an experts’ meeting report. *Eur. J. Clin. Pharmacol.* **57**(9), 621–629 (2001). <https://doi.org/10.1007/s002280100369>
51. Van Breemen, R.B., Li, Y.: Caco-2 cell permeability assays to measure drug absorption. *Expert Opin. Drug Metab. Toxicol.* **1**(2), 175–185 (2005)



52. Volpe, D.A.: Variability in Caco-2 and MDCK cell-based intestinal permeability assays. *J. Pharm. Sci.* **97**(2), 712–725 (2008). <https://doi.org/10.1002/jps>
53. Obermeier, B., Verma, A., Ransohoff, R.M.: *The Blood-Brain Barrier* (1st ed.) vol. 133. Elsevier B.V. (2016)
54. Thomas, D., Karle, C., Kiehn, J.: The cardiac hERG/IKr potassium channel as pharmacological target: structure, function, regulation, and clinical applications. *Curr. Pharm. Des.* **12**(18), 2271–2283 (2006). <https://doi.org/10.2174/138161206777585102>
55. Reisfeld, B., Mayeno, A.N.: What is computational toxicology? *Methods Mol. Biol.* **929**, 3–7 (2012). [https://doi.org/10.1007/978-1-62703-50-2\\_1](https://doi.org/10.1007/978-1-62703-50-2_1)
56. Sanderson, D.M., Earnshaw, C.G.: Computer prediction of possible toxic action from chemical structure; The DEREK system. *Hum. Exp. Toxicol.* **10**(4), 261–273 (1991). <https://doi.org/10.1177/096032719101000405>
57. Mattei, A., Li, T.: Intermolecular interactions and computational modeling. *Pharmaceut. Cryst. Sci. Eng.* 123–167 (2018)
58. Krovat, E.M., Steindl, T., Langer, T.: Recent advances in docking and scoring, 93–102 (2005)
59. Mizogami, M., Takakura, K., Tsuchiya, H.: The interactivities with lipid membranes differentially characterize selective and nonselective  $\beta$ 1-blockers. *Eur. J. Anaesthesiol.* **27**(9), 829–834 (2010). <https://doi.org/10.1097/EJA.0b013e32833bf5e4>

# Intramolecular Hydrogen Bonding Patterns and Conformational Preferences of Ouabain—A Molecule with Cardiotonic and Antiviral Activities



Liliana Mammino

**Abstract** Ouabain is a steroid-glycoside compound that has been used for decades for the treatment of heart diseases, and has also proved effective against several viruses, including coronaviruses; its potentialities against SARS-CoV-2 are currently object of various investigations. The molecule contains eight OH groups, whose mutual positions enable the simultaneous presence of several O—H...O intramolecular hydrogen bonds (IHB), although only few with bond length shorter than 2 Å and favourable directionality. Conformers corresponding to different IHB patterns have been calculated at the DFT level of theory, using both the B3LYP and the M062X functionals. Two sets of B3LYP calculations were performed, without and with the Grimme's dispersion correction, to evaluate the influence of dispersion forces on the estimation of the molecular properties. The results highlight four conformers whose relative energies are sufficiently low to make them potentially responsible for the molecule's biological activities. They also highlight the influence of the incorporation of correlation effects on the estimation of energetics and other properties.

**Keywords** Antivirals · Bioactive compounds of natural origin · Cardiotonic glycosides · Correlation effects · Intramolecular hydrogen bonding · SARS-CoV-2 · Steroid glycosides

## 1 Introduction

Ouabain (also called G-strophanthin, C<sub>29</sub>H<sub>44</sub>O<sub>12</sub>, Fig. 1) is a bioactive steroid-glycoside compound present in the roots, stems, leaves and seeds of the *Acokanthera schimperi* and *Strophanthus gratus* plants, indigenous to Eastern Africa [1, 2] and whose juices were traditionally used to poison arrows because of the toxic properties of ouabain. In small doses, it exhibits beneficial pharmaceutical activities. It has been used for decades for its cardiotonic properties, deriving from its

---

L. Mammino (✉)

School of Mathematical and Natural Sciences, University of Venda, Thohoyandou, South Africa  
e-mail: [sasdestria@yahoo.com](mailto:sasdestria@yahoo.com)

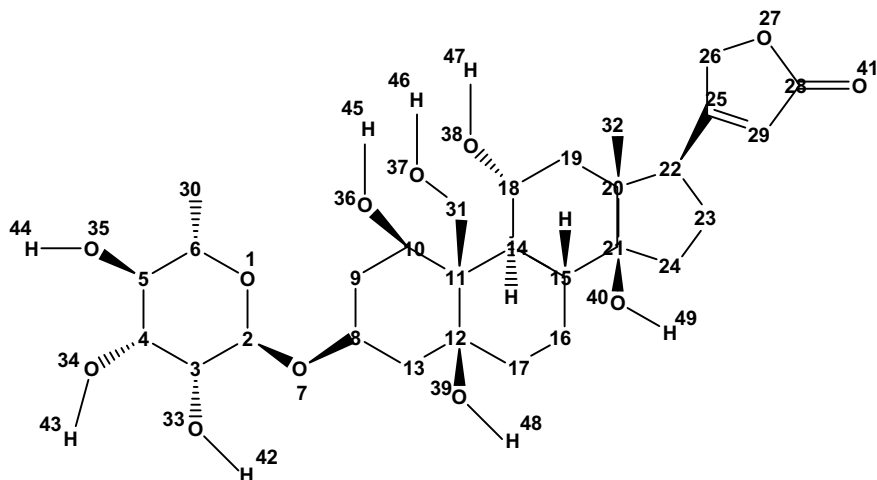


**Fig. 1** Molecular structure of the ouabain molecule and atom numbering utilised in this work. Only the H atoms attached to O atoms are numbered, because of their relevance in the discussion of hydrogen bonds. Other hydrogen atoms, if needing to be mentioned, are given the same number as the C atom to which they are attached; when more than one H atoms are attached to the same C atom, they are distinguished using subscripts (e.g., H31<sub>a</sub> and H31<sub>b</sub>)

ability to inhibit the activity of Na–K activated adenosinetriphosphatase (sodium–potassium ion pump, Na/K-ATPase), thus modulating the concentration of Na<sup>+</sup> ions and favouring intracellular calcium. Extensive research has focused on the investigation of this mechanism and its effects on various organs and conditions [3–25]. Its antiviral properties were recognised some decades ago [26], and [27, 28] specifically list coronaviruses among the viruses against which it is active. With the appearance of the SARS-CoV-2 pandemic and the consequent urgent search for drugs that can treat it, new investigations about its potentialities have been carried out [29–36]. The fact that it combines antiviral properties and anti-inflammatory properties ([16], probably related to its steroid moiety) is likely to constitute an additional advantage, as it may simultaneously fight the virus and provide relief for the inflammation it causes.

The current work presents the results of a computational study of the ouabain molecule, meant to highlight its conformational preferences, the characteristics of its intramolecular hydrogen bonds (IHBs) and other computable molecular properties. It is important to determine the molecular properties of biologically active substances with good accuracy because their biological activities may depend on the finest details of these properties [36]. Particular attention is here given to IHBs, because of their roles in determining conformational preferences (as the frequently strongest non-covalent interactions within a molecule) and of their potential participation in determining site-reactivity, molecular recognition and other features relevant to the mechanisms with which biological activities are exerted [37–42]. The results show the simultaneous presence of several IHBs, although only few with bond length

shorter than 2 Å and favourable directionality, and confirm their stabilising effects. They also highlight four conformers whose relative energies are sufficiently low to make them potentially responsible for the molecule's biological activities.

## 2 Computational Details

Calculations in vacuo (ideal gas phase) are preliminary to any other type of calculations, by providing an initial picture of a molecule's conformational preferences and the factors influencing them. All the calculations presented in this work were performed in vacuo, with fully relaxed geometry. Three calculation sets were performed at the DFT (Density Functional Theory) level, with three different options: using the B3LYP functional [43–45], using the B3LYP functional with the inclusion of a D3-type Grimme's dispersion correction [46–54], and using the M062X functional, which incorporates the consideration of correlation in a different form [55]. The B3LYP-D3 option has been described as among the best to provide reasonably accurate molecular geometries of organic molecules [53], and the comparison of B3LYP calculations with and without the Grimme's correction enables an evaluation of the consideration of correlation and dispersion effects on the estimation of molecular properties. The inclusion of dispersion effects is important for the description of H-bonds [56, 57], above all for weak H-bonds, as is the case of several of the IHBs in the conformers of the ouabain molecule. The use of two different functionals (B3LYP and M062X) is expedient to the purpose of identified-trends verification. Hartree Fock (HF) calculations were added for the same verification purpose (HF being an ab initio method, i.e., a method with a different nature than DFT) and to obtain realistic reference values for the HOMO–LUMO energy gaps. All the calculations utilised the 6–31+G(d,p) basis set, that had proved adequate for the description of other IHB-containing molecules [58–60]; the presence of diffuse functions is generally advisable for a better description of H-bonds [61–63].

IR vibrational frequencies (harmonic approximation) were calculated for the three selected options at the DFT level. No imaginary frequency was present, confirming that the identified stationary points correspond to minima on the potential energy surface of the molecule. The comparison of the lowering of the IR frequency of OH groups when engaged in IHBs as donors and when they are free enables approximate comparisons of the strengths of the various IHBs. Frequency calculations also provide the ZPE (zero-point energy) corrections, thus enabling the evaluation of ZPE-corrected relative energies.

All the calculations were performed with Gaussian-16 [64]. The visualisation of molecular structures utilised GaussView [65] and Chem3D [66]; the visualisation of bond vibrations utilised Gabedit [67].

For the sake of conciseness in the text and in the captions of tables and figures, the calculation methods are denoted with the following acronyms: B3LYP for DFT/B3LYP/6–31+G(d,p), B3LYP-D3 for DFT/B3LYP/6–31+G(d,p) with the

Grimme's correction, M062X for DFT/M062X/6-31+G(d,p) and HF for HF/6-31+G(d,p).

### 3 Results

#### 3.1 Conformational Preferences and Energetics

Figure 1 shows the structure of the ouabain molecule and the atom numbering utilised in this work. O7 bridges the glycoside moiety and the steroid moiety. The presence and positions of the eight OH groups and the other four O atoms enable the formation of a number of simultaneous O–H...O IHBs in each conformer. Depending on the conformer's geometry, the following IHBs are possible: H44...O1, H45...O1, H42...O7, H45...O7, H43...O33, H42...O34, H46...O36, H42...O36, H45...O37, H47...O37, H48...O37, H46...O38, and H46...O39.

Inputs were prepared considering possible patterns of simultaneous IHBs, with particular attention to the patterns enabling maximum number of simultaneous IHBs. This criterion is considered reliable because IHBs are often the dominant stabilising factors in the molecules in which their formation is possible. Furthermore, the consideration of different IHB patterns includes the absence of certain IHBs from certain inputs, thus expanding the conformers' range to include at least some of the higher energy ones. In some cases, an input with a certain IHB pattern optimised to a geometry with a different pattern, which was thus obtained from more than one input (the one containing it and the ones that optimised to it).

Ten conformers were thus identified; they are denoted by acronyms starting with 'ou' followed by a number; the numbers are progressive according to increasing relative energies sequence in the B3LYP-D3 results. Table 1 reports the relative energies of the calculated conformers. Figure 2 shows their optimised geometries,

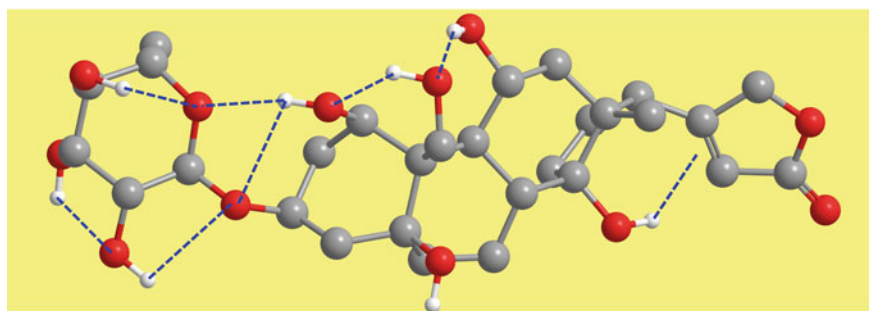
**Table 1** Relative energies of the calculated conformers of ouabain in the results of the four computational methods utilised

Conformer	Relative energy (kcal/mol)			
	B3LYP	B3LYP-D3	M062X	HF
ou-1	0.392	0.000	0.000	0.708
ou-2	1.085	0.683	1.011	1.661
ou-3	0.000	0.967	0.975	0.000
ou-4	1.310	1.873	2.430	1.564
ou-5	3.275	3.297	3.364	3.946
ou-6	4.889	5.454	5.926	5.194
ou-7	4.545	6.150	6.227	5.198

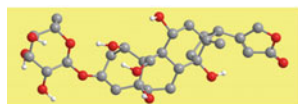
(continued)

**Table 1** (continued)

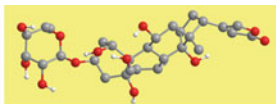
Conformer	Relative energy (kcal/mol)			
	B3LYP	B3LYP-D3	M062X	HF
ou-8	5.288	6.683	7.038	5.358
ou-9	7.534	6.780	6.567	9.071
ou-10	8.923	8.335	5.451	4.120



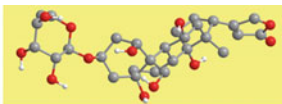
ou-1



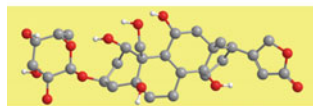
ou-2



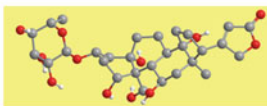
ou-3



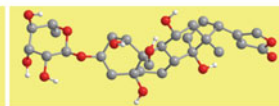
ou-4



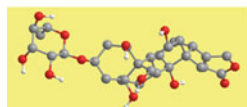
ou-5



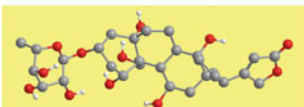
ou-6



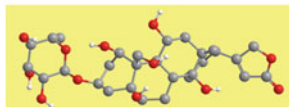
ou-7



ou-8



ou-9



ou-10

**Fig. 2** B3LYP/6-31+G(d,p) optimised geometries of the calculated conformers of ouabain in vacuo. The H atoms bonded to C atoms have been hidden to better highlight the conformer's geometry and the intramolecular hydrogen bonds (IHBs). The IHBs present in ou-1 are shown explicitly, representing them as blue dashed segments.

orienting each structure in a way that facilitates the identification of its IHBs; the IHBs of ou-1 are shown explicitly.

The different calculation methods highlight largely similar trends for the relative energies (diagram (a), Fig. 3), although the identification of the lowest energy conformers differs between the two methods incorporating correlation corrections (B3LYP-D3 and M062X) and the other two methods (B3LYP and HF). In addition, noticeable differences appear for the higher energy conformers ou-9 and ou-10.

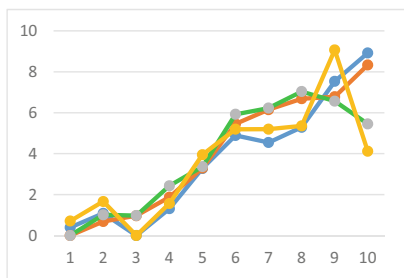
Any of the four lowest energy conformers (ou-1, ou-2, ou-3 and ou-4) may in principle be responsible for the biological activity of ouabain, although ou-1 has likely greater probability (the conformer responsible for the biological activity of a molecule is one of the sufficiently populated ones, i.e., one of those with sufficiently low relative energy—often, but not always, the lowest energy one).

Table 2 offers a synopsis of the relative energies not corrected and corrected for ZPE and the relative free energies of the calculated conformers in the results of the three sets of DFT calculations. Figure 3 visualizes the comparisons: trends of the same relative-energy type in the results of different calculation methods (diagrams a, b and c) and trends of different energy-types in the results of the same calculation methods (diagrams d, e, f). The diagrams offer complete information about the comparisons.

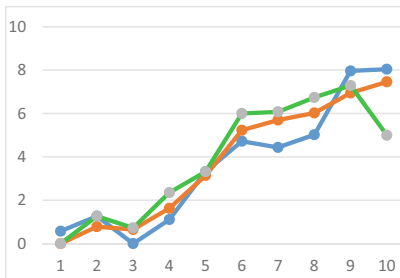
Table 3 compares relevant effect-types. Block A shows the effect of the inclusion of the Grimme's dispersion correction on the energy estimations in the B3LYP calculations; the B3LYP-D3 energy is lower than the B3LYP one, by 83.4–85.2 kcal/mol for the energies not corrected for ZPE, 81.7–83.8 kcal/mol for the energies corrected for ZPE and 80.7–83.1 kcal/mol for the Gibbs free energies. Block B compares the energy estimations with the two functionals utilised: the B3LYP energy is lower than the M062X one, by 494.1–496.8, 500.8–503.2 and 502.0–504.9 kcal/mol respectively for the energies not corrected and corrected for ZPE and for the Gibbs free energies. The last block reports the values of the ZPE correction as estimated by the three DFT options utilised. Diagrams (g), (h) and (i) in Fig. 3 visualise the comparisons for the quantities considered in each of these blocks and highlight large trend-similarities within the same block.

### 3.2 Characteristics of the Intramolecular Hydrogen Bonds

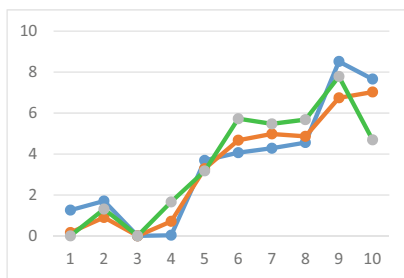
Up to seven O–H...O IHBs may be simultaneously present in a conformer (eight in ou-9). As already mentioned, the inputs' selection considered options with maximum or close-to-maximum numbers of IHBs, to identify all low energy conformers. Options with smaller number of IHBs were considered as samples, and not all the possibilities were included. For instance, the option with H42...O34 replacing H43...O33 and H42...O7 was considered only in one case (ou-5) because comparison between ou-5 and ou-2 (having the same other IHBs and differing only for this replacement) confirms the expectation that replacing two IHBs by one brings significant energy increase. Options in which O35–H44 does not form the H44...O1 IHB



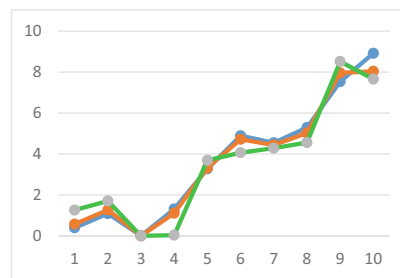
(a)



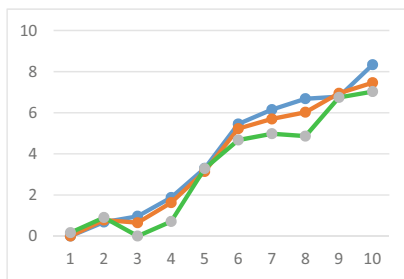
(b)



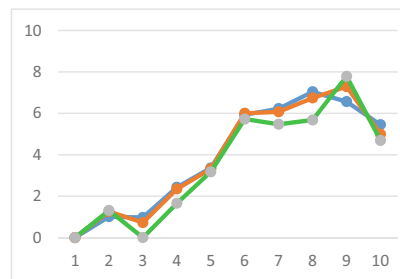
(c)



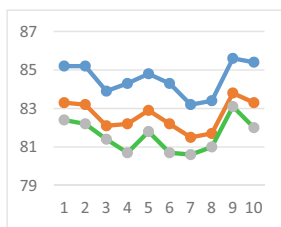
(d)



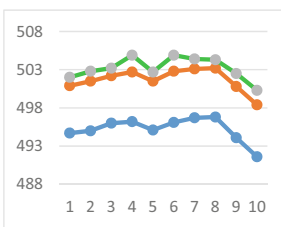
(e)



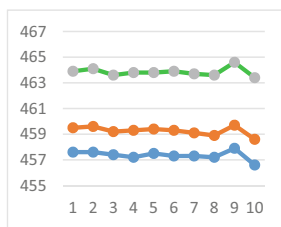
(f)



(g)



(h)



(i)



◀**Fig. 3** Relevant comparisons of the relative energies of the calculated conformers of ouabain. For each diagram, the specified energies (kcal/mol) are reported on the vertical axis and the conformers (denoted by the numbers in their acronyms) on the horizontal axis. The following quantities are reported on the vertical axes: **a** Relative energies not corrected for ZPE, in the results of the four calculation methods utilised. **b** Relative energies corrected for ZPE, in the results of the three DFT methods utilised. **c** Relative free energies, in the results of the three DFT methods utilised. **d** Relative energies not corrected for ZPE and corrected for ZPE, and relative Gibbs free energies, in the B3LYP results. **e** Relative energies not corrected for ZPE and corrected for ZPE, and relative Gibbs free energies, in the B3LYP-D3 results. **f** Relative energies not corrected for ZPE and corrected for ZPE, and relative Gibbs free energies, in the M062X results. **g** Lowering effect of the inclusion of the Grimme's dispersion correction on the energy estimation using the B3LYP functional. **h** Difference in the energy estimation between the B3LYP and the M062X functionals. **i** Zero point energy correction. Legend: In diagrams (a), (b), (c) and (j): B3LYP ( —●— ), B3LYP-D3 ( —●— ), M062X ( —●— ) and HF ( —●— , when present) results. In diagrams (d), (e), (f), (g) and (h): quantities not corrected for ZPE ( —●— ), corrected for ZPE ( —●— ), and related to the free energies ( —●— )

**Table 2** Synopsis of the relative energies not corrected for ZPE ( $\Delta E$ ) and corrected for ZPE ( $\Delta E_{\text{corr}}$ , sum of electronic and zero-point energies), and relative free energies ( $\Delta G$ , sum of electronic and thermal free energies) of the calculated conformers of ouabain in the results of the three DFT calculation-sets performed

Conformer	Relative energies (kcal/mol)								
	B3LYP			B3LYP-D3			M062X		
	$\Delta E$	$\Delta E_{\text{corr}}$	$\Delta G$	$\Delta E$	$\Delta E_{\text{corr}}$	$\Delta G$	$\Delta E$	$\Delta E_{\text{corr}}$	$\Delta G$
ou-1	0.392	0.572	1.258	0.000	0.000	0.167	0.000	0.000	0.000
ou-2	1.085	1.264	1.705	0.683	0.781	0.902	1.011	1.266	1.311
ou-3	0.000	0.000	0.000	0.967	0.651	0.000	0.975	0.727	0.002
ou-4	1.310	1.108	0.033	1.873	1.628	0.710	2.430	2.353	1.660
ou-5	3.275	3.317	3.690	3.297	3.144	3.284	3.364	3.320	3.176
ou-6	4.889	4.720	4.067	5.454	5.227	4.672	5.926	6.003	5.725
ou-7	4.545	4.436	4.282	6.150	5.697	4.980	6.227	6.076	5.474
ou-8	5.288	5.023	4.560	6.683	6.023	4.863	7.038	6.740	5.680
ou-9	7.534	7.964	8.520	6.780	6.947	6.745	6.567	7.290	7.786
ou-10	8.923	8.041	7.661	8.335	7.460	7.027	5.451	4.998	4.691

were not considered, because of the expectation that the removal of this IHB will cause an energy increase.

Table 4 reports the lengths of all the IHBs in each conformer. It is opted to consider the O—H...O interaction as an IHB in all the cases in which the H...O distance is smaller than the sum of the van der Waals radii of H and O (2.7 Å) [68]; slightly greater lengths are reported only when they appear in the results of some methods, while the length of the same IHB is shorter in the results of other methods. Lengths greater than 3.0 Å are not included; the absence of values for a certain method indicates that the H...O distance for the given IHB with that method is greater than

**Table 3** Relevant comparisons of energy estimations, and values of the zero-point energy (ZPE) corrections, in the DFT results of the calculated conformers of ouabain

Conformer	Relevant energy differences (kcal/mol)						ZPE correction (kcal/mol)		
	A			B			B3 LYP	B3L YP-D3	M06 2X
	E	E <sub>corr</sub>	G	E	E <sub>corr</sub>	G			
ou-1	85.2	83.3	82.4	494.7	500.9	502.0	457.6	459.5	463.9
ou-2	85.2	83.2	82.2	495.0	501.5	502.8	457.6	459.6	464.1
ou-3	83.9	82.1	81.4	496.0	502.2	503.2	457.4	459.2	463.6
ou-4	84.3	82.2	80.7	496.2	502.7	504.9	457.2	459.3	463.8
ou-5	84.8	82.9	81.8	495.1	501.5	502.7	457.5	459.4	463.8
ou-6	84.3	82.2	80.7	496.1	502.8	504.9	457.3	459.3	463.9
ou-7	83.2	81.5	80.6	496.7	503.1	504.4	457.3	459.1	463.7
ou-8	83.4	81.7	81.0	496.8	503.2	504.3	457.2	458.9	463.6
ou-9	85.6	83.8	83.1	494.1	500.8	502.5	457.9	459.7	464.6
ou-10	85.4	83.3	82.0	491.6	498.4	500.3	456.6	458.6	463.4

The column headings in the second headings-row for the differences section have the following meanings:

A: Effect of the addition of the dispersion correction on the B3LYP calculations (difference taken as B3LYP result minus B3LYP-D3 results);

B: Energy difference between corresponding results with the two functionals utilised (difference taken as M062X result minus B3LYP results);

The column-headings in the third headings-row have the following meanings:

E: electronic energies not corrected for ZPE;

E<sub>corr</sub>: energies corrected for ZPE (sum of electronic and zero point energies);

G: free energies (sum of electronic and thermal free energies)

3.0 Å. Several of the possible IHBs have rather poor or poor directionality, what makes them weaker. Figure 4 offers space-filling images of ou-1, to better highlight the IHB directionalities, and Table 5 reports the O $\hat{H}$ O bond angles in the B3LYP and B3LYP-D3 results, to highlight the directionality differences of the various IHBs in each conformer and across conformers, as well as possible effects of the inclusion of correlation on the estimation of the angles.

The IHBs within the glucoside moiety (H44...O1, H43...O33, H42...O34) have the poorest directionality, with bond angles not greater than 110° for H44...O1 and H43...O33, and only slightly greater for H42...O34. H44...O1 has long bond distance, while the length of H43...O33 is intermediate. Two such IHBs are present in each conformer.

The IHBs within the steroid moiety (H46...O36, H45...O37, H47...O37, H46...O38, H46...O39 and H48...O37) have the shortest lengths. Their bond angles range from 127° to 158°. Two such IHBs are present in most conformers (three in ou-8 and ou-9 and only one in ou-10).

By bridging the two moieties, O7 can be acceptor to donors from either moiety. H42...O7 is present in all the calculated conformers except ou-5 (where H42 is

**Table 4** Lengths of the O–H...O intramolecular hydrogen bonds (IHBs) in the calculated conformers of ouabain

Conformer	IHB	IHB length (Å)			
		B3LYP	B3LYP-D3	M062X	HF
ou-1	H44...O1	2.533	2.508	2.269	2.538
	H43...O33	2.269	2.295	2.249	2.316
	H42...O7	2.528	2.496	2.479	2.552
	H45...O1	2.042	1.941	2.014	2.467
	H45...O7	2.601	2.596	2.539	2.549
	H46...O36	1.916	1.929	1.963	2.036
	H47...O37	1.854	1.854	1.894	1.988
ou-2	H44...O1	2.540	2.513	2.450	2.543
	H43...O33	2.266	2.294	2.245	2.313
	H42...O7	2.530	2.499	2.482	2.549
	H45...O1	2.020	1.919	1.993	2.311
	H45...O7	2.596	2.589	2.553	2.602
	H46...O36	1.932	1.917	1.940	2.013
	H48...O37	1.966	1.971	1.973	2.019
ou-3	H44...O1	2.513	2.454	2.426	2.525
	H43...O33	2.249	2.278	2.227	2.299
	H42...O7	2.490	2.454	2.438	2.507
	H45...O7	2.129	2.118	2.147	2.369
	H46...O36	1.935	1.951	1.972	2.045
	H47...O37	1.859	1.860	1.902	1.990
ou-4	H44...O1	2.512	2.493	2.424	2.522
	H43...O33	2.247	2.274	2.224	2.229
	H42...O7	2.482	2.450	2.429	2.490
	H45...O7	2.183	2.154	2.188	2.765
	H46...O36	1.930	1.928	1.949	2.008
	H47...O37	1.949	1.961	1.966	2.004
ou-5	H44...O1	2.470	2.454	2.396	2.497
	H42...O34	2.133	2.165	2.136	2.182
	H45...O1	2.102	1.965	2.050	2.726
	H45...O7	2.538	2.548	2.476	2.356
	H46...O36	1.915	1.927	1.952	2.032
	H48...O37	1.849	1.851	1.893	1.985
ou-6	H44...O1	2.505	2.483	2.417	2.521
	H43...O33	2.233	2.226	2.196	2.291

(continued)

**Table 4** (continued)

Conformer	IHB	IHB length (Å)			
		B3LYP	B3LYP-D3	M062X	HF
	H42...O7	2.454	2.372	2.322	2.489
	H42...O36		2.168	2.164	
	H45...O37	1.854	1.808	1.825	1.974
	H46...O39	1.988	1.988	1.999	2.086
ou-7	H44...O1	2.503	2.483	2.418	2.520
	H43...O33	2.231	2.256	2.212	2.285
	H42...O7	2.459	2.433	2.412	2.485
	H45...O37	1.891	1.917	1.937	1.979
ou-8	H46...O38	1.819	1.815	1.830	1.903
	H44...O1	2.506	2.485	2.422	2.521
	H43...O33	2.237	2.264	2.217	2.290
	H42...O7	2.474	2.445	2.429	2.502
ou-9	H45...O37	1.943	1.965	1.974	2.056
	H46...O39	2.017	2.026	2.034	2.014
	H44...O1	2.548	2.511	2.421	2.533
	H43...O33	2.249	2.260	2.201	2.277
ou-10	H42...O7	2.617	2.602	2.581	2.485
	H42...O36	1.975	1.923	1.950	3.452
	H45...O7	2.679	2.393	2.187	3.204
	H45...O37	1.988	2.055	2.028	2.036
	H46...O39	2.099	2.170	2.202	2.107
	H47...O37	2.773	2.560	2.254	
ou-10	H44...O1	2.529	2.505	2.438	2.520
	H43...O33	2.256	2.284	2.238	2.286
	H42...O7	2.514	2.484	2.465	2.482
	H45...O1	2.237	2.028	2.082	
	H45...O7	2.237	2.596	2.558	2.594
	H48...O37	1.810	1.832	1.924	1.982

engaged in the H42...O34 IHB); its directionality is poor, with a 100–104° bond angle, and it is among the longest IHBs in these conformers. H45...O7 is present in all the lower energy conformers; it has long bond distance and poor directionality (bond angle 109–113°) when H45...O1 is also present (which implies bifurcation on H45), while it is shorter and has better directionality (bond angle 138–143°) when H45...O1 is not present.

H45...O1 is an IHB bridging the two moieties; its directionality is good (164–168°), and its bond length is comparatively short. H42...O36 also bridges the two

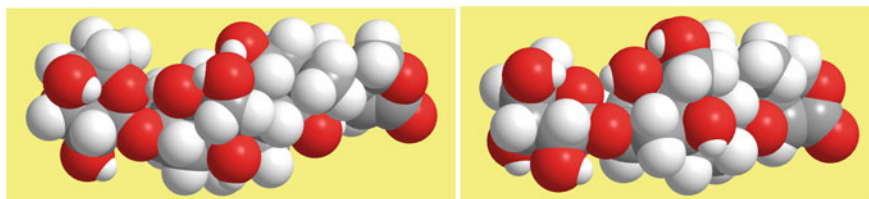


**Fig. 4** Space-filling models of the ou-1 conformer of the ouabain molecule, from two different points of view, to better highlight the intramolecular hydrogen bonds present and their directionalities. B3LYP-D3 results

moieties, when it forms; it is present in ou-9 and shows best directionality (the closest angle to  $180^\circ$ ) and short bond length; it is also present in the B3LYP-D3 and M062X results for ou-6, but not in the B3LYP and HF results, what further stresses the role of the consideration of dispersion corrections for a more complete description of H-bonding in a molecule.

Evaluating the influence of the different IHB patterns on the conformers' energies is not easy. In the low energy conformers, H44...O1, H43...O33 and H42...O7 are always present; H45 forms IHBs with O1, or O7, or both; O36 is acceptor to H46, and O37 is acceptor to H47 or H48. The mutual orientation of the two moieties also appears to have considerable influence on the energy. The two conformers in which H42...O36 appears (ou-9 and ou-6) have reversed orientation with respect to the other conformers, and their energies are not low, although the IHBs in the steroid moiety are comparable with the others. Altogether, it appears that major energy influencing role pertains to the complete IHB pattern of a conformer, including the weaker IHBs present in it and the moieties' orientation associated with it.

Evaluating the strength of individual IHBs is not easy because the removal of a specific IHB by  $180^\circ$  rotation of the donor brings about geometry and interaction changes, which also contribute to the energy difference between the conformers with and without that IHB. A rough comparison of the strengths of different IHBs may be based on the comparison of their lengths (H...O distance), on the basis that shorter IHBs are likely stronger. Another comparison may make use of the lowering effects that they have on the IR vibrational frequencies of the donor OHs.

Table 6 reports the IR stretching frequencies of the OH groups in all the calculated conformers. The decrease (red shift) in the vibrational frequency of an OH when it acts as H-bond donor should be calculated with respect to its vibration when it is free (not engaged in an H-bond); however, in the case of ouabain, it is possible to obtain conformers in which an OH is free only for some OHs, but not for all of them (the optimisation procedure will rotate certain OHs to form IHBs). It was therefore decided to choose an 'external' reference, selecting the OH of cyclohexanol for the OHs of ouabain attached to one or another ring, and the OH of ethanol for O37–H46, which is attached to a methylene group. Their vibrational frequencies were calculated with the same levels of theory (values reported in the caption of Table 7). Although this option does not provide the actual red shift for each specific OH, it has a meaning for comparison purposes.

**Table 5** Bond angles of the intramolecular hydrogen bonds (IHB) in the calculated conformers of ouabain. BLYP/6-31+G(d,p) results in vacuo

Conformer	IHB	Bond-angle (°)		IHB	Bond-angle (°)	
		B3LYP	B3LYP-D3		B3LYP	B3LYP-D3
ou-1	H44...O1	107.0	107.5	H45...O7	109.2	109.2
	H43...O33	107.9	107.3	H46...O36	127.5	127.2
	H42...O7	101.3	102.6	H47...O37	146.9	146.5
	H45...O1	165.2	165.9			
ou-2	H44...O1	106.8	107.3	H45...O7	110.9	111.1
	H43...O33	108.1	107.4	H46...O36	132.4	133.1
	H42...O7	101.2	102.4	H48...O37	133.6	133.0
	H45...O1	166.7	167.4			
ou-3	H44...O1	107.7	108.2	H45...O7	142.7	142.2
	H43...O33	108.6	107.9	H46...O36	126.7	126.2
	H42...O7	102.9	104.0	H47...O37	146.6	146.1
ou-4	H44...O1	107.8	108.2	H45...O7	137.7	138.3
	H43...O33	108.9	108.2	H46...O36	134.1	134.3
	H42...O7	103.4	104.4	H48...O37	134.7	133.7
ou-5	H44...O1	108.0	108.2	H45...O7	112.8	111.9
	H42...O34	114.9	113.7	H46...O36	127.4	127.2
	H45...O1	167.9	168.2	H47...O37	147.3	146.8
ou-6	H44...O1	107.9	108.6	H42...O36		157.8
	H43...O33	109.9	110.9	H45...O37	147.2	151.7
	H42...O7	103.6	105.2	H46...O39	125.9	126.2
ou-7	H44...O1	107.9	108.3	H45...O37	136.8	135.8
	H43...O33	110.1	109.5	H46...O38	158.0	158.3
	H42...O7	103.8	104.7			
ou-8	H44...O1	107.8	108.3	H45...O37	138.2	136.4
	H43...O33	109.5	108.9	H46...O39	124.7	124.2
	H42...O7	103.3	104.3			
ou-9	H44...O1	107.3	108.2	H45...O37	133.1	128.6
	H43...O33	110.2	109.8	H46...O39	122.1	120.0
	H42...O7	99.8	101.3	H47...O37	130.2	136.0
	H42...O36	178.0	177.2			
ou-10	H44...O1	107.2	107.6	H45...O1	163.6	165.5
	H43...O33	108.8	108.1	H45...O7	111.3	110.7
	H42...O7	101.9	103.0	H48...O37	145.5	143.2

**Table 6** IR vibrational frequencies (harmonic approximation) of the O–H groups in the calculated conformers of ouabain

Conformer	OH group considered	Frequencies (cm <sup>-1</sup> )		
		B3LYP	B3LYP-D3	M062X
ou-1	O33–H42	3818.05	3813.11	3873.68
	O34–H43	3792.30	3795.56	3851.60
	O35–H44	3796.36	3794.46	3851.60
	O36–H45	3698.15	3678.93	3785.96
	O37–H46	3698.15	3706.54	3805.12
	O38–H47	3623.04	3629.41	3746.99
	O39–H48	3807.35	3811.31	3870.93
	O40–H49	3808.71	3814.64	3881.81
ou-2	O33–H42	3816.10	3711.57	3874.61
	O34–H43	3791.24	3794.69	3850.96
	O35–H44	3797.36	3795.88	3854.12
	O36–H45	3684.31	3659.07	3767.73
	O37–H46	3708.67	3690.74	3804.53
	O38–H47	3825.80	3826.94	3885.97
	O39–H48	3694.11	3709.20	3789.92
	O40–H49	3809.85	3816.11	3879.40
ou-3	O33–H42	3817.61	3812.69	3872.12
	O34–H43	3789.81	3793.51	3850.45
	O35–H44	3795.06	3793.76	3852.51
	O36–H45	3775.09	3777.77	3853.05
	O37–H46	3727.98	3732.09	3821.74
	O38–H47	3631.55	3640.74	3770.79
	O39–H48	3806.78	3810.83	3871.23
	O40–H49	3808.42	3814.49	3879.95
ou-4	O33–H42	3814.22	3809.76	3870.39
	O34–H43	3787.48	3791.86	3849.61
	O35–H44	3795.88	3794.38	3852.56
	O36–H45	3769.49	3767.04	3840.34
	O37–H46	3684.96	3690.71	3809.87
	O38–H47	3831.61	3831.37	3894.23
	O39–H48	3684.96	3690.71	3790.38
	O40–H49	3826.96	3815.36	3881.17
ou-5	O33–H42	3758.92	3766.40	3836.88
	O34–H43	3847.84	3850.66	3891.53

(continued)

**Table 6** (continued)

Conformer	OH group considered	Frequencies (cm <sup>-1</sup> )		
		B3LYP	B3LYP-D3	M062X
	O35–H44	3787.01	3785.50	3841.22
	O36–H45	3724.99	3687.46	3291.47
	O37–H46	3704.33	3708.63	3814.97
	O38–H47	3617.23	3626.02	3770.38
	O39–H48	3807.36	3811.18	3870.21
	O40–H49	3809.29	3815.77	3880.23
ou-6	O33–H42	3796.54	3665.72	3734.92
	O34–H43	3783.05	3776.23	3837.97
	O35–H44	3791.14	3788.62	3845.98
	O36–H45	3660.71	3609.20	3710.10
	O37–H46	3735.63	3730.89	3826.38
	O38–H47	3826.57	3835.08	3892.80
	O39–H48	3806.58	3810.52	3867.32
	O40–H49	3806.86	3811.22	3877.72
ou-7	O33–H42	3810.70	3807.06	3867.24
	O34–H43	3784.72	3788.78	3848.32
	O35–H44	3789.27	3787.36	3845.73
	O36–H45	3671.17	3685.45	3791.83
	O37–H46	3634.35	3642.11	3745.71
	O38–H47	3804.18	3806.53	3871.67
	O39–H48	3808.65	3811.90	3871.88
	O40–H49	3808.83	3814.73	3880.05
ou-8	O33–H42	3816.50	3812.74	3871.28
	O34–H43	3787.53	3791.43	3848.63
	O35–H44	3790.15	3788.08	3846.96
	O36–H45	3709.60	3723.81	3815.59
	O37–H46	3750.11	3755.74	3840.98
	O38–H47	3817.57	3817.27	3865.52
	O39–H48	3807.25	3812.63	3868.74
	O40–H49	3807.59	3813.06	3878.51
ou-9	O33–H42	3587.21	3569.78	3677.81
	O34–H43	3775.60	3778.58	3838.42
	O35–H44	3800.21	3798.25	3853.83

(continued)



**Table 6** (continued)

Conformer	OH group considered	Frequencies (cm <sup>-1</sup> )		
		B3LYP	B3LYP-D3	M062X
	O36–H45	3679.23	3684.30	3717.89
	O37–H46	3768.42	3790.61	3871.14
	O38–H47	3810.40	3796.56	3819.57
	O39–H48	3805.52	3810.08	3865.06
	O40–H49	3808.10	3814.32	3787.99
ou-10	O33–H42	3813.54	3080.91	3870.23
	O34–H43	3789.15	3793.01	3851.27
	O35–H44	3794.16	3792.57	3847.07
	O36–H45	3762.97	3727.33	3811.52
	O37–H46	3851.64	3854.02	3902.63
	O38–H47	3811.79	3814.55	3887.09
	O39–H48	3674.54	3686.88	3807.40
	O40–H49	3809.87	3815.51	3881.20

In the cases where the vibrations of two OHs are coupled, the smallest value is reported

Table 7 offers a synopsis in which the bond lengths of the various IHBs are matched to the decreases that their formation causes in the vibrational frequencies of their donors. The trends of the frequency-decreases correspond to the trends noted for the lengths and directionalities of the various IHBs. The smallest decreases (weakest IHBs) correspond to H42...O7 when there is no bifurcation on H42. A slightly greater decrease corresponds to the IHBs within the glucoside moiety (H44...O1, H43...O33, H42...O34), followed by H45...O7 when there is no bifurcation on H45. Considerable greater decreases correspond to the IHBs within the steroid moiety (H46...O36, H45...O37, H47...O37, H46...O38, H46...O39 and H48...O37), with a broad range of values, depending on the IHB and on the conformer. The combined effects of H45...O1 and H45...O7 (bifurcation on H45) may reach values comparable with those of the IHBs within the steroid moiety. The greatest decrease corresponds to H42...O36 in ou-9.

Cooperativity often strengthens H-bonds with respect to when they are isolated, and may influence some aspects of the molecule's behaviour [69–72]. Cooperative IHBs are present in most low energy conformers of ouabain. For instance, H45...O1, H46...O36 and H47...O37 in ou-1 are consecutive and likely cooperative; the same applies to H45...O1, H46...O36 and H48...O37 in ou-2, H45...O7, H46...O36 and H47...O37 in ou-3, H45...O7, H46...O36 and H48...O37 in ou-3, and so on.

IHBs weaker than the O–H...O ones often play non-negligible stabilising roles and are increasingly recognized as important for the interpretation of various phenomena, including the conformations of organic compounds [72–74]. An IHB of the O–H... $\pi$  type forms between O40–H49 and the C25=C29  $\pi$  bond. It is not possible to identify an actual bond length for IHBs of this type, because the acceptor

**Table 7** Synopsis considering the bond lengths of the intramolecular hydrogen bonds and the changes that their formation causes in the IR frequencies of the donors

Conformer	IHB	IHB length (Å)			IR frequency change (cm <sup>-1</sup> )		
		B3LYP	B3LYP-D3	M062X	B3LYP	B3LYP-D3	M062X
ou-1	H44...O1	2.533	2.508	2.269	25.35	28.33	39.73
	H43...O33	2.269	2.295	2.249	29.41	27.23	39.73
	H42...O7	2.528	2.496	2.479	3.66	9.68	17.65
	H45...O1	2.042	1.941	2.014	123.56	143.86	105.37
	H45...O7	2.601	2.596	2.539			
	H46...O36	1.916	1.929	1.963	123.56	116.25	86.21
	H47...O37	1.854	1.854	1.894	212.40	205.54	165.52
ou-2	H44...O1	2.540	2.513	2.450	24.35	26.91	37.21
	H43...O33	2.266	2.294	2.245	30.47	28.10	40.37
	H42...O7	2.530	2.499	2.482	5.61	111.22	16.72
	H45...O1	2.020	1.919	1.993	137.40	163.72	123.60
	H45...O7	2.596	2.589	2.553			
	H46...O36	1.932	1.917	1.940	126.77	132.05	101.41
	H48...O37	1.966	1.971	1.973	127.60	132.05	101.41
ou-3	H44...O1	2.513	2.454	2.426	26.65	29.03	38.82
	H43...O33	2.249	2.278	2.227	31.90	29.28	40.88
	H42...O7	2.490	2.454	2.438	4.10	10.10	19.21
	H45...O7	2.129	2.118	2.147	46.62	45.02	38.28
	H46...O36	1.935	1.951	1.972	93.73	90.70	69.59
	H47...O37	1.859	1.860	1.902	203.89	194.21	141.72
	ou-4	H44...O1	2.512	2.493	2.424	25.83	28.41
H43...O33		2.247	2.274	2.224	34.23	30.93	41.72
H42...O7		2.482	2.450	2.429	7.49	13.03	20.94
H45...O7		2.183	2.154	2.188	52.22	55.75	50.99
H46...O36		1.930	1.928	1.949	136.75	132.08	81.46
H48...O37		1.949	1.961	1.966	136.75	132.08	100.95
ou-5		H44...O1	2.470	2.454	2.396	34.70	37.29
	H42...O34	2.133	2.165	2.136	62.79	56.39	54.45
	H45...O1	2.102	1.965	2.050	96.72	135.33	599.86
	H45...O7	2.538	2.548	2.476			
	H46...O36	1.915	1.927	1.952	131.11	126.32	97.54
	H47...O37	1.849	1.851	1.893	204.48	196.77	120.95
ou-6	H44...O1	2.505	2.483	2.417	30.57	34.17	45.35
	H43...O33	2.233	2.226	2.196	38.66	46.56	53.36

(continued)

**Table 7** (continued)

Conformer	IHB	IHB length (Å)			IR frequency change (cm <sup>-1</sup> )		
		B3LYP	B3LYP-D3	M062X	B3LYP	B3LYP-D3	M062X
	H42...O7	2.454	2.372	2.322	25.17	157.07	156.41
	H42...O36		2.168	2.164			
	H45...O37	1.854	1.808	1.825	161.00	213.59	181.23
	H46...O39	1.988	1.988	1.999	86.08	91.90	64.95
ou-7	H44...O1	2.503	2.483	2.418	32.44	35.43	45.60
	H43...O33	2.231	2.256	2.212	36.99	34.01	43.01
	H42...O7	2.459	2.433	2.412	11.01	15.73	24.09
	H45...O37	1.891	1.917	1.937	150.54	137.34	99.50
	H46...O38	1.819	1.815	1.830	201.09	192.84	166.80
ou-8	H44...O1	2.506	2.485	2.422	31.56	34.71	44.37
	H43...O33	2.237	2.264	2.217	34.18	31.36	42.70
	H42...O7	2.474	2.445	2.429	5.21	10.05	20.05
	H45...O37	1.943	1.965	1.974	112.11	98.98	75.74
	H46...O39	2.017	2.026	2.034	71.60	67.05	50.35
ou-9	H44...O1	2.548	2.511	2.421	21.50	24.54	37.50
	H43...O33	2.249	2.260	2.201			
	H42...O36	1.975	1.923	1.950	234.50	253.01	213.52
	H42...O7	2.617	2.602	2.581			
	H45...O37	1.988	2.055	2.028	142.48	138.49	173.44
	H45...O7	2.679	2.393	2.187			
	H46...O39	2.099	2.170	2.202	53.29	32.18	20.19
	H47...O37	2.773	2.560	2.254	25.04	38.39	92.94
ou-10	H44...O1	2.529	2.505	2.438	27.55	30.22	44.26
	H43...O33	2.256	2.284	2.238			
	H42...O7	2.514	2.484	2.465	8.17	741.88	21.10
	H45...O1	2.237	2.028	2.082			
	H45...O7	2.237	2.596	2.558	58.74	95.46	79.81
	H48...O37	1.810	1.832	1.924			

Based on the values in Tables 5 and 6 and the reference vibrational frequencies of the OH in cyclohexanol (3821.71/B3LYP, 3822.79/B3LYP-D3 and 3891.33/M062X) for the other OHs and ethanol (3835.44/B3LYP, 3834.95/B3LYP-D3 and 3912.51/M062X) for O37–H46. When two IHBs are bifurcated on the H atom of the donor, the change is reported as a value referred to both IHBs

**Table 8** H49...C25 and H49...C29 distances (Å) of the H49 atom from the two atoms forming the C25=C29  $\pi$  bond in the calculated conformers of ouabain

Conformer	B3LYP		B3LYP-D3		M062X		HF	
	49...25	49...29	49...25	49...29	49...25	49...29	49...25	49...29
ou-1	2.574	2.443	2.528	2.380	2.499	2.360	2.639	2.382
ou-2	2.587	2.456	2.541	2.392	2.514	2.372	2.657	2.530
ou-3	2.572	2.443	2.526	2.380	2.499	2.361	2.639	2.516
ou-4	2.906	2.784	2.541	2.391	2.517	2.371	3.026	2.932
ou-5	2.574	2.447	2.528	2.383	2.500	2.364	2.640	2.519
ou-6	2.580	2.444	2.540	2.383	2.512	2.363	2.648	2.517
ou-7	2.542	2.387	2.542	2.387	2.515	2.366	2.663	2.530
ou-8	2.580	2.445	2.533	2.380	2.507	2.361	2.647	2.517
ou-9	2.578	2.440	2.532	2.379	2.505	2.360	2.647	2.518
ou-10	2.604	2.463	2.555	2.399	2.513	2.372	2.659	2.532

Only the numbers of the atoms are indicated in the column-headings, for space reasons

is a  $\pi$  cloud. The only parameters that can be considered are the distances of the donor H from the C atoms forming the  $\pi$  bond. Table 8 reports the distances between H49 and C25 or C29; these distances are shorter than the sum of the van der Waals radii of C and H (2.7 Å). Because of the possibility of this IHB, inputs in which O40–H49 is oriented away from C25=C29 were not considered, as this orientation would not contribute any intramolecular interaction.

C–H...O IHBs also have stabilising effects and influence conformational geometries [72, 74–77]. Various C–H...O IHBs are present in each conformer. Table 9 lists the ones present in ou-1 and reports their lengths (considering them when the length is shorter than the sum of the van der Waals radii of the two atoms); most of them can also be easily identified from the two images in Fig. 4.

### 3.3 Other Molecular Properties

Several molecular properties of biologically active molecules are used as quantum chemical descriptors for the investigation of Quantitative Structure Activity Relationships (QSAR). The energy gap between the frontiers orbitals (HOMO and LUMO) and the dipole moment of the calculated conformers of ouabain are considered in this work.

The HOMO–LUMO energy gap is related to a molecule's reactivity, which is obviously important for its biological activity. Table 10 reports the values of the gap for the calculated conformers. It is interesting to note that, while the addition of the dispersion correction to the B3LYP calculations does not appear to have any effect on the estimation of the gap, the M062X functional shows considerable improvement

**Table 9** Lengths of the C–H...O intramolecular hydrogen bonds (IHBs) in the lowest energy (ou-1) conformer of ouabain

C–H...O IHB	IHB length (Å)				C–H...O IHB	IHB length (Å)			
	B3L YP	B3LYP-D3	M06 2X	HF		B3L YP	B3LYP-D3	M06 2X	HF
H2...O1	2.091	2.093	2.084	2.054	H31 <sub>a</sub> ...O36	2.636	2.618	2.584	2.595
H6...O1	2.009	2.010	2.005	1.985	H31 <sub>a</sub> ...O37	2.065	2.066	2.062	2.036
H3...O1	2.666	2.650	2.645	2.635	H31 <sub>b</sub> ...O37	2.037	2.040	2.035	2.010
H2...O7	2.066	2.066	2.060	2.034	H18...O37	2.597	2.578		2.504
H3...O7	2.525	2.539	2.536	2.516	H18...O38	2.056	2.057	2.690	2.028
H8...O7	2.061	2.061	2.054	2.033	H10...O38	2.274	2.258	2.247	2.278
H9 <sub>a</sub> ...O7	2.649	2.654	2.620	2.583	H19 <sub>a</sub> ...O38	2.573	2.562	2.552	2.530
H3...O33	2.081	2.084	2.078	2.050	H19 <sub>b</sub> ...O38	2.512	2.512	2.502	2.488
H4...O33	2.688	2.430	2.682	2.671	H13 <sub>a</sub> ...O39	2.626	2.627	2.622	2.602
H2...O33	2.672	2.668	2.645	2.637	H13 <sub>b</sub> ...O39	2.630	2.635	2.638	2.604
H5...O34	2.551	2.557	2.076	2.525	H16 <sub>a</sub> ...O39	2.701	2.655	2.659	2.685
H4...O34	2.080	2.083	2.565	2.049	H17 <sub>a</sub> ...O39	2.699	2.707	2.659	2.666
H30 <sub>a</sub> ...O34	2.448	2.412	2.378	2.477	H31 <sub>a</sub> ...O39	2.373	2.373	2.370	2.381
H5...O35	2.025	2.029	2.027	2.003	H31 <sub>b</sub> ...O39	2.526	2.514	2.482	2.490
H4...O35	2.540	2.500	2.548	2.515	H15 <sub>a</sub> ...O40	2.677	2.458	2.445	2.431
H6...O35	2.498	2.546	2.492	2.472	H24 <sub>a</sub> ...O40	2.478	2.472	2.463	2.460
H10...O36	2.070	2.071	2.068	2.036	H26 <sub>a</sub> ...O27	2.066	2.069	2.059	2.040
H13...O36	2.589	2.530	2.482	2.549	H26 <sub>b</sub> ...O27	2.062	2.063	2.056	2.035

**Table 10** HOMO–LUMO energy gap of the calculated conformers of ouabain

Conformer	HOMO–LUMO energy gap (kcal/mol)			
	B3LYP	B3LYP-D3	M062X	HF
ou-1	120.92	120.46	182.75	269.96
ou-2	121.64	121.33	182.20	271.66
ou-3	122.63	122.33	184.37	270.49
ou-4	125.65	123.63	184.06	271.24
ou-5	119.75	119.30	181.46	269.67
ou-6	121.81	115.57	178.83	274.73
ou-7	116.48	116.50	180.24	272.71
ou-8	122.75	122.58	185.49	274.00
ou-9	116.18	118.44	183.77	273.72
ou-10	115.59	114.30	178.67	270.83

**Table 11** Dipole moments of the calculated conformers of ouabain

Conformer	Dipole moment (debye)			
	B3LYP	B3LYP-D3	M062X	HF
ou-1	6.8088	6.7857	6.5459	6.7524
ou-2	7.0003	7.1179	6.9520	7.1451
ou-3	6.0710	5.9991	5.8213	6.2757
ou-4	6.2071	5.8764	5.7994	6.6137
ou-5	10.9233	10.8375	10.7935	11.1385
ou-6	0.8304	2.1437	2.1551	1.2643
ou-7	3.9804	4.0962	4.0522	3.7731
ou-8	1.4927	1.5247	1.5314	2.0478
ou-9	1.6036	1.8997	2.5695	2.2358
ou-10	6.6031	6.8757	5.6344	5.7092

of the estimation. As already mentioned, the HF results constitute the best reference for the gap evaluation.

The dipole moment is related to various aspects of a molecule's behaviour, and may also be related to its biological activity [36]. Table 11 reports the dipole moments of the calculated conformers of ouabain. It is obvious to expect that the values are largely determined by the orientations of the OH groups. The first four conformers (ou-1, ou-2, ou-3 and ou-4) have rather close dipole moments. The ou-5 conformer has the highest, likely because of the opposite orientations of O34–H43 and O33–H42 with respect to all the other conformers. Conformers ou-6, ou-8 and ou-9 have the smallest dipole moments, and ou-10 has a dipole moment comparable to those of the first four conformers.

## 4 Discussion and Conclusions

The obtained results identify the lowest energy conformers of ouabain and some of the higher energy ones. The use of different computational approaches provides validation of identified trends through their similarities (which, for some quantities, are more remarkable for the low energy conformers).

The calculated properties may be useful as QSAR descriptors. The predictive reliability of QSAR descriptors depends on the accuracy of their evaluation. It had been shown [69] that the incorporation of electron-correlation in the computational approach improves the accuracy of descriptors-estimation and enables satisfactory predictive abilities of QSAR using those descriptors.

It is generally to be expected that the inclusion of dispersion correction results in lower estimated energies. The extent of the effect for the ouabain molecule is considerable. Given the absence of aromatic rings in the molecule, it may be hypothesized that the effect-extent is mostly related to the presence of several IHBs.

Since DFT is a variational method, it can be inferred that B3LYP-D3 gives the best energy estimations among the methods utilized in this work (followed by B3LYP). Therefore, the B3LYP-D3 can be considered the most accurate (with the usual exception of the estimation of the HOMO–LUMO energy gaps).

The detailed analysis of intramolecular hydrogen bonds and their characteristics is expected to be expedient for further interpretations of the biological activities of ouabain and its interactions with biological targets.

Since biological processes occur in a medium, it is important to investigate the effect of suitably selected solvent on the molecular properties of ouabain. This will be the object of a separate study.

**Acknowledgements** The author wishes to express her gratitude to the Centre for High Performance Computing in Cape Town (South Africa) for providing the facilities to perform the calculations needed for this study.

## References

1. Wikipedia. Accessed on 18–02–2022
2. Neuwinger, H.D.: *African Ethnobotany: Poisons and Drugs*. Chapman & Hall, Weinheim (1996)
3. Lambert, B., Donn, A.: Effect of Ouabain on active transport of sodium in the Cornea. *Arch. Ophthalmol.* **72**(4), 525–528 (1964). <https://doi.org/10.1001/archoph.1964.00970020525017>
4. Dunn, M.J.: Ouabain- uninhibited sodium transport in human erythrocytes evidence against a second pump. *J. Clin. Invest.* **52**(3), 658–670 (1973). <https://doi.org/10.1172/JCI107227>
5. Read, N.W., Krejs, G.J., Jones, V.E., Fordtran, J.S.: Effect of ouabain on Na K-ATPase and electrolyte transport in the dog ileum in vivo. *Gut* **20**, 356–365 (1979)
6. Kaji, R., Summer, A.J.: Ouabain reverses conduction disturbances in single demyelinated nerve fibers. *Neurology* **39**(10) 1989. <https://doi.org/10.1212/WNL.39.10.1364>
7. Aizman, O., Uhlén, P., Lal, M., Brismar, H., Aperia, A.: Ouabain, a steroid hormone that signals with slow calcium oscillations. *PNAS* **98**(23), 13420–13424 (2001). <https://doi.org/10.1073/pnas.221315298>
8. Li, J., Zelenin, S., Aperia, A., Aizman, O.: Low doses of ouabain protect from serum deprivation– triggered apoptosis and stimulate kidney cell proliferation via activation of NF- $\kappa$ B. *J. Am. Soc. Nephrol.* **17**, 1848–1857 (2006). <https://doi.org/10.1681/ASN.2005080894>
9. Li, J., Khodus, G.R., Kruusmägi, M., Kamali-Zare, P., Liu, X.-L., Eklöf, A.C., Zelenin, S., Brismar, H., Aperia, A.: Ouabain protects against adverse developmental programming of the kidney. *Nat. Comm.* **1**(4), 42 (2010). <https://doi.org/10.1038/ncomms1043>
10. Hauke, F.: Ouabain—The insulin of the heart. *Int. J. Clin. Pract.* **64**(12), 1591 (2010). <https://doi.org/10.1111/j.1742-1241.2010.02395.x>
11. Abe, K., Tani, K., Fujiyoshi, Y.: Conformational rearrangement of gastric H<sup>+</sup>, K<sup>+</sup>- ATPase induced by an acid suppressant. *Nat. Commun.* **2**, 155 (2011). <https://doi.org/10.1038/ncomms1154>

12. Romero-Canelón, I., Pizarro, A.M., Habtemariam, A., Sadler, P.J.: 1279 Contrasting cellular uptake pathways for chlorido and iodido iminopyridine ruthenium arene anticancer complexes. *Metallomics* **4**, 1271–1279 (2012). <https://doi.org/10.1039/c2mt20189e>
13. Hauke, F.: On the differences between ouabain and digitalis glycosides. *Am. J. Therapeut.* **21**(1), 35–42 (2014). <https://doi.org/10.1097/MJT.0b013e318217a609>
14. Laursen, M., Lindholt Gregersen, J., Yatime, L., Nissena, P., Fedosova, N.U.: Structures and characterization of digoxin- and bufalin-bound Na<sup>+</sup>,K<sup>+</sup>-ATPase compared with the ouabain-bound complex. *PNAS* **112**(6), 1755–1760 (2015). <https://doi.org/10.1073/pnas.1422997112>
15. Renata, H., Zhou, Q., Dünstl, G., Felding, J., Merchant, R.R., Yeh, C.H., Baran, P.S.: Development of a concise synthesis of ouabagenin and hydroxylated corticosteroid analogues. *J. Am. Chem. Soc.* **137**, 1330–1340 (2015)
16. Kubala, M., Čechová, P., Geletičová, J., Biler, M., Štenclová, T., Trouillas, P., Biedermann, D.: Flavonolignans as a novel class of sodium pump inhibitors. *Front. Physiol.* (2016). <https://doi.org/10.3389/fphys.2016.00115>
17. Kaplan, W.P.: Drug-Oriented Synthesis of Cardiotoxic Steroids. PhD dissertation, University of Michigan (2017)
18. Cavalcante-Silva, L.H.A., de Almeida Lima, É., Carvalho, D.C.M., de Sales-Neto, J.M., de Abreu Alves, A.K., Galvão, J.G.F.M., de França da Silva, J.S., Rodrigues-Mascarenhas, S.: Much more than a cardiotoxic steroid: modulation of inflammation by ouabain. *Front. Physiol.* (2017). <https://doi.org/10.3389/fphys.2017.00895>
19. Cui, X.Y., Xie, Z.J.: Protein interaction and Na/K-ATPase-mediated signal transduction. *Molecules* **22**, 990 (2017). <https://doi.org/10.3390/molecules22060990>
20. Ou, Y., Pan, C.X., Zuo, J., van der Hoorn, F.A.: Ouabain affects cell migration via Na, K-ATPase-p130cas and via nucleus-centrosome association. *PLoS ONE* **12**(8), e0183343 (2017). <https://doi.org/10.1371/journal.pone.0183343>
21. Venugopal, J., Blanco, G.: On the many actions of ouabain: pro-cystogenic effects in autosomal dominant polycystic kidney disease. *Molecules* **22**(5), 729 (2017). <https://doi.org/10.3390/molecules22050729>
22. Sultana Syeda, S., Sánchez, G., Hong, K.H., Hawkinson, J.E., Georg, G.I., Blanco, G.: Design, synthesis, in vitro and in vivo evaluation of ouabain analogs as potent and selective Na,K-ATPase  $\alpha 4$  isoform inhibitors for male contraception. *J. Medic. Chem.* (2018). <https://doi.org/10.1021/acs.jmedchem.7b00925>
23. El-Mallakh, S., Gao, Y.L., You, P.: Role of endogenous ouabain in the etiology of bipolar disorder. *Int. J. Bipolar Disord.* **9**, 6 (2021). <https://doi.org/10.1186/s40345-020-00213-1>
24. Hauke, F.: Ouabain: a gift from paradise Kindle Edition. Books on Demand (2018)
25. Wang, L., Cai, W., Han, B., Zhang, J., Yu, B., Chen, M.: Ouabain exhibited strong anti-cancer effects in melanoma cells via induction of apoptosis, G2/M phase arrest, and migration inhibition *Onco. Targets. Ther.* **14**, 1261–1273 (2014)
26. Nagai, Y., Maeno, K., Iinuma, M., Yoshida, T., Matsumoto, T.: Inhibition of virus growth by ouabain: effect of ouabain on the growth of HVJ in chick embryo cells. *J. Virol.* **9**(2), 234–243 (1972)
27. Yang, C.-W., Chang, H.-Y., Lee, Y.-Z., Hsu, H.-Y., Lee, S.-J.: The cardenolide ouabain suppresses coronavirus replication via augmenting a Na<sup>+</sup>/K<sup>+</sup>-ATPase-dependent PI3K\_PDK1 axis signalling. *Toxicol. Appl. Pharmacol.* **356**, 90–97 (2018). <https://doi.org/10.1016/j.taap.2018.07.028>
28. Reddy, D., Kumavath, R., Barh, D., Azevedo, V., Ghosh, P.: Anticancer and antiviral properties of cardiac glycosides: a review to explore the mechanism of actions. *Molecules* **25**, 3596 (2020). <https://doi.org/10.3390/molecules25163596>
29. Yang, C.-W., Hsu, H.-Y., Chang, H.-Y., Lee, Y.-Z., Lee, S.-J.: Natural cardenolides suppress coronavirus replication by downregulating JAK1 via a Na<sup>+</sup>/K<sup>+</sup>-ATPase independent proteolysis. *Biochem. Pharmacol.* **180**, 114–122 (2020)
30. Cho, J.H., Lee, Y.J., Kim, J.H., Kim, S., Kim, S.S., Choi, B.S., Choi, J.H.: Antiviral activity of digoxin and ouabain against SARS-CoV-2 infection and its implication for COVID-19. *Sci. Rep.* **10**, 16200 (2020). <https://doi.org/10.1038/s41598-020-72879-7>



31. Ahmed, M., Farag, A., Boys, I.N., Wang, P., Eitson, J.L., Ohlson, M.B., Fan, W., McDougal, M.B., Menendez-Montes, I., Nguyen, N.U.N., Mar, K., Ortiz, F., Kim, S.Y., Williams, N., Iemoff, A.L., De Berardinis, L., Schoggins, J.W., Sadek, H.: Identification of atovaquone and mebendazole as repurposed drugs with antiviral activity against SARS-CoV-2 (version 6) (2021). <https://doi.org/10.26434/chemrxiv-2021-b3fv1-v7>
32. Hauke, F.: Solid evidence- ouabain is an effective therapeutic for the treatment of COVID-19, Preprint. December (2021). <https://doi.org/10.13140/RG.2.2.26048.05128>
33. Caohuy, H., Eidelman, O., Chen, T., Yang, Q., Bera, A., Walton, N., Pollard, H.B.: Common cardiac medications potently inhibit ACE2 binding to the SARS-CoV-2 Spike, and block virus penetration into human lung cells. Pre-print. <https://doi.org/10.1101/2021.06.02.446343>
34. Corrêa Souza e Souza, K.F., Tavares Moraes, B.P., Nunes de Palmer Paixão, I.C., Burth, P., Ribeiro Silva, A., Gonçalves-de-Albuquerque, C.F.: Na<sup>+</sup>/K<sup>+</sup>-ATPase as a target of cardiac glycosides for the treatment of SARS-CoV-2 infection. *Front. Pharmacol.* (2021). <https://doi.org/10.3389/fphar.2021.624704>
35. Caohuy, H., Eidelman, O., Chen, T., Yang, Q., Walton, N.I., Pollard, H.B.: Inflammation in the COVID-19 airway is due to inhibition of CFTR signaling by the SARS-CoV-2 Spike protein. *bioRxiv – Microbiology*. Pub Date : 2022-01-21. <https://doi.org/10.1101/2022.01.18.476803>
36. Bushelyev, S.N., Stepanov, N.F.: *Elektronnaya Struktura y Biologhicheskaya Aktivnost Molecul. Khimiya, Snanye, Moscow* (1989)
37. Hernandez, E.G., Garza, J.: Reactivity sites in dopamine depend on its intramolecular hydrogen bond. *J. Mex. Chem. Soc.* **61**, 222–228 (2017)
38. Fersht, A.R.: The hydrogen bond in molecular recognition. *Trend. Biochem. Sci.* **12**, 301–304 (1987)
39. Desiraju, G.R.: Chemistry beyond the molecule. *Nature* **412**, 397–400 (2001)
40. Nguyen, H.P., Seto, L.O.N., Cai, Y., Leinala, E.K., Borisova, S.N., Palcic, M.N., Evans, S.V.: The influence of an intramolecular hydrogen bond in a differential recognition of inhibitory acceptor analogs by human ABO(H) blood group A and B glycosyltransferases. *J. Biol. Chem.* **49**, 4191–4195 (2003)
41. Sanchez, G.: Introduction to “Intramolecular hydrogen bonding 2018.” *Molecules* **24**, 2858 (2019). <https://doi.org/10.3390/molecules24162858>
42. Yunta, M.J.R.: It is important to compute intramolecular hydrogen bonding in drug design? *Am. J. Model. Optim.* **5**, 24–57 (2017)
43. Lee, C., Yang, W., Parr, R.G.: Development of the Colle-Salvetti correlation-energy formula into a functional of the electron density. *Phys. Rev. B* **37**, 785–789 (1998)
44. Becke, A.D.: A new mixing of Hartree-Fock and local density-functional theories. *J. Chem. Phys.* **98**, 1372–1377 (1993)
45. Becke, A.D.: Density functional thermochemistry III. The role of exact exchange. *J. Chem. Phys.* **98**, 5648–5652 (1993)
46. Grimme, S.: Semiempirical GGA-type density functional constructed with a long-range dispersion correction. *J. Comput. Chem.* **27**, 1787–1799 (2006)
47. Schwabe, T., Grimme, S.: Double-hybrid density functionals with long-range dispersion corrections: Higher accuracy and extended applicability. *Phys. Chem. Chem. Phys.* **9**, 3397–3406 (2007)
48. Neese, F., Schwabe, T., Grimme, S.: Analytic derivatives for perturbatively corrected “double hybrid” density functionals: theory, implementation, and applications. *J. Chem. Phys.* **126**, 124115 (2007)
49. Grimme, S.: Density functional theory with London dispersion corrections. *Wiley Interdiscip. Rev. WIREs Comput. Mol. Sci.* **1**, 211–228 (2011)
50. Grimme, S., Ehrlich, S., Goerigk, L.: Effect of the damping function in dispersion corrected density functional theory. *J. Comput. Chem.* **32**, 1456–1465 (2011)
51. Hujo, W., Grimme, S.: Comparison of the performance of dispersion-corrected density functional theory for weak hydrogen bonds. *Phys. Chem. Chem. Phys.* **13**, 13942–13950 (2011)
52. Grimme, S., Goerigk, L., Fink, R.F.: Spin-component-scaled electron correlation methods. *WIREs Comput. Mol. Sci.* **2**, 886–906 (2012). <https://doi.org/10.1002/wcms.1110>

53. Grimme, S., Steinmetz, M.: Effects of London dispersion correction in density functional theory on the structures of organic molecules in the gas phase. *Phys. Chem. Chem. Phys.* **15**, 16031–16042 (2013)
54. Grimme, S., Hansen, A., Brandenburg, J.G., Bannwarth, C.: Dispersion-corrected mean-field electronic structure methods. *Chem. Rev.* **116**, 5105–5154 (2016)
55. Zhao, Y., Truhlar, D.G.: The M06 suite of density functionals for main group thermochemistry, thermochemical kinetics, noncovalent interactions, excited states, and transition elements: two new functionals and systematic testing of four M06-class functionals and 12 other functionals. *Theor. Chem. Acc.* **120**, 215–241 (2008). <https://doi.org/10.1007/s00214-007-0310-x>
56. McDonagh, J., Silva, A.F., Vincent, M., Popelier, P.: Quantifying electron correlation of the chemical bond. *J. Phys. Chem. Lett.* **8**, 1937–1942 (2017)
57. Alagona, G., Ghio, C.: Competitive H-bonds in vacuo and in aqueous solution for N-protonated adrenaline and its monohydrated complexes. *J. Mol. Struct. (Theochem)* **811**, 223–240 (2007)
58. Mammino, L., Kabanda, M.M.: A study of the intramolecular hydrogen bond in acylphloroglucinols. *J. Mol. Struct.* **901**, 210–219 (2009)
59. Mammino, L.: Intramolecular hydrogen bonding patterns, conformational preferences and molecular properties of dimeric acylphloroglucinols: an ab initio and DFT study. *J. Mol. Struct.* **1176**, 488–500 (2019)
60. Mammino, L.: Correlation effects in trimeric Acylphloroglucinols. *Computation* **9**, 121 (2021). <https://doi.org/10.3390/computation9110121>
61. Vos, R.J., Hendriks, R., Van Duijneveldt, F.B.: SCF, MP2, and CEPA-1 calculations on the OH...O hydrogen bonded complexes (H<sub>2</sub>O)<sub>2</sub> and (H<sub>2</sub>O–H<sub>2</sub>CO). *J. Comp. Chem.* **11**, 1–18 (1990)
62. Mó, O., Yáñez, M., Elguero, J.: Cooperative (nonpairwise) effects in water trimers: An ab initio molecular orbital study. *J. Chem. Phys.* **97**, 6628–6638 (1992)
63. Ferrari, A.M., Garrone, E., Ugliengo, P.: Ab initio study of the gas-phase equilibrium between (H<sub>2</sub>O)<sub>4</sub> and (H<sub>2</sub>O)<sub>8</sub>. *Chem. Phys. Lett.* **212**, 644–648 (1993)
64. Frisch, M.J., Trucks, G.W., Schlegel, H.B., Scuseria, G.E., Robb, M.A., Cheeseman, J.R., Scalmani, G., Barone, V., Petersson, G.A., Nakatsuji, H., Li, X., Caricato, M., Marenich, A.V., Bloino, J., Janesko, B.G., Gomperts, R., Mennucci, B., Hratchian, H.P., Ortiz, J.V., Izmaylov, A.F., Sonnenberg, J.L., Williams-Young, D., Ding, F., Lipparini, F., Egidi, F., Goings, J., Peng, B., Petrone, A., Henderson, T., Ranasinghe, D., Zakrzewski, V.G., Gao, J., Rega, N., Zheng, G., Liang, W., Hada, M., Ehara, M., Toyota, K., Fukuda, R., Hasegawa, J., Ishida, M., Nakajima, T., Honda, Y., Kitao, O., Nakai, H., Vreven, T., Throssell, K., Montgomery, J.A., Jr., Peralta, J.E., Ogliaro, F., Bearpark, M.J., Heyd, J.J., Brothers, E.N., Kudin, K.N., Staroverov, V.N., Keith, T.A., Kobayashi, R., Normand, J., Raghavachari, K., Rendell, A.P., Burant, J.C., Iyengar, S.S., Tomasi, J., Cossi, M., Millam, J.M., Klene, M., Adamo, C., Cammi, R., Ochterski, J.W., Martin, R.L., Morokuma, K., Farkas, O., Foresman, J.B., Fox, D.J., Gaussian, Inc., Wallingford CT (2016)
65. GaussView 4.1; Gaussian Inc.: Pittsburgh, PA, USA (2006)
66. Chem3D, version 8.0.3; Chemoffice, Cambridge Software: St Neots, UK (2003)
67. Allouche, A.R., Gabedit (2017). <http://gabedit.sourceforge.net/>
68. Horowitz, S., Trievel, R.C.: Carbon-oxygen hydrogen bonding in biological structure and function. *J. Biol. Chem.* **287**, 41576–41582 (2012)
69. López de la Paz, M., Ellis, G., Pérez, M., Perkins, J., Jiménez-Barbero, J., Vicent, C.: Carbohydrate hydrogen-bonding cooperativity—Intramolecular hydrogen bonds and their cooperative effect on intermolecular processes—Binding to a Hydrogen-bond acceptor molecule. *Eur. J. Org. Chem.* **5**, 840–855 (2002)
70. Deshmukh, M.M., Bartolotti, L.J., Gadre, S.R.: Intramolecular Hydrogen bonding and cooperative interactions in carbohydrates via the molecular tailoring approach. *J. Chem. Phys. A* **112**, 312–321 (2008)
71. Dashnau, J.L., Sharp, K.A., Vanderkooi, J.M.: Carbohydrate intramolecular hydrogen bonding cooperativity and its effect on water structure. *J. Phys. Chem. B* **109**, 24152–24159 (2005)
72. Karas, L.J., Wu, C.-H., Das, R., Wu, J. I.-C.: Hydrogen bond design principles. *WIREs Comput. Mol. Sci.* **10**, e1477 (2020). <https://doi.org/10.1002/wcms.1477>

73. Meyer, E.A., Castellano, R.K., Diederich, F.: Interactions with aromatic rings in chemical and biological recognition. *Angew Chem Int Ed.*; **42**(11), 1210–1250 (2003)
74. Mammino, L., Kabanda, M.M.: Computational study of the patterns of weaker intramolecular hydrogen bonds stabilizing acylphloroglucinols. *Int. J. Quantum Chem.* **112**, 2650–2658 (2012)
75. Gu, Y.L., Kar, T., Scheiner, S.: Fundamental properties of the CH $\cdots$ O interaction: Is it a true hydrogen bond? *J. Am. Chem. Soc.* **121**, 9411–9422 (1999)
76. Desiraju, G.R.: The C-H $\cdots$ O hydrogen bond: structural implications and supramolecular design. *Acc. Chem. Res.* **29**, 441–449 (1996)
77. Reenu, V.: Evaluating the role of electron-correlation in the external prediction of the toxicity of nitrobenzenes towards *Tetrahymena pyriformis*. *New J. Chem.* **40**, 2343–2353 (2016)

# Molecular Modeling of Acetylcholinesterase Inhibitors for the Treatment of Alzheimer's Disease



**Anderson Mendes Oliveira, Anna Eláyne da Silva Silva,  
Abraão Alves Pinheiro, Lenir Cabral Correia, Francinaldo Sarges Braga,  
Laira Rafaelle Pinto Gemaque, Cleydson Breno Rodrigues dos Santos,  
Carlos Henrique Tomich de Paula da Silva, Carlton A. Taft,  
and Lorane Izabel da Silva Hage-Melim**

**Abstract** Alzheimer's disease (AD) is a neurodegenerative disorder characterized clinically by the loss of recent memory, communication and learning ability, and that its natural history can evolve to the death of the patient. Histopathologically, AD is marked primarily by the death of cholinergic neurons, with the appearance of characteristic markers such as neurofibrillary tangles and insoluble structures from amorphous fragments arising from an abnormal metabolic process involving beta-amyloid protein. Its current treatment works as a palliative method, based only on the attempt to stabilize the patient's clinical condition through the use of anti-cholinesterase agents, which, even with its limitations, can improve the individual's quality of life. This study aims to study compounds described in the literature as AChE inhibitors and, from these, to select what best fit the study parameters as a possible drug candidate for the treatment of AD. For this, at first, the crystallographic structure of AChE and 30 inhibitor compounds were obtained. Of the latter, the pharmacophoric group was identified (with 2 aromatic groups, 1 hydrogen acceptor, 1 hydrogen donor and 4 hydrophobic donors) and were submitted to the analysis of their physicochemical properties (in which 18 structures presented two or more violations of RO5) and molecular, where structure 25 showed the best results in 4 of the

---

A. M. Oliveira · A. E. da S. Silva · A. A. Pinheiro · L. C. Correia · L. I. da S. Hage-Melim (✉)  
Laboratory of Pharmaceutical and Medicinal Chemistry (PharMedChem), Federal University of  
Amapá, Macapá, Amapá, Brazil  
e-mail: [loranehage@gmail.com](mailto:loranehage@gmail.com)

F. S. Braga · L. R. P. Gemaque · C. B. R. dos Santos  
Laboratory of Modeling and Computational Chemistry, Federal University of Amapá, Macapá,  
Amapá, Brazil

C. H. T. de P. da Silva  
Computational Laboratory of Pharmaceutical Chemistry, School of Pharmaceutical Sciences of  
Ribeirão Preto, University of São Paulo, Ribeirão Preto, São Paulo, Brazil

C. A. Taft  
Centro Brasileiro de Pesquisas Físicas, Rio de Janeiro, Brazil

L. I. da S. Hage-Melim  
Departamento de Ciências Biológicas e da Saúde, Universidade Federal de Amapá, Macapá,  
Brazil

5 properties studied, in addition to ADME/Tox properties. The molecular docking analysis presented structure 1 as the one with the best interaction with the biological receptor. Based on the analysis of these results and the pharmacological hypothesis generated, the structure was chosen with the potential to become a drug for the treatment of Alzheimer's, aiming at the conception of a new drug with greater efficiency and safety for the treatment of patients with this pathology.

**Keywords** Alzheimer's disease · AChE inhibitors · Molecular modeling · Molecular descriptors · QSAR · Molecular docking · Pharmacophoric grouping · ADME/Tox properties

## 1 Introduction

Alzheimer's disease (AD) is a neurodegenerative disorder that progresses gradually and culminates in the death of the patient, also occurring cognitive and memory deterioration, progressive impairment of daily life activities and a variety of neuropsychiatric symptoms and behavioral changes [1], making it the largest cause of death in older people [2].

As for the evolution of the disease, it is possible to observe atrophy predominantly in the cerebral cortex, more pronounced in the temporal lobe, mainly in the hippocampus region, and accompanied by a diffuse increase of the cortical grooves and fissures due to the reduction of encephalic mass. The areas most affected by AD progress are the cortical, limbic, paralimbic and cortex regions. Primary areas, such as the motor cortex or the visual or auditory cortex, it is preserved until the most advanced stage of the disease [1, 3]. The senile plaques are classified as neuritic when they contain neurites, fragments of axons or degenerate dendrites when they do not contain dystrophic neurite are called diffuse plaques [4].

The lack of evidence of the causes that lead to the development of AD, and many mechanisms not yet elucidated in the progression of the disease, hinder the development of a drug that can change the course of the disease, so that the drugs used in current AD therapy act only improving the behavioral, psychic and memory loss symptoms caused by the advancement of dementia [5].

Even with mechanisms not fully elucidated yet, AD is characterized by the selective loss of populations of neurons, especially cholinergic neurons [3], implying a marked decline in levels of acetylcholine (ACh) available in the nervous system. This justifies the cholinergic hypothesis and the attempt to propose drugs that increase the bioavailability of ACh, such as acetylcholinesterase inhibitors (AChE), responsible for metabolizing ACh, which would provide a better quality of life for patients with AD [6]. The present study aimed to propose new drug candidates, AChE inhibitors, to be used in the treatment of AD, and it is possible to observe improved pharmacokinetic and activity patterns from modifications made using molecular modeling calculations, in the rational planning of drugs.

## 2 Materials and Method

### 2.1 Inhibitors and Crystallographic Structure of PDB Studied

Knowing the coordinates of the three-dimensional structure of the target protein, or biological receptor, for the new proposals is important when designing selective structures with well-defined biological activity. This information can be found in the Protein Data Bank—PDB ([www.pdb.org](http://www.pdb.org)), through the information and experimentally resolved crystallographic structures deposited in it [7]. The structure chosen was the 2CKM access code with 2.15 Å resolution, where the complex formed by the enzyme AChE and the N, N'-di-1,2,3,4-tetrahydroacridin-9-ylheptane- 1,7-diamine [8].

Then, a group of ligands with known structure and that had inhibitory activity for the AChE enzyme, were obtained from the database BindingDB ([www.bindingdb.org/bind/index.jsp](http://www.bindingdb.org/bind/index.jsp)) [9]. The ligands available on the BindingDB were ordered by IC50, and the 30 most active compounds were selected, which were optimized and had their energy minimized in the program **HyperChem 6.0.2** [10] by semi-empirical method AM1.

### 2.2 Calculation of Molecular Properties

Two classes of molecular properties were calculated, (a) those that describe the global reactivity, through the program **GaussView 5.0** [11] using the Density Functional Theory (DFT) method that allows deducing the external potential, based on the knowledge of the fundamental state density of a many electron system [12], and the base set B3LYP/6-31G\*\* implemented with the **Gaussian 03** program [12], and (b) those describing the relation between the structure and activity (QSAR), with **HyperChem 6.02** [10] as its main tool.

#### 2.2.1 Global Reactivity Descriptors

The GaussView 5.0 program [13] was used to calculate the first properties that refer to the molecular properties of global reactivity of the structures, which sum a total of 21, namely: total energy (TE), Mulliken's electronegativity ( $\chi$ ), molecular hardness ( $\eta$ ), molecular softness ( $1/\eta$ ), chemical potential ( $\mu$ ), global electrophilicity index ( $\omega$ ), Highest Occupied Molecular Orbital (HOMO), a level below the Highest Occupied Molecular Orbital (HOMO-1), Lowest Unoccupied Molecular Orbital (LUMO), a level above the Lowest Unoccupied Molecular (LUMO+1), energy difference between HOMO and LUMO ( $GAP = HOMO - LUMO$ ). These descriptors are indicators of stability and chemical reactivity [14]. The construction of the boundary

orbitals (HOMO and LUMO) for the studied compounds were visualized with the help of the **Molekel** program [15].

### 2.2.2 Molecular Descriptors of Structure–activity Relationship

As regards the QSAR properties, represented by the following descriptors: total surface area (TSA), molecular volume (MV), molecular refractivity (MR), molecular polarizability (MP), lipophilicity coefficient (logP), molecular mass (MM) and hydration energy (HE), the program **HyperChem 6.02** was used. These descriptors, after their selection, provide information on the electronic, steric, hydrophilic and hydrophobic influence on the selected inhibitors.

### 2.3 *Electrostatic Potential Maps—MEP*

The correlation of the pharmacophoric region of the studied compounds occurs through the characteristics of the maps of electrostatic potential. MEP allows the use of a qualitative analysis to locate reactive sites of a structure, and to determine the roles played by both electronic and steric effects (size/shape) on its potency, and it is of paramount importance that MEP visualization provides qualitative information about the structures, such as the behavior of the interaction between a ligand and the receptor. The MEP at a given point (x, y, z) in the vicinity of a structure is defined in terms of the interaction energy between the electric charge generated from the electrons of the structures, nuclei and a positive test charge (a proton) located in r [16].

In the methodology applied in this work, the MEPs were generated from the atomic charge at the DFT level B3LYP/6-31G\*\* calculated in the **Gaussian 03** program, and the results were visualized with the help of the **Molekel** program [16].

### 2.4 *Molecular Docking*

The molecular docking method consists in predicting the possible interaction of two structures [17], when provided with their atomic coordinates [18], in an attempt to reproduce a real interaction. For this, the AutoDock Vina program [19] was used, which fits the ligands at the active sites of the macrostructure, showing, as a result, the orientations with probability of occurrence. The necessity of ordering these orientations is supplied by the AutoDock Vina by means of the affinity energy calculation, which makes the fittings obtained by the program more favorable (with lower affinity energy) to less favorable (with higher values of affinity energy) [19].

To perform the molecular docking, the crystallographic structure of AChE deposited in the PDB with the 2CKM code was used. As in a standard docking procedure, the inhibitor complexed to it was removed and two different files were created, one containing only the biological target structure and the other with the isolated ligand structure, so that the simulation was performed in the program AutoDock Vina, where it was defined the region where the program would be free to search for the best orientations of the ligand (region of the active site defined by Rydberg and collaborators [8]), by means of the dimensions Grid Box, that received the following three-dimensional coordinates: center = 1.838, and center = 63.579, center = 68.48. After the simulation for the crystallographic inhibitor, the method was validated by RMSD calculation and the docking simulation occurred for the other structures selected from the literature.

## 2.5 Hypothesis of the Pharmacophoric Group

Pharmacophore is the chemical segment of a structure responsible for its biological activity, being defined as the arrangement of characteristics necessary to promote an interaction between a structure and a biological target [19].

The PharmaGist web server [19] was used in this step for pharmacophoric derivation, by submitting the 30 structures selected from BindingDB. One of the features of the PharmaGist is to allow the analyzed structures to be aligned from a pivot structure informed at the time of submission to the program. The ligand indicated as pivot was the structure 1, chosen to present with lower value of IC<sub>50</sub> and, consequently, as the most active.

## 2.6 ADME/Tox Screening

Pharmacokinetic characteristics make up the so-called ADME properties (Administration, Distribution, Metabolism—or Biotransformation, and Excretion). The prediction of these properties can be predicted through the PreADMET server (<http://preadmet.bmdrc.org/>), human intestinal absorption (HIA), cell permeability in Caco-2 and MDCK cells, binding to plasma proteins (PPB) and permeability in the blood brain barrier (BBB), in addition to toxicological tests, which include investigations of carcinogenicity in rats and mice, and mutagenicity, so that these 3 properties are presented without quantification factor.



### 3 Results and Discussions

#### 3.1 Structures Studied

We selected 30 structures with inhibitory activity for BindingDB AChE, where the selection was given by the lower values of IC<sub>50</sub> values for the larger ones (Fig. 1), whereas the 2CKM crystallographic complex was obtained from the PDB with the coordinates well-defined three-dimensional and 2.15 Å resolution.

#### 3.2 Analysis of Physicochemical Properties

Search in the BindingDB database allowed us to select 30 compounds which are effective inhibitors of AchE, Fig. 1. It was also possible to obtain, from this base, four parameters related to oral bioavailability according to the Lipinski's Rule [20]. These four parameters were formulated from the study of 1500 drugs used in the United States with good penetration into the CNS. According to the rule, a drug is expected to have the following properties so that it also has good absorption by the CNS: Molecular weight  $\leq 400$ ; Hydrogen bond donor  $\leq 3$ ; Hydrogen bond acceptor  $\leq 7$  and Log p  $\leq 5$ . The results revealed that the lipophilicity coefficient (logP) of 12 of the inhibitors (compounds 1–30) exceeded 5.0, the other compounds studied were in agreement with Lipinski, being this an important characteristic for good absorption of a drug administered orally (Table 1) [21, 22].

The data obtained showed that there was violation of the rule of five parameters, where 26 of the 30 structures studied had molecular weight higher than 400 Da, and the number of hydrogen donor regions ranging from 0–5. For the hydrogen bonding acceptor regions, only compounds 16 and 27 do not obey the Rule of Five according to Table 1. Thus, only 12 of the compounds studied (11, 13, 18, 20, 21, 22, 24, 25, 26, 28, 29 and 30) did not violate more than one parameter of the rule of five, being possible drug candidates with good bioavailability for oral administration, developing pharmacological effect on the CNS. In addition, the molecular weight of the compounds (1–30) range from MW = 284.11 to 737.22 Da, according to Table 1, indicated that 10 of the compounds studied had a lower molecular weight or more similar than 80% of the commercially available drug (MW < 450 Da) [21].

#### 3.3 Calculation of Molecular Properties

All molecular descriptors presented in the methodology, whether global reactivity or QSAR, were arranged in a table for a better visualization of the results, with the determination of all the descriptors. For statistical analysis, it was necessary to construct and standardize a data matrix  $X = (n, m)$ , where the analyzed compounds

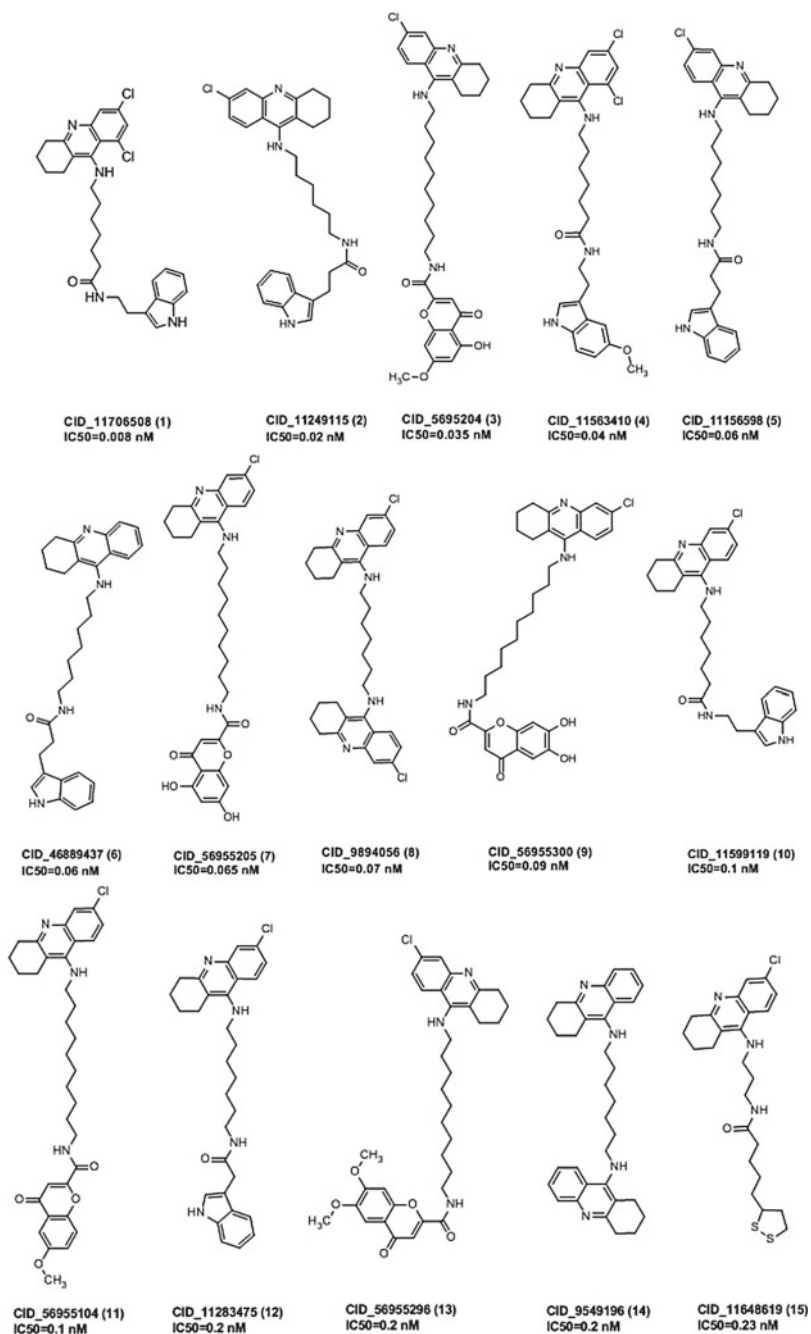


**Fig. 1** Structures with AChE inhibitory activity obtained on BindingDB

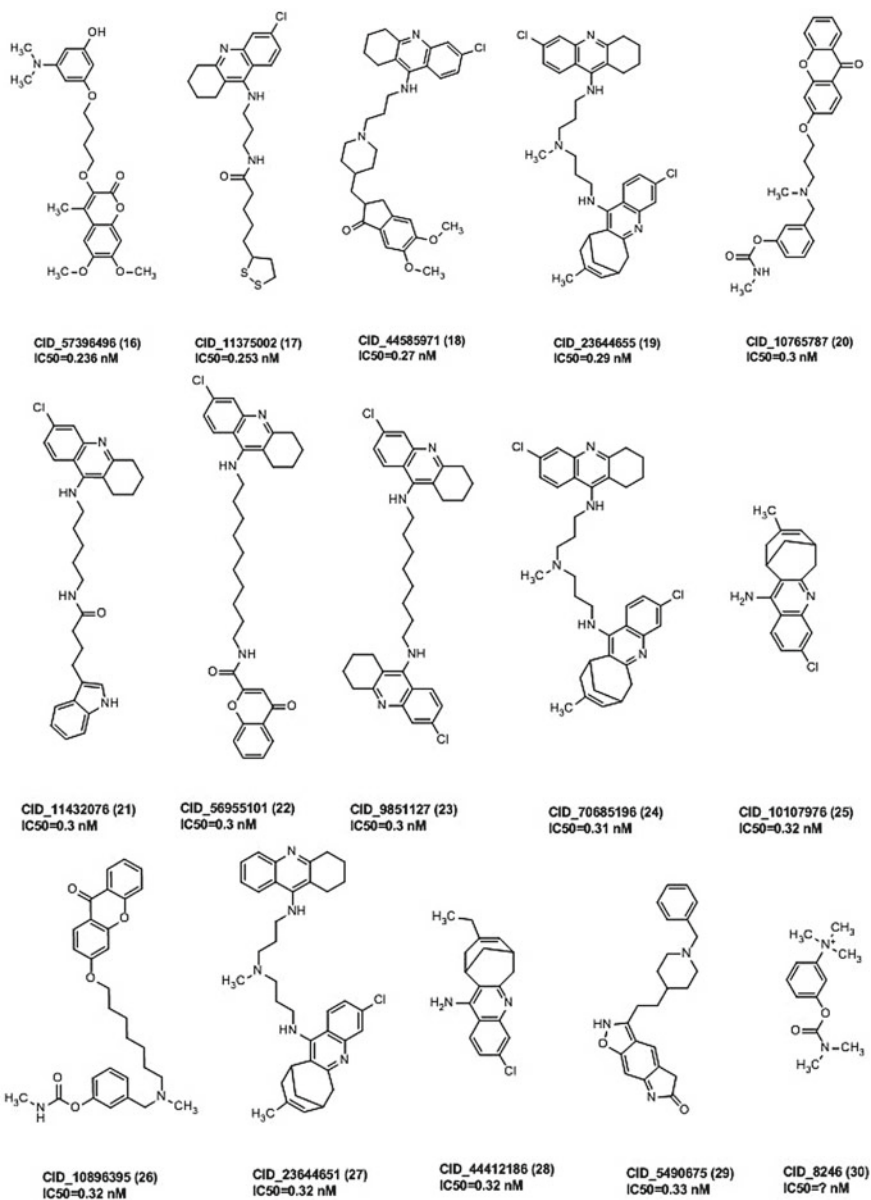


Fig. 1 (continued)

**Table 1** Physicochemical properties of the 30 structures selected in BindingDB

Structure	MW	HBD	HBA	LogP	Number of violations
1	536.21	3	3	7.60	2
2	502.25	3	3	6.80	2
3	641.25	4	7	0.35	2
4	602.20	3	4	7.60	2
5	516.26	3	3	7.30	2
6	482.30	3	3	6.70	2
7	627.23	5	7	0.51	2
8	560.25	2	4	9.80	2
9	627.00	5	7	0.32	2
10	502.25	3	3	7.00	2
11	625.25	3	6	1.37	1
12	502.25	3	3	7.00	2
13	655.26	3	7	0.38	1
14	490.32	2	4	8.50	2
15	477.17	2	5	6.10	2
16	443.19	1	8	4.10	2
17	477.17	2	5	6.10	2
18	597.25	2	6	0.68	1
19	737.22	5	5	1.58	2
20	446.18	1	6	4.40	1
21	503.08	3	3	0.49	1
22	595.24	3	5	2.37	1
23	574.00	2	4	10.30	2
24	663.27	3	5	1.48	1
25	284.11	1	2	3.70	0
26	423.01	0	5	3.10	1
27	703.25	5	10	5.00	3
28	298.12	1	2	4.10	0
29	375.20	1	4	2.90	0
30	302.06	0	3	1.18	0

were distributed in the lines and each calculated descriptor occupied a column distinct from the matrix. The objective of standardization was to give each variable an equal weight in mathematical terms, each variable was centered in the mean and scaled to the unit variance.

With the matrix completed, the Pearson's correlation ( $r$ ) was calculated to verify the existence of a linear correlation between the molecular properties of the compounds ( $r$  can assume values between 1 and  $-1$ ). Positive values indicate directly

proportional linear correlation between two variables, negative values refer to linear inversely proportional correlation, and  $r$  values equal to 0 indicate that there is no linear correlation between variables. The result of the analysis of Pearson demonstrated that the properties LUMO + 1, Log P, surface area, volume, hydration energy, refractivity, polarizability, mass, softness, total energy and IC50 have some type of correlation, as shown in Table 2.

The surface area is directly related to the rate of dissolution and absorption, because the higher the area of contact the faster the dissolution and the easier the absorption [23]. Also in Table 2, it is observed that the range of surface area change from 486.92 to 1050.26 Å<sup>2</sup> for the structures studied, and compounds 25 and 13 have the lowest and highest values of this property. The structure 26 is more likely to be diluted and absorbed. The Pearson's correlation value for the surface area with IC 50 was  $-0.389917$  (Table 2).

The molar volume of drugs causes greater stereochemical impediment, they can block the receptor to interact with the corresponding substrate [24]. The molecular volume variation was 810.80 (structure 25) at 1799.62 Å<sup>3</sup> (structure 13). The lower value indicates a possible improvement in the interaction of the receptor with the substrate, showing in Table 2 that compound 25 would be a better choice among the compounds. The Pearson's correlation value of IC 50 with the molar volume was  $-0.355343$  (Table 2).

Hydration energy is the energy released when water structures are separated from each other and are attracted by structures or ions of a solute that is dissociating in water. The hydration energy comprises the solvent-solvent and solute-solvent interactions [25]. The Table 2 shows the minimum and maximum values being  $-16.66$  and  $-1.37$ , respectively for structures 9 and 23. It should also be noted that compound 9 is the one which has the highest stability because it has the lowest hydration energy. When correlating with biological activity, the Pearson's correlation value was  $0.399899$  (Table 2).

The polarizability of physicochemical properties is very important in SAR/QSAR studies, which can be correlated with lipophilicity, molar volume and steric impediments, to help interpret the mechanisms of interaction between a compound and its biological receptor [24]. Table 2 shows the polarizability values for the compounds studied ranged from 32.13 (25) to 71.30 Å<sup>3</sup> (24). Thus, compound 24 with higher polar volume facilitates hydrogen bridge and dipole-dipole interactions. The Pearson correlation value for the polarity with IC50 was  $-0.372785$  (Table 2).

The molecular mass, although it is indirectly related to the volume value of each structure, does not conveniently express its three-dimensional profile, being, nevertheless, also used as a steric parameter in QSAR studies [26]. Table 2 shows the range of molecular mass of the compounds, being minimum and maximum, 284.79 and 628.69, the lowest value of structure 25 being the highest of structure 24, thus indicating that structure 25 has lower stereochemistry among the others. When correlating with biological activity, the Pearson's correlation value was  $-0.378167$  (Table 2), however, it was not possible to obtain parameters for the structure 30, since it is protonated, making it impossible to perform calculations for it.

**Table 2** Pearson's correlation

Structure	Surface area grid (Å <sup>2</sup> )	Volume (Å <sup>3</sup> )	Hydration energy (kcal/mol)	Polarizability (Å <sup>3</sup> )	Mass (amu)	IC 50
1	892.25	1527.93	-6.57	59.35	537.53	0.008
2	877.63	1495.09	-7.08	57.42	503.09	0.02
3	1014.29	1742.37	-10.16	65.41	606.16	0.035
4	925.55	1600.66	-8.19	61.82	567.56	0.04
5	908.87	1549.52	-6.71	59.25	517.11	0.06
6	883.82	1507.87	-7.10	57.33	482.67	0.06
7	984.54	1690.11	-15.24	63.57	592.13	0.065
8	920.16	1598.28	-1.73	65.58	561.60	0.07
9	982.87	1687.14	-16.66	63.57	592.13	0.09
10	870.40	1495.54	-7.01	57.42	503.09	0.10
11	1011.91	1723.09	-6.60	64.77	590.16	0.10
12	877.99	1494.28	-6.81	57.42	503.09	0.20
13	1050.26	1799.62	-6.22	67.24	620.19	0.20
14	874.77	1511.87	-2.41	59.72	492.71	0.20
15	801.12	1366.30	-4.20	52.60	478.11	0.23
16	762.56	1286.79	-14.20	46.41	443.50	0.236
17	800.96	1366.31	-4.20	52.60	478.11	0.253
18	921.32	1603.69	-3.77	62.27	298.82	0.27
19	996.18	1757.71	-1.87	63.37	594.24	0.29
20	762.17	1291.00	-9.22	48.45	446.50	0.30
21	874.90	1495.50	-7.06	57.42	503.09	0.30
22	960.77	1646.58	-4.41	62.30	560.14	0.30
23	952.00	1658.11	-1.37	65.41	575.62	0.30
24	992.51	1764.36	-1.73	71.30	628.69	0.31
25	486.92	810.80	-3.26	32.13	284.79	0.32
26	895.38	1512.927	-8.76	55.79	502.61	0.32
27	959.04	1713.08	-2.44	63.37	594.24	0.32
28	515.18	864.20	-2.90	33.96	298.82	0.32
29	649.10	1105.28	-8.14	42.32	375.47	0.33
30	-	-	-	-	-	-
Surface area grid (Å <sup>2</sup> )		0.996550	-0.108684	0.974569	0.860055	-0.389917
Volume (Å <sup>3</sup> )			-0.060285	0.982288	0.860329	-0.355343

(continued)

**Table 2** (continued)

Structure	Surface area grid ( $\text{\AA}^2$ )	Volume ( $\text{\AA}^3$ )	Hydration energy (kcal/mol)	Polarizability ( $\text{\AA}^3$ )	Mass (amu)	IC 50
Hydration energy (kcal/mol)				0.026939	-0.124880	0.398299
Polarizability ( $\text{\AA}^3$ )					0.841304	-0.372785
Mass (amu)						-0.378167

### 3.4 Molecular Electrostatic Potential Maps—MEP

The molecular electrostatic potential (MEP) map, which enabled a qualitative analysis to locate reactive sites on a structure and to determine the roles played by both electronic and steric effects (size/shape) on its potency [27], is an important tool for the analysis of recognition processes by another structure, such as drug-receptor interactions and enzyme-substrate types, because it is through its potential that one species sees another in a biological recognition process (Fig. 3).

When analyzing the generated MEP images for the 30 structures used in this study, it is possible to note a pattern among them, considering that regions with nucleophilic attack potential (regions with red staining—negative regions) always coincide in oxygen structures, being able or not to change the position, depending on the structure, as for example the case of two compounds, where two structures of oxygen identified as red region in an aromatic ring, and others along the chain. The red regions when they do not mark the oxygen, are located very near. And regions potentially capable of nucleophilic attack (blue regions—positive regions) appear along the chain, encompassing carbon and hydrogen structures. After the analysis, it is noted that the regions that can potentially bind to the active site, would be the regions close to the oxygen atom, because the oxygen is capable of performing nucleophilic attack, thus providing the bond (Fig. 2).

### 3.5 Molecular Docking

The investigation of the orientations and the possible forms of interaction between the ligands described in the literature and the biological target was carried out using the molecular docking methodology. The docking simulates the complex formation between the enzyme and the linker [28], that is, how the inhibitor binds to the target protein.

In this work for the simulation of molecular docking, the AutoDock Vina [18] was used, which presents the possible orientations that the ligand can assume in the protein, ordering them by means of the affinity energy, expressed in Kcal/mol,

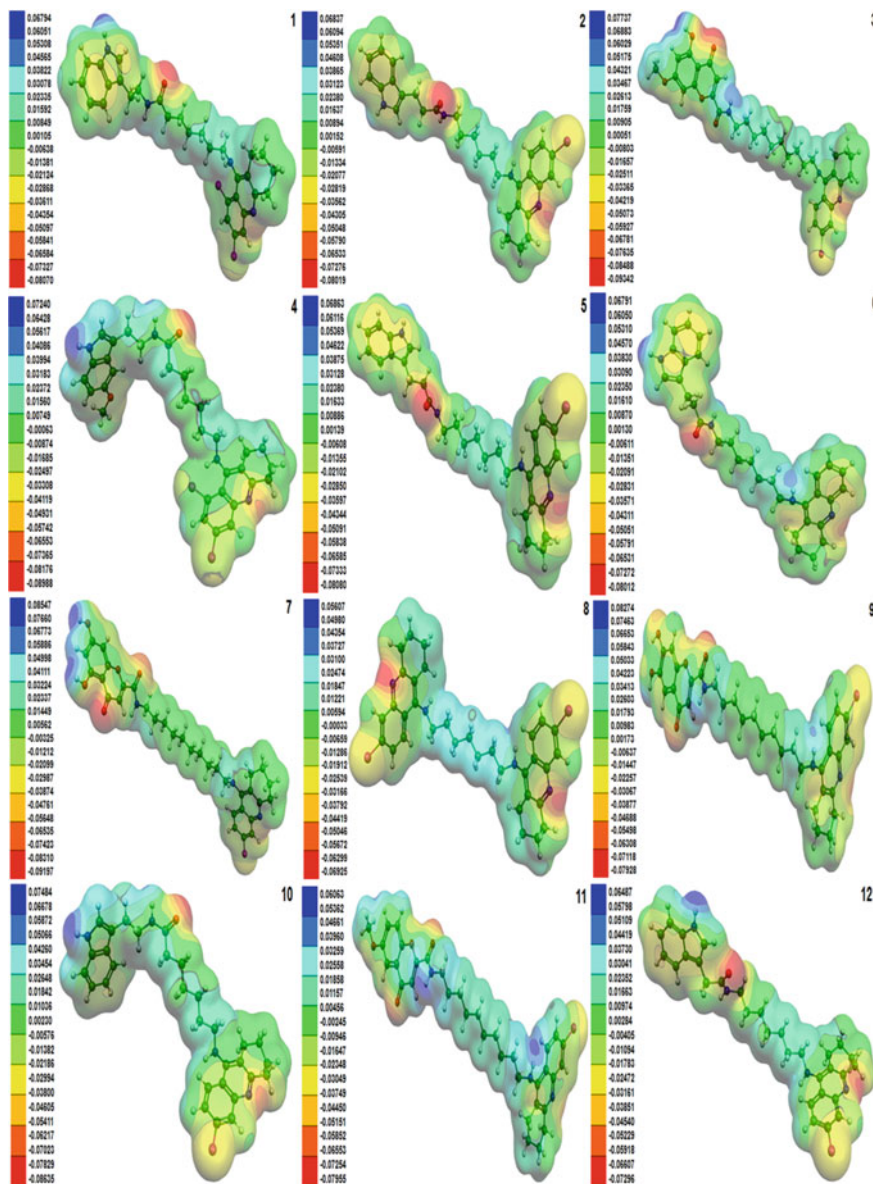


Fig. 2 Map of electrostatic potential of compounds



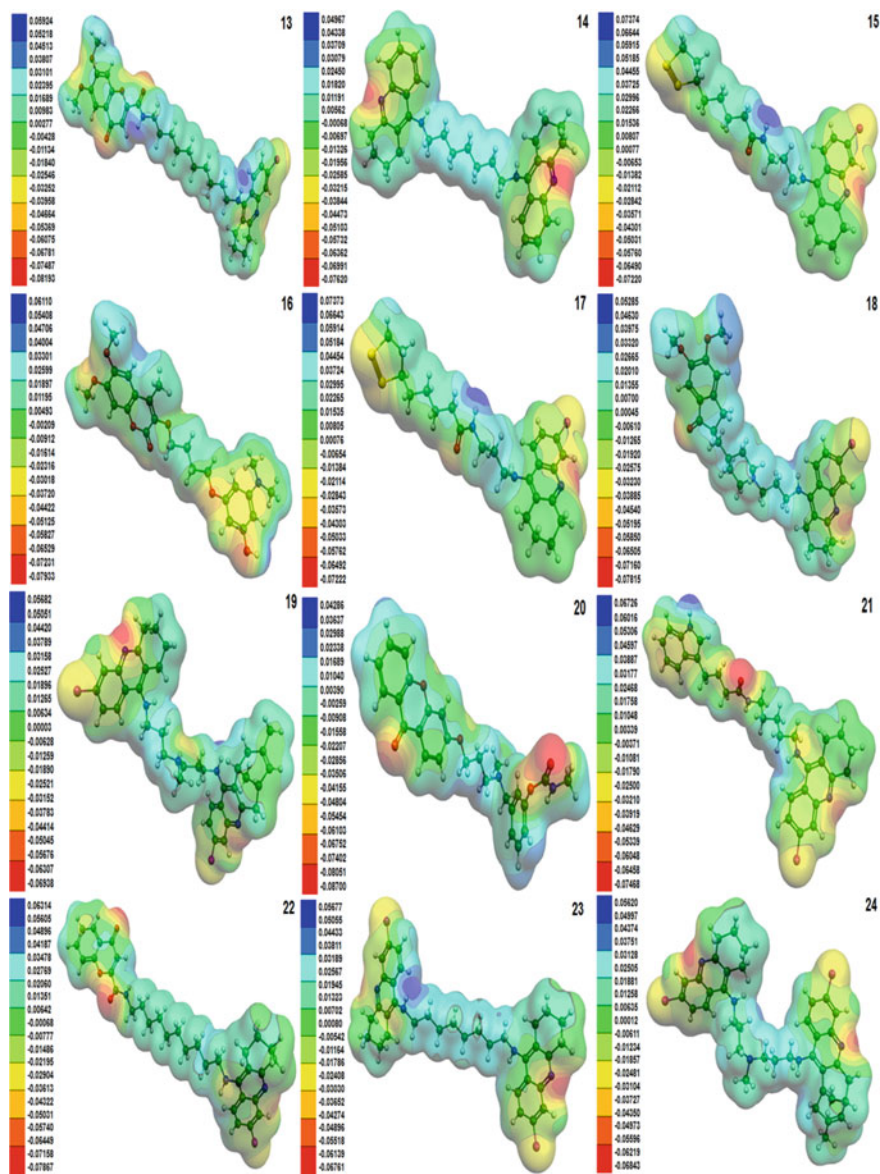


Fig. 2 (continued)

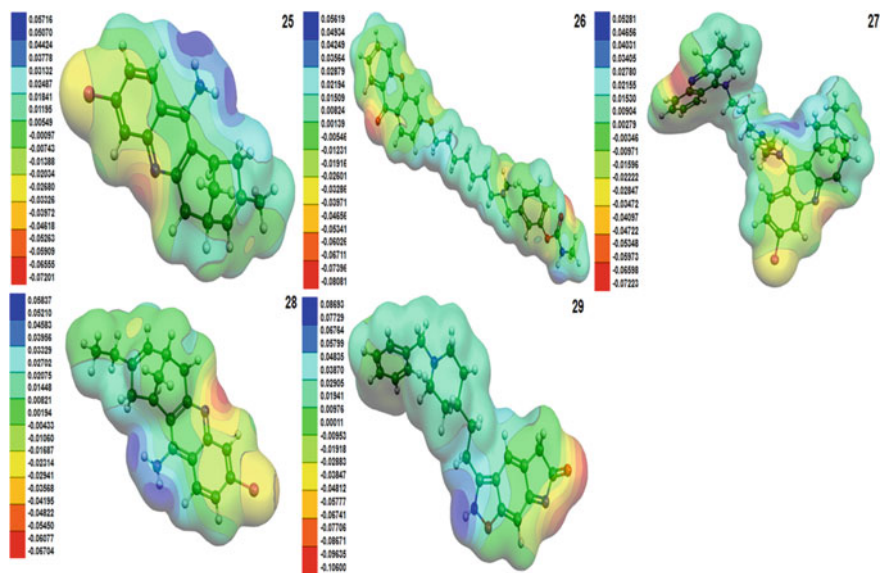


Fig. 2 (continued)

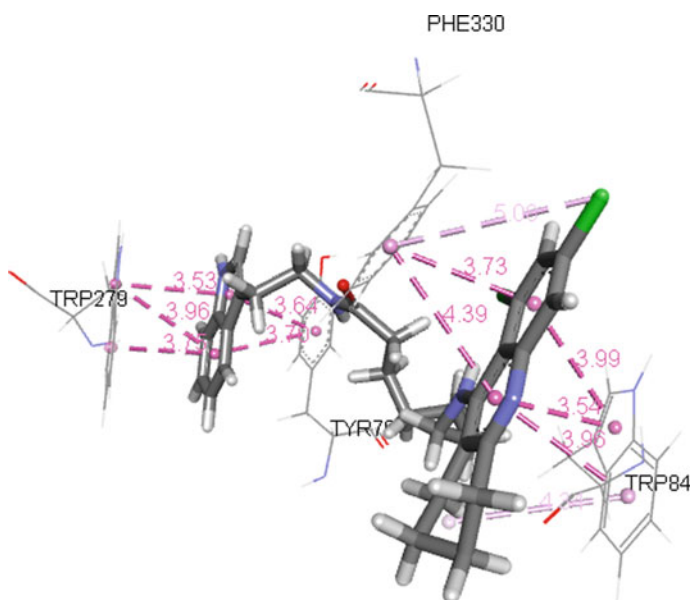


Fig. 3 Docking orientation generated by AutoDock Vina. Structure 1 (CID\_11706508)

necessary in the formation of each complex. The lower the energy spent for the ligand to complex the target, the better the interaction and affinity between them.

It was necessary to validate the docking methodology used to guarantee that it can reproduce *in silico*, with good approximation, the formation of complex already solved experimentally. For this to be possible, the docking simulation was performed for the AChE and the crystallographic inhibitor obtained from the 2CKM complex of the PDB database. This methodology to simulate molecular anchoring was previously performed in studies with inhibitors of GSK-3 $\beta$  and  $\beta$ -secretase [29], also studied as biological targets involved in the natural history of AD, where the AutoDock Vina was able to reproduce *in silico*, with relative accuracy, the results obtained experimentally, clarifying possible orientations that the active inhibitors possibly assume in the catalytic site of the enzymes.

The validation was done by calculating the RMSD of the coordinates of the crystallographic inhibitor and the results generated by the AutoDock Vina, which should assume values smaller or equal to 2.0 Å. The RMSD was calculated in the Discovery Visualizer program [30] and the value found for this solution proposed by AutoDock Vina was 0.412 Å. With the validation of molecular docking, this methodology was extended to the structures obtained from BindingDB and the best orientation for each of the structures was taken as the result for analysis of the interaction between the respective structure and the biological target.

According to the program guidelines, structure 1 was the best one that interacted among the structures obtained in BindingDB with the enzyme AChE in the region of its active site, which comprises amino acid residues Tyr70, Trp84, Trp279 and Phe330, as observed in Fig. 3, having its affinity energy equal to  $-12.4$  kcal/mol, and structure 23, which also demonstrated interactions with all active site amino acid fragments and affinity energy equal to  $-12.3$  kcal/mol, while the ligand removed from the 2CKM complex had affinity energy equal to  $-18.8$  kcal/mol also interacting with all expected amino acid fragments. Structures 6, 8 and 29 also presented affinity energy values that approximate those obtained by structures 1 and 23, however with a much smaller number of interactions demonstrated by molecular docking.

This information helps to understand how interactions between biological ligand and target must occur in a real reaction, which makes it possible to infer what the necessary conditions that an inhibitor should have in relation to the target structure. Analyzing the interactions between the ligands and the biological target, it was observed that they are mostly of the hydrophobic type, hydrogen bonding interactions and rare electrostatics were also noticed.

### 3.6 Hypothesis of the Pharmacophoric Group

Knowing the generic or common structure of most ligands, through derivation of the pharmacophoric grouping, is extremely important to know the regions that possibly confer activity to the inhibitors and, when designing new structures, to apply this information in line with the interactions that the docking indicated as the most frequent and that allow the ligand to dock at the active site of the protein [31, 32].

The Pharmagist web server [1], used in pharmacophore generation, performed multiple alignments from the 30 selected compounds, aiming at overlapping what is common among them. The alignment of the compounds, made from the pivot (1) structure, and its three-dimensional spatial characteristics were presented in the generated result, allowing a good analysis of the information obtained, and graphical presentation of the donor and acceptor regions of hydrogen, hydrophobic and aromatic regions, common to aligned structures. Regarding the result obtained, the server was able to align 23 of the structures submitted to it, and this alignment received a score value equal to 53.973.

In this result, as observed in Fig. 4, the pharmacophore has 2 aromatic groups (translucent sphere), 1 hydrogen acceptor (green sphere), 1 hydrogen donor (yellow sphere) and 4 hydrophobic (white spheres) donors. These are regions that are important, by the definition of pharmacophore itself, in the design of new structures with anticholinesterase activity.

Picanço and collaborators [6], Pinheiro and collaborators [33], both used the same methodology to generate the pharmacophore hypothesis for structures that are potential therapeutic targets for AD, Glycogen synthase kinase-3 (GSK-3 $\beta$ ) and  $\beta$ -secretase (BACE -1), respectively. Picanço and collaborators found hydrophobic rings and regions of adjacent hydrogen acceptors [6], while Pinheiro and collaborators found aromatic, hydrophobic, donor and receptor regions of hydrogen bonding [33]. The

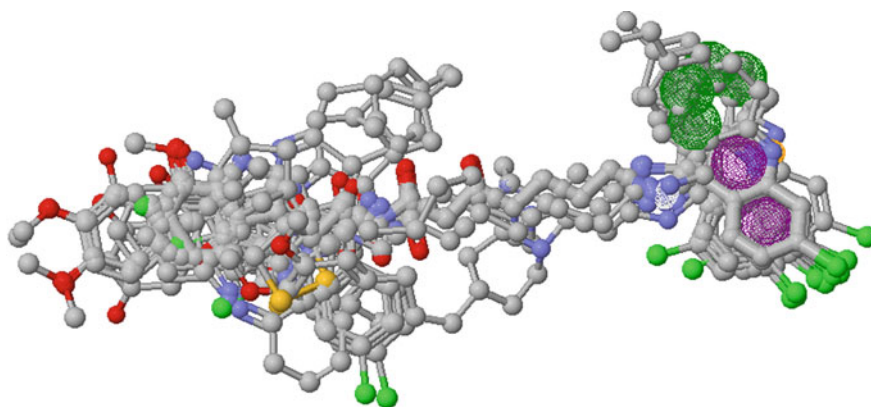


Fig. 4 Pharmacophore hypothesis for the alignment of 6 structures

results of Pinheiro and collaborators are similar, even for different biological targets, to that found in this study regarding the upper region of Fig. 4 [33].

### 3.7 ADME/Tox Screening

It is known that the chemical structure of a compound is not only responsible for pharmacological effects but also for adverse and toxicological effects [32]. For an accurate analysis of the pharmacokinetic and toxicological profile of compounds studied in this work, as well as of the developed proposals, it was necessary *in silico* predictions using the web server PreADMET (<http://preadmet.bmdrc.org/>), being possible to obtain parameters (Absorption, Distribution, Metabolism, Excretion and Toxicity) simulating human intestinal absorption (HIA), permeability in Caco-2 and MDCK cells, plasma protein binding (PPB), penetration in the blood–brain barrier (BBB) (Table 3), mutagenicity and carcinogenicity in rats and mice (Table 4) [34].

For pharmacokinetic parameters, all structures are well absorbed by the human intestine, with values above 70%; all with medium permeability in Caco2 cells, with values within the range of 4 to 70. All the compounds showed high absorption by the BBB, except the structures 2, 7 and 29, with values lower than 0.1—indicating low absorption—, and the structures 1, 6, 8, 12 and 16, with results in the range of 2.0 ~ 0.1—suggesting average absorption of the structures by BBB.

Regarding plasma protein binding, 17 obtained PPB values greater than 90%, indicating a strong binding of these to plasma proteins, whereas the other structures (1, 2, 7, 9, 10, 11, 18, 19, 21, 22, 29 and 30) demonstrate poor binding to these proteins.

Compounds 1, 2, 7, 8, 10–22, 29 and 30 showed low permeability in MDCK cells (less than 25 nm/s), while the other 11 compounds studied were predicted to be medium permeability (between 25 and 500 nm/s).

By observing the *in silico* toxicological tests for which the structures described in the literature had to be submitted, it is possible to notice that 86.7% shows a potential mutagenic activity, except for compounds 15, 16, 17 and 21. Regarding the carcinogenicity factors, according to the parameters determined by the algorithm employed (where the predictive value expressed as negative indicates that there is clear evidence of carcinogenic activity, whereas predictive values expressed as positive, indicate that there is no clarity regarding the evidence of activity carcinogenicity), all compounds showed evidence of carcinogenicity in rats, and structures 1, 4, 7, 8, 10, 11, 12, 14, 19, 21, 22, 23, 24, 25, 27 and 28 were evidence of carcinogenicity to mice.

**Table 3** Absorption, distribution in PPB percentages and BBB penetration for the AChE inhibitors investigated

Structure	Absorption			Distribution	
	HIA (%)	P <sub>Caco2</sub> (nm/s)	P <sub>MDCK</sub> (nm/s)	PPB (%)	C <sub>Brain</sub> /C <sub>Blood</sub>
1	100.00	39.94	9.98	27.40	1.25
2	96.01	44.03	11.33	40.98	0.02
3	95.74	50.26	38.68	98.06	15.63
4	95.73	53.17	45.76	100.00	17.20
5	95.73	52.44	42.17	100.00	17.32
6	96.98	21.13	31.85	100.00	1.34
7	96.43	48.17	0.09	84.63	0.04
8	96.68	53.35	0.20	85.01	0.40
9	94.02	47.97	26.98	89.06	11.78
10	93.95	46.19	15.88	88.70	11.41
11	93.95	46.72	15.88	88.05	10.87
12	96.56	53.27	0.17	91.87	1.27
13	93.95	46.20	4.40	93.29	11.18
14	94.20	48.48	7.78	91.55	10.29
15	93.95	46.84	4.40	93.12	10.96
16	96.56	53.27	0.17	91.87	1.27
17	94.27	48.22	10.56	92.11	12.30
18	95.92	52.06	0.16	84.70	13.49
19	95.86	52.70	0.09	85.69	14.59
20	97.02	23.43	19.07	100.00	2.24
21	97.54	49.77	1.92	88.98	2.55
22	93.61	50.67	24.78	86.86	10.41
23	96.87	38.31	64.12	99.03	8.08
24	96.98	39.72	57.63	97.91	6.61
25	95.89	26.58	36.61	99.39	5.64
26	94.26	21.31	27.16	100.00	4.95
27	96.94	40.81	61.26	95.41	5.22
28	94.26	21.52	53.78	100.00	4.93
29	96.99	53.22	3.04	88.09	0.03
30	95.86	52.70	0.09	85.69	14.59

**Table 4** Toxicological properties mutagenicity (Ames Test) and carcinogenicity for AChE inhibitors selected

Structure	Mutagenicity	Carcinogenicity	
		Rat	Mouse
1	Mutagenic	Negative	Positive
2	Mutagenic	Negative	Negative
3	Mutagenic	Negative	Negative
4	Mutagenic	Negative	Positive
5	Mutagenic	Negative	Negative
6	Mutagenic	Negative	Negative
7	Mutagenic	Negative	Positive
8	Mutagenic	Negative	Positive
9	Mutagenic	Negative	Negative
10	Mutagenic	Negative	Positive
11	Mutagenic	Negative	Positive
12	Mutagenic	Negative	Positive
13	Mutagenic	Negative	Negative
14	Mutagenic	Negative	Positive
15	Non-Mutagenic	Negative	Negative
16	Non-Mutagenic	Negative	Negative
17	Non-Mutagenic	Negative	Negative
18	Mutagenic	Negative	Negative
19	Mutagenic	Negative	Positive
20	Mutagenic	Negative	Negative
21	Non-Mutagenic	Negative	Positive
22	Mutagenic	Negative	Positive
23	Mutagenic	Negative	Positive
24	Mutagenic	Negative	Positive
25	Mutagenic	Negative	Positive
26	Mutagenic	Negative	Negative
27	Mutagenic	Negative	Positive
28	Mutagenic	Negative	Positive
29	Mutagenic	Negative	Negative
30	Mutagenic	Negative	Negative

## 4 Conclusion

By making a more accurate observation of the results obtained until the present moment, a kind of pattern is observed in some structures that appear as the best, time in some properties, time in other properties analyzed. Among these, the structure 25 can be assigned a special character because it is listed as the best evaluated structure in 4 properties (surface area, volume, polarizability and molecular mass) among the 5 molecular properties that constituted the analysis and still did not violate even a property of the Lipinski's Rule. In addition, structure 25 is among the structures with the best results in ADME predictions. With regard to toxicity predictions, it is present in the group of most structures presenting only one satisfactory predictive value among the three analyzed (only structure 21 had two desired values).

In view of the foregoing, it can be inferred that the structure 25 contains important properties within parameters desired for a structure to be considered a good proposal for prototype of a new drug, so that molecular modifications applied to it can potentiate its pharmacokinetic and toxicological properties, in addition to improving those that do not yet meet the ideal parameters, making possible the development of a safer and more efficient drug.

**Acknowledgements** We thank the Institute of Exact and Natural Sciences of the Federal University of Pará for the use of the GaussView and Gaussian softwares.

**Conflict of Interest** The authors confirm that this article content has no conflict of interest.

## Supplementary Material



Analysis of molecular docking generated from AutoDock Vina							
Structure	Active site of amino acid	Atoms involved	Type of interaction	Distance (Å)	Affinity (Kcal/mol)		
Ligand	Tyr70	Tyr70 – Ligand	Hydrophobic	3.73	-18.8		
		Tyr70 – Ligand	Hydrophobic	3.62			
	Trp84	Trp84 – Ligand	Hydrophobic	3.53			
		Trp84 – Ligand	Hydrophobic	4.16			
		Trp84 – Ligand	Hydrophobic	4.12			
		Trp84 – Ligand	Hydrophobic	4.37			
	Trp279	Trp279 – Ligand	Hydrophobic	3.81			
		Trp279 – Ligand	Hydrophobic	3.81			
		Trp279 – Ligand	Hydrophobic	3.70			
	Phe330	Phe330 – Ligand	Hydrophobic	4.15			
		Phe330 – Ligand	Hydrophobic	3.78			
	I	Tyr70	Tyr70 – Ligand	Hydrophobic		3.70	-12.4
			Ligand – Tyr70	Hydrophobic		3.64	
	Trp84	Trp84 – Ligand	Trp84 – Ligand	Hydrophobic		3.54	
Trp84 – Ligand			Hydrophobic	3.99			
Trp84 – Ligand			Hydrophobic	3.96			
Trp84 – Ligand			Hydrophobic	4.34			
Trp279	Trp279 – Ligand	Trp279 – Ligand	Hydrophobic	3.53			
		Trp279 – Ligand	Hydrophobic	3.96			
		Trp279 – Ligand	Hydrophobic	3.75			
Phe330	Phe330 – Ligand	Phe330 – Ligand	Hydrophobic	4.39			

(continued)

(continued)

Analysis of molecular docking generated from AutoDock Vina					
Structure	Active site of amino acid	Atoms involved	Type of interaction	Distance (Å)	Affinity (Kcal/mol)
2		Phe330 – Ligand	Hydrophobic	3.73	-11.7
		Phe330 – Cl	Hydrophobic	5.08	
	Tyr70	Tyr70 – Ligand	Hydrophobic	4.41	
		Tyr70 – Ligand	Hydrophobic	4.09	
	Trp84	Trp84 – Ligand	Hydrophobic	3.77	
		Ligand – Trp84	Hydrophobic	4.51	
	Trp279	Trp279 – Ligand	Hydrophobic	4.32	
		Trp279 – Ligand	Hydrophobic	3.67	
	Phe330	Trp279 – Ligand	Hydrophobic	3.81	
		Phe330 – Ligand	Hydrophobic	3.72	
3		Ligand – Phe330	Hydrophobic	3.84	
		Tyr70 – Ligand	Hydrophobic	4.01	
	Tyr70	Tyr70 – Ligand	Hydrophobic	3.58	
		Trp84 – Ligand	Hydrophobic	4.28	
	Trp84	Trp84 – Ligand	Hydrophobic	3.65	
		Trp84 – Ligand	Hydrophobic	4.87	
	Trp279	Trp84 – Ligand	Hydrophobic	3.97	
		Trp279 – Ligand	Hydrophobic	3.89	
		Trp279 – Ligand	Hydrophobic	3.61	
		Trp279 – Ligand	Hydrophobic	3.79	

(continued)

(continued)

Analysis of molecular docking generated from AutoDock Vina					
Structure	Active site of amino acid	Atoms involved	Type of interaction	Distance (Å)	Affinity (Kcal/mol)
4	Phe330	Phe330 – Ligand	Hydrophobic	5.70	-11.1
		Phe330 – Ligand	Hydrophobic	4.54	
	Tyr70	Tyr70 – Ligand	Hydrophobic	5.99	
		Tyr70 – Ligand	Hydrophobic	4.13	
		Tyr70 – Cl	Hydrophobic	4.02	
		Trp84 – Ligand	Hydrophobic	4.15	
	Trp279	Trp84 – Ligand	Hydrophobic	3.75	
		Trp84 – Ligand	Hydrophobic	3.96	
		Trp279 – Ligand	Hydrophobic	4.47	
		Trp279 – Ligand	Hydrophobic	3.55	
Trp279 – Ligand		Hydrophobic	4.63		
Trp279 – Ligand		Hydrophobic	3.70		
Phe330	Trp279 – Ligand	Trp279 – Ligand	Hydrophobic	4.02	
		Trp279 – Cl	Hydrophobic	4.85	
	Tyr70	Trp279 – Cl	Hydrophobic	4.11	
		Phe330 – Ligand	Hydrophobic	4.67	
		Ligand – Phe330	Hydrophobic	5.81	
		Phe330 – Ligand	Hydrophobic	5.18	
		Tyr70 – Ligand	Hydrophobic	3.70	
		Ligand – Tyr70	Hydrophobic	3.64	
Trp84	Trp84 – Ligand	Hydrophobic	3.54		
		Hydrophobic	3.54		

(continued)

(continued)

Analysis of molecular docking generated from AutoDock Vina					
Structure	Active site of amino acid	Atoms involved	Type of interaction	Distance (Å)	Affinity (Kcal/mol)
6		Trp84 – Ligand	Hydrophobic	3.99	-12.1
		Trp84 – Ligand	Hydrophobic	3.96	
		Trp84 – Ligand	Hydrophobic	4.34	
		Trp279 – Ligand	Hydrophobic	3.53	
		Trp279 – Ligand	Hydrophobic	3.96	
		Trp279 – Ligand	Hydrophobic	3.75	
		Ligand – Trp279	Hydrophobic	4.20	
		Phe330 – Ligand	Hydrophobic	4.39	
		Phe330 – Ligand	Hydrophobic	3.73	
		Phe330 – Cl	Hydrophobic	5.08	
7		Tyr70 – Ligand	Hydrophobic	3.68	-9.3
		Ligand – Tyr70	Hydrophobic	3.67	
		Trp84 – Ligand	Hydrophobic	3.77	
		Trp84 – Ligand	Hydrophobic	3.97	
		Trp84 – Ligand	Hydrophobic	5.45	
		Trp279 – Ligand	Hydrophobic	3.53	
		Trp279 – Ligand	Hydrophobic	3.81	
		Phe330 – Ligand	Hydrophobic	4.15	
		Phe330 – Ligand	Hydrophobic	3.75	
		Tyr70	-	-	
Trp84	Trp84 – Ligand	Hydrophobic	3.81		

(continued)

(continued)

Analysis of molecular docking generated from AutoDock Vina					
Structure	Active site of amino acid	Atoms involved	Type of interaction	Distance (Å)	Affinity (Kcal/mol)
8	Trp279	Trp84 – Ligand	Hydrophobic	3.82	-12.1
		Trp84 – Ligand	Hydrophobic	4.80	
	Phe330	Phe330 – Ligand	Hydrophobic	4.32	
		Phe330 – Ligand	Hydrophobic	4.68	
	Tyr70	Tyr70 – Cl	Hydrophobic	4.61	
	Trp84	Trp84 – Ligand	Hydrophobic	3.80	
		Trp84 – Ligand	Hydrophobic	3.82	
		Trp84 – Ligand	Hydrophobic	5.01	
		Trp84 – Ligand	Hydrophobic	4.84	
	Trp279	Trp279 – Ligand	Hydrophobic	5.87	
Trp279 – Ligand		Hydrophobic	5.46		
Phe330	Phe330 – Ligand	Hydrophobic	4.30		
	Phe330 – Ligand	Hydrophobic	4.70		
9	Tyr70	–	–	–	-10.7
	Trp84	Trp84 – Ligand	Hydrophobic	4.05	
		Trp84 – Ligand	Hydrophobic	4.30	
		Trp84 – Ligand	Hydrophobic	4.00	
	Trp279	Trp279 – N8	Hydrogen Bond	2.02	
		H – Ligand	Hydrogen Bond	2.55	
	Trp279 – Ligand	Hydrophobic	5.24		

(continued)

(continued)

Analysis of molecular docking generated from AutoDock Vina						
Structure	Active site of amino acid	Atoms involved	Type of interaction	Distance (Å)	Affinity (Kcal/mol)	
10	Phe330	Phe330 – Ligand	Hydrophobic	5.19	-10.7	
		Phe330 – Ligand	Hydrophobic	5.98		
	Tyr70	Tyr70 – Ligand	Hydrophobic	5.95		
		Tyr70 – Ligand	Hydrophobic	4.10		
	Trp84	Trp84 – Ligand	Hydrophobic	3.99		
		Trp84 – Ligand	Hydrophobic	3.64		
		Trp84 – Ligand	Hydrophobic	4.51		
		Trp279 – Ligand	Hydrophobic	3.53		
	Trp279	Trp279 – Ligand	Hydrophobic	4.68		
		Trp279 – Ligand	Hydrophobic	3.81		
Phe330 – Ligand		Hydrophobic	3.78			
11	Phe330	Ligand – Phe330	Hydrophobic	4.14	-11.0	
		Phe330 – Ligand	Hydrophobic	5.14		
	Tyr70	-	-			
	Trp84	Trp84 – Ligand	Hydrophobic	3.57		
Trp84 – Ligand		Hydrophobic	4.01			
Trp84 – Ligand		Hydrophobic	4.05			
Trp84 – Ligand		Hydrophobic	5.12			
Trp84 – Ligand		Hydrophobic	4.46			
Trp279	Trp279 – O3	Hydrophobic	2.34			
	Phe330 – Ligand	Hydrophobic	4.30			

(continued)

(continued)

Analysis of molecular docking generated from AutoDock Vina						
Structure	Active site of amino acid	Atoms involved	Type of interaction	Distance (Å)	Affinity (Kcal/mol)	
12		Phe330 – Ligand	Hydrophobic	3.71		
	Tyr70	Tyr70 – Ligand	Hydrophobic	4.49		-11.4
	Trp84	Trp84 – Ligand	Hydrophobic	3.77		
		Trp84 – Ligand	Hydrophobic	3.87		
		Ligand – Trp84	Hydrophobic	4.77		
		Trp279 – Ligand	Hydrophobic	4.69		
		Trp279 – Ligand	Hydrophobic	3.60		
		Trp279 – Ligand	Hydrophobic	3.86		
		Phe330 – Ligand	Hydrophobic	3.72		
		Ligand – Phe330	Hydrophobic	4.01		
13		Phe330 – Ligand	Hydrophobic	5.27		
	Tyr70	-	-	-		-10.8
	Trp84	Trp84 – Ligand	Hydrophobic	3.69		
		Trp84 – Ligand	Hydrophobic	4.08		
		Trp84 – Ligand	Hydrophobic	4.14		
	Trp279	Trp279 – O2	Hydrogen Bond	2.25		
		H1 – Ligand	Hydrogen Bond	2.99		
		Phe330 – Ligand	Hydrophobic	4.20		
14		Phe330 – Ligand	Hydrophobic	3.67		
	Tyr70	-	-	-		-11.9
	Trp84	Trp84 – Ligand	Hydrophobic	3.83		

(continued)

(continued)

Analysis of molecular docking generated from AutoDock Vina						
Structure	Active site of amino acid	Atoms involved	Type of interaction	Distance (Å)	Affinity (Kcal/mol)	
15		Trp84 – Ligand	Hydrophobic	4.07		
		Trp84 – Ligand	Hydrophobic	5.25		
	Trp279	Trp279 – Ligand	Hydrophobic	5.48		
	Phe330	Phe330 – Ligand	Hydrophobic	3.98		
		Phe330 – Ligand	Hydrophobic	3.80		
	Tyr70	–	–	–	–11.0	
	Trp84	Trp84 – Ligand	Hydrophobic	3.62		
		Trp84 – Ligand	Hydrophobic	4.06		
		Trp84 – Ligand	Hydrophobic	4.06		
		Trp84 – Ligand	Hydrophobic	5.14		
16		Trp84 – Ligand	Hydrophobic	4.46		
	Trp279	–	–	–		
	Phe330	Phe330 – Ligand	Hydrophobic	4.26		
		Phe330 – Ligand	Hydrophobic	3.71		
	Tyr70	–	–	–	–9.5	
	Trp84	Trp84 – Ligand	Hydrophobic	4.07		
		Trp84 – Ligand	Hydrophobic	4.79		
	Trp279	Trp279 – Ligand	Hydrophobic	4.92		
		Trp279 – Ligand	Hydrophobic	5.18		
	Phe330	H8 – Phe330	Hydrophobic	2.66		
	Phe330 – C19	Hydrophobic	4.54			

(continued)



(continued)

Analysis of molecular docking generated from AutoDock Vina					
Structure	Active site of amino acid	Atoms involved	Type of interaction	Distance (Å)	Affinity (Kcal/mol)
17	Tyr70	–	–	–	–10.0
	Trp84	Trp84 – Ligand	Hydrophobic	3.50	
		Trp84 – Ligand	Hydrophobic	4.27	
		Trp84 – Ligand	Hydrophobic	4.28	
		Trp84 – Ligand	Hydrophobic	4.68	
		Trp84 – Ligand	Hydrophobic	4.41	
	Trp279	–	–	–	
	Phe330	Phe330 – Ligand	Hydrophobic	4.05	
		Phe330 – Ligand	Hydrophobic	3.73	
	18	Tyr70	–	–	–
Trp84		Trp84 – Ligand	Hydrophobic	3.53	
		Trp84 – Ligand	Hydrophobic	4.14	
		Trp84 – Ligand	Hydrophobic	4.55	
		Trp84 – Ligand	Hydrophobic	4.84	
		Trp84 – Ligand	–	–	
Trp279		–	–	–	
Phe330		Phe330 – Ligand	Hydrophobic	4.14	
		Phe330 – Ligand	Hydrophobic	3.74	
		Phe330 – Ligand	Hydrophobic	5.48	
19	Tyr70	H13 – O	Hydrogen Bond	2.93	–11.2
		Tyr70 – Ligand	Hydrophobic	4.22	
		Tyr70 – Ligand	Hydrophobic	3.62	

(continued)

(continued)

Analysis of molecular docking generated from AutoDock Vina					
Structure	Active site of amino acid	Atoms involved	Type of interaction	Distance (Å)	Affinity (Kcal/mol)
20	Trp84	Trp84 – Ligand	Hydrophobic	3.51	
		Trp84 – Ligand	Hydrophobic	4.17	
		Trp84 – Ligand	Hydrophobic	4.01	
		Trp84 – Ligand	Hydrophobic	4.86	
		Trp84 – Ligand	Hydrophobic	4.27	
	Trp279	Trp279 – Ligand	Hydrophobic	4.05	
		Trp279 – Ligand	Hydrophobic	3.68	
		Trp279 – Ligand	Hydrophobic	3.69	
	Phe330	Phe330 – Ligand	Hydrophobic	4.21	
		Phe330 – Ligand	Hydrophobic	3.73	
Phe330 – Cl		Hydrophobic	5.30		
Tyr70	–	–	–	–11.4	
Trp84	Trp84 – Ligand	Trp84 – Ligand	Hydrophobic	5.02	
		Trp84 – Ligand	Hydrophobic	3.84	
		Trp84 – Ligand	Hydrophobic	4.00	
		Trp84 – Ligand	Hydrophobic	5.19	
	Trp84 – Ligand	Trp84 – Ligand	Hydrophobic	5.14	
		Trp279 – O5	Hydrogen Bond	2.16	
		Phe330 – Ligand	Hydrophobic	5.46	
		Phe330 – Ligand	Hydrophobic	4.00	
Phe330	Phe330 – Ligand	Hydrophobic	3.79		

(continued)

(continued)

Analysis of molecular docking generated from AutoDock Vina					
Structure	Active site of amino acid	Atoms involved	Type of interaction	Distance (Å)	Affinity (Kcal/mol)
21	Tyr70	Tyr70 – Ligand	Hydrophobic	4.45	-11.7
		Tyr70 – Ligand	Hydrophobic	3.58	
	Trp84	Trp84 – Ligand	Hydrophobic	3.84	
		Trp84 – Ligand	Hydrophobic	3.89	
		Ligand – Trp84	Hydrophobic	4.36	
		Trp279 – Ligand	Hydrophobic	4.16	
	Phe330	Trp279 – Ligand	Hydrophobic	3.64	
		Trp279 – Ligand	Hydrophobic	3.82	
		Phe330 – Ligand	Hydrophobic	3.80	
		Ligand – Phe330	Hydrophobic	3.88	
Tyr70 – Ligand		Hydrophobic	4.37		
Trp84 – Ligand		Hydrophobic	3.81		
22	Trp84	Trp84 – Ligand	Hydrophobic	3.81	-11.5
		Trp279 – Ligand	Hydrophobic	4.59	
	Trp279	Trp279 – Ligand	Hydrophobic	3.60	
		Trp279 – Ligand	Hydrophobic	4.86	
		Trp279 – Ligand	Hydrophobic	3.78	
		Phe330 – Ligand	Hydrophobic	4.34	
	Phe330	Phe330 – Ligand	Hydrophobic	3.73	
		Phe330 – Ligand	Hydrophobic	5.36	
		Tyr70 – Ligand	Hydrophobic	4.74	
		Tyr70	Hydrophobic	-12.3	

(continued)

(continued)

Analysis of molecular docking generated from AutoDock Vina					
Structure	Active site of amino acid	Atoms involved	Type of interaction	Distance (Å)	Affinity (Kcal/mol)
		Tyr70 – Ligand	Hydrophobic	3.76	-10.2
		Tyr70 – Cl	Hydrophobic	4.01	
	Trp84	Trp84 – Ligand	Hydrophobic	3.91	
		Trp84 – Ligand	Hydrophobic	3.91	
	Trp279	Trp279 – Ligand	Hydrophobic	4.01	
		Trp279 – Ligand	Hydrophobic	3.58	
		Trp279 – Ligand	Hydrophobic	4.84	
		Trp279 – Ligand	Hydrophobic	3.64	
		Trp279 – Cl	Hydrophobic	4.87	
		Trp279 – Cl	Hydrophobic	4.70	
Phe330	Phe330 – Ligand	Hydrophobic	4.22		
	Phe330 – Ligand	Hydrophobic	3.59		
24	Tyr70	H18 – O	Hydrogen Bond	2.28	
		Tyr70 - Ligand	Hydrophobic	4.75	
Trp84		Trp84 – Ligand	Hydrophobic	3.52	
		Trp84 – Ligand	Hydrophobic	4.18	
		Trp84 – Ligand	Hydrophobic	4.14	
		Trp84 – Ligand	Hydrophobic	4.84	
		Trp84 – Ligand	Hydrophobic	4.35	
		Trp279 – Ligand	Hydrophobic	4.01	
Trp279		Trp279 – Ligand	Hydrophobic	5.39	
		Trp279 – Ligand	Hydrophobic		

(continued)

(continued)

Analysis of molecular docking generated from AutoDock Vina							
Structure	Active site of amino acid	Atoms involved	Type of interaction	Distance (Å)	Affinity (Kcal/mol)		
25	Phe330	Phe330 – Ligand	Hydrophobic	4.18			
		Phe330 – Ligand	Hydrophobic	3.72			
		Phe330 – Cl	Hydrophobic	5.31			
	Tyr70	Tyr70 – C15	Hydrophobic	4.49		-8.4	
	Trp84	Trp84 – Ligand	Hydrophobic	Hydrophobic	3.83		
		Trp84 – Ligand	Hydrophobic	Hydrophobic	4.24		
Trp84 – Ligand		Hydrophobic	Hydrophobic	5.36			
Trp84 – Ligand		Hydrophobic	Hydrophobic	5.31			
Trp279	-	-	-	-			
26	Phe330	Phe330 – Ligand	Hydrophobic	4.04			
		Phe330 – Ligand	Hydrophobic	3.76			
	Tyr70	H22 – OH	Hydrogen Bond	2.84		-10.8	
	Trp84	Tyr70 - Ligand	Hydrophobic	Hydrophobic	4.70		
		Trp84 – Ligand	Hydrophobic	Hydrophobic	5.12		
		Trp84 – Ligand	Hydrophobic	Hydrophobic	3.87		
Trp84 – Ligand		Hydrophobic	Hydrophobic	3.96			
Trp279	Trp84 – Ligand	Hydrophobic	Hydrophobic	5.04			
	Trp84 – Ligand	Hydrophobic	Hydrophobic	5.09			
	Trp279 – Ligand	Hydrophobic	Hydrophobic	3.89			
Phe330	Trp279 – Ligand	Hydrophobic	Hydrophobic	4.22			
	Phe330 – Ligand	Hydrophobic	Hydrophobic	5.19			

(continued)

(continued)

Analysis of molecular docking generated from AutoDock Vina					
Structure	Active site of amino acid	Atoms involved	Type of interaction	Distance (Å)	Affinity (Kcal/mol)
27		Phe330 – Ligand	Hydrophobic	3.86	
		Phe330 – Ligand	Hydrophobic	3.85	
	Tyr70	Tyr70 – Ligand	Hydrophobic	4.12	-10.8
	Trp84	Trp84 – Ligand	Hydrophobic	4.67	
		Trp84 – Ligand	Hydrophobic	3.89	
		Trp84 – Ligand	Hydrophobic	4.45	
	Trp279	Trp279 – Ligand	Hydrophobic	3.52	
		Trp279 – Ligand	Hydrophobic	4.63	
		Trp279 – Ligand	Hydrophobic	3.73	
		Phe330 – Ligand	Hydrophobic	4.01	
28		Ligand – Phe330	Hydrophobic	5.07	
		Phe330 – Ligand	Hydrophobic	5.20	
	Tyr70	–	–	–	-10.7
	Trp84	Trp84 – Ligand	Hydrophobic	3.64	
		Trp84 – Ligand	Hydrophobic	4.23	
		Trp84 – Ligand	Hydrophobic	4.36	
		Trp84 – Ligand	Hydrophobic	4.84	
		Trp84 – Ligand	Hydrophobic	4.96	
		Trp84 – Ligand	Hydrophobic	4.65	
		Trp84 – Ligand	Hydrophobic	4.59	
	Trp279	–	–	–	

(continued)

(continued)

Analysis of molecular docking generated from AutoDock Vina						
Structure	Active site of amino acid	Atoms involved	Type of interaction	Distance (Å)	Affinity (Kcal/mol)	
29	Phe330	Phe330 – Ligand	Hydrophobic	3.97	-12.2	
		Phe330 – Ligand	Hydrophobic	3.74		
	Tyr70	Tyr70 – Ligand	Hydrophobic	3.71		
	Trp84	Trp84 – Ligand	Hydrophobic	5.53		
		Trp84 – Ligand	Hydrophobic	4.81		
		Trp84 – Ligand	Hydrophobic	5.20		
		Trp279 – Ligand	Hydrophobic	3.62		
30	Phe330	Trp279 – Ligand	Hydrophobic	3.70	-7.5	
			–	–		
	Tyr70	–	–			
	Trp84	N3 – Trp84		4.84		
		N3 – Trp84	Electrostatics	4.26		
		Trp84 – Ligand	Electrostatics	3.63		
		Trp84 – Ligand	Hydrophobic	4.32		
Trp279	Trp84 – C16	Hydrophobic	5.39			
	–	–	–			
	Phe330 – Ligand	Hydrophobic	4.12			

## References

1. Takacs, R., Ungvari, G.S., Gasdag, G.: Reasons for acute psychiatric admission of patients with dementia. *Neuropsychopharmacologia Hungarica* **3** (2015)
2. Teixeira, J.B., Souza Junior, P.R.B., Higa, J., Theme Filha, M.M.: Mortality from Alzheimer's disease in Brazil, 2000–2009. *Cad. Saúde Pública* **31**(4), 1–12 (2015)
3. Sereniki, A., Vital, M.A.B.F.: A doença de Alzheimer: aspectos fisiopatológicos e farmacológicos. *Rev. Psiquiatr. Rio Gd. Sul* **30**(1) (2008)
4. Duyckaerts, C., Dickson, D.: *Neuropathology of Alzheimer's Disease*. Neuropath Press, 47–65 (2003)
5. Downey, D.: Pharmacologic management of Alzheimer disease. *J. Neurosci. Nurs.* **40**(1), 55–59 (2008)
6. Picanço, L.C.S., Castro, L.L., Pinheiro, A.A., Silva, K.S., Souza, L.R., Braga, F.S., Da Silva, C.H.T.P., Hage-Melim, L.I.S., Dos Santos, C.B.R.: Study of molecular docking, physicochemical and pharmacokinetic properties of GSK-3 $\beta$  inhibitors. *Br. J. Pharm. Res.* 3–4 (2015)
7. Berman, M.H., Westbrook, J., Feng, Z., Gilliland, G., Bhat, T.N., Weissig, H., Shindyalov, I.N., Bourne, P.E.: The protein data bank. *Nucleic Acids Res.* **28**(1), 235–242 (2000)
8. Rydberg, E.H., Brumshtein, B., Greenblatt, H.M., Wong, D.M., Williams, L.D., Carlier, P.F., Pang, Y.P., Silman, I., Sussman, J.L.: Complexes of alkylene-linked tacrine dimers with Torpedo californica acetylcholinesterase: binding of bis5-tracine produces a dramatic rearrangement in the active-site gorge. *J. Med. Chem.* **49**, 5491–5500 (2006)
9. Liu, T., Lin, Y., Wen, X., Jorissen, R.N., Gilson, M.K.: BindingDB: a web-accessible database of experimentally determined protein-ligand binding affinities. *Nucleic Acids Res.* **35**, 198–201 (2007)
10. Chemplus.: Modular extensions for HyperChem release 6.02, molecular modeling for windows. HyperClub, Inc. (2000)
11. Dennington, R., Keith, T., Millam, J.: GaussView, version 5. SemiChem Inc. (2009)
12. Hohenberg, P., Kohn, W.: Inhomogeneous electron gas. *Am. Phys. Soc.* **136**(3B), B864–B871 (1964)
13. Frish, M.J.G., Trucks, W., Schlegel, H.B., Scuseira, G.E., Robb, M.A., Cheeseman, J.R., Montgomery, J.A., Vreven, J.R.T., Kudin, K.N., Burant, J.C., Millam, J.M., Iyengar, S.S., Tomasi, J., Barone, V., Mennucci, B., Cossi, M., Scalmani, G., Rega, N., Petersson, G.A., Nakatsuji, H., Hada, M., Ehara, M., Toyota, K., Fukuda, R., Hasegawa, J., Ishida, M., Nakajima, T., Honda, Y., Kitao, O., Nakai, H., Klene, M., Li, X., Knox, J.E., Hratchian, H.P., Cross, J.B., Adamo, C., Jaramillo, J., Gomperts, R., Stratmann, R.E., Yazyev, O., Austin, A.J., Cammi, R., Pomelli, C., Ochterski, J.W., Ayala, P.Y., Morokuma, K., Voth, G.A., Salvador, P., Dannenberg, J.J., Zakrzewski, V.G., Dapprich, S., Daniels, A.D., Strain, M.C., Farkas, O., Malick, D.K., Rabuck, A.D., Raghavachari, K., Foresman, J.B., Ortiz, J.V., Cui, Q., Baboul, A.G., Clifford, S., Cioslowski, J., Stefanov, B.B., Liu, G., Liashenko, A., Piskorz, P., Komaromi, I., Martin, R.L., Fox, D.J., Keith, T., Al-Laham, M.A., Peng, C.Y., Nanayakkara, A., Challacombe, M., Gill, P.M.W., Johnson, B., Chen, W., Wong, W., Gonzalez, C., Pople, J.A.: Gaussian 03, Revision A.1 (2003)
14. Padmanabhan, J., Parthasarathi, R., Elango, M., Subramanian, V., Krishnamoorthy, B.S., Gutierrez-Oliva, S., Toro-Labbé, A., Roy, D.R., Chattaraj, P.K.: Multiphilic descriptor for chemical reactivity and selectivity. *J. Phys. Chem. A* **111**(37), 9130–9138 (2007)
15. Plukiger, P., Lutthi, H.P., Portmann, S., Webber, J.: Molekel 4.1, Swiss Center for Scientific Computing. Switzerland (2001)
16. Silva, N.S.R., Santos, C.F., Gonçalves, L.K.S., Braga, F.S., Almeida, J.R., Lima, C.S., Brasil, D.S.B., Silva, C.H.T.P., Hage-Melim, L.I.S., Santos, C.B.R.: *Br. J. Pharm. Res.* **7**(4), 2–263 (2015)
17. Halperin, I., Ma, B., Wolfson, H., Nussinov, R.: Principles of Docking: an overview of search algorithms and a guide to scoring functions. *PROTEINS: structure, function and genetics* **47**, 409–443 (2002)



18. Trott, O., Olson, A.J.: AutoDockVina: improving the speed and accuracy of docking with a new scoring function, efficient optimization. *J. Comput. Chem.* **31**(2), 445–461 (2010)
19. Schneidman-Duhovny, D., Dror, O., Inbar, Y., Nussinov, R., Wolfson, H.J.: PharmaGist: a webserver for ligand-based pharmacophore detection. *Nucl. Acids. Res.* **36**, W223–W228 (2008)
20. Lipinski, C.A., Lombardo, F., Dominy, B.W., Feeney, P.J.: Experimental and computational approaches to estimate solubility and permeability in drug Discovery and development settings. *Adv. Drug Deliv. Rev.* **23**, 3–25 (1997)
21. Pajouhesh, H., Lenz, G.R.: Medicinal chemical properties of successful central nervous system drugs. *Neuro Rx* **2**(4), 541–553 (2005)
22. Lipinski, C.A.: Lead and drug-like compounds: the rule-of-five revolution. *Drug Discov. Today Technol.* **1**, 337–341 (2004)
23. Atkins, P.W.: *Físico-Química*, 6th edn. LTC, Rio de Janeiro (1997)
24. Santos, C.B.R., Vieira, J.B., Lobato, C.C., Hage-Melim, L.I.S., Souto, R.N.P., Lima, C.S., Costa, E.V.M., Brasil, D.S.B., Macêdo, W.C.V., Carvalho, J.C.T.: A SAR and QSAR study of new artemisinin compounds with antimalarial activity. *Molecules* **19**, 367–399 (2014)
25. Wulfsberg, G.: *Principles of Descriptive Inorganic Chemistry*. Cole Pub. Co., Brooks (1987)
26. Tavares, L.C.: QSAR: a abordagem de Hansh. *Quim. Nova* **27**(4), 631–639 (2004)
27. Politzer, P., Murray, J.S.: The fundamental nature and role of the electrostatic potential in atoms and structures. *Theor. Chem. Acc.* **108**, 134–142 (2002)
28. Coddig, P.W.: *Structure-Based Drug Design*. Kluwer Academic Publisher, 289 (1998)
29. Pinheiro, A.A., Silva, K.R., Silva, A.E.S., Braga, F.S., Silva, C.H.T.P., Santos, C.B.R., Hage-Melim, L.I.S.: *In silico* identification of novel potential BACE-1 inhibitors of Alzheimer's disease treatment: Molecular docking, pharmacophore modeling and activity and synthetic accessibility predictions. *Br. Pharm. Res.* **7**(3), 217–229 (2015)
30. Dietrich, S.W.: *Burger's Medicinal Chemistry and Drug Discovery: Principles and Practice*, 5th edn. John Wiley, New York (1995)
31. Lengauer, T., Rarey, M.: Computational methods for biomolecular docking. *CurOp in StrucBio* **6**(3), 402–406 (1996)
32. Morgon, N.H., Coutinho, K.: *Theoretical Chemistry and Molecular Modeling Methods*. 1st ed., São Paulo, Livraria da Física (2007)
33. Pinheiro, A.A., Silva, K., Silva, A., Braga, F., Silva, C., Santos, C., Hage-Melim, L.: *In silico* identification of novel potential BACE-1 inhibitors for Alzheimer's disease treatment: molecular docking, pharmacophore modeling and activity and synthetic accessibility predictions. *Br. J. Pharm. Res.* **7**, 217–229 (2015)
34. Cunha, E.L., Santos, C.F., Braga, F.S., Costa, J.S., Silva, R.C., Favacho, H.A.S., Hage-Melim, L.I.S., Silva, C.H.T.P., Santos, C.B.R.: Computational investigation of antifungal compounds using molecular modeling and prediction of ADME/Tox properties. *J. Comput. Theor. Nanosci.* **12**, 3682–3691 (2015)